



# 重慶大學

近十年《Cell》《Nature》《Science》及子刊

論文匯編

科学技术发展研究院 前沿交叉学科研究院

2018年3月



# 目 录

## CONTENTS

### 第一部分 《Cell》《Nature》《Science》正刊

生物工程学院

- Aging, alopecia, and stem cells  
Lei Mingxing (雷明星), Chuong Cheng-Ming ..... 1
- Universal physical responses to stretch in the living cell  
Trepas Xavier, Deng Linhong (邓林红), An Steven S., Navajas Daniel, Tschumperlin Daniel J., Gerthoffer William T., et al. .... 3

生命科学学院

- Complete Resequencing of 40 Genomes Reveals Domestication Events and Genes in Silkworm (Bombyx)  
Xia Qingyou (夏庆友), Guo Yiran, Zhang Ze (张泽), Li Dong, Xuan Zhaoling, Li Zhuo, Cheng Tingcai (程廷才), et al. .... 7

### 第二部分 《Cell》《Nature》《Science》子刊

物理学院

- Direct observation of valley-polarized topological edge states in designer surface plasmon crystals  
Wu Xiaoxiao, Meng Yan (孟岩), Tian Jingxuan, Huang Yingzhou (黄映洲), Xiang Hong (向红), Han Dezhan (韩德专), Wen Weijia (温维佳) ..... 11
- Eye motion triggered self-powered mechnosensational communication system using triboelectric nanogenerator  
Pu Xianjie (蒲贤洁), Guo Hengyu (郭恒宇), Chen Jie (陈杰), Wang Xue (王雪), Xi Yi (奚伊), Hu Chenguo (胡成果), Wang Zhong Lin ..... 20
- Self-powered textile for wearable electronics by hybridizing fiber-shaped nanogenerators, solar cells, and supercapacitors  
Wen Zhen, Yeh Min-Hsin, Guo Hengyu (郭恒宇), Zhu Lei, Wang Xin, Hu Chenguo (胡成果), et al. .... 27
- Force-dependent conformational switch of alpha-catenin controls vinculin binding  
Yao Mingxi, Qiu Wu, Liu Ruchuan (刘如川), Efremov Artem K, Cong Peiwen, et al. .... 35

- Feshbach resonances in the exit channel of the  $F + CH_3OH \rightarrow HF + CH_3O$  reaction observed using transition-state spectroscopy  
Weichman Marissa L., DeVine Jessalyn A., Babin Mark C., **Li Jun(李军)**, Guo Lifan, Ma Jianyi, Guo Hua, Neumark Daniel M. ....46
- Unravelling the hidden link of lithium halides and application in the synthesis of organocuprates  
Yi Hong, Yang Dali, Xin Jie, **Qi Xiaotian(戚啸天)**, **Lan Yu(蓝宇)**, Deng Yi, Pao Chih-Wen, Lee Jyh-Fu, Lei Aiwen .....52
- Biomimetically inspired asymmetric total synthesis of (+)-19-dehydroxyl arisandilactone A  
Han Yi-Xin, Jiang Yan-Long, Li Yong, Yu Hai-Xin, Tong Bing-Qi, Niu Zhe, Zhou Shi-Jie, **Liu Song**, **Lan Yu(蓝宇)**, et al. ....58
- Catalytic N-radical cascade reaction of hydrazones by oxidative deprotonation electron transfer and TEMPO mediation  
Hu Xiao-Qiang, **Qi Xiaotian**, Chen Jia-Rong, Zhao Quan-Qing, Wei Qiang, **Lan Yu(蓝宇)**, Xiao Wen-Jing .....71
- Micro-cable structured textile for simultaneously harvesting solar and mechanical energy  
Chen Jun, **Huang Yi**, **Zhang Nannan**, Zou Haiyang, Liu Ruiyuan, **Tao Changyuan(陶长元)**, **Fan Xing(范兴)**, Wang Zhong Lin .....83
- Towards a general diastereoselective route to oxabicyclo[3.2.1]octanes via a gold-catalysed cascade reaction  
Fu Junkai, Gu Yueqing, Yuan Hao, Luo Tuoping, **Liu Song**, **Lan, Yu(蓝宇)**, Gong Jianxian, Yang Zhen .....91
- Copper-catalyzed aerobic oxidative coupling: From ketone and diamine to pyrazine  
Wu Kun, Huang Zhiliang, **Qi Xiaotian**, **Li Yingzi**, Zhang Guanghui, Liu Chao, Yi Hong, Meng Linghui, Bunel, Emilio E., Miller Jeffrey T., Pao Chih-Wen, Lee Jyh-Fu, **Lan Yu(蓝宇)**, Lei Aiwen .....100
- Asymmetric total synthesis of (-)-lingzhiol via a Rh-catalysed [3+2] cycloaddition  
Long Rong, Huang Jun, Shao Wenbin, **Liu Song**, **Lan, Yu(蓝宇)**, Gong Jianxian, Yang Zhen .....107

- Identification of XBP1-u as a novel regulator of the MDM2/p53 axis using an shRNA library  
**Huang Can**, **Wu Shourong(吴寿荣)**, **Ji Hong**, **Yan Xuesong**, **Xie Yudan**, Murai Saomi, Zhao Hezhao, Miyagishi Makoto, **Kasim Vivi(江启慧)** .....117
- RBFOX2 Binds Nascent RNA to Globally Regulate Polycomb Complex 2 Targeting in Mammalian Genomes  
Wei Chaoliang, Xiao Rui, Chen Liang, **Cui Hanwei**, Zhou Yu, Xue Yuanchao, Hu Jing, Zhou Bing, Tsutsui Taiki, Qiu Jinsong, **Li Hairi**, **Tang Liling(唐丽灵)**, et al. ....131
- Time-dependent, protein-directed growth of gold nanoparticles within a single crystal of lysozyme  
Wei Hui, Wang Zidong, Zhang Jiong, House Stephen, Gao Yi-Gui, **Yang Limin**, Xing Hang, **Hou Changjun(侯长军)**, et al. ....147

- Fast and slow dynamics of the cytoskeleton  
**Deng Linhong (邓林红)**, Trepat Xavier, Butler James P., Millet Emil, Morgan Kathleen G., Weitz David A., Fredberg Jeffrey J. ....175

生命科学学院

- Proline Catabolism Modulates Innate Immunity in *Caenorhabditis elegans*  
**Tang, Haiqing (唐海清)** ; **Pang, Shanshan (庞珊珊)** .....180
- The Methyl-CpG-Binding Protein MBD7 Facilitates Active DNA Demethylation to Limit DNA Hyper-Methylation and Transcriptional Gene Silencing  
Lang Zhaobo, Lei Mingguang, Wang Xingang, Tang Kai, Miki Daisuke, Zhang Huiming, Mangrauthia Satendra K., **Liu Wenshan (刘玫杉)**, et al. ....189

药学院

- Versatile Protein Recognition by the Encoded Display of Multiple Chemical Elements on a Constant Macrocyclic Scaffold  
**Yizhou Li(李亦舟)**, Roberto De Luca, Samuele Cazzamalli, Francesca Pretto, Davor Bajic, et al. ....203
- Clinical Success of Drug Targets Prospectively Predicted by In Silico Study  
**Zhu Feng (朱峰)**, **Li Xiao Xu (李晓旭)**, Yang Sheng Yong, Chen Yu Zong. ....211
- A Radical Cascade Enabling Collective Syntheses of Natural Products  
Wang Xiaobei, Xia Dongliang, **Qin Wenfang (秦文芳)**, Zhou Ruijie, Zhou Xiaohan, **Zhou Qilong (周启龙)**, **Liu Wentao (刘文涛)**, **Dai Xiang (戴翔)**, **Wang Huijing (王慧婧)**, **Wang Shuqing (王树青)**, et al. ....214

动力工程学院

- Microalgal Cultivation in Treating Liquid Digestate from Biogas Systems  
**Xia Ao (夏昇)**, Murphy Jerry D. ....229
- A molecular nematic liquid crystalline material for high-performance organic photovoltaics  
**Sun Kuan (孙宽)**, Xiao Zeyun, Lu Shirong, Zzajczkowski Wojciech, Pisula Wojciech, Hanssen Eric, et al. ....241

资源与环境科学学院

- Determination of the CYP1A-inducing potential of single substances, mixtures and extracts of samples in the micro-EROD assay with H4IIE cells  
Schiwy Andreas, Brinkmann Markus, Thiem Ines, Guder Gabriele, Winkens Kerstin, Eichbaum Kathrin, **Hollert Henner**, et al. ....250

材料科学与工程学院

- Twinning-like lattice reorientation without a crystallographic twinning plane  
Liu Bo-Yu, Wang Jian, Li Bin, Lu Lu, **Zhang Xi-Yan (张喜燕)**, Shan Zhi-Wei, Li Ju, Jia Chun-Lin, Sun Jun, Ma Evan. ....264

光电工程学院

- Chalcogenide glass-on-graphene photonics  
Lin Hongtao, Song Yi, Huang Yizhong, Kita Derek, Deckoff-Jones Skylar, Wang Kaiqi, Li Lan, Li **Junying (李钧颖)**, Zheng Hanyu, et al. ....270

confirming the nature of the electrical signals that are read out in their devices. As expected, there is almost no sensitivity to applied magnetic fields. All this was performed at room temperature.

This breakthrough reveals fertile ground for new spintronics device concepts based on antiferromagnets. The lack of magnetic moment and concomitant insensitivity to fields means that data stored in such a memory will be stable against any attempt (planned or accidental) to externally wipe it with a magnetic field. The devices can also be packed arbitrarily densely on a chip without fear of their disturbing one another's state. Because antiferromagnets display resonances in the terahertz frequency range, versus gigahertz for ferromagnets, they offer the prospect of extremely fast operation.

However, major obstacles to a competitive memory technology remain. The device presented by Wadley *et al.* produces a very small readout signal, but this problem could be ameliorated by using a tunnel-junction readout technique, where it is already known that the readout signals can be large (10). Such a vertical device geometry could also help to increase memory cell density in an array architecture; at the moment, the "Union Jack" lateral geometry will occupy a prohibitively large footprint. Solving these problems will entail some interesting device engineering projects. Of more fundamental interest is the slow relaxation of the antiferromagnetic order into its rotated state, which sometimes requires many pulses, each of tens of milliseconds, to induce the full resistance change. Determining whether current-driven dynamics can truly happen at terahertz frequencies remains an outstanding challenge. Nonetheless, identifying this promising class of antiferromagnets that can display this remarkable behavior is a breakthrough that will be seized upon by many other laboratories, not least because these effects are predicted in other materials systems (11). Given the vast number of antiferromagnets, it is unlikely that the optimal material has been discovered at this early stage. The search is now on to find it. ■

#### REFERENCES

1. A. Hoffmann, S. Bader, *Phys. Rev. Appl.* **4**, 047001 (2015).
2. B. Dieny *et al.*, *Phys. Rev. B* **43**, 1297(R) (1991).
3. J. S. Moodera *et al.*, *Phys. Rev. Lett.* **74**, 3273 (1995).
4. J. A. Katine *et al.*, *Phys. Rev. Lett.* **84**, 3149 (2000).
5. L. Liu *et al.*, *Science* **336**, 555 (2012).
6. P. Wadley *et al.*, *Science* **351**, 587 (2016).
7. J. Železný *et al.*, *Phys. Rev. Lett.* **113**, 157201 (2014).
8. P. Wadley *et al.*, *Nat. Commun.* **4**, 2322 (2013).
9. X. Marti *et al.*, *Nat. Mater.* **13**, 367 (2014).
10. B. G. Park *et al.*, *Nat. Mater.* **10**, 347 (2011).
11. V. M. T. S. Barthem, *Nat. Commun.* **4**, 2892 (2013).

10.1126/science.aad8211

#### STEM CELLS

# Aging, alopecia, and stem cells

## Intrinsic epigenetic status and extrinsic environmental factors affect hair follicle stem cells

By Mingxing Lei,<sup>1,2</sup> and Cheng-Ming Chuong<sup>1,3</sup>

Many tissues turn over during adult life, and declines in this process are associated with the progression of aging. Whether renewal is continual (as in the intestinal villi) or episodic (as in hair follicles), it is mainly attributed to somatic stem cells. One fundamental question is whether a decline of tissue renewal reflects the lifelong accumulation of external insults or the internal progression of a clock within stem cells? On pages 613 and 575 of this issue, Wang *et al.* (1) and Matsuura *et al.* (2), respectively, gain insight into this phenomenon by examining hair follicle growth and aging.

Slowing down aging and moving toward regenerative medicine requires understanding fundamental principles of tissue renewal. If intrinsic changes in stem cells play a major role, the basis for their use to prevent aging weakens. If environmental factors play a dominant role, rebuilding stem cell niches or modifying the global body environment will be important.

The hair follicle is an excellent model for studying regeneration because the follicle contains stem cells that can be activated cyclically, reflected in the growing (anagen) and resting (telogen) phases of the hair cycle (3, 4) (see the second figure). The longer the growth phase, the longer the hair. Thus, the vitality of stem cells, reflected in the duration of the growth phase, is a measurable capacity. Because hair can show different phenotypes in different life stages and in different anatomical locations (5), it provides a highly accessible window to peek into

the cellular and molecular basis of stem cell activity in growth and aging. Indeed, androgenetic alopecia (hair loss) is a common sign of aging.

During cyclic quiescence and activation, hair follicle stem cells (HFSCs) in resting phase constantly "sum up" the input of activators and inhibitors. When total activators become dominant, the follicle enters growth phase (4–6). The secreted proteins bone morphogenetic protein (BMP) and Wnt display competing inhibitor and activator activities, respectively, leading to stem cell quiescence (telogen) or entrance into hair growth (anagen). Yet the internal status of stem cells determines the response to these external factors (7, 8). For example, deletion of DNA methyltransferase-1 (DNMT1) from the epidermis (in mice) decreases the probability

of successful stem cell activation in every hair cycle, leading to progressive alopecia (9). This indicates that an intrinsic mechanism affecting the epigenetic landscape is involved in the response of HFSCs to external factors. As well, transcription factors such as LIM homeobox 2 (Lhx2), transcription factor 3/4 (TCF3/4), SRY-box 9 (Sox9), Tbox 1 (Tbx1), and nuclear factor of activated T cells, cytoplasmic 1 (Nfatc1) are critical to HFSC properties, and their absence results in accelerated entry into

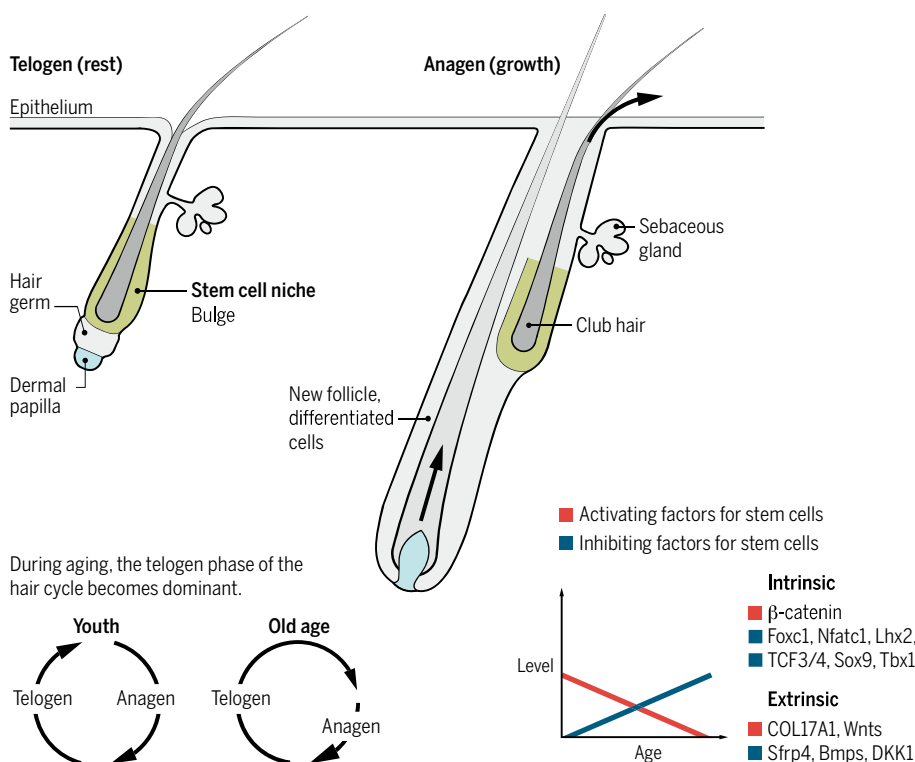
the hair growth cycle (10).

In androgenetic alopecia, hair fibers become shorter, thinner, and fewer as thick terminal scalp hairs are gradually replaced by fine vellus hairs. Yet in the early stages of this condition, HFSCs appear generally normal; a failure in their activation to form hair germ cells was the problem (11). Hair germ arises from activated HFSCs and migrate out of the bulge during early catagen to support the generation of a new hair. This suggests that the environment affects HFSCs. Such effects are not limited to the intrafollicle niche (the bulge); they also include the extrafollicular dermal environment and body hormone



**Hair follicle.** The Foxc1 transcription factor (magenta) is present in stem cells (green) and their niche (white) during self renewal.

<sup>1</sup>Department of Pathology, Keck School of Medicine, University of Southern California, Los Angeles, CA, USA. <sup>2</sup>"111" Project Laboratory of Biomechanics and Tissue Repair, College of Bioengineering, Chongqing University, Chongqing, China. <sup>3</sup>Integrative Stem Cell Center, China Medical University, Taichung, Taiwan. E-mail: cmchuong@usc.edu



**Hair growth and aging.** Renewal capacity of the hair cycle decreases with aging. Intrinsic and extrinsic factors affect hair follicle stem cells. During aging, there is a shift from an activator-dominant to an inhibitor-dominant environment.

status (12). In aged mice, secreted factors in the intradermal adipose tissue that inhibit Wnt signaling [e.g., dickkopf wnt signaling pathway inhibitor 1 (DKK1) and secreted frizzled-related protein 4 (Sfrp4)] are present in a wider dermal region and persist for long amounts of time, thus blocking activation of hair growth and decreasing hair regeneration ability. The aging phenotype of the skin of an old mouse was partially rescued when transplanted into the dermal environment of a young mouse (13). Thus, the control of hair cycling during aging is likely affected by both intrinsic stem cell properties and extrinsic environmental factors. We need to learn more about how these different regulatory compartments interact to control HFSC activation.

The downstream effectors of dynamic histone modifications during hair cycling are considered to be good candidates for driving epigenetic change. Among these effectors is the transcription factor forkhead box C1 (Foxc1) (8). Wang *et al.* show in mice that Foxc1 is expressed dynamically in HFSCs during hair cycling (see the first figure). It is absent during telogen (when stem cells are quiescent) but is expressed throughout the entire bulge when the next new hair cycle is initiated. Reducing Foxc1 expression in the basal hair follicle layer, where stem cells are located, resulted in a shortened telogen phase and loss of the old hair. Its absence in

the suprabasal bulge caused a loss of club hairs (as new hair is formed, the hair fiber from the previous cycle—the club hair—is pushed upward in the follicle and eventually out). These results indicate that Foxc1 promotes HFSC quiescence and also maintains the niche structure. Wang *et al.* also show that genes that maintain HFSC quiescence are down-regulated in the HFSCs of mice lacking Foxc1. Chromatin immunoprecipitation (ChIP) sequencing and assay for transposase-accessible chromatin (ATAC) sequencing data revealed that several genes controlling HFSC quiescence contain Foxc1 binding sites in their promoter or enhancer regions. Remarkably, these include genes encoding Bmp and Nfatc1, factors that suppress HFSC activation. The findings push our understanding of hair cycle control from the morphogen level to an epigenetic level.

Extracellular matrix is a major component of the follicle stem cell niche. Among the matrix constituents, type XVII collagen is required to maintain both HFSCs and melanocyte stem cells (14). But how is the homeostasis of type XVII collagen regulated? Matsumura *et al.* show that during repetitive hair cycling, HFSCs accumulate DNA damage, which leads to proteolysis of type XVII collagen. They found that aging dorsal skin proceeds in a stepwise manner (in the mouse). Gene ontology analyses showed

that genes involved in the DNA damage response are enriched in aged HFSCs, implying the accumulation of DNA damage during aging. Aged HFSCs produce ELA2/neutrophil elastase (ELANE) and other proteases that degrade COL17A1, the alpha chain constituent of type XVII collagen. Without COL17A1, HFSCs lose their self-renewal property and differentiate into an epidermal lineage. Thus, Matsumura *et al.* reveal an explicit mechanism for how aging-related DNA damage in HFSCs loops back to alter the stem cell microenvironment. Maintaining COL17A1 in the skin protected HFSCs against aging and reduced hair loss in mice. The study links DNA damage with changes of key extracellular matrix components in the stem cell niche, resulting in altered stem cell fate, depletion of stem cell numbers, reduction of organ size (miniature hairs), and reduced hair numbers. This finding also raises the possibility of rejuvenating HFSCs, because the microenvironment is seemingly easier to modulate than the HFSCs themselves.

Tissue regenerative ability after wounding also declines during aging. In large wound-induced follicle neogenesis, new follicles form in addition to the regeneration of hair from the original follicles. However, this ability declines gradually with aging (15). Hair regeneration in aging persons is hormone-dependent and region-specific. Androgens suppress hair growth in the scalp but enhance hair growth in beards and eyebrows (5). The findings of Wang *et al.* and Matsumura *et al.* should facilitate a multidimensional understanding of stem cell regulation and management during aging. It may also provide some hope for restoring hair growth in people with alopecia. ■

#### REFERENCES AND NOTES

1. L. Wang *et al.*, *Science* **351**, 613 (2016).
2. H. Matsumura *et al.*, *Science* **351**, aad4395 (2016).
3. Y. C. Hsu, E. Fuchs, *Nat. Rev. Mol. Cell Biol.* **13**, 103 (2012).
4. E. Kandyba *et al.*, *Proc. Natl. Acad. Sci. U.S.A.* **110**, 1351 (2013).
5. C. M. Chuong *et al.*, *Physiology* **27**, 61 (2012).
6. V. Greco *et al.*, *Cell Stem Cell* **4**, 155 (2009).
7. V. A. Botchkarev, M. R. Gdula, A. N. Mardaryev, A. A. Sharov, M. Y. Fessing, *J. Invest. Dermatol.* **132**, 2505 (2012).
8. W. H. Lien *et al.*, *Cell Stem Cell* **9**, 219 (2011).
9. J. Li *et al.*, *J. Invest. Dermatol.* **132**, 2681 (2012).
10. B. E. Keyes *et al.*, *Proc. Natl. Acad. Sci. U.S.A.* **110**, E4950 (2013).
11. L. A. Garza *et al.*, *J. Clin. Invest.* **121**, 613 (2011).
12. M. V. Plikus *et al.*, *Nature* **451**, 340 (2008).
13. C. C. Chen *et al.*, *J. Invest. Dermatol.* **134**, 2086 (2014).
14. S. Tanimura *et al.*, *Cell Stem Cell* **8**, 177 (2011).
15. M. Ito *et al.*, *Nature* **447**, 316 (2007).

#### ACKNOWLEDGMENTS

C.-M.C. is supported by NIH grants AR42177 and AR60306. M.L. is supported by Fundamental Research Funds for the Central Universities (106112015CDJRC231206), Special Funding for Postdoctoral Research Projects in Chongqing (Xm2015093), and a fellowship from the China Scholarship Council (2011605042). We thank R. Widelitz, L. Yang, and T. Yang for discussion.

10.1126/science.aaf1635

sciencemag.org **SCIENCE**

## LETTERS

# Universal physical responses to stretch in the living cell

Xavier Trepat<sup>1</sup>, Linhong Deng<sup>1,2</sup>, Steven S. An<sup>1,3</sup>, Daniel Navajas<sup>4</sup>, Daniel J. Tschumperlin<sup>1</sup>, William T. Gerthoffer<sup>5</sup>, James P. Butler<sup>1</sup> & Jeffrey J. Fredberg<sup>1</sup>

With every beat of the heart, inflation of the lung or peristalsis of the gut, cell types of diverse function are subjected to substantial stretch. Stretch is a potent stimulus for growth, differentiation, migration, remodelling and gene expression<sup>1,2</sup>. Here, we report that in response to transient stretch the cytoskeleton fluidizes in such a way as to define a universal response class. This finding implicates mechanisms mediated not only by specific signalling intermediates, as is usually assumed, but also by non-specific actions of a slowly evolving network of physical forces. These results support the idea that the cell interior is at once a crowded chemical space<sup>3</sup> and a fragile soft material in which the effects of biochemistry, molecular crowding and physical forces are complex and inseparable, yet conspire nonetheless to yield remarkably simple phenomenological laws. These laws seem to be both universal and primitive, and thus comprise a striking intersection between the worlds of cell biology and soft matter physics.

Soft materials such as tomato ketchup, shaving foam and toothpaste tend to fluidize when subjected to shear<sup>4-7</sup>, as do granular materials including sugar in a bowl, coffee beans in a chute<sup>8</sup> and even certain geophysical strata during an earthquake<sup>9</sup>; each transforms from a solid-like to a fluid-like phase, stiffness falls, and the material flows. Underlying microscopic stress-bearing elements, or clusters of elements, interact with neighbours to form a network of force transmission, but how flow is initiated and the nature of energy barriers that must be overcome remain the subject of much current attention<sup>5-9</sup>.

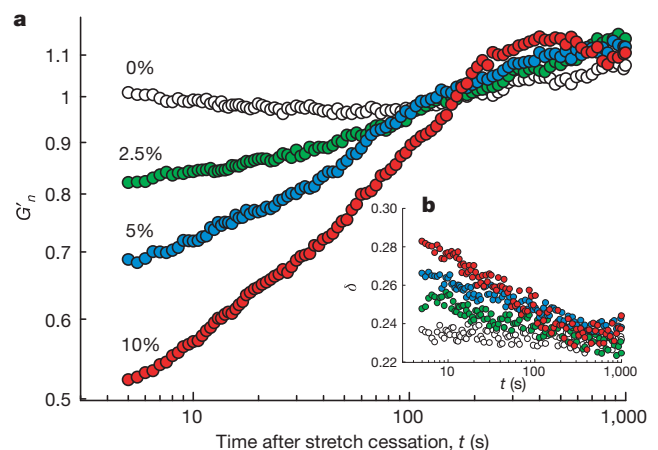
The response of a living cell to transient stretch would seem to be a different matter altogether. Very early literature shows that in response to application of a physical force the cell acutely softens (Supplementary Note 4), but more recent literature uniformly emphasizes stiffening (Supplementary Note 5)<sup>1,10</sup>. Nevertheless, we demonstrate here that the living cell promptly fluidizes and then slowly re-solidifies much as do the inert systems described above. Moreover, underlying structural rearrangements on the nanometre scale promptly accelerate and then slowly relax. In addition, in experiments spanning wide differences in cellular interventions, cell type and even integrative scale, these physical events conform to universal relationships.

Shear fluidization of inert matter is usually attributed to the presence of physical interactions that possess energy barriers that are so large that thermal energies by themselves are insufficient to drive microconfigurations to thermodynamic equilibrium. The material is then unable to explore its configuration space<sup>5</sup>, and structural rearrangements become limited by long-lived microconfigurations in which the system becomes trapped. If these microconfigurations were metastable, then their longevity could depend upon agitation

energy of some non-thermal origin. In the case of living cells, one such source of non-thermal agitation is ATP-dependent conformational changes of proteins<sup>11</sup>, which release energy of about  $20k_B T$  per event, where  $k_B$  is Boltzmann's constant and  $T$  is temperature, whereas another is energy injected into the system by stretch.

To test this last idea, we developed a novel experimental system in which we could subject the adherent human airway smooth muscle (HASM) cell to a transient isotropic biaxial stretch–unstretch manoeuvre of 4 seconds duration with zero residual macroscale strain. We could then monitor, on the nanometre scale, cell mechanical properties, remodelling dynamics and their changes (Methods; Supplementary Fig. 1; Supplementary Note 2).

Stiffness after stretch relative to stiffness of the same cell immediately before was denoted  $G'_n$ . When no stretch was applied, this fractional stiffness did not change, but immediately after cessation of a single transient stretch  $G'_n$  promptly decreased and then slowly recovered (Fig. 1a). These responses varied systematically with the amplitude of the imposed stretch, but little with the number of imposed stretch cycles (Supplementary Fig. 2). Immediately after stretch cessation, the phase angle  $\delta = \tan^{-1}(G''/G')$  promptly increased and then slowly recovered (Fig. 1b), where for a hookean



**Figure 1 | A single transient stretch drives fractional stiffness  $G'_n$  down and the phase angle  $\delta$  up, indicating fluidization of the cytoskeleton. a**, Evolution of  $G'_n$  of HASM cells after a single transient stretch of 0% (no stretch, open circles), 2.5% (green), 5% (blue) and 10% (red). The response of each bead was normalized to its pre-stretch value. **b**, Evolution of the phase angle after stretch application. Compare with Box 1 in Supplementary Note 7.

<sup>1</sup>Program in Molecular and Integrative Physiological Sciences, Harvard School of Public Health, Boston, Massachusetts 02115, USA. <sup>2</sup>'111 project' Laboratory of Biomechanics and Tissue Repair, Bioengineering College, Chongqing University, Chongqing 400044, China. <sup>3</sup>Division of Physiology, Johns Hopkins Bloomberg School of Public Health, Baltimore, Maryland 21205, USA. <sup>4</sup>Unitat de Biofísica i Bioenginyeria, Universitat de Barcelona-IDIBAPS, Ciber Enfermedades Respiratorias, and Institut de Bioenginyeria de Catalunya, 08036 Barcelona, Spain. <sup>5</sup>Department of Pharmacology, School of Medicine, University of Nevada, Reno, Nevada 89557, USA.



solid  $\delta = 0$  and for a newtonian fluid  $\delta = \pi/2$ . In the living cell  $0.15 < \delta < 0.50$ , thus placing the living cell closer to the solid-like state, and  $\delta$  is virtually invariant with changes of frequency, thus setting cytoskeleton rheology within the paradigms of structural damping and scale-free dynamics<sup>12–17</sup>. These prompt changes establish that shear tended to fluidize the cell, and did so in a manner comparable to the effect of shear on soft materials including colloidal glasses, emulsions and pastes<sup>4,5</sup> (Supplementary Note 7). However, fluidization in response to transient stretch contrasts with strain-stiffening behaviour that is observed in response to sustained stretch of cells<sup>15</sup> or reconstituted crosslinked actin gels<sup>18,19</sup>; in Supplementary Note 6 we reconcile these seemingly contradictory behaviours.

To assess the robustness of these responses, we pre-treated cells with an extensive set of mechanistically distinct drugs. These interventions caused expected changes in baseline material properties (Supplementary Table 1). Despite wide differences in baseline values, each cell could serve as its own pre-stretch control. Across the panel of interventions, fluidization–resolidification responses to stretch were similar in quality but markedly disparate in magnitude and time course (Fig. 2a). When F-actin was stabilized with jasplakinolide, stretch caused the largest fractional decrease in stiffness and displayed the fastest recovery, whereas when F-actin was depolymerized with

latrunculin A, stretch caused the smallest fractional decrease of stiffness and a relatively slow recovery. Inhibition of the myosin light chain kinase with ML7 blocked contractile activation as expected (Supplementary Fig. 3), but the time course of  $G'_n$  remained almost unchanged. Similarly, when extracellular calcium was chelated with EGTA to prevent calcium influx through stretch-activated channels, the time course of  $G'_n$  remained largely unchanged. In contrast, ATP depletion caused stiffness recovery to slow dramatically. In all experimental conditions, the phase angle showed a rapid increase followed by a slow decrease (Fig. 2b).

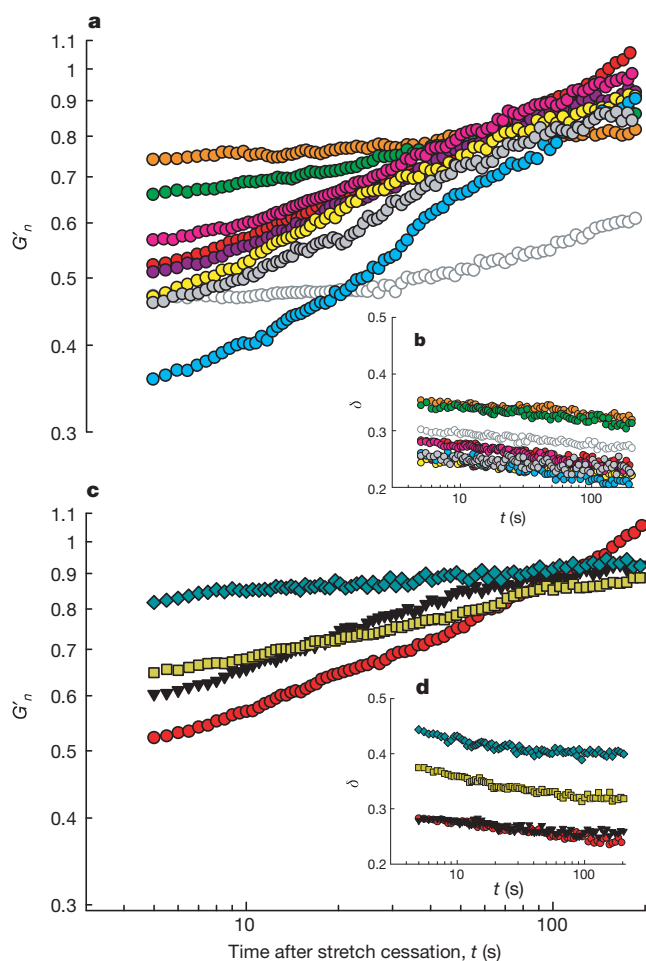
To assess the generality of these results, we also evaluated human lung fibroblasts (HLF), Madin–Darby canine kidney epithelial cells (MDCK) and human bronchial epithelial cells (HBE). Again, we found responses that were similar in quality but disparate in magnitude and time course (Fig. 2c, d).

A striking unification of these diverse responses was established when we focused on the prompt stiffness reduction  $G'_n$  (assessed at the earliest measurable time point,  $t = 5$  s) and its initial rate of recovery  $\alpha$  (assessed from the fit of  $G'_n$  to  $t^{\alpha}$  for the first 30 s of response). Despite the broad diversity of drug interventions and cellular systems, when  $G'_n$  (at  $t = 5$  s) was plotted against the pre-stretch value of the phase angle ( $\delta_0$ ), all data collapsed onto a single unifying relationship (Fig. 3a). Similarly, when the rate of stiffness recovery was plotted against  $\delta_0$  another master relationship was defined, although ATP depletion fell off that relationship (Fig. 3b). Moreover, at the level of an isolated bovine airway smooth muscle tissue strip mounted in a muscle bath, maximally activated, and then stretched using a servo-controller<sup>20</sup>, data fell onto the very same relationships as did single cells in culture (Fig. 3).

Although these wide ranges of cellular systems, interventions and integrative scales might have led to a quagmire of inconsistencies, they instead unveiled a pattern of consistency (Fig. 3). The closer the system was to the solid-like state before being subjected to transient stretch, the greater was the extent of its fluidization and, except in the case of ATP depletion, the faster was its subsequent resolidification (Fig. 3). Behaviour of this kind is crudely reminiscent of that observed in inert soft materials such as hard-sphere colloids and is predicted by coarse-grained trap models of soft glassy rheology (Fig. 3c; Supplementary Note 7).

To test this interpretation further, we made direct observations of molecular-scale structural rearrangements. Cells were subjected to 10% transient stretch–unstretch, but instead of measuring forced bead motions using optical magnetic twisting cytometry (OMTC), as above, we measured spontaneous nanoscale bead motions and used them as a direct index of the rate of molecular-scale structural rearrangements<sup>16</sup>. The evolution of mean square bead displacement (MSD) on the nanometre scale—both before the transient stretch and at different waiting times ( $t_w$ ) after stretch cessation—showed that when no stretch was applied the MSD evolved as we have reported previously<sup>16,21</sup> (Fig. 4). But when a transient stretch was applied, the rate of remodelling kinetics accelerated promptly and by more than an order of magnitude; comparatively, macromolecular mobility in unstretched cells was markedly retarded. However, as  $t_w$  increased, those kinetics progressively slowed, but relaxed more slowly than any exponential process<sup>5–7</sup> (Fig. 4b). This constellation of out-of-equilibrium features (Figs 1–4) represents the strongest evidence yet available to suggest slow relaxation of a glassy phase (Supplementary Note 7).

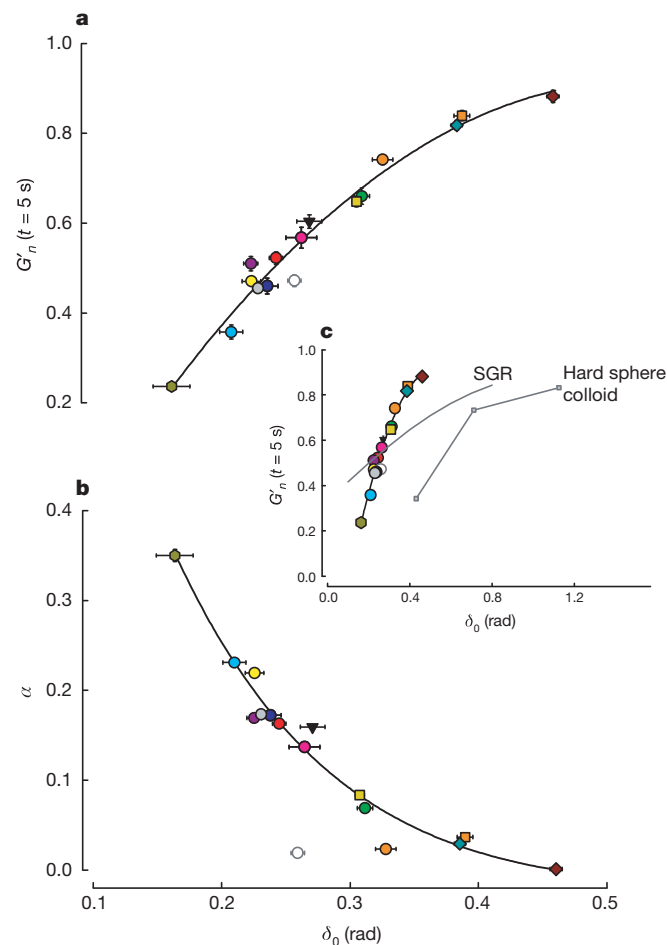
The conventional understanding of cytoskeleton dynamics has been based on the ideas that physical forces act to stiffen the network through both passive mechanical strain-stiffening<sup>18,19</sup> and active signalling-mediated reinforcement<sup>1,10</sup>. The results presented here show this viewpoint to be incomplete. Rather than merely triggering biochemical signalling cascades, as is usually assumed, cell stretch is seen to set into motion ongoing physical events in cell signalling that are not limited to the initiating upstream molecular transducers: physical forces seem to be more than a trigger. The absence of molecular



**Figure 2 | A broad variety of cell systems were fluidized by a transient stretch of 10% amplitude.** a, b,  $G'_n$  (a) and  $\delta$  (b) of pharmacologically treated HASM cells after application of a single transient stretch of 10% amplitude (see Methods and Supplementary Table 1 for pre-stretch baseline values and treatment details). Groups are latrunculin A (orange), DBcAMP (green), ML7 (10 min incubation, bright pink; 45 min incubation, dark pink), histamine (yellow), EGTA (grey), jasplakinolide (bright blue), ATP depletion (open symbols), and untreated cells (red).  $G'_n$  (c) and  $\delta$  (d) of MDCK (blue diamonds), HBE (yellow squares), HLF (black triangles) and HASM (red circles). Compare with Box 1 in Supplementary Note 7.

specificity in the early events of this process is highlighted by the fact that over wide ranges of systems and circumstances, the abilities of a cell to fluidize suddenly in response to stretch and to resolidify subsequently (Figs 3 and 4) seem to be insensitive to molecular details, and instead depend solely on the proximity of the cell to a solid-like state before the stretch ( $\delta_0$ ). This simple result is remarkable, but as more data accrue the cases in which this universality class is violated are likely to be most instructive.

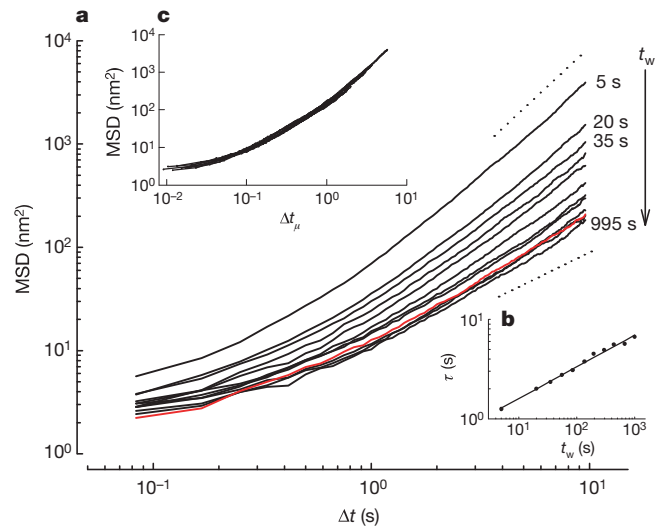
These findings of universality and non-specificity, taken together with the striking analogy to dynamics in inert glassy systems (Fig. 3c; Supplementary Note 7), imply ongoing actions of a network of slowly evolving physical forces, but it remains unclear if these observations can be interpreted in terms of the onset of a non-equilibrium phase transition controlled by external stress that separates a jammed phase from a flowing phase<sup>5,22</sup>. Despite the underlying variety of molecular



**Figure 3 | Two unifying relationships describe the response to stretch of a broad variety of cell systems.** In every case, the closer the system was to the solid-like state ( $\delta_0 = 0$ ) before being subjected to transient stretch, the greater was the extent of its fluidization and, except for the case of ATP depletion, the faster was its subsequent recovery. Master curves of  $G'_n$  at the earliest time point recorded after stretch (a) and of the initial rate of stiffness recovery  $\alpha$  versus the pre-stretch phase angle  $\delta_0$  (b).  $\alpha$  was assessed by fitting a power-law  $G'_n \propto t^\alpha$  to the first 30 s of response after stretch cessation. Error bars indicate standard errors. When plotted again over the full range possibilities (c), cells are seen to lie much closer to the solid-like ( $\delta_0 = 0$ ) than the fluid-like ( $\delta_0 = \pi/2$ ) state. In response to shear of similar magnitude, cells show a fluidization response comparable to but to the left of hard sphere colloids (data adapted from ref. 4). Soft glassy rheology theory<sup>5</sup> (Supplementary Note 7) captures these trends but substantially underestimates sensitivity to changes of  $\delta_0$ .  $n$  values are given in Supplementary Table 1. Colours are as in Fig. 2 with the addition of HASM PBS (dark blue), HBE Latrunculin A (orange squares), MDCK cytochalasin D (brown diamonds) and BASM tissue (green hexagons).

mechanisms, all such glassy systems are thought to have one feature in common—structural rearrangements that are slow, localized and inelastic—and the applicability of such a point of view is justified by the universality of the phenomenology, including inert matter<sup>4–7,23</sup>, proteins<sup>24</sup>, cells<sup>16,25,26</sup> and integrated tissues<sup>20</sup>. In the case of physical interactions between cytoskeletal molecules, such inelastic rearrangements might include disruption or unfolding of crosslinking proteins, resolution of steric constraints, detachment of myosin crossbridges, rupture of hydrogen bonds or cytoskeleton filaments, or actions of force-dependent capping proteins controlling filament polymerization<sup>27</sup>.

While fluidization of living and inert systems clearly differ (Fig. 3c), the constellation of out-of-equilibrium features displayed by the cytoskeleton of the living cell is seen to be rich, nontrivial and unexplained, and would appear to describe a glassy matrix close to a glass transition. We now have firm phenomenological evidence, moreover, that dynamics in the cytoskeleton of the living adherent cell revolve around the master parameter  $\delta_0$  (or, equivalently,  $\alpha$ ; Supplementary Note 7), which sets the power-law rheology exponent<sup>12,13</sup>, the rate of nanoscale structural rearrangements and their relaxation (Fig. 4)<sup>16</sup>, the extent of fluidization in response to stretch (Figs 2 and 3a) and the rate of subsequent resolidification (Fig. 3b). In turn, this master parameter  $\delta_0$  is set by cytoskeletal tension (pre-stress)<sup>28</sup>.



**Figure 4 | Structural relaxation takes place on timescales that grow with the time elapsed since the application of stretch and is slower than any exponential process.** a, Spontaneous motions of beads bound to HASM cells at different  $t_w$  after stretch cessation ( $n = 1,062$  beads). Waiting times are 5, 20, 35, 55, 85, 135, 195, 295, 435, 665 and 995 s from top to bottom. The red line is the MSD before stretch application. The dashed lines indicate diffusion exponents of 1 and 2. b, To characterize the progressive slowing of rearrangement kinetics, we defined a time  $\tau$  at which  $\text{MSD}(\tau) = d^2$ , where  $d$  was taken as an arbitrary threshold and  $\tau$  thus represented the average time required for a bead to move (diffuse) a distance  $d$ . For any value of  $d$ , we found that  $\tau$  increased with  $t_w$  as a power law  $\tau \propto t_w^\mu$  with  $\mu \approx 0.3$ , indicating that the decay was slower than any exponential process, and that within the experimental time window no steady state was achieved. Data are shown for  $d^2 = 100 \text{ nm}^2$  and the solid line is a fit to a power law with exponent  $\mu = 0.32$ . c, After rescaling the time axis using  $\Delta t_\mu = \Delta t / t_w^\mu$  with  $\mu = 0.32$ , all data collapsed onto a master curve. This indicates that the kinetics at each waiting time were self-similar. In inert soft glassy materials, such slowing of rearrangement kinetics as well as the absence of a steady state is referred to as physical ageing and  $\mu$  is identified as the ageing coefficient. Physical ageing can be interrupted by injection of mechanical energy through shear; shear drives inelastic structural rearrangements<sup>7,23</sup>, in which case it is presumed that elements can then 'hop' out of the deep energy wells in which they are trapped, erase system memory, and push the system farther from thermodynamic equilibrium. In inert soft materials these events reset system evolution to some earlier time and for that reason are called physical rejuvenation<sup>6,7</sup>.

As such, two major concepts in cytoskeletal biology that are each understood in its own right to be highly unifying are now seen to be linked intimately to one another—cytoskeletal tension on the one hand and glassy dynamics on the other. Although a mechanism explaining why this might be so is unknown<sup>29</sup> (Supplementary Notes 7, 8), these phenomena, taken together, define the most primitive features of the cytoskeletal phenotype, namely, its abilities to deform, to contract and to remodel, and might have arisen as early as the cytoskeleton itself, about two billion years ago<sup>30</sup> (Supplementary Note 9).

We traditionally think about molecular interactions within the cytoskeleton as being highly specific, whereas in a crowded<sup>3</sup> glassy phase the nature of molecular interactions and their rate of progression become highly constrained, severely regularized, and non-specific (Figs 3 and 4; Supplementary Note 8). Conventional descriptions of physical interactions based upon viscoelasticity, the fluctuation-dissipation theorem, specific signalling cascades, dilute solution chemistry, and even emerging notions of protein interaction maps, fail to account for these dynamics. Because physical interactions are now seen to play out within a glassy phase, they will have to be rethought within a rather different conceptual perspective.

## METHODS SUMMARY

**Cell culture.** HASM, HLF, HBE and MDCK cells were grown on collagen I-coated silastic substrates (Flexcell) for 5–14 days, depending on the cell type. Cells were allowed to reach confluence before being serum-deprived for experiments.

**Measurement of cell rheology.** We measured cell rheology using OMTC<sup>12,13</sup> (Supplementary Notes 2). Ferrimagnetic beads (4.5 μm) coated with a synthetic Arg–Gly–Asp (RGD)-containing peptide are allowed to bind integrins on the cell surface and become tightly anchored to the cytoskeleton through focal contacts. The beads are permanently magnetized in the horizontal plane of the cell culture and subsequently twisted in an oscillatory magnetic field with frequency 0.75 Hz. The twisting field causes each bead to rotate towards alignment with the oscillatory field and, as result, a weak mechanical torque is applied to the cell. The complex modulus of the cells ( $G^*$ ) is computed from the Fourier transform of the applied mechanical torque ( $T$ ) and of the resulting lateral bead displacement ( $D$ ):

$$G^* = G' + jG'' = \tilde{T}/\tilde{D} \quad (1)$$

where  $*$  denotes a complex number, the tilde overbar denotes the Fourier domain, and  $j^2 = -1$ . For each experimental condition, data are reported as medians of the bead populations (215–719 beads on a similar number of cells per experimental condition).

**Spontaneous bead motions.** Spontaneous bead motions were measured by tracking the position of the centroid of each bead. Data were recorded during time intervals of 10 s starting at different waiting times  $t_w$  after stretch cessation. We computed the MSD of each bead  $i$  as:

$$\text{MSD}_i(\Delta t, t_w) = \langle (x_i(t + \Delta t, t_w) - x_i(t, t_w))^2 \rangle \quad (2)$$

where  $\Delta t$  is the time lag,  $x$  is the bead coordinate, and brackets indicate an average over  $t$ . The distribution of the MSD( $\Delta t, t_w$ ) from bead to bead was approximately log-normal. Accordingly, data are reported as the median of the bead population.

**Full Methods** and any associated references are available in the online version of the paper at [www.nature.com/nature](http://www.nature.com/nature).

Received 14 November 2006; accepted 10 April 2007.

- Vogel, V. & Sheetz, M. Local force and geometry sensing regulate cell functions. *Nature Rev. Mol. Cell Biol.* **7**, 265–275 (2006).
- Ingber, D. E. & Tensegrity, I. I. How structural networks influence cellular information processing networks. *J. Cell Sci.* **116**, 1397–1408 (2003).
- Minton, A. P. How can biochemical reactions within cells differ from those in test tubes? *J. Cell Sci.* **119**, 2863–2869 (2006).
- Mason, T. G. & Weitz, D. A. Linear viscoelasticity of colloidal hard sphere suspensions near the glass transition. *Phys. Rev. Lett.* **75**, 2770–2773 (1995).
- Sollich, P., Lequeux, F., Hebraud, P. & Cates, M. E. Rheology of soft glassy materials. *Phys. Rev. Lett.* **78**, 2020–2023 (1997).

- Cloitre, M., Borrega, R. & Leibler, L. Rheological aging and rejuvenation in microgel pastes. *Phys. Rev. Lett.* **85**, 4819–4822 (2000).
- Viasnoff, V. & Lequeux, F. Rejuvenation and overaging in a colloidal glass under shear. *Phys. Rev. Lett.* **89**, 065701 (2002).
- Corwin, E. I., Jaeger, H. M. & Nagel, S. R. Structural signature of jamming in granular media. *Nature* **435**, 1075–1078 (2005).
- Johnson, P. A. & Jia, X. Nonlinear dynamics, granular media and dynamic earthquake triggering. *Nature* **437**, 871–874 (2005).
- Matthews, B. D., Overby, D. R., Mannix, R. & Ingber, D. E. Cellular adaptation to mechanical stress: role of integrins, Rho, cytoskeletal tension and mechanosensitive ion channels. *J. Cell Sci.* **119**, 508–518 (2006).
- Lau, A. W., Hoffman, B. D., Davies, A., Crocker, J. C. & Lubensky, T. C. Microrheology, stress fluctuations, and active behavior of living cells. *Phys. Rev. Lett.* **91**, 198101 (2003).
- Fabry, B. *et al.* Scaling the microrheology of living cells. *Phys. Rev. Lett.* **87**, 148102 (2001).
- Fabry, B. *et al.* Time scale and other invariants of integrative mechanical behavior in living cells. *Phys. Rev. E* **68**, 041914 (2003).
- Alcaraz, J. *et al.* Microrheology of human lung epithelial cells measured by atomic force microscopy. *Biophys. J.* **84**, 2071–2079 (2003).
- Trepatt, X. *et al.* Viscoelasticity of human alveolar epithelial cells subjected to stretch. *Am. J. Physiol. Lung Cell. Mol. Physiol.* **287**, L1025–L1034 (2004).
- Bursac, P. *et al.* Cytoskeletal remodelling and slow dynamics in the living cell. *Nature Mater.* **4**, 557–561 (2005).
- Deng, L. *et al.* Fast and slow dynamics of the cytoskeleton. *Nature Mater.* **5**, 636–640 (2006).
- Gardel, M. L. *et al.* Elastic behavior of cross-linked and bundled actin networks. *Science* **304**, 1301–1305 (2004).
- Storm, C., Pastore, J. J., MacKintosh, F. C., Lubensky, T. C. & Janmey, P. A. Nonlinear elasticity in biological gels. *Nature* **435**, 191–194 (2005).
- Fredberg, J. J. *et al.* Airway smooth muscle, tidal stretches, and dynamically determined contractile states. *Am. J. Respir. Crit. Care Med.* **156**, 1752–1759 (1997).
- Hoffman, B. D., Massiera, G., Van Citters, K. M. & Crocker, J. C. The consensus mechanics of cultured mammalian cells. *Proc. Natl Acad. Sci. USA* **103**, 10259–10264 (2006).
- Miguel, M. C. & Zapperi, S. Materials science. Fluctuations in plasticity at the microscale. *Science* **312**, 1151–1152 (2006).
- Bulatov, V. V. & Argon, A. S. A stochastic-model for continuum elastoplastic behavior. 2. A study of the glass-transition and structural relaxation. *Model. Simul. Mater. Sci. Eng.* **2**, 185–202 (1994).
- Brujic, J., Hermans, R. I., Walthers, K. A. & Fernandez, J. M. Single-molecule force spectroscopy reveals signatures of glassy dynamics in the energy landscape of ubiquitin. *Nature Phys.* **2**, 282–286 (2006).
- Moazzam, F., DeLano, F. A., Zweifach, B. W. & Schmid-Schonbein, G. W. The leukocyte response to fluid stress. *Proc. Natl Acad. Sci. USA* **94**, 5338–5343 (1997).
- Yap, B. & Kamm, R. D. Mechanical deformation of neutrophils into narrow channels induces pseudopod projection and changes in biomechanical properties. *J. Appl. Physiol.* **98**, 1930–1939 (2005).
- Kozlov, M. M. & Bershadsky, A. D. Processive capping by formin suggests a force-driven mechanism of actin polymerization. *J. Cell Biol.* **167**, 1011–1017 (2004).
- Stamenovic, D., Suki, B., Fabry, B., Wang, N. & Fredberg, J. J. Rheology of airway smooth muscle cells is associated with cytoskeletal contractile stress. *J. Appl. Physiol.* **96**, 1600–1605 (2004).
- Rosenblatt, N., Alencar, A. M., Majumdar, A., Suki, B. & Stamenovic, D. Dynamics of prestressed semiflexible polymer chains as a model of cell rheology. *Phys. Rev. Lett.* **97**, 168101 (2006).
- Kirschner, M. W. & Gerhart, J. C. *The Plausibility of Life: Resolving Darwin's Dilemma* (Yale Univ., New Haven, 2005).

**Supplementary Information** is linked to the online version of the paper at [www.nature.com/nature](http://www.nature.com/nature).

**Acknowledgements** These studies were supported by grants from National Institutes of Health and from the Spanish Ministries of Education and Science and Health. We thank R. Panettieri for providing cells, and R. Farré, D. Fletcher, F. Ritort and V. Viasnoff for discussions.

**Author Contributions** X.T. and J.J.F. designed research and wrote the manuscript. J.P.B. conducted the theoretical analysis. X.T. and D.N. designed and implemented the experimental system. X.T., L.D. and S.S.A. optimized experimental conditions and treatments. W.T.G. and D.J.T. helped to design experimental protocols and interpret data. D.J.T. provided cells and reagents. X.T. performed all stretch experiments and data analysis. J.J.F. oversaw the project.

**Author Information** Reprints and permissions information is available at [www.nature.com/reprints](http://www.nature.com/reprints). The authors declare no competing financial interests. Correspondence and requests for materials should be addressed to J.J.F. ([jeffrey\\_fredberg@harvard.edu](mailto:jeffrey_fredberg@harvard.edu)).

would use nuclear transfer to combine a haploid somatic nucleus (e.g., by somatic cell haploidization) from one parent and a haploid female or male gamete nucleus from the other parent into a mature oocyte. If a female gamete nucleus is used, a haploid somatic nucleus is directly introduced into a normal oocyte without enucleation. SC would allow for biparental contribution to the progeny and create a new and unpredictable combination of genetic traits from both parents similar to normal fertilization (22). We tested SC directly by producing mosaic oocytes in medaka. We labeled  $i^1$ -derived HX1a cells (Fig. 2H) with nuclear GFP and transplanted their nuclei into nonenucleated mature oocytes of  $i^3$  albino. Just as the F1 hybrid zygote from normal fertilization between these two albino strains produces wild-type pigmentation (fig. S1A), the mosaic oocyte from the SC procedure would also contain one HX1a-derived haploid  $i^1$  nucleus and one  $i^3$  oocyte nucleus and thus might generate offspring with black pigmentation and GFP expression. Out of 667 oocytes, 7 reached the hatching stage, and 3 hatched out to swimming fry (table S4). These nuclear transplants indeed exhibited black pigmentation and nuclear GFP in many tissues (Fig. 4, A to C). One of the nuclear transplant fry grew into a fertile female (Fig. 4D) that exhibited continuous GFP expression from the haploid ES genome and similar pigmentation to the fertilization hybrid between  $i^1$  and  $i^3$  albinos (fig. S1A and Fig. 4E), demonstrating the functional contribution from both the oocyte and HX1a nuclei, instead of meiotic genome duplication. We call this SC-derived fertile nuclear transplant Holly. Holly showed normal fertility and germline transmission upon test crosses to both  $i^1$  and  $i^3$  males, producing four types of F1 progeny: albino or pigmented and GFP-positive or -negative (Fig. 4, F to I). Pigmented and albino progeny were segregated at the Mendelian 1:1 ratio, albeit GFP-positive progeny represented only 23% (table S5). We raised the F1 animals to adulthood and examined their germline transmission again by test crosses. When crossed to nontransgenic  $i^1$  fish, pigmented F1 animals heterozygous for GFP produced the same four different phenotypes in F2 generation. Female and male progeny from Holly were not different in exhibiting the 1:1 Mendelian segregation of pigmentation and GFP expression in F2 (table S6) and F3 generations (fig. S10), suggesting the absence of apparent parental defects. Because genomic abnormalities cannot support embryogenesis to advanced stages in mammals (22) and medaka (18), the production of Holly and its germline transmission demonstrates the retention of genetic stability and integrity in medaka haploid ES cultures. Hence, mosaic oocytes created by combining a haploid mitotic nucleus and a haploid meiotic nucleus can generate viable and fertile fish offspring. Holly and its progeny over three generations show normal embryonic and adult development (Fig. 4 and fig. S10). Uniparental diploid ES cell lines have been obtained from gynogenetic mammalian embryos (23). Whether

mammalian haploid ES cells could be generated and participate in a normal developmental program is unknown.

The lack of haploid human cell lines has led to alternative approaches such as using unstable near-haploid leukemia cultures (11) or human-rodent cell fusions to convert diploidy to haploidy (24). Featuring haploidy and pluripotency, the medaka haploid ES cell lines we obtained will provide a unique yeast-like system for directly analyzing recessive and disease phenotypes in various cell lineages of a vertebrate in vitro.

#### References and Notes

1. D. Botstein, G. R. Fink, *Science* **240**, 1439 (1988).
2. A. M. Wobus, K. R. Boheler, *Physiol. Rev.* **85**, 635 (2005).
3. J. A. Thomson *et al.*, *Science* **282**, 1145 (1998).
4. Y. Hong, C. Winkler, M. Scharl, *Mech. Dev.* **60**, 33 (1996).
5. M. J. Evans, M. H. Kaufman, *Nature* **292**, 154 (1981).
6. K. Takahashi, S. Yamanaka, *Cell* **126**, 663 (2006).
7. S. P. Otto, A. C. Gerstein, *Curr. Biol.* **18**, R1121 (2008).
8. J. J. Freed, L. Mezger-Freed, *Proc. Natl. Acad. Sci. U.S.A.* **65**, 337 (1970).
9. A. Debrec, *Exp. Cell Res.* **151**, 236 (1984).
10. A. Debrec, *Nature* **274**, 255 (1978).
11. M. Kotecki, P. S. Reddy, B. H. Cochran, *Exp. Cell Res.* **252**, 273 (1999).
12. M. H. Kaufman, E. J. Robertson, A. H. Handyside, M. J. Evans, *J. Embryol. Exp. Morphol.* **73**, 249 (1983).
13. J. Wittbrodt, A. Shima, M. Scharl, *Natl. Rev.* **3**, 53 (2002).

14. Y. Hong, C. Winkler, M. Scharl, *Proc. Natl. Acad. Sci. U.S.A.* **95**, 3679 (1998).
15. Y. Hong *et al.*, *Proc. Natl. Acad. Sci. U.S.A.* **101**, 8011 (2004).
16. Y. Hong, C. Winkler, M. Scharl, *Dev. Genes Evol.* **208**, 595 (1998).
17. Y. Hong, M. Scharl, *Methods Mol. Biol.* **329**, 3 (2006).
18. K. Araki, H. Okamoto, A. C. Graveson, I. Nakayama, H. Nagoya, *Dev. Growth Differ.* **43**, 591 (2001).
19. D. Kobayashi, T. Jindo, K. Naruse, H. Takeda, *Dev. Growth Differ.* **48**, 283 (2006).
20. J. Bejar, Y. Hong, M. Scharl, *Development* **130**, 6545 (2003).
21. H. Uwa, Y. Ojima, *Proc. Jpn. Acad.* **57**, 39 (1981).
22. R. Yanagimachi, *Reprod. Biomed. Online* **10**, 247 (2005).
23. Q. Mai *et al.*, *Cell Res.* **17**, 1008 (2007).
24. H. Yan *et al.*, *Nature* **403**, 723 (2000).
25. Supported by the Biomedical Research Council of Singapore (R-05-1-21-19-404, R-08-1-21-19-585, and SBIC-SSCC C-002-2007), the Ministry of Education of Singapore (R-154-000-285-112), the National University of Singapore, and the Lee Hiok Kwee donation (R-154-000-153-720). We thank J. Deng for fish breeding.

#### Supporting Online Material

www.sciencemag.org/cgi/content/full/326/5951/430/DC1  
Materials and Methods

Figs S1 to S10

Tables S1 to S6

Movies S1 to S6

References

20 April 2009; accepted 21 August 2009

10.1126/science.1175151

## Complete Resequencing of 40 Genomes Reveals Domestication Events and Genes in Silkworm (*Bombyx*)

Qingyou Xia,<sup>1,2\*</sup> Yiran Guo,<sup>3\*</sup> Ze Zhang,<sup>1,2\*</sup> Dong Li,<sup>1,3\*</sup> Zhaoling Xuan,<sup>3\*</sup> Zhuo Li,<sup>3\*</sup> Fangyin Dai,<sup>1</sup> Yingrui Li,<sup>3</sup> Daojun Cheng,<sup>1</sup> Ruiqiang Li,<sup>3,4</sup> Tingcai Cheng,<sup>1,2</sup> Tao Jiang,<sup>3</sup> Celine Becquet,<sup>5†</sup> Xun Xu,<sup>3</sup> Chun Liu,<sup>1</sup> Xingfu Zha,<sup>1</sup> Wei Fan,<sup>3</sup> Ying Lin,<sup>1</sup> Yihong Shen,<sup>1</sup> Lan Jiang,<sup>3</sup> Jeffrey Jensen,<sup>5</sup> Ines Hellmann,<sup>5</sup> Si Tang,<sup>5</sup> Ping Zhao,<sup>1</sup> Hanfu Xu,<sup>1</sup> Chang Yu,<sup>3</sup> Guojie Zhang,<sup>3</sup> Jun Li,<sup>3</sup> Jianjun Cao,<sup>3</sup> Shiping Liu,<sup>1</sup> Ningjia He,<sup>1</sup> Yan Zhou,<sup>3</sup> Hui Liu,<sup>3</sup> Jing Zhao,<sup>3</sup> Chen Ye,<sup>3</sup> Zhouhe Du,<sup>1</sup> Guoqing Pan,<sup>1</sup> Aichun Zhao,<sup>1</sup> Haojing Shao,<sup>3,7</sup> Wei Zeng,<sup>3</sup> Ping Wu,<sup>3</sup> Chunfeng Li,<sup>1</sup> Minhui Pan,<sup>1</sup> Jingjing Li,<sup>3</sup> Xuyang Yin,<sup>3</sup> Dawei Li,<sup>3</sup> Juan Wang,<sup>3</sup> Huisong Zheng,<sup>3</sup> Wen Wang,<sup>3</sup> Xiuqing Zhang,<sup>3</sup> Songgang Li,<sup>3</sup> Huanming Yang,<sup>3</sup> Cheng Lu,<sup>1</sup> Rasmus Nielsen,<sup>4,5</sup> Zeyang Zhou,<sup>1,6</sup> Jian Wang,<sup>3</sup> Zhonghuai Xiang,<sup>1†</sup> Jun Wang,<sup>3,4†</sup>

A single-base pair resolution silkworm genetic variation map was constructed from 40 domesticated and wild silkworms, each sequenced to approximately threefold coverage, representing 99.88% of the genome. We identified ~16 million single-nucleotide polymorphisms, many indels, and structural variations. We find that the domesticated silkworms are clearly genetically differentiated from the wild ones, but they have maintained large levels of genetic variability, suggesting a short domestication event involving a large number of individuals. We also identified signals of selection at 354 candidate genes that may have been important during domestication, some of which have enriched expression in the silk gland, midgut, and testis. These data add to our understanding of the domestication processes and may have applications in devising pest control strategies and advancing the use of silkworms as efficient bioreactors.

The domesticated silkworm, *Bombyx mori*, has a mid-range genome size of ~432 Mb (1), is the model insect for the order Lepidoptera, has economically important values (e.g., silk and bioreactors production), and has been domesticated for more than 5000 years (2). Be-

cause of human selection, silkworms have evolved complete dependence on humans for survival (3), and more than 1000 inbred domesticated strains are kept worldwide (3). Archaeological and genetic evidences indicate that the domesticated silkworm originated from the Chinese wild silkworm

worm, *Bombyx mandarina*, that is found throughout Asia, where modern sericulture and silkworm domestication were initiated.

The origin of the domesticated silkworm is a long-standing question that has not been settled by previous limited biochemical and molecular analyses. Two hypotheses suggested a unique domestication but disagreed on the ancestral variety.

<sup>1</sup>The Key Sericultural Laboratory of Agricultural Ministry, College of Biotechnology, Southwest University, Chongqing 400715, China. <sup>2</sup>Institute of Agronomy and Life Sciences, Chongqing University, Chongqing 400044, China. <sup>3</sup>BGI-Shenzhen, Shenzhen 518083, China. <sup>4</sup>Department of Biology, University of Copenhagen, Universitetsparken 15, 2100 Kbh Ø, Denmark. <sup>5</sup>Departments of Integrative Biology and Statistics, University of California Berkeley, Berkeley, CA 94720, USA. <sup>6</sup>Chongqing Normal University, Chongqing 400047, China. <sup>7</sup>Innovative Program for Undergraduate Students, South China University of Technology, Guangzhou 510006, China.

\*These authors contributed equally to this work.

†Present address: Institute for Human Genetics, University of California San Francisco, San Francisco, CA 94143-0794, USA.

‡To whom correspondence should be addressed. E-mail: wangj@genomics.org.cn (J.W.); xbxzh@swu.edu.cn (Z.X.)

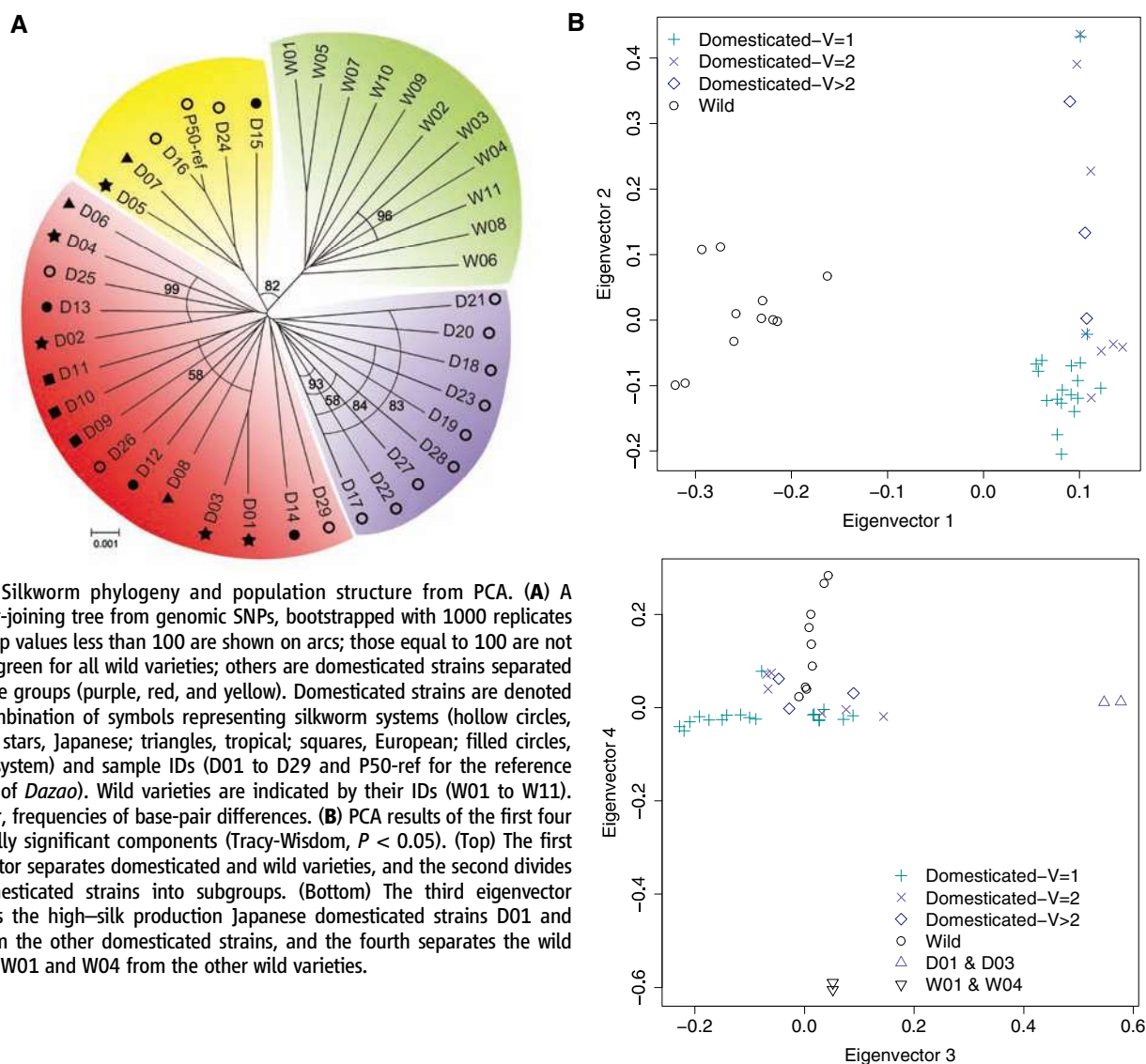
One hypothesis, based on isoenzyme polymorphism, proposed mono-voltinism as ancestral variety (voltinism represents number of generations per annum), from which bi- and multi-voltine were derived by artificial selection (4); the other proposed the reverse path considering evidence from archaeology, history, and genetics (5). An alternative hypothesis based on random amplification of polymorphic DNA indicated that the ancestral domestic silkworm strains were issued, not from a unique variety, but from mixed geographic locations and ecological types (6). These theories are conflicting, probably because they were derived from incomplete genetic information. Consequently, we present here a genome-wide detailed genetic variation map in hopes to help reconstruct the silkworm domestication history.

The data consisted of 40 samples from 29 phenotypically and geographically diverse domesticated silkworm lines [categorized by geographical regions (3): Chinese, Japanese, tropical, European lineages, and the mutant system], as well as 11 wild silkworms from various mulberry fields

in China (table S1). We sequenced each genome at approximately threefold coverage, after creating single- and paired-end (PE) libraries with inserts of PEs ranging from base pairs 137 to 307 (7).

Raw short reads were mapped against the refined 432-Mb reference genome from *Dazao* (1) with the program SOAP (8). We pooled all reads from the 40 complete genomes and identified 15,986,559 single-nucleotide polymorphisms (SNPs) using SoapSNP (7, 9) (table S3A). The accuracy of the SNP calling was evaluated with Sequenom (San Diego, California) genotyping of a representative subset of variants in all 40 varieties, resulting in a 96.7% validation rate (7).

We then pooled separately all 29 domesticated strains and all 11 wild varieties and obtained SNP sets for each (7). The number of SNPs in the domestic versus wild varieties was 14,023,573 and 13,237,865, respectively (table S3A). To account for the different number of domestic and wild strains, we used the population-size scaled mutation rate  $\theta_s$  to measure genetic varia-



**Fig. 1.** Silkworm phylogeny and population structure from PCA. **(A)** A neighbor-joining tree from genomic SNPs, bootstrapped with 1000 replicates (bootstrap values less than 100 are shown on arcs; those equal to 100 are not shown) for all wild varieties; others are domesticated strains separated into three groups (purple, red, and yellow). Domesticated strains are denoted by a combination of symbols representing silkworm systems (hollow circles, Chinese; stars, Japanese; triangles, tropical; squares, European; filled circles, mutant system) and sample IDs (D01 to D29 and P50-ref for the reference genome of *Dazao*). Wild varieties are indicated by their IDs (W01 to W11). Scale bar, frequencies of base-pair differences. **(B)** PCA results of the first four statistically significant components (Tracy-Wisdom,  $P < 0.05$ ). (Top) The first eigenvector separates domesticated and wild varieties, and the second divides the domesticated strains into subgroups. (Bottom) The third eigenvector separates the high-silk production Japanese domesticated strains D01 and D03 from the other domesticated strains, and the fourth separates the wild varieties W01 and W04 from the other wild varieties.

tion (10) (table S3B). We found that  $\theta_{S,domesticated}$  (0.0108) was significantly smaller than  $\theta_{S,wild}$  (0.0130) [Mann-Whitney  $U$  (MWU),  $P = 1.10 \times 10^{-7}$ ], which may reflect differences in effective population size and demographic history (including domestication and artificial selection). The rate of heterozygosity in domesticated strains was more than twofold lower than that of wild varieties (0.0032 versus 0.0080, respectively) (MWU,  $P = 3.33 \times 10^{-6}$ ). This reduction in heterozygosity is most likely due to inbreeding or the bottleneck experienced by domesticated lines.

In addition to SNPs, we also identified 311,608 small insertion-deletions (indels) (table S4A), a subset of which were validated with polymerase chain reaction (7). The  $\theta_S$  values for the indels (table S4B) were in agreement with a lower effective population size in domesticated versus wild varieties. A mate-pair relationship method (7, 11) identified 35,093 structural variants (SVs) among the 40 varieties (table S5). Over three-fourths of the SVs overlapped with transposable elements (TEs), suggesting that SV events in silkworm are probably due to TE content (12) and mobility (11). The SNPs, indels, and SVs all con-

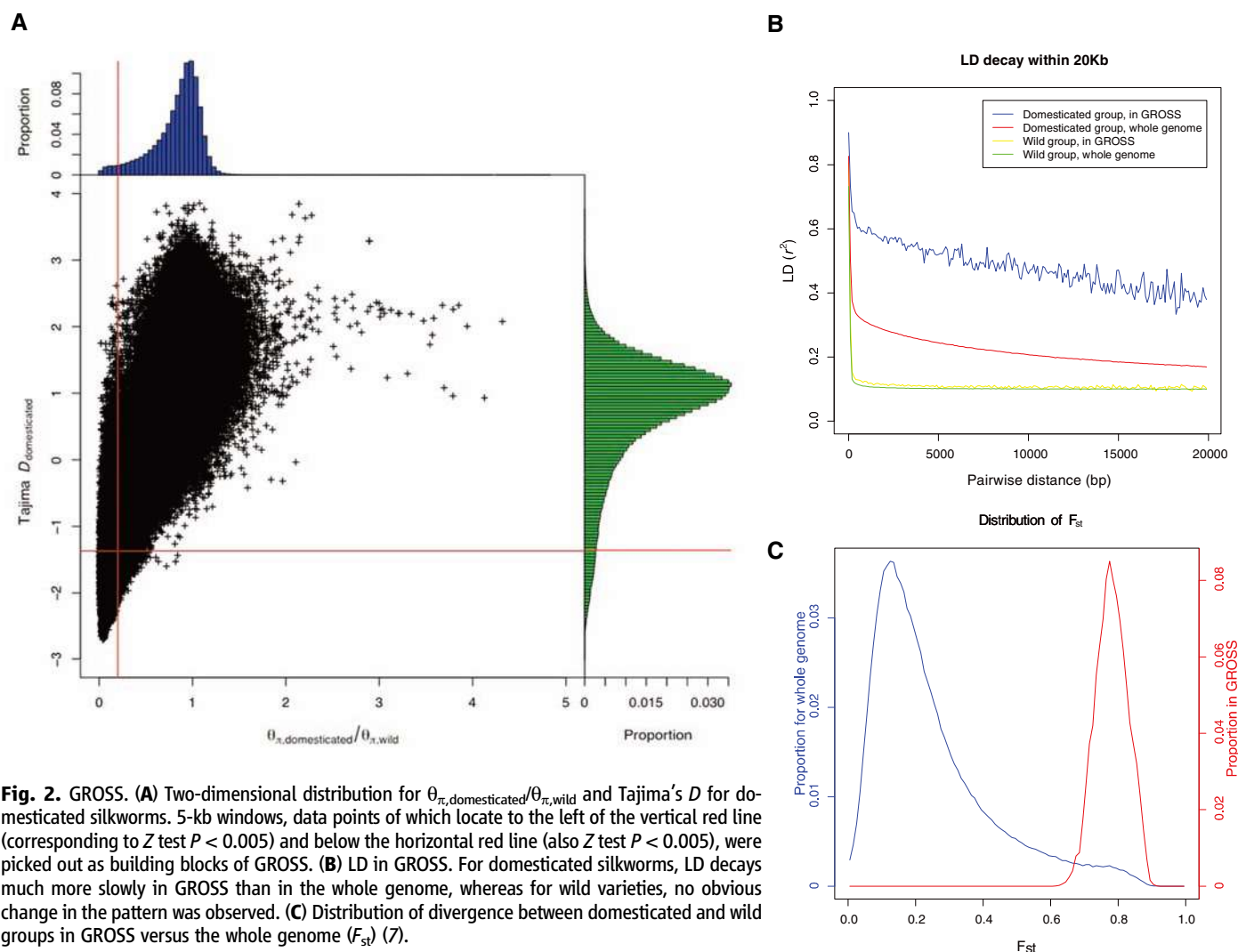
tributed to a comprehensive genetic variation map for the silkworm.

To elucidate the phylogeny of silkworms beyond previous studies (6, 13, 14), we used our identified SNPs to estimate a neighbor-joining tree (7) on the basis of a dissimilarity measure of genetic distance (Fig. 1A). This tree represents an average of distances among strains, so lineages cannot be directly interpreted as representing phylogenetic relationships. Instead, the distances may reflect gene flow and other population level processes related to human activities such as ancient commercial trade. The unrooted radial relationship reveals a clear split between the domesticated and wild varieties, and the domestic strains cluster into several subgroups (Fig. 1A).

A principal components analysis (PCA) (7) classified the first four eigenvectors as significant (table S6; Tracy-Widom,  $P < 0.05$ ). The first eigenvector clearly separates the domesticated and wild varieties, whereas the second eigenvector divides the domesticated strains into subgroups correlated with voltinism (Fig. 1B, top). The third principal component separates D01 and D03 (which are high-silk producing Japanese domes-

ticated strains) from the other domesticated strains, whereas the fourth separates W01 and W04 from the other wild varieties (Fig. 1B, bottom). Results of population structure analysis (7) (fig. S3) confirmed the results of the PCA, as well as the neighbor-joining analysis. The clear genetic separation between domesticated and wild varieties suggests a unique domestication event and relatively little subsequent gene flow between the two groups.

One puzzling observation is that, although domesticated strains are clearly genetically differentiated from the wild ones, they still harbor ~83% of the variation observed in the wild varieties. This suggests that the population-size bottleneck at domestication only reduced genetic variability mildly (7); that is, a large number of individuals must have been selected for initial domestication or else domestication occurred simultaneously in many places. To quantify this observation, we fit a simple coalescence-based genetic bottleneck model to the SNP frequency spectrum (7). The estimated model suggests that the domestication event lead to a 90% reduction in effective population size during the initial bottleneck (fig. S2). Additionally, we observed no



**Fig. 2. GROSS. (A)** Two-dimensional distribution for  $\theta_{\pi,domesticated}/\theta_{\pi,wild}$  and Tajima's  $D$  for domesticated silkworms. 5-kb windows, data points of which locate to the left of the vertical red line (corresponding to Z test  $P < 0.005$ ) and below the horizontal red line (also Z test  $P < 0.005$ ), were picked out as building blocks of GROSS. **(B)** LD in GROSS. For domesticated silkworms, LD decays much more slowly in GROSS than in the whole genome, whereas for wild varieties, no obvious change in the pattern was observed. **(C)** Distribution of divergence between domesticated and wild groups in GROSS versus the whole genome ( $F_{st}$ ) (7).

excess of low-frequency variants in the domesticated varieties compared with the wild varieties, suggesting that there has not been obvious population growth since the domestication event and that the domestic lines probably have had a generally stable effective population size.

Our measure of pairwise linkage disequilibrium (LD) (7) showed that LD decays rapidly in silkworms, with correlation coefficient  $r^2$  decreasing to half of its maximum value at distances of ~46 and 7 base pairs for the domesticated and wild varieties, respectively (fig. S1). The fast decay of LD implies that regions affected by selective sweeps are probably relatively small. To detect regions with significant ( $Z$  test,  $P < 0.005$ ) signatures of selective sweep, we measured SNP variability and frequency spectrum following a genome-wide sliding window strategy (7) (Fig. 2A). Though the significance of our  $Z$  tests (7) cannot be interpreted literally due to correlations in LD and shared ancestral history between the two populations, the  $Z$  tests suggest differences in frequency spectra and amounts of variability between the two groups. We termed the candidate regions genomic regions of selective signals (GROSS).

We identified a total of 1041 GROSS (7), covering 12.5 Mb (2.9%) of the genome, which may reflect genomic footprints left by artificial selection during domestication. A region affected by selective sweep typically has an elevated level of LD (15, 16), and in our GROSS, the level of LD among SNP pairs less than 20-kb apart was 2.3 times higher than genome average (Fig. 2B), consistent with the hypothesis that selection is affecting these regions. In all these regions, divergence levels (7) between the domesticated and wild groups were also elevated (Fig. 2C), confirming the differentiation of the two subpopulations.

*B. mori* has experienced intense artificial selection, represents a completely domesticated insect (3), and has become totally dependent on humans for survival. Artificial selection has also enhanced important economic traits such as cocoon size, growth rate, and digestion efficiency (3). Moreover, compared to its wild ancestor *B. mandarina*, *B. mori* has gained some representative behavioral characteristics (such as tolerance to human proximity and handling, as well as extensive crowding) and lost other traits (such as flight, predators, and diseases avoidance). However, to date no genes have been identified as domestication genes under artificial selection. Within GROSS, we identified 354 protein-coding genes that represent good candidates for domestication genes (table S9). Their Gene Ontology annotation (17) showed the most representation in the categories of “binding” and “catalytic” in molecular function, as well as “metabolic” and “cellular” in biological process (fig. S4).

Considering published expression profiles performed on different tissues in fifth-instar day 3 of *Dazao* with genome-wide microarray (18), we found that 159 of our GROSS genes exhibit differential expression. Of these, 4, 32, and 54 genes are enriched in tissues of silk gland, midgut, and

testis, respectively (fig. S5). Among the genes enriched in the silk gland is silk gland factor-1 (*Sgf-1*), a homolog of a *Drosophila melanogaster* *Fkh* gene. *Sgf-1* regulates the transcription of the *B. mori* glue protein-encoding *sericin-1* gene and of three fibroin genes encoding fibroin light chain, fibroin heavy chain, and *fhx/P25* (19, 20). Another silk gland-enriched gene, *BGIBMGA005127*, homologous to the *Drosophila* *sage* gene, was overexpressed fourfold in a high-silk strain compared with *Dazao* (fig. S6). In *Drosophila*, the products of *Fkh* and *sage* genes cooperate to regulate the transcription of the glue genes *SG1* and *SG2*, which are crucial for the synthesis and secretion of glue proteins (21, 22). Additionally, midgut- and testis-enriched genes suggest that genes involved in energy metabolism and reproduction have also been under artificial selection during domestication (7). Specifically, we identified three likely candidates for artificial selection: (i) *NM\_001130902* is homologous to paramyosin protein in *Drosophila* and may be related to flight (23). (ii) *NM\_001043506* is homologous to fatty-acyl desaturase (*desat1*) in *Drosophila*, which is related to courtship behaviors, because mutations in *desat1* can change the pattern of sex pheromones production and discrimination (24). Finally, (iii) *BGIBMGA000972* is homologous to tyrosine-protein kinase *Btk29A* in *Drosophila*, which is involved in male genitalia development (25).

In sericulture, silkworms are typically categorized by their geographic origins (3). Voltinism, which results from adaptation to ecological conditions, and geographic systems have been central to previous studies of silkworm origin and domestication (4–6). Our findings indicate that a unique domestication event occurred and, although voltinism correlates with genetic distances, major genetically cohesive strains cannot be identified on the basis of voltinism. We observed no correlation between longitudes of the sample origins and any of the principal components, but we did find a significant correlation between the latitudes and eigenvectors 2 and 4 in the PCA (table S7). Although this correlation might be due to isolation by distance, this result also agrees with previous studies suggesting that climate affects silkworm biology (2).

The silkworm data reported here represent a large body of genome sequences for a lepidopteran species and offer a source of near-relatives in this clade for comparative genomic analysis. We further proposed a set of candidate domestication genes that, in addition to being putatively under artificial selection, also show higher expression levels in tissues important for silkworm economic traits. Because a proportion of the GROSS genes were probably important in domestication, functional verification of these candidate genes may enable a comprehensive understanding of the differences of biological characteristics between *B. mori* and *B. mandarina*. Moreover, domesticated silkworms have been used as bioreactors (26, 27), and such an effort may provide useful clues to help improve the capacity and capability of silkworms to produce foreign proteins (26). These findings may also aid

in the understanding of how to enhance traits of interest in other organisms in an environmentally safe manner and, because the wild silkworm is a destructive pest, allow new approaches for pest control.

#### References and Notes

- The International Silkworm Genome Consortium, *Insect Biochem. Mol. Biol.* **38**, 1036 (2008).
- Z. Xiang, J. Huang, J. Xia, C. Lu, *Biology of Sericulture* (China Forestry Publishing House, Beijing, 2005).
- M. R. Goldsmith, T. Shimada, H. Abe, *Annu. Rev. Entomol.* **50**, 71 (2005).
- N. Yoshitake, *J. Sericult. Sci. Japan* **37**, 83 (1967).
- Y. Jiang, *Agric. Archaeol.* **14**, 316 (1987).
- C. Lu, H. Yu, Z. Xiang, *Agric. Sci. China* **1**, 349 (2002).
- Materials and methods are available as supporting material on Science Online.
- R. Li, Y. Li, K. Kristiansen, J. Wang, *Bioinformatics* **24**, 713 (2008).
- R. Li et al., *Genome Res.* **19**, 1124 (2009).
- G. A. Watterson, *Theor. Popul. Biol.* **7**, 256 (1975).
- J. Wang et al., *Nature* **456**, 60 (2008).
- Biology Analysis Group et al., *Science* **306**, 1937 (2004).
- Q. Xia, Z. Zhou, C. Lu, Z. Xiang, *Acta Entomol. Sinica* **41**, 32 (1998).
- M. Li et al., *Genome* **48**, 802 (2005).
- R. Nielsen, *Annu. Rev. Genet.* **39**, 197 (2005).
- M. Slatkin, *Nat. Rev. Genet.* **9**, 477 (2008).
- J. Ye et al., *Nucleic Acids Res.* **34**, W293 (2006).
- Q. Xia et al., *Genome Biol.* **8**, R162 (2007).
- B. Horard, E. Julien, P. Nony, A. Garel, P. Couble, *Mol. Cell. Biol.* **17**, 1572 (1997).
- V. Mach et al., *J. Biol. Chem.* **270**, 9340 (1995).
- E. W. Abrams, W. K. Mihoulides, D. J. Andrew, *Development* **133**, 3517 (2006).
- T. R. Li, K. P. White, *Dev. Cell* **5**, 59 (2003).
- H. Liu et al., *Proc. Natl. Acad. Sci. U.S.A.* **102**, 10522 (2005).
- F. Marcillac, Y. Grosjean, J. F. Ferveur, *Proc. Biol. Sci.* **272**, 303 (2005).
- K. Baba et al., *Mol. Cell. Biol.* **19**, 4405 (1999).
- S. Maeda, *Annu. Rev. Entomol.* **34**, 351 (1989).
- S. Maeda et al., *Nature* **315**, 592 (1985).
- We thank two anonymous referees, L. Goodman, L. Bolund, and K. Kristiansen for providing valuable comments. This work was supported by the Ministry of Science and Technology of China (grants 2005CB121000, 2007CB815700, 2006AA10A117, 2006AA10A118, 2006AA02Z177, and 2006AA10A121), the Ministry of Education of China (Program for Changjiang Scholars and Innovative Research Team in University, grant IRT0750), Chongqing Municipal Government, the 111 Project (grant B07045), the National Natural Science Foundation of China (grants 30725008, 30890032, and 90608010), the International Science and Technology Cooperation Project (grant 0806), the Chinese Academy of Science (grant GJHZ0701-6), the Danish Platform for Integrative Biology, the Ole Rømer grant from the Danish Natural Science Research Council, and the Solexa project (grant 272-07-0196). Raw genome data are deposited in the National Center for Biotechnology Information/Short Read archive database with accession number SRA009208; silkworm genetic variations, GROSS information, and microarray data can be found in <http://silkworm.swu.edu.cn/silkdb/resequencing.html>.

#### Supporting Online Material

[www.sciencemag.org/cgi/content/full/1176620/DC1](http://www.sciencemag.org/cgi/content/full/1176620/DC1)  
Materials and Methods  
SOM Text  
Figs. S1 to S7  
Tables S1 to S10  
References

21 May 2009; accepted 12 August 2009

Published online 27 August 2009;

10.1126/science.1176620

Include this information when citing this paper.

ARTICLE

DOI: 10.1038/s41467-017-01515-2

OPEN

# Direct observation of valley-polarized topological edge states in designer surface plasmon crystals

Xiaoxiao Wu<sup>1,2</sup>, Yan Meng<sup>1,2</sup>, Jingxuan Tian<sup>3</sup>, Yingzhou Huang<sup>1</sup>, Hong Xiang<sup>1</sup>, Dezhan Han<sup>1</sup> & Weijia Wen<sup>1,2</sup>

The extensive research of two-dimensional layered materials has revealed that valleys, as energy extrema in momentum space, could offer a new degree of freedom for carrying information. Based on this concept, researchers have predicted valley-Hall topological insulators that could support valley-polarized edge states at non-trivial domain walls. Recently, several kinds of photonic and sonic crystals have been proposed as classical counterparts of valley-Hall topological insulators. However, direct experimental observation of valley-polarized edge states in photonic crystals has remained difficult until now. Here, we demonstrate a designer surface plasmon crystal comprising metallic patterns deposited on a dielectric substrate, which can become a valley-Hall photonic topological insulator by exploiting the mirror-symmetry-breaking mechanism. Topological edge states with valley-dependent transport are directly visualized in the microwave regime. The observed edge states are confirmed to be fully valley-polarized through spatial Fourier transforms. Topological protection of the edge states at sharp corners is also experimentally demonstrated.

<sup>1</sup>Department of Applied Physics, Chongqing University, Chongqing 401331, China. <sup>2</sup>Department of Physics, The Hong Kong University of Science and Technology, Clear Water Bay, Kowloon, Hong Kong China. <sup>3</sup>Department of Mechanical Engineering, Faculty of Engineering, The University of Hong Kong, Hong Kong China. Xiaoxiao Wu and Yan Meng contributed equally to this work. Correspondence and requests for materials should be addressed to D.H. (email: [dzhan@cqu.edu.cn](mailto:dzhan@cqu.edu.cn)) or to W.W. (email: [phwen@ust.hk](mailto:phwen@ust.hk))

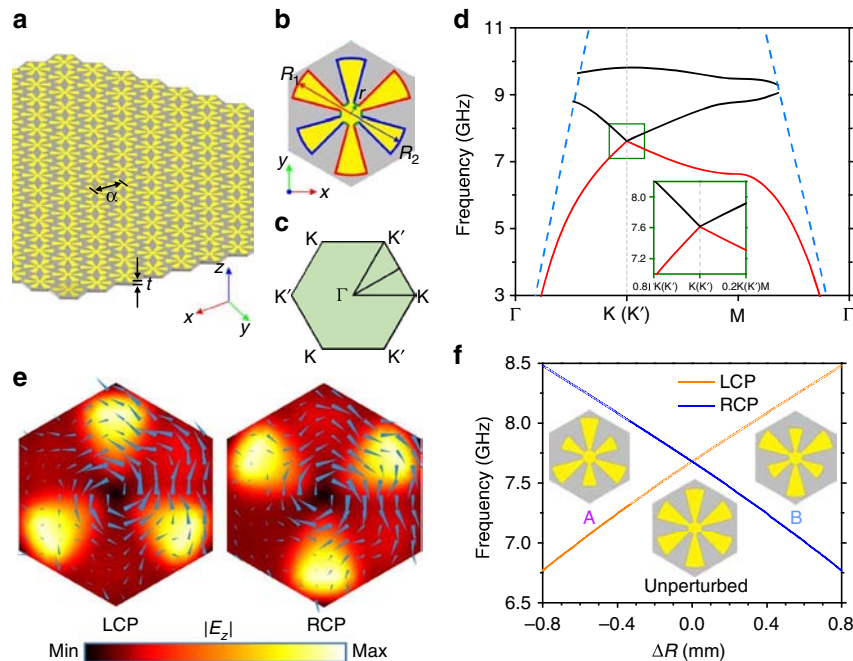


Two-dimensional (2D) layered materials, such as graphene and transition metal dichalcogenides, exhibit a pair of degenerate but inequivalent energy extrema in the momentum space (or reciprocal space), called valleys<sup>1–4</sup>. As a new potential carrier for information, valleys have opened up a novel research area referred to as valleytronics<sup>5–9</sup> aimed at engineering the degree of freedom. Many works have predicted that if the degeneracy between the two valleys is lifted, 2D materials could exhibit the quantum valley-Hall effect, which is manifested by a pair of counter-propagating edge states with opposite valley-polarization at non-trivial domain walls in the absence of inter-valley scattering<sup>10–14</sup>. These materials are sometimes referred to as valley-Hall topological insulators<sup>14,15</sup>. Regarding the classical counterparts of this kind of quantum topological electronic system, several photonic crystals have been proposed as possible valley-Hall photonic topological insulators (PTIs) and numerically investigated<sup>16–19</sup>. Moreover, a sonic crystal comprising anisotropic scatters has been proposed and experimentally demonstrated as a valley-Hall sonic topological insulator (STI)<sup>20</sup>.

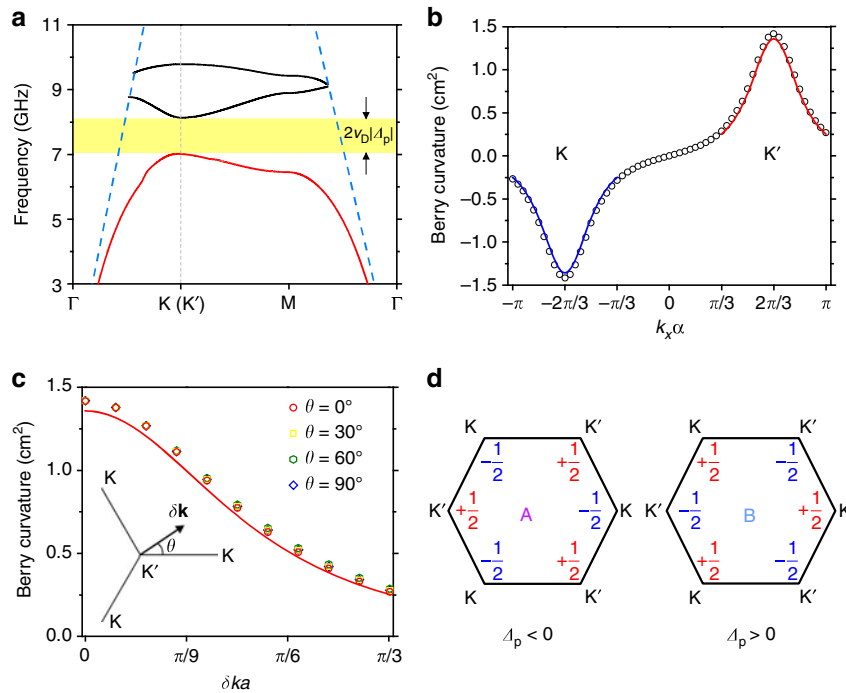
The topological phase transition in the STI is induced by mirror symmetry breaking in the sonic crystal. However, currently proposed PTIs and STIs usually require covers to confine the waves in the vertical direction to prevent radiative leakage into free space<sup>20–25</sup>. In experiments, the covers will largely hamper probing inside the photonic or sonic crystals and the experimental mapping of the fields inside the structure becomes a difficult challenge. As a result, there are few direct experimental

observations of valley-polarized edge states. Until now, valley-dependent transport has been experimentally reported in STIs<sup>20,26</sup>, serving as an important but indirect observation for valley-polarized edge states. In order to achieve direct observations, the edge states need to be vertically confined in free space to eliminate covers<sup>27</sup>, and the elimination of covers is also beneficial for both manufacturing and applications.

In view of these demands, designer surface plasmons (DSPs), also dubbed spoof surface plasmons<sup>28–39</sup>, can become a potential platform for constructing valley-Hall PTIs. DSPs are non-leaky electromagnetic (EM) surface modes similar to the famous surface plasmons at optical and infrared regimes but arise at much lower frequencies in periodic subwavelength metallic structures, and these structures can be called DSP crystals. Owing to its vertical confinement in free space, DSPs have been successfully employed in realizing time-reversal-invariant PTIs aimed at directly detecting topological phenomena of classical waves in recent works<sup>40–42</sup>. Compared with previous PTIs that utilize magneto-optical effect<sup>21,43</sup>, PTIs based on DSP crystals are time-reversal-invariant and do not rely on external magnetic fields. Further, since the realization of a topological bandgap now does not involve coupled-resonator optical waveguides or the coupling between transverse-electric and transverse-magnetic modes, complex structures such as ring-resonator networks<sup>44,45</sup> or three-dimensional resonators<sup>22,23,46</sup> in previous time-reversal-invariant PTIs are no longer needed, which can offer more compactness for the PTIs in applications.



**Fig. 1** Conceptual illustration of the DSP crystal and frequency split of circularly polarized valley states. **a** Schematic illustration of the triangular-lattice designer surface plasmon (DSP) crystal consisting of metallic patterns (yellow) on a dielectric F4B substrate (gray). **b** Top-view Wigner-Seitz unit cell of the lattice. The metallic pattern consists of an inner circle with radius  $r = 1$  mm and six radial fans with sector angle  $30^\circ$ , three of them marked by red outlines having radius  $R_1$ , the other three marked by blue outlines having radius  $R_2$ . **c** First Brillouin zone (FBZ) of the triangular lattice. **d** Calculated band structure of the DSP crystal along the special directions of the FBZ with  $R_1 = R_2 = 5.55$  mm. The blue dashed lines represent the dispersion of EM wave in air (light line) and only the guided part of the band structure is shown. The inset enlarges the area enclosed by the green rectangle around K/K' valley, showing the gapless Dirac cone. **e** Simulated field maps of  $E_z$  component on the  $xy$  plane 1 mm above the surface, showing the two degenerate states at the K valley with energy flux represented by blue arrows. The circulating energy flux of the states is either left-hand circularly polarized (LCP) or right-hand circularly polarized (RCP). The color indicates the amplitude of  $E_z$  component. **f** Calculated eigenfrequencies of the LCP and RCP states at the K valley when the parameter  $\Delta R = R_1 - R_2$  varies while the mean radius  $R = (R_1 + R_2)/2 = 5.55$  mm is kept constant. The inversion of frequency order of the LCP and RCP states indicates a topological phase transition when  $\Delta R$  crosses zero. The evolution of the unit cell is indicated in the inset, where pattern A corresponds to  $\Delta R = -0.5$  mm, the unperturbed pattern corresponds to  $\Delta R = 0$ , and pattern B corresponds to  $\Delta R = 0.5$  mm. The difference between  $R_1$  and  $R_2$  are exaggerated for a clearer visualization



**Fig. 2** Band structure of the DSP crystal with breaking of  $\Gamma K$ -mirror symmetry and topological property of its first band. **a** Calculated band structure of the DSP crystal along the special directions of the FBZ when  $\Delta R = \pm 0.5$  mm (pattern A or B). Blue dashed lines represent the light line and only the guided part of the band structure is shown. The light yellow shaded region represents the full bandgap. **b** Berry curvature of the first band for pattern A along the K (blue solid line) or K' (red solid line) valley. **c** Berry curvature for pattern A around a K' valley as a function of  $\delta k$  for different polar angles  $\theta$  (open symbols). The red solid line represents the isotropic result from the effective Hamiltonian model. The inset shows the definition of  $\delta k$  and  $\theta$  in the reciprocal space. **d** Valley Chern numbers summarized for pattern A and pattern B

In this paper, we experimentally realize a valley-Hall PTI operating in the microwave regime and demonstrate the measured near-field maps of the valley-polarized edge states. The valley-Hall PTI is constructed using a DSP crystal, and the topological phase transition is realized through perturbations that break mirror symmetry and generate non-trivial valley Chern numbers. Valley-polarized edge states and their valley-dependent transport are directly observed in a beam splitter. The topological protection of these edge states at sharp corners is also demonstrated in a Z-shaped waveguide. The valley-Hall PTI should have potential in applications considering its planar geometry and ultrathin thickness and may serve as a prototype for future development of telecommunication devices.

**Results**

**Topological phase transition and valley-Hall PTIs.** The starting point for our consideration is a triangular-lattice DSP crystal comprising metallic patterns deposited on a dielectric substrate as illustrated in Fig. 1a. The substrate is a conventional high-frequency dielectric material, F4B, with a relative permittivity of 2.65 and a loss tangent of 0.001. The lattice constant is  $a = 12$  mm and the thickness of the substrate is  $t = 1$  mm. A top-view Wigner–Seitz unit cell of the DSP crystal is shown in Fig. 1b. The metallic pattern in each unit cell is a thin layer of copper with thickness  $t_m = 35 \mu\text{m}$ , comprising an inner circle with a radius  $r = 1$  mm and six radial fans with a sector angle of  $30^\circ$ . Of the six fans, the three marked by red outlines have the radius  $R_1$  and the other three marked by blue outlines have the radius  $R_2$ . The first Brillouin zone (FBZ) of the triangular lattice is depicted in Fig. 1c.

We first consider a detailed situation when the unit cell possesses mirror symmetry along  $\Gamma K$  direction ( $\Gamma K$ -mirror

symmetry) and assume that  $R_1 = R_2 = 5.55$  mm. The band structure of the DSP crystal is numerically calculated (see Methods section) and the guided part<sup>27,47</sup> of the first three bands along special directions of the FBZ is shown in Fig. 1d, while the dispersion of EM wave in air (light line) is represented by the blue dashed lines. The first band is highlighted by the red solid line and other bands are represented by black solid lines. It can be observed that the first and second bands linearly touch each other at the Dirac frequency  $\omega_D = 2\pi \times 7.61$  GHz at the K and K' valleys due to the  $C_{3v}$  symmetry of the valleys in the reciprocal space<sup>48</sup>. Dirac cones are then formed at each valley by the two bands, with details displayed in the inset that enlarges the area enclosed by the green rectangle.

We then plot the cross-sectional field maps of  $E_z$  component of the two degenerate states at the K valley in Fig. 1e, where the blue arrows represent the time-averaged Poynting vectors (energy flux). As displayed in the field maps, the energy flux of the two states are either left circularly polarized (LCP) or right circularly polarized (RCP), and are invariant under a rotation through  $120^\circ$ . The fields at the K' valley could be obtained by the time-reversal operation, which reverses the direction of the energy flux and hence the circular polarization of the state<sup>16,49</sup>. Since the valley states are in the guide part of the band structure and far away from the light line, the electric field is tightly confined near the metallic surface in the  $z$  (vertical) direction (See Supplementary Fig. 1 for electric field distribution in the  $z$  direction).

We then introduce a perturbation to break the  $\Gamma K$ -mirror symmetry of the unit cell, which will lift the degeneracy at the valleys and hence open a bandgap<sup>20,49</sup>. This could be accomplished by perturbing the radii  $R_1$  and  $R_2$  such that they become unequal, and hence a parameter  $\Delta R = R_1 - R_2$  is defined to characterize the perturbation. After varying this parameter, the

eigenfrequencies of the LCP and RCP states at the K valley are calculated and plotted as a function of  $\Delta R$  in Fig. 1f. For comparison, the mean radius  $\bar{R} = (R_1 + R_2)/2$  is kept constant ( $\bar{R} = 5.55$  mm) when we vary  $\Delta R$ . The evolution of the unit cell when varying  $\Delta R$  is visualized in the inset in Fig. 1f, pattern A corresponding to  $\Delta R = -0.5$  mm, the unperturbed pattern corresponding to  $\Delta R = 0$  mm, pattern B corresponding to  $\Delta R = 0.5$  mm. As expected, the LCP and RCP states become non-degenerated when  $\Delta R$  becomes non-zero and the degeneracy is lifted. However, the  $C_3$  symmetry is intact under the perturbation; hence the circular polarizations of the valley states are not mixed<sup>16</sup>. More interestingly, the frequency order of the LCP and RCP states at the K valley is inverted when  $\Delta R$  crosses zero, which signals a topological phase transition.

For further analysis, we first study the band structure of pattern A with  $\Delta R = -0.5$  mm, that is,  $R_1 = 5.3$  mm and  $R_2 = 5.8$  mm. Because of the time-reversal symmetry as no magnetic materials are introduced, the band structures of pattern A and pattern B are exactly the same, and the guided part of their band structure is shown in Fig. 2a. As can be seen, the full bandgap indicated by the yellow shaded region confirms that the breaking of  $\Gamma K$ -mirror symmetry indeed lifts the degeneracy between the first band and the second band at the valleys. Further, it is noted that though pattern A and pattern B share the same band structure, the circular polarizations of their energy flux at the K and K' valleys are exactly opposite (Supplementary Fig. 2) as dictated by the time-reversal symmetry.

**Theoretical modeling and numerical verifications.** To model the topological phase transition from pattern A to pattern B, which could not be fully investigated from the band structure, we construct an effective Hamiltonian using  $\mathbf{k}\cdot\mathbf{p}$  method in the vicinity of K/K' valley<sup>50,51</sup> (See Supplementary Note 1 for the first-principal derivation)

$$H_{K/K'}(\delta\mathbf{k}) = \pm v_D \delta k_x \sigma_x + v_D \delta k_y \sigma_y + v_D \Delta_p \sigma_z, \quad (1)$$

in which  $v_D$  is the group velocity,  $\delta\mathbf{k} = \mathbf{k} - \mathbf{k}_{K/K'}$  is the displacement of the wave vector  $\mathbf{k}$  to the K/K' valley represented by  $\mathbf{k}_{K/K'}$  in the reciprocal space,  $\sigma_i$  ( $i = x, y, z$ ) are the Pauli matrices acting on the orbital degree of freedom, and  $\Delta_p$  is proportional to the bandwidth of the bandgap ( $2v_D|\Delta_p|$ ) between the first and second bands (see Methods section). Using the eigenvector from this effective Hamiltonian, the local Berry curvature ( $z$  component) of the first band at the K/K' valley can be analytically calculated (see Supplementary Note 2)

$$\Omega_{z,K/K'}(\delta\mathbf{k}) = \pm \frac{\Delta_p}{2(\delta k^2 + \Delta_p^2)^{3/2}}, \quad (2)$$

in which  $\delta k = |\delta\mathbf{k}|$  is the norm of the displacement in the reciprocal space, and the result is expectedly localized around the valleys ( $\delta k = 0$ ). In order to consolidate the above analytical results, we numerically calculate the Berry curvature along the line  $k_y = 2\pi/(\sqrt{3}a)$  in the reciprocal space that includes a pair of K and K' valleys (see Methods section). The numerical result is shown as open circles in Fig. 2b. We also analytically calculate the Berry curvature according to Eq. (2) with fitted parameters ( $v_D = 5.42 \times 10^7$  m s<sup>-1</sup> and  $\Delta_p = -60.68$  m<sup>-1</sup>, see Methods section), and this result, which is essentially derived from the effective Hamiltonian model near K/K' valley, is separately plotted as the blue and red solid lines in Fig. 2b. Quantitative agreement can be observed between the numerical calculation and effective Hamiltonian model. However, the anisotropy of the local Berry curvature is not embodied in Eq. (2) because Eq. (1) is a lowest-order effective Hamiltonian that only includes the linear isotropic

terms, and higher order anisotropic terms, such as warping terms, are neglected.

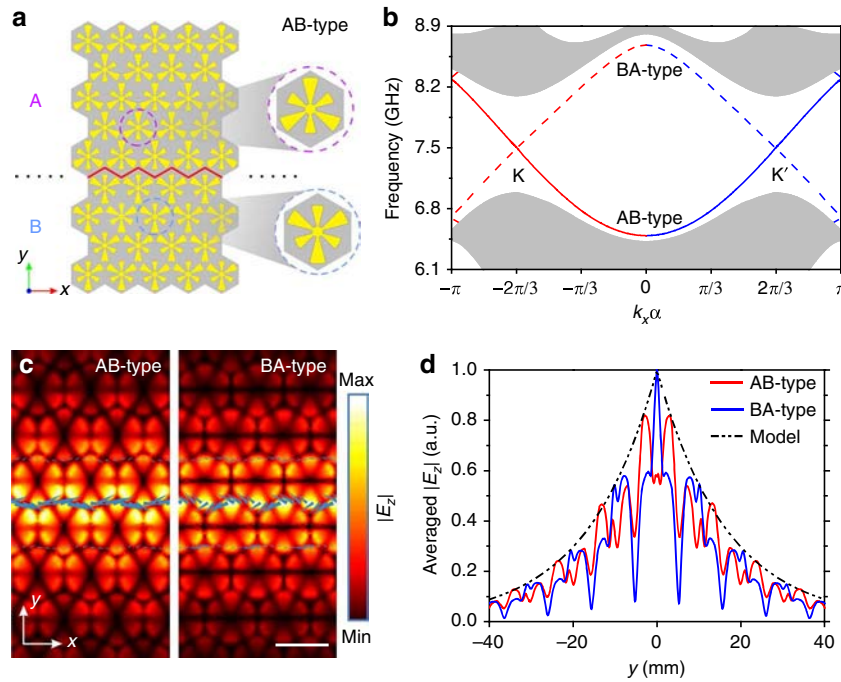
To evaluate the anisotropy, we numerically calculate the Berry curvature around a K' valley along lines in the reciprocal space with different polar angle  $\theta$ , and the corresponding results are plotted as a function of  $\delta k$  in Fig. 2c, represented by differently colored open symbols. For comparison, we also plot the isotropic result from the effective Hamiltonian model as the red solid line. From the results, we could conclude that the anisotropy is indeed negligible and the Berry curvature calculated from the effective Hamiltonian is satisfactorily accurate. Therefore, we can safely calculate the valley Chern numbers of the first band by integrating the local Berry curvature derived from the effectively Hamiltonian

$$C^{K/K'} = \frac{1}{2\pi} \int_{\text{HBZ}} \Omega_{K/K'}(\delta\mathbf{k}) d\mathbf{S} = \pm \frac{1}{2} \text{sgn}(\Delta_p), \quad (3)$$

in which the integral is carried out in half of a Brillouin zone (HBZ) surrounding the K/K' valley. Eq. (3) shows that for each valley, the valley Chern number is  $\pm 1/2$  with the sign solely determined by the sign of  $\Delta_p$ . This dependence stems from the fact that the sign of  $\Delta_p$  solely determines the frequency order of the LCP and RCP states in the band structure, and their frequency order determines the topological phase of the DSP crystal. The calculation using Eq. (3) is straightforward since  $\Delta_p$  is negative for pattern A and hence positive for pattern B. The calculated valley Chern numbers for pattern A and pattern B are summarized in Fig. 2d. These results indicate that when  $\Delta R$  is nonzero, the proposed DSP crystal becomes a valley-Hall PTI because of the full bandgap and nontrivial valley Chern numbers<sup>16,19</sup>.

**Bulk-boundary correspondence and valley-polarized topological edge states.** The above conclusion could be reinforced by the famous bulk-boundary correspondence, which states that the valley topological property of a bandgap is determined by the sum of the valley Chern numbers of the bands below it<sup>52</sup>. Therefore, non-trivial edge states should emerge in the first bandgap at a domain wall between pattern A and pattern B, because the difference of valley Chern numbers of their first band gives  $|\Delta C^{K/K'}| = |C_A^{K/K'} - C_B^{K/K'}| = 1$ <sup>16,19</sup>. We hence combine pattern A and pattern B to construct a domain wall as shown in Fig. 3a, which is referred to as AB-type because pattern A is replicated in the upper domain and pattern B is replicated in the lower domain. Alternatively, we can also replicate pattern A in the lower domain and pattern B in the upper domain, which forms a domain wall referred to as BA-type. It should be emphasized that an AB-type domain wall cannot be converted to a BA-type domain wall through SO(3) operations, and vice versa. For convenience, we assume that the domain wall is periodic along the  $x$  direction and centered along  $y = 0$ .

The band structures of the two domain walls are then simulated using a supercell consisting of total 25 unit cells in the  $y$  direction (see Methods section) and the simulated band structure is shown in Fig. 3b, in which the shaded regions represent the projections of bulk bands. As expected, gapped edge states are observed in the first bandgap for each domain wall, and they do not connect the first and second bands because time-reversal symmetry is preserved here<sup>19</sup>. The edge states of the AB-type and BA-type domain walls are represented by the solid and dashed lines, respectively, and the edge states of the two domain walls intersect each other at the K/K' valley at the frequency 7.50 GHz, in the middle of the first bandgap (Supplementary



**Fig. 3** Edge states at domain walls between two valley-Hall PTIs. **a** Sketch of an AB-type domain wall, in which pattern A is replicated at the upper domain and pattern B is replicated at the lower domain, respectively. The domain wall is marked by the red solid lines. **b** Calculated band structure of an AB-type (solid line) domain wall and a BA-type (dashed line) domain wall. The shaded regions represent the projection of the bulk bands. The red lines indicate positive group velocity (forward) and the blue lines indicate negative group velocity (backward). **c** Simulated field maps of  $E_z$  component on the  $xy$  plane 1 mm above the surface, showing the edge states of AB-type domain wall and BA-type domain wall at the  $K'$  valley, respectively. The color indicates the amplitude of  $E_z$  component. The blue arrows represent the energy flux. The scale bar is 12 mm. **d** The averaged  $|E_z|$  (averaged along the  $x$  direction in a unit cell) of the edge states shown in **c**. The black dash-dotted line represents the corresponding result calculated from the effective Hamiltonian model

Note 3). We use red and blue colors to denote the part of the edge states near  $K$  and  $K'$  valleys, respectively.

It is seen that the propagating directions of an edge state for  $K$  and  $K'$  valleys are exactly opposite, no matter at an AB-type or BA-type domain wall. This is a manifestation of valley-chirality of the valley-Hall effect, in other words, the valley-polarized edge states are locked to one propagating direction in the absence of inter-valley scattering<sup>14,20</sup>. For example, at the  $K$  valley, the edge state of the AB-type domain wall is backward, while at the  $K'$  wall it is forward. This phenomenon could be predicted by the valley Chern number, as  $\Delta C_{AB}^K = C_A^K - C_B^K = -1$  and  $\Delta C_{AB}^{K'} = C_A^{K'} - C_B^{K'} = 1$ . The simulated field maps of  $E_z$  component of edge states at the  $K'$  valley are plotted in Fig. 3c, and both map show that the field is concentrated along the domain wall and decays into the bulk, which is a characteristic of edge states. Further, the blue arrows represent the energy flux and their directions verify that at the  $K'$  valley, the edge state of AB-type is forward, while that of BA-type is backward, consistent with the band structure in Fig. 3b.

We also use three phase-matched dipoles<sup>16</sup> to excite the edge states at domain walls, and the observed one-way propagation in simulations and experiments confirms the valley chirality of the edge states (See Supplementary Note 5 and Supplementary Figs. 5 and 6). Then in order to analyze the decay character of the edge states in the bulk,  $|E_z|$  is averaged along the  $x$  direction in a unit cell and plotted as a function of  $y$  in Fig. 3d. It can be observed that the averaged  $|E_z|$ , which represents spatial amplitude profiles of the edge states, symmetrically decay into the bulk with respect to  $y=0$ .

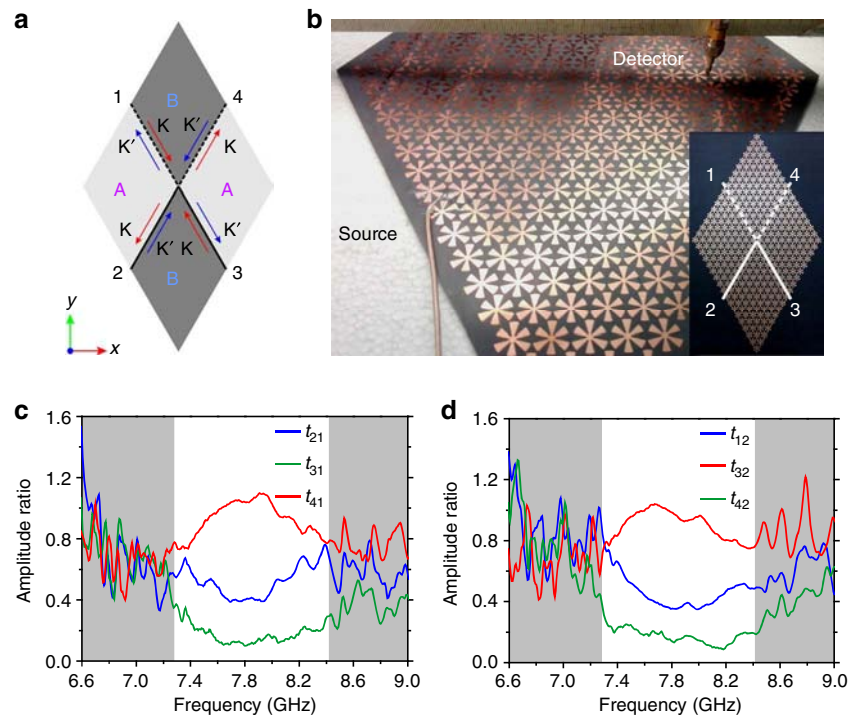
The analytic form of the edge states can also be directly deduced from the effective Hamiltonian model, which proves the bulk-boundary correspondence in our structure, and the decay of

the edge state is predicted to be  $|E_z| \propto e^{-\Delta_p|y|}$  (Supplementary Note 3). As can be observed in Fig. 3d, the prediction from the effective Hamiltonian model plotted as the black dashed line agrees well with the envelopes of the averaged  $|E_z|$  from simulations. Therefore, the symmetric decay of the edge states should be attributed to the same  $\Delta_p$ , or the same decay length in the bulk, shared by pattern A and pattern B lying on the two sides of the domain walls.

**Observation of valley-dependent transport in a beam splitter.**

In order to selectively excite valley-polarized edge states, a rhombus-shaped beam splitter is designed and its diagram is shown in Fig. 4a. The beam splitter consists of four domains. The upper and lower domains are filled with patterns A, while the left and right domains are filled with patterns B, with each domain containing  $9 \times 9$  unit cells. Between the domains, two AB-type domain walls and two BA-type domain walls are formed and they are denoted by the dashed lines and solid lines, respectively. At the outer ends of the domain walls, there exist four terminals labeled as 1–4. The valley-polarized edge states supported at the four domain walls are indicated in Fig. 4a, in which red or blue arrows imply  $K$  or  $K'$  valley-polarized edge states.

A real sample of the beam splitter is fabricated by etching a  $35\text{-}\mu\text{m}$  thick copper layer on a 1-mm thick F4B substrate using standard printed circuit board etching techniques. The experiment setup is shown in Fig. 4b, in which the source and detector are connected to port 1 and port 2 of a vector network analyzer and the scattering parameter  $S_{21}$  proportional to the  $E_z$  component is measured (see Methods section). The inset of Fig. 4b shows a top-view photograph of the fabricated sample and indicates the domain walls and terminals of the sample. The



**Fig. 4** Topological transport of valley-polarized edge states. **a** Schematic diagram of the beam splitter used for selective excitation of valley-polarized edge states. The beam splitter comprises two domains of patterns A and two domains of patterns B. The black dashed lines and solid lines represent AB-type domain walls and BA-type domain walls, respectively. The red and blue arrows represent edges states near K and K' valleys, respectively. **b** Photograph of the experiment setup. Two monopole antennas are used in experiments (see Methods section). DSPs are excited by one of the antennas and  $E_z$  component of the transmitted wave is measured by the other one. Inset shows a top-view photograph of the fabricated beam splitter. **c, d** Measured  $E_z$  amplitude ratio  $t_{ij}$  (outgoing terminal  $i$ , incident terminal  $j$ ) when the source is placed at terminal 1 (**c**) or terminal 2 (**d**). The unshaded region corresponds to the bandgap obtained from experimental measurement

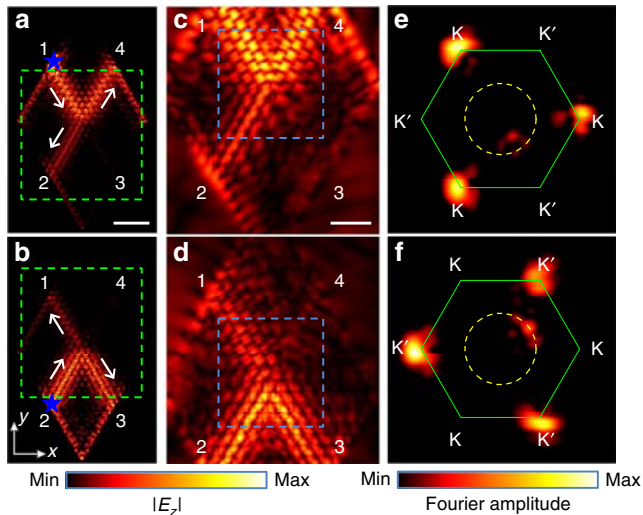
measured  $S_{21}$  data are regarded as  $E_z$  and the amplitude ratios of  $S_{21}$  between the outgoing terminals and the incident terminal are plotted in Fig. 4c, d, in which the source is attached at terminal 1 and terminal 2, respectively. The measured  $E_z$  amplitude ratios are labeled as  $t_{ij}$  by the outgoing terminal  $i$  and incident terminal  $j$ . The unshaded region corresponds to the measured bandgap of the fabricated DSP crystal samples (See Supplementary Fig. 3 for measurement of the bandgap). Compared with the simulated bandgap (7.05–8.12 GHz), the measured bandgap (7.28–8.42 GHz) is shifted about 3.7% toward higher frequency, and this small deviation could be attributed to fabrication errors, such as the errors in thickness and relative permittivity of the commercial F4B substrates. Nevertheless, these fabrication errors do not introduce any essential difference in the physics of valley-dependent transport in our investigated DSP crystal, and only slightly shifts the frequency of bandgap edges (See Supplementary Fig. 4 for detailed results).

From the measured amplitude ratios, it can be observed that the transports of edge states involving opposite valleys ( $t_{31}$  in Fig. 4c and  $t_{42}$  in Fig. 4d) are heavily suppressed compared with those involving the same valley in the bandgap. In the bandgap, the sum of the measured  $E_z$  amplitude ratio involving the same valley is at least 14 dB larger than those involving opposite valleys, whenever the source is attached at terminal 1 or terminal 2. The measurements hence indicate that the excited edge states of the DSP crystal adhere to a valley-dependent topological transport, a feature of valley-polarized edge states<sup>20</sup>. The total thickness (1.035 mm) of the fabricated DSP crystal is smaller than 1/38 of the wavelength (40 mm) at 7.50 GHz, and this deep-subwavelength thickness could be further decreased if we use a dielectric substrate with higher permittivity.

**Direct mapping and analysis of topological edge states.** Next, we scan the  $E_z$  component on the  $xy$  plane above the sample with the same experiment setup for the purpose of directly visualizing the edge states and analyzing their valley polarizations. For reference, simulated field maps of  $E_z$  component at 7.50 GHz are plotted in Fig. 5a, b, in which the blue star denotes the source and the gray arrows denote the directions of the propagating edge states. The source is placed at terminal 1 and terminal 2, respectively, in Fig. 5a, b. We then experimentally scanned the  $E_z$  component in the regions denoted by green dashed rectangles in Fig. 5a, b. The two regions are both of the area  $205 \times 220 \text{ mm}^2$ . The scanned field maps at 7.50 GHz are plotted in Fig. 5c, d, respectively (see Supplementary Fig. 7 for scanned field maps at other frequencies).

The field maps from simulations and experiments show similar distributions of the electric fields and clearly demonstrate the suppression of the inter-valley edge states, which has been indicated in Fig. 4c, d. Spatial Fourier transforms<sup>49</sup> are then performed on the interior regions (denoted by the blue dashed rectangles in Fig. 5c, d) of the scanned complex  $E_z$  component at 7.50 GHz, which excludes the interfaces between DSP crystals and air. The amplitudes of the spatial Fourier transforms, or so-called spatial Fourier spectra, are then plotted in Fig. 5e, f, respectively, where the green solid hexagons denote the FBZs and the yellow dashed circles denote the 7.50-GHz isofrequency contours of the light cone.

From the spatial Fourier spectra, it is observed that wherever the source is attached at terminal 1 or terminal 2, only three equivalent corners of the FBZ, corresponding to one valley, are bright in each situation. In contrast, the three dark corners of the FBZ clearly imply that the opposite valley corresponding to each



**Fig. 5** Near-field maps of valley-polarized edge states and corresponding spatial Fourier spectra. **a, b** Simulated field maps of  $E_z$  component at 7.50 GHz on the  $xy$  plane 1 mm above the metallic surface. The source denoted by the blue star is placed at terminal 1 in **a** and terminal 2 in **b**. Gray arrows denote the direction of the valley-polarized edge states. Green dashed rectangles denote the regions of the area  $205 \times 220 \text{ mm}^2$  scanned in experiments. The scale bar is 60 mm. **c, d** Measured field maps of  $E_z$  component at 7.50 GHz in the region of the sample denoted by green dashed rectangles in **a** and **b**, respectively. The blue dashed rectangles denote the interior regions where we perform Fourier transforms. The scale bar is 40 mm. **e, f** Spatial Fourier spectra of the scanned  $E_z$  component. The green solid hexagons represent the FBZs and the yellow dashed circles represent the 7.50-GHz isofrequency contours of the light cone. The color indicates the amplitude of  $E_z$  component in field maps and the amplitude of spatial Fourier transforms in spatial Fourier spectra, respectively

situation is heavily suppressed. The small faint regions on the light cone (yellow dashed circles) further imply that the non-zero  $t_{31}$  or  $t_{42}$  in Fig. 4c, d are largely owing to the existence of the uncoupled EM wave propagating in air, rather than inter-valley scatterings of the edge states.

We have scanned the background field when there are no metallic patterns on the F4B substrate and the corresponding spatial Fourier spectra also show similar faint regions on the light cone (See Supplementary Note 6 and Supplementary Fig. 8 for detailed experiment setup and results). The small faint regions inside the light cone could be attributed to the evanescent states created by the scatterings of the edge states at the center of the beam splitter<sup>53</sup>. The spatial Fourier spectra hence directly confirm that the excited propagating edge states are fully valley-polarized and their valley-polarizations totally agree with the diagram in Fig. 4a. In other words, the spatial Fourier spectra experimentally confirm that the observed edge states could propagate with negligible inter-valley scattering along zigzag domain walls, which has been theoretically predicted and numerically confirmed for EM waves in previous works<sup>16</sup>. This feature indicates that we can exploit the valley-Hall PTIs to design planar topological waveguides since the suppression of inter-valley scattering will suppress scattering losses at sharp corners in conventional waveguides owing to the valley-chirality of the edge states. Compared with previous counterparts<sup>21–23</sup>, the topological waveguide does not require external magnetic fields or three-dimensional structures for realizing this topological protection, thus benefiting both manufacturing and applications. Moreover, the planar geometry and ultrathin thickness of the topological waveguide will also facilitate its integration with existing electronic systems.

**Topological protection in a Z-shaped waveguide.** For proof of principle, we designed and fabricated a Z-shaped waveguide featuring two sharp corners using patterns A and patterns B. The schematic diagram of the waveguide is shown in Fig. 6a, in which the corner angle  $\alpha = 60^\circ$ . The waveguide is essentially a curved BA-type domain wall and the two ends of the interface are denoted as terminal 1 and terminal 2. In experiments, the source is attached at terminal 1 and the  $E_z$  amplitude is measured around terminal 1 and terminal 2. We also measured the  $E_z$  amplitude near two reference terminals 1' and 2', which are in fact in the bulk of patterns A or patterns B. The measured amplitude ratios show a good contrast between  $t_{21}$  and  $t_{1'1}$  or  $t_{2'1}$  in the bandgap (Supplementary Fig. 11a), which implies a good confinement of the edge state.

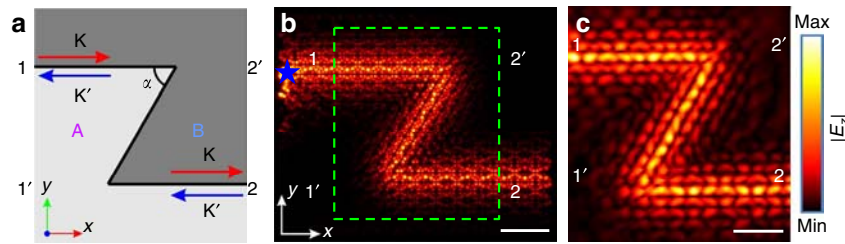
We then scanned the  $E_z$  component above the waveguide with the same experiment setup used for scanning the beam splitter. For comparison, the simulated field map of  $E_z$  component at 7.50 GHz is shown in Fig. 6b, in which the green dashed rectangle denotes the region of the area  $208 \times 220 \text{ mm}^2$  scanned in experiments. The scanned field map at 7.50 GHz is shown in Fig. 6c, which agrees well with the simulated field map and shows that there are no observable scattering losses at the bends (See Supplementary Fig. 9 for scanned field maps at other frequencies).

We have also measured the transport of the edge state in a straight topological waveguide also comprised of a BA-type domain wall and it is observed that the transport behaviors of the two waveguides are generally similar in the bandgap, but show remarkable differences in the bulk bands (Supplementary Fig. 11b). We have also numerically investigated other geometric configurations in which the corner angle  $\alpha$  of the topological waveguides varies, and no notable scattering losses are observed in all cases (See Supplementary Fig. 10 for simulated field maps.), even when the corner becomes incompatible with the triangular lattice ( $\alpha = 30^\circ, 90^\circ, 150^\circ$ )<sup>20</sup>. The overall results hence confirm that the corners in the topological waveguides only have weak influences on transport of the edge states, compared with conventional non-topological waveguides<sup>23</sup>.

According to previous theoretical studies, a random arrangement of the unit cells of valley-Hall PTIs only results in a higher-order perturbation  $O(\Delta_p^2)$  between the two circularly polarized states in  $K/K'$  valley, which is usually much smaller than the first-order perturbation  $v_D \Delta_p$  caused by breaking  $\Gamma K$ -mirror symmetry<sup>16</sup>. This feature of valley-Hall PTIs leads to the suppression of scattering losses in our topological waveguides, where the unit cells (patterns A and patterns B) are arranged to generate a curved domain wall. Since the underlying mechanism is independent of specific waves, this suppression of scattering losses are also observed for acoustic waves in the topological waveguides made from a valley-Hall STI where the topological bandgap is similarly introduced by breaking the  $\Gamma K$ -mirror symmetry of the unit cell<sup>20</sup>.

## Discussion

In summary, we have designed an ultrathin valley-Hall PTI based on mirror-symmetry-breaking mechanism using a DSP crystal. Selective excitation and direct observation of valley-polarized edge states is experimentally demonstrated and confirmed. Our research suggests that DSP crystals that support non-leaky DSPs could become an ideal platform for exploring various phenomena involving topological properties, which are originally proposed in electronic systems. The intrinsic non-leaky feature of DSPs in an open environment facilitates the scanning of near fields, which is difficult for many classical systems, and hence paves the way for more direct experimental studies on topological phenomena of



**Fig. 6** Topological protection of the edge state in a Z-shaped waveguide. **a** Schematic diagram of a Z-shaped topological waveguide formed between patterns A and patterns B. The corner angle  $\alpha = 60^\circ$ . **b** Simulated field map of  $E_z$  component at 7.50 GHz. The green dashed rectangle denotes the region of the area  $208 \times 220 \text{ mm}^2$  scanned in experiments. The color indicates the amplitude of  $E_z$  component. The scale bar is 60 mm. **c** Measured field map of  $E_z$  component at 7.50 GHz. The color indicates the amplitude of  $E_z$  component. The scale bar is 40 mm

classical waves. Moreover, the proposed valley-Hall PTI could also be useful in telecommunications because of its ease in large-scale fabrication using standard techniques, its planar geometry, and ultrathin thickness without any covers, and its topological edge states which can travel through sharp corners with negligible scattering, a critical concern in conventional waveguides. The one-way propagation of valley-polarized edge states may also be exploited to design an on-demand flow switch of EM wave. Finally, we note that though proposed in the microwave regime, the design principle of the valley-Hall PTI should be valid in other frequency regimes, such as the terahertz and near-infrared regimes, and even the optical regime because the basic mirror-symmetry-breaking mechanism does not rely on particular material properties.

## Methods

### Effective Hamiltonian model.

In the effective Hamiltonian,  $H_{K/K'}(\delta\mathbf{k}) = \pm v_D \delta k_x \sigma_x + v_D \delta k_y \sigma_y + v_D \Delta_p \sigma_z$ , the first two terms describe the gapless Dirac cones at the K/K' valley shown in Fig. 1b, while the third term comes from the geometric perturbation that breaks the  $\Gamma$ K-mirror symmetry. The third term is also called the mass term<sup>20</sup>, which lifts the degeneracy at valleys and opens a full band gap with bandwidth  $2v_D|\Delta_p|$  shown in Fig. 2a. Here  $v_D$  is the group velocity,  $\delta\mathbf{k} = \mathbf{k} - \mathbf{k}_{K/K'}$  is the displacement of the wave vector  $\mathbf{k}$  to the K/K' valley ( $\mathbf{k}_{K/K'}$ ), and  $\sigma_i$  ( $i = x, y, z$ ) are Pauli matrices acting on the orbital degree of freedom comprising the first and second bands at the K/K' valley. Since the circular polarizations of the first and second bands at the K/K' valley are exactly opposite as aforementioned, the two circularly polarized states are represented as  $A_R = [1; 0]$ ,  $A_L = [0; 1]$  at the K valley and  $A_R = [0; 1]$ ,  $A_L = [1; 0]$  at the K' valley<sup>16</sup>, respectively. By fitting the dispersions around the valleys calculated from the effective Hamiltonian to the numerical band structures shown in Figs. 1b, 2a, it is found that for pattern A, the parameters  $v_D = 5.42 \times 10^7 \text{ m s}^{-1}$  and  $\Delta_p = -60.68 \text{ m}^{-1}$ , both quantitatively agreeing with the values obtained from the first-principal derivation and the deviation is smaller than 1% (Supplementary Note 1). Likewise, for pattern B,  $v_D = 5.42 \times 10^7 \text{ m s}^{-1}$  and  $\Delta_p = 60.68 \text{ m}^{-1}$ .

**Simulations.** Throughout this paper, all full-wave simulations (or numerical calculations) are performed using commercial finite element method software COMSOL Multiphysics, in which the module EM waves, frequency domain (emw) is used. When calculating the bulk (edge) band structure, Floquet periodic boundary conditions are imposed on periodic surfaces of the unit cell (supercell). Second order scattering boundary conditions for plane waves are used to terminate the simulation domain. In all simulations, the maximum scale of the mesh is smaller than 1/20 of the wavelength (40 mm) of 7.50-GHz EM wave in air. All  $xy$ -plane field maps are recorded at the plane 1 mm above the metallic surface.

**Numerical calculations of berry curvature.** When numerically calculating Berry curvature of a point in the reciprocal space, we first integrate Berry connection along an infinitesimal square contour around the point. Then, according to Stokes' theorem, the line integral is equal to the surface integral of Berry curvature over the infinitesimal square that includes the point<sup>54</sup>. Hence, the line integral divided by the area of the infinitesimal square is exactly the Berry curvature of the point. In real numerical calculations, the side length of the square contour is chosen to be  $\delta k = 1.0 \text{ m}^{-1}$ , and the path integrals are discretized into summations. Further details are given in Supplementary Note 4 and Supplementary Fig. 12.

**Experiment setup.** In experiments, two monopole antennas are used to act as the source and the detector, and the sample is supported by a piece of foam that is

mounted on a stepper motor-driven stage. A vector network analyzer (VNA, Agilent N5232A) is employed throughout the measurements and the source connected to port 1 of the VNA is closely attached to the surface of the sample to excite DSPs, while the detector connected to port 2 of the VNA are placed  $\sim 1 \text{ mm}$  above the metallic surface of the sample to measure the  $E_z$  component of the electric field. In measurements, the scattering parameter  $S_{21}$  is recorded, which is proportional to the  $E_z$  component of the electric field. When scanning the  $E_z$  component above the sample, the resolution in the  $xy$  plane is  $1 \times 1 \text{ mm}^2$ .

**Data availability.** The data which support the figures and other findings within this paper are available from the corresponding authors upon request.

Received: 8 March 2017 Accepted: 21 September 2017

Published online: 03 November 2017

## References

- McCann, E. et al. Weak-localization magnetoresistance and valley symmetry in graphene. *Phys. Rev. Lett.* **97**, 146805 (2006).
- Rycerz, A., Tworzydło, J. & Beenakker, C. Valley filter and valley valve in graphene. *Nat. Phys.* **3**, 172–175 (2007).
- Xiao, D., Yao, W. & Niu, Q. Valley-contrasting physics in graphene: magnetic moment and topological transport. *Phys. Rev. Lett.* **99**, 236809 (2007).
- Lebegue, S. & Eriksson, O. Electronic structure of two-dimensional crystals from ab initio theory. *Phys. Rev. B* **79**, 115409 (2009).
- Yao, W., Xiao, D. & Niu, Q. Valley-dependent optoelectronics from inversion symmetry breaking. *Phys. Rev. B* **77**, 235406 (2008).
- Behnia, K. Condensed-matter physics: polarized light boosts valleytronics. *Nat. Nanotechnol.* **7**, 488–489 (2012).
- Jariwala, D., Sangwan, V. K., Lauhon, L. J., Marks, T. J. & Hersam, M. C. Emerging device applications for semiconducting two-dimensional transition metal dichalcogenides. *ACS Nano* **8**, 1102–1120 (2014).
- Mak, K. F., McGill, K. L., Park, J. & McEuen, P. L. The valley Hall effect in MoS2 transistors. *Science* **344**, 1489–1492 (2014).
- Schaibley, J. R. et al. Valleytronics in 2D materials. *Nat. Rev. Mater.* **1**, 16055 (2016).
- Yao, W., Yang, S. A. & Niu, Q. Edge states in graphene: from gapped flat-band to gapless chiral modes. *Phys. Rev. Lett.* **102**, 096801 (2009).
- Zhang, F., Jung, J., Fiete, G. A., Niu, Q. & MacDonald, A. H. Spontaneous quantum Hall states in chirally stacked few-layer graphene systems. *Phys. Rev. Lett.* **106**, 156801 (2011).
- Qiao, Z., Tse, W.-K., Jiang, H., Yao, Y. & Niu, Q. Two-dimensional topological insulator state and topological phase transition in bilayer graphene. *Phys. Rev. Lett.* **107**, 256801 (2011).
- Zhang, F., MacDonald, A. H. & Mele, E. J. Valley Chern numbers and boundary modes in gapped bilayer graphene. *Proc. Natl Acad. Sci. USA* **110**, 10546–10551 (2013).
- Ju, L. et al. Topological valley transport at bilayer graphene domain walls. *Nature* **520**, 650–655 (2015).
- Song, Z. et al. Quantum spin Hall insulators and quantum valley Hall insulators of BiX/SbX (X=H, F, Cl and Br) monolayers with a record bulk band gap. *NPG Asia Mater.* **6**, e147 (2014).
- Ma, T. & Shvets, G. All-Si valley-Hall photonic topological insulator. *New J. Phys.* **18**, 025012 (2016).
- Dong, J.-W., Chen, X.-D., Zhu, H., Wang, Y. & Zhang, X. Valley photonic crystals for control of spin and topology. *Nat. Mater.* **16**, 298–302 (2016).
- Chen, X.-D. & Dong, J.-W. Valley-protected backscattering suppression in silicon photonic graphene. Preprint at <https://arxiv.org/abs/1602.03352> (2016).

19. Chen, X.-D., Zhao, F.-L., Chen, M. & Dong, J.-W. Valley-contrasting physics in all-dielectric photonic crystals: orbital angular momentum and topological propagation. *Phys. Rev. B* **96**, 020202 (2017).
20. Lu, J. et al. Observation of topological valley transport of sound in sonic crystals. *Nat. Phys.* **13**, 369–374 (2016).
21. Wang, Z., Chong, Y., Joannopoulos, J. & Soljačić, M. Observation of unidirectional backscattering-immune topological electromagnetic states. *Nature* **461**, 772–775 (2009).
22. Chen, W.-J. et al. Experimental realization of photonic topological insulator in a uniaxial metacrystal waveguide. *Nat. Commun.* **5**, 5782 (2014).
23. Ma, T., Khanikaev, A. B., Mousavi, S. H. & Shvets, G. Guiding electromagnetic waves around sharp corners: topologically protected photonic transport in metawaveguides. *Phys. Rev. Lett.* **114**, 127401 (2015).
24. Wu, L.-H. & Hu, X. Scheme for achieving a topological photonic crystal by using dielectric material. *Phys. Rev. Lett.* **114**, 223901 (2015).
25. Cheng, X. et al. Robust reconfigurable electromagnetic pathways within a photonic topological insulator. *Nat. Mater.* **15**, 542–548 (2016).
26. Ye, L. et al. Observation of acoustic valley vortex states and valley-chirality locked beam splitting. *Phys. Rev. B* **95**, 174106 (2017).
27. Barik, S., Miyake, H., DeGottardi, W., Waks, E. & Hafezi, M. Two-dimensionally confined topological edge states in photonic crystals. *New J. Phys.* **18**, 113013 (2016).
28. Pendry, J., Martin-Moreno, L. & Garcia-Vidal, F. Mimicking surface plasmons with structured surfaces. *Science* **305**, 847–848 (2004).
29. Garcia-Vidal, F., Martin-Moreno, L. & Pendry, J. Surfaces with holes in them: new plasmonic metamaterials. *J. Opt. A* **7**, S97 (2005).
30. Maier, S. A., Andrews, S. R., Martin-Moreno, L. & Garcia-Vidal, F. Terahertz surface plasmon-polariton propagation and focusing on periodically corrugated metal wires. *Phys. Rev. Lett.* **97**, 176805 (2006).
31. Williams, C. R. et al. Highly confined guiding of terahertz surface plasmon polaritons on structured metal surfaces. *Nat. Photonics* **2**, 175–179 (2008).
32. Yu, N. et al. Designer spoof surface plasmon structures collimate terahertz laser beams. *Nat. Mater.* **9**, 730–735 (2010).
33. Kats, M. A., Woolf, D., Blanchard, R., Yu, N. & Capasso, F. Spoof plasmon analogue of metal-insulator-metal waveguides. *Opt. Express* **19**, 14860–14870 (2011).
34. Pors, A., Moreno, E., Martin-Moreno, L., Pendry, J. B. & Garcia-Vidal, F. J. Localized spoof plasmons arise while texturing closed surfaces. *Phys. Rev. Lett.* **108**, 223905 (2012).
35. Shen, X., Cui, T. J., Martin-Cano, D. & Garcia-Vidal, F. J. Conformal surface plasmons propagating on ultrathin and flexible films. *Proc. Natl Acad. Sci. USA* **110**, 40–45 (2013).
36. Shen, X. & Cui, T. J. Ultrathin plasmonic metamaterial for spoof localized surface plasmons. *Laser Photon. Rev.* **8**, 137–145 (2014).
37. Liao, Z. et al. Combined system for efficient excitation and capture of LSP resonances and flexible control of SPP transmissions. *ACS Photonics* **2**, 738–743 (2015).
38. Gao, F. et al. Vertical transport of subwavelength localized surface electromagnetic modes. *Laser Photon. Rev.* **9**, 571–576 (2015).
39. Gao, Z., Gao, F., Shastri, K. K. & Zhang, B. Frequency-selective propagation of localized spoof surface plasmons in a graded plasmonic resonator chain. *Sci. Rep.* **6**, 25576 (2016).
40. Gao, F. et al. Probing topological protection using a designer surface plasmon structure. *Nat. Commun.* **7**, 11619 (2016).
41. Meng, Y. et al. Topological interface states in multiscale spoof-insulator-spoof waveguides. *Opt. Lett.* **41**, 3698–3701 (2016).
42. Yang, Y. et al. Hyperbolic spoof plasmonic metasurfaces. *NPG Asia Mater.* **9**, e428 (2017).
43. Skirlo, S. A. et al. Experimental observation of large Chern numbers in photonic crystals. *Phys. Rev. Lett.* **115**, 253901 (2015).
44. Hafezi, M., Demler, E. A., Lukin, M. D. & Taylor, J. M. Robust optical delay lines with topological protection. *Nat. Phys.* **7**, 907–912 (2011).
45. Hafezi, M., Mittal, S., Fan, J., Migdall, A. & Taylor, J. Imaging topological edge states in silicon photonics. *Nat. Photonics* **7**, 1001–1005 (2013).
46. Xiao, B. et al. Exciting reflectionless unidirectional edge modes in a reciprocal photonic topological insulator medium. *Phys. Rev. B* **94**, 195427 (2016).
47. Johnson, S. G., Fan, S., Villeneuve, P. R., Joannopoulos, J. D. & Kolodziejski, L. Guided modes in photonic crystal slabs. *Phys. Rev. B* **60**, 5751 (1999).
48. Lu, J. et al. Dirac cones in two-dimensional artificial crystals for classical waves. *Phys. Rev. B* **89**, 134302 (2014).
49. Lu, J., Qiu, C., Ke, M. & Liu, Z. Valley vortex states in sonic crystals. *Phys. Rev. Lett.* **116**, 093901 (2016).
50. Mei, J., Wu, Y., Chan, C. & Zhang, Z.-Q. First-principles study of Dirac and Dirac-like cones in phononic and photonic crystals. *Phys. Rev. B* **86**, 035141 (2012).
51. Wang, H., Xu, L., Chen, H. & Jiang, J.-H. Three-dimensional photonic Dirac points stabilized by point group symmetry. *Phys. Rev. B* **93**, 235155 (2016).
52. Ezawa, M. Topological Kirchhoff law and bulk-edge correspondence for valley Chern and spin-valley Chern numbers. *Phys. Rev. B* **88**, 161406 (2013).
53. Brendel, C., Peano, V., Painter, O. & Marquardt, F. Snowflake topological insulator for sound waves. Preprint at <https://arxiv.org/abs/1701.06330> (2017).
54. Fukui, T., Hatsugai, Y. & Suzuki, H. Chern numbers in discretized Brillouin zone: efficient method of computing (spin) Hall conductances. *J. Phys. Soc. Jpn* **74**, 1674–1677 (2005).

## Acknowledgements

We thank C.T. Chan and M. Xiao for fruitful discussions. The work is supported by the Areas of Excellence Scheme grant (AOE/P-02/12) from Research Grant Council (RGC) of Hong Kong, and the Special Fund for Agro-scientific Research in the Public Interest from Ministry of Agriculture of the Peoples' Republic of China (no. 201303045), and two grants from National Natural Science Foundation of China (NSFC) (no. 11574037 and no. 91630205).

## Author contributions

X.W. and W.W. conceived the original idea. X.W., D.H. and Y.M. performed the simulations and derived the theory. Y.H. supported the fabrication process of the sample. X.W. and Y.M. carried out the experiments. H.X. helped in the experiment setup. X.W., D.H., Y.M. and J.T. analyzed the data, prepared the figures, and wrote the manuscript. W.W. and D.H. supervised the project. All authors contributed to scientific discussions of the manuscript.

## Additional information

**Supplementary Information** accompanies this paper at doi:10.1038/s41467-017-01515-2.

**Competing interests:** The authors declare no competing financial interests.

**Reprints and permission** information is available online at <http://npg.nature.com/reprintsandpermissions/>

**Publisher's note:** Springer Nature remains neutral with regard to jurisdictional claims in published maps and institutional affiliations.



**Open Access** This article is licensed under a Creative Commons Attribution 4.0 International License, which permits use, sharing, adaptation, distribution and reproduction in any medium or format, as long as you give appropriate credit to the original author(s) and the source, provide a link to the Creative Commons license, and indicate if changes were made. The images or other third party material in this article are included in the article's Creative Commons license, unless indicated otherwise in a credit line to the material. If material is not included in the article's Creative Commons license and your intended use is not permitted by statutory regulation or exceeds the permitted use, you will need to obtain permission directly from the copyright holder. To view a copy of this license, visit <http://creativecommons.org/licenses/by/4.0/>.

© The Author(s) 2017



## APPLIED SCIENCES AND ENGINEERING

## Eye motion triggered self-powered mechnosensational communication system using triboelectric nanogenerator

Xianjie Pu,<sup>1\*</sup> Hengyu Guo,<sup>1,2\*</sup> Jie Chen,<sup>1</sup> Xue Wang,<sup>1</sup> Yi Xi,<sup>1</sup> Chenguo Hu,<sup>1†</sup> Zhong Lin Wang<sup>2†</sup>

Mechnosensational human-machine interfaces (HMIs) can greatly extend communication channels between human and external devices in a natural way. The mechnosensational HMIs based on biopotential signals have been developing slowly owing to the low signal-to-noise ratio and poor stability. In eye motions, the corneal-retinal potential caused by hyperpolarization and depolarization is very weak. However, the mechanical micromotion of the skin around the corners of eyes has never been considered as a good trigger signal source. We report a novel triboelectric nanogenerator (TENG)-based micromotion sensor enabled by the coupling of triboelectricity and electrostatic induction. By using an indium tin oxide electrode and two opposite tribomaterials, the proposed flexible and transparent sensor is capable of effectively capturing eye blink motion with a super-high signal level (~750 mV) compared with the traditional electrooculogram approach (~1 mV). The sensor is fixed on a pair of glasses and applied in two real-time mechnosensational HMIs—the smart home control system and the wireless hands-free typing system with advantages of super-high sensitivity, stability, easy operation, and low cost. This TENG-based micromotion sensor is distinct and unique in its fundamental mechanism, which provides a novel design concept for intelligent sensor technique and shows great potential application in mechnosensational HMIs.

## INTRODUCTION

Human beings have never stopped their pursuit of making their life more convenient and fascinating. A human-machine interface (HMI)—a novel communication channel between a human and an external device—is one way to turn a virtual thought into realistic action. Unlike traditional HMIs as hand operation, speech input, etc., HMIs based on bioelectrical signals (1–4) have advantages of “hands-free” or “aphasia,” especially for patients suffering from amyotrophic lateral sclerosis. To date, the bioelectrical signals applied to HMIs include neuron signals (1, 2, 5), as well as electrocorticogram (6), electroencephalogram (EEG) (3), electromyogram (EMG) (7), electrooculogram (EOG) signals (8–10), etc. Among these techniques, EEG, EMG, and EOG are noninvasive. EEG-based HMI is the most commonly used method and has been proven useful for paralyzed patients to communicate with the external world to relatively low cost (3, 11). However, the low signal-to-noise ratio (SNR) of the scalp-recorded EEG signals (in microvolts), the lack of efficient resolution in modeling, and consequently higher requirements for the classification algorithm (12, 13), as well as a long period of training, limit the wide use of EEG-based HMIs (14). Furthermore, a multielectrode with electrolyte gel [usually named “wet electrode” (15)] takes much time to prepare, and the gel can only keep excellent electrical conductivity for 2 hours. These drawbacks make EEG-based HMIs stable only under favorable laboratory conditions, and unstable in daily life because of various disturbances, including mechanical artifacts such as EMG and EOG signals (4). Nevertheless, EMG and EOG can be used as good control signals for healthy people and even “lock-in” patients who could still blink their eyes (16). As to these people, EMG and EOG techniques are more practical for everyday situations than EEG-based HMIs (4, 16). In particular for EOG, it is a technique serving both healthy and disabled persons. EOG is based on signal collection from the corneal-retinal potential difference

in the process of eye movements. The fundus is usually defined as the negative pole and the cornea as the positive pole (17). The potential difference is determined in principle at least on two exposed electrodes (usually Ag/AgCl electrodes as wet electrodes) pasted around the sensitive eyes, which bring discomfort and poor aesthetics. In addition, the amplitude of EOG is very weak, ranging between 50  $\mu$ V and 3.5 mV (17), which is often masked by noise and difficult to detect without sophisticated and expensive electronics. Also, as for these weak signals, facial muscle movement can easily produce artifacts (17). Therefore, EOG would be inappropriate for some applications, such as driving a car, piloting a plane, or operating a motorized wheelchair. A noninvasive and sensitive aesthetic sensor that is usable, stable, and comfortable is desired for serving the particular groups of people discussed above to solve these problems in bioelectrical-based HMI systems.

In recent years, the fast development of nanotechnology has provided possible strategies for problems in the field of bioelectric signal collection and HMIs (18–20). Among these technologies, a new system—the triboelectric nanogenerator (TENG) (21–24)—was invented and quickly developed on the basis of contact electrification and electrostatic induction (25, 26), with unique advantages of high output, low cost, light weight, applicability of structure design, prominent stability, robustness, etc. (27–30). Because TENGs can generate electricity from almost all types of mechanical motions, including touching (31), sliding (32, 33), rotation (34, 35), vibration (36), etc., they can serve as self-powered sensors for a similarly wide range of motions, such as touch/pressure sensors (37), vibration sensors (38), biomechanical sensors (39), electronic skin sensors (40), acoustic sensors (41), pulse wave sensors (42), synthesized multifunctional sensors (43), and more. For the pulse wave sensor, Yang *et al.* (42) have reported a bionic membrane sensor that non-invasively monitors the extremely weak arterial pulse from the subject's carotid artery, chest, and wrist. This inspired us to consider whether a TENG-based micromotion sensor could be used as a novel sensing device as an alternative to traditional EOG technique and could make a significant breakthrough on the mechnosensational HMI.

Here, a noninvasive, highly sensitive (~750 mV), easy-to-fabricate, stable, small, light, transparent, flexible, skin-friendly, low-cost, durable, and reusable TENG-based sensor for translating the real-time micromotion

<sup>1</sup>Department of Applied Physics, Chongqing University, Chongqing 400044, P. R. China. <sup>2</sup>Beijing Institute of Nanoenergy and Nanosystems, Chinese Academy of Sciences, National Center for Nanoscience and Technology, Beijing 100083, P. R. China.

\*These authors contributed equally to this work.

†Corresponding author. Email: hucg@cqu.edu.cn (C.H.); zhong.wang@mse.gatech.edu (Z.L.W.)

of eye blink into control command is presented. This mechnosensational TENG (msTENG) [as a sensor, it can be regarded as a type of the present ongoing “dry electrode” (15, 19)] with a multifilm structure is designed on the basis of a single-electrode mode and thus could be flexibly mounted and hidden behind an eyeglass arm to form a wearable sensor (44). The voltage curves of the device with different parameter structures are tested systematically, and synchronous measurement illustrates that voltage amplitude from the msTENG is significantly larger (hundred times) than that from an EOG. On the basis of this high sensitivity, the as-fabricated msTENG smart sensor glasses are used to control household appliances with a simple signal processing circuit. Furthermore, a wireless module is introduced to develop a hands-free virtual keyboard typing system. This work for the first time brings a TENG-based sensor to the field of mechnosensational HMIs, and it promises to make a significant breakthrough on mechnosensational HMIs in conditions of daily life.

## RESULTS

As illustrated in Fig. 1A, the circular msTENGs are mounted on the inner side arms of ordinary glasses with adjustable fixators in consideration of invisibility, aesthetics, and convenience. The small fixator (Fig. 1A, 1) assembled with two acrylic sheets, two screws, and two springs provides a flexible mechanical support for the msTENGs. The msTENG (Fig. 1A, 2) designed in the single-electrode mode has a multilayered structure using a thin layer of polyethylene terephthalate (PET) in a tadpole-like shape as a supporting substrate. A fluorinated ethylene propylene (FEP) thin film as one electrification layer coated with indium tin oxide (ITO) as the back electrode is laminated onto the PET substrate. The natural latex used as the opposite electrification layer, which will contact the skin near the eyes, is located on the top. Compared with other thin films, such as nylon and synthetic latex, the natural latex has advantages of super-high elasticity, high tensile strength, air permeability, durability, and being skin-friendly for sensitive eyes. To realize vertical contact/separation, we tightly attached an acrylic thin annulus as a spacer between the natural latex film and the FEP layer. The thickness and diameter of the annulus will determine the pressure detection limit and range of the msTENG. The tiny cylindrical cavity formed between the natural latex and FEP serves as an air spacer for the charge generation and transfer. Five pores with diameters of 0.5 mm are punched through the PET, ITO, and FEP layers, acting as air breathing channels. Fabrication of the TENG-based sensor is described in the Materials and Methods section. Photographs in Fig. 1 (B to D) illustrate a pair of glasses mounted with msTENG on its arms, the simple fixator, and the flexible and transparent msTENG (transmittance is shown in fig. S1). To enhance triboelectrification, we created vertically aligned polymer nanowires onto the FEP surface for better contact with the natural latex. A scanning electron microscopy (SEM) image of FEP nanowires is shown in Fig. 1A2 (inset).

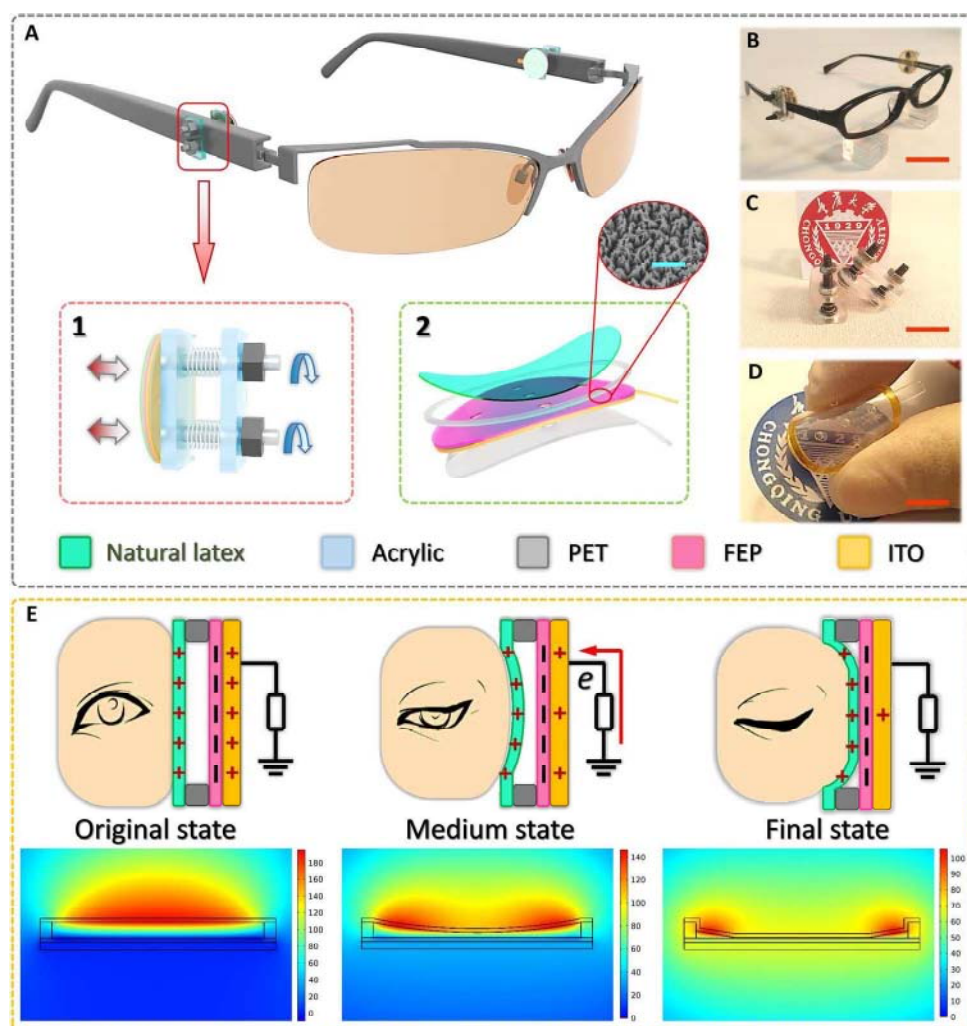
The working principle of the msTENG is based on the coupling of contact electrification and electrostatic induction. The electricity generation process when the eye is blinking is illustrated in Fig. 1E. Here, both the schematic diagram of charge distribution (top) and simulation of potential distribution by COMSOL (bottom) are presented. In the original eye-open stage, there are positive charges on the natural latex and negative charges on FEP, which are obtained by several friction cycles between the natural latex and FEP layers. In the middle stage of the eye-blinking process, the muscle around the eye pushes the natural latex film close to the FEP layer. As the potential difference between the two layers gradually becomes lower, the electrons flow to the ITO

electrode from the ground in the external circuit. When the eye is fully closed at the final stage, the natural latex film is then in contact with the FEP layer in a large area, so the bound charges are almost in neutralization. Consequently, because there is almost no potential difference across the ITO electrode and ground, the electron flow stops, and then, when the eye is back to open stage, there is an opposite current flowing in the external circuit. This is the full cycle of the electricity generation process.

To characterize the performance of the msTENG sensor, a computer-controlled linear motor and a force gauge are used. At the skin-contact side of msTENG, a silicon rubber pad is used to simulate the skin, and it is fixed on a linear motor tip to apply pressure uniformly onto the natural latex film. Meanwhile, at the other side of the msTENG, a small glass plate with the same dimension is placed between the PET substrate and the tip of the force gauge. As shown in Fig. 2A, the applied pressures and corresponding output voltage under variable deformation degrees from 0.8 to 1.0 mm are measured at a contact-separate frequency of 0.5 Hz. In a cycle of the dynamic deformation, increasing and decreasing pressure is realized through a linear motor, which simulates the deformation induced by eye blinking. From the curves in Fig. 2A, we can see that stronger blinking induces a better signal. To further investigate the frequency response and stability of the msTENG, we measured the voltage signals under an applied pressure of 1 N at deformation frequencies of 0.5, 1.0, 1.5, 2.0, and 3.0 Hz (Fig. 2B). Short-circuit current at different frequencies and a durability test for 10,000 cycles are shown in figs. S2 and S3, respectively. The voltage amplitude reveals a high repeatability, stability, and durability of the msTENG. It is also noted that both the open-circuit voltage and the load voltage increase significantly with a rise in frequency, meaning that a stronger signal can be obtained when the eye blinks faster. To summarize the results of Fig. 2 (A and B), we can conclude that voluntary and fast blinking is different from an involuntary light blink (to be discussed later in the paper), showing that the msTENG has great potential in stable and reliable mechnosensational controlling.

Furthermore, the influence of gap and area size of the air spacer in the msTENG is evaluated (Fig. 2, C and D, respectively). The dynamic pressure is applied with a constant frequency of 1 Hz. Figure 2C shows that when a light force (for example, <2 N) is applied, the msTENG is more sensitive to that force when there is a smaller gap (a larger output voltage under the same force). On the other hand, a smaller gap means a smaller linear range and quicker saturation. Notably, when the gap is relatively large (such as 0.8 mm in Fig. 2C), voltage versus pressure response curve exhibits two distinct regions with different slopes. To theoretically explain the result, we used the finite element method (FEM) to simulate the approaching and contacting process. The result is shown in fig. S4, which matches well the experimental results. In Fig. 2C, in the low-applied pressure region (<4 N), a lower pressure sensitivity is experimentally observed, whereas in the high-pressure region (>4 N), well-behaved linear variation in the output voltage shows a superior pressure sensitivity. This tells us that the msTENG can be used as a microforce (also, deformation or motion) sensor, and different gaps are needed to make the msTENG work in linear range in different applications. For the area size of the air spacer, Fig. 2D shows that higher sensitivity to force is obtained under a larger area, but the voltage curve is quicker to saturation. To summarize the results of Fig. 2 (C and D), a larger area size and a smaller gap create superior sensitivity to the microdeformation caused by blinking.

Synchronous measurement is taken to compare the output sensitivity of the as-fabricated msTENG with traditional EOG. Figure 2E illustrates the sensor placement method for msTENG and EOG. For the msTENG, one skin-friendly sensor is concealed on the eyeglass arms, whereas for the EOG, two exposed Ag/AgCl electrodes are firmly pasted

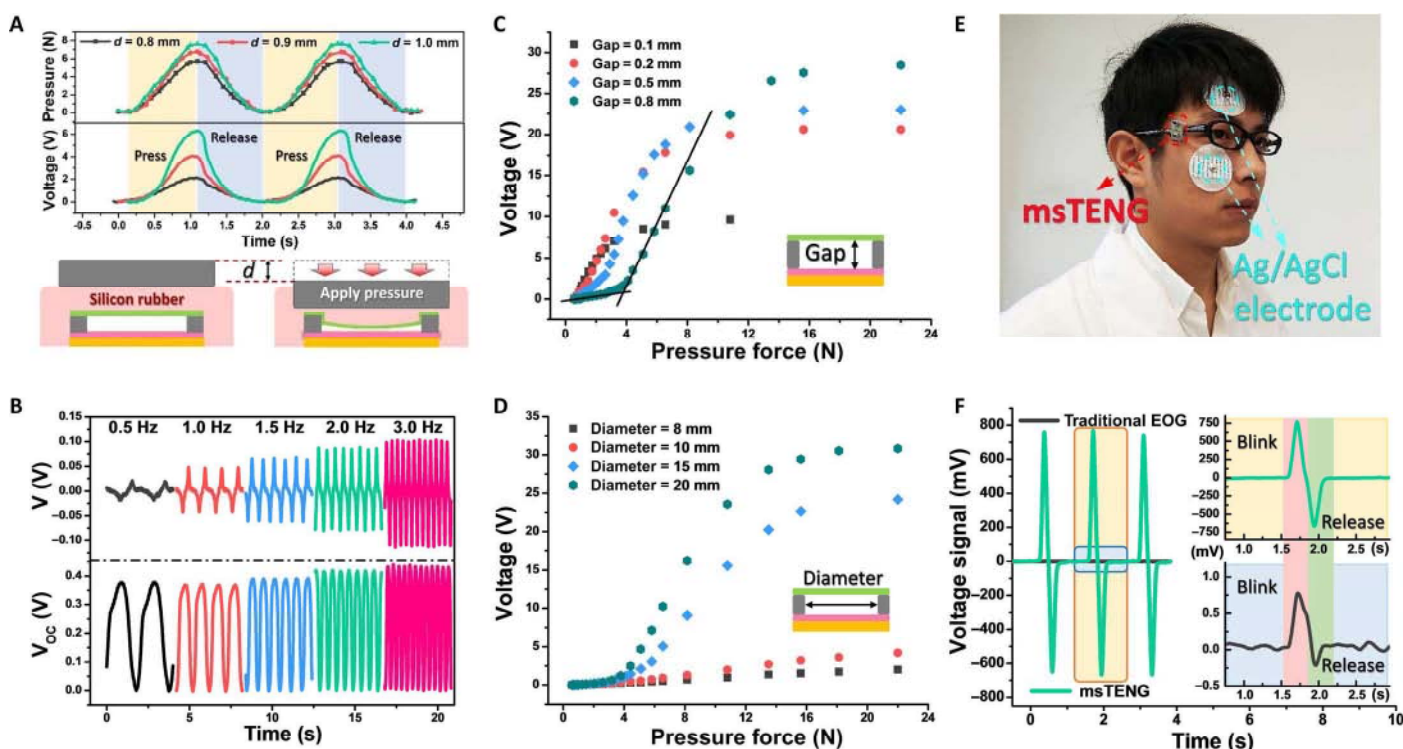


**Fig. 1. Structure, and working mechanism of the msTENG.** (A) Schematic structure of a pair of ordinary glasses mounted with msTENG. Bottom left: Structure of the fixing device for convenient adjustment. Bottom right: Schematic diagram of the msTENG. Inset: An SEM image of FEP nanowires. Scale bar, 5  $\mu\text{m}$ . (B) Photograph of an ordinary glasses mounted with an as-fabricated msTENG. Scale bar, 2 cm. (C and D) Photographs of the simple fixator (C) and the flexible and transparent msTENG (D). Scale bars, 1 cm. (E) Schematics of the operating principle of msTENG. Top: Charge behavior when the eye is at different states during the blinking process. Bottom: Potential simulation by COMSOL to elucidate the working principle.

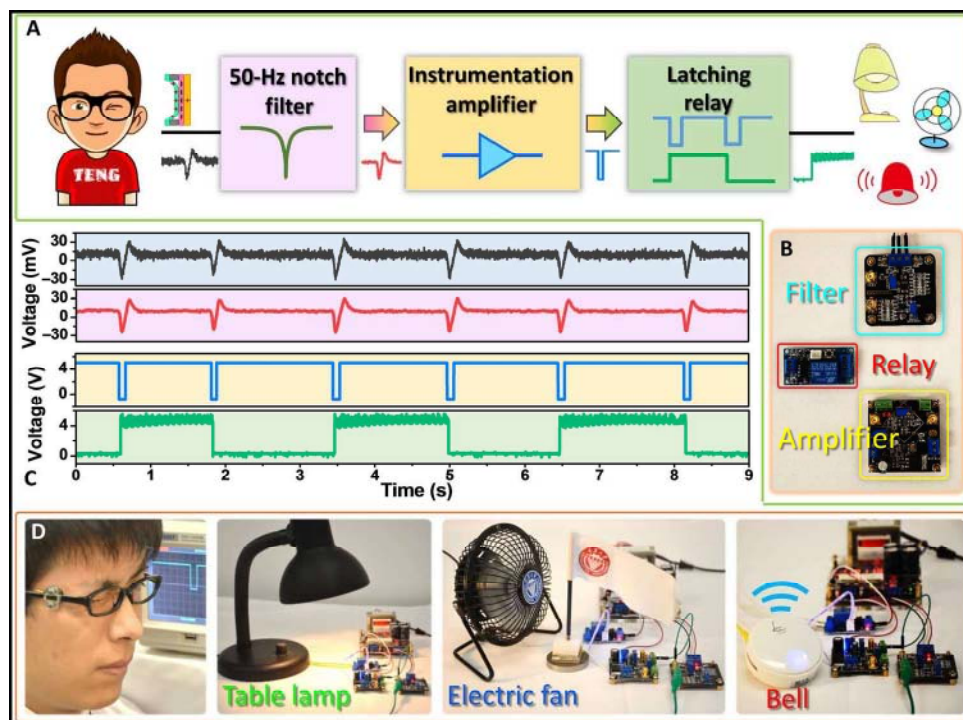
around sensitive eyes, which would lead to dim sight because of the connecting lead (the principle of EOG measurement is shown in fig. S5). A real-time profile of the output voltage from msTENG and EOG is demonstrated in Fig. 2F. The insets show a compressed view of the msTENG signal (top) and an enlarged view of the EOG signal (bottom) in one cycle, indicating that an output signal from msTENG is much larger (more than 750 times) than that from EOG within the same response time. This result demonstrates the high sensitivity of the msTENG, and it is superior to any EOG reported in literature. A super-high sensitivity in an equal response time warrants the use of the msTENG to detect micromotions of eye blinking as a control signal in HMI.

On the basis of the strong advantages of the msTENG demonstrated above, we develop a smart home control system, comprised of a person, a pair of glasses mounted with the msTENG, a simple signal processing circuit, and some electrical appliances, such as a table lamp, an electric fan, and a doorbell (Fig. 3A). The signal processing circuit consists of three parts: a 50-Hz notch filter to eliminate power-line interference, an AD623-based instrumentation amplifier to amplify the filtered signal to

drive a relay, and a latching relay based on a single-chip microcomputer (SCM). For conditioning other signals such as EEG, EOG, etc., the circuit should always include more parts (10), aside from those illustrated above because of their poor SNR. Three small real circuit boards ( $\leq 5 \times 5$  cm) are shown in Fig. 3B (a detailed diagram is shown in fig. S6). The procedure of signal processing based on these circuits is presented in Fig. 3C. From top to bottom, the first signal is the original blinking signal from the msTENG, followed by the signals after being filtered, amplified, and relay-converted, respectively. Then, the output terminal of latching relay is connected in series with the electrical appliances (lamp, fan, or bell, as shown in Fig. 3D) and a power outlet. When a user is blinking, the signal detected by the msTENG attached to the skin of the in-task eye is conditioned and converted into a switching signal for the electrical appliances (Fig. 3D and movies S1 to S3). This demonstration presents many potential applications for the msTENG in daily life, such as hands-free phone answering while driving, ringing a doorbell when a person's two hands are fully occupied, self-care for the disabled, and so on. The msTENG functions as the extra hand you always dream of.



**Fig. 2. Characterizing the performance of msTENG.** (A) Measurement of the force and output voltage under variable deformation degrees from 0.8 to 1.0 mm. In this measurement, silicon rubber was used to simulate the skin. (B) Load voltage (top) and open-circuit voltage (bottom) of the msTENG under different deformation frequency from 0.5 to 3.0 Hz. (C and D) The influence of gap distance (C) and area size (D). (E) Demonstration of eye movement signal acquisition through msTENG versus EOG. (F) Synchronous measurement of voltage signals from msTENG and EOG. Top right: Compressed curve from msTENG. Bottom right: Enlarged curve from EOG.



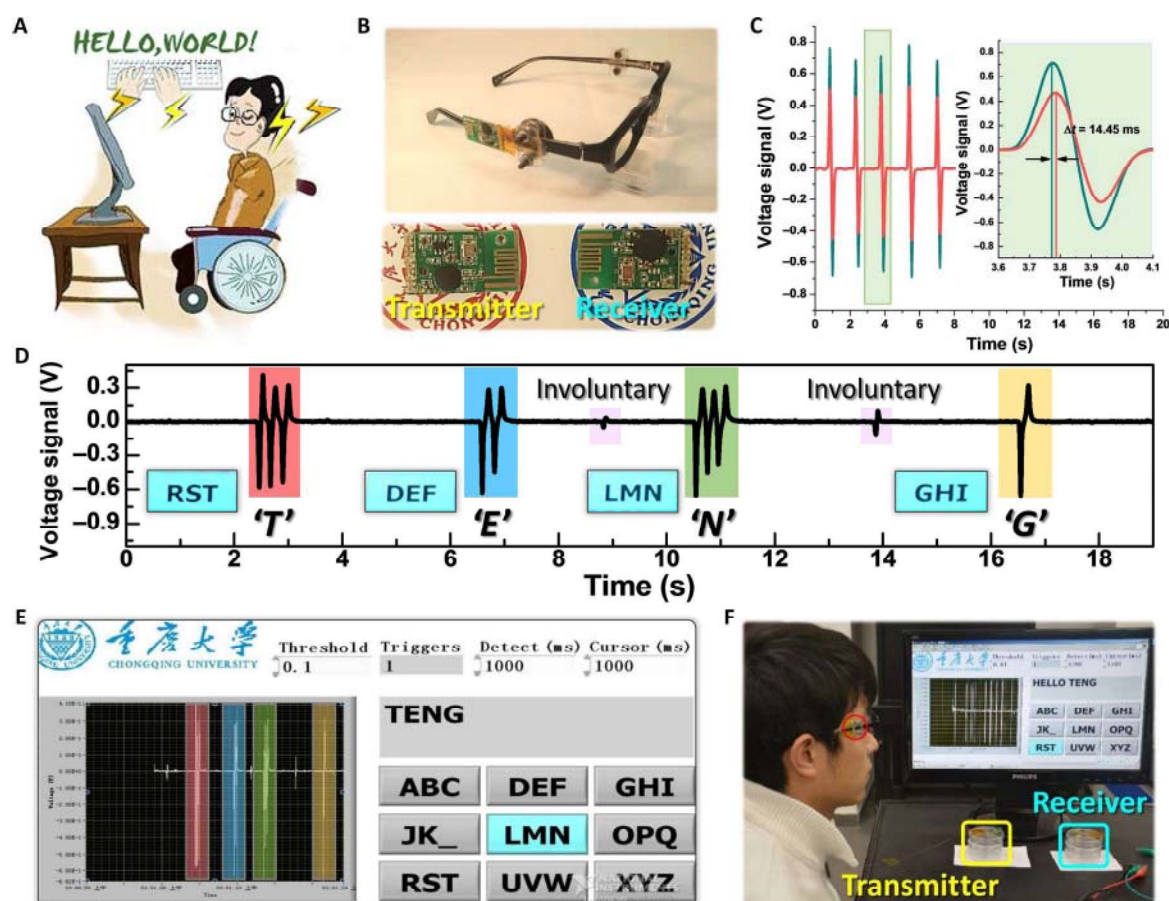
**Fig. 3. Application of the msTENG in smart home control for both healthy and disabled people.** (A) Scheme diagram of an msTENG-involved smart home control system. After simple filtering and amplifying, a blinking signal can be converted into a trigger signal to control the appliances. (B) The circuits for signal conditioning. (C) From top to bottom, the first signal is the original blinking signal from the msTENG, and as follows are the signals after being filtered, amplified, and converted, respectively. (D) Demonstration of the controlling of a table lamp, an electric fan, and a doorbell.

To make the msTENG easier to use, a wireless transceiver module is utilized, and then, a hands-free typing system (typing with eye blinking) is developed (Fig. 4A). Figure 4B shows the smart sensor glasses fabricated with the transmitter module. All the devices in this sensor system are of small sizes and could be encased in a specially designed glasses frame in the future. An eye blink signal from the receiver has a delay of 14.45 ms compared with a wire signal in synchronous measurement (Fig. 4C), which would not affect common operations in daily life. The typing system is designed on the basis of the virtual instrument software platform LabVIEW as a virtual keyboard in the front panel (Fig. 4E). On this keyboard, all the letters (A to Z) and a spacebar (“\_”, set after “JK,” as shown in Fig. 4E) are divided into nine groups. The blue cursor keeps shifting to each of these groups at a certain speed [for example, 1000 ms per group, set in a box of “Cursor (ms)”. To select a letter in a group when the cursor is shifting on it, the user is supposed to voluntarily blink over a specified period of time [for example, 1000 ms, set in a box of “Detect (ms)”: once, the first letter will be typed to the above textbox; twice, the second letter; and thrice, the third letter (a query table is illustrated in table S1). Because of a high spelling success rate (table S2), “backspace” and “clear” are rarely used. Thus, the strategies for “backspace” and “clear” are designed as four and five consecutive voluntary blinks, instead of adding an extra group labeled “backspace” and “clear” on the screen,

which may affect the concision and the spelling efficiency. Furthermore, a more complete scheme of a virtual full keyboard with two channels (for both eyes) is preliminarily framed (fig. S7). The threshold to classify a blink as voluntary or not can be adjusted according to each individual. The process flow of the whole typing system is illustrated in fig. S8. In Fig. 4E, the word “TENG” has been typed with eye blinking by a user. Each signal corresponding to a certain letter is enlarged in Fig. 4D, from which we could understand the operating process and attest the significant difference between voluntary and involuntary blink, as predicted in Fig. 2. To verify the performance of this wireless virtual keyboard typing system, a user with two trials to find the best msTENG placement demonstrates a simple operation process (Fig. 4F and movie S4). Excellent performance of this system could be proof for the msTENG as a super-sensitive sensor to be applied in computer control. We believe that on the basis of the msTENG, many kinds of mechnosensational computer games will spring out to make life more fascinating.

## DISCUSSION

Nowadays, keeping pace with the rapid development of artificial intelligence is an important and urgent task for the sensor technology. Here,



**Fig. 4. Application of the msTENG in a hands-free typing system.** (A) Sketch of the msTENG as a way to help people suffering from “locked-in syndrome” to communicate with the world. (B) The msTENG glasses are assembled with wireless transceiver module to make it easier to use. (C) Synchronous acquisition of wired (green) versus wireless (red) signal. (D) Correspondence between signals and letters typed in the demonstration of a hands-free typing system (E) with adjustable threshold, detecting time, and cursor shift interval. (F) Demonstration of the msTENG-based hands-free wireless typing system. The words on the screen are typed with eye blinking.

we have developed a TENG-based, highly sensitive, noninvasive micro-motion sensor that is skin-friendly, reusable, small, and light to translate eye blink to control command for HMIs and have mounted it on the arms of glasses to construct two practical HMI systems—the smart home control system and the hands-free typing system. Both systems performed extremely well on the basis of simple hardware circuit and software program. These systems are merely ordinary demonstrations that bring us inspiration to apply new technology to a traditional research field. To benefit from TENG, the msTENG sensor is distinct and unique in its fundamental mechanism, which can effectively avoid problems, such as poor SNR and inconvenient operation in mechno-sensational HMIs. Moreover, considering the easy fabrication process and the common materials used, the msTENG sensor is cost-effective and suitable for mass production to serve people dependent on ambient intelligence. With the innovative assembly of msTENGs in different body places, people can foresee great potential of TENG-based sensors in intelligent robotics.

## MATERIALS AND METHODS

### Fabrication of the TENG-based sensor

The fabrication process of the msTENG started from a piece of PET slice. Typically, a PET film (thickness, ~0.2 mm) was cut into tadpole-like pieces (head, diameter of 15 mm; tail, rectangle of 5 × 2 mm) to act as the substrate and the single electrode using a laser cutter after depositing an ITO layer (~50 nm) by electron beam deposition. Then, a nanostructured FEP film (thickness, 20 μm; etched by inductively coupled plasma-reactive ion etching) was adhered over the ITO layer to work as the negative tribolayer. It should be noted that several pores should be created on the as-prepared bottom slice to avoid forming an enclosed chamber. Later, a PET film (thickness, ~0.2 mm) was cut into an annulus (outer diameter, 15 mm; inner diameter, 13 mm), followed by covering a natural latex film (thickness, 0.05 mm) to work as the positive tribolayer. Finally, the as-prepared two parts were assembled to msTENG.

### Signal processing circuit

To convert the raw signal into a command, it is necessary to filter the power-line interference and to amplify the filtered signal. First, a two-stage twin-T 50-Hz notch filter with tunable Q-factor (a detailed diagram is shown in fig. S6) was adopted. Then, the filtered signal was amplified by an AD623-based instrumentation amplifying circuit with tunable magnification and dc bias (fig. S6). All the parameters were adjusted carefully to meet the needs of command translation. The commercial latching relay based on a programmed SCM was easy to be driven by the processed signal.

### Characterization and measurement

Field-emission SEM (Hitachi SU8010) was used to characterize the surface morphology of the nanostructured FEP film. For the electric output measurement of the TENG-based sensor, a linear motor (LinMot E1100) was used to form alternative motions and drive the sensor to contact and separate for quantified measurement. Meanwhile, a force meter was also used to measure the corresponding pressure force. A programmable electrometer (Keithley 6514) was adopted to test the open-circuit voltage and short-circuit current. In addition, NI 6259 was used to collect data. A software platform was constructed on the basis of LabVIEW, which is capable of realizing real-time data acquisition control and analysis.

## SUPPLEMENTARY MATERIALS

Supplementary material for this article is available at <http://advances.sciencemag.org/cgi/content/full/3/7/e1700694/DC1>

- fig. S1. Transmittance spectra of the msTENG.
- fig. S2. Short-circuit current curve of the msTENG under various working frequencies.
- fig. S3. Durability test of the msTENG during 10,000 working cycles.
- fig. S4. The voltage distribution on the sensor under different displacements by FEM simulation in Fig. 2C.
- fig. S5. Principle of EOG measurement.
- fig. S6. Main circuit diagrams for conditioning signal from TENG.
- fig. S7. Virtual full keyboard with grouping strategy.
- fig. S8. Process flow of the typing system.
- table S1. Query table for eye blink typing.
- table S2. Success rate of the eye blink typing test.
- movie S1. Demonstration of the msTENG in controlling a table lamp.
- movie S2. Demonstration of the msTENG in controlling an electric fan.
- movie S3. Demonstration of the msTENG in controlling a doorbell.
- movie S4. Demonstration of the msTENG-based hands-free wireless typing system.

## REFERENCES AND NOTES

1. L. R. Hochberg, Turning thought into action. *N. Engl. J. Med.* **359**, 1175–1177 (2008).
2. L. R. Hochberg, D. Bacher, B. Jarosiewicz, N. Y. Masse, J. D. Simeral, J. Vogel, S. Haddadin, J. Liu, S. S. Cash, P. van der Smagt, J. P. Donoghue, Reach and grasp by people with tetraplegia using a neurally controlled robotic arm. *Nature* **485**, 372–375 (2012).
3. N. Birbaumer, N. Ghanayim, T. Hinterberger, I. Iversen, B. Kotchoubey, A. Kubler, J. Perelmouter, E. Taub, H. Flor, A spelling device for the paralysed. *Nature* **398**, 297–298 (1999).
4. M. A. Lebedev, M. A. L. Nicolelis, Brain-machine interfaces: Past, present and future. *Trends Neurosci.* **29**, 536–546 (2006).
5. L. R. Hochberg, M. D. Serruya, G. M. Friehs, J. A. Mukand, M. Saleh, A. H. Caplan, A. Branner, D. Chen, R. D. Penn, J. P. Donoghue, Neuronal ensemble control of prosthetic devices by a human with tetraplegia. *Nature* **442**, 164–171 (2006).
6. E. C. Leuthardt, G. Schalk, J. R. Wolpaw, J. G. Ojemann, D. W. Moran, A brain-computer interface using electrocorticographic signals in humans. *J. Neural Eng.* **1**, 63–71 (2004).
7. R. Okuno, M. Yoshida, K. Akazawa, Compliant grasp in a myoelectric hand prosthesis. *IEEE Eng. Med. Biol. Mag.* **24**, 48–56 (2005).
8. X. Guo, W. Pei, Y. Wang, Y. Chen, H. Zhang, X. Wu, X. Yang, H. Chen, Y. Liu, R. Liu, A human-machine interface based on single channel EOG and patchable sensor. *Biomed. Signal Process. Control* **30**, 98–105 (2016).
9. A. N. Belkacem, D. Shin, H. Kambara, N. Yoshimura, Y. Koike, Online classification algorithm for eye-movement-based communication systems using two temporal EEG sensors. *Biomed. Signal Process. Control* **16**, 40–47 (2015).
10. A. B. Usakli, S. Gurkan, Design of a novel efficient human-computer interface: An electrooculogram based virtual keyboard. *IEEE Trans. Instrum. Meas.* **59**, 2099–2108 (2010).
11. X. Chen, Y. Wang, M. Nakanishi, X. Gao, T.-P. Jung, S. Gao, High-speed spelling with a noninvasive brain-computer interface. *Proc. Natl. Acad. Sci. U.S.A.* **112**, E6058–E6067 (2015).
12. T. Zhang, T. Liu, F. Li, M. Li, D. Liu, R. Zhang, H. He, P. Li, J. Gong, C. Luo, D. Yao, P. Xu, Structural and functional correlates of motor imagery BCI performance: Insights from the patterns of fronto-parietal attention network. *Neuroimage* **134**, 475–485 (2016).
13. W. Speier, C. Arnold, N. Pouratian, Integrating language models into classifiers for BCI communication: A review. *J. Neural Eng.* **13**, 031002 (2016).
14. J. R. Wolpaw, N. Birbaumer, D. J. McFarland, G. Pfurtscheller, T. M. Vaughan, Brain-computer interfaces for communication and control. *Clin. Neurophysiol.* **113**, 767–791 (2002).
15. E. Forvi, M. Bedoni, R. Carabona, M. Soncini, P. Mazzoleni, F. Rizzo, C. O'Mahony, C. Morasso, D. G. Cassarà, F. Gramatica, Preliminary technological assessment of microneedles-based dry electrodes for biopotential monitoring in clinical examinations. *Sens. Actuators A Phys.* **180**, 177–186 (2012).
16. N. Birbaumer, Brain-computer-interface research: Coming of age. *Clin. Neurophysiol.* **117**, 479–483 (2006).
17. R. Barea, L. Boquete, M. Mazo, E. Lopez, System for assisted mobility using eye movements based on electrooculography. *IEEE Trans. Neural Syst. Rehabil. Eng.* **10**, 209–218 (2003).
18. T. Someya, Z. Bao, G. G. Malliaras, The rise of plastic bioelectronics. *Nature* **540**, 379–385 (2016).
19. J.-W. Jeong, W.-H. Yeo, A. Akhtar, J. J. S. Norton, Y.-J. Kwack, S. Li, S.-Y. Jung, Y. Su, W. Lee, J. Xia, H. Cheng, Y. Huang, W.-S. Choi, T. Bretl, J. A. Rogers, Materials and optimized

- designs for human-machine interfaces via epidermal electronics. *Adv. Mater.* **25**, 6839–6846 (2013).
20. C. Xie, L. Hanson, W. Xie, Z. Lin, B. Cui, Y. Cui, Noninvasive neuron pinning with nanopillar arrays. *Nano Lett.* **10**, 4020–4024 (2010).
  21. G. Zhu, J. Chen, Y. Liu, P. Bai, Y. S. Zhou, Q. Jing, C. Pan, Z. L. Wang, Linear-grating triboelectric generator based on sliding electrification. *Nano Lett.* **13**, 2282–2289 (2013).
  22. G. Zhu, J. Chen, T. Zhang, Q. Jing, Z. L. Wang, Radial-arrayed rotary electrification for high performance triboelectric generator. *Nat. Commun.* **5**, 3426 (2014).
  23. G. Zhu, B. Peng, J. Chen, Q. Jing, Z. L. Wang, Triboelectric nanogenerators as a new energy technology: From fundamentals, devices, to applications. *Nano Energy* **14**, 126–138 (2015).
  24. Z. L. Wang, J. Chen, L. Lin, Progress in triboelectric nanogenerators as a new energy technology and self-powered sensors. *Energy Environ. Sci.* **8**, 2250–2282 (2015).
  25. R. G. Horn, D. T. Smith, Contact electrification and adhesion between dissimilar materials. *Science* **256**, 362–364 (1992).
  26. H. T. Baytekin, A. Z. Patashinski, M. Branicki, B. Baytekin, S. Soh, B. A. Grzybowski, The mosaic of surface charge in contact electrification. *Science* **333**, 308–312 (2011).
  27. J. Chen, G. Zhu, W. Yang, Q. Jing, P. Bai, Y. Yang, T. C. Hou, Z. L. Wang, Harmonic-resonator-based triboelectric nanogenerator as a sustainable power source and a self-powered active vibration sensor. *Adv. Mater.* **25**, 6094–6099 (2013).
  28. H. Guo, J. Chen, M.-H. Yeh, X. Fan, Z. Wen, Z. Li, C. Hu, Z. L. Wang, An ultrarobust high-performance triboelectric nanogenerator based on charge replenishment. *ACS Nano* **9**, 5577–5584 (2015).
  29. H. Guo, M. H. Yeh, Y.-C. Lai, Y. Zi, C. Wu, W. Zhen, C. Hu, Z. L. Wang, All-in-one shape-adaptive self-charging power package for wearable electronics. *ACS Nano* **10**, 10580–10588 (2016).
  30. Z. Wen, M.-H. Yeh, H. Guo, J. Wang, Y. Zi, W. Xu, J. Deng, L. Zhu, X. Wang, C. Hu, L. Zhu, X. Sun, Z. L. Wang, Self-powered textile for wearable electronics by hybridizing fiber-shaped nanogenerators, solar cells, and supercapacitors. *Sci. Adv.* **2**, e1600097 (2016).
  31. G. Zhu, W. Q. Yang, T. Zhang, Q. Jing, J. Chen, Y. S. Zhou, P. Bai, Z. L. Wang, Self-powered, ultrasensitive, flexible tactile sensors based on contact electrification. *Nano Lett.* **14**, 3208–3213 (2014).
  32. H. Guo, L. Qiang, X. He, M. Wang, J. Chen, C. Hu, X. Yi, A triboelectric generator based on checker-like interdigital electrodes with a sandwiched PET thin film for harvesting sliding energy in all directions. *Adv. Energy Mater.* **5**, 1400790 (2015).
  33. Z. Wen, J. Chen, M.-H. Yeh, H. Guo, Z. Li, X. Fan, T. Zhang, L. Zhu, Z. L. Wang, Blow-driven triboelectric nanogenerator as an active alcohol breath analyzer. *Nano Energy* **16**, 38–46 (2015).
  34. H. Guo, J. Chen, Q. Leng, Y. Xi, M. Wang, X. He, C. Hu, Spiral-interdigital-electrode-based multifunctional device: Dual-functional triboelectric generator and dual-functional self-powered sensor. *Nano Energy* **12**, 626–635 (2015).
  35. X. S. Meng, H. Y. Li, G. Zhu, Z. L. Wang, Fully enclosed bearing-structured self-powered rotation sensor based on electrification at rolling interfaces for multi-tasking motion measurement. *Nano Energy* **12**, 606–611 (2015).
  36. G. Liu, H. Guo, L. Chen, X. Wang, D. Wei, C. Hu, Double-induced-mode integrated triboelectric nanogenerator based on spring steel to maximize space utilization. *Nano Res.* **9**, 3355–3363 (2016).
  37. J. Chen, G. Zhu, J. Yang, Q. Jing, P. Bai, W. Yang, X. Qi, Y. Su, Z. L. Wang, Personalized keystroke dynamics for self-powered human-machine interfacing. *ACS Nano* **9**, 105–116 (2015).
  38. Q. Liang, Z. Zhanga, X. Yan, Y. Gu, Y. Zhao, G. Zhang, S. Lu, Q. Liao, Y. Zhang, Functional triboelectric generator as self-powered vibration sensor with contact mode and non-contact mode. *Nano Energy* **14**, 209–216 (2015).
  39. Y. Fang, X. Wang, S. Niu, S. Li, Y. Yin, K. Dai, G. Zhang, L. Long, W. Zhen, H. Guo, J. Wang, M.-H. Yeh, Y. Zi, Q. Liao, Z. You, Y. Zhang, Z. L. Wang, A highly shape-adaptive, stretchable design based on conductive liquid for energy harvesting and self-powered biomechanical monitoring. *Sci. Adv.* **2**, e1501624 (2016).
  40. M. Ma, Z. Zhang, Q. Liao, F. Yi, L. Han, G. Zhang, S. Liu, X. Liao, Y. Zhang, Self-powered artificial electronic skin for high-resolution pressure sensing. *Nano Energy* **32**, 389–396 (2017).
  41. X. Fan, J. Chen, J. Yang, P. Bai, Z. Li, Z. L. Wang, Ultrathin, rollable, paper-based triboelectric nanogenerator for acoustic energy harvesting and self-powered sound recording. *ACS Nano* **9**, 4236–4243 (2015).
  42. J. Yang, J. Chen, Y. Su, Q. Jing, Z. Li, F. Yi, X. Wen, Z. Wang, Z. L. Wang, Eardrum-inspired active sensors for self-powered cardiovascular system characterization and throat-attached anti-interference voice recognition. *Adv. Mater.* **27**, 1316–1326 (2015).
  43. M. Ma, Q. Liao, G. Zhang, Z. Zhanga, Q. Liang, Y. Zhang, Self-recovering triboelectric nanogenerator as active multifunctional sensors. *Adv. Funct. Mater.* **25**, 6489–6494 (2015).
  44. W. Gao, S. Emaminejad, H. Y. Y. Nyein, S. Challa, K. Chen, A. Peck, H. M. Fahad, H. Ota, H. Shiraki, D. Kiriya, D.-H. Lien, G. A. Brooks, R. W. Davis, A. Javey, Fully integrated wearable sensor arrays for multiplexed in situ perspiration analysis. *Nature* **529**, 509–514 (2016).

#### Acknowledgments

**Funding:** This research was supported by the National Natural Science Foundation of China (51572040), the Natural Science Foundation of Chongqing (cstc2014jcyjA50030), the Fundamental Research Funds for the Central Universities (CQDXWL-2014-001), and the National High Technology Research and Development Program (863 Program) of China (2015AA034801). **Author contributions:** X.P., H.G., C.H., and Z.L.W. conceived the idea and designed the msTENG. X.P. and H.G. fabricated the msTENG and designed and performed the experiments. X.P., H.G., C.H., and Z.L.W. analyzed the data and prepared the manuscript. All authors discussed the results and commented on the manuscript. **Competing interests:** Z.L.W., C.H., X.P., and H.G. are authors on a patent application related to this work, filed with the State Intellectual Property Office of the P. R. China (serial no. 2017061400947090, application no. 201710445108.5; filed on 14 June 2017). The other authors declare that they have no competing interests. **Data and materials availability:** All data needed to evaluate the conclusions in the paper are present in the paper and/or the Supplementary Materials. Additional data related to this paper may be requested from the authors.

Submitted 9 March 2017

Accepted 16 June 2017

Published 28 July 2017

10.1126/sciadv.1700694

**Citation:** X. Pu, H. Guo, J. Chen, X. Wang, Y. Xi, C. Hu, Z. L. Wang, Eye motion triggered self-powered mechnosensational communication system using triboelectric nanogenerator. *Sci. Adv.* **3**, e1700694 (2017).

## WEARABLE TECHNOLOGY

# Self-powered textile for wearable electronics by hybridizing fiber-shaped nanogenerators, solar cells, and supercapacitors

Zhen Wen,<sup>1,2,3\*</sup> Min-Hsin Yeh,<sup>1,4\*</sup> Hengyu Guo,<sup>1,5\*</sup> Jie Wang,<sup>1</sup> Yunlong Zi,<sup>1</sup> Weidong Xu,<sup>3</sup> Jianan Deng,<sup>1</sup> Lei Zhu,<sup>6</sup> Xin Wang,<sup>1</sup> Chenguo Hu,<sup>5</sup> Liping Zhu,<sup>2</sup> Xuhui Sun,<sup>3</sup> Zhong Lin Wang<sup>1,7†</sup>

2016 © The Authors, some rights reserved; exclusive licensee American Association for the Advancement of Science. Distributed under a Creative Commons Attribution NonCommercial License 4.0 (CC BY-NC).

Wearable electronics fabricated on lightweight and flexible substrate are believed to have great potential for portable devices, but their applications are limited by the life span of their batteries. We propose a hybridized self-charging power textile system with the aim of simultaneously collecting outdoor sunshine and random body motion energies and then storing them in an energy storage unit. Both of the harvested energies can be easily converted into electricity by using fiber-shaped dye-sensitized solar cells (for solar energy) and fiber-shaped triboelectric nanogenerators (for random body motion energy) and then further stored as chemical energy in fiber-shaped supercapacitors. Because of the all-fiber-shaped structure of the entire system, our proposed hybridized self-charging textile system can be easily woven into electronic textiles to fabricate smart clothes to sustainably operate mobile or wearable electronics.

## INTRODUCTION

Wearable electronics fabricated on lightweight and flexible substrate are widely believed to have great potential for portable devices (1–3). Several promising applications, for example e-skin, smartwatches, and bracelets, have been successfully achieved for the replacement of conventional electronic gadgets (4–6). Lightweight and wearable power supply modules with high energy storage performance are desirable for wearable technology. One strategy is to directly integrate a conventional rechargeable energy storage device, such as a battery or a supercapacitor (SC), into fabrics (7–10). This self-powered system is a favorable power platform to be integrated into wearable electronic systems. Fu *et al.* (11) designed a new type of integrated power fiber by incorporating a dye-sensitized solar cell (DSSC) and a solar cell for harvesting solar energy and storage to realize a self-powered system for driving a commercial light-emitting diode (LED). Du *et al.* (12) also proposed self-powered electronics by integration of flexible graphene-based SCs into perovskite hybrid solar cells. However, a photovoltaic cell works only under sufficient light illumination, and solar energy is not always available, strongly depending on the weather, working conditions, and so on. The intermittent and unpredictable nature of solar energy is an inevitable challenge for its expansion as a reliable power supply system in wearable electronics. The question of how to scavenge alternative energy from the environment with different types of energy harvesters, to compensate for the insufficient part of the solar energy, is urgent.

To develop a practical strategy to simultaneously scavenge multiple types of energies from the environment, the concept of a hybridized energy harvester incorporating two kinds of conversion cells for concurrently scavenging solar and mechanical energies was proposed, so that the energy resources could be effectively and complementarily used (13–18). Triboelectric nanogenerators (TENGs), are based on the coupling effect of contact electrification and electrostatic induction, and these have now been widely studied to harvest different mechanical energies from the environment (19–23). By using TENGs as the power supply, different types of self-powered systems were successfully demonstrated and realized, such as wireless sensors, chemical sensors, electrochemical reactions, home appliances, and security detection systems (24–28). Furthermore, to expand the practical applications of a TENG-based self-powered system, various structure types of flexible TENGs have been designed for harvesting ambient mechanical energy and, more adequately, for integration into wearable electronic devices (29–31). The high operating voltage of SCs can be directly achieved by charging them using a single TENG unit without additional in-series connection, which compensates for insufficient solar energy (32, 33).

Here, we present a prototype of a fabric-hybridized self-charging power system not only for harvesting solar energy from ambient light but also for gathering mechanical energy from human motion. Both of the harvested energies can be easily converted into electricity by using fiber-shaped DSSCs (F-DSSCs) (for solar energy) and fiber-shaped TENGs (F-TENGs) (for mechanical energy) and then further stored as chemical energy in fiber-shaped SCs (F-SCs). Our proposed hybridized self-charging textile not only achieves reasonable energy conversion and storage capacity but also is inexpensive and can be easily fabricated. In addition, because of the all-fiber-based shape in each device, our proposed hybridized self-charging textile system can be easily woven into electronic textiles to fabricate smart clothes which operate wearable electronic devices.

## RESULTS AND DISCUSSION

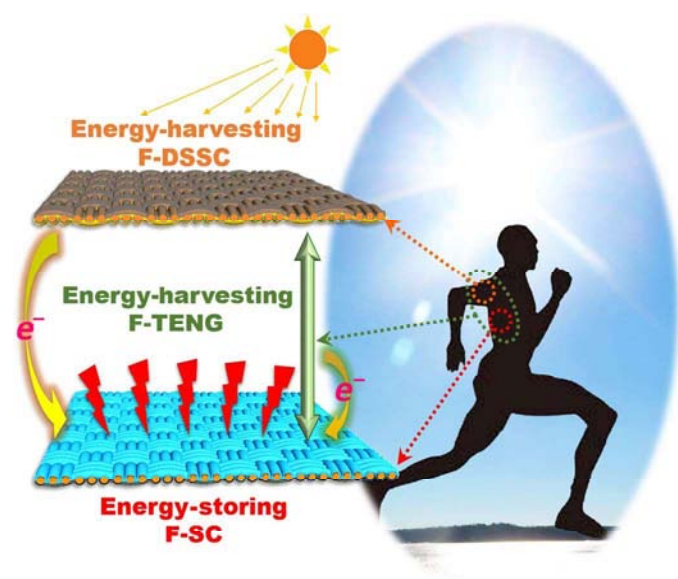
The double-layer structure of our proposed hybridized self-charging power textile is schematically illustrated in Fig. 1. Three kinds of

<sup>1</sup>School of Material Science and Engineering, Georgia Institute of Technology, Atlanta, GA 30332-0245, USA. <sup>2</sup>State Key Laboratory of Silicon Materials, School of Materials Science and Engineering, Cyrus Tang Center for Sensor Materials and Applications, Zhejiang University, Hangzhou 310027, China. <sup>3</sup>Jiangsu Key Laboratory for Carbon-Based Functional Materials and Devices, Institute of Functional Nano and Soft Materials, Soochow University, Suzhou, Jiangsu 215123, China. <sup>4</sup>Department of Chemical Engineering, National Taiwan University of Science and Technology, Taipei 10607, Taiwan. <sup>5</sup>Department of Applied Physics, Chongqing University, Chongqing 400044, China. <sup>6</sup>School of Material Science and Engineering, China University of Mining and Technology, Xuzhou, Jiangsu 221116, China. <sup>7</sup>Beijing Institute of Nanoenergy and Nanosystems, Chinese Academy of Sciences; National Center for Nanoscience and Technology, Beijing 100083, China.

\*These authors contributed equally to this work.

†Corresponding author. Email: zhong.wang@mse.gatech.edu





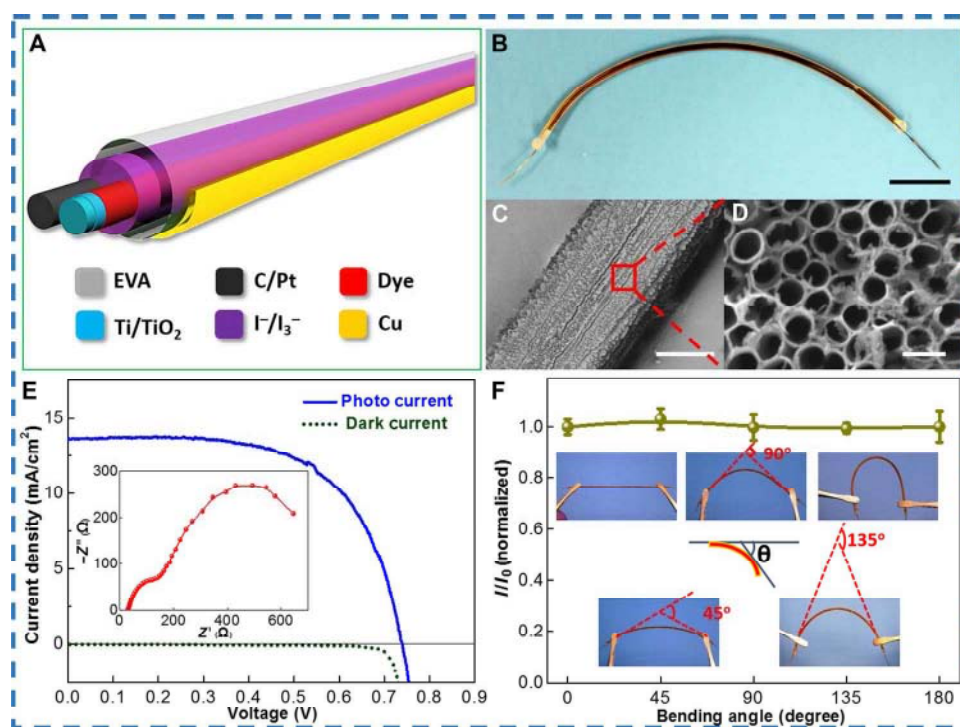
**Fig. 1. Schematic of the self-charging power textile.** Scheme of a fiber-based self-charging power system, which is made of an F-TENG, an F-DSSC as an energy-harvesting fabric, and an F-SC as an energy-storing fabric.

functional devices, including F-DSSCs, F-SCs, and F-TENGs, can be integrated spontaneously into a conventional textile structure. First, the top layer of the hybridized self-charging power textile is the F-DSSC-based textile, which is woven of several F-DSSC units for harvesting solar energy. Here, DSSC is chosen from numerous photovoltaic cells because DSSC materials and dyes can be tuned for optimization in a variety of lighting conditions, making it suitable for indoor and outdoor applications. Also, DSSCs can also be applied to a variety of substrates that are favorable for constructing the TENG structure. The F-SC-based textile acts as the bottom layer for storing the harvested energies. Meanwhile, each F-DSSC and F-SC unit is connected to one another, forming a single F-TENG unit; this F-TENG-based textile system is built to simultaneously scavenge body motion energy. Transparent and flexible ethylene vinyl acetate (EVA) tubing was used to build the basic unit of the self-charging power textile. Before the concurrent operation of the textile, the characterization of each functional device was carried out individually to evaluate its performance.

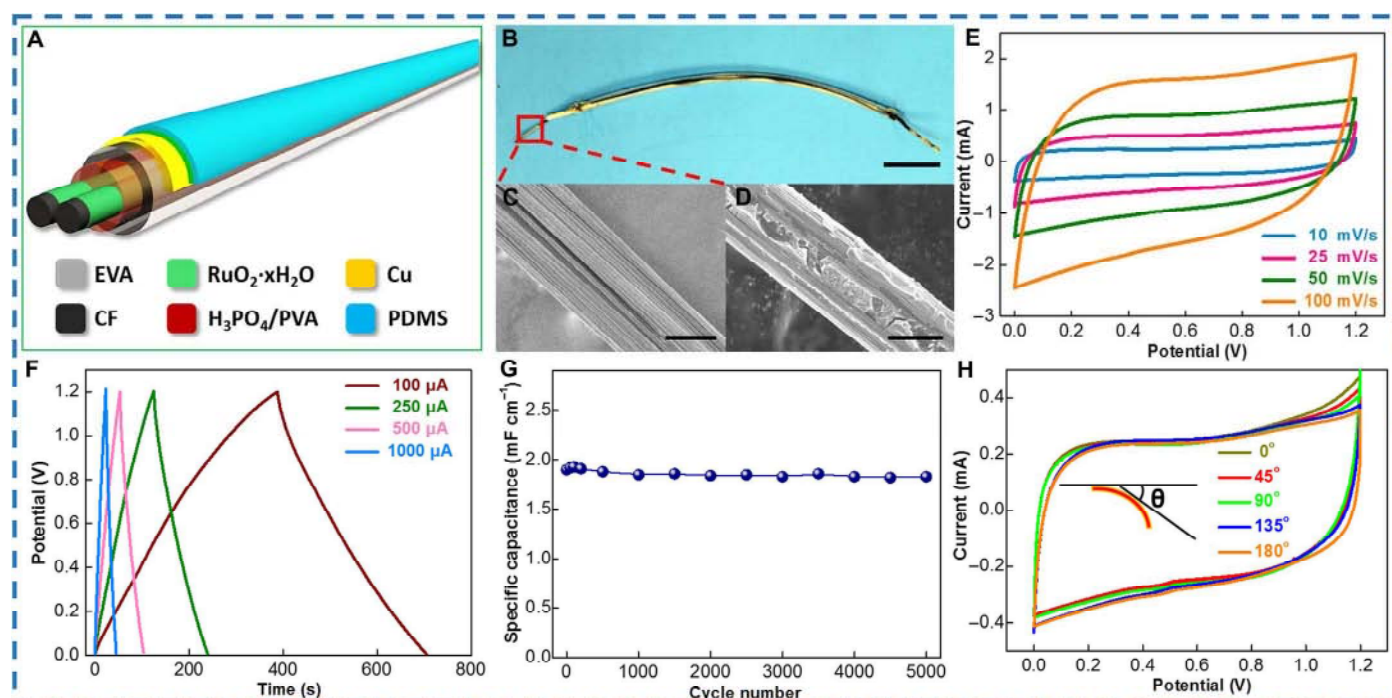
Initially, a single F-DSSC unit with a length of  $\sim 10$  cm is constructed using N719 dye-sensitized  $\text{TiO}_2$  nanotube arrays on a Ti wire as a working electrode and a Pt-coated carbon fiber as a counter electrode (CE), which is sealed into Cu-coated EVA tubing containing an  $\Gamma/I_3^-$ -based electrolyte. Cu-coated EVA tubing acts not only as the holder for fabricating an F-DSSC but also as one electrode for F-TENG, which will be discussed later. The wire structure of the F-DSSC unit is schematically illustrated in detail in Fig. 2A. A photograph of a single F-DSSC unit is also presented in Fig. 2B. Figure 2C shows a low-magnification scanning electron microscopy (SEM) image of a Ti wire with a diameter of  $\sim 200$   $\mu\text{m}$  after anodic oxidation. A top-view high-magnification SEM image presented in Fig. 2D shows that the vertically oriented array of one-dimensional (1D)  $\text{TiO}_2$  nanotubes is well grown on the Ti wire surface via electrochemical anodization, with a similar diameter of  $\sim 50$  nm. Furthermore, the crystalline phases of the as-prepared  $\text{TiO}_2$  nanotubes were examined by x-ray diffraction (XRD) patterns, as shown in fig. S1. Peaks corresponding to (101),

(103), (004), (200), (105), and (211) of the  $\text{TiO}_2$  anatase phase are observed (34). On the other hand, the SEM images of the Pt-coated carbon fiber and the bare carbon fiber are shown in fig. S2. It can be observed that the diameter of a single fiber (for both the Pt-coated carbon fiber and the pure carbon fiber) is  $\sim 10$   $\mu\text{m}$ . Homogeneous Pt nanoparticles were well dispersed on the surface of the carbon fiber, as a result of a thermally decomposed process. Afterward, the current-voltage ( $I$ - $V$ ) characteristic of a single F-DSSC unit was evaluated under standard illumination ( $100 \text{ mW cm}^{-2}$ ; AM1.5). Figure 2E shows the photocurrent density-voltage ( $J$ - $V$ ) curve of a single F-DSSC. The single F-DSSC unit exhibits a short-circuit current density ( $J_{\text{SC}}$ ), an open-circuit voltage ( $V_{\text{OC}}$ ), and a fill factor (FF) of  $11.92 \text{ mA cm}^{-2}$ ,  $0.74 \text{ V}$ , and  $0.64$ , respectively, corresponding to an overall power conversion efficiency of  $5.64\%$ . The dark current is also added in the figure as the reference. The performance of a single F-DSSC with bare carbon fibers is also examined for comparison, as shown in fig. S4. The performance of a single F-DSSC unit at different incident light angles is shown in fig. S5, and a detailed discussion can be found in the Supplementary Materials. A nonvolatile  $\Gamma/I_3^-$ -based electrolyte was used in our study to enhance the long-term stability of the F-DSSC unit. The inset to Fig. 2E shows the electrochemical impedance spectra of a single F-DSSC unit for evaluating the charge transfer resistance in the device, which was measured under  $V_{\text{OC}}$  with an alternating current (ac) amplitude of  $10 \text{ mV}$  in the  $100 \text{ kHz}$  to  $10 \text{ MHz}$  frequency range. The ohmic series resistance ( $R_s$ ) of a single F-DSSC unit can be determined in the high-frequency region of a Nyquist plot where the phase is zero. The first semicircle in the Nyquist plot at the high-frequency range corresponded to the impedance at the CE/electrolyte interface ( $R_{\text{ct1}}$ ) for the reduction reaction of  $I_3^-$  ions, whereas the second semicircle at the middle frequency range corresponded to the charge-transfer impedance at the  $\text{TiO}_2/\text{dye}/\text{electrolyte}$  interface ( $R_{\text{ct2}}$ ). The above results provide solid evidence that F-DSSCs had been successfully prepared for harvesting solar energy. To further apply F-DSSCs in our proposed self-charging power textile, the output performance of the F-DSSC at different bending angles should be considered. Figure 2F shows the normalized current density of a single F-DSSC at different bending degrees (from  $0^\circ$  to  $180^\circ$ ) under a constant incident light intensity, where the value of the current density ( $\sim 12 \text{ mA cm}^{-2}$ ) rarely changed under various bending angles, showing the stability of the photovoltaic device.

F-SCs are introduced in the self-charging power textile as the energy storage unit for F-DSSCs. A single F-SC unit with a length of  $10 \text{ cm}$  is symmetrically assembled with two carbon fibers coated with  $\text{RuO}_2 \cdot x\text{H}_2\text{O}$  in the  $\text{H}_3\text{PO}_4/\text{PVA}$  [poly(vinyl alcohol)] electrolyte and packaged into the polydimethylsiloxane (PDMS)-covered Cu-coated EVA tubing, as schematically shown in Fig. 3A. PDMS-covered Cu-coated EVA tubing acts not only as the holder for fabricating an F-SC but also as one electrode for F-TENG, which will be discussed later. Two bundles of carbon fibers were separated by a cellulose-based paper septum. A photograph of a single F-SC is shown in Fig. 3B. Here, long-ordered carbon fibers without any binders were directly used as the substrate for fabricating the F-SC owing to their excellent chemical stability and outstanding conductivity (35).  $\text{RuO}_2 \cdot x\text{H}_2\text{O}$  was synthesized on carbon fiber bundles by using a vapor-phase hydrothermal method to form binder-free fiber electrodes (36). A low-magnification SEM image of the as-synthesized  $\text{RuO}_2 \cdot x\text{H}_2\text{O}$ -coated carbon fibers reveals that several carbon fibers were assembled into a bundle, as shown in Fig. 3C. Figure 3D shows a high-magnification SEM image of  $\text{RuO}_2 \cdot x\text{H}_2\text{O}$  coated on a single carbon fiber with a



**Fig. 2. Structural design of an F-DSSC.** (A) Schematic diagram and (B) photograph (scale bar, 1 cm) of a single F-DSSC, consisting of N719 dye-adsorbed TiO<sub>2</sub> nanotube arrays on a Ti wire as a working electrode and a Pt-coated carbon fiber as a CE in an I<sup>-</sup>/I<sub>3</sub><sup>-</sup>-based electrolyte. (C) Low-magnification and (D) high-magnification SEM images of the TiO<sub>2</sub> nanotube arrays on the Ti wire [scale bars, 100 μm (C) and 100 nm (D)]. (E) J-V curve of a single F-DSSC, which is measured under V<sub>OC</sub> with frequencies ranging from 100 kHz to 10 MHz. (F) Normalized current density of the single F-DSSC at different bending angles (0° to 180°) (insets show the photograph of a single F-DSSC at different bending angles).

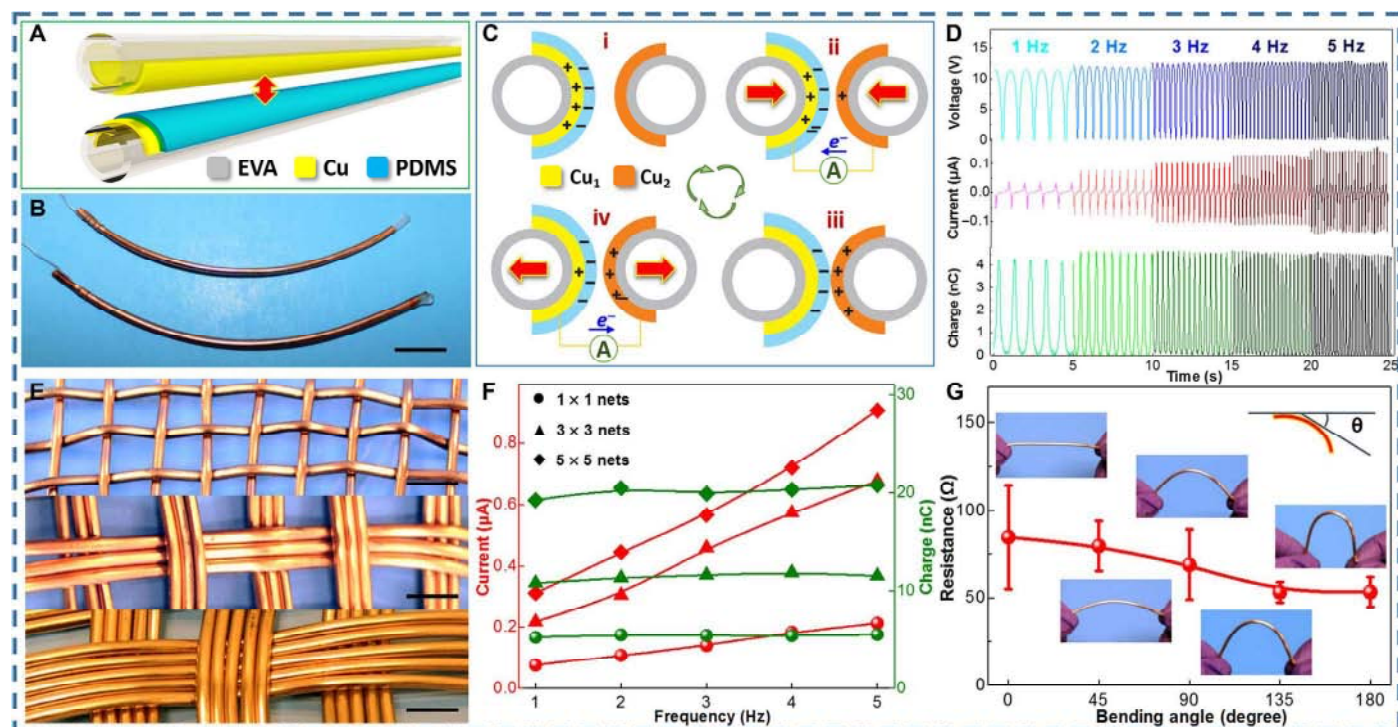


**Fig. 3. Structural design of an F-SC.** (A) Schematic diagram and (B) photograph (scale bar, 1 cm) of a single F-SC, consisting of two carbon fibers coated with RuO<sub>2</sub>·xH<sub>2</sub>O in the H<sub>3</sub>PO<sub>4</sub>/PVA electrolyte. (C) Low-magnification and (D) high-magnification SEM images of the RuO<sub>2</sub>·xH<sub>2</sub>O-coated carbon fiber electrode [scale bars, 100 μm (C) and 5 μm (D)]. (E) CV of the single F-SC at different scanning rates (10 to 100 mV/s). (F) GCD curve of a single F-SC at different current densities (100 to 1000 μA). (G) Cycling performance of a single F-SC unit. (H) CV curves of the single F-SC at different bending angles (0° to 180°).

diameter of  $\sim 10\ \mu\text{m}$ ; it presents the typical “cracked mud” morphology on the surface of carbon fibers. Moreover, the crystalline phase of the as-synthesized fibers is confirmed by XRD patterns (fig. S5), and the peaks for each XRD pattern can be assigned to a typical amorphous  $\text{RuO}_2 \cdot x\text{H}_2\text{O}$  with a partly rutile crystalline structure, which is an essential phase to simultaneously obtain high ion and high electron conductivity (37). The electrochemical capacitance properties of a single F-SC unit were further evaluated by cyclic voltammetry (CV) and galvanostatic charging/discharging (GCD) techniques. To evaluate the fast charge/discharge ability of the F-SC, we examined CV at different scan rates (from 10 to  $100\ \text{mV s}^{-1}$ ), as shown in Fig. 3E. It can be observed that the CV curves do not distort significantly as the scan rate increases, indicating their good capacitive behavior and high-rate capability. Figure 3F shows the charge/discharge curves of the F-SC at different current densities (from 100 to  $1000\ \mu\text{A}$ ), with the potential ranging from 0 to 1.2 V. The symmetrically triangle-shaped GCD curves of the F-SC under various current densities can be observed. Moreover, no obvious  $IR$ -drop phenomenon can be found even at a short discharging time of 23 s, which reconfirms the outstanding capacitance behavior and the promising charging/discharging performance of the F-SC. As a comparison, the energy storage performances of the carbon fiber without incorporating  $\text{RuO}_2$  were also measured, as shown in fig. S6. Because the mass-specific capacitance ( $\text{F g}^{-1}$ ) is not suitable for F-SC, the length-specific capacitance ( $\text{F cm}^{-1}$ ) was evaluated and then calculated in this study. Our results reveal that the specific capacitance of  $1.9\ \text{mF cm}^{-1}$  can still be retained at a high level under a high current density of  $1000\ \mu\text{A}$ , and its energy density is up to  $1.37\ \text{mJ cm}^{-1}$ , both of which

demonstrate a fast charging/discharging ability and a reasonable energy density. The cycling stability of SC is also a critical issue that should be considered. The cycling performance of a single F-SC unit was investigated, as shown in Fig. 3G. No obvious capacitance change can be observed after 5000 cycles at a charging/discharging current of  $1000\ \mu\text{A}$ . The PVA/ $\text{H}_3\text{PO}_4$  gel electrolyte has also demonstrated excellent cycling stability in our previous work (34). Finally, the capacitance of a single F-SC at different bending angles (from  $0^\circ$  to  $180^\circ$ ) was also examined, as shown in Fig. 3H. All of the CV curves for a single F-SC unit with various bending angles exhibit typical and almost overlapping rectangle-like curves, indicating that it is a reliable platform for storing harvested energies with excellent flexibility and promising stability under various bending conditions.

As mentioned before, a pair of single F-TENG units can be built by pairing the F-DSSC with Cu-coated EVA tubing and the F-SC with PDMS-covered Cu-coated EVA tubing. A schematic diagram and a digital photograph of a pair of single F-TENG units are shown in Fig. 4 (A and B, respectively). To elucidate the working mechanism in a simplified model, the relative motion of the two fiber tubes can be simplified as the contact-separation process that occurs between Cu and PDMS, as illustrated in Fig. 4C. In the original state (i), the PDMS surface was charged with negative electrostatic charges and the  $\text{Cu}_1$  electrode produced positive charges, due to the electrostatic induction and conservation of charges. When the F-TENG was pressed (ii), a shrinkage of the gap between the  $\text{Cu}_2$  electrode and PDMS would result in induced positive charges accumulating in the  $\text{Cu}_2$  layer because of the electrostatic induction. Accordingly, free electrons in  $\text{Cu}_2$  would flow to the  $\text{Cu}_1$  layer to balance the field. This

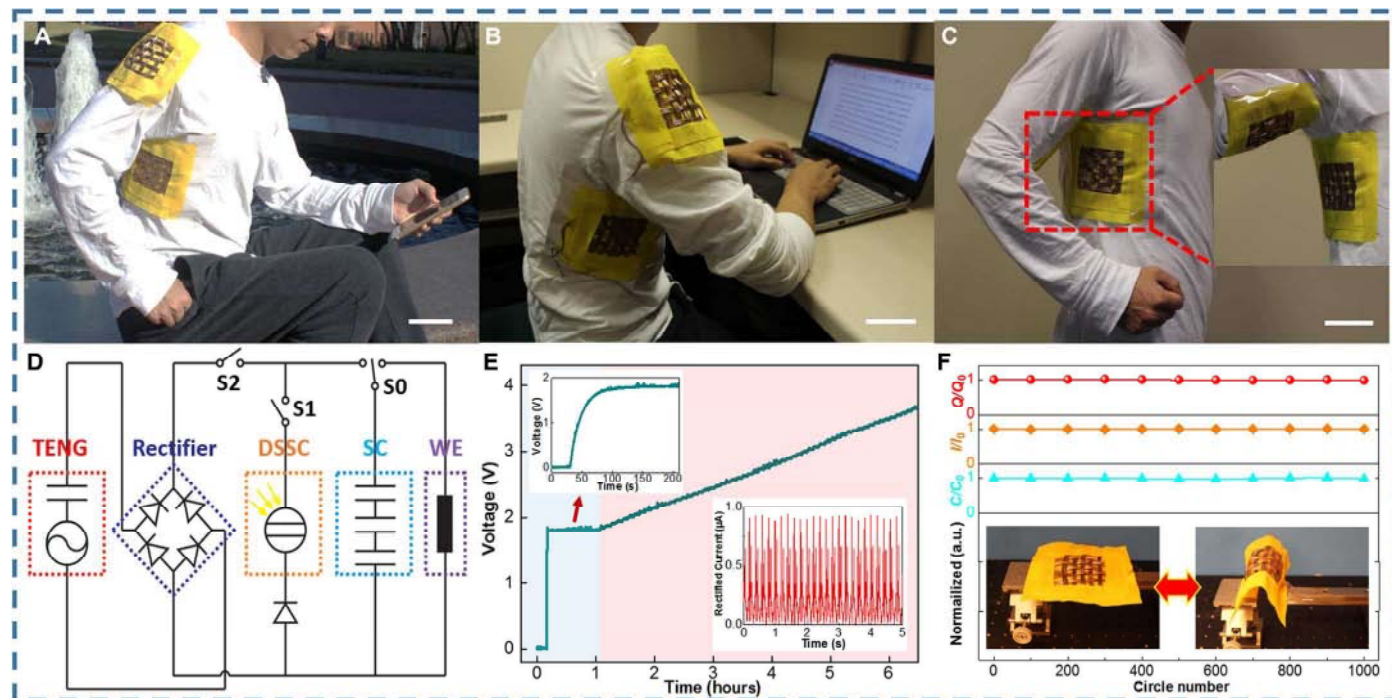


**Fig. 4. Structural design of an F-TENG.** (A) Schematic diagram and (B) photograph (scale bar, 1 cm) of a pair of single F-TENG units, consisting of a Cu-coated EVA tube and a PDMS-covered Cu-coated EVA tube. (C) Schematic illustration of the working mechanism of the F-TENG under parallel contact-separation motion. (D) Electrical outputs of a pair of F-TENG units, which included  $V_{\text{OC}}$ ,  $I_{\text{SC}}$  and  $Q_{\text{SC}}$  at various motion frequencies (1 to 5 Hz). (E) Photograph of the wearable self-charging powered textile with knitting patterns of  $1 \times 1$ ,  $3 \times 3$ , and  $5 \times 5$  nets (all scale bars, 1 cm). (F) Triboelectric output performance of the three network textiles. (G) The electric resistance of the Cu-coated EVA tube at different bending angles ( $0^\circ$  to  $180^\circ$ ) (insets show the photograph of the Cu-coated EVA tube at different bending angles).

process produces an instantaneous positive current. It is necessary to note that the charges on PDMS will not be annihilated even when it makes contact with the  $\text{Cu}_2$  electrode (iii), because the electrostatic charges are naturally impregnated into the insulator PDMS. In the reverse case, when the F-TENG was released (iv), it would recover back to its original state (i) and the internal gap would be increased. Thus, an instantaneous negative current could be produced. Therefore, a contact-separation process of the F-TENG will generate an ac through the load (38–41). The output performance of power generation for a pair of single F-TENG units with a length of  $\sim 10$  cm was systematically studied via the periodic motion of contacting and separating under controlled frequencies. To analyze the output capability of the F-TENG, we used a linear motor to trigger the pair of single F-TENG units, wherein the maximum distance between the two tubing systems was purposely set at 10 mm. As shown in Fig. 4D, when motion frequencies vary from 1 to 5 Hz, the  $V_{OC}$  and transferred charges ( $Q_{SC}$ ) remain constant ( $\sim 12.6$  V and  $\sim 4.5$  nC, respectively). The short-circuit current ( $I_{SC}$ ) increases from  $\sim 0.06$  to  $\sim 0.15$   $\mu\text{A}$ , revealing a clear increasing trend with the increase in frequency. In other words, the increase in frequency is favorable for the magnitude of  $I_{SC}$ . Furthermore, three kinds of F-TENG-based textile with knitting patterns of  $1 \times 1$ ,  $3 \times 3$ , and  $5 \times 5$  nets are fabricated and then characterized under various motion frequencies (1 to 5 Hz), as shown in Fig. 4 (E and F, respectively). It indicates that the values of  $Q_{SC}$  and  $I_{SC}$  at 5 Hz increase with the increase in braided density from  $1 \times 1$  nets (5.4 nC and 0.21  $\mu\text{A}$ ) to  $3 \times 3$  nets (11.6 nC and 0.68  $\mu\text{A}$ ) and  $5 \times 5$  nets (20.8 nC and 0.91  $\mu\text{A}$ ), as a result of the further en-

largement of its conductive surface area for electrostatic induction. The  $V_{OC}$  remains almost constant because of the unchanged motion distance, as shown in fig. S7. As for wearable energy-harvesting textiles, the capability of F-TENG to withstand harsh bending or deformation is an essential requirement. Therefore, a flexibility test was performed, as shown in Fig. 4E and movie S1. No apparent change in resistance could be observed when a single Cu-coated EVA tubing was bent at different angles (from  $0^\circ$  to  $180^\circ$ ). The photograph of the Cu-coated EVA at different bending angles is also shown as insets.

To construct the hybridized self-charging power textile, several F-DSSC and F-SC units were woven into an individual fabric as the textile structure with in-series/parallel connection. An F-TENG-based textile system can be built after connecting both textiles. Figure 5 (A to C) shows a tester who wore our designed hybridized self-charging power textile attached to a T-shirt, which harvests light energy and motion energy based on the tester's daily outdoor and indoor activities, respectively. It is also worth noting that the DSSC can efficiently generate electric power under weak light (42). The equivalent circuit of the hybridized self-charging power textile is shown in Fig. 5D. A bridge rectifier is used to convert the generated current of F-TENG from ac to direct current before charging the F-DSSC, a diode is used to block the current of F-TENG that goes through an F-DSSC, and all the switches are used to control the circuit. Although the rectifier, diode, and switches are not flexible, it is possible to design them into either a logo or a button, considering their small size. To simply demonstrate the performance of the as-prepared hybridized self-charging power textile, we design the textile structure in a



**Fig. 5. Demonstration of the self-charging powered textile and its operation under outdoor and indoor conditions.** Photograph of the self-charging power textile woven with F-TENGs, F-DSSCs, and F-SCs under outdoor (A), indoor (B), and movement (C) conditions. (D) Circuit diagram of the self-charging powered textile for wearable electronics (WE). (E) Charging curve of the F-DSSC and the F-TENG, where the light blue-shaded area corresponds to the charging curve of the F-DSSC and the light red-shaded area corresponds to the charging curve of the F-DSSC-F-TENG hybrid. The top left corner inset shows an enlarged curve during the F-DSSC charging period, and the bottom right corner inset shows the rectified  $I_{SC}$  of F-TENGs. (F) Normalized  $Q_{SC}$  values of F-TENGs,  $I_{SC}$  values of F-DSSCs, and capacitances of F-SCs bent between  $0^\circ$  and  $180^\circ$  for 1000 cycles. Insets show the photographs of the two final bending statuses (both scale bars, 1 cm). a.u., arbitrary units.

3 × 3 network, meaning that each fabric was connected to three individual F-DSSC or six F-SC units in series and then woven separately. Figure 5E shows the characteristics of the self-charging behavior by harvesting solar and mechanical contact-separation motion energies via the as-prepared hybridized self-charging power textile. Turning the switch S0 on to connect the F-SC to the circuit, while switch S1 is on and switch S2 is off, will linearly increase the voltage of the F-SC (which takes about 69 s to charge from 0 to 1.8 V), indicating the stable output of F-DSSCs. The top left corner inset in Fig. 5E shows the enlarged curve during the charging period of the F-DSSCs. The *I*-*V* curve of three F-DSSCs with in-series connection is shown in fig. S8. However, the F-SCs remained at 1.8 V because of the low output voltage of the F-DSSCs limits their reliability and practicality, as shown in the light blue-shaded area. One effective method to solving this problem is to mimic the in-series structure of F-SCs for electrocytes in the electric eel to produce high working voltages, as reported by Sun *et al.* (43). Here, we introduced the TENG with a high voltage output to directly charge the electrochemical capacitors to a high level, which compensates for the weakness of the DSSC. After turning the switch S2 on, the F-SCs can be charged continuously by the F-TENGs to a higher voltage. The corresponding charging curve is plotted in the light red-shaded area. The bottom right corner inset in Fig. 5E shows the rectified  $I_{SC}$  of three-series F-TENGs. It should be noted that further improvement in the charging efficiencies can be achieved by obtaining impedance matching among DSSCs, TENGs, and SCs, because the internal impedance of TENGs is generally several orders of magnitude higher than that of DSSCs and SCs. Traditional electronic devices, such as LEDs, digital watches, and a variety of sensors for temperature, pressure, or medical diagnosis, can be easily powered. We believe that, after large-scale fabrication and further improvement, high-power electronic devices—for example, smart bracelets and portable MP3 players—could be charged by our novel self-powered textile in the near future. Last, the durability of the hybridized self-charging power textile was examined under continuous bending motion for 1000 cycles by the linear motor, as shown in Fig. 5F and movie S2. Normalized  $Q_{SC}$  values of F-TENGs,  $I_{SC}$  values of F-DSSCs, and capacitances of F-SCs were recorded after every 100 times of bending. The insets also display photographs of the textile bent from 0° to 180°. As shown in Fig. 5F, on the basis of their performance, each device showed no significant degradation in performance, confirming their excellent flexibility and stability. The increasing demand for lightweight, highly flexible, stretchable, and washable power modules is one of the critical challenges for the progress of self-powered wearable textiles.

## CONCLUSION

In summary, we demonstrate the concept of a hybridized self-charging power textile system with the aim of simultaneously collecting outdoor sunshine and random body motion energies and then transferring them to an energy-storing cell to sustainably operate mobile or wearable electronics. For a single F-DSSC unit, a  $V_{OC}$  of 0.74 V and a  $J_{SC}$  of 11.92 mA cm<sup>-2</sup> were achieved, corresponding to an overall power conversion efficiency of 5.64%. The F-TENG can take advantage of human motions, such as jogging, to deliver an output current of up to 0.91 μA. The F-SC unit with the excellent pseudocapacitance of the as-synthesized RuO<sub>2</sub>·xH<sub>2</sub>O exhibits a promising specific capacitance (1.9 mF cm<sup>-1</sup>), which makes it an effective and

flexible electronic energy storage device. Because of the all-fiber-based shape in each device, our proposed hybridized self-charging textile system can be easily woven into electronic textiles to fabricate smart clothes to operate wearable electronic devices. This work presents a welcome advancement for self-powered systems in wearable technology, which will initiate promising improvements in self-powered flexible displays and wearable electronics, among others. A more complicated design is possible because all of the textiles started from 1D building blocks.

## MATERIALS AND METHODS

### Materials

Lithium iodide (LiI), iodine (I<sub>2</sub>), sodium hydroxide (NaOH), ethanol (EtOH), 4-*tert*-butylpyridine (tBP), *tert*-butyl alcohol (tBA), ammonium fluoride (NH<sub>4</sub>F), hexachloroplatinic(IV) acid hexahydrate (H<sub>2</sub>PtCl<sub>6</sub>·6H<sub>2</sub>O), ruthenium(III) chloride (RuCl<sub>3</sub>), PVA ( $M_w = 89,000$  to 98,000), phosphoric acid solution (H<sub>3</sub>PO<sub>4</sub>), 3-methoxypropionitrile (MPN), acetonitrile (ACN), titanium tetrachloride (TiCl<sub>4</sub>), ethylene glycol (EG), 1,2-dimethyl-3-propylimidazolium iodide (DMPII), and *cis*-diisothiocyanato-bis(2,2'-bipyridyl-4,4'-dicarboxylato)ruthenium(II) bis(tetra-butylammonium) (N719 dye) were obtained from Sigma-Aldrich. All chemicals were used as received without further treatment. Miniature clear EVA tubing (length, 10 cm; inside diameter, 0.04"; outer diameter, 0.07"; wall thickness, 0.015") was purchased from McMaster-Carr. Ti wires (diameter, 0.02"; purity, ~99.99%) and PDMS (Sylgard 184 silicone elastomer) were purchased from Alfa Aesar and Dow Corning, respectively.

### Fabrication of the energy-harvesting F-DSSC

Ti wires were polished to remove residual metal oxides and then sequentially cleaned with a neutral cleaner, deionized water, and acetone. A highly ordered TiO<sub>2</sub> nanotube was fabricated on the Ti wire surface by anodization in 0.3 wt % NH<sub>4</sub>F/EG solution containing 8 wt % H<sub>2</sub>O at a voltage of 60 V via a two-electrode electrochemical cell with a Pt wire as a CE for 6 hours (44). After rinsing the surface of the anodized Ti wire with deionized water, the as-prepared Ti wires were gradually annealed to a temperature of 500°C for 1 hour. Afterward, the annealed Ti wires were immersed in 40 mM TiCl<sub>4</sub> solution at 70°C for 30 min and then annealed again at 450°C for 30 min. After cooling to 80°C, the annealed Ti wires were immersed in a 3 × 10<sup>-4</sup> M solution of N719 dye in ACN and tBA (*v/v* = 1/1) at room temperature for 24 hours. To fabricate the fiber-based CE, we soaked carbon fiber in an H<sub>2</sub>PtCl<sub>6</sub>·6H<sub>2</sub>O aqueous solution (5 mg/ml) for 5 min and then thermally decomposed it at 400°C for 30 min to obtain the Pt-coated carbon fiber, which is used as a CE. To obtain the F-DSSC, we simultaneously inserted a Pt-coated carbon fiber and a dye-sensitized Ti wire into the Cu-coated EVA tubing in parallel and we injected a nonvolatile I<sup>-</sup>/I<sub>3</sub><sup>-</sup>-based electrolyte (0.1 M LiI, 0.05 M I<sub>2</sub>, 0.6 M DMPII, and 0.5 M tBP in MPN) into the tubing. Finally, the ends of the tubing were sealed with sealing glue to prevent leakage of the electrolyte.

The solar-to-electrical energy conversion efficiency ( $\eta$ ) for a solar cell is given by the  $J_{SC}$ , the  $V_{OC}$ , and the FF of the cell, and the intensity of the incident light ( $P_{in}$ ), as shown in Eq. 1

$$\eta = \frac{J_{SC} \times V_{OC} \times FF}{P_{in}} \quad (1)$$

FF can be defined by the ratio of the maximum power ( $P_{\max}$ ) of the solar cell per unit area divided by the  $V_{OC}$  and  $J_{SC}$ , as shown in Eq. 2

$$FF = \frac{P_{\max}}{J_{SC} \times V_{OC}} \quad (2)$$

where  $P_{\max}$  is obtained as the product of the photocurrent and photovoltage, with the power output of the cell being maximal.

### Fabrication of the energy-storing F-SC

A bunch of carbon fibers were ultrasonically cleaned in a mixed solution of acetone, EtOH, and deionized water for 10 min and then coated with  $\text{RuCl}_3$  slurry made from 0.1 g of  $\text{RuCl}_3$  and 4 ml of EtOH. After drying at 60°C, the carbon fibers were fixed on a shelf and then placed in a 50-ml Teflon-lined stainless steel autoclave with 1 ml of 0.1 M NaOH solution. The autoclave was kept in an oven at 190°C for 5 hours and then cooled down to room temperature in air. After washing and drying,  $\text{RuO}_2 \cdot x\text{H}_2\text{O}$ -coated carbon fibers were obtained. The PVA/ $\text{H}_3\text{PO}_4$  gel electrolyte was prepared by adding 5 g of  $\text{H}_3\text{PO}_4$  and 5 g of PVA powder into 50 ml of deionized water. The mixture was heated to 85°C under stirring until the solution became clear. The as-prepared  $\text{RuO}_2 \cdot x\text{H}_2\text{O}$ -coated carbon fibers were immersed into PVA/ $\text{H}_3\text{PO}_4$  solution for 10 min, with their two-end parts kept above the solution. After being taken out, two fibers were assembled into PDMS-covered Cu-coated tubing, separated by a paper septum and leaving aside the bare part as the electrode terminal.

The length-specific capacitance and energy density can be calculated from the GCD curve by using Eqs. 3 and 4, respectively

$$C = \frac{I \times \Delta t}{\Delta V \times l} \quad (3)$$

$$E = \frac{1}{2} C \times \Delta V^2 \quad (4)$$

where  $C$  is the length-specific capacitance of F-SC,  $I$  is the constant current,  $\Delta t$  is the discharge time,  $\Delta V$  is the voltage change during the discharge process,  $l$  is the total length for both carbon electrodes, and  $E$  is the energy density.

### Fabrication of the energy-harvesting F-TENG

Commercial miniature clear EVA tubing was used to fabricate the F-TENG. The tubing was cleaned with isopropanol and then washed with abundant deionized water by ultrasonic cleaning. After drying, a copper lead wire was attached to the tubing with conductive adhesive epoxy. Subsequently, a layer of copper electrode was deposited onto one side of the EVA tubing surface by physical vapor deposition with a power of 100 W under Ar atmosphere for 40 min (layer thickness, 1  $\mu\text{m}$ ). Afterward, the PDMS elastomer and the curing agent were mixed (w/w = 10/1) and then coated on the surface of the as-prepared Cu-coated EVA tubing through a “dipping and drying” process (45, 46). After drying at room temperature for 12 hours, PDMS-covered Cu-coated EVA tubing was obtained. A single F-TENG unit can be assembled by connecting Cu-coated EVA tubing as a triboelectric electrode and PDMS-covered Cu-coated EVA tubing as another electrode.

### Fabrication of the hybridized self-charging power textile

First, the as-prepared F-DSSCs and F-SCs could be easily woven as the textile with different net structures, as shown in Fig. 1. The output voltage and capacitance of the as-woven textile could be easily tuned by in-series and/or parallel connection to drive real wearable electronics. To fabricate the hybridized self-charging power textile, the woven F-DSSC textile was used as the top layer to harvest sunlight energy, and the woven F-SC textile was used as the bottom layer to store harvested energies. Meanwhile, both woven textiles simultaneously played as triboelectric layers to gather mechanical energies from human motion, which were then also collected via the woven F-SC textile after rectification.

### Characterization and measurement

Field-emission SEM (Hitachi SU8010) was used to measure the morphology and size of the  $\text{TiO}_2$  nanotube arrays on the Ti wire and  $\text{RuO}_2 \cdot x\text{H}_2\text{O}$ -coated carbon fibers. The crystal phase identification of both the as-prepared  $\text{TiO}_2$  nanotube and  $\text{RuO}_2 \cdot x\text{H}_2\text{O}$  was investigated by the XRD system (Bede D1) with Cu-K $\alpha$ 1 radiation ( $\lambda = 0.15406$  nm). For the electric output measurement of the F-TENG, a linear motor (Linmot E1100) was applied to mimic human motions, driving the TENG contact-separation process. A programmable electrometer (Keithley 6514) was adopted to test the  $V_{OC}$ ,  $I_{SC}$ , and  $Q_{SC}$ . The software platform was constructed on the basis of LabVIEW, which is capable of realizing real-time data acquisition control and analysis. The  $J$ - $V$  characteristic of the F-DSSC was recorded by a Keithley 2400 electrometer under illumination (100  $\text{mW}/\text{cm}^2$ ) of simulated solar light (Oriel 91160-1000 equipped with a 450-W Xe lamp; AM1.5). The light intensity was calibrated using a reference Si solar cell (Oriel 70260). The effective area of the F-DSSC was defined by multiplying the length by the diameter of the photoanode. The F-DSSC body remained vertical with the light, whether straight or bending. The electrochemical performance of the F-SC was measured by an electrochemical workstation (Princeton Applied Research VersaSTAT 3). A potentiostat was used to test capacitance properties with CV and GCD techniques. The charging/discharging process of the self-charging power system was tested with a battery analyzer.

### SUPPLEMENTARY MATERIALS

Supplementary material for this article is available at <http://advances.sciencemag.org/cgi/content/full/2/10/e1600097/DC1>

- fig. S1. XRD pattern of the anodized  $\text{TiO}_2$  nanotube arrays on a Ti wire.
- fig. S2. SEM images of the pure carbon fiber and the Pt-coated carbon fiber.
- fig. S3.  $J$ - $V$  curve of an F-DSSC based on bare carbon fibers.
- fig. S4. Dependence of an F-DSSC at different incident light angles.
- fig. S5. XRD pattern of the  $\text{RuO}_2 \cdot x\text{H}_2\text{O}$ .
- fig. S6. CV and GCD curves of an F-SC based on bare carbon fibers.
- fig. S7.  $V_{OC}$  outputs of F-TENG network textiles.
- fig. S8.  $I$ - $V$  curve of three F-DSSCs with in-series connection.
- movie S1. Flexibility test of Cu-coated EVA tubing.
- movie S2. Stability test of hybridized self-charging power textile.

### REFERENCES AND NOTES

1. D. Son, J. Lee, S. Qiao, R. Ghaffari, J. Kim, J. E. Lee, C. Song, S. J. Kim, D. J. Lee, S. W. Jun, S. Yang, M. Park, J. Shin, K. Do, M. Lee, K. Kang, C. S. Hwang, N. Lu, T. Hyeon, D.-H. Kim, Multifunctional wearable devices for diagnosis and therapy of movement disorders. *Nat. Nanotechnol.* **9**, 397–404 (2014).
2. M. J. Cima, Next-generation wearable electronics. *Nat. Biotechnol.* **32**, 642–643 (2014).
3. M. Ha, J. Park, Y. Lee, H. Ko, Triboelectric generators and sensors for self-powered wearable electronics. *ACS Nano* **9**, 3421–3427 (2015).

4. H.-H. Chou, A. Nguyen, A. Chortos, J. W. F. To, C. Lu, J. Mei, T. Kurosawa, W.-G. Bae, J. B.-H. Tok, Z. Bao, A chameleon-inspired stretchable electronic skin with interactive colour changing controlled by tactile sensing. *Nat. Commun.* **6**, 8011 (2015).
5. E. Dolgin, Technology: Dressed to detect. *Nature* **511**, S16–S17 (2014).
6. R. Hinchet, W. Seung, S.-W. Kim, Recent progress on flexible triboelectric nanogenerators for self-powered electronics. *ChemSusChem* **8**, 2327–2344 (2015).
7. J. Deng, Y. Zhang, Y. Zhao, P. Chen, X. Cheng, H. Peng, A shape-memory supercapacitor fiber. *Angew. Chem. Int. Ed.* **54**, 15419–15429 (2015).
8. J. Bae, M. K. Song, Y. J. Park, J. M. Kim, M. Liu, Z. L. Wang, Fiber supercapacitors made of nanowire-fiber hybrid structures for wearable/flexible energy storage. *Angew. Chem. Int. Ed.* **50**, 1683–1687 (2011).
9. T. Chen, L. Qiu, Z. Yang, Z. Cai, J. Ren, H. Li, H. Lin, X. Sun, H. Peng, An integrated “energy wire” for both photoelectric conversion and energy storage. *Angew. Chem. Int. Ed.* **51**, 11977–11980 (2012).
10. Z. Zhang, X. Chen, P. Chen, G. Guan, L. Qiu, H. Lin, Z. Yang, W. Bai, Y. Luo, H. Peng, Integrated polymer solar cell and electrochemical supercapacitor in a flexible and stable fiber format. *Adv. Mater.* **26**, 466–470 (2014).
11. Y. Fu, H. Wu, S. Ye, X. Cai, X. Yu, S. Hou, H. Kafafy, D. Zou, Integrated power fiber for energy conversion and storage. *Energy Environ. Sci.* **6**, 805–812 (2013).
12. P. Du, X. Hu, C. Yi, H. C. Liu, P. Liu, H.-L. Zhang, X. Gong, Self-powered electronics by integration of flexible solid-state graphene-based supercapacitors with high performance perovskite hybrid solar cells. *Adv. Funct. Mater.* **25**, 2420–2427 (2015).
13. C. Xu, Z. L. Wang, Compact hybrid cell based on a convoluted nanowire structure for harvesting solar and mechanical energy. *Adv. Mater.* **23**, 873–877 (2011).
14. C. Xu, X. Wang, Z. L. Wang, Nanowire structured hybrid cell for concurrently scavenging solar and mechanical energies. *J. Am. Chem. Soc.* **131**, 5866–5872 (2009).
15. C. Xu, C. Pan, Y. Liu, Z. L. Wang, Hybrid cells for simultaneously harvesting multi-type energies for self-powered micro/nanosystems. *Nano Energy* **1**, 259–272 (2012).
16. Y. Yang, H. Zhang, G. Zhu, S. Lee, Z.-H. Lin, Z. L. Wang, Flexible hybrid energy cell for simultaneously harvesting thermal, mechanical, and solar energies. *ACS Nano* **7**, 785–790 (2013).
17. Y. Yang, Z. L. Wang, Hybrid energy cells for simultaneously harvesting multi-types of energies. *Nano Energy* **14**, 245–256 (2015).
18. Q. Liang, X. Yan, Y. Gu, K. Zhang, M. Liang, S. Lu, X. Zheng, Y. Zhang, Highly transparent triboelectric nanogenerator for harvesting water-related energy reinforced by antireflection coating. *Sci. Rep.* **5**, 9080 (2015).
19. Z. L. Wang, J. Chen, L. Lin, Progress in triboelectric nanogenerators as a new energy technology and self-powered sensors. *Energy Environ. Sci.* **8**, 2250–2282 (2015).
20. Y. Zi, S. Niu, J. Wang, Z. Wen, W. Tang, Z. L. Wang, Standards and figure-of-merits for quantifying the performance of triboelectric nanogenerators. *Nat. Commun.* **6**, 8376 (2015).
21. J. Chen, J. Yang, Z. Li, X. Fan, Y. Zi, Q. Jing, H. Guo, Z. Wen, K. C. Pradel, S. Niu, Z. L. Wang, Networks of triboelectric nanogenerators for harvesting water wave energy: A potential approach toward blue energy. *ACS Nano* **9**, 3324–3331 (2015).
22. R. Zhang, S. Wang, M.-H. Yeh, C. Pan, L. Lin, R. Yu, Y. Zhang, L. Zheng, Z. Jiao, Z. L. Wang, A streaming potential/current-based microfluidic direct current generator for self-powered nanosystems. *Adv. Mater.* **27**, 6482–6487 (2015).
23. Q. Liang, X. Yan, X. Liao, S. Cao, X. Zheng, H. Si, S. Lu, Y. Zhang, Multi-unit hydroelectric generator based on contact electrification and its service behavior. *Nano Energy* **16**, 329–338 (2015).
24. H. Guo, Z. Wen, Y. Zi, M.-H. Yeh, J. Wang, L. Zhu, C. Hu, Z. L. Wang, A water-proof triboelectric–electromagnetic hybrid generator for energy harvesting in harsh environments. *Adv. Energy Mater.* **6**, 1501593 (2015).
25. Z. Wen, J. Chen, M.-H. Yeh, H. Guo, Z. Li, X. Fan, T. Zhang, L. Zhu, Z. L. Wang, Blow-driven triboelectric nanogenerator as an active alcohol breath analyzer. *Nano Energy* **16**, 38–46 (2015).
26. M.-H. Yeh, H. Guo, L. Lin, Z. Wen, Z. Li, C. Hu, Z. L. Wang, Rolling friction enhanced free-standing triboelectric nanogenerators and their applications in self-powered electrochemical recovery systems. *Adv. Funct. Mater.* **26**, 1054–1062 (2015).
27. Z. Wen, H. Guo, Y. Zi, M.-H. Yeh, X. Wang, J. Deng, J. Wang, S. Li, C. Hu, L. Zhu, Z. L. Wang, Harvesting broad frequency band blue energy by a triboelectric–electromagnetic hybrid nanogenerator. *ACS Nano* **10**, 6526–6534 (2016).
28. Z. Li, J. Chen, J. Yang, Y. Su, X. Fan, Y. Wu, C. Yu, Z. L. Wang,  $\beta$ -Cyclodextrin enhanced triboelectrification for self-powered phenol detection and electrochemical degradation. *Energy Environ. Sci.* **8**, 887–896 (2015).
29. X. Pu, L. Li, H. Song, C. Du, Z. Zhao, C. Jiang, G. Cao, W. Hu, Z. L. Wang, A self-charging power unit by integration of a textile triboelectric nanogenerator and a flexible lithium-ion battery for wearable electronics. *Adv. Mater.* **27**, 2472–2478 (2015).
30. W. Seung, M. K. Gupta, K. Y. Lee, K.-S. Shin, J.-H. Lee, T. Y. Kim, S. Kim, J. Lin, J. H. Kim, S.-W. Kim, Nanopatterned textile-based wearable triboelectric nanogenerator. *ACS Nano* **9**, 3501–3509 (2015).
31. C. Pan, W. Guo, L. Dong, G. Zhu, Z. L. Wang, Optical fiber-based core–shell coaxially structured hybrid cells for self-powered nanosystems. *Adv. Mater.* **24**, 3356–3361 (2012).
32. H. Guo, X. He, J. Zhong, Q. Zhong, Q. Leng, C. Hu, J. Chen, L. Tian, Y. Xi, J. Zhou, A nanogenerator for harvesting airflow energy and light energy. *J. Mater. Chem. A* **2**, 2079–2087 (2014).
33. Y. Zi, L. Lin, J. Wang, S. Wang, J. Chen, X. Fan, P.-K. Yang, F. Yi, Z. L. Wang, Triboelectric–pyroelectric–piezoelectric hybrid cell for high-efficiency energy-harvesting and self-powered sensing. *Adv. Mater.* **27**, 2340–2347 (2015).
34. J. Wang, X. Li, Y. Zi, S. Wang, Z. Li, L. Zheng, F. Yi, S. Li, Z. L. Wang, A flexible fiber-based supercapacitor–triboelectric-nanogenerator power system for wearable electronics. *Adv. Mater.* **27**, 4830–4836 (2015).
35. S. Pan, Z. Yang, P. Chen, X. Fang, G. Guan, Z. Zhang, J. Deng, H. Peng, Carbon nanostructured fibers as counter electrodes in wire-shaped dye-sensitized solar cells. *J. Phys. Chem. C* **118**, 16419–16425 (2014).
36. J. Park, J. W. Lee, B. U. Ye, S. H. Chun, S. H. Joo, H. Park, H. Lee, H. Y. Jeong, M. H. Kim, J. M. Baik, Structural evolution of chemically-driven RuO<sub>2</sub> nanowires and 3-dimensional design for photo-catalytic applications. *Sci. Rep.* **5**, 11933 (2015).
37. Z.-S. Wu, D.-W. Wang, W. Ren, J. Zhao, G. Zhou, F. Li, H.-M. Cheng, Anchoring hydrous RuO<sub>2</sub> on graphene sheets for high-performance electrochemical capacitors. *Adv. Funct. Mater.* **20**, 3595–3602 (2010).
38. X. Fan, J. Chen, J. Yang, P. Bai, Z. Li, Z. L. Wang, Ultrathin, rollable, paper-based triboelectric nanogenerator for acoustic energy harvesting and self-powered sound recording. *ACS Nano* **9**, 4236–4243 (2015).
39. S. Li, S. Wang, Y. Zi, Z. Wen, L. Lin, G. Zhang, Z. L. Wang, Largely improving the robustness and lifetime of triboelectric nanogenerators through automatic transition between contact and noncontact working states. *ACS Nano* **9**, 7479–7487 (2015).
40. J. Chen, J. Yang, H. Guo, Z. Li, L. Zheng, Y. Su, Z. Wen, X. Fan, Z. L. Wang, Automatic mode transition enabled robust triboelectric nanogenerators. *ACS Nano* **9**, 12334–12343 (2015).
41. X. Li, M.-H. Yeh, Z.-H. Lin, H. Guo, P.-K. Yang, J. Wang, S. Wang, R. Yu, T. Zhang, Z. L. Wang, Self-powered triboelectric nanosensor for microfluidics and cavity-confined solution chemistry. *ACS Nano* **9**, 11056–11063 (2015).
42. G. Liu, M. Peng, W. Song, H. Wang, D. Zou, An 8.07% efficient fiber dye-sensitized solar cell based on a TiO<sub>2</sub> micron-core array and multilayer structure photoanode. *Nano Energy* **11**, 341–347 (2015).
43. H. Sun, X. Fu, S. Xie, Y. Jiang, H. Peng, Electrochemical capacitors with high output voltages that mimic electric eels. *Adv. Mater.* **28**, 2070–2076 (2016).
44. Z. Yang, J. Deng, X. Sun, H. Li, H. Peng, Stretchable, wearable dye-sensitized solar cells. *Adv. Mater.* **26**, 2643–2647 (2014).
45. J. Zhong, Y. Zhang, Q. Zhong, Q. Hu, B. Hu, Z. L. Wang, J. Zhou, Fiber-based generator for wearable electronics and mobile medication. *ACS Nano* **8**, 6273–6280 (2014).
46. J. Zhong, Q. Zhong, Q. Hu, N. Wu, W. Li, B. Wang, B. Hu, J. Zhou, Stretchable self-powered fiber-based strain sensor. *Adv. Funct. Mater.* **25**, 1798–1803 (2015).

#### Acknowledgments

**Funding:** Research was supported by the Hightower Chair Foundation, the National Key R&D Project from the Ministry of Science and Technology (2016YFA0202704), and the “Thousands Talents” program for pioneer researcher and his innovation team of China. Z.W. thanks the China Scholarship Council for supporting research at the Georgia Institute of Technology, USA.

**Author contributions:** Z.W., M.-H.Y., and Z.L.W. conceived the idea. Z.W., M.-H.Y., and H.G. designed the experiments. Z.W., M.-H.Y., H.G., and J.W. performed the F-SC experiments. M.-H.Y., H.G., W.X., L.Z., X.W., and X.S. performed the F-DSSC experiments. Z.W., H.G., and J.D. performed the F-TENG experiments. Z.W., M.-H.Y., H.G., Y.Z., C.H., and L.Z. graphed and analyzed the data. Z.W., M.-H.Y., and Z.L.W. wrote the paper. All authors discussed the results and commented on the manuscript. **Competing interests:** The authors declare that they have no competing interests.

**Data and materials availability:** All data needed to evaluate the conclusions in the paper are present in the paper and/or the Supplementary Materials. Additional data related to this paper may be requested from the authors.

Submitted 19 January 2016

Accepted 26 September 2016

Published 26 October 2016

10.1126/sciadv.1600097

**Citation:** Z. Wen, M.-H. Yeh, H. Guo, J. Wang, Y. Zi, W. Xu, J. Deng, L. Zhu, X. Wang, C. Hu, L. Zhu, X. Sun, Z. L. Wang, Self-powered textile for wearable electronics by hybridizing fiber-shaped nanogenerators, solar cells, and supercapacitors. *Sci. Adv.* **2**, e1600097 (2016).

ARTICLE

Received 4 Feb 2014 | Accepted 25 Jun 2014 | Published 31 Jul 2014

DOI: 10.1038/ncomms5525

# Force-dependent conformational switch of $\alpha$ -catenin controls vinculin binding

Mingxi Yao<sup>1,\*</sup>, Wu Qiu<sup>2,3,\*</sup>, Ruchuan Liu<sup>2,3</sup>, Artem K. Efremov<sup>1</sup>, Peiwen Cong<sup>1,4</sup>, Rima Seddiki<sup>5</sup>, Manon Payre<sup>5</sup>, Chwee Teck Lim<sup>1,6</sup>, Benoit Ladoux<sup>1,5</sup>, René-Marc Mège<sup>5</sup> & Jie Yan<sup>1,3,6,7</sup>

Force sensing at cadherin-mediated adhesions is critical for their proper function.  $\alpha$ -Catenin, which links cadherins to actomyosin, has a crucial role in this mechanosensing process. It has been hypothesized that force promotes vinculin binding, although this has never been demonstrated. X-ray structure further suggests that  $\alpha$ -catenin adopts a stable auto-inhibitory conformation that makes the vinculin-binding site inaccessible. Here, by stretching single  $\alpha$ -catenin molecules using magnetic tweezers, we show that the subdomains M<sub>I</sub> vinculin-binding domain (VBD) to M<sub>III</sub> unfold in three characteristic steps: a reversible step at  $\sim 5$  pN and two non-equilibrium steps at 10–15 pN. 5 pN unfolding forces trigger vinculin binding to the M<sub>I</sub> domain in a 1:1 ratio with nanomolar affinity, preventing M<sub>I</sub> domain refolding after force is released. Our findings demonstrate that physiologically relevant forces reversibly unfurl  $\alpha$ -catenin, activating vinculin binding, which then stabilizes  $\alpha$ -catenin in its open conformation, transforming force into a sustainable biochemical signal.

<sup>1</sup>Mechanobiology Institute, National University of Singapore, Singapore 117411, Singapore. <sup>2</sup>Department of Physics, National University of Singapore, Singapore 117542, Singapore. <sup>3</sup>College of Physics, Chongqing University, No. 55 Daxuecheng South Road, Chongqing 401331, China. <sup>4</sup>Singapore-MIT Alliance for Research and Technology, National University of Singapore, Singapore 117543, Singapore. <sup>5</sup>Institut Jacques Monod, CNRS UMR 7592, Université Paris Diderot, Paris 75013, France. <sup>6</sup>Department of Bioengineering, National University of Singapore, Singapore 117542, Singapore. <sup>7</sup>Centre for Bioimaging Sciences, National University of Singapore, Singapore 117546, Singapore. \* These are joint first authors. Correspondence and requests for materials should be addressed to R.-M.M. (email: mege@ijm.univ-paris-diderot.fr) or to J.Y. (email: phyyj@nus.edu.sg).



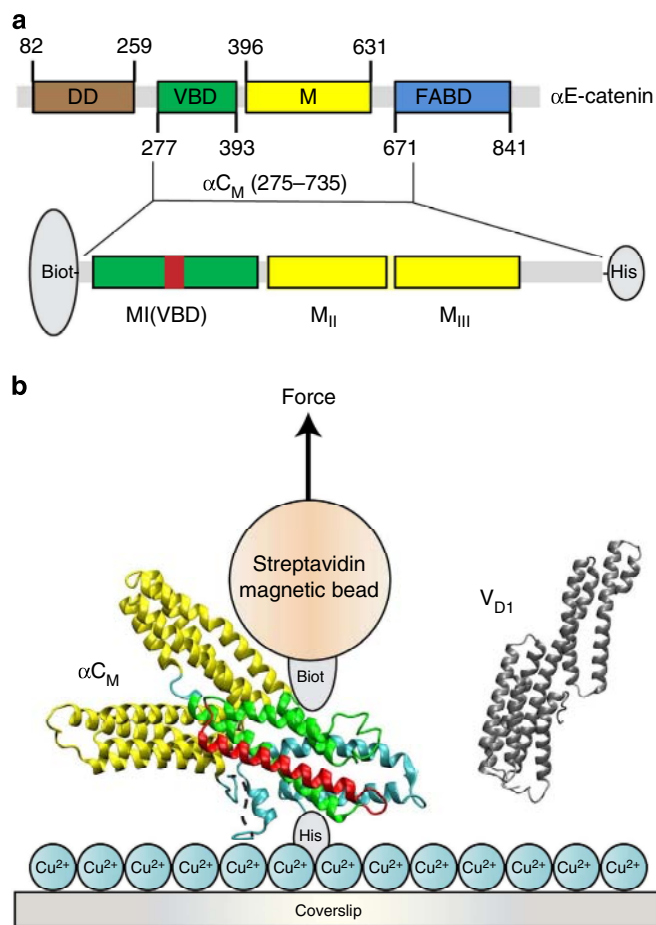
Cell–matrix and cell–cell adhesions are required in morphogenesis during embryogenesis, tissue development during fetal life, as well as tissue maintenance during adulthood<sup>1</sup>. In addition to mere cell membrane adhesion, fine-tuning of transmission of mechanical load from cell to extracellular matrix (ECM) and cell to cell is also essential to these processes<sup>2,3</sup>. The molecular mechanisms underlying cell–ECM mechanosensing processes have been partly unraveled. Although cell–ECM mechanotransduction may rely on more global adaptation of the actomyosin viscoelastic networks<sup>4</sup> and activation of mechanosensitive channels<sup>5</sup>, pioneering works have demonstrated the existence of integrin-associated cytoplasmic proteins with buried sites of phosphorylation such as p130Cas<sup>6</sup>, and of protein–protein interactions such as talin<sup>7,8</sup> that are unmasked upon myosin II-dependent stretching. The tension-dependent conformation switch of these proteins may thus initiate the force-dependent building of adaptor complexes linking cell–matrix adhesions to the tension-generating actomyosin network.

By analogy, cadherin-associated adhesion complexes might have an essential role in transducing forces at cell–cell junctions<sup>9,10</sup>. These complexes are tension adaptive, actin-cytoskeleton-associated structures, responsive to both external load and tensile force produced by intracellular myosin motors<sup>11,12</sup>. The mechanism of mechanosensing at cell–cell contacts has only been very recently investigated<sup>13,14</sup>, and  $\alpha$ -catenin appears as a central component of the force transmission pathway.

The  $\alpha E$  isoform of  $\alpha$ -catenin is expressed ubiquitously in early embryonic cells, and then restricted to epithelia. Its deletion is associated with impaired cadherin-mediated adhesion<sup>15,16</sup>, tissue growth, and homeostasis<sup>17–19</sup>. It has been recently hypothesized that  $\alpha E$ -catenin may act as a mechanotransducer in the pathway that converts mechanical strain on cadherin adhesions into a cue for junction strengthening<sup>11</sup>. Because vinculin accumulates at mature cell–cell junctions upon actomyosin generated tension<sup>11,20–22</sup> and binds  $\alpha E$ -catenin<sup>23–25</sup>, it has been proposed that  $\alpha$ -catenin functions in concert with vinculin. Further analysis of cadherin adhesion strengthening by cell doublet force separation measurement indicates that  $\alpha$ -catenin, vinculin and their direct interaction are required for tension-dependent intercellular junction strengthening<sup>26</sup>. These proteins appear as key candidates for mechanotransduction at cell–cell junctions.

Vinculin is a cytoplasmic actin-binding protein enriched in both focal adhesions and adherens junctions, essential for embryonic development<sup>27</sup>. At focal adhesions, vinculin has a critical function in linking integrins to F-actin. Vinculin is a compact globular protein composed of successive four  $\alpha$ -helix bundles. Five of these  $\alpha$ -helix bundles constitute the vinculin head binding to various partners such as talin, whereas the C-terminal constitutes the vinculin tail binding to F-actin. In the cytosol, vinculin is under an inactive head to tail conformation presenting only weak affinity for actin. In contrast, vinculin captured at focal adhesions by force-dependent activated talin is stabilized under an open conformation characterized by head to tail dissociation, stabilized by binding of the head to talin and high affinity binding of the tail to F-actin<sup>28</sup>.

$\alpha$ -Catenin is a complex protein with strong homology with the vinculin head domain, sharing a  $\lambda$ -shape arrangement of  $\alpha$ -helix bundles<sup>29</sup>. At cell–cell junctions,  $\beta$ -catenin directly binds to the N-terminus of  $\alpha$ -catenin<sup>30,31</sup> and to the intracellular tail of cadherins<sup>32,33</sup>, forming the cadherin/ $\beta$ / $\alpha$ -catenin complex.  $\alpha$ -Catenin possesses a domain of homodimerization and dimerizes in solution (Fig. 1a: DD domain); however, this domain overlaps with a N-terminal  $\beta$ -catenin-binding domain, and homodimerization of  $\alpha$ -catenin is inhibited by  $\beta$ -catenin



**Figure 1 | Domain map and experimental setup.** (a) Domain mapping of full-length and sub-domains of mouse  $\alpha E$ -catenin.  $\alpha E$ -catenin consists of an N-terminal dimerization domain (DD), followed by vinculin-binding domain (VBD; also referred to the  $M_I$  domain). Interaction between VBD and two other modulation domains ( $M_{II}$ – $M_{III}$ ) is suggested to inhibit vinculin binding.  $\alpha E$ -catenin contains a C-terminal F-actin-binding domain (FABD) that binds to F-actin and transmits mechanical forces generated by actomyosin contraction. The  $\alpha C_M$  construct (residues 275–735) is enclosed in the top bracket. (b) Schematics of experimental setup. A single  $\alpha C_M$  molecule is tethered between a cover glass surface and a paramagnetic bead through NTA-His tag and streptavidin-biotin linkages, respectively. The modulatory  $M_I$  (VBD) domain is shown in green,  $M_{II}$  and  $M_{III}$  domains in yellow. The vinculin-binding helix is marked in red. The  $V_{D1}$  molecule, which is also a helix bundle, is shown in silver. Force was applied to the paramagnetic bead using a pair of permanent magnets.  $\alpha C_M$  constructs were stretched in the absence or in the presence of  $V_{D1}$  of various concentrations. The model of  $\alpha C_M$  is adopted from PDB structure 4IGG.

binding<sup>29,34</sup>. The C-terminus of  $\alpha$ -catenin contains an F-actin-binding site<sup>25,35</sup>, which associates the tertiary cadherin/ $\beta$ -catenin/ $\alpha$ -catenin complex to the actin filaments<sup>36</sup>. Although direct binding has not been observed between the purified components of this complex in solution<sup>37</sup>, it is still acknowledged that  $\alpha$ -catenin dynamically links the complex to F-actin directly, indirectly or both, allowing force transduction and strengthening of adhesions<sup>13,26,38</sup>.  $\alpha$ -Catenin binds to other actin-binding proteins, such as vinculin<sup>18,24,25,39</sup>, ZO-1 (refs 25,40), afadin<sup>41</sup> and formin-1 (ref. 42), through sites distributed in the central part of the molecule. The actin-binding domain of  $\alpha$ -catenin located at the C-terminus of the molecule (Fig. 1a: FABD domain) appears to bind to the side of actin filaments, inducing

conformational changes of individual filaments and preventing the binding of the branching complex Arp2/3 and the severing protein cofilin<sup>43</sup>. Thus,  $\alpha$ -catenin binding to actin may favour assembly of unbranched filaments that are more protected from severing than dynamic, branched filament arrays<sup>44</sup>.

The  $\alpha$ -catenin central domain ( $\alpha$ C<sub>M</sub>, Fig. 1a: VBD + M domains) is an adhesion modulation domain<sup>25,45</sup>, composed of a vinculin-binding domain M<sub>I</sub> or VBD<sup>23,46</sup>, followed by the so-called modulation domains M<sub>II</sub> and M<sub>III</sub> (ref. 47). Biochemical and structural data suggest that the vinculin helix bundle (V<sub>D1</sub>) forming the vinculin head binds to a single vinculin-binding  $\alpha$ -helix (residues 305–355) within the  $\alpha$ -catenin VBD domain<sup>39,46</sup>. Structural data further indicate that  $\alpha$ -catenin can adopt an auto-inhibitory conformation<sup>48</sup> whereby the VBD domain is interacting with both M<sub>II</sub> and M<sub>III</sub> helix bundles, thus preventing accessibility of the vinculin-binding domain. Vinculin may only bind to  $\alpha$ -catenin when the VBD-M<sub>II</sub>-M<sub>III</sub> helix bundles are in an open conformation<sup>46–48</sup>. Altogether, these data suggest that  $\alpha$ -catenin may unfurl in a tension-dependent manner, allowing the recruitment of vinculin, and further strengthening of the cadherin complex/F-actin linkage. This pathway may be responsible for the mechanosensitive maturation of intercellular junctions. However, crucial experiments are lacking in support of this hypothesis. No direct evidence demonstrates the force-dependent unfurling exposing the VBD  $\alpha$ -helix and the binding of  $\alpha$ -catenin to vinculin under force.

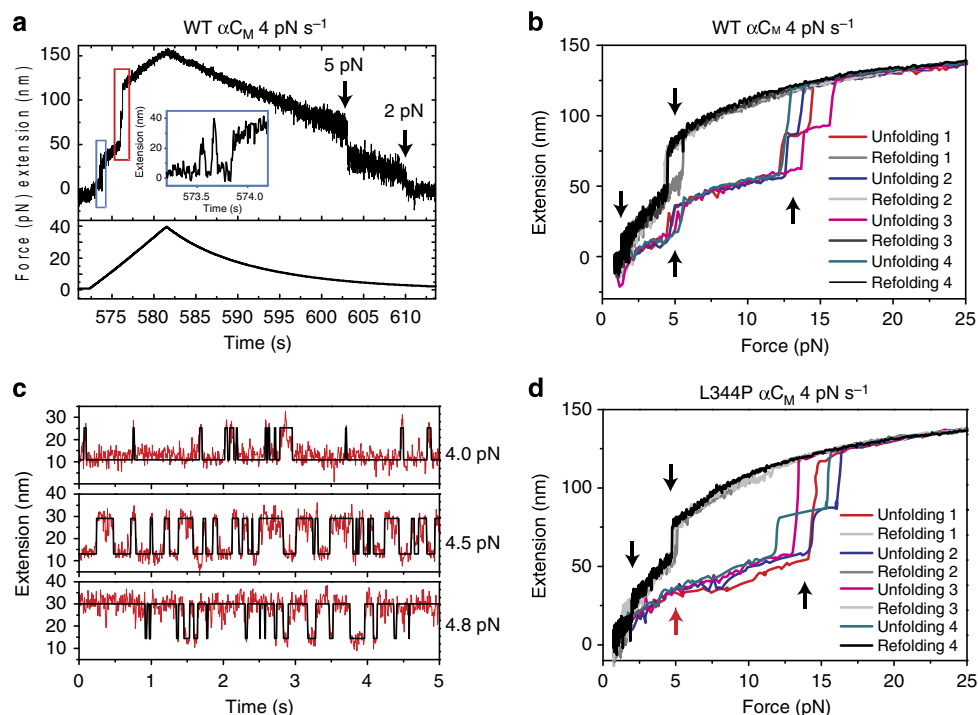
To investigate the role of  $\alpha$ -catenin in force transduction, we use single-molecule assays that allow us to obtain direct experimental evidence that physiological-range forces regulate  $\alpha$ -catenin conformation and  $\alpha$ -catenin–vinculin interaction.

Thus, we provide here a molecular mechanism by which forces are locally transformed into biochemical signal at cadherin-mediated adhesions, which has significant implications for adherens junction assembly and regulation.

## Results

**$\alpha$ C<sub>M</sub> unfolds in three characteristic steps under force.** To experimentally test the hypothesis that the modulation domain of  $\alpha$ E-catenin ( $\alpha$ C<sub>M</sub>) containing the VBD-M<sub>II</sub>-M<sub>III</sub> helix bundles can unfurl upon application of physiological-range forces<sup>39</sup>, we first investigated the force response of  $\alpha$ C<sub>M</sub> domain of mouse  $\alpha$ E-catenin (275–735), produced with a biotin tag at the N-terminal and a 6-His tag at the C-terminal (Fig. 1a), thanks to a stable high-force magnetic tweezers instrument<sup>49–51</sup>. For this set of experiments, we specifically tethered single  $\alpha$ C<sub>M</sub> molecules between an NTA-Cu<sup>2+</sup> functionalized coverslip and a streptavidin-coated paramagnetic bead and subjected the tethered molecules to forces exerted by a pair of permanent magnets (Fig. 1b). We recorded the extension change of the  $\alpha$ C<sub>M</sub> molecule based on the diffraction pattern of the bead at a sampling rate of 200 Hz with nanometer resolution<sup>49</sup>.

To obtain a mechanical characterization of the molecule, single  $\alpha$ C<sub>M</sub> tethers were subjected to force scanning cycles. In each cycle, force was increased at a constant loading rate of 4 pN s<sup>-1</sup> from ~1 pN to ~40 pN, which was followed with a force-decrease step, reducing force exponentially with time back to <1 pN that minimizes duration of the tether being held at large forces (Fig. 2a). The chosen loading rate of 4 pN s<sup>-1</sup> is within a physiologically relevant range, as recently estimated for integrin



**Figure 2 | Force response of  $\alpha$ C<sub>M</sub>.** (a) Extension change of  $\alpha$ C<sub>M</sub> recorded at 200 Hz in a typical force cycle experiment. During the stretch phase (force-increase) at a loading rate of 4 pN s<sup>-1</sup>, an unfolding step was observed at ~5 pN (blue box), and two additional ones occurred at higher forces (~15 pN; red box). Two refolding events, one at ~5 pN with >20 nm and another at ~2 pN with >10 nm, were observed during relaxation (force-decrease). The inset shows that the extension at ~5 pN is reversible. (b) Four force-extension curves recorded in four sequential stretch-relax cycles. The stretch curves are indicated in colour, whereas the relax curves are indicated in grey scale. Unfolding steps are marked by up arrows and refolding steps are marked by down arrows. Data in **b** are smoothed using 0.05-s time intervals. (c) Stepwise extension fluctuation at constant forces. Raw data are shown in red, and the black lines are fitted states using Hidden Markov method (Methods: ‘Determination of transition rates at constant forces’). (d) Typical force-extension curves obtained from four force cycles for L344P  $\alpha$ C<sub>M</sub> mutant on a single tether. The red up arrow marks the missing ~5 pN unfolding step.

stretching during cell retraction<sup>52</sup>. During the force-increase step, we identified unfolding events by sudden increases in the extension of the  $\alpha_{\text{CM}}$  tether, whereas we also identified refolding events during the force-decrease step by sudden decreases in the extension. To allow refolding of the  $\alpha_{\text{CM}}$  molecule following the force-decrease step, we held the  $\alpha_{\text{CM}}$  tether at  $<1$  pN for 1 min. During this period of time, the refolding of  $\alpha_{\text{CM}}$  appeared taking place with a  $>90\%$  probability (Supplementary Fig. 1a). The unfolding and refolding force-responses that we observed indicate that  $\alpha_{\text{CM}}$  behaves like a nonlinear spring, which may be important for its potential *in vivo* function as a mechanosensor.

In a typical force-increase scan, we found that the  $\alpha_{\text{CM}}$  unfolded in three characteristic steps (Fig. 2a). Because both extension and force at any time were known, the time traces of extension and force could be converted into force-extension curves (Fig. 2b). Representative unfolding and refolding force-extension curves obtained during successive force cycles on a single  $\alpha_{\text{CM}}$  tether shows remarkable reproducibility (Fig. 2b). We confirmed this reproducibility on multiple ( $>10$ ) independent  $\alpha_{\text{CM}}$  molecules (Supplementary Fig. 1b for another example).

At a constant loading rate of  $4 \text{ pN s}^{-1}$ , the first step occurred at  $5.2 \pm 0.7$  pN (mean  $\pm$  s.d.) and involved a reversible extension change of  $16.3 \pm 4$  nm (mean  $\pm$  s.d.) between two conformational states, which can be understood by unfolding the bundled  $\alpha$ -helices in the VBD domain into a linear chain of extended  $\alpha$ -helices as discussed in the Discussion section. The inset in Fig. 2a clearly shows that the extension of the tether fluctuates at forces  $\sim 5$  pN indicating that the transition of the corresponding domain is near equilibrium when the  $\alpha_{\text{CM}}$  tether is subjected to this force magnitude.

The two higher force steps were overlapping at about  $12.5 \pm 2.0$  pN and had similar step sizes of  $23.3 \pm 6.6$  nm corresponding to  $105 \pm 30$  residues. These unfolding sizes fit the domain sizes of  $\alpha_{\text{CM}}$  (VBD: 277–393,  $\text{M}_{\text{II}}\text{-M}_{\text{III}}$ : 396–631, Fig. 1a)<sup>25,45</sup>. As the unfolding forces of the two higher force steps were close to each other, they could combine into a single large step of  $\sim 50$  nm. During the following force-decrease scan, we observed two apparent refolding steps at low forces, one at  $\sim 5$  pN, and another at  $\sim 2$  pN (Fig. 2a).

The co-existence of unfolding and refolding steps of same sizes around 5 pN during the stretching process suggests that it corresponds to a near-equilibrium transition operating in this range of forces (Supplementary Fig. 1c). We were particularly interested in this transition because its force dependence is close to the range of forces generated by a single myosin motor<sup>53</sup>. If this transition is near-equilibrium in this range of forces it should be largely insensitive to loading rate. To further demonstrate the reversibility of this transition, constant force experiments were carried out in the 4–5 pN range (Fig. 2c). Slight increase in force from  $\sim 4.1$  to  $\sim 4.8$  pN switched the predominant folded state to the predominant unfolded state. Analysis of the dwell times of each state determined the force-dependent unfolding and refolding transition rates and a critical force of  $\sim 4.7$  pN (Supplementary Fig. 1d). These results confirmed that the  $\sim 5$  pN transition was insensitive to loading rate in the range tested and reversible around a force of 5 pN, which may be important for physiological myosin-driven conformational switch of  $\alpha$ -catenin.

Altogether, the highly reproducible force-extension curve we observed characterizes the mechanical response of  $\alpha_{\text{CM}}$ , and can serve as the basis for further analysis of the force-dependent interaction between  $\alpha_{\text{CM}}$  and the  $\text{V}_{\text{D1}}$  domain of the vinculin head.

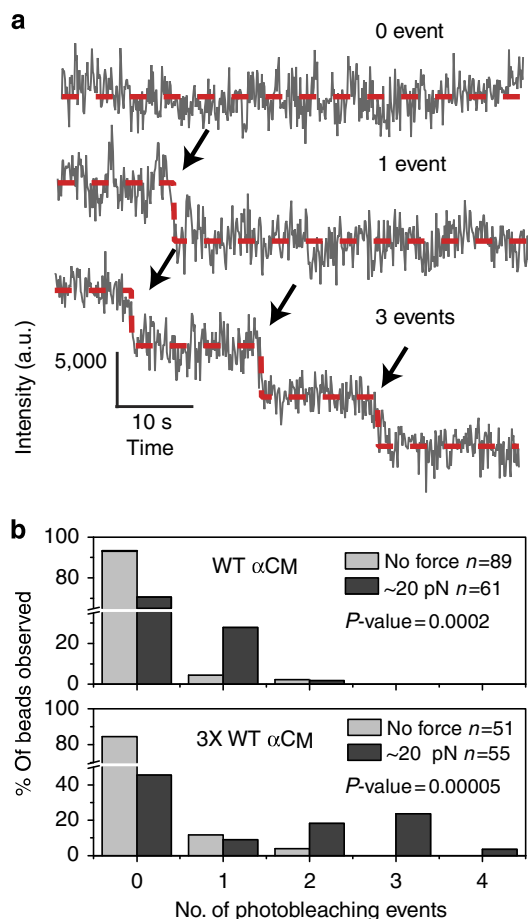
**$\sim 5$  pN force unfurls  $\alpha_{\text{CM}}$  exposing the vinculin-binding site.** To determine whether the  $\alpha_{\text{CM}}$  near-equilibrium unfolding at

$\sim 5$  pN corresponds to the unfurling of the VBD domain allowing the stabilization of the  $\text{V}_{\text{D1}}$ -binding  $\alpha$ -helix predicted by structural data<sup>39,48</sup>, we performed glutathione S-transferase (GST) pull-down experiments. WT  $\alpha_{\text{CM}}$  proteins were specifically pulled down with GST- $\text{V}_{\text{D1}}$  (Supplementary Fig. 2a), as expected from the presence of the VBD domain. To disrupt the  $\text{V}_{\text{D1}}$ -binding  $\alpha$ -helix, we introduced a leucine to proline point mutation in the middle of the  $\alpha$ -helix (construct L344P  $\alpha_{\text{CM}}$ )<sup>39</sup>. As previously reported<sup>39</sup>, this mutation inhibited the binding of  $\alpha_{\text{CM}}$  to GST- $\text{V}_{\text{D1}}$  (Supplementary Fig. 2a). We repeated the force-cycling experiments on L344P  $\alpha_{\text{CM}}$ . The 5 pN reversible unfolding/refolding step was not observed with the mutant protein (Fig. 2d and Supplementary Fig. 2b,c) indicating that the  $\text{V}_{\text{D1}}$ -binding  $\alpha$ -helix was required for proper unfolding/refolding of  $\alpha_{\text{CM}}$  at  $\sim 5$  pN. It further suggested that the transition at  $\sim 5$  pN involves the unfurling of the VBD domain allowing the formation of the vinculin-binding  $\alpha$ -helix.

We then determined whether  $\alpha_{\text{CM}}$  mechanical stretching influences  $\text{V}_{\text{D1}}$  binding. To do so, we counted the number of photobleaching events of Alexa 488-labelled  $\text{V}_{\text{D1}}$  bound to  $\alpha_{\text{CM}}$  maintained or not under force. Alexa 488 was conjugated to  $\text{V}_{\text{D1}}$  following the  $\text{V}_{\text{D1}}$  labelling protocol used in a previous study of talin- $\text{V}_{\text{D1}}$  binding<sup>7</sup> (Methods: 'Photobleaching counting'). Three typical time trajectories of the fluorescence intensity with zero, one and three photobleaching events, respectively, are presented in Fig. 3a. The number of photobleaching events was very low when no force was applied and increased fivefold when force was increased from 0 to 20 pN (Fig. 3b, upper panel). Significantly, more tethers showed one photobleaching event at 20 pN force compared with that at 0 pN force. This result is consistent with previous reports suggesting the binding of only one vinculin-binding  $\alpha$ -helix per  $\alpha$ -catenin central domain<sup>24</sup>. We performed similar experiments with a construct containing three  $\alpha_{\text{CM}}$  domains. Consistently, using this artificial 3x WT  $\alpha_{\text{CM}}$  molecule-bearing three potential vinculin-binding sites, we also observed an increase of photobleaching events when forces were increased from 0 to 20 pN, with a number of photobleaching events reaching three at 20 pN (Fig. 3b). The rare cases where we observed more than one photobleaching event on WT  $\alpha_{\text{CM}}$ , or more than three photobleaching events on 3x WT, were likely due to low probability of double or multiple coupling of the Alexa 488 dyes on some  $\text{V}_{\text{D1}}$  molecules. Altogether these results demonstrate that the mechanical stretching of  $\alpha_{\text{CM}}$  strongly activates the binding of a single  $\text{V}_{\text{D1}}$  per VBD domain.

**$\text{V}_{\text{D1}}$  binds stretched  $\alpha_{\text{CM}}$  and inhibits  $\text{M}_{\text{I}}$  domain refolding.** To correlate the force-dependent binding of  $\text{V}_{\text{D1}}$  to one of the specific unfolding steps of the  $\alpha_{\text{CM}}$  molecule described above, we investigated the effect of  $\text{V}_{\text{D1}}$  on the force responses of  $\alpha_{\text{CM}}$ . We carried out force cycle experiments in the presence of  $\text{V}_{\text{D1}}$  in the solution. In a typical force cycle in the presence of 10 nM  $\text{V}_{\text{D1}}$ , the  $\sim 5$  pN unfolding step disappeared in the force-increase phase, whereas the two unfolding steps at 10–18 pN remained (Fig. 4a). In the force-decrease phase, we observed a small ( $\sim 2.5$  nm) step at  $\sim 9$  pN, which was not observed in the absence of  $\text{V}_{\text{D1}}$ , followed by two larger ( $>15$  nm) steps at lower forces also observed in the absence of  $\text{V}_{\text{D1}}$ .

Figure 4b shows unfolding force distributions normalized by the number of force cycles at different  $\text{V}_{\text{D1}}$  concentrations recorded during force-increase phases on a single tether with more than 30 unfolding events for each condition, which clearly reveals that the frequency of the  $\sim 5$  pN transition decreases as the  $\text{V}_{\text{D1}}$  concentration increases. Figure 4c summarizes results from eight different tethers recorded in the absence or in the presence of  $\text{V}_{\text{D1}}$  at 1 and 10 nM concentrations. The  $\sim 5$  pN



**Figure 3 | Photobleaching counting of  $V_{D1}$  bound to WT  $\alpha_{CM}$  and 3X WT  $\alpha_{CM}$  under force.** (a) Three representative time-lapse traces of the fluorescent intensity measured below individual tethered beads: 0 (WT  $\alpha_{CM}$ , no  $V_{D1}$  in solution), 1 (WT  $\alpha_{CM}$ ,  $V_{D1}$  in solution) and 3 photobleaching events (3x WT  $\alpha_{CM}$ ,  $V_{D1}$  in solution) were shown for each case. Dashed lines are drawn for visual guidance. (b) Histograms of the percentage of beads with different numbers of photobleaching events observed for WT  $\alpha_{CM}$  and 3x WT  $\alpha_{CM}$  constructs. The number of individual tethered beads tested for each condition is denoted by 'n' in figure panel. The  $P$ -value was obtained from the  $\chi^2$  test with the null hypothesis that the photobleaching statistics is independent on whether force is applied.

unfolding events were significantly reduced in the presence of 1 nM  $V_{D1}$ , and nearly disappeared in the presence of 10 nM  $V_{D1}$ . Similar results were obtained at higher  $V_{D1}$  concentrations (Supplementary Fig. 3).

Interestingly, we found an additional unfolding step at  $> 35$  pN associated with a very small step size of  $\sim 3.0$  nm appearing in the presence of  $V_{D1}$  in solution, which was not observed in the absence of  $V_{D1}$  (Fig. 4a). Considering that high forces could favour a transition of the vinculin-binding  $\alpha$ -helix from the  $V_{D1}$ -bound state to a  $V_{D1}$ -unbound, extended random coiled peptide chain state, this step could be interpreted as the dissociation of  $V_{D1}$  bound to the vinculin-binding  $\alpha$ -helix. Therefore, at a sufficiently high force,  $V_{D1}$  dissociation should occur, accompanied by a small unfolding step during the subsequent helix-to-coil transition of the vinculin-binding  $\alpha$ -helix. The  $\sim 3$  nm unfolding step size observed at  $\sim 39$  pN was consistent with the estimated extension increase during helix-to-coil transition of the vinculin-binding  $\alpha$ -helix at 30–40 pN (Methods: 'Helix-to-coil transition').

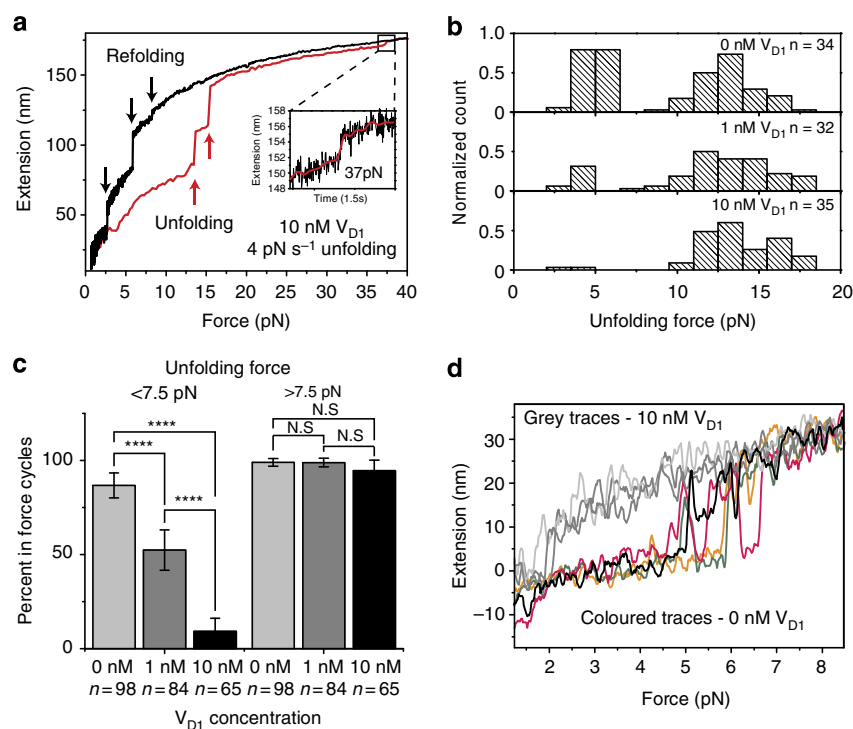
The fact that we observed only one  $\sim 3$  nm unfolding step at high forces again strongly indicated that a single  $V_{D1}$ -binding helix exists in the  $\alpha_{CM}$  construct, which was consistent with our photobleaching experiments (Fig. 3). Similarly, the  $\sim 2.5$  nm refolding step at  $\sim 9$  pN that we only observed in the presence of  $V_{D1}$  may be due to the re-binding of  $V_{D1}$  to the unfolded vinculin-binding  $\alpha$ -helix of  $\alpha_{CM}$ , which induces formation of the  $\alpha$ -helix structure of the vinculin-binding site. Consistently, when experiments were performed, at a lower concentration of  $V_{D1}$  (1 nM) to reduce the chance of re-binding during force decrease, we observed that displacement of the bound  $V_{D1}$  at high force could restore the  $\sim 5$  pN transitions (Supplementary Fig. 3c).

To investigate whether activation of  $V_{D1}$  binding to  $\alpha_{CM}$  requires or not complete unfolding of  $\alpha_{CM}$ , we performed force-cycling experiments up to 9 pN at a loading rate of  $4$  pN  $s^{-1}$ . We selected this maximal force because it only allowed unfolding of the weakest domain at  $\sim 5$  pN. We found that unfolding the weakest domain was sufficient to activate  $V_{D1}$  binding that abolished the  $\sim 5$  pN unfolding/refolding events (Fig. 4d). The results indicated that unfolding the VBD domain alone was sufficient to activate  $V_{D1}$  binding. Taken together, these results suggested that the vinculin-binding  $\alpha$ -helix in  $\alpha_{CM}$  could be reversibly exposed by mechanical force of  $\sim 5$  pN. In addition, they indicated that  $V_{D1}$  binding to the exposed vinculin-binding  $\alpha$ -helix inhibited  $\alpha_{CM}$  refolding at low force, and that the bound  $V_{D1}$  could be displaced at large forces.

**$V_{D1}$  binds to and locks  $\alpha_{CM}$  in its open conformation.** To evaluate to which extent mechanical force increased the affinity of  $V_{D1}$  binding to  $\alpha_{CM}$ , we incubated  $\alpha_{CM}$  tethers in the presence of 10–100 nM  $V_{D1}$  at low force (1–2 pN) for 10 min before the first stretching. Should  $V_{D1}$  spontaneously bind to the  $\alpha_{CM}$  tether at low force during the time, we would expect to observe a loss of the  $\sim 5$  pN unfolding/refolding step during the first force-increase scan. In three out of four independent experiments, we observed the  $\sim 5$  pN transition and the two higher force unfolding steps in the first force-increase scan (Fig. 5a, and Supplementary Fig. 4a,b), indicating that no  $V_{D1}$  binding had occurred within 10 min incubation at  $\sim 2$  pN. In addition, we found that the  $\sim 5$  pN transition was lost in the subsequent force cycles, whereas the two higher force species remained. These results were consistent with  $V_{D1}$  binding occurring after the first stretching procedure, which locked the vinculin-binding  $\alpha$ -helix of the  $M_I$  domain in an open state. In the fourth experiment at 100 nM  $V_{D1}$ , the  $\sim 5$  pN transition step disappeared in the first force-increase scan, indicating  $V_{D1}$  binding before the force-increase scan. A close examination of the extension time trace revealed that a spontaneous binding of  $V_{D1}$  occurred at  $\sim 2$  pN at minutes after we introduced  $V_{D1}$  solution, as indicated by an abrupt extension increase (Fig. 5b). As  $V_{D1}$  binds to unfolded  $\alpha_{CM}$  in seconds under  $> 5$  pN forces, these results indicated that mechanical forces above 5 pN strongly promoted  $V_{D1}$  binding to  $\alpha_{CM}$ .

**$V_{D1}$  bound to exposed VBD has a slow off-rate at low force.** Then, to quantify the stability of  $V_{D1}$  association to mechanically exposed  $V_{D1}$ -binding  $\alpha$ -helix under force, we carried out force-jump experiments in which force was alternated between 8 pN to promote rapid  $V_{D1}$  binding, and a high force to dissociate the  $V_{D1}$  from the  $V_{D1}$ -binding  $\alpha$ -helix. We found that a single  $V_{D1}$  dissociation event, indicated by a  $\sim 3$ -nm unfolding step, occurred within 10 s after force was switched to  $\sim 40$  pN (Fig. 6a), which was not observed for the L344P mutant (Fig. 6b).

To quantify the force-dependent off-rate of  $V_{D1}$  bound to  $\alpha_{CM}$ , we repeated such force-jump for many cycles on native  $\alpha_{CM}$  at a



**Figure 4 | Unfolding and refolding of  $\alpha C_M$  in the presence of  $V_{D1}$ .** (a) Force-extension curve of  $\alpha C_M$  in a typical stretch-relax force cycle in the presence of 10 nM  $V_{D1}$ . The inset shows a  $\sim 3$  nm  $V_{D1}$  dissociation unfolding step at  $\sim 37$  pN. (b) Unfolding force histogram obtained from repeating stretch-relax force cycles on a single  $\alpha C_M$  at different  $V_{D1}$  concentrations. (c) Percentages of observed unfolding events at  $<7.5$  pN and  $>7.5$  pN unfolding cycles at different  $V_{D1}$  concentrations. The significance indicated by the asterisks is based on  $P$ -value calculation from the  $\chi^2$  test with the null hypothesis that the percentages of the unfolding events are independent on the  $V_{D1}$  concentration. Four asterisks denote a  $P$ -value smaller than 0.0001. The data were collected from eight independent tethers. The error bar denotes 95% confidence interval of probability estimation. (d) Three force-extension curves recorded during three sequential stretch processes between 1 and 9 pN in the presence of 0 nM  $V_{D1}$  (coloured traces), where only the  $\sim 5$  pN unfolding/refolding events occurred. After each stretch, force was jumped to 0.1 pN for 1 min for refolding before the next stretch was performed in the presence of 10 nM  $V_{D1}$  (black and grey traces). The  $\sim 5$  pN unfolding/refolding event was observed during the first stretch cycle (black), but was lost in the subsequent three stretches. Data in d are smoothed using 0.05-s time interval.

variety of forces. The cumulative dissociation time distribution (the percentage of vinculin dissociated at time  $t$ ) at various high forces from three independent tethers was obtained (Fig. 6c). At each force, the time window of observation was chosen so that in more than 90% of the force-jump cycles vinculin dissociation events were observed. The cumulative dissociation distributions were fitted by an exponential decay function  $1 - \exp(-tK_{off})$ , where the parameter  $K_{off}$  characterizes the rate of dissociation at force  $f$ . We found that the logarithm of  $K_{off}(f)$  roughly linearly depended on force (Fig. 6d), from which the off-rate at low forces could be estimated by linear extrapolation. At  $<10$  pN, the extrapolated off-rate is  $<10^{-5} s^{-1}$ . Such an ultraslow dissociation rate of  $V_{D1}$  from exposed  $V_{D1}$ -binding  $\alpha$ -helix may explain why the bound  $V_{D1}$  could inhibit refolding of  $\alpha C_M$ . Altogether, these data indicated a strong stability of the vinculin/ $\alpha$ -catenin complex with a rapid formation and slow dissociation in the tension range 5–30 pN.

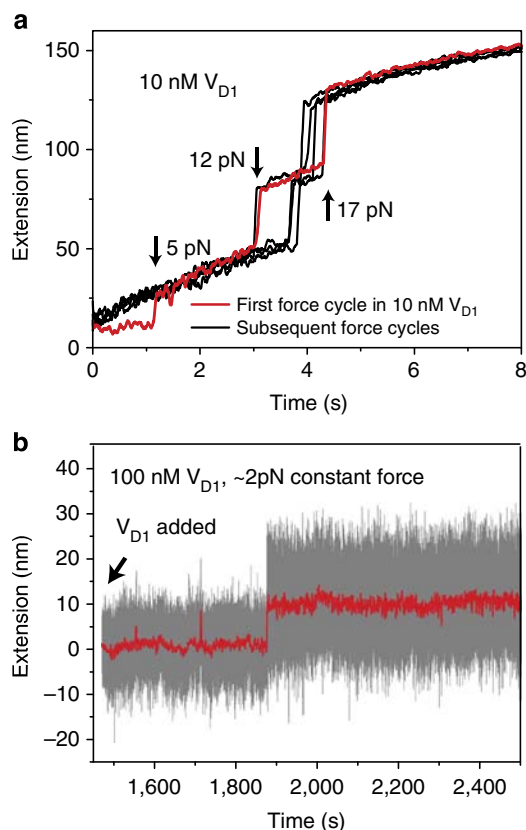
## Discussion

We report here on the mechanical response of the central domain of  $\alpha E$ -catenin ( $\alpha C_M$ ) and its force-dependent binding to the vinculin head ( $V_{D1}$ ), characterized at the single-molecule level, in a physiologically relevant range of forces. Our results show that  $\alpha C_M$  displays three major unfolding steps, occurring at different forces in the range of 5–20 pN under a physiologically loading rate of  $4 pN s^{-1}$ . We identified the  $M_I/VBD$  domain of  $\alpha$ -catenin,

which contains the  $V_{D1}$ -binding site made of a single  $\alpha$ -helix, as the weakest domain that unfolded at  $\sim 5$  pN. This unfolding step was lost when a single point mutation (L344P) is introduced in the  $\alpha$ -helix<sup>39</sup>, as well as when  $V_{D1}$  is bound to  $\alpha C_M$ .

The two larger force-unfolding events are unrelated to binding of  $V_{D1}$ , and are attributed to the unfolding of the sub-domains  $M_{II}$  and  $M_{III}$  also constituted of helix bundles but not predicted to contain vinculin-binding sites. Structural data suggest that in the folded state,  $M_I/VBD$  interacts with both  $M_{II}$  and  $M_{III}$  (ref. 47); therefore this interaction may stabilize VBD in its closed conformation, as well as contributing to the stabilization of the  $M_I$ - $M_{III}$  subdomains. Our results are consistent with a hypothesis that the interaction of the three sub-domains contributes to the stabilization of  $\alpha$ -catenin under its close conformation, whereas a moderate 5 pN stretching force disrupt this inter-domain interaction resulting in exposing the vinculin-binding site in the  $M_I/VBD$  domain.

The  $\sim 5$  pN unfolding and folding transitions are nearly at equilibrium within the loading rates tested in the experiments. These transitions involved a step size of  $\sim 16$  nm with a critical force of  $\sim 4.7$  pN at which folding and unfolding are balanced. This transition cannot be explained by the disruption of the inter-domain interactions alone; otherwise much smaller transition steps would be expected as each subdomain has a dimension of only  $\sim 3$  nm in the folded state. Together with data obtained from L344P mutation and  $V_{D1}$ -binding studies, the  $\sim 16$  nm step involved in this transition is consistent with a picture that the



**Figure 5 | Mechanical stretching activates  $V_{D1}$  binding to  $\alpha_{C_M}$ .** (a)

Extension change of  $\alpha_{C_M}$  in multiple stretch-relax force cycles in the presence of 10 nM  $V_{D1}$ . The  $V_{D1}$  solution was slowly introduced at a low force ( $\sim 1$  pN) to avoid  $\alpha_{C_M}$  unfolding by fluid-drag force. After the  $V_{D1}$  solution was introduced, the  $\alpha_{C_M}$  molecule was held at  $\sim 2$  pN for 10 min in the  $V_{D1}$  solutions before being stretched for the first time. Data were smoothed with 0.05-s time window. (b) In one out of four experiments after introduction of 100 nM  $V_{D1}$  solution at 2 pN, spontaneous binding of  $V_{D1}$  occurred indicated by a stepwise unfolding event. For clarity, data are smoothed using 0.5-s time interval.

disruption of the inter-domain interactions at  $\sim 5$  pN leads to a subsequent unfolding of the  $M_1$ /VBD  $\alpha$ -helix bundle. The extension of an unfolded peptide in random coil and in  $\alpha$ -helix conformations is similar,  $\sim 17$  nm estimated for a chain of extended helices with total  $\sim 32$  helical turns of 116 residues in the  $M_1$  domain, and  $\sim 15$  nm of the same number of residues in the random coil conformation at  $\sim 5$  pN estimated based on the worm-like chain polymer model with a bending persistence length of  $\sim 0.5$  nm (reported from 0.4–0.6 nm)<sup>54–57</sup>. Considering that  $V_{D1}$ -binding occurred at this force range, we reason that the unbundled  $\alpha$ -helices in the  $M_1$  domain at  $\sim 5$  pN likely assumed a conformation as a chain of extended  $\alpha$ -helices rather than a randomly coiled peptide chain.

We then demonstrated and characterized in details the kinetics of the force-dependent binding of the  $V_{D1}$  to  $\alpha_{C_M}$ . Indeed, our results revealed that a characteristic force response of  $\alpha_{C_M}$  controlled the level of  $V_{D1}$  binding.  $\alpha_{C_M}$  unfolding at  $\sim 5$  pN was sufficient to trigger  $V_{D1}$  binding at a nanomolar concentration, which prevented refolding of  $\alpha_{C_M}$  VBD even after force was released. This binding was observed in the presence of  $V_{D1}$  at concentrations as low as 1 nM and was maximum in the presence of 10 nM  $V_{D1}$ , implying a strong affinity of  $V_{D1}$  to  $\alpha_{C_M}$  VBD triggered by  $> 5$  pN force. Overall, the effect of  $V_{D1}$  binding to the vinculin-binding  $\alpha$ -helix in  $\alpha_{C_M}$  on the characteristic force

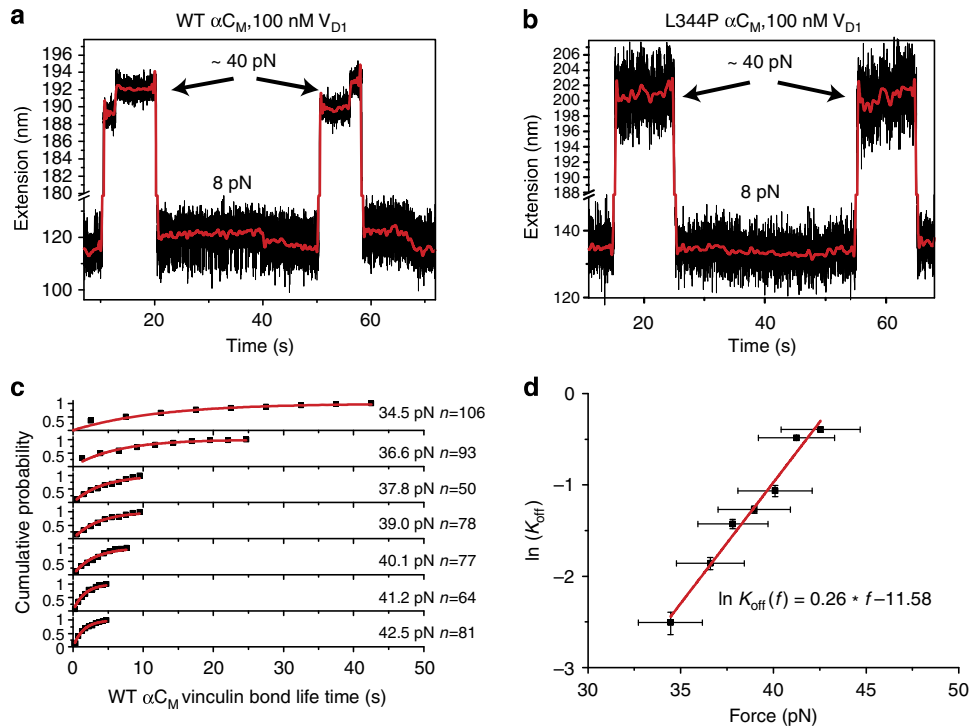
response of  $\alpha_{C_M}$  is similar to the leucine to proline mutation at the residue 344 of  $\alpha_{C_M}$ , both abolishing the  $\sim 5$  pN unfolding/refolding transitions. These results are also consistent with our observation that  $V_{D1}$  did not bind to L344P  $\alpha_{C_M}$  in *in-vitro* pull-down assays.

To estimate the increase in the binding affinity of  $V_{D1}$  to  $\alpha_{C_M}$  by force, we used results from published isothermal titration calorimetry studies, which indicate a  $K_D$  of  $82 \pm 19$  nM for  $\alpha_{C_M}$  binding to  $V_{D1}$  at zero force<sup>58</sup>. Based on these calculations, and considering that the apparent  $V_{D1}$  binding to mechanically stretched  $\alpha_{C_M}$  at  $\sim 5$  pN was observed at  $\sim 1$  nM  $V_{D1}$  and maximum at  $\sim 10$  nM  $V_{D1}$ , we estimated that a force of several piconewton increased the binding affinity of  $V_{D1}$  to  $\alpha_{C_M}$  by about 100-folds, which may be sufficient to activate auto-inhibited vinculin by competing off its head-to-tail association<sup>59</sup>. Overall, these data provide molecular evidences in strong support of  $\alpha$ -catenin as being the force-dependent molecular switch acting at cell–cell junctions to recruit vinculin (Fig. 7), at the basis of the reported tension-dependent growth and adaptation of these junctions<sup>12,22,26,60</sup>.

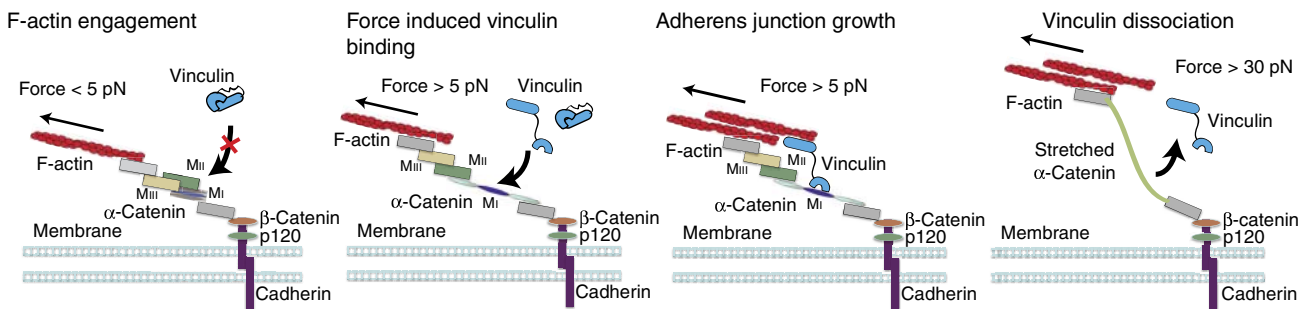
Our results revealed that vinculin head binding is biphasically dependent on force. In the small force range ( $< 5$  pN) where  $\alpha_{C_M}$  existed as natively folded, auto-inhibitory helical bundles, and in the high force range ( $> 30$  pN) where the  $V_{D1}$ -binding site was converted from its  $\alpha$ -helix conformation to an extended random coiled peptide chain, binding of  $V_{D1}$  was strongly inhibited. Between 5 and 30 pN, binding of  $V_{D1}$  was significantly promoted. As 5 pN is close to the force that can be exerted by a single myosin motor<sup>53</sup>, the low-force regime is likely involved during early adhesion formation with low myosin activity. The high-force  $V_{D1}$  dissociation is also physiologically relevant, as a 30-pN force can be produced by several cooperative myosins or external forces exerted on cells. Ultimately, locking  $\alpha$ -catenin in a partially unfolded conformation may regulate cellular adhesion strengthening in a force-dependent manner. Similarly, high forces achieved upon mobilization of multiple myosin molecules pulling on a single  $\alpha$ E-catenin molecule via F-actin may eventually release vinculin at  $> 30$  pN and then lead to the disruption of the mechanosensitive link<sup>61</sup>. This may explain the disruption of cadherin adhesions observed upon increased cell contraction obtained by increasing RhoA activity<sup>62</sup>. To elucidate these mechanisms, further experiments *in cellulo* will be required in the future.

The force-dependent process centered on  $\alpha$ -catenin we unraveled here may further cooperate with the binding of other  $\alpha$ -catenin partners to regulate the strength of the cytoskeleton linkage to cell–cell junctions. A  $\sim 5$  pN force deforms the modulation domain of  $\alpha$ -catenin and initializes binding of  $V_{D1}$ . The resulting lockage of  $\alpha$ -catenin in a partially unfolded conformation may have a downstream impact on interactions between  $\alpha$ -catenin and other junctional and cytoskeleton proteins, such as  $\alpha$ -catenin itself, afadin, ZO-1,  $\alpha$ -actinin and F-actin. However, further understanding of these processes will require precise structural and biochemical data on these complexes that are lacking so far. Up to date, a complete structural description of  $\alpha$ E-catenin under both its closed and open conformations is still lacking.

The exact sequential mechanistic pathway by which  $\alpha$ -catenin and vinculin bind together at cell–cell contacts has been highly debated within the field. Bakolitsa *et al.* proposed that  $\alpha$ E-catenin VBD binding to vinculin can activate vinculin<sup>58</sup>; however, previous data suggested that  $\alpha$ E-catenin lacking the actin-binding domain, or the VBD domain alone, bound poorly to full-length vinculin in solution unless F-actin is present in the solution<sup>39,46</sup>. These results suggested that  $\alpha$ E-catenin or the VBD domain alone were not sufficient to activate vinculin by direct



**Figure 6 | High force displaces the bound  $V_{D1}$  from the vinculin-binding site in  $\alpha_{C_M}$ .** (a) Extension change of WT  $\alpha_{C_M}$  during force jump between ~8 and ~40 pN in the presence of 100 nM  $V_{D1}$ . (b) Extension change of L344P  $\alpha_{C_M}$  during the same force jump procedure. (c) The histogram of lifetime of  $V_{D1}$  bound to  $\alpha_{C_M}$  at different forces. Red curves are fittings with exponential decay function from which the dissociation rates were obtained. The number of events observed in each condition is denoted by 'n' in figure panel. The data were obtained from three individual tethers. (d) The logarithm of the dissociation rate is roughly linearly dependent on force. Red line denotes linear fitting of the log-scaled force-dependent off-rate. From the slope, the transition distance is estimated to be ~1 nm, and the dissociation rate at no force is estimated to be  $9.3 \times 10^{-6} s^{-1}$  by extrapolation based on the Bell's model<sup>69</sup>. Y error bars denote 95% confidence interval of off-rate estimation, X error bars denote the ~5% relative error of our force calibration method.



**Figure 7 | Schematics of biphasic dependence of  $V_{D1}$  binding to  $\alpha_{C_M}$  on force.** At low force (<5 pN),  $\alpha_{C_M}$  exists under an auto-inhibited helix bundle conformation that prevents  $V_{D1}$  binding. At high force (>30 pN),  $V_{D1}$  binding is also inhibited because the  $\alpha$ -helix conformation of the vinculin-binding site bound with  $V_{D1}$  is unstable. In the intermediate force range (5–30 pN), the auto-inhibited conformation of  $\alpha_{C_M}$  is released, and the vinculin-binding site is exposed for  $V_{D1}$  binding.

interaction with the vinculin head. Nonetheless, as  $\alpha$ E-catenin and the VBD domain were not placed under force in those experiments, those results do not rule out the possibility that  $\alpha$ E-catenin alone can directly activate vinculin when it is placed under force. Our results demonstrated that  $V_{D1}$  bound to mechanically exposed VBD in  $\alpha_{C_M}$  under 5–30 pN forces with a nanomolar dissociation constant. This is significantly lower than the  $K_D = \sim 50\text{--}90$  nM determined for the head-to-tail association of vinculin<sup>59,63</sup>. Such a strong affinity between  $V_{D1}$  and mechanically stretched  $\alpha$ E-catenin suggests that it may be able to compete off the vinculin head-to-tail association of auto-inhibited vinculin, which warrants future studies. In *in vivo* conditions, such stably associated activated vinculin may then

bind itself to other molecular partners of the junctional complex, such as of F-actin,  $\beta$ -catenin<sup>64</sup> and PtdIns(4,5)P<sub>2</sub> (ref. 58), further contributing to the tension-dependent maintenance, strengthening and force-adaptation of cell–cell junctions.

To our knowledge, this work provides the first molecular demonstration of a tension-dependent conformational switch for a cadherin-associated protein. It provides a molecular mechanism explaining the local mechanosensitivity of cell–cell junctions, based on tension-dependent unfurling of  $\alpha$ -catenin and recruitment of vinculin, a pathway that has been overwhelmingly hypothesized but surprisingly never proven so far. Further studies will be needed to determine whether the pathway is unique at cell–cell junctions or cooperate with similarly operating

molecular mechanosensors and/or with more globally distributed mechano-adaptation of the actomyosin cytoskeleton<sup>4</sup>. Together with previous studies on force-dependent binding of vinculin to talin at integrin-mediated cell–matrix adhesions<sup>7,8</sup>, this work indicates that tension-dependent unfurling of mechanosensitive proteins and recruitment of actin-binding adaptor proteins to adhesion plaques is a central mode of mechanotransduction at adhesion sites. Further dissection of cell-context modulation of this pathway has broad implications for the understanding of cell adaptation to cell–ECM and cell–cell transduced mechanical load, an important factor of tissue reshaping, tumour progression and collective cell migration.

## Methods

**Protein expression and purification.** A PCR product of the mouse  $\alpha$ E-catenin central domain ( $\alpha$ C<sub>M</sub>; residues: 275–735) was cloned into the di-cistronic pDW363 vector, co-expressing the *Escherichia coli* biotin holoenzyme synthetase (Bir A)<sup>65</sup>. Briefly, the 822–2266 nucleotide fragment of the coding sequence of the mouse  $\alpha$ E-catenin cDNA (NM\_009818) was amplified by PCR and cloned in phase between the *Xho*I and *Bam*HI sites in N-terminal of the lysine-containing sequence recognized by Bir A, replacing the MalE-coding sequence. A 6His-coding sequence followed by a stop codon was added in C-terminal of the  $\alpha$ E-catenin sequences. Unique *Kpn*I and *Apa*I sites were introduced on both sides of the recombinant  $\alpha$ E-catenin, thanks to the following forward: 5'-CTGGTGGCTCGAGCGGTACCGGGCGAGAGCTGGCATACTGCT-3', and reverse: 5'-ATGACCGACTTCACCCGAGGCAAAGGGCCCGGGCCGGGCATCATCACCATTGAGGATCCATCATC-3' primers. We then derived by PCR from this WT Biot- $\alpha$ Ecat-6His construct, designated WT  $\alpha$ C<sub>M</sub> throughout this study, a L344P Biot- $\alpha$ Ecat-6His named thereafter L344P  $\alpha$ C<sub>M</sub> bearing the L344P point mutation in the VBD domain reported previously to impair vinculin binding<sup>39</sup>. A 3 × WT  $\alpha$ C<sub>M</sub> biotin and 6His-tagged construct, bearing three repeats of the *Kpn*I-*Apa*I fragment, was also constructed in the pDW363 vector by combination of PCR amplification and In-Fusion recombination (Clontech). All constructs were validated by full sequencing of the open reading frame. Recombinant Biot-6His fusion proteins were expressed in *E. coli* BL21 strain and purified using Protino Ni-TED columns (Macherey-Nagel). Protein purity was evaluated by SDS–polyacrylamide gel electrophoresis and protein concentration measured using absorbance at 280 nm. The V<sub>D1</sub> (residues: 1–258) construct was expressed as described in previous studies<sup>7</sup>.

**GST pull-down and western blotting.** A measure of 10  $\mu$ g of Biot- $\alpha$ Ecat-6His (WT  $\alpha$ C<sub>M</sub> or L344P  $\alpha$ C<sub>M</sub>) and 4  $\mu$ g of GST-V<sub>D1</sub> (or GST) were mixed gently with 10  $\mu$ l of glutathione-sepharose beads in PBS (final volume, 200  $\mu$ l) for 30 min at room temperature. The beads were washed three times with PBS, then centrifuged for 2 min at 4 °C and incubated in 50  $\mu$ l of 20 mM reduced glutathione, 50 mM Tris-HCl buffer pH 8 for 10 min at room temperature. GST-V<sub>D1</sub> (or GST) with associated  $\alpha$ E-catenin were recovered in the supernatant after centrifugation. Proteins were resolved on 10% polyacrylamide gels (Invitrogen) by conventional SDS–polyacrylamide gel electrophoresis and Coomassie blue staining.

**Single-molecule manipulation.** The single-molecule  $\alpha$ -catenin pulling experiments were done on a home-made high-force magnetic tweezers setup with laminar flow channels with a NTA-Cu<sup>2+</sup> functionalized coverslip for specific immobilization of  $\alpha$ C<sub>M</sub>. The force calibration was done for each individual tethered bead measured in experiments, which had an ~5% relative error. The details of the design and control of the magnetic tweezers setup were published previously<sup>49</sup>. Protocols of coverslip functionalization, sample preparation, single-protein stretching experiments and force calibration have been published in our previous studies of Filamin A protein<sup>50,51</sup>.

Briefly, the channels were prepared by the following procedure: 20 × 32 mm<sup>2</sup> 1.5# coverslips were cleaned by ultrasonication in detergent, acetone and isopropanol for 30 min each, followed by 15 min of oxygen plasma treatment. The cleaned coverslips were silanized by incubation in 1% APTES (Sigma) in methanol for 20 min, rinsed thoroughly with methanol and cured for 20 min in oven at 110 °C. A laminar flow channel was made by sandwiching the silanized coverslip and a 20 × 20 mm<sup>2</sup> clean non-functionalized coverslip with two parallel stripes of double-sided tape as spacer. The laminar flow channel was further treated by 0.5% glutaraldehyde for 1 h followed by incubation with 3  $\mu$ m diameter amine-coated polystyrene beads (polysciences) for 20 min and then with 10  $\mu$ g ml<sup>-1</sup> NH<sub>2</sub>-NTA for 6 h. The channel was then treated with 500 mM Tris pH 7.4 for 20 min and 0.04% (w/v) CuSO<sub>4</sub> for 10 min. The Cu<sup>2+</sup> charged channels were then blocked in PBS, 1% BSA, 0.0002% Tween-20 overnight before stretching experiment.

6His and biotin double-tagged  $\alpha$ C<sub>M</sub> molecule (0.002 mg ml<sup>-1</sup>) were introduced in the channel and incubated for 20 min before introduction of 2.8  $\mu$ m diameter streptavidin-coated paramagnetic beads (M270 streptavidin, Dynabeads) to form

tethers. A syringe pump was used for slow buffer exchange (~5  $\mu$ l min<sup>-1</sup>). The drag force applied to  $\alpha$ C<sub>M</sub> during buffer exchange was estimated to be less than 1 pN. The pulling experiments were done in 40 mM phosphate buffer pH 7.4, 300 mM NaCl, 5 mM  $\beta$ -mercaptoethanol and 10 mg ml<sup>-1</sup> BSA at 22 °C with various V<sub>D1</sub> concentrations.

Raw extension data were recorded at a sampling rate of 200 Hz. In Figs 2b,d, 4a,d and 5a,b, those are smoothed using the fast Fourier transform (FFT)-smooth function of OriginPro 9.0 in order to improve the clarity of data representation. The unfolding steps of the molecule were detected using an in-house written Matlab programme. Briefly, a delta-function was calculated from the raw time lapse data. Candidate unfolding step positions were picked by peaks in the delta-function with height above a threshold of 10 nm. To determine the unfolding step size, the data points across the individual steps were fitted to a Heaviside step function with an additional linear term that take into account the continuous extension increase because of force change in the force scans. Finally, a *t*-test was carried out to test the height difference before and after the individual identified steps. Only statistically significant (*P*-value < 0.01) steps were considered.

**Force calibrations methods.** The force applied to a bead depends on both the magnets–bead distance and the maximal magnetization of the bead. The latter is determined by the number of nano-magnetites in the bead, which has a large variation from one bead to another. At a fixed magnets–bead distance, this results in a large variation in force. According to our previous studies, forces applied to the weakest and the strongest M280 dynabeads at the same magnets–bead distance can differ by 100% (ref. 49).

In the single-protein manipulation studies of unfolding and refolding of  $\alpha$ C<sub>M</sub> molecules, force was calibrated for individual beads based on their thermal fluctuations under force. A small relative error in force calibration (~5%) was ensured, which was mainly caused by the variation in the size of beads<sup>49</sup>.

In the photobleaching assay, a fixed magnets–bead distance was maintained and the sample chamber was scanned over 1 h time scale such that tethers in the chamber were subjected to the force as homogeneous as possible. Then, photobleaching assay was performed. As in this assay, the thermal motions of the beads were not tracked, the force estimated represented the average force and therefore had a significantly larger error compared with the single-molecule manipulation assay. To ensure most beads were subject to large enough force to unfold the  $\alpha$ C<sub>M</sub> molecules, a fixed magnets–bead distance was chosen to have a relatively large average value of 20 pN.

**Photobleaching counting.** The photobleaching counting of the number of Alexa 488-labelled V<sub>D1</sub> bound to a single WT  $\alpha$ C<sub>M</sub> or 3X  $\alpha$ C<sub>M</sub> under force were carried out using a total internal reflection microscope similar to the one described in the previous study of talin–vinculin interactions<sup>7</sup>. Force estimated in the photobleaching assay represented the average force and therefore has a significantly larger error compared with the single-molecule manipulation assay. Labelling and purification of the V<sub>D1</sub> with Alexa 488 dye were based on the commercial microscale protein labelling kit (A30006) following the manufacturer's protocol. The Alexa Fluoro-488 reactive dye has a tetrafluorophenyl ester, which reacts efficiently with primary amines of proteins to form stable dye–protein conjugates.

The solution containing 50  $\mu$ g ml<sup>-1</sup> labelled V<sub>D1</sub> was added to the flow-chamber coated with WT  $\alpha$ C<sub>M</sub> or WT 3X  $\alpha$ C<sub>M</sub> constructs. These constructs were subjected to force and incubated for 1 h, then unbound V<sub>D1</sub> was flushed away before counting the number of bound V<sub>D1</sub> by photobleaching events similar to previous studies of talin–vinculin interaction.

The images of TIRF fluorescence at 488 nm were taken for 1 min using Olympus IX71 (TIRF) microscope with a 1.45 numerical aperture, ×100 objective. Images were further analysed using in-house written Igor programme. Briefly, a region of interest containing a tethered magnetic bead was chosen and the total fluorescence intensity of this region of interest was recorded. The auto-fluorescence of the magnetic beads contributed to a background intensity, which was stable at our experimental time (~60 s) without any abrupt changes. For a tether with bound labelled V<sub>D1</sub>, photobleaching of single-dye molecules showed an abruptly decrease in fluorescence intensity, which allowed us to count the number of labelled V<sub>D1</sub> associated to the tether.

Single-dye photobleaching events were identified following the method developed by del Rio *et al.* in their paper on force-dependent vinculin binding to talin<sup>7</sup>. Spontaneous stepwise decreases of fluorescent intensity in the time trajectories of the total fluorescence underneath the magnetic beads were identified as photobleaching steps of Alexa 488-labelled V<sub>D1</sub>. These photobleaching steps were not present in control experiments when Alexa 488-labelled V<sub>D1</sub> was not added. In that case, only smooth exponential decay of auto-fluorescence of the bead was observed.

The number of tethered beads tested for the WT  $\alpha$ C<sub>M</sub> at no force and 20 pN of applied force was 89 and 61, respectively. For the WT 3X  $\alpha$ C<sub>M</sub>, the total number of tethered beads tested was 51 and 55 for no force and 20 pN force, respectively.

**Determination of transition rates at constant forces.** The force-dependent kinetic rates of the near-equilibrium unfolding/refolding transitions between 4 and 6 pN were obtained by fitting constant force extension fluctuation time traces to a



Modified Hidden Markov model. An in-house written Matlab programme based on the Viterbi algorithm was used to find emission distribution and corresponding folded/unfolded state sequence with maximum likelihood<sup>66</sup>. The lifetime distributions of each state were then fitted to an exponential distribution to obtain their characteristic lifetime  $t$ . The unfolding and refolding transition rates at a given force were calculated as the inverse of the fitted characteristic lifetime of the unfolded and folded states. The distance to the transition state was calculated by the slope of the linear fit of the natural logarithm of the unfolding and refolding rates at different forces as described previously<sup>67</sup>.

**Helix-to-coil transition estimation.** Crystal structures were available for vinculin head binding to the  $V_{D1}$ -binding  $\alpha$ -helix of  $\alpha$ E-catenin such as 4EHP.  $V_{D1}$  can only bind to the VBD of  $\alpha$ E-catenin if the  $V_{D1}$ -binding domain is under  $\alpha$ -helix conformation. When interacting with  $V_{D1}$ , the vinculin-binding site of  $\alpha$ E-catenin adopts an  $\alpha$ -helical structure with six turns of alpha helix that consists of around 22 residues and span a length of around 3.2 nm (0.54 nm per turn). Although at 25–40 pN, the length of a random coil of 22 amino acids is predicted to be 6.1–6.7 nm based on the worm-like-chain polymer model<sup>68</sup> with a persistent length of 0.5 nm estimated from previous protein unfolding experiments<sup>56</sup> (0.4–0.6 nm). Therefore, the size of steps expected for the helix-to-coil transition of the vinculin-binding  $\alpha$ -helices when the vinculin head domain dissociates is  $\sim$ 2.9–3.5 nm.

## References

- Edelman, G. M. Cell adhesion molecules in the regulation of animal form and tissue pattern. *Annu. Rev. Cell Biol.* **2**, 81–116 (1986).
- Mammoto, T. & Ingber, D. E. Mechanical control of tissue and organ development. *Development* **137**, 1407–1420 (2010).
- Zhang, H. & Labouesse, M. Signalling through mechanical inputs: a coordinated process. *J. Cell Sci.* **125**, 3039–3049 (2012).
- Trichet, L. *et al.* Evidence of a large-scale mechanosensing mechanism for cellular adaptation to substrate stiffness. *Proc. Natl Acad. Sci. USA* **109**, 6933–6938 (2012).
- Morris, C. E. Mechanosensitive ion channels. *J. Membr. Biol.* **113**, 93–107 (1990).
- Sawada, Y. *et al.* Force sensing by mechanical extension of the Src family kinase substrate p130Cas. *Cell* **127**, 1015–1026 (2006).
- del Rio, A. *et al.* Stretching single talin rod molecules activates vinculin binding. *Science* **323**, 638–641 (2009).
- Yao, M. *et al.* Mechanical activation of vinculin binding to talin locks talin in an unfolded conformation. *Sci. Rep.* **4**, 4610 (2014).
- Mege, R. M., Gavaud, J. & Lambert, M. Regulation of cell-cell junctions by the cytoskeleton. *Curr. Opin. Cell Biol.* **18**, 541–548 (2006).
- Ganz, A. *et al.* Traction forces exerted through N-cadherin contacts. *Biol. Cell* **98**, 721–730 (2006).
- Yonemura, S., Wada, Y., Watanabe, T., Nagafuchi, A. & Shibata, M. Alpha-catenin as a tension transducer that induces adherens junction development. *Nat. Cell Biol.* **12**, 533–542 (2010).
- Ladoux, B. *et al.* Strength dependence of cadherin-mediated adhesions. *Biophys. J.* **98**, 534–542 (2010).
- Huveneers, S. & de Rooij, J. Mechanosensitive systems at the cadherin-F-actin interface. *J. Cell Sci.* **126**, 403–413 (2013).
- Dufour, S., Mege, R. M. & Thiery, J. P. Alpha-catenin, vinculin, and F-actin in strengthening E-cadherin cell-cell adhesions and mechanosensing. *Cell. Adh. Migr.* **7**, 345–350 (2013).
- Watabe, M., Nagafuchi, A., Tsukita, S. & Takeichi, M. Induction of polarized cell-cell association and retardation of growth by activation of the E-cadherin-catenin adhesion system in a dispersed carcinoma line. *J. Cell Biol.* **127**, 247–256 (1994).
- Hirano, S., Kimoto, N., Shimoyama, Y., Hirohashi, S. & Takeichi, M. Identification of a neural alpha-catenin as a key regulator of cadherin function and multicellular organization. *Cell* **70**, 293–301 (1992).
- Silvis, M. R. *et al.* Alpha-catenin is a tumor suppressor that controls cell accumulation by regulating the localization and activity of the transcriptional coactivator Yap1. *Sci. Signal* **4**, ra33 (2011).
- Kobiela, A. & Fuchs, E. Alpha-catenin: at the junction of intercellular adhesion and actin dynamics. *Nat. Rev. Mol. Cell Biol.* **5**, 614–625 (2004).
- Lien, W. H., Klezovitch, O., Fernandez, T. E., Delrow, J. & Vasioukhin, V. AlphaE-catenin controls cerebral cortical size by regulating the hedgehog signaling pathway. *Science* **311**, 1609–1612 (2006).
- Sumida, G. M., Tomita, T. M., Shih, W. & Yamada, S. Myosin II activity dependent and independent vinculin recruitment to the sites of E-cadherin-mediated cell-cell adhesion. *BMC Cell Biol.* **12**, 48 (2011).
- Miyake, Y. *et al.* Actomyosin tension is required for correct recruitment of adherens junction components and zonula occludens formation. *Exp. Cell Res.* **312**, 1637–1650 (2006).
- le Duc, Q. *et al.* Vinculin potentiates E-cadherin mechanosensing and is recruited to actin-anchored sites within adherens junctions in a myosin II-dependent manner. *J. Cell Biol.* **189**, 1107–1115 (2010).
- Watabe-Uchida, M. Alpha-catenin-vinculin interaction functions to organize the apical junctional complex in epithelial cells. *J. Cell Biol.* **142**, 847–857 (1998).
- Weiss, E. E., Kroemker, M., Rudiger, A. H., Jockusch, B. M. & Rudiger, M. Vinculin is part of the cadherin-catenin junctional complex: complex formation between alpha-catenin and vinculin. *J. Cell Biol.* **141**, 755–764 (1998).
- Imamura, Y., Itoh, M., Maeno, Y., Tsukita, S. & Nagafuchi, A. Functional domains of alpha-catenin required for the strong state of cadherin-based cell adhesion. *J. Cell Biol.* **144**, 1311–1322 (1999).
- Thomas, W. A. *et al.*  $\alpha$ -Catenin and vinculin cooperate to promote high E-cadherin-based adhesion strength. *J. Biol. Chem.* **288**, 4957–4969 (2013).
- Peng, X., Nelson, E. S., Maier, J. L. & DeMali, K. A. New insights into vinculin function and regulation. *Int. Rev. Cell. Mol. Biol.* **287**, 191–231 (2011).
- Izard, T. *et al.* Vinculin activation by talin through helical bundle conversion. *Nature* **427**, 171–175 (2004).
- Rangarajan, E. S. & Izard, T. Dimer asymmetry defines alpha-catenin interactions. *Nat. Struct. Mol. Biol.* **20**, 188–193 (2013).
- Huber, O., Krohn, M. & Kemler, R. A specific domain in alpha-catenin mediates binding to beta-catenin or plakoglobin. *J. Cell Sci.* **110**(Pt 15): 1759–1765 (1997).
- Aberle, H. *et al.* Assembly of the cadherin-catenin complex *in vitro* with recombinant proteins. *J. Cell Sci.* **107**, 3655–3663 (1994).
- Stappert, J. & Kemler, R. A short core region of E-cadherin is essential for catenin binding and is highly phosphorylated. *Cell Commun. Adhes.* **2**, 319–327 (1994).
- Huber, A. H., Nelson, W. J. & Weis, W. I. Three-dimensional structure of the armadillo repeat region of beta-catenin. *Cell* **90**, 871–882 (1997).
- Pokutta, S. & Weis, W. I. Structure of the dimerization and beta-catenin-binding region of alpha-catenin. *Mol. Cell* **5**, 533–543 (2000).
- Pokutta, S., Drees, F., Yamada, S., Nelson, W. J. & Weis, W. I. Biochemical and structural analysis of alpha-catenin in cell-cell contacts. *Biochem. Soc. Trans.* **36**, 141–147 (2008).
- Nagafuchi, A., Ishihara, S. & Tsukita, S. The roles of catenins in the cadherin-mediated cell adhesion: functional analysis of E-cadherin-alpha catenin fusion molecules. *J. Cell Biol.* **127**, 235–245 (1994).
- Yamada, S., Pokutta, S., Drees, F., Weis, W. I. & Nelson, W. J. Deconstructing the cadherin-catenin-actin complex. *Cell* **123**, 889–901 (2005).
- Desai, R. *et al.* Monomeric alpha-catenin links cadherin to the actin cytoskeleton. *Nat. Cell Biol.* **15**, 261–273 (2013).
- Peng, X., Maier, J. L., Choudhury, D., Craig, S. W. & DeMali, K. A. Alpha-Catenin uses a novel mechanism to activate vinculin. *J. Biol. Chem.* **287**, 7728–7737 (2012).
- Itoh, M. Involvement of ZO-1 in cadherin-based cell adhesion through its direct binding to alpha catenin and actin filaments. *J. Cell Biol.* **138**, 181–192 (1997).
- Pokutta, S., Drees, F., Takai, Y., Nelson, W. J. & Weis, W. I. Biochemical and structural definition of the 1-fadin- and actin-binding sites of alpha-catenin. *J. Biol. Chem.* **277**, 18868–18874 (2002).
- Kobiela, A., Pasolli, H. A. & Fuchs, E. Mammalian formin-1 participates in adherens junctions and polymerization of linear actin cables. *Nat. Cell Biol.* **6**, 21–30 (2004).
- Hansen, S. D. *et al.* Alpha-E-catenin actin binding domain alters actin filament conformation and regulates binding of nucleation and disassembly factors. *Mol. Biol. Cell* **24**, 3710–3720 (2013).
- Benjamin, J. M. *et al.* AlphaE-catenin regulates actin dynamics independently of cadherin-mediated cell-cell adhesion. *J. Cell Biol.* **189**, 339–352 (2010).
- Yang, J., Dokurno, P., Tonks, N. K. & Barford, D. Crystal structure of the M-fragment of alpha-catenin: implications for modulation of cell adhesion. *EMBO J.* **20**, 3645–3656 (2001).
- Choi, H. J. *et al.* alphaE-catenin is an autoinhibited molecule that coactivates vinculin. *Proc. Natl Acad. Sci. USA* **109**, 8576–8581 (2012).
- Ishiyama, N. *et al.* An autoinhibited structure of alpha-catenin and its implications for vinculin recruitment to adherens junctions. *J. Biol. Chem.* **288**, 15913–15925 (2013).
- Rangarajan, E. S. & Izard, T. The cytoskeletal protein alpha-catenin unfurls upon binding to vinculin. *J. Biol. Chem.* **287**, 18492–18499 (2012).
- Chen, H. *et al.* Improved high-force magnetic tweezers for stretching and refolding of proteins and short DNA. *Biophys. J.* **100**, 517–523 (2011).
- Chen, H. *et al.* Differential mechanical stability of filamin A rod segments. *Biophys. J.* **101**, 1231–1237 (2011).
- Chen, H. *et al.* Mechanical perturbation of filamin A immunoglobulin repeats 20–21 reveals potential non-equilibrium mechanochemical partner binding function. *Sci. Rep.* **3**, 1642 (2013).
- Moore, S. W., Roca-Cusachs, P. & Sheetz, M. P. Stretchy proteins on stretchy substrates: the important elements of integrin-mediated rigidity sensing. *Dev. Cell* **19**, 194–206 (2010).

53. Finer, J. T., Simmons, R. M. & Spudich, J. A. Single myosin molecule mechanics: piconewton forces and nanometre steps. *Nature* **368**, 113–119 (1994).
54. Gao, Y., Sirinakis, G. & Zhang, Y. Highly anisotropic stability and folding kinetics of a single coiled coil protein under mechanical tension. *J. Am. Chem. Soc.* **133**, 12749–12757 (2011).
55. Maillard, R.A. *et al.* ClpX(P) Generates mechanical force to unfold and translocate its protein substrates. *Cell* **145**, 459–469 (2011).
56. Junker, J. P., Ziegler, F. & Rief, M. Ligand-dependent equilibrium fluctuations of single calmodulin molecules. *Science* **323**, 633–637 (2009).
57. Carrion-Vazquez, M. *et al.* Mechanical and chemical unfolding of a single protein: a comparison. *Proc. Natl Acad. Sci. USA* **96**, 3694–3699 (1999).
58. Bakolitsa, C. *et al.* Structural basis for vinculin activation at sites of cell adhesion. *Nature* **430**, 583–586 (2004).
59. Bois, P. R. J., O'Hara, B. P., Nietlispach, D., Kirkpatrick, J. & Izzard, T. The vinculin binding sites of talin and alpha-actinin are sufficient to activate vinculin. *J. Biol. Chem.* **281**, 7228–7236 (2006).
60. Barry, A. K. *et al.* Alpha-catenin cytomechanics - role in cadherin-dependent adhesion and mechanotransduction. *J. Cell. Sci.* **127**, 1779–1791 (2014).
61. Huvneers, S. *et al.* Vinculin associates with endothelial VE-cadherin junctions to control force-dependent remodeling. *J. Cell. Biol.* **196**, 641–652 (2012).
62. Gavard, J. *et al.* Lamellipodium extension and cadherin adhesion: two cell responses to cadherin activation relying on distinct signalling pathways. *J. Cell. Sci.* **117**, 257–270 (2004).
63. Cohen, D. M., Chen, H., Johnson, R. P., Choudhury, B. & Craig, S. W. Two distinct head-tail interfaces cooperate to suppress activation of vinculin by talin. *J. Biol. Chem.* **280**, 17109–17117 (2005).
64. Peng, X., Cuff, L. E., Lawton, C. D. & DeMali, K. A. Vinculin regulates cell-surface E-cadherin expression by binding to beta-catenin. *J. Cell. Sci.* **123**, 567–577 (2010).
65. Tsao, K. L., DeBarbieri, B., Michel, H. & Waugh, D. S. A versatile plasmid expression vector for the production of biotinylated proteins by site-specific, enzymatic modification in *Escherichia coli*. *Gene* **169**, 59–64 (1996).
66. Viterbi, A. Error bounds for convolutional codes and an asymptotically optimum decoding algorithm. *IEEE Trans. Inf. Theory* **13**, 260–269 (1967).
67. Elms, P. J., Chodera, J. D., Bustamante, C. & Marqusee, S. The molten globule state is unusually deformable under mechanical force. *Proc. Natl Acad. Sci. USA* **109**, 3796–3801 (2012).
68. Bustamante, C., Marko, J. F., Siggia, E. D. & Smith, S. Entropic elasticity of lambda-phage DNA. *Science* **265**, 1599–1600 (1994).
69. Bell, G. I. Models for the specific adhesion of cells to cells. *Science* **200**, 618–627 (1978).

### Acknowledgements

We thank the Mechanobiology Institute Protein Expression Facility for V<sub>D1</sub> expression and purification services. We thank Anne Houllier for her help in the construction and production of the tagged  $\alpha$ -catenin recombinant proteins. We also thank Didier Chatenay, Michael Sheetz and André Sobel for stimulating discussions and critical reading of the manuscript. Work in Singapore was supported by the National Research Foundation of Singapore through the Mechanobiology Institute at National University of Singapore (to J.Y., B.L., C.L. and R.L.); work in France was supported by grants from CNRS, ARC, as well as from Human Frontier Science Program (HFSP grant RPG0040/2012), and Agence Nationale de la Recherche (ANR 2010 Blan1515). R.S. was supported by an Ile de France Region fellowship cNano.

### Author contributions

J.Y., R.-M.M., B.L., C.T.L. and R.L. designed the research and supervised the experiments. R.S. and M.P. expressed  $\alpha$ C<sub>M</sub> constructs and carried out the GST-VinH pull-down experiments. M.Y. performed the magnetic tweezers experiments and W.Q. performed the photobleaching counting experiments. M.Y., W.Q., J.Y., A.K.E., P.C. and R.-M.M. analysed the data. M.Y., J.Y., R.-M.M. and B.L. wrote the paper.

### Additional information

**Supplementary Information** accompanies this paper at <http://www.nature.com/naturecommunications>

**Competing financial interests:** The authors declare no competing financial interests.

**Reprints and permission** information is available online at <http://npg.nature.com/reprintsandpermissions/>

**How to cite this article:** Yao, M. *et al.* Force-dependent conformational switch of  $\alpha$ -catenin controls vinculin binding. *Nat. Commun.* 5:4525 doi: 10.1038/ncomms5525 (2014).

# Feshbach resonances in the exit channel of the $F + CH_3OH \rightarrow HF + CH_3O$ reaction observed using transition-state spectroscopy

Marissa L. Weichman<sup>1</sup>, Jessalyn A. DeVine<sup>1</sup>, Mark C. Babin<sup>1</sup>, Jun Li<sup>2\*</sup>, Lifan Guo<sup>3</sup>, Jianyi Ma<sup>3</sup>, Hua Guo<sup>4</sup> and Daniel M. Neumark<sup>1,5\*</sup>

**The transition state governs how chemical bonds form and cleave during a chemical reaction and its direct characterization is a long-standing challenge in physical chemistry. Transition state spectroscopy experiments based on negative-ion photodetachment provide a direct probe of the vibrational structure and metastable resonances that are characteristic of the reactive surface. Dynamical resonances are extremely sensitive to the topography of the reactive surface and provide an exceptional point of comparison with theory. Here we study the seven-atom  $F + CH_3OH \rightarrow HF + CH_3O$  reaction using slow photoelectron velocity-map imaging spectroscopy of cryocooled  $CH_3OH^-$  anions. These measurements reveal spectral features associated with a manifold of vibrational Feshbach resonances and bound states supported by the post-transition state potential well. Quantum dynamical calculations yield excellent agreement with the experimental results, allow the assignment of spectral structure and demonstrate that the key dynamics of complex bimolecular reactions can be captured with a relatively simple theoretical framework.**

Since the development of crossed molecular beam experiments in the 1960s<sup>1,2</sup>, studies of reaction dynamics via reactive scattering experiments and accompanying theoretical advances have led to major insights into the fundamental interactions that govern chemical reactivity<sup>3</sup>. A key concept in chemistry is that during the course of a reactive collision, chemical bond formation and cleavage occur in the transition-state (TS) region of the potential energy surface (PES)<sup>4–6</sup>. Hence, there is much interest in characterizing the reaction TSs experimentally and theoretically<sup>7</sup>.

Increasingly sophisticated scattering experiments that involve state-selective reactant preparation and state-resolved product detection provide new ways to observe properties of the TS—such as the reaction barrier height and geometry—that dictate the mode specificity and the most favourable reactant orientation to promote a reactive collision<sup>8–10</sup>. However, such experiments do not probe the TS region of the PES directly. Complementary experiments based on negative-ion photodetachment yield a vibrationally resolved structure characteristic of the TS<sup>11</sup>, and have been applied with considerable success to benchmark bimolecular<sup>12</sup> and unimolecular<sup>13,14</sup> reactions.

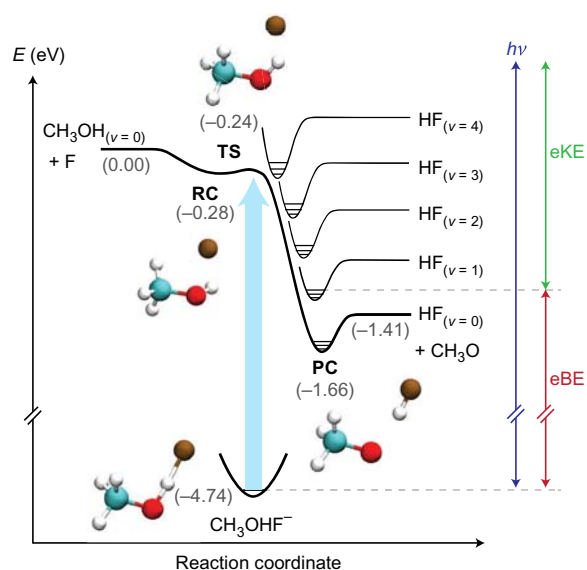
Here we report a joint high-resolution photoelectron imaging and theoretical quantum dynamics study of the  $F + CH_3OH \rightarrow HF + CH_3O$  hydrogen-abstraction reaction, based on the photodetachment of the stable  $CH_3OH^-$  anion. The spectra are obtained via slow photoelectron velocity-map imaging of cryogenically cooled anions (cryo-SEVI)<sup>15–17</sup>, which yields photoelectron spectra of complex species with a kinetic-energy resolution as high as  $1 \text{ cm}^{-1}$  (refs 18,19). The resolution of the cryo-SEVI spectra of  $CH_3OH^-$  and  $CH_3OD^-$  is substantially improved over previous photodetachment experiments<sup>20,21</sup>; it reveals low-frequency progressions assigned to the exit-channel-bound states and Feshbach

resonances and provides new insights into the TS region of this polyatomic reaction. The experimental spectrum is assigned with the help of reduced-dimensional quantum dynamical calculations on a global PES determined by fitting a large number of high-level *ab initio* points in full dimensionality.

Dynamical Feshbach resonances of the type probed here are transient metastable states supported by the reactive PES. These resonances have sufficient vibrational energy to dissociate, but decay slowly because of the inefficient energy flow from the excited modes to the reaction coordinate. Quantum-scattering calculations indicate that the energies and widths of these resonances are exquisitely sensitive to the topography of the reactive PES<sup>9,12,22</sup>. Dynamical resonances can strongly mediate reactivity and can manifest as peaks in the integral or differential cross-section as a function of collision energy<sup>23–26</sup>. These effects have been sought out and, in some cases, clearly observed in molecular beam reactive scattering experiments<sup>9,26–30</sup>.

Anion photoelectron TS spectroscopy offers an alternative and often more direct means to detect dynamical resonances<sup>11,12</sup>. In such an experiment, a bound anion similar in geometry to the neutral TS is photodetached. The vibrational wavefunction of the anion is vertically projected onto the neutral PES, and the kinetic energy of the nascent photoelectron reports on the wave-packet evolution under the influence of the neutral Hamiltonian. The resulting photoelectron spectrum may show a broad structure if the photodetachment accesses a repulsive Franck–Condon region of the neutral PES. However, direct detachment to discrete bound or quasi-bound neutral states will manifest as sharp, well-defined features in the photoelectron spectrum<sup>31</sup>. These features provide valuable information on the neutral PES in strongly interacting regions, such as reactive intermediate wells and TSs. Resonances identified

<sup>1</sup>Department of Chemistry, University of California, Berkeley, California 94720, USA. <sup>2</sup>School of Chemistry and Chemical Engineering, Chongqing University, Chongqing 401331, China. <sup>3</sup>Institute of Atomic and Molecular Physics, Sichuan University, Chengdu, Sichuan 610065, China. <sup>4</sup>Department of Chemistry and Chemical Biology, University of New Mexico, Albuquerque, New Mexico 87131, USA. <sup>5</sup>Chemical Sciences Division, Lawrence Berkeley National Laboratory, Berkeley, California 94720, USA. \*e-mail: [jli15@cqu.edu.cn](mailto:jli15@cqu.edu.cn); [dneumark@berkeley.edu](mailto:dneumark@berkeley.edu)



**Figure 1 | Schematic energy diagram for the photodetachment of the  $\text{CH}_3\text{OHF}^-$  anion to the neutral  $\text{F} + \text{CH}_3\text{OH} \rightarrow \text{HF} + \text{CH}_3\text{O}$  reactive PES.** The upper bold line is the ZPE-corrected surface that connects the reactants and products in their ground vibrational states, and the curves sketched above it are the product-well HF stretching VAPs. The lower bold line represents the bound anion potential. Geometries are shown for the anion, RC, TS and PC stationary points; C, blue; O, red; H, white; F, brown. Energies derived from the fitted PIP-NN surface, shown in grey text, are given in electronvolts relative to the reactant asymptote. The relationship between the photon energy ( $h\nu$ ), eBE and electron kinetic energy (eKE) in a SEVI experiment is also indicated.

in studies of TS spectroscopy offer an exceptional point of comparison with quantum theory, which can provide assignments based on the nodal structure of the resonance wavefunctions. Thus far, such comparisons have been limited to triatomic<sup>12,32,33</sup> and tetratomic<sup>34</sup> systems, and the somewhat irregular structure in the entrance channel of the  $\text{F} + \text{CH}_4$  reaction<sup>35</sup>.

Here we exploit the high resolution of cryo-SEVI spectra to observe and identify dynamical resonances in the more complex seven-atom  $\text{F} + \text{CH}_3\text{OH}$  hydrogen-atom abstraction reaction. This reaction can proceed either at the hydroxyl or the methyl site, and leads to methoxy ( $\text{CH}_3\text{O}$ ) or hydroxymethyl ( $\text{CH}_2\text{OH}$ ) radical products, respectively. The methoxy and hydroxymethyl pathways are exothermic by 1.357(4) and 1.767(4) eV, respectively<sup>36</sup>, and both are predicted to proceed without a barrier<sup>37–39</sup>. The  $\text{F} + \text{CH}_3\text{OH}$  branching ratio for abstraction from the hydroxyl group is considerably higher than the value of 25% expected if the branching were statistical<sup>38–44</sup>. This is attributed to the fact that the hydroxyl-group abstraction proceeds through a reactant complex (RC) and TS stabilized by hydrogen-bonding interactions<sup>37</sup>. The hydrogen-bonded  $\text{CH}_3\text{OHF}^-$  anion is similar in geometry to the hydroxyl-abstraction TS<sup>20,21,45–47</sup>, as shown schematically in Fig. 1; further details on the calculated reactive surface are given in Results. This system is an ideal case for TS spectroscopy, but simultaneously poses a challenge, particularly to theory, with 15 degrees of freedom potentially involved in the dynamics.

## Results

Experimental cryo-SEVI spectra of  $\text{CH}_3\text{OHF}^-$  and  $\text{CH}_3\text{ODF}^-$  are shown in Fig. 2b,c. The spectra are dominated by broad steps (labelled *a*, *b*, *c*, *d*, *e*), with an *a*–*b* spacing of  $\sim 3,600\text{ cm}^{-1}$  in the  $\text{CH}_3\text{OHF}^-$  spectrum and  $\sim 2,700\text{ cm}^{-1}$  for the  $\text{CH}_3\text{ODF}^-$  spectrum. These features were also seen in the lower-resolution photoelectron spectroscopy results of Bradforth *et al.*<sup>20</sup> and in a recent photoelectron–photofragment coincidence study by Ray *et al.*<sup>21</sup> Both

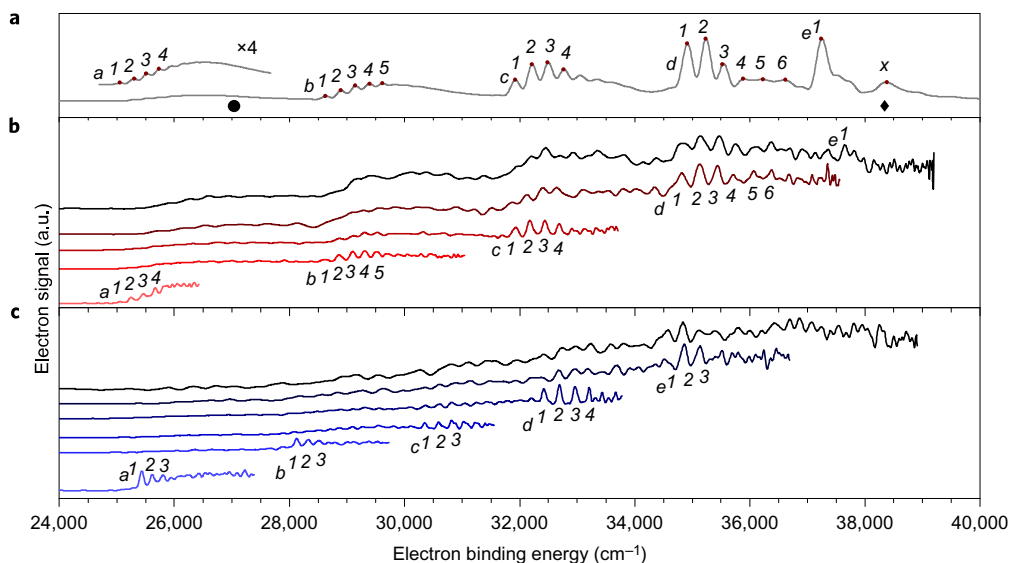
prior studies assigned this stepped structure to an HF stretching progression of the  $\text{CH}_3\text{O}-\text{HF}$  product complex (PC). The considerably higher spectral resolution afforded by cryo-SEVI reveals an additional layer of vibrational structure not seen previously. We now resolve a much finer structure spaced by  $\sim 200\text{ cm}^{-1}$  superimposed on the broad steps with typical peak widths of  $75\text{--}125\text{ cm}^{-1}$  (full-width at half-maximum (FWHM)). Peak positions and spacings are listed in Supplementary Tables 1 and 2. A key trend is that the spacing of resonances within each step increases with increasing HF stretching excitation. For example, the *a1*–*a2*, *b1*–*b2*, *c1*–*c2* and *d1*–*d2* gaps are measured experimentally as 192, 248, 255 and  $315\text{ cm}^{-1}$ , respectively.

Accurate quantum dynamical studies on a reactive PES are necessary to interpret the experimental spectra. We model the  $\text{F} + \text{CH}_3\text{OH}$  reaction using a full 15-dimensional (15D) PES constructed with  $\sim 121,000$  points calculated at the explicitly correlated unrestricted coupled cluster level with singles, doubles and perturbative triples<sup>48</sup> with the augmented correlation-consistent polarized valence double zeta basis set and core electrons frozen (FC-UCCSD(T)-F12a/AVDZ). The CCSD(T)-F12/AVDZ method is expected to yield results of a quality comparable to that of the conventional CCSD(T)/AVQZ level. The PES is fit using the permutation invariant polynomial–neural network (PIP-NN) method<sup>49</sup>.

Figure 1 shows a schematic of the  $\text{F} + \text{CH}_3\text{OH} \rightarrow \text{HF} + \text{CH}_3\text{O}$  reaction path. The upper bold line is the zero-point energy (ZPE) corrected minimum energy path that connects the reactants and products in their ground vibrational states. The reported stationary point energies derived from the PIP-NN PES are in good agreement with prior work (Supplementary Fig. 1 gives a detailed comparison)<sup>21,37</sup>. The TS, RC and PC all lie below the energy of the free reactants. The RC is a covalent three-electron two-centre hemi-bonded complex, similar to that between F and  $\text{H}_2\text{O}$  (ref. 50), which is bound by 0.28 eV relative to the free reactants, but lies only slightly lower in energy than the TS. The PC is a hydrogen-bonded complex between HF and the methoxy radical bound by 0.25 eV relative to the free products. The stationary point geometries are consistent across different levels of theory and agree well with the available experimental results (Supplementary Figs 2 and 3). The corresponding harmonic frequencies of these stationary points are compared in Supplementary Table 3.

To simulate the photoelectron spectrum, wave-packet-based quantum dynamics were investigated with a reduced 6D model by freezing the methyl moiety. The  $\text{CH}_3\text{OHF}^-$  detachment spectrum simulated with a  $\sim 200\text{ fs}$  wave-packet propagation is given in Fig. 2a and compares favourably with the experimental results. The electron-binding energy (eBE) of the bottom of the PC well is calculated to lie at  $24,810\text{ cm}^{-1}$ , close to the experimental onset of the structure at  $25,058(25)\text{ cm}^{-1}$  (peak *a1*) and to previous measurements<sup>20,21</sup>. The simulated spectrum has therefore been shifted to a higher eBE by  $250\text{ cm}^{-1}$ , so that the onset of the structure at a low eBE matches that observed experimentally. Experimental and theoretical peak positions are compared for the  $\text{CH}_3\text{OHF}^-$  detachment in Supplementary Table 1; the theory reproduces the trend of increasing resonance peak spacings mentioned above.

The product asymptote for the  $\text{F} + \text{CH}_3\text{OH} \rightarrow \text{HF} + \text{CH}_3\text{O}$  reaction lies at  $26,820\text{ cm}^{-1}$ , while the reactant asymptote lies at  $38,220\text{ cm}^{-1}$  on the ZPE-corrected PIP-NN surface. These asymptotes are marked in Fig. 2a with filled circle and diamond symbols, respectively, and have also been shifted to higher eBE by  $250\text{ cm}^{-1}$  for comparison with the experiment. The energies of these asymptotes indicate that much of the observed structure can lie only in the PC well. The peaks in the *a* manifold fall below the product asymptote and are thus bound with respect to free HF +  $\text{CH}_3\text{O}$  products. Ray *et al.*<sup>21</sup> accordingly found that the *a* manifold was associated with the production of non-dissociating neutral complexes, whereas the higher-lying peaks were correlated largely with



**Figure 2 | Experimental and theoretical photodetachment spectra of  $\text{CH}_3\text{OHF}^-$  and  $\text{CH}_3\text{ODF}^-$  showing transitions to resonances in the  $\text{F} + \text{CH}_3\text{OH} \rightarrow \text{HF} + \text{CH}_3\text{O}$  product well.** **a**, Theoretical simulation of the  $\text{CH}_3\text{OHF}^-$  photoelectron spectrum obtained with an estimated 200 fs propagation time (grey). **b,c**, Experimental cryo-SEVI spectra of  $\text{CH}_3\text{OHF}^-$  (**b**) and  $\text{CH}_3\text{ODF}^-$  (**c**) detachment. The experimental overview spectra are plotted in black and the high-resolution traces taken at progressively lower photon energies are plotted in colour. The filled circle and filled diamond symbols represent the PIP-NN product and reactant asymptotes, respectively. In all the panels, the broad steps *a–e* represent transitions to the PC states with increasing HF stretching vibrational excitation. The numbered features associated with each step represent resonances supported by the HF(DF) stretching VAPs (see Fig. 1) with increasing  $\text{CH}_3\text{O–HF}$  stretching excitation. a.u., arbitrary units.

dissociated fragments. The agreement of experiment and theory unambiguously identifies the newly resolved low-frequency progressions as derived from discrete bound states and Feshbach resonances on the product side of the TS.

## Discussion

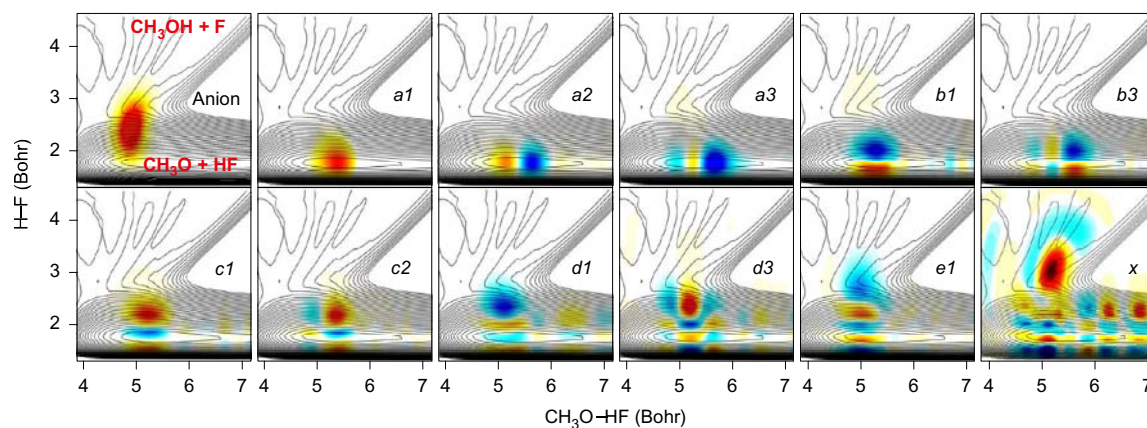
The presence of the low-frequency progressions and the trend of their increasing spacing within steps *a–d* can be explained intuitively with reference to the vibrational adiabatic potentials (VAPs) shown in Fig. 1. These VAPs correspond to the HF vibrational levels plotted along the reaction coordinate and correlate to vibrationally excited free  $\text{HF}(\nu) + \text{CH}_3\text{O}$  products. The HF vibrational adiabaticity is expected to be strong because of its high vibrational frequency, which couples weakly with the dissociation coordinate. Each spectral step *a–e* represents a detachment to an  $\text{HF}(\nu = 0–4)$  VAP. The finely spaced progressions within each step are resonances supported in the wells of the VAPs and reflect increasing quanta of excitation in the low-frequency  $\text{CH}_3\text{O–HF}$  stretching mode. The VAP wells deepen as the HF excitation is increased, resulting in more widely spaced states within each well. The deepening of the PC VAPs can be explained by dynamical vibrational bonding. It is a well-known phenomenon in heavy–light–heavy<sup>51–53</sup> and other triatomic<sup>9,54</sup> systems that VAPs can support increasingly stabilized wells as the vibrationally excited light atom is more delocalized between the two outer fragments.

To better understand the vibrational character of the observed spectral features, the simulated wavefunctions of all the peaks were extracted. Relevant examples are shown in Fig. 3. From the localized character of these wavefunctions, it is clear that they are stable bound states or metastable resonances supported by the PC well. The  $\sim 100 \text{ cm}^{-1}$  FWHM peak widths of the observed spectral features allow us to place a lower bound of 50 fs on the lifetimes of the Feshbach resonance states that lie above the  $\text{HF} + \text{CH}_3\text{O}$  dissociation limit, although the highest-resolution theoretical results suggest that these states are much longer lived. The final dissociation of these resonance states is expected to proceed via vibrational pre-dissociation facilitated by energy flow from

the HF stretching coordinate to translational motion along the dissociation coordinate. The large frequency mismatch means that such an energy flow is expected to be slow and result in long lifetimes for these resonances. Similar long-lived Feshbach resonance states were observed in  $\text{F} + \text{H}_2\text{O}$  (ref. 34) and this picture holds even in the presence of many degrees of freedom for the  $\text{F} + \text{CH}_3\text{OH}$  system.

Vibrational assignments can be confirmed by examining the resonance wavefunction nodal structure. Peaks in the *a1–b1–c1–d1–e1* progression show an increasing integer number of nodes along the HF stretching coordinate (vertical axis in Fig. 3). Therefore, the broad shelves in the spectrum indeed correspond to a progression of the HF stretching vibrational states of the PC. The isotope effect observed in the  $\text{CH}_3\text{ODF}^-$  cryo-SEVI spectrum (Fig. 2c) further validates this assignment. The increasing number of nodes in the *a1–a2–a3* progression along the  $\text{CH}_3\text{O–HF}$  coordinate (horizontal axis in Fig. 3) confirms that the finely spaced progressions are resonances with increasing quanta of excitation in the stretching mode between the product fragments. The experimental and theoretical Franck–Condon factors increase along with HF stretching excitation, as the PC vibrational states with higher quanta of excitation in the HF stretch have more wavefunction density at a larger HF displacement. Compare, for instance, the vibrational wavefunctions for peaks *a1* and *d1*: the latter has a substantially better Franck–Condon overlap with the anion wavefunction, which leads to an increased intensity in the photoelectron spectrum.

To illustrate the evolution of these resonances further, a simulated photoelectron spectrum is shown in Supplementary Fig. 4 for three different propagation times. The low-resolution spectrum obtained in the first 40 fs of propagation suggests that the short-time dynamics on the neutral PES are along the HF vibrational coordinate, as the spectrum clearly resolves peaks related to the HF vibrational frequency. By 200 fs, the fine-structure peaks emerge because of the recursion of the wave packet along the  $\text{CH}_3\text{O–HF}$  dissociation coordinate. By 800 fs, the fine-structure peaks split further into sharper peaks related to  $\text{H}_3\text{C–O–HF}$  bending excitation, although these are not resolved experimentally.



**Figure 3 |** Cuts of the  $\text{CH}_3\text{OHF}^-$  anion vibrational ground-state wavefunction and representative  $\text{F} + \text{CH}_3\text{OH} \rightarrow \text{HF} + \text{CH}_3\text{O}$  resonance wavefunctions. The labels correspond to the related peaks in the simulated photodetachment spectrum of  $\text{CH}_3\text{OHF}^-$  (Fig. 2a). Wavefunctions are superimposed on the neutral PES contours plotted with respect to the  $\text{CH}_3\text{O-HF}$  and  $\text{H-F}$  bond distances with the other four coordinates relaxed. The locations of the entrance and exit channels are labelled in red in the upper-left plot. The  $a1$ ,  $b1$ ,  $c1$ ,  $d1$  and  $e1$  wavefunctions are localized in the exit channel and demonstrate a growing number of nodes along the HF axis, which confirms that steps  $a$ - $e$  in Fig. 2 represent a progression of PC HF stretching states. The  $a1$ ,  $a2$  and  $a3$  wavefunctions show a growing number of nodes along the  $\text{CH}_3\text{O-HF}$  axis, which indicates that the finely spaced peaks correspond to vibrational progressions in the stretching mode between the product fragments.

The vibrational assignments made here are also sensible in the context of the Franck–Condon principle. Comparison of the anion and PC geometries (Supplementary Figs 2 and 3) indicates that photodetachment to the PC well should be accompanied by vibrational excitation in the HF stretching and the  $\text{CH}_3\text{O-HF}$  stretching and bending modes. Indeed, the HF bond length in the anion (1.32 Å) is considerably longer than that of free HF (0.92 Å). The geometry of the methyl moiety is largely unchanged by detachment, so freezing its internal degrees of freedom during the quantum dynamical calculations does not have an adverse impact on the accuracy of the simulation. In this regard, the TS spectrum of  $\text{F} + \text{CH}_3\text{OH}$  is analogous to that predicted and observed for the  $\text{F} + \text{H}_2\text{O}$  system<sup>34,55</sup>. In  $\text{F} + \text{H}_2\text{O}$ , photodetachment predominantly accesses the  $\text{OH} + \text{HF}$  product well and is accompanied by considerable HF vibrational excitation, with the OH fragment acting as a spectator, as  $\text{CH}_3\text{O}$  does here.

We do not find evidence of resonances supported by the RC well. All sharp features that fall below the reactant asymptote (marked with a filled diamond in Fig. 2a) have wavefunctions localized on the product side of the TS (Fig. 3). Ray *et al.*<sup>21</sup> tentatively assigned a spectral feature that lies below the reactant asymptote to an RC resonance, as it appeared to have a longer lifetime than neighbouring peaks. In the cryo-SEVI spectra this feature is resolved as peaks  $d4$ ,  $d5$  and  $d6$ , which are well-reproduced by theory as resonances in the PC well. On the other hand, the long-lived feature observed by Ray *et al.*<sup>21</sup> represents a sufficiently small fraction of the total dissociative signal that there may not be a reasonable expectation of resolving it in our present experiment. Furthermore, such a state may not be captured accurately by our simulations as the reduced-dimensional model, which is ideal for the  $\text{HF} + \text{CH}_3\text{O}$  product channel, might not be sufficient for the  $\text{F} + \text{CH}_3\text{OH}$  reactant channel.

The resonances we report here are non-reactive as they are submerged below the energy of the free reactants. These states cannot, for instance, be accessed in an  $\text{F} + \text{CH}_3\text{OH}$  scattering experiment and are therefore uniquely accessible with anion photoelectron spectroscopy. It is expected that reactive resonances also exist at higher energies, similar to the predictions for  $\text{F} + \text{H}_2\text{O}$  (refs 34,55). The lowest-lying reactive resonance that is predicted theoretically underlies the feature labelled  $x$  in Fig. 2a. The wavefunction for this feature is shown in Fig. 3 and clearly has an intensity that extends into the reactant channel. Unfortunately, no

unambiguous evidence of this feature is resolved experimentally, as the spectrum becomes congested at higher photon energies.

The poor agreement between the experimental and theoretical results for the position and intensity of peak  $e1$  could also be caused by experimental congestion. The laser-noise background becomes a limiting factor at high photon energies. It is also possible that detachment to excited  $\text{F} + \text{CH}_3\text{OH}$  surfaces, analogous to those predicted in  $\text{F} + \text{H}_2\text{O}$  (ref. 55), contributes at higher eBE, and leads to the increased baseline of the experimental spectra compared with theory. Additionally, the Wigner threshold law<sup>56</sup> can distort relative peak intensities close to the threshold, which may further hamper our ability to resolve peaks  $e1$  and  $x$  at the relatively low electron kinetic energies accessible here.

In conclusion, we investigated the photodetachment of  $\text{CH}_3\text{OHF}^-$  and its singly deuterated isotopologue using slow photoelectron velocity-map imaging spectroscopy and quantum dynamical calculations on a new *ab initio* based PES. The cryo-SEVI spectrum is dominated by Feshbach resonances supported in the product well of the  $\text{F} + \text{CH}_3\text{OH} \rightarrow \text{HF} + \text{CH}_3\text{O}$  reaction. These resonances are fully reproduced by theory, which allows their unambiguous assignment to the vibrational HF and  $\text{CH}_3\text{O-HF}$  stretching states of the PC. This work demonstrates the utility of cryo-SEVI TS spectroscopy experiments for probing detailed multidimensional dynamical features near the TS as well as theoretical advances in modelling the dynamics of increasingly complex bimolecular reactions. It also illustrates that, despite much increased complexity, the key dynamical features of this seven-atom reaction remain largely local and can still be captured by a relatively simple physical picture.

## Methods

The cryo-SEVI method has been described in detail elsewhere<sup>15–17</sup>.  $\text{CH}_3\text{OHF}^-$  and  $\text{CH}_3\text{ODF}^-$  anions are prepared by expanding trace  $\text{NF}_3$  and either methanol or methanol- $d_1$  vapour in helium gas through an Even–Lavie pulsed valve<sup>57</sup> fitted with a circular filament ionizer. Dissociative electron attachment to  $\text{NF}_3$  produces  $\text{F}^-$  atomic ions, which then cluster with methanol(- $d_1$ ). The anions are cooled by collisions with an 80:20 He:H<sub>2</sub> buffer gas mixture in a radiofrequency ion trap held at 5 K. After thermalization to their ground vibrational and electronic states, the ions are extracted from the trap and mass-selected by time-of-flight. The ions are photodetached at various photon energies with tunable light from the frequency-doubled output of a dye laser pumped by either the second or third harmonic of a neodymium:yttrium–aluminium–garnet laser. The electron kinetic energy distribution of the resulting photoelectrons is measured with a velocity-map imaging spectrometer<sup>58</sup> using relatively low extraction voltages. This magnifies the electron image on the detector and achieves a  $1 \text{ cm}^{-1}$  instrumental energy resolution for slow electrons<sup>18</sup>.

The quantum dynamical calculations are performed with a reduced-dimensional model, in which the methyl moiety is fixed at the geometry associated with the PC well. This is a reasonable approximation as the methyl group behaves largely as a spectator in the  $F + \text{CH}_3\text{OH} \rightarrow \text{HF} + \text{CH}_3\text{O}$  channel. The remaining six coordinates are represented by the diatom–diatom Jacobi coordinates, in the same fashion as in our recent work on  $F(\text{H}_2\text{O})$  photodetachment<sup>55</sup>. The photodetachment process is simulated within the Condon approximation, in which the anion wavefunction is placed on the neutral PES in a vertical transition. The subsequent dynamics are followed by propagating the initial wave packet in the Chebyshev order domain and the photoelectron spectrum is computed by a discrete cosine transform of the Chebyshev autocorrelation function<sup>59</sup>. Additional theoretical details, including descriptions of the benchmark calculations and the construction of the PESs, are given in the Supplementary Information.

**Data availability.** The experimental and theoretical data that support the findings of this study are available from the corresponding authors on reasonable request.

Received 13 March 2017; accepted 19 May 2017;  
published online 10 July 2017

## References

- Herschbach, D. R. Reactive collisions in crossed molecular beams. *Discuss. Faraday Soc.* **33**, 149–161 (1962).
- Lee, Y. T., McDonald, J. D., LeBreton, P. R. & Herschbach, D. R. Molecular beam reactive scattering apparatus with electron bombardment detector. *Rev. Sci. Instrum.* **40**, 1402–1408 (1969).
- Levine, R. D. *Molecular Reaction Dynamics* (Cambridge Univ. Press, 2005).
- Eyring, H. The activated complex in chemical reactions. *J. Chem. Phys.* **3**, 107–115 (1935).
- Truhlar, D. G., Garrett, B. C. & Klippenstein, S. J. Current status of transition-state theory. *J. Phys. Chem.* **100**, 12771–12800 (1996).
- Guo, H. & Liu, K. Control of chemical reactivity by transition-state and beyond. *Chem. Sci.* **7**, 3992–4003 (2016).
- Polanyi, J. C. & Zewail, A. H. Direct observation of the transition state. *Acc. Chem. Res.* **28**, 119–132 (1995).
- Zare, R. N. Laser control of chemical reactions. *Science* **279**, 1875–1879 (1998).
- Yang, T. et al. Extremely short-lived reaction resonances in  $\text{Cl} + \text{HD} (\nu = 1) \rightarrow \text{DCl} + \text{H}$  due to chemical bond softening. *Science* **347**, 60–63 (2015).
- Liu, K. Vibrational control of bimolecular reactions with methane by mode, bond, and stereoselectivity. *Annu. Rev. Phys. Chem.* **67**, 91–111 (2016).
- Neumark, D. M. Probing the transition state with negative ion photodetachment: experiment and theory. *Phys. Chem. Chem. Phys.* **7**, 433–442 (2005).
- Kim, J. B. et al. Spectroscopic observation of resonances in the  $F + \text{H}_2$  reaction. *Science* **349**, 510–513 (2015).
- Ervin, K. M., Ho, J. & Lineberger, W. C. A study of the singlet and triplet states of vinylidene by photoelectron spectroscopy of  $\text{H}_2\text{CC}^-$ ,  $\text{D}_2\text{CC}^-$  and  $\text{HDCC}^-$ . Vinylidene–acetylene isomerization. *J. Chem. Phys.* **91**, 5974–5992 (1989).
- Wenthold, P. G., Hrovat, D. A., Borden, W. T. & Lineberger, W. C. Transition-state spectroscopy of cyclooctatetraene. *Science* **272**, 1456–1459 (1996).
- Osterwalder, A., Nee, M. J., Zhou, J. & Neumark, D. M. High resolution photodetachment spectroscopy of negative ions via slow photoelectron imaging. *J. Chem. Phys.* **121**, 6317–6322 (2004).
- Neumark, D. M. Slow electron velocity-map imaging of negative ions: applications to spectroscopy and dynamics. *J. Phys. Chem. A* **112**, 13287–13301 (2008).
- Hock, C., Kim, J. B., Weichman, M. L., Yacovitch, T. I. & Neumark, D. M. Slow photoelectron velocity-map imaging spectroscopy of cold negative ions. *J. Chem. Phys.* **137**, 244201 (2012).
- Weichman, M. L., DeVine, J. A., Levine, D. S., Kim, J. B. & Neumark, D. M. Isomer-specific vibronic structure of the 9-, 1-, and 2-anthracenyl radicals via slow photoelectron velocity-map imaging. *Proc. Natl Acad. Sci. USA* **113**, 1698–1705 (2016).
- DeVine, J. A. et al. Non-adiabatic effects on excited states of vinylidene observed with slow photoelectron velocity-map imaging. *J. Am. Chem. Soc.* **138**, 16417–16425 (2016).
- Bradforth, S. E., Arnold, D. W., Metz, R. B., Weaver, A. & Neumark, D. M. Spectroscopy of the transition state: hydrogen abstraction reactions of fluorine. *J. Phys. Chem.* **95**, 8066–8078 (1991).
- Ray, A. W., Agarwal, J., Shen, B. B., Schaefer, H. F. & Continetti, R. E. Energetics and transition-state dynamics of the  $F + \text{HOCH}_3 \rightarrow \text{HF} + \text{OCH}_3$  reaction. *Phys. Chem. Chem. Phys.* **18**, 30612–30621 (2016).
- Schatz, G. C., Bowman, J. M. & Kuppermann, A. Exact quantum, quasiclassical, and semiclassical reaction probabilities for the collinear  $F + \text{H}_2 \rightarrow \text{FH} + \text{H}$  reaction. *J. Chem. Phys.* **63**, 674–684 (1975).
- Wyatt, R. E. & Redmon, M. J. Quantum–mechanical differential reaction cross sections for the  $F + \text{H}_2 (\nu = 0) \rightarrow \text{FH} (\nu' = 2,3) + \text{H}$  reaction. *Chem. Phys. Lett.* **96**, 284–288 (1983).
- Schatz, G. C. Detecting resonances. *Science* **288**, 1599–1600 (2000).
- Zare, R. N. Resonances in reaction dynamics. *Science* **311**, 1383–1385 (2006).
- Liu, K. Quantum dynamical resonances in chemical reactions: from  $A + \text{BC}$  to polyatomic systems. *Adv. Chem. Phys.* **149**, 1–46 (2012).
- Neumark, D. M., Wodtke, A. M., Robinson, G. N., Hayden, C. C. & Lee, Y. T. Molecular beam studies of the  $F + \text{H}_2$  reaction. *J. Chem. Phys.* **82**, 3045–3066 (1985).
- Skodje, R. T. et al. Observation of a transition state resonance in the integral cross section of the  $F + \text{HD}$  reaction. *J. Chem. Phys.* **112**, 4536–4552 (2000).
- Qiu, M. et al. Observation of Feshbach resonances in the  $F + \text{H}_2 \rightarrow \text{HF} + \text{H}$  reaction. *Science* **311**, 1440–1443 (2006).
- Ren, Z., Sun, Z., Zhang, D. & Yang, X. A review of dynamical resonances in  $A + \text{BC}$  chemical reactions. *Rep. Prog. Phys.* **80**, 026401 (2017).
- Russell, C. L. & Manolopoulos, D. E. How to observe the elusive resonances in  $F + \text{H}_2$  reactive scattering. *Chem. Phys. Lett.* **256**, 465–473 (1996).
- Garand, E., Zhou, J., Manolopoulos, D. E., Alexander, M. H. & Neumark, D. M. Nonadiabatic interactions in the  $\text{Cl} + \text{H}_2$  reaction probed by  $\text{ClH}_2^-$  and  $\text{ClD}_2^-$  photoelectron imaging. *Science* **319**, 72–75 (2008).
- Waller, I. M., Kitsopoulos, T. N. & Neumark, D. M. Threshold photodetachment spectroscopy of the  $I + \text{HI}$  transition-state region. *J. Phys. Chem.* **94**, 2240–2242 (1990).
- Otto, R. et al. Imaging dynamics on the  $F + \text{H}_2\text{O} \rightarrow \text{HF} + \text{OH}$  potential energy surfaces from wells to barriers. *Science* **343**, 396–399 (2014).
- Westermann, T. et al. Resonances in the entrance channel of the elementary chemical reaction of fluorine and methane. *Angew. Chem. Int. Ed.* **53**, 1122–1126 (2014).
- Active Thermochemical Tables Values based on v. 1.118 of the Thermochemical Network (Argonne National Laboratory 2015); <http://ATcT.anl.gov>
- Feng, H., Randall, K. R. & Schaefer, H. F. Reaction of a fluorine atom with methanol: potential energy surface considerations. *J. Phys. Chem. A* **119**, 1636–1641 (2015).
- Glauser, W. A. & Koszykowski, M. L. Anomalous methoxy radical yields in the fluorine + methanol reaction. 2. Theory. *J. Phys. Chem.* **95**, 10705–10713 (1991).
- Jodkowski, J. T., Rayez, M.-T., Rayez, J.-C., Bérces, T. & Dóbe, S. Theoretical study of the kinetics of the hydrogen abstraction from methanol. 1. Reaction of methanol with fluorine atoms. *J. Phys. Chem. A* **102**, 9219–9229 (1998).
- Meier, U., Grotheer, H. H. & Just, T. Temperature dependence and branching ratio of the  $\text{CH}_3\text{OH} + \text{OH}$  reaction. *Chem. Phys. Lett.* **106**, 97–101 (1984).
- Wickramaaratchi, M. A., Setser, D. W., Hildebrandt, H., Körbitzer, B. & Heydtmann, H. Evaluation of HF product distributions deduced from infrared chemiluminescence. II. F atom reactions. *Chem. Phys.* **94**, 109–129 (1985).
- Khatoun, T. & Hoyermann, K. The reactions of fluorine atoms with normal and deuterated methanols. *Ber. Bunsen-Ges. Phys. Chem.* **92**, 669–673 (1988).
- Durant, J. L. Anomalous methoxy radical yields in the fluorine + methanol reaction. 1. Experiment. *J. Phys. Chem.* **95**, 10701–10704 (1991).
- Dóbe, S., Bérces, T., Temps, F., Wagner, H. G. & Ziemer, H. Formation of methoxy and hydroxymethyl free radicals in selected elementary reactions. *25th Symp. Int. Combust. Proc.* **25**, 775–781 (1994).
- Wladkowski, B. D., East, A. L. L., Mihalick, J. E., Allen, W. D. & Brauman, J. I. The proton-transfer surface of  $\text{CH}_3\text{OH}^-$ . *J. Chem. Phys.* **100**, 2058–2088 (1994).
- Sun, L., Song, K., Hase, W. L., Sena, M. & Riveros, J. M. Stationary points for the  $\text{OH}^- + \text{CH}_3\text{F} \rightarrow \text{CH}_3\text{OH} + \text{F}^-$  potential energy surface. *Int. J. Mass Spectrom.* **227**, 315–325 (2003).
- Gonzales, J. M. et al. Definitive *ab initio* studies of model  $\text{S}_{\text{N}}2$  reactions  $\text{CH}_3\text{X} + \text{F}^- (\text{X} = \text{F}, \text{Cl}, \text{CN}, \text{OH}, \text{SH}, \text{NH}_2, \text{PH}_2)$ . *Chem. Eur. J.* **9**, 2173–2192 (2003).
- Knizia, G., Adler, T. B. & Werner, H.-J. Simplified CCSD(T)-F12 methods: theory and benchmarks. *J. Chem. Phys.* **130**, 054104 (2009).
- Jiang, B., Li, J. & Guo, H. Potential energy surfaces from high fidelity fitting of *ab initio* points: the permutation invariant polynomial–neural network approach. *Int. Rev. Phys. Chem.* **35**, 479–506 (2016).
- Li, J., Li, Y. & Guo, H. Covalent nature of  $\text{X} \cdots \text{H}_2\text{O}$  ( $\text{X} = \text{F}, \text{Cl}$ , and  $\text{Br}$ ) interactions. *J. Chem. Phys.* **138**, 141102 (2013).
- Manz, J., Meyer, R., Pollak, E. & Romelt, J. A new possibility of chemical bonding. vibrational stabilization of IHI. *Chem. Phys. Lett.* **93**, 184–187 (1982).
- Manz, J., Meyer, R. & Schor, H. H. R. Interplay of vibrational and van der Waals type bonding. *J. Chem. Phys.* **80**, 1562–1568 (1984).
- Fleming, D. G., Manz, J., Sato, K. & Takayanagi, T. Fundamental change in the nature of chemical bonding by isotopic substitution. *Angew. Chem. Int. Ed.* **53**, 13706–13709 (2014).
- Levine, R. D. & Wu, S. F. Resonances in reactive collisions: computational study of the  $\text{H} + \text{H}_2$  collision. *Chem. Phys. Lett.* **11**, 557–561 (1971).
- Ma, J. & Guo, H. Reactive and nonreactive Feshbach resonances accessed by photodetachment of  $\text{FH}_2\text{O}^-$ . *J. Phys. Chem. Lett.* **6**, 4822–4826 (2015).
- Wigner, E. P. On the behavior of cross sections near thresholds. *Phys. Rev.* **73**, 1002–1009 (1948).
- Even, U., Jortner, J., Noy, D., Lavie, N. & Cossart-Magos, C. Cooling of large molecules below 1 K and He clusters formation. *J. Chem. Phys.* **112**, 8068–8071 (2000).

58. Eppink, A. T. J. B. & Parker, D. H. Velocity map imaging of ions and electrons using electrostatic lenses: application in photoelectron and photofragment ion imaging of molecular oxygen. *Rev. Sci. Instrum.* **68**, 3477–3484 (1997).
59. Guo, H. A time-independent theory of photodissociation based on polynomial propagation. *J. Chem. Phys.* **108**, 2466–2472 (1998).

### Acknowledgements

This work is funded by the US Air Force Office of Scientific Research (Grants no. FA9550-16-1-0097 to D.M.N. and no. FA9550-15-1-0305 to H.G.), and the National Natural Science Foundation of China (Contracts no. 21573027 to J.L. and no. 91441107 to J.M.). M.L.W. thanks the National Science Foundation for a graduate research fellowship.

### Author contributions

The experimental research was conceived and supervised by D.M.N. The experiments were carried out by M.L.W., J.A.D. and M.C.B. Experimental data analysis and interpretation

was performed by M.L.W. Theoretical calculations were conceived by J.L., J.M. and H.G. and performed by J.L., L.G. and J.M. The paper was written by M.L.W., with the theoretical sections contributed by J.L., J.M. and H.G. All of the authors contributed to discussions about the results and manuscript.

### Additional information

Supplementary information is available in the [online version of the paper](#). Reprints and permissions information is available online at [www.nature.com/reprints](http://www.nature.com/reprints). Publisher's note: Springer Nature remains neutral with regard to jurisdictional claims in published maps and institutional affiliations. Correspondence and requests for materials should be addressed to J.L. and D.M.N.

### Competing financial interests

The authors declare no competing financial interests.



ARTICLE

Received 10 Aug 2016 | Accepted 1 Feb 2017 | Published 16 Mar 2017

DOI: 10.1038/ncomms14794

OPEN

# Unravelling the hidden link of lithium halides and application in the synthesis of organocuprates

Hong Yi<sup>1</sup>, Dali Yang<sup>1</sup>, Jie Xin<sup>1</sup>, Xiaotian Qi<sup>2</sup>, Yu Lan<sup>2</sup>, Yi Deng<sup>1</sup>, Chih-Wen Pao<sup>3</sup>, Jyh-Fu Lee<sup>3</sup> & Aiwen Lei<sup>1,4</sup>

As a versatile metal, copper has demonstrated a wide application in acting as both organometallic reagent and catalyst. Organocuprates are among the most used organometallic reagents in the formation of new carbon-carbon bonds in organic synthesis. Therefore, revealing the real structures of organocuprates in solution is crucial to provide insights into the reactivity of organocuprates. Here we provide several important insights into organocuprate chemistry. The main finding contains the following aspects. The Cu(O) particles were detected via the reduction of CuX by *n*BuLi or PhLi. The Cu(II) precursors CuX<sub>2</sub> (X = Cl, Br) could be used for the preparation of Gilman reagents. In addition, we provide direct evidence for the role and effect of LiX in organocuprate synthesis. Moreover, the EXAFS spectrum provides direct evidence for the exact structure of Li<sup>+</sup> CuX<sub>2</sub><sup>-</sup> ate complex in solution. This work not only sheds important light on the role of LiX in the formation of organocuprates but also reports two new routes for organocuprate synthesis.

<sup>1</sup>College of Chemistry and Molecular Sciences, The Institute for Advanced Studies (IAS), Wuhan University, Wuhan, Hubei 430072, China. <sup>2</sup>School of Chemistry and Chemical Engineering, Chongqing University, Chongqing 400030, China. <sup>3</sup>National Synchrotron Radiation Research Center, Hsinchu 30076, Taiwan. <sup>4</sup>State Key Laboratory of Organometallic Chemistry, Shanghai Institute of Organic Chemistry, Chinese Academy of Sciences, Shanghai 200032, China. Correspondence and requests for materials should be addressed to Y.D. (email: yideng@whu.edu.cn) or to A.L. (email: aiwenlei@whu.edu.cn).

Since the pioneering work of Gilman *et al.*,<sup>1</sup> organocuprates have been widely employed as organometallic reagents in organic synthesis (including conjugate additions, the opening of epoxides and cross-coupling reactions)<sup>2–7</sup>. In the textbook, organocuprates are usually prepared through transmetalation of lithium, magnesium or zinc organometallics with Cu(I) salts<sup>8</sup>. Different coordination environments always drastically affect the reactivity or stabilities of organocuprates<sup>9</sup>. Up to now, a lot of synthetic methodologies involving organocuprate reagents have been developed, while great uncertainty still exists in the related mechanism<sup>10</sup>. Although several important crystal structures of organocuprates were reported<sup>11–14</sup>, it should be noted that solid-state structures often reflect the most thermodynamically stable species and are not necessarily the same as in solution state. Besides, organocuprates can exhibit complex behaviour in solution, often existing as a number of different species in equilibrium, thus further complicating their characterization. For that reason, the structure of organocuprate compounds in solution cannot be inferred directly from crystal structures and must be determined independently.

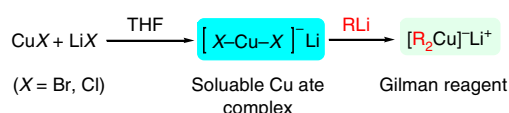
The structures of organocuprate reagents in an ethereal solution have received wide attention, because they are strongly relevant to reactivity in real reaction conditions<sup>15–17</sup>. Nuclear magnetic resonance<sup>18–20</sup> and electrospray ionization–mass spectrometry<sup>21,22</sup> served as powerful tools and have been widely used in determining the structures of organocuprates in solution. The linear bonding geometry of the C–Cu–C moiety in cuprates such as MeCu(CN)Li, Me<sub>2</sub>CuLi and Me<sub>2</sub>CuLi<sub>3</sub>LiX (X = I, CN) has been well established. In 1996, Knochel and colleagues<sup>23,24</sup> first introduced the extended X-ray absorption fine structure (EXAFS) to study the local structure of organocuprates from the reaction between CuCN and *n*BuLi. EXAFS spectroscopy provides a unique probe of the local structural environment of metal ions in non-crystalline systems<sup>25–33</sup>. The preliminary structure for lithium cyanocuprates based on EXAFS data has been elucidated. However, the role of cyanide and the difference between cyanide and other halide atoms still remain in debate<sup>9</sup>. Lipshutz *et al.*<sup>21</sup> and Koszinowski and colleagues<sup>34</sup> have

pointed out the LiX could have a positive effect on the solubility of CuX (X = I, Br, Cl, CN) independently. The electrospray ionization–mass spectrometry was used to study the structure of formed ate complex<sup>21,34</sup>. However, determination of the exact structure, the role for LiX and application in organocuprates have still been not well-studied up to date. We started our research by investigating the effect of anion on organocuprates preparation. Here we show the anion effect of different Cu(I) precursors on Gilman reagent preparation. The EXAFS reveals that the LiX (X = Br, Cl) serves as the hidden link for organocuprates preparation from unfavoured CuX. A soluble cupric bromide anion intermediate is evidenced by EXAFS when adding LiBr to CuBr in tetrahydrofuran (THF). This CuX<sub>2</sub><sup>−</sup> Li<sup>+</sup> ate complex serves as a key intermediate in the generation of Gilman reagent (Fig. 1). In addition, we also shed two other important findings in this work. First, the detection of copper nanoparticles produced after the addition of *n*BuLi or PhLi to CuX. Second, the Cu(II) precursors CuX<sub>2</sub> (X = Cl, Br) can be used for the preparation of Gilman reagents.

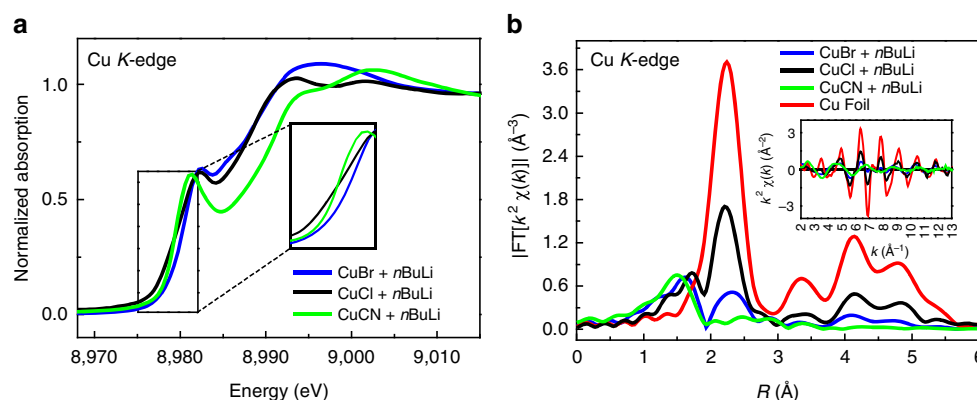
## Results

**Detection of Cu(0) particles via the reduction of CuX.** In organic synthesis, different Cu(I) precursors are always applied in different reaction systems<sup>10</sup>. Initially, we investigated different cuprous salts with excess *n*BuLi in THF under −78 °C for organocuprates synthesis. From X-ray absorption near-edge spectroscopy (XANES) spectra (Fig. 2a), we observed the difference of reactions from CuCN and CuX (X = Br, Cl). In Fourier-transformed EXAFS spectra, an obvious copper nanoparticle feature at high shells in CuBr and CuCl complexes appeared (Fig. 2b). However, such peaks at 3.4, 4.1 and 4.8 Å were not detected in the CuCN system, which is accordance with previous literature<sup>23</sup> that CuCN is a good precursor to Gilman reagent. In addition, such results also indicate that organocuprates made by CuBr or CuCl are very unstable to decompose into zero valance copper nanoparticle. Meanwhile, it seemed that the smaller the anion atom is, the more Cu(0) particle is formed.

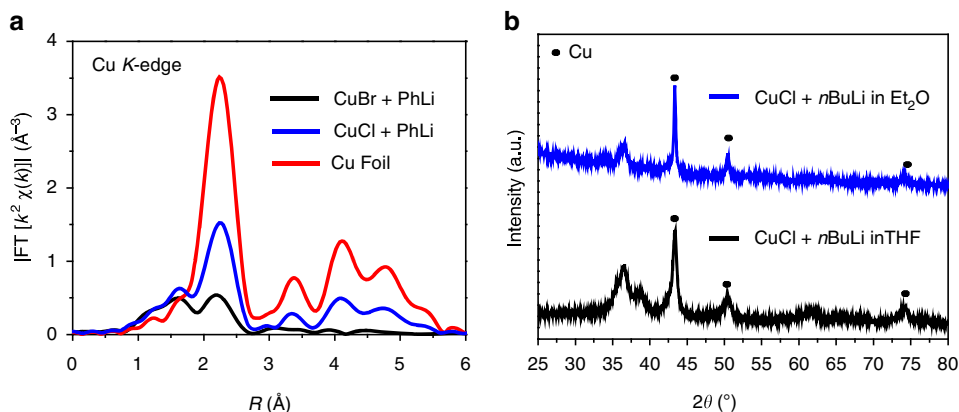
Then, we also used X-ray absorption spectroscopy (XAS) to study the reaction between CuX (X = Br, Cl) and PhLi. The XANES spectra were shown in Supplementary Fig. 1. From the EXAFS spectra in Fig. 3a, we found that the mixture of Cu(0) and Cu(I) species was formed when mixing CuBr or CuCl with PhLi. The CuCl was easier to be reduced to Cu(0) particle than CuBr by PhLi, which was consistent with the reaction with *n*BuLi. In addition, we also investigated the solvent effect on this process. We found that the reduction process was even faster when using



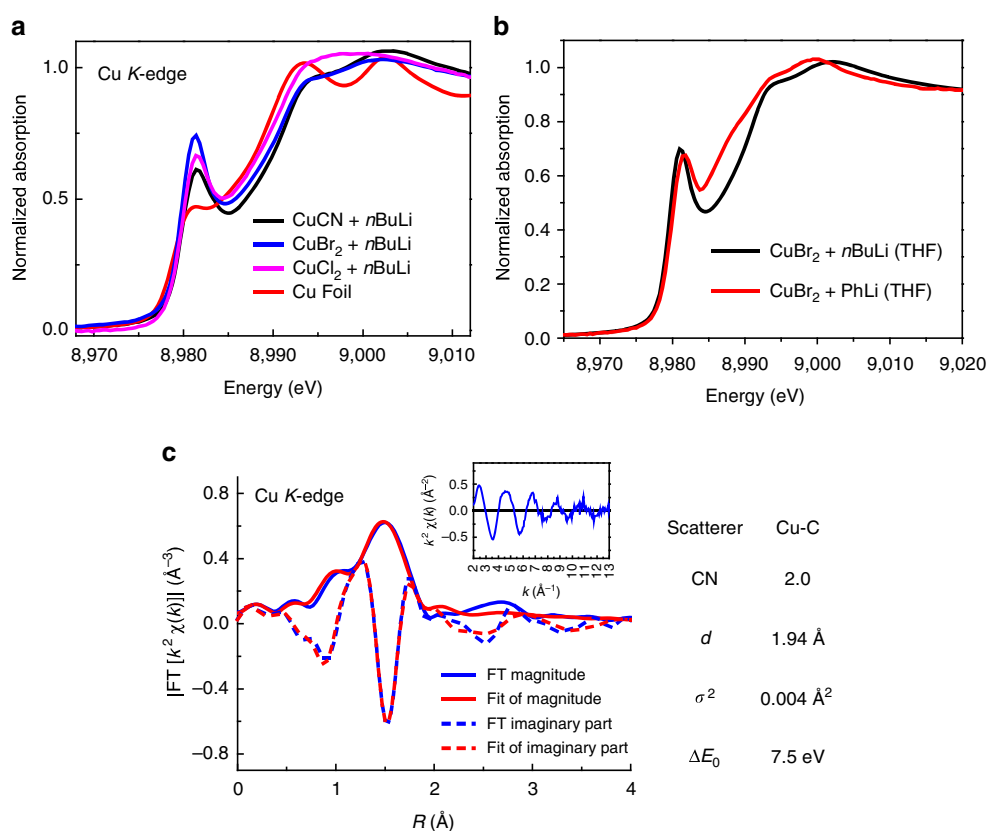
**Figure 1 | Hidden link of lithium halides.** Scheme of the role of LiX (X = Br, Cl) and application in Gilman reagent preparation.



**Figure 2 | XAFS analysis of CuX reduction.** (a) XANES spectra of various cuprous salts with excess *n*BuLi in THF under −78 °C. (b) Comparison of FT magnitudes of  $k^2$ -weighted EXAFS of various Cu(I) species mixed with excess *n*BuLi in THF under −78 °C. ( $3.0 \text{ \AA}^{-1} < k < 12.4 \text{ \AA}^{-1}$ ).



**Figure 3 | EXAFS and X-ray powder diffraction analysis.** (a) EXAFS spectra of CuBr and CuCl mixed with excess PhLi in THF under  $-78\text{ }^{\circ}\text{C}$ . (b) X-ray powder diffraction experiments, blue line: CuCl + 5.0 equiv *n*BuLi in Et<sub>2</sub>O, black line: CuCl + 5.0 equiv *n*BuLi in THF.

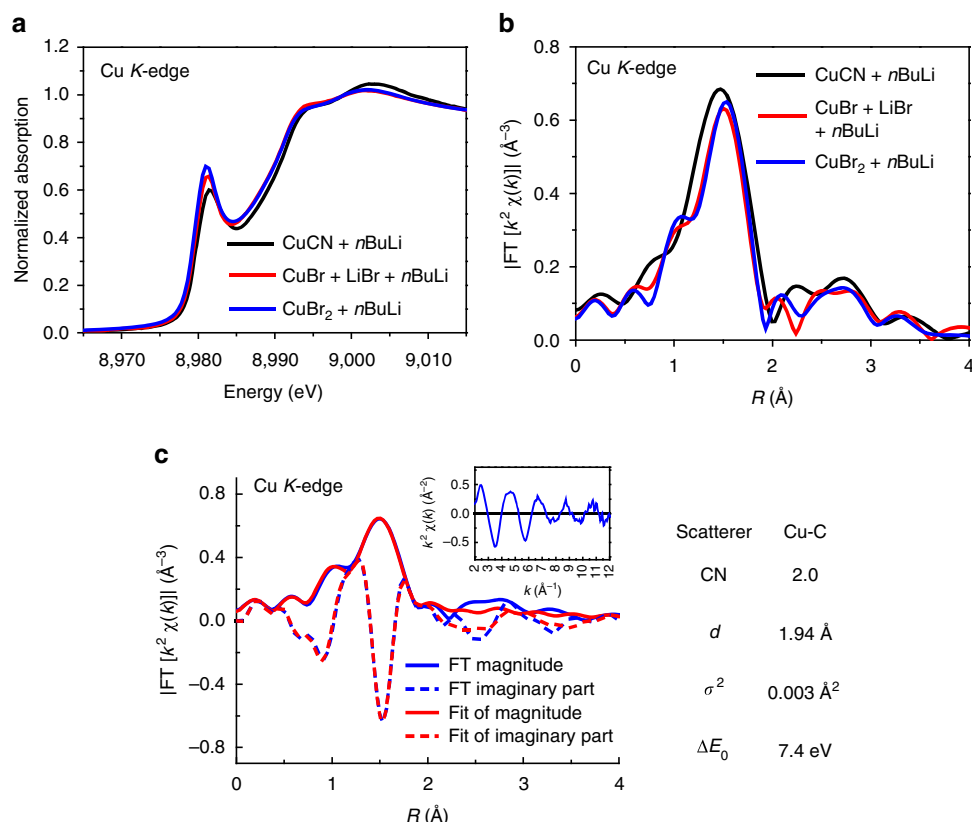


**Figure 4 | XAFS analysis of CuX<sub>2</sub> reduction.** (a) XANES spectra of CuCN, CuBr<sub>2</sub> and CuCl<sub>2</sub> mixed with excess *n*BuLi in THF under  $-78\text{ }^{\circ}\text{C}$ . (b) XANES spectra of CuBr<sub>2</sub> mixed with excess PhLi in THF under  $-78\text{ }^{\circ}\text{C}$ . (c) Fitting result for CuBr<sub>2</sub> + 5.0 equiv *n*BuLi in THF solution ( $2.910\text{ }^{\circ}\text{Å}^{-1} < k < 11.472\text{ }^{\circ}\text{Å}^{-1}$  and  $1.065\text{ }^{\circ}\text{Å} < R < 2.127\text{ }^{\circ}\text{Å}$ ).

ethyl ether (Et<sub>2</sub>O) as the solvent (Supplementary Figs 2 and 3). To further evidence the Cu(0) species and this reduction process, X-ray powder diffraction experiments were performed and the results are shown in Fig. 3b. The figure shows the main existence of Cu in the reaction between CuCl and *n*BuLi in THF or Et<sub>2</sub>O, in which the three peaks at 43.3°, 50.4° and 74.1° are corresponding to the (111), (200) and (220) planes of Cu (JCPDS number 04-0836), respectively.

**Reduction of Cu(II) precursors.** As the *n*BuLi could serve as a reductant to reduce CuX (*X* = Br, Cl) to Cu(0) species, we also employed EXAFS to investigate the reactions between Cu(II) salts

and *n*BuLi. We are very excited to discover that instead of using Cu(I) as the starting reagent, more stable and cheaper Cu(II) halide salts could also be good Gilman reagent precursors in the presence of excess organolithium reagent. EXAFS provided us a direct view of these transformations. Compared with traditional Gilman reagent prepared from CuCN, we could see that in the presence of 5.0 equivalent of *n*BuLi in THF under  $-78\text{ }^{\circ}\text{C}$ , both CuBr<sub>2</sub> and CuCl<sub>2</sub> were reduced into Cu(I) with edge energies about 8979.9 and 8980.0 eV, respectively, in the XANES spectra (Fig. 4a). The PhLi could also reduce CuBr<sub>2</sub> to corresponding Cu(I) species (Fig. 4b). The fitting result further verified the existence of 2-coordinated [C-Cu(I)-C] short-range structure (Fig. 4c). Owing to the fact that CuX<sub>2</sub> is stable and easy to store,



**Figure 5 | Role of lithium halides in the synthesis of organocuprates.** (a) XANES spectra of CuCN (black), CuBr + 1.0 eq LiBr (red) and CuBr<sub>2</sub> (blue) with excess *n*BuLi in THF under  $-78^\circ\text{C}$ . (b) EXAFS spectra of CuCN (black), CuBr + 1 eq LiBr (red) and CuBr<sub>2</sub> (blue) with excess *n*BuLi in THF under  $-78^\circ\text{C}$ . (c) Fitting results of *R*-space  $k^2$ -weighted EXAFS spectra of CuBr + 1 equiv LiBr in 5.0 equiv *n*BuLi THF solution ( $2.957 \text{ \AA}^{-1} < k < 11.145 \text{ \AA}^{-1}$  and  $1.172 \text{ \AA} < R < 1.914 \text{ \AA}$ ).

this method will be a new route for organocuprates preparation from CuX<sub>2</sub>. We also applied this method to organic synthesis. When adding the electrophile such as benzyl bromide or (2-bromoethyl)benzene into the reaction system, the desired C–C bond formation was formed, which implied that this method for organocuprates could be used for cross-coupling reactions. The detail application of this method in complicated molecular synthesis is on the way in our lab.

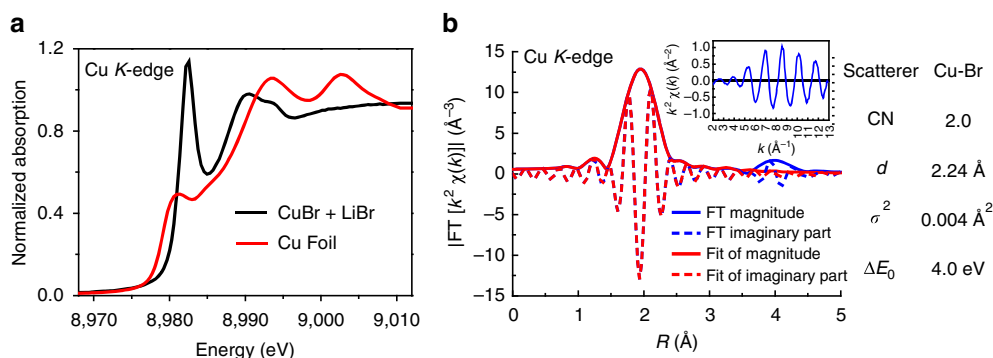
#### Role of lithium halides in the synthesis of organocuprates.

The lithium salts may have an effect on the formation of organocuprates, which has been awaked by several groups<sup>21,34–39</sup>. Although knowing this phenomenon for a long time, determination of the exact structure, the role for LiX and application in organocuprates have still been not well researched. When one equivalent LiBr was added to the mixture of CuBr and 5 equivalent *n*BuLi, we obtained a similar XANES spectra of which obtained from CuCN and excess *n*BuLi under low temperature (Fig. 5a). The edge energy was determined as 8979.7 and 8979.9 eV, respectively. Furthermore, high shell features for copper nanoparticle disappeared in the EXAFS spectrum, which indicates the formation of relatively pure organocuprate compound (Fig. 5b). The results of fitting show two carbon atoms at 1.94 Å around the copper atom equally (Fig. 5c). Thus, we developed a new method of preparing Gilman reagents using CuX with the help of LiX, which is very similar to what we get from mostly used cuprous cyanide in traditional synthesis route.

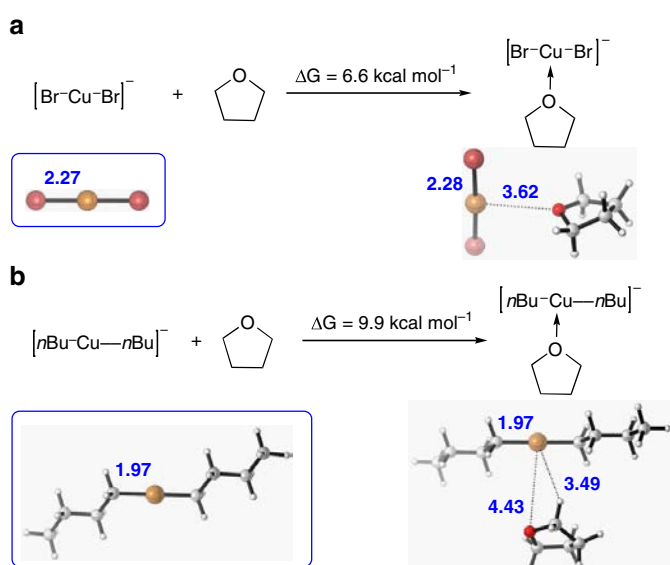
To further elucidate the role of LiX in preparing Gilman reagent, the mixture of LiBr and CuBr in THF was used

for demonstration. As shown in Supplementary Fig. 4, the CuBr species alone look polymer-like and very insoluble in THF. In contrast, CuBr can be dissolved in THF with the aid of one equivalent quantity of LiBr. A green solution is quickly formed after adding 1 equivalent LiBr into the system. This result indicated that the CuBr has an interaction with LiBr and a new copper species is possibly formed. The interaction between CuBr and LiBr might be the key to stabilizing the Gilman reagents prepared through this method. Valance alternation in cuprous bromide was invisible in the presence of LiBr from XANES spectra (Fig. 6a, edge energy of 8980.9 eV). In addition, EXAFS fitting results indicate two bromine atoms coordinated to the copper(I) centre (Fig. 6b). Thus, we claim that this type of ate complex was a  $[\text{Br-Cu-Br}]^- \text{Li}^+$  anion. This  $[\text{CuBr}_2]^-$  ate complex shows good solubility and serves as a key intermediate in the generation of Gilman reagent.

**Density functional theory calculations.** Density functional theory calculation was also performed to provide support for the EXAFS fitting results. As shown in Fig. 7a, the coordination of THF to  $[\text{Br-Cu-Br}]^-$  anion is endergonic by 6.6 kcal mol<sup>-1</sup>. The optimized structure suggests that the Cu–O distance is 3.62 Å, which means the interaction between Cu and O is very weak. As previous reports, the monomer state of organocuprates was always present in more polar solvent such as THF. Thus, the monomer structure of organocuprate was calculated. Meanwhile, the coordination of THF to  $[\text{nBu-Cu-nBu}]^-$  anion is found to be endergonic by 9.9 kcal mol<sup>-1</sup> and the corresponding Cu–O distance is determined to be 4.43 Å (Fig. 7b). Thus,



**Figure 6 | XAFS analysis of reaction between CuX and LiX.** (a) XANES spectra of CuBr + LiBr in THF species. (b) Fitting results of  $k^2$ -weighted  $R$ -space EXAFS spectra of CuBr + 1.0 equiv LiBr ( $2.890 \text{ \AA}^{-1} < k < 12.134 \text{ \AA}^{-1}$  and  $1.487 \text{ \AA} < R < 2.376 \text{ \AA}$ ).



**Figure 7 | Density functional theory calculation.** Density functional theory calculation for the coordination of THF to (a)  $[\text{Br-Cu-Br}]^-$  anion and (b)  $[\text{nBu-Cu-nBu}]^-$  anion.

the coordination of THF to  $[\text{Br-Cu-Br}]^-$  and  $[\text{nBu-Cu-nBu}]^-$  anion are both energetically unfavourable<sup>19,20,40</sup>. Moreover, optimized structures reveal that the bond length of Cu-Br in  $[\text{Br-Cu-Br}]^-$  anion is 2.27  $\text{\AA}$  and the bond length of Cu-C in  $[\text{nBu-Cu-nBu}]^-$  anion is 1.97  $\text{\AA}$ , which are very close to that obtained from EXAFS (2.24 and 1.94  $\text{\AA}$ ). Consequently, the theoretical study and EXAFS fitting results have reached the same conclusion.

## Discussion

To sum up, we elucidate LiX ( $X = \text{Br}, \text{Cl}$ ) as a hidden link in the preparation of organocuprate reagents from CuX ( $X = \text{Br}, \text{Cl}$ ) with a key intermediate  $\text{CuX}_2^- \text{Li}^+$  ate complex evidenced by EXAFS. Meanwhile, this Cu(I) ate complex can serve as a good precursor to prepare Gilman reagents following a tandem process. In addition, we also developed the organocuprate reagents synthesis from Cu(II) precursors. This discovery might help open a new perspective in understanding the organocopper chemistry and mechanisms of copper-catalysed reactions as well.

## Methods

**General information.** X-ray absorption measurements were acquired in transmission mode at beamline 17C1 at National Synchrotron Radiation Research

Center in Taiwan. A pure Cu foil spectrum (edge energy 8979 eV) was acquired simultaneously with each measurement for energy calibration. Multiple scans were taken to reduce the noise. The Supplementary Tables 1–3 revealed the detailed parameters of the XAFS spectral.

**Reaction system.** Cu salt (0.5 mmol) was added to the schlenk tube cell in a glovebox beforehand. Then, 5.0 ml of THF was injected into the cell and the solution was stirred under  $\text{N}_2$  at  $-78^\circ\text{C}$  for 20 min. Subsequently, RLi (2.5 mmol) was added into the system and stirred for 30 min. As the last step, the liquid nitrogen was quickly added to reaction system, which would be frozen into solid immediately, and it was transferred into the XAFS cell with the protection of nitrogen gas.

**Detection system (beamline).** The detection system was cooled using cooled nitrogen gas. The Supplementary Fig. 5 was the picture of cell holder used in the beamline. This hold connected with a liquid nitrogen cooled gas stream. The Supplementary Fig. 6 showed our idea for low-temperature system. We used a gas stream passing through the liquid nitrogen Dewar to cool the system. The temperature could be controlled by the tuning of the flow rate. The Supplementary Fig. 7 was the whole picture of experimental set-up in beamline.

**Data availability.** Data supporting the findings of this study are available within this article and its Supplementary Information file and from the corresponding authors on reasonable request.

## References

- Gilman, H., Jones, R. G. & Woods, L. A. The preparation of methylcopper and some observations on the decomposition of organocopper compounds. *J. Org. Chem.* **17**, 1630–1634 (1952).
- House, H. O., Respass, W. L. & Whitesides, G. M. The chemistry of carbanions. XII. The role of copper in the conjugate addition of organometallic reagents. *J. Org. Chem.* **31**, 3128–3141 (1966).
- Cherney, A. H., Kadunce, N. T. & Reisman, S. E. Enantioselective and enantiospecific transition-metal-catalyzed cross-coupling reactions of organometallic reagents to construct C-C bonds. *Chem. Rev.* **115**, 9587–9652 (2015).
- Surry, D. S. & Spring, D. R. The oxidation of organocuprates—an offbeat strategy for synthesis. *Chem. Soc. Rev.* **35**, 218–225 (2006).
- Whitesides, G. M., Fischer, W. F., San Filippo, J., Bashe, R. W. & House, H. O. Reaction of lithium dialkyl- and diarylcuprates with organic halides. *J. Am. Chem. Soc.* **91**, 4871 (1969).
- Krause, N. & Gerold, A. Regio- and stereoselective syntheses with organocopper reagents. *Angew. Chem. Int. Ed.* **36**, 186 (1997).
- Corey, E. J. & Posner, G. H. Selective formation of carbon-carbon bonds between unlike groups using organocopper reagents. *J. Am. Chem. Soc.* **89**, 3911 (1967).
- Knochel, P. & Singer, R. D. Preparation and reactions of polyfunctional organozinc reagents in organic synthesis. *Chem. Rev.* **93**, 2117 (1993).
- Neumeier, M. & Gschwind, R. M. Elongated Gilman cuprates: the key to different reactivities of cyano- and iodocuprates. *J. Am. Chem. Soc.* **136**, 5765–5772 (2014).
- Yoshikai, N. & Nakamura, E. Mechanisms of nucleophilic organocopper(I) reactions. *Chem. Rev.* **112**, 2339–2372 (2012).
- Dupuis, J. *et al.* Electron transfer from trialkyltin radicals to nitrosugars: the synthesis of C-glycosides with tertiary anomeric carbon atoms. *J. Am. Chem. Soc.* **107**, 4332 (1985).

12. Olmstead, M. M. & Power, P. P. Isolation and first structural characterization of dimethyl sulfide solvates of phenyllithium, phenylcopper, and lower and higher order lithium phenylcuprate reagents. *J. Am. Chem. Soc.* **112**, 8008 (1990).
13. Davies, R. P. The structures of lithium and magnesium organocuprates and related species. *Coordin. Chem. Rev.* **255**, 1226 (2011).
14. Bertz, S. H., Hardin, R. A., Heavey, T. J. & Ogle, C. A. The X-ray crystal structure of a cuprate-carbonyl pi-complex. *Angew. Chem. Int. Ed.* **52**, 10250–10252 (2013).
15. Lipshutz, B. H., Keith, J. & Buzard, D. J. An electrospray ionization mass spectrometry study of the aggregation states of organocopper complexes in solution. *Organometallics* **18**, 1571 (1999).
16. Bertz, S. H. New copper chemistry. 20. Lithium cyanocuprates,  $\text{RCu(CN)Li}$ : first observation of two-bond carbon-13-carbon-13 NMR couplings in organocuprates. *J. Am. Chem. Soc.* **113**, 5470 (1991).
17. Putau, A., Brand, H. & Koszinowski, K. Tetraalkylcuprates(III): formation, association, and intrinsic reactivity. *J. Am. Chem. Soc.* **134**, 613–622 (2012).
18. Lipshutz, B. H., Kozlowski, J. A. & Wilhelm, R. S. Higher order, mixed organocuprates. 12. Chemical and spectroscopic observations on the properties and composition of higher order, mixed organocuprates,  $\text{R}_2\text{Cu(CN)Li}_2$ . *J. Org. Chem.* **49**, 3943 (1984).
19. Gschwind, R. M., Xie, X., Rajamohanam, P. R., Auel, C. & Boche, G.  $\text{Me}_2\text{CuLi}^+\text{LiCN}$  in diethyl ether prefers a homodimeric core structure  $[\text{Me}_2\text{CuLi}]_2$  and not a heterodimeric one  $[\text{Me}_2\text{CuLi}^+\text{LiCN}]$ :  $^1\text{H}$ ,  $^6\text{Li}$  HOE and  $^1\text{H}$ ,  $^1\text{H}$  NOE studies by NMR. *J. Am. Chem. Soc.* **123**, 7299–7304 (2001).
20. Gschwind, R. M. Organocuprates and diamagnetic copper complexes: structures and nmr spectroscopic structure elucidation in solution. *Chem. Rev.* **108**, 3029–3053 (2008).
21. Lipshutz, B. H., Stevens, K. L., James, B., Pavlovich, J. G. & Snyder, J. P. Analyses of anioniccuprate(I) complexes via electrospray mass spectrometry. *J. Am. Chem. Soc.* **118**, 6796 (1996).
22. Putau, A. & Koszinowski, K. Association and dissociation of lithium cyanocuprates in ethereal solvents. *Organometallics* **30**, 4771 (2011).
23. Stemmler, T., Penner-Hahn, J. E. & Knochel, P. Structural characterization of organocopper reagents by EXAFS spectroscopy. *J. Am. Chem. Soc.* **115**, 348 (1993).
24. Stemmler, T. L. *et al.* Structural characterization of organocuprate reagents. EXAFS spectroscopy and *ab initio* calculations. *J. Am. Chem. Soc.* **117**, 12489 (1995).
25. Koningsberger, D. & Prins, R. *X-Ray Absorption: Principles, Applications, Techniques of EXAFS, SEXAFS, and XANES* (Wiley, 1988).
26. Nelson, R. C. & Miller, J. T. An introduction to X-ray absorption spectroscopy and its in situ application to organometallic compounds and homogeneous catalysts. *Catal. Sci. Technol.* **2**, 461 (2012).
27. Zhang, G. *et al.* Direct observation of reduction of Cu(II) to Cu(I) by terminal alkynes. *J. Am. Chem. Soc.* **136**, 924–926 (2014).
28. Yi, H. *et al.* Evidence of Cu(I)/Cu(II) redox process by X-ray absorption and EPR spectroscopy: direct synthesis of dihydrofurans from beta-ketocarbonyl derivatives and olefins. *Chem. Eur. J.* **21**, 18925–18929 (2015).
29. Lu, Q. *et al.* Operando X-ray absorption and EPR evidence for a single electron redox process in copper catalysis. *Chem. Sci.* **6**, 4851 (2015).
30. Rabeah, J., Bentrup, U., Stosser, R. & Bruckner, A. Selective alcohol oxidation by a copper TEMPO catalyst: mechanistic insights by simultaneously coupled operando EPR/UV-Vis/ATR-IR spectroscopy. *Angew. Chem. Int. Ed.* **54**, 11791–11794 (2015).
31. Welther, A., Bauer, M., Mayer, M. & Jacobi von Wangelin, A. Iron(0) particles: catalytic hydrogenations and spectroscopic studies. *ChemCatChem* **4**, 1088 (2012).
32. Bauer, M. & Gastl, C. X-Ray absorption in homogeneous catalysis research: the iron-catalyzed Michael addition reaction by XAS, RIXS and multi-dimensional spectroscopy. *Phys. Chem. Chem. Phys.* **12**, 5575–5584 (2010).
33. Schoch, R., Desens, W., Werner, T. & Bauer, M. X-ray spectroscopic verification of the active species in iron-catalyzed cross-coupling reactions. *Chem. Eur. J.* **19**, 15816–15821 (2013).
34. Putau, A., Wilken, M. & Koszinowski, K. Ionic aggregates of lithium organocuprates. *Chem. Eur. J.* **19**, 10992–10999 (2013).
35. Lipshutz, B. H., Kozlowski, J. A. & Breneman, C. M. Chemical and spectroscopic studies on copper iodide derived organocuprates: new insight into the composition of Gilman's reagent. *J. Am. Chem. Soc.* **107**, 3197 (1985).
36. Krasovskiy, A., Malakhov, V., Gavryushin, A. & Knochel, P. Efficient synthesis of functionalized organozinc compounds by the direct insertion of zinc into organic iodides and bromides. *Angew. Chem. Int. Ed.* **45**, 6040–6044 (2006).
37. Bertz, S. H., Vellekoop, A. S., Smith, R. A. J. & Snyder, J. P. New copper chemistry. 23. Preparation of ethereal lithium dimethylcuprates  $(\text{Me}_2\text{CuLi})_2$  and  $\text{Me}_2\text{CuLi}\cdot\text{LiI}$  displaying narrow line width  $^{13}\text{C}$  NMR resonances. *Organometallics* **14**, 1213 (1995).
38. Feng, C., Cunningham, D. W., Easter, Q. T. & Blum, S. A. Role of LiCl in generating soluble organozinc reagents. *J. Am. Chem. Soc.* **138**, 11156–11159 (2016).
39. Nakamura, E., Mori, S. & Morokuma, K. Theoretical studies on  $\text{S}_{\text{N}}2$ -reaction of MeBr with  $\text{Me}_2\text{CuLi}\cdot\text{LiCl}$ . Solvent and cluster effects on oxidative addition/reductive elimination pathway. *J. Am. Chem. Soc.* **120**, 8273 (1998).
40. John, M. *et al.* The relation between ion pair structures and reactivities of lithium cuprates. *Chem. Eur. J.* **6**, 3060–3068 (2000).

### Acknowledgements

This work was supported by the 973 Program (2012CB725302), the National Natural Science Foundation of China (21390400, 21520102003, 21272180 and 21302148), the Hubei Province Natural Science Foundation of China (2013CFA081), the Research Fund for the Doctoral Program of Higher Education of China (20120141130002) and the Ministry of Science and Technology of China (2012YQ120060). The Program of Introducing Talents of Discipline to Universities of China (111 Program) is also appreciated. The X-ray absorption spectroscopy studies were carried out at the beamline 17C1 of the National Synchrotron Radiation Research Center (NSRRC) in Taiwan. We thank Ms Z. Alaji and Dr Atul K. Singh for kind discussions.

### Author contributions

H.Y. and A.L. conceived the project. H.Y., D.Y., X.J., D.Y., C.-W.P. and J.-F.L. performed the experiments, analysed the data and discussed the results. X.Q. and Y.L. performed the density functional theory calculations. H.Y., D.Y. and A.L. wrote the paper. H.Y. and D.Y. wrote the Supplementary Information and contributed other related materials. H.Y. and D.Y. contributed equally to this work. All the authors checked the manuscript.

### Additional information

**Supplementary Information** accompanies this paper at <http://www.nature.com/naturecommunications>

**Competing interests:** The authors declare no competing financial interests.

**Reprints and permission** information is available online at <http://npg.nature.com/reprintsandpermissions/>

**How to cite this article:** Yi, H. *et al.* Unravelling the hidden link of lithium halides and application in the synthesis of organocuprates. *Nat. Commun.* **8**, 14794 doi: 10.1038/ncomms14794 (2017).

**Publisher's note:** Springer Nature remains neutral with regard to jurisdictional claims in published maps and institutional affiliations.



This work is licensed under a Creative Commons Attribution 4.0 International License. The images or other third party material in this article are included in the article's Creative Commons license, unless indicated otherwise in the credit line; if the material is not included under the Creative Commons license, users will need to obtain permission from the license holder to reproduce the material. To view a copy of this license, visit <http://creativecommons.org/licenses/by/4.0/>

© The Author(s) 2017

ARTICLE

Received 28 May 2016 | Accepted 12 Dec 2016 | Published 31 Jan 2017

DOI: 10.1038/ncomms14233

OPEN

# Biomimetically inspired asymmetric total synthesis of (+)-19-dehydroxyl arisandilactone A

Yi-Xin Han<sup>1,\*</sup>, Yan-Long Jiang<sup>1,\*</sup>, Yong Li<sup>1</sup>, Hai-Xin Yu<sup>1</sup>, Bing-Qi Tong<sup>1</sup>, Zhe Niu<sup>1</sup>, Shi-Jie Zhou<sup>1</sup>, Song Liu<sup>2</sup>, Yu Lan<sup>2</sup>, Jia-Hua Chen<sup>1</sup> & Zhen Yang<sup>1,3,4</sup>

Complex natural products are a proven and rich source of disease-modulating drugs and of efficient tools for the study of chemical biology and drug discovery. The architectures of complex natural products are generally considered to represent significant barriers to efficient chemical synthesis. Here we describe a concise and efficient asymmetric synthesis of 19-dehydroxyl arisandilactone A—which belongs to a family of architecturally unique, highly oxygenated nortriterpenoids isolated from the medicinal plant *Schisandra arisanensis*. This synthesis takes place by means of a homo-Michael reaction, a tandem retro-Michael/Michael reaction, and Cu-catalysed intramolecular cyclopropanation as key steps. The proposed mechanisms for the homo-Michael and tandem retro-Michael/Michael reactions are supported by density functional theory (DFT) calculation. The developed chemistry may find application for the synthesis of its other family members of *Schisandraceae* nortriterpenoids.

<sup>1</sup>Key Laboratory of Bioorganic Chemistry and Molecular Engineering of Ministry of Education, Beijing National Laboratory for Molecular Science (BNLMS), College of Chemistry and Molecular Engineering, Peking-Tsinghua Center for Life Sciences, Peking University, Beijing 100871, China. <sup>2</sup>School of Chemistry and Chemical Engineering, Chongqing University, Chongqing 400030, China. <sup>3</sup>Laboratory of Chemical Genomics, School of Chemical Biology and Biotechnology, Peking University Shenzhen Graduate School, Shenzhen 518055, China. <sup>4</sup>Key Laboratory of Marine Drugs, Chinese Ministry of Education, School of Medicine and Pharmacy, Ocean University of China, 5 Yushan Road, Qingdao 266003, China. \* These authors contributed equally to this work. Correspondence and requests for materials should be addressed to Y.L. (email: lanyu@cqu.edu.cn) or to J.-H.C. (email: jhchen@pku.edu.cn) or to Z.Y. (email: zyang@pku.edu.cn).

*Schisandra chinensis* is also known as wu wei zi in China, which translates to five-flavour berry, a description given to it because it possesses all five basic flavours of salty, sweet, sour, spicy and bitter. Records show that for over 2,000 years five-flavour berries have been used as sedatives and tonic agents, as well as for the treatment of rheumatic lumbago and related diseases<sup>1,2</sup>.

Because *S. chinensis* is a traditional Chinese herbal medicine, it has been targeted in medicinal chemistry to identify lead compounds for drug discovery. There has been considerable progress in the discovery of bioactive triterpenoids from the *Schisandraceae* family over the past two decades. To date, over 200 nortriterpenoids have been structurally characterized<sup>1,2</sup>, and some representative structures **1–6** are shown in Fig. 1. Preliminary biological assays have indicated that some of the nortriterpenoids possess inhibitory activity toward hepatitis, tumours and HIV-1 (refs 1,2).

Natural sources of these compounds are scarce, which hampers systematic studies of their biological activities. Synthesis of these products is needed to continue biomedical research in this area, and much effort has been devoted to total synthesis of these nortriterpenoids ('Synthetic studies on Schisandraceae triterpenoids', see ref. 3 and related references therein). From this research, total syntheses of schindilactone A<sup>4</sup>, rubrifloridilactone A<sup>5,6</sup>, schilancitrilactones B and C<sup>7</sup> and propindilactone G<sup>8</sup> (see **3–6** in Fig. 1) have been developed.

In 2010, Shen isolated (+)-arisandilactone A<sup>9</sup> and (+)-arisanolactone C<sup>10</sup> (**1** and **2** in Fig. 1) from *S. arisanensis*, which is found in Taiwan. The structures of these compounds were confirmed by X-ray crystallography. Among the nortriterpenoids, arisandilactone A (**1**) is unique in that it has an oxa-bridged 7-9-5 tricyclic carbon core, which has not been encountered in natural products before. Because of this structural feature, arisandilactone A (**1**) is a challenging target for total synthesis. To the best of our

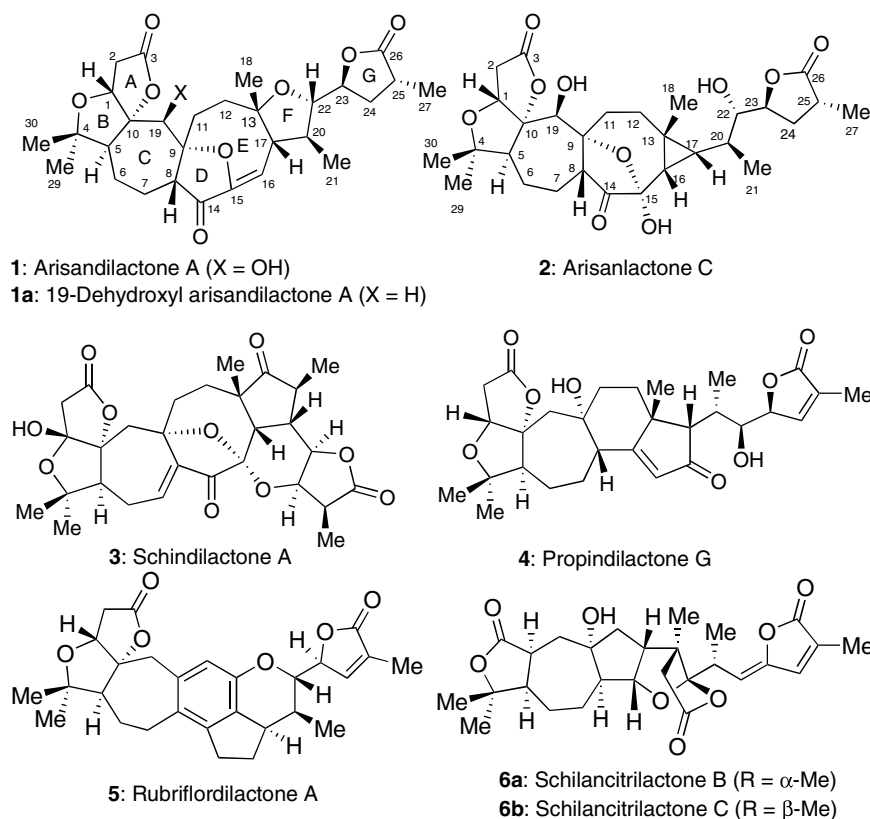
knowledge, no synthesis of arisandilactone A (**1**) has been reported to date.

Natural products with unique and complex architectures are challenging in organic synthesis (for an excellent review, see ref. 11). In this regard, biomimetic approaches for the formation of complex natural products have proven to be effective strategies in organic synthesis<sup>12</sup>. Among the various biomimetic reactions, Michael-type reaction can be regarded as one of the most powerful reactions in the biosynthesis of natural products<sup>13</sup>. Here, we report an asymmetric total synthesis of (+)-19-dehydroxyl arisandilactone A (**1a**), a derivative of arisandilactone A (**1**), using a biomimetic synthesis involving a homo-Michael reaction and a tandem retro-Michael/Michael reaction as key steps.

## Results

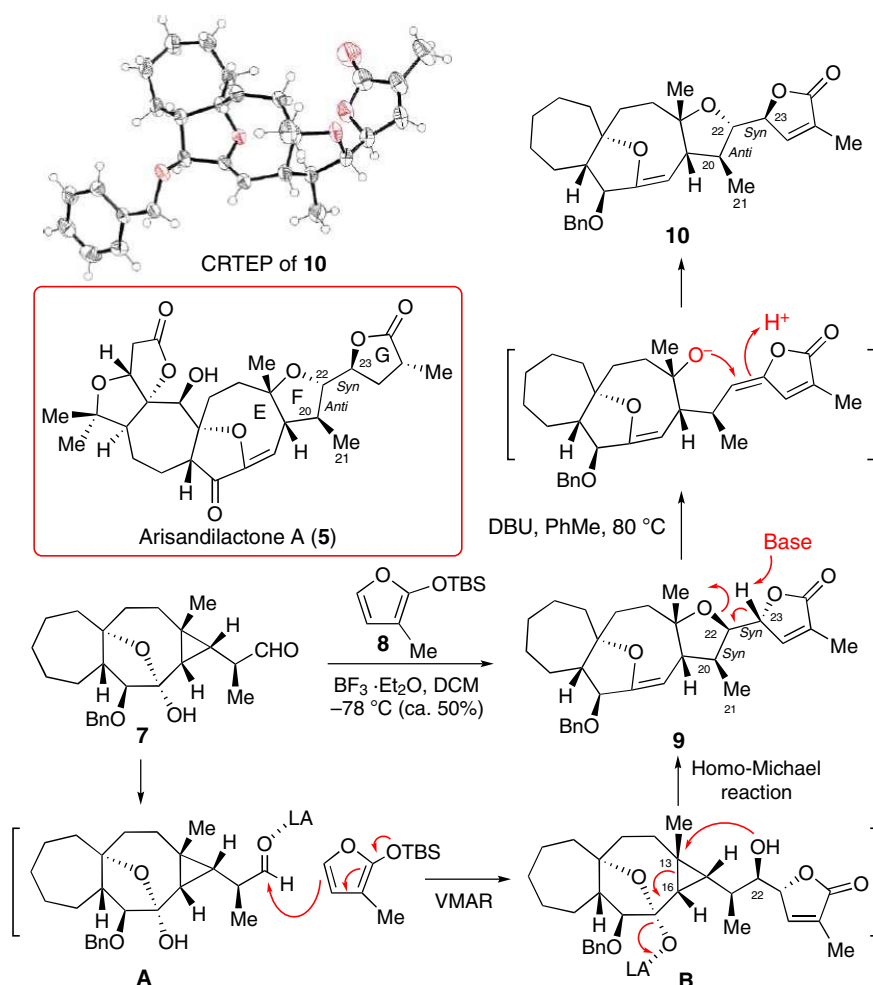
**Retrosynthetic analysis.** For the total synthesis of arisandilactone A (**1**), construction of its strained transannular 10-oxabicyclo[5.2.1]dec-6-en-8-one core (DE ring) bearing an oxa-bridged  $\alpha,\beta$ -unsaturated ketone subunit is the most difficult task in the entire total synthesis. Thus, from a synthetic strategy point of view, this fragment should be introduced at a late stage in the total synthesis, and preferable by a biomimetic synthesis because of its high sensitivity and instability.

While conducting the model study toward the total synthesis of arisanolactone C (**2**), we serendipitously found that this strained bicyclic core could be constructed via an intramolecular oxa-homo-Michael reaction (Fig. 2). In the event, we first synthesized aldehyde **7** and then coupled with tert-butyl dimethyl((3-methylfuran-2-yl)oxy)silane (**8**) via a vinylogous Mukaiyama aldol reaction (VMAR). To our surprise, product **9** was obtained in approximately 50% yield when the reaction was carried out at  $-78^\circ\text{C}$  in the presence of  $\text{BF}_3 \cdot \text{Et}_2\text{O}$  in  $\text{CH}_2\text{Cl}_2$ . The reaction



**Figure 1** | *Schisandraceae* family. Naturally occurring nortriterpenoids (**1–6**) and 19-dehydroxyl arisandilactone A (**1a**, a derivative of **1**).





**Figure 2 | Model study.** Unified biosynthetic approach featuring homo-Michael and retro-Michael/Michael reactions for formation of the 7/9/5 tricyclic core of arisandilactone A (**1**).

was proposed to proceed through a typical VMAR to form intermediate **B**. This was followed by a homo-Michael reaction<sup>14,15</sup> through the cleavage of its carbon-carbon bond at C13 and C16 and simultaneous formation of the five-membered F ring (see Fig. 2). The newly generated three stereogenic centres at C20, C22 and C23 in product **9** formed a *syn/syn* stereotriad. The arrangements of groups at the stereogenic centres at C22 and C23 were opposite to those in arisandilactone A, which has an *anti/syn* stereotriad. Stereoselective synthesis of the *anti/syn* stereotriad has proven to be challenging<sup>16,17</sup>.

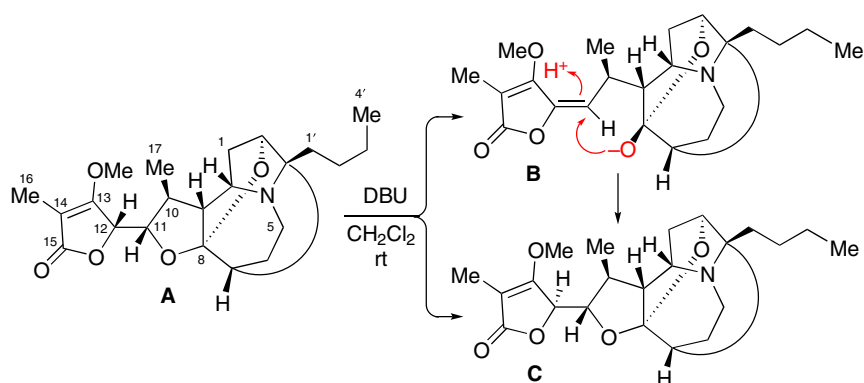
On inspection of the structure of product **9**, we found that **9** could be epimerized at its C22 and C23 stereogenic centres by treatment with 1,8-diazabicyclo[5.4.0]undec-7-ene (DBU) via a tandem retro-Michael/Michael reaction. This strategy has been used by Pyne and co-workers in the total synthesis of *Stemona* alkaloid (11*S*, 12*R*)-dihydrostemofoline (**C**) from (11*S*, 12*S*)-dihydrostemofoline (**A**) through intermediate **B** (Fig. 3)<sup>18</sup>. The stereochemical outcome of the DBU-initiated ring opening reaction of **A** can be rationalized as occurring through a deprotonation of **A** by DBU at the acidic  $\gamma$ -position of the lactone ring which would result in the anionic intermediate **B**, and then lead to (11*S*, 12*R*)-dihydrostemofoline (**C**) to avoid the unfavourable steric interaction between the methoxy (C13) and methyl (C10) groups in the intermediate **B** (Fig. 3).

To explore the feasibility of this strategy, we treated **9** with DBU in toluene at 80 °C. As expected, the desired product **10** was

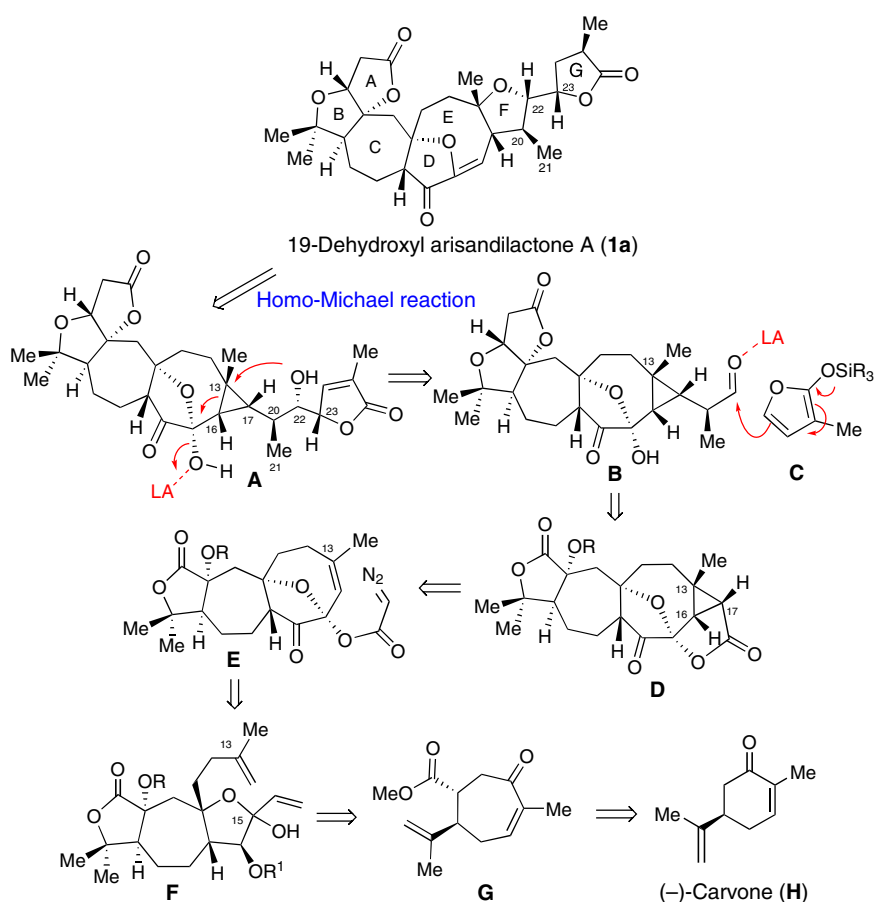
obtained in 48% yield (Fig. 2), and its structure was tentatively confirmed through X-ray crystallography; however, the data were of insufficient quality to allow a definitive determination of the structure. Inspired by these results, we applied this knowledge to the total synthesis of 19-dehydroxyl arisandilactone A (**1a**) using the homo-Michael and the tandem retro-Michael/Michael reactions as key steps.

Figure 4 illustrates our proposed biomimetic total synthesis of 19-dehydroxyl arisandilactone A. Based on the chemistry presented above, we expected the target **1a** could be produced from precursor **A** using the developed tandem retro-Michael/Michael reaction as a key step. The intermediate **A**, in turn, could be produced from **B** via nucleophilic attack of the silyl ether **C** on the aldehyde in intermediate **B** via a VMAR, followed by the key intramolecular homo-Michael reaction as shown above. Precursor aldehyde **B** could be prepared from lactone **D** via a series of functional group interconversions.

It is conceivable that the *cis*-fused 8/3-bicyclic domain in lactone **D** could be constructed via a Cu-catalysed intramolecular cyclopropanation<sup>19</sup> of **E** by taking advantage of conformation control of the substrate. This reaction would generate **D** with three contiguous stereogenic centres at C13, C16 and C17, as well as a lactone fragment, which could serve as a handle to install the side chain. To the best of our knowledge, synthesis of a *cis*-fused 8/3-bicyclic ring fragment in **D** is unprecedented. Thus, our retrosynthetic analysis could trace back to the synthesis of the



**Figure 3 | retro-Michael/Michael reaction.** DBU mediated a biomimetic tandem retro-Michael/Michael reaction for the formation of (11S, 12R)-dihydrostemofoline (**C**) from (11S, 12S)-dihydrostemofoline (**A**) through intermediate **B**.

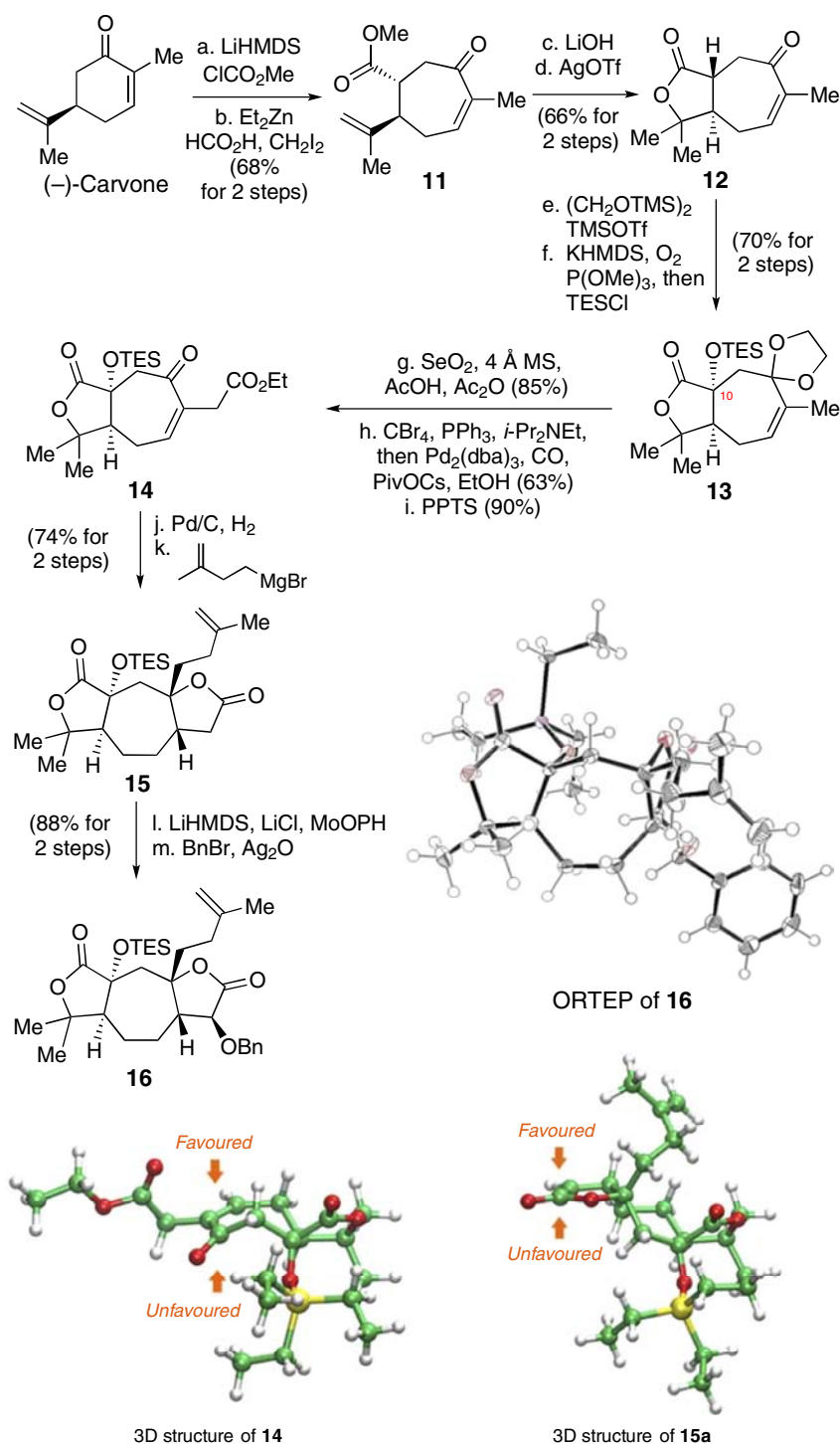


**Figure 4 | Retrosynthetic analysis of 19-dehydroxyl arisandilactone A (1a).** The Homo-Michael/Michael reaction were used as key steps to construct core structure of 19-dehydroxyl arisandilactone A (1a).

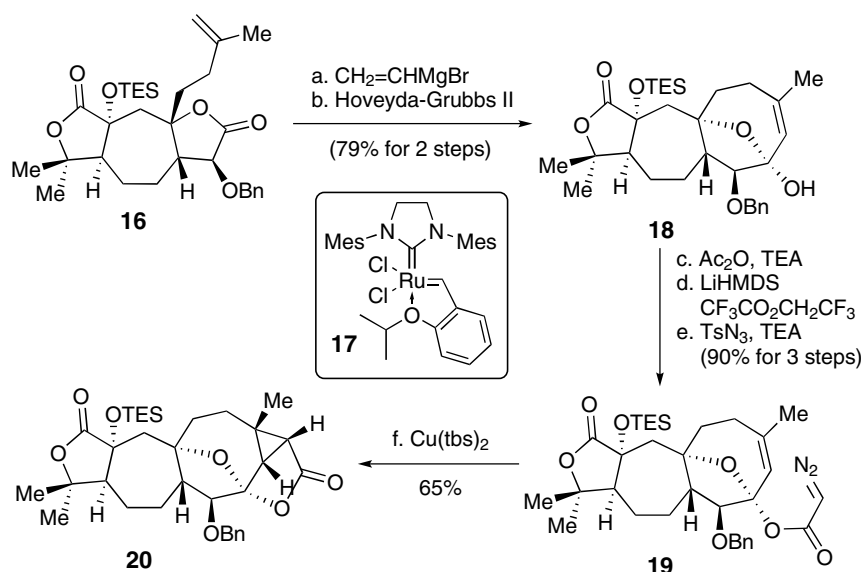
oxa-bridged ‘tri-substituted’ cyclooctene ring in **E**, which could be generated from diene **F** using a ring-closing metathesis (RCM) reaction, a method that was utilized in our total synthesis of schindilactone **A**<sup>5</sup> (**3** in Fig. 1). Diene **F**, in turn, could be made from ketoester **G** by modifying the methods applied in our total synthesis of schindilactone **A**. Thus, (*R*)-(-)-carvone (**H**) is a logical starting material for the preparation of ketoester **G**.

**Asymmetric synthesis of 19-dehydroxyl arisandilactone A (1a).** Our synthesis began with asymmetric construction of the fully functionalized bislactone **16** from (*R*)-(-)-carvone (Fig. 5).

A two-step procedure for the conversion of (*R*)-(-)-carvone to cycloheptenone was accomplished using a Mander’s methoxycarbonylation, followed by a sequence of cyclopropanation/ring-expansion reactions<sup>20,21</sup> to afford **11** in 68% yield. Compound **11** was hydrolysed with LiOH, and the resulting acid then underwent an AgOTf-mediated lactonisation<sup>22</sup> to afford **12** in 66% overall yield. To install the C10 silyloxy group of **13**, **12** was first exposed to TMSO(CH<sub>2</sub>)<sub>2</sub>OTMS/TMSOTf<sup>23</sup>, and the resultant ketal ester was then reacted with potassium bis(trimethylsilyl)amide in the presence of P(OMe)<sub>3</sub> under an O<sub>2</sub> atmosphere<sup>24</sup>, followed by reaction with triethylchlorosilane to afford **13** in 70% yield as a single diastereoisomer.



**Figure 5 | Synthesis of compound 16.** (a) (-)-carvone (1.0 eq), LiHMDS (2.1 eq), ClCOOMe (1.5 eq), THF,  $-78^\circ\text{C}$ , 2 h, 90%; (b)  $\text{Et}_2\text{Zn}$  (2.3 eq),  $\text{CH}_2\text{I}_2$  (2.3 eq),  $\text{HCOOH}$  (2.3 eq), DCM,  $0^\circ\text{C}$ , 75%; (c) LiOH (2.2 eq),  $\text{MeCN}/\text{H}_2\text{O}$  (1:1), rt, 92%; (d) AgOTf (0.05 eq),  $\text{ClCH}_2\text{CH}_2\text{Cl}$ , reflux, 72%; (e)  $\text{TMSOCH}_2\text{CH}_2\text{OTMS}$  (1.4 eq), TMSOTf (0.1 eq), DCM,  $-78$  to  $-20^\circ\text{C}$ , 87%; (f) KHMDS (2.0 eq),  $\text{P(OMe)}_3$  (1.6 eq),  $-78^\circ\text{C}$ , THF, under a balloon filled with  $\text{O}_2$ , then TESCI (1.4 eq), 81%; (g)  $\text{SeO}_2$  (3.0 eq),  $\text{Ac}_2\text{O}$  (1.0 eq), AcOH (0.16 eq), 4 Å MS (120% mass fraction), dioxane,  $65^\circ\text{C}$ , 85%; (h)  $\text{CBr}_4$  (1.2 eq),  $\text{PPh}_3$  (1.2 eq),  $i\text{-Pr}_2\text{NEt}$  (0.4 eq), DCM,  $0^\circ\text{C}$ , 3 h, then  $\text{Pd}_2(\text{dba})_3$  (0.05 eq), PivOCs (0.5 eq),  $i\text{-Pr}_2\text{NEt}$  (0.8 eq), EtOH, under a balloon filled with CO,  $0^\circ\text{C}$  to rt, 63%; (i) PPTS (0.1 eq), acetone/ $\text{H}_2\text{O}$  (10:1),  $60^\circ\text{C}$ , 90%; (j) Pd/C (10% mass fraction), EtOAc, under balloon filled with  $\text{H}_2$ , rt, 92%; (k) Grignard reagent (3.0 eq), THF,  $-20^\circ\text{C}$ , 80%; (l) LiHMDS (2.0 eq), LiCl (2.0 eq), MoOPH (1.5 eq), THF,  $-78^\circ\text{C}$ , 91%; and (m) BnBr (2.0 eq),  $\text{Ag}_2\text{O}$  (2.0 eq), DCM, rt, 97%. LiHMDS, lithium hexamethyldisilylamide. KHMDS, potassium hexamethyldisilylamide. MoOPH, oxodiperoxymolybdenum(pyridine)(hexamethylphosphoric triamide), also referred to as Vedejs' reagent; 4 Å MS, molecular sieves, type 4A;  $\text{Pd}_2(\text{dba})_3$ , tris(dibenzylideneacetone)dipalladium(0); PivOCs, cesium pivalate; PPTS, pyridium *p*-toluenesulfonate; TESCI, triethylsilyl chloride.



**Figure 6 | Synthesis of the lactone 20.** (a) Grignard reagent (1.5 eq), THF, rt; (b) Hoveyda-Grubbs II (**17**, 0.05 eq), PhMe, 80 °C, 79% in two steps; (c)  $\text{Ac}_2\text{O}$  (2.0 eq), DMAP (0.5 eq),  $\text{Et}_3\text{N}$  (5.0 eq), DCM, rt, 97%; (d) LiHMDS (2.5 eq),  $\text{CF}_3\text{CO}_2\text{CH}_2\text{CF}_3$  (1.5 eq), THF,  $-78^\circ\text{C}$  to  $0^\circ\text{C}$ . (e)  $\text{TsN}_3$  (1.4 eq),  $\text{Et}_3\text{N}$  (3.0 eq), MeCN, rt, 93% in two steps; (f)  $\text{Cu}(\text{tbs})_2$  (0.1 eq), PhMe, 80 °C, 4.5 h, 65%. ;  $\text{Cu}(\text{tbs})_2$ , bis(*N*-tert-butylsalicylaldiminato) copper(II); DMAP, 4-dimethylaminopyridine;  $\text{TsN}_3$ , tosylazide.

Next, we treated **13** with  $\text{SeO}_2$  in the presence of  $\text{AcOH}^{25}$ ,  $\text{Ac}_2\text{O}$  and 4 Å molecular sieves for an allylic oxidation. The resulting allylic alcohol was then converted to its corresponding carboxylic ester by bromination<sup>26</sup> and Pd-catalysed carbonylation<sup>27</sup> to give an ester in 63% yield in one step. After deprotection, enone **14** was obtained in 90% yield. To synthesize bislactone **16** from enone **14**, we adopted the strategy developed in our total synthesis of schindilactone **A**<sup>5</sup>. Enone **14** was sequentially subjected to a Pd-catalysed hydrogenation (92%) and Grignard reaction (80%) to give **15** in 74% yield as a single diastereoisomer. The observed diastereoselectivity could be attributed to the steric bulk of the triethylsilyloxy group in substrate **14**, which allows both the hydrogenation and Grignard reactions to occur at the less-hindered face (see three-dimensional structure of **14** in Fig. 5)

To achieve facially selective  $\alpha$ -hydroxylation, bislactone **15** was treated with LiHMDS in the presence of  $\text{LiCl}^{28}$  at  $-78^\circ\text{C}$  in THF. The resulting enolate complex was subsequently oxidized with  $\text{MoOPH}^{29}$  to afford a secondary alcohol, which was then treated with  $\text{BnBr}/\text{Ag}_2\text{O}^{30}$  to give bislactone **16** in 88% overall yield as a single diastereoisomer. The relative stereochemistry of **16** was confirmed by X-ray crystallography (Fig. 5).

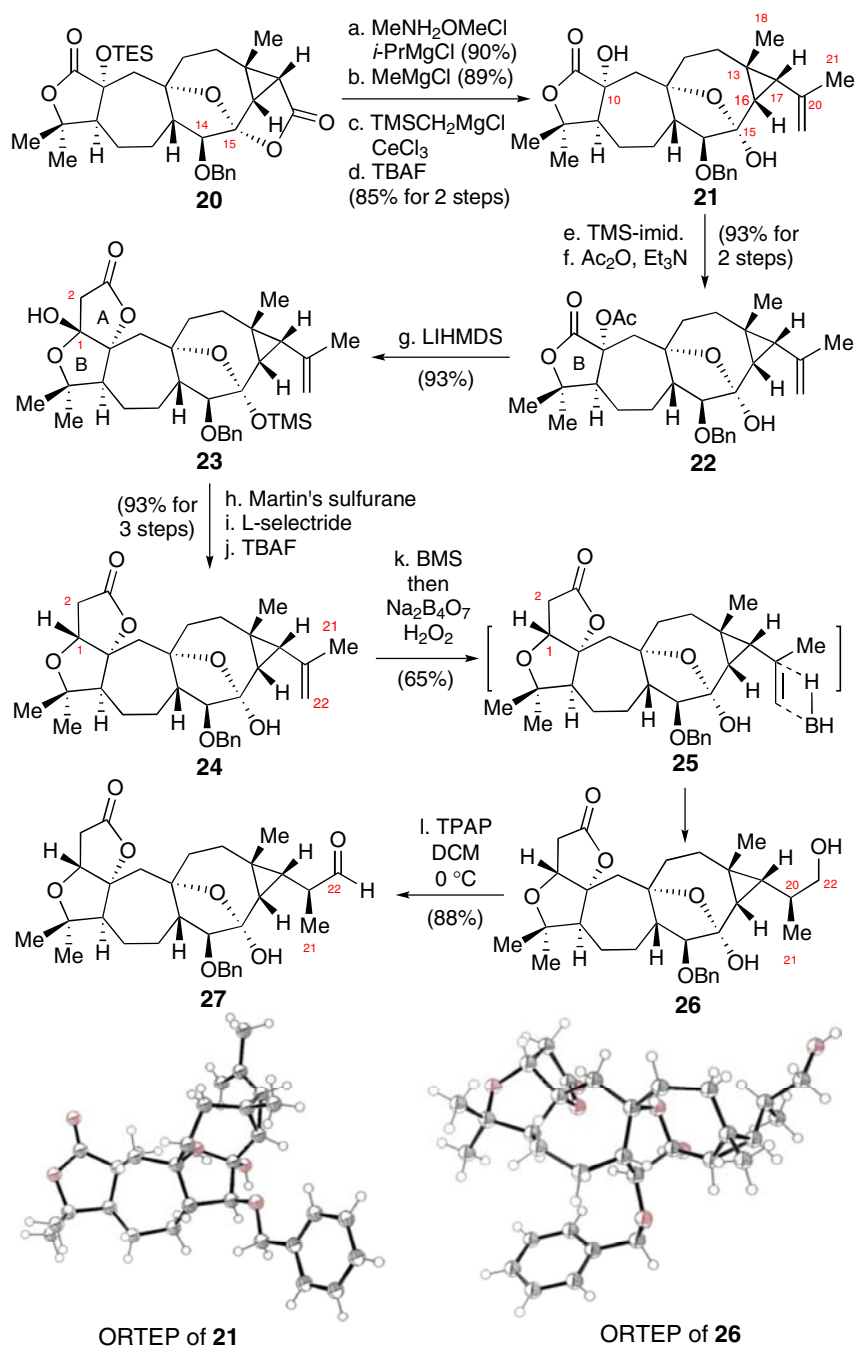
This highly stereoselective  $\alpha$ -hydroxylation was also likely promoted by the steric effect of the triethylsilyloxy group in enolate **15a**, which was generated *in situ* during the treatment of **15** with LiHMDS, forcing the oxidant to approach from the less-hindered face (see three-dimensional structure of **15a** in Fig. 5).

We then investigated our proposed RCM reaction to construct the medium-sized ring-based<sup>31</sup> tri-substituted cyclooctene in compound **18** (Fig. 6). By screening various reaction conditions (for example, catalysts, solvents, additives and reaction temperatures), we determined that the use of the second-generation Hoveyda-Grubbs catalyst (**17**) in toluene at  $80^\circ\text{C}$  afforded the best results. Considering the potential for *in situ* epimerization of hemiketal during the RCM reaction<sup>5,32</sup>, we treated bislactone **16** with vinyl magnesium bromide<sup>33</sup>. The resulting dienes, as an epimeric mixture of hemiketals, were then subjected to a RCM reaction in the presence of catalyst **17** (ref. 34; 5% amount-of-substance fraction) in toluene at  $80^\circ\text{C}$  for 18 h. To our delight,

the desired product **18** was obtained as a single diastereoisomer in an overall 79% yield for the two steps.

For stereoselective formation of the 8/3 bicyclic-ring system in **20**, an efficient method was required to prepare  $\alpha$ -diazoacetate **19** from hemiketal **18**. Initial attempts to prepare **19** by esterification coupling of **18** with  $\text{ClCOCH}=\text{NNHTs}^{35}$  in the presence of a base produced only a trace amount of the desired product. This could be attributed to steric hindrance at the C15 hydroxyl group in **18**. Consequently, we carried out a systematic study for the synthesis of **19**. We found out that **19** could be effectively generated by the treatment of **18** with  $\text{Ac}_2\text{O}/\text{Et}_3\text{N}$  in the presence of DMAP followed by reaction with LiHMDS in the presence of  $\text{CF}_3\text{CO}_2\text{CH}_2\text{CF}_3$  at  $-78^\circ\text{C}$ , and then treated with  $\text{TsN}_3$  to afford **19** in an overall 90% yield for the three steps. We next investigated the conditions for synthesis of the rigid and highly strained intermediate **20** from **19** via the proposed intramolecular cyclopropanation reaction. To date, intramolecular cyclopropanation for the formation of an 8/3 fused bicyclic ring system has not been reported. Consequently, it was unknown whether such a rigid and highly strained intermediate could be generated. We hypothesized that strategic positioning of  $\alpha$ -diazoacetate could be used to facilitate the cyclopropanation in a diastereoselective manner. To achieve this goal, we systematically profiled the cyclopropanation reaction with different metal catalysts, including  $\text{CuSO}_4$ ,  $\text{CuCl}$ , bis(2,4-pentanedionato) copper(II) ( $\text{Cu}(\text{acac})_2$ ),  $\text{CuI}$ ,  $\text{Rh}_2(\text{OAc})_4$  and  $\text{Cu}(\text{tbs})_2$ . We found that the  $\text{Cu}(\text{tbs})_2$ -catalysed cyclopropanation<sup>36</sup> of **19** afforded **20** in 65% yield as a single diastereoisomer. The structure of **20** was confirmed by two-dimensional NMR spectroscopy.

With lactone **20** in hand, we next investigated its transformation to aldehyde **27**. As illustrated in Fig. 7, the first synthetic task was the conversion of the lactone ring in **20** to the terminal olefin in **21**. Exposure of **20** to a solution of *N,O*-dimethylhydroxylamine hydrochloride and isopropylmagnesium chloride in THF at  $-20^\circ\text{C}$  (ref. 37) formed a Weinreb amide in 90% yield, which was reacted with methylmagnesium chloride to afford a ketone in 89% yield. This ketone then underwent Peterson olefination<sup>38</sup> by reaction with freshly produced (trimethylsilyl)methylmagnesium



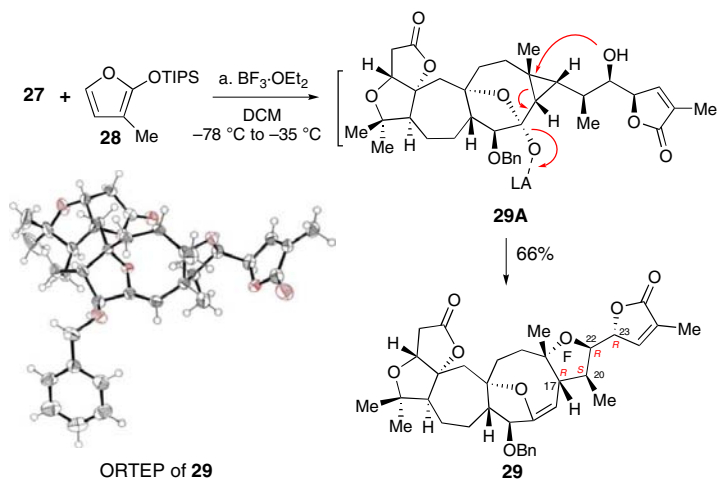
**Figure 7 | Synthesis of alcohol 27.** (a)  $\text{MeNHOMe}\cdot\text{HCl}$  (5.0 eq),  $^i\text{PrMgCl}$  (10.0 eq), THF,  $-20^\circ\text{C}$ , 90%; (b)  $\text{MeMgCl}$  (3.0 eq), THF,  $0^\circ\text{C}$ , 89%; (c)  $\text{TMSCH}_2\text{MgCl}$  (5.0 eq),  $\text{CeCl}_3$  (5.0 eq), THF,  $0^\circ\text{C}$ , then silica gel, DCM, 83%; (d) TBAF (3.0 eq), THF,  $0^\circ\text{C}$ , 99%; (e) TMS-imid. (10.0 eq), DCM,  $0^\circ\text{C}$ , 95%; (f)  $\text{Ac}_2\text{O}$  (15.0 eq), DMAP (1.0 eq),  $\text{Et}_3\text{N}$  (15.0 eq), PhMe, rt, 98%; (g) LiHMDS (3.0 eq), THF,  $-78$  to  $-35^\circ\text{C}$ , 93% b.r.s.m.; (h) Martin's sulfurane (1.2 eq), DCM, rt; (i) L-selectride (3.0 eq),  $-78^\circ\text{C}$ ; (j) TBAF (5.0 eq), THF,  $0^\circ\text{C}$ , 93% in three steps; (k) BMS (10.0 eq), THF,  $0^\circ\text{C}$ , 0.75 h, then  $\text{Na}_2\text{B}_4\text{O}_7$  (excess),  $\text{H}_2\text{O}_2$  (excess), rt, 65%; (l) TPAP (1.3 eq), DCM,  $0^\circ\text{C}$ , 88%. BMS, borane-dimethylsulfide complex; b.r.s.m., based on recovered starting material; L-selectride, lithium tri-*sec*-butylborohydride; Martin's sulfurane, bis[ $\alpha,\alpha$ -bis(trifluoromethyl) benzenemethanolato]-diphenylsulfur; TBAF, tetra-*n*-butylammonium fluoride; TMS-imid., 1-(trimethylsilyl)-1*H*-imidazole; TPAP, tetra-*n*-propylammonium perruthenate(VII).

chloride in the presence of  $\text{CeCl}_3$  (ref. 39) in THF at  $0^\circ\text{C}$ , and the resultant mixture was worked up by the treatment with silica gel to give an olefin, which, without purification, was then subjected to a desilylation with TBAF to give 21 in 82% yield for the two steps. The structure of 21 was confirmed by X-ray crystallography.

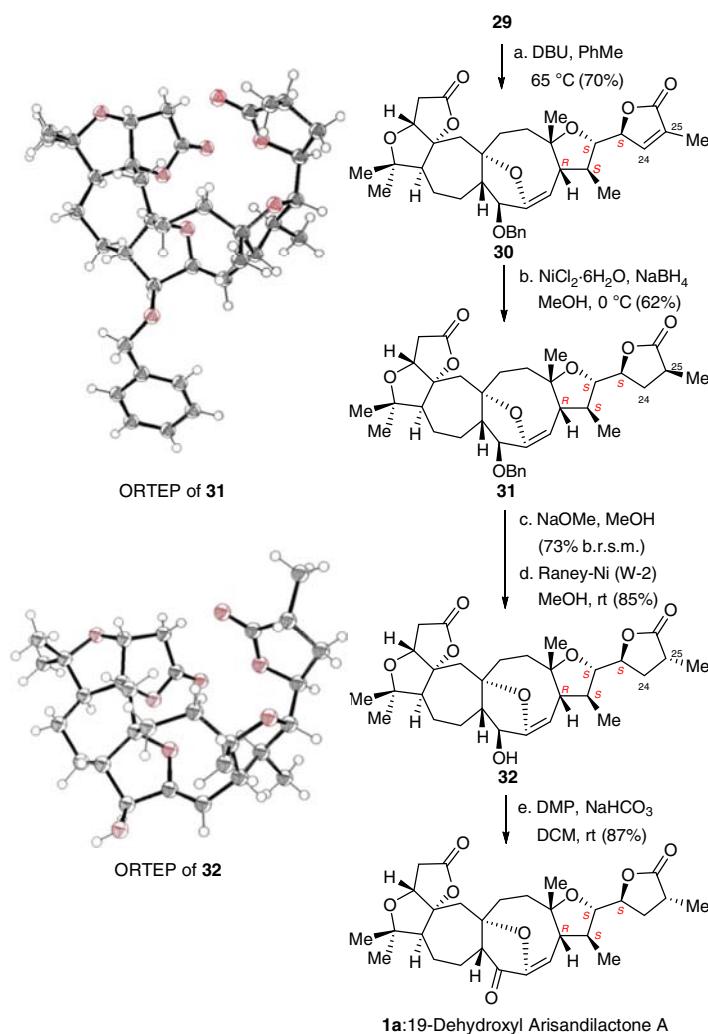
It is worthwhile to mention that when the ketone derived from the Weinreb amide was directly reacted with a Wittig reagent

derived from methyltriphenylphosphonium bromide, the expected olefination proceeded. However, epimerization occurred at C17 of the product 21.

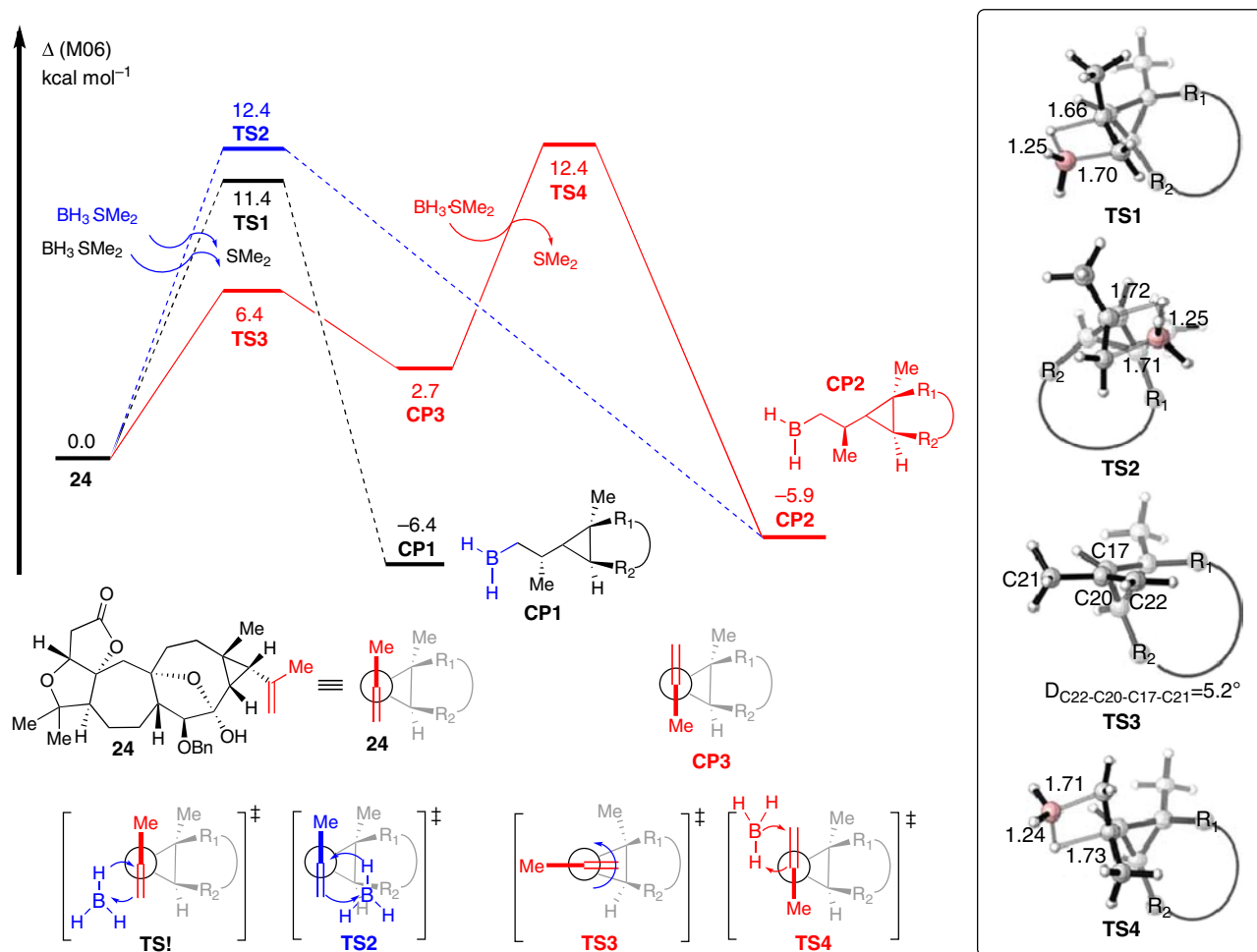
The next task in the synthesis of aldehyde 27 was A ring formation in intermediate 24. Diol 21 was selectively protected by sequential treatment with TMS-imid. and  $\text{Ac}_2\text{O}$ /DMAP, to give 22 in an overall 93% yield for the two steps. Dieckmann-type condensation<sup>4</sup> of 22 proceeded smoothly to afford product 23



**Figure 8 | Total synthesis of 29.** (a) **28** (3.0 eq),  $\text{BF}_3 \cdot \text{OEt}_2$  (3.3 eq), DCM,  $-78$  to  $-35^\circ\text{C}$ , 66%.



**Figure 9 | Total synthesis of 19-dehydroxyl-arisandilactone A (1a).** (a) DBU (15.0 eq), PhMe,  $65^\circ\text{C}$ , 70%; (b)  $\text{NiCl}_2 \cdot 6\text{H}_2\text{O}$  (1.0 eq),  $\text{NaBH}_4$  (3.0 eq), MeOH,  $0^\circ\text{C}$ , 62%; (c) 5% NaOMe/MeOH, rt, 73% (b.r.s.m.); (d) W-2 Raney Ni, EtOH, rt, 85%; (e) DMP (2.0 eq),  $\text{NaHCO}_3$  (5.0 eq), DCM, rt, 87%. b.r.s.m., based on recovered starting material; DMP, Dess-Martin periodinane.



**Figure 10 | Energy profiles for the hydroboration of 24.** The values given by kcal mol<sup>-1</sup> are the relative free energies calculated by M06 method in tetrahydrofuran solvent.

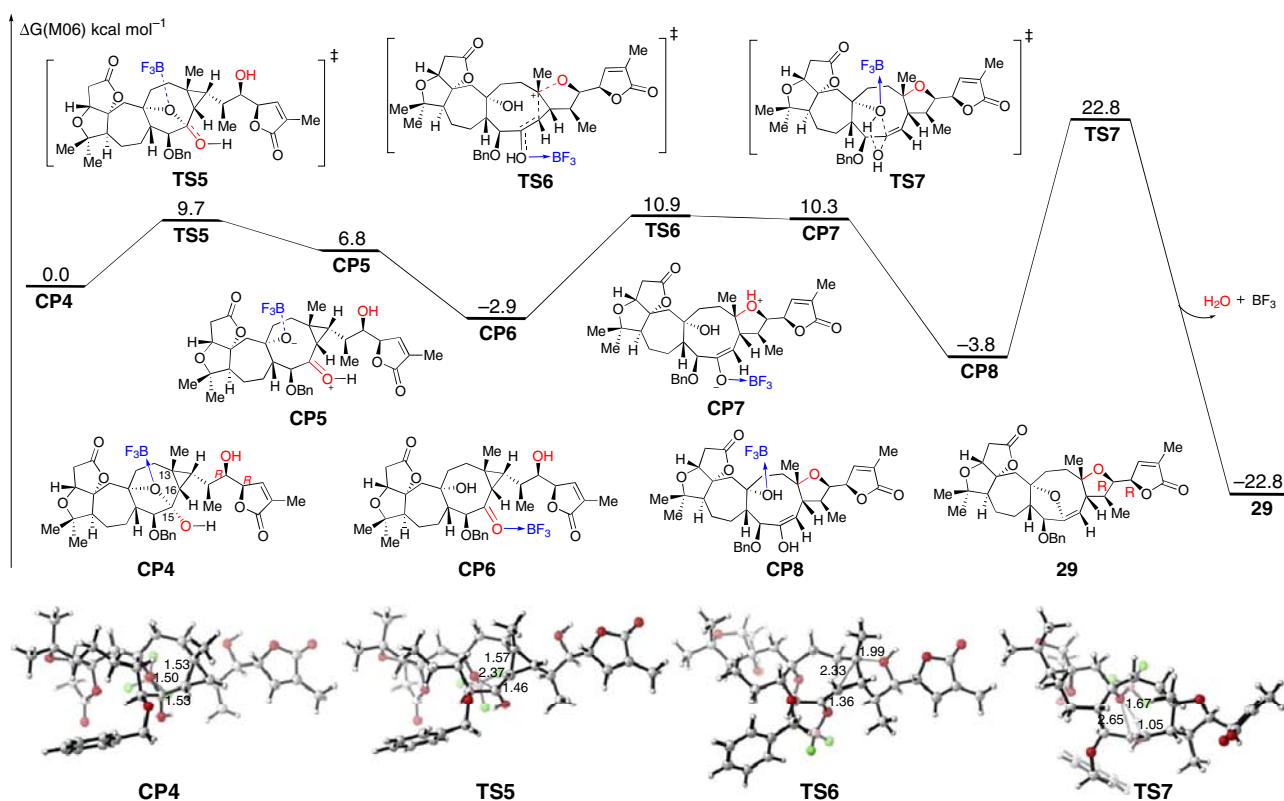
in 93% yield. Dehydration of the C1 hydroxyl group in **23** was achieved by treatment with Martin's sulfuran<sup>40</sup>, and the resultant  $\alpha,\beta$ -unsaturated lactone was reduced with *L*-selectride<sup>41</sup>, followed by desilylation to give **24** as a single diastereoisomer in 93% yield for three steps.

The synthesis of alcohol **26** proved challenging because **24** contained a lactone and a highly rigid three-membered ring-linked olefin<sup>42</sup>. These groups are sensitive to both hydroboration and basic conditions. Thus, after intensive experimentation, we found that treatment of **24** with BMS<sup>43</sup> in THF at 0 °C, followed by oxidation with a solution of H<sub>2</sub>O<sub>2</sub> (30%) in the presence of a weak base (Na<sub>2</sub>B<sub>4</sub>O<sub>7</sub>; ref. 44), product **26** could be obtained in 65% yield, together with its diastereoisomer (16% yield). The stereochemistry at C20 in **26** was confirmed by X-ray crystallography. Thus, synthesis of aldehyde **27** could be achieved in 88% yield by oxidation of substrate **26** with TPAP.

With synthesis of aldehyde **27** achieved, we attempted the proposed biomimetic synthesis of 19-dehydroxyl arisandilactone A (**1a**) (Fig. 8). In the event, **27** was coupled with **28** in the presence of BF<sub>3</sub>·Et<sub>2</sub>O in CH<sub>2</sub>Cl<sub>2</sub> at -78 °C, and the resultant mixture was then stirred at -35 °C for 1 h, followed by workup to give product **29** in 66% yield as a single diastereoisomer. The reaction actually proceeded through a typical VMAR followed by the proposed homo-Michael reaction. The structure of **29** was confirmed by X-ray crystallography, which indicated that the stereogenic centers at C22 and C23 were opposite to those in the natural product.

We now move to the stage for the completion of the total synthesis. To this end, substrate **29** was treated with DBU in toluene at 65 °C, as a result, product **30** was obtained in 70% yield with inversion of the stereogenic centres at C22 and C23 (Fig. 9). Thus, further treatment of **30** with NiCl<sub>2</sub>·6H<sub>2</sub>O/NaBH<sub>4</sub>, the double bonds at C24 and C25 in **30** could be chemo-selectively saturated to give product **31** in 62% yield. However, X-ray crystallographic analysis of **31** indicated that its stereochemistry at C25 was opposite to that in the natural form. We, therefore, treated **31** with NaOMe in methanol to invert its stereochemistry at C25, and the resultant product was then subjected to Raney nickel-mediated debenzoylation to give product **32** in 73% yield and 85% yield, respectively. The structure of **32** was confirmed by X-ray crystallography. Thus, our total synthesis of 19-dehydroxyl arisandilactone A (**1a**) was eventually achieved in 87% yield by oxidation of **32** with DMP. Overall, this asymmetric synthesis consists of 37 steps in its longest linear sequence from (*R*)-(-)-carvone.

**Computational study.** DFT calculations were carried out using the Gaussian 09 program (Gaussian Inc., Wallingford, CT, USA) to determine the diastereoselectivity for the hydroboration step to stereoselectively form **26** from **24** (see Fig. 10). The method B3LYP with 6-31G(d) basis set was used for geometry optimizations in gas phase. M06 functional with larger basis set 6-311+G(d) was used for solvation single point calculations



**Figure 11 | Energy profiles for the homo-Michael step.** The values given by kcal mol<sup>-1</sup> are the relative free energies calculated by M06 method in dichloromethane solvent.

in THF based on gas-phase stationary points using the continuum solvation model SMD (see Supplementary Methods for details).

As shown in Fig. 10, olefin **24** was set to relative zero for the free energy profiles. Initially, the Cossy model<sup>43</sup> was considered to explain the diastereoselectivity. We found that the relative free energy of **TS1** was 1.0 kcal mol<sup>-1</sup> lower than that of **TS2**, which could be attributed to the repulsion between the borane moiety and the substituents on cyclopropane in the transition state **TS2**. The diastereoisomer **CP1**, which is the precursor of alcohol **26**, is the major product generated via transition state **TS1**. This result is consistent with experimental observations. Moreover, we also found that rotation of an alkenyl could take place via transition state **TS3** with a barrier of only 6.4 kcal mol<sup>-1</sup>. The relative free energy of the rotational isomer **CP3** was 2.7 kcal mol<sup>-1</sup> higher than that of compound **24**. This was attributed to the larger size of R<sub>2</sub> compared with R<sub>1</sub>, and the closer positioning of R<sub>2</sub> to the methyl group in **CP3**. However, when hydroboration takes place from **CP3** via transition state **TS4**, the hybridization of C22 changes from sp<sup>2</sup> to sp<sup>3</sup>, and the size difference between the methyl and methylene groups is reduced. Therefore, the relative free energy of **TS4** was only 1.0 kcal mol<sup>-1</sup> higher than that of **TS1**. The DFT calculations indicated that favourable pathway for the generation of major intermediate **CP1** takes place via the same transition state **TS1** in both the Cossy model and our proposed reaction model. However, there are two different pathways for the generation of side intermediate **CP2** including the Cossy model via transition state **TS2** and our proposed model via transition state **TS4**, the barriers for which are closed.

We applied the same method to study the mechanism of the homo-Michael reaction. As shown in Fig. 11, complex **CP4**, which is formed by reaction between aldehyde **27** and silyl ether

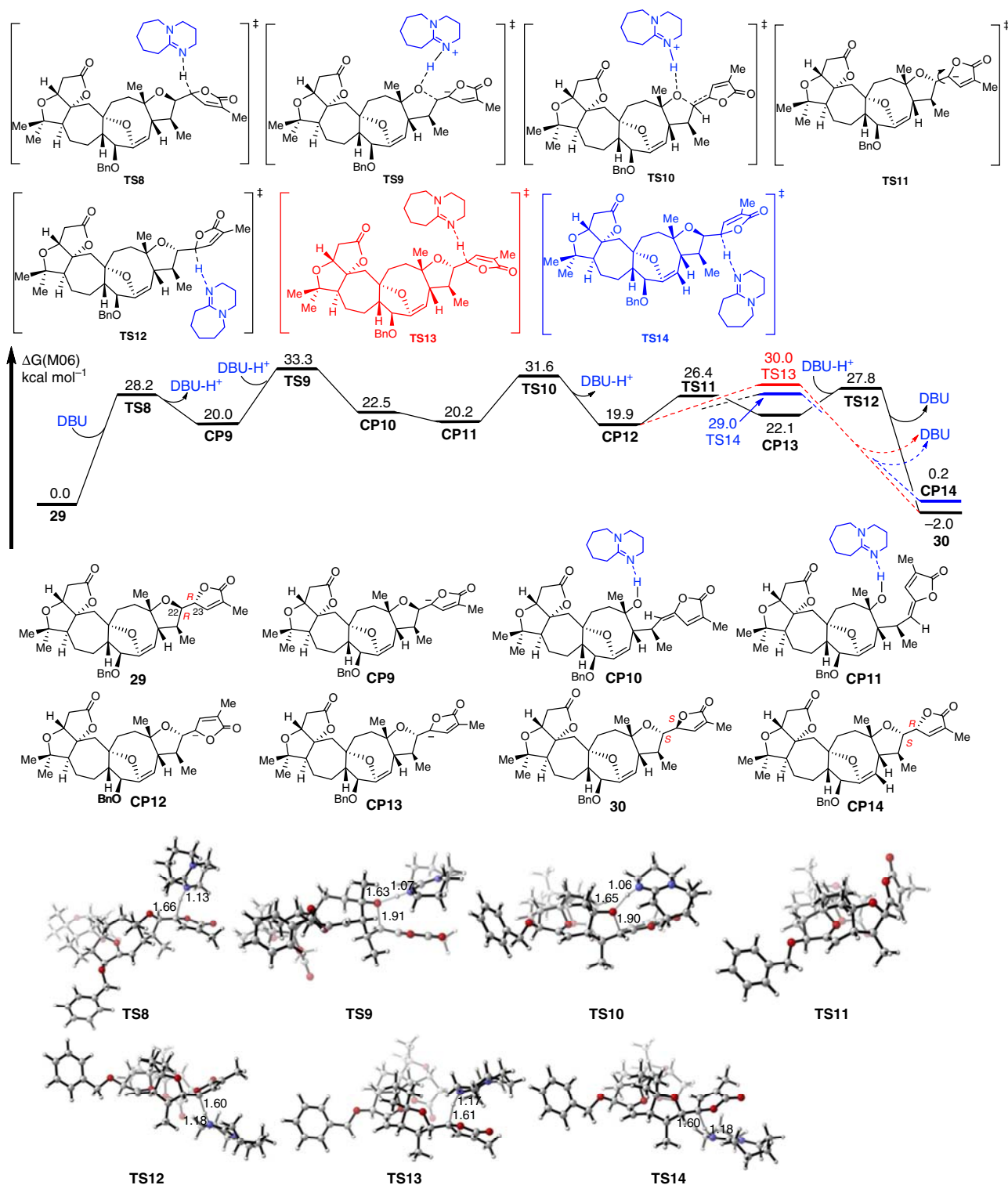
**28** with the coordination of BF<sub>3</sub> is set to the relative zero for the free-energy profiles of this reaction. With the activation of BF<sub>3</sub>, the C–O bond cleavage forms a protonated ketone intermediate **CP5** via transition state **TS5** with a barrier of only 9.7 kcal mol<sup>-1</sup>. The subsequent isomerization generates intermediate **CP6** with 9.7 kcal mol<sup>-1</sup> exothermic. With the activation of BF<sub>3</sub>·Et<sub>2</sub>O, C13 and C16 is more electron-deficient. Therefore, the nucleophilic addition with hydroxyl takes place via transition state **TS6** with a barrier of 13.8 kcal mol<sup>-1</sup>. After a proton transfer, an enol intermediate **CP8** is formed. The followed cyclization occurs via transition state **TS7** with a barrier of 26.6 kcal mol<sup>-1</sup>. After releasing of one molecule water coordinated BF<sub>3</sub>, product **29** is formed exothermically.

Finally, we used the same method to study the mechanism of the isomerization of **29** to **30**. As shown in Fig. 12, the intermolecular electrophilic deprotonation by DBU of substrate **29**, which gives intermediate **CP9** endothermically, occurs via transition state **TS8** with a barrier of 28.2 kcal mol<sup>-1</sup>. Subsequently, the retro-Michael addition takes place via transition state **TS9** to break the C–O bond, with the help of DBU-H<sup>+</sup> to stabilize the formed ionic oxygen atom, to generate intermediate **CP10** reversibly with a barrier of 13.3 kcal mol<sup>-1</sup>.

In **CP10** rotation of the C22–C20 single bond affords **CP11** in a 2.3 kcal mol<sup>-1</sup> exothermic step. The Michael addition takes place at the *Si*-face of the alkene moiety in **CP11** via transition state **TS10**, with a barrier of 11.4 kcal mol<sup>-1</sup>, and generates intermediate **CP12** reversibly. The direct protonation of **CP12** by DBU-H<sup>+</sup> could occur via transition state **TS13** or **TS14**.

However, **30** was not the major product because the relative free energy of **TS14**, which leads to the formation of **CP14** was 1.0 kcal mol<sup>-1</sup> lower than that of **TS13** which leads to **30**. Alternatively, we found that a single C–C bond in **CP12** could rotate rapidly via transition state **TS11**, and isomer **CP13** could





**Figure 12 | Energy profiles for the reversible retro-oxa-Michael reaction of 29.** The values given in kcal mol<sup>-1</sup> are the relative free energies calculated by the M06 method in tetrahydrofuran solvent.

be formed reversibly. The protonation of CP13 via transition state TS12 could also afford product 30, and the relative free energy of TS12 was 1.2 kcal mol<sup>-1</sup> lower than that of TS14. Moreover, the relative free energy of 30 was 2.2 kcal mol<sup>-1</sup> lower than that of CP14, and 2.0 kcal mol<sup>-1</sup> lower than that of 29. Therefore, 30 was also a thermodynamically stable product, which was observed experimentally.

## Discussion

In conclusion, we successfully developed an asymmetric total synthesis of (+)-19-dehydroxyl arisandilactone A (1a). Construction of an oxa-bridged and moderately sized DE ring involved an unprecedented tandem VMAR and oxa-homo-Michael type reaction. Stereoselective formation of stereogenic centres at C22 and C23 of 1a were achieved by a tandem and

biomimetic retro-Michael/Michael reaction. Key steps in this total synthesis also included a RCM reaction for the diastereoselective formation of the fully functionalized eight-membered DE ring system, and an interesting Cu-catalysed intramolecular cyclopropanation that resulted in stereoselective formation of the central 8/3 *cis*-fused bicyclic ring system. The structure of 19-dehydroxyl (+)-arisandilactone A (**1a**) was confirmed by X-ray crystallography of its precursor alcohol **32**. Details of the reactions for the hydroboration, homo-Michael, and tandem retro-Michael/Michael reactions were determined by DFT calculations. The biological investigation of the synthesized (+)-19-dehydroxyl arisandilactone A (**1a**), as well as the advanced intermediates in this total synthesis is currently underway in our laboratory.

## Methods

**General.** All reactions were carried out under a nitrogen atmosphere under anhydrous conditions and all reagents were purchased from commercial suppliers without further purification. Solvent purification was conducted according to *Purification of Laboratory Chemicals* (Peerrin, D. D.; Armarego, W. L. and Perrins, D. R., Pergamon Press: Oxford, 1980). Yields refer to chromatographically and spectroscopically (<sup>1</sup>H NMR) homogeneous materials. Reactions were monitored by Thin Layer Chromatography on plates (GF254) supplied by Yantai Chemicals (China) visualized by ultraviolet or stained with ethanolic solution of phosphomolybdic acid and cerium sulfate, basic solution of KMnO<sub>4</sub> and iodine vapour. If not specially mentioned, flash column chromatography was performed using E. Merck silica gel (60, particle size 0.040–0.063 mm). NMR spectra were recorded on Bruker AV400, Bruker AV500 instruments and calibrated by using residual undeuterated chloroform ( $\delta$ H = 7.26 p.p.m.) and CDCl<sub>3</sub> ( $\delta$ C = 77.16 p.p.m.), partially deuterated methylene chloride ( $\delta$ H = 5.32 p.p.m.) and methylene chloride-*d*2 ( $\delta$ C = 53.84 p.p.m.), partially-deuterated methanol ( $\delta$ H = 3.31 ppm) and methanol-*d*4 ( $\delta$ C = 49.00 p.p.m.) as internal references. The following abbreviations were used to explain the multiplicities: s = singlet, d = doublet, t = triplet, q = quartet, br = broad, td = triple doublet, dt = double triplet, dq = double quartet, m = multiplet. Infrared (IR) spectra were recorded on a Thermo Nicolet Avatar 330 FT-IR spectrometer. High-resolution mass spectra were recorded on a Bruker Apex IV FTMS mass spectrometer using ESI (electrospray ionization) as ionization method.

For detailed experimental procedures, see Supplementary Methods. For NMR spectra of the synthesized compounds in this article, see Supplementary Figs 1–34. For the comparison of NMR spectra of the natural arisandilactone A and synthetic 19-dehydroxyl arisandilactone A, see Supplementary Table 1. For ORTEP diagrams for compounds **10**, **16**, **21**, **26**, **29**, **31** and **32**, see Supplementary Figs 35–41. For computational calculation details, see Supplementary Methods and Supplementary Data 1. For calculation results using other methods, see Supplementary Figs 42–44.

**Data availability.** The X-ray crystallographic coordinates for structures reported in this article have been deposited at the Cambridge Crystallographic Data Centre (CCDC), under deposition numbers CCDC 1509144 for compound **10**, CCDC 1508989 for compound **16**, CCDC 1509314 for compound **21**, CCDC 1509138 for compound **26**, CCDC 1507976 for compound **29**, CCDC 1507977 for compound **31**, and CCDC 1507978 for compound **32**. These data can be obtained free of charge from the Cambridge Crystallographic Data Centre via [http://www.ccdc.cam.ac.uk/data\\_request/cif](http://www.ccdc.cam.ac.uk/data_request/cif).

## References

- Xiao, W. L., Li, R. T., Huang, S. X., Pu, J. X. & Sun, H. D. Triterpenoids from the *Schisandraceae* family. *Nat. Prod. Rep.* **25**, 871–891 (2008).
- Shi, Y. M., Xiao, W. L., Pu, J. X. & Sun, H. D. Triterpenoids from the *Schisandraceae* family: an update. *Nat. Prod. Rep.* **32**, 367–410 (2015).
- Bartoli, A., Chouraqui, G. & Parrain, J. L. Collective domino approach toward the core of molecules isolated from the Genus *Schisandra*. *Org. Lett.* **14**, 122–125 (2012).
- Xiao, W. L. Diastereoselective total synthesis of ( $\pm$ )-Schindilactone A. *Angew. Chem. Int. Ed.* **50**, 7373–7377 (2011).
- Li, J., Yang, P., Yao, M., Deng, J. & Li, A. Total synthesis of Rubrifloridilactone A. *J. Am. Chem. Soc.* **136**, 16477–16480 (2014).
- Goh, S. S. *et al.* Total synthesis of (+)-Rubrifloridilactone A. *Angew. Chem. Int. Ed.* **54**, 12618–12621 (2015).
- Wang, L., Wang, H.-T., Li, Y.-H. & Tang, P.-P. Total synthesis of Schilancitrilactones B and C. *Angew. Chem. Int. Ed.* **54**, 5732–5735 (2015).
- You, L. *et al.* Asymmetric total synthesis of Propindilactone G. *J. Am. Chem. Soc.* **137**, 10120–10123 (2015).
- Cheng, Y. B. *et al.* Arisandilactone A, a new triterpenoid from the fruits of *Schisandra arisanensis*. *Org. Lett.* **12**, 1016–1019 (2010).
- Cheng, Y. B. *et al.* Nortriterpene lactones from the fruits of *Schisandra arisanensis*. *J. Nat. Prod.* **73**, 1228–1233 (2010).
- Nicolaou, K. C., Vourloumis, D., Winssinger, N. & Baran, P. S. The art and science of total synthesis at the dawn of the twenty-first century. *Angew. Chem. Int. Ed.* **39**, 44–122 (2000).
- Breslow, R. Biomimetic chemistry: biology as an inspiration. *J. Biol. Chem.* **284**, 1337–1342 (2009).
- Marchetti, R. & Levine, M. Biomimetic catalysis. *ACS Catal.* **1**, 1090–1118 (2011).
- Reissig, H.-U. & Zimmer, R. Donor-acceptor-substituted cyclopropane derivatives and their application in organic synthesis. *Chem. Rev.* **103**, 1151–1196 (2003).
- Carson, C. A. & Kerr, M. A. Heterocycles from cyclopropanes: applications in natural product synthesis. *Chem. Soc. Rev.* **38**, 3051–3060 (2009).
- Hoffman, R. W. Stereoselective syntheses of building blocks with three consecutive stereogenic centers: important precursors of polyketide natural products. *Angew. Chem. Int. Ed. Engl.* **26**, 489–594 (1987).
- Hoffmann, R. W., Dahmann, G. & Andersen, M. W. Stereoselective synthesis of alcohols. XLV: recent developments in the generation of the stereotriad 'D'. *Synthesis* **1994**, 629–638 (1994).
- Sastrarajji, K. *et al.* Structural revision of stemoburkilline from an *E*-alkene to a *Z*-alkene. *J. Nat. Prod.* **72**, 316–318 (2009).
- Corey, E. J. & Myers, A. G. Efficient synthesis and intramolecular cyclopropanation of unsaturated diazoacetic esters. *Tetrahedron Lett.* **25**, 3559–3562 (1984).
- Mander, L. N. & Sethi, S. P. Regioselective synthesis of  $\beta$ -ketoesters from lithium enolates and methyl cyanofornate. *Tetrahedron Lett.* **24**, 5425–5428 (1983).
- Xue, S., Liu, Y.-K., Li, L.-Z. & Guo, Q.-X. Zinc-mediated ring-expansion and chain-extension reactions of  $\beta$ -keto esters. *J. Org. Chem.* **70**, 8245–8247 (2005).
- Yang, C.-G., Reich, N. W., Shi, Z. & He, C. Intramolecular additions of alcohols and carboxylic acids to inert olefins catalyzed by silver(I) triflate. *Org. Lett.* **7**, 4553–4556 (2005).
- Hwu, J. R. & Wetzel, J. M. The trimethylsilyl cationic species as a bulky proton. Application to chemoselective dioxolanation. *J. Org. Chem.* **50**, 3946–3948 (1985).
- Gardner, J. N., Carlon, F. E. & Gnoj, O. One-step procedure for the preparation of tertiary  $\alpha$ -ketols from the corresponding ketones. *J. Org. Chem.* **33**, 3294–3299 (1968).
- Näf, R., Velluz, A., Decorzant, R. & Näf, F. Structure and synthesis of two novel ionone-type compounds identified in quince brandy (*Cydonia oblonga* Mil.). *Tetrahedron Lett.* **32**, 753–756 (1991).
- Appel, R. Tertiary phosphane/tetrachloromethane, a versatile reagent for chlorination, dehydration, and P-N Linkage. *Angew. Chem. Int. Ed.* **14**, 801–811 (1975).
- Milstein, D. Mild, low-pressure carbonylation of ( $\pi$ -allyl)palladium complexes. *Organometallics* **1**, 888–890 (1982).
- Adam, W. & Prechtel, F. Highly efficient hydroxylation of carbonyl compounds with dimethyldioxirane. *Chem. Ber.* **124**, 2369–2375 (1991).
- Vedejs, E., Engler, D. A. & Telschow, J. E. Transition-metal peroxide reactions. Synthesis of  $\alpha$ -hydroxycarbonyl compounds from enolates. *J. Org. Chem.* **43**, 188–196 (1978).
- Van Hijfte, L. & Little, R. D. Intramolecular 1,3-diyl trapping reactions. A formal total synthesis of ( $\pm$ )-coriolin. *J. Org. Chem.* **50**, 3940–3942 (1985).
- Maier, M. E. Synthesis of medium-sized rings by the ring-closing metathesis reaction. *Angew. Chem. Int. Ed.* **39**, 2073–2077 (2000).
- Scholl, M. & Grubbs, R. H. Total synthesis of (–) and ( $\pm$ )-frontalin via ring-closing metathesis. *Tetrahedron Lett.* **40**, 1425–1428 (1999).
- Figuerola, R., Hsung, R. P. & Guevarra, C. C. An enantioselective total synthesis of (+)-aigialospirol. *Org. Lett.* **9**, 4857–4857 (2007).
- Garber, S. B., Kingsbury, J. S., Gray, B. L. & Hoveyda, A. H. Efficient and recyclable monomeric and dendritic Ru-based metathesis catalysts. *J. Am. Chem. Soc.* **122**, 8168–8179 (2000).
- Danheiser, R. L., Miller, R. F., Brisbois, R. G. & Park, S. Z. An improved method for the synthesis of  $\alpha$ -diazo ketones. *J. Org. Chem.* **55**, 1959–1964 (1990).
- Yu, M., Lynch, V. & Pagenkopf, B. L. Intramolecular cyclopropanation of glycals: studies toward the synthesis of canadensolide, sporothriolide, and xylobovide. *Org. Lett.* **3**, 2563–2567 (2001).
- Williams, J. M. *et al.* A new general method for preparation of *N*-methoxy-*N*-methylamides. Application in direct conversion of an ester to a ketone. *Tetrahedron Lett.* **36**, 5461–5464 (1995).
- Peterson, D. J. Carbonyl olefination reaction using silyl-substituted organometallic compounds. *J. Org. Chem.* **33**, 780–784 (1968).
- Li, W.-D. Z. & Yang, J.-H. A novel synthesis of functionalized allylsilanes. *Org. Lett.* **6**, 1849–1852 (2004).
- Martin, J. C. & Arhart, R. J. Sulfuranes. III. Reagent for the dehydration of alcohols. *J. Am. Chem. Soc.* **93**, 4327–4329 (1971).
- Ganem, B. & Fortunato, J. M. Unique methodology for the conjugate reduction and reductive alkylation of  $\alpha,\beta$ -unsaturated carboxylic esters. *J. Org. Chem.* **40**, 2846–2848 (1975).

42. Goodman, A. L. & Eastman, R. H. Conjugation effects in phenylcyclopropanes. *J. Am. Chem. Soc.* **86**, 908–911 (1964).
43. Cossy, J., Balnchard, N., Hamel, C. & Meyer, C. Diastereoselective hydroboration of isopropenylcyclopropanes. *J. Org. Chem.* **64**, 2608–2609 (1999).
44. Brown, H. C. & Rangaishenvi, M. V. Organoboranes: LI. Convenient procedures for the recovery of pinanediol in asymmetric synthesis via one-carbon homologation of boronic esters. *J. Organomet. Chem.* **358**, 15–30 (1988).

### Acknowledgements

This work is supported by the National Science Foundation of China (Natural Science Foundation of China (Grant No. 21272015, 21372016, 21472006, 21572009 and 21372266). J.-H. C. and Z. Y. are very grateful to Prof Jian Hao from Beijing University of Chemical Technology, and Prof Fuling Yin from Peking University Health Science Center for rescuing help on XRD analysis. Prof Wenxiang Zhang and Prof Nengdong Wang from Peking University also supported the research by primary XRD analysis.

### Author contributions

Y.-X.H. and Y.-L.J. contributed equally to this work. Y.-X.H., Y.-L.J., Y.Li, J.-H.C. and Z.Y. conceived the project and analysed the experimental results. Y.-X.H., Y.-L.J., Y.Li, H.-X.Y., B.-Q.T. and Z.N. performed the synthesis and characterization. S.L. and Y.Lan performed the theoretical calculations. Y.Lan and Z.Y. composed the manuscript with input from all the authors.

### Additional information

**Supplementary Information** accompanies this paper at <http://www.nature.com/naturecommunications>

**Competing financial interests:** The authors declare no competing financial interests.

**Reprints and permission** information is available online at <http://npg.nature.com/reprintsandpermissions/>

**How to cite this article:** Han, Y.-X. *et al.* Biomimetically inspired asymmetric total synthesis of (+)-19-dehydroxyl arisandilactone *A. Nat. Commun.* **8**, 14233 doi: 10.1038/ncomms14233 (2017).

**Publisher's note:** Springer Nature remains neutral with regard to jurisdictional claims in published maps and institutional affiliations.



This work is licensed under a Creative Commons Attribution 4.0 International License. The images or other third party material in this article are included in the article's Creative Commons license, unless indicated otherwise in the credit line; if the material is not included under the Creative Commons license, users will need to obtain permission from the license holder to reproduce the material. To view a copy of this license, visit <http://creativecommons.org/licenses/by/4.0/>

© The Author(s) 2017

ARTICLE

Received 1 Oct 2015 | Accepted 25 Feb 2016 | Published 6 Apr 2016

DOI: 10.1038/ncomms11188

OPEN

# Catalytic N-radical cascade reaction of hydrazones by oxidative deprotonation electron transfer and TEMPO mediation

Xiao-Qiang Hu<sup>1</sup>, Xiaotian Qi<sup>2</sup>, Jia-Rong Chen<sup>1</sup>, Quan-Qing Zhao<sup>1</sup>, Qiang Wei<sup>1</sup>, Yu Lan<sup>2</sup> & Wen-Jing Xiao<sup>1</sup>

Compared with the popularity of various C-centred radicals, the N-centred radicals remain largely unexplored in catalytic radical cascade reactions because of a lack of convenient methods for their generation. Known methods for their generation typically require the use of N-functionalized precursors or various toxic, potentially explosive or unstable radical initiators. Recently, visible-light photocatalysis has emerged as an attractive tool for the catalytic formation of N-centred radicals, but the pre-incorporation of a photolabile groups at the nitrogen atom largely limited the reaction scope. Here, we present a visible-light photocatalytic oxidative deprotonation electron transfer/2,2,6,6-tetramethylpiperidine-1-oxyl (TEMPO)-mediation strategy for catalytic N-radical cascade reaction of unsaturated hydrazones. This mild protocol provides a broadly applicable synthesis of 1,6-dihydropyridazines with complete regioselectivity and good yields. The 1,6-dihydropyridazines can be easily transformed into diazinium salts that showed promising *in vitro* antifungal activities against fungal pathogens. DFT calculations are conducted to explain the mechanism.

<sup>1</sup>CCNU-uOttawa Joint Research Centre, Key Laboratory of Pesticide and Chemical Biology, Ministry of Education, College of Chemistry, Central China Normal University, 152 Luoyu Road, Wuhan 430079, China. <sup>2</sup>School of Chemistry and Chemical Engineering, Chongqing University, Chongqing 400030, China. Correspondence and requests for materials should be addressed to J.-R.C. (email: chenjiarong@mail.ccnu.edu.cn).

Synthetic chemists continuously strive for fast, selective and high yielding reactions under mild conditions. Radical reactions, especially the radical cascades, provide a potential access to such ideal transformations and have attracted considerable attention of synthetic community because of their typically mild conditions, short reaction times and high efficiency<sup>1,2</sup>. Although various carbon radicals have been widely used in catalytic radical-based cascade reactions<sup>3–5</sup>, however, the chemistry of N-centred radicals in this regard remains largely unexplored because of a lack of convenient and general methods for their generation<sup>6,7</sup>. Known methods for their generation typically require the use of N-functionalized precursors or various toxic, potentially explosive or unstable radical initiators. Pioneered by Nicolaou's discovery of the *o*-iodoxybenzoic acid-mediated conversion of *N*-aryl amides and carbamates into the corresponding nitrogen radicals<sup>8</sup>, the groups of Chiba<sup>9</sup> and Lei<sup>10</sup>, respectively, developed two efficient methods for the generation of 1,3-diazaallyl and amidyl radicals by Cu- and Ni-catalyzed oxidative cleavage of N–H bonds of amidines and *N*-alkoxyamides using O<sub>2</sub> and di-tertiary butyl peroxide as terminal oxidants at high temperatures. Recently, Li<sup>11</sup> and Chemler<sup>12</sup> also independently reported the Cu- and Ag-catalyzed oxidative formation of amidyl radicals in the presence of stoichiometric MnO<sub>2</sub> and Selectfluor reagents as oxidants. Despite these impressive advancements, the search for new efficient protocols for direct catalytic conversion of the N–H bonds into the corresponding N-centred radicals under mild conditions has become an increasingly significant, yet challenging priority in the development of new N-radical cascade reactions.

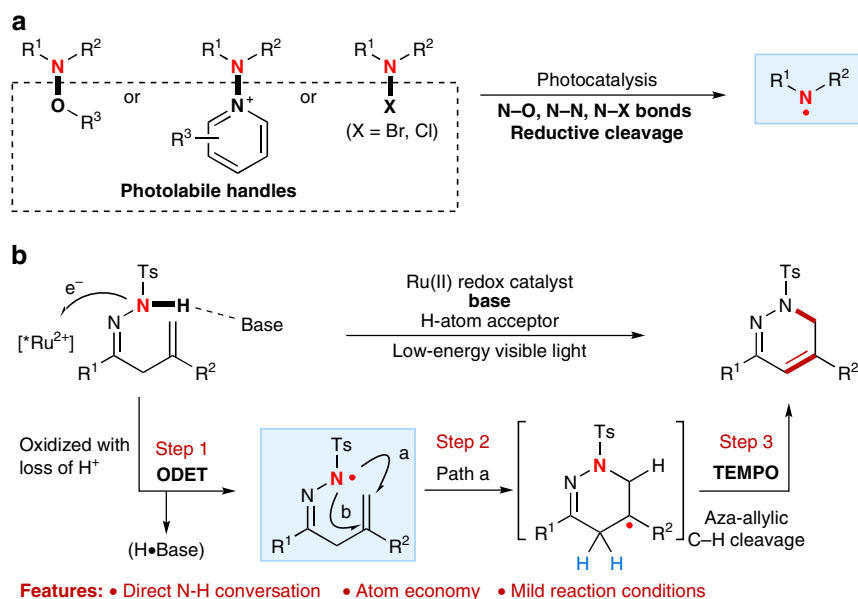
In recent years, the visible-light photocatalysis has been established as a powerful technique that facilitates selectively activating organic molecules and chemical bonds to identify new chemical reactions under mild conditions<sup>13–16</sup>. As the notable early studies by MacMillan<sup>17</sup> and Sanford<sup>18</sup> on neutral N-centred radical-mediated photocatalytic C–H amination of aldehydes and (hetero)arenes, several promising visible-light photocatalytic protocols have been developed by other groups for generating N-centred radicals and C–N bond formation (Fig. 1a)<sup>19–23</sup>. Despite their advantages, these methods require the introduction of a photolabile substituent at the nitrogen atom as a handle for

photo-activation. The use of the visible-light photocatalysis in initiating strong N–H bond activation and application in neutral N-centred radical-mediated catalytic cascade reactions have been, until recently, very limited. The Knowles' group recently reported an elegant combination of iridium photocatalyst and phosphate base for a direct homolytic cleavage of strong N–H bonds of *N*-arylamides to access amidyl radicals by a concerted proton-coupled electron transfer, which allowed an efficient radical cascade reaction towards N-heterocycle synthesis<sup>24</sup>. Exploring new reactivity of N-containing compounds in the field of visible-light photocatalysis is an integral part of our recent ongoing research endeavours<sup>25–28</sup>. For example, our group has recently developed a direct catalytic conversion of the N–H bonds of  $\beta,\gamma$ -unsaturated hydrazones into N-centred hydrazoneyl radicals by visible-light-induced photoredox catalysis, which enables an efficient and mild approach to intramolecular alkene hydroamination and oxyamination for synthesis of 4,5-dihydropyrazole derivatives<sup>28</sup>. In this reaction, a highly regioselective 5-exo radical cyclization of an N-centred radical was observed. It should be noted that the groups of Han<sup>29,30</sup> and Chiba<sup>31</sup> have also independently reported stoichiometric amounts of tetramethylpiperidine-1-oxyl (TEMPO)-mediated intramolecular cyclization of hydrazoneyl radicals for pyrazoline synthesis. Inspired by these studies, we considered exploration of the reactivity of hydrazones in catalytic N-radical cascade reactions to assemble biologically and synthetically important dihydropyrazine scaffolds<sup>32</sup>, inaccessible using other thermal methods<sup>29–31,33</sup> or our own previous protocols.

To this end, herein, we report an oxidative deprotonation electron transfer (ODET)/TEMPO-mediation strategy for direct N–H bond activation and catalytic N-radical cascade reactions of unsaturated hydrazones (Fig. 1b). This mild protocol represents the first, to our knowledge, broadly applicable synthesis of 1,6-dihydropyrazines with good regioselectivity and yield, achieved by merge of visible-light photocatalysis and TEMPO mediation.

## Results

**Reaction design.** To realize the target catalytic N-radical cascade reaction of unsaturated hydrazones as shown in Fig. 1b, several



**Figure 1 | Reaction design.** (a) Visible-light-induced photocatalytic generation of N-centred radicals from N-functionalized precursors. (b) Our blueprint for catalytic N-radical cascade reaction of hydrazones: merge of oxidative deprotonation electron transfer (ODET) activation of N–H bond with TEMPO mediation.

major challenges would probably be encountered, such as the controlled formal homolysis of the recalcitrant N–H bond for the formation of the neutral N-centred hydrazonyl radical, regioselectivity of the N-radical cyclization step (for example, 6-*endo* and 5-*exo*, path a versus path b)<sup>34,35</sup> and selective homolytic activation of aza-allylic C–H bond in C-centred radical intermediate. Notably, it has been recently documented by MacMillan<sup>36,37</sup>, Knowles<sup>24,38,39</sup> and our group<sup>28,40</sup> that the addition of a suitable Brønsted acid, Lewis acid or base could facilitate some otherwise inaccessible photocatalytic event by weakening chemical bonds of reactants and co-catalysts or modulating their redox potential. It has also been demonstrated by López and Gómez that complete 6-*endo*-selectivity over 5-*exo* ring closure in radical cyclization of C-centred radicals can be controlled by the radical property, substitution pattern at C-5 or ring strain of substrate<sup>34,35</sup>. Quite recently, the MacMillan group also first integrated elementary hydrogen atom transfer (HAT) process into H-bond catalysis, and achieved a highly selective photoredox  $\alpha$ -alkylation/lactonization cascade of alcohols<sup>41</sup>. Based on these inspiring studies, we hypothesized that the aforementioned regioselective N-radical cascade reaction could possibly be achieved by merging visible-light photoredox with TEMPO-mediated HAT process, wherein the N–H bond might be directly converted into the corresponding N-centred hydrazonyl radical through an ODET and the aza-allylic C–H bond can probably be homolytically cleaved by a suitable H-atom acceptor such as TEMPO<sup>42</sup>.

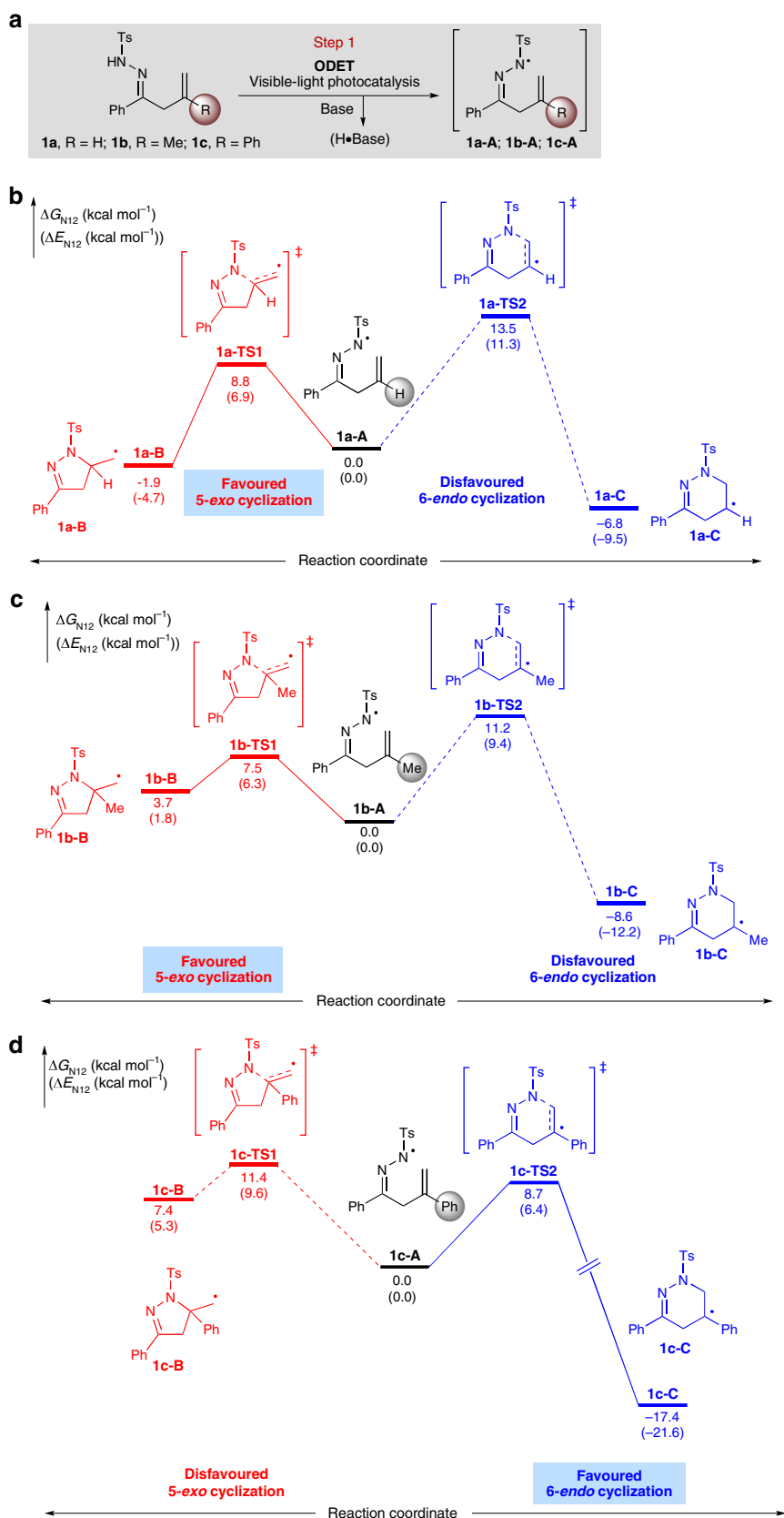
To test the feasibility of this strategy, we initially conducted density functional theory (DFT) calculations on the cyclization step of N-centred radical intermediates **1a-A**, **1b-A** and **1c-A** with sterically and electronically diverse substituents at the 2-position of the alkene (Fig. 2a; see Supplementary Notes 1–3 for details). The energies given in this work are N-12//6-311 + G(d, p)//B3LYP/6-31G(d) calculated Gibbs free energies in chloroform. See the Supplementary Information for more computational details.<sup>43</sup> As expected, both 5-*exo* and 6-*endo* N-radical-mediated radical cyclizations are possible pathways. For example, the study showed that the 5-*exo*-trig radical cyclization of **1a-A** with an activation free energy of only 8.8 kcal mol<sup>-1</sup> via **1a-TS1** is much more favoured than its 6-*endo*-trig variant (activation free energy of 13.5 kcal mol<sup>-1</sup>; Fig. 1b). It was also found that **1b-A** would undergo 5-*exo* cyclization through **1b-TS1** more feasibly than its 6-*endo* cyclization via **1b-TS2**, as shown by their activation free energy (Fig. 1c, 7.5 versus 11.2 kcal mol<sup>-1</sup>). Interestingly, the 6-*endo* cyclization of **1c-A** with a phenyl group at the 2-position of the alkene moiety proved to be easier to accomplish through **1c-TS2**, with a relatively low activation free energy of 8.7 kcal mol<sup>-1</sup>, to give the C-centred radical intermediate **1c-C** (Fig. 1d). Encouraged by these computational results, we proceeded to perform experimental studies with these substrates to explore the feasibility of the desired 6-*endo* radical cyclization.

Under our previously developed visible-light photocatalytic conditions for hydroamination of  $\beta,\gamma$ -unsaturated hydrazones<sup>28</sup>, substrates **1a** and **1b** indeed underwent 5-*exo* radical cyclization reactions smoothly to give the corresponding products **2a** and **2b** in 68% and 81% yields, respectively (Fig. 3a). These results also provided a solid support for the above computational investigations into these substrates. Interestingly, the reaction of **1c** resulted in the formation of a complex mixture with a complete conversion (Fig. 3b). Careful analysis of the reaction mixture revealed that an inseparable mixture of products **2c** and **3** can be obtained in 21% yield with a ratio of 1:0.9. Meanwhile, product **4** was also isolated in 16% yield, which might be formed through another radical cascade reaction between **1c** and the reaction solvent CHCl<sub>3</sub> via radical intermediate **1c-B**. The

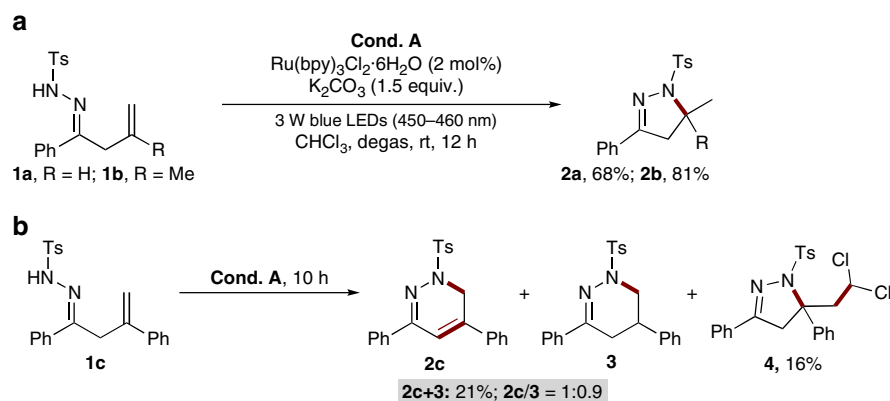
structures of **2a-2c**, **3** and **4** were fully characterized by their <sup>1</sup>H and <sup>13</sup>C NMR spectra and mass data, and compound **4** was further characterized by single-crystal X-ray analysis (see Supplementary Fig. 79 for details). Note that the biologically significant 1,6-dihydropyridazines of type **2c** cannot be easily prepared using traditional methods<sup>33</sup>. These observations suggested that further optimization of reaction parameters might result in the exclusive formation of the desired 1,6-dihydropyridazines.

**Optimization of reaction conditions.** Encouraged by these initial results, we continued to optimize the reaction conditions with **1c** as a model substrate to further improve the selectivity and yield (Table 1). Inspired by the recently demonstrated wide applicability of nitroxides in organic synthesis and their unique properties<sup>44,45</sup>, we initially focused on nitroxides as potential additives. Surprisingly, it was found that the addition of TEMPO (1.0 equiv.) did not quench the reaction; instead, it resulted in a clean reaction and gave the desired 1,6-dihydropyridazine **2c** in 89% yield (entry 1). Based on our blueprint of the reaction, we postulated that TEMPO might serve as a H-atom acceptor to abstract aza-allylic H-atom by an HAT process<sup>41</sup>. Then, we simply screened inorganic bases such as NaOH, Na<sub>2</sub>CO<sub>3</sub> and Na<sub>2</sub>HPO<sub>4</sub>, and established that the base also played an important role in the reaction, with K<sub>2</sub>CO<sub>3</sub> identified as the best choice (entries 2–4). With K<sub>2</sub>CO<sub>3</sub> as the base, we also briefly examined several other common solvents and CHCl<sub>3</sub> proved to be the best reaction media with tetrahydrofuran, MeOH, dimethylformamide and CH<sub>3</sub>CN giving relatively low yields (entries 5–8). Then, we evaluated the effect of photocatalysts on the reaction under otherwise identical conditions. Interestingly, the use of Ir(ppy)<sub>2</sub>(dtbbpy)PF<sub>6</sub> as a photocatalyst provided comparable results, whereas organic photocatalyst Eosin Y was ineffective for the reaction (entries 9–10). It has been well documented that TEMPO can serve not only as a radical scavenger but also as an oxidant in transition-metal catalysis<sup>44,45</sup>. Thus, we continued to test several other oxidants, such as K<sub>2</sub>S<sub>2</sub>O<sub>8</sub> and 2,3-dichloro-5,6-dicyano-1,4-benzoquinone (see Supplementary Table 1 for details). However, all the reactions with these oxidants resulted in a complex mixture without formation of any desired product, suggesting that TEMPO might act as a radical trap to abstract the  $\alpha$ -hydrogen atom from intermediate **1c-C** to facilitate the target N-radical cascade reaction pathway (entries 11–12). In the control experiments with CHCl<sub>3</sub> or CH<sub>3</sub>CN as the solvent, only very little or no desired products were detected in the absence of photocatalyst, base, TEMPO or light; large amounts of starting materials remained intact, highlighting the critical role of all the parameters in the reaction (entries 13–16; see Supplementary Table 2 for details).

**Substrate scope.** Under the optimized conditions, we then evaluated the substrate scope of this transformation with a variety of  $\beta,\gamma$ -unsaturated hydrazones (Fig. 4). First, we examined the effects of arene substitution using a wide range of  $\beta,\gamma$ -unsaturated hydrazones **1c-Ii**. It was found that the reaction with various  $\beta,\gamma$ -unsaturated hydrazones bearing electron-neutral, electron-poor (for example, Cl, Br, CF<sub>3</sub>) or electron-rich (for example, Me) substituents at the 2-, 3- or 4-position of the aromatic ring proceeded well to deliver the corresponding products **2c-2i** with yields ranging from 61 to 85%. Notably, those aryl bromides are amenable to further synthetic elaborations through transition-metal-catalyzed C–C coupling reactions. Product **2f** was also characterized by single-crystal X-ray analysis (see Supplementary Fig. 79 for details). Moreover, 2-naphthyl substituted hydrazone **1j** reacted well to afford product **2j** in 86% yield. Considering the

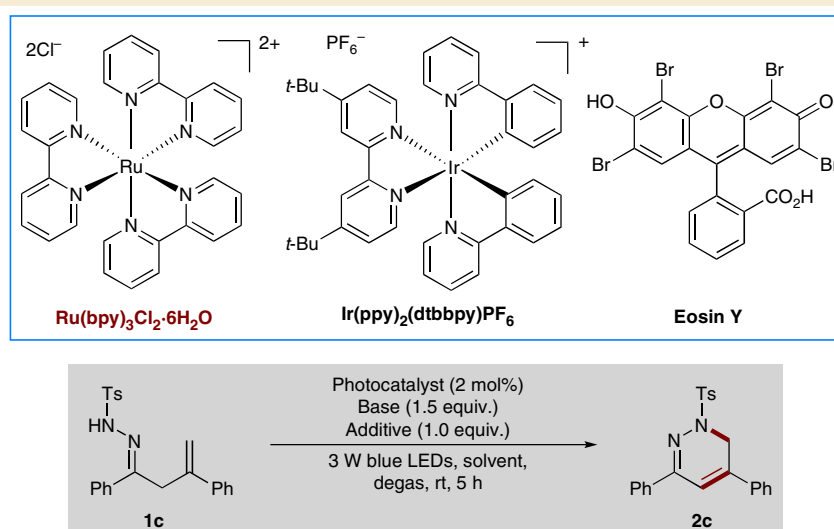


**Figure 2 | Reaction development.** (a) Generation of N-radicals by visible-light photocatalysis. (b) Free energy profiles for 5-*exo* and 6-*endo* radical cyclizations of **1a-A**. (c) Free energy profiles for 5-*exo* and 6-*endo* radical cyclizations of **1b-A**. (d) Free energy profiles for 5-*exo* and 6-*endo* radical cyclizations of **1c-A**.



**Figure 3 | Initial results.** (a) Reaction of substrate **1a** and **1b** under condition **A**. (b) Reaction of substrate **1c** under condition **A**. Unless otherwise noted, condition **A**: reaction were run with **1** (0.2 mmol), Ru(bpy)<sub>3</sub>Cl<sub>2</sub>·6H<sub>2</sub>O (2 mol%), K<sub>2</sub>CO<sub>3</sub> (0.3 mmol), 3 W blue light-emitting diodes (450–460 nm) irradiation and CHCl<sub>3</sub> (4.0 mL) at rt for 10–12 h.

**Table 1 | Optimization of conditions for catalytic N-radical cascade reaction of unsaturated hydrazone **1c**.**



Entry	Photocatalyst	Base	Solvent	Additive	Yield (%) <sup>*</sup>
1	Ru(bpy) <sub>3</sub> Cl <sub>2</sub> ·6H <sub>2</sub> O	K <sub>2</sub> CO <sub>3</sub>	CHCl <sub>3</sub>	TEMPO	89
2	Ru(bpy) <sub>3</sub> Cl <sub>2</sub> ·6H <sub>2</sub> O	NaOH	CHCl <sub>3</sub>	TEMPO	81
3	Ru(bpy) <sub>3</sub> Cl <sub>2</sub> ·6H <sub>2</sub> O	Na <sub>2</sub> CO <sub>3</sub>	CHCl <sub>3</sub>	TEMPO	72
4	Ru(bpy) <sub>3</sub> Cl <sub>2</sub> ·6H <sub>2</sub> O	Na <sub>2</sub> HPO <sub>4</sub>	CHCl <sub>3</sub>	TEMPO	8
5	Ru(bpy) <sub>3</sub> Cl <sub>2</sub> ·6H <sub>2</sub> O	K <sub>2</sub> CO <sub>3</sub>	THF	TEMPO	51
6	Ru(bpy) <sub>3</sub> Cl <sub>2</sub> ·6H <sub>2</sub> O	K <sub>2</sub> CO <sub>3</sub>	MeOH	TEMPO	23
7	Ru(bpy) <sub>3</sub> Cl <sub>2</sub> ·6H <sub>2</sub> O	K <sub>2</sub> CO <sub>3</sub>	DMF	TEMPO	26
8	Ru(bpy) <sub>3</sub> Cl <sub>2</sub> ·6H <sub>2</sub> O	K <sub>2</sub> CO <sub>3</sub>	CH <sub>3</sub> CN	TEMPO	48
9	Ir(ppy) <sub>2</sub> (dtbbpy)PF <sub>6</sub>	K <sub>2</sub> CO <sub>3</sub>	CHCl <sub>3</sub>	TEMPO	83
10	Eosin Y	K <sub>2</sub> CO <sub>3</sub>	CHCl <sub>3</sub>	TEMPO	Trace
11	Ru(bpy) <sub>3</sub> Cl <sub>2</sub> ·6H <sub>2</sub> O	K <sub>2</sub> CO <sub>3</sub>	CHCl <sub>3</sub>	K <sub>2</sub> S <sub>2</sub> O <sub>8</sub>	Trace
12	Ru(bpy) <sub>3</sub> Cl <sub>2</sub> ·6H <sub>2</sub> O	K <sub>2</sub> CO <sub>3</sub>	CHCl <sub>3</sub>	DDQ	Trace
13	—	K <sub>2</sub> CO <sub>3</sub>	CHCl <sub>3</sub>	TEMPO	0
14	Ru(bpy) <sub>3</sub> Cl <sub>2</sub> ·6H <sub>2</sub> O	—	CHCl <sub>3</sub>	TEMPO	0
15	Ru(bpy) <sub>3</sub> Cl <sub>2</sub> ·6H <sub>2</sub> O	K <sub>2</sub> CO <sub>3</sub>	CHCl <sub>3</sub>	—	11
16 <sup>†</sup>	Ru(bpy) <sub>3</sub> Cl <sub>2</sub> ·6H <sub>2</sub> O	K <sub>2</sub> CO <sub>3</sub>	CHCl <sub>3</sub>	TEMPO	0

DDQ, 2,3-dichloro-5,6-dicyano-1,4-benzoquinone; DMF, dimethylformamide; Eosin Y, tetrabromofluorescein; TEMPO, 2,2,6,6-tetramethylpiperidine-1-oxyl; THF, tetrahydrofuran.

Reaction conditions: **1c** (0.2 mmol), photocatalyst (0.004 mmol, 2.0 mol %), TEMPO (0.2 mmol), K<sub>2</sub>CO<sub>3</sub> (0.3 mmol) and solvent (4.0 ml) at room temperature for 5 h under irradiation from a 3-W blue light-emitting diodes (450–460 nm).

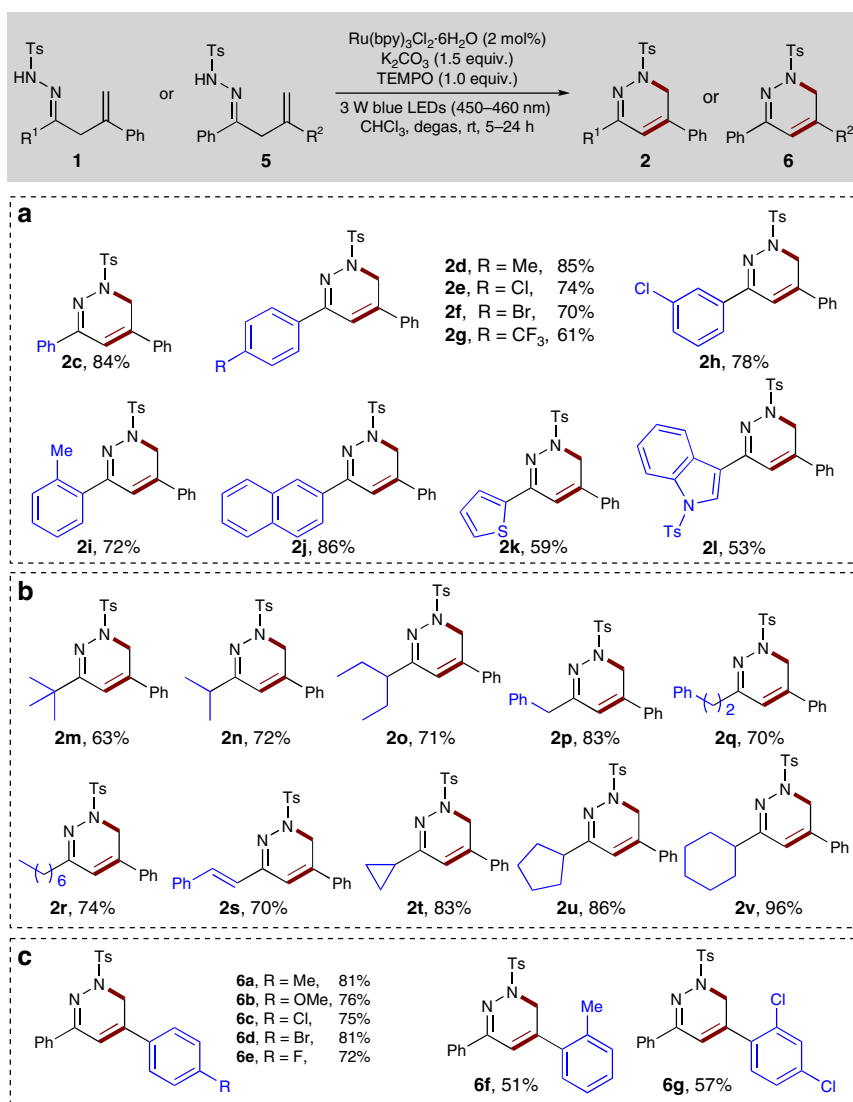
<sup>\*</sup>Isolated yields based on **1c**.

<sup>†</sup>Without visible-light irradiation.

known medicinal chemistry, it is noteworthy that various heterocycles can be incorporated into the hydrazone substrates with no apparent deleterious effect on the reaction efficiency. For

example, 2-thiophenyl and 3-indolyl substituted hydrazones were tolerated well to give the desired products **2k** and **2l** in 59% and 53% yields, respectively. More importantly, the substrate scope of





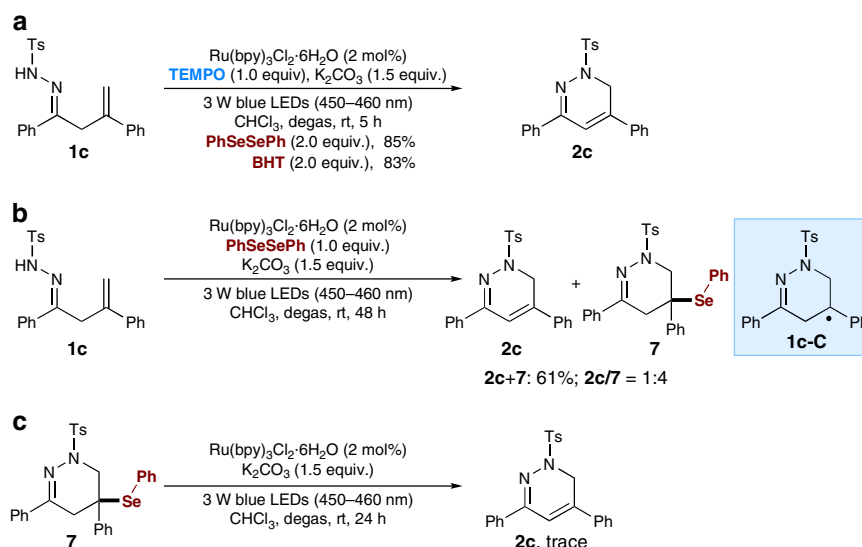
**Figure 4 | Reaction scope of unsaturated hydrazones.** (a) Investigation of the effects of arene substitution of hydrazones. (b) Substrate scope of aliphatic unsaturated hydrazones. (c) Substrate scope of alkene moieties. Unless otherwise noted, reactions were run with **1** or **5** (0.3 mmol),  $\text{Ru}(\text{bpy})_3\text{Cl}_2 \cdot 6\text{H}_2\text{O}$  (0.006 mmol, 2.0 mol%),  $\text{K}_2\text{CO}_3$  (0.45 mmol), TEMPO (0.3 mmol) and  $\text{CHCl}_3$  (6.0 ml) at rt for 5–24 h under irradiation with 3 W blue light-emitting diodes (450–460 nm).

the current protocol can be successfully extended to aliphatic  $\beta,\gamma$ -unsaturated hydrazones. Thus, the reaction with a series of linear and branched aliphatic  $\beta,\gamma$ -unsaturated hydrazones **1m–1r** can undergo the radical cascade reaction smoothly under standard conditions, although with prolonged reaction times, to afford the products **2m–2r** in 63–83% yield. The  $\beta,\gamma$ -unsaturated hydrazone **1s** bearing a styryl group also appeared to be viable for the reaction, producing a 70% yield of **2s**. Remarkably, cyclic substituents, such as cyclopropyl, cyclopentyl and cyclohexyl groups, could also be easily incorporated into the 1,6-dihydropyridazine scaffold with high yields (**2t–2v**, 83–96%).

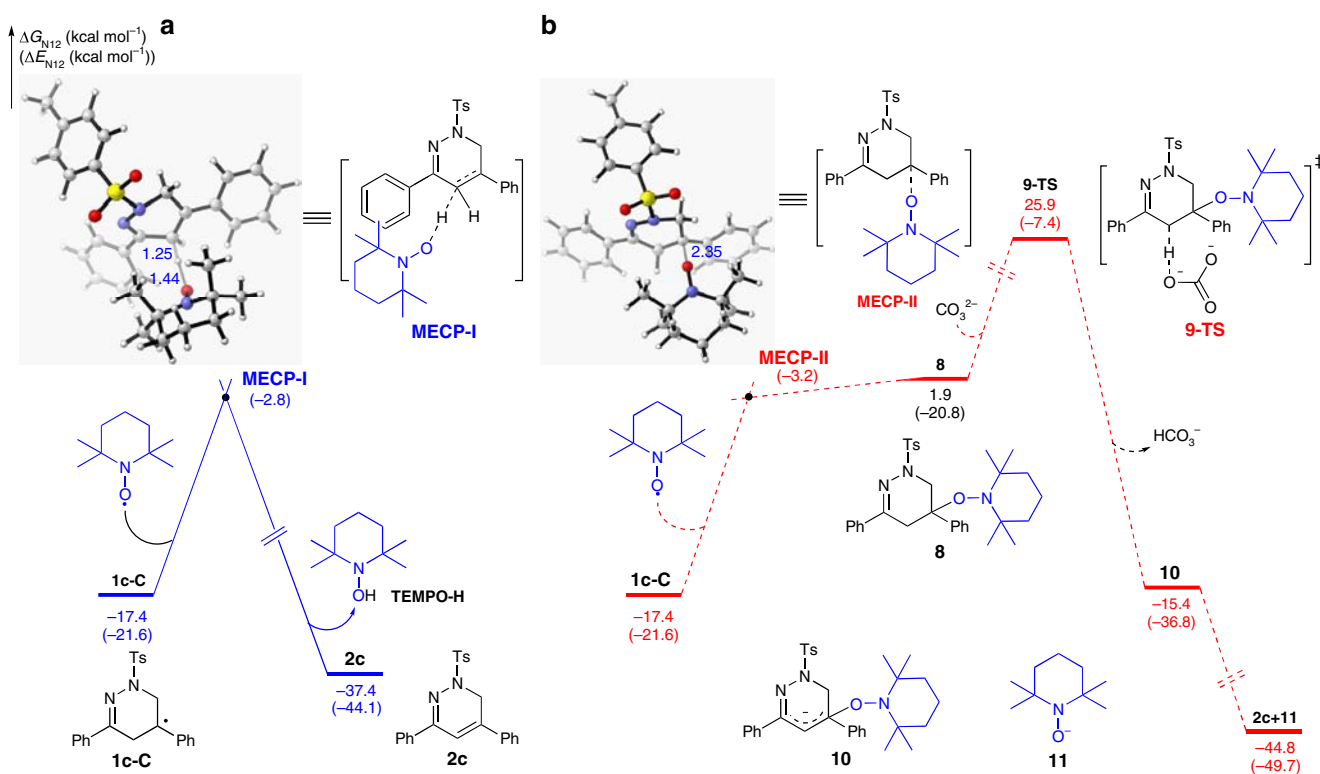
Encouraged by these results, we proceeded to examine the scope of alkene moieties by incorporation of various substituents into the phenyl ring. As highlighted in Fig. 4c, the substitution patterns and electronic properties of the aromatic ring showed no apparent effect on the reaction efficiency either. For example, all the electron-releasing (for example, 4-Me, 2-Me and 4-MeO) and electron-withdrawing (for example, 4-F, 4-Cl, 4-Br, 2,4-2Cl) groups were well tolerated under the standard conditions, furnishing the expected products **6a–6g** in 51–81% yield.

Interestingly, during our subsequent biological studies with 1,6-dihydropyridazines **2**- and **6**-derived diazinium salts, it was found that such aromatic substituents at the 2-position of the alkene are critical to their antifungal *in vitro* activities. It should be noted that we did not detect any 5-*exo* cyclization products in all cases<sup>29,30</sup>.

**Mechanistic investigations.** To gain additional insights into the reaction mechanism, several control experiments were conducted with model substrate **1c** (Fig. 5; see Supplementary Discussion for details). To further confirm the formation of C-centred intermediate of type **1c-C** during the reaction, common radical trapping agents (PhSeSePh or 2,6-di-*tert*-butyl-4-methylphenol, BHT) were added to the reaction system to capture the radical intermediate (Fig. 5a). However, no trapping products were observed; instead, only the 1,6-dihydropyridazine **2c** was produced and isolated in 85% and 83% yields, respectively. In contrast, without addition of TEMPO, the reaction with PhSeSePh as a radical trapping agent furnished a mixture of desired **2c** and selenide-adduct **7** (61% yield, 1:4 ratio; see Supplementary Fig. 78



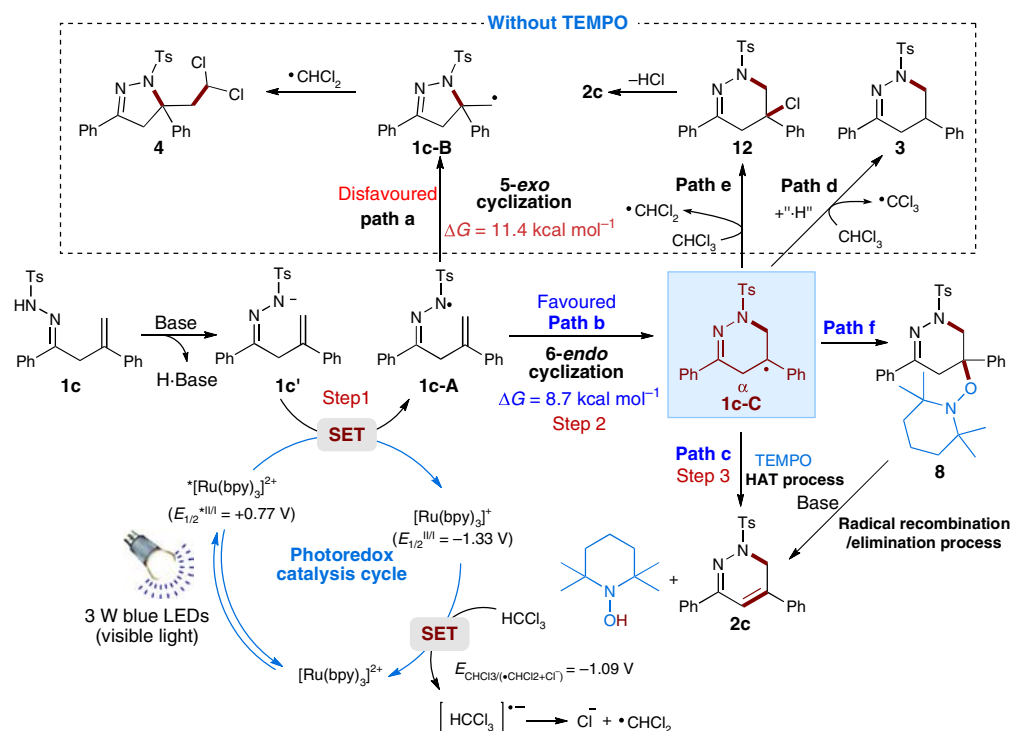
**Figure 5 | Mechanistic investigations.** (a) Trapping the C-centred intermediate by addition of PhSeSePh or BHT under the standard conditions. (b) Trapping the C-centred intermediate by addition of PhSeSePh under the standard conditions in the absence of TEMPO. (c) Control experiment with selenide-adduct **7** under the standard conditions.



**Figure 6 | Calculation studies.** (a) Free energy profile for the transformation of C-centred radical **1c-C** into product **2c** through a TEMPO-mediated HAT process. (b) Free energy profile for the transformation of C-centred radical **1c-C** into product **2c** through carbon radical trapping/elimination process.

for details), and compound **7** should be formed from radical intermediate **1c-C** and PhSeSePh (Fig. 5b). Then, we obtained the pure selenide-adduct **7** by semi-preparative high-performance liquid chromatography purification and re-subjected it to the standard reaction conditions without TEMPO (Fig. 5c). However, we did not detect any desired product **2c** even after 24 h and compound **7** remained intact, suggesting that selenide-adduct **7** should not be the possible intermediate for the formation of 1,6-dihydropyridazine **2c**.

To further determine the role of TEMPO, we also calculated the free energy of the subsequent transformation of C-centred radical intermediate **1c-C** into the final product **2c** via the minimum energy crossing point (MECP; Fig. 6)<sup>43</sup>. As shown in Fig. 6a, the computational results showed that the TEMPO might facilitate the conversion of the intermediate **1c-C** into the final product **2c** through a TEMPO-mediated HAT process, because the calculated energy barrier ( $\Delta E$ ) for the aza-allylic hydrogen atom abstraction via **MECP-I** is only 18.8 kcal mol<sup>-1</sup>. Moreover,



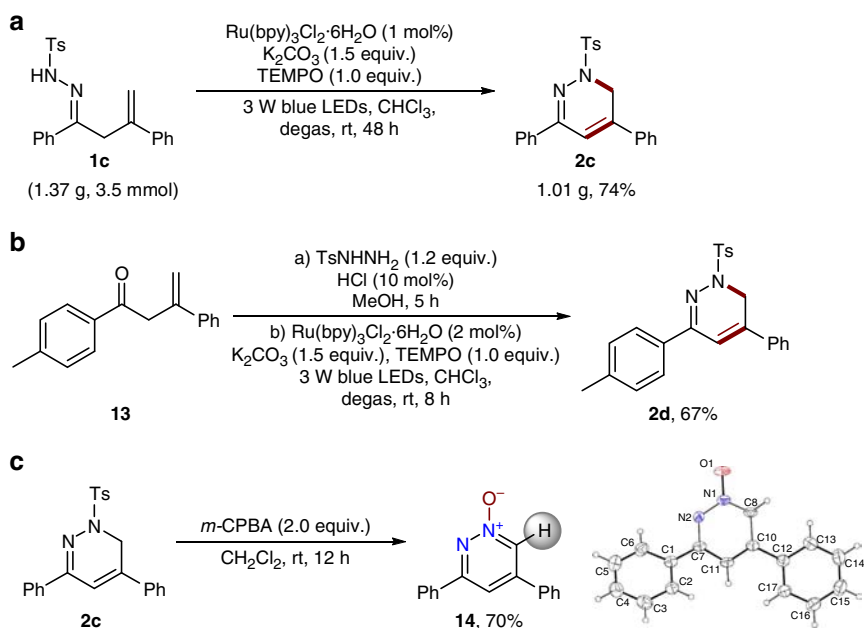
**Figure 7 | Proposed catalytic cycle.** The plausible mechanism involves oxidative deprotonation electron transfer (ODET) activation of N-H bond into N-centred radical by visible light photoredox catalysis and TEMPO-mediated N-radical cyclization.

the generation of product **2c** is exergonic by  $20.0 \text{ kcal mol}^{-1}$  compared with the intermediate **1c-C**. Recently, a similar trapping of carbon radical and elimination of TEMPO-H process in the presence of base has been identified by Chiba's group as the possible pathway in TEMPO-mediated C-H bond oxygenation of oximes and hydrazones<sup>46</sup>. Inspired by this work, another possible pathway involving carbon radical trapping/elimination sequence of **1c-C** in the presence of base was also considered in calculation. As shown in Fig. 6b, the combination of radical **1c-C** with TEMPO occurs through **MECP-II**, and the energy barrier ( $\Delta E$ ) of which is  $18.4 \text{ kcal mol}^{-1}$ . Although this energy barrier is close to that of **MECP-I** formation (Fig. 6a), the formation of TEMPO-adduct **8** is endergonic by  $19.3 \text{ kcal mol}^{-1}$  compared with **1c-C**. Moreover, the activation free energy of subsequent deprotonation, which occurs via transition state **9-TS**, reaches as high as  $43.3 \text{ kcal mol}^{-1}$ . According to these results, the sequential combination of carbon radical **1c-C** with TEMPO and elimination process appears to be thermodynamically unfavourable. Moreover, we also intended to isolate the possible intermediate **8** upon  $\sim 50\%$  conversion of model substrate **1c**. Unfortunately, all the attempts met failure, although a trace amount of intermediate **8** was detected by the high-resolution mass spectrometry analysis of the reaction mixture (see Supplementary Information). Another possible pathway for base-free elimination of TEMPO-H from **8** by direct radical elimination with C-O bond homolysis is not considered as the stoichiometric base is necessary in our reaction system<sup>47-49</sup>. Taken together, although the calculation studies support the TEMPO-mediated HAT process as the likely mechanism for the transformation of C-centred radical intermediate **1c-C** into the final product **2c**, at present we cannot rule out the carbon radical recombination/elimination pathway (see Supplementary Figs 80 and 81 and Supplementary Notes 1-3 for details). More detailed mechanistic studies are currently underway in our laboratory.

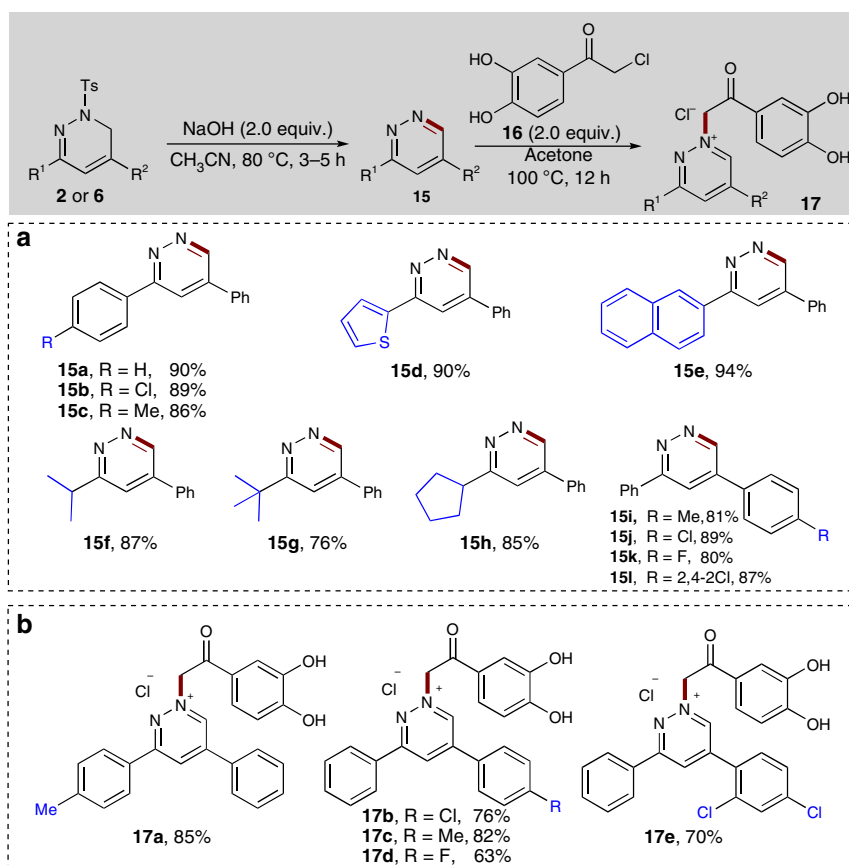
According to our blueprint for ODET activation of N-H bond, the addition of  $\text{K}_2\text{CO}_3$  proved be critical for the reaction as a base

and this phenomenon was indeed observed during the optimization study (Table 1, entry 14). To further evaluate the role of base in these reactions, we continue to study the mechanism of N-centred hydrazonyl radical formation by luminescence quenching experiments, NMR and electrochemical analysis with **1c** as a model substrate (see Supplementary Figs 82-86 for details). Stern-Volmer analysis demonstrated that hydrazone **1c** alone is unable to quench the excited state of  $^*\text{[Ru(bpy)}_3\text{)]}^{2+}$  in dimethylformamide at  $25^\circ\text{C}$ , implying that the excited state ruthenium complex does not oxidize the hydrazone **1c** directly. However, upon addition of  $\text{K}_2\text{CO}_3$  as a base, a significant decrease of luminescence emission intensity was observed. In addition, the  $^1\text{H NMR}$  analysis of a solution containing both **1c** and  $\text{K}_2\text{CO}_3$  exhibited that the addition of  $\text{K}_2\text{CO}_3$  resulted in complete disappearance of the signal of N-H, suggesting that  $\text{K}_2\text{CO}_3$  serve to abstract the proton of N-H bond to generate nitrogen anion intermediate **1c'** (Fig. 7 and Supplementary Information). Moreover, cyclic voltammetry data confirmed that the excited photocatalyst  $^*\text{[Ru(bpy)}_3\text{)]}^{2+}$  ( $E_{1/2}^{*II/I} = +0.77 \text{ V}$  versus SCE in  $\text{CH}_3\text{CN}$ ) is likely to be sufficiently oxidizing to oxidize the nitrogen anion **1c'** ( $E_{\text{p}}^{\text{red}} = 0.56 \text{ V}$  versus SCE) to generate the corresponding N-centred radical intermediate **1c-A** (Fig. 7). Taken together, although we could not completely exclude the concerted proton-coupled electron transfer mechanism at the current stage<sup>24,38,39</sup>, the above results are more consistent with an ODET activation mechanism involving sequential deprotonation of hydrazone substrates by the  $\text{K}_2\text{CO}_3$  and visible-light photocatalytic single-electron transfer (SET) oxidation.

Ultimately, a plausible mechanism is outlined in Fig. 7 using **1c** as an example. Initially, the  $\beta,\gamma$ -unsaturated hydrazone **1c** is transformed into anionic intermediate **1c'** upon deprotonation, which is then oxidized to the N-centred radical **1c-A** by the excited photocatalyst  $^*\text{[Ru(bpy)}_3\text{)]}^{2+}$  through a SET process. Then, the key intermediate **1c-A** undergoes a 6-endo radical cyclization to afford the C-centred benzylic radical intermediate **1c-C**, which can be conveniently transformed into the final



**Figure 8 | Synthetic application.** (a) Gram-scale reaction. (b) One-pot process for synthesis of 1,6-dihydropyridazine **2d**. (c) Synthesis of pyridazine *N*-oxide **14**.



**Figure 9 | Application to the synthesis of pyridazines and diazinium salts.** (a) Reactions were run with **2** or **6** (0.2 mmol), NaOH (0.6 mmol) and CH<sub>3</sub>CN (4.0 ml) at 80 °C for 3–5 h. (b) Reactions were run with **15** (0.3 mmol), **16** (0.6 mmol) and acetone (3.0 ml) at 100 °C for 12 h.

product **2c** by an HAT process in the presence of TEMPO (path c). However, as for the transformation of C-centred radical intermediate **1c-C** into the final product **2c**, at the current stage, we cannot rule out the carbon radical recombination/elimination

pathway that involves TEMPO-adduct **8** as the key intermediate (path f, see Supplementary Information). In the absence of TEMPO, the intermediate **1c-C** can abstract a hydrogen atom directly from CHCl<sub>3</sub> to give 1,4,5,6-tetrahydropyridazine **3**

(path d). Meanwhile, the intermediate **1c-C** can also abstract a chlorine radical from chloroform to give rise to dichloromethyl radical and labile tertiary chloride adduct **12** intermediate<sup>50</sup>, which can undergo facile elimination to give the product **2c**. Moreover, without addition of TEMPO, the intermediate N-centred radical **1c-A** could also undergo a 5-*exo* radical cyclization (path a) to furnish **1c-B**, partly because of the relatively small activation free energy difference between **1c-B** and **1c-C** (Fig. 2d). In the photocatalytic cycle, chloroform can regenerate the photocatalyst [Ru(bpy)<sub>3</sub>]<sup>2+</sup> by an SET oxidation process with the concomitant release of the chloroform radical anion, which rapidly dechlorinated to give chloride ion and the dichloromethyl radical<sup>51–54</sup>. The formation of a dichloromethyl radical in the reaction was also confirmed by the isolation of side product **4**, resulting from the radical cross coupling between the dichloromethyl radical and **1c-B** intermediate.

**Synthetic application.** To further demonstrate the synthetic potential of this method, a gram-scale reaction of  $\beta,\gamma$ -unsaturated hydrazone **1c** was conducted in the presence of 1 mol% of photocatalyst under standard reaction conditions, and the desired product **2c** was still successfully obtained in 74% yield after 48 h (Fig. 8a). A key benefit of this photocatalytic radical cyclization strategy is that the  $\beta,\gamma$ -unsaturated hydrazone starting materials are easily accessed from the corresponding  $\beta,\gamma$ -unsaturated ketones and tosyl hydrazine. Thus, we examined the photocatalytic radical cyclization with  $\beta,\gamma$ -unsaturated ketone **13** and tosyl hydrazine in a two-step one-pot process (Fig. 8b). Pleasingly, the desired 1,6-dihydropyridazine **2d** was obtained in 67% overall yield. Recently, heteroaromatic *N*-oxides have been widely employed in transition-metal-catalyzed aromatic C–H activation/functionalization reactions to access various valuable heterocyclic molecules<sup>55</sup>. We found that the present method could provide a new approach to the synthesis of pyridazine *N*-oxides. For example, treatment of **2c** with *m*-CPBA as the oxidant resulted in the facile formation of pyridazine *N*-oxide **14** in a 70% yield that was also clearly determined by X-ray analysis (Fig. 8c; see Supplementary Fig. 79 for details).

Moreover, it was then established that the 1,6-dihydropyridazine products can also be easily transformed into the corresponding biologically important pyridazines under mild conditions (2.0 equiv. NaOH in CH<sub>3</sub>CN at 80 °C). As highlighted in Fig. 9a, the electronic and steric properties of the substituents on both of the aromatic rings showed no significant effect on the reaction efficiency. A series of substrates with electron-rich or electron-poor substituents worked well to give the desired products in good yields (**15a–15d**, 86–90% yield; **15i–15l**, 81–89% yield). In addition, 2-thiophenyl and 2-naphthyl-substituted 1,6-dihydropyridazines reacted well to give the corresponding pyridazine products **15d** and **15e** in 90% and 94% yield, respectively. Remarkably, the 1,6-dihydropyridazines bearing alkyl groups such as isopropyl, *tert*-butyl and cyclohexyl substituents, were well tolerated to deliver the desired products **15f–15h** in high yields (76–87%).

It has recently been documented that the pyridazine derivatives, such as diazinium salts bearing a dihydroxyacetophenone core, showed promising biological activities against a variety of microorganisms (germs and fungi)<sup>56</sup>. Thus, we further attempted to transform a range of representative pyridazines **15** into the corresponding diazinium salts **17** and preliminarily explored their potential structure–activity relationships (Fig. 9b). By refluxing a mixture of pyridazines **15** and 2-chloro-3',4'-dihydroxyacetophenone **16** in acetone for 12 h, a series of diazinium salts **17a–17e** were easily obtained in 63–85% yield after a simple filtration.

Over the past decades, the incidence of invasive fungal infections and the associated morbidity and mortality rates have risen remarkably due to the over-use of broad-spectrum antibiotics, serious medical interventions and immune deficiency disorders, such as AIDS<sup>57,58</sup>. Despite recent additions to the antifungal drug family, the limitations of the current antifungal drugs involve narrow activity spectra, detrimental drug–drug interactions and antifungal resistance, necessitating the development of new antifungal agents or leads. With diazinium salts **17a–17e** in hand, we evaluated the *in vitro* antifungal activities of these compounds against eight human pathogenic fungi, compared with commercially available fluconazole. In contrast to the antibacterial activities reported for related diazinium salts<sup>56</sup>, our results demonstrated that some of these compounds showed promising activities against four common clinical pathogenic fungi (*Candida albicans*, *C. parapsilosis*, *C. neoformans* and *C. glabrata*; see Supplementary Tables 3 and 4 for details). These results also confirmed that the substitution patterns and electronic properties of the substituents at both of the phenyl rings are critical to their *in vitro* antifungal activities. Gratifyingly, the MIC<sub>80</sub> values of most of the compounds (**17b–17e**) against *C. parapsilosis*, *C. neoformans* and *C. glabrata* (0.5–4  $\mu\text{g ml}^{-1}$ ) were comparable to those of fluconazole, which should be valuable for our future biological studies.

## Discussion

We have developed a novel ODET/HAT strategy, which we used to directly convert the N–H bond of  $\beta,\gamma$ -unsaturated hydrazones to the N-centred radical, and developed an efficient catalytic N-radical cascade reaction. This mild protocol represents the first, to our knowledge, broadly applicable synthesis of 1,6-dihydropyridazines with good regioselectivity and yield, achieved by the merge of visible-light photocatalysis and TEMPO mediation. The 1,6-dihydropyridazines could also be conveniently transformed into biologically important diazinium salts bearing dihydroxyacetophenone core, which showed promising antifungal *in vitro* activities against various fungal pathogens. Control experiments and DFT calculations have been performed to help explain the mechanism. Owing to the wide occurrence of various N–H bonds, we believe that this strategy may find wide use for generation of other various *N*-centred radicals and new reaction developments with these reactive species<sup>59</sup>.

## Methods

**Materials.** Unless otherwise noted, materials were purchased from commercial suppliers and used without further purification. All the solvents were treated according to general methods. Flash column chromatography was performed using 200–300 mesh silica gel. The manipulations for photocatalytic N-radical cascade reactions were carried out with standard Schlenk techniques under Ar by visible-light irradiation. See Supplementary Methods for experimental details.

**General methods.** <sup>1</sup>H NMR spectra were recorded on 400 or 600 MHz spectrophotometers. Chemical shifts are reported in delta ( $\delta$ ) units in parts per million (p.p.m.) relative to the singlet (0 p.p.m.) for tetramethylsilane. Data are reported as follows: chemical shift, multiplicity (s = singlet, d = doublet, t = triplet, dd = doublet of doublets, m = multiplet), coupling constants (Hz) and integration. <sup>13</sup>C NMR spectra were recorded on 100 or 150 MHz with complete proton-decoupling spectrophotometers (CDCl<sub>3</sub>: 77.0 p.p.m. or DMSO-*d*<sub>6</sub>: 39.5 p.p.m.). <sup>19</sup>F NMR spectra were recorded on 376 MHz with complete proton-decoupling spectrophotometers. Mass spectra were measured on MS spectrometer (EI) or liquid chromatography-mass spectrometry (LC/MS), or electrospray ionization mass spectrometry (ESI-MS). High-resolution mass spectrometry was recorded on Bruker ultrafleXtreme matrix-assisted laser desorption/ionization–time-of-flight (TOF)/TOF mass spectrometer. <sup>1</sup>H NMR, <sup>13</sup>C NMR and <sup>19</sup>F NMR spectra are supplied for all compounds: see Supplementary Figs 1–77.

**General procedure for catalytic nitrogen radical cascade reaction of hydrazones.** In a flame-dried Schlenk tube under Ar, **1c** (117.0 mg, 0.3 mmol), Ru(bpy)<sub>3</sub>Cl<sub>2</sub>·6H<sub>2</sub>O

(0.006 mmol), TEMPO (46.9 mg, 0.3 mmol) and  $K_2CO_3$  (61.2 mg, 0.45 mmol) were dissolved in  $CHCl_3$  (6.0 ml). Then, the resulting mixture was degassed via 'freeze-pump-thaw' procedure (three times). After that, the solution was stirred at a distance of ~5 cm from a 3-W blue light-emitting diodes (450–460 nm) at room temperature ~5 h until the reaction was completed as monitored by thin-layer chromatography analysis. The crude product was purified by flash chromatography on silica gel (petroleum ether/ethyl acetate 20:1~10:1) directly to give the desired product **2c** in 84% yield as a white solid. Full experimental details and characterization of new compounds can be found in the Supplementary Methods.

## References

1. Chatgililoglu, C. & Studer, A. *Encyclopedia of Radicals in Chemistry, Biology and Materials* (John Wiley & Sons, 2012).
2. Zard, S. Z. *Radical Reactions in Organic Synthesis* (Oxford Univ., 2003).
3. Sebrén, L. J., Devery, III J. J. & Stephenson, C. R. Catalytic radical domino reactions in organic synthesis. *ACS Catal.* **4**, 703–716 (2014).
4. Wille, U. Radical cascades initiated by intermolecular radical addition to alkynes and related triple bond systems. *Chem. Rev.* **113**, 813–853 (2013).
5. Chen, J.-R., Yu, X.-Y. & Xiao, W.-J. Tandem radical cyclization of N-arylacrylamides: an emerging platform for the construction of 3,3-disubstituted oxindoles. *Synthesis* **47**, 604–629 (2015).
6. Zard, S. Z. Recent progress in the generation and use of nitrogen-centred radicals. *Chem. Soc. Rev.* **37**, 1603–1618 (2008).
7. Minozzi, M., Nanni, D. & Spagnolo, P. From azides to nitrogen-centered radicals: applications of azide radical chemistry to organic synthesis. *Chem. Eur. J.* **15**, 7830–7840 (2009).
8. Nicolaou, K. C. *et al.* Iodine (V) reagents in organic synthesis. Part 3. New routes to heterocyclic compounds via o-iodoxybenzoic acid-mediated cyclizations: generality, scope, and mechanism. *J. Am. Chem. Soc.* **124**, 2233–2244 (2002).
9. Wang, Y.-F., Chen, H., Zhu, X. & Chiba, S. Copper-catalyzed aerobic aliphatic C-H oxygenation directed by an amidine moiety. *J. Am. Chem. Soc.* **134**, 11980–11983 (2012).
10. Zhou, L.-L. *et al.* Transition-metal-assisted radical/Radical cross-coupling: a new strategy to the oxidative  $C(sp^3)$ -H/N-H cross-coupling. *Org. Lett.* **16**, 3404–3407 (2014).
11. Li, Z.-D., Song, L.-Y. & Li, C.-Z. Silver-catalyzed radical aminofluorination of unactivated alkenes in aqueous media. *J. Am. Chem. Soc.* **135**, 4640–4643 (2013).
12. Liwosz, T. W. & Chemler, S. R. Copper-catalyzed oxidative amination and allylic amination of alkenes. *Chem. Eur. J.* **19**, 12771–12777 (2013).
13. Dai, C., Narayanam, J. M. R. & Stephenson, C. R. J. Visible-light-mediated conversion of alcohols to halides. *Nat. Chem.* **3**, 140–145 (2011).
14. Xuan, J. & Xiao, W.-J. Visible-light photoredox catalysis. *Angew. Chem. Int. Ed.* **51**, 6828–6838 (2012).
15. Prier, C. K., Rankic, D. A. & Macmillan, D. W. Visible light photoredox catalysis with transition metal complexes: applications in organic synthesis. *Chem. Rev.* **113**, 5322–5363 (2013).
16. Schultz, D. M. & Yoon, T. P. Solar synthesis: prospects in visible light photocatalysis. *Science* **343**, 985–994 (2014).
17. Cecere, G., König, C. M., Alleva, J. L. & MacMillan, D. W. Enantioselective direct alpha-amination of aldehydes via a photoredox mechanism: a strategy for asymmetric amine fragment coupling. *J. Am. Chem. Soc.* **135**, 11521–11524 (2013).
18. Allen, L. J., Cabrera, P. J., Lee, M. & Sanford, M. S. N-Acyloxypthalimides as nitrogen radical precursors in the visible light photocatalyzed room temperature C-H amination of arenes and heteroarenes. *J. Am. Chem. Soc.* **136**, 5607–5610 (2014).
19. Qin, Q.-X. & Yu, S.-Y. Visible-light-promoted redox neutral C-H amidation of heteroarenes with hydroxylamine derivatives. *Org. Lett.* **16**, 3504–3507 (2014).
20. Kim, H., Kim, T., Lee, D. G., Roh, S. W. & Lee, C. Nitrogen-centered radical-mediated C-H imidation of arenes and heteroarenes via visible light induced photocatalysis. *Chem. Commun.* **50**, 9273–9276 (2014).
21. Greulich, T. W., Daniliuc, C. G. & Studer, A. N-Aminopyridinium salts as precursors for N-centered radicals-direct amidation of arenes and heteroarenes. *Org. Lett.* **17**, 254–257 (2015).
22. Miyazawa, K., Koike, T. & Akita, M. Regiospecific intermolecular aminohydroxylation of olefins by photoredox catalysis. *Chem. Eur. J.* **21**, 11677–11680 (2015).
23. Jiang, H. *et al.* Visible-light-promoted iminyl-radical formation from acyl oximes: A unified approach to pyridines, quinolines, and phenanthridines. *Angew. Chem. Int. Ed.* **54**, 4055–4059 (2015).
24. Choi, G. J. & Knowles, R. R. Catalytic alkene carboaminations enabled by oxidative proton-coupled electron transfer. *J. Am. Chem. Soc.* **137**, 9226–9229 (2015).
25. Zou, Y.-Q. *et al.* Visible-light-induced oxidation/[3 + 2] cycloaddition/oxidative aromatization sequence: a photocatalytic strategy to construct pyrrolo[2,1-*a*] isoquinolines. *Angew. Chem. Int. Ed.* **50**, 7171–7175 (2011).
26. Xuan, J. *et al.* Visible-light-induced formal [3 + 2] cycloaddition for pyrrole synthesis under metal-free conditions. *Angew. Chem. Int. Ed.* **53**, 5653–5656 (2014).
27. Xuan, J. *et al.* Redox-neutral  $\alpha$ -allylation of amines by combining palladium catalysis and visible-light photoredox catalysis. *Angew. Chem. Int. Ed.* **54**, 1625–1628 (2015).
28. Hu, X.-Q. *et al.* Photocatalytic generation of N-centered hydrazonyl radicals: a strategy for hydroamination of  $\beta,\gamma$ -unsaturated hydrazones. *Angew. Chem. Int. Ed.* **53**, 12163–12167 (2014).
29. Duan, X.-Y. *et al.* Hydrazone radical promoted vicinal difunctionalization of alkenes and trifunctionalization of allyls: synthesis of pyrazolines and tetrahydropyridazines. *J. Org. Chem.* **78**, 10692–10704 (2013).
30. Duan, X.-Y. *et al.* Transition from  $\pi$  radicals to  $\sigma$  radicals: substituent-yuned cyclization of hydrazonyl radicals. *Angew. Chem. Int. Ed.* **53**, 3158–3162 (2014).
31. Zhu, X. & Chiba, S. TEMPO-mediated allylic C-H amination with hydrazones. *Org. Biomol. Chem.* **12**, 4567–4570 (2014).
32. Maison, W. & Küchenthal, C.-H. Synthesis of cyclic hydrazino  $\alpha$ -carboxylic acids. *Synthesis* **2010**, 719–740 (2010).
33. Potikha, L., Turelik, A. & Kovtunenkov, V. Synthesis and properties of *z*-1,3-bis-(aryl)-4-bromo-2-buten-1-ones. *Chem. Heterocycl. Compd* **45**, 1184–1189 (2009).
34. Gómez, A. M., Company, M. D., Uriel, C., Valverde, S. & López, J. C. 6-*Endo* versus 5-*exo* radical cyclization: streamlined syntheses of carbahexopyranoses and derivatives by 6-*endo-trig* radical cyclization. *Tetrahedron Lett.* **48**, 1645–1649 (2007).
35. Gómez, A. M., Uriel, C., Company, M. D. & López, J. C. Synthetic strategies directed towards 5a-carbahexopyranoses and derivatives based on 6-*endo-trig* radical cyclizations. *Eur. J. Org. Chem.* **2011**, 7116–7132 (2011).
36. Cuthbertson, J. D. & MacMillan, D. W. C. The direct arylation of allylic  $sp^3$  C-H bonds via organic and photoredox catalysis. *Nature* **519**, 74–77 (2015).
37. Jin, J. & MacMillan, D. W. C. Alcohols as alkylating agents in heteroarene C-H functionalization. *Nature* **525**, 87–90 (2015).
38. Miller, D. C., Choi, G. J., Orbe, H. S. & Knowles, R. R. Catalytic olefin hydroamination enabled by proton-coupled electron transfer. *J. Am. Chem. Soc.* **137**, 13492–13495 (2015).
39. Tarantino, K. T., Miller, D. C., Callon, T. A. & Knowles, R. R. Bond-weakening catalysis: conjugate aminations enabled by the soft homolysis of strong N-H bonds. *J. Am. Chem. Soc.* **137**, 6440–6443 (2015).
40. Zhou, Q.-Q. *et al.* Decarboxylative alkylation and carbonylative alkylation of carboxylic acids enabled by visible-light photoredox catalysis. *Angew. Chem. Int. Ed.* **54**, 11196–11199 (2015).
41. Jeffrey, J. L., Terrett, J. A. & MacMillan, D. W. C. O-H hydrogen bonding promotes H-atom transfer from C-H bonds for C-alkylation of alcohols. *Science* **349**, 1532–1536 (2015).
42. Mayer, J. M. Understanding hydrogen atom transfer: from bond strengths to Marcus theory. *Acc. Chem. Res.* **44**, 36–46 (2011).
43. The reference for Harvey's program Harvey, J. N., Aschi, M., Schwarz, H. & Koch, W. The singlet and triplet states of phenyl cation. A hybrid approach for locating minimum energy crossing points between non-interacting potential energy surfaces. *Theor. Chem. Acc.* **99**, 95–99 (1998).
44. Tebben, L. & Studer, A. Nitroxides: applications in synthesis and in polymer chemistry. *Angew. Chem. Int. Ed.* **50**, 5034–5068 (2011).
45. Bagryanskaya, E. G. & Marque, S. R. A. Scavenging of organic C-centered radicals by nitroxides. *Chem. Rev.* **114**, 5011–5056 (2014).
46. Zhu, X., Wang, Y.-F., Ren, W., Zhang, F.-L. & Chiba, S. TEMPO-Mediated aliphatic C-H oxidation with oximes and hydrazones. *Org. Lett.* **15**, 3214–3217 (2013).
47. Li, Y. & Studer, A. Transition-metal-free trifluoromethylaminoxylation of alkenes. *Angew. Chem. Int. Ed.* **51**, 8221–8224 (2012).
48. Hartmann, M., Li, Y. & Studer, A. Transition-metal-free oxyarylation of alkenes with aryl diazonium salts and TEMPO. *J. Am. Chem. Soc.* **134**, 16516–16519 (2012).
49. Maity, S. *et al.* Efficient and stereoselective nitration of mono- and disubstituted olefins with  $AgNO_2$  and TEMPO. *J. Am. Chem. Soc.* **135**, 3355–3358 (2013).
50. Recupero, F. *et al.* Enhanced nucleophilic character of the 1-adamantyl radical in chlorine atom abstraction and in addition to electron-poor alkenes and to protonated heteroaromatic bases. Absolute rate constants and relationship with the Gif reaction. *J. Chem. Soc. Perkin Trans 2*, 2399–2406 (1997).
51. Bertran, J., Gallardo, I., Moreno, M. & Saveant, J. M. Dissociative electron transfer. Ab initio study of the carbon-halogen bond reductive cleavage in methyl and perfluoromethyl halides. Role of the solvent. *J. Am. Chem. Soc.* **114**, 9576–9583 (1992).
52. Zhang, W., Yang, L., Wu, L.-M., Liu, Y.-C. & Liu, Z.-L. Photoinduced electron transfer retro-pinacol reaction of 4-(*N,N*-dimethylamino)phenyl pinacols in chloroform. *J. Chem. Soc. Perkin Trans 2*, 1189–1194 (1998).
53. Costentin, C., Robert, M. & Savéant, J.-M. Successive removal of chloride ions from organic polychloride pollutants. mechanisms of reductive electrochemical elimination in aliphatic gem-polychlorides,  $\alpha,\beta$ -polychloroalkenes, and  $\alpha,\beta$ -polychloroalkanes in mildly protic medium. *J. Am. Chem. Soc.* **125**, 10729–10739 (2003).

54. Studer, A. & Curran, D. P. The electron is a catalyst. *Nat. Chem.* **6**, 765–773 (2014).
55. Seregin, I. V. & Gevorgyan, V. Direct transition metal-catalyzed functionalization of heteroaromatic compounds. *Chem. Soc. Rev.* **36**, 1173–1193 (2007).
56. Balan, A. M. *et al.* Diazinium salts with dihydroxyacetophenone skeleton: syntheses and antimicrobial activity. *Eur. J. Med. Chem.* **44**, 2275–2279 (2009).
57. Ostrosky-Zeichner, L., Casadevall, A., Galgiani, J. N., Odds, F. C. & Rex, J. H. An insight into the antifungal pipeline: selected new molecules and beyond. *Nat. Rev. Drug Discov.* **9**, 719–727 (2010).
58. Brown, G. D., Denning, D. W. & Levitz, S. M. Tackling human fungal infections. *Science* **336**, 647–647 (2012).
59. Chen, J.-R., Hu, X.-Q., Lu, L.-Q. & Xiao, W.-J. Visible light photoredox-controlled reactions of N-radicals and radical ions. *Chem. Soc. Rev.* <http://dx.doi.org/10.1039/C5CS00655D> (2016).

### Acknowledgements

We are grateful to the National Science Foundation of China (NO. 21272087, 21472058, 21472057 and 21232003), and the Youth Chen-Guang Project of Wuhan (No. 2015070404010180). This work was also financially supported by the self-determined research funds of CCNU from the colleges' basic research and operation of MOE (No. CCNU15A02009). X.Q. and Y.L. are grateful to the National Science Foundation of China (NO. 21372266 and 51302327) for financial support. We also thank the anonymous referees for helpful suggestions.

### Author contributions

X.-Q.H., J.-R.C., Q.-Q.Z. and Q.W. are responsible for the plan and implementation of the experimental work. X.Q. and Y.L. are responsible for the calculation study. J.-R.C.

and W.-J.X. designed and guided this project and co-wrote the manuscript. All authors discussed the results and commented on the manuscript.

### Additional information

**Accession codes:** The X-ray crystallographic coordinates for structures reported in this Article have been deposited at the Cambridge Crystallographic Data Centre (CCDC), under deposition numbers CCDC 1407651 (2f), 1407652 (4), 1407653 (14). These data can be obtained free of charge from the Cambridge Crystallographic Data Centre via [http://www.ccdc.cam.ac.uk/data\\_request/cif](http://www.ccdc.cam.ac.uk/data_request/cif).

**Supplementary Information** accompanies this paper at <http://www.nature.com/naturecommunications>

**Competing financial interests:** The authors declare no competing financial interests.

**Reprints and permission** information is available online at <http://npg.nature.com/reprintsandpermissions/>

**How to cite this article:** Hu, X.-Q. *et al.* Catalytic N-radical cascade reaction of hydrazones by oxidative deprotonation electron transfer and TEMPO mediation. *Nat. Commun.* **7**:11188 doi: 10.1038/ncomms11188 (2016).



This work is licensed under a Creative Commons Attribution 4.0 International License. The images or other third party material in this article are included in the article's Creative Commons license, unless indicated otherwise in the credit line; if the material is not included under the Creative Commons license, users will need to obtain permission from the license holder to reproduce the material. To view a copy of this license, visit <http://creativecommons.org/licenses/by/4.0/>

# Micro-cable structured textile for simultaneously harvesting solar and mechanical energy

Jun Chen<sup>1†</sup>, Yi Huang<sup>2†</sup>, Nannan Zhang<sup>2</sup>, Haiyang Zou<sup>1</sup>, Ruiyuan Liu<sup>1</sup>, Changyuan Tao<sup>2</sup>, Xing Fan<sup>2\*</sup> and Zhong Lin Wang<sup>1,3\*</sup>

**Developing lightweight, flexible, foldable and sustainable power sources with simple transport and storage remains a challenge and an urgent need for the advancement of next-generation wearable electronics. Here, we report a micro-cable power textile for simultaneously harvesting energy from ambient sunshine and mechanical movement. Solar cells fabricated from lightweight polymer fibres into micro cables are then woven via a shuttle-flying process with fibre-based triboelectric nanogenerators to create a smart fabric. A single layer of such fabric is 320  $\mu\text{m}$  thick and can be integrated into various cloths, curtains, tents and so on. This hybrid power textile, fabricated with a size of 4 cm by 5 cm, was demonstrated to charge a 2 mF commercial capacitor up to 2 V in 1 min under ambient sunlight in the presence of mechanical excitation, such as human motion and wind blowing. The textile could continuously power an electronic watch, directly charge a cell phone and drive water splitting reactions.**

In light of concerns about global warming and energy crises, searching for renewable energy resources that are not detrimental to the environment is one of the most urgent challenges to the sustainable development of human civilization<sup>1–3</sup>. Generating electricity from natural forces provides a superior solution to alleviate expanding energy needs on a sustainable basis<sup>4–9</sup>. With the rapid advancement of modern technologies, developing lightweight, flexible, sustainable and stable power sources remains both highly desirable and a challenge<sup>10–16</sup>. Solar irradiance and mechanical motion are clean and renewable energy sources<sup>17–24</sup>. Fabric-based materials are most common for humans and fibre-based textiles can effectively accommodate the complex deformations induced by body motion<sup>25–32</sup>. A smart textile that generates electrical power from absorbed solar irradiance and mechanical motion could be an important step towards next-generation wearable electronics.

Here, we present a foldable and sustainable power source by fabricating an all-solid hybrid power textile with economically viable materials and scalable fabrication technologies. Based on lightweight and low-cost polymer fibres, the reported hybrid power textile introduces a new module fabrication strategy by weaving it in a staggered way on an industrial weaving machine via a shuttle-flying process. Colourful textile modules with arbitrary size and various weaving patterns are demonstrated. Featuring decent breathability and robustness, the hybrid power textile was demonstrated to harvest energy simultaneously from ambient sunshine and human biomechanical movement in a wearable manner with or without encapsulation. The hybrid power textile is highly deformable in response to human motion. Mixed with colourful wool fibres, the hybrid power textile with a size of 4 cm by 5 cm is capable of stably delivering an output power of 0.5 mW with a wide range of loading resistances from 10 K $\Omega$  to 10 M $\Omega$  for a human walking under sunlight of intensity 80 mW cm<sup>-2</sup>. More importantly, the power textile can be also adopted for large-area application such as curtains and tents. Under ambient sunlight with movement of a car or wind blowing, the textile delivered sufficient power to charge

a 2 mF commercial capacitor up to 2 V in 1 min, continuously drive an electronic watch, directly charge a cell phone, as well as drive the water splitting reactions.

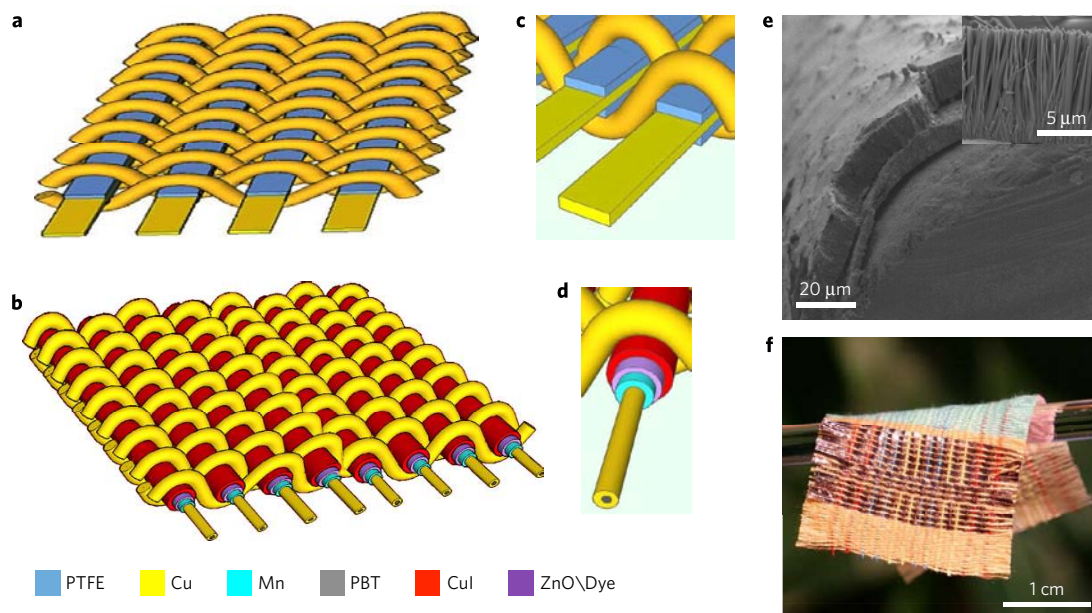
## Structural design

The main idea for the design is to use a polymer-fibre-based solar cell as the basic component in fabricating a triboelectric nanogenerator (TENG) so that both light and mechanical energy can be harvested simultaneously. The wearable all-solid hybrid power textile has a single-layer interlaced structure, which is a mixture of two polymer-wire-based energy harvesters, including both a fabric TENG to convert mechanical movement into electricity and a photovoltaic textile to gather power from ambient sunlight, as schematically illustrated in Fig. 1a,b, respectively. An enlarged view of the interlaced structure is presented for both the fabric TENG (Fig. 1c) and photovoltaic textile (Fig. 1d). A scanning electron microscopy (SEM) image of the photoanode in the photovoltaic textile is shown in Fig. 1e. A counter electrode was also made of Cu-coated polymer fibre. It is worth noting that assembled on polymer fibres via a low-temperature wet process, all of the electrodes are fully compatible with high-throughput textile processing. Strings of the wire-shaped photoanodes, Cu-coated polytetrafluoroethylene (PTFE) stripes and copper electrodes were woven in a staggered way on an industrial weaving machine to fabricate the hybrid power textile via a shuttle-flying process<sup>33</sup>, as shown in Supplementary Video 1. Here, to simplify the structural design of the hybrid power textile, both the photovoltaic textile and the fabric TENG employed copper as one of the electrodes. In the meanwhile, lightweight polymer fibre was chosen as the photoanode substrate of the photovoltaic component to improve its mechanical strength and flexibility, which greatly contribute to an effective combination of the two components in the hybrid power textile for simultaneously harvesting solar and mechanical energy. Figure 1f is a photograph of a piece of as-woven hybrid power textile mixed with commercial wool fibres, which is highly flexible, colourful and

<sup>1</sup>School of Materials Science and Engineering, Georgia Institute of Technology, Atlanta, Georgia 30332, USA. <sup>2</sup>College of Chemistry and Chemical Engineering, Chongqing University, Chongqing 400044, China. <sup>3</sup>Beijing Institute of Nanoenergy and Nanosystems, Chinese Academy of Sciences, National Center for Nanoscience and Technology (NCNST), Beijing 100083, China. <sup>†</sup>These authors contributed equally to this work.

\*e-mail: foxcqx@cqu.edu.cn; zhong.wang@mse.gatech.edu





**Figure 1 | Structural design of the hybrid power textile.** **a, b**, Schematic illustration of the hybrid power textile, which is a mixture of two textile-based all-solid energy harvesters: fabric TENG (**a**) and photovoltaic textile (**b**). **c, d**, Enlarged view of the interlaced structure of both the fabric TENG (**c**) and the photovoltaic textile (**d**). **e**, SEM image of the photoanode employed in the photovoltaic textile. Inset: the ZnO-nanowire arrays grown on the Mn-plated polymer wire substrate. **f**, A photograph of the hybrid power textile mixed with coloured wool wires.

wearable, with a thickness of about 0.32 mm. As demonstrated in Supplementary Video 2, it is highly sensitive and deformable in response to external mechanical excitation.

### Electrical signal generation

The working principle of the hybrid power textile for electrical signal generation can be elucidated from two aspects, namely, the photovoltaic textile to generate power from absorbed solar irradiance, and the fabric TENG to convert mechanical movement into electricity. In the first aspect, Supplementary Fig. 1 shows the working principle of the photovoltaic textile for solar energy harvesting. Excited by the photons, the holes and electrons on the ZnO\dye interface become separated and form hole–electron pairs. Then, the holes are injected into and travel along the axial direction in the all-solid hole-transporting layer, and are eventually collected by the wire-shaped counter electrode. Meanwhile, electrons are transported via the conducting band of the semiconductor, and finally collected by the photoanode. In this process, the absorbed solar energy was converted into electricity in the external load.

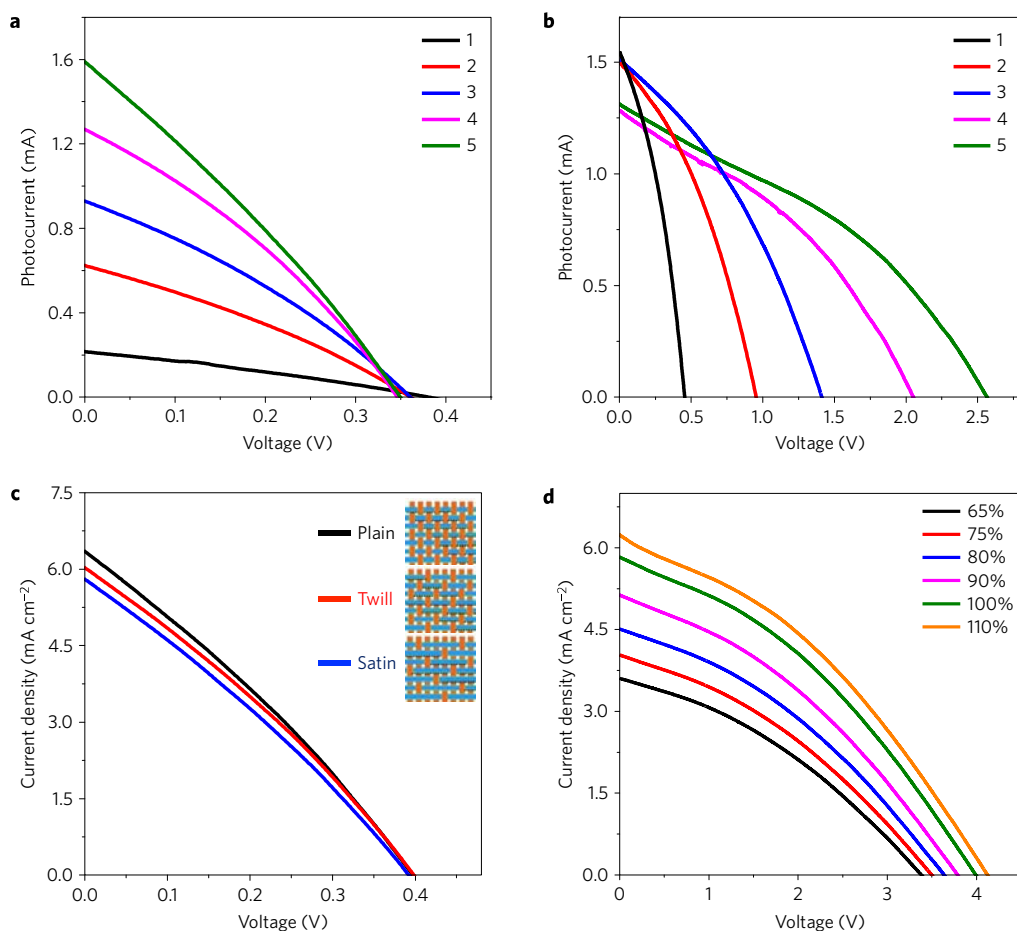
In the other aspect, as illustrated in Supplementary Fig. 2, taking two adjacent PTFE strips in the fabric TENG as an example, the interlaced copper electrodes can be brought into contact with PTFE stripes under a mechanical excitation applied to the power textile. The difference in electron affinity between the copper and PTFE causes a charge transfer at the interface, which results in positively charged copper and negatively charged PTFE. When the deformed fabric is released, the mechanical-motion-induced separation between the charged copper and PTFE results in a flow of electrons from the PTFE back-coated electrode to the copper strings<sup>34,35</sup>. Another return contact between the charged copper strings and PTFE strips generates a back flow of the electrons between the electrodes. This describes a full cycle of the electricity generation process of the fabric TENG for mechanical energy conversion.

### Optimization of the photovoltaic textile

To comprehensively investigate the hybrid power textile, the first step taken was to study and optimize the individual components. Different from orthodox mosaic-like solar modules composed of

small solar units, strings of the wire-shaped photoanodes and counter electrodes were woven in an interlaced manner, to form a single-layered textile. First, the electrical connection among the strings in the photovoltaic textile is a key factor to achieve a desired power output. As shown in Fig. 2a, in parallel connection, the current of the textile could be obviously improved by increasing the number of strings in the wire-shaped photoanode from one to five, without a serious negative impact on the textile voltage output. Meanwhile, the voltage output of the textile could be effectively improved by electrically connecting multiple strings in series, as demonstrated in Fig. 2b. As a result, the electrical output of the photovoltaic textile can be designed by tuning the number of strings and their electrical connections, providing great convenience in matching the power delivery from the fabric TENG part, and fulfilling the power requirements of various portable electronic devices.

The weaving patterns used in the photovoltaic textile also have an impact on the ambient solar energy conversion. To investigate this, three basic weaving patterns, plain, twill and satin, were employed to study the weaving-pattern-dependent photovoltaic performance of the textile. The detailed procedures for obtaining various weaving patterns for the power textile are presented in Supplementary Note 1. As elucidated in Fig. 2c, the photovoltaic textile works well in different weaving patterns. Also it is found that the overall energy conversion efficiency is a monotonically increasing function of the ratio of the effective illuminated area of the textile, namely, the textile projected area, as illustrated in Supplementary Fig. 3. Also, for the mixed textile composed of both wire-shape solar cells and other fibres, the projected area of other fibres was deducted in the calculation. Of the three basic weaving patterns, the plain-weave structure has the largest effective illumination area ratio of 96.1%, which delivers the highest current density of 6.35 mA cm<sup>-2</sup>, and the satin-weave pattern has the smallest effective illumination area ratio of 87.3%, corresponding to the lowest current output of 5.8 mA cm<sup>-2</sup>. The light-intensity-dependent photovoltaic performance of the textile was also studied, as shown in Fig. 2d. Here, 100% represents the standard one-sun condition, corresponding to a light intensity of 1,000 W m<sup>-2</sup>. A



**Figure 2 | Photovoltaic textile and its electrical output characterization.** **a, b**, Electrical output of the photovoltaic textile with an increasing number of strings connected in parallel (**a**) and in series (**b**). **c**, Weaving-pattern-dependent photovoltaic performance of the textile. **d**, Light-intensity-dependent photovoltaic performance of the as-fabricated photovoltaic textile. Here, 100% represents the standard one-sun condition, corresponding to a light intensity of  $1,000 \text{ W m}^{-2}$ .

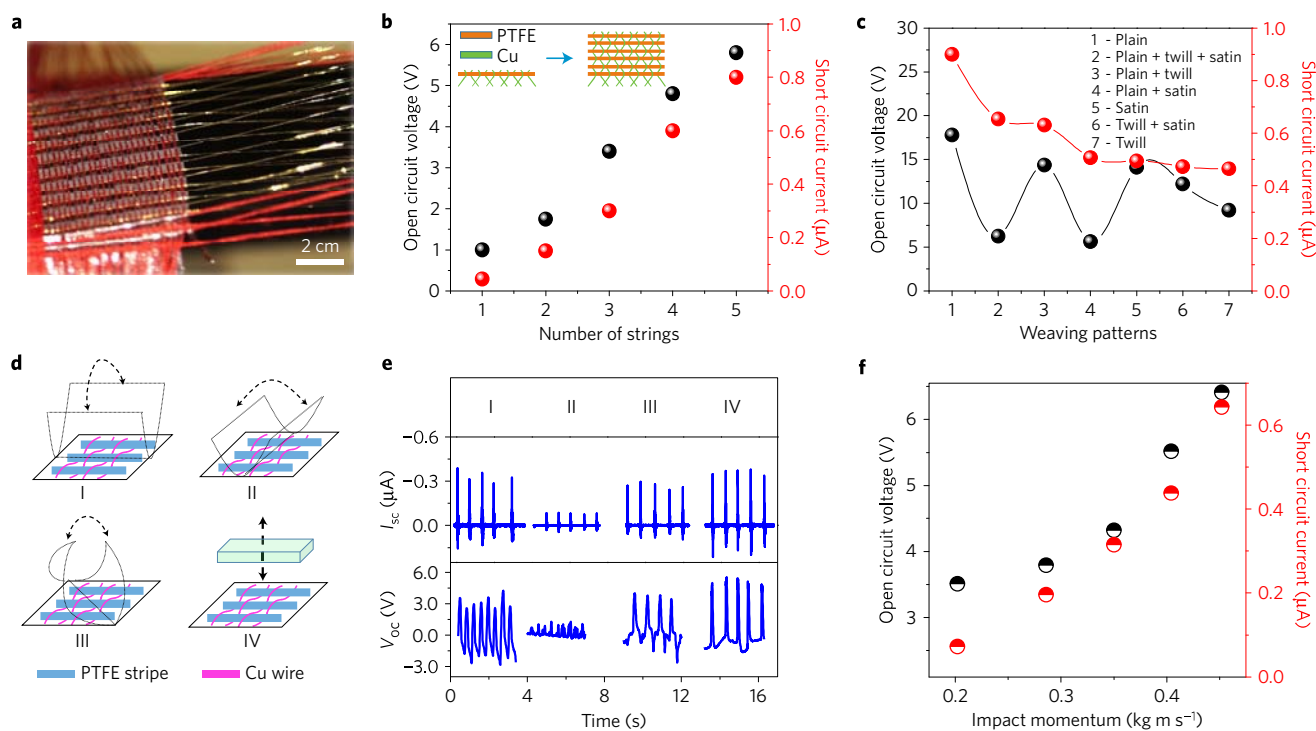
larger power output is expected at a higher light intensity for the photovoltaic textile.

### Optimization of the fabric TENG

Another pivotal component of the hybrid power textile, the fabric TENG, was also systematically investigated and optimized. Figure 3 reports a fibre-based TENG and characterization of its electrical output. The fabric TENG was fabricated via a shuttle-flying process, as pictured in Fig. 3a. Given that all the copper electrodes are simply connected in parallel, both the voltage and current output of the fabric TENG increase with an increasing number of PTFE stripes. Here, an average of nine deformation cycles were needed before reaching a stable electrical output, which is mainly ascribed to the requirement for surface charge accumulation and a saturation process in the course of contact electrification<sup>36,37</sup>. Furthermore, as a wearable textile, the weaving patterns of the fabric TENG are not only important for commercial applications, but also have a great impact on its electrical output, as demonstrated in Fig. 3b. Under mechanical excitation, such as hand clapping, the electrical output with three basic weaving patterns—plain, satin and twill, as well as their mixed patterns—was systematically investigated, as shown in Fig. 3c. To ensure quantitative and reproducible results in the experiment, the hand clapping was simulated by the impact force of a flat object with controllable heights of fall and acceleration, as elaborated in Supplementary Fig. 4. The results indicated that the output performance of the fabric TENG is dependent on the pattern, and works well for various weaving patterns. Of all the weaving patterns, the

plain-weave structure delivers the highest electrical output, while the twill-weave pattern exhibits the lowest. This is mainly attributed to a disparity in the effective contact area due to a variation in string-packing density between the PTFE stripes and copper electrodes in the weaving patterns<sup>38,39</sup>. Also it is interesting to find that the output performance of the fabric TENGs with mixed weaving patterns is intermediate between the corresponding basic patterns.

To systematically investigate the fabric TENG for mechanical energy conversion, four basic excitation modes were studied for the plain-woven fabric TENG, as illustrated in Fig. 3d. Excitation modes I and II are respectively to fold the textile parallel or perpendicular to the PTFE stripes. Mode III is to fold the textile along its diagonal line, while mode IV is to clap the textile with a flat surface, as illustrated in Supplementary Fig. 5. As presented in Fig. 3e, of all the excitation modes, the output power from mode IV is the highest, followed by mode I, and then modes II and III. In addition, a further step was taken to study the dependence of the electrical output on the impact momentum under excitation mode IV. As shown in Fig. 3f, the output power of fabric TENG is an increasing function of the external impact momentum. This observation is mainly attributed to the fact that, under external impact, both contact separation and relative sliding could occur between the electrodes and the PTFE stripes, where the relative-movement-induced friction would contribute a large portion to the total electrical output. At larger impact momentum, the air gaps between the electrodes and PTFE strips obviously decreased, which contributed to a larger electrical output<sup>40,41</sup>.



**Figure 3 | Fabric TENG and its electrical output characterization.** **a**, Photograph showing the textile weaving process. **b**, Influence of number of PTFE stripes on the textile electrical output. **c**, Weaving-pattern-dependent electrical output. **d, e**, Sketch showing the four basic excitation modes of the fabric TENG (**d**) and the corresponding directly measured electrical signals (**e**). **f**, Dependence of the electrical output of the fabric TENG on the impact momentum under working mode IV.

### Optimization of the hybrid power textile

After a comprehensive investigation of the individual components of the hybrid power textile, the electrical connections and hybridization patterns between components need also to be systematically optimized to maximize its energy efficiency. On one hand, due to a much lower internal impedance of the photovoltaic textile than that of the fabric TENG, the two are complementary in electricity generation and the latter delivers a relatively low current output in comparison to its voltage output<sup>42–45</sup>. A mismatch of the impedance would result in a large current leakage, which will seriously contaminate the final output power of the hybrid textile. As illustrated in Fig. 4a and Supplementary Fig. 6, three electrical connection strategies—in series, in parallel and regulated with unidirectional blocking diodes—were systematically designed and tested to optimize the electrical inter-connection between the triboelectric and photovoltaic textile components. Owing to the high internal impedance of the fabric TENG, a direct series connection between the two would lead to a dominance of the current and voltage by the fabric TENG, and thus a low electrical output of the hybrid power textile. In the case of a direct parallel inter-connection, due to the lower impedance of the photovoltaic textile, the fabric TENG will be shorted, rendering the hybrid power textile ineffective for mechanical energy harvesting. Taking this into account, functioning as a unidirectional blocking unit, a diode was employed as an inter-component connection to prevent this short circuit case, without harming the output of the solar cell as a large resistor would do, and thus effectively combining the output power of the two textile components, as shown in Supplementary Fig. 7.

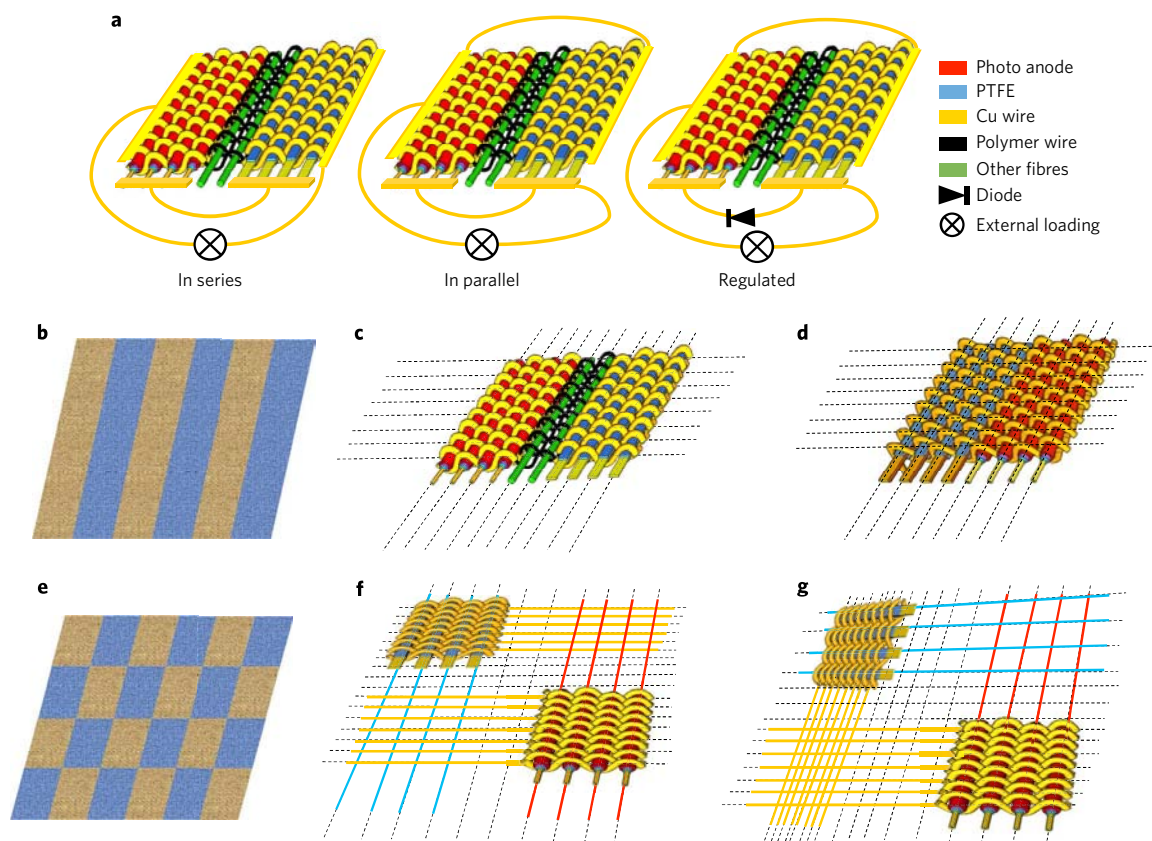
On the other hand, the hybridization pattern between components is another concern towards maximizing the textile conversion efficiency. Based on the diode-regulated electrical connection, two representative hybridization patterns, stripy and mosaic patterns, were extensively investigated for the hybrid power textile. Figure 4b shows an illustration of the power textile with a stripy pattern

produced by parallel weaving the triboelectric and photovoltaic textile components. Here, two configurations were specifically investigated for the stripy pattern. One is with the two textile components connected via insulating polymer wires (Fig. 4c), the other is with the two components sharing the copper electrodes (Fig. 4d).

The mosaic pattern is another common and basic weaving mode employed in textile production, as illustrated in Fig. 4e. Two configurations were also studied for the mosaic hybridization pattern. One used photoanodes of the photovoltaic textile interlaced with the copper electrodes of the fabric TENG (Fig. 4f), whereas the other used photoanodes interlaced with the PTFE stripes of the fabric TENG (Fig. 4g). As demonstrated in Supplementary Figs 8–11, different hybridization patterns under identical light and mechanical excitation could realize comparable electrical output. In relative terms, with the stripy hybridization pattern, the photovoltaic textile could be optimally employed in areas with greater light illumination, whereas the mosaic pattern is more suitable for applications in areas with uniformly dispersed light illumination. Furthermore, the electrode alignment of the fabric TENG should be designed to match the direction of larger strain change to deliver greater electrical power.

### Hybrid power textile as a flexible power source

Through optimization of the structure and weaving pattern of individual component textiles, and a further investigation of the inter-component electrical connection and structural hybridization, a piece of comprehensively optimized hybrid power textile was woven with a size of 4 cm by 5 cm, including a triboelectric component of 4 cm by 4 cm, and a photovoltaic component of 4 cm by 1 cm, mixed with wool fibres. The photovoltaic textile was made from 15 wire-shaped solar-cell units connected in series, with the photoanode in each unit having a length of 3 cm. With plain weaving patterns, the textiles were electrically connected via a diode as a regulated unit. For quantitative characterization, a linear



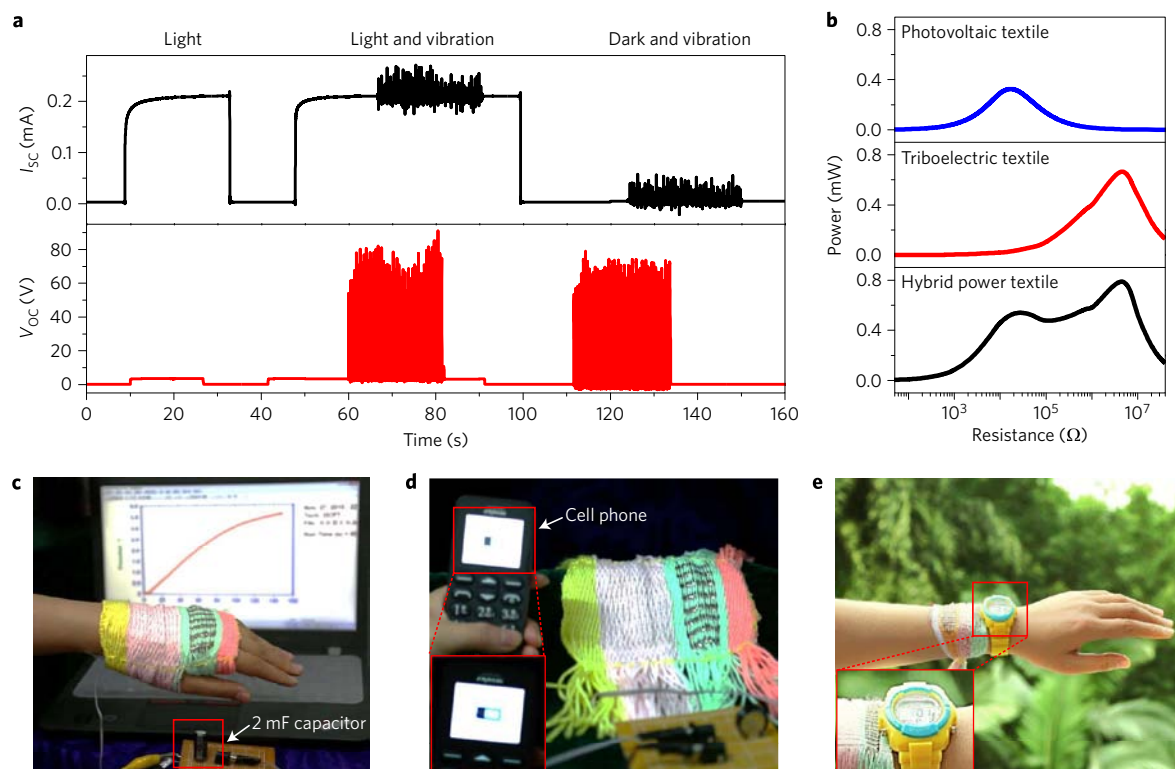
**Figure 4 | Electrical connection- and weaving-pattern-optimized hybrid textiles.** **a**, Illustration of three electrical connection strategies: in series, in parallel and regulated with blocking diodes. **b**, Schematic illustration of a power textile with a stripy pattern. **c**, Stripy pattern with fabric TENG and photovoltaic textile separated by insulating polymer wires. **d**, Stripy pattern with fabric TENG and photovoltaic textile sharing the copper electrodes. **e**, Illustration of a power textile with a mosaic pattern. **f**, Mosaic pattern with the copper electrodes of the fabric TENG interlaced with the photoanodes of the photovoltaic textile. **g**, Mosaic pattern with the PTFE stripes of the fabric TENG interlaced with the photoanodes of the photovoltaic textile.

motor with mechanical transmission kit was employed to mimic various environmental mechanical movements. Figure 5a shows the electrical output of the textile under different circumstances. When the textile is at rest in sunlight, the photovoltaic component is capable of delivering power by converting solar irradiance, which also works for the triboelectric part under mechanical excitation. When the textile is exposed to light with mechanical excitation, for instance, when people wear the textile and walk in sunlight, it can generate power simultaneously from both ambient sunshine and human biomechanical movement. Resistors were utilized as external loads to further investigate the output power of the hybrid textile. As displayed in Supplementary Fig. 12, all the current amplitudes drop with increasing load resistances owing to ohmic loss, whereas the voltages follow a reverse trend. As a result, the instantaneous peak power is maximized at matched load resistances for the hybrid textile and its components. The hybrid power textile with a size of 4 cm by 5 cm is capable of stably delivering an average output power of 0.5 mW under a remarkably wide range of load resistances from 10 K $\Omega$  to 10 M $\Omega$  for a human walking under a solar intensity of 80 mW cm<sup>-2</sup> (Fig. 5b). Here, the light intensity was calibrated by a standard silicon solar cell, as certified in Supplementary Fig. 13. Consequently, via hybridization optimization, not only was the output power evidently enhanced compared to that of individual components, but also the range of load resistances was greatly expanded, which is a significant improvement in using the hybrid textile as a power source since the operational resistances of small electronics vary considerably.

To demonstrate the capability and feasibility of the hybrid power textile as a flexible and sustainable power source for practical

applications, a colourful, lightweight, larger thin textile with various weaving patterns was fabricated into cloths. Under natural daylight with human biomechanical movement, such as hand shaking, the power delivered from the woven fabric is capable of charging a 2 mF commercial capacitor up to 2 V in 1 min (Fig. 5c and Supplementary Fig. 14 and Supplementary Video 3). It can also act as a wearable power source to directly charge a cell phone (Fig. 5d and Supplementary Video 4), as well as continuously drive an electronic watch (Fig. 5e and Supplementary Video 5). It is worth noting that the hybrid power textile is not limited to wearable applications. It can also act as a piece of flag, harvesting energy from sunlight and ambient wind blowing, and the delivered power is also capable of charging personal electronics as well as driving electrochemical reactions for self-powered water splitting (Supplementary Fig. 15 and Supplementary Video 6). In addition, the hybrid power textile was also demonstrated to generate power from weak sunlight and wind from a moving car in a city location on a cloudy day (Supplementary Fig. 16 and Supplementary Video 7), which also indicates its decent capability of working even in a harsh environment.

As a sustainable power source, the robustness of the hybrid power textile was also systematically investigated. As elaborated in Supplementary Note 2, it had sufficient mechanical durability and chemical stability for practical applications. In addition, the influence of environmental humidity on the power textile was also studied. As demonstrated in Supplementary Note 3, at fixed pressure and applied impact, the electrical output of the triboelectric component gradually decreased to ~73.5% of its original value as the relative humidity increased from 10% to 90%. This is mainly attributed to the negative impact of humidity on the triboelectric



**Figure 5 | Demonstration of the power textile to drive portable electronics.** **a**, Electrical output of the wearable all-solid hybrid power textile under various circumstances. **b**, Dependence of the output power of hybrid power textile as well as individual components on the load resistances. Under natural daylight with mechanical excitation, the delivered power from a small piece of hybrid power textile is capable of charging a 2 mF commercial capacitor up to 2 V in 1 min **(c)**, directly charging a cell phone **(d)** and continuously powering an electronic watch in a wearable manner **(e)**.

charging process<sup>46,47</sup>. It is worth mentioning that the performance degradation can be recovered if the textile is subsequently dried, and this negative impact can be easily resolved by device encapsulation.

## Conclusions

In summary, we have presented a lightweight, flexible, foldable and sustainable power source by fabricating an all-solid wearable hybrid power textile in a staggered way on an industrial weaving machine via a shuttle-flying process. Based on the lightweight and low-cost polymer fibres, the reported hybrid power textile introduces an innovative module fabricating strategy with greatly reduced device thickness, weight, total cost and suitability for mass production. Having an ultrathin single-layered interlaced structure with a thickness of 320  $\mu\text{m}$ , the power textile is highly deformable, breathable, and easy to transport and store. Under ambient sunlight with mechanical excitation, such as human motion, car movement and wind blowing, the as-woven textile was capable of generating sufficient power for various practical applications, including charging a 2 mF commercial capacitor up to 2 V in 1 min, continuously driving an electronic watch, directly charging a cell phone and driving the water splitting reactions. The hybrid power textile could be extensively applied not only to self-powered electronics but also possibly to power generation on a larger scale.

## Methods

**Fabrication of the photoanode.** A layer of copper was first deposited on insulated polybutylene terephthalate (PBT) polymer wire with a diameter of 0.26 mm via a chemical plating method<sup>48</sup>. Mn was then plated on the Cu-coated wire substrates via an electroplating method. A layer of ZnO-nanowire arrays was grown on the Mn-plated substrate in a solution of zinc acetate (0.03 M) and hexamethylene tetramine (0.03 M) at 95 °C for 10 h. After cleaning with de-ionized water and drying in vacuum, the as-prepared photoanode was sensitized in an ethanol solution of N719 (Solaronix, Switzerland) for 24 h. After dye sensitization, a layer of CuI was deposited onto the ZnO nanoarrays as the

hole-transfer material, using CuI/CH<sub>3</sub>CN solution at 130 °C under a N<sub>2</sub> atmosphere, thus avoiding possible contamination of traditional liquid-state electrolyte onto human skin<sup>49–51</sup>.

**Fabrication of PTFE electrode.** To fabricate the wire-shaped PTFE electrodes, copper foil (thickness  $\sim 30 \mu\text{m}$ ) sandwiched between two polytetrafluoroethylene (PTFE) layers (thickness  $\sim 33 \mu\text{m}$ ) was cut into narrow strips with a width of 0.3 mm via a slicing machine. The copper layer was lead out from the tip of the strips via conductive silver paste and copper wire with a diameter of 33  $\mu\text{m}$ .

**Weaving process for the hybrid power textile.** PBT wires of different thickness coated with a layer of chemical-plated Cu were employed as the counter electrodes for both the TENG and the photovoltaic textile. Different wire-shaped electrodes were woven into plain, twill and satin patterns on an industrial weaving machine via a shuttle-flying process. The tensional stress on the strings was finely controlled and kept constant during the whole weaving process by means of a specially designed pulley system. To stabilize the contact status of strings inside the textile, the edge of the textile is fixed by sticking strings of photoanodes onto strings of counter electrodes. For the fabric TENG and photovoltaic textile, wire-shaped counter electrodes were employed as the fixed shuttle, and photoanodes or PTFE electrodes were inserted as the flying shuttle. To weave different hybridized patterns, the fixed shuttle or flying shuttle could alternate with others. It worth noting that, due to the woven fibre structure, different power sources could be integrated and hybridized freely in a single piece, which could not only harvest the ambient energy efficiently via a thin and light textile, but also provide comfortable and safe contact to human skin, owing to its excellent flexibility, breathability and freedom from electrolyte leakage. The fabrication procedures of the hybrid power textile are straightforward and compatible with possible large-scale manufacturing. More details of fabric weaving can be found in Supplementary Video 1, Supplementary Fig. 6 and Supplementary Note 1.

**Weaving strategy for the stripy pattern.** For the stripy pattern with TENG and photovoltaic textile separated by insulative polymer wires, polymer wires coated with a segmentally distributed Cu layer were employed as the fixed shuttle in the longitudinal direction, while the wire-shaped photoanodes and PTFE electrodes were respectively inserted as the flying shuttle into different segments in the latitudinal direction. For the stripy pattern with fabric TENG and photovoltaic

textile sharing the copper electrodes, Cu-coated polymer wires were employed as the fixed shuttle in the longitudinal direction, while the wire-shaped photoanodes and PTFE electrodes were inserted as the flying shuttle in the latitudinal direction.

**Weaving strategy for the mosaic pattern.** For the mosaic pattern with the copper electrodes of fabric TENG interlaced with the photoanode of photovoltaic textile, Cu-coated polymer wires were employed as the fixed shuttle in the longitudinal direction. Wire-shaped photoanode and PTFE electrode were inserted as flying shuttle in the latitudinal direction, sectionally, while their Cu cores were led out and aligned in different directions. For the mosaic pattern with the PTFE stripes of fabric TENG interlaced with the photoanodes of the photovoltaic textile, Cu-coated polymer wires and photoanodes with their copper cores leading out were employed as the fixed shuttle and aligned in the longitudinal direction. Wire-shaped PTFE electrodes with their copper cores leading out and other Cu-coated polymer wires were inserted as the flying shuttle in the latitudinal direction.

**Structure and performance characterization.** The morphology of the electrode was characterized using scanning electron microscopy (SEM) (S570, Hitachi). The photo-electrochemical tests were conducted on an electrochemical working station (CHI660D, Shanghai Chenhua). The ambient light intensity of 80 mW cm<sup>-2</sup> was calibrated by a standard silicon solar cell. The effective area employed in the photocurrent density calculation was the projected area of the photoanodes. For a quantitative characterization of the hybrid textile for power delivery, a linear motor with mechanical transmission kit was employed to mimic various mechanical movements.

Received 19 April 2016; accepted 8 August 2016;  
published 12 September 2016

## References

- Wang, Z. L. & Song, J. Piezoelectric nanogenerators based on zinc oxide nanowire arrays. *Science* **312**, 242–246 (2006).
- Qin, Y., Wang, X. & Wang, Z. L. Microfibre-nanowire hybrid structure for energy scavenging. *Nature* **451**, 809–813 (2008).
- Tian, B. *et al.* Coaxial silicon nanowires as solar cells and nanoelectronic power sources. *Nature* **449**, 885–889 (2007).
- Zhu, G., Chen, J., Zhang, T., Jing, Q. & Wang, Z. L. Radial-arrayed rotary electrification for high performance triboelectric generator. *Nat. Commun.* **5**, 3426 (2014).
- Grazel, M. Photoelectrochemical cells. *Nature* **414**, 338–344 (2001).
- Yang, R., Qin, Y., Dai, L. & Wang, Z. L. Power generation with laterally packaged piezoelectric fine wires. *Nat. Nanotech.* **4**, 34–39 (2009).
- Wang, X., Song, J., Liu, J. & Wang, Z. L. Direct-current nanogenerator driven by ultrasonic waves. *Science* **316**, 102–105 (2007).
- Zhong, J. *et al.* Fiber-based generator for wearable electronics and mobile medication. *ACS Nano* **8**, 6273–6280 (2014).
- Chen, J. *et al.* Harmonic-resonator-based triboelectric nanogenerator as a sustainable power source and a self-powered active vibration sensor. *Adv. Mater.* **25**, 6094–6099 (2013).
- Son, D. *et al.* Multifunctional wearable devices for diagnosis and therapy of movement disorders. *Nat. Nanotech.* **9**, 397–404 (2014).
- Xu, S. *et al.* Soft microfluidic assemblies of sensors, circuits, and radios for the skin. *Science* **344**, 70–74 (2014).
- Park, S. I. *et al.* Soft, stretchable, fully implantable miniaturized optoelectronic systems for wireless optogenetics. *Nat. Biotechnol.* **33**, 1280–1286 (2015).
- Weng, W., Chen, P., He, S., Sun, X. & Peng, H. Smart electronic textiles. *Angew. Chem. Int. Ed.* **55**, 6140–6169 (2016).
- Xu, S. *et al.* Stretchable batteries with self-similar serpentine interconnects and integrated wireless recharging systems. *Nat. Commun.* **4**, 1543 (2013).
- Zhang, Z. *et al.* Weaving efficient polymer solar cell wires into flexible power textiles. *Adv. Energy Mater.* **4**, 1301750 (2014).
- Kim, K. N. *et al.* Highly stretchable 2D fabrics for wearable triboelectric nanogenerator under harsh environments. *ACS Nano* **9**, 6394–6400 (2015).
- Lee, M. R. *et al.* Solar power wires based on organic photovoltaic materials. *Science* **324**, 232–235 (2009).
- Huynh, W. U., Dittmer, J. J. & Alivisatos, A. P. Hybrid nanorod-polymer solar cells. *Science* **295**, 2425–2427 (2002).
- Xu, C., Wang, X. & Wang, Z. L. Nanowire structured hybrid cell for concurrently scavenging solar and mechanical energies. *J. Am. Chem. Soc.* **131**, 5866–5872 (2009).
- Wang, Z. L., Chen, J. & Lin, L. Progress in triboelectric nanogenerators as a new energy technology and self-powered sensors. *Energy Environ. Sci.* **8**, 2250–2282 (2015).
- Fan, Z. & Javey, A. Photovoltaics: solar cells on curtains. *Nat. Mater.* **7**, 835–836 (2008).
- Yoon, J. *et al.* Ultrathin silicon solar microcells for semitransparent, mechanically flexible and microconcentrator module designs. *Nat. Mater.* **7**, 907–915 (2008).
- Zheng, L. *et al.* A hybridized power panel to simultaneously generate electricity from sunlight, raindrops, and wind around the clock. *Adv. Energy Mater.* **5**, 1501152 (2015).
- Yang, Y. *et al.* Hybrid energy cell for degradation of methyl orange by self-powered electrocatalytic oxidation. *Nano Lett.* **13**, 803–808 (2013).
- Zeng, W. *et al.* Fiber-based wearable electronics: a review of materials, fabrication, devices, and applications. *Adv. Mater.* **26**, 5310–5336 (2014).
- Service, R. F. Technology-electronic textiles charge ahead. *Science* **301**, 909–911 (2003).
- Stuart, M. A. C. *et al.* Emerging applications of stimuli-responsive polymer materials. *Nat. Mater.* **9**, 101–113 (2010).
- Cherenack, K. *et al.* Smart textiles: challenges and opportunities. *J. Appl. Phys.* **112**, 091301 (2012).
- Hamedi, M., Forchheimer, R. & Inganäs, O. Towards woven logic from organic electronic fibres. *Nat. Mater.* **6**, 357–362 (2007).
- Avila, A. G. & Hinestroza, J. P. Smart textiles: tough cotton. *Nat. Nanotech.* **3**, 458–459 (2008).
- Rossi, D. D. *et al.* Electronic textiles: a logical step. *Nat. Mater.* **6**, 328–329 (2007).
- Hu, L. & Cui, Y. Energy and environmental nanotechnology in conductive paper and textiles. *Energy Environ. Sci.* **5**, 6423–6435 (2012).
- Zhang, N. *et al.* A wearable all-solid photovoltaic textile. *Adv. Mater.* **28**, 263–269 (2016).
- Fan, X. *et al.* Ultrathin, rollable, paper-based triboelectric nanogenerator for acoustic energy harvesting and self-powered sound recording. *ACS Nano* **9**, 4236–4243 (2015).
- Zi, Y. *et al.* Triboelectric-pyroelectric-piezoelectric hybrid cell for high-efficiency energy-harvesting and self-powered sensing. *Adv. Mater.* **27**, 2340–2347 (2015).
- Zhou, Y. *et al.* *In situ* quantitative study of nanoscale triboelectrification and patterning. *Nano Lett.* **13**, 2771–2776 (2013).
- Zhou, Y. *et al.* Manipulating nanoscale contact electrification by an applied electric field. *Nano Lett.* **14**, 1567–1572 (2014).
- Baytekin, H. T. *et al.* The mosaic of surface charge in contact electrification. *Science* **333**, 308–312 (2011).
- Grzybowski, B. A., Winkleman, A., Wiles, J. A., Brumer, Y. & Whitesides, G. M. Electrostatic self-assembly of macroscopic crystals using contact electrification. *Nat. Mater.* **2**, 241–245 (2003).
- Niu, S. *et al.* Theory of sliding-mode triboelectric nanogenerators. *Adv. Mater.* **25**, 6184–6193 (2013).
- Niu, S. & Wang, Z. L. Theoretical systems of triboelectric nanogenerators. *Nano Energy* **14**, 161–192 (2015).
- Yang, W. *et al.* Harvesting energy from the natural vibration of human walking. *ACS Nano* **7**, 11317–11324 (2013).
- Zi, Y. *et al.* Effective energy storage from a triboelectric nanogenerator. *Nat. Commun.* **7**, 10987 (2016).
- Zhang, C., Tang, W., Han, C., Fan, F. & Wang, Z. L. Theoretical comparison, equivalent transformation, and conjunction operations of electromagnetic induction generator and triboelectric nanogenerator for harvesting mechanical energy. *Adv. Mater.* **26**, 3580–3591 (2014).
- Niu, S., Wang, X., Yi, F., Zhou, Y. S. & Wang, Z. L. A universal self-charging system driven by random biomechanical energy for sustainable operation of mobile electronics. *Nat. Commun.* **6**, 8975 (2015).
- Pence, S., Novotny, V. J. & Diaz, A. F. Effect of surface moisture on contact charge of polymers containing ions. *Langmuir* **10**, 592–596 (1994).
- Nguyen, V. & Yang, R. Effect of humidity and pressure on the triboelectric nanogenerator. *Nano Energy* **2**, 604–608 (2013).
- Feng, H. *et al.* From wires to veins: wet-process fabrication of light-weight reticulation photoanodes for dye-sensitized solar cells. *Chem. Commun.* **50**, 3509–3511 (2014).
- Fu, Y. *et al.* Integrated power fiber for energy conversion and storage. *Energy Environ. Sci.* **6**, 805–812 (2013).
- Fu, Y. *et al.* Conjunction of fiber solar cells with groovy micro-reflectors as highly efficient energy harvesters. *Energy Environ. Sci.* **4**, 3379–3383 (2011).
- Fan, X. *et al.* Wire-shaped flexible dye-sensitized solar cells. *Adv. Mater.* **20**, 592–595 (2008).

## Acknowledgements

Research was supported by the Hightower Chair foundation, KAUST, the ‘Thousands Talents’ Program for pioneer researcher and his innovation team, China, National Natural Science Foundation of China (Grant No. 51432005, 5151101243, 51561145021) and the National Key R&D Project from the Minister of Science and Technology (2016YFA0202704). X.F. and Y.H. also would like to acknowledge the Program for New

Century Excellent Talents in University of China (NCET-13-0631) and the Fundamental Research Funds for the Central Universities (106112016CDJZR225514).

### Author contributions

J.C., X.F. and Z.L.W. conceived the idea, designed the experiment and guided the project. Y.H., J.C., X.F., N.Z., R.L., H.Z. and C.T. fabricated the device and performed electrical measurements. J.C., X.F. and Z.L.W. analysed the experimental data, drew the figures and prepared the manuscript.

### Additional information

Supplementary information is [available for this paper](#). Reprints and permissions information is available at [www.nature.com/reprints](http://www.nature.com/reprints). Correspondence and requests for materials should be addressed to X.F. or Z.L.W.

### Competing interests

The authors declare no competing financial interests.

ARTICLE

Received 25 May 2015 | Accepted 10 Sep 2015 | Published 16 Oct 2015

DOI: 10.1038/ncomms9617

OPEN

# Towards a general diastereoselective route to oxabicyclo[3.2.1]octanes via a gold-catalysed cascade reaction

Junkai Fu<sup>1,2</sup>, Yueqing Gu<sup>1,2</sup>, Hao Yuan<sup>1,2</sup>, Tuoping Luo<sup>2</sup>, Song Liu<sup>3</sup>, Yu Lan<sup>3</sup>, Jianxian Gong<sup>1,2</sup> & Zhen Yang<sup>1,2,4</sup>

The development of an efficient diastereoselective synthesis of the oxabicyclo[3.2.1]octane ring system bearing two oxygenated quaternary chiral centres represents a significant challenge. This motif can be found in a wide range of natural products with significant biological activities. Here we report the synthesis of such kind of scaffold using a cyclohexane-*trans*-1,4-diol with an alkyne side chain in the presence of Au(I) catalyst. This is a domino process in which two C-H, two C-O and one C-C bond is assembled through a sequence of cyclization/semi-pinacol rearrangements. This strategy has been successfully applied to the asymmetric formal total synthesis of (+)-cortistatins.

<sup>1</sup>Laboratory of Chemical Genomics, School of Chemical Biology and Biotechnology, Peking University Shenzhen Graduate School, Shenzhen 518055, China. <sup>2</sup>Key Laboratory of Bioorganic Chemistry and Molecular Engineering of Ministry of Education, Beijing National Laboratory for Molecular Science (BNLMS) and Peking-Tsinghua Center for Life Sciences, Peking University, Beijing 100871, China. <sup>3</sup>School of Chemistry and Chemical Engineering, Chongqing University, Chongqing 400030, China. <sup>4</sup>Key Laboratory of Marine Drugs, Chinese Ministry of Education, School of Medicine and Pharmacy, Ocean University of China, 5 Yushan Road, Qingdao 266003, China. Correspondence and requests for materials should be addressed to Z.Y. (email: zyang@pku.edu.cn) or to J.G. (email: gongjx@pku.edu.cn) or to Y.L. (email: lanyu@cqu.edu.cn).



A wide variety of intriguing natural products with 8-oxabicyclo[3.2.1]octane motifs (1–8, Fig. 1) have been shown to exhibit significant biological activities.

The cortistatins (1–4) are a family of 11 steroidal alkaloids, with unique structures and prominent biological activities<sup>1,2</sup>. They were isolated from the marine sponge *Corticium simplex* by the Kobayashi group in 2006 and 2007. Among them, cortistatin A (1) has proved to be the strongest inhibitor of the migration and proliferation of human umbilical vein endothelial cells at concentrations as low as 100 pM, and with a therapeutic index of over 3,300. Englerin A (5) is isolated from the stem bark of *Phyllanthus engleri* in Tanzania. It is a guaiane sesquiterpene and has been reported to selectively inhibit the growth of renal cancer cell lines at the nanomolar level<sup>3</sup>. Platensimycin (6) comes from the fermentation broth of *Streptomyces platensis*. It is a broad-spectrum antibiotic against Gram-positive bacteria and exerts its antibacterial effect by selectively inhibiting the  $\beta$ -ketoacyl-(acyl-carrier-protein)synthase (FabF), one of the key enzymes in bacterial fatty acid biosynthesis<sup>4,5</sup>. Hedyosumin C (7), isolated from *Hedyosmum orientale*, represents a novel type of sesquiterpenoid with cytotoxic activity against human lung adenocarcinoma and leukaemia tumour cell lines<sup>6</sup>. Linearol (8), isolated from dried *Dictyota Indica*, has a significant inhibitory effect on herbivores<sup>7</sup>.

The biological properties, together with their complex structures have elevated them to be prominent targets for total synthesis<sup>8–13</sup>. However, the challenges associated with the diastereoselective synthesis of the 8-oxabicyclo[3.2.1]octane core reside in construction of the two oxygenic quaternary chiral centres. A general diastereoselective route for the development of divergent synthetic processes to produce assortments of skeletally diverse and densely functionalized oxabicyclo[3.2.1]octane scaffolds is always highly desirable, despite the excellent progress made thus far<sup>14–24</sup>. Herein we report a general strategy using a semi-pinacol rearrangement cascade reaction of substituted 1-ethynylcyclohexane-*trans*-1,4-diols. This goes via a highly strained oxonium ion generated *in situ* and is derived from nucleophilic addition of a hydroxyl group onto a gold-activated alkyne. This chemistry has been successfully applied to the asymmetric formal total synthesis of (+)-cortistatins.

The cascade reaction<sup>25</sup> allows several bond-forming and/or -cleaving events to occur in a single synthetic operation, thus minimizing the costs and waste. Over the past 10 years, gold catalysts have risen to the forefront of cycloisomerization due to

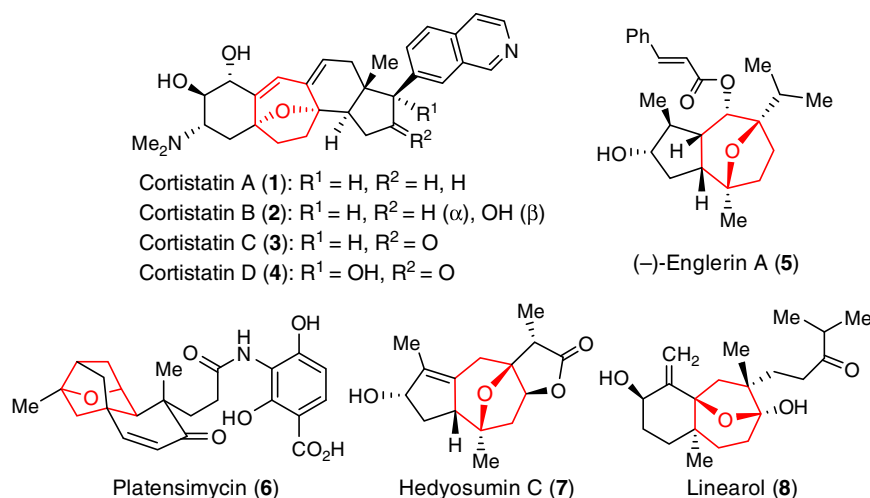
their high activities and the mild reaction conditions, and a wide variety of organic scaffolds are available by these methods<sup>26–29</sup>. As a soft Lewis-acid catalyst, gold complex could selectively activate alkynes and promote the addition of nucleophiles<sup>30</sup>. In this context, the intramolecular nucleophilic addition of a hydroxyl group to a Au-activated carbon–carbon triple bond, followed by a compatible synthetic transformation has proven to be a powerful method for the synthesis of structurally diverse scaffolds (Fig. 2a)<sup>31–33</sup>.

On the other hand, 1,2-alkyl migration has been considered as a key element in numbers of novel gold-catalysed cascade reactions<sup>34</sup>, and it could be induced through oxonium ions<sup>35,36</sup> or gold carbenoids<sup>37–40</sup>. Recently, the electrophile-induced intermolecular addition of enol ether, followed by semi-pinacol-type 1,2-migration of the resulting oxonium ions has been well documented to be a powerful method to synthesize several complex natural products by Tu and colleagues<sup>41</sup> (Fig. 2b). In accordance with our goal, an oxygenated quaternary chiral center was generated from the corresponding hydroxyl vinyl ether.

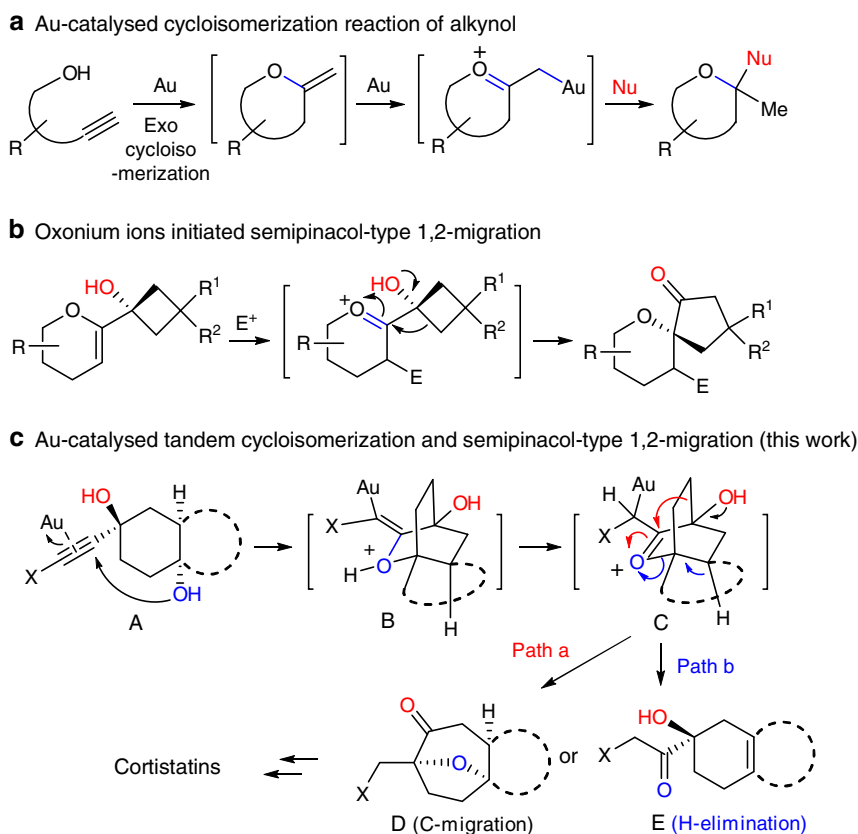
On the basis of previous work in our laboratory using gold-catalysed tandem reactions of alkynes with internal nucleophiles<sup>42,43</sup>, we wondered if oxabicyclo[3.2.1]octane scaffolds **D** could be constructed from 1-ethynyl-cyclohexane-*trans*-1,4-diol **A** via a gold-catalysed cascade reaction (Fig. 2c). Formation of the tricyclic oxabicyclo[3.2.1]octane scaffold **D** was envisioned to come about from an intramolecular 6-exo-dig nucleophilic addition of the OH group in substrate **A** onto the Au-activated triple bond, and the resultant exo-cyclic enol ether **B** was expected to undergo an isomerization to the highly strained oxonium ion **C**, followed by a semi-pinacol-type 1,2-alkyl migration (path a) to give the oxabicyclo[3.2.1]octane scaffold **D**, or via a  $\beta$ -hydrogen elimination (path b) to the bicyclic product **E**. Whilst this proposed cascade reaction is unknown, there have been reports of Au-catalysed nucleophilic addition of hydroxyl groups to alkynes<sup>44</sup>, Au-catalysed isomerization of an exo-cyclic enol ether<sup>45,46</sup> and the oxonium-induced semi-pinacol rearrangement<sup>34,41</sup>.

## Results

**Optimization of reaction conditions.** Model substrates were first used to test the feasibility of the proposed strategy outlined in Fig. 2 (Table 1). To this end, 1-ethynyldecahydro-naphthalene-1,4-diol **9** was treated with AuCl and AuCl<sub>3</sub> in 1,2-dichloroethane

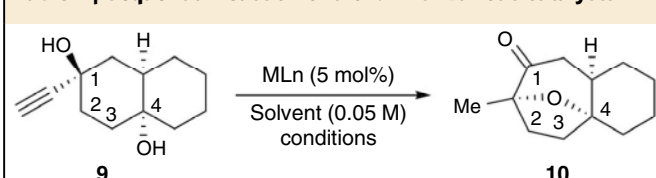


**Figure 1 | Representative natural products containing oxa-bridged seven-membered carbocycles.** Selected biologically active natural products bearing functionalized 8-oxabicyclo[3.2.1]octane rings.



**Figure 2 | Gold-catalysed sequential reactions.** (a) Au-catalysed cycloisomerization of alkynol to generate structurally diverse oxacycles; (b) semi-pinacol-type 1,2-migration of oxonium ions to construct oxaspirocycles; (c) our strategy to access oxabicyclo[3.2.1]octane ring systems via Au-catalysed annulations and the application to cortistatins synthesis.

**Table 1 | Sequential reaction of diol **9** with various catalysts\*.**



Entry	Catalyst	Solvent	Time	Yield (%) <sup>†</sup>
1	AuCl	DCE	1h	69
2	AuCl <sub>3</sub>	DCE	1h	48
3	lprAuNTf <sub>2</sub>	DCE	2h	58
4	Ph <sub>3</sub> PAuNTf <sub>2</sub>	DCE	2h	72
5	Ph <sub>3</sub> PAuSbF <sub>6</sub>	DCE	2h	70
6	[(Ph <sub>3</sub> PAu) <sub>3</sub> O]BF <sub>4</sub>	DCE	2h	0
7	Ph <sub>3</sub> PAuNTf <sub>2</sub>	toluene	2h	78
8	Ph <sub>3</sub> PAuNTf <sub>2</sub>	DCM	2h	85
9 <sup>‡</sup>	Ph <sub>3</sub> PAuNTf <sub>2</sub>	DCM	2h	83
10	K <sub>2</sub> PtCl <sub>6</sub>	DCM	2h	0
11	PtCl <sub>2</sub>	DCM	2h	28
12	NIS	DCM	2h	0
13	PTSA	DCM	2h	0
14	none	DCM	2h	0

DCE, dichloroethane; NIS, *N*-iodosuccinimide; PTSA, *p*-toluenesulfonamide.

\*1-Ethynylcyclohexane-*trans*-1,4-diol **9** (0.2 mmol) and MLn (5 mol%) in solvent (5 ml), stirred at room temperature.

<sup>†</sup>Product **10** was isolated via flash column chromatography.

<sup>‡</sup>MLn (2.5 mol%).

at room temperature. This gave the desired 8-oxabicyclo[3.2.1]octane **10** in 69% and 48%, respectively (entries 1 and 2; Table 1). Tests revealed Ph<sub>3</sub>PAuNTf<sub>2</sub> (5 mol%) to be the

optimum gold catalyst when used at room temperature for 2 h and gave **10** in 72% yield (entries 3–6; Table 1). In terms of solvent, dichloromethane (DCM) gave better results than dichloroethane and toluene (entries 7 and 8). Decreasing the loading of Ph<sub>3</sub>PAuNTf<sub>2</sub> had little effect on the yield (entry 9). Platinum catalysts can also be used for alkyne-based hydroelement addition reactions. However, in this case only starting material was recovered when K<sub>2</sub>PtCl<sub>6</sub> was used and for PtCl<sub>2</sub> a yield of only 28% was observed (entries 10 and 11). Alternative Lewis acid or Brønsted acid, such as *N*-iodosuccinimide or *p*-toluenesulfonamide had no effect on the reaction, however substrate decomposition was observed when the reaction time was extended or the temperature increased (entries 12 and 13). A control experiment in the absence of gold catalyst gave no desired product, indicating that Ph<sub>3</sub>PAuNTf<sub>2</sub> is essential (entry 14). In light of these results, the optimized conditions for this reaction are Ph<sub>3</sub>PAuNTf<sub>2</sub> (2.5 mol%) in DCM at room temperature. The experimental conditions were particularly practical because neither flame-dried glassware, an inert atmosphere nor carefully dried solvent were required.

**Substrate scope.** A number of substituted 1-ethynyldecahydronaphthalene-1,4-diols (Table 2) were used to assess the generality of this reaction. These substrates bearing electron-withdrawing groups, such as bromide, iodide and ester on the terminal alkyne were synthesized (**11a–11c**). The corresponding products **12a–12c** were obtained in good yields, allowing the further functional group inter-conversion to facilitate the synthetic transformation (entries 1–3). In addition, when the terminal alkynes had phenyl, allyl or alkyl substituents (**11d–11f**), the expected annulated products (**12d–12f**) were formed albeit in

slightly lower yields (entries 4–6). Notably, when the alkyne moiety had an alkyl group, hydrogen elimination was a potential competing reaction and gave **13f** in 21% yield (entry 6).

Methoxyethoxymethyl (MEM) protection of the hydroxyl group at C4 led to product **12g** in 65% yield, indicating the reaction might proceed via the intramolecular nucleophilic addition of the MEM ether to the Au-activated alkyne, followed by deprotection of the MEM group (entry 7). Furthermore, the [6,5]-fused bicyclic substrates also underwent the sequential reaction to give the desired products in excellent yields (entries 8–11). The relative stereochemistry of **12k** was confirmed by X-ray crystallography. The bulky alkyl group and electronic effect of the ester in substrates **11c**, **11f** and **11k** meant that the reaction had to be carried out at higher temperature (70 °C) to accelerate the addition of the tertiary hydroxyl group to the triple bond.

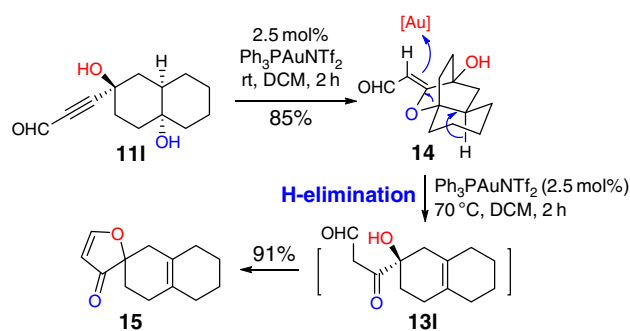
It is worthwhile to mention that when substrate **11l** was used, **14** was obtained in 85% yield. This supports our proposed formation of intermediate **B** (Fig. 2c). Interestingly, further treatment of **14** with gold catalyst at high temperature (70 °C) afforded **15** in 91% yield, presumably through intermediate **13l** (Fig. 3). Alternative acids, such as TsOH, HCl, AcOH, AlCl<sub>3</sub> and AlMe<sub>3</sub>, all failed to promote this transformation.

The Au-catalysed sequential reaction of monocyclic diol substrates were also tested (Table 3) for the synthesis of 8-oxabicyclo[3.2.1]octane derivatives equipped with several functional groups. These are useful in the synthesis of natural products containing this basic skeleton, such as (–)-englerin A (**5**), platensimycin (**6**), hedyosumin C (**7**) and linearol (**8**), and also for the preparation of a variety of valuable functionalized cyclic compounds.

The reaction of substrates **16a–16h** generated desired products **17a–17h** in good yields (Table 3). Substrates bearing a terminal alkyne and those substituted with halogen atoms or an ester tolerated the reaction conditions. These groups allow further functional group manipulation (entries 1–4; Table 3). R group has proven to be compatible with a variety of functional groups, such as alkyl group, allyl group or even just H atom (entries 5–8). In the case where R=H (entry 8), a higher temperature was required. This may be because the distance between the secondary hydroxyl group and the alkyne is greater than that in the case of tertiary alcohol-based substrates.

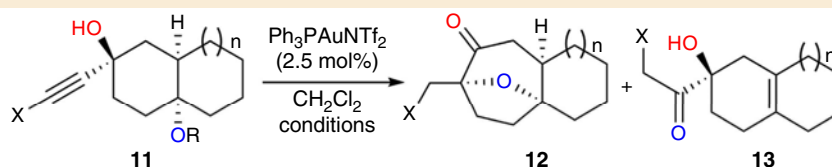
**Mechanistic investigation.** In our proposed mechanism for this Au-catalysed cascade reaction (Fig. 4), the alkyne moiety of the substrate is first activated by the active catalyst Ph<sub>3</sub>PAuNTf<sub>2</sub>, which is generated from the reaction between Ph<sub>3</sub>PAuCl and AgNTf<sub>2</sub> (ref. 47), to form  $\pi$ -coordinated intermediate **A**. The subsequent intramolecular nucleophilic attack by the hydroxyl group takes place to form a [2.2.2] bicyclic intermediate **B**, which would isomerize to a highly strained oxonium intermediate **C** through a proton shift<sup>48</sup>. Oxonium ion-initiated semi-pinacol rearrangement could afford intermediate **D** or **E** through pathway 1 or 2 and release ring strain. The following proton shift would form product **10** or side product **10'**, respectively, and regenerate the active catalyst Ph<sub>3</sub>PAuNTf<sub>2</sub> (ref. 49).

Alternatively, H-elimination followed by C–O bond cleavage would form intermediate **F**, which could lead to the generation of another side product **10''** (pathway 3)<sup>50</sup>. Although path 3 was observed in some cases (for substrate **11f** and **11l**), path 2 was never detected. To gain further insights into the mechanism and the origins of the excellent regioselectivity of the semi-pinacol type of 1,2-alkyl migration, we completed detailed density functional theory (DFT) calculations.



**Figure 3 | H-elimination pathway for the propargyl aldehyde substrate.** A cyclization intermediate **14** could be isolated from the Au-catalysed reaction of propargyl aldehyde substrate **11l**. Further treatment with gold catalyst in higher temperature, **14** could undergo H-elimination, followed by a condensation to afford spiro-compound **15**.

**Table 2 | Au-catalysed sequential reactions with alkyne-substituted bicyclic diols\*.**



Entry	Substrate	<i>n</i>	Conditions	Product <sup>†</sup>
1	<b>11a</b> (X = Br, R = H)	1	rt, 2 h	<b>12a</b> (75%)
2	<b>11b</b> (X = I, R = H)	1	rt, 2 h	<b>12b</b> (80%)
3	<b>11c</b> (X = CO <sub>2</sub> Et, R = H)	1	70 °C, 2 h	<b>12c</b> (76%)
4	<b>11d</b> (X = Ph, R = H)	1	rt, 2 h	<b>12d</b> (68%)
5	<b>11e</b> (X = CH <sub>2</sub> CH = CH <sub>2</sub> , R = H)	1	rt, 2 h	<b>12e</b> (52%)
6	<b>11f</b> (X = (CH <sub>2</sub> ) <sub>3</sub> CH <sub>3</sub> , R = H)	1	70 °C, 2 h	<b>12f</b> (58%) <b>13f</b> (21%)
7	<b>11g</b> (X = H, R = MEM)	1	rt, 2 h	<b>12g</b> (65%)
8	<b>11h</b> (X = H, R = H)	0	rt, 2 h	<b>12h</b> (85%)
9	<b>11i</b> (X = Br, R = H)	0	rt, 2 h	<b>12i</b> (78%)
10	<b>11j</b> (X = I, R = H)	0	rt, 2 h	<b>12j</b> (81%)
11	<b>11k</b> (X = CO <sub>2</sub> Et, R = H)	0	70 °C, 2 h	<b>12k</b> (81%) <sup>‡</sup>

\*1-Ethynylcyclohexane-trans-1,4-diols **11** (0.2 mmol) and MLn (2.5 mol%) in solvent (5 ml) and the reaction was stirred at room temperature (rt).

<sup>†</sup>Products **12** and **13** were isolated via flash column chromatography.

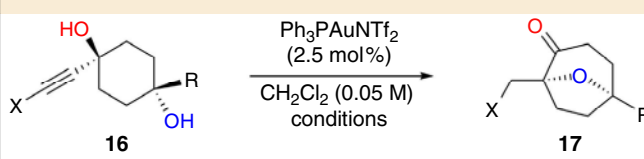
<sup>‡</sup>The structure of **12k** was confirmed by X-ray crystallography.

**Computational study.** The M11-L/6-311 + G(d)//B3LYP/6-31 + G(d) (Stuttgart/Dresden effective core potentials (SDD) basis set for Au atom) calculated free-energy profiles for the Au-catalysed annulation reaction are shown in Fig. 5a to clarify the mechanisms proposed in Fig. 4. All of the DFT calculations conducted in this study were carried out using the GAUSSIAN 09 series of programs<sup>51</sup>. DFT method B3LYP (refs 52,53) with a standard 6-31 + G(d) basis set (SDD basis set for Au) was used

for the geometry optimizations. The M11-L functional, proposed by Peverati and Truhlar<sup>54</sup>, was used with a 6-311 + G(d) basis set (SDD basis set for Au) to calculate the single point energies. The solvent effects were taken into consideration using single point calculations based on the gas-phase stationary points with a SMD continuum solvation model<sup>55–57</sup>. The energies presented in this paper are the M11-L calculated Gibbs free energies in a DCM solvent with B3LYP calculated thermodynamic corrections.

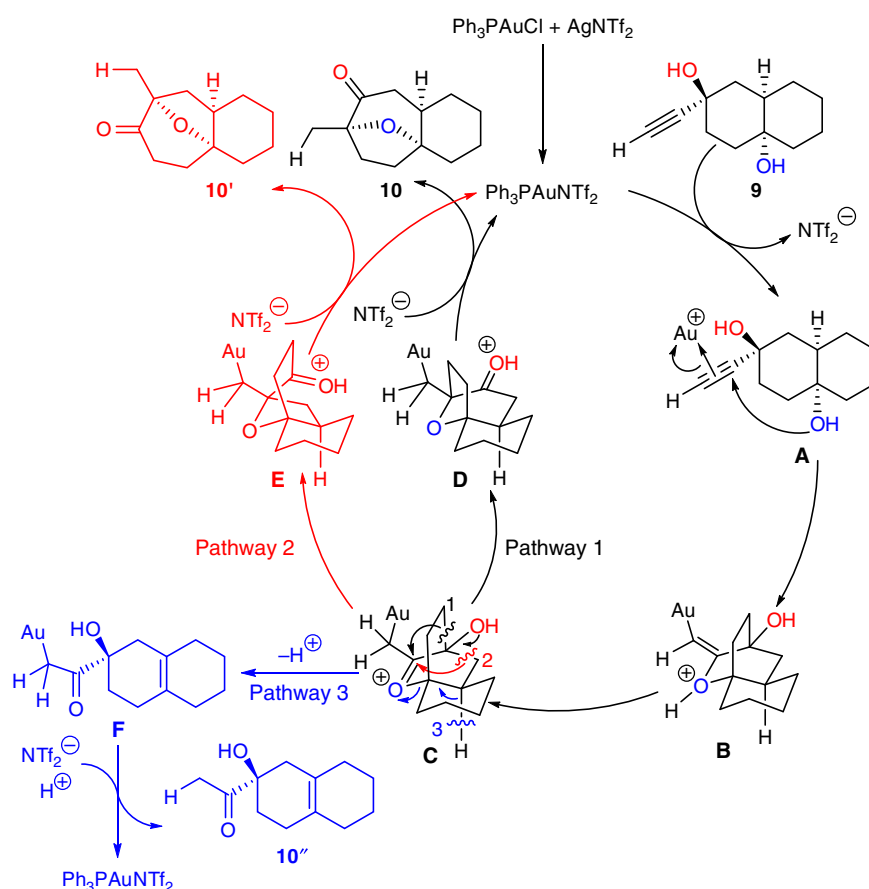
Initially, the alkynediol-coordinated Au-complex **CP1** was set to the relative zero of the relative free energy. The ring flip, which gives intermediate **CP2** with boat conformation, occurs via a twisted boat transition state **TS1** with a barrier of 8.4 kcal mol<sup>-1</sup>. The Au-activated alkynediol **CP2** might undergo an intramolecular nucleophilic addition of its hydroxyl group to the triple bond in an exo-selective manner to give oxonium ionic intermediate **CP3**, via transition state **TS2** with an energetic span of 4.7 kcal mol<sup>-1</sup>. The intermolecular hydrogen shift between intermediate **CP3** and **9** (or water<sup>58</sup>) irreversibly gives carbocation intermediate **CP4**, via transition state **TS3** with an energetic span of 16.9 kcal mol<sup>-1</sup>. Subsequently, the conformational isomerization of **CP4** gives carbocation intermediate **CP5**, via transition state **TS4** with a barrier of 20.4 kcal mol<sup>-1</sup>. The carbocation intermediate **CP5** undergoes a semi-pinacol rearrangement via transition state **TS5** with a barrier of 21.7 kcal mol<sup>-1</sup> to give intermediate **CP6**. The following proton shift and coordination of **9** gives the major product **10** with 31.0 kcal mol<sup>-1</sup> exothermic. Alternatively, side product **10'** would also be formed by the semi-pinacol rearrangement of another carbon atom via transition state **TS6** from **CP4**. The relative free energy of transition state **TS6** is

**Table 3 | Au-catalysed sequential reactions of alkyne-substituted monocyclic diols\*.**

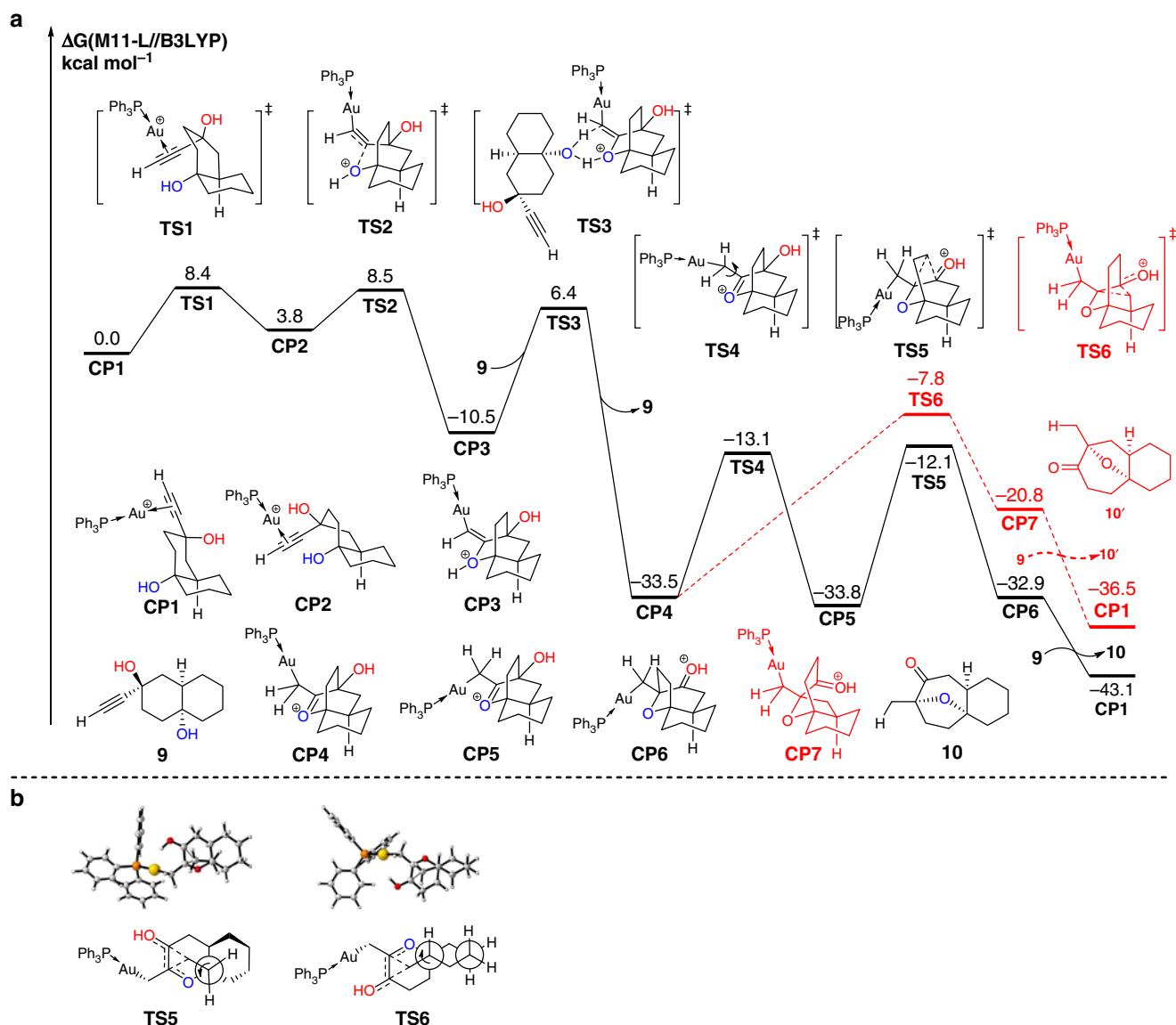


Entry	Substrate	Conditions	Product (yield) <sup>†</sup>
1	<b>16a</b> (X = H, R = Me)	rt, 2 h	<b>17a</b> (86%)
2	<b>16b</b> (X = Br, R = Me)	rt, 2 h	<b>17b</b> (81%)
3	<b>16c</b> (X = I, R = Me)	rt, 2 h	<b>17c</b> (78%)
4	<b>16d</b> (X = CO <sub>2</sub> Et, R = Me)	70 °C, 2 h	<b>17d</b> (73%)
5	<b>16e</b> (X = H, R = CH(CH <sub>3</sub> ) <sub>2</sub> )	rt, 2 h	<b>17e</b> (85%)
6	<b>16f</b> (X = H, R = CH(CH <sub>2</sub> ) <sub>5</sub> )	rt, 2 h	<b>17f</b> (86%)
7	<b>16g</b> (X = H, R = CH <sub>2</sub> CH = CH <sub>2</sub> )	rt, 2 h	<b>17g</b> (86%)
8	<b>16h</b> (X = H, R = H)	70 °C, 2 h	<b>17h</b> (77%)

\*1-Ethynylcyclohexane-trans-1,4-diol **16** (0.2 mmol) and MLn (2.5 mol%) in solvent (5 ml) was stirred at room temperature (rt).  
<sup>†</sup>Product **17** were isolated via flash column chromatography.



**Figure 4 | Proposed mechanism for the Au-catalysed annulation reaction.** The proposed mechanism involves the sequential intramolecular nucleophilic addition/ 1,3-proton shift/ oxonium ion-initiated semi-pinacol rearrangement (pathways 1 and 2) or hydrogen elimination (pathway 3).



**Figure 5 | Free-energy profiles for the two competing mechanisms.** (a) SMD-M11-L/6-311 + G(d)//B3LYP/6-31 + G(d) (SDD for Au) calculated free-energy profile for the sequence of intramolecular nucleophilic addition/semi-pinacol rearrangement of 1-ethynylcyclohexane-*trans*-1,4-diols established in this study for the reaction of key intermediate **CP1**. This indicates that the semi-pinacol rearrangement is the rate-determining step of this reaction and formation of complex **10** via transition state **TS5** is both thermodynamically and kinetically favourable (see Supplementary Tables 1 and 2). (b) The Newman projections of transition states **TS5** and **TS6**.

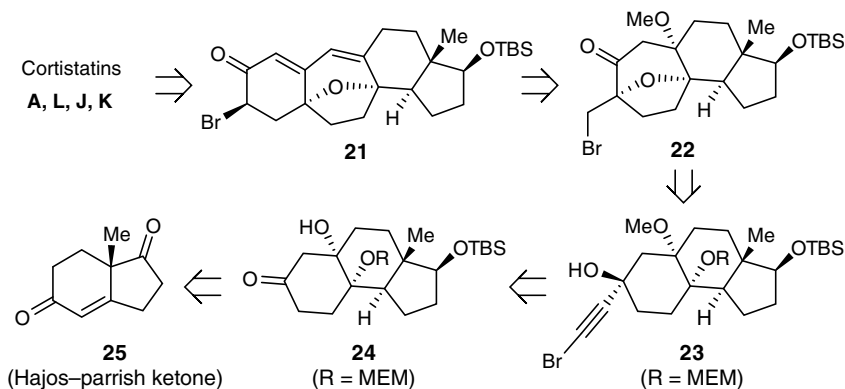
4.3 kcal mol<sup>-1</sup> higher than that of transition state **TS5**. Therefore, complex **10'** cannot be observed experimentally. This result is consistent with the experimental observation.

The Newman projections of transition states **TS5** and **TS6** are shown in Fig. 5b to further demonstrate the regioselectivity of the semi-pinacol rearrangement, in which the axis in the projections is supposed to rotate accordingly along with the migration. In transition state **TS5**, when the carbon atom migrates, the axis of Newman projection, being located out of the cyclohexane ring, rotates anticlockwise without restriction. In transition state **TS6**, however, the cyclohexane ring restricts the free rotation of the axis on it in Newman projection. Hence, the strain coming from the conformational change of the cyclohexane ring in transition state **TS6** blocks the carbocation rearrangement.

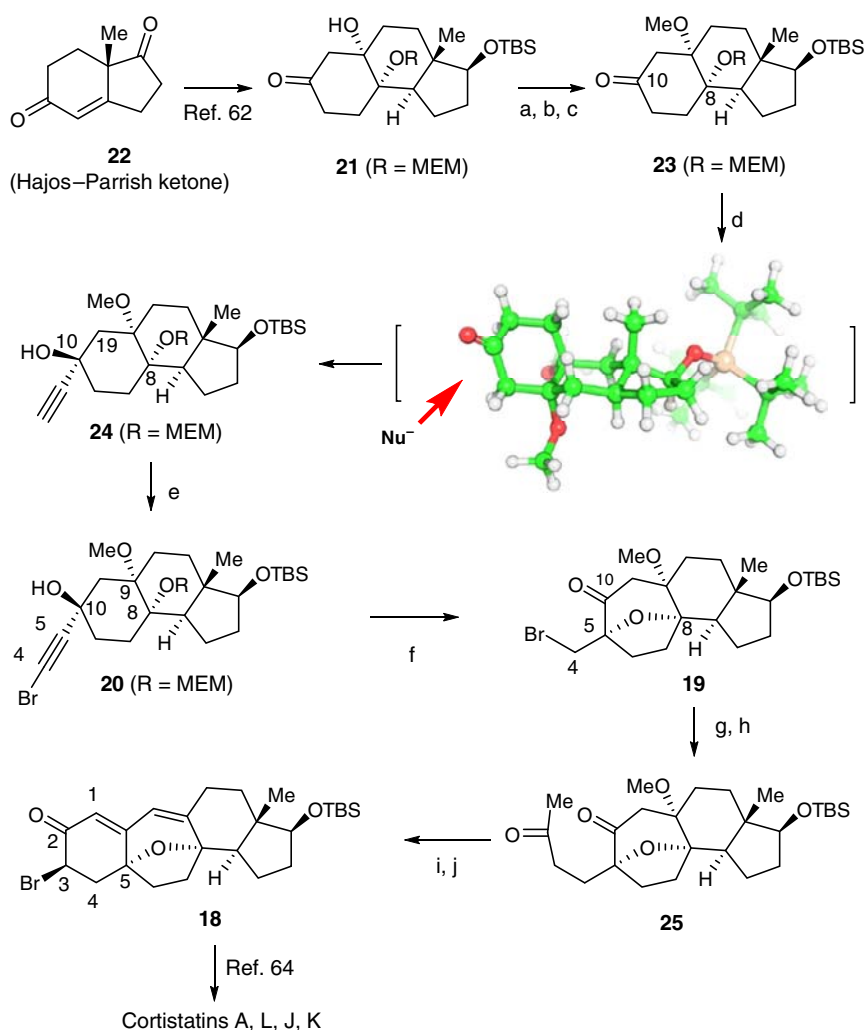
**Formal synthesis of the cortistatins.** The high yields and mild reaction conditions make this reaction to be a desirable method to

construct oxabicyclo[3.2.1]octane scaffolds. These are present in the cortistatins and inspired us to attempt their total synthesis<sup>59–67</sup>. Our retrosynthetic analysis of cortistatins **A**, **L**, **J** and **K** is shown in Fig. 6. Inspiration came from the highly efficient synthesis of cortistatins from tetracyclic intermediate **18** reported by Myers and colleagues<sup>65</sup>. Ketone **19** (Br being a substituent capable of S<sub>N</sub>2 displacement) could be a precursor to intermediate **18**, and it might be synthesized by our gold-catalysed cascade reaction from alcohol **20**, which in turn could be made from ketone **21** via an alkylation. This ketone could be derived from Hajos–Parrish ketone **22**.

Our synthesis commenced with known compound **21** (Fig. 7), which was prepared from Hajos–Parrish ketone **22** by a modified procedure reported by Shair and colleagues<sup>63</sup> (see Supplementary Methods). Initial attempts to protect the tertiary alcohol as the methyl ether were unsuccessful. Decomposition was observed presumably because of the ketone at the β-position of the tertiary



**Figure 6 | Retrosynthetic analysis of cortistatins.** The current Au-catalysed annulation reaction was used as a key step to construct the oxabicyclo[3.2.1]octane ring.



**Figure 7 | Formal total synthesis of the cortistatins.** (a) 2,2-Dimethylpropane-1,3-diol, Pyridinium p-Toluenesulfonate (PPTS) benzene, 50 °C, 4 h, 80%; (b) KH, MeI, THF, 0 °C to room temperature (rt), 92%; (c) CAN, borate buffer (pH = 8.0), 60 °C, 5 h, 55%; (d) ethynylmagnesium chloride, THF, 0 °C to rt, 75% + 20% diastereomer; (e) NBS,  $\text{AgNO}_3$ , acetone, rt, 0.5 h, 90%; (f)  $\text{Ph}_3\text{PAuNTf}_2$  (2.5 mol%), DCM, rt, 1 h, 81%; (g) allyl( $\text{Bu}$ ) $_3\text{Sn}$ , azodiisobutyronitrile (AIBN) benzene, 80 °C, 18 h, 78%; (h)  $\text{PdCl}_2$ , CuCl,  $\text{O}_2$ , DMF- $\text{H}_2\text{O}$  (7:1), rt, 12 h, 90%; (i) NaOMe, MeOH, rt, 10 h, 70%; (j) TMSOTf,  $\text{Et}_3\text{N}$ , THF, 0 °C, 0.5 h, then NBS, THF, 0 °C, 1 h, 80%.

hydroxyl group. A stepwise approach was adopted, whereby **21** was first treated with Pyridinium p-Toluenesulfonate (PPTS) in the presence of 2,2-dimethylpropane-1,3-diol and the resultant ketal was then protected as its methyl ether using MeI/KH in

tetrahydrofuran (THF). Removal of the ketal group<sup>68</sup> gave **23** in 40% yield over the three steps.

To prepare intermediate **20**, ketone **23** was reacted with ethynylmagnesium chloride in THF at 0 °C to afford desired

product **24** in 75% yield, together with its diastereoisomer in 20% yield. The diastereoselective formation of product **24** could be a result of the chair-like transition state adopted by **23**, which might guide the nucleophile approaching from the bottom face of the ketone to achieve the minimum level of steric interaction (see three-dimensional structure of **23** in Fig. 7). Thus, bromination of the alkyne moiety in **24** with *N*-bromosuccinimide (NBS) in the presence of AgNO<sub>3</sub> in acetone at room temperature gave **20** in 90% yield. Treatment of substrate **20** with Ph<sub>3</sub>PAuNTf<sub>2</sub> (2.5 mol%) in DCM at room temperature for 1 h, gave desired product **19** in 81% yield.

The structure of **19** was confirmed by X-ray crystallography of its derivative (see Supplementary Fig. 69). Product **19** was subjected to a radical-type allylation by reacting it with allyltributyl stannane in the presence of azodiisobutyronitrile (AIBN) and the resultant terminal alkene was then oxidized to diketone **25** via the Wacker oxidation to give diketone **25** in 70% yield over two steps. Thus, further treatment of diketone **25** with NaOMe in MeOH to initiate a cascade aldol condensation/ $\beta$ -elimination<sup>69</sup>, followed by an  $\alpha$ -bromination with NBS in THF at 0 °C afforded **18** in 56% yield over two steps<sup>70</sup>. This compound has been used by Myers and colleagues<sup>65</sup> in the total synthesis of corstatins **A**, **L**, **J** and **K**.

## Discussion

In summary, a novel strategy for the diastereoselective synthesis of structurally diverse oxabicyclo[3.2.1]octane scaffolds has been achieved via a gold-catalysed cascade reaction, which is consisted of three individual reactions, featuring (1) a gold-catalysed intramolecular nucleophilic addition of the OH group onto the carbon-carbon triple bond; (2) a gold-catalysed isomerization of exo-cyclic enol ether to a highly strained oxonium ion; (3) the oxonium-induced semi-pinacol rearrangement. This chemistry has also been demonstrated in the formal total synthesis of the cortistatins. DFT calculations reveal the necessity for the selective 1,2-alkyl migration to form oxabicyclo[3.2.1]octane scaffolds. Further applications of this methodology to other biologically active natural products with the oxabicyclo[3.2.1]heptane scaffold are currently underway in our laboratory.

## Methods

**Materials.** For <sup>1</sup>H and <sup>13</sup>C NMR spectra of the compounds in this article, see Supplementary Figs 1–67. For ORTEP diagrams, see Supplementary Figs 68 and 69.

**General.** All reactions were conducted in oven-dried glassware under an inert atmosphere of dry nitrogen. All reagents were purchased and used without further purification unless otherwise specified. Solvents for flash column chromatography were technical grade and distilled before use. Analytical thin-layer chromatography was performed using silica gel plates with HSGF 254 (0.15–0.2 mm) manufactured by Shandong Huanghai Chemical Company (Qingdao, China). Visualization was performed by measuring ultraviolet absorbance (254 nm) and using the appropriate stain. Flash column chromatography was performed using Qingdao Haiyang Chemical HG/T2354-92 silica gel (45–75  $\mu$ m). <sup>1</sup>H and <sup>13</sup>C NMR data were recorded on a Bruker 500 MHz (125 MHz for <sup>13</sup>C NMR) or a Bruker 400 MHz (100 MHz for <sup>13</sup>C NMR) nuclear resonance spectrometer unless otherwise specified. Chemical shifts ( $\delta$ ) in p.p.m. are reported relative to the residual chloroform signal (<sup>1</sup>H 7.26 p.p.m. and <sup>13</sup>C 77.16 p.p.m.). Multiplicities are described as follows: s (singlet), bs (broad singlet), d (doublet), t (triplet), q (quartet) and m (multiplet). Coupling constants (*J*) are reported in Hertz (Hz). <sup>13</sup>C NMR spectra were recorded with total proton decoupling. High-resolution mass spectrometry electrospray ionization analysis was performed by the Analytical Instrumentation Center at Peking University, and High-resolution mass spectrometry data are reported as ion mass/charge (*m/z*) ratios in atomic mass units.

**General procedure for the gold-catalysed cascade reactions.** A mixture of Ph<sub>3</sub>PAuNTf<sub>2</sub> (2.5 mg, 0.005 mmol, 0.025 equiv) and AgNTf<sub>2</sub> (1.9 mg, 0.005 mmol, 0.025 equiv) in DCM (1.0 ml) was stirred for 0.5 h to generate the active gold catalyst *in situ*. The mixture was then added to a stirred solution of the substrate

(0.20 mmol, 1.0 equiv) in DCM (4.0 ml) and stirred at ambient temperature for 2 h. The solvent was removed *in vacuo*, and the residue was purified by flash chromatography on silica gel to provide the desired product. For additional procedures see Supplementary Methods.

## References

- Aoki, S. *et al.* Cortistatins A, B, C and D, anti-angiogenic steroidal alkaloids, from the marine sponge *Corticium simplex*. *J. Am. Chem. Soc.* **128**, 3148–3149 (2006).
- Aoki, S. *et al.* Structure-activity relationship and biological property of cortistatins, anti-angiogenic spongian steroidal alkaloids. *Bioorg. Med. Chem.* **15**, 6758–6762 (2007).
- Ratnayake, R., Covell, D., Ransom, T. T., Gustafson, K. R. & Beutler, J. A. Englerin A, a selective inhibitor of renal cancer cell growth, from *Phyllanthus engleri*. *Org. Lett.* **11**, 57–60 (2009).
- Wang, J. *et al.* Platensimycin is a selective FabF inhibitor with potent antibiotic properties. *Nature* **441**, 358–361 (2006).
- Zhang, C. *et al.* Platensimycin and platencin congeners from *Streptomyces platensis*. *J. Nat. Prod.* **74**, 329–340 (2011).
- Su, Z.-S. *et al.* Sesquiterpenoids from *Hedyosmum orientale*. *J. Nat. Prod.* **71**, 1410–1413 (2008).
- Pereira, R. C., Pinheiro, M. D., Teixeira, V. L. & Gama, B. A. P. Feeding preferences of the endemic gastropod *Astraea latispina* in relation to chemical defenses of Brazilian tropical seaweeds. *Braz. J. Biol.* **62**, 33–40 (2002).
- Ylijoki, K. E. O. & Stryker, J. M. [5 + 2] Cycloaddition reactions in organic and natural product synthesis. *Chem. Rev.* **113**, 2244–2266 (2013).
- Jones, D. E. & Harmata, M. *Application of the [4 + 3] Cycloaddition Reaction to the Synthesis of Natural Products, in Methods and Applications of Cycloaddition Reactions in Organic Syntheses* (ed. Nishiwaki, N.) (John Wiley & Sons, Inc., 2014).
- Jiménez-Núñez, E., Claverie, C. K., Nieto-Oberhuber, C. & Echavarren, A. M. Prins cyclizations in Au-catalyzed reactions of enynes. *Angew. Chem. Int. Ed.* **45**, 5452–5455 (2006).
- Jiménez-Núñez, E., Molawi, K. & Echavarren, A. M. Stereoselective gold-catalyzed cycloaddition of functionalized ketoenynes: synthesis of (+)-orientalol F. *Chem. Commun.* 7327–7329 (2009).
- Molawi, K., Delpont, N. & Echavarren, A. M. Enantioselective synthesis of (–)-englerin A and B. *Angew. Chem. Int. Ed.* **49**, 3517–3519 (2010).
- Zhou, Q., Chen, X. & Ma, D. Asymmetric, protecting-group-free total synthesis of (–)-englerin A. *Angew. Chem. Int. Ed.* **49**, 3513–3516 (2010).
- Singh, V., Krishna, U. M., Vikrant & Trivedi, V. G. K. Cycloaddition of oxidopyrylium species in organic synthesis. *Tetrahedron* **64**, 3405–3428 (2008).
- Wender, P. A., Lee, H. Y., Wilhelm, R. S. & Williams, P. D. Studies on tumor promoters. 7. The synthesis of a potentially general precursor of the tiglianes, daphnanes, and ingenanes. *J. Am. Chem. Soc.* **111**, 8954–8957 (1989).
- Kitagaki, S. *et al.* Enantiocontrol in tandem carbonyl ylide formation and intermolecular 1,3-dipolar cycloaddition of  $\alpha$ -diazo ketones mediated by chiral dirhodium(II) carboxylate catalyst. *J. Am. Chem. Soc.* **121**, 1417–1418 (1999).
- Xiong, H., Hsung, R. P., Berry, C. R. & Rameshkumar, C. The first epoxidations of 1-amidoallenes. A general entry to nitrogen-substituted oxyallyl cations in highly stereoselective [4 + 3] cycloadditions. *J. Am. Chem. Soc.* **123**, 7174–7175 (2001).
- Molander, G. A., St. Jean, Jr D. J. & Haas, J. Toward a general route to the eunicellin diterpenes: the asymmetric total synthesis of deacetoxyalcyonin acetate. *J. Am. Chem. Soc.* **126**, 1642–1643 (2004).
- Chung, W. K. *et al.* Inter- and intramolecular [4 + 3] cycloadditions using epoxy enol silanes as functionalized oxyallyl cation precursors. *J. Am. Chem. Soc.* **131**, 4556–4557 (2009).
- Ishida, K., Kusama, H. & Iwasawa, N. Enantioselective preparation of 8-oxabicyclo[3.2.1]octane derivatives via asymmetric [3 + 2]-cycloaddition of platinum-containing carbonyl ylides with vinyl ethers. *J. Am. Chem. Soc.* **132**, 8842–8843 (2010).
- Burns, N. Z., Witten, M. R. & Jacobsen, E. N. Dual catalysis in enantioselective oxidopyrylium-based [5 + 2] cycloadditions. *J. Am. Chem. Soc.* **133**, 14578–14581 (2011).
- Li, B., Zhao, Y.-J., Lai, Y.-C. & Loh, T.-P. Asymmetric syntheses of 8-oxabicyclo[3.2.1]octanes: a cationic cascade cyclization. *Angew. Chem. Int. Ed.* **51**, 8041–8045 (2012).
- Obradors, C. & Echavarren, A. M. Intermolecular gold-catalyzed cycloaddition of alkynes with oxoalkenes. *Chem. Eur. J.* **19**, 3547–3551 (2013).
- Faustino, H., Alonso, I., Mascareñas, J. L. & López, F. Gold(I)-catalyzed cascade cycloadditions between allenamides and carbonyl-tethered alkenes: an enantioselective approach to oxa-bridged medium-sized carbocycles. *Angew. Chem. Int. Ed.* **52**, 6526–6530 (2013).
- Nicolau, K. C., Edmonds, D. J. & Bulger, P. G. Cascade reactions in total synthesis. *Angew. Chem. Int. Ed.* **45**, 7134–7186 (2006).

26. Friend, C. M. & Hashmi, A. S. K. Gold catalysis. *Acc. Chem. Res.* **47**, 729–730 (2014).
27. Hashmi, A. S. K. & Rudolph, M. Gold catalysis in total synthesis. *Chem. Soc. Rev.* **37**, 1766–1775 (2008).
28. Rudolph, M. & Hashmi, A. S. K. Gold catalysis in total synthesis—an update. *Chem. Soc. Rev.* **41**, 2448–2462 (2012).
29. Fürstner, A. From understanding to prediction: Gold- and platinum-based  $\pi$ -acid catalysis for target oriented synthesis. *Acc. Chem. Res.* **47**, 925–938 (2014).
30. Dorel, R. & Echavarren, A. M. Gold(I)-catalyzed activation of alkynes for the construction of molecular complexity. *Chem. Rev.* **115**, 9028–9072 (2015).
31. Hashmi, A. S. K. Gold-catalyzed organic reactions. *Chem. Rev.* **107**, 3180–3211 (2007).
32. Hashmi, A. S. K. & Hutchings, G. J. Gold catalysis. *Angew. Chem. Int. Ed.* **45**, 7896–7936 (2006).
33. Hashmi, A. S. K. *et al.* Gold catalysis: tandem reactions of diyne–diols and external nucleophiles as an easy access to tricyclic cage-like structures. *Chem. Eur. J.* **16**, 9846–9854 (2010).
34. Crone, B. & Kirsch, S. F. 1,2-Alkyl migration as a key element in the invention of cascade reactions catalyzed by  $\pi$ -acids. *Chem. Eur. J.* **14**, 3514–3522 (2008).
35. Kirsch, S. F., Binder, J. T., Liébert, C. & Menz, H. Gold(III)- and platinum(II)-catalyzed domino reaction consisting of heterocyclization and 1,2-migration: efficient synthesis of highly substituted 3(2H)-furanones. *Angew. Chem. Int. Ed.* **45**, 5878–5880 (2006).
36. Zhang, J. & Schmalz, H.-G. Gold(I)-catalyzed reaction of 1-(1-alkynyl)-cyclopropyl ketones with nucleophiles: a modular entry to highly substituted furans. *Angew. Chem. Int. Ed.* **45**, 6704–6707 (2006).
37. Wang, T. *et al.* Synthesis of highly substituted 3-formylfurans by a gold(I)-catalyzed oxidation/1,2-alkynyl migration/cyclization cascade. *Angew. Chem. Int. Ed.* **53**, 3715–3719 (2014).
38. Wang, T., Huang, L., Shi, S., Rudolph, M. & Hashmi, A. S. K. Synthesis of highly substituted *N*-(furan-3-ylmethylene)benzenesulfonamides by a gold(I)-catalyzed oxidation/1,2-alkynyl migration/cyclization cascade. *Chem. Eur. J.* **20**, 14868–14871 (2014).
39. Nösel, P. *et al.* 1,6-Carbene transfer: gold-catalyzed oxidative diyne cyclizations. *J. Am. Chem. Soc.* **135**, 15662–15666 (2013).
40. Lauterbach, T. *et al.* Gold-Catalyzed carbenoid transfer reactions of diynes – pinacol rearrangement *versus* retro-Buchner reaction. *Adv. Synth. Catal.* **357**, 775–781 (2015).
41. Song, Z.-L., Fan, C.-A. & Tu, Y.-Q. Semipinacol rearrangement in natural product synthesis. *Chem. Rev.* **111**, 7523–7556 (2011).
42. Shi, H. *et al.* Total syntheses of Drimane-type sesquiterpenoids enabled by a gold-catalyzed tandem reaction. *J. Am. Chem. Soc.* **133**, 14944–14947 (2011).
43. Yue, G. *et al.* Collective synthesis of cladiellins based on the gold-catalyzed cascade reaction of 1,7-diyne. *Angew. Chem. Int. Ed.* **53**, 1837–1840 (2014).
44. Widenhoefer, R. A. & Song, F. *Gold-Catalyzed Addition of Oxygen Nucleophiles to C-C Multiple Bonds, in Catalyzed Carbon-Heteroatom Bond Formation* (ed Yudin, A. K.) (Wiley-VCH Verlag GmbH & Co. KGaA, 2010).
45. Barluenga, J., Diéguez, A., Fernández, A., Rodríguez, F. & Fañanás, F. J. Gold- or platinum-catalyzed tandem cycloisomerization/Prins-type cyclization reactions. *Angew. Chem. Int. Ed.* **45**, 2091–2093 (2006).
46. Barluenga, J., Fernández, A., Diéguez, A., Rodríguez, F. & Fañanás, F. J. Gold- or platinum-catalyzed cascade processes of alkynol derivatives involving hydroalkoxylation reactions followed by Prins-type cyclizations. *Chem. Eur. J.* **15**, 11660–11667 (2009).
47. Mézailles, N., Ricard, L. & Gagosz, F. Phosphine gold(I) bis-(trifluoromethanesulfonyl)imidate complexes as new highly efficient and air-stable catalysts for the cycloisomerization of enynes. *Org. Lett.* **7**, 4133–4136 (2005).
48. Krauter, C. M., Hashmi, A. S. K. & Pernpointner, M. A new insight into gold(I)-catalyzed hydration of alkynes: proton transfer. *ChemCatChem* **2**, 1226–1230 (2010).
49. Hashmi, A. S. K. Homogeneous gold catalysis beyond assumptions and proposals—characterized intermediates. *Angew. Chem. Int. Ed.* **49**, 5232–5241 (2010).
50. Xu, M., Ren, T.-T. & Li, C.-Y. Gold-catalyzed oxidative rearrangement of homopropargylic ether via oxonium ylide. *Org. Lett.* **14**, 4902–4905 (2012).
51. Frisch, M. J. *et al.* Gaussian 09 (Gaussian, Inc., Wallingford, CT, 2013).
52. Becke, A. D. Density-functional thermochemistry. III. The role of exact exchange. *J. Chem. Phys.* **98**, 5648–5652 (1993).
53. Lee, C., Yang, W. & Parr, R. G. Development of the Colle-Salvetti correlation-energy formula into a functional of the electron density. *Phys. Rev. B* **37**, 785–789 (1988).
54. Peverati, R. & Truhlar, D. G. Improving the accuracy of hybrid meta-GGA density functionals by range separation. *J. Phys. Chem. Lett.* **2**, 2810–2817 (2011).
55. Cances, E., Mennucci, B. & Tomasi, J. A new integral equation formalism for the polarizable continuum model: theoretical background and applications to isotropic and anisotropic dielectrics. *J. Chem. Phys.* **107**, 3032–3041 (1997).
56. Cossi, M., Barone, V., Cammi, R. & Tomasi, J. Ab initio study of solvated molecules: a new implementation of the polarizable continuum model. *J. Chem. Phys. Lett.* **255**, 327–335 (1996).
57. Barone, V., Cossi, M. & Tomasi, J. Geometry optimization of molecular structures in solution by the polarizable continuum model. *J. Comput. Chem.* **19**, 404–417 (1998).
58. Xia, Y. *et al.* An unexpected role of a trace amount of water in catalyzing proton transfer in phosphine-catalyzed (3 + 2) cycloaddition of allenolates and alkenes. *J. Am. Chem. Soc.* **129**, 3470–3471 (2007).
59. Narayan, A. R. H., Simmons, E. M. & Sarpong, R. Synthetic strategies directed towards the Cortistatin family of natural products. *Eur. J. Org. Chem.* **2010**, 3553–3567 (2010).
60. Shenvi, R. A., Guerrero, C. A., Shi, J., Li, C.-C. & Baran, P. S. Synthesis of (+)-cortistatin A. *J. Am. Chem. Soc.* **130**, 7241–7243 (2008).
61. Shi, J. *et al.* Scalable synthesis of cortistatin A and related structures. *J. Am. Chem. Soc.* **133**, 8014–8027 (2011).
62. Nicolaou, K. C., Sun, Y.-P., Peng, X.-S., Polet, D. & Chen, D. Y.-K. Total synthesis of (+)-cortistatin A. *Angew. Chem. Int. Ed.* **47**, 7310–7313 (2008).
63. Lee, H. M., Nieto-Oberhuber, C. & Shair, M. D. Enantioselective synthesis of (+)-cortistatin A, a potent and selective inhibitor of endothelial cell proliferation. *J. Am. Chem. Soc.* **130**, 16864–16866 (2008).
64. Nicolaou, K. C. *et al.* Total synthesis and biological evaluation of cortistatins A and J and analogues thereof. *J. Am. Chem. Soc.* **131**, 10587–10597 (2009).
65. Flyer, A. N., Si, C. & Myers, A. G. Synthesis of cortistatins A, J, K and L. *Nat. Chem.* **2**, 886–892 (2010).
66. Nilson, M. G. & Funk, R. L. Total synthesis of ( $\pm$ )-cortistatin J from furan. *J. Am. Chem. Soc.* **133**, 12451–12453 (2010).
67. Yamashita, S., Iso, K., Kitajima, K., Himuro, M. & Hiramata, M. Total synthesis of cortistatins A and J. *J. Org. Chem.* **76**, 2408–2425 (2011).
68. Markó, I. E. *et al.* Cerium(IV)-catalyzed deprotection of acetals and ketals under mildly basic conditions. *Angew. Chem. Int. Ed.* **38**, 3207–3209 (1999).
69. Tan, D. S., Dudley, G. B. & Danishefsky, S. J. Synthesis of the functionalized tricyclic skeleton of guanacastepene A: a tandem epoxide-opening  $\beta$ -elimination/Knoevenagel cyclization. *Angew. Chem. Int. Ed.* **41**, 2185–2188 (2002).
70. Fang, L. *et al.* Formal synthesis of cortistatins. *J. Org. Chem.* **76**, 2479–2487 (2011).

## Acknowledgements

This work is supported by the National Science Foundation of China (Grant Nos. 21372016, 21472006 and 21402002), 863 Program (2013AA092903), Guangdong Natural Science Foundation (2014A030312004), NSFC-Shandong Joint Fund for Marine Science Research Centers (U1406402) and Shenzhen Basic Research Program (Grant Nos. JCY20130329180217059, ZDSYS20140509094114168 and JSGG20140717102922014).

## Author contributions

Z.Y., J.F. and T.L. conceived the project and analysed the experimental results. J.F., Y.G., H.Y. and J.G. performed the synthesis and characterization. S.L. and Y.L. performed the theoretical calculations. Y.L., J.G. and Z.Y. composed the manuscript with input from all authors.

## Additional information

**Accession codes.** The X-ray crystallographic coordinates for the structures reported in this article have been deposited at the Cambridge Crystallographic Data Centre (CCDC), under deposition number CCDC 1059110 (for **510**) and 1059111 (for **12k**). These data can be obtained free of charge from the Cambridge Crystallographic Data Centre via [http://www.ccdc.cam.ac.uk/data\\_request/cif](http://www.ccdc.cam.ac.uk/data_request/cif).

**Supplementary Information** accompanies this paper at <http://www.nature.com/naturecommunications>

**Competing financial interests:** The authors declare no competing financial interests.

**Reprints and permission** information is available online at <http://npg.nature.com/reprintsandpermissions/>

**How to cite this article:** Fu, J. *et al.* Towards a general diastereoselective route to oxabicyclo[3.2.1]octanes via a gold-catalysed cascade reaction. *Nat. Commun.* 6:8617 doi: 10.1038/ncomms9617 (2015).



This work is licensed under a Creative Commons Attribution 4.0 International License. The images or other third party material in this article are included in the article's Creative Commons license, unless indicated otherwise in the credit line; if the material is not included under the Creative Commons license, users will need to obtain permission from the license holder to reproduce the material. To view a copy of this license, visit <http://creativecommons.org/licenses/by/4.0/>



# Copper-catalyzed aerobic oxidative coupling: From ketone and diamine to pyrazine

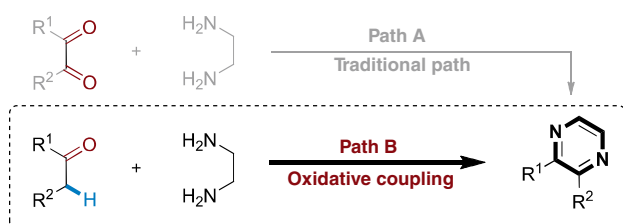
Kun Wu,<sup>1\*</sup> Zhiliang Huang,<sup>1,2\*</sup> Xiaotian Qi,<sup>3</sup> Yingzi Li,<sup>3</sup> Guanghui Zhang,<sup>1,2</sup> Chao Liu,<sup>1</sup> Hong Yi,<sup>1</sup> Lingkui Meng,<sup>1</sup> Emilio E. Bunel,<sup>2</sup> Jeffrey T. Miller,<sup>2</sup> Chih-Wen Pao,<sup>4</sup> Jyh-Fu Lee,<sup>4</sup> Yu Lan,<sup>3†</sup> Aiwen Lei<sup>1,2,5†</sup>

Copper-catalyzed aerobic oxidative C–H/N–H coupling between simple ketones and diamines was developed toward the synthesis of a variety of pyrazines. Various substituted ketones were compatible for this transformation. Preliminary mechanistic investigations indicated that radical species were involved. X-ray absorption fine structure experiments elucidated that the Cu(II) species 5 coordinated by two N atoms at a distance of 2.04 Å and two O atoms at a shorter distance of 1.98 Å was a reactive one for this aerobic oxidative coupling reaction. Density functional theory calculations suggested that the intramolecular coupling of cationic radicals was favorable in this transformation.

## INTRODUCTION

Oxidative cross-coupling reactions have recently shown great potential in carbon-carbon and carbon-heteroatom bond formation (1–4). Generally, organometallic compounds (R–M) can be used as one of the reaction partners in these transformations, but alcohols, amines, and hydrocarbons (R–H) can be directly used as well (5–13). Compared with R–M, R–H is an “ideal” reactant in view of atom-economical synthesis. Up to now, seeking and applying different R–H in oxidative C–H/C–H or C–H/Y–H (Y = N, O, S, etc.) coupling reactions remains a challenge.

Pyrazine, which is one of the well-known and important classes of heterocyclic compounds, exhibits extraordinary biological and pharmaceutical properties (14–18). In recent years, pyrazines have received a lot of attention because of their applications in the field of luminescent materials (19). Therefore, exploring effective methods toward the synthesis of pyrazines is appealing and important. Traditionally, condensation of  $\alpha$ -diketone and diamine is a predominant method for the construction of pyrazines (Scheme 1, Path A) (20–25). Most  $\alpha$ -diketones are often not commercially available, and the preparation processes are energy-consuming and complicated (26–28). Hence, if simple ketones could be applied instead of  $\alpha$ -diketones in this synthesis, it would be a more attractive strategy to access pyrazines (Scheme 1, Path B).



**Scheme 1.** Traditional and theoretical pathways for the synthesis of pyrazines.

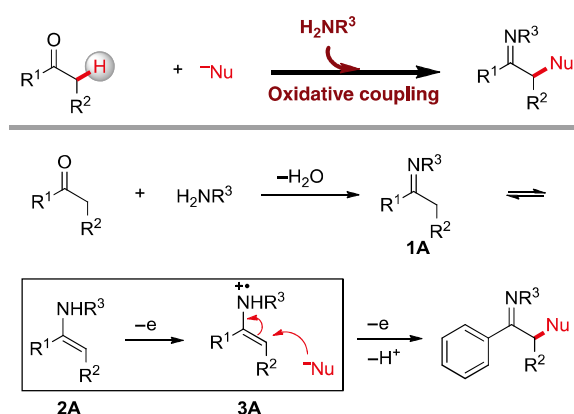
<sup>1</sup>College of Chemistry and Molecular Sciences, Institute for Advanced Studies, Wuhan University, Wuhan 430072, China. <sup>2</sup>Chemical Sciences and Engineering Division, Argonne National Laboratory, 9700 South Cass Avenue, Argonne, IL 60439, USA. <sup>3</sup>School of Chemistry and Chemical Engineering, Chongqing University, Chongqing 400030, China. <sup>4</sup>National Synchrotron Radiation Research Center, Hsinchu 30076, Taiwan. <sup>5</sup>National Research Center for Carbohydrate Synthesis, Jiangxi Normal University, Nanchang 330022, China.

\*These authors contributed equally to this work.

†Corresponding author. E-mail: aiwenlei@whu.edu.cn (A.L.); lanyu@cqu.edu.cn (Y.L.)

2015 © The Authors, some rights reserved; exclusive licensee American Association for the Advancement of Science. Distributed under a Creative Commons Attribution NonCommercial License 4.0 (CC BY-NC). 10.1126/sciadv.1500656

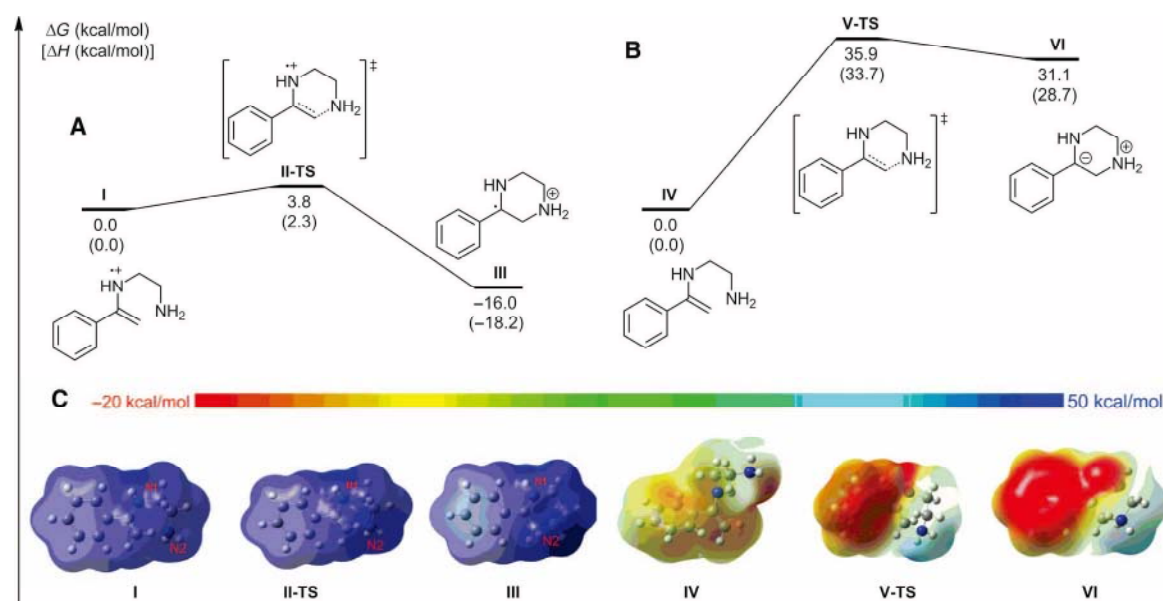
A C–N bond formation involving the  $\alpha$ -C–H of ketones and N–H of primary amines is required to realize the designed transformation. Both are known nucleophiles and cannot directly react to form C–N bonds. There are some clues in the literature regarding the C–N bond formation involving a Csp<sup>3</sup>–H and an N–H under oxidative conditions (29–37). However, to the best of our knowledge, only a few examples in which I<sub>2</sub>, N-bromosuccinimide, or hypervalent iodine was used as oxidant were developed to construct the C–N bond by using  $\alpha$ -C–H of simple ketones and N–H of primary amines (38–41). Herein, we proposed a strategy (Scheme 2) to achieve this transformation by utilizing copper salt as the catalyst and O<sub>2</sub> as the oxidant. Initially, a primary amine was introduced to react with ketone to produce imine **1A** (42), which could isomerize to enamine **2A** (43, 44). The isomer might be oxidized by losing one electron in the presence of a catalyst [Cu(II)] and an oxidant (O<sub>2</sub>) to form enamine radical cation **3A** (45, 46). As a relatively electron-deficient species, **3A** might be attacked by nucleophiles (N–H) (47, 48). After losing another electron, the bond formation between  $\alpha$ -C–H of ketones and N–H of primary amines could be realized. In this regard, we attempt to demonstrate an oxidative coupling between ketones and diamines toward the synthesis of pyrazines by single electron transfer.



**Scheme 2.** The proposed strategy for oxidative coupling reactions between simple ketones and nucleophiles.

## RESULTS AND DISCUSSION

The density functional theory (DFT) method B3LYP was initially performed to further analyze the practicality of our proposed strategy



**Fig. 1.** Density functional theory (DFT) calculations for energy comparisons. (A to C) Free energy profile for the intramolecular cyclization process (A and B), and the corresponding electrostatic potential (ESP) maps (C).

(49). As illustrated in Fig. 1A, the nucleophilic addition of cationic radical **I** takes place via transition state **II-TS** with only a 3.8-kcal/mol barrier, after which the generated cationic radical **III** (16.0 kcal/mol) becomes more stable than cationic radical **I**. As a comparison, the corresponding cyclization of neutral enamine **IV** has also been calculated. The free energy profile (Fig. 1B) shows that the activation free energy of intramolecular cyclization via transition state **V-TS** is 35.9 kcal/mol, which is 32.1 kcal/mol higher than that of cationic radical **I**. The relative free energy of the formed complex **VI** is 31.1 kcal/mol higher than that of complex **IV**. The calculated ESP (Fig. 1C) could rationalize this difference. From the ESP results, the cyclization from **I** to **III** is a charge transfer process, whereas that from **IV** to **VI** is a charge separation process. The latter is much more difficult than the former; that is, oxidative coupling between ketones and diamines toward the synthesis of pyrazines by single electron transfer is much more facile.

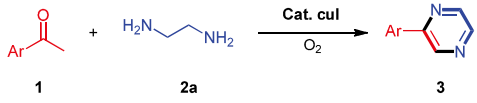
On the basis of the DFT calculations, the C–N bond formation reaction of acetophenone **1a** and ethylenediamine **2a** toward the synthesis of pyrazine was commenced by using 30 mol% of copper(I) iodide as the catalyst and O<sub>2</sub> as the oxidant, because these reaction parameters are standard for the formation of radical cations (42, 50, 51). After several potential solvents were evaluated, dimethyl acetamide (DMA)/Et<sub>3</sub>N (2:1) proved to be the most effective, and the corresponding pyrazine product was obtained in moderate yield (Table 1, entry 1). Various additives were also examined (Table 1, entries 2 to 4). The efficiency of the reaction was significantly improved by the addition of the inexpensive and readily available lithium chloride (Table 1, entry 5). In addition, CuI plays a critical role in the reaction with only trace amounts of **3a** formed in its absence (Table 1, entry 13). Other copper salts, such as CuCl, CuBr, CuCl<sub>2</sub>, and Cu(OTf)<sub>2</sub>, were less effective (Table 1, entries 6 to 9). The reaction also took place efficiently with lower loadings of CuI (Table 1, entries 10 to 12). When DMA was used as the sole solvent, the yield of the desired product was slightly lower (Table 1, entry 14). Finally, the reaction conditions described in entry 11 were selected as the standard conditions for further investigations.

**Table 1.** Impact of reaction parameters on oxidative C–H/N–H coupling reaction. For more details on metals, solvents, temperature, ratio of substrates, and the amount of LiCl, see tables S1 to S5.

Entry	[Cu](equiv)	Additive	Solvent	3a <sup>a</sup> [%]
1	CuI(0.3)	---	DMA/Et <sub>3</sub> N(2:1)	55
2	CuI(0.3)	LiBr	DMA/Et <sub>3</sub> N(2:1)	60
3	CuI(0.3)	KI	DMA/Et <sub>3</sub> N(2:1)	78
4	CuI(0.3)	ZnCl <sub>2</sub>	DMA/Et <sub>3</sub> N(2:1)	74
5	CuI(0.3)	LiCl	DMA/Et <sub>3</sub> N(2:1)	79(74)
6	CuCl(0.3)	LiCl	DMA/Et <sub>3</sub> N(2:1)	37
7	CuBr(0.3)	LiCl	DMA/Et <sub>3</sub> N(2:1)	36
8	CuCl <sub>2</sub> (0.3)	LiCl	DMA/Et <sub>3</sub> N(2:1)	17
9	Cu(OTf) <sub>2</sub> (0.3)	LiCl	DMA/Et <sub>3</sub> N(2:1)	5
10	CuI(0.2)	LiCl	DMA/Et <sub>3</sub> N(2:1)	80(74)
11	CuI(0.1)	LiCl	DMA/Et <sub>3</sub> N(2:1)	78(75)
12	CuI(0.05)	LiCl	DMA/Et <sub>3</sub> N(2:1)	68
13	---	LiCl	DMA/Et <sub>3</sub> N(2:1)	<1
14	CuI(0.3)	LiCl	DMA	60

<sup>a</sup>Gas chromatography yield based on **1a** with biphenyl used as the internal standard.

To further investigate the scope of this catalytic system, we used a variety of aryl methyl ketones to couple with ethylenediamine **2a** under the optimized reaction conditions (Table 2). All substrates proceeded well and afforded corresponding products in moderate to good yields. Aryl methyl ketones with an electron-donating group (OMe) or an electron-withdrawing group (CN, CF<sub>3</sub>) could react with **2a** smoothly to afford the desired products in moderate to good yields (Table 2, entries 5 and 10 to 13). Acetophenones with halogen substituents (F, Cl, and Br) were also suitable substrates to yield the corresponding

**Table 2. Copper-catalyzed oxidative C–H/N–H coupling of aryl ketone and 2a.**


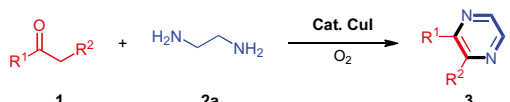
Entry	Substrate 1	Product 3	Yield*
1			R = H, <b>3a</b> : 75%
2			R = Ph, <b>3b</b> : 71%
3			R = F, <b>3c</b> : 38% <sup>†</sup>
4			R = Br, <b>3d</b> : 60%
5			R = CN, <b>3e</b> : 65% <sup>†</sup>
6			<b>3f</b> : 75%
7			<b>3g</b> : 2-Cl, 56%
8			<b>3h</b> : 3-Cl, 72% <sup>†</sup>
9			<b>3i</b> : 4-Cl, 70%
10			<b>3j</b> : 3-CF <sub>3</sub> , 67%
11			<b>3k</b> : 4-CF <sub>3</sub> , 68%
12			<b>3l</b> : 3-OMe, 56%
13			<b>3m</b> : 4-OMe, 66% <sup>†</sup>
14			<b>3n</b> : 72%
15			<b>3o</b> : 71%
16			<b>3p</b> : 60%

\*Conditions: **1** (0.5 mmol), **2a** (2.5 mmol), CuI (0.05 mmol), LiCl (1.0 mmol), DMA/Et<sub>3</sub>N = 2:1 (1.5 ml), 120°C, 15 hours, under O<sub>2</sub> (1 atm). Isolated yields. <sup>†</sup>Twenty-four hours.

products, which enabled a potential application for further functionalization (Table 2, entries 3, 4, and 7 to 9). 1-(1,1'-Biphenyl)-4-yl)ethanone and 1-(naphthalen-2-yl)ethanone were also suitable substrates for this transformation (Table 2, entries 2 and 6). In addition, heterocyclic methyl ketones could react well with **2a** to give the corresponding products in good yields (Table 2, entries 14 to 16).

In addition to aryl ketones, various other ketones were also reacted with **2a**, and the results are given in Table 3. The reaction between **2a** and propiophenone or 2-phenyl-1-(*p*-tolyl)ethanone proceeded to give the desired products in good yields (Table 3, entries 1 and 2). For the reaction of 1-phenylbutane-1,3-dione with **2a**, **3a** was obtained in 71% yield (Table 3, entry 3). In this reaction, C–C bond cleavage also occurred. The reaction of 1-(4-methoxyphenyl)propan-2-one with 2-phenylacetaldehyde produced the pyrazine ring as well (Table 3, entries 4 and 5). 3,4-Dihydronaphthalen-1(2*H*)-one was suitable for this reaction, generating benzo[*f*]quinoxaline in 40% yield (Table 3, entry 6). The reactions of **2a** with simple alkyl ketones, such as cycloheptanone, cyclooctanone, and 3,3-dimethylbutan-2-one, proceeded to afford the desired pyrazines (Table 3, entries 7 to 9).

As shown in Table 4, various diamines other than **2a** also gave pyrazine products in this copper-catalyzed aerobic oxidative C–H/N–H coupling reaction. For example, 1,2-diphenylethane-1,2-diamine reacted

**Table 3. Copper-catalyzed oxidative C–H/N–H coupling of other ketones and 2a.** For more attempts between other ketones and ethylenediamine, see table S6.


Entry	Substrate 1	Product 3	Yield*
1			<b>3q</b> : 60%
2			<b>3r</b> : 65%
3			<b>3a</b> : 71% <sup>†</sup>
4			<b>3t</b> : 30%
5			<b>3a</b> : 44%
6			<b>3v</b> : 40% <sup>†</sup>
7			<b>3w</b> : 18% <sup>‡</sup>
8			<b>3x</b> : 21% <sup>‡</sup>
9			<b>3y</b> : 7% <sup>‡,  </sup>

\*Conditions: **1** (0.5 mmol), **2a** (2.5 mmol), CuI (0.05 mmol), LiCl (1.0 mmol), DMA/Et<sub>3</sub>N = 2:1 (1.5 ml), 120°C, 15 hours, under O<sub>2</sub> (1 atm). Isolated yields. <sup>†</sup>Twenty-four hours. <sup>‡</sup>Cul (30 mol%). <sup>||</sup>Nuclear magnetic resonance yield.

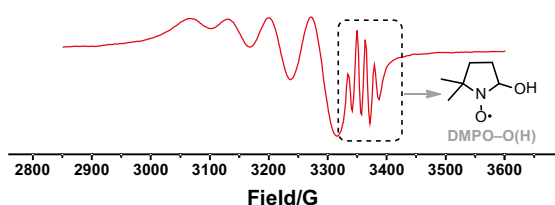
with acetophenone, 1-(4-chlorophenyl)ethan-1-one, and propiophenone to afford the corresponding products in moderate yields (Table 4, entries 1 to 3). The reaction of propane-1,2-diamine with acetophenone gave two products in 43 and 29% yields (Table 4, entry 4). In addition, when other unsymmetrical 1,2-diamines were used with **1a**, a similar selectivity was obtained (Table 4, entries 5 and 6).

As proposed, the copper-catalyzed aerobic oxidative C–H/N–H cross-coupling might undergo a radical process. To investigate this possibility, we performed a radical-trapping experiment. In the presence of 1 eq of 2,6-bis(1,1-dimethylethyl)-4-methylphenol, no product **3a** was obtained under the standard conditions (see Supporting Information, scheme S3). The reaction between acetophenone (**1a**) and ethylenediamine (**2a**) was also monitored by electron paramagnetic resonance (EPR), and the results are shown in Fig. 2. Cu(II) signal was detected during the reaction (Fig. 2A) (52, 53). In addition, when 5,5-dimethyl-1-pyrroline *N*-oxide (DMPO) was added to the reaction, the signal corresponding to DMPO–O(H) was identified (Fig. 2B), which is seen as four classical

**Table 4. Copper-catalyzed oxidative C–H/N–H coupling of 1 and 2.**

Entry	Product*	Entry	Product*
1	 4a: 66%	2	 4b: 66%
3	 4c: 58%	4	 4d: 72%, 60:40 (1/2)
5	 4e: 60%, 62:38 (1/2)	6	 4f: 62%, 65:35 (1/2)

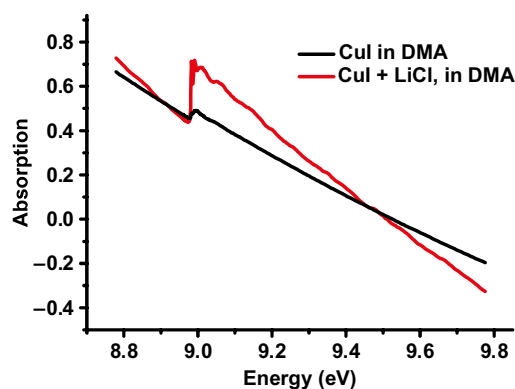
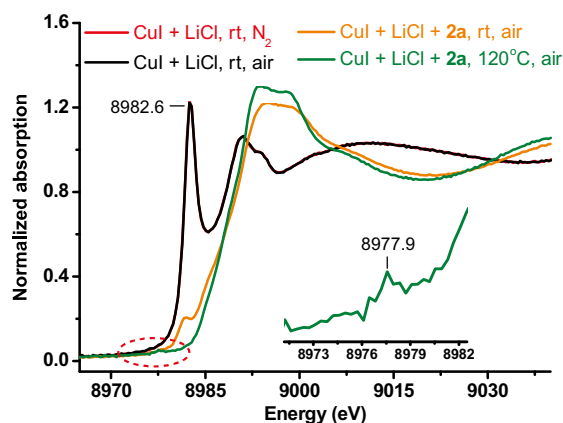
\*Conditions: **1** (0.5 mmol), **2** (2.5 mmol), CuI (0.05 mmol), LiCl (1.0 mmol), DMA/Et<sub>3</sub>N = 2:1 (1.5 ml), 120°C, 15 hours, under O<sub>2</sub> (1 atm). Isolated yields.

**A 1a + 2a under standard conditions****B 1a + 2a + DMPO under standard conditions****Fig. 2. The capture experiment of hydroxyl radical.** (A and B) The EPR spectra (X band, 9.4 GHz, room temperature) of (A) the reaction mixture of **1a** and **2a** under standard conditions and (B) the reaction mixture of **1a** and **2a** with the addition of DMPO under standard conditions.

peaks (54–56). The calculated hyperfine splittings are  $g_0$  (2.0069),  $\alpha^H$  (14.9 G), and  $\alpha^N$  (14.5 G). This result suggests that a hydroxyl radical may be involved in this transformation.

To further elucidate the mechanism, we performed experiments using x-ray absorption fine structure (XAFS) spectroscopy. As illustrated in Fig. 3, the DMA solution of CuI with LiCl and that without LiCl were tested. In the presence of LiCl, the edge step of copper K-edge spectrum is 0.31; however, it is only 0.05 without LiCl. Because the edge step is linearly proportional to the concentration of copper species, LiCl increases the solubility of CuI in DMA. We do observe that the turbid DMA solution of CuI became clear after the addition of LiCl, which is consistent with the XAFS.

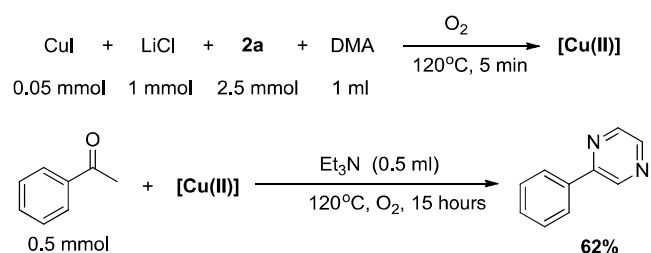
The oxidation of Cu(I) to Cu(II) was also studied. As shown in Fig. 4, under N<sub>2</sub> or air, the XANES (x-ray absorption near-edge struc-

**Fig. 3. Copper K-edge spectrum** (black line, 0.6 mmol of CuI in 12 ml of DMA; red line, 0.6 mmol of CuI and 12 mmol of LiCl in 12 ml of DMA).**Fig. 4. XANES spectra** [red line, 0.6 mmol of CuI and 12 mmol of LiCl in 12 ml of DMA at room temperature (rt) under N<sub>2</sub> for 5 min; black line, 0.6 mmol of CuI and 12 mmol of LiCl in 12 ml of DMA at rt under air for 5 min; brown line, 0.6 mmol of CuI, 12 mmol of LiCl, and 30 mmol of **2a** in 12 ml of DMA at rt under air for 5 min; green line, 0.6 mmol of CuI, 12 mmol of LiCl, and 30 mmol of **2a** in 12 ml of DMA at 120°C under air for 5 min].

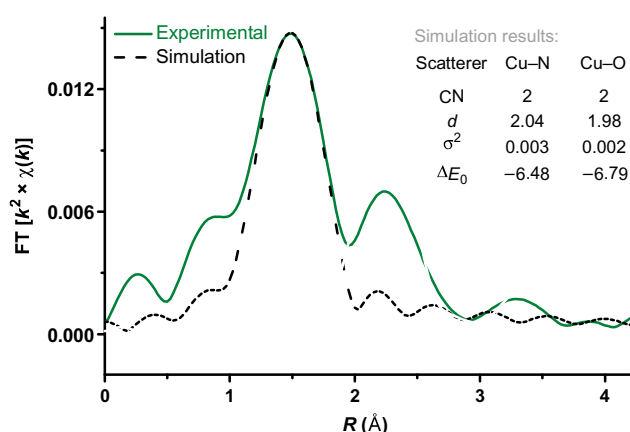
ture) spectrum of the mixture of CuI, LiCl, and DMF displays a peak at 8982.6 eV, which is assigned to a 1s → 4p Cu(I) transition. Upon addition of **2a**, Cu(I) is oxidized to Cu(II) by air at room temperature (partially oxidized) or at 120°C (completely oxidized in 5 min) as evidenced by the decrease in the Cu(I) pre-edge and a shift in the edge-energy position to 8984.9 eV. The small pre-edge peak at 8977.9 eV is also consistent with Cu(II) (Fig. 4, green line) (57, 58). These results are consistent with the coordination of **2a** to Cu(I), increasing the electron density of the copper center, which then facilitates this oxidation.

The reactivity of this Cu(II) intermediate was also investigated (59–63). As illustrated in Scheme 3, when the Cu(II) was used in the oxidative C–H/N–H coupling reaction, the desired product could be obtained in 62% yield. The results indicated that the Cu(II) species obtained by oxidizing the mixture of CuI, LiCl, **2a**, and DMA with air or O<sub>2</sub> was active for the oxidative C–H/N–H coupling reaction.

The structure of this active Cu(II) was determined by fitting of the EXAFS data. As shown in Fig. 5, the Fourier transform of the raw EXAFS data and the obtained EXAFS fit for the first shell data are given. The

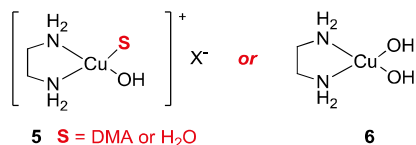


**Scheme 3.** Reactivity of the Cu(II) species in the oxidative C–H/N–H coupling reaction.

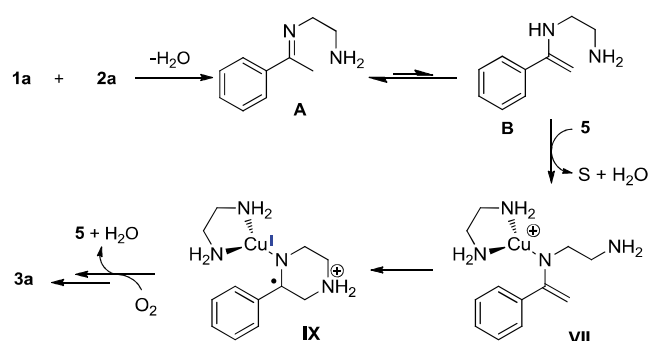


**Fig. 5.** The mixture of CuI, LiCl, 2a, and DMA in the presence of air at 120°C for 5 min [green line, FT (Fourier transform) = 2.62 to 9.42 Å<sup>–1</sup>] and simulation (black line, fitting range = 1.09 to 1.84 Å). CN, coordination number, *d*, bond distance.

obtained fitting parameters revealed that the Cu(II) center was coordinated by two N atoms at a distance of 2.04 Å and two O atoms at a shorter distance of 1.98 Å. Additionally, no Cu–Cu scattering peak was found in the raw EXAFS data, whereas the second shell might be attributed to the Cu–C at long distance (64). These results indicated that the Cu(II) species should be a monomer. Therefore, we propose the structure of the Cu(II) species to be similar to **5** or **6**. However, only a small amount of the desired product was produced when Cu(OH)<sub>2</sub>, instead of CuI, was used as the catalyst in this transformation (see table S1), suggesting that **5** rather than **6** might be the right structure.



According to the design in Scheme 2, the intramolecular cyclization of the enamine cationic radical should be the key step for the formation of pyrazine. Therefore, the DFT method B3LYP was also used to study this step (49). On the basis of the experimental results above, the copper(II)-involved cationic radical nucleophilic addition has also been considered in Fig. 6A. The transformation starts from complex **VII** and then the cyclization product **IX** could be generated through transition state **VIII-ts** with an activation energy of 16.4 kcal/mol. Cationic radical **IX** owns two resonance structures, which are described



**Scheme 4.** Putative mechanism.

as structures **IX** and **X**. To confirm the structure of **X**, an ESP map has been calculated. The dark blue color around the nitrogen atom in Fig. 6B suggests that most of the positive charge is located on nitrogen, rather than on copper. The spin density map also indicates that minimal unpaired electron density is located on copper, whereas most of the unpaired electron is shared by nitrogen and four carbon atoms (Fig. 6C). Therefore, the cyclization product prefers to exist in the form of structure **IX**.

On the basis of the results of mechanistic investigations and DFT calculations, a putative and simplified reaction pathway was proposed for these copper-catalyzed oxidative coupling reactions (Scheme 4). Initially, condensation between acetophenone and ethylenediamine occurred to afford imine **A**, which could isomerize to enamine **B**. In the presence of Cu species **5**, the intermediate **B** turned to the **VII** species via a well-known process. Subsequently, intramolecular cyclization of intermediate **VII** occurs by way of a radical pathway. Finally, the desired pyrazine was produced along with further oxidative dehydrogenation.

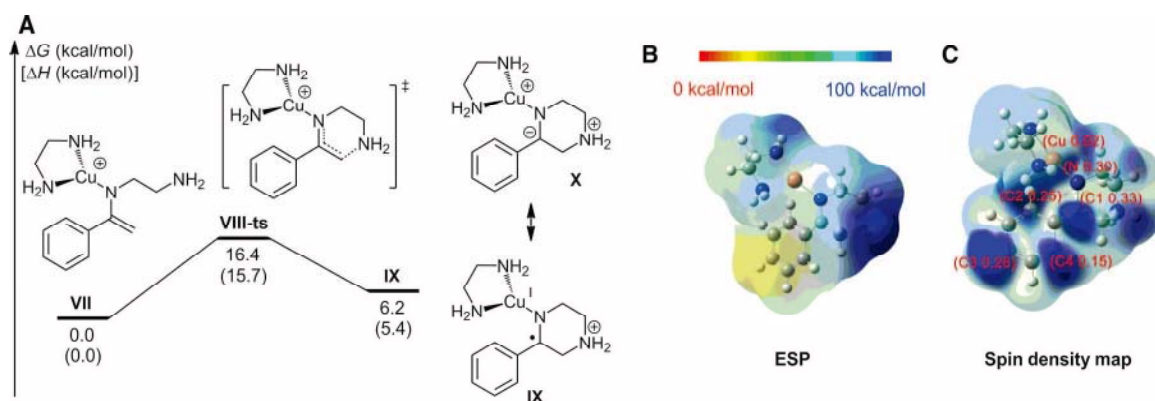
## CONCLUSION

In conclusion, we have developed a copper-catalyzed aerobic oxidative C–H/N–H coupling of ketones with diamines to construct aromatic pyrazine derivatives. By utilizing simple CuI as the catalyst and O<sub>2</sub> as the oxidant, various substituted ketones were suitable for this transformation. Compared with the traditional pyrazine syntheses from diketones with diamines, this protocol provided a more attractive approach. Preliminary mechanistic investigations indicated that radical species were involved in the transformation. Moreover, a structure of the reactive catalyst intermediate was proposed according to the XAFS experimental results. DFT calculations suggested that the intramolecular coupling of cationic radicals was a favorable pathway for this transformation. On the basis of the current mechanistic investigations, a simplified mechanism was proposed, which could be helpful for understanding the copper-catalyzed aerobic reactions. Further detailed mechanistic studies are under way in our laboratory and will be reported in the future.

## MATERIALS AND METHODS

### General procedure

CuI (9.5 mg, 0.05 mmol) and LiCl (42 mg, 1.0 mmol) were added to an oven-dried Schlenk tube that was then sealed with septa and fitted with an oxygen balloon. Subsequently, DMA (1 ml), ketone (0.5 mmol), Et<sub>3</sub>N (0.5 ml), and diamine (2.5 mmol) were injected via a syringe or



**Fig. 6.** Density functional theory (DFT) calculations for intramolecular cyclization of the enamine cationic radical. (A) Free energy profile for copper(II)-involved cyclization. (B) ESP map of complex IX. (C) Spin density map of complex IX. The numbers in parentheses are the corresponding Mulliken spin density located on each atom.

microsyringe. Finally, the Schlenk tube was allowed to stir at 120°C for 15 hours. After completion of the reaction, it was quenched by water and extracted with ethyl ether (3 × 10 ml). The organic layers were combined and dried over sodium sulfate. The pure product was obtained by flash column chromatography on silica gel (petroleum ether/ethyl acetate, 100:1).

## SUPPLEMENTARY MATERIALS

Supplementary material for this article is available at <http://advances.sciencemag.org/cgi/content/full/1/9/e1500656/DC1>

General information

General procedure

Table S1. The evaluation of several metal salts.

Table S2. The effects of other solvents.

Table S3. The effects of reaction temperature.

Table S4. The effects of the ratio of substrates.

Table S5. The effects of LiCl loading.

Table S6. Oxidative C–H/N–H coupling between ketone and ethylenediamine under standard reaction conditions.

Scheme S1. Gas chromatography–mass spectrometry analysis of the reaction between **1a** and **2a**.

Scheme S2. Gas chromatography–mass spectrometry analysis of the reaction between **1a** and **2e**.

EPR experiments

Radical trapping experiments

Scheme S3. Radical trapping experiment using BHT [2,6-bis(1,1-dimethylethyl)-4-methylphenol] as the scavenger.

Scheme S4. Radical trapping experiment using TEMPO (2,2,6,6-tetramethylpiperidinyloxy) as the scavenger.

XAS experiments

General computational calculation details

Detailed descriptions for products

NMR data

References (65–73)

## REFERENCES AND NOTES

- C.-L. Sun, B.-J. Li, Z.-J. Shi, Pd-catalyzed oxidative coupling with organometallic reagents via C–H activation. *Chem. Commun.* **46**, 677–685 (2010).
- C. Liu, H. Zhang, W. Shi, A. Lei, Bond formations between two nucleophiles: Transition metal catalyzed oxidative cross-coupling reactions. *Chem. Rev.* **111**, 1780–1824 (2011).
- W. Shi, C. Liu, A. Lei, Transition-metal catalyzed oxidative cross-coupling reactions to form C–C bonds involving organometallic reagents as nucleophiles. *Chem. Soc. Rev.* **40**, 2761–2776 (2011).
- G. J. Hutchings, M. S. Scurrell, J. R. Woodhouse, Oxidative coupling of methane using oxide catalysts. *Chem. Soc. Rev.* **18**, 251–283 (1989).
- C.-J. Li, Cross-Dehydrogenative coupling (CDC): Exploring C–C bond formations beyond functional group transformations. *Acc. Chem. Res.* **42**, 335–344 (2009).
- X. Chen, K. M. Engle, D.-H. Wang, J.-Q. Yu, Palladium(II)-catalyzed C–H activation/C–C cross-coupling reactions: Versatility and practicality. *Angew. Chem. Int. Ed.* **48**, 5094–5115 (2009).
- C. S. Yeung, V. M. Dong, Catalytic dehydrogenative cross-coupling: Forming carbon–carbon bonds by oxidizing two carbon–hydrogen bonds. *Chem. Rev.* **111**, 1215–1292 (2011).
- S. H. Cho, J. Y. Kim, J. Kwak, S. Chang, Recent advances in the transition metal-catalyzed twofold oxidative C–H bond activation strategy for C–C and C–N bond formation. *Chem. Soc. Rev.* **40**, 5068–5083 (2011).
- R. Giri, B.-F. Shi, K. M. Engle, N. Maugel, J.-Q. Yu, Transition metal-catalyzed C–H activation reactions: Diastereoselectivity and enantioselectivity. *Chem. Soc. Rev.* **38**, 3242–3272 (2009).
- T. W. Lyons, M. S. Sanford, Palladium-catalyzed ligand-directed C–H functionalization reactions. *Chem. Rev.* **110**, 1147–1169 (2010).
- G. Dyker, *Handbook of C–H Transformations. Applications in Organic Synthesis* (Wiley-VCH, Weinheim, Germany, 2005).
- T. Hamada, X. Ye, S. S. Stahl, Copper-catalyzed aerobic oxidative amidation of terminal alkynes: Efficient synthesis of enamides. *J. Am. Chem. Soc.* **130**, 833–835 (2008).
- L. V. Desai, H. A. Malik, M. S. Sanford, Oxone as an inexpensive, safe, and environmentally benign oxidant for C–H bond oxygenation. *Org. Lett.* **8**, 1141–1144 (2006).
- N. Sato, *Comprehensive Heterocyclic Chemistry II* (Pergamon, Oxford, UK, 1996).
- S. Berg, M. Bergh, S. Hellberg, K. Högdin, Y. Lo-Alfredsson, P. Söderman, S. von Berg, T. Weigelt, M. Ormo, Y. Xue, J. Tucker, J. Neelissen, E. Jerning, Y. Nilsson, R. Bhat, Discovery of novel potent and highly selective glycogen synthase kinase-3 $\beta$  (GSK3 $\beta$ ) inhibitors for Alzheimer's disease: Design, synthesis, and characterization of pyrazines. *J. Med. Chem.* **55**, 9107–9119 (2012).
- A. Gazit, H. App, G. McMahon, J. Chen, A. Levitzki, F. D. Bohmer, Tyrphostins. 5. Potent inhibitors of platelet-derived growth factor receptor tyrosine kinase: Structure–activity relationships in quinoxalines, quinolines, and indole tyrphostins. *J. Med. Chem.* **39**, 2170–2177 (1996).
- L. E. Seitz, W. J. Suling, R. C. Reynolds, Synthesis and antimycobacterial activity of pyrazine and quinoxaline derivatives. *J. Med. Chem.* **45**, 5604–5606 (2002).
- S. Yanagisawa, K. Ueda, T. Taniguchi, K. Itami, Potassium *t*-butoxide alone can promote the biaryl coupling of electron-deficient nitrogen heterocycles and haloarenes. *Org. Lett.* **10**, 4673–4676 (2008).
- S. Achelle, C. Baudequin, N. Plé, Luminescent materials incorporating pyrazine or quinoxaline moieties. *Dyes Pigm.* **98**, 575–600 (2013).
- S. A. Raw, C. D. Wilfred, R. J. K. Taylor, Preparation of quinoxalines, dihydropyrazines, pyrazines and piperazines using tandem oxidation processes. *Chem. Commun.* **39**, 2286–2287 (2003).
- S. A. Kotharkar, D. B. Shinde, Pb(NO<sub>3</sub>)<sub>2</sub> mediated synthesis of pyrazine. *Chin. J. Chem.* **25**, 105–107 (2007).
- P. Ghosh, A. Mandal, Greener approach toward one pot route to pyrazine synthesis. *Green Chem. Lett. Rev.* **5**, 127–134 (2012).
- T.-Q. Huang, W.-Y. Qu, J.-C. Ding, M.-C. Liu, H.-Y. Wu, J.-X. Chen, Catalyst-free protocol for the synthesis of quinoxalines and pyrazines in PEG. *J. Heterocycl. Chem.* **50**, 293–297 (2013).
- P. J. Steel, G. B. Caygill, Cyclometallated compounds V. Double cyclopalladation of diphenyl pyrazines and related ligands. *J. Organomet. Chem.* **395**, 359–373 (1990).
- S. A. Raw, C. D. Wilfred, R. J. K. Taylor, Tandem oxidation processes for the preparation of nitrogen-containing heteroaromatic and heterocyclic compounds. *Org. Biomol. Chem.* **2**, 788–796 (2004).
- Z. Zheng, X. Zhou, Metal-free oxidation of  $\alpha$ -hydroxy ketones to 1,2-diketones catalyzed by mesoporous carbon nitride with visible light. *Chin. J. Chem.* **30**, 1683–1686 (2012).
- C. Qi, H. Jiang, L. Huang, Z. Chen, H. Chen, DABCO-catalyzed oxidation of deoxybenzoins to benzils with air and one-pot synthesis of quinoxalines. *Synthesis* **2011**, 387–396 (2010).

28. A. Gao, F. Yang, J. Li, Y. Wu, Pd/Cu-catalyzed oxidation of alkynes into 1,2-diketones using DMSO as the oxidant. *Tetrahedron* **68**, 4950–4954 (2012).
29. A. K. Bagdi, M. Rahman, S. Santra, A. Majee, A. Hajra, Copper-catalyzed synthesis of imidazo[1,2-*a*]pyridines through tandem imine formation-oxidative cyclization under ambient air: One-step synthesis of zolimidine on a gram-scale. *Adv. Synth. Catal.* **355**, 1741–1747 (2013).
30. Z.-J. Cai, S.-Y. Wang, S.-J. Ji, Copper(II) iodide/boron trifluoride etherate-cocatalyzed aerobic dehydrogenative reactions applied in the synthesis of substituted heteroaromatic imidazo[1,2-*a*]pyridines. *Adv. Synth. Catal.* **355**, 2686–2692 (2013).
31. Y. Cui, C. He, A silver-catalyzed intramolecular amidation of saturated C–H bonds. *Angew. Chem. Int. Ed.* **43**, 4210–4212 (2004).
32. H. M. L. Davies, M. S. Long, Recent advances in catalytic intramolecular C–H aminations. *Angew. Chem. Int. Ed.* **44**, 3518–3520 (2005).
33. F. Collet, R. H. Dodd, P. Dauban, Catalytic C–H amination: Recent progress and future directions. *Chem. Commun.* **45**, 5061–5074 (2009).
34. C. G. Espino, P. M. Wehn, J. Du Bois, Synthesis of 1,3-difunctionalized amine derivatives through selective C–H bond oxidation. *J. Am. Chem. Soc.* **123**, 6935–6936 (2001).
35. X. Liu, Y. Zhang, L. Wang, H. Fu, Y. Jiang, Y. Zhao, General and efficient copper-catalyzed amidation of saturated C–H bonds using *N*-halosuccinimides as the oxidants. *J. Org. Chem.* **73**, 6207–6212 (2008).
36. G. Pelletier, D. A. Powell, Copper-catalyzed amidation of allylic and benzylic C–H bonds. *Org. Lett.* **8**, 6031 (2006).
37. R. W. Evans, J. R. Zbieg, S. Zhu, W. Li, D. W. C. MacMillan, Simple catalytic mechanism for the direct coupling of  $\alpha$ -carbonyls with functionalized amines: A one-step synthesis of plavix. *J. Am. Chem. Soc.* **135**, 16074–16077 (2013).
38. X. Xu, Y. Deng, X. Li, Z. Zhao, W. Fang, X. Yan, Iodine (III)-mediated one-pot synthesis of quinoxaline by tandem nucleophilic substitution and cyclization. *J. Chem. Res.* **35**, 605–607 (2011).
39. Z.-J. Cai, S.-Y. Wang, S.-J. Ji, CuI/BF<sub>3</sub>·Et<sub>2</sub>O cocatalyzed aerobic dehydrogenative reactions of ketones with benzylamines: Facile synthesis of substituted imidazoles. *Org. Lett.* **14**, 6068–6071 (2012).
40. M.-Y. Chang, T.-W. Lee, R.-T. Hsu, T.-L. Yen, Synthesis of quinoxaline analogues. *Synthesis* **2011**, 3143–3151 (2011).
41. M. Lian, Q. Li, Y. Zhu, G. Yin, A. Wu, Logic design and synthesis of quinoxalines via the integration of iodination/oxidation/cyclization sequences from ketones and 1,2-diamines. *Tetrahedron* **68**, 9598–9605 (2012).
42. S. E. Allen, R. R. Walvoord, R. Padilla-Salinas, M. C. Kozlowski, Aerobic copper-catalyzed organic reactions. *Chem. Rev.* **113**, 6234–6458 (2013).
43. R. Shi, L. Lu, H. Zhang, B. Chen, Y. Sha, C. Liu, A. Lei, Palladium/copper-catalyzed oxidative C–H alkenylation/*N*-dealkylative carbonylation of tertiary anilines. *Angew. Chem. Int. Ed.* **52**, 10582–10585 (2013).
44. J. Ke, C. He, H. Liu, M. Li, A. Lei, Oxidative cross-coupling/cyclization to build polysubstituted pyrroles from terminal alkynes and  $\beta$ -enamino esters. *Chem. Commun.* **49**, 7549–7551 (2013).
45. Z. Li, C.-J. Li, Highly efficient copper-catalyzed nitro-mannich type reaction: Cross-dehydrogenative-coupling between sp<sup>3</sup> C–H bond and sp<sup>3</sup> C–H bond. *J. Am. Chem. Soc.* **127**, 3672–3673 (2005).
46. T. D. Beeson, A. Mastrocchio, J.-B. Hong, K. Ashton, D. W. C. MacMillan, Enantioselective organocatalysis using SOMO activation. *Science* **316**, 582–585 (2007).
47. S.-I. Murahashi, N. Komiya, H. Terai, Ruthenium-catalyzed oxidative cyanation of tertiary amines with hydrogen peroxide and sodium cyanide. *Angew. Chem. Int. Ed.* **44**, 6931–6933 (2005).
48. C. Wei, C.-J. Li, Enantioselective direct-addition of terminal alkynes to imines catalyzed by copper(I)pybox complex in water and in toluene. *J. Am. Chem. Soc.* **124**, 5638–5639 (2002).
49. Computational details are listed in the Supporting Information.
50. M. Nishino, K. Hirano, T. Satoh, M. Miura, Copper-catalyzed oxidative direct cyclization of *N*-methylanilines with electron-deficient alkenes using molecular oxygen. *J. Org. Chem.* **76**, 6447–6451 (2011).
51. G. Rossé, J. Strickler, M. Patek, Efficient solid-phase synthesis of disubstituted 1,3-dihydroimidazol-2-ones. *Synlett* **2004**, 2167–2168 (2004).
52. I. Caretti, E. Carter, I. A. Fallis, D. M. Murphy, S. Van Doorslaer, Interactions of an asymmetric amine with a non-C<sub>2</sub> symmetric Cu–salen complex: An EPR/ENDOR and HSCORE investigation. *Phys. Chem. Chem. Phys.* **13**, 20427–20434 (2011).
53. P. Håkansson, T. Nguyen, P. B. Nair, R. Edge, E. Stulz, Cu(II)-porphyrin molecular dynamics as seen in a novel EPR/Stochastic Liouville equation study. *Phys. Chem. Chem. Phys.* **15**, 10930–10941 (2013).
54. A. Samuni, C. M. Krishna, P. Riesz, E. Finkelstein, A. Russo, Superoxide reaction with nitroxide spin-adducts. *Free Radic. Biol. Med.* **6**, 141–148 (1989).
55. H. Zhao, J. Joseph, H. Zhang, H. Karoui, B. Kalyanaram, Synthesis and biochemical applications of a solid cyclic nitron spin trap: A relatively superior trap for detecting superoxide anions and glutathyl radicals. *Free Radic. Biol. Med.* **31**, 599–606 (2001).
56. C. Zhang, P. Feng, N. Jiao, Cu-catalyzed esterification reaction via aerobic oxygenation and C–C bond cleavage: An approach to  $\alpha$ -ketoesters. *J. Am. Chem. Soc.* **135**, 15257–15262 (2013).
57. R. Bai, G. Zhang, H. Yi, Z. Huang, X. Qi, C. Liu, J. T. Miller, A. J. Kropf, E. E. Bunel, Y. Lan, A. Lei, Cu(II)–Cu(I) synergistic cooperation to lead the alkyne C–H activation. *J. Am. Chem. Soc.* **136**, 16760–16763 (2014).
58. G. Zhang, H. Yi, G. Zhang, Y. Deng, R. Bai, H. Zhang, J. T. Miller, A. J. Kropf, E. E. Bunel, A. Lei, Direct observation of reduction of Cu(II) to Cu(I) by terminal alkynes. *J. Am. Chem. Soc.* **136**, 924–926 (2014).
59. A. N. Campbell, S. S. Stahl, Overcoming the “Oxidant Problem”: Strategies to use O<sub>2</sub> as the oxidant in organometallic C–H oxidation reactions catalyzed by Pd (and Cu). *Acc. Chem. Res.* **45**, 851–863 (2012).
60. S. D. McCann, S. S. Stahl, Copper-catalyzed aerobic oxidations of organic molecules: Pathways for two-electron oxidation with a four-electron oxidant and a one-electron redox-active catalyst. *Acc. Chem. Res.* **48**, 1756–1766 (2015).
61. A. E. Wendlandt, A. M. Suess, S. S. Stahl, Copper-catalyzed aerobic oxidative C–H functionalizations: Trends and mechanistic insights. *Angew. Chem. Int. Ed.* **50**, 11062–11087 (2011).
62. A. E. King, L. M. Huffman, A. Casitas, M. Costas, X. Ribas, S. S. Stahl, Copper-catalyzed aerobic oxidative functionalization of an arene C–H bond: Evidence for an aryl-copper(III) intermediate. *J. Am. Chem. Soc.* **132**, 12068–12073 (2010).
63. A. M. Suess, M. Z. Ertem, C. J. Cramer, S. S. Stahl, Divergence between organometallic and single-electron-transfer mechanisms in copper(II)-mediated aerobic C–H oxidation. *J. Am. Chem. Soc.* **135**, 9797–9804 (2013).
64. M. Tromp, G. P. F. van Strijdonck, S. S. van Berkel, A. van den Hoogenband, M. C. Feiters, B. de Bruin, S. G. Fiddy, A. M. J. van der Eerden, J. A. van Bokhoven, P. W. N. M. van Leeuwen, D. C. Koningsberger, Multitechnique approach to reveal the mechanism of copper(II)-catalyzed arylation reactions. *Organometallics* **29**, 3085–3097 (2010).
65. A. D. Becke, Density-functional thermochemistry. III. The role of exact exchange. *J. Chem. Phys.* **98**, 5648 (1993).
66. C. Lee, W. Yang, R. G. Parr, Development of the Colle-Salvetti correlation-energy formula into a functional of the electron density. *Phys. Rev. B Condens Matter* **37**, 785 (1988).
67. S. Miertuš, E. Scrocco, J. Tomasi, Electrostatic interaction of a solute with a continuum. A direct utilization of ab initio molecular potentials for the prevision of solvent effects. *Chem. Phys.* **55**, 117–129 (1981).
68. S. Miertuš, J. Tomasi, Approximate evaluations of the electrostatic free energy and internal energy changes in solution processes. *Chem. Phys.* **65**, 239–245 (1982).
69. P. P. Singh, S. K. Aithagani, M. Yadav, V. P. Singh, R. A. Vishwakarma, Iron-catalyzed cross-coupling of electron-deficient heterocycles and quinone with organoboron species via innate C–H functionalization: Application in total synthesis of pyrazine alkaloid botryllazine A. *J. Org. Chem.* **78**, 2639–2648 (2013).
70. C. F. Harris, D. Ravindranathan, S. Huo, Oxidative addition of heteroaromatic halides to Negishi reagent and subsequent cross-coupling reactions. *Tetrahedron Lett.* **53**, 5389–5392 (2012).
71. M. Li, R. Hua, Gold(I)-catalyzed direct C–H arylation of pyrazine and pyridine with aryl bromides. *Tetrahedron Lett.* **50**, 1478–1481 (2009).
72. C.-L. Deng, S.-M. Guo, Y.-X. Xie, J.-H. Li, Mild and ligand-free palladium-catalyzed cross-couplings between aryl halides and arylboronic acids for the synthesis of biaryls and heterocycle-containing biaryls. *Eur. J. Org. Chem.* **2007**, 1457–1462 (2007).
73. R. J. Bergeron, P. Hoffman, Application of *N*-phenyltrifluoromethanesulfonamides to the synthesis of pyrazines. *J. Org. Chem.* **45**, 161–163 (1980).

**Funding:** This work was supported by the 973 Program (grants 2012CB725302 and 2011CB808600), the National Natural Science Foundation of China (grants 21390400, 21272180, 21302148, 21372266, and 51302327), the Research Fund for the Doctoral Program of Higher Education of China (grant 20120141130002), the Program for Changjiang Scholars and Innovative Research Team in University (grant IRT1030), and the Ministry of Science and Technology of China (grant 2012YQ120060). The Program of Introducing Talents of Discipline to Universities of China (111 Program) is also appreciated. This work was also funded by the Chemical Sciences and Engineering Division, Argonne National Laboratory. Use of the Advanced Photon Source was supported by the U.S. Department of Energy, Office of Science, Office of Basic Energy Sciences, under contract no. DE-AC02-06CH11357. MRCAT (Materials Research Collaborative Access Team) operations are supported by the Department of Energy and the MRCAT member institutions. Part of XAFS data were collected at beamline 17C1 of the National Synchrotron Radiation Research Center, Taiwan. **Author contributions:** A.L. conceived the project. K.W. and Z.H. designed and performed the synthetic work, and designed the work for mechanistic investigation. X.Q., Y. Li, and Y. Lan performed the DFT calculations. Z.H., G.Z., J.T.M., C.-W.P., and J.-F.L. performed the XAS experiments. C.L., L.M., Y. Lan, and E.E.B. discussed the results and designed part of the experiments. K.W. and H.Y. performed the EPR experiments. K.W., Z.H., and A.L. wrote the manuscript. K.W. and Z.H. wrote the supplementary materials and contributed other related materials. **Competing interests:** The authors declare that they have no competing interests. **Data and materials availability:** Data will be made available upon request by emailing aiwenlei@whu.edu.cn.

Submitted 21 May 2015

Accepted 22 July 2015

Published 9 October 2015

10.1126/sciadv.1500656

**Citation:** K. Wu, Z. Huang, X. Qi, Y. Li, G. Zhang, C. Liu, H. Yi, L. Meng, E. E. Bunel, J. T. Miller, C.-W. Pao, J.-F. Lee, Y. Lan, A. Lei, Copper-catalyzed aerobic oxidative coupling: From ketone and diamine to pyrazine. *Sci. Adv.* **1**, e1500656 (2015).

ARTICLE

Received 12 Jun 2014 | Accepted 30 Oct 2014 | Published 8 Dec 2014

DOI: 10.1038/ncomms6707

# Asymmetric total synthesis of (–)-lingzhiol via a Rh-catalysed [3 + 2] cycloaddition

Rong Long<sup>1,2,\*</sup>, Jun Huang<sup>1,2,\*</sup>, Wenbin Shao<sup>1,2</sup>, Song Liu<sup>3</sup>, Yu Lan<sup>3</sup>, Jianxian Gong<sup>1,2</sup> & Zhen Yang<sup>1,2,4</sup>

The development of efficient reactions for the one-pot construction of bicyclic ring systems bearing two quaternary carbon centres at their bridgehead positions represents a significant challenge to synthetic chemistry. The development of new methods capable of overcoming this challenge is highly desirable, because this motif can be found in a wide range of natural products with significant biological activities. Herein, we report an efficient [3 + 2] cycloaddition reaction between an enal and an allenyl rhodium species, which was generated *in situ* from the corresponding enynol via a retro metal-propargylation reaction, to give [3.3.0] and [3.4.0] bicyclic systems bearing two quaternary atoms at their bridgehead positions. The developed chemistry has been successfully applied to the asymmetric total synthesis of natural product (–)-lingzhiol (**4**) for the first time in 17 steps.

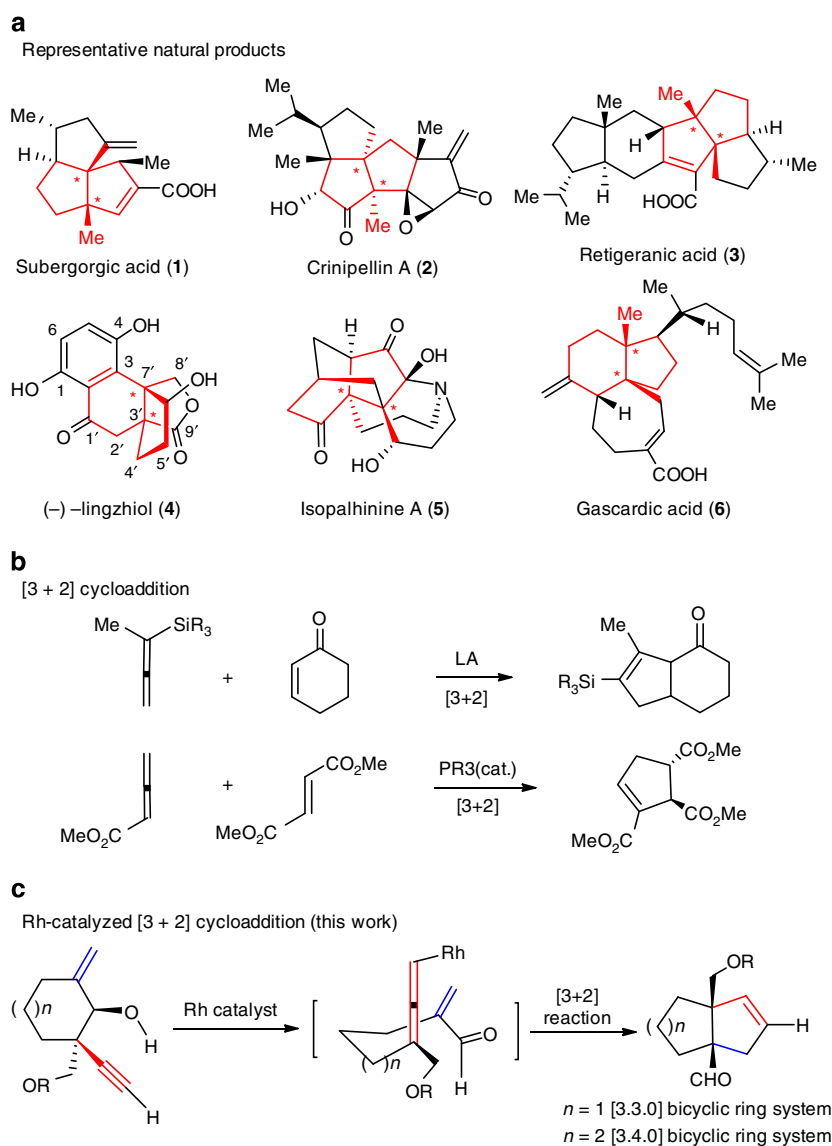
<sup>1</sup>Laboratory of Chemical Genomics, School of Chemical Biology and Biotechnology, Peking University Shenzhen Graduate School, Shenzhen 518055, China. <sup>2</sup>Key Laboratory of Bioorganic Chemistry and Molecular Engineering of Ministry of Education, Beijing National Laboratory for Molecular Science (BNLMS), and Peking-Tsinghua Center for Life Sciences and Academy for Advanced Interdisciplinary Studies, Peking University, Beijing 100871, China. <sup>3</sup>School of Chemistry and Chemical Engineering, Chongqing University, Chongqing 400030, China. <sup>4</sup>Key Laboratory of Marine Drugs, Chinese Ministry of Education, School of Medicine and Pharmacy, Ocean University of China, 5 Yushan Road, Qingdao 266003, China. \* These authors contributed equally to this work. Correspondence and requests for materials should be addressed to Y.L. (email: lanyu@cqu.edu.cn) or to J.G. (email: gongjx@pku.edu.cn) or to Z.Y. (email: zyang@pku.edu.cn)



A wide variety of intriguing natural products with five-membered [3.3.0] and [4.3.0] carbobicyclic ring systems and two vicinal stereogenic quaternary carbon centres at the ring junction have been identified to exhibit significant biological activities that could potentially be used to develop new drugs<sup>1–6</sup>. Subergorgic acid (**1** in Fig. 1a), isolated from the Pacific gorgonian coral *Subergorgia suberosa*, showed cardiotoxic activity<sup>1</sup>. Crinipellin A (**2**), isolated from the fungus *Crinipellis stipitaria* (Agaricales), has been reported to exhibit potent antibiotic activity<sup>2</sup>. Retigeranic acid (**3**) is a representative member of the sesterterpenoid family of compounds and exhibits a broad range of biological activities<sup>3–7</sup>. Although compounds of this type are well known to elicit a variety of interesting biological responses, efficient methods for their construction are scarce. New synthetic strategies and methodologies are therefore required to provide facile access to these natural products and their analogues, to allow for the development of new therapeutic agents and drugs.

The construction of vicinal quaternary carbon centres, however, represents a significant challenge in natural-product synthesis<sup>8</sup>. Despite significant progress in this area during the last two decades towards the stereoselective synthesis of vicinal quaternary carbon centres<sup>9–16</sup>, there are currently no efficient reactions available for the enantioselective construction of [3.3.0] and [4.3.0] bicyclic ring systems<sup>17,18</sup> bearing two quaternary carbon centres at their bridgehead positions. This lack of suitable synthetic methodologies has therefore limited the in-depth exploitation of the biological and pharmaceutical value of these natural products.

Five-membered carbocycles can be constructed according to reactions between 3-C and 2-C units<sup>19,20</sup>. Danheiser and Becker<sup>21</sup> reported the use of an allene as a three-carbon synthon in their [3 + 2] cycloaddition reaction of Si-substituted allenes (Fig. 1b). In a separate study, Lu *et al.*<sup>22,23</sup> reported the development of a phosphine catalysed [3 + 2] cycloaddition reaction. Recently, phosphine-catalysed regio- and enantio-selective



**Figure 1 | Representative natural products containing five-membered carbocycles and their synthetic methods.** (a) Selected biologically active natural products bearing bridgehead functionalized [3.3.0] fused rings and [3.4.0] fused rings. (b) Lewis acid-promoted and phosphine-catalysed [3 + 2] cycloaddition of allenates to construct five-membered carbocycles. (c) Our strategy to access both [3.3.0] and [4.3.0] bicyclic ring systems via Rh-catalysed [3 + 2] cycloaddition.

[3 + 2] cycloadditions of allenates with electron-deficient olefins and imines—a process that provided efficient access to a variety of synthetically useful carbo- and heterocycles—have received considerable research interest, and significant progresses have been elegantly demonstrated by different groups<sup>24–33</sup>. Despite the above impressive achievements, there is an urgent need for the development of efficient [3 + 2] cycloaddition reaction to enable the direct and stereoselective syntheses of [3.3.0] and [4.3.0] bicyclic ring systems bearing two quaternary carbon centres at their bridgehead positions.

As a useful nucleophile, allenyl metal species can react with a wide variety of electrophiles<sup>34–36</sup> and, consequently, these adducts have been applied to the syntheses of a broad range of structurally diverse compounds<sup>37–39</sup>. However, the use of allenyl rhodium species in organic synthesis remains scarce<sup>40–42</sup>.

With this in mind, and as part of our ongoing work towards the development of efficient methods for the total synthesis of natural products, we investigated the use allenyl rhodium species as three-carbon synthons in organic synthesis. It was envisaged that the use of an  $\alpha,\beta$ -unsaturated aldehyde linked to an allenyl rhodium moiety could be used for an intramolecular [3 + 2] cycloaddition reaction, which would allow for the formation of a cyclopentane ring<sup>43,44</sup>. Herein, we report the development of a new [3 + 2] cycloaddition reaction between an enal and an allenyl rhodium species, which was generated *in situ* by the Rh(I)-mediated retro-propargylation of homo-propargyl alcohol<sup>45</sup>, to give [3.3.0] and [4.3.0] bicyclic ring systems bearing two quaternary carbon centres at the bridgehead positions (Fig. 1c). Notably, the use of chiral starting materials in this reaction led to the unprecedented synthesis of enantiomerically pure [3.3.0] bicyclic products, representing a significant development in terms of the application of this reaction to the total synthesis of naturally occurring biologically active chiral molecules. Furthermore, this newly developed reaction has been successfully applied to the total synthesis of natural product

lingzhiol, which is reported to be an important agent for the study and treatment of diabetic nephropathy<sup>4</sup>.

## Results

**Optimization of the reaction conditions.** During the course of this study, compound **7a** (entry 1 in Table 1), which contained a homo-propargyl alcohol and a terminal alkene, was converted to **7b** in 23% yield as a single diastereoisomer in the presence of  $[\text{RhCl}(\text{cod})_2]$  (5 mol%) under a balloon pressure of CO. The structure of **7a** was confirmed by X-ray crystallographic analysis of its precursor diol, and this observation inspired us to investigate this reaction in greater detail.

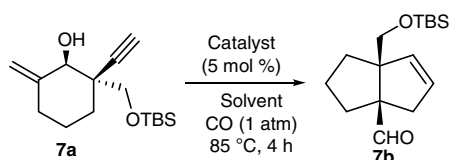
Initial optimization of the reaction conditions have been performed on studying the effects of various reaction parameters on the outcome of the reaction, including the type of rhodium catalyst, the solvent and the temperature. Of the different rhodium catalysts and solvents tested,  $[\text{RhCl}(\text{CO})_2]_2$  (refs 46–48) in  $\text{ClCH}_2\text{CH}_2\text{Cl}$  was found to be optimal. To demonstrate the catalytic role of the rhodium catalyst, the annulation reaction of **7a** was conducted in the absence of  $[\text{RhCl}(\text{CO})_2]_2$ ; as a result, no annulated product **7b** was observed, indicating that the rhodium catalyst was essential to the success of the reaction. We then carried out the reaction below 80 °C and the reaction became sluggish, which resulted in lower yields of the annulated product **7b**. The results of these screening experiments were combined into a single optimized procedure involving the use of a catalytic amount of  $[\text{RhCl}(\text{CO})_2]_2$  (5 mol%) at a temperature of 85 °C under a positive pressure of CO (balloon) in  $\text{ClCH}_2\text{CH}_2\text{Cl}$ , which gave the annulated **7b** in an isolated yield of 87% (entry 7 in Table 1).

It is noteworthy that these reactions had to be conducted under an atmosphere of CO. When the reaction was conducted in the absence of CO, the desired product **7b** was formed in a reduced yield of only 45% (entry 8 in Table 1). To determine whether the observed low yield occurred as a consequence of a Rh-catalysed decarbonylation<sup>49</sup> reaction, we monitored the reaction by high-resolution mass spectroscopy, although the results of this analysis failed to identify the formation of a decarbonylative species during the course of the reaction (Supplementary Fig. 80). Based on these results, it was proposed that under an atmosphere of CO, the decomposition of  $[\text{RhCl}(\text{CO})_2]_2$  catalyst was in part prohibited, thus facilitating the conversion from **7a** to **7b**.

**Substrate scope.** To assess the scope and generality of the optimized reaction conditions, we prepared enynols **8a–14a** in their racemic forms and investigated their annulation under the conditions listed in Table 2. Substrates **8a–11a**, bearing an ether, ester or carboxylate substituent (Table 2, entries 2–4), can give the corresponding annulated products **8b–11b** in good-to-excellent yields (68–98%). Furthermore, the alkyne moiety of the substrate could be substituted with an aromatic group, which demonstrated that moderate reaction yields could be achieved in most cases (Table 2, entry 6). However, when the substrates bear a bromine substituent at the terminal alkyne position (entry 5, **12a**), or two methyl groups at the exocyclic methylene positions (entry 7, **14a**), the yields for the annulation are relatively low due to the substrate decomposition under the standard conditions.

The annulation reaction is also compatible with the presence of a bromine substituent at the terminal alkyne position, although the corresponding [3 + 2] product **12b** was isolated in low yield due to the stability problems. The substitution of the exocyclic methylene group with two methyl groups was also well tolerated under the optimized conditions (Table 2, entry 7), with the annulated product **14b** being isolated in a yield of 43%. This particular example highlights the potential value of applying our

**Table 1 | Catalyst screening and reaction optimization conditions.**



Entry	Catalyst	Solvent	Yield (%) <sup>†</sup>
1	$[\text{RhCl}(\text{cod})_2]$	Toluene	23
2	$[\text{RhCl}(\text{cod})_2]$	$\text{ClCH}_2\text{CH}_2\text{Cl}$	75
3	$\text{Rh}(\text{PPh}_3)_3\text{Cl}$	$\text{ClCH}_2\text{CH}_2\text{Cl}$	0
4	$\text{RhCO}(\text{PPh}_3)_3\text{Cl}$	$\text{ClCH}_2\text{CH}_2\text{Cl}$	< 5
5	$[\text{Rh}(\text{C}_7\text{H}_5)_2]\text{BF}_4$	$\text{ClCH}_2\text{CH}_2\text{Cl}$	16
6	$[\text{RhOH}(\text{cod})_2]$	$\text{ClCH}_2\text{CH}_2\text{Cl}$	48
7	$[\text{RhCl}(\text{CO})_2]_2$	$\text{ClCH}_2\text{CH}_2\text{Cl}$	87
8	$[\text{RhCl}(\text{CO})_2]_2$	$\text{ClCH}_2\text{CH}_2\text{Cl}$	45 <sup>†</sup>
9	$[\text{RhCl}(\text{CO})_2]_2$	MeCN	< 5
10	$[\text{RhCl}(\text{CO})_2]_2$	THF	17
11	$[\text{RhCl}(\text{CO})_2]_2$	1,4-dioxane	0

<sup>†</sup>Isolated yield after silica gel column chromatography.

<sup>†</sup>The reaction was carried out in the absence of CO.

**Table 2 | Synthesis of the [3,3,0]-bicyclic scaffolds.**

Entry	Substrate	Product	Time (h)	Yield*
1			8	82%
2			8	68%
3			8	98%
P = NO <sub>2</sub> PhCO		X-ray crystallography		
4			8	85%
5			24	30%
6				
		<b>13ba</b> (R <sup>3</sup> = H)	24	50%
		<b>13bb</b> (R <sup>3</sup> = <i>p</i> -Me)	24	61%
		<b>13bc</b> (R <sup>3</sup> = <i>p</i> -OMe)	8	55%
		<b>13bd</b> (R <sup>3</sup> = <i>p</i> -F)	8	45%
		<b>13be</b> (R <sup>3</sup> = <i>o</i> -OMe)	72	16%
		<b>13bf</b> (R <sup>3</sup> = <i>o</i> -NO <sub>2</sub> )	72	6%
7			8	43%

\*Isolated yield after silica gel column chromatography.

method as a strategy for the construction of up to three vicinal quaternary carbon centres. The structure of **10b** was confirmed by X-ray crystallographic analysis.

We also investigated the application of our newly developed reaction as a general method for the construction of [4,3,0] ring systems (Table 3). Enynols **15a–19a** were prepared and subjected to the optimized reaction conditions to afford the corresponding products **15b–19b** in good-to-acceptable yields, bearing two

**Table 3 | Syntheses of the [3,4,0]-bicyclic scaffolds.**

Entry	Substrate	Product	Yield*
1			92%
2			95%
R = NO <sub>2</sub> PhCO		X-ray crystallography	
3			51%
4			79%
		X-ray crystallography	
5			31%

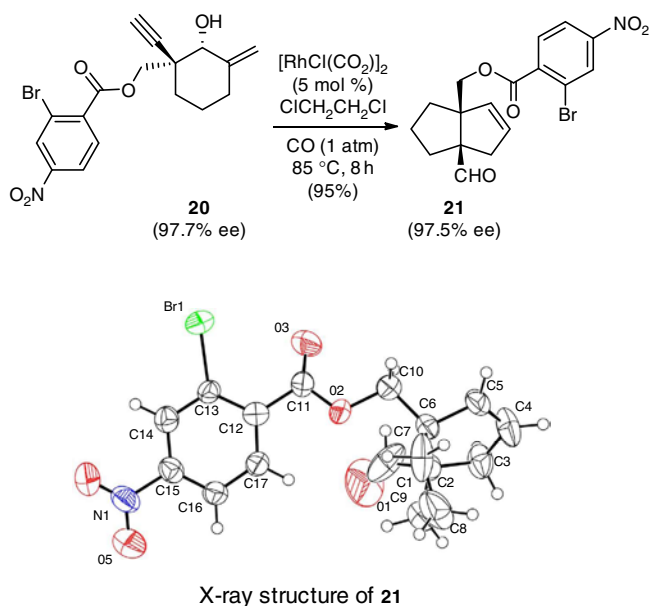
\*Isolated yield after flash silica gel column chromatography.

*syn*-configured vicinal quaternary stereocentres. These results highlight the robust nature of our method as a general strategy for the construction of ring systems of different sizes. The structure of **16b** was confirmed by X-ray crystallographic analysis.

It is particularly important that optically active molecules can be readily and reliably generated during the course of a total synthesis of natural product, because the optical properties of a molecule can have a significant impact on its biological activities. With this in mind, we evaluated the ability of optical enynols to undergo a stereospecific [3 + 2] cycloaddition reaction without affecting their original enantiomeric excess (ee).

The chiral enynol ester **20** (97.7% ee, Fig. 2) was readily synthesized from the corresponding chiral enynol via a coupling reaction with 2-bromo-4-nitrobenzoic acid. The application of the optimized annulation conditions to **20** resulted in the formation of the cycloaddition product **21** (97.5% ee) in 95% yield (Supplementary Figs 77 and 78). The stereochemistry of **21** was confirmed through X-ray crystallography. These results indicated that this [3 + 2] cycloaddition reaction occurred in a stereospecific manner, and that the chirality of the substrate was effectively transferred to the product.

**Mechanism investigation.** Although the mechanism of this reaction is not completely elucidated, we proposed a mechanism to account for the stereochemical outcome of the reaction (Fig. 3a). It was envisaged that [RhCl(CO)<sub>2</sub>]<sub>2</sub> would react



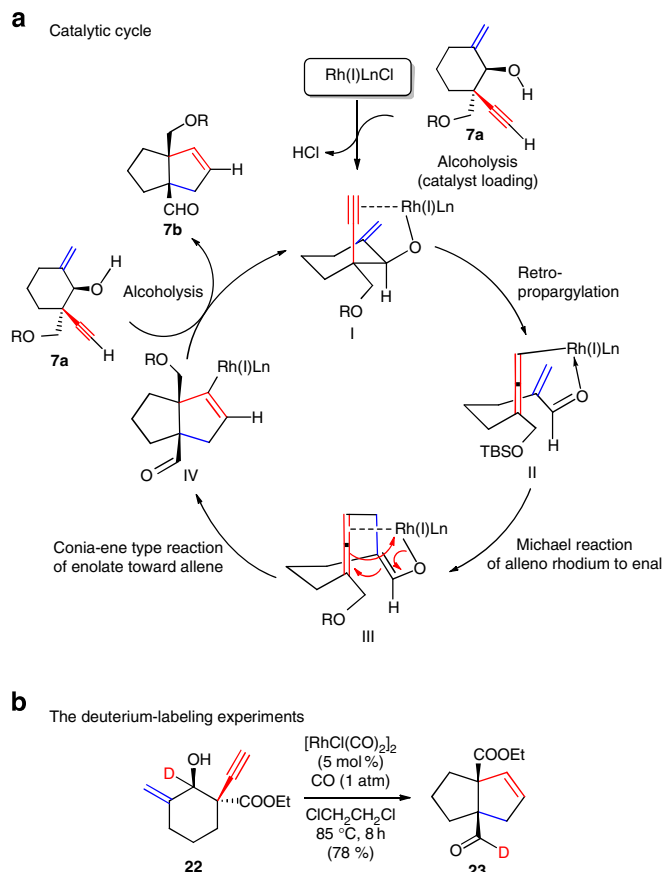
**Figure 2 | Chirality transfer.** Enantiomerically enriched substrate **20** underwent Rh-catalysed [3+2] cycloaddition to yield enantiomerically enriched product **21**.

with compound **7a** to afford complex **I** (refs 50,51), which would undergo a Rh(I)-mediated retro-propargylation of the homopropargyl alcohol to afford complex **II** (Fig. 3a).

Complex **II** would then undergo the intramolecular Michael addition<sup>52–56</sup> of the allenyl rhodium to the enal, to give the allenyl rhodium species **III** bearing an enolate moiety and a Rh-coordinate allene moiety. The transformation of **III** to **IV** can be interpreted as a Conia-ene<sup>57</sup>-type reaction between the Rhoda-enolate species and the allene. Finally, protonolysis<sup>58–60</sup> of complex **IV** with **7a** would give product **7b**, which contains a [3.3.0] bicyclic ring moiety, together with the regeneration of complex **I**, which would allow for the completion of the catalytic cycle.

To support our proposed reaction mechanism, the deuterated enynol **22** was prepared as a probe to confirm that the Rh(I)-catalysed retro- $\beta$ -carbon elimination reaction was the key step in our catalytic cycle (Fig. 3a). The annulation of **22** under the optimized reaction conditions gave the desired product **23** in 78% yield with the retention of deuterium (Fig. 3b). This result indicated that the aldehyde substituent at the C1 position was generated via a Rh-mediated C–C bond cleavage reaction, rather than the oxidation of the corresponding alcohol.

**Computational study.** To further support our proposed reaction mechanism, density functional theory method M11-L, recently proposed by Peverati and Truhlar<sup>61</sup>, is employed to elucidate the mechanism of Rh-catalysed reaction cycle (Supplementary Tables 1 and 2). The free-energy profile, shown in Fig. 4, indicates that intramolecular retro metal propargylation from **CP1** to **CP2** occurs via a concerted transition state **TS1** with an activation-free energy of  $16.9 \text{ kcal mol}^{-1}$ . The allene–rhodium complex **CP2** then forms reversibly, with the chirality of the allene being determined by the  $\alpha$ -carbon of the alkyne moiety in **CP1**. In **CP2**, the enone moiety is activated by rhodium (similar to the Lewis acid activation of enones), because the oxygen atom in the enone moiety coordinates to the rhodium atom. The second step, which is the rate limit, in this process is a relatively facile Michael-type addition of alleno–rhodium to the activated enone via **TS2**, with an activation-free energy of

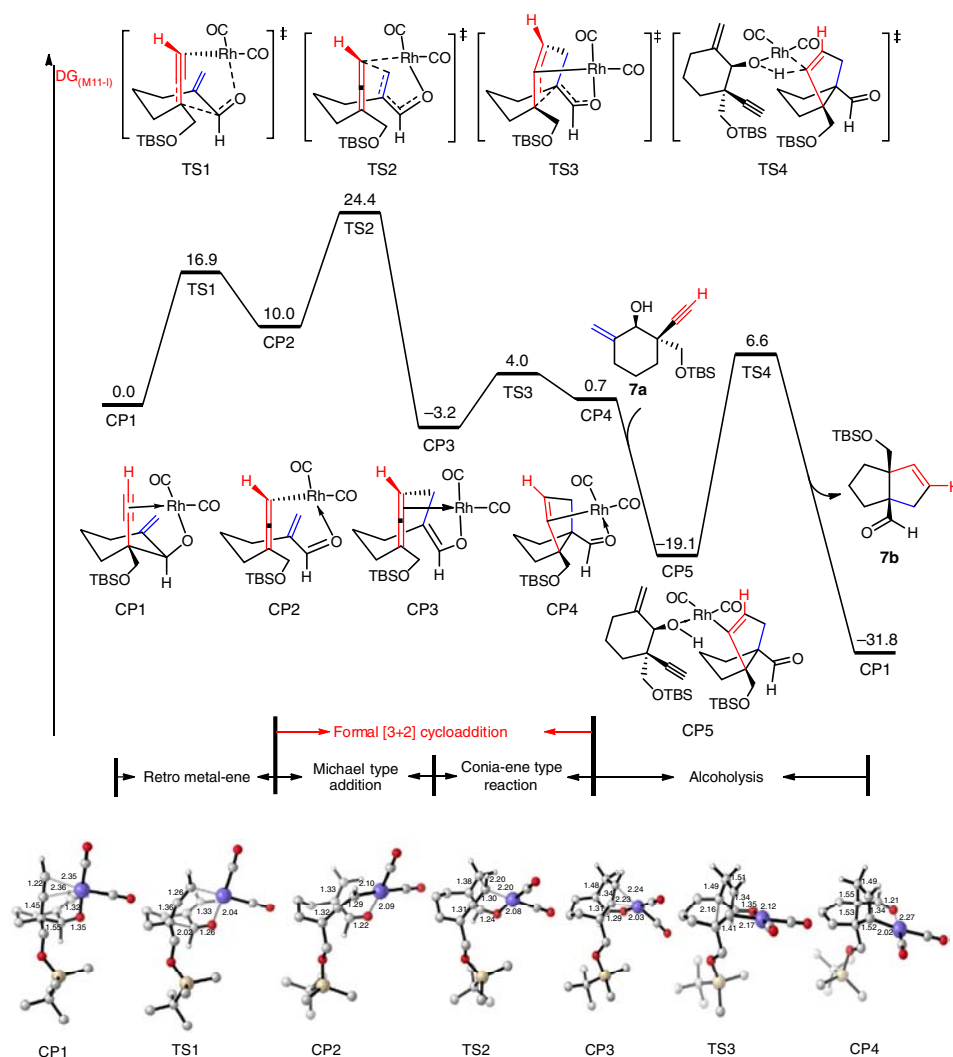


**Figure 3 | Proposed Rh-catalysed reaction cycle and deuterium-labelling experiments.** (a) The possible mechanism involves the sequential Rh-catalysed retro-propargylation/intramolecular Michael addition/Conia-ene-type reaction/alcoholsysis. (b) The deuterium-labelling experiments indicate that the aldehyde is generated via a Rh-mediated C–C bond cleavage reaction.

$24.4 \text{ kcal mol}^{-1}$ . This Michael-type addition reaction affords intermediate **CP3**, which contains an enolate moiety and an allene moiety.

The allene moiety in **CP3** is activated by its coordination to the rhodium centre. The subsequent reaction is alkylation of the enolate by the activated allene via a Conia-ene-type reaction. This alkylation step via **TS3** is facile and gives the formal intramolecular [3+2] cycloadduct **CP4**, with an activation-free energy of  $7.2 \text{ kcal mol}^{-1}$ . The last step is demetalation by the alcohol moiety of the substrate, which begins with ligand exchange between **CP4** and the starting material **7a** to give **CP5**. Next, the C–Rh bond in complex **CP5** is protonated via four-membered-ring transition state **TS4** (ref. 62). Following the release of product **7b**, the active intermediate **CP1** is regenerated irreversibly to complete the catalytic cycle. This mechanism also well explains how the chirality in the starting molecule can be transferred to the final [3+2] cycloadduct.

**Total synthesis of (–)-lingzhiol.** To demonstrate the utility of our newly developed methodology, we applied the annulation reaction in the asymmetric total synthesis of (–)-lingzhiol (**4**)<sup>4</sup>. As a pair of rotary door-shaped meroterpenoidal enantiomers, (–)-lingzhiol (**4**) and its enantiomer (+)-lingzhiol were isolated from *Ganoderma lucidum* by Hou and colleagues<sup>4</sup>, who had to use 80 kg of *G. lucidum* to obtain 25 mg of both pure (–)-lingzhiol and (+)-lingzhiol. *G. lucidum* is a well-known



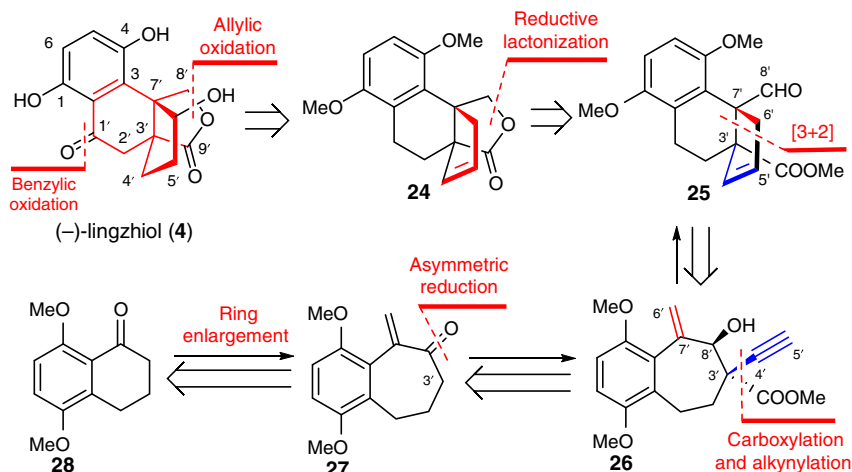
**Figure 4 | Density functional theory calculations.** Free-energy profiles and geometric information for catalytic cycle of rhodium-catalysed synthesis of bicyclo[3.3.0]octane **7b**.

mushroom that is used extensively in Asia as a super-grade medicine. Biological studies of the chemicals contained in this mushroom have indicated that both of the enantiomers of lingzhiols show potent and selective inhibitory activity towards the phosphorylation of Smad3 in transforming growth factor- $\beta$ 1-induced rat renal proximal tubular cells and activate Nrf2/Keap1 in mesangial cells under diabetic conditions<sup>4</sup>. In light of the important biological activities of lingzhiol-type compounds and their potential application as lead compound for the development of therapeutic agents against chronic kidney disease, there is an urgent need for the development of a synthetic method capable of providing facile access to these materials to allow for detailed studies of their structure–activity relationship.

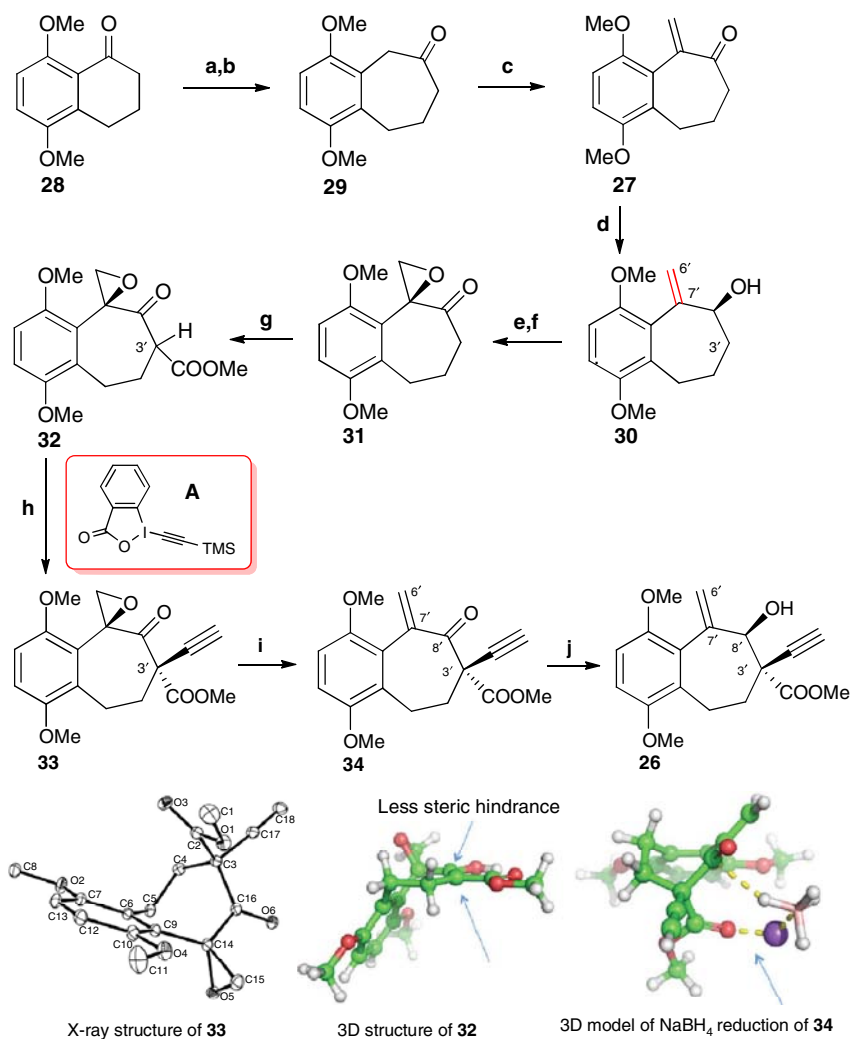
From a chemical perspective, (–)-lingzhiol (**4**) represents a formidable challenge for total synthesis. (–)-Lingzhiol (**4**) possesses an intricate structure, which is decorated with two *syn*-configured vicinal quaternary carbon centres at the bridgehead carbons. This compound is also composed of a highly compact carbobicyclo[4.3.0]nonane core, which is known as a dihydroquinone-fused propellane. The development of an efficient synthesis for (–)-lingzhiol (**4**) that proceeds with good stereoselectivity would allow for the preparation of the natural product as well as its analogues in large-enough quantities to facilitate an adequate evaluation of their biological activities.

Our synthetic strategy was devised to provide rapid access to asymmetric synthesis of (–)-lingzhiol (**4**) and to address the synthetic issues associated with the construction of the highly compact carbobicyclo[4.3.0]nonane core belonging to this structural class. It was envisaged that our newly developed Rh-catalysed intramolecular [3 + 2] cycloaddition reaction could be used for the stereoselective formation of the carbobicyclo[4.3.0]nonane core of (–)-lingzhiol (**4**), because this reaction would allow for the installation of the two bridgehead and *syn*-configured vicinal quaternary carbon centres in a single step.

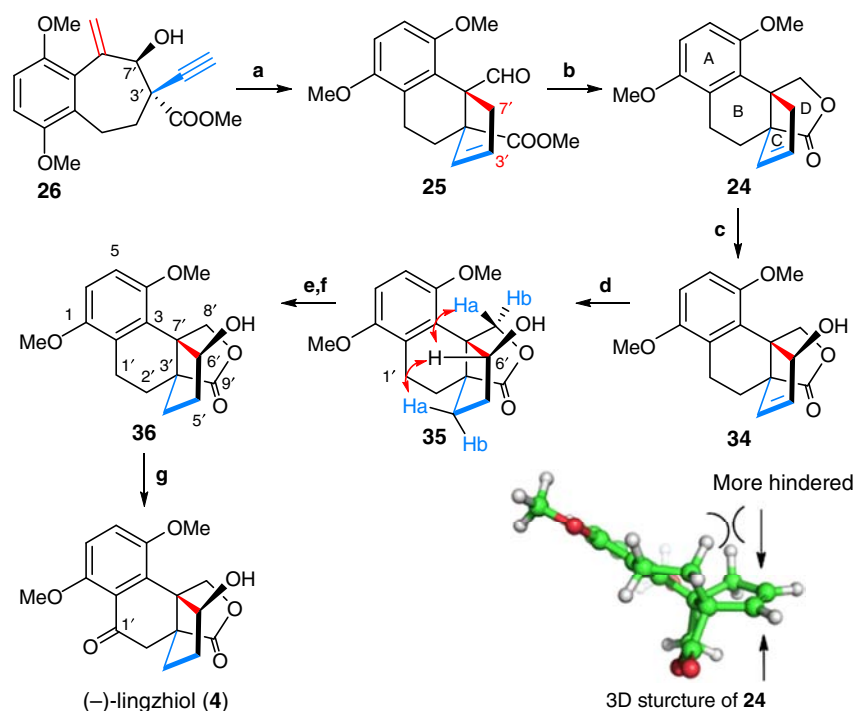
Our retrosynthetic analysis of (–)-lingzhiol (**4**) is shown in Scheme 3. It was envisaged that the application of allylic oxidation, benzylic oxidation and demethoxylation reactions would allow for the successful elaboration and conversion of chiral lactone **24** into the final product (–)-lingzhiol (**4**). Lactone **24** could be synthesized directly from the tricyclic precursor aldehyde **25** via a reductive lactonization reaction. The disconnections of the C3'–C7' and C4'–C6' bonds of **25** led to the homopropargyl alcohol **26**, which could undergo our newly developed Rh-catalysed intramolecular [3 + 2] cycloaddition reaction to form the tricyclic core of **25** in a diastereoselective manner. The chiral homopropargyl alcohol **26** could be prepared from enone **27** via sequential asymmetric ketone reduction with (*R*)-CBS/BH<sub>3</sub> (ref. 63), carboxylation and alkylation<sup>64</sup>



**Figure 5 | Retrosynthetic analysis of (-)-lingzhiol.** The current Rh-catalysed [3+2] cycloaddition was used as a key step to construct the [4.3.0]-bicyclic ring moiety in (-)-lingzhiol.



**Figure 6 | Synthetic pathways for the construction of intermediate 26.** (a) PPh<sub>3</sub>CH<sub>3</sub>Br, THF, KHMDS 0 °C to 25 °C, 98%; (b) PhI(OAc)<sub>2</sub>, p-TSA, MeCN, 0 °C, 95%; (c) Et<sub>3</sub>N · HCl, Et<sub>2</sub>NH, (CH<sub>2</sub>O)<sub>n</sub>, 1,4-dioxane, 105 °C, 98%; (d) (R)-CBS, BH<sub>3</sub>, THF, -20 °C, 91%, 92% ee; (e) meta-chloroperoxybenzoic acid (*m*-CPBA), NaHPO<sub>4</sub>, PhH, 25 °C; (f) Dess-Martin periodinane, NaHCO<sub>3</sub>, DCM, 25 °C, 81% for two steps; (g) LiHMDS, NCCOOMe, THF, -78 °C; (h) tetra-*n*-butylammonium fluoride, **A**, THF, -30 °C, 62% for two steps; (i) NaI, MeCN, CF<sub>3</sub>COOH, 0 °C, 92%; (j) NaBH<sub>4</sub>, CeCl<sub>3</sub> · 7H<sub>2</sub>O, EtOH, 0 °C, 63%. KHMDS: Potassium bis(trimethylsilyl)amide.



**Figure 7 | Total synthesis of (–)-lingzhiol.** (a)  $[\text{Rh}(\text{CO})_2\text{Cl}]_2$  (5 mol%), CO, DCE, 85 °C, 86%; (b)  $\text{NaBH}_4$ , MeOH, 0 °C, 89%; (c)  $\text{SeO}_2$ , 1,4-dioxane, 110 °C, 65%; (d) Pd-C (10%),  $\text{H}_2$ , MeOH, 25 °C, 95%; (e) *N*-bromosuccinimide, benzoyl peroxide (BPO),  $\text{NaHCO}_3$ ,  $\text{H}_2\text{O}$ ,  $\text{CCl}_4$ , 80 °C; (f)  $\text{MnO}_2$ ,  $\text{CH}_2\text{Cl}_2$ , 25 °C, 71% for two steps; (g)  $^t\text{BuSH}$ ,  $\text{AlCl}_3$ , DCM, 40 °C, 71%.

reactions. In this way, our retrosynthetic analysis was traced back to the preparation of enone **27**, which could be made from commercially available 5,8-dimethoxy-3,4-dihydronaphthalen-1(2*H*)-one (**28**) (Fig. 5).

Our total synthesis of (–)-lingzhiol (**4**) began with the asymmetric preparation of the homo-propargyl alcohol **26** (Fig. 6). Treatment of commercially available 5,8-dimethoxy-3,4-dihydronaphthalen-1(2*H*)-one (**28**) with a mixture of  $\text{Ph}_3\text{PCH}_2\text{Br}$  and potassium bis(trimethylsilyl)amide (KHMDs) in tetrahydrofuran (THF) resulted in the formation of the expected olefin in 98% yield, which was subsequently reacted with Koser's reagent<sup>65</sup> in the presence of *p*-TSA in MeCN to give the benzoannulene **29** in 95% yield via a ring-expansion reaction. Compound **29** was initially reacted with formaldehyde under a variety of different conditions. Unfortunately, however, the desired aldol reaction did not occur under these conditions, presumably because of the poor reactivity of formaldehyde. Alternatively, starting from Eschenmoser's salt, which was prepared by the reaction of formaldehyde with  $\text{Et}_2\text{NH} \cdot \text{HCl}/\text{Et}_2\text{NH}$ , the aldol reaction with ketone **29** in 1,4-dioxane at 105 °C furnished the expected enone **27** in almost quantitative yield, which then subjected to an asymmetric reduction with (*R*)-CBS/ $\text{BH}_3$  to afford the chiral allylic alcohol **30** in 91% yield with 94% ee.

With the chiral allylic alcohol **30** in hand, we turned our attention towards its elaboration to the key intermediate **26**. To this end, allylic alcohol **30** was first subjected to a substrate-controlled asymmetric epoxidation by reaction with meta-chloroperoxybenzoic acid to afford an epoxide, which was then oxidized to ketone **31** in 81% yield in two steps by the treatment with Dess–Martin periodinane in the presence of  $\text{NaHCO}_3$  in  $\text{CH}_2\text{Cl}_2$ . To install the functional groups at its C3' position, ketone **31** was reacted with LiHMDS in THF at –78 °C, followed by reaction with methyl carbonocyanide to give the  $\beta$ -ketoester **32** as a pair of ketone-enol isomers. Compound **32** was found to be unstable and was therefore immediately reacted with Waser's reagent<sup>66</sup> in the presence of tetra-*n*-butylammonium fluoride in

THF at –30 °C to give compound **33** in 62% yield in two steps, together with 10% of its diastereoisomer. The stereochemistry of **33** was confirmed through X-ray crystallography and the observed diastereoselectivity presumably occurred as a consequence of the less steric hindrance of the top face of **32** (see the three-dimensional (3D) structure of **32** in Fig. 6). Thus, the treatment of compound **33** with NaI in the presence of  $\text{CF}_3\text{COOH}$  in MeCN provided ketoester **34** in 92% yield. Finally, the Luche reduction<sup>67</sup> of ketoester **34** with  $\text{NaBH}_4$  in the presence of  $\text{CeCl}_3 \cdot 7\text{H}_2\text{O}$  in ethanol at 0 °C gave the homo-propargyl alcohol **26** in 63% yield as a single isomer. To account for the observed diastereoselectivity, we proposed that the ester group of **34** could coordinate with  $\text{NaBH}_4$  in such a way as to facilitate the delivery of the hydride to the ketone from its bottom face (see 3D model of complex **34** in Fig. 6).

We then proceeded to evaluate our newly developed Rh-catalysed [3 + 2] cycloaddition reaction with the homo-propargyl alcohol **26** for the stereoselective construction of the critical intermediate **25**, which featured two quaternary carbon centres at its bridgehead carbons (Fig. 7). Compound **26** was treated with  $[\text{RhCl}(\text{CO})_2]_2$  (5 mol%) at 85 °C under an atmosphere of CO (balloon) in  $\text{ClCH}_2\text{CH}_2\text{Cl}$ . Pleasingly, this reaction proceeded with excellent diastereoselectivity to give the desired product **25** in 86% yield. Subsequent treatment of **25** with  $\text{NaBH}_4$  gave lactone **24** in 89% yield, which was subjected to a  $\text{SeO}_2$ -mediated allylic oxidation in 1,4-dioxane at 110 °C to give the allylic alcohol **35** in 65% yield as a single diastereoisomer. The excellent diastereoselectivity observed in this reaction was attributed to the steric bulk over the top face of substrate **24**, which would direct the  $\text{SeO}_2$  to approach the double bond from its bottom face (see the 3D structure of **24** in Fig. 7). Compound **35** was then subjected to a Pd-catalysed hydrogenation reaction to give product **36** in 95% yield. The stereochemistry of **36** as depicted in Scheme 5 was determined by rotating-frame overhauser effect spectroscopy experiments. Furthermore, nuclear overhauser effect (NOE) experiments revealed a correlation between the H-6', Ha-4' and H-6' protons.

With the entire lingzhiol skeleton installed, all that remained was to introduce the final oxygen atom at C1' of **36** and remove its two methoxyl groups. Unfortunately, however, none of the typical benzylic oxidation reaction conditions tested resulted in the desired product **37**. Given that the benzylic position could readily undergo a radical-mediated halogenation reaction, we designed a stepwise protocol involving sequential halogenation/substitution/oxidation reactions to achieve this transformation. Following a period of experimentation, it was established that substrate **36** could be effectively converted to ketone **37** in 73% yield by the sequential treatment of **36** with *N*-bromosuccinimide (NBS) in the presence of benzoyl peroxide<sup>68</sup>, as well as a trace amount of water in carbon tetrachloride, followed by MnO<sub>2</sub>-mediated oxidation of the resultant benzylic alcohol in CH<sub>2</sub>Cl<sub>2</sub> at room temperature. Finally, removal of the both methoxyl groups of **37** with AlCl<sub>3</sub> in the presence of an excess of <sup>t</sup>BuSH in CH<sub>2</sub>Cl<sub>2</sub> resulted in the formation of (–)-lingzhiol in 78% yield. The spectroscopic data for the synthetic (–)-lingzhiols were identical to the published values of the natural products<sup>4</sup> and the optical rotation for (–)-lingzhiol (**4**) was in good agreement with the literature values (Supplementary Tables 3–5).

## Discussion

In summary, we have developed a new intramolecular [3 + 2] cycloaddition reaction between an enal and an allenic rhodium, which was generated *in situ* from the Rh(I)-mediated retro-propargylation of the corresponding homo-propargyl alcohol, to give [3.3.0] and [4.3.0] bicyclic ring systems with two quaternary carbon centres at their bridgehead positions. This reaction also allowed for the asymmetric synthesis when it was applied to chiral starting materials. To account for the observed reaction, we proposed a mechanism, which suggested that the reaction might involve an Rh-catalysed ring opening of a 2-alkynyl cycloalkanol moiety followed by the intramolecular [3 + 2] cycloaddition on an allenic rhodium species to an enal. The application of this reaction to the synthesis of the natural product (–)-lingzhiol has been also achieved for the first time in 17 steps from a commercially available starting material.

## Methods

**General.** For <sup>1</sup>H and <sup>13</sup>C spectra of the compounds in this article, see Supplementary Figs 1–69. For ORTEP diagrams, see Supplementary Figs 70–76. For HPLC traces, see Supplementary Figs 77–79.

**General procedure for the synthesis of 8b–19b.** To a solution of an enynol in anhydrous ClCH<sub>2</sub>CH<sub>2</sub>Cl (0.025 M) was added [RhCl(CO)<sub>2</sub>]<sub>2</sub> (0.5 mg, 1.25 μmol, 5% mol) at CO atmosphere at room temperature and the mixture was degassed with CO for five times. The reaction mixture was then stirred at 85 °C for the time listed in the Tables 2 and 3. After cooling to room temperature, the solvent was removed under vacuum and the residue was purified by a flash chromatography on silica gel to provide the desired product. For additional procedures, see Supplementary Methods.

## References

- Groweiss, A. *et al.* Subergorgic acid, a novel tricyclopentanoid cardiotoxin from the Pacific gorgonian coral. *Tetrahedron Lett.* **26**, 2379–2382 (1985).
- Anke, T. *et al.* Crinipellins, the first natural products with a tetraquinane skeleton. *Angew. Chem. Int. Ed.* **24**, 709–711 (1986).
- Kaneda, M., Takahashi, R., Iitaka, Y. & Shibata, S. Retigeranic acid, a novel sesterterpene isolated from the lichens of *lobaria retigera* group. *Tetrahedron Lett.* **13**, 4609–4612 (1972).
- Yan, Y.-M. *et al.* Lingzhiols, unprecedented rotary door-shaped meroterpenoids as potent and selective inhibitors of p-Smad3 from *Ganoderma lucidum*. *Org. Lett.* **15**, 5488–5491 (2013).
- Dong, L.-B. *et al.* Isopalhinine A, a unique pentacyclic lycopodium alkaloid from *palhinhaea cernua*. *Org. Lett.* **15**, 3570–3573 (2013).
- Boeckman, Jr R. K., Blum, D. M., Arnold, E. U. & Clardy, J. The structure of gascardic acid from an X-ray diffraction study. *Tetrahedron Lett.* **20**, 4609–4694 (1979).
- Hog, D. T., Mayer, P. & Trauner, D. A unified approach to *trans*-hydrindane sesterterpenoids. *J. Org. Chem.* **77**, 5838–5843 (2012).
- Steven, A. & Overman, L. E. Total synthesis of complex cyclotryptamine alkaloids: stereocontrolled construction of quaternary carbon stereocenters. *Angew. Chem. Int. Ed.* **46**, 5488–5508 (2007).
- Nicolaou, K. C., Vassilikogiannakis, G., Mägerlein, W. & Kranich, R. Total synthesis of colombiasin A. *Angew. Chem. Int. Ed.* **40**, 2482–2486 (2001).
- Birman, V. B. & Danishefsky, S. J. The total synthesis of (±)-merrillactone A. *J. Am. Chem. Soc.* **124**, 2080–2081 (2002).
- Overman, L. E., Larrow, J. F., Stearns, B. A. & Vance, J. M. Enantioselective construction of vicinal stereogenic quaternary centers by dialkylation: practical total syntheses of (+)- and meso-chimonanthine. *Angew. Chem. Int. Ed.* **39**, 213–215 (2000).
- Crimmins, M. T. *et al.* Total synthesis of (±)-ginkgolide B. *J. Am. Chem. Soc.* **121**, 10249–10250 (1999).
- Overman, L. E., Paone, D. V. & Stearns, B. A. Direct stereo- and enantiocontrolled synthesis of vicinal stereogenic quaternary carbon centers. Total syntheses of meso- and (–)-chimonanthine and (+)-calycanthine. *J. Am. Chem. Soc.* **121**, 7702–7703 (1999).
- Hatcher, J. M. & Coltart, D. M. Copper(I)-catalyzed addition of Grignard reagents to *in situ*-derived *N*-sulfonyl azoalkenes: An umpolung alkylation procedure applicable to the formation of up to three contiguous quaternary centers. *J. Am. Chem. Soc.* **132**, 4546–4547 (2010).
- Kikushima, K., Holder, J. C., Gatti, M. & Stoltz, B. M. Palladium-catalyzed asymmetric conjugate addition of arylboronic acids to five-, six-, and seven-membered β-substituted cyclic enones: enantioselective construction of all-carbon quaternary stereocenters. *J. Am. Chem. Soc.* **133**, 6902–6905 (2011).
- Trost, B. M. & Osipov, M. Palladium-catalyzed asymmetric construction of vicinal all-carbon quaternary stereocenters and its application to the synthesis of cyclotryptamine alkaloids. *Angew. Chem. Int. Ed.* **52**, 9176–9181 (2013).
- Zhang, Y. & Danishefsky, S. J. Total synthesis of (±)-aplykurodione-1: traceless stereochemical guidance. *J. Am. Chem. Soc.* **132**, 9567–9569 (2010).
- Jiao, L., Lin, M. & Yu, Z. -X. Rh(I)-catalyzed intramolecular [3 + 2] cycloaddition reactions of 1-ene-, 1-yne- and 1-allene- vinylcyclopropanes. *Chem. Commun.* **46**, 1059–1061 (2010).
- Yamago, S. & Nakamura, E. *Org. React.* **61**, 1–217 (2002).
- Chan, D. M. T. in *Comprehensive Organic Synthesis* Vol. 3 (eds Trost, B. M. & Fleming, I.) 271–314 (Pergamon, 1991).
- Becker, D. A. & Danheiser, R. L. A new synthesis of substituted azulenes. *J. Am. Chem. Soc.* **111**, 389–391 (1989).
- Zhang, C. & Lu, X. Phosphine-catalyzed cycloaddition of 2,3-butadienoates or 2-butyonoates with electron-deficient olefins. A novel [3 + 2] annulation approach to cyclopentenes. *J. Org. Chem.* **60**, 2906–2908 (1995).
- Lu, X., Zhang, C. & Xu, Z. Reactions of electron-deficient alkynes and allenes under phosphine catalysis. *Acc. Chem. Res.* **34**, 535–544 (2001).
- Zhu, G. *et al.* Asymmetric [3 + 2] cycloaddition of 2,3-butadienoates with electron-deficient olefins catalyzed by novel chiral 2,5-dialkyl-7-phenylphosphabicyclo[2.2.1]heptanes. *J. Am. Chem. Soc.* **119**, 3836–3837 (1997).
- Wilson, J. E. & Fu, G. C. Synthesis of functionalized cyclopentenes through catalytic asymmetric [3 + 2] cycloadditions of allenes with enones. *Angew. Chem. Int. Ed.* **45**, 1426–1429 (2006).
- Cowen, B. J. & Miller, S. J. Enantioselective [3 + 2]-cycloadditions catalyzed by a protected, multifunctional phosphine-containing α-amino acid. *J. Am. Chem. Soc.* **129**, 10988–10989 (2007).
- Fang, Y. Q. & Jacobsen, E. N. Cooperative, highly enantioselective phosphinothiourea catalysis of imine-allene [3 + 2] cycloadditions. *J. Am. Chem. Soc.* **130**, 5660–5661 (2008).
- Voituriez, A., Panossian, A., Fleury-Brégeot, N., Retailleau, P. & Marinetti, A. 2-Phospha[3]ferrocenophanes with planar chirality: synthesis and use in enantioselective organocatalytic [3 + 2] cyclizations. *J. Am. Chem. Soc.* **130**, 14030–14031 (2008).
- Sampath, M. & Loh, T. -P. Highly entantio-, region- and diastereo-selective one-pot [2 + 3]-cycloaddition reaction via isomerization of 3-butyonoates to allenates. *Chem. Sci.* **1**, 739–742 (2010).
- Xiao, H. *et al.* Asymmetric [3 + 2] cycloaddition of allenates and dual activated olefins catalyzed by simple bifunctional *N*-acyl aminophosphines. *Angew. Chem. Int. Ed.* **49**, 4467–4470 (2010).
- Fujiwara, Y. & Fu, G. C. Application of a new chiral phosphine to the catalytic asymmetric synthesis of highly functionalized cyclopentenes that bear an array of heteroatom-substituted quaternary stereocenters. *J. Am. Chem. Soc.* **133**, 12293–12297 (2011).
- Zhang, X.-N. & Shi, M. Phosphine-catalyzed [3 + 2] cycloaddition of 4,4-dicyano-2-methylenebut-3-enoates with benzyl buta-2,3-dienate and penta-3,4-dien-2-one. *ACS Catal.* **3**, 507–512 (2013).
- Han, X. Y., Wang, Y. Q., Zhong, F. R. & Lu, Y. X. Enantioselective [3 + 2] cycloaddition of allenes to acrylates catalyzed by dipeptide-derived phosphines:



- facile creation of functionalized cyclopentenes containing quaternary stereogenic centers. *J. Am. Chem. Soc.* **133**, 1726–1729 (2011).
34. Marshall, J. A., Gung, B. W. & Grachan, M. L. in *Modern Allene Chemistry* Vol. 2 (eds Krause, N. & Hashmi, A. S. K.) 493–592 (Wiley-VCH, 2004).
35. Krause, N. & Hoffmann-Roder, A. Synthesis of allenes with organometallic reagents. *Tetrahedron* **60**, 11671–11694 (2004).
36. Marshall, J. A. Chiral allylic and allenic metal reagents for organic synthesis. *J. Org. Chem.* **72**, 8153–8166 (2007).
37. Ruitenbergh, K., Kleijn, H., Meijer, J., Oostveen, E. A. & Vermeer, P. Palladium(0)-promoted cross-coupling of allenylmetal compounds with aryl and vinyl iodides. A novel route to aryl- and vinyl-substituted allenes. *J. Organomet. Chem.* **224**, 399–405 (1982).
38. Russell, C. E. & Hegedus, L. S. Palladium-catalyzed acylation of unsaturated halides by anions of enol ethers. *J. Am. Chem. Soc.* **105**, 943–949 (1983).
39. de Graaf, W., Boersma, J., van Koten, G. & Elsevier, C. J. Chiral induction in the synthesis of 4,4-dimethyl-1-phenylpenta-1,2-diene (1-Ph-3-t-Bu-allene) catalyzed by chiral phosphine complexes of palladium. *J. Organomet. Chem.* **378**, 115–124 (1989).
40. Werner, H., Rappert, T., Wiedemann, R., Wolf, J. & Mahr, N. Mononuclear (allenylidene)metal complexes of a d8 system: synthesis and molecular structure of *trans*-[RhCl(C:C:CRR')(PiPr<sub>3</sub>)<sub>2</sub>]. *Organometallics* **13**, 2721–2727 (1994).
41. Banerjee, M. & Roy, S. Rhodium(I)-catalyzed carbonyl allenylation versus propargylation via redox transmetalation across tetragonal Tin(II) oxide. *Org. Lett.* **6**, 2137–2140 (2004).
42. Werner, H. *et al.* Unusual pathways for metal-assisted C–C and C–P coupling reactions using allenylidenerhodium complexes as precursors. *J. Am. Chem. Soc.* **124**, 6966–6980 (2002).
43. Wang, J.-C., Ng, S.-S. & Krische, M. J. Catalytic diastereoselective synthesis of diquinanes from acyclic precursors. *J. Am. Chem. Soc.* **125**, 3682–3683 (2003).
44. Jones, R. A. & Krische, M. Asymmetric Total synthesis of the iridoid β-glucoside (+)-geniposide via phosphine organocatalysis. *Org. Lett.* **11**, 1849–1851 (2009).
45. Hayashi, S., Hirano, K., Yorimitsu, H. & Oshima, K. Synthesis of arylallenes by palladium-catalyzed retro-propargylation of homopropargyl alcohols. *J. Am. Chem. Soc.* **130**, 5048–5049 (2008).
46. Wender, P. A. *et al.* Transition metal-catalyzed [5 + 2] cycloadditions of allenes and vinylcyclopropanes: first studies of *endo-exo* selectivity, chemoselectivity, relative stereochemistry, and chirality transfer. *J. Am. Chem. Soc.* **121**, 5348–5349 (1999).
47. Wender, P. A. *et al.* Transition metal-catalyzed [5 + 2] cycloadditions with substituted cyclopropanes: first studies of regio- and stereoselectivity. *J. Am. Chem. Soc.* **121**, 10442–10443 (1999).
48. Wender, P. A. & Christy, J. P. Rhodium(I)-catalyzed [4 + 2 + 2] cycloadditions of 1,3-dienes, alkenes, and alkynes for the synthesis of cyclooctadienes. *J. Am. Chem. Soc.* **128**, 5354–5355 (2006).
49. Marshall, J. A. & Robinson, E. D. A mild method for the synthesis of furans. Application to 2,5-bridged furano macrocyclic compounds. *J. Org. Chem.* **55**, 3450–3451 (1990).
50. Zhao, P., Incarvito, C. D. & Hartwig, J. F. Direct observation of β-aryl eliminations from Rh(I) alkoxides. *J. Am. Chem. Soc.* **128**, 3124 (2006).
51. Zhao, P., Incarvito, C. D. & Hartwig, J. F. Carbon–oxygen bond formation between a terminal alkoxo ligand and a coordinated olefin. Evidence for olefin insertion into a rhodium alkoxide. *J. Am. Chem. Soc.* **128**, 9642 (2006).
52. Ma, S. & Negishi, E.-I. Palladium-catalyzed cyclization of ω-haloallenes. A new general route to common, medium, and large ring compounds via cyclic carbopalladation. *J. Am. Chem. Soc.* **117**, 6345–6357 (1995).
53. Gibson, S. E., Guillo, N., Middleton, R. J., Thuilliez, A. M. & Tozer, J. Synthesis of conformationally constrained phenylalanine analogues via 7-, 8- and 9-endo Heck cyclisations. *J. Chem. Soc. Perkin Trans. 1*, 447–456 (1997).
54. Takasu, K., Mizutani, S., Noguchi, M., Makita, K. & Ihara, M. Stereoccontrolled total synthesis of (±)-culmorin via the intramolecular double michael addition. *Org. Lett.* **1**, 391–393 (1999).
55. Burns, A. R., McAllister, G. D., Shanahan, S. E. & Taylor, R. J. Total Synthesis and structural reassignment of (+)-dictyosphaeric acid A: a tandem intramolecular michael addition/alkene migration approach. *Angew. Chem. Int. Ed.* **49**, 5574–5577 (2010).
56. Takasu, K., Mizutani, S., Noguchi, M., Makita, K. & Ihara, M. Total Synthesis of (±)-culmorin and (±)-longiborneol: an efficient construction of tricyclo[6.3.0.0.3,9]undecan-10-one by intramolecular double michael addition. *J. Org. Chem.* **65**, 4112–4119 (2000).
57. Conia, J. M. & Le Perche, P. The thermal cyclisation of unsaturated carbonyl compounds. *Synthesis* **1**, 1–19 (1975).
58. Senda, T., Ogasawara, M. & Hayashi, T. Rhodium-catalyzed asymmetric 1,4-addition of organoboron reagents to 5,6-dihydro-2(1H)-pyridinones. asymmetric synthesis of 4-aryl-2-piperidinones. *J. Org. Chem.* **66**, 6852–6856 (2001).
59. Hayashi, T., Takahashi, M., Takaya, Y. & Ogasawara, M. Catalytic cycle of rhodium-catalyzed asymmetric 1,4-addition of organoboronic acids. arylrhodium, oxa-π-allylrhodium, and hydroxorhodium intermediates. *J. Am. Chem. Soc.* **124**, 5052–5058 (2002).
60. Sun, Z.-M. & Zhao, P. Rhodium-mediated decarboxylative conjugate addition of fluorinated benzoic acids: stoichiometric and catalytic transformations. *Angew. Chem. Int. Ed.* **48**, 6726–6730 (2009).
61. Peverati, R. & Truhlar, D. G. Improving the accuracy of hybrid meta-GGA density functionals by range separation. *J. Phys. Chem. Lett.* **2**, 2810–2817 (2011).
62. Shi, F.-Q. Density functional theory study on the mechanism of Rh-catalyzed decarboxylative conjugate addition: diffusion- and ligand-controlled selectivity toward hydrolysis or β-hydride elimination. *Org. Lett.* **13**, 736–739 (2011).
63. Corey, E. J., Bakshi, R. K. & Shibata, S. Highly enantioselective borane reduction of ketones catalyzed by chiral oxazaborolidines mechanism and synthetic implications. *J. Am. Chem. Soc.* **109**, 5551–5553 (1987).
64. Poulsen, T. B., Bernardi, L., Alemán, J., Overgaard, J. & Jørgensen, K. A. Organocatalytic asymmetric direct α-alkynylation of cyclic β-ketoesters. *J. Am. Chem. Soc.* **129**, 441–449 (2007).
65. Justik, M. W. & Koser, G. F. Oxidative rearrangements of arylalkenes with [hydroxy(tosyloxy)iodo]benzene in 95% methanol: a general, regioselective synthesis of α-aryl ketones. *Tetrahedron Lett.* **45**, 6159–6163 (2004).
66. González, D. F., Brand, J. P. & Waser, J. Ethynyl-1,2-benziodoxol-3(1 H)-one (EBX): an exceptional reagent for the ethynylation of keto, cyano, and nitro esters. *Chem. Eur. J.* **16**, 9457–9461 (2010).
67. Luche, J.-L. Lanthanides in organic chemistry. 1. Selective 1,2 reductions of conjugated ketones. *J. Am. Chem. Soc.* **100**, 2226–2227 (1978).
68. Nomura, K., Okazaki, K., Hori, K. & Yoshii, E. Total synthesis of (±)-granaticin. *J. Am. Chem. Soc.* **109**, 3402–3408 (1987).

## Acknowledgements

We thank Professors Zhixiang Yu of Peking University and Junmin Quan of Peking University Shenzhen Graduate School for their helpful discussions. This work is supported by the National Science Foundation of China (grant numbers 21372016 and 21402002), 863 Program (grant number 2013AA092903), 973 Program (grant numbers 2010CB833201 and 2012CB722602), NSFC-Shandong Joint Fund for Marine Science Research Centers (U1406402) and Shenzhen Basic Research Program (grant numbers JCY20130329180217059, GJHS20120628101219325, ZYC201105170335A and ZYC201105170358A).

## Author contributions

R.L. and J.H. contributed equally to this work. R.L., J.H. and Z.Y. conceived the project and analysed the experimental results. R.L., J.H., W.S. and J.G. performed the synthesis and characterization. S.L. and Y.L. performed the theoretical calculations. Y.L., J.G. and Z.Y. composed the manuscript with input from all authors.

## Additional information

**Accession codes:** The X-ray crystallographic coordinates for structures reported in this article have been deposited at the Cambridge Crystallographic Data Centre (CCDC), under deposition numbers CCDC 1026082–1026089. These data can be obtained free of charge from the Cambridge Crystallographic Data Centre via [http://www.ccdc.cam.ac.uk/data\\_request/cif](http://www.ccdc.cam.ac.uk/data_request/cif)

**Supplementary Information** accompanies this paper at <http://www.nature.com/naturecommunications>

**Competing financial interests:** The authors declare no competing financial interests.

**Reprints and permission** information is available online at <http://npg.nature.com/reprintsandpermissions/>

**How to cite this article:** Long, R. *et al.* Asymmetric total synthesis of (–)-lingzhiol via a Rh-catalysed [3 + 2] cycloaddition. *Nat. Commun.* 5:5707 doi: 10.1038/ncomms6707 (2014).

## CELL BIOLOGY

# Identification of XBP1-u as a novel regulator of the MDM2/p53 axis using an shRNA library

Can Huang,<sup>1</sup> Shourong Wu,<sup>1,2\*</sup> Hong Ji,<sup>1</sup> Xuesong Yan,<sup>1</sup> Yudan Xie,<sup>1</sup> Saomi Murai,<sup>3</sup> Hezhao Zhao,<sup>4</sup> Makoto Miyagishi,<sup>5</sup> Vivi Kasim<sup>1,2\*</sup>

Cell cycle progression is a tightly controlled fundamental process in living cells, with any defects being closely linked to various abnormalities. The tumor suppressor p53/p21 axis is a core pathway controlling cell cycle progression; however, its regulatory mechanism has not been fully elucidated. In an effort to unravel this crucial network, we screened a short hairpin RNA expression vector library and identified unspliced X-box binding protein 1 (XBP1-u) as a novel and critical regulator of the p53/p21 axis. Specifically, XBP1-u negatively regulates the p53/p21 axis by enhancing p53 ubiquitination, which in turn down-regulates p21 expression. We show that XBP1-u suppression induces G<sub>0</sub>-G<sub>1</sub> phase arrest and represses cell proliferation. We further report that the carboxyl terminus of XBP1-u, which differs from that of its spliced form (XBP1-s) due to a codon shift, binds and stabilizes mouse double minute homolog 2 (MDM2) protein, a negative regulator of p53, by inhibiting its self-ubiquitination. Concomitantly, XBP1-u overexpression enhances tumorigenesis by positively regulating MDM2. Together, our findings suggest that XBP1-u functions far beyond being merely a precursor of XBP1-s and, instead, is involved in fundamental biological processes. Furthermore, this study provides new insights regarding the regulation of the MDM2/p53/p21 axis.

## INTRODUCTION

Cell cycle is a critical event controlling cell proliferation. It progresses in a directional manner following well-ordered events: DNA replication, spindle assembly, nuclear division, and cytokinesis. Cell cycle progression is regulated by numerous proteins, including cyclins and cyclin-dependent kinases (CDKs), whose expression oscillates throughout the cell cycle and is tightly controlled. *p21* was the first reported CDK inhibitor and was identified as a tumor suppressor gene induced by *p53* (1, 2). It binds to cyclins and CDKs and thus negatively regulates cell cycle progression (3). It also participates in other important physiological processes, such as DNA repair, stem cell maintenance, differentiation, and senescence; thus, loss of *p21* might lead to various disorders including tumorigenesis (3–5). Mice lacking *p21* display higher tumorigenesis potential, and their embryonic fibroblast cells can bypass the G<sub>1</sub>-S checkpoint upon exposure to DNA damage (6). Despite functioning as a tumor suppressor and being down-regulated in various malignancies (7, 8), *p21* itself is rarely mutated in human cancers (3, 9). These findings underscore the importance of the regulatory pathways controlling *p21* gene expression, which have not been fully elucidated.

Here, in an effort to unravel the regulatory mechanism of the p53/p21 axis, we screened a short hairpin RNA (shRNA) vector library and identified X-box binding protein 1 (XBP1) as a negative regulator of p21 transcriptional activity. XBP1 has been characterized as a bZIP (basic-region leucine zipper) transcription factor that interacts specifically with the conserved X2 boxes of major histocompatibility complex class II gene promoters (10). *XBP1* yields two isoforms: unspliced XBP1 (XBP1-u) and spliced XBP1 (XBP1-s). Upon exposure to endoplasmic

reticulum (ER) stress, XBP1-u is spliced, and the 26 nucleotides located between +541 and +566 of XBP1-u are excised, causing a codon frameshift in XBP1-s and distinct C-terminal regions between the two isoforms (11, 12). XBP1-s is considered the active form, playing a pivotal role in the unfolded protein response (UPR) network (12). However, we report herein that the regulatory effect on p21 is specific to the poorly characterized XBP1-u isoform but not to the well-known XBP1-s isoform. The C terminus of XBP1-u binds to mouse double minute 2 homolog [MDM2 (also known as HDM2)] and inhibits its homodimerization and self-ubiquitination. The accumulation of MDM2 protein, in turn, accelerates the ubiquitination and proteasomal degradation of p53, which is a positive regulator of p21 transcription. Together, our findings uncover a pivotal role of XBP1-u in regulating the cell cycle and its link to the conventional MDM2/p53 axis.

## RESULTS

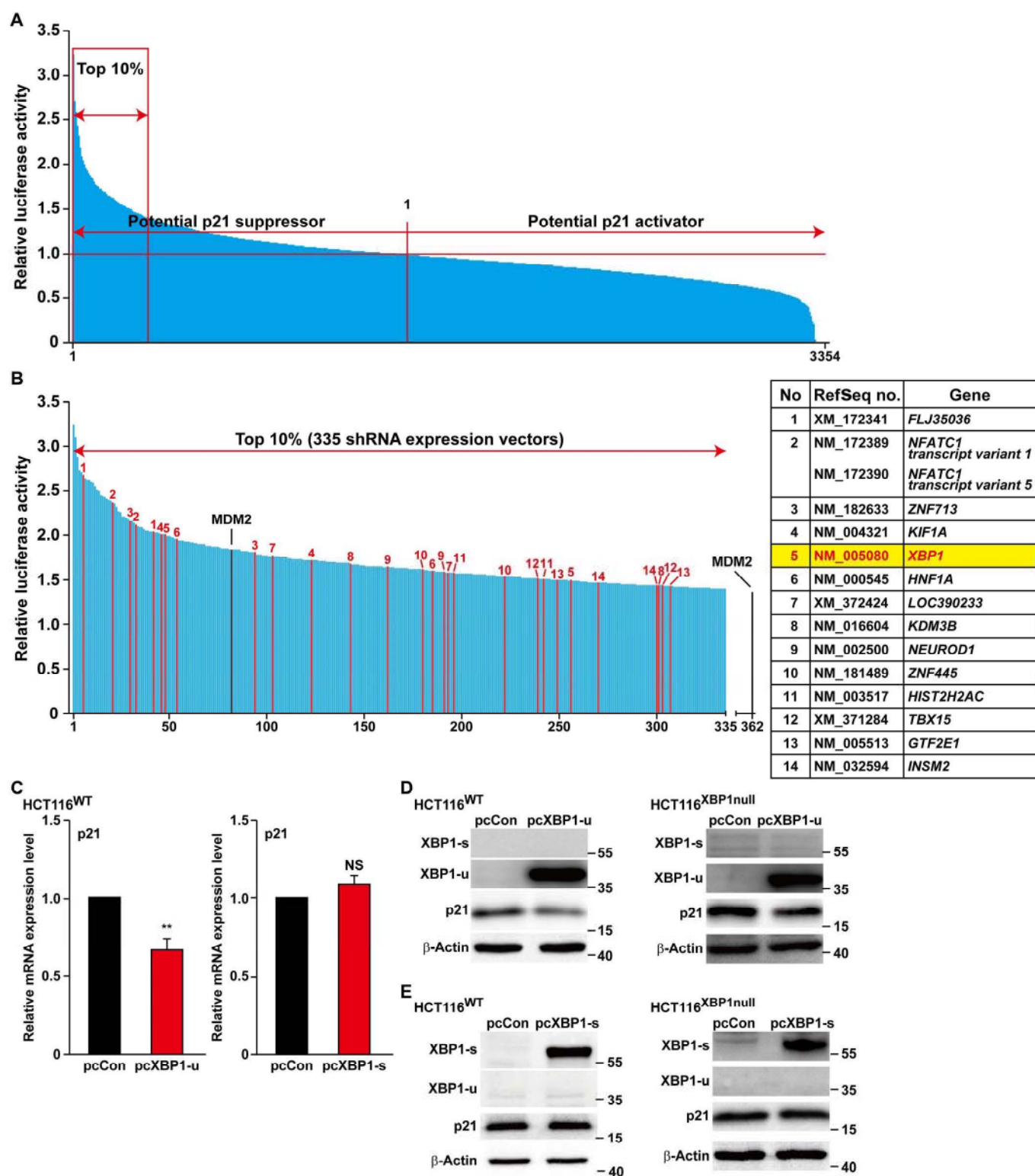
### Screening of shRNA expression vector library leads to the identification of factors involved in p21 transcriptional regulation

We established a screening system using an shRNA expression vector library and a p21 reporter gene in HCT116<sup>WT</sup> human colon carcinoma cells. The system was validated with shRNA against positive (p53) and negative (MDM2) regulators of p21: Silencing of *p53* significantly decreased p21 reporter activity, whereas silencing of *MDM2* robustly increased it (fig. S1A).

Next, we screened an shRNA expression vector library containing 3354 shRNA expression vectors covering 2065 genes (Fig. 1A): 1289 genes with two vectors targeting different sites per gene and 776 genes with one shRNA expression vector per gene. This screening led to the identification of more than 300 candidates or around 10% of the overall screened genes, for which p21 reporter activity was stronger than with shMDM2, and thus, those candidates were considered potential p21 suppressors (Fig. 1B, left, and table S1). To reduce the false-positive results caused by the off-target effect of shRNA, we gave priority to the 14 genes with two shRNA expression vectors among the top 10% of potential p21 suppressors. Among them, we noticed the presence

<sup>1</sup>Key Laboratory of Biorheological Science and Technology, Ministry of Education, College of Bioengineering, Chongqing University, Chongqing 400044, China. <sup>2</sup>111 Project Laboratory of Biomechanics and Tissue Repair, College of Bioengineering, Chongqing University, Chongqing 400044, China. <sup>3</sup>Department of Chemistry and Biotechnology, Graduate School of Engineering, The University of Tokyo, Tokyo 113-8656, Japan. <sup>4</sup>Chongqing Cancer Institute, Chongqing 400030, China. <sup>5</sup>Molecular Composite Medicine Research Group, Biomedical Research Institute, National Institute of Advanced Industrial Science and Technology (AIST), Tsukuba 305-8566, Japan.

\*Corresponding author. Email: vivikasim@cqu.edu.cn (V.K.); shourongwu@cqu.edu.cn (S.W.)



**Fig. 1. Screening for p21 regulators using an shRNA expression vector library.** (A) Screening results of a library containing 3354 shRNA expression vectors. Relative luciferase activity was calculated as the ratio of firefly and *Renilla* luciferase activities. The ratios were then normalized with the average ratio of the measurement of each 96-well plate. (B) Top 10% potential p21 suppressors. Genes with both shRNA expression vectors included in the top 10% are shown in red and listed above in the right panel; *MDM2* is shown in black. (C) p21 mRNA expression level in HCT116<sup>WT</sup> cells transfected with either pcXBP1-u or pcXBP1-s, as determined by quantitative reverse transcription polymerase chain reaction (qPCR). pcCon, pcDNA3.1(+); NS, not significant. (D and E) p21 protein expression level in HCT116<sup>WT</sup> and HCT116<sup>XBP1null</sup> cells transfected with either pcXBP1-u (D) or pcXBP1-s (E), as determined by Western blotting. Cells transfected with pcCon were used as control.  $\beta$ -Actin was used for qPCR normalization and as Western blotting loading control. qPCR data were shown relative to control and expressed as the mean  $\pm$  SEM of three independent experiments.  $^{**}P < 0.01$  [analysis of variance (ANOVA)].

of *XBPI* (Fig. 1B, right). *XBPI* has been known as a critical player in ER stress (12); however, its role within the p21 network remains unknown.

### **XBPI-u negatively regulates p21 transcriptional activity**

We further confirmed the regulatory effect of *XBPI* on the p21 promoter using two more shRNA expression vectors against *XBPI* (sh*XBPI*-3 and sh*XBPI*-4) and by establishing HCT116<sup>*XBPI*null</sup> cells using the CRISPR (clustered regularly interspaced short palindromic repeats)/Cas9 method. The p21 reporter activity was enhanced in both *XBPI*-silenced cells and HCT116<sup>*XBPI*null</sup> cells (fig. S1, B and C). Consistently, both *XBPI* silencing and knockout robustly increased mRNA and protein expression levels of p21 (fig. S1, D to F). Together, these results indicate that *XBPI* might be a novel p21 transcriptional regulator.

*XBPI* is expressed as *XBPI*-u, which is spliced into *XBPI*-s upon ER stress (fig. S2, A and B). We then investigated the effect of thapsigargin, which induced *XBPI* splicing and increased *XBPI*-s levels (fig. S2C), on p21 expression. Surprisingly, instead of suppressing it, thapsigargin promoted p21 expression (fig. S2, D and E). It should be noted that in contrast to the condition with thapsigargin addition, both the protein level and copy number of *XBPI*-u were significantly higher than those of *XBPI*-s under basal condition (that is, without thapsigargin addition), and thus, under basal condition, the sh*XBPI* vectors described above mainly affected the levels of *XBPI*-u (fig. S2, E to G). Hence, we assumed that the effect of *XBPI* silencing and knockout described in this work could be attributed to the absence of *XBPI*-u. Next, we selectively overexpressed *XBPI*-u and *XBPI*-s in HCT116<sup>WT</sup> cells (fig. S3, A and B). Only overexpression of *XBPI*-u could significantly suppress p21 mRNA and protein expression, whereas *XBPI*-s overexpression failed to produce any significant changes (Fig. 1, C to E, and fig. S3C). Similar results were also obtained with HCT116<sup>*XBPI*null</sup> cells (Fig. 1, D and E, and fig. S3C). It should be noted that *XBPI*-u overexpression did not affect the levels of *XBPI*-s and its downstream genes *ATF4*, *CHOP*, and *BIP* (fig. S3, A and D). Together, these results strongly indicate that *XBPI*-u, but not *XBPI*-s, is a negative regulator of p21.

### **XBPI-u suppression induces G<sub>0</sub>-G<sub>1</sub> arrest**

Knowing that p21 is a master regulator of cell cycle progression, we investigated the role of *XBPI*-u in cell cycle regulation. Both *XBPI* silencing and knockout significantly reduced HCT116<sup>WT</sup> cell number (Fig. 2A and fig. S4A). *XBPI* suppression robustly reduced cell proliferation, as indicated by the number of ethynyl deoxyuridine (EdU)-positive cells (Fig. 2B), and largely increased the percentage of G<sub>0</sub>-G<sub>1</sub> cells (Fig. 2C and fig. S4B, for *XBPI* silencing and *XBPI* knockout, respectively). Concomitantly, the expression of G<sub>1</sub> regulatory factors cyclin D and CDK4 was suppressed in *XBPI*-silenced cells (Fig. 2D and fig. S4C). Furthermore, the suppression of cyclin D and CDK4 expression was also observed in *XBPI* knockout and thapsigargin-treated cells (fig. S4, D and E). In contrast, the levels of these factors increased substantially following overexpression of *XBPI*-u, but not *XBPI*-s, in both *XBPI*-silenced HCT116<sup>WT</sup> cells (Fig. 2E and fig. S4, F and G) and HCT116<sup>*XBPI*null</sup> cells (fig. S4H). The same pattern was also observed for other cyclins and CDK (fig. S4, I and J).

### **p53 plays a crucial role in *XBPI*-u-regulated transcription of p21**

It is well known that the tumor suppressor p53 blocks cell cycle progression by positively regulating p21 transcriptional activity (13). Thus, we investigated the role of p53 in the *XBPI*-u-mediated regulation of p21. Both *XBPI* silencing and knockout promoted the accumulation of

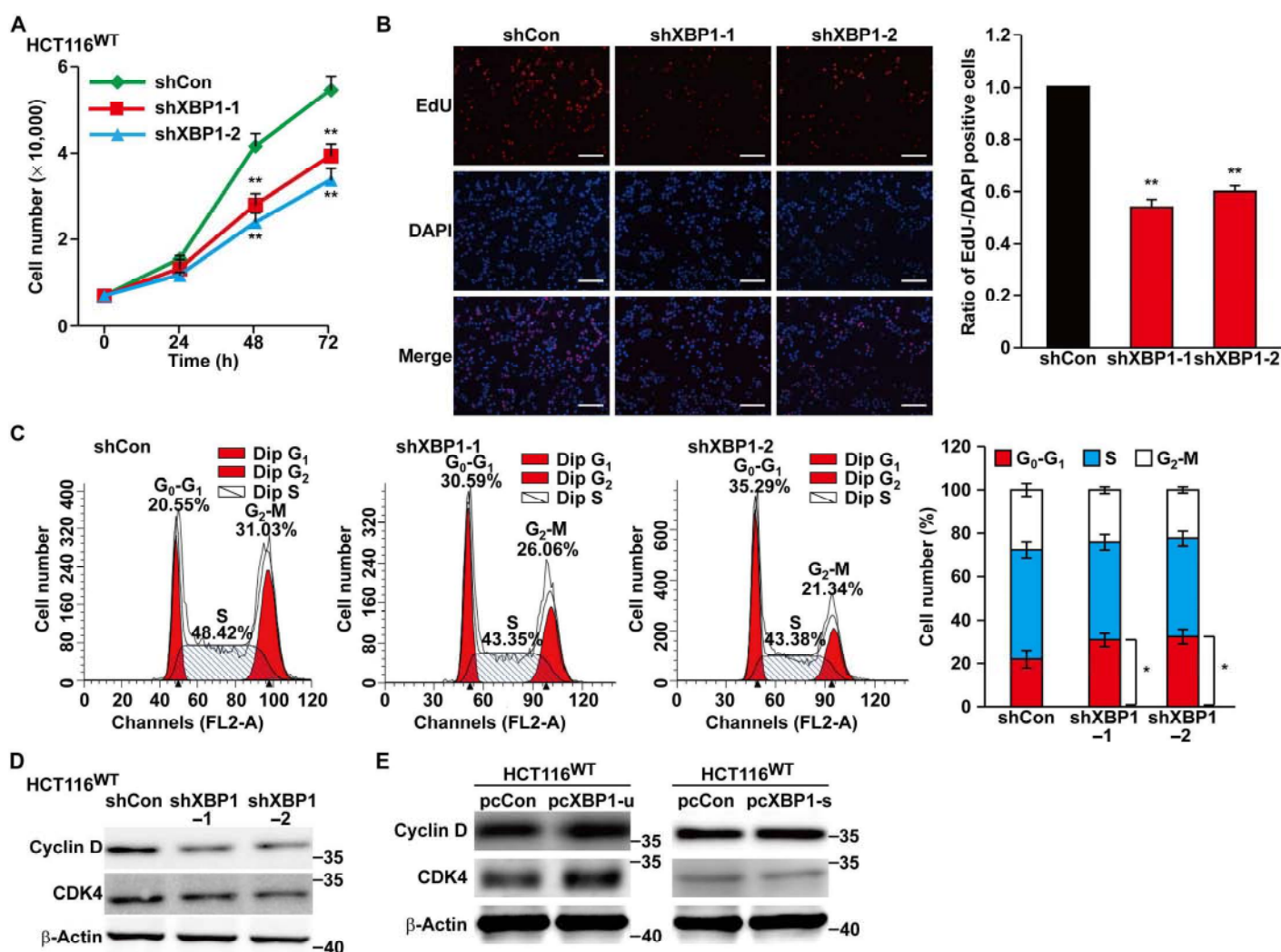
p53 protein but not its mRNA, a pattern that was reversed by *XBPI*-u overexpression (Fig. 3, A and B, and fig. S5A). Next, we constructed a mutant p21 reporter vector without the p53 binding site (p21<sup>mut</sup>-luc). We found that overall luciferase activities in HCT116<sup>WT</sup> cells cotransfected with p21<sup>mut</sup>-luc were significantly lower than those in HCT116<sup>WT</sup> cells cotransfected with a wild-type p21 reporter, irrespective of *XBPI* status (fig. S5B). A similar tendency was also observed in HCT116<sup>p53null</sup> cells cotransfected with a wild-type p21 reporter (fig. S5B). Moreover, *XBPI* silencing failed to promote p21 mRNA expression in p53-null cells (Fig. 3C) and only slightly affected p21 protein accumulation (fig. S5C), as well as cyclins and CDKs expression (fig. S5, D and E). Concomitantly, the effect of *XBPI* silencing on the characteristics of HCT116<sup>p53null</sup> cells, that is, total cell number (fig. S6, A and B), induction of G<sub>0</sub>-G<sub>1</sub> arrest (fig. S6C), and colony-forming potential (fig. S6, D and E), was significantly weaker than the effect on the characteristics of HCT116<sup>WT</sup> cells.

Given that p53 had been reported to be degraded by the proteasomal pathway, we investigated the role of *XBPI*-u in the ubiquitination of p53. *XBPI* silencing significantly reduced p53 ubiquitination, whereas overexpression of *XBPI*-u robustly increased it (Fig. 3, D and E). These results suggest that *XBPI*-u regulates p21 mainly at a transcriptional level and in a p53-dependent manner via increased p53 ubiquitination. Previous studies reported that factors such as p14(ARF) and ribosomal proteins, for example, RPL11 and RPS14, could form complexes with MDM2, a negative regulator of p53 protein stability (14), and suppress its stimulation of p53 ubiquitination (15–17). Therefore, we investigated whether *XBPI*-u affected the binding of these factors to MDM2. As shown in Fig. 3F, overexpression of *XBPI*-u had no significant effect on the binding of p14(ARF), RPL11, or RPS14 to MDM2, indicating that *XBPI*-u did not exert its function in degrading p53 through any of these pathways.

### **XBPI-u regulates the p53/p21 axis by promoting MDM2 protein accumulation**

Next, we investigated whether *XBPI*-u exerted its inhibitory effect on the p53/p21 axis through a positive regulation of MDM2. We found that silencing of *XBPI*, as well as knocking out *XBPI* and decreasing *XBPI*-u level by inducing its splicing, resulted in a significant decrease in MDM2 protein level, whereas overexpressing *XBPI*-u, but not *XBPI*-s, induced its accumulation (Fig. 4A and fig. S7, A to D). Furthermore, MDM2 overexpression repressed the p21 and p53 up-regulation observed in *XBPI*-silenced cells (fig. S7E). Next, we constructed HCT116<sup>*XBPI*null</sup>/pcMDM2 as well as control (HCT116<sup>WT</sup>/pcDNA3 and HCT116<sup>*XBPI*null</sup>/pcDNA3) stable cell lines (Fig. 4B and fig. S7F). Analysis of total cell numbers of these cell lines revealed that MDM2 overexpression in *XBPI*-null cells successfully restored high cell numbers (fig. S7G). Together, these results suggest that *XBPI*-u most likely regulates the p53/p21 axis in an MDM2-dependent manner. Furthermore, *XBPI*-u/MDM2/p53 regulatory pathways could also be found in hepatocarcinoma and breast cancer cell lines (fig. S8, A and B), indicating that this mechanism is common to various human carcinomas.

However, MDM2 mRNA expression in *XBPI*-silenced HCT116<sup>WT</sup> cells and *XBPI*-knocked out (HCT116<sup>*XBPI*null</sup>) cells, as well as in HCT116<sup>WT</sup> cells overexpressing *XBPI*-u, did not show any significant changes (fig. S9, A and B). These results were intriguing, as a previous study (18) revealed that MDM2 transcription could be regulated by two promoters: the p53-irresponsive p1 promoter and the p53-responsive p2 promoter; thus, MDM2 transcription is also regulated by p53



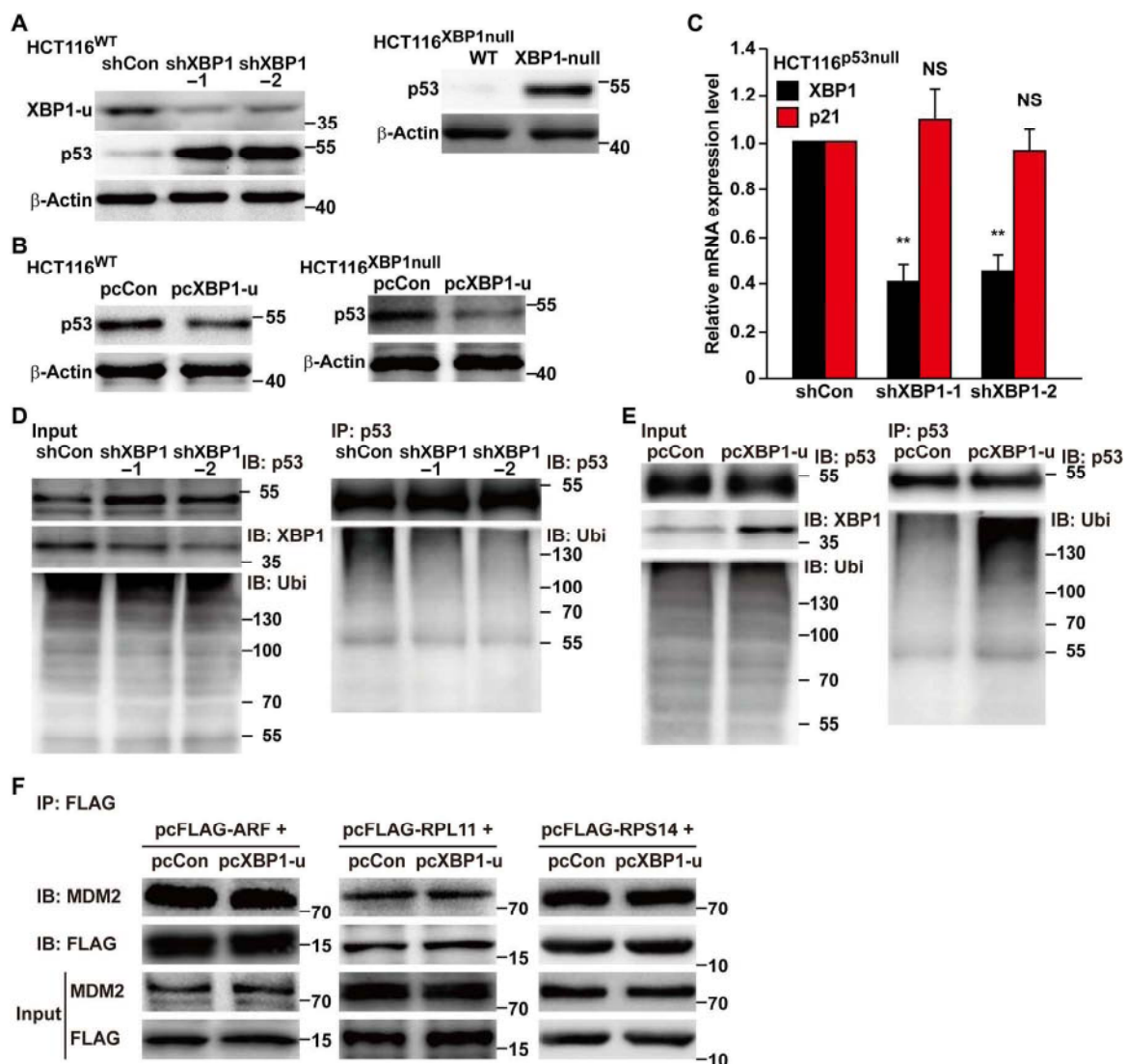
**Fig. 2. XBP1-u regulates cell cycle progression and cell proliferation.** (A) Total cell number of *XBP1*-silenced HCT116<sup>WT</sup> cells at the indicated time points. (B) Number of proliferating *XBP1*-silenced HCT116<sup>WT</sup> cells, as determined by the EdU incorporation assay. Representative images (left) and the ratio of EdU-positive cells (right) are shown. Cells transfected with control vector (shCon) were used as control. 4,6'-Diamidino-2-phenylindole (DAPI) was used to stain the nuclei. Proliferating cells were calculated as the ratio of EdU-positive and DAPI-positive cells and are shown relative to the control. Scale bars, 200  $\mu$ m. (C) Different cell cycle phases of *XBP1*-silenced HCT116<sup>WT</sup> cells. Cells were stained using propidium iodide, and the percentages were determined by flow cytometry. Representative images are shown (left), and the average percentage of cells in each cell cycle phase from three independent experiments was calculated (right). (D and E) Protein expression levels of cyclin D and CDK4 in *XBP1*-silenced HCT116<sup>WT</sup> cells (D) or HCT116<sup>WT</sup> cells transfected with either pcXBP1-u or pcXBP1-s (E), as analyzed by Western blotting.  $\beta$ -Actin was used as loading control. Quantitative data are expressed as the mean  $\pm$  SEM of three independent experiments. \* $P$  < 0.05, \*\* $P$  < 0.01 (ANOVA).

through a feedback mechanism (19–21). Similar to the effect of *XBP1* silencing on mRNA in HCT116<sup>WT</sup> cells, our results showed that *XBP1* silencing did not affect the activities of both p1 and p2 reporters (fig. S9C). Next, we assessed the effect of *XBP1* silencing on the MDM2 mRNA expression level in HCT116<sup>p53null</sup> cells and found that in the absence of p53, *XBP1* silencing significantly suppressed MDM2 mRNA expression level (fig. S9D). The same tendency was observed for the activity of the p2 reporter (fig. S9E) in *XBP1*-silenced HCT116<sup>p53null</sup> cells. Thus, these results indicate that *XBP1* silencing might also down-regulate MDM2 at its transcriptional level. Furthermore, these results suggest that the overall effect of *XBP1* silencing on MDM2 transcriptional activity in HCT116<sup>WT</sup> cells was the accumulative effect of both *XBP1* suppression and p53-induced feedback mechanism. In other words, the increase of p53 restored the decrease

of MDM2 transcriptional activity caused by *XBP1* suppression, resulting in the overall unchanged MDM2 mRNA expression level in *XBP1*-silenced HCT116<sup>WT</sup> cells.

### XBP1-u enhances MDM2 protein stability by inhibiting its homodimerization and self-ubiquitination

The fact that XBP1-u could positively regulate MDM2 protein accumulation even in cells with wild-type p53, in which no significant change in overall MDM2 mRNA expression could be observed, suggested that XBP1-u might regulate MDM2 at the protein level. Ubiquitin-mediated proteasomal degradation is the canonical pathway for regulating MDM2 homeostasis and is thus critical for fine regulation of the cell cycle and proliferation (22). Time-dependent protein degradation rate assays showed that, compared to HCT116<sup>WT</sup>, the degradation rate of

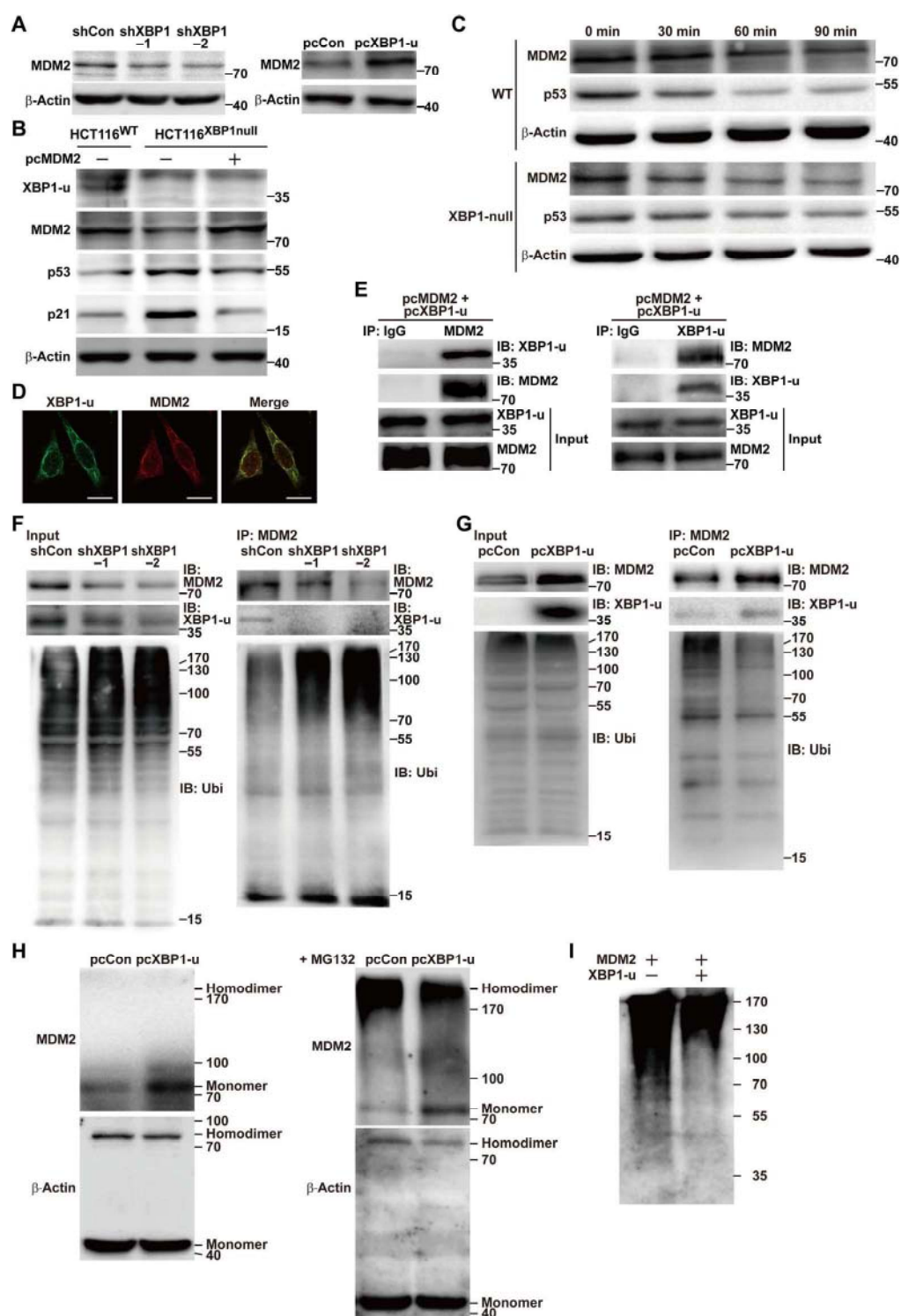


**Fig. 3. XBP1-u promotes p53 protein degradation.** (A and B) Protein expression level of p53 in *XBP1*-silenced HCT116<sup>WT</sup> cells and *XBP1*-knocked out HCT116<sup>XBP1null</sup> cells (A) or in HCT116<sup>WT</sup> cells and HCT116<sup>XBP1null</sup> cells transfected with pcXBP1-u (B), as determined by Western blotting. (C) p21 mRNA expression level in *XBP1*-silenced HCT116<sup>p53null</sup> cells, as analyzed by qPCR. Data are shown relative to those of cells transfected with shCon and expressed as the mean  $\pm$  SEM of three independent experiments. (D and E) p53 ubiquitination levels in HCT116<sup>WT</sup> cells transfected with pc53, pcUbi, and shXBP1 (D) or pcXBP1-u (E) were analyzed by anti-ubiquitin immunoblotting (IB) of cell lysates immunoprecipitated with anti-p53 antibody. Ubi, ubiquitin. (F) Physical interactions between MDM2 and ARF, RPL11, or RPS14 in HCT116<sup>WT</sup> cells transfected with corresponding FLAG-conjugated overexpression vectors, MDM2 and pcXBP1-u, as determined by immunoprecipitation (IP). Cell lysates were immunoprecipitated with anti-FLAG antibody; binding was detected by immunoblotting against anti-MDM2 antibody.  $\beta$ -Actin was used for qPCR normalization and as Western blotting loading control. \*\* $P < 0.01$  (ANOVA).

MDM2 in HCT116<sup>XBP1null</sup> cells was substantially faster (Fig. 4C), in contrast with the pattern for p53 degradation. Endogenous XBP1-u and MDM2 colocalized to the cytoplasm, and they could be reciprocally immunoprecipitated (Fig. 4, D and E). Moreover, silencing *XBP1* significantly enhanced MDM2 ubiquitination, whereas overexpressing XBP1-u reduced it (Fig. 4, F and G).

Given that MDM2 could form homodimers and face degradation via self-ubiquitination (23, 24), we examined the effect of XBP1-u on MDM2 homodimerization and self-ubiquitination. To this end, we performed an *in vivo* chemical cross-linking assay using disuccinimidyl suberate (DSS), a chemical cross-linking reagent that promotes protein homodimerization (25, 26). Compared to the control,

XBP1-u overexpression significantly increased MDM2 monomer level (Fig. 4H, left). The MDM2 homodimer could not be detected in control or in XBP1-u-overexpressing cells (Fig. 4H, left); however, its accumulation was significantly stronger in control cells upon treatment with the proteasome inhibitor MG132 (Fig. 4H, right). These results strongly suggest that XBP1-u inhibited the formation of the MDM2 homodimer, which, as reported previously, is unstable and undergoes proteasomal degradation (26, 27). To further confirm that XBP1-u prevented MDM2 self-ubiquitination, we examined the MDM2 self-ubiquitination potential in the presence of XBP1-u. An *in vitro* assay showed that the ubiquitination level of MDM2 decreased significantly in the presence of XBP1-u (Fig. 4I). Together, these results revealed



**Fig. 4. XBP1-u stabilizes MDM2 protein by inhibiting its self-ubiquitination.** (A and B) MDM2 protein expression level in *XBP1*-silenced or pcXBP1-u-transfected HCT116<sup>WT</sup> cells (A) or MDM2, p53, and p21 in HCT116<sup>XBP1null</sup>/pcMDM2, HCT116<sup>XBP1null</sup>/pcDNA3, and HCT116<sup>WT</sup>/pcDNA3 stable cell lines (B), as determined by Western blotting. (C) Degradation rates of MDM2 and p53 in HCT116<sup>WT</sup> and HCT116<sup>XBP1null</sup> cells. The levels of MDM2 and p53 protein at the indicated time points after the addition of cycloheximide, which inhibits new protein synthesis, were analyzed using Western blotting. (D) Colocalization of MDM2 and XBP1-u, as determined by immunofluorescence staining. Scale bars, 20  $\mu$ m. (E) Physical interaction between XBP1-u and MDM2, as determined by anti-XBP1 immunoblotting of cell lysate immunoprecipitated with anti-MDM2 antibody and vice versa. IgG, immunoglobulin G. (F and G) MDM2 ubiquitination level in HCT116<sup>WT</sup> cells transfected with shXBP1 (F) or pcXBP1-u (G), as determined by anti-ubiquitin immunoblotting of cell lysates immunoprecipitated with anti-MDM2 antibody. (H) Homodimerization of MDM2 in HCT116<sup>WT</sup> cells transfected with pcXBP1-u, as analyzed by DSS-induced chemical cross-linking assay with or without MG132. (I) Ubiquitination level of MDM2 in the presence or absence of XBP1-u, as analyzed by an *in vitro* ubiquitination assay.  $\beta$ -Actin was used as loading control.

that XBP1-u could form a complex with MDM2, enhance MDM2 stability by preventing its homodimerization and self-ubiquitination, and promote p53 protein degradation.

Next, we overexpressed FLAG-conjugated full-length XBP1-u, FLAG-conjugated XBP1-u N-terminal region, or FLAG-conjugated XBP1-u C-terminal region (FLAG-XBP1-u, FLAG-XBP1-u-N, and FLAG-XBP1-u-C, respectively). Immunoprecipitation with anti-FLAG antibody revealed that only the C terminus (and not the N terminus) of XBP1-u could bind MDM2 (Fig. 5A). A glutathione *S*-transferase (GST) pull-down assay using GST-conjugated MDM2 (GST-MDM2) and His-conjugated XBP1-u fragments (His-XBP1-u, His-XBP1-u-N, and His-XBP1-u-C for the full-length XBP1-u, the N terminus of XBP1-u, and the C terminus of XBP1-u, respectively) further confirmed the above results: Only His-XBP1-u and His-XBP1-u-C could be pulled down by GST-MDM2 (Fig. 5B). We also showed that overexpression of XBP1-u-C suppressed the formation of the MDM2 homodimer (Fig. 5C) and inhibits MDM2 self-ubiquitination (Fig. 5D). These effects could not be observed with XBP1-u-N (fig. S10, A and B). Thus, it is most likely that the C terminus of XBP1-u could bind to MDM2 and suppress its homodimerization, resulting in the decrease of MDM2 self-ubiquitination. We showed that overexpression of FLAG-XBP1-u-C was functionally sufficient to block intracellular MDM2 ubiquitination (Fig. 5E). Concomitantly, XBP1-u-C overexpression induced MDM2 protein accumulation and reduced p53 and p21 protein levels in HCT116<sup>WT</sup> and HCT116<sup>XBP1null</sup> cells (Fig. 5F). Together, these results reveal that XBP1-u could bind MDM2, suppress its ubiquitination, and thus regulate the p53/p21 pathway. Moreover, all these functions could be attributed to the C terminus of XBP1-u.

### The XBP1-u/MDM2 pathway is critical for tumorigenesis

To elucidate the pathological function of the XBP1-u/MDM2 pathway *in vivo*, especially during tumorigenesis, we transplanted HCT116<sup>WT</sup>/pcDNA3, HCT116<sup>XBP1null</sup>/pcDNA3, and HCT116<sup>XBP1null</sup>/pcMDM2 stable cell lines subcutaneously into BALB/c-nu/nu mice. XBP1 deficiency significantly reduced the tumorigenesis potential of HCT116 cells; however, MDM2 overexpression restored it (Fig. 6, A and B). Furthermore, Western blotting results revealed that the expression of MDM2 was negatively regulated in XBP1 knockout cells. Conversely, the expression of p53 and p21 was enhanced but was then suppressed by MDM2 overexpression (Fig. 6C). Immunohistochemistry of tissue sections from xenografted tumors further confirmed the above results (Fig. 6D).

Finally, we found that XBP1-u, MDM2, and p21 were aberrantly expressed in clinical human colon carcinoma samples (Fig. 6, E and F). XBP1-u and MDM2 demonstrated a positive correlation because both were up-regulated in tumor lesions compared to tumor adjacent tissues. At the same time, the mRNA and protein levels of XBP1-u were up-regulated in tumor tissues, whereas those of p21 were down-regulated.

We found that XBP1-u localization to the nucleus was enhanced in tumor lesions, in which expression of both XBP1 and MDM2 was up-regulated (Fig. 6F). Similarly, we found that whereas XBP1-u localized predominantly to the cytoplasm under basal condition or when it was overexpressed alone, it colocalized with MDM2 to the nucleus when both of them were overexpressed (fig. S11A). Furthermore, using sequential immunoprecipitation, we observed that XBP1-u, MDM2, and p53 interacted physically, indicating that they could form at least a tertiary complex (fig. S11, B and C). Given that MDM2 interacts with and degrades p53 protein in the nucleus, these results indicate that XBP1-u might shuttle to the nucleus upon binding to MDM2 and then

be involved in p53 degradation. These mechanisms resemble the conventional and highly conserved MDM2/MDMX/p53 regulatory pathway (28, 29). Human homolog of double minute X [MDMX (also known as MDM4)], a homolog of MDM2 that could form a heteromeric complex with MDM2, inhibits MDM2 homodimerization and, as a result, suppresses MDM2 self-ubiquitination in the cytoplasm and promotes p53 degradation (23, 24). However, MDMX itself localizes only to the cytoplasm and enters the nucleus solely upon binding to MDM2 (29, 30). Despite similarities on inhibition of MDM2 homodimerization and self-ubiquitination, we found that XBP1-u could not be immunoprecipitated with MDMX (fig. S12). Thus, it is most likely that this novel and specific regulatory pathway is irrelevant to the conventional, well-known MDM2/MDMX/p53 pathway. Together, these findings reveal that XBP1-u is a novel oncogene responsible for regulating the MDM2/p53 axis through an unconventional pathway (Fig. 6G).

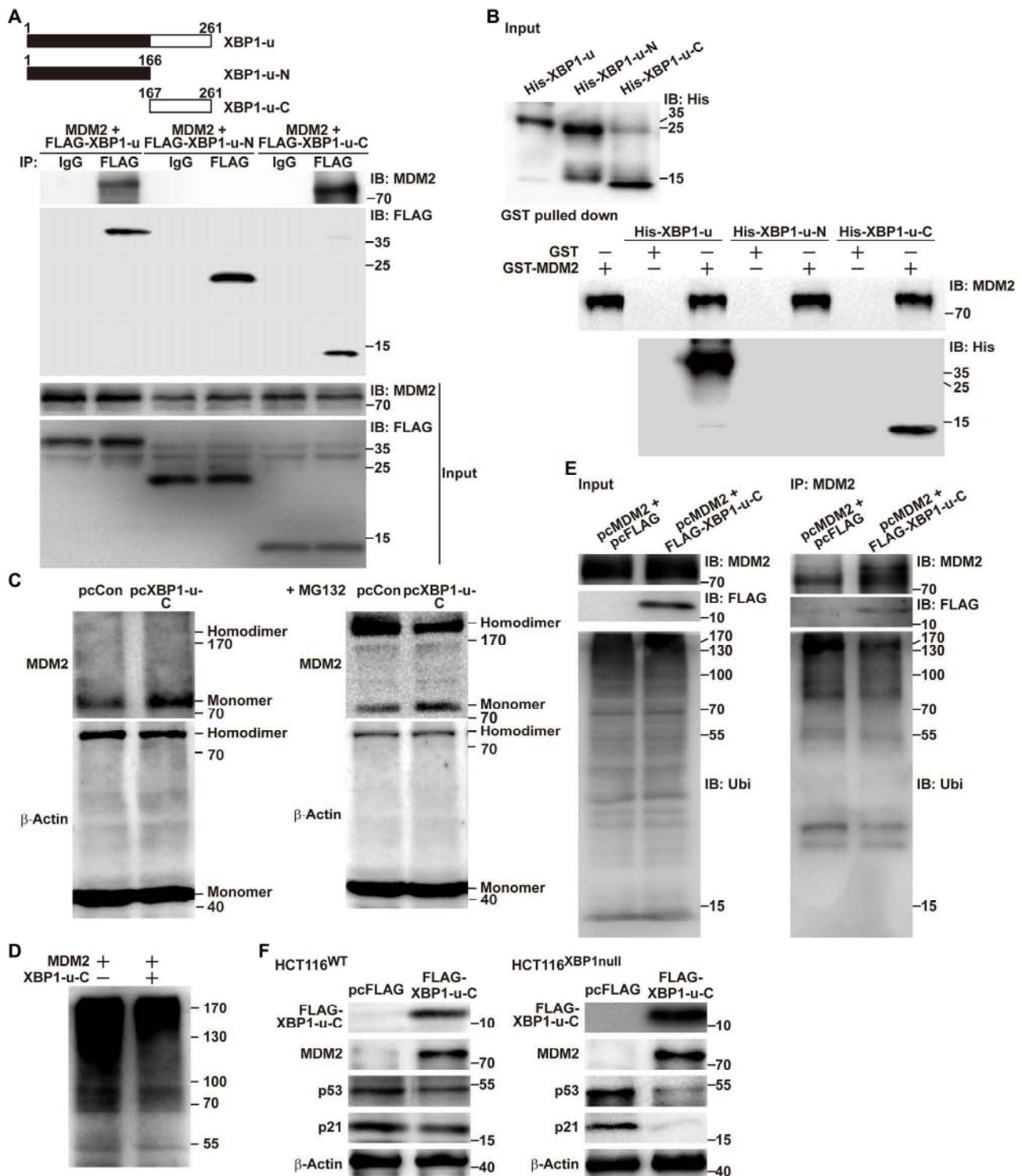
### DISCUSSION

Tight control of cell cycle progression is critical for maintaining normal biological functions, and the p53/p21 axis plays a critical role in this regulation. Loss of control of this mechanism leads to several abnormalities, including tumors and embryonic lethality. Besides mutations in p53, which could be observed in approximately half of all human malignancies, many tumors with wild-type p53 exhibit abnormal expression of p53 regulators. MDM2 is a crucial negative regulator of p53 that promotes its degradation by the ubiquitin proteasomal degradation pathway (14). Our findings describe a novel regulatory mechanism of the MDM2/p53 pathway: XBP1-u binds to MDM2, inhibits its self-ubiquitination, stabilizes it, and thus enhances p53 degradation. This subsequently leads to the down-regulation of p21 and accelerated cell cycle progression as well as cell proliferation (Fig. 6G).

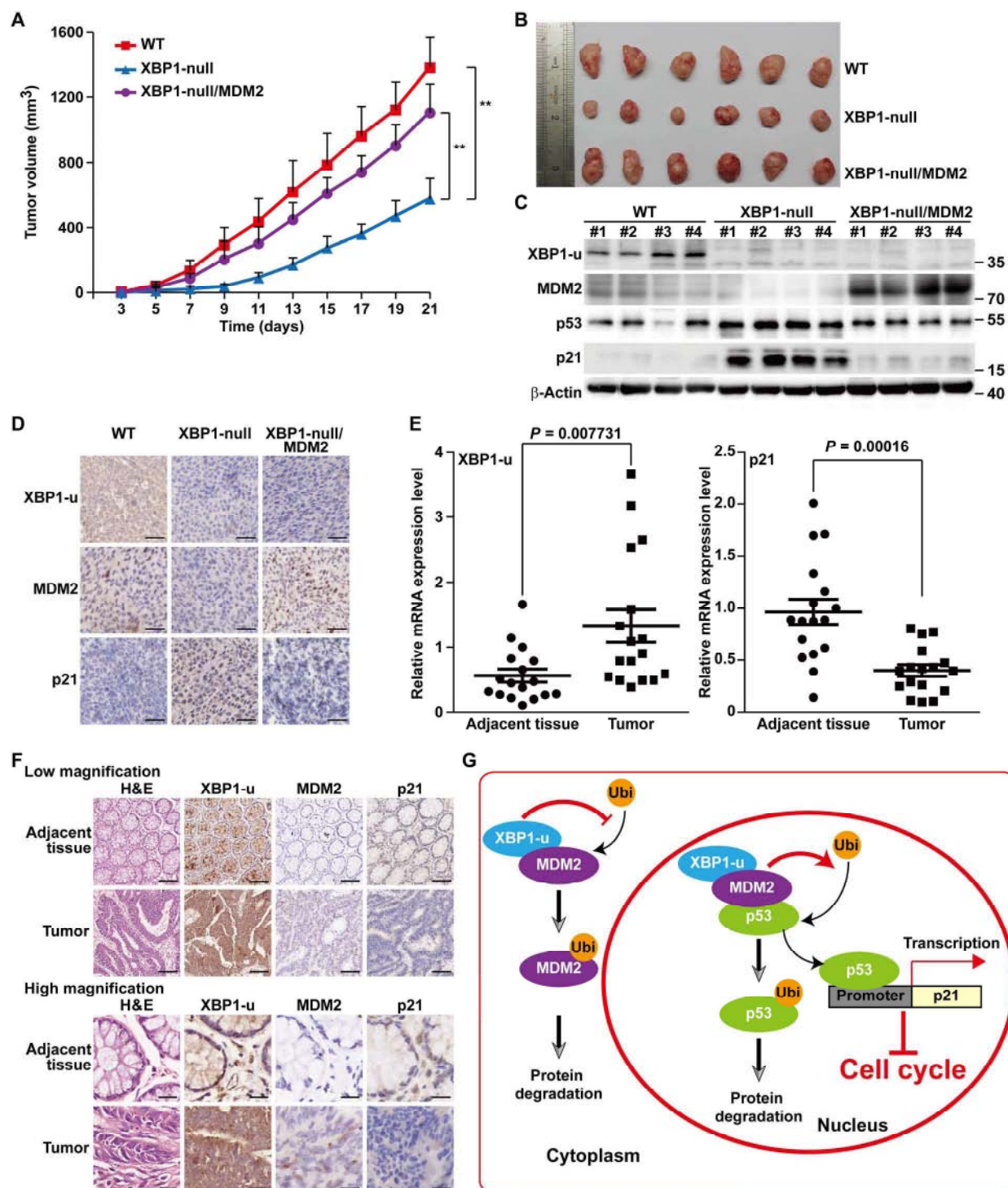
XBP1 was initially identified for its spliced active form, XBP1-s (12). In response to ER stress, the mRNA of XBP1-u is spliced to generate XBP1-s, which regulates ER homeostasis by binding to a subset of genes and components of the ER-associated degradation pathway (31). XBP1-s has been reported to be involved in various biological and physiological contexts, such as adaptive and innate immunity, circadian rhythm, and oxidative stress (32–34). However, Nekrutenko and He (35) demonstrated that XBP1 evolved in a fashion that was consistent only if both reading frames were functional. Unlike XBP1-s, the specific role of XBP1-u has remained poorly understood. This may be due to the high sequence similarity between XBP1-u and XBP1-s and to the low expression level of XBP1-u under ER stress condition, making it difficult to perform a gene function analysis specific to XBP1-u. Although recent studies have shown that XBP1-u is involved in the protection of endothelial cells from oxidative stress by promoting Akt1 (AKT serine/threonine kinase 1) phosphorylation and in the suppression of autophagy by promoting the degradation of forkhead box 1 (36, 37), knowledge of any specific, ER stress-independent functions of XBP1-u remains minimal. Our findings show that XBP1-u intersects with the MDM2/p53 pathway. The latter is a fundamental regulatory pathway critical for tumorigenesis and other biological and pathological functions, such as embryogenesis, DNA repair, and senescence (38, 39). Hence, our results elucidate a novel function of XBP1-u in pivotal biological functions.

MDM2 is an oncogene that belongs to the RING domain-containing E3 ligase family (14, 40, 41). MDM2 could shuttle between the nucleus, where it enhances p53 ubiquitination, and the cytoplasm,





**Fig. 5. The C terminus of XBP1-u suppresses MDM2 ubiquitination.** (A) In vivo binding capacity of XBP1-u fragments to MDM2, as determined by immunoprecipitation. HCT116<sup>WT</sup> cells were transfected with pcMDM2 and pcFLAG-XBP1-u, pcFLAG-XBP1-u-N, or pcFLAG-XBP1-u-C. Cell lysates were immunoprecipitated against IgG or anti-FLAG antibody. The presence of MDM2 was detected by immunoblotting. (B) Binding capacity of XBP1-u fragments to MDM2, as determined by an in vitro GST pull-down assay. His-tagged XBP1-u peptides were mixed with GST-MDM2 peptides and pulled down using a GST column. The presence of XBP1-u fragments was detected using anti-His immunoblotting. (C) Homodimerization of MDM2 in HCT116<sup>WT</sup> cells transfected with pcXBP1-u-C, as analyzed by DSS-induced chemical cross-linking assay with or without MG132. (D) Ubiquitination level of MDM2 in the presence or absence of XBP1-u-C, as analyzed by an in vitro ubiquitination assay. (E) MDM2 ubiquitination level in HCT116<sup>WT</sup> cells transfected with pcFLAG-XBP1-u-C, pcMDM2, and pcUbi, as analyzed by anti-ubiquitin immunoblotting of cell lysates immunoprecipitated with anti-MDM2 antibody. (F) Protein expression levels of MDM2, p53, and p21 in HCT116<sup>WT</sup> and HCT116<sup>XBP1null</sup> cells transfected with FLAG-XBP1-u-C, as determined by Western blotting. β-Actin was used as loading control.



**Fig. 6. XBP1-u is involved in MDM2-mediated tumorigenesis.** (A and B) Tumorigenesis potentials of HCT116<sup>WT</sup>/pcDNA3, HCT116<sup>XBP1null</sup>/pcDNA3, and HCT116<sup>XBP1null</sup>/pcMDM2 stable cell lines, as determined in vivo by subcutaneous injection into BALB/c-nu/nu mice ( $n = 6$ ). The volume of the generated tumor was measured at the indicated time points (A), and morphological images are shown (B). (C) Protein expression levels of XBP1-u, MDM2, p53, and p21 in the generated tumors, as determined by Western blotting.  $\beta$ -Actin was used as loading control. (D) Immunohistochemistry staining showing the localization of MDM2, XBP1-u, and p21 in tissue sections of xenografted tumors in BALB/c-nu/nu mice injected with the indicated cell lines. Scale bars, 20  $\mu$ m. (E) mRNA expression levels of XBP1-u and p21 in clinical human colon carcinoma and adjacent tissues samples ( $n = 17$ ), as determined by qPCR. Data were normalized with  $\beta$ -actin.  $P$  values were determined by ANOVA. (F) Immunohistochemistry staining showing localization of MDM2, XBP1-u, and p21 in clinical human colon carcinoma and adjacent tissues samples. Low-magnification (top) and high-magnification (bottom) images are shown. Scale bars, 100  $\mu$ m (top) and 20  $\mu$ m (bottom). H&E, hematoxylin and eosin. (G) Schematic diagram showing the mechanism of XBP1-u regulation on the MDM2/p53/p21 axis.

where its protein regulation occurs. Unlike XBP1-s, which localizes to the nucleus (42), we show here that XBP1-u is detected predominantly in the cytoplasm. Furthermore, the MDM2-stabilizing function of XBP1-u could be attributed to its C terminus, which is different from that of XBP1-s, and has been reported to have a strong nuclear exclusion signal (42). These facts strongly support our conclusion that the MDM2-stabilizing function is specific to XBP1-u. Intriguingly, when overexpressed, MDM2 could promote XBP1-u localization to the nucleus, where MDM2 functions as a negative regulator of p53. Although the detailed mechanism needs to be investigated further, these results indicate that XBP1-u might not only stabilize MDM2 protein but also be involved in MDM2-induced p53 degradation. Taking into account the fact that XBP1-u is sufficient to inhibit MDM2 self-ubiquitination in vitro and that it neither immunoprecipitates with MDMX nor affects the binding of MDM2 to factors that inhibit its ubiquitination activity such as ARF and ribosomal proteins RPL11 and RPS14, the XBP1-u/MDM2/p53 axis represents a novel pathway. Hence, although further investigation is required to elucidate whether XBP1-u competes with MDMX in stabilizing MDM2, our findings unraveled a critical, unconventional pathway for the regulation of MDM2 and p53.

Besides regulating p53, recent reports have shown that MDM2 could also promote cell proliferation and tumorigenesis in a p53-independent manner (20), raising the possibility that XBP1-u/MDM2 might also contribute to tumorigenesis in a p53-independent manner. Our results show that *XBP1* silencing could still suppress cell cycle progression, cell proliferation, and colony-forming potential in p53-null cells, although the effects are significantly lower than in wild-type cells. This could be mediated, at least in part, through the induction of p21 protein accumulation. This result conforms to the notion that MDM2 could directly regulate p21 protein stability (43). Therefore, it is most likely that although p53 is critical for the involvement of XBP1-u/MDM2 in tumorigenesis, the XBP1-u/MDM2 pathway could also participate in p53-independent tumorigenic processes. This fact further highlights the importance of XBP1-u/MDM2 in regulating both cell cycle and tumorigenesis.

p53 could regulate MDM2 transcription through a feedback mechanism, which would give rise to an oscillated expression pattern of both proteins (19–21). However, our results indicate that in the presence of p53, XBP1-u did not significantly affect MDM2 mRNA expression. This intriguing result is most plausibly due to the accumulative effects of XBP1-u positive regulation on MDM2 transcription and p53-induced feedback mechanism. To our knowledge, unlike its spliced form, XBP1-s, which had been reported to act as a transcriptional factor for its downstream genes (44), there is no report regarding the transcriptional function of XBP1-u at present. The transcriptional functions of XBP1-s should be attributed to its C terminus (44), which is different from that of XBP1-u. Nevertheless, although the detailed mechanism of XBP1-u regulation on MDM2 transcription needs further investigation, the fact that MDM2 protein accumulation is suppressed by *XBP1* silencing even in the presence of p53 reveals that the contribution of XBP1-u is even more significant at the protein stability level. On the other hand, the fact that XBP1-u could positively regulate MDM2 on both transcriptional and translational levels strongly suggests the clinical significance of its oncogenic function. Given that p53 down-regulation could also be observed even in many tumors with wild-type p53 (45), our results indicate that XBP1-u could mask the feedback regulation of p53 on MDM2 and thus might be involved in the aberrant high expression of MDM2 in many cancers with wild-type p53 (21).

In summary, by performing shRNA library screening, as well as in vitro and in vivo experiments, we uncover a previously unknown function of XBP1-u in regulating the MDM2/p53 axis and elucidate the new, critical role of XBP1-u in cell cycle and tumorigenesis. The fact that the MDM2/p53 pathway is also involved in other processes, including embryogenesis and senescence, indicates that the importance of XBP1-u has been underestimated and might indeed have a far-reaching impact. Finally, these findings give a new perspective regarding the regulation of the basic, conventional MDM2/p53 axis.

## MATERIALS AND METHODS

### shRNA expression vector and shRNA expression vector library

shRNA target sites were predicted using the algorithm for predicting specific target sites, and the shRNA expression vector library was constructed as described previously (46). The library contains 3354 shRNA expression vectors against 2065 genes (1 or 2 shRNA expression vectors with different target sequences for each gene). The specific target sites for shXBP1-1, shXBP1-2, shXBP1-3, and shXBP1-4 were GTA AGA AAT ATT ACT ATA A, AGT AAG AAA TAT TAC TAT A, GCT GGA AGC CAT TAA TGA A, and GAA CCA GGA GTT AAG ACA G, respectively; the target sites for p53 (NM\_000546.5) were GCA AGA AGG GAG ACA AGA T and GAG AAG AGT TGG AAC AGA A; and the target sites for MDM2 (NM\_002392.5) were GAC TAA ACG ATT ATA TGA T and AGG CAA ATG TGC AAT ACC A. The shRNA expression vectors were constructed as described previously (47). Briefly, the oligonucleotides with a hairpin structure, overhanging sequences, and a terminator were synthesized, annealed, and inserted into the Bsp MI sites of a pcPUR+U6i cassette vector containing the U6 promoter as described previously.

For XBP1-u (NM\_005080.3) and XBP1-s (NM\_001079539.1) overexpression vectors (pcXBP1-u and pcXBP1-s, respectively), the oligonucleotides of the coding sequences were synthesized and cloned into pUC57 (Invitrogen) before they were subcloned into the Bam HI and Not I sites of pcDNA3.1(+) (Invitrogen). For p53 and MDM2 overexpression vectors (pcp53 and pcMDM2, respectively), the corresponding regions were amplified using the Takara PrimeSTAR Max DNA Polymerase (Takara Bio) from human complementary DNA (cDNA) obtained by reverse-transcribing the total RNA extracted from HCT116<sup>WT</sup> cells using the PrimeScript RT Reagent Kit with gDNA Eraser (Takara Bio) and cloned into the Bam HI and Not I sites of pcDNA3.1(+). XBP1-u C-terminal (1 to 498 regions) and N-terminal (499 to 786 regions) overexpression vectors (pcXBP1-u-C and pcXBP1-u-N, respectively) were cloned in a similar way, except that pcXBP1-u and pcXBP1-s were used as templates.

For pcFLAG, the FLAG sequence was inserted into the Nhe I and Hind III sites of pcDNA3.1(+). For FLAG-tagged MDMX (NM\_002393.4), FLAG-tagged ARF (NM\_000077.4), FLAG-tagged RPL11 (NM\_000975.3), and FLAG-tagged RPS14 (NM\_001025071.1) overexpression vectors (FLAG-MDMX, FLAG-ARF, FLAG-RPL11, and FLAG-RPS14, respectively), the coding sequences were amplified from human cDNA as described above, whereas for FLAG-tagged XBP1-u, XBP1-u C terminus, and XBP1-u N terminus (FLAG-XBP1-u, FLAG-XBP1-u-C, and FLAG-XBP1-u-N, respectively), the XBP1-u, XBP1-u-C, and XBP1-u-N fragments were amplified from pcXBP1-u, pcXBP1-u-C, and pcXBP1-u-N, respectively. These fragments were then inserted into the Bam HI and Not I sites of pcFLAG.

For the p21 wild-type promoter reporter vector containing –65 to +2586 p21 promoter region (p21-luc) and MDM2 promoter reporter vectors (MDM2-p1-luc and MDM2-p2-luc, containing –2410 to –1 and +317 to +841 of MDM2 promoter regions, respectively), the corresponding promoter regions were amplified using the Takara PrimeSTAR Max DNA Polymerase (Takara Bio) from human genome DNA extracted from HCT116<sup>WT</sup> cells using the TIANamp Genomic DNA Kit (Tiangen Biotech) and cloned into the Bgl II and Hind III sites of pGL4.13 vector (Promega). p21-luc vector lacking the p53 binding site (p21<sup>mut</sup>-luc) was constructed on the basis of the site-specific mutagenesis method (48).

### Cell cultures and cell lines

The wild-type and p53-null HCT116 colon carcinoma cell lines (HCT116<sup>WT</sup> and HCT116<sup>p53null</sup>, respectively) were provided by B. Vogelstein (Johns Hopkins University School of Medicine). The HepG2 human liver carcinoma cell line and the MCF-7 human breast carcinoma cell line were obtained from the Cell Bank of the Chinese Academy of Sciences, Shanghai. Cells were maintained in medium [McCoy's 5A medium (Gibco) for HCT116 cells or Dulbecco's modified Eagle's medium (Gibco) for HepG2 and MCF-7 cells] supplemented with 10% fetal bovine serum (Biological Industries). All cell lines were routinely tested and found negative for mycoplasma contamination using Mycoplasma Detection Kit-QuickTest (Biotool).

The XBP1-null HCT116 (HCT116<sup>XBP1null</sup>) cell line was established using CRISPR/Cas9 technology. Briefly, human XBP-1 CRISPR/Cas9 KO Plasmid and human XBP-1 HDR Plasmid (Santa Cruz Biotechnology) were transfected into the HCT116<sup>WT</sup> cells using Lipofectamine 2000 (Invitrogen). Twenty-four hours later, puromycin selection (0.8 µg/ml) was performed to eliminate untransfected cells for 7 days. Cell line was then established from a single clone. The elimination of XBP1 was confirmed by analyzing the sequence of the corresponding genome DNA: The nucleotides located at the +570 to +616 region (47 base pairs) of XBP1-u were deleted.

To construct the XBP1-null stable cell line overexpressing MDM2, MDM2 overexpression vector pcMDM2 was transfected into HCT116<sup>XBP1null</sup> cells. To construct control stable cells lines, pcDNA3.1(+) vector was transfected into HCT116<sup>XBP1null</sup> or HCT116<sup>WT</sup> cells. Transfection was performed using Lipofectamine 2000 according to the manufacturer's instruction. The transfected cells were then selected using G418 (final concentration, 400 µg/ml), and stable cell lines were established from single clones.

For gene silencing experiments, cells were transfected with 2 µg of indicated shRNA expression vector using Lipofectamine 2000 (Invitrogen). Twenty-four hours later, cells were subjected to puromycin selection (final concentration, 1.2 µg/ml) to eliminate untransfected cells. mRNA and protein samples were collected 36 hours after puromycin selection.

For overexpression experiments, cells were transfected with 2 µg of indicated overexpression vector using Lipofectamine 2000 (Invitrogen). Twenty-four hours later, mRNA and protein samples were collected and subjected for further analysis.

For rescue experiments, cells were transfected with 1 µg of indicated shRNA expression vector and 1 µg of overexpression vector using Lipofectamine 2000 (Invitrogen). Cells were subjected to puromycin selection (final concentration, 1.2 µg/ml) to eliminate untransfected cells. mRNA and protein samples were collected 36 hours after puromycin selection.

For thapsigargin treatment,  $1 \times 10^6$  cells were seeded and cultured for 24 hours. After being treated with thapsigargin (final concentration, 1 nM) for 6 hours, mRNA and protein were collected.

### Animal experiment

For the in vivo tumor study, BALB/c-nu/nu mice (male; body weight, 18 to 22 g; 6 weeks old) were purchased from the Third Military Medical University (Chongqing, China; permit number SYXK-PLA-20120031). Animal studies were carried out in the Third Military Medical University and approved by the Laboratory Animal Welfare and Ethics Committee of the Third Military Medical University. All animal experiments conformed to the approved guidelines of the Animal Care and Use Committee of the Third Military Medical University. All efforts to minimize suffering were made.

To generate an experimental subcutaneous tumor model, BALB/c-nu/nu mice were divided into three groups ( $n = 6$ ), and each group was injected subcutaneously with  $5 \times 10^6$  HCT116<sup>WT</sup>/pcDNA, HCT116<sup>XBP1null</sup>/pcDNA, or HCT116<sup>XBP1null</sup>/pcMDM2 stable cells. Tumor size ( $V$ ) was evaluated by a caliper every 2 days with reference to the following equation:  $V = a \times b^2/2$ , where  $a$  and  $b$  are the major and minor axes of the tumor, respectively (47). Mice were randomly divided into three groups ( $n = 6$ ). The investigator was blinded to the group allocation and during the assessment.

### Clinical human colon carcinoma specimens

Human colon carcinoma specimens were obtained from colon carcinoma patients undergoing surgery at Chongqing Cancer Institute (Chongqing, China) and stored in the Biological Specimen Bank of Chongqing Cancer Institute. Patients did not receive chemotherapy, radiotherapy, or other adjuvant therapies before the surgery. The specimens were snap-frozen in liquid nitrogen. Patients' written informed consents were obtained, and the experiments were approved by the Institutional Research Ethics Committee of Chongqing Cancer Institute.

### Dual-Luciferase Reporter System and library screening

Cells were seeded onto 24-well plates for luciferase reporter assay or 96-well plates for library screening. Twenty-four hours later, cells were cotransfected with the indicated shRNA expression vectors, reporter vector, and the *Renilla* luciferase expression vector (pRL-SV40, Promega) as internal control using Lipofectamine 2000. Twenty-four hours after cotransfection, the luciferase activities were then measured with the Dual-Luciferase Reporter Assay System (Promega).

### RNA extraction and quantitative RT-PCR analysis

Total RNAs were extracted using TRIzol (Invitrogen) according to the manufacturer's instruction. Each total RNA sample (1 µg) was reverse-transcribed into cDNA using the PrimeScript RT Reagent Kit with gDNA Eraser (Takara Bio), and quantitative reverse transcription PCR (qPCR) was performed to assess the mRNA expression levels with SYBR Premix Ex Taq (Takara Bio). The sequences of the primers used for quantitative RT-PCR are shown in table S2.  $\beta$ -Actin was used to normalize sample amplification. The results are shown relative to the expression level in the corresponding controls, which are assumed as 1.

### Western blotting

For cell culture experiments, cells were collected and lysed with radioimmunoprecipitation assay (RIPA) lysis buffer with protease inhibitor and phosphatase inhibitor cocktail (complete cocktail, Roche Applied Science). Equal amounts of the sample proteins were electrophoresed on SDS polyacrylamide gel and transferred to a polyvinylidene fluoride membrane (Millipore) with a pore size of 0.45 or 0.22 µm (for protein,  $\leq 15$  kDa). The antibodies used are listed in table S3,

and immunoblotting with anti- $\beta$ -actin antibody was conducted to ensure equal protein loading. The signals were measured using Super-Signal West Femto Maximum Sensitivity Substrate detection system (Thermo Fisher Scientific). Images of uncropped blots are shown in fig. S13 (A to Q). Quantification was performed using Quantity One software.

For protein degradation assay,  $1 \times 10^6$  cells were seeded in a 3.5-cm dish. Cycloheximide was added at the final concentration of 200  $\mu$ g/ml. Protein samples were collected at the indicated time points and were subjected to Western blotting as described above.

#### Quantification of total cell number

HCT116<sup>WT</sup> cells or HCT116<sup>p53null</sup> cells were first transfected with the indicated vectors using Lipofectamine 2000 (Invitrogen). Twenty-four hours after transfection, puromycin selection (final concentration, 1.2  $\mu$ g/ml) was performed to eliminate untransfected cells. The transfected cells were seeded into 96-well plates. The cell numbers were measured by Cell Counting Kit-8 (Dojindo) at the indicated time points.

#### EdU incorporation assay and colony formation assay

Cells were transfected with the indicated shRNA expression vectors and selected using puromycin as indicated above. For EdU incorporation assay, after puromycin selection, EdU incorporation and staining were performed using Cell-Light EdU Apollo488 In Vitro Imaging Kit (RiboBio) according to the manufacturer's instruction. Nuclei were stained with DAPI. Images were taken with DMI6000B (Leica). Quantification of EdU-positive and DAPI-positive cells was performed using Microsystems LAS AF-TCS MP5 (Leica), and the results are shown as the ratio of EdU-positive cells to DAPI-positive cells. For colony formation assay, 300 cells were cultured in a six-well plate for 8 days. Cells were then fixed with 30% ethanol and stained with methylene blue. The colonies were then counted. The investigator was blinded during the assessment.

#### Cell cycle analysis

HCT116<sup>WT</sup> cells or HCT116<sup>p53null</sup> cells were transfected with the indicated shRNA expression vectors and selected using puromycin selection as described above. Cells were subjected for starvation for 24 hours before they were incubated further for 24 hours under normal conditions and then harvested and stained with propidium iodide (KeyGen Biotech). The percentages of the cells in each cell cycle phase were determined by flow cytometry.

#### Immunoprecipitation and in vivo ubiquitination assay

Cells were seeded in a 10-cm dish ( $5 \times 10^6$  cells per dish) and transfected with 16  $\mu$ g of shRNA expression vectors or overexpression vectors as described above. Total protein samples were collected and lysed with RIPA lysis buffer with protease inhibitor and phosphatase inhibitor cocktail (complete cocktail, Roche Applied Science) and cleared by centrifugation at 12,000 rpm. The supernatants were incubated at 4°C for 2 hours with protein A+G beads (Beyotime Biotechnology) in the presence of indicated antibodies or IgG as control. Then, the immunoprecipitated proteins were subjected to immunoblotting as described in Western blotting.

For ubiquitination assay, cells were transfected with the ubiquitin overexpression vector (pcUbi) and the indicated shRNA expression vector or overexpression vector, as well as the pcp53 or pcMDM2 vector (6  $\mu$ g each). Twenty-four hours later, cells were treated with MG132 (final concentration, 20  $\mu$ M) for 8 hours, and then the lysates

were collected as described above. Immunoprecipitation was performed using the indicated antibodies, and then the immunoprecipitated proteins were subjected to immunoblotting using anti-ubiquitin antibody and other antibodies as indicated.

#### GST pull-down assay

His-tagged N-terminal and C-terminal fragments, as well as the full-length XBP1-u proteins, were purchased from Proteintech. The GST-MDM2 protein was purchased from Boston Biochem and mixed with GST beads (GE Healthcare Life Sciences) in the binding buffer [phosphate-buffered saline (PBS) + 2 mM EDTA + 0.05% Tween 20 + 3% milk powder] at 4°C for 1 hour. The mixtures were then washed four times with wash buffer (PBS + 2 mM EDTA + 0.05% Tween 20 + 150 mM NaCl). His-tagged XBP1 fragments were added into the mixture and mixed in the abovementioned binding buffer at 4°C for 2 hours. The mixtures were then washed four times with wash buffer as mentioned above, and the protein complexes were eluted using 1% SDS. The pulled-down proteins were subjected to Western blotting as described above.

#### In vivo chemical cross-linking assay

Cells were transfected with the indicated vectors. After culturing for 24 hours, cells were collected and washed with cold PBS. The cell suspensions were treated with DSS for 30 min at 25°C, and the reaction was stopped using tris-buffered saline (pH 7.5). Cells were then lysed with RIPA lysis buffer with protease inhibitor and phosphatase inhibitor cocktail (complete cocktail, Roche Applied Science) before they were subjected to Western blotting as described above. For assay with MG132, cells were treated with MG132 (final concentration, 20  $\mu$ M) for 8 hours before they were collected and treated with DSS.

#### In vitro ubiquitination assay

Fifty nanograms of E1 (Boston Biochem), 100 ng of UBE2D2 (Boston Biochem), 5  $\mu$ g of ubiquitin (Boston Biochem), and 4  $\mu$ g of each protein as indicated were mixed in a buffer containing 50 mM tris (pH 7.6), 5 mM MgCl<sub>2</sub>, 2 mM adenosine triphosphate, and 2 mM dithiothreitol. The mixtures were then incubated at 30°C for 90 min, and the reactions were then stopped using 5 $\times$  SDS-polyacrylamide gel electrophoresis loading buffer. The samples were resolved on 10% SDS polyacrylamide gel and subjected to Western blotting against anti-MDM2 antibody as described above.

#### Immunohistochemical analysis

Paraffin-embedded sections were obtained from fresh colon carcinoma and adjacent tissues or xenografted tumors (4  $\mu$ m thick) using a cryostat and subjected to immunohistochemistry. Briefly, the tissue sections were incubated with primary antibodies for 1 hour. The specimens were then incubated with the corresponding second antibodies conjugated with horseradish peroxidase. Visualization was performed using a DAB (diaminobenzidine) Kit (DAKO) under a microscope. Nuclei were then counterstained with hematoxylin, followed by dehydration and coverslip mounting. The antibodies used are listed in table S2. Images were taken using Panoramic Midi (3DHistech).

#### Immunofluorescence staining

Cells were seeded in 3.5-cm culture dishes ( $2 \times 10^5$  cells per dish), fixed for 30 min at room temperature with 4% paraformaldehyde, permeabilized for 5 min with PBS containing 0.1% Triton X-100, blocked with 1% bovine serum albumin for 1 hour, and incubated with anti-XBP1-u and anti-MDM2 antibodies for 2 hours. Cells were then incubated with

fluorescent second antibodies for 1 hour. Nuclei were stained with DAPI (Beyotime Biotechnology) for 15 min. Images were taken with laser scanning confocal microscopy (Leica Microsystems TCS SP5).

### Sequential immunoprecipitation

Sequential immunoprecipitation was performed as described previously (49). Briefly, HCT116<sup>WT</sup> cells seeded in a 10-cm dish (5 × 10<sup>6</sup> cells per dish) were transfected with pcFLAG-XBP1u, pcMDM2, and pcp53 (6 μg each) as described above. Total protein samples were treated as described in the “Immunoprecipitation and in vivo ubiquitination assay” section, except that after immunoprecipitation with IgG or anti-FLAG antibody, the immunoprecipitants were again immunoprecipitated with IgG or anti-MDM2 antibody. Then, the immunoprecipitants were subjected to immunoblotting as described above.

### Statistical analysis

Quantification data were analyzed by one-way ANOVA conducted using SPSS Statistics v17.0. Statistical significance was defined as  $P < 0.05$ , and  $P < 0.01$  was considered highly significant.

### SUPPLEMENTARY MATERIALS

Supplementary material for this article is available at <http://advances.sciencemag.org/cgi/content/full/3/10/e1701383/DC1>

- fig. S1. XBP1 is a novel regulator of p21.  
 fig. S2. Expression levels of unspliced XBP1 (XBP1-u) and spliced XBP1 (XBP1-s).  
 fig. S3. Overexpression of XBP1-u suppresses p21 expression without inducing UPR.  
 fig. S4. XBP1-u promotes cell cycle progression and cell proliferation.  
 fig. S5. XBP1-u regulates p21 translation p53-dependently.  
 fig. S6. XBP1-u regulates cell cycle and colony-forming potential mainly through the p53 axis.  
 fig. S7. XBP1-u regulates p21 through the MDM2/p53 axis.  
 fig. S8. XBP1-u regulates the MDM2/p53/p21 axis in hepatocarcinoma and breast cancer cells.  
 fig. S9. p53 feedback mechanism restores XBP1-u regulation on the MDM2 mRNA expression level.  
 fig. S10. The N terminus of XBP1-u does not inhibit MDM2 homodimerization and self-ubiquitination.  
 fig. S11. Simultaneous up-regulation of XBP1-u and MDM2 induces the formation of XBP1-u/MDM2/p53 complex.  
 fig. S12. XBP1-u does not interact with MDMX.  
 fig. S13. Uncropped Western blots with the indicated areas of selection in Figs. 1 to 6 and figs. S1, S2, S4, S5, S7, S8, S10, S11, and S12.  
 table S1. List of the genes in the top 10% of the screening results.  
 table S2. Primers used for gene quantification by qPCR.  
 table S3. Antibodies used for Western blotting, immunohistochemistry, immunofluorescence, and immunoprecipitation.

### REFERENCES AND NOTES

- W. S. el-Deiry, T. Tokino, V. E. Velculescu, D. B. Levy, R. Parsons, J. M. Trent, D. Lin, W. E. Mercer, K. W. Kinzler, B. Vogelstein, WAF1, a potential mediator of p53 tumor suppression. *Cell* **75**, 817–825 (1993).
- J. W. Harper, G. R. Adami, N. Wei, K. Keyomarsi, S. J. Elledge, The p21 Cdk-interacting protein Cip1 is a potent inhibitor of G1 cyclin-dependent kinases. *Cell* **75**, 805–816 (1993).
- T. Abbas, A. Dutta, p21 in cancer: intricate networks and multiple activities. *Nat. Rev. Cancer* **9**, 400–414 (2009).
- F. Di Cunto, G. Topley, E. Calautti, J. Hsiao, L. Ong, P. K. Seth, G. P. Dotto, Inhibitory function of p21<sup>Cip1/WAF1</sup> in differentiation of primary mouse keratinocytes independent of cell cycle control. *Science* **280**, 1069–1072 (1998).
- H.-S. Kim, J.-I. Heo, S.-H. Park, J.-Y. Shin, H.-J. Kang, M.-J. Kim, S. C. Kim, J. Kim, J.-B. Park, J.-Y. Lee, Transcriptional activation of p21<sup>WAF1/CIP1</sup> is mediated by increased DNA binding activity and increased interaction between p53 and Sp1 via phosphorylation during replicative senescence of human embryonic fibroblasts. *Mol. Biol. Rep.* **41**, 2397–2408 (2014).
- G. Lozano, G. P. Zambetti, What have animal models taught us about the p53 pathway? *J. Pathol.* **205**, 206–220 (2005).
- A. Dhyani, J. A. Machado-Neto, P. Favaro, S. T. Olalla Saad, ANKHD1 represses p21 (WAF1/CIP1) promoter and promotes multiple myeloma cell growth. *Eur. J. Cancer* **51**, 252–259 (2015).
- P. Zhang, C. Wong, D. Liu, M. Finegold, J. W. Harper, S. J. Elledge, p21<sup>CIP1</sup> and p57<sup>KIP2</sup> control muscle differentiation at the myogenin step. *Genes Dev.* **13**, 213–224 (1999).
- M. Shiohara, W. S. el-Deiry, M. Wada, T. Nakamaki, S. Takeuchi, R. Yang, D. L. Chen, B. Vogelstein, H. P. Koeffler, Absence of WAF1 mutations in a variety of human malignancies. *Blood* **84**, 3781–3784 (1994).
- H. C. Liou, M. R. Boothby, P. W. Finn, R. Davidon, N. Nabavi, N. J. Zeleznik-Le, J. P. Ting, L. H. Glimcher, A new member of the leucine zipper class of proteins that binds to the HLA DR alpha promoter. *Science* **247**, 1581–1584 (1990).
- K. Yanagitani, Y. Kimata, H. Kadokura, K. Kohno, Translational pausing ensures membrane targeting and cytoplasmic splicing of XBP1u mRNA. *Science* **331**, 586–589 (2011).
- H. Yoshida, T. Matsui, A. Yamamoto, T. Okada, K. Mori, XBP1 mRNA is induced by ATF6 and spliced by IRE1 in response to ER stress to produce a highly active transcription factor. *Cell* **107**, 881–891 (2001).
- Y. Li, H. Feng, H. Gu, D. W. Lewis, Y. Yuan, L. Zhang, H. Yu, P. Zhang, H. Cheng, W. Miao, W. Yuan, S.-Y. Cheng, S. M. Gollin, T. Cheng, The p53–PUMA axis suppresses iPSC generation. *Nat. Commun.* **4**, 2174 (2013).
- S. Fang, J. P. Jensen, R. L. Ludwig, K. H. Vousden, A. M. Weissman, Mdm2 is a RING finger-dependent ubiquitin protein ligase for itself and p53. *J. Biol. Chem.* **275**, 8945–8951 (2000).
- C. M. Eischen, J. D. Weber, M. F. Roussel, C. J. Sherr, J. L. Cleveland, Disruption of the ARF–Mdm2–p53 tumor suppressor pathway in Myc-induced lymphomagenesis. *Genes Dev.* **13**, 2658–2669 (1999).
- R. Fähræus, V. Olivares-Illana, MDM2's social network. *Oncogene* **33**, 4365–4376 (2014).
- X. Zhou, Q. Hao, J. Liao, Q. Zhang, H. Lu, Ribosomal protein S14 unties the MDM2–p53 loop upon ribosomal stress. *Oncogene* **32**, 388–396 (2013).
- A. Zauberman, D. Flusberg, Y. Haupt, Y. Barak, M. Oren, A functional p53-responsive intronic promoter is contained within the human *mdm2* gene. *Nucleic Acids Res.* **23**, 2584–2592 (1995).
- Y. Barak, T. Juven, R. Haffner, M. Oren, *mdm2* expression is induced by wild type p53 activity. *EMBO J.* **12**, 461–468 (1993).
- O. Karni-Schmidt, M. Lokshin, C. Prives, The roles of MDM2 and MDMX in cancer. *Annu. Rev. Pathol.* **11**, 617–644 (2016).
- M. Wade, Y.-C. Li, G. M. Wahl, MDM2, MDMX and p53 in oncogenesis and cancer therapy. *Nat. Rev. Cancer* **13**, 83–96 (2013).
- C. Fan, X. Wang, Mdm2 Splice isoforms regulate the p53/Mdm2/Mdm4 regulatory circuit via RING domain-mediated ubiquitination of p53 and Mdm4. *Cell Cycle* **16**, 660–664 (2017).
- H. Kawai, V. Lopez-Pajares, M. M. Kim, D. Wiederschain, Z.-M. Yuan, RING domain-mediated interaction is a requirement for MDM2's E3 ligase activity. *Cancer Res.* **67**, 6026–6030 (2007).
- S. Tanimura, S. Ohtsuka, K. Mitsui, K. Shirouzu, A. Yoshimura, M. Ohtsubo, MDM2 interacts with MDMX through their RING finger domains. *FEBS Lett.* **447**, 5–9 (1999).
- J. D. Chavez, N. L. Liu, J. E. Bruce, Quantification of protein–protein interactions with chemical cross-linking and mass spectrometry. *J. Proteome Res.* **10**, 1528–1537 (2011).
- T. Liu, H. Zhang, J. Xiong, S. Yi, L. Gu, M. Zhou, Inhibition of MDM2 homodimerization by XIAP IRES stabilizes MDM2, influencing cancer cell survival. *Mol. Cancer* **14**, 65 (2015).
- K. Itahana, H. Mao, A. Jin, Y. Itahana, H. V. Clegg, M. S. Lindström, K. P. Bhat, V. L. Godfrey, G. I. Evan, Y. Zhang, Targeted inactivation of Mdm2 RING finger E3 ubiquitin ligase activity in the mouse reveals mechanistic insights into p53 regulation. *Cancer Cell* **12**, 355–366 (2007).
- C. R. Coffill, A. P. Lee, J. W. Siau, S. M. Chee, T. L. Joseph, Y. S. Tan, A. Madhumalar, B.-H. Tay, S. Brenner, C. S. Verma, F. J. Ghadessy, B. Venkatesh, D. P. Lane, The p53–Mdm2 interaction and the E3 ligase activity of Mdm2/Mdm4 are conserved from lampreys to humans. *Genes Dev.* **30**, 281–292 (2016).
- P. Dolezelova, K. Cetkowska, K. H. Vousden, S. Uldrijan, Mutational analysis of Mdm2 C-terminal tail suggests an evolutionarily conserved role of its length in Mdm2 activity toward p53 and indicates structural differences between Mdm2 homodimers and Mdm2/MdmX heterodimers. *Cell Cycle* **11**, 953–962 (2012).
- J. Gu, H. Kawai, L. Nie, H. Kitao, D. Wiederschain, A. G. Jochemsen, J. Parant, G. Lozano, Z.-M. Yuan, Mutual dependence of MDM2 and MDMX in their functional inactivation of p53. *J. Biol. Chem.* **277**, 19251–19254 (2002).
- D. Acosta-Alvarez, Y. Zhou, A. Blais, M. Tsikitis, N. H. Lents, C. Arias, C. J. Lennon, Y. Kluger, B. D. Dynlacht, XBP1 controls diverse cell type- and condition-specific transcriptional regulatory networks. *Mol. Cell* **27**, 53–66 (2007).
- G. Cretenet, M. Le Clech, F. Gachon, Circadian clock-coordinated 12 Hr period rhythmic activation of the IRE1α pathway controls lipid metabolism in mouse liver. *Cell Metab.* **11**, 47–57 (2010).
- Y. He, S. Sun, H. Sha, Z. Liu, L. Yang, Z. Xue, H. Chen, L. Qi, Emerging roles for XBP1, a sUPER transcription factor. *Gene Expr.* **15**, 13–25 (2010).
- N. N. Iwakoshi, A.-H. Lee, P. Vallabhajosyula, K. L. Otipoby, K. Rajewsky, L. H. Glimcher, Plasma cell differentiation and the unfolded protein response intersect at the transcription factor XBP-1. *Nat. Immunol.* **4**, 321–329 (2003).

35. A. Nekrutenko, J. He, Functionality of unspliced *XBP1* is required to explain evolution of overlapping reading frames. *Trends Genet.* **22**, 645–648 (2006).
36. D. Martin, Y. Li, J. Yang, G. Wang, A. Margariti, Z. Jiang, H. Yu, A. Zampetaki, Y. Hu, Q. Xu, L. Zeng, Unspliced X-box-binding protein 1 (*XBP1*) protects endothelial cells from oxidative stress through interaction with histone deacetylase 3. *J. Biol. Chem.* **289**, 30625–30634 (2014).
37. Y. Zhao, X. Li, M.-Y. Cai, K. Ma, J. Yang, J. Zhou, W. Fu, F.-Z. Wei, L. Wang, D. Xie, W.-G. Zhu, *XBP-1*u suppresses autophagy by promoting the degradation of FoxO1 in cancer cells. *Cell Res.* **23**, 491–507 (2013).
38. S. L. Harris, A. J. Levine, The p53 pathway: positive and negative feedback loops. *Oncogene* **24**, 2899–2908 (2005).
39. R. Montes de Oca Luna, D. S. Wagner, G. Lozano, Rescue of early embryonic lethality in *mdm2*-deficient mice by deletion of *p53*. *Nature* **378**, 203–206 (1995).
40. P. H. Kussie, S. Gorina, V. Marechal, B. Elenbaas, J. Moreau, A. J. Levine, N. P. Pavletich, Structure of the MDM2 oncoprotein bound to the p53 tumor suppressor transactivation domain. *Science* **274**, 948–953 (1996).
41. D.-H. Kwon, G. H. Eom, J. H. Ko, S. Shin, H. Joung, N. Choe, Y. S. Nam, H.-K. Min, T. Kook, S. Yoon, W. Kang, Y. S. Kim, H. S. Kim, H. Choi, J.-T. Koh, N. Kim, Y. Ahn, H.-J. Cho, I.-K. Lee, D. H. Park, K. Suk, S. B. Seo, E. R. Wissing, S. M. Mendrysa, K.-I. Nam, H. Kook, MDM2 E3 ligase-mediated ubiquitination and degradation of HDAC1 in vascular calcification. *Nat. Commun.* **7**, 10492 (2016).
42. H. Yoshida, M. Oku, M. Suzuki, K. Mori, pXBP1(U) encoded in *XBP1* pre-mRNA negatively regulates unfolded protein response activator pXBP1(S) in mammalian ER stress response. *J. Cell Biol.* **172**, 565–575 (2006).
43. H. Xu, Z. Zhang, M. Li, R. Zhang, MDM2 promotes proteasomal degradation of p21<sup>Waf1</sup> via a conformation change. *J. Biol. Chem.* **285**, 18407–18414 (2010).
44. A. N. Shajahan, R. B. Riggins, R. Clarke, The role of X-box binding protein-1 in tumorigenicity. *Drug News Perspect.* **22**, 241–246 (2009).
45. P. Hainaut, K. G. Wiman, 30 years and a long way into p53 research. *Lancet Oncol.* **10**, 913–919 (2009).
46. V. Kasim, S. Wu, K. Taira, M. Miyagishi, Determination of the role of DDX3 a factor involved in mammalian RNAi pathway using an shRNA-expression library. *PLOS ONE* **8**, e59445 (2013).
47. S. Wu, V. Kasim, M. R. Kano, S. Tanaka, S. Ohba, Y. Miura, K. Miyata, X. Liu, A. Matsushashi, U.-i. Chung, L. Yang, K. Kataoka, N. Nishiyama, M. Miyagishi, Transcription factor YY1 contributes to tumor growth by stabilizing hypoxia factor HIF-1 $\alpha$  in a p53-independent manner. *Cancer Res.* **73**, 1787–1799 (2013).
48. T. A. Kunkel, Rapid and efficient site-specific mutagenesis without phenotypic selection. *Proc. Natl. Acad. Sci. U.S.A.* **82**, 488–492 (1985).
49. N. Okamoto, M. Yasukawa, C. Nguyen, V. Kasim, Y. Maida, R. Possemato, T. Shibata, K. L. Ligon, K. Fukami, W. C. Hahn, K. Masutomi, Maintenance of tumor initiating cells of defined genetic composition by nucleostemin. *Proc. Natl. Acad. Sci. U.S.A.* **108**, 20388–20393 (2011).

**Acknowledgments:** We thank B. Vogelstein (Johns Hopkins University School of Medicine) for providing HCT116<sup>WT</sup> and HCT116<sup>p53null</sup> cell lines. **Funding:** This work was supported by grants from the National Natural Science Foundation of China (31301119 and 81372202), the Natural Science Foundation of Chongqing (cstc2014jcyjA10058), the Fundamental Research Funds for the Central Universities (106112016CDJZR235516), the Graduate Scientific Research and Innovation Foundation of Chongqing (CYB17039), the National Institute of Advanced Industrial Science and Technology (AAZ30368), and the New Energy and Industrial Technology Development Organization (P00013). **Author contributions:** V.K. and S.W. conceived the project, designed the experiments, analyzed and interpreted the experimental results, and wrote the manuscript. M.M. designed the shRNA target sequences, constructed the shRNA expression vector library, supervised the library screening, and analyzed the data. C.H. performed most of the experiments and analyzed the experimental data. H.J. carried out Western blotting and qPCR analysis. S.M. performed library screening. H.Z. collected human clinical samples. Y.X. and X.Y. carried out part of the animal and clinical sample experiments. **Competing interests:** The authors declare that they have no competing interests. **Data and materials availability:** All data needed to evaluate the conclusions in the paper are present in the paper and/or the Supplementary Materials. Additional data related to this paper may be requested from the authors.

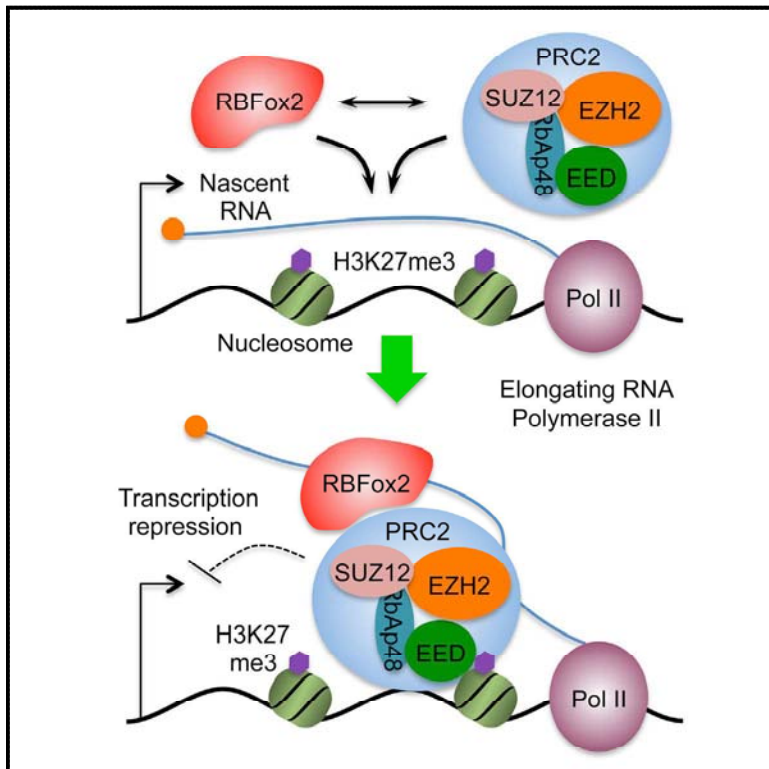
Submitted 10 May 2017  
Accepted 13 September 2017  
Published 18 October 2017  
10.1126/sciadv.1701383

**Citation:** C. Huang, S. Wu, H. Ji, X. Yan, Y. Xie, S. Murai, H. Zhao, M. Miyagishi, V. Kasim, Identification of *XBP1-u* as a novel regulator of the MDM2/p53 axis using an shRNA library. *Sci. Adv.* **3**, e1701383 (2017).

# Molecular Cell

## RBFOX2 Binds Nascent RNA to Globally Regulate Polycomb Complex 2 Targeting in Mammalian Genomes

### Graphical Abstract



### Authors

Chaoliang Wei, Rui Xiao, Liang Chen, ..., Hairi Li, Liling Tang, Xiang-Dong Fu

### Correspondence

xdfu@ucsd.edu

### In Brief

PRC2 is known to interact with RNA, but it has been unclear whether this process requires additional regulators. Wei et al. report that the RNA binding protein RBFOX2 is a global regulator of PRC2 recruitment to active genes, particularly those with bivalent histone modifications, to mediate dynamic transcriptional control.

### Highlights

- RBFOX2 has a direct role in transcriptional control besides splicing regulation
- Nascent RNAs are required for RBFOX2 interaction with chromatin
- RBFOX2 directly interacts with PRC2 to mediate PRC2 targeting genome-wide
- Gene-body-associated nascent RNA serves as feedback sensor for transcription output

### Accession Numbers

GSE57926



Wei et al., 2016, *Molecular Cell* 62, 875–889  
 June 16, 2016 © 2016 Elsevier Inc.  
<http://dx.doi.org/10.1016/j.molcel.2016.04.013>

CellPress



# RBFox2 Binds Nascent RNA to Globally Regulate Polycomb Complex 2 Targeting in Mammalian Genomes

Chaoliang Wei,<sup>1,4</sup> Rui Xiao,<sup>1,4</sup> Liang Chen,<sup>1,4</sup> Hanwei Cui,<sup>1,3,4</sup> Yu Zhou,<sup>1,4</sup> Yuanchao Xue,<sup>1</sup> Jing Hu,<sup>1</sup> Bing Zhou,<sup>1</sup> Taiki Tsutsui,<sup>1</sup> Jinsong Qiu,<sup>1</sup> Hairi Li,<sup>3</sup> Liling Tang,<sup>3</sup> and Xiang-Dong Fu<sup>1,2,\*</sup>

<sup>1</sup>Department of Cellular and Molecular Medicine

<sup>2</sup>Institute of Genomic Medicine

University of California, San Diego, La Jolla, CA 92093-0651, USA

<sup>3</sup>Key Laboratory of Biorheological Science and Technology, Ministry of Education, College of Bioengineering, Chongqing University, Chongqing 400044, China

<sup>4</sup>Co-first author

\*Correspondence: [xdfu@ucsd.edu](mailto:xdfu@ucsd.edu)

<http://dx.doi.org/10.1016/j.molcel.2016.04.013>

## SUMMARY

Increasing evidence suggests that diverse RNA binding proteins (RBPs) interact with regulatory RNAs to regulate transcription. RBFox2 is a well-characterized pre-mRNA splicing regulator, but we now encounter an unexpected paradigm where depletion of this RBP induces widespread increase in nascent RNA production in diverse cell types. Chromatin immunoprecipitation sequencing (ChIP-seq) reveals extensive interaction of RBFox2 with chromatin in a nascent RNA-dependent manner. Bayesian network analysis connects RBFox2 to Polycomb complex 2 (PRC2) and H3K27me3, and biochemical experiments demonstrate the ability of RBFox2 to directly interact with PRC2. Strikingly, RBFox2 inactivation eradicates PRC2 targeting on the majority of bivalent gene promoters and leads to transcriptional depression. Together, these findings uncover a mechanism underlying the enigmatic association of PRC2 with numerous active genes, highlight the importance of gene body sequences to gauge transcriptional output, and suggest nascent RNAs as critical signals for transcriptional feedback control to maintain homeostatic gene expression in mammalian genomes.

## INTRODUCTION

RNA binding proteins (RBPs) and ribonucleoprotein particles (RNPs) have been increasingly appreciated for their involvement in multiple layers of regulated gene expression beyond their traditional roles in RNA processing, which likely act in conjunction with diverse regulatory RNAs expressed in mammalian genomes (Fu, 2014; Rinn and Chang, 2012). For instance, the splicing commitment factor SRSF2 is now known to play a key role in facilitating RNA Polymerase II (Pol II) pause release from

gene promoters (Ji et al., 2013) and modulating transcriptional elongation in gene bodies (Lin et al., 2008). The small nuclear ribonucleoprotein particle U1 small nuclear RNP (snRNP), besides its role in 5' splice site definition, helps prevent cryptic transcriptional termination and premature polyadenylation (Kaida et al., 2010). The regulatory functions of RBPs via specific non-coding RNAs (ncRNAs) in transcriptional control are also exemplified by the interaction of FUS/TLS with a *cyclin D1* promoter-associated ncRNA to repress transcription in response to DNA damage (Wang et al., 2008) and by the ability of both hnRNP U and hnRNP K to bind the *Xist* ncRNA to mediate transcriptional repression (Chu et al., 2015). These findings mark an emerging trend for wide participation of RBPs in transcriptional control, likely via numerous ncRNAs expressed in mammalian genomes (ENCODE Project Consortium, 2012).

The mechanism underlying ncRNA-mediated epigenetic control of gene expression is perhaps best illustrated with Polycomb complex 2 (PRC2), which catalyzes H3K27 trimethylation on chromatin (Cao et al., 2002) and is critical for X-inactivation in the mouse (Lee and Bartolomei, 2013) and responsible for establishing bivalent promoters in different cell lineages (Voigt et al., 2013). Interestingly, at least two components of PRC2 (EZH2 and SUZ12) appear to have the capacity to directly bind RNA, but whether they bind with a degree of specificity has been a subject of debate (Davidovich et al., 2013; Kaneko et al., 2013; Kanhere et al., 2010; Zhao et al., 2010). A more recent biochemical comparison suggests that PRC2 does have a degree of preference for different RNAs despite its capacity to bind diverse RNAs with high affinity, suggesting that promiscuous and specific RNA-binding activities of PRC2 do not have to be mutually exclusive (Davidovich et al., 2015).

Genome-wide analysis of PRC2-RNA interactions reveals that RNAs from modestly expressed protein-coding genes constitute the vast majority of the PRC2 interactome (Kaneko et al., 2013; Zhao et al., 2010). Because PRC2 does not bind all RNAs, especially from highly expressed genes, this has been part of ongoing debate on direct or indirect mechanisms for PRC2 recruitment in mammalian genomes, leading to speculation for the involvement of certain RBPs as adaptors (Bonasio and Shiekhattar, 2014). The observation that bivalency is established

during the transition from naive to primed embryonic stem (ES) cells suggests that PRC2 targeting is a highly regulated process (Marks et al., 2012; Theunissen et al., 2014). Consistently, a recent study reveals a key role of the DNA/RBP ATRX in *Xist* loading/spreading on X chromosome and in facilitating PRC2 targeting to many other genomic loci (Sarma et al., 2014).

The RBFox family of RBPs has been characterized as splicing regulators (Kuroyanagi, 2009) by recognizing the evolutionarily conserved GCAUG motif (Jin et al., 2003; Zhang et al., 2008) to induce alternative splicing in a position-dependent manner (Jangi et al., 2014; Yeo et al., 2009). *RBFox1* (a.k.a. *A2BP1*) is expressed in muscles and brain; *RBFox2* (a.k.a. *RMB9* or *Fxh*) is more ubiquitously expressed with higher abundance in most cell types; and *RBFox3* (a.k.a. *NeuN*) is predominantly detected in mature neurons (Underwood et al., 2005). It is also important to bear in mind that RBFox1 was first discovered as a X chromosome dosage-compensation regulator in *C. elegans* (Hodgkin et al., 1994; Nicoll et al., 1997); RBFox2 was found earlier as a co-transcriptional repressor in nuclear-receptor-regulated gene expression (Norris et al., 2002); and RBFox3/NeuN was recently shown to modulate microRNA (miRNA) processing (Kim et al., 2014). This literature information suggests that RBFox proteins may regulate gene expression at different levels and via multiple mechanisms.

We recently dissected the RBFox2-regulated splicing program during pressure overloading-induced heart failure (Wei et al., 2015). However, many specific cardiac phenotypes caused by *RBFox2* ablation could not readily be attributed to altered splicing (unpublished data), suggesting the need to investigate the function of RBFox2 in regulated gene expression without being confined to the traditional framework. Here, we present evidence that RBFox2 broadly interacts with nascent RNA on chromatin to mediate transcriptional repression through its functional interplay with PRC2. Strikingly, *RBFox2* ablation causes genome-wide eradication of PRC2-chromatin interactions and dynamic H3K27me3 deposition on gene promoters in diverse cell types. This reveals RBFox2 as a global regulator of PRC2 targeting in mammalian genomes, which also supports the concept that nascent RNAs from both non-coding and protein-coding genes act as *cis*-acting signals for dynamic control of mammalian gene expression.

## RESULTS

### Widespread Transcriptional Induction in Response to *RBFox2* Knockout

As part of our ongoing efforts to understand severe cardiomyopathy triggered by *RBFox2* knockout in the mouse heart (Wei et al., 2015), we noted transcriptional induction of multiple mature miRNAs, which is coincident with the development of cardiac phenotype (Figure S1A). Unlike the reported role of RBFox3/NeuN in modulating post-transcriptional miRNA processing (Kim et al., 2014), however, we found miRNA induction at the pri-miRNA level without significant changes at the pre-miRNA level, which applies to all induced and at least a subset of repressed miRNAs we detected at mature miRNA levels (Figures S1A–S1C). This finding indicates a previously unrecognized function of RBFox2 in transcriptional control. Although we were able to link some induced miRNAs to a spe-

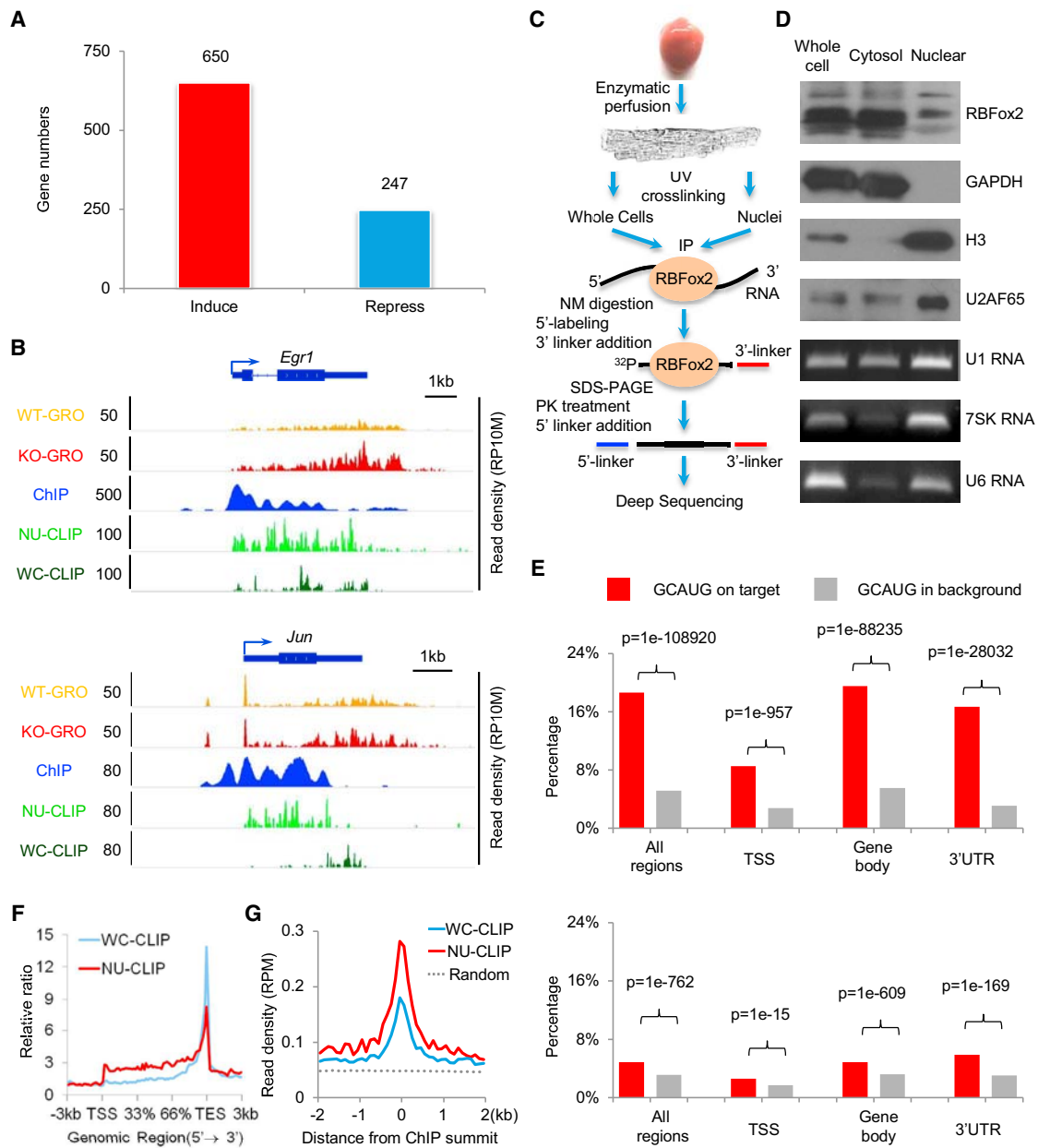
cific cardiac defect (unpublished data), we suspected an even greater altered transcription program that may underlie the overall disease phenotype in our animal model. We therefore decided to first pursue this intriguing and unexpected paradigm for RBFox2-regulated gene expression.

We isolated primary cardiomyocytes from WT and *RBFox2* knockout heart by enzymatic perfusion and performed global nuclear run-on coupled with deep sequencing (GRO-seq) to detect nascent RNA production (Table S1A). We found that *RBFox2* ablation caused a >1.5-fold change in nascent RNA production among 650 upregulated genes and 247 downregulated genes, indicating a dominant role (directly or indirectly at this point) of RBFox2 in transcriptional repression (Figure 1A). This includes a set of miRNAs we examined by real-time RT-PCR (Figure S1A), which corroborates with increased GRO-seq signals (Figure S1D), both at the primary miRNA level. Importantly, we also detected elevated transcription from a large number of protein-coding genes, as illustrated for *Egr1* and *Jun* (Figure 1B). These data provide initial evidence for a critical role of RBFox2 in transcriptional control, which we decided to rigorously pursue in both primary cardiomyocytes and more experimentally manipulable cellular models.

### RBFox2 Interaction with RNA and DNA

Because RBFox2 is an RBP that has been implicated in regulated RNA metabolism in both the nucleus and the cytoplasm, we hypothesized that RBFox2 might interact with RNA on chromatin during co-transcriptional pre-mRNA splicing to influence transcription. We therefore mapped its interaction with RNA by cross-linking immunoprecipitation followed by deep sequencing (CLIP-seq) on fractionated primary cardiomyocytes from WT mouse heart (Figure 1C). We optimized the cell fractionation protocol for cardiomyocytes, which involves a more elaborated procedure to disrupt multi-nuclei muscle cells (see [Experimental Procedures](#)), and showed the expected distribution of cytoplasmic and nuclear proteins (e.g., GAPDH and histone 3) and nuclear RNAs (e.g., 7SK and U6), despite a degree of leakage of nuclear components into the cytosolic fraction (i.e., U2AF65 and U1), which is common in preparing nuclear extracts even from cultured cells (Figure 1D). Such leakage would in fact enrich for RBFox2-RNA interactions on chromatin.

From 67 and 22 million initially mapped reads, we obtained 14.9 million whole-cell (WC) CLIP-seq reads and 3.2 million nuclear (NU) CLIP-seq reads that were uniquely mapped to the mouse genome after removing PCR duplicates (Table S1B). In line with the prediction by Ray et al. (2013), a large fraction of the WC RBFox2 CLIP-seq reads were mapped in 3' UTRs, which becomes further evident after size normalization (Figure S1E). The WC RBFox2 CLIP-seq reads are enriched with the expected GCAUG motif (Figures 1E and S1F), similar to our early report on ES cells (Yeo et al., 2009). Interestingly, RBFox2 appears to interact with RNA near gene promoters (from the transcription start site [TSS] to +/-1 kb downstream sequences) with much reduced specificity, as indicated by less frequent association of the consensus motif with its binding events near the TSS relative to gene body or 3' UTR (Figure 1E, top). In contrast, the NU RBFox2 CLIP-seq signals showed a general underrepresentation of the GCAUG motif underlying RBFox2 binding events (Figure 1E, bottom), which also exhibited a 5' shift toward promoter



**Figure 1. RBFox2 Knockout-Induced Transcription in Primary Cardiomyocytes**

(A) Significantly induced and repressed genes in *RBFox2* knockout cardiomyocytes. The data are based on a >1.5-fold change and p value < 0.1 from GRO-seq analysis. See also Figures S1A–S1C.

(B) *RBFox2* knockout-induced gene expression detected by GRO-seq in comparison with *RBFox2*-RNA interactions detected by CLIP-seq and *RBFox2*-DNA interactions detected by ChIP-seq on two representative protein-coding genes, *Egr1* and *Jun*. All experiments were on isolated cardiomyocytes from 9-week-old mice. The scale on the y axis indicates the read density per 10 million of total normalized reads (RP10M). See also Figure S1D and Table S1.

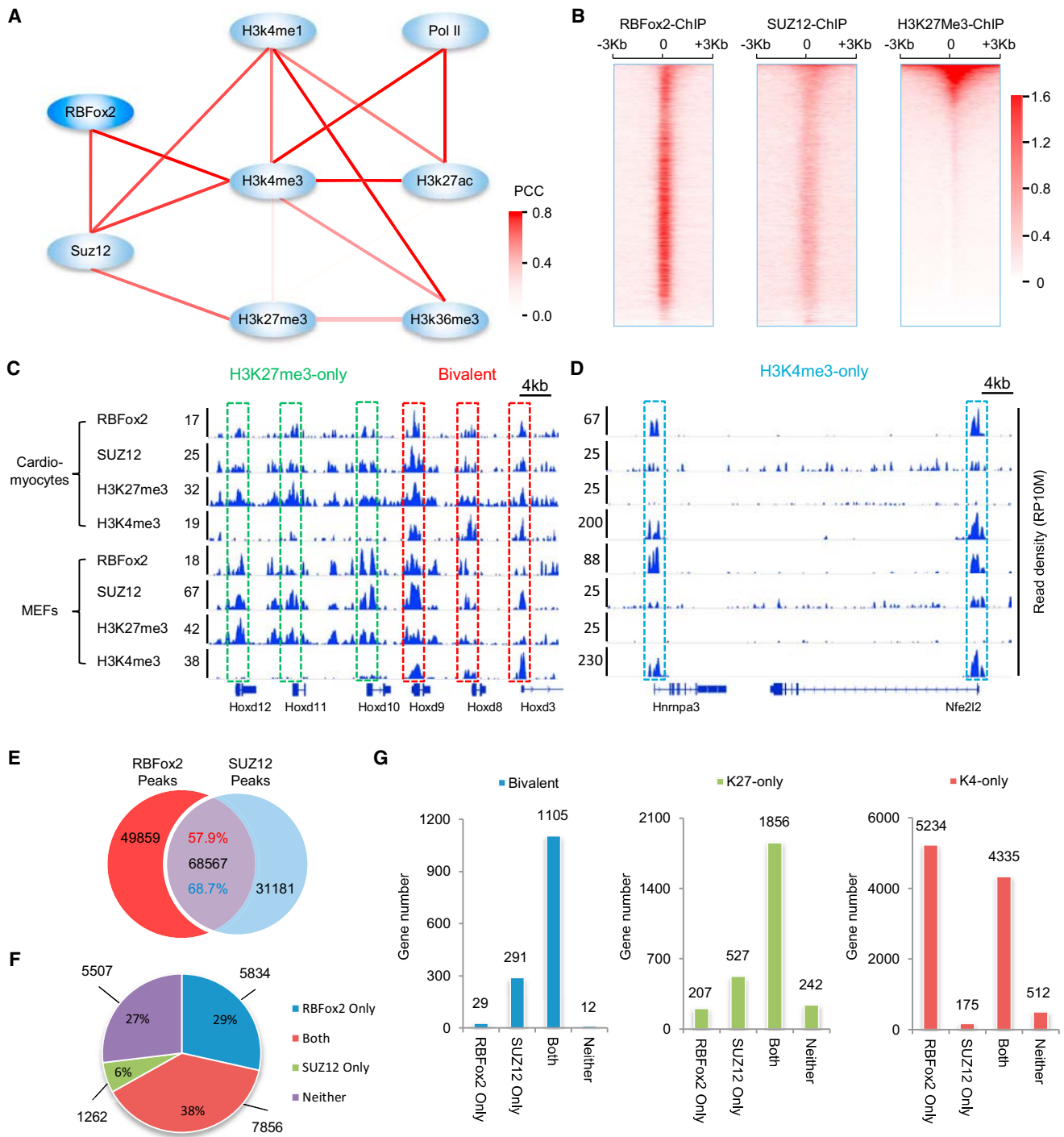
(C) Diagram showing key steps in CLIP-seq analysis on whole-cell or nuclear-enriched cardiomyocytes.

(D) Characterization of fractionated cardiomyocytes by western blotting using both cytoplasmic (GAPDH) and nuclear proteins (histone H3 and U2AF65) and RNAs (U1, 7SK, and U6) as markers.

(E) Distribution of the GCAUG motif in *RBFox2* WC CLIP-seq reads (top) or NU CLIP-seq reads (bottom) in different regions of RefSeq coding genes (red bars) relative to background (gray bars). TSS, transcription start site to  $\pm 1$  kb downstream regions; gene body, regions in RefSeq coding genes without a TSS and 3' UTR. See also Figures S1E and S1F.

(F) Meta-gene analysis of whole-cell (WC; blue) and nuclear (NU; red) *RBFox2* CLIP-seq signals on all RefSeq protein-coding genes by the ngsplot program.

(G) Alignment of the WC (blue) and NU (red) *RBFox2* CLIP-seq signals on the center of *RBFox2* ChIP-seq signals. Randomized signals (dashed line) served as control.



**Figure 2. Connecting RBFox2-DNA Interactions to PRC2**

(A) Bayesian network analysis of the interactions in gene promoter regions (TSS  $\pm$  1 kb) among RBFox2, SUZ12, Pol II and key histone modifications by SeqSpider program. The color intensity of an edge indicates the Pearson correlation coefficient (PCC) between paired nodes based on the total reads counts in their promoter regions.

(B) Heatmaps of RBFox2 ChIP-seq signals in comparison with SUZ12 and H3K27me3 ChIP-seq signals  $\pm$ 3 kb from the TSS. The RBFox2 and SUZ12 ChIP-seq data were generated on isolated cardiomyocytes from 9-week-old wild-type (WT) mice. The H3K27me3 ChIP-seq dataset was extracted from the GEO database (GEO: GSM1000131). All heatmaps were normalized by total reads, input signals subtracted, and sorted by mean H3K27me3 density. The numbers beside the color bar indicate the read density per 10 million total reads.

(legend continued on next page)

and gene body from 3' UTR (Figure 1F). These observations hint on a more relaxed binding mode for RBFox2 to interact with chromatin-associated RNA.

We next hypothesized that chromatin-associated RNA might mediate RBFox2 association with chromatin and thus performed RBFox2 chromatin immunoprecipitation sequencing (ChIP-seq) on isolated cardiomyocytes, obtaining 26 million uniquely mapped reads (Table S2). As anticipated, we detected extensive RBFox2 interaction with genomic DNA near the TSS as well as within the gene body, which was correlated with induced nascent RNA production, as illustrated on representative *Egr1* and *Jun* genes (Figure 1B). By relating RBFox2 CLIP-seq peaks to its ChIP-seq signals, we observed that RBFox2-DNA interactions were more related to its RNA binding activities enriched in the nucleus (Figure 1G). This suggests that RBFox2 may become associated with chromatin via nascent RNA, which we later demonstrate to be the case both on representative genes and at a global level (see below).

### RBFox2 Binding in Relationship with Key Chromatin Features

To uncover potential mechanism(s) underlying RBFox2-mediated transcriptional repression, we performed Bayesian network analysis, a bioinformatics approach for inferring global relationships among detected binding events (Liu et al., 2013), by relating RBFox2 ChIP-seq signals to public ChIP-seq data from mouse heart near the TSS region (see [Experimental Procedures](#)). The resulting network suggests a connection of RBFox2 to SUZ12, which is linked to the repressive H3K27me3 mark on chromatin (Figure 2A). This was further confirmed by meta-gene analysis near the TSS with RBFox2 and SUZ12 ChIP-seq signals generated on the same cardiomyocytes (Table S2; Figure 2B). These relationships therefore predicted a functional interplay between RBFox2 binding and PRC2 targeting, raising an intriguing possibility that RBFox2 might mediate transcription repression via PRC2. We seized this opportunity to understand the enigmatic association with PRC2 with numerous active genes in mammalian genomes.

Because PRC2-regulated gene expression applies to all cell types in mammals (Davidovich et al., 2013), we next extended the analysis to mouse embryonic fibroblasts (MEFs), which would minimize potential compound effects in knockout animals and allow efficient experimental manipulations. As on cardiomyocytes, we fractionated MEFs to obtain nuclear enriched RBFox2, noting that RBFox2 appears to be predominantly associated with the nuclear fraction in MEFs (Figure S2A). To begin to investigate the potential contribution of nascent RNA to RBFox2's association with chromatin, we briefly treated MEFs for 3 hr with the transcription inhibitor 5,6-dichloro-1- $\beta$ -D-ribofuranosylbenzimidazole (DRB),

which targets the active site in the kinase p-TEFb required for Pol II pause release (Adelman and Lis, 2012). While the treatment did not affect RBFox2 at the protein level (Figure S2B, bottom), we noted that RBFox2 immunofluorescence signals became greatly dispersed (Figure S2B, top). Furthermore, RNase A and DNase I treatment on Triton X-100-permeabilized MEFs essentially eliminated RBFox2 staining signals (Figure S2B, top). These data indicate the requirement of RNA for RBFox2 to interact with DNA in the nucleus.

We next performed both WC and NU CLIP-seq for RBFox2 in MEFs (Table S3A). Duplicated experiments based on 2 to 3 million uniquely mapped reads in the mouse genome demonstrated the reproducibility of RBFox2 WC and NU CLIP-seq analyses (Figures S2C and S2D). As indicated by biochemical fractionation, RBFox2 appears to be tightly retained in the nucleus of MEFs (Figure S2A), and consequently, both datasets showed the enriched GCAUG motif, but with much reduced representation underlying RBFox2 binding events across all genic regions (Figures S2E and S2F), which is similar to the trend observed with RBFox2 NU CLIP-seq on primary cardiomyocytes (see Figure 1E, bottom).

In mammalian genomes, H3K4me3 and H3K27me3 generally mark active and repressed genes, respectively (Rivera and Ren, 2013). However, many are associated with both chromatin marks, known as bivalent genes, and such bivalent genes are thought to be particularly sensitive to regulatory signals during development (Bernstein et al., 2006; Mikkelsen et al., 2007). To link RBFox2 and SUZ12 binding to specific histone modification events under uniform conditions, we generated an elaborated set of ChIP-seq data with 10 to 25 million uniquely mapped reads in each (Table S3B). In both cardiomyocytes and MEFs, we noted concordant ChIP-seq signals for RBFox2, SUZ12, and H3K27me3 on both repressed (marked exclusively with H3K27me3) and bivalent genes (Figure 2C), while RBFox2 ChIP-seq signals were also prevalent on active genes marked exclusively with H3K4me3 (Figure 2D). These reflect a global trend: RBFox2 and SUZ12 ChIP-seq signals overlap on more than half of their peaks (Figure 2E), which is particularly significant (38%) on protein-coding genes (Figure 2F). RBFox2 and SUZ12 ChIP-seq peaks are largely co-incident on both bivalent (both H3K4me3 and H3K27me3) and largely repressed genes (H3K27me3-only), as well as on approximately half of active genes (H3K4me3-only) (Figure 2G). These observations indicate extensive functional interplay between RBFox2 and PRC2 in the mouse genome.

### RBFox2 Mediates Global PRC2 Targeting Near Gene Promoters via Nascent RNA

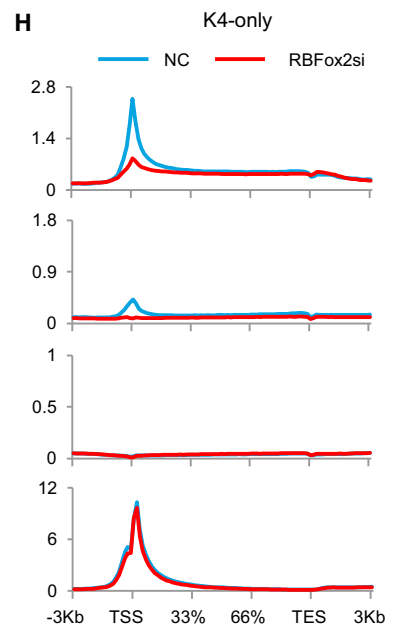
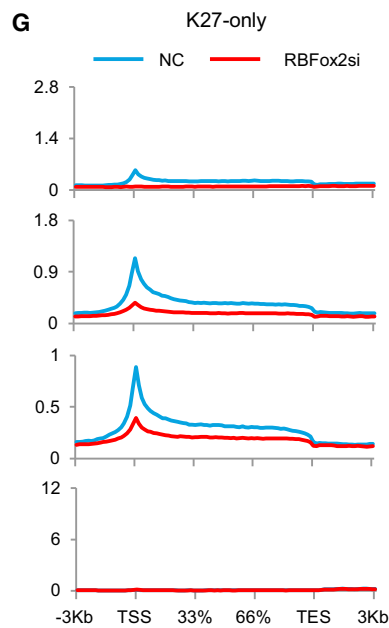
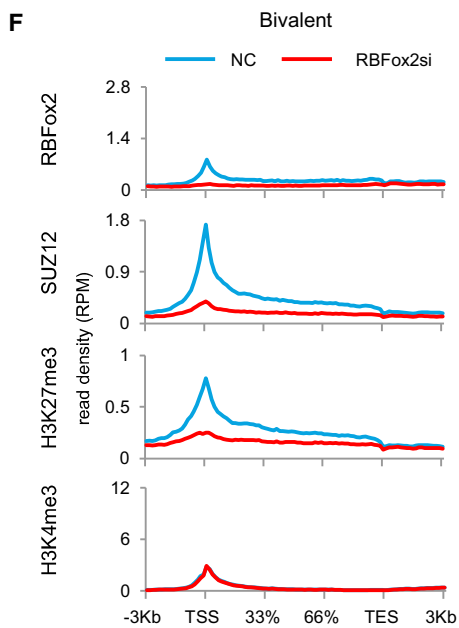
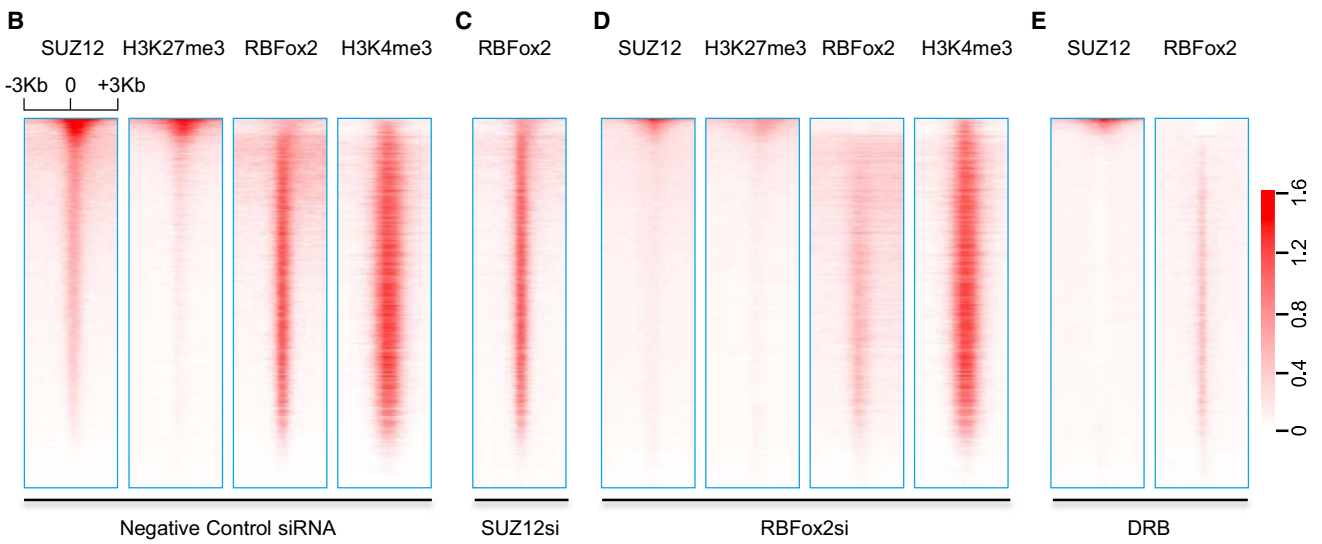
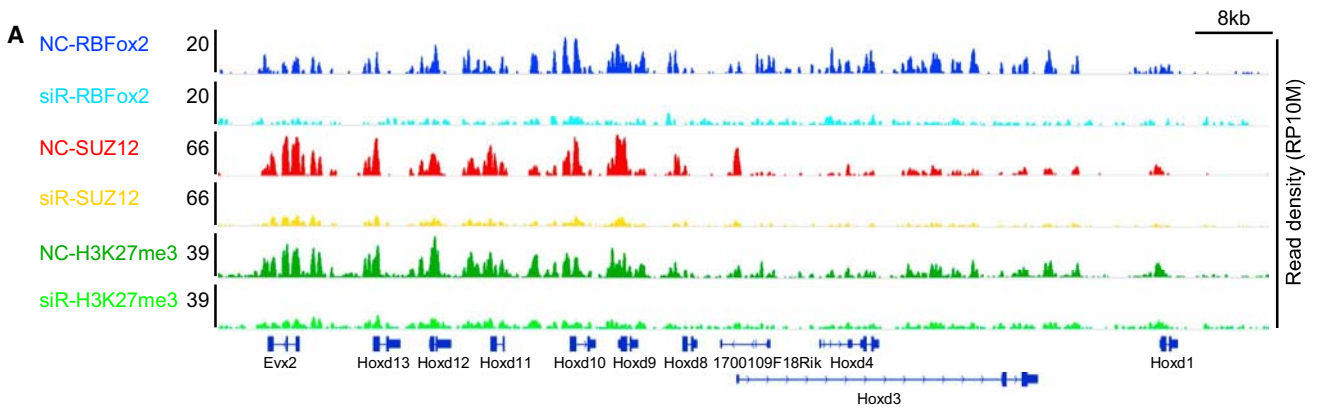
To determine potential function of RBFox2 in PRC2 targeting, we performed functional perturbation in response to small interfering RNA (siRNA)-mediated knockdown of *RBFox2* and *SUZ12*

(C and D) RBFox2, SUZ12, H3K27me3 and H3K4me3 ChIP-seq signals on representative genes. Bivalent genes (red in C) are highlighted in comparison with genes exclusively marked by H3K27me3 (green in C) and with genes exclusively marked with H3K4me3 (blue in D).

(E) Overlap between RBFox2 and SUZ12 ChIP-seq peaks. Shown are both the number and the relative percentage of overlapped peaks on each class of genes. Hypergeometric test shows the overlapping is extremely significant ( $p < 1e-10$ ).

(F) Distribution of protein-coding genes with or without RBFox2 or/and SUZ12 binding at TSS regions. Hypergeometric test shows the overlapping is extremely significant ( $p < 1e-10$ ).

(G) RBFox2 and/or SUZ12 ChIP binding genes on different groups of genes classified by the presence of H3K4me3, H3K27me3, or both (bivalent) on their promoter regions. See also Figure S2 and Table S2.



(legend on next page)

in MEFs. In comparison with MEFs treated with nonspecific control siRNA (NC), two independent *siRBFox2* reduced RBFox2 protein, and two independent *siSUZ12* reduced not only SUZ12 but also EZH2 (likely due to destabilized PRC2 in the cell) (Figure S3A). Interestingly, in comparison with significant reduction of H3K27me3 levels in *siSUZ12*-treated MEFs, we detected little effect on this histone modification at the global level in *siRBFox2*-treated MEFs (Figure S3A), which is consistent with unaltered expression of all key PRC2 components at both the mRNA and protein levels (data not shown).

We next performed ChIP-seq on SUZ12, H3K27me3, and H3K4me3 in response to *siRBFox2* in MEFs (Figure S3B; Table S3B). Strikingly, in comparison with control siRNA-treated MEFs, *siRBFox2* not only abolished RBFox2 ChIP-seq signals, as expected (this also helps validate the specificity of anti-RBFox2 antibody in ChIP-seq analysis), but also significantly reduced ChIP-seq signals for both SUZ12 and H3K27me3, as shown on a representative genomic segment in the *HoxD* locus (Figure 3A). Focusing on TSS-associated ChIP-seq signals, we found that RBFox2 ChIP signals were unaffected by *siSUZ12*, indicating that PRC2 is not required for RBFox2 to interact with chromatin (Figures 3B and 3C). By contrast, *siRBFox2* not only diminished global RBFox2 binding but also abolished SUZ12 and H3K27me3 ChIP-seq signals around the TSS, without measurable impact on H3K4me3 ChIP-seq signals (Figure 3D).

Because *siRBFox2* had little effect on the global level of H3K27me3 (Figure S3A), we determined whether *siRBFox2* caused redistribution of PRC2 in the mouse genome, as reported in comparing between mouse naive and primed ES cells (Marks et al., 2012). We computed the genomic distribution of H3K27me3 peaks by binning H3K27me3-enriched regions to tag density per peak (based on normalization of total tags to 10 million), as described earlier (Marks et al., 2012), and found that, in control siRNA-treated MEFs (Figure S3C, left), more than half of H3K27me3 peaks with high tag density were associated with gene promoters (blue), but in response to *RBFox2* knockdown (Figure S3C, right), those peaks were significantly reduced near the TSS with accompanying increases in intergenic regions (green). Together, these data suggest that RBFox2 may not be essential for general PRC2 activities but are critical for PRC2 targeting to dynamically regulated gene promoters.

Given RBFox2 is a well-established RBP, we next asked whether the coordinated events for factor binding and histone modification were RNA dependent. By treating MEFs with the transcription inhibitor DRB for 2 hr to block nascent RNA production in the gene body, we observed a major reduction of both RBFox2 and SUZ12 ChIP-seq signals (Figure 3E), which we further validated on specific genes by ChIP-qPCR (Figure S3D).

While we cannot rule out other potential indirect effects of DRB, the data strongly suggest the requirement for nascent RNAs to mediate the association of RBFox2 with active genes, which in turn recruits PRC2.

Because RBFox2 frequently interacts with PRC2 on bivalent genes, we separately analyzed the functional impact of *siRBFox2* on different gene classes. We found that *RBFox2* knockdown in MEFs greatly reduced SUZ12 and H3K27me3 ChIP-seq signals on bivalent genes as well as on largely repressed genes that were exclusively marked by H3K27me3 (Figures 3F and 3G), but without detectable effect on H3K4me3 signals on most active genes that are exclusively decorated with this chromatin mark (Figure 3H).

To generalize the function of RBFox2 in global PRC2 targeting to gene promoters, we extended the analysis to C2C12 cells (Table S4). RBFox2 mainly bound bivalent and active genes in C2C12 cells (Figure S4A), and in response to *siRBFox2*, global H3K27me3 (Figure S4B), but not H3K4me3 (Figure S4C), went down. Interestingly, the Pol II ChIP-seq signals were also modestly increased, consistent with a role of RBFox2 in global transcriptional repression in C2C12 cells (Figure S4D). These data suggest a general requirement for RBFox2 to mediate global PRC2 targeting in diverse cell types.

### Functional Consequence of RBFox2-Regulated PRC2 Targeting

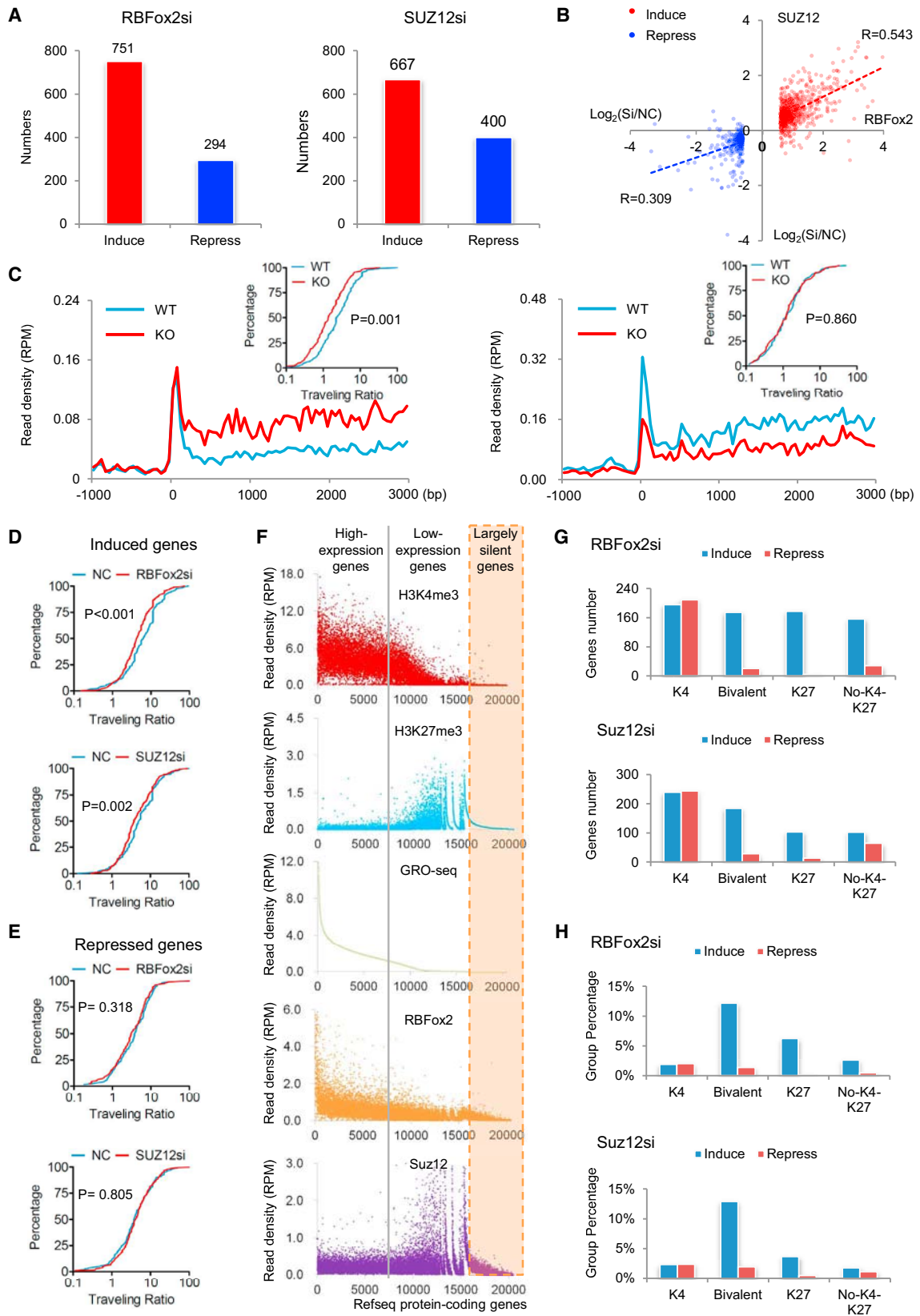
A previous study recorded little functional consequence in response to PRC2 knockdown based on analysis of steady-state mRNA by RNA-sequencing, which led to a “junk mail” model for PRC2 targeting, emphasizing additional requirements in conjunction with PRC2 to have measurable functional consequences on a rather restricted subset of PRC2-targeted genes (Davidovich et al., 2013). We revisited this critical issue by using more sensitive GRO-seq to measure transcriptional response at the levels of nascent RNA production, as we could clearly detect transcriptional response in *RBFox2* knockout cardiomyocytes (see Figures 1A and 1B), and more importantly, we wished to relate RBFox2-mediated PRC2 targeting to the functional impact on gene expression, at least on a subset of PRC2-targeted genes. In MEFs with 6–7 million unique GRO-seq reads under individual conditions (Table S5), we detected both up- and down-regulated nascent RNA production in response to *siRBFox2* and *siSUZ12* treatment, and as observed on cardiomyocytes, de-repressed genes outnumbered repressed genes in both cases (Figure 4A). By comparing the responsive genes with DNA binding evidence for both RBFox2 and SUZ12, we found that *siRBFox2* and *siSUZ12* had similar effects on induced genes ( $R = 0.543$ ), but much less so on repressed genes ( $R = 0.309$ ).

### Figure 3. Functional Requirement for RBFox2 to Mediate Global PRC2 Targeting

(A) ChIP-seq signals on a representative chromosomal segment for RBFox2, SUZ12, and H3K27me3 before and after siRNA-mediated *RBFox2* knockdown (*siR*) in MEFs. The y axis indicates the read density per 10 million total reads (RP10M).

(B–E) Sorted ChIP-seq signals for SUZ12, H3K27me3, RBFox2, and H3K4me3 at TSS regions in control siRNA-treated (B), *SUZ12* siRNA-treated (C), *RBFox2* siRNA-treated (D), and DRB-treated (E) MEFs. The data were sorted according to mean SUZ12 ChIP-seq signals in control siRNA-treated MEFs. All ChIP-seq data were normalized by total reads after subtracting input signals. The numbers beside the color bar indicate the read density per million. See also Figure S3 and Table S3.

(F–H) Responses of the indicated ChIP-seq signals to *RBFox2* knockdown on different gene classes (bivalent, H3K27me3 only, or H3K4me3 only) in MEFs. See also Figure S4 and Table S4 on related functional data from C2C12 cells.



(legend on next page)



(Figure 4B). These results support a more related function of RBFox2 and SUZ12 in transcriptional repression than activation, the latter of which likely results from various indirect effects.

Based on the GRO-seq signals from both cardiomyocytes (Table S1A) and MEFs (Table S5), which reflect transcriptionally engaged Pol II (Ji et al., 2013), we calculated the Pol II traveling ratio [TR, defined by the read density at the TSS divided by the read density in the gene body, see (Rahl et al., 2010)] for both induced and repressed genes and plotted the data in the accumulative fashion (inserts in Figure 4C). In *RBFox2* knockout cardiomyocytes, we linked decreased TR to induced gene expression (Figure 4C, left) but detected little difference with repressed genes (Figure 4C, right). We made similar observations with MEFs treated with *siRBFox2* or *siSUZ12* (Figures 4D and 4E). Note that the differences are not as striking as on cardiomyocytes, but still statistically significant, which was likely due to incomplete knockdown versus knockout in combination with ~5-fold fewer GRO-seq reads from MEFs (Table S5) relative to cardiomyocytes (Table S1A). Nonetheless, these findings are consistent with one another, together suggesting that RBFox2 and PRC2 may act in a coordinated fashion to induce Pol II pausing near the promoters of a set of responsive genes.

Sorting the GRO-seq signals in MEFs further revealed a positive correlation of gene expression with H3K4me3 and a negative correlation with H3K27me3 and SUZ12 binding, and largely silent genes (orange-shaded) typically lacked either mark (Figure 4F). While higher on highly expressed genes, the RBFox2 ChIP-seq signals were also associated with bivalent genes, but much less or none on largely silent genes (Figure 4F). We further observed that, while *siRBFox2* and *siSUZ12* caused induction and repression of approximately equal numbers of genes among those exclusively marked with H3K4me3, perhaps indicative of both direct and indirect effects, both treatments preferentially de-repressed bivalent genes as well as a significant number of largely repressed genes exclusively marked by H3K27me3 and genes that lacked detectable H3K4me3 and H3K27me3 (Figure 4G). The preferential impact on bivalent genes became more evident when comparing the relative percentages of induced versus repressed genes in different gene classes (Figure 4H). Together, these results strongly suggest that RBFox2 is directly involved in the dynamic regulation of transcriptional repression via PRC2.

### Interactions between RBFox2 and PRC2 In Vivo and In Vitro

Finally, to understand the molecular basis for RBFox2-dependent recruitment of PRC2, we performed co-immunoprecipitation (co-IP) on MEFs. We detected the association of RBFox2 with multiple components of PRC2 as well as several key components of PRC1 we examined (Figure 5A). To determine whether RNA is required to mediate and/or stabilize the interaction, we treated the cell lysate with RNase A (R) or Benzonase (B, which degrades both DNA and RNA) and found that neither treatment affected reciprocal immunoprecipitation between SUZ12 and RBFox2 (Figure 5B). In these immunoprecipitation experiments, GAPDH (Figures 5A and 5B) as well as abundant nuclear protein SRSF1 and histone H3 (data not shown) served as negative controls, suggesting that RBFox2 is part of larger Polycomb complexes in the cell.

Given efficient co-IP between RBFox2 and PRC2, we explored a possibility that RBFox2 might directly interact with PRC2. We expressed core PRC2 components individually as well as together to form the PRC2 complex in baculovirus-infected Sf9 cells, and purified these proteins to nearly homogeneity via the maltose-binding protein (MBP) tag (Figure S5A) according to the established conditions (Davidovich et al., 2013). We also prepared the PRC2 complex after removing the MBP tags from individual components. We then used these pure proteins for glutathione S-transferase (GST) pull-down assays with bacterially expressed GST-RBFox2, finding that GST-RBFox2, but not GST alone, efficiently pulled down the PRC2 complex with or without the MBP tag (Figure S5B). Interestingly, under the same conditions, we detected little binding with individual PRC2 components (data not shown), which might be due to induced conformation in both EZH2 and SUZ12 that only occurs within the fully assembled PRC2 complex (Jiao and Liu, 2015). Given their direct interaction, we performed sequential ChIP on two SUZ12-positive loci (*Egr2* and *Arx4*) and one negative locus (*Slc6a12*), finding the ability of RBFox2 and SUZ12 to simultaneously interact with both positive loci (Figure 5C).

We further mapped the domain in RBFox2 responsible for PRC2 binding and found that its RNA binding domain, which is conserved among all RBFox family members, is not required, and the C-terminal domain (CTD), which is unique in RBFox2, is sufficient to pull down PRC2 (Figure 5D). Interestingly, we

### Figure 4. Transcription Repression Coordinately Regulated by RBFox2 and PRC2

(A) Induced and repressed genes according to a >1.5-fold change and p value < 0.1 in GRO-seq in response to knockdown of *RBFox2* (left) or *SUZ12* (right) relative to control siRNA-treated MEFs. See also Table S5.

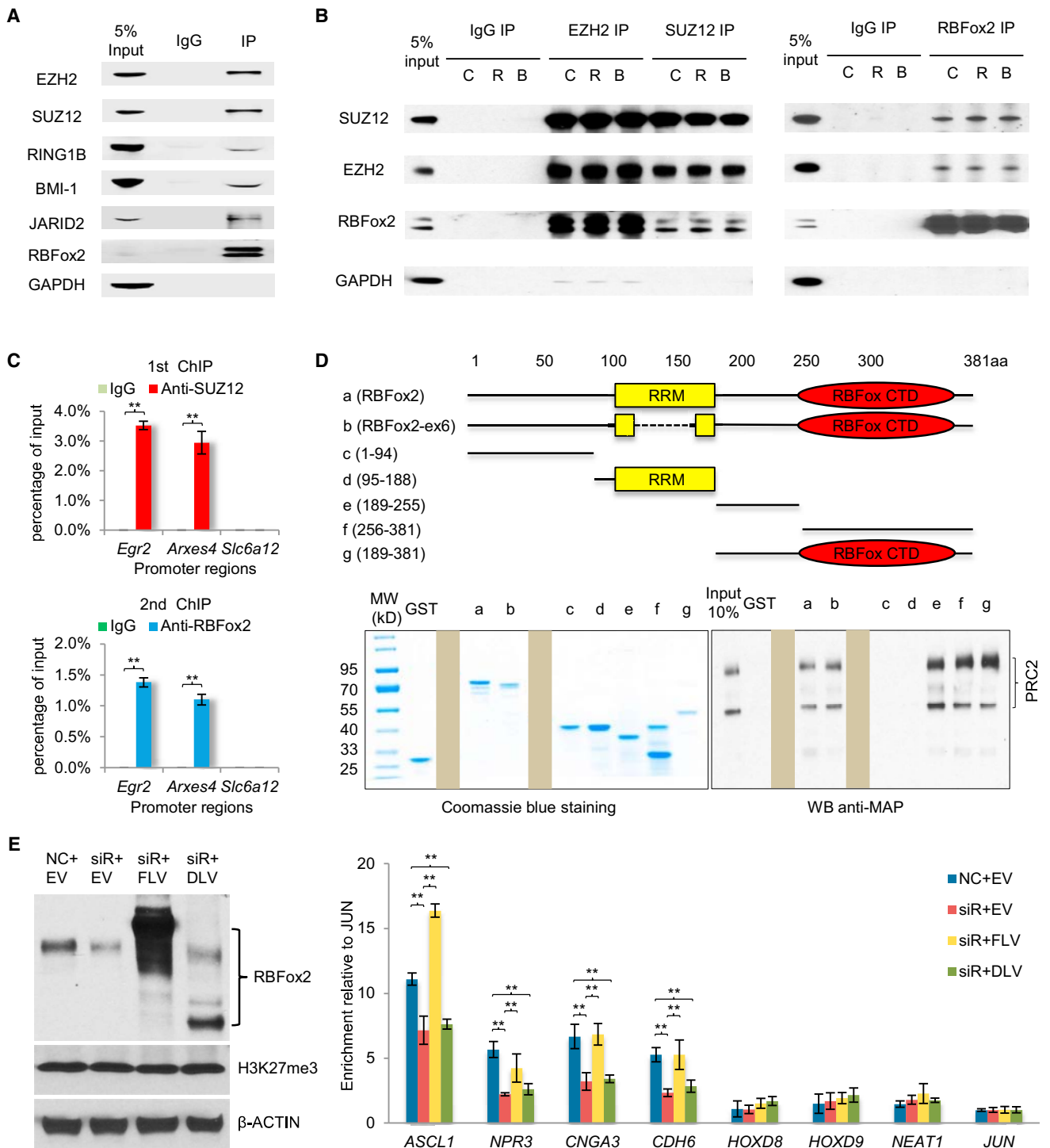
(B) Comparison between induced and repressed transcription (in log<sub>2</sub>) in response to knockdown of *RBFox2* and *SUZ12*, showing a significant concordance between *RBFox2* and *SUZ12* siRNA treatments among induced, but not repressed, genes.

(C) Meta-gene analysis of GRO-seq signals and the distribution of the traveling ratio (TR) of induced (left) or repressed genes (right) in *RBFox2* knockout cardiomyocytes. A total of 209 and 138 significantly induced and repressed genes were selected for the analysis. The x axis indicates the distance from the TSS and the y axis shows the read density per million (RPM). The inserts show changes in TRs plotted in the accumulative fashion. Statistical significance was determined using the Kolmogorov-Smirnov test.

(D and E) Calculated TR changes in response to knockdown of *RBFox2* and *SUZ12* in MEFs based on significantly induced genes (476 genes from the *siRBFox2* group and 435 genes from the *siSUZ12* group) (D) and repressed genes (196 genes from the *siRBFox2* group and 222 genes from the *siSUZ12* group) (E).

(F) Sorting of protein-coding genes according to GRO-seq levels at TSS regions (±3 kb) to segregate highly active (left from the gray line), intermediately expressed (between the gray line and orange-shaded regions), and largely silent genes (orange shaded), relative to their association with levels of H3K4me3, H3K27me3, SUZ12, and RBFox2.

(G and H) Association (G) and percentage (H) of induced and repressed genes in response to knockdown of *RBFox2* or *SUZ12* with active and/or repressive chromatin marks.



**Figure 5. Interaction between RBFox2 and PRC2**

(A) Co-IP of RBFox2 with key components of PRC1 and PRC2 in MEFs.

(B) Reciprocal co-IP of RBFox2 with PRC2 in a RNA-independent manner. Before immunoprecipitation, whole-cell extracts were treated with either RNase A (R) or benzonase (B) for 30 min at room temperature. GAPDH served as negative control for immunoprecipitation.

(C) Re-ChIP confirms co-binding of SUZ12 and RBFox2 on the TSS regions of two bivalent genes (*Egr2* and *Arxes4*), but not on *Slc6a12* without H3K4me3 or H3K27me3 signals. ChIP signals are presented as percentage of input. Data are compared to immunoglobulin G control and are presented as mean  $\pm$  SEM. \*\* $p < 0.01$ .

(legend continued on next page)

found that two segments in the RBFox2 CTD were able to interact with PRC2, indicating multiple contacts between RBFox2 and PRC2 (Figure 5D). Finally, we performed the functional rescue experiments with full-length FLAG- and Strep-tagged RBFox2 (FLV) and its C-terminal deletion mutant (DLV) in transfected 293T cells (Figure 5E, left), finding that full-length RBFox2, but not the mutant, could rescue RBFox2-dependent H3K27me3 deposition on four SUZ12-positive loci, but not four SUZ12-negative loci, as previously reported (Gao et al., 2012) (Figure 5E, right). Together, these findings provide a biochemical basis for RBFox2-dependent PRC2 targeting in mammalian cells. Combining the current observations with the existing information in literature, we propose a model for dynamic control of gene expression through nascent RNA-mediated and context-dependent functional interplays between RBFox2 and PRC2 (Figure 6; see Discussion).

## DISCUSSION

### Multifaceted Functions of RBPs in Mammalian Cells

Through pursuing altered transcription programs in *RBFox2* knockout heart and extending the analysis to additional model cell lines, we discovered a general role of RBFox2 as a transcription repressor. A conservative estimate based on RBPs cross-linked to oligo-dT captured mRNA suggests that ~1,000 RBPs are expressed in the human genome (Castello et al., 2012). However, many RBPs have been studied in their traditional frameworks, which are largely confined to their originally elucidated functions in RNA metabolism. Our current findings, together with earlier work demonstrating the splicing-independent role of U1 snRNP in genome protection (Kaida et al., 2010) and the involvement of SRSF2 in transcription pause release (Ji et al., 2013), suggest the direct participation of RBPs in gene expression before engaging in co-transcriptional RNA processing. Given the pervasive transcription of mammalian genomes, various forms of ncRNAs must enlist specific RBPs to execute their regulatory functions in the genome (Cech and Steitz, 2014; Fu, 2014).

### Distinct RBFox2 Binding Modes with Different RNA Populations

RBPs execute biological functions by binding to their target RNAs. In isolation, each RBP shows distinct binding affinity and specificity, and related RNA binding specificities have been observed with RBPs that bear similar RNA recognition motifs (Ray et al., 2013). However, even with purified RBPs, each RBP appears to bind diverse motifs (Lambert et al., 2014). This is also the case with RBFox2, which appears to be capable of binding multiple RNA motifs that can fit into its RNA binding pocket (Auweter et al., 2006; Lambert et al., 2014). Inside cells, individual RBPs

may have even more complex binding profiles, as indicated by numerous published CLIP-seq studies. In some extreme cases, such as PTB and U2AF, most of their in vivo binding events are associated with their in vitro binding consensus – pyrimidine-rich sequences (Shao et al., 2014; Xue et al., 2009), but the CLIP-seq data for many other RBPs show diverse motifs underlying their binding peaks with the best consensus representing only a fraction of their binding events in the cell. An extreme case is exemplified by RBFox3/NeuN, which seems to bind RNA with much relaxed specificity in vivo (Kim et al., 2014). While these variable modes of RNA binding may be affected by the quality of CLIP-seq data generated in individual studies, such variations may also reflect the influence of RNA secondary structure and the involvement of more than one RBP, as well as the interaction with different populations of RNAs in different cellular compartments.

Here, we found that even within the same cell type, RBFox2 binds RNA from different genic regions with different specificities. The general trend is that RBFox2 binds chromatin-associated RNA, especially those near gene promoters, with much reduced specificity during transcription relative to its interaction with late RNA segments during co- and post-transcriptional RNA processing. The reduced RNA binding specificity is likely due to the action of RBFox2 as part of larger protein complexes, including PRC2. Because PRC2 has intrinsic RNA binding capability, but with much less specificity (Davidovich et al., 2015; Kaneko et al., 2013), RBFox2 and PRC2 (perhaps other RBPs) in the complex may undertake some coordinated interactions with RNA to regulate a broad spectrum of genes in mammalian cells.

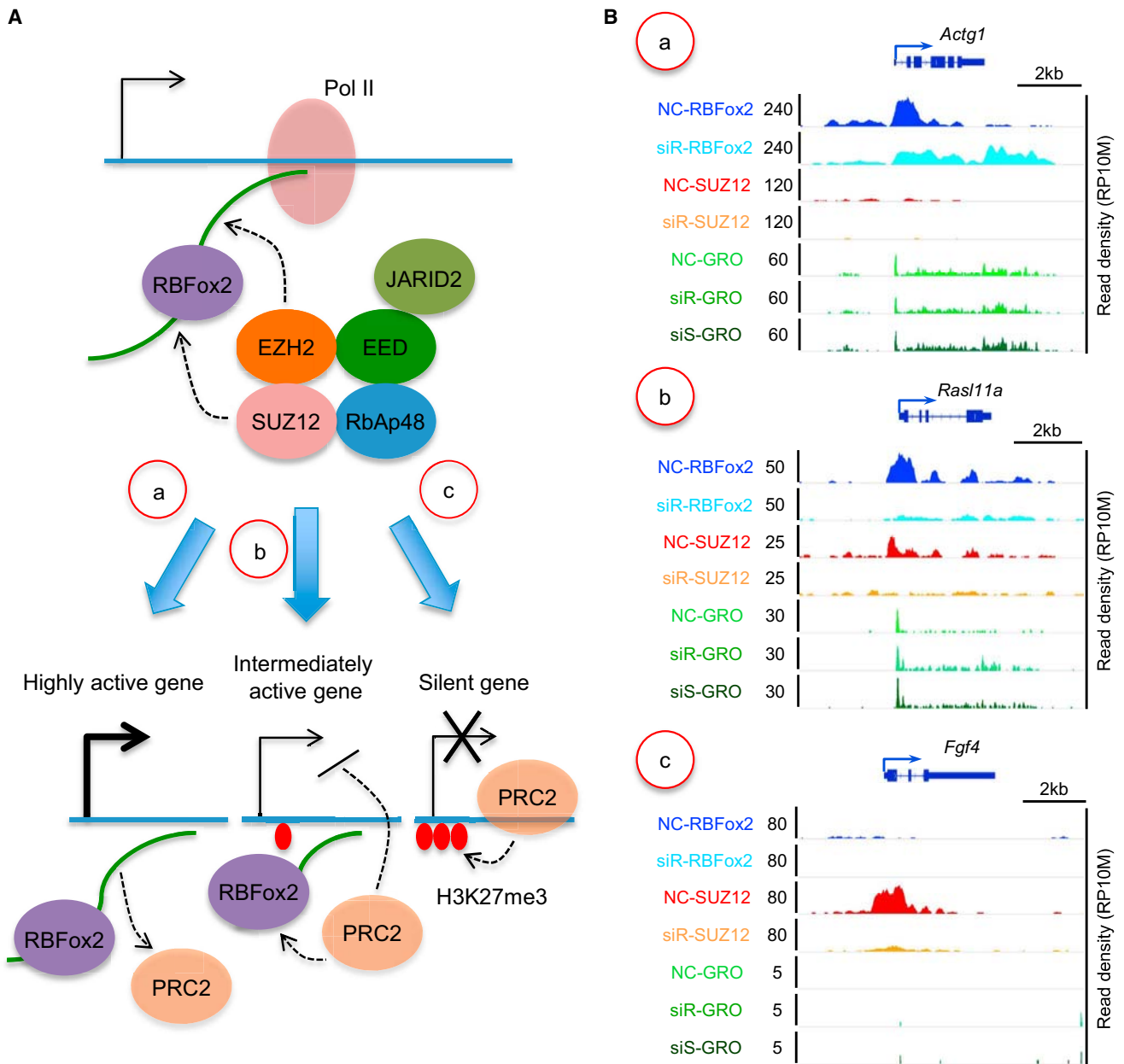
### Regulated Targeting of Polycomb Complexes

The most striking discovery here is the unexpected function of RBFox2 in directing PRC2 targeting in the genome. Polycomb complexes are well known to play vital roles in developmental control of gene expression (Schuettengruber et al., 2007). Polycomb complexes have two separate cores, PRC1 and PRC2, acting either separately or in a concerted fashion to induce gene silencing (Simon and Kingston, 2013). PRC2 contains four major subunits (Cao et al., 2002), with EZH2/SUZ12 for catalyzing H3K27me2/3, EED for amplifying repressive signals via its affinity for H3K27me3, and Rbap48 capable of interacting with histone H4 (Voigt et al., 2013).

EZH2/SUZ12 may target PRC2 to specific genomic loci via RNA, but because PRC2 does not bind RNAs proportional to their abundance in the cell, this process appears to be regulated. A recent study demonstrates a role of the DNA/RBP ATRX in *Xist* loading and spreading on X chromosome as well as in global regulation of PRC2 targeting; however, it remains unclear whether such regulatory function is mediated by its DNA and/or RNA binding activity (Sarma et al., 2014). A recent proteomic

(D) The RBFox2 CTD responsible for interactions with PRC2. Full-length and various deletion constructs of RBFox2 are depicted (top). Individual proteins were expressed and purified from bacteria (bottom left), which were used to conduct GST pull-down assays with baculovirus expressed PRC2 complex (bottom right). Two irrelevant lanes in each gel were blocked.

(E) Western blotting analysis of endogenous RBFox2 (middle band), overexpressed full-length RBFox2 containing N-terminally tagged FLAG and Strep (top band), and similarly tagged C-terminal deletion mutant (bottom band), H3K27me3, and actin in transfected 293T cells (left). NC, negative siRNA control; EV, empty pcDNA3.0 vector; siR, RBFox2 RNAi; FLV, full-length RBFox2 vector; DLV, C-terminal deletion RBFox2 vector. Right panel shows ChIP-qPCR analysis of H3K27me3 levels on the TSS regions of four positive and four negative genes in 293T cells. Results was calculated as fold-changes normalized to *JUN* and are presented as mean  $\pm$  SEM. \*\*p < 0.01. See also Figure S5.



**Figure 6. Proposed Model for Functional Interplays of RBFox2, PRC2, and H3K27me3 that Result in Different Gene Classes**

(A) Model for nascent RNA-mediated, RBFox2-dependent recruitment of PRC2. (a) On highly expressed genes, nascent RNA may modulate the RNA sensor function of PRC2 to cause PRC2 repulsion. (b) On modestly expressed genes, functional interplay between RBFox2 and PRC2 may dynamically regulate homeostatic gene expression, as a modest increase or decrease in nascent RNA production may cause increased or decreased PRC2 recruitment to induce feedback controls. A level of pre-deposited H3K27me3 may help stabilize recruited PRC2. (c) On nearly silent genes, interaction of PRC2 with chromatin is switched from RNA-dependent to EED-mediated interactions, leading to the amplification of the repressive signal to eventually shut down the genes. It is important to also emphasize that functional outcomes on individual genes likely depend on the contribution of transcription regulators in conjunction with specific nucleosome states.

(B) Representative genes in different classes based on the genomic data generated in the current study: NC, siR, and siS represent ChIP-seq or GRO-seq signals in nonspecific control siRNA-, *siRBFox2*-, and *siSUZ12*-treated MEFs, respectively. (a–c) Examples of specific gene in each class described in (A, a–c), showing RBFox2 and SUZ12 binding before and after *RBFox2* knockdown, as well as nascent RNA production before and after *RBFox2* or *SUZ12* knockdown. NC, non-specific siRNA; siR, *siRBFox2*; siS, *siSUZ12*.

analysis of *Xist*-containing RNP reveals a large number of proteins associated with this long ncRNA, and we noted that RBFox2 is actually part of this large RNP (Chu et al., 2015). PRC2 has also been proposed to act as an RNA sensor because RNA can effectively block its enzymatic activity both in vitro and inside cells (Kaneko et al., 2013). These findings suggest that Polycomb Complex targeting is likely regulated by various RNAs and RBPs in mammalian cells.

### Mechanisms for Sorting Genes in Different Functional States

As depicted in Figure 6A and exemplified on representative genes in Figure 6B, our data in combination with literature information suggest that RBFox2 may initially interact with nascent RNA on chromatin and then recruit PRC2 via protein-protein interactions. In this process, the level of nascent RNA may provide a key sensory function: On highly active genes, as proposed earlier (Kaneko et al., 2013), high RNA levels coupled with relatively open chromatin may prevent stable PRC2 binding on chromatin, even initially recruited (Figures 6A and 6Ba). On modestly expressed genes, nascent RNA together with JARID2 (da Rocha et al., 2014; Kaneko et al., 2014a) may help initial recruitment of PRC2, which may become stabilized by relatively compacted chromatin (Yuan et al., 2012) and a degree of predisposed H3K27me3 for EED to bind (Margueron et al., 2009). As a result, increased RNA production would elevate RNA-mediated recruitment of PRC2, leading to increased chromatin compaction, whereas stabilized PRC2 would then limit nascent RNA production, thereby damping further PRC2 recruitment (Figures 6A and 6Bb). This mechanism may help maintain the bivalent nature of those genes for homeostatic expression at intermediate levels. Finally, on a subset of these initially bivalent genes, diminished nascent RNA production may cause a switch from RNA-dependent to H3K27me3-mediated PRC2 recruitment, likely due to excessive chromatin compaction, predisposed H3K27me3, and the action of EED, among other mechanisms, as suggested by a recent study (Kaneko et al., 2014b), together leading to eventual silencing of those genes (Figures 6A and 6Bc).

Last, but not least, our findings emphasize the regulatory function of RNA, even from protein-coding genes. Interestingly, nascent RNA appears to use multiple strategies to regulate the expression of their host genes. A recent study showed that nascent RNA base pairs with a virus-encoded long ncRNA to facilitate the recruitment of the transcription factor PAX5 to regulate the expression of neighbor genes during replication of Epstein-Barr virus (Lee et al., 2015). Our findings now suggest that nascent RNAs produced from active protein-coding genes are not only products of transcription but also critical signals for the regulation of gene expression. Therefore, RNAs are also multitasking in mammalian cells regardless of whether they are ncRNAs or part of RNAs from protein-coding genes.

### EXPERIMENTAL PROCEDURES

#### ***RBFox2* Knockout, miRNA Profiling, Immunostaining, Western Blotting, Co-IP, GST Pull-Down, and RNAi**

Handling of mice was approved by the IRB of University of California, San Diego. Conditional *RBFox2* knockout mice were previously described

(Wei et al., 2015). Immunostaining, western blotting, co-IP, GST pull-down, and RNAi assays were conducted with various antibodies listed in Supplemental Experimental Procedures. The siRNA sequences used in the current study and primer sequences for RT-PCR are listed in Table S6.

#### **CLIP-Seq, ChIP-Seq, and GRO-Seq**

CLIP-seq was performed as described previously (Xue et al., 2009). Isolation of nuclei from cardiomyocytes was performed according to Widnell et al. (1967). To break up myofilaments and release nuclei from cardiomyocytes, cells were homogenized with a homogenizer (Kinematica, POLYTRON PT 2100) at maximum speed for 30 s and ice cooled for 30 s for three rounds. To perform CLIP-seq, WCs or isolated nuclei were digested with 0.1 U/ $\mu$ l RQ1 DNase and 2 U/ $\mu$ l RNaseOUT in lysis buffer (1xPBS buffer with 0.3% SDS, 0.5% deoxycholate sodium, and 0.5% NP-40) for 5 min at 37°C. Each lysate was processed for CLIP-seq with rabbit polyclonal anti-RBFox2 antibody (Bethyl, A300-864A). ChIP-seq was performed as described previously (Ji et al., 2013) using anti-RBFox2 (Bethyl, A300-864A), anti-SUZ12 (Cell Signaling, D39F6), anti-H3K27me3 (Active Motif, 61017), anti-H3K4me3 (Active Motif, 39159) or anti-Pol II (Santa Cruz Biotechnology, sc-899). GRO-seq was performed as described previously (Wang et al., 2011).

#### **Analysis of Genomic Data**

Bayesian network construction was performed according to Liu et al. (2013) by using the RBFox2 and SUZ12 ChIP-seq data generated on isolated cardiomyocytes from 9-week-old mice and the following publically available datasets generated from mouse heart: GSM769017 (for H3K4me3), GSM769025 (for H3K4me1), GSM1000130 (for H3K36me3), GSM1000131 (for H3K27me3), GSM1000093 (for H3K27ac), and GSM918723 (for total Pol II). SeqSpider software (Liu et al., 2013) was used to generate binding matrix and construct the network. Other details on data analysis can be found in Supplemental Experimental Procedures.

#### **ACCESSION NUMBERS**

The accession number for the CLIP-seq, ChIP-seq, and GRO-seq data reported in this paper and summarized in Tables S1–S5 is GEO: GSE57926.

#### **SUPPLEMENTAL INFORMATION**

Supplemental Information includes Supplemental Experimental Procedures, five figures, and six tables and can be found with this article online at <http://dx.doi.org/10.1016/j.molcel.2016.04.013>.

#### **AUTHOR CONTRIBUTIONS**

C.W. and X.-D.F. designed the study; R.X., C.W., L.C., and H.C. generated most data; Y.X. and J.H. performed CLIP-seq and cell fractionation; T.T., J.Q., and H.L. contributed to expression of recombinant proteins and deep sequencing; Y.Z. and B.Z. analyzed genomic data; L.T. guided H.C. in initial study; and C.W. and X.-D.F. wrote the paper.

#### **ACKNOWLEDGMENTS**

The authors are grateful to members of the X.-D.F. lab for cooperation, reagent sharing, and stimulating discussion during the course of this investigation. We are grateful to Dr. Tom Cech for providing the expression plasmids for individual PRC2 subunits and to Drs. Yi Zhang and John Lis for critical comments on the manuscript. H.C. was supported by China Scholarship Council. This work was supported by National Institutes of Health grants GM049369 and HG004659 (to X.-D.F.).

Received: November 30, 2015

Revised: March 23, 2016

Accepted: April 11, 2016

Published: May 19, 2016; corrected online: May 30, 2016

## REFERENCES

- Adelman, K., and Lis, J.T. (2012). Promoter-proximal pausing of RNA polymerase II: emerging roles in metazoans. *Nat. Rev. Genet.* *13*, 720–731.
- Auweter, S.D., Fasan, R., Reymond, L., Underwood, J.G., Black, D.L., Pitsch, S., and Allain, F.H. (2006). Molecular basis of RNA recognition by the human alternative splicing factor Fox-1. *EMBO J.* *25*, 163–173.
- Bernstein, B.E., Mikkelsen, T.S., Xie, X., Kamal, M., Huebert, D.J., Cuff, J., Fry, B., Meissner, A., Wernig, M., Plath, K., et al. (2006). A bivalent chromatin structure marks key developmental genes in embryonic stem cells. *Cell* *125*, 315–326.
- Bonasio, R., and Shiekhattar, R. (2014). Regulation of transcription by long noncoding RNAs. *Annu. Rev. Genet.* *48*, 433–455.
- Cao, R., Wang, L., Wang, H., Xia, L., Erdjument-Bromage, H., Tempst, P., Jones, R.S., and Zhang, Y. (2002). Role of histone H3 lysine 27 methylation in Polycomb-group silencing. *Science* *298*, 1039–1043.
- Castello, A., Fischer, B., Eichelbaum, K., Horos, R., Beckmann, B.M., Strein, C., Davey, N.E., Humphreys, D.T., Preiss, T., Steinmetz, L.M., et al. (2012). Insights into RNA biology from an atlas of mammalian mRNA-binding proteins. *Cell* *149*, 1393–1406.
- Cech, T.R., and Steitz, J.A. (2014). The noncoding RNA revolution—trashing old rules to forge new ones. *Cell* *157*, 77–94.
- Chu, C., Zhang, Q.C., da Rocha, S.T., Flynn, R.A., Bharadwaj, M., Calabrese, J.M., Magnuson, T., Heard, E., and Chang, H.Y. (2015). Systematic discovery of Xist RNA binding proteins. *Cell* *161*, 404–416.
- da Rocha, S.T., Boeva, V., Escamilla-Del-Arenal, M., Ancelin, K., Granier, C., Matias, N.R., Sanulli, S., Chow, J., Schulz, E., Picard, C., et al. (2014). Jarid2 is implicated in the initial Xist-induced targeting of PRC2 to the inactive X chromosome. *Mol. Cell* *53*, 301–316.
- Davidovich, C., Zheng, L., Goodrich, K.J., and Cech, T.R. (2013). Promiscuous RNA binding by Polycomb repressive complex 2. *Nat. Struct. Mol. Biol.* *20*, 1250–1257.
- Davidovich, C., Wang, X., Cifuentes-Rojas, C., Goodrich, K.J., Gooding, A.R., Lee, J.T., and Cech, T.R. (2015). Toward a consensus on the binding specificity and promiscuity of PRC2 for RNA. *Mol. Cell* *57*, 552–558.
- ENCODE Project Consortium (2012). An integrated encyclopedia of DNA elements in the human genome. *Nature* *489*, 57–74.
- Fu, X.D. (2014). Non-coding RNA: a new frontier in regulatory biology. *Natl. Sci. Rev.* *1*, 190–204.
- Gao, Z., Zhang, J., Bonasio, R., Strino, F., Sawai, A., Parisi, F., Kluger, Y., and Reinberg, D. (2012). PCGF homologs, CBX proteins, and RYBP define functionally distinct PRC1 family complexes. *Mol. Cell* *45*, 344–356.
- Hodgkin, J., Zellan, J.D., and Albertson, D.G. (1994). Identification of a candidate primary sex determination locus, fox-1, on the X chromosome of *Caenorhabditis elegans*. *Development* *120*, 3681–3689.
- Jangi, M., Boutz, P.L., Paul, P., and Sharp, P.A. (2014). Rbfox2 controls autoregulation in RNA-binding protein networks. *Genes Dev.* *28*, 637–651.
- Ji, X., Zhou, Y., Pandit, S., Huang, J., Li, H., Lin, C.Y., Xiao, R., Burge, C.B., and Fu, X.D. (2013). SR proteins collaborate with 7SK and promoter-associated nascent RNA to release paused polymerase. *Cell* *153*, 855–868.
- Jiao, L., and Liu, X. (2015). Structural basis of histone H3K27 trimethylation by an active polycomb repressive complex 2. *Science* *350*, aac4383.
- Jin, Y., Suzuki, H., Maegawa, S., Endo, H., Sugano, S., Hashimoto, K., Yasuda, K., and Inoue, K. (2003). A vertebrate RNA-binding protein Fox-1 regulates tissue-specific splicing via the pentanucleotide GCAUG. *EMBO J.* *22*, 905–912.
- Kaida, D., Berg, M.G., Younis, I., Kasim, M., Singh, L.N., Wan, L., and Dreyfuss, G. (2010). U1 snRNP protects pre-mRNAs from premature cleavage and polyadenylation. *Nature* *468*, 664–668.
- Kaneko, S., Son, J., Shen, S.S., Reinberg, D., and Bonasio, R. (2013). PRC2 binds active promoters and contacts nascent RNAs in embryonic stem cells. *Nat. Struct. Mol. Biol.* *20*, 1258–1264.
- Kaneko, S., Bonasio, R., Saldaña-Meyer, R., Yoshida, T., Son, J., Nishino, K., Umezawa, A., and Reinberg, D. (2014a). Interactions between JARID2 and noncoding RNAs regulate PRC2 recruitment to chromatin. *Mol. Cell* *53*, 290–300.
- Kaneko, S., Son, J., Bonasio, R., Shen, S.S., and Reinberg, D. (2014b). Nascent RNA interaction keeps PRC2 activity poised and in check. *Genes Dev.* *28*, 1983–1988.
- Kanhere, A., Viiri, K., Araújo, C.C., Rasaiyaah, J., Bouwman, R.D., Whyte, W.A., Pereira, C.F., Brookes, E., Walker, K., Bell, G.W., et al. (2010). Short RNAs are transcribed from repressed polycomb target genes and interact with polycomb repressive complex-2. *Mol. Cell* *38*, 675–688.
- Kim, K.K., Yang, Y., Zhu, J., Adelstein, R.S., and Kawamoto, S. (2014). Rbfox3 controls the biogenesis of a subset of microRNAs. *Nat. Struct. Mol. Biol.* *21*, 901–910.
- Kuroyanagi, H. (2009). Fox-1 family of RNA-binding proteins. *Cell. Mol. Life Sci.* *66*, 3895–3907.
- Lambert, N., Robertson, A., Jangi, M., McGeary, S., Sharp, P.A., and Burge, C.B. (2014). RNA Bind-n-Seq: quantitative assessment of the sequence and structural binding specificity of RNA binding proteins. *Mol. Cell* *54*, 887–900.
- Lee, J.T., and Bartolomei, M.S. (2013). X-inactivation, imprinting, and long noncoding RNAs in health and disease. *Cell* *152*, 1308–1323.
- Lee, N., Moss, W.N., Yario, T.A., and Steitz, J.A. (2015). EBV noncoding RNA binds nascent RNA to drive host PAX5 to viral DNA. *Cell* *160*, 607–618.
- Lin, S., Coutinho-Mansfield, G., Wang, D., Pandit, S., and Fu, X.D. (2008). The splicing factor SC35 has an active role in transcriptional elongation. *Nat. Struct. Mol. Biol.* *15*, 819–826.
- Liu, Y., Qiao, N., Zhu, S., Su, M., Sun, N., Boyd-Kirkup, J., and Han, J.D. (2013). A novel Bayesian network inference algorithm for integrative analysis of heterogeneous deep sequencing data. *Cell Res.* *23*, 440–443.
- Margueron, R., Justin, N., Ohno, K., Sharpe, M.L., Son, J., Drury, W.J., 3rd, Voigt, P., Martin, S.R., Taylor, W.R., De Marco, V., et al. (2009). Role of the polycomb protein EED in the propagation of repressive histone marks. *Nature* *461*, 762–767.
- Marks, H., Kalkan, T., Menafra, R., Denissov, S., Jones, K., Hofemeister, H., Nichols, J., Kranz, A., Stewart, A.F., Smith, A., and Stunnenberg, H.G. (2012). The transcriptional and epigenomic foundations of ground state pluripotency. *Cell* *149*, 590–604.
- Mikkelsen, T.S., Ku, M., Jaffe, D.B., Issac, B., Lieberman, E., Giannoukos, G., Alvarez, P., Brockman, W., Kim, T.K., Koche, R.P., et al. (2007). Genome-wide maps of chromatin state in pluripotent and lineage-committed cells. *Nature* *448*, 553–560.
- Nicoll, M., Akerib, C.C., and Meyer, B.J. (1997). X-chromosome-counting mechanisms that determine nematode sex. *Nature* *388*, 200–204.
- Norris, J.D., Fan, D., Sherk, A., and McDonnell, D.P. (2002). A negative coregulator for the human ER. *Mol. Endocrinol.* *16*, 459–468.
- Rahl, P.B., Lin, C.Y., Seila, A.C., Flynn, R.A., McCuine, S., Burge, C.B., Sharp, P.A., and Young, R.A. (2010). c-Myc regulates transcriptional pause release. *Cell* *141*, 432–445.
- Ray, D., Kazan, H., Cook, K.B., Weirauch, M.T., Najafabadi, H.S., Li, X., Gueroussov, S., Albu, M., Zheng, H., Yang, A., et al. (2013). A compendium of RNA-binding motifs for decoding gene regulation. *Nature* *499*, 172–177.
- Rinn, J.L., and Chang, H.Y. (2012). Genome regulation by long noncoding RNAs. *Annu. Rev. Biochem.* *81*, 145–166.
- Rivera, C.M., and Ren, B. (2013). Mapping human epigenomes. *Cell* *155*, 39–55.
- Sarma, K., Cifuentes-Rojas, C., Ergun, A., Del Rosario, A., Jeon, Y., White, F., Sadreyev, R., and Lee, J.T. (2014). ATRX directs binding of PRC2 to Xist RNA and Polycomb targets. *Cell* *159*, 869–883.
- Schuettengruber, B., Chourrout, D., Vervoort, M., Leblanc, B., and Cavalli, G. (2007). Genome regulation by polycomb and trithorax proteins. *Cell* *128*, 735–745.

- Shao, C., Yang, B., Wu, T., Huang, J., Tang, P., Zhou, Y., Zhou, J., Qiu, J., Jiang, L., Li, H., et al. (2014). Mechanisms for U2AF to define 3' splice sites and regulate alternative splicing in the human genome. *Nat. Struct. Mol. Biol.* *21*, 997–1005.
- Simon, J.A., and Kingston, R.E. (2013). Occupying chromatin: Polycomb mechanisms for getting to genomic targets, stopping transcriptional traffic, and staying put. *Mol. Cell* *49*, 808–824.
- Theunissen, T.W., Powell, B.E., Wang, H., Mitalipova, M., Faddah, D.A., Reddy, J., Fan, Z.P., Maetzel, D., Ganz, K., Shi, L., et al. (2014). Systematic identification of culture conditions for induction and maintenance of naive human pluripotency. *Cell Stem Cell* *15*, 471–487.
- Underwood, J.G., Boutz, P.L., Dougherty, J.D., Stoilov, P., and Black, D.L. (2005). Homologues of the *Caenorhabditis elegans* Fox-1 protein are neuronal splicing regulators in mammals. *Mol. Cell. Biol.* *25*, 10005–10016.
- Voigt, P., Tee, W.W., and Reinberg, D. (2013). A double take on bivalent promoters. *Genes Dev.* *27*, 1318–1338.
- Wang, X., Arai, S., Song, X., Reichart, D., Du, K., Pascual, G., Tempst, P., Rosenfeld, M.G., Glass, C.K., and Kurokawa, R. (2008). Induced ncRNAs allosterically modify RNA-binding proteins in cis to inhibit transcription. *Nature* *454*, 126–130.
- Wang, D., Garcia-Bassets, I., Benner, C., Li, W., Su, X., Zhou, Y., Qiu, J., Liu, W., Kaikkonen, M.U., Ohgi, K.A., et al. (2011). Reprogramming transcription by distinct classes of enhancers functionally defined by eRNA. *Nature* *474*, 390–394.
- Wei, C., Qiu, J., Zhou, Y., Xue, Y., Hu, J., Ouyang, K., Banerjee, I., Zhang, C., Chen, B., Li, H., et al. (2015). Repression of the central splicing regulator RBFox2 is functionally linked to pressure overload-induced heart failure. *Cell Rep.* *10*, 1521–1533.
- Widnell, C.C., Hamilton, T.H., and Tata, J.R. (1967). The isolation of enzymically active nuclei from the rat heart and uterus. *J. Cell Biol.* *32*, 766–770.
- Xue, Y., Zhou, Y., Wu, T., Zhu, T., Ji, X., Kwon, Y.S., Zhang, C., Yeo, G., Black, D.L., Sun, H., et al. (2009). Genome-wide analysis of PTB-RNA interactions reveals a strategy used by the general splicing repressor to modulate exon inclusion or skipping. *Mol. Cell* *36*, 996–1006.
- Yeo, G.W., Coufal, N.G., Liang, T.Y., Peng, G.E., Fu, X.D., and Gage, F.H. (2009). An RNA code for the FOX2 splicing regulator revealed by mapping RNA-protein interactions in stem cells. *Nat. Struct. Mol. Biol.* *16*, 130–137.
- Yuan, W., Wu, T., Fu, H., Dai, C., Wu, H., Liu, N., Li, X., Xu, M., Zhang, Z., Niu, T., et al. (2012). Dense chromatin activates Polycomb repressive complex 2 to regulate H3 lysine 27 methylation. *Science* *337*, 971–975.
- Zhang, C., Zhang, Z., Castle, J., Sun, S., Johnson, J., Krainer, A.R., and Zhang, M.Q. (2008). Defining the regulatory network of the tissue-specific splicing factors Fox-1 and Fox-2. *Genes Dev.* *22*, 2550–2563.
- Zhao, J., Ohsumi, T.K., Kung, J.T., Ogawa, Y., Grau, D.J., Sarma, K., Song, J.J., Kingston, R.E., Borowsky, M., and Lee, J.T. (2010). Genome-wide identification of polycomb-associated RNAs by RIP-seq. *Mol. Cell* *40*, 939–953.

## Time-dependent and protein-directed growth of gold nanoparticles within a single crystal of lysozyme

Hui Wei, Zidong Wang, Jiong Zhang, Stephen House, Yi-Gui Gao, Limin Yang, Howard Robinson, Li Huey Tan, Hang Xing, Changjun Hou, Ian M. Robertson, Jian-Min Zuo and Yi Lu

### Materials and Methods

**Materials.** Chloroauric acid, 2,2'-thiodiethanol, tris(2-carboxyethyl)phosphine, and lysozyme lyophilized powder (from chicken egg white) were purchased from Sigma-Aldrich Chemical Co. All other chemicals were obtained from Fisher Scientific Inc. The  $\text{ClAuS}(\text{CH}_2\text{CH}_2\text{OH})_2$  (**Au(I)**) in 0.1 M sodium acetate (pH=4.5) was freshly prepared before use according to a literature method<sup>S1</sup>.  $\text{Au}_{102}(\text{para-mercaptobenzoic acid})_{44}$  was prepared according to a literature method<sup>S2</sup>. 5 nm gold nanoparticles stabilized by citrate with a concentration of 82 nM were purchased from Ted Pella, Inc. 13 nm gold nanoparticles stabilized by citrate with a concentration of 17 nM were prepared according to a literature method<sup>S3</sup>. The water used throughout all experiments was purified by a Milli-Q system (Millipore, Bedford, MA, USA).

**Crystal Growth and X-ray Crystallographic Studies.** Crystals of the lysozyme-**Au(I)** complex were grown by hanging drop vapour diffusion at room temperature. Specifically, 5  $\mu\text{L}$  75 mg/mL lysozyme in 0.1 M sodium acetate (pH=4.5) were mixed with 3  $\mu\text{L}$  35 mM **Au(I)** in 0.1 M sodium acetate (pH=4.5) at room temperature for 5 minutes. Then the crystal trays were set up by mixing 7  $\mu\text{L}$  of the as-prepared lysozyme-**Au(I)** complex and 3  $\mu\text{L}$  of the well solution. The well solution was 6.5% NaCl (w/v) in 0.1 M sodium acetate (pH 4.5). The well of the crystal tray was filled with 800  $\mu\text{L}$  of the same solution. Colourless crystals were observed after one day of growth. The crystals changed from colourless to pink, then to red as the growth time increased. Crystals at different stages of growth were collected and soaked in a cryoprotectant solution, then flash frozen in liquid  $\text{N}_2$  before data collection.



To fine-tune the growth rate of gold nanoparticles within the lysozyme crystals,  $\sim 0.2 \mu\text{L}$  of chemicals ( $\text{Hg}^{2+}$  or TCEP) were added to the crystal drop solution after one day of growth.

A crystal of lysozyme- $\text{HAuCl}_4$  was grown by hanging drop vapour diffusion at room temperature. Specifically,  $3 \mu\text{L}$   $75 \text{ mg/mL}$  lysozyme in  $0.1 \text{ M}$  sodium acetate ( $\text{pH}$  4.8) was mixed with  $3 \mu\text{L}$   $2 \text{ mM}$   $\text{HAuCl}_4$  aqueous solution at room temperature for 5 min. Then the crystal trays were set up by mixing  $6 \mu\text{L}$  of the as-prepared lysozyme- $\text{HAuCl}_4$  complex and  $3 \mu\text{L}$  of the well solution. The well solution was  $6.5\%$   $\text{NaCl}$  (w/v) in  $0.1 \text{ M}$  sodium acetate ( $\text{pH}$  4.8). The well of the crystal tray was filled with  $800 \text{ mL}$  of the same solution. A colourless crystal was obtained, collected, and soaked in a cryoprotectant solution, then flash frozen in liquid  $\text{N}_2$  before data collection.

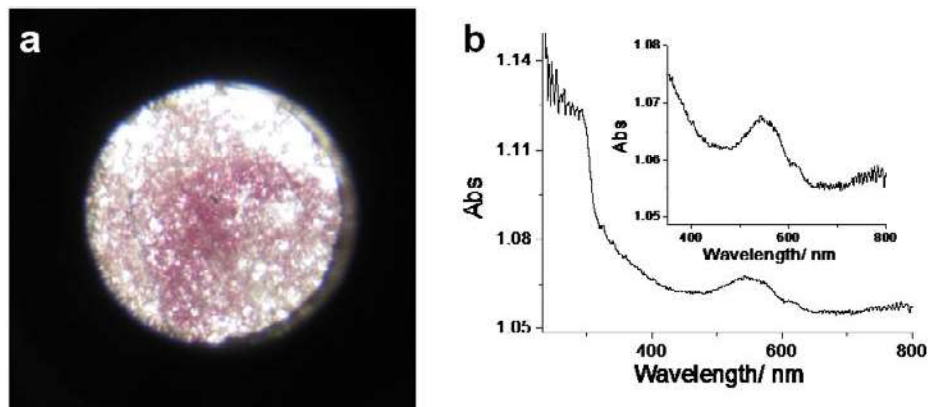
As control experiments, crystals of lysozyme were also grown from lysozyme and different as-prepared gold nanoparticles by hanging drop vapour diffusion at room temperature. (i) For  $\sim 1 \text{ nm}$   $\text{Au}_{102}(\text{para-mercaptobenzoic acid})_{44}$ ,  $7.5 \mu\text{L}$   $75 \text{ mg/mL}$  lysozyme in  $0.1 \text{ M}$  sodium acetate ( $\text{pH}$  4.5) was mixed with  $5 \mu\text{L}$   $\sim 1 \text{ nm}$   $\text{Au}_{102}(\text{para-mercaptobenzoic acid})_{44}$  ( $1 \text{ mM}$ ) at room temperature for 5 min. Then the crystal trays were set up by mixing  $5 \mu\text{L}$  of the sample and  $5 \mu\text{L}$  of the well solution. (ii) For  $5 \text{ nm}$  gold nanoparticles stabilized by sodium citrate,  $5 \mu\text{L}$   $120 \text{ mg/mL}$  lysozyme in  $0.1 \text{ M}$  sodium acetate ( $\text{pH}$  4.5) was mixed with  $5 \mu\text{L}$   $5 \text{ nm}$  gold nanoparticles stabilized by sodium citrate ( $82 \text{ nM}$ ) at room temperature for 5 min. Then the crystal trays were set up by mixing  $5 \mu\text{L}$  of the sample and  $5 \mu\text{L}$  of the well solution. (iii) For  $13 \text{ nm}$  gold nanoparticles stabilized by sodium citrate,  $5 \mu\text{L}$   $75 \text{ mg/mL}$  lysozyme in  $0.1 \text{ M}$  sodium acetate ( $\text{pH}$  4.5) was mixed with  $5 \mu\text{L}$   $13 \text{ nm}$  gold nanoparticles stabilized by sodium citrate ( $17 \text{ nM}$ ) at room temperature for 5 min. Then the crystal trays were set up by mixing  $5 \mu\text{L}$  of the sample and  $5 \mu\text{L}$  of the well solution. For all the three samples, the well solution was  $6.5\%$   $\text{NaCl}$  (w/v) in  $0.1 \text{ M}$  sodium acetate ( $\text{pH}$  4.5). The well of the crystal tray was filled with  $800 \text{ mL}$  of the same solution.

X-ray diffraction data were collected at the National Synchrotron Light Source X12C beamline (Brookhaven National Laboratory, USA). All data were integrated using the program HKL2000<sup>S4</sup>.

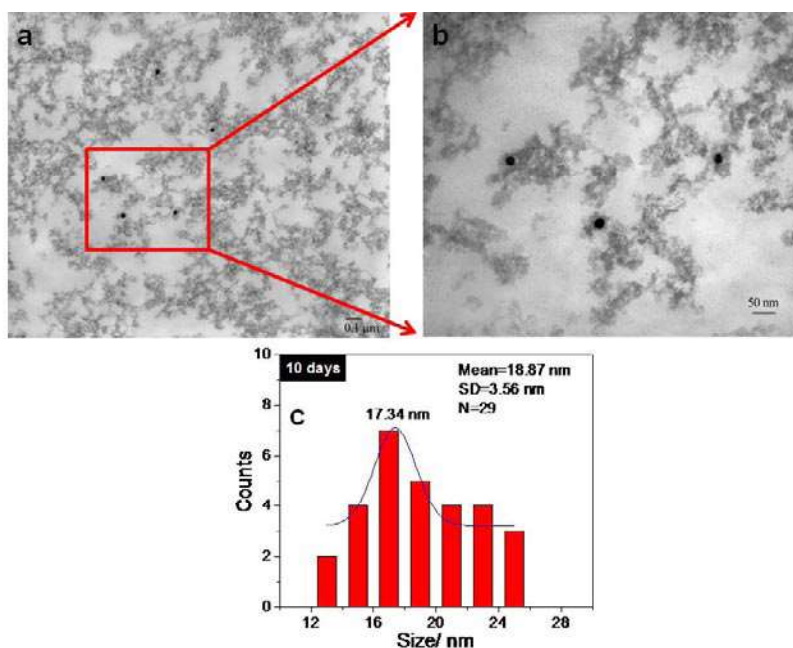
The crystal structures were solved by the molecular replacement method using MOLREP in the CCP4 Package<sup>S5</sup>. The refinement was performed using X-plor<sup>S6</sup> and SHELX'97<sup>S7</sup>. VMD and PyMol were used for visualization of lysozyme protein<sup>S8,S9</sup>.

**Electron Tomography.** A tilt series of HAADF STEM images for three-dimensional electron tomography was obtained on a JEOL 2010F field-emission scanning transmission electron microscope with a camera length of 15 cm at an acceleration voltage of 200 kV. A tilt series of HAADF-STEM images of the relatively thin sample area were recorded from  $-51^{\circ}$  to  $51^{\circ}$  at  $3^{\circ}$  intervals. The images were aligned and the tomography was reconstructed using EM3D<sup>S10</sup>. The reconstruction was visualized using Chimera<sup>S11</sup>.

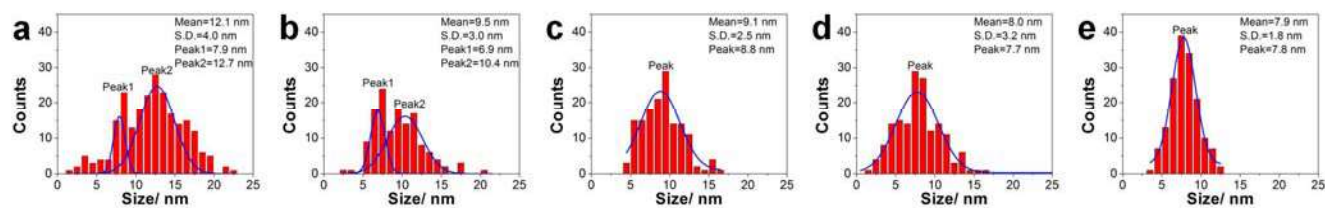
**Instrumentation.** Absorption spectra were obtained on a Cary 5000 spectrophotometer (Varian, USA). Powder X-ray diffraction (XRD) data were collected on a Siemens-Bruker D5000 XRD diffractometer. TEM images were obtained on a JEOL 2010 LaB<sub>6</sub> (or JEOL 2100 LaB<sub>6</sub>) transmission electron microscope at an acceleration voltage of 200 kV. (S)TEM samples were prepared by grinding the crystals into a fine powder with mortar and pestle, then transferring the crystal powder onto copper TEM grids. Photographs of the crystals were taken with a Canon digital camera.



**Figure S1.** The red lysozyme-Au(I) crystal powder immobilized onto a Cary 5000 sample holder (a) and the corresponding solid state absorption spectra (b). Inset of panel (b) is the zoomed-in spectra. A 580-nm surface plasmon resonance absorption peak from the gold nanoparticles grown within the lysozyme single crystals was observed, which gave the crystal its red colour. The 280 nm peak from lysozyme could not be measured due to the limit of the powder-based absorption measurement method.

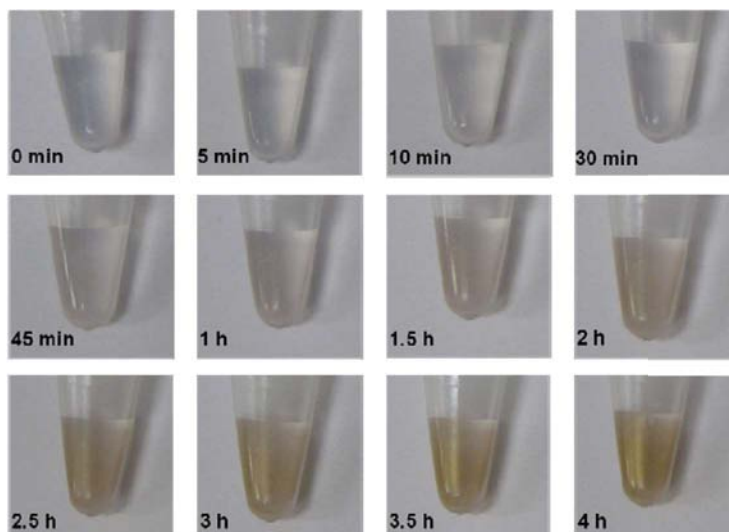


**Figure S2.** Cross-sectional TEM images (**a** and **b**) and the corresponding size histograms (**c**) of the gold nanoparticles within the lysozyme-Au(I) crystal after 10 days of growth. The crystal was stained with uranyl acetate and lead citrate and then sectioned by a Leica/Reichert Microtome. The sectioned crystal was placed on a TEM supporting grid and dried in air. The TEM images of the sectioned crystals were taken on a H600 Hitachi transmission electron microscopy at an acceleration voltage of 75 kV. **Note:** the particle size obtained from the stained and sectioned TEM samples (18.87 nm) was consistent with that from powder TEM samples (16.87 nm) (**Fig. 1b**). This confirmed that the TEM sample preparation method used in this study was valid and correct.



**Figure S3.** The size distribution histograms of the gold nanoparticles within the crystals grown from lysozyme-**Au(I)** in the absence (**a**) and presence (**b-d**) of histidine after 3 days of growth. From **b** to **d**, the molar ratios of histidine to **Au(I)** were 1:4, 1:1, 4:1, and 10:1.

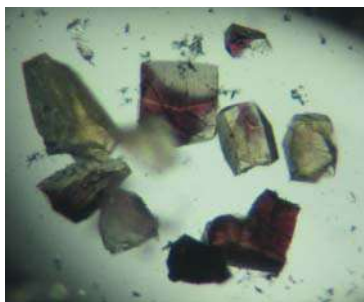
**The possible mechanism of the transformation of the bimodal distribution of gold nanoparticles size into a single peak.** We propose that the small gold nanoparticles were formed from the **Au(I)** bound to His15 of lysozyme, as observed in the crystal structures shown in Fig. 1e. Because the **Au(I)** ions are bound to the protein and stabilized by the coordination, their transformation into gold nanoparticles is slower resulting in small gold nanoparticles; on the other hand, the large gold nanoparticles are proposed to be formed from the free **Au(I)** diffused into the lysozyme crystals, where their transformation into gold nanoparticles is faster. Therefore a bimodal size distribution of gold nanoparticles size would be observed in the intermediate stage of crystal growth. With increasing time, **Au(I)** bound to His15 of lysozyme would be consumed (see Figs. 1e and 1g) and thus no more small gold nanoparticles would be formed. Finally, further growth of the small and large gold nanoparticles into larger ones would result in the final single peak. To further support this proposed scheme and understand the transformation of the bimodal distribution of gold nanoparticles size into a single peak, we carried out the following experiment. We added free histidine as a competing agent for free **Au(I)** diffused into the lysozyme crystals. As shown in Fig. S3, with the increase of the ratio between histidine over **Au(I)** and at the same time point, the bimodal distribution of gold nanoparticles size transformed into a single peak and shifted to the smaller size region. These results suggest the role of histidine ligand in slowing down the growth gold nanoparticles to smaller sizes and that external ligands such as histidine can help influence the kinetics of the free **Au(I)** diffused into the crystals and thus final size distributions.



**Figure S4.** Time-dependent photos of the disproportionation of 35 mM **Au(I)** in aqueous solution as a control. As the disproportionation reaction proceeded, the solution changed from colourless to yellowish due to the formation of bulk gold. Compared with the **Au(I)** within lysozyme crystals, **Au(I)** in aqueous solution disproportionated much faster.



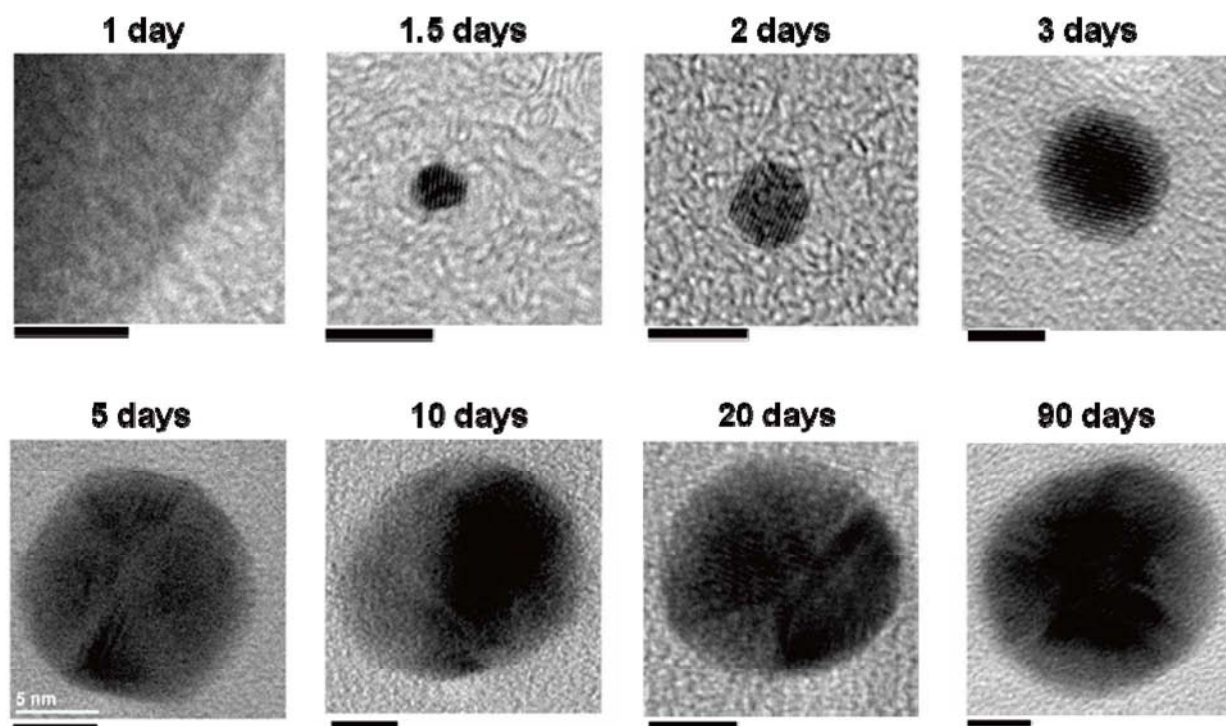
**Figure S5.** Photos of the crystals grown from lysozyme and preformed gold nanoparticles of different sizes. **(a)** 13 nm gold nanoparticles stabilized by sodium citrate (17 nM), **(b)** 5 nm gold nanoparticles stabilized by sodium citrate (82 nM), and **(c)**  $\sim 1$  nm  $\text{Au}_{102}(\text{para-mercaptobenzoic acid})_{44}$  (1 mM).



**Figure S6.** The image of the crystals grown from 75mg/mL lysozyme, followed by 35 mM  $\text{HAuCl}_4$  soaking and 100 mM  $\text{NaBH}_4$  reduction.

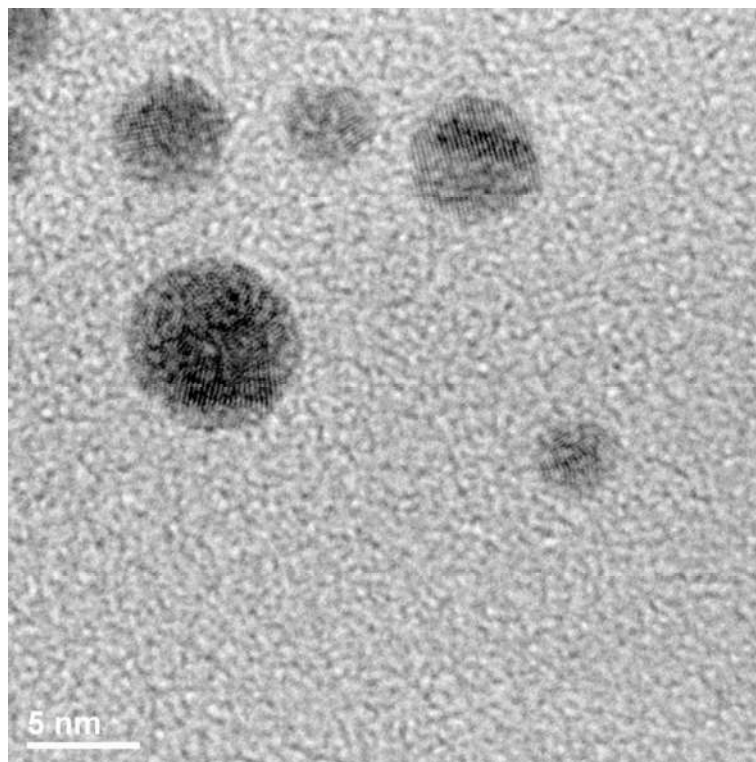
The host crystals were usually quite stable at the described conditions we used to grow the nanoparticles (see Fig. 1a). However, we did find that if strong reducing agents such as  $\text{NaBH}_4$  were used to reduce the gold salt fast, not only did the crystals lose the integrity, but also the crystals formed were not uniform (see Fig. S6). This negative control result supports the novel approach presented in the current work.



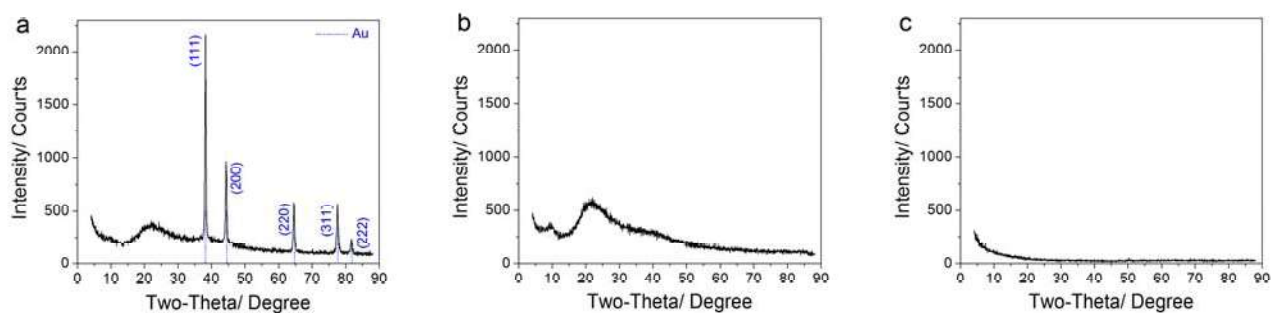


**Figure S7.** High-resolution TEM images of the gold particles within the crystals grown from lysozyme and **Au(I)** at different growth stages (after 1 day, 1.5 days, 2 days, 3 days, 5 days, 10 days, 20 days, and 90 days of growth; the scale bar is 5 nm).

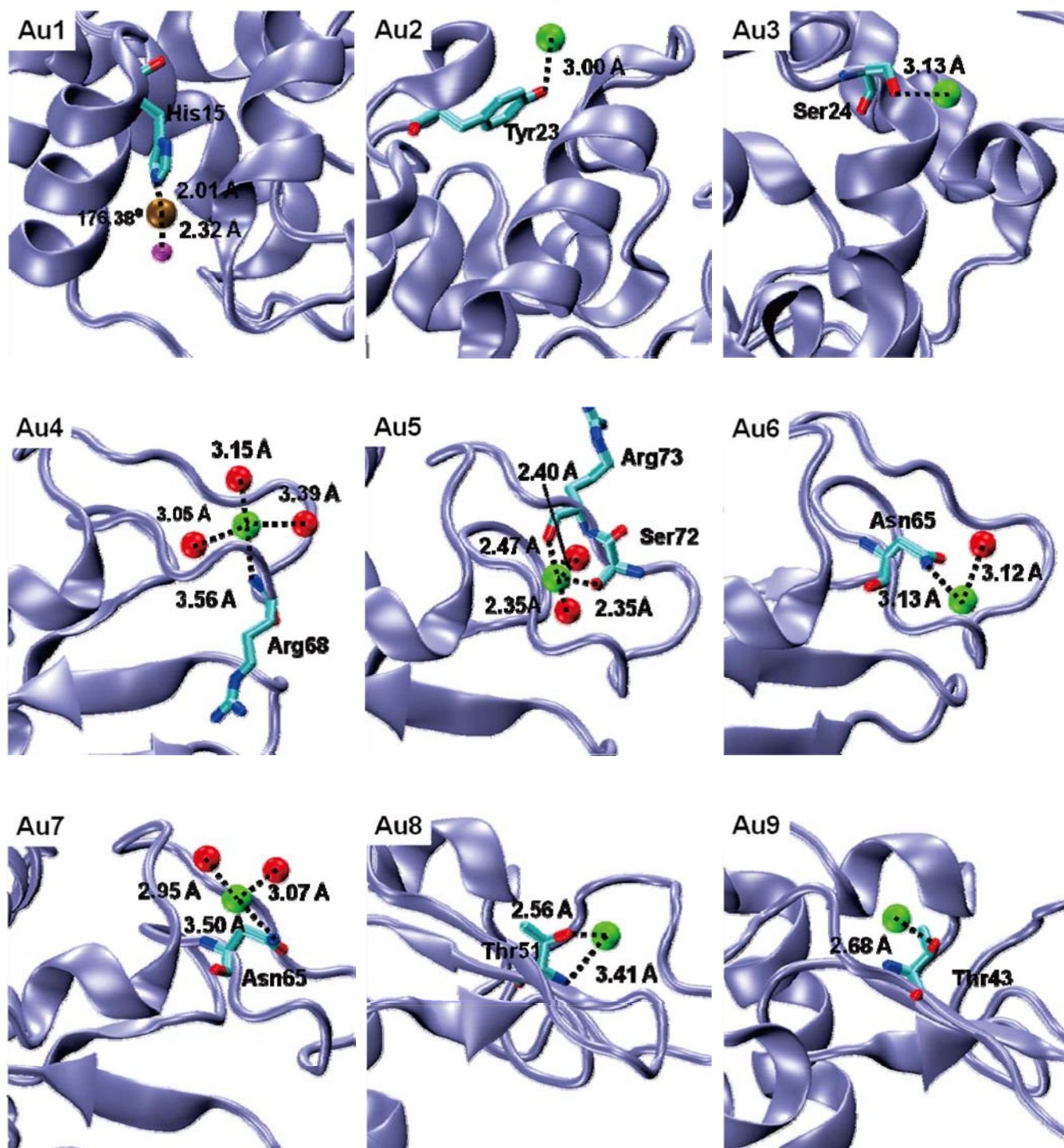
As shown in Fig. S7, at the early stages, gold single crystals were observed; while at the late stages, twinned structures of gold were observed. The appearance of the twinned structures was probably due to their more low energy facets<sup>S12</sup>. This observation was also be further confirmed by the solution-based synthesis, where gold nanoparticles with twinned structures could also be observed (see Fig. S8). These results suggest that the gold crystallites structural properties were not changed dramatically by growing them within the protein crystals.



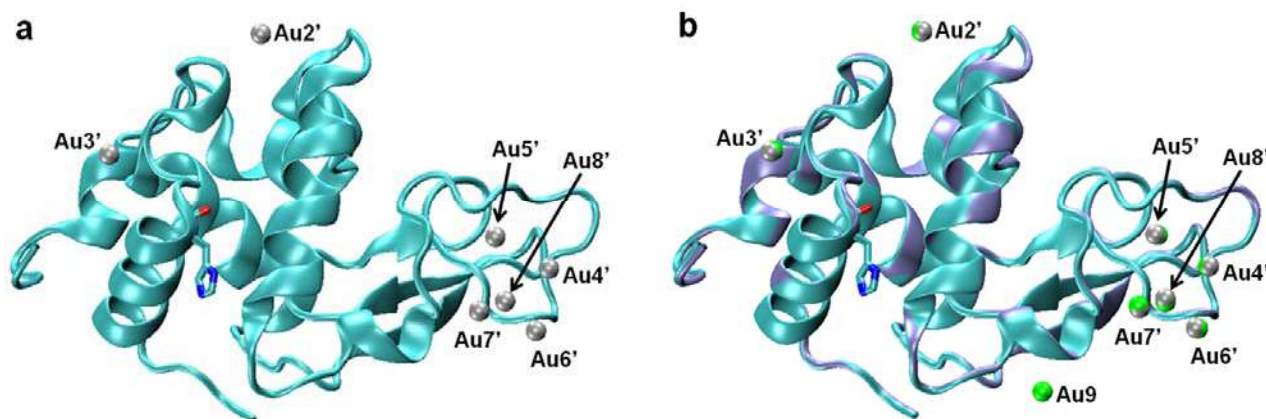
**Figure S8.** A TEM image of gold nanoparticles stabilized by lysozyme. The gold nanoparticles were prepared via a solution based reduction of 35 mM **Au(I)** in the presence of 75 mg/mL lysozyme using as the reducing agent  $\text{NaBH}_4$  as the reducing agent.



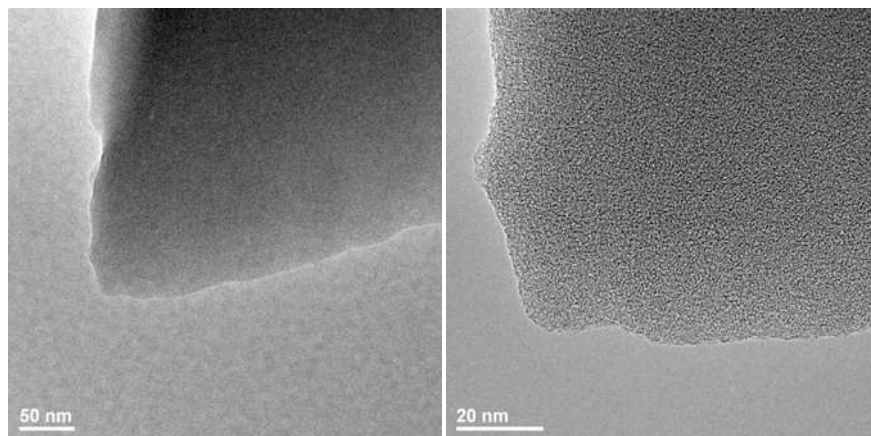
**Figure S9.** The powder XRD patterns of the crystals grown from lysozyme-Au(I) after 10 days (**a**) and the crystals grown from lysozyme alone (**b**). (**c**) shows the background response of the quartz sample holder used. The broad peaks between 15° and 30° in panels (**a**) and (**b**) were assigned to lysozyme, which was consistent with previous report<sup>S13</sup>.



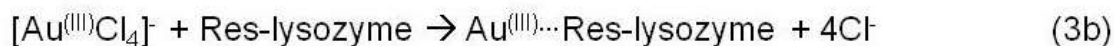
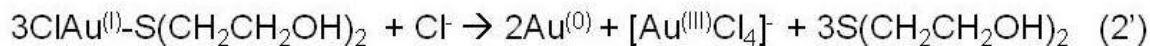
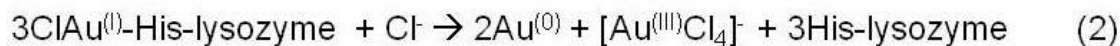
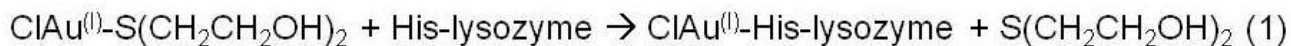
**Figure S10.** The binding motifs of the gold atoms and lysozyme. In all panels Au(I) is shown in ochre, Au(III) in green, carbon in cyan, nitrogen in blue, oxygen (or water in the ball) in red, and chloride in magenta. VMD was used for visualization<sup>S8</sup>.



**Figure S11.** X-ray crystallographic structure of the lysozyme single crystal grown from lysozyme and  $\text{HAuCl}_4$  (**a**) and its overlay with the ninetieth day lysozyme single crystal grown from lysozyme and **Au(I)** (**b**). In all panels Au(III) is shown in green or silver, carbon in cyan, nitrogen in blue, oxygen in red, and chloride in magenta. The PDB code of **a** is 3P68. VMD was used for visualization<sup>S8</sup>.



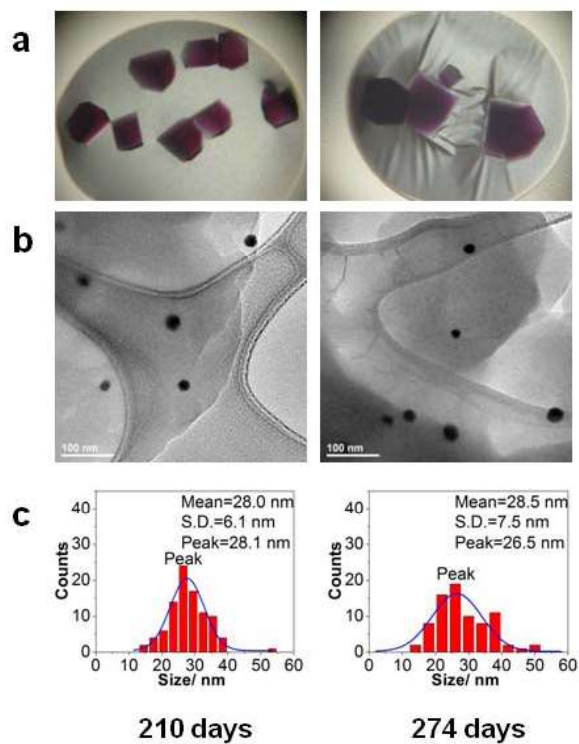
**Figure S12.** TEM images of the crystals grown from 2 mM  $\text{HAuCl}_4$  and 75 mg/mL lysozyme after 45 days of growth. No gold nanoparticles could be observed under this condition.



His-lysozyme, the His15 of lysozyme;

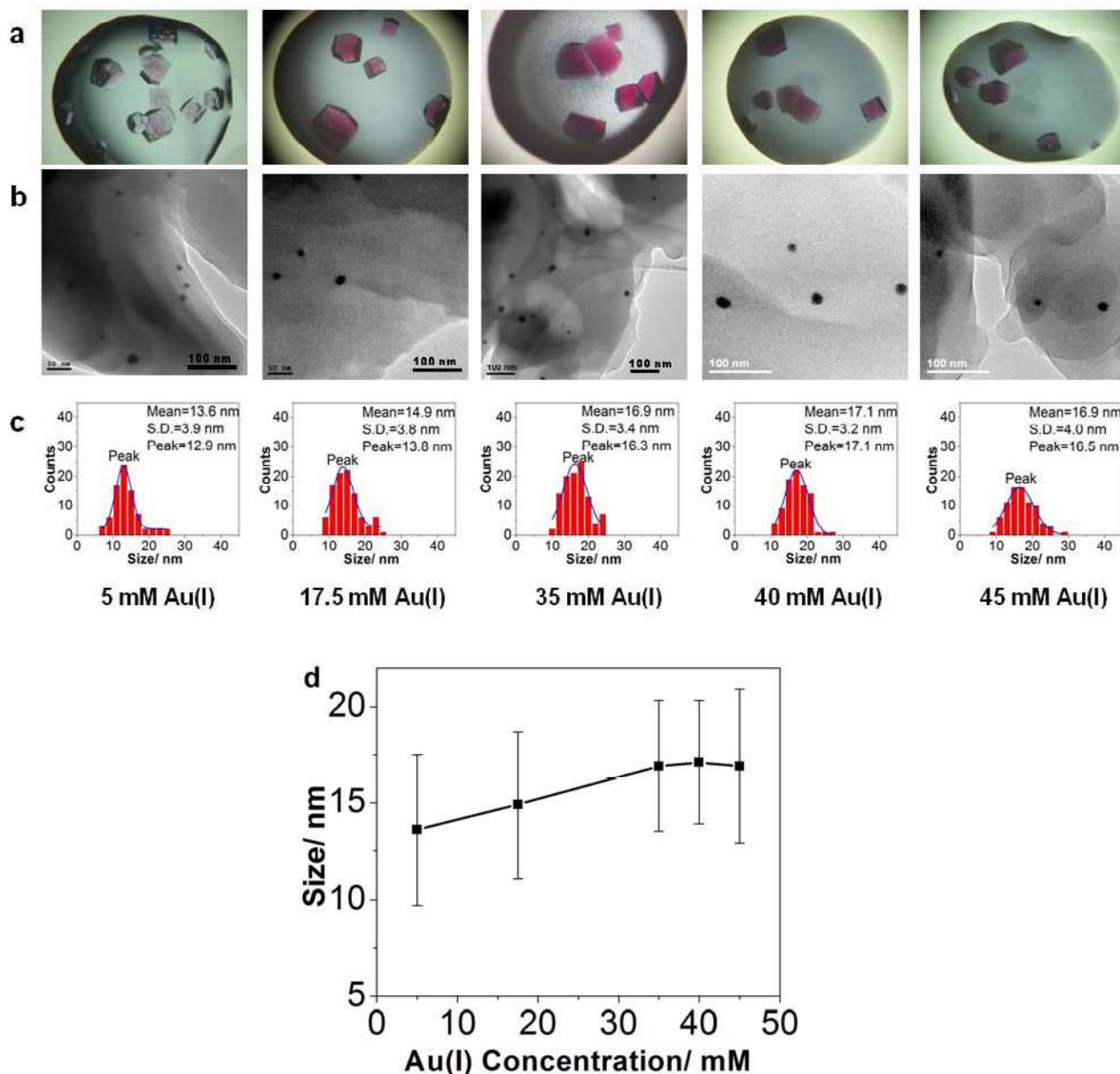
Res-lysozyme, other gold binding sites of lysozyme.

**Figure S13.** The reactions involved in this study.



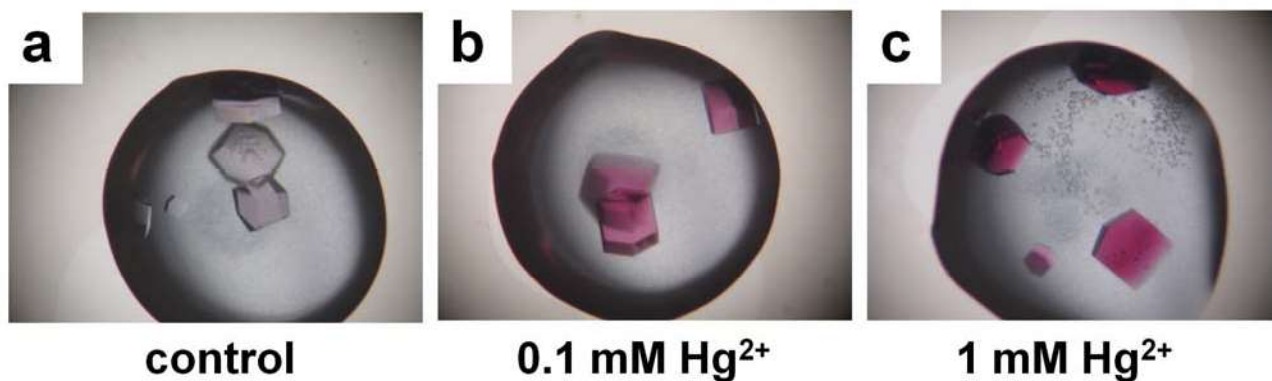
**Figure S14.** The images of the crystals grown from 75mg/mL lysozyme and 35 mM **Au(I)** at longer growth stages (210 and 274 days) (a), the corresponding TEM images (b) and the size distribution histograms of the gold nanoparticles within the crystals (c).



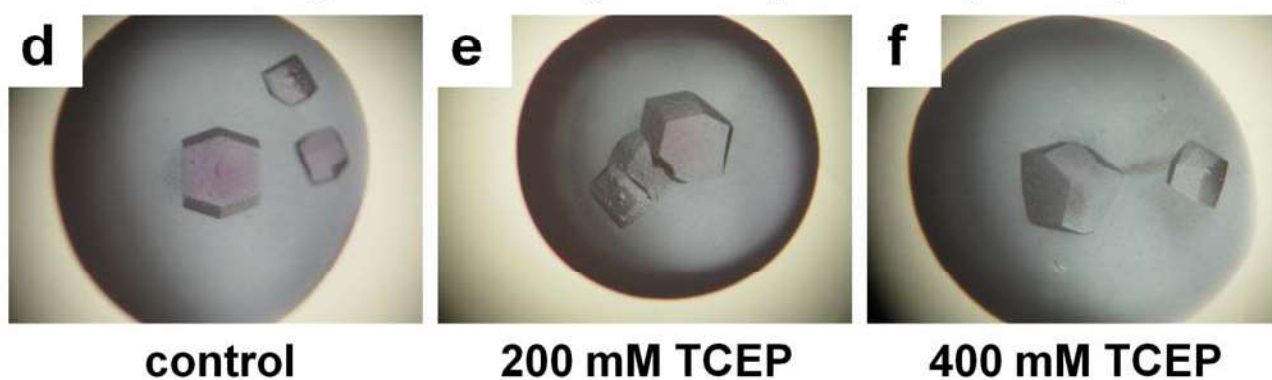


**Figure S15.** The images of the crystals grown from 75mg/mL lysozyme and different concentrations of **Au(I)** (a), the corresponding TEM images (b) and the size distribution histograms of the gold nanoparticles within the crystals (c). The plots of gold nanoparticles size vs. **Au (I)** concentration (d). The data were collected after 10 days of growth.

## Accelerate the growth rate of gold nanoparticles by adding Hg(II)

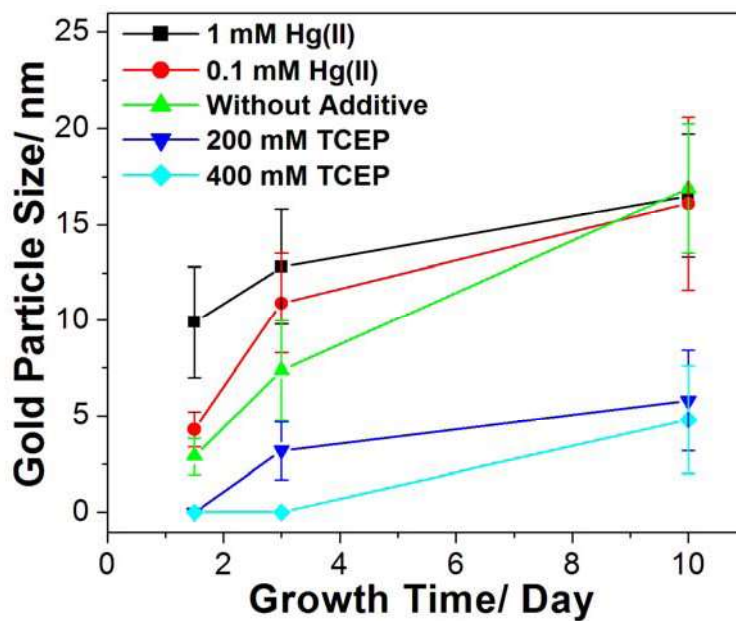


## Decelerate the growth rate of gold nanoparticles by adding TCEP

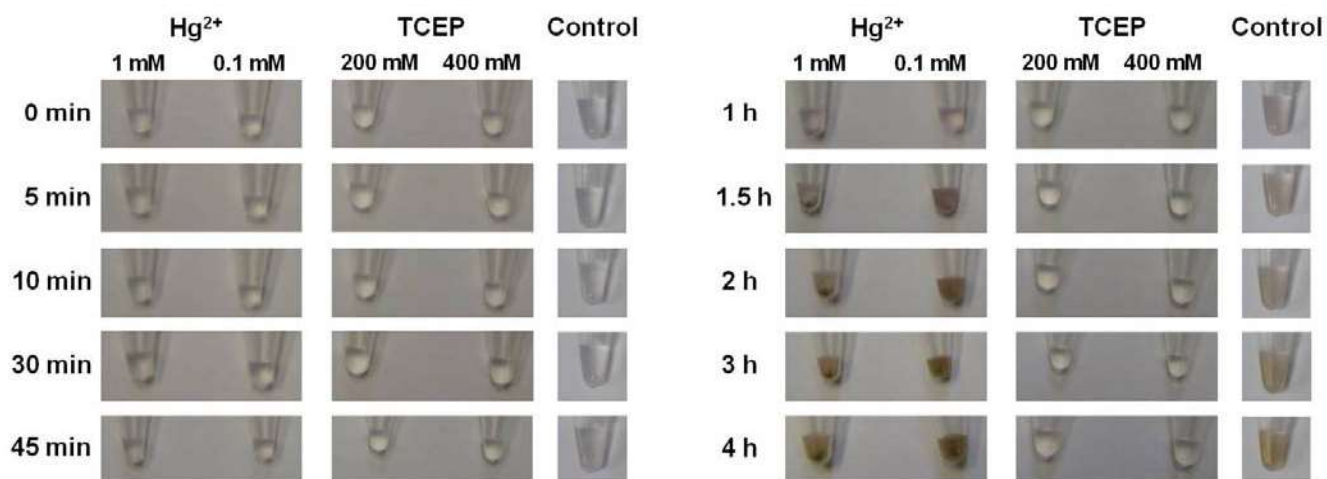


**Figure S16. Fine-tuning the gold nanoparticles growth rates within the lysozyme crystals.**

**a-c**, Accelerating the growth rate by using Hg(II) as an additive. **d-f**, Decelerating the rate of the growth by using TCEP as an additive. **a-c** were taken after ca. 1.5 days of growth, while **d-f** were taken after ca. 3 days of growth.

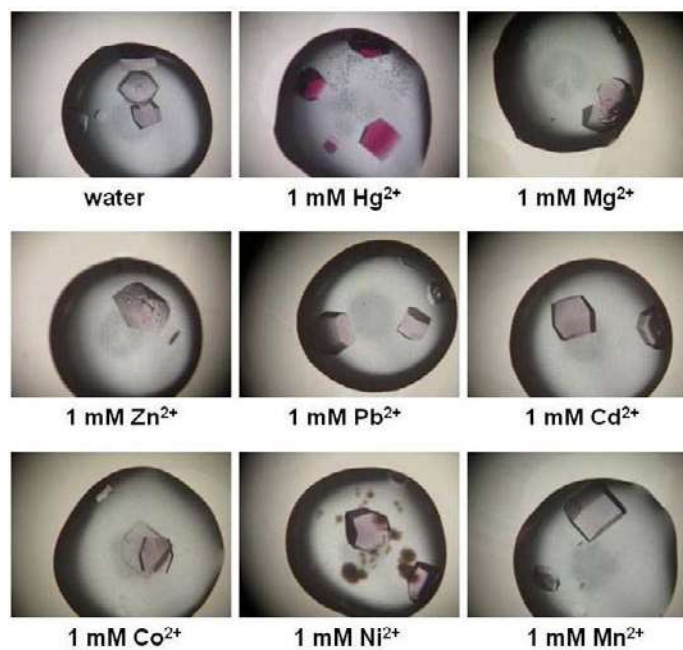


**Figure S17.** The plots of gold nanoparticles size within lysozyme crystals vs. growth time in the absence and presence of different additives.

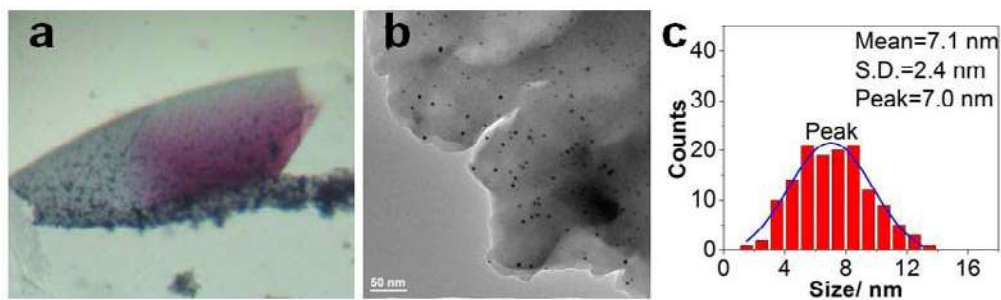


**Figure S18.** Time dependent photos of the disproportionation of 35 mM Au(I) aqueous solution in the absence and presence of  $\text{Hg}^{2+}$  (or TCEP).

The effects  $\text{Hg}^{2+}$  and TCEP of on the **Au(I)** disproportionation were further verified by a solution based study. As shown in Fig. S18,  $\text{Hg}^{2+}$  could accelerate the **Au(I)** disproportionation while TCEP could decelerate the reaction in aqueous solution. The specific interaction between  $\text{Hg}^{2+}$  and **Au(I)** was also demonstrated by a selectivity study as shown in Fig. S19.



**Figure S19.** Photos of the crystals grown from 75 mg/mL lysozyme and 35 mM Au(I) with and without 1 mM metal ions as additives. The photos were taken after about 1.5 days of growth.



**Figure S20.** An image of the crystals grown from 50 mg/mL thaumatin (from *Thaumatococcus daniellii*) and 35 mM **Au(I)** by using 1 mM  $\text{Hg}^{2+}$  as an additive (a), the corresponding TEM image (b) and the size distribution histograms of the gold nanoparticles within the crystal (c).

**Movie files of tomography.**

**S1-Aligned\_Tilt\_Series.avi:** This movie shows the aligned results of the tilt series from  $-51^\circ$  to  $+51^\circ$  with a step size of  $3^\circ$ .

**S1-Reconstruction.avi:** The corresponding three-dimensional reconstructions of the previous movie.

**Table S1.** Data collection and refinement data statistics of lysozyme with **Au(I)**.

<i>Crystal Data</i>	<b>1 Day</b>	<b>2 Days</b>	<b>3 Days</b>	<b>90 Days</b>
Space Group	P4 <sub>3</sub> 2 <sub>1</sub> 2	P4 <sub>3</sub> 2 <sub>1</sub> 2	P4 <sub>3</sub> 2 <sub>1</sub> 2	P4 <sub>3</sub> 2 <sub>1</sub> 2
Unit Cell				
<i>a</i> (Å)	78.584	78.567	78.641	78.543
<i>b</i> (Å)	78.584	78.567	78.641	78.543
<i>c</i> (Å)	37.121	36.794	37.130	37.154
$\alpha$ (°)	90.00	90.00	90.00	90.00
$\beta$ (°)	90.00	90.00	90.00	90.00
$\gamma$ (°)	90.00	90.00	90.00	90.00
<i>Data collection statistics</i>				
Wavelength (Å)	1.1	1.1	1.1	1.1
Resolution (Å)	1.60 (1.66 – 1.60)	1.31 (1.36 – 1.31)	1.31(1.36 – 1.31)	1.31 (1.36 – 1.31)
Total number of reflections	396,076	777,626	775,235	782,959
Number of unique reflections	15,391	28,400	28,645	28,492
R-merge	0.157(0.496)	0.079 (0.454)	0.043 (0.211)	0.162 (0.136)
Redundancy	25.7(26.9)	27.4 (26.8)	27.1 (26.3)	27.5 (26.8)
Completeness (%)	97.5(100.0)	99.8 (100.0)	99.8(99.6)	97.3 (81.6)
I/SigmaI	29.1(11.8)	48.8(4.6)	65.5(16.7)	62.2(24.8)
<i>Refinement statistics</i>				
Resolution (Å)	10.0 – 1.60	10.0 – 1.30	10 – 2.10	10.0 – 1.36
R-all (%)	19.33	20.44	21.03	21.92
R-work (%)	19.33	20.20	20.85	21.59
R-free (%)	23.58	23.41	22.51	24.33
RMS Bond lengths (Å)	0.007	0.011	0.010	0.010
RMS Bond angles (°)	1.943	2.269	2.131	2.118
Metal Ion	1 CL, 2 AU	1 CL, 4 AU	1 CL, 5 AU	8 AU
No. of water molecules	237	202	161	210



**Table S2.** Data collection and refinement data statistics of lysozyme with Au<sup>3+</sup>.

<i>Crystal Data</i>	<b>Lyso-Au<sup>3+</sup></b>
Space Group	P4 <sub>3</sub> 2 <sub>1</sub> 2
Unit Cell	
<i>a</i> (Å)	78.400
<i>b</i> (Å)	78.400
<i>c</i> (Å)	37.224
$\alpha$ (°)	90.00
$\beta$ (°)	90.00
$\gamma$ (°)	90.00
<b><i>Data collection statistics</i></b>	
Wavelength (Å)	1.1
Resolution (Å)	1.50 (1.55 – 1.50)
Total number of reflections	493,833
Number of unique reflections	19,283
R-merge	0.110(0.476)
Redundancy	25.6(23.3)
Completeness (%)	100.0(100.0)
I/SigmaI	29.1(11.8)
<b><i>Refinement statistics</i></b>	
Resolution (Å)	10.0 – 1.60
R-all (%)	21.72
R-work (%)	21.66
R-free (%)	25.50
RMS Bond lengths (Å)	0.008
RMS Bond angles (°)	1.985
Metal Ion	7 AU
No. of water molecules	179

**Table S3.** The B-factors and occupancies of the gold atoms in the lysozyme crystals at different growth stages. The numbering of gold atoms was the same as **Fig. 4**.

1 Day									
	Au1	Au2	Au3	Au4	Au5	Au6	Au7	Au8	Au9
B. F.	72.45	55.10							
Occ.	1.00	0.50							
A. A.	H15	Y23							
2 Days									
	Au1	Au2	Au3	Au4	Au5	Au6	Au7	Au8	Au9
B. F.	62.15	53.98	66.21	53.22					
Occ.	0.50	1.00	1.00	0.50					
A. A.	H15	Y23	S24	R68					
3 Days									
	Au1	Au2	Au3	Au4	Au5	Au6	Au7	Au8	Au9
B. F.	63.95	49.89	59.36	65.44	48.63				
Occ.	0.30	1.00	1.00	1.00	0.50				
A. A.	H15	Y23	S24	R68	R73				
90 Days									
	Au1	Au2	Au3	Au4	Au5	Au6	Au7	Au8	Au9
B. F.		48.48	57.10	48.98	50.95	63.92	75.96	55.59	59.31
Occ.		1.00	1.00	1.00	1.00	1.00	1.00	0.50	1.00
A. A.		Y23	S24	R68	R73	N65	N65	T51	T43

B.F. : B-factor,

Occ. : Occupancy,

A. A. : Amino Acid residues that interacted with the corresponding gold atoms.

**References**

- S1. McCleskey, T.M., Mizoguchi, T.J., Richards, J.H. & Gray, H.B. Electronic spectroscopy of gold(I) Pseudomonas aeruginosa azurin derivatives. *Inorg. Chem.* **35**, 3434-3435 (1996)
- S2. Jadzinsky, P.D., Calero, G., Ackerson, C.J., Bushnell, D.A. & Kornberg, R.D. Structure of a thiol monolayer-protected gold nanoparticle at 1.1 angstrom resolution. *Science* **318**, 430-433 (2007).
- S3. Grabar, K.C., Freeman, R.G., Hommer, M.B. & Natan, M.J. Preparation and Characterization of Au Colloid Monolayers. *Anal. Chem.* **67**, 735-743 (1995).
- S4. Otwinowski, Z. & Minor, W. Processing of X-ray diffraction data collected. *Methods Enzymol.* **276**, 307-326 (1997).
- S5. Vagin, A. & Teplyakov, A. MOLREP: an automated program for molecular replacement. *J. Appl. Crystallogr.* **30**, 1022-1025 (1997).
- S6. Brunger, A.T. et al. Crystallography & NMR system: A new software suite for macromolecular structure determination. *Acta Crystallogr. Sect. D-Biol. Crystallogr.* **54**, 905-921 (1998).
- S7. Sheldrick, G.M. & Schneider, T.R. SHELXL: high-resolution refinement. *Methods Enzymol.* **277**, 319-343 (1997).
- S8. Humphrey, W., Dalke, A. & Schulten, K. VMD: Visual molecular dynamics, *J. Mol. Graph.* **14**, 33-38 (1996).
- S9. PyMOL The PyMOL Molecular Graphics System, Version 1.3, Schrödinger, LLC.
- S10. Harlow, M.L., Ress, D., Stoschek, A., Marshall, R.M. & McMahan, U.J. The architecture of active zone material at the frog's neuromuscular junction. *Nature* **409**, 479-484 (2001).
- S11. Pettersen, E.F. et al. UCSF chimera - A visualization system for exploratory research and analysis. *J. Comput. Chem.* **25**, 1605-1612 (2004).
- S12. Marks, L. D. Experimental studies of small-particle structures, *Rep. Prog. Phys.* **57**, 603-649 (1994).
- S13. Bernardo, A., Calmanovici, C. E. & Miranda, E. A. Observance of polymorphic behavior during dissolution of insulin and lysozyme, *Braz. J. Chem. Eng.* **22**, 331-339 (2005).

# Fast and slow dynamics of the cytoskeleton

LINHONG DENG<sup>1,2\*</sup>, XAVIER TREPAT<sup>1</sup>, JAMES P. BUTLER<sup>1</sup>, EMIL MILLET<sup>1</sup>, KATHLEEN G. MORGAN<sup>3,4</sup>, DAVID A. WEITZ<sup>5</sup> AND JEFFREY J. FREDBERG<sup>1</sup>

<sup>1</sup>Program in Molecular and Integrative Physiological Sciences, Harvard School of Public Health, Boston, Massachusetts 20115, USA

<sup>2</sup>Bioengineering College, Chongqing University, Chongqing 400044, China

<sup>3</sup>Boston Biomedical Research Institute, Watertown, Massachusetts 02472, USA

<sup>4</sup>Department of Medicine, Harvard Medical School, Boston, Massachusetts 20115, USA

<sup>5</sup>Department of Physics, Harvard University, Cambridge, Massachusetts 02138, USA

\*e-mail: ldeng@hsph.harvard.edu

Published online: 9 July 2006; doi:10.1038/nmat1685

**M**aterial moduli of the cytoskeleton (CSK) influence a wide range of cell functions<sup>1–3</sup>. There is substantial evidence from reconstituted F-actin gels that a regime exists in which the moduli scale with frequency with a universal exponent of 3/4. Such behaviour is entropic in origin and is attributable to fluctuations in semiflexible polymers driven by thermal forces<sup>4–7</sup>, but it is not obvious *a priori* that such entropic effects are responsible for the elasticity of the CSK. Here we demonstrate the existence of such a regime in the living cell, but only at high frequencies. Fast events scaled with frequency in a manner comparable to semiflexible-polymer dynamics, but slow events scaled with a non-universal exponent that was systematically smaller than 3/4 and probably more consistent with a soft-glass regime<sup>8,9</sup>. These findings strongly suggest that at smaller timescales elasticity arises from entropic fluctuations of a semiflexible-filament network, whereas on longer timescales slow (soft-glass-like) dynamics of a different origin prevail. The transition between these two regimes occurred on timescales of the order of 0.01 s, thus setting within the slow glassy regime cellular events such as spreading, crawling, contracting, and invading.

A major constituent of the CSK is F-actin. Reconstituted F-actin gels *in vitro* show clear evidence of semiflexible-polymer network dynamics<sup>6,7,10,11</sup>. At lower frequencies,  $f$ , network elasticity is frequency-independent, but at higher frequencies the elasticity approaches a regime where it increases as  $f^{3/4}$ , consistent with the theoretical prediction<sup>4,12–16</sup>

$$G^*(f) \sim (\rho \kappa l_p / 15) (4i \zeta \pi f / \kappa)^{3/4}, \quad (1)$$

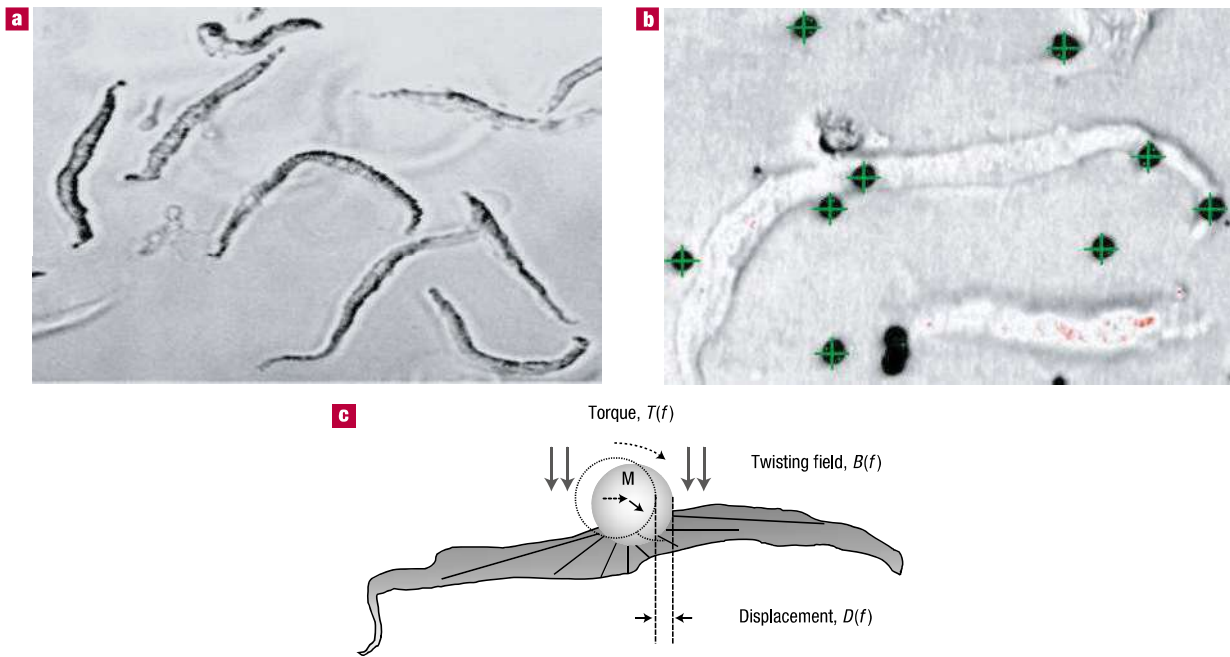
where  $G^*(f)$  is the complex modulus,  $\rho$ ,  $\kappa$ ,  $\zeta$ , and  $l_p$  are the density, bending stiffness, lateral drag coefficient, and persistence length of actin filaments in the gel, respectively, and  $i^2 = -1$ ; here we have suppressed a small newtonian viscosity that contributes little except at very high frequencies. Equation (1) is a consequence of filament entropy wherein elasticity at high frequencies becomes dominated

by lateral bending fluctuations of semiflexible filaments (F-actin) driven by thermal perturbations<sup>4,12,15,16</sup>. This behaviour has been found to hold in a variety of F-actin solutions over wide ranges of actin concentration, extent of entanglement, and gel crosslinking<sup>14</sup>.

Dynamics of this type have yet to be observed in the living cell<sup>4–7</sup>. Moreover, in the highly crosslinked and short-filament networks of the cell, and under the appreciable pre-stress to which the cell is subjected<sup>17</sup>, it is not obvious that entropic effects can be responsible for the elasticity. Indeed, in a variety of cell types, as well as in F-actin gels that are pre-stressed and crosslinked by filamin, dynamics of a rather different type have recently been reported<sup>8,9,18–20</sup>.

To fill this gap and to assess the existence of a regime comparable to that suggested by equation (1), here we report rheological properties of the freshly isolated living airway smooth muscle (ASM) cell. Compared with the CSK of the smooth muscle cell passaged in culture, that of the freshly isolated smooth muscle cell has substantially more organization<sup>21</sup>, higher density of contractile filaments, more smooth-muscle-specific actin-binding proteins (h-caldesmon, h-1 calponin, and sm22) and myofibril bundles, but fewer microtubules (K.M., personal communication). In addition, the freshly dissociated ASM cell has a long worm-like shape that more closely approximates the morphology of the ASM cell *in situ*<sup>22,23</sup> (Fig. 1a). In these cells, we measured  $G^*$  as described in the Methods section. Collectively, data spanned baseline, relaxation, and contraction conditions, and spanned four orders of magnitude in frequency.

Variability of  $G'$  (the real part of  $G^*$ ) from bead-to-bead was extensive and approximated a log-normal distribution, as is found in other cell preparations<sup>19,24</sup>. Nonetheless, from bead-to-bead the frequency dependence of  $G'$  was highly consistent (Fig. 2a).  $G''$  (the imaginary part of  $G^*$ ) exhibited a comparable degree of variability and increased systematically with frequency (Fig. 2b). Although both  $G'$  and  $G''$  were highly variable across cells, the variability of their ratio (loss tangent,  $\eta$ ) was slight (Fig. 2b, inset). Pooled data for  $G'$  (geometric mean and geometric standard error) increased



**Figure 1** Freshly isolated bovine trachea smooth muscle cells, with bound beads, and the twisting cytometry method. **a**, Photomicrograph of freshly isolated bovine trachea smooth muscle cells (typically 150 to 200 micrometres long) adhered to a poly-L-lysine substrate. Note the typical long worm-like appearance. 4–5 h after first settling on the substrate, healthy cells usually established firm attachment with various contact points. **b**, Bovine trachea smooth muscle cells with beads attached. RGD-coated ferrimagnetic beads were introduced and allowed to bind to the integrin receptors on the surface of the adherent cells (20 min). A charge-coupled device camera was used to identify each bead, which was then marked with a cross-hair determined by the centre position of its image. **c**, Schematic diagram of the magnetic twisting cytometry method in which the bead was oscillated at a frequency,  $f$ , from 0.09 to 1,000 Hz by a torque,  $T$ , caused by a sinusoidal magnetic field,  $B$ , of 20 G magnitude at  $f$ . The resultant sinusoidal displacement,  $D$ , of the bead was measured from the recorded bead positions during the oscillation.

slowly with frequency at frequencies below 100 Hz, but much more rapidly at frequencies greater than 100 Hz (Fig. 3). Compared with the frequency dependence of  $G'$ , that of  $G''$  was smaller at lower frequencies but higher at higher frequencies.

On a cell-by-cell basis, we fitted these data in the complex plane (see the Methods section) to the relationship  $G^*(f) = A(if)^\alpha + B(if)^\beta$ .  $G'$  data were well represented by the best fit, but  $G''$  data at lower frequencies fell systematically above and had weaker frequency dependence than indicated by the best fit (Fig. 3, solid lines); similar discrepancies have been reported in bronchial epithelial cells, macrophages and neutrophils<sup>24</sup>, and are a signature of soft glassy materials that are ageing<sup>25–28</sup>.

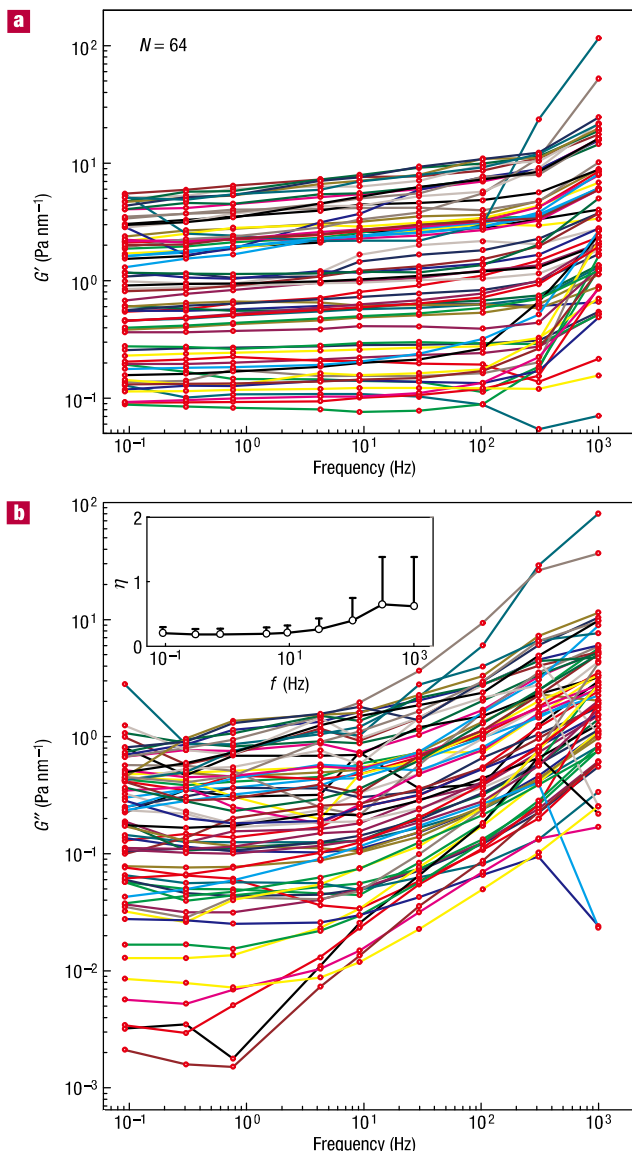
Although our technology is limited to frequencies below 1 kHz, our data were sufficient to resolve the exponents  $\alpha$  and  $\beta$  and put relatively narrow bounds on their values (see the additional comments on statistical tests in the Supplementary Information). Across the cell population ( $N = 64$ ), the distributions of  $\alpha$  and  $\beta$  were approximately normal (Fig. 4). The mean of  $\alpha$  was 0.05 (95% confidence interval 0.04–0.06) and was different from zero ( $p < 0.00001$ ); as described below, this implies that at low frequencies the system did not approach a hookean limit. The mean of  $\beta$  was 0.75, (95% confidence interval 0.69–0.79) and was different from unity ( $p < 0.00001$ ); as described below, this implies that at high frequencies the system did not approach a newtonian limit. Indeed, setting  $\beta$  to unity degraded the fit and adding a newtonian viscous term led to a result that was physically unrealizable (see the Supplementary Information).

Distinct values of  $\alpha$  and  $\beta$  imply that the rheology in these cells was characterized by two distinct regimes. In excess of 100 Hz, the complex modulus approached  $f^{0.75}$ , a scaling behaviour consistent

with that predicted by the theory of semiflexible polymers<sup>4,12,15,16</sup>. Such high-frequency dynamics have not been noted previously in the living cell although, in retrospect, a hint of such behaviour is evident in cells passaged in culture<sup>24</sup>. In contrast, at lower frequencies semiflexible-polymer dynamics became subdominant, with the complex modulus scaling as  $f^{0.05}$ . This exponent was non-universal, as shown below, and was systematically smaller than that observed in ASM cells passaged in culture, where, typically,  $0.1 < \alpha < 0.3$  (refs 8,17,24,29), but is comparable to that found in intact activated ASM strips (data not shown).

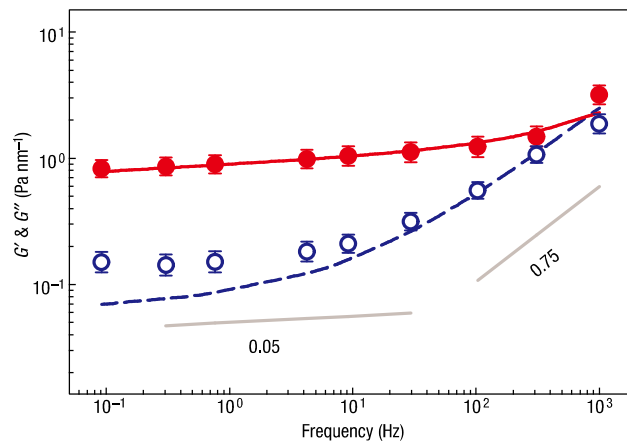
$G^*$  increased with contractile activation (KCl, 80 mM) and decreased with relaxation (dibutyl cAMP, 1 mM) (Supplementary Information, Fig. S1). The exponent  $\beta$  was not influenced by relaxation, but decreased during contraction from 0.75 to 0.64 (95% confidence interval 0.57 to 0.71) (Supplementary Information Fig. S2, top), suggesting that contraction altered the qualitative nature of the high-frequency behaviour, whereas relaxation did not. Values of  $\beta$  smaller than 3/4 are consistent with behaviour observed in pre-stressed F-actin gels<sup>14</sup>. Indeed, pre-stress in cells<sup>17,30</sup> and in filamin-crosslinked gels<sup>20</sup> is known to be a major determinant of dynamics in the slow glassy regime, but the role of pre-stress in the fast regime could not be addressed in the experiments described here and remains a major open question. The exponent  $\alpha$  decreased slightly during cell contraction, but during cell relaxation it increased from 0.05 to 0.08 (95% confidence interval 0.06 to 0.09) (Supplementary Information, Fig. S2, bottom).

Why should material moduli at low frequencies scale with a weak non-universal exponent? When taken together with other observations, such behaviour has been taken as strong evidence



**Figure 2** Storage modulus ( $G'$ ) and loss modulus ( $G''$ ) as a function of frequency for all beads measured ( $N=64$ ). a,b,  $G'$  (a) and  $G''$  (b) varied broadly across beads, approximately log-normally. However, the hysteresivity or loss tangent  $\eta = G''/G'$  varied little across beads, and only weakly with frequency (inset, mean  $\pm$  standard deviation).

for non-equilibrium behaviour and, in particular, a glassy regime of CSK dynamics has been suggested<sup>8,9</sup>. The ability of a liquid to form a glass is related to slowly relaxing degrees of freedom which, under certain conditions, may persist out of equilibrium<sup>31</sup>. By the term ‘slow’, here we mean processes that decay more slowly than any exponential, such as logarithmic or weak power-law decay. In various inert glassy systems, slow degrees of freedom have been attributed to a variety of possibilities, including slow motions of polymer chains constrained by chemical crosslinks, entanglements or loops, slow turnover of covalent or non-covalent bonds connecting constituent structures to form a bond network, slow relaxation towards energetically favourable configurations, and slow structural rearrangements arising from crowding, caging, and jamming<sup>32–35</sup>. Despite this variety, traditional glassy systems share one feature in common: slow localized inelastic rearrangements,



**Figure 3** Pooled data of  $G'$  (red, filled circles) and  $G''$  (blue, open circles) from all individual beads, together with the average two-term power-law fit (solid lines). The data presented are the geometric mean, and the corresponding error bars represent the geometric standard error defined as the standard error of the data set in logarithmic space. The solid lines represent the two-term power-law fit with geometric means of  $A$  and  $B$ , and arithmetic means of  $\alpha$  and  $\beta$ . This graph clearly demonstrates the two regimes of frequency dependence measured in the freshly isolated ASM cell. At lower frequencies, the moduli increased with frequency as a weak power law with exponent 0.05. At higher frequencies, the moduli increased as a stronger power law with exponent 0.75. The transition occurred at about 100 Hz. The straight grey lines denote slopes of 0.05 and 0.75.

and the applicability of such a point of view is justified by the universality of the phenomenology<sup>25,31</sup>. In the living cell, none of the above can be ruled out and, as we suggested previously, ATP-dependent rearrangements might modify CSK microconfigurations and thereby provide an alternate means of exploring new network configurations<sup>9</sup>. ATP hydrolysis can drive both conformational changes and polymerization/depolymerization cycles of CSK proteins, either or both of which could conceivably resolve constraints and drive structural rearrangements.

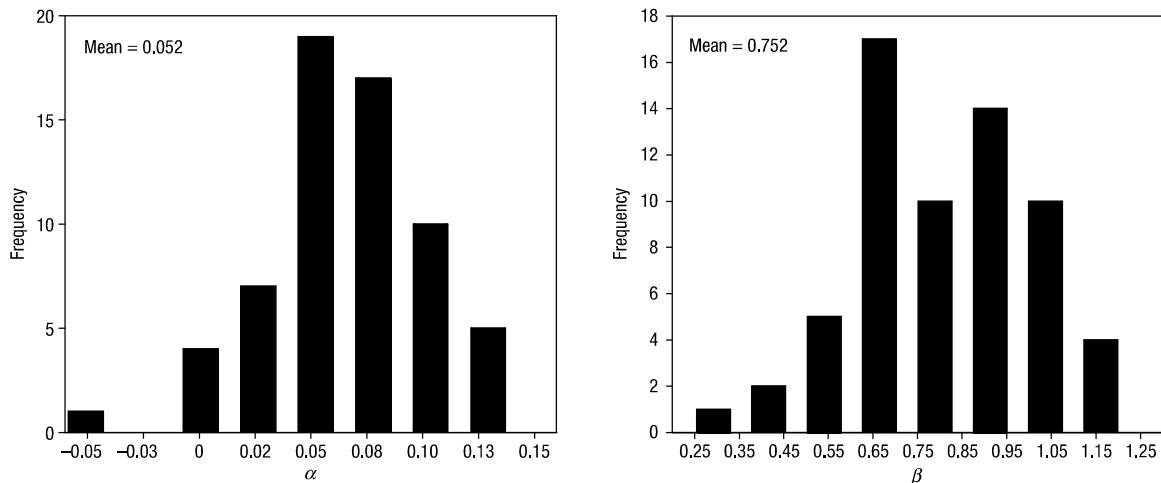
Consistent with that physical picture<sup>9,25,36</sup>, but in contrast with equation (1), the complex modulus of the ASM cell passaged in culture has been shown to go as<sup>8,24</sup>

$$G^*(f) \sim G_0 \Gamma(1-\alpha) \{i2\pi f / \Phi_0\}^\alpha, \quad (2)$$

where  $\Gamma()$  is the gamma function, and  $G_0$  and  $\Phi_0$  are scale factors for stiffness and frequency, respectively, and again we have suppressed a small newtonian viscosity.

We suggest that equations (1) and (2) describe the high-frequency [ $B(if)^{3/4}$ ] and low-frequency [ $A(if)^\alpha$ ] terms of the best fit, respectively. As regards low-frequency behaviour of the CSK<sup>8,18,19,24,29</sup> and equation (2), the non-universal exponent  $\alpha$  becomes a continuous measure of proximity of the CSK to solid-like ( $\alpha = 0$ ;  $G'' = 0$ ) versus fluid-like ( $\alpha = 1$ ;  $G' = 0$ ) behaviours. In contrast, the observation of  $G^*$  approaching  $f^{3/4}$  at higher frequencies suggests the emergence of entropic dynamics associated with semiflexible polymers and in this report it is identified for the first time in living cells. Despite uncertainties in the values of the various factors in equation (1), values found in the literature yield a prefactor,  $B$ , that is within an order of magnitude of that which was observed experimentally; this correspondence represents independent evidence that the fast regime indeed arises from dynamics of semiflexible polymers.

Therefore, we conclude that in the living cell the dynamics of semiflexible polymers and soft glasses coexist, but each dominates



**Figure 4** Distributions of the two exponents,  $\alpha$  and  $\beta$ , that characterize the two distinct regimes of CSK dynamics. These were both approximately normal. The mean and standard deviation of  $\alpha$  were 0.05 and 0.036, respectively (95% confidence interval 0.04–0.06). The mean and standard deviation of  $\beta$  were 0.75 and 0.19 (95% confidence interval 0.69–0.79). A Student's *t*-test verified that  $\alpha$  was significantly different from zero ( $p < 0.00001$ ), and  $\beta$  was significantly different from unity ( $p < 0.00001$ ), but not different from 0.75 ( $p > 0.5$ ).

on different timescales. On shorter timescales (higher frequencies), there is insufficient time for inelastic structural rearrangements and, as such, relatively fast thermal fluctuations drive bending of semiflexible CSK filaments and determine material properties of the CSK. In this fast regime, as crosslink density increases, entropic contributions to the elasticity diminish relative to the enthalpic contributions<sup>14</sup>. However, on longer timescales (lower frequencies) slow inelastic rearrangements of the CSK prevail<sup>8,9</sup>, and the effects of thermally driven filament bending become subdominant. Such an interpretation implies sustained departure from thermodynamic equilibrium and is consistent with the finding that in the living ASM cell on longer timescales the generalized Stokes–Einstein relationship breaks down<sup>9</sup>.

It was not obvious *a priori* that entropic effects could be responsible for cell elasticity. The results presented here are the first evidence to suggest that they are. As these results resemble so clearly what is seen in simple reconstituted but crosslinked actin networks, they also strongly support the idea that the bead-twisting probe we used is most sensitive to the cytoskeletal actin network. All prior measurements in other cell systems show power-law responses with non-universal exponents in the range 0.1–0.3 (refs 8,17–19,24,29), and it was not clear from those measurements if a distinct high-frequency regime might exist. The results presented here show that such a regime does exist and that its exponent is 3/4.

As such, data reported here unify within the same cell these two distinct schools of thought, and suggest that the transition between regimes occurs on timescales of the order of  $10^{-2}$  s. Accordingly, these data set within the slow glassy regime timescales typical of integrated mechanical events of the cell such as spreading, crawling, contracting, and invading.

## METHODS

All chemical reagents, standard buffer solutions, and media were purchased from Sigma unless stated otherwise.

### PREPARATION OF INTACT LIVING CELLS

Single ASM cells were freshly isolated from bovine trachea by enzymatic digestion, which was adopted from a previously described method<sup>23</sup>. Briefly, a

bovine trachea was obtained from an abattoir and transported to the laboratory within 2 h of excision. Before use, the tissue was maintained at 4 °C in an oxygenated (95% O<sub>2</sub> and 5% CO<sub>2</sub>) buffer containing 1:1 Hank's balanced salt solution and Dulbecco's modified Eagle's medium, and 1,000 Unit ml<sup>-1</sup> of penicillin and streptomycin. Subsequently, in constantly oxygenated Krebs solution (120 mM NaCl, 5.9 mM KCl, 1.2 mM NaH<sub>2</sub>PO<sub>4</sub>, 25 mM NaHCO<sub>3</sub>, 11.5 mM dextrose, 1 mM CaCl<sub>2</sub>, and 1.4 mM MgCl<sub>2</sub>), 50 mg wet weight of ASM was dissected from the trachea and cut into 2 × 3 mm pieces. The tissue was then transferred into a siliconized, that is, coated with SigmaCote, flask containing an enzymatic digestion solution. The digestion solution consisted of 182 Unit ml<sup>-1</sup> Type 2 collagenase (Worthington), 3.0 Unit ml<sup>-1</sup> Grade II elastase (Roche Diagnostics), and 5,000 Unit ml<sup>-1</sup> Type II-S soybean trypsin inhibitor in a Ca<sup>2+</sup> and Mg<sup>2+</sup> free buffer consisting of 137 mM NaCl, 5.4 mM KCl, 5.6 mM dextrose, 4.2 mM NaHCO<sub>3</sub>, 0.42 mM Na<sub>2</sub>HPO<sub>4</sub>, 0.44 mM KH<sub>2</sub>PO<sub>4</sub>, and 0.075% bovine serum albumin. The tissue was incubated in this digestion solution in a shaking water bath (9.6 cycles min<sup>-1</sup>) at 34 °C and oxygenated atmosphere for 40 min. The dissociated cells were filtered through nylon gauze (526 μm mesh size) and rinsed with 10 ml of the Ca<sup>2+</sup> and Mg<sup>2+</sup> free buffer. More cells may be harvested by repeatedly incubating the remaining tissue in the digestion solution, but in a progressively reduced concentration of collagenase.

Dissociated cells were poured over glass coverslips or 96 wells coated with poly L-lysine and incubated for 40 min on ice. Cell viability was verified by KCl-induced contraction of sample cells in each batch of harvested cells.

Because these cells were adherent on a rigid substrate at the time of measurement, all contractions were isometric. Although we did not use traction microscopy to measure contractile stresses, as we have in our previous work<sup>17,30</sup>, these cells probably do maintain appreciable axial tension.

### MEASUREMENT OF THE DYNAMIC MODULUS

To probe the microrheology of CSK, ferrimagnetic beads (4.5 μm diameter) were coated with a synthetic peptide containing the Arg–Gly–Asp (RGD; Peptide 2000, Integra Life Sciences) sequence and allowed to adhere to the apical cell surface. These beads become tightly tethered to the F-actin CSK through transmembrane integrin receptors, mostly  $\alpha_5\beta_1$ ; these receptors bind to the RGD ligand in the extracellular domain and the focal adhesion and actin filaments in the intracellular domain<sup>1,8,24,29,37–39</sup> (Fig. 1b). We then measured the complex modulus as a function of frequency by applying an oscillatory magnetic field and measuring the resultant oscillatory bead motions with light microscopy<sup>24,37</sup> (Fig. 1c). When the oscillatory magnetic field of frequency  $f$  was applied to the bead, it resulted in an oscillatory torque  $\tilde{T}$ , where the tilde overbar denotes the Fourier domain. The induced lateral displacement of the

bead,  $\tilde{D}$ , was measured using a charge-coupled device camera attached to an inverted optical microscope (Leica Microsystems). The complex modulus is then simply

$$G^*(f) = \tilde{T}/\tilde{D}.$$

$G^*$  measured in this way has units of torque per unit bead volume per unit bead displacement, or Pa nm<sup>-1</sup>. This can be converted to familiar material moduli with the use of a length scale derived from a model of cell deformation<sup>40</sup>, but to avoid model-dependent assumptions here we report all data in primary measurement units of Pa nm<sup>-1</sup>.

#### DATA ANALYSIS AND FITTING

Denote the complex modulus of the  $n$ th bead at frequency  $f_m$  by  $G_n^*(f_m)$ . For each bead (that is, for each  $n$ ), the two-term power-law model,  $G^*(f) = A(if)^\alpha + B(if)^\beta$  was fitted to these data by minimizing  $\sum_{m=1, M} |\log G_n^*(f_m) - \log G_n^*(f_m)|^2$  with respect to the parameters  $A, B, \alpha, \beta$ .  $M$  is the number of frequencies used, typically 9, spanning 0.1 Hz to 1 kHz in half log increments. The distributions of the parameters obtained from this bead-by-bead fit were examined statistically. R project, a freely available statistical software package ([www.r-project.org](http://www.r-project.org)), was used to fit the model to the data and for statistical analysis. One-way analysis of variance, and Student's  $t$ -test were used to examine the differences in the parameters when compared among multiple conditions or between two conditions, respectively. Differences with  $p < 0.05$  were considered statistically significant.

Received 17 February 2006; accepted 19 May 2006; published 9 July 2006.

#### References

- Chicurel, M. E., Chen, C. S. & Ingber, D. E. Cellular control lies in the balance of forces. *Curr. Opin. Cell Biol.* **10**, 232–239 (1998).
- Discher, D. E., Janmey, P. & Wang, Y. L. Tissue cells feel and respond to the stiffness of their substrate. *Science* **310**, 1139–1143 (2005).
- Janmey, P. A. & Weitz, D. A. Dealing with mechanics: mechanisms of force transduction in cells. *Trends Biochem. Sci.* **29**, 364–370 (2004).
- Gittes, F., Schnurr, B., Olmsted, P. D., MacKintosh, F. C. & Schmidt, C. F. Microscopic viscoelasticity: Shear moduli of soft materials determined from thermal fluctuations. *Phys. Rev. Lett.* **79**, 3286–3289 (1997).
- Morse, D. C. Viscoelasticity of concentrated isotropic solutions of semiflexible polymers. 2. Linear response. *Macromolecules* **31**, 7044–7067 (1998).
- Gardel, M. L., Valentine, M. T., Crocker, J. C., Bausch, A. R. & Weitz, D. A. Microrheology of entangled F-actin solutions. *Phys. Rev. Lett.* **91**, 158302 (2003).
- Gardel, M. L. *et al.* Elastic behavior of cross-linked and bundled actin networks. *Science* **304**, 1301–1305 (2004).
- Fabry, B. *et al.* Scaling the microrheology of living cells. *Phys. Rev. Lett.* **87**, 148102 (2001).
- Bursac, P. *et al.* Cytoskeletal remodeling and slow dynamics in the living cell. *Nature Mater.* **4**, 557–561 (2005).
- Kas, J., Strey, H. & Sackmann, E. Direct imaging of reptation for semiflexible actin filaments. *Nature* **368**, 226–229 (1994).
- MacKintosh, F. C., Kas, J. & Janmey, P. A. Elasticity of semiflexible biopolymer networks. *Phys. Rev. Lett.* **75**, 4425–4428 (1995).
- Gittes, F. & MacKintosh, F. C. Dynamic shear modulus of a semiflexible polymer network. *Phys. Rev. E* **58**, R1241–R1244 (1998).
- Gisler, T. & Weitz, D. A. Scaling of the microrheology of semidilute F-actin solutions. *Phys. Rev. Lett.* **82**, 1606–1609 (1999).
- Gardel, M. L. *et al.* Scaling of F-actin network rheology to probe single filament elasticity and dynamics. *Phys. Rev. Lett.* **93**, 188102 (2004).
- Morse, D. C. Viscoelasticity of tightly entangled solutions of semiflexible polymers. *Phys. Rev. E* **58**, R1237–R1240 (1998).
- Morse, D. C. Viscoelasticity of concentrated isotropic solutions of semiflexible polymers. 1. Model and stress tensor. *Macromolecules* **31**, 7030–7043 (1998).
- Stamenovic, D., Suki, B., Fabry, B., Wang, N. & Fredberg, J. J. Rheology of airway smooth muscle cells is associated with cytoskeletal contractile stress. *J. Appl. Physiol.* **96**, 1600–1605 (2004).
- Alcaraz, J. *et al.* Microrheology of human lung epithelial cells measured by atomic force microscopy. *Biophys. J.* **84**, 2071–2079 (2003).
- Desprat, N., Richert, A., Simeon, J. & Asnacios, A. Creep function of a single living cell. *Biophys. J.* **88**, 2224–2233 (2005).
- Gardel, M. L. *et al.* Prestressed F-actin networks cross-linked by hinged filamins replicate mechanical properties of cells. *Proc. Natl Acad. Sci. USA* **103**, 1762–1767 (2006).
- Draeger, A., Stelzer, E., Herzog, M. & Small, J. Unique geometry of actin-membrane anchorage sites in avian gizzard smooth muscle cells. *J. Cell Sci.* **94**, 703–711 (1989).
- Bagby, R. M., Young, A. M., Dotson, R. S., Fisher, B. A. & McKinnon, K. Contraction of single smooth muscle cells from *Bufo marinus* stomach. *Nature* **234**, 351–352 (1971).
- DeFeo, T. T. & Morgan, K. G. Responses of enzymatically isolated mammalian vascular smooth muscle cells to pharmacological and electrical stimuli. *Pflugers Arch.* **404**, 100–102 (1985).
- Fabry, B. *et al.* Time scale and other invariants of integrative mechanical behavior in living cells. *Phys. Rev. E* **68**, 041914 (2003).
- Sollich, P., Lequeux, F., Hebraud, P. & Cates, M. E. Rheology of soft glassy materials. *Phys. Rev. Lett.* **78**, 2020–2023 (1997).
- Cates, M. E. & Sollich, P. in *Foams and Emulsions* (eds Sadoc, J. F. & Rivier, N.) 207–236 (Kluwer Academic, Dordrecht, 1999).
- Mason, T. G., Gisler, T., Kroy, K., Frey, E. & Weitz, D. A. Rheology of F-actin solutions determined from thermally driven tracer motion. *J. Rheol.* **44**, 917–928 (2000).
- Gopal, A. D. & Durian, D. J. Relaxing in foam. *Phys. Rev. Lett.* **91**, 188303 (2003).
- Puig-de-Morales, M. *et al.* Cytoskeletal mechanics in adherent human airway smooth muscle cells: probe specificity and scaling of protein-protein dynamics. *Am. J. Physiol. Cell Physiol.* **287**, C643–C654 (2004).
- Wang, N. *et al.* Cell prestress. 1. Stiffness and prestress are closely associated in adherent contractile cells. *Am. J. Physiol. Cell Physiol.* **282**, C606–C616 (2002).
- Bulatov, V. V. & Argon, A. S. A stochastic-model for continuum elastoplastic behavior. 2. A study of the glass-transition and structural relaxation. *Modelling Simul. Mater. Sci. Eng.* **2**, 185–202 (1994).
- Weeks, E. R., Crocker, J. C., Levitt, A. C., Schofield, A. & Weitz, D. A. Three-dimensional direct imaging of structural relaxation near the colloidal glass transition. *Science* **287**, 627–631 (2000).
- Mazurin, O. V. Theory of glass-transition—chemical-equilibria approach. *J. Non-Cryst. Solids* **129**, 259–265 (1991).
- Kovacs, A. J., Aklonis, J. J., Hutchinson, J. M. & Ramos, A. R. Isobaric volume and enthalpy recovery of glasses. 2. Transparent multi-parameter theory. *J. Polym. Sci. Polym. Phys.* **17**, 1097–1162 (1979).
- Chen, H. S. & Turnbull, D. Evidence of a glass-liquid transition in a gold-germanium-silicon alloy. *J. Chem. Phys.* **48**, 2560–2571 (1968).
- Sollich, P. Rheological constitutive equation for a model of soft glassy materials. *Phys. Rev. E* **58**, 738–759 (1998).
- Wang, N., Butler, J. P. & Ingber, D. E. Mechanotransduction across the cell surface and through the cytoskeleton. *Science* **260**, 1124–1127 (1993).
- Deng, L., Fairbank, N. J., Fabry, B., Smith, P. G. & Maksym, G. N. Localized mechanical stress induces time-dependent actin cytoskeletal remodeling and stiffening in cultured airway smooth muscle cells. *Am. J. Physiol. Cell Physiol.* **287**, C440–C448 (2004).
- Choquet, D., Felsenfeld, D. P. & Sheetz, M. P. Extracellular matrix rigidity causes strengthening of integrin-cytoskeleton linkages. *Cell* **88**, 39–48 (1997).
- Mijailovich, S. M., Kojic, M., Zivkovic, M., Fabry, B. & Fredberg, J. J. A finite element model of cell deformation during magnetic bead twisting. *J. Appl. Physiol.* **93**, 1429–1436 (2002).

#### Acknowledgements

The authors would like to thank C. Gallant for her assistance in the adaptation of the cell isolation method. X.T. is supported by a postdoctoral fellowship from the Spanish Ministerio de Educación y Ciencia. This study was financially supported by NIH HL65960, HL33009 and HL31704. Correspondence and requests for materials should be addressed to L.D. Supplementary Information accompanies this paper on [www.nature.com/naturematerials](http://www.nature.com/naturematerials).

#### Competing financial interests

The authors declare that they have no competing financial interests.

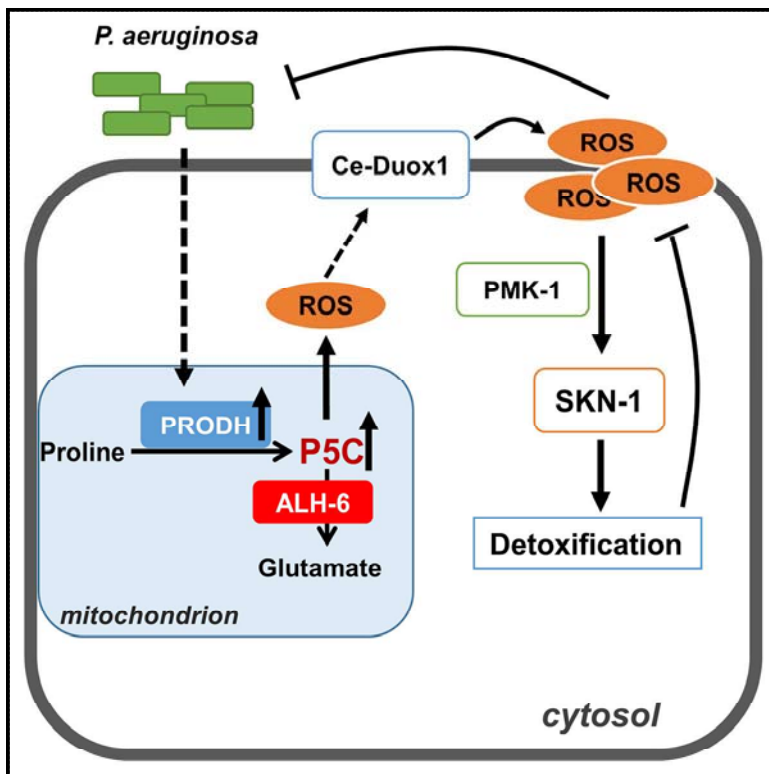
Reprints and permission information is available online at <http://npg.nature.com/reprintsandpermissions/>



# Cell Reports

## Proline Catabolism Modulates Innate Immunity in *Caenorhabditis elegans*

### Graphical Abstract



### Authors

Haiqing Tang, Shanshan Pang

### Correspondence

hqtang@cqu.edu.cn (H.T.),  
sspang@cqu.edu.cn (S.P.)

### In Brief

Tang and Pang show that proline catabolism is a component of the innate immune system in *C. elegans*. In response to *P. aeruginosa* infection, proline catabolic enzymes modulate ROS homeostasis and subsequent SKN-1 activation, likely through metabolic intermediate P5C and dual-oxidase Ce-Duox1/BLI-3.

### Highlights

- Mitochondrial proline catabolism is essential for pathogen resistance in *C. elegans*
- Proline catabolism regulates infection-induced SKN-1 activation through ROS
- Metabolic intermediate P5C may account for ROS production and SKN-1 activation
- Ce-Duox1/BLI-3 is required for proline catabolism-induced ROS and SKN-1 responses



Tang & Pang, 2016, Cell Reports 17, 2837–2844  
December 13, 2016 © 2016 The Author(s).  
<http://dx.doi.org/10.1016/j.celrep.2016.11.038>

CellPress

# Proline Catabolism Modulates Innate Immunity in *Caenorhabditis elegans*

Haiqing Tang<sup>1,\*</sup> and Shanshan Pang<sup>1,2,\*</sup>

<sup>1</sup>School of Life Sciences, Chongqing University, Chongqing 401331, China

<sup>2</sup>Lead Contact

\*Correspondence: [hqtang@cqu.edu.cn](mailto:hqtang@cqu.edu.cn) (H.T.), [sspang@cqu.edu.cn](mailto:sspang@cqu.edu.cn) (S.P.)

<http://dx.doi.org/10.1016/j.celrep.2016.11.038>

## SUMMARY

Metabolic pathways are regulated to fuel or instruct the immune responses to pathogen threats. However, the regulatory roles for amino acid metabolism in innate immune responses remains poorly understood. Here, we report that mitochondrial proline catabolism modulates innate immunity in *Caenorhabditis elegans*. Modulation of proline catabolic enzymes affects host susceptibility to bacterial pathogen *Pseudomonas aeruginosa*. Mechanistically, proline catabolism governs reactive oxygen species (ROS) homeostasis and subsequent activation of SKN-1, a critical transcription factor regulating xenobiotic stress response and pathogen defense. Intriguingly, proline catabolism-mediated activation of SKN-1 requires cell-membrane dual-oxidase Ce-Duox1/BLI-3, highlighting the importance of interaction between mitochondrial and cell-membrane components in host defense. Our findings reveal how animals utilize metabolism of a single amino acid to defend against a pathogen and identify proline catabolism as a component of innate immune signaling.

## INTRODUCTION

Cellular metabolism is regulated or reprogrammed to support immune functions (Ganeshan and Chawla, 2014; Pearce and Pearce, 2013). Metabolic reprogramming provides activated immune cells with sufficient ATP to match their considerable energetic demands. Metabolic pathways, such as glycolysis, glutaminolysis, and fatty acid oxidation, are preferentially utilized by various immune cells to generate energy (Ganeshan and Chawla, 2014). On the other hand, metabolic intermediates can act as signaling molecules in immune responses. For example, the rise of succinate, a metabolite from tricarboxylic acid (TCA) cycle, is identified as an endogenous danger signal to initiate proinflammatory responses in macrophages (Tannahill et al., 2013). The metabolism of amino acids, representing an essential pool of nutrients utilized for cellular energy production, also plays regulatory roles in immune functions. Catabolism of arginine and tryptophan is found to be critical for regulation of T cell functions

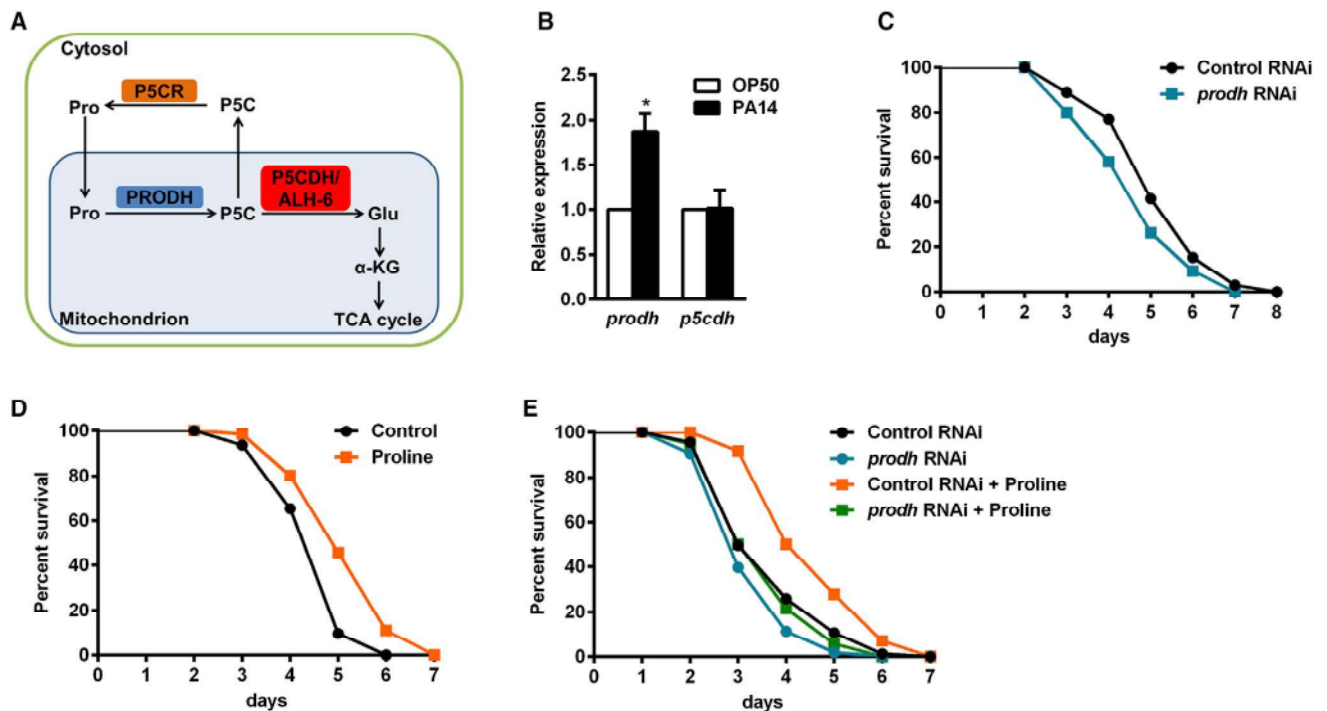
(Bronte and Zanovello, 2005; Bronte et al., 2003; Grohmann and Bronte, 2010). However, the regulatory roles for other amino acid metabolisms in immune responses, especially innate immunity, remain poorly understood.

Proline is one of amino acids whose metabolism impacts multiple cellular functions. Mitochondrial proline dehydrogenase (PRODH), the first enzyme of proline catabolism, is a well-known tumor regulator involved in cancer cell autophagy, proliferation, and apoptosis (Liu et al., 2012a, 2012b, 2006, 2009). PRODH also promotes fat utilization in starved adipocytes to prevent cell death (Lettieri Barbato et al., 2014). Both we and others have shown that, under nutrient stress, *C. elegans* utilizes proline catabolism to promote stress responses, which impacts animal survival (Pang and Curran, 2014; Zarse et al., 2012). Despite the essential roles for proline catabolism in multiple fundamental cellular processes, its contribution to animal innate immunity is unclear.

Innate immunity is an ancient and conserved system that serves as the first line of defense against invading pathogens. During infection, antimicrobial reactions are activated to directly eliminate invading pathogens. Meanwhile, host-resistant responses, such as detoxification, are exploited to limit the deleterious impact caused by pathogen infection (Schneider and Ayres, 2008). *C. elegans* provides a valuable genetic model for studying the conserved players of animal innate immune systems. One major factor responsible for host immunity in *C. elegans* is the Nrf protein ortholog SKN-1, a transcription factor that promotes host resistance by inducing genes involved in detoxification of reactive oxygen species (ROS) and harmful bacterial components (Hoeven et al., 2011; Papp et al., 2012). In response to bacterial pathogen, cell-membrane dual-oxidase Ce-Duox1/BLI3 generates ROS, which are important for pathogen resistance by acting as microbicidal molecules (Chávez et al., 2009). On the other hand, ROS could also function as signaling molecules to induce SKN-1 activation in a p38/PMK-1-dependent manner (Hoeven et al., 2011); however, the signaling components of this key host immune pathway remain poorly defined.

In this study, we investigated the role for mitochondrial proline catabolism in *C. elegans* host defense. We identified proline catabolism as part of innate immunity by governing ROS homeostasis and SKN-1 activation. Given that the function of amino acid metabolism is highly conserved, we propose that mechanisms identified here might be applied in other organisms, including mammals.





**Figure 1. Proline Dehydrogenase Promotes Pathogen Resistance**

(A) Schematic of mitochondrial proline catabolism pathway. (B) The mRNA levels of *prodh* and *p5cdh* in worms exposed to *E. coli* OP50 and *P. aeruginosa* PA14. (C) Effects of *prodh* RNAi on host survival upon *P. aeruginosa* PA14 infection. (D) Proline supplementation promotes pathogen resistance. (E) Effects of *prodh* RNAi on pathogen resistance induced by exogenous proline. Data are presented as mean  $\pm$  SEM. \* $p < 0.05$  versus respective controls. See also Figure S1 and Table S1.

## RESULTS AND DISCUSSION

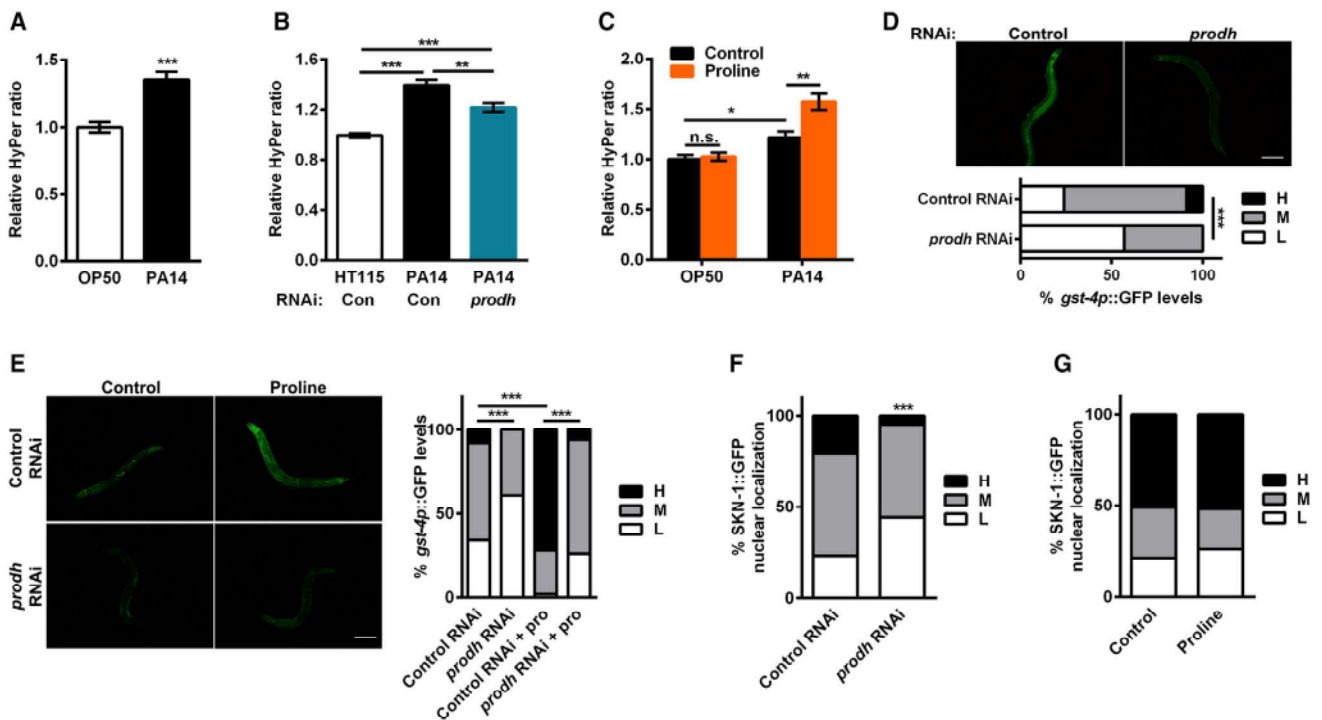
### Proline Dehydrogenase Promotes Pathogen Resistance

Mitochondrial proline catabolism comprises two consecutive enzymatic reactions. First, proline is catabolized to pyrroline-5-carboxylate (P5C) through proline dehydrogenase (PRODH). P5C dehydrogenase (P5CDH) then further oxidizes P5C to glutamate, which is converted to  $\alpha$ -ketoglutarate and fed into the TCA cycle (Figure 1A). Both *prodh* and *p5cdh* genes are encoded in the nuclear DNA. We studied the involvement of proline catabolism in pathogen resistance by using the *C. elegans*-*P. aeruginosa* host-pathogen system. First, the expression of proline catabolic enzymes was examined. qRT-PCR results revealed that the mRNA levels of *prodh/B0513.5*, the *C. elegans* PRODH-encoded gene, were significantly upregulated by *P. aeruginosa* infection, while the levels of *alh-6/p5cdh*, the *C. elegans* P5CDH-encoded gene, were unaffected (Figure 1B), implicating a possible role for PRODH in pathogen resistance. By using RNAi strategy to efficiently downregulate the expression of *prodh* during infection (Figure S1A), we found that knockdown of *prodh* increased the susceptibility of *C. elegans* to *P. aeruginosa* (Figure 1C; Table S1), indicating the requirement of this enzyme in host defense. Supporting this idea, proline supplementation promoted host survival during infection (Figure 1D; Table S1), and, more importantly, RNAi targeting host *prodh* largely

suppressed the effects of proline (Figure 1E; Table S1), suggesting that exogenous proline acts, at least in part, through host PRODH to promote pathogen resistance. We also examined the involvement of PRODH in pathogen load. Congruent with pathogen resistance, *prodh* RNAi treatment increased *P. aeruginosa* load, while proline supplementation decreased pathogen load in the intestine (Figures S1B and S1C).

### PRODH Promotes ROS Production and SKN-1 Activation during Infection

PRODH can promote pathogen resistance by either replenishing the TCA cycle intermediates to generate ATP (Figure 1A) or executing a regulatory function to certain immune pathways. Induction of PRODH is found to activate a mitochondrial ROS signal to promote lifespan in long-lived *C. elegans* (Zarse et al., 2012). ROS, generated from NADPH oxidase or mitochondria, are implicated in direct killing of pathogens as well as activation of essential immune pathways in innate immune cells (Bedard and Krause, 2007; Sena and Chandel, 2012). These findings inspired the hypothesis that infection-caused increases in ROS levels might be dependent on PRODH. By measuring the ratio of oxidized to reduced HyPer, an established indicator of hydrogen peroxide (Back et al., 2012; Knoefler et al., 2012; Pang and Curran, 2014), we found that *P. aeruginosa* PA14 infection indeed significantly increased host ROS levels (Figure 2A),



**Figure 2. Proline Dehydrogenase Regulates ROS Generation and SKN-1 Activation during Infection**

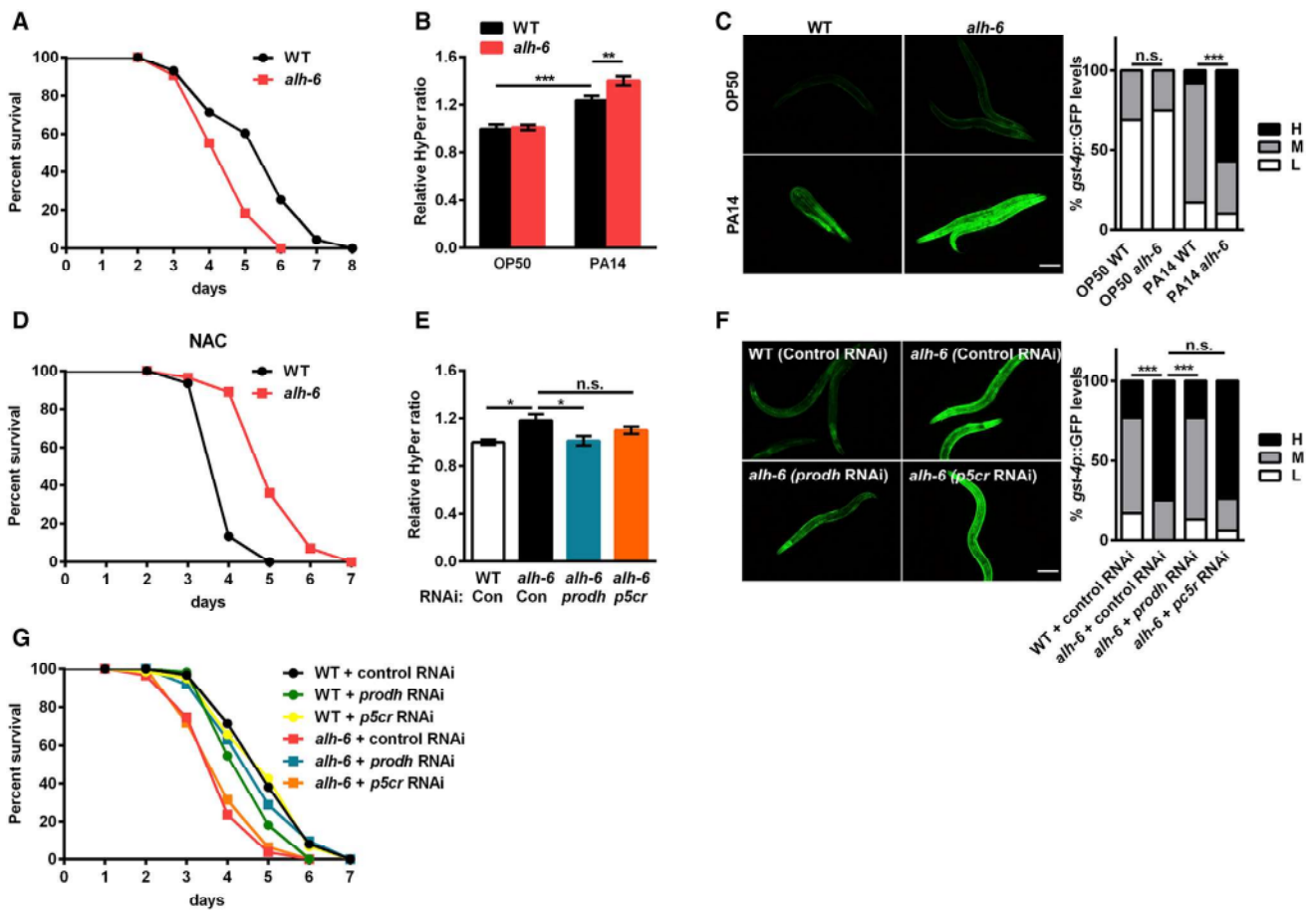
(A) ROS levels in animals fed with *E. coli* OP50 and pathogen *P. aeruginosa* PA14. (B) *prodh* RNAi treatment reduces ROS levels in *P. aeruginosa* PA14-infected worms. (C) Effects of proline supplementation on ROS levels in worms fed with *E. coli* OP50 and *P. aeruginosa* PA14. (D) *prodh* RNAi reduces *gst-4p::GFP* expression in *P. aeruginosa* PA14-infected worms. Upper panel: representative images. Lower panel: quantification of GFP expression levels, scored as low (L), medium (M), and high (H). (E) Effect of *prodh* RNAi on proline-induced *gst-4p::GFP* expression upon *P. aeruginosa* infection. Left panel, representative images. Right panel, quantification of GFP expression levels. (F and G) Effects of *prodh* RNAi and proline supplementation on SKN-1::GFP nuclear localization induced by *P. aeruginosa* infection. ROS levels were measured by HyPer ratio. Scale bar, 100  $\mu$ m. Data are presented as mean  $\pm$  SEM. \* $p < 0.05$ , \*\* $p < 0.01$ , \*\*\* $p < 0.001$  versus respective controls unless specifically indicated. See also Figure S2.

similar to *E. faecalis* infection (Chávez et al., 2009). The ROS increases during infection were also detected by 2',7'-dichlorofluorescein diacetate (DCF-DA) (Figure S2A), a well-known dye sensitive to ROS in *C. elegans* (Lee et al., 2010; Schulz et al., 2007; Yang and Hekimi, 2010).

We next examined the involvement of PRODH in ROS production. Knockdown of *prodh* largely abrogated infection-induced ROS production (Figures 2B and S2B), implying that ROS reduction may, at least in part, be responsible for compromised survival in *prodh* RNAi-treated worms. Exogenous proline supplementation, on the other hand, further increased ROS levels, specifically during infection (Figures 2C and S2C). Proline-induced ROS increases were important for pathogen resistance, as treatment with ROS inhibitor N-acetyl-L-cysteine (NAC) completely abolished the effects of proline on host survival upon infection (Figure S2D; Table S1).

SKN-1, a central transcription factor involved in detoxification and innate immunity, is activated by ROS during infection (Hoeven et al., 2011). We therefore evaluated the possible function of PRODH on SKN-1 activation. By using SKN-1 transcriptional activity reporter *gst-4p::GFP*, we verified that *P. aeruginosa*

infection indeed activated the SKN-1 reporter gene (Figure S2E) (Hoeven et al., 2011; Papp et al., 2012). Congruent with a role for PRODH in ROS regulation, *prodh* RNAi significantly inhibited the expression of SKN-1 reporter *gst-4p::GFP* (Figure 2D), as well as the mRNA levels of other SKN-1 target genes (Figure S2F), suggesting that PRODH is a critical regulator of SKN-1 transcriptional activity during infection. On the other hand, exogenous proline supplementation further activated *gst-4p::GFP* (Figure 2E) as well as SKN-1 targets in infected worms (Figure S2G). More importantly, both host PRODH and ROS were required for proline-induced *gst-4p::GFP* expression (Figures 2E and S2H), indicating that the involvement of PRODH and ROS in proline-induced SKN-1 targets activation. To further characterize SKN-1 activation, we examined SKN-1::GFP nuclear translocation (Hoeven et al., 2011; Papp et al., 2012). RNAi of *prodh* significantly inhibited SKN-1 nuclear accumulation upon infection (Figures 2F and S2I). However, we did not observe further increases in SKN-1 nuclear accumulation in proline-treated worms (Figure 2G), possibly due to saturated SKN-1 nuclear translocation, as previous reports showed that PA14 infection could induce SKN-1 nuclear accumulation as strong as the intense



**Figure 3. P5CDH/ALH-6 Prevents Excessive ROS Production and SKN-1 Activation in Response to Infection**

(A) Survival of *alh-6* mutants in response to *P. aeruginosa* PA14 infection. (B) ROS levels of WT and *alh-6* mutants fed with *E. coli* OP50 and *P. aeruginosa* PA14. (C) The expression of *gst-4p::GFP* in WT and *alh-6* mutants fed with *E. coli* OP50 and *P. aeruginosa* PA14. (D) Effects of NAC treatment on the survival of *alh-6* mutants during infection. (E–G) Effects of RNAi targeting *prodh* and *p5cr* on ROS levels (E), *gst-4p::GFP* expression (F), and survival (G) of *alh-6* mutants in response to *P. aeruginosa* PA14 infection. For *gst-4p::GFP* expression, left panel is representative images, and right panel is quantification of GFP expression levels. ROS levels were measured by HyPer ratio. Scale bar, 100  $\mu$ m. Data are presented as mean  $\pm$  SEM. \* $p < 0.05$ , \*\* $p < 0.01$ , \*\*\* $p < 0.001$  as indicated. See also Figure S3 and Table S1.

SKN-1 activator paraquat (An and Blackwell, 2003; Hoeven et al., 2011). These data suggest that PRODH promotes ROS generation and SKN-1 activation in response to infection, which may confer host resistance to pathogen infection.

### P5CDH/ALH-6 Functions in an Opposite Way to PRODH in Regulating ROS Production and SKN-1 Activation

To further explore the mechanism of proline catabolism-mediated immune responses, we evaluated the role for P5CDH (Figure 1A) in pathogen resistance. Our previous study has shown that mutation of *alh-6*, the worm ortholog of *p5cdh*, increases mitochondrial ROS levels in older gravid adults but not in larva or young adult worms (Pang and Curran, 2014). When we infected L4 stage worms with *P. aeruginosa*, *alh-6* mutants showed reduced survival (Figure 3A; Table S1), indicating that *alh-6* might have a similar function to that of *prodh*. However,

*alh-6* mutation increased ROS levels specifically in infected *C. elegans* (Figures 3B and S3A), which was opposite to *prodh*. Congruent with this finding, infected *alh-6* mutants exhibited robust activation of SKN-1 target *gst-4p::GFP* in the intestine (Figure 3C), whereas uninfected mutants only showed moderate *gst-4p::GFP* activation specifically in the muscle (Figure 3C) as previously reported (Pang and Curran, 2014). RNAi targeting *alh-6* phenocopied the activation of *gst-4p::GFP* upon infection (Figure S3B). *skn-1* RNAi completely silenced the *gst-4p::GFP* activation in *alh-6* mutants (Figure S3C). These data indicate that *alh-6* mutation enhances infection-induced generation of ROS and transcriptional activation of SKN-1.

We previously showed that *gst-4p::GFP* activation in muscle of *alh-6* mutants was independent on ROS (Pang and Curran, 2014). Nevertheless, we found that treatment with ROS inhibitor NAC significantly silenced *gst-4p::GFP* hyper-activation in the

intestine of *alh-6* mutants (Figure S3D), suggesting an essential role for ROS in activating SKN-1 targets in *P. aeruginosa*-infected *alh-6* mutants. Consistently, PMK-1/p38, a kinase mediating ROS-induced SKN-1 activation under oxidative and pathogenic stresses (Hoeven et al., 2011; Inoue et al., 2005), was also required for *gst-4p::GFP* activation caused by *alh-6* mutation (Figure S3E). These results may reflect the mechanistic differences in SKN-1 activation under different circumstances. Together, these data indicate that PRODH and P5CDH/ALH-6, two consecutive enzymes in proline catabolism, act oppositely to govern ROS production and subsequent SKN-1 activation during infection.

It is widely known that excessive ROS may cause cell damages and therefore be deleterious to the host. We previously showed that *alh-6* mutation caused excessive accumulation of ROS and ultimately accelerated animal aging in *C. elegans* (Pang and Curran, 2014). We proposed that, during infection, mutation of *alh-6* compromised host survival due to ROS accumulation. As expected, we found that treatment with ROS inhibitor NAC completely abolished the survival reduction in infected *alh-6* mutants (Figure 3D; Table S1). Intriguingly, *alh-6* mutation even increased host resistance to infection under NAC treatment (Figure 3D). During the aging process, low levels of ROS extend lifespan, whereas high levels of ROS shorten lifespan, which is defined as mitohormesis (Schulz et al., 2007). Our findings imply that it might also be the case during pathogen infection that PRODH acts to generate ROS to fight against pathogen invasion, while *alh-6* mutation causes excessive accumulation of ROS, which are harmful to the host.

### Metabolic Intermediate P5C Likely Accounts for ROS Homeostasis and SKN-1 Activation

How could two consecutive enzymes of proline catabolism function in opposite ways to modulate ROS levels and SKN-1 activation? Mutation of *alh-6* causes accumulation of its substrate P5C during infection when *prodh* is induced (Figures 1A and 1B). Also, we previously found that accumulation of P5C induced mitochondrial stress and excessive ROS generation during aging (Pang and Curran, 2014). Given the differential effects of PRODH and P5CDH/ALH-6 on the levels of metabolic intermediate P5C, we proposed that accumulation of P5C might be the key event for initiating the downstream ROS and SKN-1 responses. If so, knockdown of *prodh* should alleviate accumulation of P5C and abolish the effects of *alh-6* mutation. As expected, RNAi of *prodh* largely inhibited the ROS elevation (Figure 3E) as well as *gst-4p::GFP* activation (Figure 3F) in infected *alh-6* mutants. Remarkably, although *prodh* RNAi shortened the survival of wild-type worms, it reversed the survival reduction of *alh-6* mutants (Figure 3G; Table S1). These results suggest that PRODH-generated P5C may account for observed phenotypes in *alh-6* mutants.

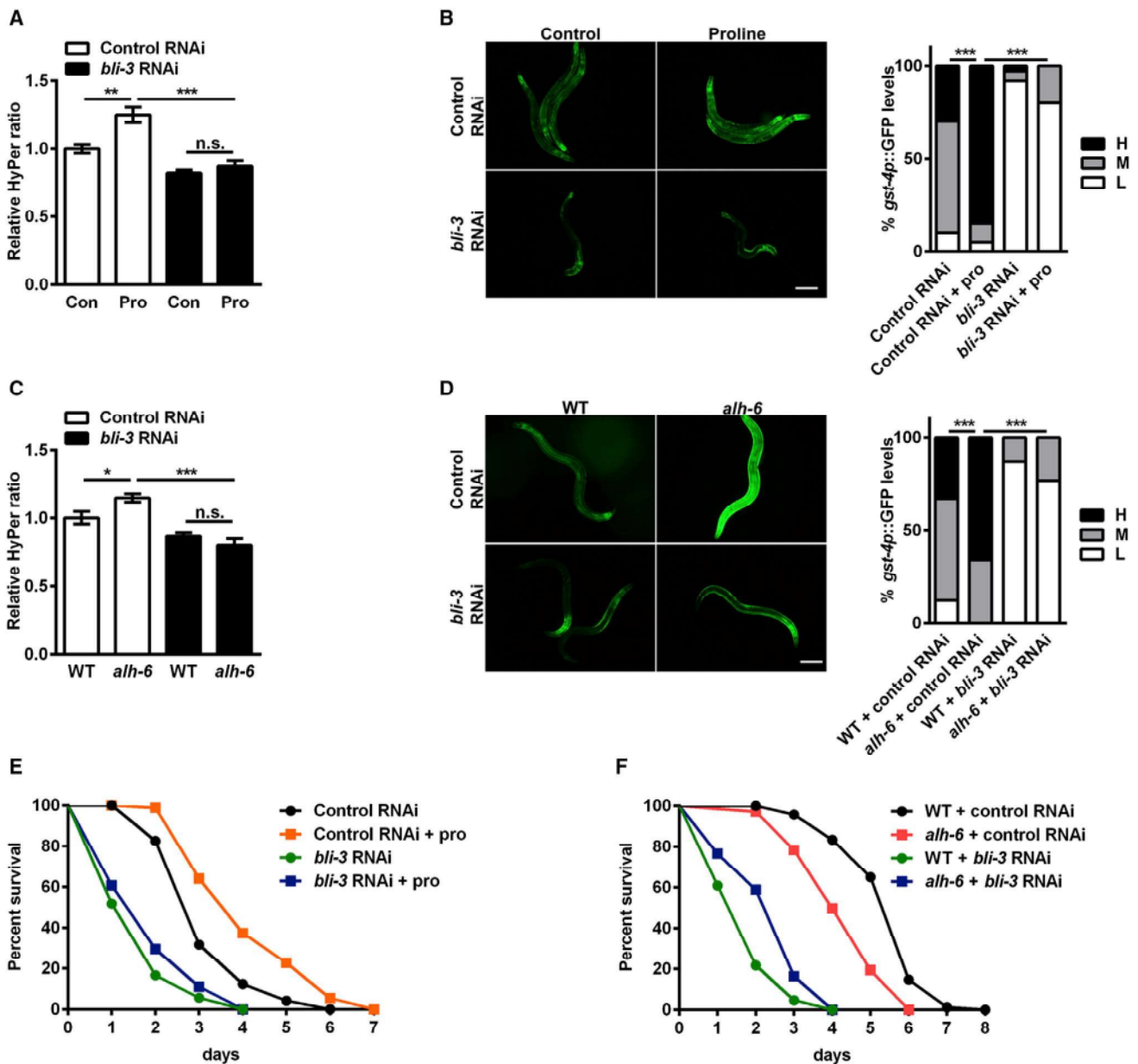
Excessive P5C due to *alh-6* mutation may be converted back to proline through P5C reductase (P5CR), which forms intensive proline-P5C cycle (Figure 1A). This enhanced proline-P5C cycle concomitantly increases the transfer of electrons to mitochondrial electrons transfer chain (mETC), which supports ROS generation (Miller et al., 2009). However, we found that *p5cr* RNAi treatment, which disrupted intensive proline-P5C cycle but not P5C accumu-

lation, did not affect ROS levels (Figure 3E), SKN-1 reporter expression (Figure 3F), or survival rate (Figure 3G; Table S1) of *P. aeruginosa* infected *alh-6* mutants, ruling out a major role for enhanced proline-P5C cycle in these observed phenotypes. These results imply that, during infection, PRODH increases levels of P5C, which may act as an endogenous danger/toxic signal to induce ROS and SKN-1 activation. P5CDH/ALH-6, by catabolizing P5C to glutamate, inhibits excessive accumulation of P5C and therefore prevents ROS overproduction.

### Ce-Duox1/BLI-3 Is Required for ROS Production and SKN-1 Activation Induced by Modulation of Proline Catabolism

Cell-membrane NADPH oxidase and mitochondria are two major sources of ROS production during infection. The crosstalk between NADPH oxidase and mitochondria in many pathophysiological processes has been reported, during which mitochondria may represent critical nodes in the activation of NADPH oxidase (Dikalov, 2011). Ce-Duox1/BLI-3 is a cell-membrane dual oxidase responsible for ROS production and SKN-1 activation in *C. elegans*. *bli-3* RNAi-treated worms exhibit low levels of ROS and are hyper-sensitive to bacterial pathogen infection (Hoeven et al., 2011). Our finding that mitochondrial proline catabolism governs ROS homeostasis and SKN-1 activation during infection raises an interesting question: is there any crosstalk between mitochondrial proline catabolism and cell-membrane Ce-Duox1/BLI-3? Intriguingly, we found that *bli-3* RNAi suppressed the ROS increases and SKN-1 reporter *gst-4p::GFP* expression in proline-treated animals (Figures 4A and 4B), suggesting an essential role for Ce-Duox1/BLI-3 in proline-induced ROS homeostasis. Supporting this idea, *bli-3* RNAi also dramatically inhibited the ROS generation and *gst-4p::GFP* activation in *alh-6* mutants (Figures 4C and 4D). Moreover, Ce-Duox1/BLI-3 was largely required for improved pathogen resistance promoted by proline supplementation (Figure 4E; Table S1). Mutation of *alh-6* moderately reversed the hyper-susceptibility of *bli-3* RNAi-treated animals to *P. aeruginosa* infection (Figure 4F; Table S1). These data implicate that mitochondrial proline catabolism may act through cell-membrane NADPH oxidase in governing ROS homeostasis and SKN-1 activation (Figure S4).

How does mitochondrial proline catabolism act upstream of NADPH oxidase to regulate ROS production? In mammalian endothelial cells, modulation of mitochondrial ROS levels could affect cell-membrane NADPH oxidase activity, as well as ROS production by NADPH oxidase, in response to angiotensin treatment (Dikalov, 2011; Dikalova et al., 2010). In addition, mitochondrial ROS signal was reported to stimulate NADPH oxidase activity and its production of ROS through a signaling cascade involving PI3K and Rac1 in human 293T cells (Lee et al., 2006). Given that studies have well established a role for proline catabolism in generation of mitochondrial ROS (Nishimura et al., 2012; Zarse et al., 2012), it is intriguing to postulate that, during infection, activation of PRODH promotes mitochondrial ROS production, which, in turn, acts as an initiating signal to activate NADPH oxidase (Ce-Duox1/BLI-3) to amplify the ROS pool (Figure S4). Further studies testing this model and identification of possible molecules linking mitochondria and NADPH oxidase would be of great interest.



**Figure 4. Interaction between Proline Catabolism and Ce-Duox1/BLI-3 during Infection**

(A and B) Effects of *bli-3* RNAi on ROS production (A) and *gst-4p::GFP* expression (B) induced by proline supplementation during infection. (C and D) Effects of *bli-3* RNAi on ROS production (C) and *gst-4p::GFP* expression (D) in *alh-6* mutants in response to *P. aeruginosa* PA14 infection. (E and F) Effects of *bli-3* RNAi on the survival of wild-type worms treated with exogenous proline (E) and *alh-6* mutants (F) upon infection. For *gst-4p::GFP* expression, left panel is representative images, and right panel is quantification of GFP expression levels. ROS levels were measured by HyPer ratio, 100  $\mu$ m. Data are presented as mean  $\pm$  SEM. \* $p < 0.05$ , \*\* $p < 0.01$ , \*\*\* $p < 0.001$  as indicated. See also Figure S4 and Table S1.

### Concluding Remarks

In this study, we identify proline catabolism as a component of the *C. elegans* innate immune system. We reveal that, in response to infection, two proline catabolic enzymes, PRODH and P5CDH/ALH-6, act together to govern ROS homeostasis and SKN-1 activity. PRODH promotes ROS production and SKN-1 activation, likely through generation of metabolic interme-

diates P5C. An interesting implication is that the rise of P5C may be recognized as an endogenous toxic/danger signal that initiates ROS and SKN-1-dependent detoxification response. P5CDH/ALH-6 catalyzes the conversion of P5C to glutamate, to prevent excessive elevation of P5C, and ultimately maintains ROS homeostasis. Disruption of the balance between PRODH and P5CDH/ALH-6, such as mutation of *alh-6*, leads to ROS

overproduction and therefore compromises host defense to infection (Figure S4).

The regulation of ROS by proline catabolism is highly conserved throughout evolution (Lettieri Barbato et al., 2014; Liu et al., 2012b; Miller et al., 2009; Nomura and Takagi, 2004; Pang and Curran, 2014; Yoon et al., 2004; Zarse et al., 2012). More intriguingly, PRODH has been reported to contribute to pathogen defense in *Arabidopsis thaliana* (Cecchini et al., 2011; Qamar et al., 2015). Research in past years has revealed the mechanisms that animals and plants utilize to resist infection are surprisingly similar (Ausubel, 2005). Our finding that animals also utilize the proline catabolism pathway to defend against pathogen implicates an ancient and important role for this pathway in the host defense system. We propose that metazoan innate immunity could be governed by shared mechanisms.

## EXPERIMENTAL PROCEDURES

### *C. elegans* Growth Condition and Strains

*C. elegans* were cultured using standard techniques at 20°C (Brenner, 1974). The following strains were used: wild-type N2 Bristol, SPC321[*alh-6* (*lax105*)], CL2166[*gst4-p::gfp*], LD1[*skn-1b/c::GFP*], KU25[*pmk-1* (*km25*)], and the HyPer expression strain *jrls1*[*Prpl-17::HyPer*]. Double and triple mutants were generated by standard genetic techniques.

### Infection Assay

Infection assay was performed as previously described (Tan et al., 1999). In brief, overnight-cultured *P. aeruginosa* strain PA14 bacteria were seeded on slow killing (SK) plates and incubated at 37°C for 24 hr followed by 25°C for 24 hr. For killing assay, L4 animals were added to those plates and incubated at 25°C for survival analysis. All survival data were repeated at least twice. Worms that died of vulva burst, bagging, or crawling off plates were censored. For proline and NAC treatment, proline and NAC were added to plates at a final concentration of 10 mM.

### Fluorescent Microscopy

To analyze *gst-4p::GFP* expression, worms were infected by PA14 for 24 hr and paralyzed with 1 mM levamisole, and fluorescent microscopic images were taken after they were mounted on slides. The expression levels of GFP were scored as low, medium, and high. In brief, a dim green signal in the anterior or posterior of the intestine, a green signal throughout the intestine, and a bright signal throughout the intestine were categorized as low, medium, or high expression, respectively. To study SKN-1 nuclear localization, SKN-1B/C::GFP worms were infected by PA14 for 6 hr and mounted on slides. The levels of GFP nuclear localization were scored as previously described (An and Blackwell, 2003). In brief, no nuclear GFP, GFP signal in the nucleus of anterior or posterior intestine cells, and nuclear GFP in all intestine cells were categorized as low, medium, or high expression, respectively. For *P. aeruginosa* load, worms were infected by PA14 GFP strain for 24 hr, mounted on slides and examined for GFP signal inside the intestine. Dim GFP signal throughout the intestine, bright GFP signal in the anterior or posterior of the intestine, and bright GFP throughout the intestine were scored as low, medium, or high expression, respectively.

### ROS Measurement

ROS determined by HyPer ratio were measured as previously described (Back et al., 2012; Pang and Curran, 2014). In brief, worms of indicated genotypes and treatment were mounted on slides. The oxidized and reduced HyPer of individual worms were excited with GFP and CFP channels, respectively. Fluorescent density was calculated by using ImageJ software. The hydrogen peroxide levels were measured as the ratio of oxidized to reduced HyPer intensity. ROS determined by DCF-DA were measured as previously described (Lee et al., 2010), with modifications. In brief, about 600 worms of indicated genotypes and treatment were collected and washed twice in M9 to remove bacte-

ria. Worms were then homogenized in PBST (PBS with 0.1% Tween 20) and centrifuged at 15,000 rpm at 4°C. 50  $\mu$ L supernatants were mixed with equal volume 100  $\mu$ M DCF-DA prepared in PBS. Fluorescent intensity was measured at the excitation wavelength 488 nm and emission wavelength 535 nm after 1 hr incubation. The protein content in supernatant was determined by bicinchoninic acid (BCA) assay to normalize the fluorescent intensity.

### qRT-PCR

qRT-PCR was performed as previously described (Pang et al., 2014). In brief, worms of indicated genotype and treatment were collected, washed in M9 buffer, and then homogenized in Trizol reagent (Life Technologies). RNA was extracted according to the manufacturer's protocol. DNA contamination was digested with DNase I (Thermo Fisher Scientific), and subsequently RNA was reverse transcribed to cDNA by using the RevertAid First Strand cDNA Synthesis Kit (Thermo Fisher Scientific). qPCR was performed by using SYBR Green (Bio-Rad). The expression of *ama-1* or *pmp-3* was used to normalize samples. For measurement of *prodh* and *alh-6*, worms were cultured on PA14 plates for 24 hr. For measurement of SKN-1 targets, worms were collected 6 hr after treatment for RNA extraction.

### RNA Interference Treatment

HT115 bacteria containing specific double-stranded RNA (dsRNA)-expression plasmids were seeded on nematode growth media (NGM) plates containing 5 mM isopropyl  $\beta$ -D-1-thiogalactopyranoside (IPTG). RNAi was induced at room temperature for 24 hr. L1 worms were added to those plates to knock down indicated genes. For *bli-3* RNAi, the bacterial strain was diluted at a ratio of 1:30 to the vector control, as previously described (Hoeven et al., 2011).

### Statistics

Data were presented as mean  $\pm$  SEM. Survival data were analyzed by using the log-rank (Mantel-Cox) test. The levels of fluorescent micrographs were analyzed by using chi-square and Fisher's exact tests.  $p < 0.05$  was considered significant. Other data were analyzed by using unpaired Student's *t* test.

## SUPPLEMENTAL INFORMATION

Supplemental Information includes four figures and one table and can be found with this article online at <http://dx.doi.org/10.1016/j.celrep.2016.11.038>.

## AUTHOR CONTRIBUTIONS

H.T. and S.P. designed the study, performed the experiments, analyzed data, and wrote the manuscript.

## ACKNOWLEDGMENTS

We thank Dr. Kun Zhu for providing the *P. aeruginosa* PA14 strain, Dr. Cheng-gang Zhou for providing the PA14 GFP strain, and Dr. B. Braeckman for providing the HyPer expression strain. Some strains were provided by the CGC, which is funded by the NIH Office of Research Infrastructure Programs (P40 OD010440). This work was supported by the National Natural Science Foundation of China (grant no. 31571243 to S.P.) and the Fundamental Research Funds for the Central Universities (grant no. 106112015CDJRC291208 to H.T.).

Received: March 1, 2016

Revised: September 28, 2016

Accepted: November 10, 2016

Published: December 13, 2016

## REFERENCES

- An, J.H., and Blackwell, T.K. (2003). SKN-1 links *C. elegans* mesendodermal specification to a conserved oxidative stress response. *Genes Dev.* 17, 1882–1893.
- Ausubel, F.M. (2005). Are innate immune signaling pathways in plants and animals conserved? *Nat. Immunol.* 6, 973–979.

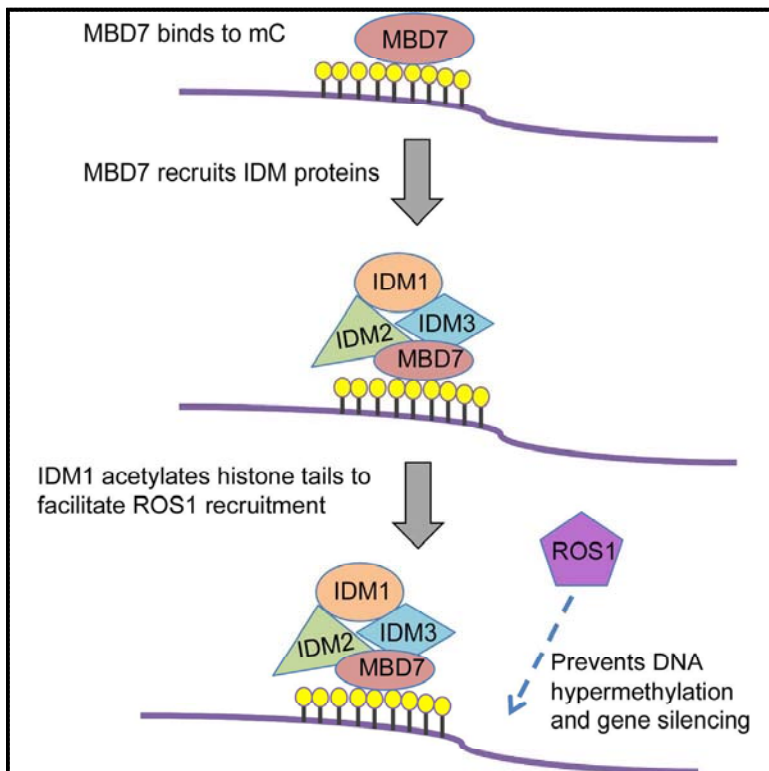


- Back, P., De Vos, W.H., Depuydt, G.G., Matthijssens, F., Vanfleteren, J.R., and Braeckman, B.P. (2012). Exploring real-time in vivo redox biology of developing and aging *Caenorhabditis elegans*. *Free Radic. Biol. Med.* **52**, 850–859.
- Bedard, K., and Krause, K.-H. (2007). The NOX family of ROS-generating NADPH oxidases: Physiology and pathophysiology. *Physiol. Rev.* **87**, 245–313.
- Brenner, S. (1974). The genetics of *Caenorhabditis elegans*. *Genetics* **77**, 71–94.
- Bronte, V., and Zanovello, P. (2005). Regulation of immune responses by L-arginine metabolism. *Nat. Rev. Immunol.* **5**, 641–654.
- Bronte, V., Serafini, P., Mazzoni, A., Segal, D.M., and Zanovello, P. (2003). L-arginine metabolism in myeloid cells controls T-lymphocyte functions. *Trends Immunol.* **24**, 302–306.
- Cecchini, N.M., Monteoliva, M.I., and Alvarez, M.E. (2011). Proline dehydrogenase contributes to pathogen defense in *Arabidopsis*. *Plant Physiol.* **155**, 1947–1959.
- Chávez, V., Mohri-Shiomi, A., and Garsin, D.A. (2009). Ce-Duox1/BLI-3 generates reactive oxygen species as a protective innate immune mechanism in *Caenorhabditis elegans*. *Infect. Immun.* **77**, 4983–4989.
- Dikalov, S. (2011). Cross talk between mitochondria and NADPH oxidases. *Free Radic. Biol. Med.* **51**, 1289–1301.
- Dikalova, A.E., Bikineyeva, A.T., Budzyn, K., Nazarewicz, R.R., McCann, L., Lewis, W., Harrison, D.G., and Dikalov, S.I. (2010). Therapeutic targeting of mitochondrial superoxide in hypertension. *Circ. Res.* **107**, 106–116.
- Ganeshan, K., and Chawla, A. (2014). Metabolic regulation of immune responses. *Annu. Rev. Immunol.* **32**, 609–634.
- Grohmann, U., and Bronte, V. (2010). Control of immune response by amino acid metabolism. *Immunol. Rev.* **236**, 243–264.
- Hoeven, R.v., McCallum, K.C., Cruz, M.R., and Garsin, D.A. (2011). Ce-Duox1/BLI-3 generated reactive oxygen species trigger protective SKN-1 activity via p38 MAPK signaling during infection in *C. elegans*. *PLoS Pathog.* **7**, e1002453.
- Inoue, H., Hisamoto, N., An, J.H., Oliveira, R.P., Nishida, E., Blackwell, T.K., and Matsumoto, K. (2005). The *C. elegans* p38 MAPK pathway regulates nuclear localization of the transcription factor SKN-1 in oxidative stress response. *Genes Dev.* **19**, 2278–2283.
- Knoefler, D., Thamsen, M., Koniczek, M., Niemuth, N.J., Diederich, A.-K., and Jakob, U. (2012). Quantitative in vivo redox sensors uncover oxidative stress as an early event in life. *Mol. Cell* **47**, 767–776.
- Lee, S.B., Bae, I.H., Bae, Y.S., and Um, H.D. (2006). Link between mitochondria and NADPH oxidase 1 isozyme for the sustained production of reactive oxygen species and cell death. *J. Biol. Chem.* **281**, 36228–36235.
- Lee, S.-J., Hwang, A.B., and Kenyon, C. (2010). Inhibition of respiration extends *C. elegans* life span via reactive oxygen species that increase HIF-1 activity. *Curr. Biol.* **20**, 2131–2136.
- Lettieri Barbato, D., Aquilano, K., Baldelli, S., Cannata, S.M., Bernardini, S., Rotilio, G., and Ciriolo, M.R. (2014). Proline oxidase-adipose triglyceride lipase pathway restrains adipose cell death and tissue inflammation. *Cell Death Differ.* **21**, 113–123.
- Liu, Y., Borchert, G.L., Surazynski, A., Hu, C.-A., and Phang, J.M. (2006). Proline oxidase activates both intrinsic and extrinsic pathways for apoptosis: The role of ROS/superoxides, NFAT and MEK/ERK signaling. *Oncogene* **25**, 5640–5647.
- Liu, Y., Borchert, G.L., Donald, S.P., Diwan, B.A., Anver, M., and Phang, J.M. (2009). Proline oxidase functions as a mitochondrial tumor suppressor in human cancers. *Cancer Res.* **69**, 6414–6422.
- Liu, W., Le, A., Hancock, C., Lane, A.N., Dang, C.V., Fan, T.W.-M., and Phang, J.M. (2012a). Reprogramming of proline and glutamine metabolism contributes to the proliferative and metabolic responses regulated by oncogenic transcription factor c-MYC. *Proc. Natl. Acad. Sci. USA* **109**, 8983–8988.
- Liu, W., Glunde, K., Bhujwala, Z.M., Raman, V., Sharma, A., and Phang, J.M. (2012b). Proline oxidase promotes tumor cell survival in hypoxic tumor microenvironments. *Cancer Res.* **72**, 3677–3686.
- Miller, G., Honig, A., Stein, H., Suzuki, N., Mittler, R., and Zilberstein, A. (2009). Unraveling delta1-pyrroline-5-carboxylate-proline cycle in plants by uncoupled expression of proline oxidation enzymes. *J. Biol. Chem.* **284**, 26482–26492.
- Nishimura, A., Nasuno, R., and Takagi, H. (2012). The proline metabolism intermediate  $\Delta$ 1-pyrroline-5-carboxylate directly inhibits the mitochondrial respiration in budding yeast. *FEBS Lett.* **586**, 2411–2416.
- Nomura, M., and Takagi, H. (2004). Role of the yeast acetyltransferase Mpr1 in oxidative stress: Regulation of oxygen reactive species caused by a toxic proline catabolism intermediate. *Proc. Natl. Acad. Sci. USA* **101**, 12616–12621.
- Pang, S., and Curran, S.P. (2014). Adaptive capacity to bacterial diet modulates aging in *C. elegans*. *Cell Metab.* **19**, 221–231.
- Pang, S., Lynn, D.A., Lo, J.Y., Paek, J., and Curran, S.P. (2014). SKN-1 and Nrf2 couples proline catabolism with lipid metabolism during nutrient deprivation. *Nat. Commun.* **5**, 5048.
- Papp, D., Csermely, P., and Söti, C. (2012). A role for SKN-1/Nrf in pathogen resistance and immunosenescence in *Caenorhabditis elegans*. *PLoS Pathog.* **8**, e1002673.
- Pearce, E.L., and Pearce, E.J. (2013). Metabolic pathways in immune cell activation and quiescence. *Immunity* **38**, 633–643.
- Qamar, A., Mysore, K.S., and Senthil-Kumar, M. (2015). Role of proline and pyrroline-5-carboxylate metabolism in plant defense against invading pathogens. *Front. Plant Sci.* **6**, 503.
- Schneider, D.S., and Ayres, J.S. (2008). Two ways to survive infection: What resistance and tolerance can teach us about treating infectious diseases. *Nat. Rev. Immunol.* **8**, 889–895.
- Schulz, T.J., Zarse, K., Voigt, A., Urban, N., Birringer, M., and Ristow, M. (2007). Glucose restriction extends *Caenorhabditis elegans* life span by inducing mitochondrial respiration and increasing oxidative stress. *Cell Metab.* **6**, 280–293.
- Sena, L.A., and Chandel, N.S. (2012). Physiological roles of mitochondrial reactive oxygen species. *Mol. Cell* **48**, 158–167.
- Tan, M.W., Rahme, L.G., Sternberg, J.A., Tompkins, R.G., and Ausubel, F.M. (1999). *Pseudomonas aeruginosa* killing of *Caenorhabditis elegans* used to identify *P. aeruginosa* virulence factors. *Proc. Natl. Acad. Sci. USA* **96**, 2408–2413.
- Tannahill, G.M., Curtis, A.M., Adamik, J., Palsson-McDermott, E.M., McGettrick, A.F., Goel, G., Frezza, C., Bernard, N.J., Kelly, B., Foley, N.H., et al. (2013). Succinate is an inflammatory signal that induces IL-1 $\beta$  through HIF-1 $\alpha$ . *Nature* **496**, 238–242.
- Yang, W., and Hekimi, S. (2010). A mitochondrial superoxide signal triggers increased longevity in *Caenorhabditis elegans*. *PLoS Biol.* **8**, e1000556.
- Yoon, K.-A., Nakamura, Y., and Arakawa, H. (2004). Identification of ALDH4 as a p53-inducible gene and its protective role in cellular stresses. *J. Hum. Genet.* **49**, 134–140.
- Zarse, K., Schmeisser, S., Groth, M., Priebe, S., Beuster, G., Kuhlow, D., Guthke, R., Platzer, M., Kahn, C.R., and Ristow, M. (2012). Impaired insulin/IGF1 signaling extends life span by promoting mitochondrial L-proline catabolism to induce a transient ROS signal. *Cell Metab.* **15**, 451–465.

# Molecular Cell

## The Methyl-CpG-Binding Protein MBD7 Facilitates Active DNA Demethylation to Limit DNA Hypermethylation and Transcriptional Gene Silencing

### Graphical Abstract



### Authors

Zhaobo Lang, Mingguang Lei, ..., Zhizhong Gong, Jian-Kang Zhu

### Correspondence

jkzhu@purdue.edu

### In Brief

Lang et al. show that MBD7 binds to highly methylated, CG-dense chromatin regions and physically associates with IDM proteins to enable these DNA demethylases to prevent aberrant spreading of DNA methylation.

### Highlights

- MBD7 and IDM3 prevent DNA hypermethylation and gene silencing
- MBD7 binds to genomic regions with a high density of CG methylation
- MBD7 prevents DNA methylation spread
- MBD7 physically associates with IDM3, and with IDM1 and IDM2

### Accession Numbers

GSE58789  
GSE58787  
GSE59712  
GSE33071  
GSE49421



Lang et al., 2015, *Molecular Cell* 57, 971–983  
March 19, 2015 ©2015 Elsevier Inc.  
<http://dx.doi.org/10.1016/j.molcel.2015.01.009>

CellPress

# The Methyl-CpG-Binding Protein MBD7 Facilitates Active DNA Demethylation to Limit DNA Hyper-Methylation and Transcriptional Gene Silencing

Zhaobo Lang,<sup>1,2,8</sup> Mingguang Lei,<sup>2,8</sup> Xingang Wang,<sup>2</sup> Kai Tang,<sup>2</sup> Daisuke Miki,<sup>1</sup> Huiming Zhang,<sup>2</sup> Satendra K. Mangrauthia,<sup>2,3</sup> Wenshan Liu,<sup>2,4</sup> Wenfeng Nie,<sup>2,5</sup> Guojie Ma,<sup>2</sup> Jun Yan,<sup>2</sup> Cheng-Guo Duan,<sup>2</sup> Chuan-Chih Hsu,<sup>6</sup> Chunlei Wang,<sup>7</sup> W. Andy Tao,<sup>6</sup> Zhizhong Gong,<sup>7</sup> and Jian-Kang Zhu<sup>1,2,\*</sup>

<sup>1</sup>Shanghai Center for Plant Stress Biology, Shanghai Institutes for Biological Sciences, Chinese Academy of Sciences, Shanghai 200032, China

<sup>2</sup>Department of Horticulture & Landscape Architecture, Purdue University, West Lafayette, IN 47906, USA

<sup>3</sup>Biotechnology Section, Directorate of Rice Research, Hyderabad 500030, India

<sup>4</sup>School of Life Sciences, Chongqing University, Chongqing 400044, China

<sup>5</sup>Department of Horticulture, Zhejiang University, Hangzhou 310058, China

<sup>6</sup>Department of Biochemistry, Purdue University, West Lafayette, IN 47907, USA

<sup>7</sup>State Key Laboratory of Plant Physiology and Biochemistry, College of Biological Sciences, China Agricultural University, Beijing 100193, China

<sup>8</sup>Co-first author

\*Correspondence: [jkzhu@purdue.edu](mailto:jkzhu@purdue.edu)

<http://dx.doi.org/10.1016/j.molcel.2015.01.009>

## SUMMARY

DNA methylation is a conserved epigenetic mark that plays important roles in plant and vertebrate development, genome stability, and gene regulation. Canonical Methyl-CpG-binding domain (MBD) proteins are important interpreters of DNA methylation that recognize methylated CG sites and recruit chromatin remodelers, histone deacetylases, and histone methyltransferases to repress transcription. Here, we show that *Arabidopsis* MBD7 and Increased DNA Methylation 3 (IDM3) are anti-silencing factors that prevent gene repression and DNA hypermethylation. MBD7 preferentially binds to highly methylated, CG-dense regions and physically associates with other anti-silencing factors, including the histone acetyltransferase IDM1 and the alpha-crystallin domain proteins IDM2 and IDM3. IDM1 and IDM2 were previously shown to facilitate active DNA demethylation by the 5-methylcytosine DNA glycosylase/lyase ROS1. Thus, MBD7 tethers the IDM proteins to methylated DNA, which enables the function of DNA demethylases that in turn limit DNA methylation and prevent transcriptional gene silencing.

## INTRODUCTION

DNA methylation, a conserved epigenetic mark in plants and vertebrates, plays important roles in development, genome stability, and in several well-known epigenetic phenomena such as genomic imprinting, paramutation, and X chromosome inactivation (He et al., 2011; Law and Jacobsen, 2010; Tariq and Pasz-

kowski, 2004). In mammals, 5-methylcytosine (5mC) occurs mainly at CG dinucleotides, whereas in plants, 5mC is found in three sequence contexts: CG, CHG, and CHH (where H is A, C, or T) (He et al., 2011; Law and Jacobsen, 2010). In plants, DNA methylation can be established through the RNA-directed DNA methylation (RdDM) pathway (Matzke and Mosher, 2014; Haag and Pikaard, 2011; Zhang and Zhu, 2011). Maintenance of CG and CHG methylation requires the Dnmt1 ortholog MET1, and the plant specific enzyme CMT3, respectively (He et al., 2011; Law and Jacobsen, 2010). CHH methylation is carried out by DRM2 through the RdDM pathway (Matzke and Mosher, 2014) and by CMT2, which requires the chromatin remodeling protein DDM1 (Zemach et al., 2013).

DNA methylation is associated with transcriptional silencing (He et al., 2011; Law and Jacobsen, 2010; Tariq and Paszkowski, 2004). Methyl-CpG-binding domain (MBD) proteins are important interpreters of DNA methylation (Hendrich and Bird, 1998). Generally, MBD proteins recognize methylated CG sites and recruit chromatin remodelers, histone deacetylases, and histone methyltransferases to repress transcription (Ng et al., 1999). Recent analysis of the genome-wide binding sites of MBD proteins in mammalian cells confirmed that MBD proteins are typically enriched at methylated genomic regions and methylation-dependent MBD protein binding at promoters coincides with gene silencing (Baubec et al., 2013). The *Arabidopsis* genome is predicted to encode 13 canonical MBD proteins, although only three of them, MBD5, MBD6, and MBD7, bind specifically to methylated CG sites in vitro (Zemach and Grafi, 2007). The functions of these plant MBD proteins are poorly understood, but the available information is consistent with a conserved role as effectors of DNA methylation that cause transcriptional repression (Zemach and Grafi, 2007).

DNA methylation is dynamically controlled by both methylation and demethylation reactions (Zhu, 2009). In vertebrates, active DNA demethylation is initiated by oxidation or deamination of

5-methylcytosine (5mC) by TET enzymes or AID/APOBECs, respectively, followed by the DNA glycosylase TDG or MBD4 (Rai et al., 2008; Kohli and Zhang, 2013), whereas in plants, active DNA demethylation is initiated by the ROS1/DME family of 5mC DNA glycosylases (Zhu, 2009). In *Arabidopsis*, ROS1 is necessary for preventing DNA hypermethylation at thousands of genomic regions (Qian et al., 2012). How the DNA demethylation enzymes are targeted to specific genomic loci is poorly understood. At a subset of these genomic regions, ROS1 function requires the histone acetyltransferase Increased DNA Methylation 1 (IDM1) (Qian et al., 2012) and its partner protein IDM2 (Qian et al., 2014).

In this study, we employed a previously described forward genetic screen to uncover MBD7 and IDM3 as anti-silencing factors in *Arabidopsis*. Our screen has identified several anti-silencing factors, such as Anti-silencing 1 (ASI1), Enhanced Downy Mildew 2 (EDM2), and IDM2, in addition to new alleles of known anti-silencing factors, such as IDM1 and ROS1 (Lei et al., 2014; Wang et al., 2013). We found that both MBD7 and IDM3 limit DNA methylation, particularly at transposable elements (TEs). MBD7 is enriched at highly methylated, CG-dense sites throughout the genome, and this enrichment coincides with its function in preventing DNA methylation spread or hypermethylation. Protein interaction analyses revealed that MBD7 associates with IDM2 and IDM3 (an IDM2-like protein) *in vitro* and *in vivo* and also associates with IDM1 *in vivo*. These results suggest a model in which MBD7 recognizes methylated DNA and recruits regulators of active DNA demethylation to prevent DNA methylation spread and transcriptional silencing.

## RESULTS

### ASI2 Is an Anti-Silencing Factor that Prevents Spread of DNA Methylation

We previously developed a screen for anti-silencing mutants in *Arabidopsis* that employs wild-type (WT) plants that express a cauliflower mosaic virus 35S promoter-driven sucrose transporter 2 (35S::SUC2) transgene and exhibit a short-root phenotype when grown on medium containing sucrose (Figure 1A) (Lei et al., 2014; Wang et al., 2013). Further, these plants express 35S promoter-driven neomycin phosphotransferase II (NPTII) and hygromycin phosphotransferase II (HPTII) transgenes and thus are resistant to kanamycin and hygromycin. We identified a recessive mutant, *asi2-1*, from a population of WT plants mutagenized with ethylmethane sulfonate. *asi2-1* mutant plants developed long roots on sucrose-containing media due to reduced SUC2 expression (Figures 1A, 1B, and S1A) and were sensitive to hygromycin and kanamycin due to reduced expression of HPTII and NPTII (Figures 1B, 1C, S1A, and S1B). We performed chromatin immunoprecipitation (ChIP) and observed reduced occupancy of RNA polymerase II (Pol II) and enrichment of the repressive chromatin mark H3K9me2 at the 35S promoter in *asi2-1* mutant plants, suggesting that reduced RNA levels are caused by decreased Pol II transcription from this promoter (Figures S1C and S1D).

Next, we analyzed DNA methylation of *asi2-1* and WT plants by genomic bisulfite sequencing. We found that part of the 35S

promoter (region A) is hypermethylated in WT plants, but this hypermethylation extends to the neighboring region (region B) in *asi2-1* mutant plants (Figure 1D). Thus, the spread of DNA methylation at the 35S promoter may silence the transgenes in *asi2-1* mutant plants. In support of this hypothesis, treatment with the DNA methylation inhibitor 5-aza-2'-deoxycytidine (5-aza) suppressed the kanamycin sensitivity of *asi2-1* mutant plants (Figure 1C) and restored the expression of NPTII and SUC2 (Figure S1E).

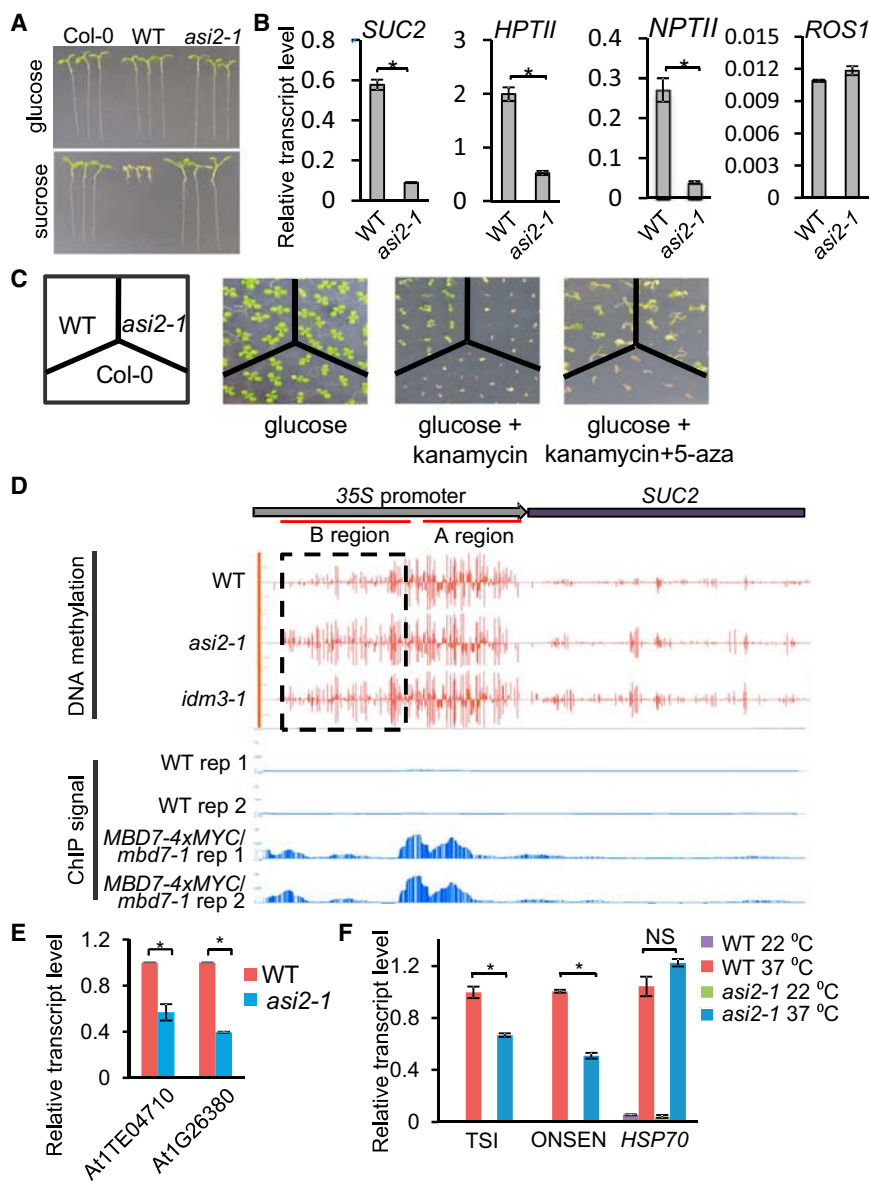
In plants, TEs and other repeats are silenced by DNA methylation and repressive histone modifications (He et al., 2011; Law and Jacobsen, 2010; Tariq and Paszkowski, 2004). We found that the expression of At1G26380, a gene in a repetitive gene cluster (Qian et al., 2012), is reduced in *asi2-1* (Figure 1E). Similarly, the expression of the TE At1TE04710 is also decreased in *asi2-1* (Figure 1E). Expression of some repeats, like *ONSEN* and *TSI*, can be induced by prolonged heat treatment (Ito et al., 2011). We observed reduced heat-induced expression of *ONSEN* and *TSI* in *asi2-1* compared to WT plants (Figure 1F). In addition, At1G26380, At1TE04710, *TSI*, and *ONSEN* display increased DNA methylation in *asi2-1* (Figures S1F). Thus, the recessive *asi2-1* mutation causes the DNA hypermethylation and silencing of transgenic and some endogenous loci, thereby indicating an anti-silencing role for ASI2.

### The Methyl CpG-Binding Protein MBD7 Is Encoded by ASI2

Through map-based cloning, we found that *asi2-1* has a C-to-T point mutation in MBD7 (AT5g59800) that creates a premature stop codon (Figure 2A). The long-root phenotype of *asi2-1* could be complemented by native promoter-driven MBD7 fused with either a 4xMYC tag or a GFP tag (Figure 2B). RT-PCR assays indicated that the MYC-tagged WT MBD7 is able to rescue the suppressed expression of 35S::SUC2 and 35S::HPTII transgenes in *asi2-1* (Figure S2A). Further, we found that MYC-tagged MBD7 protein was enriched at the 35S transgene promoter by ChIP-qPCR (Figure 2C). These results confirm that the transgene silencing in *asi2-1* was caused by the mutation in MBD7. We thus refer to the *asi2-1* mutant as *mbd7-1* hereafter. We also introduced the 35S::SUC2 transgene into a T-DNA insertion allele of MBD7 (SAIL\_697\_E08/*mbd7-2*) by crossing the T-DNA mutant with WT plants. As expected, *mbd7-2* mutant plants containing the 35S::SUC2 transgene also showed a long-root phenotype (Figure S2B). These results demonstrate that MBD7 dysfunction causes the transgene silencing phenotypes in plants.

### The *mbd7-1* Mutation Induces DNA Hypermethylation at Endogenous Genomic Regions

Whole-genome bisulfite sequencing identified 1,390 differentially methylated regions (DMRs) in *mbd7-1*, among which 1,144 are hypermethylated and 246 are hypomethylated. Five hypermethylated cytosines (HMCs) in *mbd7-1* were selected for validation by Chop-PCR, an assay in which genomic DNA is digested with a methylation-sensitive restriction endonuclease and then tested as a template for PCR with primers flanking the restriction sites. We observed amplification from genomic digests of *mbd7-1* but not WT DNA (Figure 2D), consistent with



**Figure 1. *ASI2* Antagonizes Transcriptional Silencing and Prevents DNA Hypermethylation**

(A) Isolation of the *asi2-1* mutant. Transgenic overexpression of the sucrose transporter gene *SUC2* in *Arabidopsis* (ecotype Col-0) results in hypersensitivity to exogenous sucrose, as indicated by the short root phenotype in the transgenic plants (wild-type, WT). Dysfunction of *ASI2* rescues the sucrose-inhibited root growth phenotype.

(B) RT-qPCR quantification of transgene transcript levels in *asi2-1* in comparison to WT plants. Relative *ROS1* transcript level was included as an unchanged control.

(C) *ASI2* dysfunction causes a loss of kanamycin resistance in the transgenic plants. Treatment with a DNA methylation inhibitor, 5-aza, restores kanamycin resistance in the *asi2-1* mutant.

(D) DNA methylation status and MBD7 enrichment at the 35S::*SUC2* transgene in WT, *asi2-1*, and *idm3-1* mutants. Shown are screenshots from Integrative Genome Browser (IGB) display of whole-genome bisulfite sequencing and ChIP-seq results. Vertical bars on each track indicate DNA methylation levels or MBD7 enrichment at chromatin. Two replicates of ChIP-seq data from *MBD7-4xMYC* transgenic plants and from WT control plants are displayed.

(E) RT-qPCR analysis of At1TE04710 and At1G26380 in WT and *asi2-1* plants.

(F) *ASI1* dysfunction compromises heat-induced expression of *ONSEN* and *TSI* but not *HSP70*.

In (B), (E) and (F), RT-qPCR measurements of transcript levels in the *asi2-1* mutant are relative to the corresponding values in the WT. All error bars indicate SD, n = 3. \*p < 0.01; NS, not significant (two-tailed t test).

See also Figure S1.

hypermethylation of the candidate sites in *mbd7-1*. The greater number of hypermethylated than hypomethylated regions in *mbd7-1* suggests that MBD7 mainly antagonizes DNA methylation.

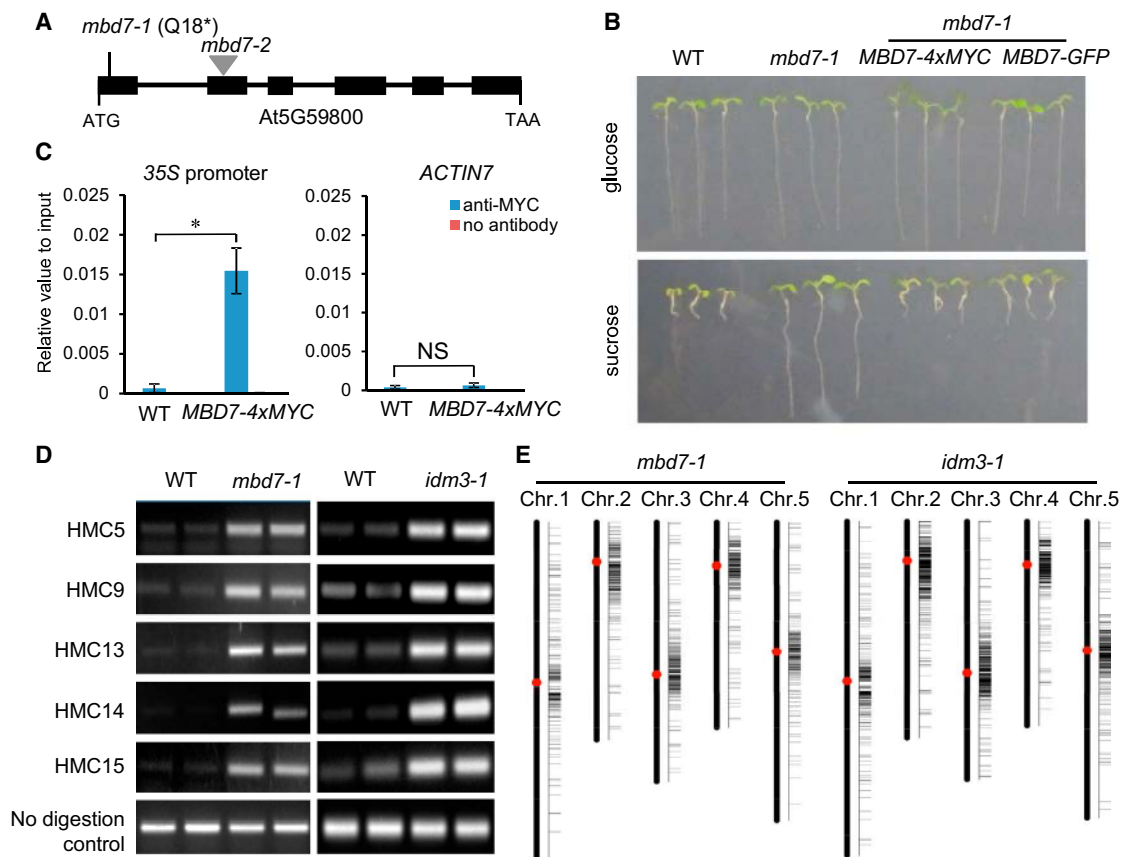
We found that about 85% (974) of the hypermethylated DMRs in *mbd7-1* are located in TEs, with no obvious preference for any specific type (Figure S2C). The DNA methylation levels are increased at these TE DMRs in CG, CHG, and CHH sequence contexts, and the increase is independent of TE length (Figure S2D).

In *mbd7-1* mutant plants, hypermethylated DMRs are concentrated near centromeric and pericentromeric regions (Figure 2E). To test whether MBD7 preferentially regulates TEs located at these regions, we compared the number of hypermethylated DMR-associated TEs to the total number of TEs across consecutive 500-kb windows. This density distribu-

tion of hypermethylated TEs across five chromosomes showed no obvious preference for centromeric or pericentromeric TEs, but rather that the concentration of hypermethylated TEs within these regions corresponds to a higher total number of TEs (Figure S2E).

#### MBD7 Associates with mCG-Dense Genomic Regions

MBD7 was previously identified as a methyl CpG-binding protein (Zemach and Grafi, 2007); however, its genomic targets are not known. To identify endogenous MBD7 targets, we performed ChIP using plants expressing native promoter-driven *MBD7-4xMYC* followed by high-throughput sequencing (ChIP-seq). We identified 2,452 peaks of MBD7 enrichment on chromatin; 1,930 (78.7%) are within TE regions, 94 (3.8%) are within intergenic regions, and 401 (16.4%) correspond to genes (202 of the genes contain annotated repeats). The pattern of chromosomal distribution of MBD7 binding peaks is similar to that of *mbd7-1* hyper-DMRs (Figures 3A and 2E), and approximately 63% of the *mbd7-1* hyper-DMRs overlap with MBD7 binding peaks.



**Figure 2. *AS12* Encodes the mCpG-Binding Protein MBD7, and *asi2-1* and *idm3-1* Methyloome Analysis**

(A) A diagram of the *MBD7* gene showing the mutation site in *mbd7-1* and the T-DNA insertion position in the *mbd7-2* allele. Boxes and lines denote exons and introns, respectively.

(B) The long root phenotype in *asi2-1* is caused by *MBD7* mutation. Transgenic expression of *MBD7* driven by its native promoter restored the short root phenotype in *mbd7-1*.

(C) Examination of MBD7 enrichment at the 35S transgene promoter using ChIP assay. Promoter of *ACTIN7* was used as a control. All error bars indicate SD,  $n = 3$ . \* $p < 0.01$ ; NS, not significant (two-tailed t test).

(D) Chop-PCR validation of hyper-DMRs identified in *mbd7-1* and *idm3-1*. Results of two biological replicates are shown. Methylation-sensitive restriction enzymes and primers are listed in Table S1.

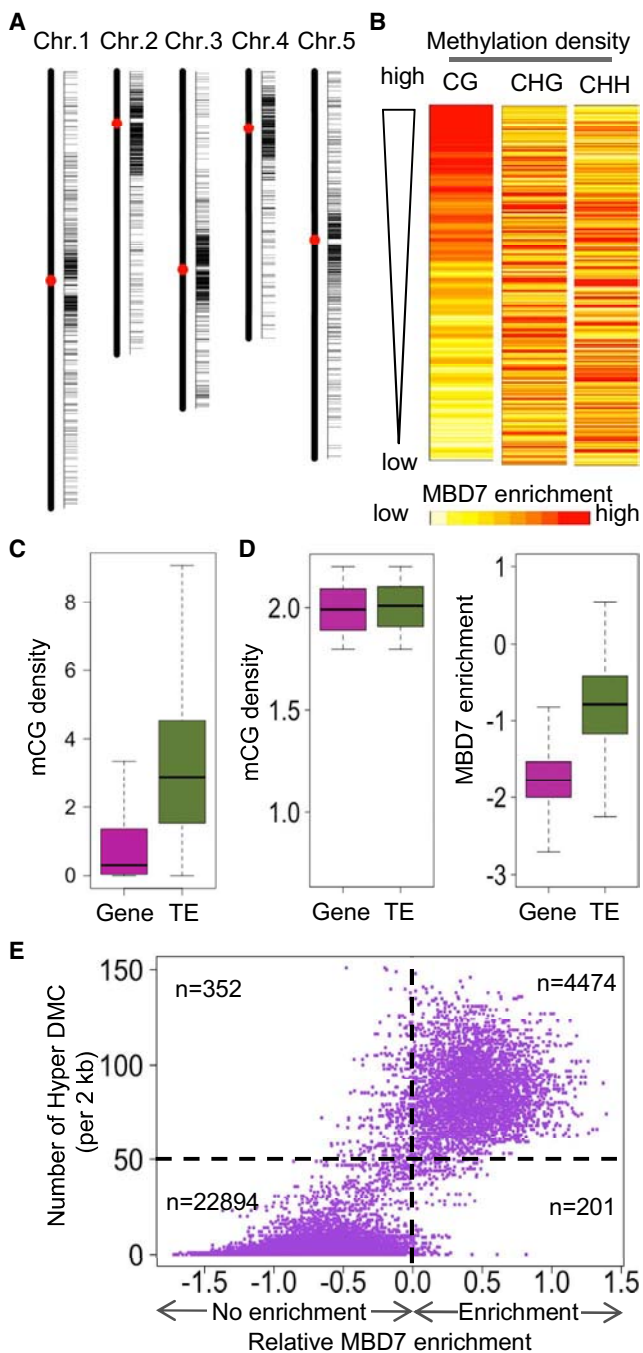
(E) Chromosomal distribution of hyper-DMRs in *mbd7-1* and *idm3-1*.

See also Figure S2.

We examined the correlation between MBD7 binding and DNA methylation in CG, CHG, and CHH contexts. First, the genome was divided into 1-kb regions, and MBD7 enrichment was calculated for each region. The top 1% of MBD7-enriched regions was selected for further analysis. To evaluate the influences of DNA methylation level on MBD7 enrichment, we ranked these regions by CG, CHG, and CHH methylation levels and generated a heat map of MBD7 enrichment. However, no pattern of MBD7 enrichment was evident for any of the three ranks (data not shown), suggesting that the methylation level of individual CG, CHG, or CHH motifs does not determine MBD7 binding.

Methylation density is a value reflecting both methylation level and methyl cytosine density for a region, and it is equal to the sum of methylation percentages of individual cytosines in a region normalized by the region length (Baubec et al., 2013). To consider not only methylation level but also the methyl cytosine

density of a region, we calculated the methylation density for 1-kb genomic regions. When these regions were ranked by mCG, mCHG, and mCHH densities, the heat map pattern indicated that MBD7 enrichment is associated with CG methylation density rather than with CHG and CHH methylation densities (Figure 3B), which is consistent with previous in vitro finding that MBD7 can bind to mCG sites but not to mCHG sites (Zemach and Grafi, 2007). The tight relationship between MBD7 enrichment and CG methylation density genome wide (instead of the top 1%) was supported by an analysis using a previously described method (Baubec et al., 2013), where all 1-kb genomic regions were ranked from left to right by their CG methylation density, and their MBD7 enrichment and CG methylation density values are indicated by red and blue lines, respectively (Figure S3A). When the same method was used, no correlation was observed between MBD7 enrichment and methylation density in either the CHG or CHH context (data not shown).



**Figure 3. MBD7 Preferentially Binds to Regions with High mCG Density and the Binding Coincides with Its Role in Preventing DNA Hypermethylation**

(A) Chromosomal distribution of MBD7 binding peaks.  
 (B) Correlation of MBD7 enrichment with DNA methylation density. The top 1% of MBD7-enriched regions was selected for analysis. For each region, MBD7 enrichment was represented by color from light yellow (lowest) to red (highest). Methylation density was examined in the contexts of CG, CHG, and CHH.  
 (C) Comparison of CG methylation density between genes and TEs in the *Arabidopsis* genome.  
 (D) Comparison of MBD7 chromatin enrichment (right panel) at a subset of Gene and TE loci that show similar mCG densities in the range of 1.8–2.2 (left panel).

The majority of MBD7 binding sites are in TE regions. We analyzed the CG methylation density of all TE-associated 1-kb windows (TE windows) and all gene-associated 1-kb windows (gene windows) and found that TE windows generally have higher CG methylation density than gene windows (Figure 3C), as expected. To test whether the TE-preferred binding of MBD7 is due to the higher CG methylation density of TE or due to other TE-specific features, we selected TE windows and gene windows with comparable CG methylation density and then compared their MBD7 enrichment (Figure 3D). We found a greater enrichment for MBD7 in TEs than in genes, even when they had comparable mCG densities (Figure 3D); this pattern was consistent for all the ranges of mCG density we tested (Figure S3C). This result suggests that MBD7 may not bind to all regions with a high mCG density, but instead it may recognize and bind to mCGs located in TEs.

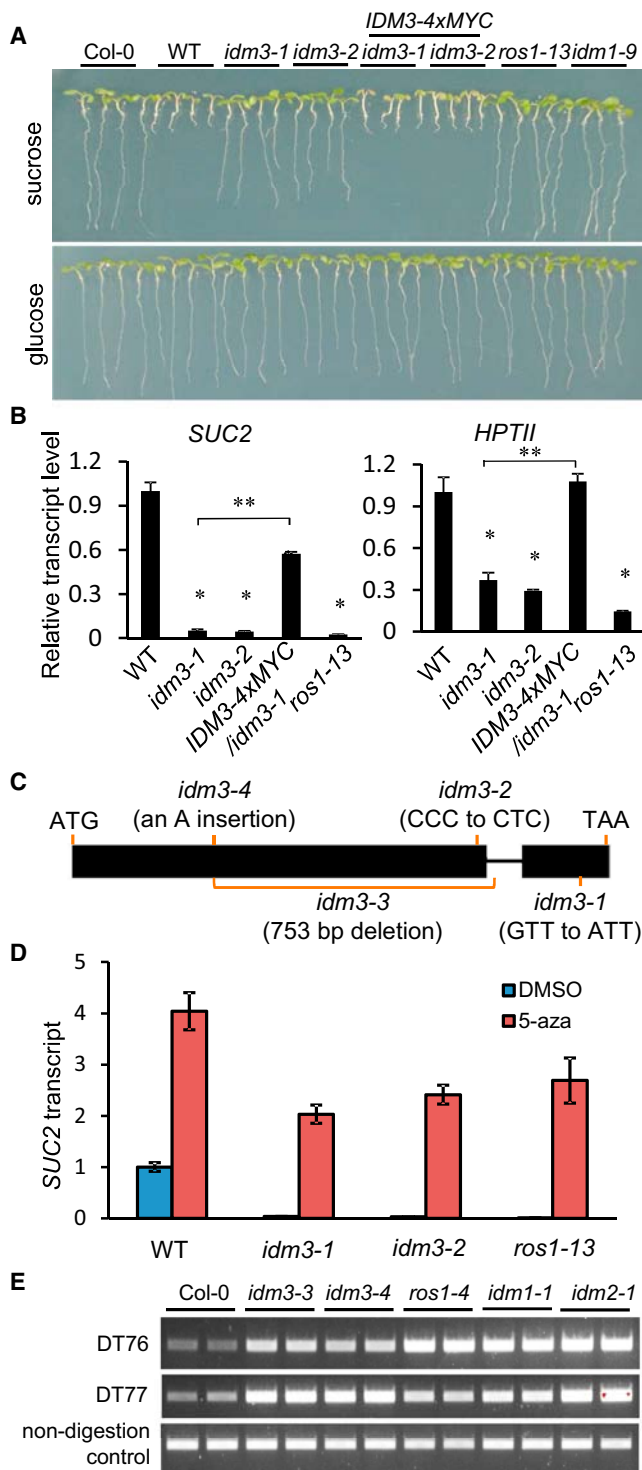
#### MBD7 Binding Coincides with Its Role in Preventing DNA Hypermethylation

To investigate the correlation of MBD7 binding with its influence on DNA methylation, we calculated MBD7 enrichment and the number of hyper differentially methylated cytosines (DMCs) in the *mbd7-1* mutant for each 2-kb genomic region. Interestingly, the numbers of hyper DMCs in the *mbd7-1* mutant positively correlated with MBD7 enrichment; most of the 2-kb bin genomic regions with MBD7 enrichment (4,474) have higher numbers of hyper DMCs (>50 per 2 kb bin), compared to the numerous 2-kb bin genomic regions without MBD7 enrichment (22,894) (Figure 3E). The result indicates that MBD7 binding to chromatin coincides with its function in preventing DNA hypermethylation.

To further understand the influence of MBD7 on DNA methylation at its binding sites, we compared the methylation levels between the WT and *mbd7-1* at MBD7-binding regions. Two groups of control regions were randomly selected, and their methylation levels were also calculated. In *mbd7-1*, mCHG, mCHH, as well as mCG levels were elevated at MBD7-binding regions but not in control regions (Figure S3C). Boxplot analysis indicated that the increase in average methylation levels at the MBD7-binding regions is due to increases in the majority of the regions rather than extremely large increases in a small number of regions (Figure S3D).

The ChIP-seq data also showed an enrichment of MBD7 protein in the 35S promoter region (Figure 1D), which is consistent with the ChIP-qPCR result (Figure 2C). In addition, the ChIP-seq data revealed MBD7 enrichment at At1G26380, At1TE04710, *ONSEN*, and *TS1* regions (Figure S1F), which had increased DNA methylation in *mbd7-1*. These results suggest that physical binding of MBD7 at these loci attenuates the silencing of these loci (Figures 1E and 1F) by preventing DNA hypermethylation.

(E) Correlation of MBD7 enrichment with DNA hypermethylation in *mbd7-1* mutant plants. For each 2-kb genomic region, the relative MBD7 enrichment and number of hyper DMCs in *mbd7-1* are calculated. The numbers of displayed 2-kb genomic regions with or without MBD7 enrichment and with >50 or <50 hyper DMCs are indicated. See also Figures S3.



**Figure 4. IDM3 Functions in Preventing Transcriptional Silencing**

(A) The *idm3* mutants were isolated based on its long root phenotype when grown with exogenous sucrose. Transgenic expression of the WT *IDM3* gene rescued *idm3* root growth phenotype. The *ros1-13* and *idm1-9* were used as controls.

(B) *IDM3* dysfunction suppresses *SUC2* and *HPTII* transgene expression. RT-qPCR results are means  $\pm$  SD of three biological replicates where the fold

#### *idm3* Mutants Phenocopy *mbd7* Mutants

From the same mutant screen, we isolated Increased DNA Methylation 3-1 (*idm3-1*) and *idm3-2*, which showed a long-root phenotype on sucrose-containing media and reduced *SUC2* and *HPTII* transcript levels (Figures 4A and 4B). Map-based cloning of *idm3-1* and *idm3-2* identified missense mutations in At1G20870 (Figure 4C). To further confirm that the mutations in At1G20870 are responsible for the anti-silencing defects in the *idm3* mutants, we transformed a native promoter-driven WT At1G20870 gene fused with 4xMYC into the *idm3* mutants and found that the root growth as well as *SUC2* and *HPTII* transgene expression phenotypes were rescued (Figures 4A and 4B). *IDM3* is predicted to encode an alpha-crystallin domain (ACD) protein localized to the nucleus (Figure S4A) and is similar to *IDM2* (Qian et al., 2014) (Figure S4B). Although both *IDM2* and *IDM3* belong to the family of small heat shock proteins, like *IDM2* (Qian et al., 2014), *IDM3* expression is not heat inducible (Figure S4C).

Genomic bisulfite sequencing of *idm3-1* mutant plants revealed that DNA methylation spread to neighboring sequence in the 35S transgene promoter (Figure 1D). Consistent with the notion that increased DNA methylation was responsible for the silencing of the transgenes, expression of the 35S::*SUC2* transgene was restored in *idm3* mutants after treatment with the cytosine methylation inhibitor 5-aza, as revealed by RT-qPCR (Figure 4D). The 5-aza treatment also increased the expression of the 35S::*SUC2* transgene in the WT (Figure 4D). The result suggests that the transgenes were already subjected to some DNA methylation-dependent silencing in WT plants, which is consistent with the high level of DNA methylation observed within region A of the 35S promoter (Figure 1D).

As in *mbd7-1*, there were many more hyper-DMRs (1,703) than hypo-DMRs (274) in *idm3-1*. Approximately 47% (799) of the hyper-DMRs are also hypermethylated in *mbd7-1*. Chop-PCR analysis confirmed that several endogenous genomic sites were hypermethylated in *idm3-1* mutant plants, as in *mbd7-1* (Figure 2D). Because we suspected that the *idm3-1* and *idm3-2* point mutations represent weak alleles, and also because we could not find any T-DNA insertion alleles of *idm3*, we used the CRISPR/Cas system (Mao et al., 2013) to generate two new alleles, *idm3-3* and *idm3-4*. In *idm3-3*, a 753-bp fragment was deleted from the *IDM3* gene. In *idm3-4*, a frameshift mutation at the 5' region of *IDM3* created a premature stop

changes are normalized to transcript levels in WT. \* $p < 0.01$  compared to WT; NS, not significant compared to WT; \*\* $p < 0.01$  compared to *idm3-1* (two-tailed t test).

(C) A diagram of the *IDM3* gene showing the mutation sites in *idm3* mutants. Boxes and lines denote exons and introns, respectively.

(D) Transcriptional silencing of 35S::*SUC2* in *idm3* mutants can be released by chemical inhibition of DNA methylation. Plants were treated with the DNA methylation inhibitor 5-aza or the solvent DMSO as a control. Gene expression levels were normalized to that of DMSO-treated WT plants. RT-qPCR results are means  $\pm$  SD of three biological replicates, where the fold changes are normalized to transcript levels in WT. Results are means  $\pm$  SD of three biological replicates.  $p < 0.01$  (two-tailed t test).

(E) Analysis of DNA methylation levels at the DT76 and DT77 loci in *idm3-3* and *idm3-4* mutants by Chop-PCR.

See also Figure S4.



codon (Figure 4C). We examined DNA methylation by Chop-PCR at two loci, DT76 and DT77 (Qian et al., 2012), in *idm3-3* and *idm3-4*. The amplification from genomic digests of the mutants but not WT DNA indicates that these loci were hypermethylated in *idm3-3* and *idm3-4* mutants, as they were in *ros1-4*, *idm1-1*, and *idm2-1* (Figure 4E). Thus, like MBD7, IDM3 is required to prevent transgene silencing and DNA hypermethylation.

### MBD7 Interacts with IDM2 and IDM3

In order to understand how MBD7 functions, we identified MBD7-interacting proteins by performing immunoprecipitation (IP) followed by liquid chromatography-tandem mass spectrometry (LC-MS/MS) with *mbd7-1* mutant plants complemented with native promoter-driven *MBD7-4xMYC*. WT plants not expressing *MBD7-4xMYC* served as controls. Of the proteins co-precipitated with anti-MYC antibodies in the *MBD7-4xMYC* transgenic plants but not in the control plants, four had been uncovered from the 35S::*SUC2* transgene-based screen as anti-silencing factors: MBD7 itself, IDM1 (Qian et al., 2012), IDM2 (Qian et al., 2014), and IDM3 (Figure 5A). Similar IP-LC-MS/MS experiments were carried out using *idm3-1* mutant plants complemented with native promoter-driven *IDM3-4xMYC*. In the anti-MYC immunoprecipitates, we identified not only IDM3 itself but also MBD7, IDM2, and IDM1 (Figure 5A). In addition, in anti-GFP immunoprecipitates from *idm1-1* mutant plants complemented with native promoter-driven *IDM1-GFP-HA*, we found IDM1 itself and IDM2, IDM3, and MBD7 (Figure 5A). These results show that MBD7 is associated with IDM3, IDM2, and IDM1 in vivo.

Yeast two-hybrid (Y2H) assays were used to determine whether MBD7 interacts directly with IDM1, IDM2, and IDM3. Yeast cells expressing binding domain (BD)-MBD7 and activation domain (AD)-IDM3 were able to grow on both minus-three media (media lacking leucine, tryptophan, and histidine) and minus-four media (media lacking leucine, tryptophan, histidine and adenine) (Figure 5B), suggesting a strong interaction between MBD7 and IDM3. BD-MBD7 and AD-IDM2 co-transfected yeast cells grew on minus-three media but not on minus-four media (Figure 5C), indicating a relatively weaker interaction between MBD7 and IDM2. MBD7 did not interact with IDM1 in the Y2H assay (data not shown). The interaction between MBD7 and IDM3 was confirmed in a split luciferase complementation assay in protoplasts (Figure 5D). The split luciferase complementation assay also indicated an interaction between MBD7 and IDM2, although this interaction is much weaker than that between MBD7 and IDM3, as indicated by the relative luciferase activities (Figure 5D).

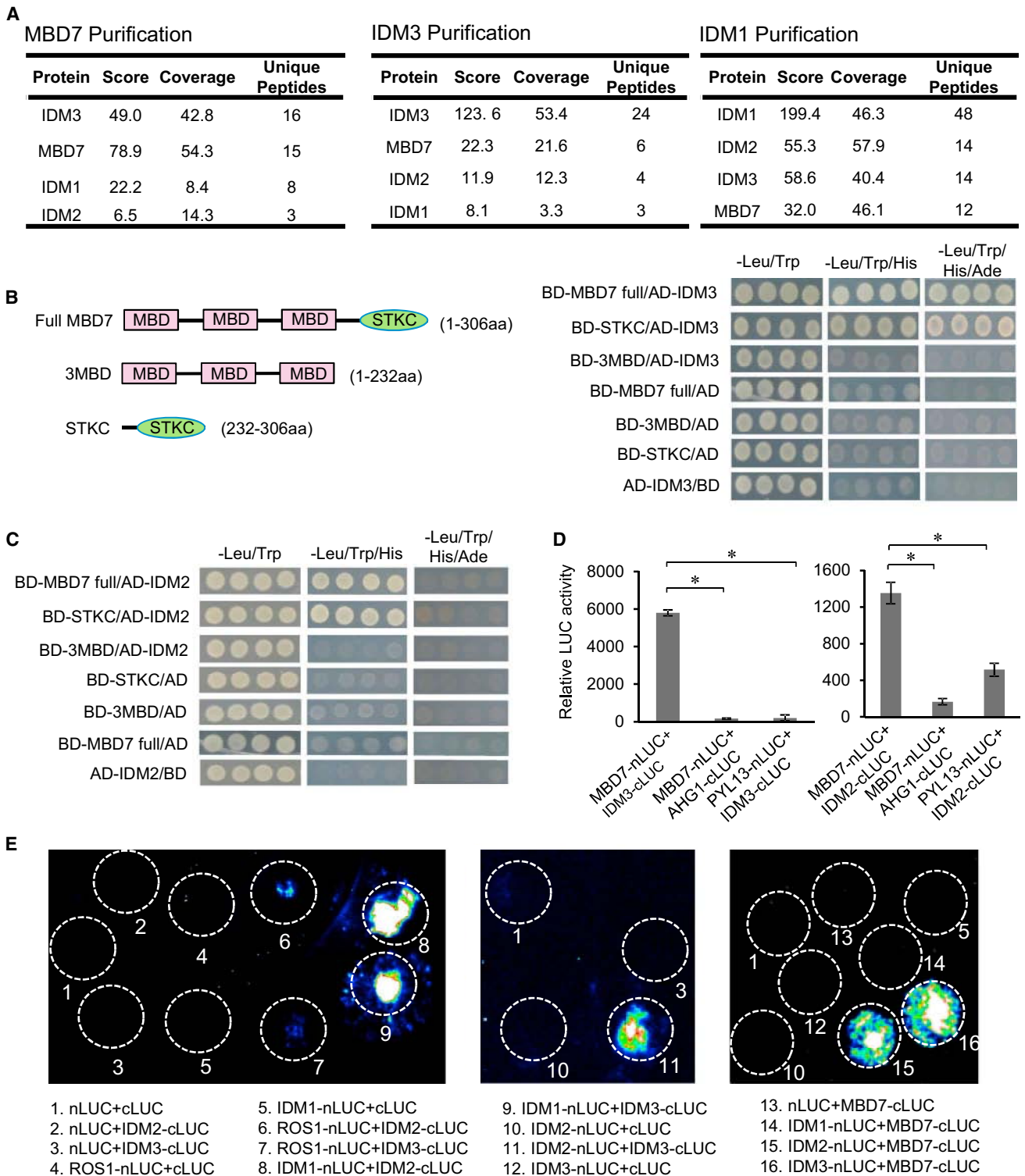
The MBD7 interactions with IDM3 and IDM2 were also confirmed using a split luciferase complementation assay in tobacco leaves (Figure 5E). Interestingly, IDM3 also interacted with IDM2 in the assay. We observed an interaction between IDM2 and IDM1 in the assay, which is consistent with previous results (Qian et al., 2014; Zhao et al., 2014). Like IDM2, IDM3 also interacted with IDM1 in the split luciferase complementation assay (Figure 5E). The Y2H and split luciferase complementation results show that MBD7 interacts with IDM3 and IDM2, and that IDM3 interacts with IDM2 and IDM1. These results are consistent with our IP-LC-MS/MS data (Figure 5A) that showed MBD7 association with IDM3, IDM2, and IDM1 in vivo.

MBD7 contains three MBD domains and a C-terminal domain known as the StkC domain (Figure 5B). We performed the Y2H assay with different deletion mutants and found that both IDM2 and IDM3 bind to the StkC domain of MBD7 but not the three MBD domains (Figures 5B and 5C). To test whether StkC, the protein interaction domain, is important for the anti-silencing function of MBD7, we separately transformed the native promoter-driven full-length *MBD7* coding sequence (*proMBD7::MBD7-4xMYC*) and native promoter-driven *MBD7* containing only the three MBD domains (*proMBD7::3MBD-4xMYC*) into *mbd7-1*. Unlike the full-length MBD7 protein, the three MBD domains could not rescue the root phenotype of *mbd7-1* (Figure S5A), indicating that the StkC domain is required for the anti-silencing function of MBD7, at least at the transgene loci.

Our IP-LC-MS/MS results indicated an association between MBD7 and IDM1 in vivo (Figure 5A). We showed previously that IDM1 is a histone H3 acetyltransferase that catalyzes H3K18 and H3K23 acetylation (Qian et al., 2012) and that H3K18ac and H3K23ac marks are reduced at the silenced 35S promoter in *idm1* mutant plants (Qian et al., 2014). ChIP-qPCR assays revealed that H3K18ac and H3K23ac levels are reduced in *mbd7-1* mutant plants at the 35S promoter, as in *idm1-9* mutants (Figures S5B and S5C). The results are consistent with the notion that MBD7 and IDM1 are in the same protein complex in vivo and suggest that MBD7 is important for IDM1 function in plants.

### MBD7 Affects a Subset of Genomic Regions Targeted for Active DNA Demethylation

IDM1 and IDM2 have been shown to be required to prevent the hypermethylation of hundreds of genomic regions that are a subset of the targets of active demethylation by ROS1, DML2, and DML3 (Qian et al., 2012, 2014). We previously determined the methylomes of the *idm1-1*, *idm2-1*, and *rdm* (*ros1*, *dml2*, and *dml3* triple mutant) mutants. We found that these methylomes could not be compared to those of the *mbd7-1* and *idm3-1* mutants because the genetic background for these mutants and their WT control (containing the 35S::*SUC2* transgene) was twice subjected to *Agrobacterium*-mediated transformation and contains several transgenes (see Experimental Procedures), and even the WT control methylome is very different from that of Col-0 control (data not shown). We therefore determined the DNA methylomes of *mbd7-2* and *idm3-3*, which are in the standard Col-0 background as *idm1-1*, *idm2-1*, and *rdm*. We found 1,014 and 1,725 DMRs with increased DNA methylation (hyper-DMRs) in *mbd7-2* and *idm3-3*, respectively. Approximately 77% (776) of the hyper-DMRs in *mbd7-2* overlap with the hyper-DMRs in *rdm*, 61% (613) overlap with the hyper-DMRs in *ros1-4*, 44% (441) overlap with the hyper-DMRs in *idm1-1*, 46% (461) overlap with the hyper-DMRs in *idm2-1*, and 42% (425) overlap with the hyper-DMRs in *idm3-3*. Several examples of shared hyper-DMRs in the *mbd7-2*, *idm1-1*, *idm2-1*, *idm3-3*, and *ros1-4* mutants are shown in Figures 6A and S6A–S6D, which also display ChIP-seq results showing MBD7 enrichment levels in these regions. Furthermore, we examined IDM1 occupancy at some of these loci using ChIP against 3xHA tagged IDM1. The ChIP assay indicated that IDM1 protein was enriched in the chromatin at the tested loci in WT plants, but



**Figure 5. MBD7 Physically Interacts with IDM2 and IDM3**

(A) Detection of proteins that associate with MBD7, IDM3, or IDM1. Proteins were detected by LC-MS/MS following IP of MYC-tagged MBD7, MYC-tagged IDM3, or GFP-tagged IDM1. There were two biological replicates for each of the protein purifications; one representative result is shown here.

(B) Tests of IDM3-MBD7 interaction by yeast two-hybrid assays. Full-length protein (MBD7 full) and truncated forms (3MBD and STKC) of MBD7 were fused with the GAL4 binding domain (BD). Full-length IDM3 was fused with the GAL4 activation domain (AD).

(legend continued on next page)

the enrichment was substantially reduced in *mbd7-1* mutant plants (Figures 6B and S6E). These results suggest that IDM1 binding to target loci is MBD7 dependent.

Our results suggest that MBD7 affects only a specific subset of genomic regions that require IDM1 or IDM2 for DNA demethylation. To understand how MBD7 may achieve this specificity, we analyzed the CG methylation density of the different groups of hyper-DMRs. In *idm1*, *idm2*, and *idm3* mutants, the hyper-DMRs that overlap with those in *mbd7-2* have higher CG methylation density than the non-overlapping hyper-DMRs. Simulations with randomly selected regions do not show a significant difference (Figure S6F). The results suggest that MBD7 functions together with IDM1 and IDM2 preferentially at genomic regions with a high CG methylation density, consistent with the requirement of high mCG density for MBD7 binding. Indeed, analyses of the MBD7 ChIP-seq data showed that MBD7 is more highly enriched at the dense mCG/overlapping hyper-DMRs than at the non-overlapping hyper-DMRs (Figure S6G). No significant difference was found using the control ChIP-seq data from WT plants (Figure S6G).

## DISCUSSION

We have found that MBD7 and IDM3 are two cellular anti-silencing factors that inhibit DNA hypermethylation at some genomic regions and prevent transcriptional gene silencing. DNA methylation is a conserved epigenetic mark that silences TEs and other invasive elements (He et al., 2011; Law and Jacobsen, 2010). Many plant and animal genomes have abundant TEs, such that the genes are islands in the sea of TEs (Bennetzen and Wang, 2014). Methylation at TEs may spread to and silence adjacent, transcriptionally active genes. Active DNA demethylation is one mechanism for preventing DNA methylation spread to protect nearby genes. For example, the *EPF2* gene, which controls the size of the stomatal stem cell population in leaf epidermis, is close to a methylated TE in *Arabidopsis*, and active DNA demethylation is required to prevent methylation spreading and transcriptional silencing of *EPF2* (Yamamuro et al., 2014). In the DNA demethylase *ros1* mutants, *EPF2* is silenced by DNA methylation that spreads from the proximal TE, resulting in an over-production of stomatal lineage cells (Yamamuro et al., 2014). Many imprinted genes in plants require the DNA demethylase DME for DNA demethylation and expression in the endosperm, because these genes evolved to have TEs in or near their regulatory sequences (Gehring et al., 2009). Our findings reveal that MBD7 associates with methylated DNA and recruits other anti-silencing factors to create a permissible chromatin environment for binding of DNA

demethylases such as ROS1. Thus, our results suggest that MBD7 and the IDM proteins limit the spread of DNA methylation by promoting active DNA demethylation.

Active DNA demethylation is also necessary for pruning the DNA methylation landscape of many TEs and is thus important for preventing over-silencing of TEs (Zhu et al., 2007). In addition, it has been known for a long time that DNA methylation can cause transcriptional silencing of transgenes in plants (Matzke et al., 1989). It is important to understand how transcriptional silencing of transgenes can be avoided or prevented in order to keep transgenic traits stable in the agricultural biotechnology industry.

The key enzymes for active DNA demethylation have been identified in recent years. In vertebrates, active DNA demethylation is initiated by deamination or oxidation of 5mC by AID/APOBECs or TET enzymes, respectively, followed by the DNA glycosylase TDG or MBD4 (Rai et al., 2008; Kohli and Zhang, 2013), whereas in plants, active DNA demethylation is initiated by the ROS1/DME family of 5mC DNA glycosylases (Zhu, 2009). How the DNA demethylation enzymes are targeted to specific genomic loci is poorly understood. In plants, the histone acetyltransferase IDM1 is required for targeting ROS1 to a subset of genomic regions for demethylation (Qian et al., 2012). Although it is not known how the H3K18 and H3K23 acetylation marks created by IDM1 affect ROS1 targeting, this regulation may be considered an “acetylation switch,” analogous to the model proposed for targeting of the chromatin remodeling complex SWR1 in yeast (Ranjan et al., 2013). Like IDM1, IDM2 regulates the demethylation of a similar subset of genomic loci targeted by the ROS1 family of demethylases (Qian et al., 2014). IDM2/ROS5 is a nuclear ACD protein that interacts with IDM1 and affects its H3K18 acetylation activity (Qian et al., 2014; Zhao et al., 2014). Interestingly, we have now identified IDM3, an ACD protein that is closely related to IDM2 and is also required to prevent DNA hypermethylation and gene silencing.

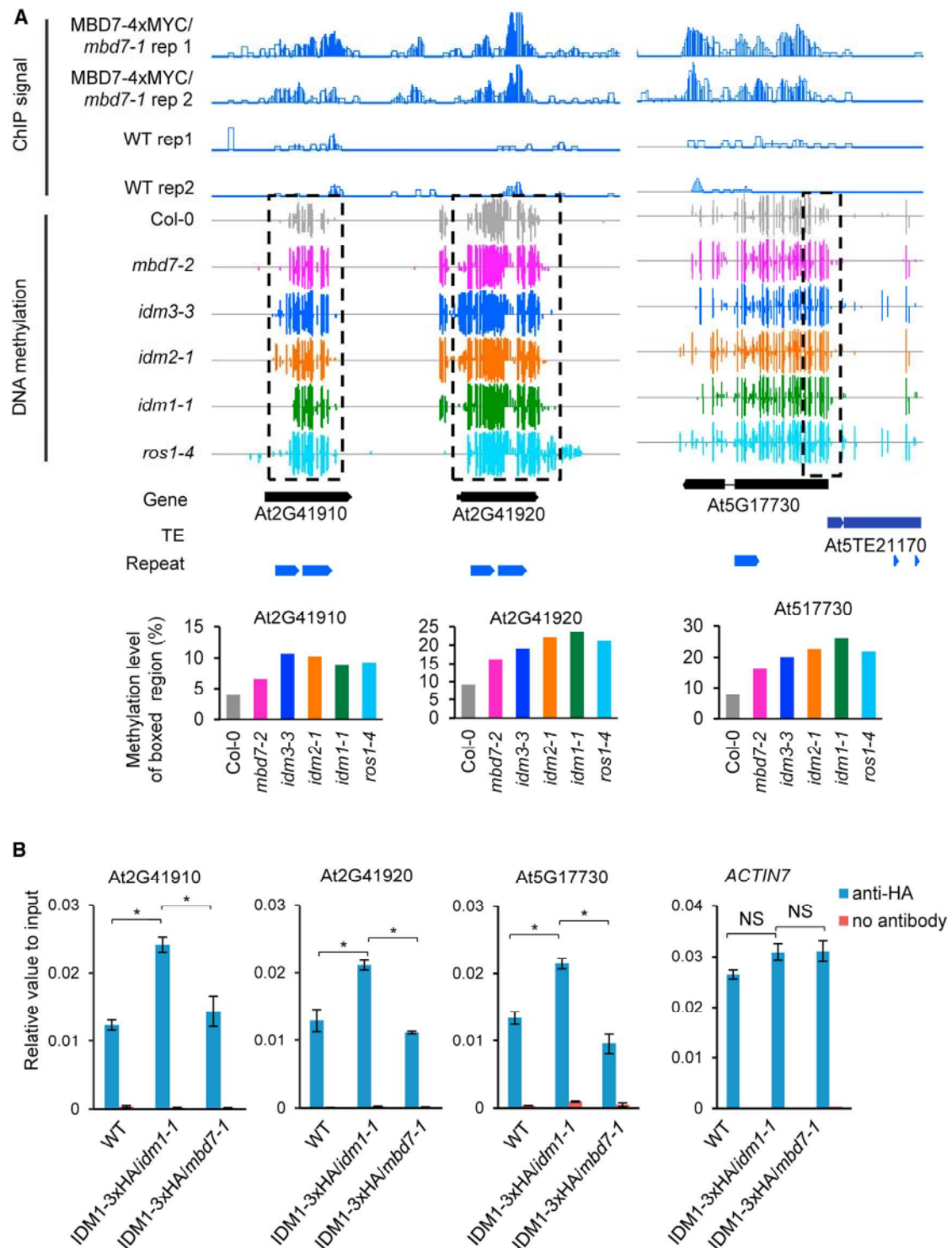
MBD7 is an MBD protein that contains three MBD domains and a C-terminal Stk domain. Consistent with its ability to bind methylated CpGs in vitro (Zemach and Grafi, 2007), our ChIP-seq assays revealed that genome-wide binding of MBD7 correlates with the density of methylated CG but not methylated CHG or CHH sites. Our results suggest that MBD7 does not bind to all regions with a high mCG density, but instead may preferentially recognize and bind to mCGs located in TEs. It is possible that in addition to high mCG density, TE features such as heterochromatic histone marks may also contribute to MBD7 binding. We showed that MBD7 binding is coincident with the role of MBD7 in preventing DNA hypermethylation. Therefore, instead

(C) Tests of IDM2-MBD7 interaction by yeast two-hybrid assays. Full-length protein (MBD7 full) and truncated forms (3MBD and STKC) of MBD7 were fused with BD. Full-length IDM2 was fused with AD.

(D) Analyses of IDM2-MBD7 and IDM3-MBD7 protein interactions by split luciferase complementation assays in *Arabidopsis* protoplasts. The co-transfected *GUS* gene was used to standardize protoplast transfection efficiency. Protoplasts expressing the tested protein and proteins unrelated to gene silencing including ABA-hypersensitive germination 1 (AHG1) and PYR1-like protein 13 (PYL13) served as negative controls.

(E) Examination of protein interactions between ROS1, IDM1, IDM2, IDM3, and MBD7 by split luciferase complementation assays in tobacco (*N. benthamiana*) leaves. Luciferase activities were detected at 48 hr post infiltration. White circles indicate leaf region that were infiltrated with *Agrobacterium* strains containing the indicated constructs.

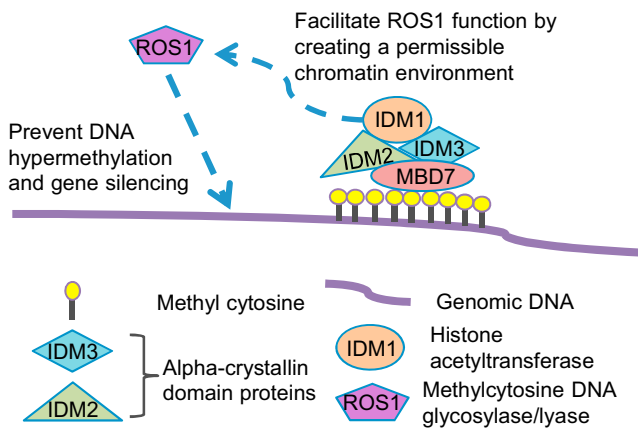
See also Figure S5.



**Figure 6. Shared Hyper-DMRs between *mbd7-2* and Other Anti-Silencing Mutants and the Effect of *mbd7* on IDM1 Binding to Chromatin**  
(A) Levels of DNA methylation and MBD7 chromatin enrichment at several shared hyper-DMRs (dashed boxes) in the *mbd7-2*, *idm3-3*, *idm2-1*, *idm1-1*, and *ros1-4* mutants. Total DNA methylation levels of boxed regions in each mutant were quantified from the whole-genome bisulfite sequencing data and shown in the bottom panel.

(B) Effect of *mbd7* on IDM1 protein enrichment at the shared hyper-DMRs. ChIP against IDM1-3xHA was performed in WT, IDM1-3xHA/*idm1-1*, and IDM1-3xHA/*mbd7-1*. Promoter of *ACTIN7* was used as a control region. All error bars indicate SD,  $n = 3$ . \* $p < 0.01$ ; NS, not significant (two-tailed t test).

See also Figure S6.



**Figure 7. A Working Model of the Functions for MBD7 and IDM3 in Anti-Silencing**

MBD7 binds to highly methylated genomic regions through its MBD motifs and uses its Stkc domain to bind to IDM3 and IDM2, thus bringing IDM1 to the methylated DNA. The H3K18ac and H3K23ac marks created by IDM1 then allow ROS1 and related DNA demethylases to be recruited to curb methylation spread or to prevent hypermethylation by active demethylation.

of reading the DNA methylation signal to cause silencing, MBD7 interprets the DNA methylation signal to avoid DNA methylation spread or hypermethylation to prevent silencing.

MBD7 interacts directly with both IDM2 and IDM3. Like IDM2 (Qian et al., 2014; Zhao et al., 2014), IDM3 also interacts with IDM1. In addition, IDM2 and IDM3 interact with each other. Our IP-LC-MS/MS results show that MBD7 is associated with IDM1 as well as with IDM2 and IDM3 in vivo. The IP-LC-MS/MS results indicated that the amounts of IDM1 and IDM2 that were co-immunoprecipitated with MBD7 or IDM3 were low, compared to the amounts of IDM3 or MBD7 (Figure 5A). The results suggest that while MBD7 and IDM3 may exist in a tight complex, IDM2 and IDM1 are more loosely or transiently associated with the complex. In addition to having three MBD motifs, MBD7 also contains a Stkc domain that is conserved in plant MBD7 orthologs but is not found in other proteins. Our results show that the Stkc domain is necessary for MBD7 function in anti-silencing in plants, consistent with the Stkc domain being responsible for mediating the interaction of MBD7 with IDM2 and IDM3.

Our results suggest a model in which MBD7 binds to methylated TEs and other repeats through its MBD motifs and uses its Stkc domain to bind to IDM3 and IDM2, thus bringing IDM1 to the methylated DNA (Figure 7). The H3K18ac and H3K23ac marks created by IDM1 then allow ROS1 and related DNA demethylases to be recruited to restrict methylation spread or to prevent hypermethylation by active demethylation (Figure 7). Consistent with this model, IDM1 recruitment to target genomic regions is dependent on MBD7 (Figures 6B and S6E), and H3K18ac and H3K23ac marks are reduced in *mbd7* mutant plants, as in *idm1* plants, at the *35S* promoter (Figures S5B and S5C). It is interesting that IDM1 also contains an MBD domain that can bind methylated CG in vitro (Qian et al., 2012). It seems that the single MBD domain of IDM1 is not sufficient to bring IDM1 to some of its target genomic regions, and the tar-

getting requires MBD7 that contains multiple MBD domains. Nevertheless, the single MBD domain may help anchor IDM1 to the genomic sites once it is recruited by MBD7.

Our results suggest that MBD7 and the three IDM proteins form a previously unknown anti-silencing complex that promotes DNA demethylation. Protein complexes that promote DNA methylation and transcriptional gene silencing have been well studied (Matzke and Mosher, 2014). In contrast, nothing has been known in any system about protein complexes that function in regulating DNA demethylation. Our results suggest that MBD7 binds to highly methylated genomic regions through its MBD motifs and uses its Stkc domain to bind to IDM3 and IDM2, thus bringing IDM1 to the methylated DNA (Figure 7). The H3K18ac and H3K23ac marks created by IDM1 then allow ROS1 and related DNA demethylases to be recruited to restrict methylation spread or to prevent hypermethylation by active demethylation (Figure 7). MBD7 may also recruit histone modification enzymes other than IDM1 to help target the DNA demethylases, since IDM1 only affects a subset of genomic regions demethylated by ROS1 and related 5mC DNA glycosylases. It is possible that at some genomic regions MBD7 may affect DNA methylation by preventing the establishment or maintenance of DNA methylation rather than by facilitating active DNA demethylation. On the other hand, not all genomic regions subjected to active DNA demethylation are affected by MBD7, indicating the presence of MBD7-independent mechanisms for targeting the DNA demethylases.

## EXPERIMENTAL PROCEDURES

### Plant Materials, Mutant Screening, and Map-Based Cloning

WT in this study refers to transgenic plants expressing the phosphate starvation responsive *AtPT2* promoter driven firefly luciferase reporter gene and *35S::NPTII* (Karthikeyan et al., 2002) that were later transformed with a construct containing the CaMV *35S* promoter-driven sucrose transporter 2 (*35S::SUC2*) and *35S::HPTII* transgenes (Lei et al., 2011). An EMS-mutagenized pool of plants was generated and screened for mutants with a long-root phenotype (Wang et al., 2013). M2 seedlings were grown vertically on 1/2 MS plates with 2% sucrose and 1% agar. WT plants exhibit severely suppressed root growth on this medium, and we screened for mutants with long-root phenotype among 7-day-old seedlings. Genetic mapping and gene cloning was performed as described previously (Lei et al., 2014). Details of plant materials and gene cloning are provided in Supplemental Experimental Procedures.

### RNA Analysis and Chop-PCR

RNA analysis and Chop-PCR assays were carried out according to Lei et al. (2014). Detailed procedures are described in the Supplemental Experimental Procedures. Primer information is included in Table S1.

### Whole-Genome Bisulfite Sequencing and Data Analysis

Fourteen-day-old seedlings were used for extraction of genomic DNA. Bisulfite conversion, library construction, and deep sequencing were performed by the Beijing Genomics Institute (BGI) in Shenzhen, China. DMRs were identified according to Qian et al. (2012) with some modifications, which are detailed in Supplemental Experimental Procedures.

### ChIP Assay

The ChIP assay was performed as described (Wierzbicki et al., 2008). Dynabeads (Invitrogen, cat# 10003D) were used for pre-clearing and antibody binding. The antibodies were anti-H3K9me2 (Abcam, cat# ab1220), anti-H3K18ac (Abcam, cat# ab1191), anti-H3K23ac (Millipore, cat#07-355), anti-MYC (Millipore, cat#05-724), and anti-Pol II (Abcam, cat#ab5408).

### MBD7 ChIP-Seq and Data Analysis

*proMBD7::gMBD7-4xMYC* transgenic plants were used for ChIP-seq, with WT plants as controls. ChIP was performed according to a previously published protocol (Wierzbicki et al., 2008). ChIP samples were sent to the Genomics Core Facilities of the Shanghai Center for Plant Stress Biology, SIBS, CAS (Shanghai, China) for library construction and Illumina sequencing.

MBD7 binding Peaks were called with SICER (Zang et al., 2009), which compared the two replicates of MBD7-Myc ChIP samples with the two replicates of WT control. The MBD7 protein enrichments were calculated according to Baubec et al. (2013) as follows:  $\text{Enrichment} = \log_2(8 + n_{\text{ChIP}}) - \log_2(8 + n_{\text{Input}} * N_{\text{ChIP}}/N_{\text{Input}})$ , where  $n_{\text{ChIP}}$  and  $n_{\text{Input}}$  represent the number of mapped ChIP and input tags in the corresponding 1-kb bin, and  $N_{\text{ChIP}}$  and  $N_{\text{Input}}$  are the sums of all mapped tags. In Figure 3E, the relative enrichment value is calculated as:  $\log_2(\text{MBD7 enrichment value}) - \log_2(\text{WT enrichment value})$ . Detailed methods are described in Supplemental Experimental Procedures.

### Yeast Two-Hybrid Assay

Coding sequences of IDM2, IDM3, MBD7, and truncated MBD7 (3MBD or STKC) with stop codon were cloned into pDEST22 or pDEST32. Yeast two-hybrid assays were performed as described (Bai et al., 2013).

### IP and LC-MS/MS Analysis

For IP, 5 g of floral tissues for each epitope-tagged transgenic line were used. Dynabeads (Thermo Fisher Scientific) conjugated with MYC antibody (Millipore, cat#05-724) were used for IP. For affinity purification as described in Law et al. (2010), the protein samples were subjected to LC-MS/MS analysis as detailed in Supplemental Experimental Procedures.

### Split Luciferase Complementation Assays

Split luciferase complementation assays were performed in tobacco leaves and *Arabidopsis* protoplasts, the details of which are provided in Supplemental Experimental Procedures.

### ACCESSION NUMBERS

All high-throughput sequencing data generated in this study were submitted to NCBI's Gene Expression Omnibus (GSE58789, GSE58787, and GSE59712). Additional data sets used in this study are GSE33071 (Qian et al., 2012) and GSE49421 (Qian et al., 2014).

### SUPPLEMENTAL INFORMATION

Supplemental Information includes six figures, one table, and Supplemental Experimental Procedures and can be found with this article online at <http://dx.doi.org/10.1016/j.molcel.2015.01.009>.

### AUTHOR CONTRIBUTIONS

J.-K.Z., Z.L., and M.L. designed the study; interpreted the data; and wrote the manuscript. Z.L. and M.L. performed much of the experimental work. X.W., H.Z., D.M., S.M., W.L., W.N., G.M., J.Y., and C.-G.D. contributed to the experiments and discussion of results. K.T. and Z.L. did the bioinformatics analysis. C.H. and W.T. performed the mass spectrometry experiments. C.W. and Z.G. contributed to discussion and interpretation of results.

### ACKNOWLEDGMENTS

This work was supported by National Institutes of Health Grants R01GM070795 and R01GM059138 and by the Chinese Academy of Sciences (to J.-K. Z.).

Received: September 4, 2014

Revised: November 21, 2014

Accepted: January 5, 2015

Published: February 12, 2015

### REFERENCES

- Bai, G., Yang, D.H., Zhao, Y., Ha, S., Yang, F., Ma, J., Gao, X.S., Wang, Z.M., and Zhu, J.K. (2013). Interactions between soybean ABA receptors and type 2C protein phosphatases. *Plant Mol. Biol.* *83*, 651–664.
- Baubec, T., Ivánek, R., Lienert, F., and Schübeler, D. (2013). Methylation-dependent and -independent genomic targeting principles of the MBD protein family. *Cell* *153*, 480–492.
- Bennetzen, J.L., and Wang, H. (2014). The contributions of transposable elements to the structure, function, and evolution of plant genomes. *Annu. Rev. Plant Biol.* *65*, 505–530.
- Gehring, M., Bubb, K.L., and Henikoff, S. (2009). Extensive demethylation of repetitive elements during seed development underlies gene imprinting. *Science* *324*, 1447–1451.
- Haag, J.R., and Pikaard, C.S. (2011). Multisubunit RNA polymerases IV and V: purveyors of non-coding RNA for plant gene silencing. *Nat. Rev. Mol. Cell Biol.* *12*, 483–492.
- He, X.J., Chen, T., and Zhu, J.K. (2011). Regulation and function of DNA methylation in plants and animals. *Cell Res.* *21*, 442–465.
- Hendrich, B., and Bird, A. (1998). Identification and characterization of a family of mammalian methyl-CpG binding proteins. *Mol. Cell. Biol.* *18*, 6538–6547.
- Ito, H., Gaubert, H., Bucher, E., Mirouze, M., Vaillant, I., and Paszkowski, J. (2011). An siRNA pathway prevents transgenerational retrotransposition in plants subjected to stress. *Nature* *472*, 115–119.
- Karthikeyan, A.S., Varadarajan, D.K., Mukatira, U.T., D'Urzo, M.P., Damsz, B., and Raghothama, K.G. (2002). Regulated expression of *Arabidopsis* phosphate transporters. *Plant Physiol.* *130*, 221–233.
- Kohli, R.M., and Zhang, Y. (2013). TET enzymes, TDG and the dynamics of DNA demethylation. *Nature* *502*, 472–479.
- Law, J.A., and Jacobsen, S.E. (2010). Establishing, maintaining and modifying DNA methylation patterns in plants and animals. *Nat. Rev. Genet.* *11*, 204–220.
- Law, J.A., Ausin, I., Johnson, L.M., Vashisht, A.A., Zhu, J.K., Wohlschlegel, J.A., and Jacobsen, S.E. (2010). A protein complex required for polymerase V transcripts and RNA-directed DNA methylation in *Arabidopsis*. *Curr. Biol.* *20*, 951–956.
- Lei, M., Liu, Y., Zhang, B., Zhao, Y., Wang, X., Zhou, Y., Raghothama, K.G., and Liu, D. (2011). Genetic and genomic evidence that sucrose is a global regulator of plant responses to phosphate starvation in *Arabidopsis*. *Plant Physiol.* *156*, 1116–1130.
- Lei, M., La, H., Lu, K., Wang, P., Miki, D., Ren, Z., Duan, C.G., Wang, X., Tang, K., Zeng, L., et al. (2014). *Arabidopsis* EDM2 promotes IBM1 distal polyadenylation and regulates genome DNA methylation patterns. *Proc. Natl. Acad. Sci. USA* *111*, 527–532.
- Mao, Y., Zhang, H., Xu, N., Zhang, B., Gou, F., and Zhu, J.-K. (2013). Application of the CRISPR-Cas system for efficient genome engineering in plants. *Mol. Plant* *6*, 2008–2011.
- Matzke, M.A., and Mosher, R.A. (2014). RNA-directed DNA methylation: an epigenetic pathway of increasing complexity. *Nat. Rev. Genet.* *15*, 394–408.
- Matzke, M.A., Primig, M., Trnovsky, J., and Matzke, A.J. (1989). Reversible methylation and inactivation of marker genes in sequentially transformed tobacco plants. *EMBO J.* *8*, 643–649.
- Ng, H.H., Zhang, Y., Hendrich, B., Johnson, C.A., Turner, B.M., Erdjument-Bromage, H., Tempst, P., Reinberg, D., and Bird, A. (1999). MBD2 is a transcriptional repressor belonging to the MeCP1 histone deacetylase complex. *Nat. Genet.* *23*, 58–61.
- Qian, W., Miki, D., Zhang, H., Liu, Y., Zhang, X., Tang, K., Kan, Y., La, H., Li, X., Li, S., et al. (2012). A histone acetyltransferase regulates active DNA demethylation in *Arabidopsis*. *Science* *336*, 1445–1448.
- Qian, W., Miki, D., Lei, M., Zhu, X., Zhang, H., Liu, Y., Li, Y., Lang, Z., Wang, J., Tang, K., et al. (2014). Regulation of active DNA demethylation by an  $\alpha$ -crystallin domain protein in *Arabidopsis*. *Mol. Cell* *55*, 361–371.

- Rai, K., Huggins, I.J., James, S.R., Karpf, A.R., Jones, D.A., and Cairns, B.R. (2008). DNA demethylation in zebrafish involves the coupling of a deaminase, a glycosylase, and gadd45. *Cell* *135*, 1201–1212.
- Ranjan, A., Mizuguchi, G., FitzGerald, P.C., Wei, D., Wang, F., Huang, Y., Luk, E., Woodcock, C.L., and Wu, C. (2013). Nucleosome-free region dominates histone acetylation in targeting SWR1 to promoters for H2A.Z replacement. *Cell* *154*, 1232–1245.
- Tariq, M., and Paszkowski, J. (2004). DNA and histone methylation in plants. *Trends Genet.* *20*, 244–251.
- Wang, X., Duan, C.-G., Tang, K., Wang, B., Zhang, H., Lei, M., Lu, K., Mangrauthia, S.K., Wang, P., Zhu, G., et al. (2013). RNA-binding protein regulates plant DNA methylation by controlling mRNA processing at the intronic heterochromatin-containing gene IBM1. *Proc. Natl. Acad. Sci. USA* *110*, 15467–15472.
- Wierzbicki, A.T., Haag, J.R., and Pikaard, C.S. (2008). Noncoding transcription by RNA polymerase Pol IVb/Pol V mediates transcriptional silencing of overlapping and adjacent genes. *Cell* *135*, 635–648.
- Yamamuro, C., Miki, D., Zheng, Z., Ma, J., Wang, J., Yang, Z., Dong, J., and Zhu, J.K. (2014). Overproduction of stomatal lineage cells in *Arabidopsis* mutants defective in active DNA demethylation. *Nat. Commun.* *5*, 4062.
- Zang, C., Schones, D.E., Zeng, C., Cui, K., Zhao, K., and Peng, W. (2009). A clustering approach for identification of enriched domains from histone modification ChIP-Seq data. *Bioinformatics* *25*, 1952–1958.
- Zemach, A., and Grafi, G. (2007). Methyl-CpG-binding domain proteins in plants: interpreters of DNA methylation. *Trends Plant Sci.* *12*, 80–85.
- Zemach, A., Kim, M.Y., Hsieh, P.H., Coleman-Derr, D., Eshed-Williams, L., Thao, K., Harmer, S.L., and Zilberman, D. (2013). The *Arabidopsis* nucleosome remodeler DDM1 allows DNA methyltransferases to access H1-containing heterochromatin. *Cell* *153*, 193–205.
- Zhang, H., and Zhu, J.K. (2011). RNA-directed DNA methylation. *Curr. Opin. Plant Biol.* *14*, 142–147.
- Zhao, Y., Xie, S., Li, X., Wang, C., Chen, Z., Lai, J., and Gong, Z. (2014). REPRESSOR OF SILENCING5 Encodes a Member of the Small Heat Shock Protein Family and Is Required for DNA Demethylation in *Arabidopsis*. *Plant Cell* *26*, 2660–2675.
- Zhu, J.K. (2009). Active DNA demethylation mediated by DNA glycosylases. *Annu. Rev. Genet.* *43*, 143–166.
- Zhu, J., Kapoor, A., Sridhar, V.V., Agius, F., and Zhu, J.K. (2007). The DNA glycosylase/lyase ROS1 functions in pruning DNA methylation patterns in *Arabidopsis*. *Curr. Biol.* *17*, 54–59.

# Versatile protein recognition by the encoded display of multiple chemical elements on a constant macrocyclic scaffold

Yizhou Li<sup>1,2\*</sup>, Roberto De Luca<sup>2</sup>, Samuele Cazzamalli<sup>2</sup>, Francesca Pretto<sup>3</sup>, Davor Bajic<sup>2</sup>, Jörg Scheuermann<sup>2\*</sup> and Dario Neri<sup>2\*</sup>

**In nature, specific antibodies can be generated as a result of an adaptive selection and expansion of lymphocytes with suitable protein binding properties. We attempted to mimic antibody-antigen recognition by displaying multiple chemical diversity elements on a defined macrocyclic scaffold. Encoding of the displayed combinations was achieved using distinctive DNA tags, resulting in a library size of 35,393,112. Specific binders could be isolated against a variety of proteins, including carbonic anhydrase IX, horseradish peroxidase, tankyrase 1, human serum albumin, alpha-1 acid glycoprotein, calmodulin, prostate-specific antigen and tumour necrosis factor. Similar to antibodies, the encoded display of multiple chemical elements on a constant scaffold enabled practical applications, such as fluorescence microscopy procedures or the selective in vivo delivery of payloads to tumours. Furthermore, the versatile structure of the scaffold facilitated the generation of protein-specific chemical probes, as illustrated by photo-crosslinking.**

The versatile and specific recognition of target proteins is a fundamentally important feature of the humoral arm of the adaptive immune system. Indeed, antibodies can be raised against virtually any antigen, by suitable immunization procedures<sup>1</sup>. This natural process of clonal selection and amplification can be mimicked in vitro by the construction of large combinatorial antibody libraries and the implementation of efficient selection systems (for example, phage display technology<sup>2</sup>), which allow the generation of man-made antibodies<sup>3–5</sup>. The selected antibodies from phage display libraries can also be used for pharmaceutical applications; for example, the tumour necrosis factor (TNF)-inhibitor Humira (one of the best-selling drugs in the world) was generated using this technology.

There is great scientific and industrial interest in isolating molecules that are substantially smaller than antibodies but retain the ability to recognize various target proteins with high binding affinity and specificity. Such molecules would be less immunogenic, should penetrate tissues more efficiently, and therefore could be advantageous for certain pharmaceutical applications<sup>6</sup>. Large combinatorial libraries of polypeptides developed from display methods (for example, phage display<sup>7</sup>, mRNA display<sup>8,9</sup>, yeast display<sup>10</sup> and ribosome display<sup>11</sup>) have demonstrated the ability to yield specific binders against different proteins. However, those polypeptides are still mainly composed of proteinogenic amino acids and are developed using biosynthetic methodologies.

Serving as a chemical solution for exponentially generating molecular diversity, DNA-encoded chemical libraries (DECLs) are increasingly being employed for the isolation of small-molecule binders against target proteins of interest<sup>12,13</sup>. The technology couples the power of genetics with chemical synthesis, allowing the generation of large sets of synthetic molecules, each linked to a distinctive DNA fragment serving as an amplifiable identification

barcode<sup>14,15</sup>. Compared with conventional screening methodologies such as high-throughput screening and non-encoded combinatorial libraries, DECL technology allows the rapid and rather inexpensive construction of very large chemical libraries of typically millions to billions of compounds, which can be quickly interrogated for target binding by affinity-based selection procedures followed by decoding with high-throughput DNA sequencing (HTDS)<sup>16</sup>.

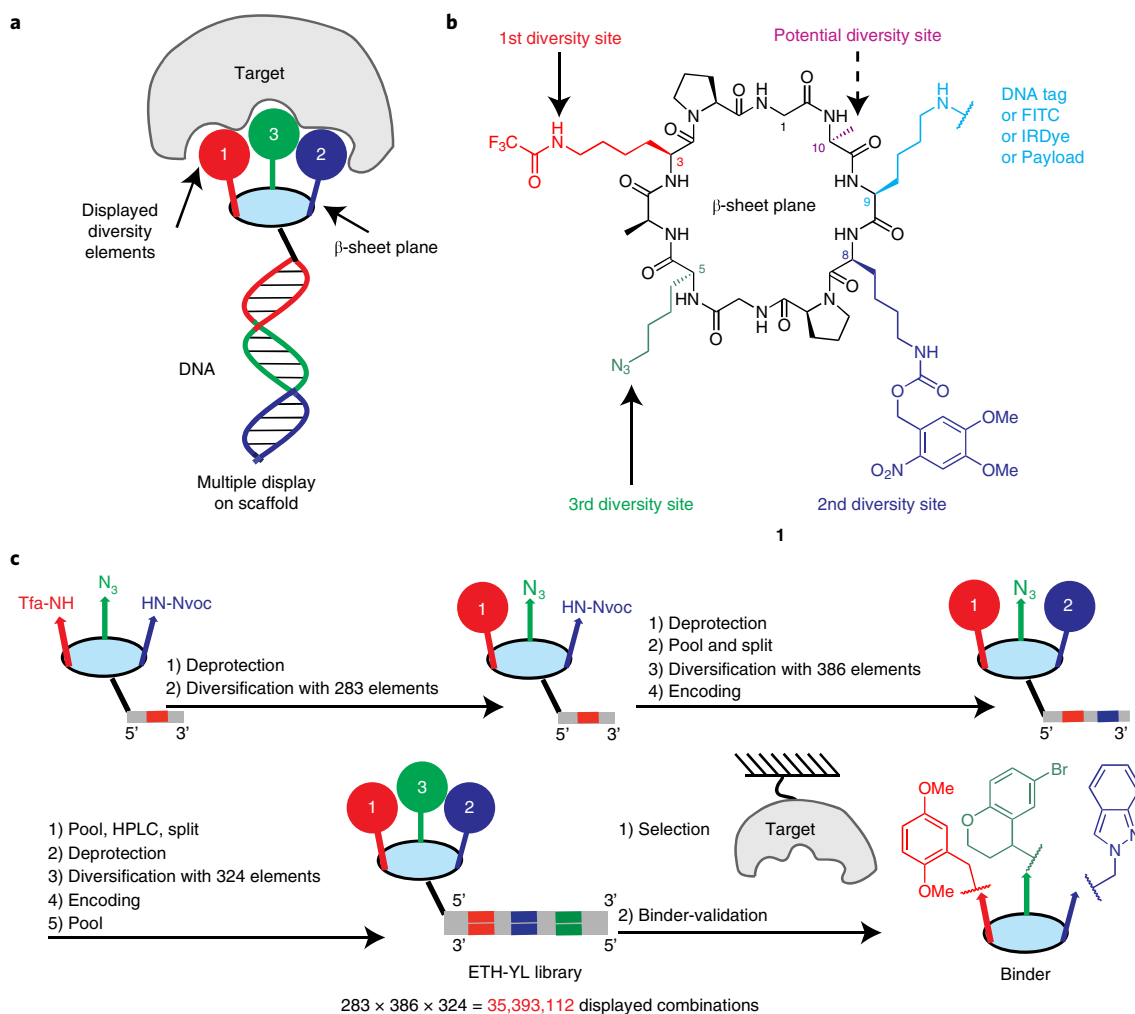
Most of the DECLs reported so far by both academia and industry were constructed by split-and-pool synthetic procedures<sup>16–18</sup>, aiming at drug-like molecules complying with Lipinski's rule of five (RO5)<sup>19</sup>. Further approaches for the construction of DECLs have been proposed featuring, for example, DNA-based routing<sup>20</sup>, DNA-templated synthesis<sup>21–23</sup> or fragment-based strategies<sup>24–27</sup>. While RO5-type DECLs may preferentially yield binders for targets with defined pockets, such as proteases<sup>28</sup>, kinases<sup>17</sup> or phosphatases<sup>29</sup>, the recognition of large surfaces of target proteins remains a challenge. The intrinsically larger size and complexity of macrocycles suggests their usefulness for the recognition of larger target surfaces; however, the pharmaceutical properties of macrocyclic binders may be difficult to optimize, because modification on the cyclic backbone may lead to unexpected conformational changes<sup>7,30</sup>.

In this Article we explore a strategy featuring the encoded combinatorial display of multiple chemical diversity elements (DEs) on a structurally defined macrocyclic scaffold, to achieve a versatile and specific recognition of different target proteins. With that aim, we sought out a fixed macrocyclic scaffold with antiparallel  $\beta$ -sheets, previously described by Manfred Mutter and Pascal Dumy, which serves as a defined platform for the presentation of multiple chemical diversity elements into one side of the  $\beta$ -sheet plane (Fig. 1a)<sup>31–33</sup>. The constant macrocyclic scaffold also contains a further chemically addressable site, which facilitates the encoding of individual synthetic combinations with distinctive DNA tags,

<sup>1</sup>Chongqing Key Laboratory of Natural Product Synthesis and Drug Research, School of Pharmaceutical Sciences, Chongqing University, Shapingba, Chongqing, China. <sup>2</sup>Department of Chemistry and Applied Biosciences, Swiss Federal Institute of Technology (ETH Zürich), Zürich, Switzerland.

<sup>3</sup>Philochem AG, Otelfingen, Switzerland. \*e-mail: [yizhouli@cqu.edu.cn](mailto:yizhouli@cqu.edu.cn); [joerg.scheuermann@pharma.ethz.ch](mailto:joerg.scheuermann@pharma.ethz.ch); [dario.neri@pharma.ethz.ch](mailto:dario.neri@pharma.ethz.ch)





**Fig. 1 | Design, synthesis, encoding and selection of the multiple display DNA-encoded chemical library.** **a**, Protein recognition by encoded multiple display of chemical elements on a constant macrocyclic scaffold. **b**, Scaffold **1**, containing three diversity sites, one potential diversity site and one site for DNA tagging. **c**, Scheme of library construction by a split-and-pool strategy employing three rounds of coupling and encoding with DNA tags. The performance of selection procedures on immobilized target proteins of interest allows the isolation of binders, whose binding affinities can be confirmed after resynthesis. A schematic representation of a possible macrocycle is illustrated as an example.

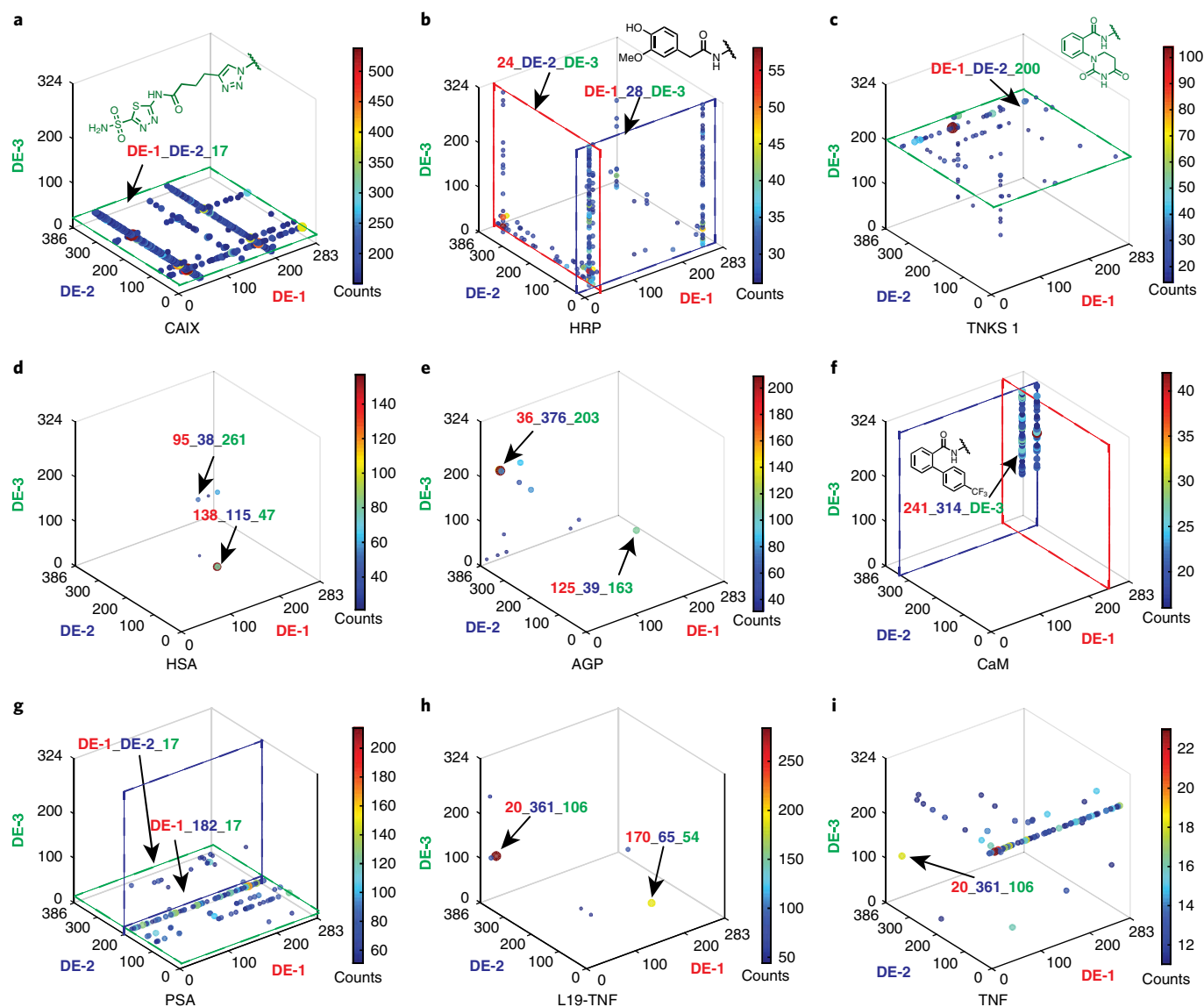
serving as amplifiable identification barcodes for further selection procedures. Alternatively, the same site can be modified with various chemical entities, thus allowing binder validation experiments or chemical biology applications<sup>34</sup>. Our strategy of the directed display of multiple diversity elements on a constant macrocyclic scaffold yielded specific binders against various target proteins, and the resulting binders exhibited antibody-like properties, enabling biochemical and biological applications.

## Results

**Library design and synthesis.** We first synthesized cyclic peptide scaffold **1** (Fig. 1b) by using a solid-phase peptide synthesis approach, followed by cyclization of the pre-organized linear precursor. Three lysine side chains (Fig. 1b: highlighted in red at position 3, green at position 5 and dark blue at position 8, pointing to one side of the  $\beta$ -sheet plane) were masked with mutually orthogonal protecting groups and subsequently coupled with sets of chemical diversity elements under DNA-compatible conditions (Supplementary Fig. 3). The lysine at position 9 (highlighted in light blue in Fig. 1b), pointing to the other side of the  $\beta$ -sheet plane, was used for the stepwise incorporation of DNA tags or for later-stage functionalization. Position 10 (highlighted

in magenta in Fig. 1b) was reserved as a fourth potential diversity site, which could be used for the conjugation of additional diversity elements or as a chemical handle for specific needs (for example, photo-crosslinking).

Library synthesis was accomplished with three rounds of chemical coupling and encoding (Fig. 1c). Scaffold **1** was conjugated to 283 individual oligonucleotides, which encoded the first diversity site (Tfa site). The resulting conjugates were further coupled with 281 carboxylic acids acting as diversity elements (**DE-1** representing the first diversity element in all three-dimensional cubes of Fig. 2), while the two residual oligonucleotides were used as controls ('Tfa-on' and 'Tfa-off'). After Nvoc deprotection by UV irradiation, the conjugates were pooled to a mixture, followed by splitting into 386 vials for subsequent modification with a second set of different carboxylic acids (**DE-2** representing the second diversity element in Fig. 2). The resulting conjugates were encoded by an enzymatic ligation procedure. After a further pool-and-split step, the third site diversification (**DE-3** representing the third diversity element in Fig. 2) was performed either through a copper-catalysed cycloaddition with a set of terminal alkynes or by Staudinger reduction, followed by the acylation with a set of carboxylic acids. The last encoding step, featuring Klenow



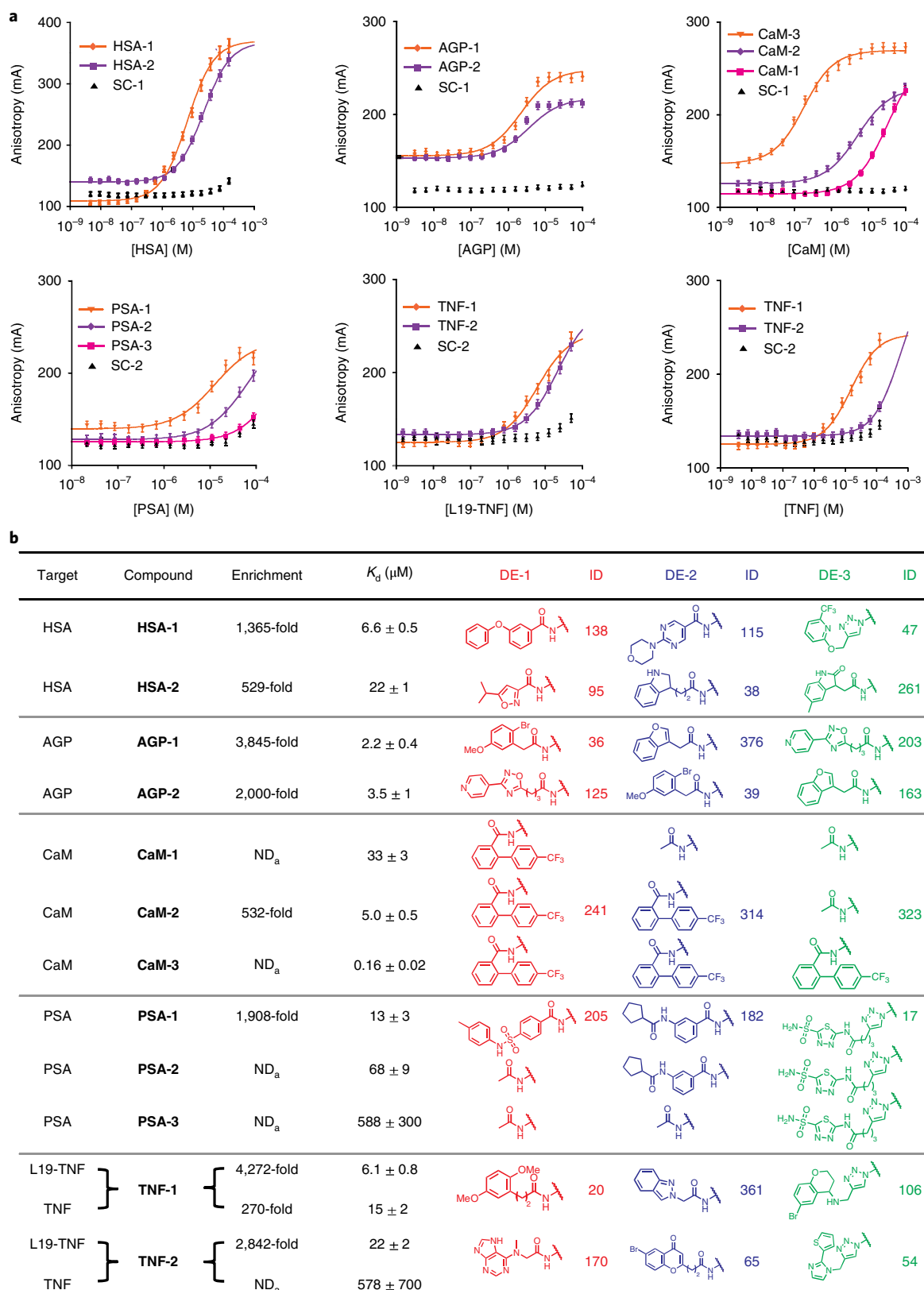
**Fig. 2 | Selection fingerprints from the multiple display DNA-encoded chemical library.** **a**, HTDS plot of a selection against CAIX. The x, y and z axes represent the first (DE-1, red), second (DE-2, dark blue) and third diversity element (DE-3, green) of the library, respectively. Jet colour scale and dot size represent HTDS sequence counts. Total sequence count (TSC) = 2,357,282, cut-off level = 150. **b**, HTDS plot of a selection against HRP. TSC = 4,269,414, cut-off level = 25. **c**, HTDS plot of a selection against TNKS 1. TSC = 2,525,256, cut-off level = 10. **d**, HTDS plot of a selection against HSA. TSC = 3,344,294, cut-off level = 20. **e**, HTDS plot of a selection against AGP. TSC = 1,929,066, cut-off level = 30. **f**, HTDS plot of a selection against CaM. TSC = 1,931,086, cut-off level = 15. **g**, HTDS plot of a selection against PSA. TSC = 2,244,812, cut-off level = 50. **h**, HTDS plot of a selection against L19-TNF. TSC = 2,353,006, cut-off level = 40. **i**, HTDS plot of a selection against TNF. TSC = 2,357,282, cut-off level = 10.

polymerization with partially complementary oligonucleotides, led to the formation of double-stranded DNA, corresponding to an encoded library comprising 35,393,112 displayed combinations on a constant macrocyclic scaffold (ETH-YL library).

The coupling efficiency of all employed chemical diversity elements to DNA was evaluated in model reactions before library construction<sup>35, 36</sup>. Shifts of the average mass of conjugate mixtures after the second and third coupling step were monitored by ultra-performance liquid chromatography-mass spectrometry (UPLC-MS)<sup>17</sup>, and only diversity elements with conversion yields of over 80% were included in the final library (Supplementary Figs. 10 and 12). The efficiency of the DNA-encoding procedure was also checked by gel electrophoresis and UPLC-MS (Supplementary Figs. 14 and 15). HTDS data of the library pool prior to selection

exhibited a uniform distribution of sequence counts, providing additional support for the homogeneity of the library construction (Supplementary Fig. 16).

**Selection experiments and binder validation.** Affinity-based selections of our library with biotinylated proteins were performed according to a previously published procedure and decoded by HTDS<sup>37</sup>. Figure 2 presents the results of affinity selections against nine different target proteins as ‘fingerprints’. The frequency of the sequenced DNA codes (counts) for each DE-1, DE-2, DE-3 combination can be plotted as individual dots, using both a jet colour code (from blue to red) and dot size (from small to large) to rank the counts of the displayed combinations, in a three-dimensional cube with axes DE-1, DE-2 and DE-3.



**Fig. 3 | Binder validation of selected combinations against HSA, AGP, CaM, PSA, L19-TNF and TNF. a**, FP measurements of selected fluorescently labeled compounds against HSA, AGP, CaM, PSA, L19-TNF and TNF. A shift of the sigmoidal curves to the left for selected compounds indicates a contribution of the displayed chemical diversity elements to the binding affinity compared to the unmodified scaffold controls (**SC-1** and **SC-2**). Error bars indicate standard deviation of three measurements. **b**, Enrichments and dissociation constants of synthesized compounds, chemical structures and corresponding identification numbers of the three diversity elements. For calculation of enrichment see Supplementary Table 7. **SC-1** and **SC-2** are two respective scaffold controls capped at the diversity sites. Detailed structures are provided in Supplementary Figs. 21 and 44. ND, not determined; ID, identification number. <sup>†</sup>Not included in the library.

Carbonic anhydrase IX (CAIX), horseradish peroxidase (HRP) and tankyrase 1 (TNKS 1) served as positive controls, as the library contained diversity elements that were known to bind to these proteins. As expected, selections against CAIX revealed one plane of enriched combinations (DE-1\_DE-2\_17, highlighted in green), which corresponds to acetazolamide, a nanomolar binder to this protein (Fig. 2a)<sup>38</sup>. Selections against HRP (Fig. 2b) revealed an enriched phenolic structure (24\_DE-2\_DE-3 and DE-1\_28\_DE-3, respectively)<sup>39</sup>. Figure 2c shows a plane of enriched compounds, featuring the presence of a chemical moiety (DE-1\_DE-2\_200, highlighted in green), which has previously been reported as a TNKS 1 binder<sup>40</sup>.

The fingerprint of the human serum albumin (HSA) selection (Fig. 2d) showed a scattered pattern of displayed combinations. We synthesized two enriched combinations (138\_115\_47 and 95\_38\_261) as fluorescein isothiocyanate (FITC)-labelled derivatives in the absence of DNA and used them in fluorescence polarization (FP) measurements, revealing dissociation constants in the single-digit micromolar range ( $K_d = 6.6 \mu\text{M}$  and  $22 \mu\text{M}$ , respectively, Fig. 3).

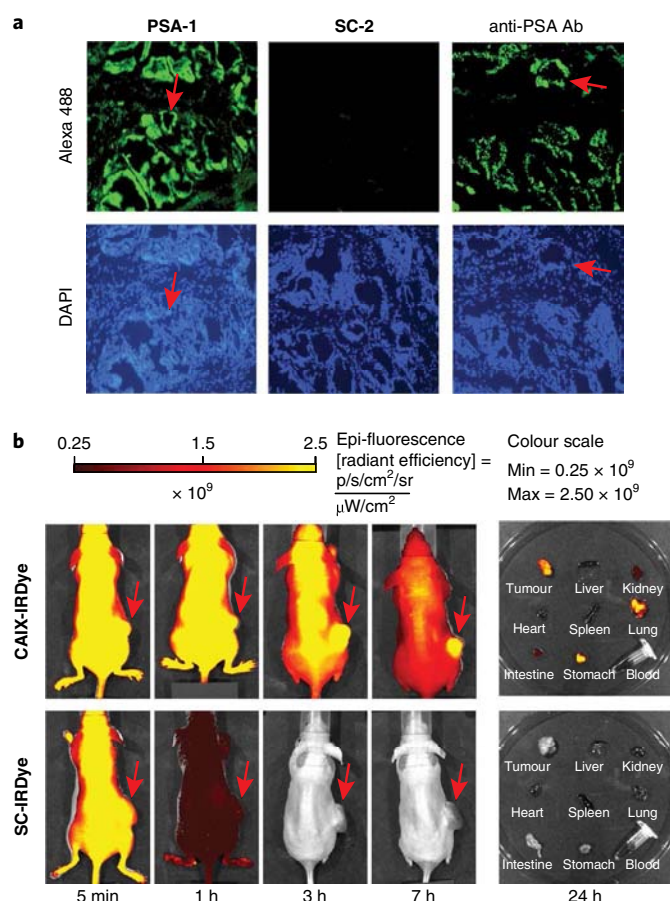
Selection against alpha-1 acid glycoprotein (AGP) revealed a preferential enrichment of two identical sets of three chemical diversity elements, which were located at different positions on the scaffold (Fig. 3b). This corresponds to a 'pseudo-rotation' of the three displayed chemical moieties along the defined scaffold. Synthetic FITC-labelled derivatives of these combinations (AGP-1 and AGP-2) showed a similar AGP binding affinity ( $2.2 \mu\text{M}$  and  $3.5 \mu\text{M}$ , respectively, Fig. 3) in FP measurements. AGP-linear, a linear analogue of AGP-1, was synthesized and exhibited a sevenfold decrease in binding affinity ( $K_d = 15 \mu\text{M}$ ), indicating a contribution of the cyclic nature of the scaffold to protein recognition (Supplementary Fig. 29).

A further selection against calmodulin (CaM) evidenced a preferential enrichment of an identical biphenyl moiety at the first and second diversity site, respectively (Fig. 2f). The corresponding bivalent binder CaM-2 had a  $K_d$  of  $5 \mu\text{M}$  (Fig. 3), while the monovalent binder CaM-1 bound to CaM with a  $K_d$  of  $33 \mu\text{M}$ . Inclusion of a third binding moiety led to the trivalent derivative CaM-3 with a submicromolar dissociation constant ( $K_d = 0.16 \mu\text{M}$ ).

The fingerprint of a selection against human prostate-specific antigen (PSA), a tumour marker, revealed lines of enriched combinations in a plane, corresponding to DE-3 = 17 (green in Fig. 2g). This finding implies that, while DE-3 = 17 plays an essential role, additional diversity elements contribute to protein recognition. The enriched combination 205\_182\_17 (PSA-1) showed  $K_d = 13 \mu\text{M}$ , while the progressive removal of individual diversity elements led to a continuous loss of binding affinity (PSA-2 and PSA-3; Fig. 3).

We also performed selections against human TNF, used both as recombinant protein (TNF) and as TNF-antibody fusion (L19-TNF). We identified two diversity element combinations (20\_361\_106 and 170\_65\_54) as individual spots in the L19-TNF selection fingerprint (Fig. 2h), with high enrichment (Fig. 3b). The corresponding synthetic derivatives TNF-1 and TNF-2 exhibited  $K_d = 6.1 \mu\text{M}$  and  $22 \mu\text{M}$ , respectively. The combination 20\_361\_106 was also enriched in the TNF selection fingerprint (Fig. 2i), indicating that binding was directed against the TNF moiety. The  $K_d$  of TNF-1 to TNF was found to be  $15 \mu\text{M}$ , while TNF-2 did not exhibit considerable TNF binding (Fig. 3).

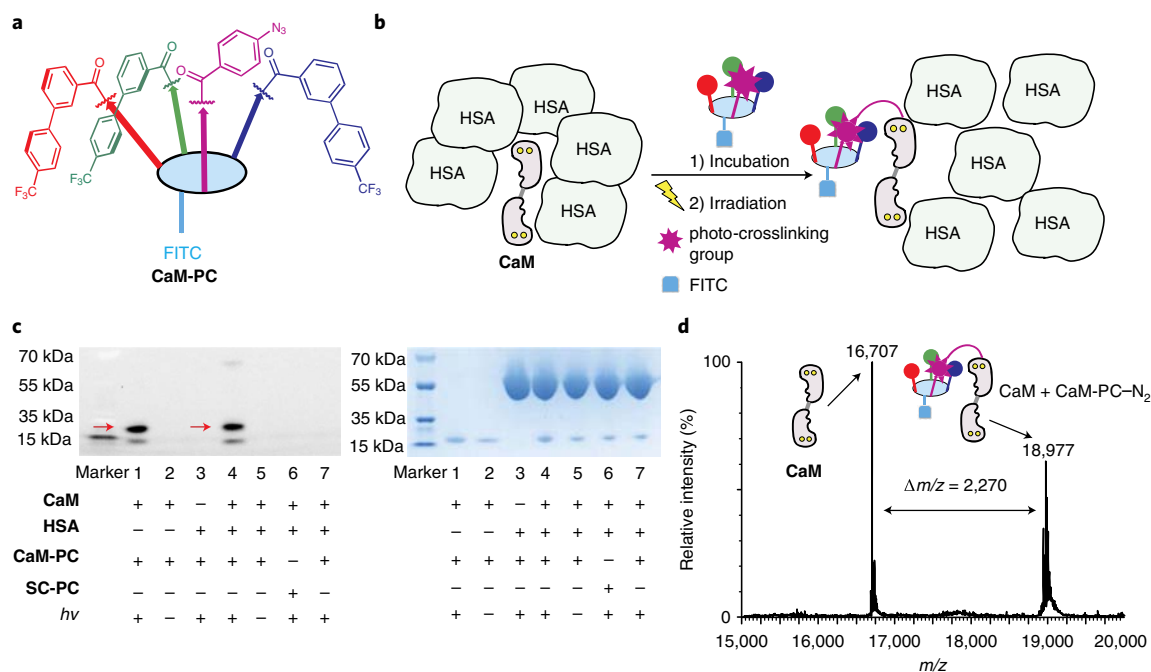
The utility of a constant macrocyclic scaffold lends itself to a further investigation of the impact of the flexibility of the scaffold and the length of the lysine side chains, which serve as linkers between the diversity elements and the scaffold itself, on the binding affinity of the selected binders. A previous study reported that substitution of two *L*-proline residues with *D*-proline in the macrocyclic backbone leads to an even more restricted  $\beta$ -hairpin conformation<sup>33</sup>. For the TNF binder d-TNF-1 and the PSA binder d-PSA-1, this substitution could be implemented, resulting in neither a significant loss nor gain of binding affinity (Supplementary Figs. 54 and



**Fig. 4 | Immunofluorescence performance of selected PSA binder and in vivo performance of CAIX binder.** **a**, Upper panels: Micrographs illustrating PSA localization by binding to **PSA-1**, **SC-2** and to a mouse anti-PSA antibody (Ab). Sections were incubated with **PSA-1** or **SC-2** ( $0.5 \mu\text{M}$  each), treated with rabbit anti-FITC antibody and detected by goat anti-rabbit antibody-Alexa 488. For comparison, the third section was incubated with mouse anti-PSA antibody and detected with goat anti-mouse antibody-Alexa 488. Lower panels: DAPI staining of the same sections. Some glandular structures are indicated with red arrows. DAPI, 4',6-diamidino-2'-phenylindole. **b**, Evaluation of the targeting performance of IRDye-680 conjugates **CAIX-IRDye** and of the control **SC-IRDye**, using near-infrared fluorescence imaging of BALB/c nu/nu mice bearing SKRC-52 xenografts, after intravenous administration of  $3 \text{ nmol}$  conjugates. Images were acquired with identical parameters at 5 min, 1 h, 3 h and 7 h after injection. Right: Imaging of excised organs and blood of injected mice 24 h after injection. Detailed structures are provided in Supplementary Figs. 68 and 70.

67). Shortening the linker side chains by one, two or three methylene groups, however, leads to a loss in binding affinity for the PSA binder (Supplementary Fig. 54). Interestingly, in the case of the TNF binder, substitution of the diversity-elements-displaying lysine with ornithine residues leads to a sixfold increase in the binding affinity of **TNF-1**, while further shortening of the linker side chains had a detrimental effect on  $K_d$  values (Supplementary Fig. 67).

**In vitro and in vivo applications of selected binders.** To test whether the selected synthetic binders could be used like antibodies in certain applications, we first investigated the performance of the binder **PSA-1** in a fluorescence microscopy analysis of human prostate tissue expressing PSA. The synthetic FITC-labelled derivative was incubated with the tissue sections and detected using an anti-FITC antibody as secondary reagent. This procedure stained



**Fig. 5 | Performance of a chemical probe developed from selected CaM binder.** **a**, Structure of the chemical probe **CaM-PC** developed from **CaM-3**. **b**, Specific labelling of CaM by **CaM-PC** in the presence of excess HSA. **c**, SDS-PAGE analysis reveals the formation of a covalent adduct (indicated with red arrows) between the **CaM-PC** probe and **CaM**. Left panel: Fluorescence imaging of FITC: a smaller proteolytic fragment of CaM is also visible. Right panel: Coomassie Brilliant Blue staining: left lane, marker; lane 1, CaM (3  $\mu$ M)/**CaM-PC** (10  $\mu$ M),  $h\nu$ ; lane 2, same as lane 1, no  $h\nu$ ; lane 3, HSA (15  $\mu$ M)/**CaM-PC** (10  $\mu$ M),  $h\nu$ ; lane 4, CaM (3  $\mu$ M)/HSA (15  $\mu$ M)/**CaM-PC** (10  $\mu$ M),  $h\nu$ ; lane 5: same as lane 4, no  $h\nu$ ; lane 6, same as lane 4 with scaffold control **SC-PC** instead of **CaM-PC**; lane 7, same as lane 4, with addition of soluble competitor **CaM-3-amino** (100  $\mu$ M). Supplementary Figs. 76 and 77 show full gel images. **d**, Electrospray ionization time-of-flight mass spectrometry spectrum of the reaction mixture containing **CaM-PC** and CaM following UV irradiation, revealing the formation of a covalent adduct. CaM (10  $\mu$ M)/**CaM-PC** (10  $\mu$ M),  $h\nu$ . Detailed structures are provided in Supplementary Figs. 72 and 74.

the glandular structures, which are known to express PSA. The same structures were also stained by an anti-PSA antibody, which served as a positive control (Fig. 4a). As negative control, the FITC-labelled capped scaffold **SC-2** was used. In a second application, we injected mice (bearing a subcutaneously grafted tumour expressing CAIX) with **CAIX-IRDye**, a derivative conjugated with acetazolamide as diversity elements and carrying a near-infrared dye for detection. Imaging at different time points revealed a preferential accumulation of the CAIX binder in the tumour, while no preferential tumour uptake could be observed when the capped scaffold **SC-IRDye** was used as negative control (Fig. 4b).

**Development of chemical probes.** We installed a photo-crosslinking moiety on the fourth diversity site of the scaffold in order to convert binders into chemical probes for specific protein labelling applications. As an illustrative example, we fused a photo-crosslinking moiety (phenyl azide) to the trivalent CaM binder (**CaM-3**), generating a probe (**CaM-PC**; Fig. 5a). Incubation of this probe with CaM in the presence of a fivefold excess of HSA, followed by UV irradiation (Fig. 5b), led to the preferential photo-crosslinking of the probe to CaM rather than to HSA, as evidenced by gel electrophoretic analysis (lane 4 in Fig. 5c). A control probe (**SC-PC**), consisting of the scaffold equipped with the photo-crosslinking moiety, but devoid of the CaM recognition elements, did not label CaM, as expected (lane 6, Fig. 5c). The formation of a covalent conjugate with CaM under irradiation was further confirmed by mass spectrometric analysis (Fig. 5d).

## Discussion

We have described the synthesis of a DNA-encoded chemical library based on the display of multiple diversity elements on a constant macrocyclic scaffold, containing over 35 million combina-

tions. We used optimized DNA-compatible synthetic procedures<sup>41</sup>, to ensure high library quality, which is a prerequisite for good performance in selections and for the identification of structure-activity relationships<sup>40, 42, 43</sup>.

The encoded library yielded binders against various, structurally diverse target proteins. This feature is reminiscent of the performance of large combinatorial libraries of antibodies (for example, phage display libraries), which produce useful binding specificities against the majority of target proteins. The typical dissociation constants for binders isolated from our library were in the single-digit micromolar range, while phage display libraries containing billions of clones typically yield antibody fragments with  $K_d$  values in the 10 nM to 1  $\mu$ M range<sup>44–46</sup>. Interestingly, it has previously been reported that the use of a smaller portion (containing only 10 million library members) of a 65-billion-membered phage-display library in selection experiments yielded binders with  $K_d$  values ranging between 0.8  $\mu$ M and 12  $\mu$ M (ref. 44). These findings suggest that binders of higher affinity may be isolated from larger libraries based on the design strategy reported in this Article, featuring the incorporation of more chemical diversity elements on the same scaffold. On the other hand, the structure-activity relationships obtained from the selection experiment for our library as fingerprints for a given target allow the construction of a next-generation library by using structural analogues of the enriched chemical diversity elements on the scaffold, in analogy to the step-wise process often used for the affinity maturation of antibodies<sup>47–49</sup>. Alternatively, we have shown that fine-tuning of certain structural features of the constant scaffold may also have an impact on dissociation constants (Supplementary Fig. 67).

An antibody recognizes its antigen as a result of numerous interactions between its multiple residues in the hypervariable loops and the contact residues of the antigen. Interestingly, specific antibodies

could also be isolated from 'designer' combinatorial libraries in which the multiple antigen-contacting sites of the hypervariable loops contain a restricted set of diversity elements<sup>50</sup>. At the other extreme, the fixed macrocyclic scaffold described in this Article displays only three spatially oriented sets of chemical diversity elements. This chemical strategy was sufficient to generate specific binders against different target proteins, providing further evidence that certain antibody properties for recognition may be minimized (that is, converted into smaller chemical structures, capable of similar performance)<sup>51</sup>. The diversity elements that could be employed in our strategy are not limited to proteinogenic amino acids, as required by antibodies, and can be chosen from a broader chemical space.

There is growing interest in the field of macrocycles for drug discovery<sup>52</sup>. However, it might be difficult to improve their pharmaceutical properties, as modifications of the backbone can lead to conformational changes<sup>30</sup>. The nature of the constant macrocyclic scaffold for this study allows the display of diversity elements in a predefined spatial orientation (as shown both by NMR studies<sup>32</sup> and by X-ray crystallography<sup>33</sup>) and facilitates the incorporation of additional chemical moieties, such as photo-crosslinkers, fluorophores or other payloads, for further applications.

In summary, we have shown that an encoded library, containing over 35 million displayed combinations on a constant macrocyclic scaffold, yielded specific binders against multiple target proteins, including difficult targets (for example, TNF). The binders discovered from our library enabled biochemical applications (for example, immunofluorescence tissue staining procedures and *in vivo* delivery of payloads to tumours) with antibody-like performance and the development of a chemical probe. Our strategy may facilitate chemical biology research and the development of novel classes of pharmaceutical products.

## Methods

Detailed methods, synthetic procedures and characterization of the presented ETH-YL library and compounds are described in the Supplementary Information.

**Library synthesis.** Scaffold **1** was conjugated to amino-modified oligonucleotides (code 1: 5'-amino-C6-GGAGCTTCTGAATCTGTGTGCTGNNNNNCGAGTCCCATGGCGC-3'-OH, N representing variable bases serving as code) using a reported 1-ethyl-3-(3-dimethylaminopropyl) carbodiimide (EDC)/1-hydroxy-7-azabenzotriazole (HOAt) method<sup>38</sup>. The conjugates were precipitated with ethanol before purification by HPLC. Tfa deprotection was performed with ammonium hydroxide (25% aq.), followed by immobilization on diethylaminoethyl (DEAE) sepharose. The first diversification elements were coupled to oligonucleotides with EDC-HCl/HOAt on pseudo-solid phase<sup>35</sup> and the resulting DNA conjugates were then isolated by ethanol precipitation. The individual conjugates with the first diversity elements were subjected to irradiation at 365 nm at 0 °C for 60 min, followed by equimolar pooling of the 283 conjugates. The first pool was further divided into 386 aliquots and coupled with the second diversity elements using the same EDC-HCl/HOAt conditions. Individual conjugates with second diversity elements were employed in an enzymatic ligation step. To the conjugates, 5'-phosphorylated-oligonucleotides (code 2: 5'-phosphate-CGGATCGACGNNNNNCGTCAGGCAGC-3'-OH) and a 'splint' oligonucleotide (5'-OH-CGTCGATCCGCGCCATGGG-3'-OH) were added, followed by addition of ligase buffer and T4 DNA ligase. The ligation was allowed for 6 h at 22 °C. Equimolar amounts of the 386 conjugates were combined to generate the second pool, followed by ethanol precipitation and HPLC purification. A portion of the second pool was divided into 136 aliquots and immobilized on DEAE sepharose. The resin was washed with aq. AcOH (3 × 0.5 ml, 10 mM), H<sub>2</sub>O (3 × 0.5 ml) and DMSO:H<sub>2</sub>O:BuOH = 4:3:1 (3 × 0.5 ml). To the resin-immobilized conjugates, a solution of the corresponding alkyne diversity element (20 mM), tris[(1-benzyl-1*H*-1,2,3-triazol-4-yl)methyl]amine (TBTA) (10 mM), CuSO<sub>4</sub> (2.5 mM) and ascorbate (10 mM) in DMSO:H<sub>2</sub>O:BuOH = 4:3:1 (0.2 ml) was added. The slurry was agitated for 4 h at 25 °C. The coupling solution was removed and the resin washed with DMSO:H<sub>2</sub>O:BuOH = 4:3:1 (6 × 0.5 ml), aq. EDTA (3 × 0.5 ml, 50 mM) and aq. AcOH (3 × 0.5 ml, 10 mM). The conjugates were eluted from the resin by incubation with aq. AcOH (3 × 0.2 ml, 3 M) for 5 min. A further portion of the second pool was dissolved in Tris-HCl (500 mM, pH 8.0) and treated with tris(2-carboxyethyl)phosphine hydrochloride (TCEP-HCl) (100 mM). The Staudinger reduction lasted for 12 h at 25 °C, and the reduction products were isolated by ethanol precipitation. The reduction products were further split into 185 aliquots and conjugated with 185 carboxylic acids using the above-mentioned

EDC-HCl/HOAt method. Individual conjugates with the third diversity elements were further subjected to polymerase extension using oligonucleotides of the following sequence for encoding (code 3: 5'-OH-GCTCTGCACGGTTCGNNNNNNGCTGCCTGACGC-3'-OH). Equimolar amounts of the 324 conjugates were combined to generate the final library of 35 million combinations. For further details, see Supplementary Section 3.

**FP measurement with FITC-labelled binders.** Freshly dissolved FITC-labelled binders (7.5 μl, final concentration 50 nM, 1% DMSO) were incubated at 22 °C for 10 min in a black 384-well plate (Greiner, non-binding) in PBS with increasing concentrations of protein to a final volume of 15 μl. The fluorescence anisotropy was measured on a Spectra Max Paradigm multimode plate reader (Molecular Devices). Experiments were performed in triplicate, and the mean anisotropy values were fitted to equation (3) in the Supplementary Section 5.

**Mass spectrometry analysis of the CaM-probe covalent complex.** In a 96-well plate, CaM (10 μM) in Dulbecco's PBS (10% DMSO) was incubated with the probe (CaM-PC, 10 μM) for 10 min at 0 °C with gentle shaking. The samples were irradiated at 365 nm for 15 min at 0 °C. Protein samples were purified on Vivaspins 500 centrifugal concentrators and dissolved in 100 μl PBS. A Xevo G2-XS Q-TOF with electrospray ionization source was used for detection.

**Reporting Summary.** Further information on experimental design is available in the Nature Research Reporting Summary linked to this article.

**Data availability.** The main data supporting the findings of this study are available within this Article and its Supplementary Information. Extra data and materials are available from the corresponding authors upon reasonable request. A Life Sciences Reporting Summary for this paper is available.

Received: 14 May 2017; Accepted: 4 January 2018;

Published online: 19 March 2018

## References

- Murphy, K., Janeway, C. A. & Mowat, A. *Janeway's Immunobiology* 8th edn (Garland Science, New York, 2012).
- Smith, G. P. Filamentous fusion phage: novel expression vectors that display cloned antigens on the virion surface. *Science* **228**, 1315–1317 (1985).
- Clackson, T., Hoogenboom, H. R., Griffiths, A. D. & Winter, G. Making antibody fragments using phage display libraries. *Nature* **352**, 624–628 (1991).
- Lerner, R. A., Kang, A. S., Bain, J. D., Burton, D. R. & Barbas, C. F. III Antibodies without immunization. *Science* **258**, 1313–1314 (1992).
- Winter, G., Griffiths, A. D., Hawkins, R. E. & Hoogenboom, H. R. Making antibodies by phage display technology. *Annu. Rev. Immunol.* **12**, 433–455 (1994).
- Thurber, G. M. et al. Single-cell and subcellular pharmacokinetic imaging allows insight into drug action *in vivo*. *Nat. Commun.* **4**, 1504 (2013).
- Heinis, C., Rutherford, T., Freund, S. & Winter, G. Phage-encoded combinatorial chemical libraries based on bicyclic peptides. *Nat. Chem. Biol.* **5**, 502–507 (2009).
- Wilson, D. S., Keefe, A. D. & Szostak, J. W. The use of mRNA display to select high-affinity protein-binding peptides. *Proc. Natl Acad. Sci. USA* **98**, 3750–3755 (2001).
- Kawakami, T. et al. Diverse backbone-cyclized peptides via codon reprogramming. *Nat. Chem. Biol.* **5**, 888–890 (2009).
- Boder, E. T. & Wittrup, K. D. Yeast surface display for screening combinatorial polypeptide libraries. *Nat. Biotechnol.* **15**, 553–557 (1997).
- Hanes, J. & Pluckthun, A. *In vitro* selection and evolution of functional proteins by using ribosome display. *Proc. Natl Acad. Sci. USA* **94**, 4937–4942 (1997).
- Goodnow, R. A. Jr, Dumelin, C. E. & Keefe, A. D. DNA-encoded chemistry: enabling the deeper sampling of chemical space. *Nat. Rev. Drug Discov.* **16**, 131–147 (2017).
- Lerner, R. A. & Brenner, S. DNA-encoded compound libraries as open source: a powerful pathway to new drugs. *Angew. Chem. Int. Ed.* **56**, 1164–1165 (2017).
- Brenner, S. & Lerner, R. A. Encoded combinatorial chemistry. *Proc. Natl Acad. Sci. USA* **89**, 5381–5383 (1992).
- Needels, M. C. et al. Generation and screening of an oligonucleotide-encoded synthetic peptide library. *Proc. Natl Acad. Sci. USA* **90**, 10700–10704 (1993).
- Mannocci, L. et al. High-throughput sequencing allows the identification of binding molecules isolated from DNA-encoded chemical libraries. *Proc. Natl Acad. Sci. USA* **105**, 17670–17675 (2008).
- Clark, M. A. et al. Design, synthesis and selection of DNA-encoded small-molecule libraries. *Nat. Chem. Biol.* **5**, 647–654 (2009).
- Litovchick, A. et al. Encoded library synthesis using chemical ligation and the discovery of sEH inhibitors from a 334-million member library. *Sci. Rep.* **5**, 10916 (2015).

19. Franzini, R. M. & Randolph, C. Chemical space of DNA-encoded libraries. *J. Med. Chem.* **59**, 6629–6644 (2016).
20. Halpin, D. R. & Harbury, P. B. DNA display I. Sequence-encoded routing of DNA populations. *PLoS Biol.* **2**, e173 (2004).
21. Gartner, Z. J. et al. DNA-templated organic synthesis and selection of a library of macrocycles. *Science* **305**, 1601–1605 (2004).
22. Hansen, M. H. et al. A yoctoliter-scale DNA reactor for small-molecule evolution. *J. Am. Chem. Soc.* **131**, 1322–1327 (2009).
23. Li, Y., Zhao, P., Zhang, M., Zhao, X. & Li, X. Multistep DNA-templated synthesis using a universal template. *J. Am. Chem. Soc.* **135**, 17727–17730 (2013).
24. Wichert, M. et al. Dual-display of small molecules enables the discovery of ligand pairs and facilitates affinity maturation. *Nat. Chem.* **7**, 241–249 (2015).
25. Reddavid, F. V., Lin, W., Lehnert, S. & Zhang, Y. DNA-encoded dynamic combinatorial chemical libraries. *Angew. Chem. Int. Ed.* **54**, 7924–7928 (2015).
26. Li, G. et al. Design, preparation, and selection of DNA-encoded dynamic libraries. *Chem. Sci.* **6**, 7097–7104 (2015).
27. Dagher, J. P. et al. DNA display of fragment pairs as a tool for the discovery of novel biologically active small molecules. *Chem. Sci.* **6**, 739–744 (2015).
28. Deng, H. et al. Discovery of highly potent and selective small molecule ADAMTS-5 inhibitors that inhibit human cartilage degradation via encoded library technology (ELT). *J. Med. Chem.* **55**, 7061–7079 (2012).
29. Barluenga, S. et al. Novel PTP1B inhibitors identified by DNA display of fragment pairs. *Bioorg. Med. Chem. Lett.* **26**, 1080–1085 (2016).
30. Maianti, J. P. et al. Anti-diabetic activity of insulin-degrading enzyme inhibitors mediated by multiple hormones. *Nature* **511**, 94–98 (2014).
31. Mutter, M., Hersperger, R., Gubernator, K. & Muller, K. The construction of new proteins. V. A template-assembled synthetic protein (TASP) containing both a 4-helix bundle and beta-barrel-like structure. *Proteins* **5**, 13–21 (1989).
32. Dumy, P., Eggleston, I. M., Esposito, G., Nicula, S. & Mutter, M. Solution structure of regioselectively addressable functionalized templates: an NMR and restrained molecular dynamics investigation. *Biopolymers* **39**, 297–308 (1996).
33. Peluso, S. et al. Crystal structure of a synthetic cyclodecapeptide for template-assembled synthetic protein design. *ChemBioChem* **2**, 432–437 (2001).
34. Salamon, H., Klika Škopic, M., Jung, K., Bugain, O. & Brunschweiler, A. Chemical biology probes from advanced DNA-encoded libraries. *ACS Chem. Biol.* **11**, 296–307 (2016).
35. Franzini, R. M. et al. Systematic evaluation and optimization of modification reactions of oligonucleotides with amines and carboxylic acids for the synthesis of DNA-encoded chemical libraries. *Bioconjug. Chem.* **25**, 1453–1461 (2014).
36. Li, Y. et al. Optimized reaction conditions for amide bond formation in DNA-encoded combinatorial libraries. *ACS Comb. Sci.* **18**, 438–443 (2016).
37. Decurtins, W. et al. Automated screening for small organic ligands using DNA-encoded chemical libraries. *Nat. Protoc.* **11**, 764–780 (2016).
38. Krall, N. et al. A small-molecule drug conjugate for the treatment of carbonic anhydrase IX expressing tumors. *Angew. Chem. Int. Ed.* **53**, 4231–4235 (2014).
39. Gilibert, M. A. A. et al. Differential substrate behaviour of phenol and aniline derivatives during oxidation by horseradish peroxidase: kinetic evidence for a two-step mechanism. *Biochim. Biophys. Acta* **1699**, 235–243 (2004).
40. Franzini, R. M. et al. Identification of structure–activity relationships from screening a structurally compact DNA-encoded chemical library. *Angew. Chem. Int. Ed.* **54**, 3927–3931 (2015).
41. Malone, M. L. & Paegel, B. M. What is a ‘DNA-compatible’ reaction? *ACS Comb. Sci.* **18**, 182–187 (2016).
42. Deng, H. et al. Discovery, SAR, and X-ray binding mode study of BCATm inhibitors from a novel DNA-encoded library. *ACS Med. Chem. Lett.* **6**, 919–924 (2015).
43. Satz, A. L. Simulated screens of DNA encoded libraries: the potential influence of chemical synthesis fidelity on interpretation of structure–activity relationships. *ACS Comb. Sci.* **18**, 415–424 (2016).
44. Griffiths, A. D. et al. Isolation of high affinity human antibodies directly from large synthetic repertoires. *EMBO J.* **13**, 3245–3260 (1994).
45. Nissim, A. et al. Antibody fragments from a ‘single pot’ phage display library as immunochemical reagents. *EMBO J.* **13**, 692–698 (1994).
46. Vaughan, T. J. et al. Human antibodies with sub-nanomolar affinities isolated from a large non-immunized phage display library. *Nat. Biotechnol.* **14**, 309–314 (1996).
47. Gram, H. et al. In vitro selection and affinity maturation of antibodies from a naive combinatorial immunoglobulin library. *Proc. Natl. Acad. Sci. USA* **89**, 3576–3580 (1992).
48. Jespers, L. S., Roberts, A., Mahler, S. M., Winter, G. & Hoogenboom, H. R. Guiding the selection of human antibodies from phage display repertoires to a single epitope of an antigen. *Biotechnology* **12**, 899–903 (1994).
49. Pini, A. et al. Design and use of a phage display library. Human antibodies with subnanomolar affinity against a marker of angiogenesis eluted from a two-dimensional gel. *J. Biol. Chem.* **273**, 21769–21776 (1998).
50. Fellouse, F. A., Wiesmann, C. & Sidhu, S. S. Synthetic antibodies from a four-amino-acid code: a dominant role for tyrosine in antigen recognition. *Proc. Natl. Acad. Sci. USA* **101**, 12467–12472 (2004).
51. Li, B. et al. Minimization of a polypeptide hormone. *Science* **270**, 1657–1660 (1995).
52. Driggers, E. M., Hale, S. P., Lee, J. & Terrett, N. K. The exploration of macrocycles for drug discovery—an underexploited structural class. *Nat. Rev. Drug Discov.* **7**, 608–624 (2008).

### Acknowledgements

This work was supported by ETH Zürich, the Swiss National Science Foundation (310030B\_163479/1 grant, 31003A\_144242 grant and CRSII2\_160699/1 Sinergia grant), the ERC Advanced Grant ‘ZauberKugel’ (Grant agreement 670603), Philochem AG and through Start-up Funding for the ‘Hundred Young-Talent Scheme’ Professorship provided by Chongqing University in China (0247001104406). The authors thank G. Annuziati for help with synthesis, C. Aquino and L. Optiz for help with high-throughput DNA sequencing, and M. Wichert, R. Franzini, G. Zimmerman, A. Dal Corso, W. Decurtins, A. Schmid, L. Sun, M. Xi and J. Zhang for discussions. Instant JChem (ChemAxon) was used for structure and data management (<http://www.chemaxon.com>).

### Author contributions

Y.L., J.S. and D.N. designed the project. Y.L. constructed the library. R.D.L. provided target proteins. Y.L. designed and performed the selections. Y.L. and J.S. analysed high-throughput DNA screening data. Y.L. performed synthesis and hit validation experiments and performed the photo-crosslinking experiments. Y.L. and F.P. performed the immunofluorescence experiments. Y.L. and S.C. performed in vivo experiments. D.B. performed the biotinylation of target proteins. Y.L., J.S. and D.N. wrote the manuscript.

### Competing interests

D.N. is a co-founder and shareholder of Philochem AG (Otelfingen, Switzerland) and J.S. is a board member of Philochem AG.

### Additional information

**Supplementary information** is available for this paper at <https://doi.org/10.1038/s41557-018-0017-8>.

**Reprints and permissions information** is available at [www.nature.com/reprints](http://www.nature.com/reprints).

**Correspondence and requests for materials** should be addressed to J.S. or D.N.

**Publisher’s note:** Springer Nature remains neutral with regard to jurisdictional claims in published maps and institutional affiliations.

<sup>1</sup>Division of Applied Regulatory Science, Office of Clinical Pharmacology, Office of Translational Sciences, Center for Drug Evaluation and Research, US Food and Drug Administration, Silver Spring, MD 20993, USA

<sup>2</sup>Office of Clinical Pharmacology, Office of Translational Sciences, Center for Drug Evaluation and Research, US Food and Drug Administration, Silver Spring, MD 20993, USA

\*Correspondence:

David.Strauss@fda.hhs.gov (D.G. Strauss).

<https://doi.org/10.1016/j.tips.2017.12.006>

#### References

- US Food and Drug Administration (2010) *Advancing Regulatory Science for Public Health. A Framework for FDA's Regulatory Science Initiative*. First Published October 2010. <https://www.fda.gov/downloads/ScienceResearch/SpecialTopics/RegulatoryScience/UCM228444.pdf>
- Rouse, R. *et al.* (2017) Translating new science into the drug review process: the US FDA's Division of Applied Regulatory Science. *Ther. Innov. Regul. Sci.* Published online July 21, 2017. <http://dx.doi.org/10.1177/2168479017720249>
- US Food and Drug Administration (2004) *Innovation or Stagnation: Challenge and Opportunity on the Critical Path to New Medical Products*. First Published March 2004. <https://www.fda.gov/downloads/ScienceResearch/SpecialTopics/CriticalPathInitiative/CriticalPathOpportunitiesReports/ucm113411.pdf>
- US Food and Drug Administration (2006) *Innovation or Stagnation: Critical Path Opportunities List*. First Published March 2006. <https://www.fda.gov/downloads/ScienceResearch/SpecialTopics/CriticalPathInitiative/CriticalPathOpportunitiesReports/UCM077258.pdf>
- US Food and Drug Administration (2011) *Advancing Regulatory Science at FDA: A Strategic Plan*. First Published August 2011. <https://www.fda.gov/downloads/ScienceResearch/SpecialTopics/RegulatoryScience/UCM268225.pdf>
- US Food and Drug Administration (2015) *Assessing CDER's Drug Safety-Related Regulatory Science Needs and Identifying Priorities*. First Published March 2015. <https://www.fda.gov/downloads/Drugs/ScienceResearch/UCM438138.pdf>
- US Food and Drug Administration (2013) *Regulatory Science in FDA's Center for Devices and Radiological Health*. First Published December 2013. <https://www.fda.gov/downloads/AboutFDA/CentersOffices/OfficeofMedicalProductsandTobacco/CDRH/CDRHReports/UCM274162.pdf>
- Pharmaceutical Technology (2017) *Counting the Cost of Failure in Drug Development*. First Published June 2017. <http://www.pharmaceutical-technology.com/features/featurecounting-the-cost-of-failure-in-drug-development-5813046/>
- US Food and Drug Administration (2014) *Guidance for Industry and FDA Staff: Qualification Process for Drug Development Tools*. First Published January 2014. <https://www.fda.gov/ucm/groups/fdagov-public/@fdagov-drugs-gen/documents/document/ucm230597.pdf>
- US Food and Drug Administration (2017) *Qualification of Medical Device Development Tools: Guidance for Industry, Tool Developers, and Food and Drug Administration Staff*. First Published August 2017. <https://www.fda.gov/ucm/groups/fdagov-public/@fdagov-meddev-gen/documents/document/ucm374432.pdf>
- FDA-NIH Biomarker Working Group (2016) *BEST (Biomarkers, Endpoints, and other Tools) Resource*. First Published 2016. [https://www.ncbi.nlm.nih.gov/books/NBK326791/pdf/Bookshelf\\_NBK326791.pdf](https://www.ncbi.nlm.nih.gov/books/NBK326791/pdf/Bookshelf_NBK326791.pdf)
- Lalonde, R.L. *et al.* (2007) Model-based drug development. *Clin. Pharmacol. Ther.* 82, 21–32
- US Food and Drug Administration (2017) *PDUFA Reauthorization Performance Goals and Procedures Fiscal Years 2018 through 2022*. First Published August 2017. <https://www.fda.gov/downloads/forindustry/userfees/prescriptiondruguserfee/ucm511438.pdf>

## Forum

### Clinical Success of Drug Targets Prospectively Predicted by *In Silico* Study

Feng Zhu,<sup>1,2,4,\*</sup> Xiao Xu Li,<sup>1,2</sup> Sheng Yong Yang,<sup>5</sup> and Yu Zong Chen<sup>3,\*</sup>

**The selection of the right drug targets is critically important for the successful and cost-effective development and clinical testing of drugs. A 2009 paper reported an *in silico* prospective prediction of the clinical potential of 156 targets of clinical trial drugs (all of these targets were without an approved drug at the time of the paper's publication). Eight years later, the assessment of the clinical status of these targets revealed impressive capability of the *in silico* method in prospectively predicting the clinical success of drug targets.**

The selection of a good target is critical for the successful discovery and clinical testing of effective drugs [1]. A 2009 paper [2] reported a prospective prediction of the clinical potential of 31, 84, and 41 targets of drugs in Phase III, II, and I clinical trials, respectively. These 156 targets were all without an approved drug at the time of that study [2]. Based on the *in silico* analysis of their sequence, structural,

physicochemical, and human systems profiles, 41 targets have been predicted as clinically promising (likely to yield an approved drug) and the remaining 115 targets as nonpromising (unlikely to yield an approved drug). Eight years later, its target prediction results can be judged by the current clinical status of the 156 targets.

The current clinical status of the targets revealed an impressive performance of the *in silico* method in predicting the clinical success of the Phase III targets (see Figure 1 and Supplemental Table S1 online). Of the 16 Phase III targets predicted as promising, 10 (62.5%) targets have since yielded Food and Drug Administration (FDA)-approved drug, two (12.5%) targets remain in Phase III, and four (25%) targets have been downgraded (1 to Phase II, 1 to Phase I, and 2 discontinued clinical trial). Of the 15 Phase III targets predicted as nonpromising, 12 (80%) targets have been downgraded (3 discontinued clinical trial, 3 to Phase I, and 6 to Phase II), two (13.3%) targets remain in Phase III, and one (6.7%) target (neutral endopeptidase) paired with a pre-existing clinically successful target (angiotensin II receptor) has yielded an FDA-approved drug combination (sacubitril/valsartan) [3]. Neutral endopeptidase has yielded no other approved drug and is currently without a drug in clinical trial. Hence, it remains unclear if neutral endopeptidase can yield an individual drug.

The *in silico* method is intended for predicting the likelihood of a target to yield an approved drug. It may be premature to judge its prediction of the Phase II and Phase I targets that are expected to take longer times to reach drug approval. Nonetheless, some indication about its prediction performance may be revealed on the basis that promising targets more likely and nonpromising targets less likely advance to or remain in the higher trial phases. Of the 22 Phase II targets predicted as promising, the majority (68.2%)



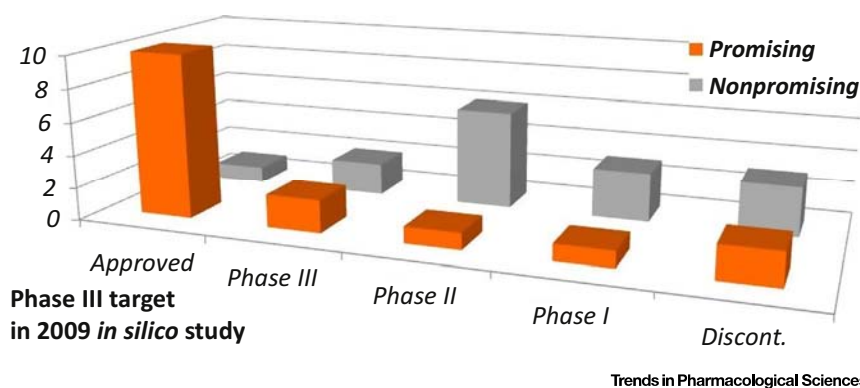


Figure 1. The Prediction Results of 31 Clinical Trial Phase III Targets Analyzed by 2009 *In Silico* Study Were Judged by Their Current Clinical Status. Discont., discontinued.

of them have advanced to a higher phase or remain in the same trial phase. Specifically, two (9.1%) targets have yielded approved drug, seven (31.8%) targets have advanced to Phase III, six targets (27.3%) remain in Phase II, and seven (31.8%) targets have been downgraded (2 to Phase I, 5 discontinued clinical trials). Of the 62 Phase II targets predicted as nonpromising, 35 targets (56.5%) have been downgraded (28 discontinued clinical trial and 7 to Phase I), 21 (33.9%) targets remain in Phase II, five (8.1%) targets have advanced to Phase III, and one (1.6%) target (interleukin-4 receptor  $\alpha$ ) has yielded an FDA-approved monoclonal antibody (mAb) drug (dupilumab) [4]. The misclassification of interleukin-4 receptor  $\alpha$  is likely due to the inadequate representation of the mAb drug targets (15 targets) in training the *in silico* method [2].

Of the three Phase I targets predicted as promising, two (66.7%) targets have advanced to a higher phase (1 to Phase III and 1 to Phase II), and one target has discontinued clinical trial. Of the 37 Phase I targets predicted as nonpromising, 20 (54.1%) targets have discontinued clinical trial, three (8.1%) targets remain in Phase I, ten (27.0%) targets have advanced to Phase II, and four (10.8%) targets have advanced to Phase III. It is noted that a comparable majority of the predicted nonpromising Phase I and Phase II

targets have been downgraded (54.1% vs. 63.2%), and a comparably small minority of the predicted nonpromising Phase I and Phase II targets have advanced to Phase III (10.8% vs. 8.1%). These quantitatively comparable levels of the majority and minority targets seem to be the result of a consistent prediction of the nonpromising targets, and the juries are still out to judge these prediction results by the future clinical trial outcomes.

The impressive capability of the *in silico* method in prospectively predicting the clinical potential of the drug targets arises from its integrated analysis of multiple druggability properties [2] reported in the literature including sequence similarity to the pre-existing targets [5], binding-site geometric and energetic features and structural similarity to the pre-existing targets [6], the physicochemical characteristics learnt by the machine learning studies of the pre-existing targets [2], and systems profiles (similarity to human proteins, pathway, and tissue distribution) derived from the analysis of the pre-existing targets [2,7]. Recent studies have indicated the importance of human protein-network topologies in target prediction and validation [7,8]. The gene expression [9] and copy number [10] profiles have been used for mAb target selection. These and other features need be

included for improved prediction of the clinical success of drug targets.

#### Author Contributions

X.X.L. analyzed the data. F.Z. and S.Y.Y. developed the program and software. F.Z. developed the concept and supervised the work. F.Z. and Y.Z.C. prepared the manuscript.

#### Acknowledgments

The authors acknowledge funding from the Academic Research Fund Singapore (R-148-000-230-114 and R-148-000-239-114), the National Natural Science Foundation of China (30772651), the Ministry of Science and Technology 863 Hi-Tech Program China (2006AA020400), the Precision Medicine Project of the National Key Research and Development Plan of China (2016YFC0902200), and the Innovation Project on Industrial Generic Key Technologies of Chongqing (cstc2015zdcy-ztzx120003).

#### Disclaimer Statement

The authors declare no competing financial interests.

#### Supplemental Information

Supplemental information associated with this article can be found online at <https://doi.org/10.1016/j.tips.2017.12.002>.

<sup>1</sup>Innovative Drug Research and Bioinformatics Group, College of Pharmaceutical Sciences, Zhejiang University, Hangzhou 310058, China

<sup>2</sup>Innovative Drug Research and Bioinformatics Group, School of Pharmaceutical Sciences, Chongqing University, Chongqing 401331, China

<sup>3</sup>Bioinformatics and Drug Design Group, Department of Pharmacy, National University of Singapore, Singapore 117543, Singapore

<sup>4</sup>State Key Laboratory Breeding Base-Shenzhen Key Laboratory of Chemical Biology, Graduate School at Shenzhen, Tsinghua University, Shenzhen Kivita Innovative Drug Discovery Institute, Shenzhen 518055, China

<sup>5</sup>State Key Laboratory of Biotherapy, Sichuan University, Chengdu 610000, China

#### \*Correspondence:

zhufeng@zju.edu.cn (F. Zhu) and  
phacyz@nus.edu.sg (Y.Z. Chen).

<https://doi.org/10.1016/j.tips.2017.12.002>

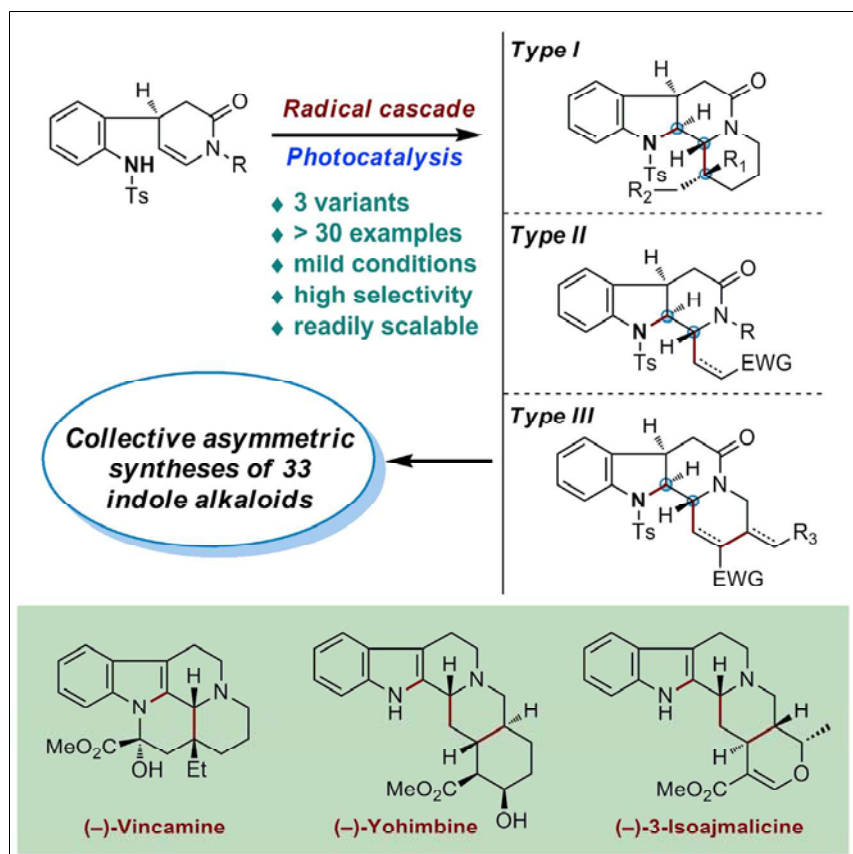
#### References

1. Rask-Andersen, M. et al. (2011) Trends in the exploitation of novel drug targets. *Nat. Rev. Drug Discov.* 10, 579–590
2. Zhu, F. et al. (2009) What are next generation innovative therapeutic targets? Clues from genetic, structural, physicochemical, and systems profiles of successful targets. *J. Pharmacol. Exp. Ther.* 330, 304–315

3. Mullard, A. (2015) 2015 FDA drug approvals. *Nat. Rev. Drug Discov.* 15, 73–76
4. Shirley, M. (2017) Dupilumab: first global approval. *Drugs* 77, 1115–1121
5. Hopkins, A.L. and Groom, C.R. (2002) The druggable genome. *Nat. Rev.* 1, 727–730
6. Hajduk, P.J. *et al.* (2005) Druggability indices for protein targets derived from NMR-based screening data. *J. Med. Chem.* 48, 2518–2525
7. Yao, L. and Rzhetsky, A. (2008) Quantitative systems-level determinants of human genes targeted by successful drugs. *Genome Res.* 18, 206–213
8. Yildirim, M.A. *et al.* (2007) Drug-target network. *Nat. Biotechnol.* 25, 1119–1126
9. Scott, A.M. *et al.* (2012) Antibody therapy of cancer. *Nat. Rev. Cancer* 12, 278–287
10. Imai, K. and Takaoka, A. (2006) Comparing antibody and small-molecule therapies for cancer. *Nat. Rev. Cancer* 6, 714–727

## Article

## A Radical Cascade Enabling Collective Syntheses of Natural Products



Qin and co-workers use photocatalytic conditions to generate a nitrogen-centered radical from aniline-type sulfonamide, which reverses the conventional reactivity between two electron-donating amine and enamine groups and initiates radical cascade reactions with excellent chemo-, regio-, and diastereoselectivity. The power of this distinct method has been demonstrated by the efficient syntheses of 33 monoterpene indole alkaloids belonging to four families.

Xiaobei Wang, Dongliang Xia, Wenfang Qin, ..., Hao Song, Xiao-Yu Liu, Yong Qin

yongqin@scu.edu.cn

**HIGHLIGHTS**

Direct generation of nitrogen-centered radical from sulfonamide by photocatalysis

Radical cascade reactions with excellent selectivities

Efficient syntheses of 33 indole alkaloids and related analogs

Potential applications for the syntheses of other nitrogen-containing molecules



Wang et al., Chem 2, 803–816  
June 8, 2017 © 2017 Elsevier Inc.  
<http://dx.doi.org/10.1016/j.chempr.2017.04.007>

## Article

# A Radical Cascade Enabling Collective Syntheses of Natural Products

Xiaobei Wang,<sup>1,3</sup> Dongliang Xia,<sup>1,3</sup> Wenfang Qin,<sup>2,3</sup> Ruijie Zhou,<sup>1,3</sup> Xiaohan Zhou,<sup>1,3</sup> Qilong Zhou,<sup>2,3</sup> Wentao Liu,<sup>2</sup> Xiang Dai,<sup>2</sup> Huijing Wang,<sup>2</sup> Shuqing Wang,<sup>2</sup> Ling Tan,<sup>1</sup> Dan Zhang,<sup>1</sup> Hao Song,<sup>1</sup> Xiao-Yu Liu,<sup>1</sup> and Yong Qin<sup>1,4,\*</sup>

## SUMMARY

Natural products have long been important inspirations for the development of chemical methodologies, theories, and technologies, and ultimately, discoveries of new drugs and materials. Chemical syntheses have traditionally yielded individual or small groups of natural products; however, methodology development allowing the synthesis of a large collection of natural products remains scarce. Here, we report an efficient photocatalytic radical cascade method that enables access to libraries of chiral and multiple-ring-fused tetrahydrocarbolinones. The radical cascade can controllably introduce complexity and functionality into products with excellent chemo-, regio-, and diastereoselectivity. The power of this distinct method has been demonstrated by the efficient syntheses of 33 monoterpenoid indole alkaloids belonging to four families.

## INTRODUCTION

Structurally complex and diverse natural products and their analogs have long been inspirations for the development of new medicines, which have greatly improved human health.<sup>1</sup> When access to such molecules from natural sources is uncertain or uneconomical, chemical synthesis is one of the most important alternative ways to obtain them.<sup>2,3</sup> Although syntheses of individual or several natural products belonging to a certain family have been achieved, a breakthrough in synthetic methods that yields diverse skeletons of natural products and that benefits the syntheses of a large collection of natural products for biological activity tests is highly anticipated. With over 15 families and more than 3,000 known members, monoterpenoid indole alkaloids represent the most stereochemically and architecturally diverse natural products.<sup>4,5</sup> Most of them have exhibited important biological activities, and some of them, such as vinblastine and reserpine,<sup>6,7</sup> have been used as clinical drugs for decades (Figure 1A). Three major types of monoterpenoid indole alkaloids, namely, corynanthe-, aspidosperma-, and iboga-type alkaloids, have been categorized on the basis of the carbon skeletons of the monoterpenoid units (bold carbon chain in Figure 1A).<sup>4</sup> All of these alkaloids can be roughly categorized into the non-rearranged families (shown in blue in Figure 1A) and the rearranged families (shown in black in Figure 1A), which are believed to have been biosynthesized originally from tryptamine and secologanin by strictosidine synthase- (STR1) and strictosidine glucosidase (SG)-catalyzed condensation.<sup>8</sup> Since the milestone syntheses of reserpine and strychnine by Woodward et al. in the 1950s,<sup>9,10</sup> the syntheses of complex monoterpenoid indole alkaloids has been an interesting and challenging topic because of their rich structural diversity and biological activities.<sup>11–14</sup>

## The Bigger Picture

Today, achieving the chemical synthesis of a single natural product is rarely out of reach with sufficient manpower. However, considering the urgent demand for chemical biology studies and drug discovery, efficient preparation of a large collection of complex natural products and natural-product-like libraries with stereochemical and architectural divergence remains highly desirable. Here, we describe a visible-light-mediated radical cascade reaction that generates a nitrogen-centered radical from aniline-type sulfonamide and reverses the conventional reactivity between two electron-donating amine and enamine groups, allowing efficient syntheses of 33 complex indole alkaloids with varied architectures and divergent stereochemistry. This approach could be expanded to intermolecular reaction patterns and could be expected to facilitate the preparation of nitrogen-containing architectures, which are of great interest for the syntheses of natural products and bioactive substances.

Radical cascades are among the most powerful reactions for bond formation.<sup>15–19</sup> However, their application in constructing complex naturally predefined architectures, and especially in resolving the major problems—namely collective syntheses of bioactive natural products<sup>20</sup>—is still underexploited.<sup>21–23</sup> This is largely because of the high reactivity of radicals, which is difficult to control with multiple functionalities in the substrate, thus resulting in poor stereoselectivity and chemoselectivity. In addition, tedious preparation of an initiating group for the classic radical reaction further impedes its application. A design for precise control of a radical pathway is required for successful assembly of complex natural products. Recent advances in photocatalytic radical reactions<sup>24–31</sup> have provided great opportunities in the synthesis of natural products.<sup>32–35</sup> Here, we report a photocatalytic radical cascade with excellent stereo-, regio-, and chemoselectivity to prepare libraries of chiral tetrahydrocarbolinones under mild conditions. This radical cascade can be scaled up and can generate two of the three monoterpenoid indole-alkaloid skeletons, including the corynanthe-type and aspidosperma-type alkaloids, by varying easily accessible substrates. This cascade provided indoline skeletons with stereochemical divergence, which is typically difficult to achieve and which requires one-by-one synthesis using traditional synthetic methods. Rapid assembly of the core structures enabled efficient syntheses of 33 complex monoterpenoid indole alkaloids belonging to four families and also four unnatural diastereoisomers.

## RESULTS AND DISCUSSION

### Radical Cascade Design

Given that efficient preparation of aspidosperma-type and corynanthe-type intermediates is expected to facilitate the syntheses of diverse families of indole alkaloids,<sup>36</sup> we envisioned that an electron-deficient nitrogen-centered radical (Ts-I; Figure 1B), initiated from chiral aniline **2** (easily synthesized from the chiral compound **1**, the preparation of which<sup>37</sup> is described in the [Supplemental Experimental Procedures](#); see also [Figures S1–S7](#)), would enable the formation of a C–N bond between both electron-donating aniline nitrogen and the  $\beta$  carbon of the enamine (Ts-I). The resultant heteroatom-associated carbon radical might intramolecularly attack the pre-installed double bond tethered to the enamine nitrogen to afford aspidosperma-type intermediate **3** (pathway a, via Ts-Ia). Similarly, the intermolecular Michael addition (Ts-IIb, pathway b) via Ts-III after radical quenching would give tetrahydrocarbolinone **4**, an important intermediate used for previous indole-alkaloid syntheses.<sup>38–40</sup> In addition, a further cascade reaction might occur via intramolecular addition of the resultant radical in Ts-III with a tethered double bond or triple bond, thus leading to the corynanthe-type intermediate **5**. Compounds **3–5** possess different ring systems and functionalities suitable for the syntheses of a variety of indole alkaloids. The untested aspect of the designed radical cascade was whether the stereochemistry of the adducts could be controlled by the chiral substrate **2**. Given that non-rearranged monoterpenoid indole alkaloids have been described with varying configurations at the C15 and C20 positions,<sup>41</sup> this concern was partly diminished.

### Radical Cascade Results

The first key task in achieving the above radical cascade was the direct initiation of a nitrogen-centered radical from Ts-protected aniline by cleavage of the N–H bond in **2**. Classic generation of amide-type nitrogen-centered radicals usually requires cleavage of an N–heteroatom bond.<sup>42,43</sup> Direct conversion of an N–H bond of aniline-type amide to a nitrogen-centered radical via photocatalysis is promising but has proved challenging and unprecedented; there are only a few recent examples on alkyl-type amide substrates.<sup>44–47</sup> With the above radical cascade strategy for

<sup>1</sup>Key Laboratory of Drug Targeting and Drug Delivery Systems of the Ministry of Education, West China School of Pharmacy, State Key Laboratory of Biotherapy, Sichuan University, Collaborative Innovation Center, Chengdu 610041, China

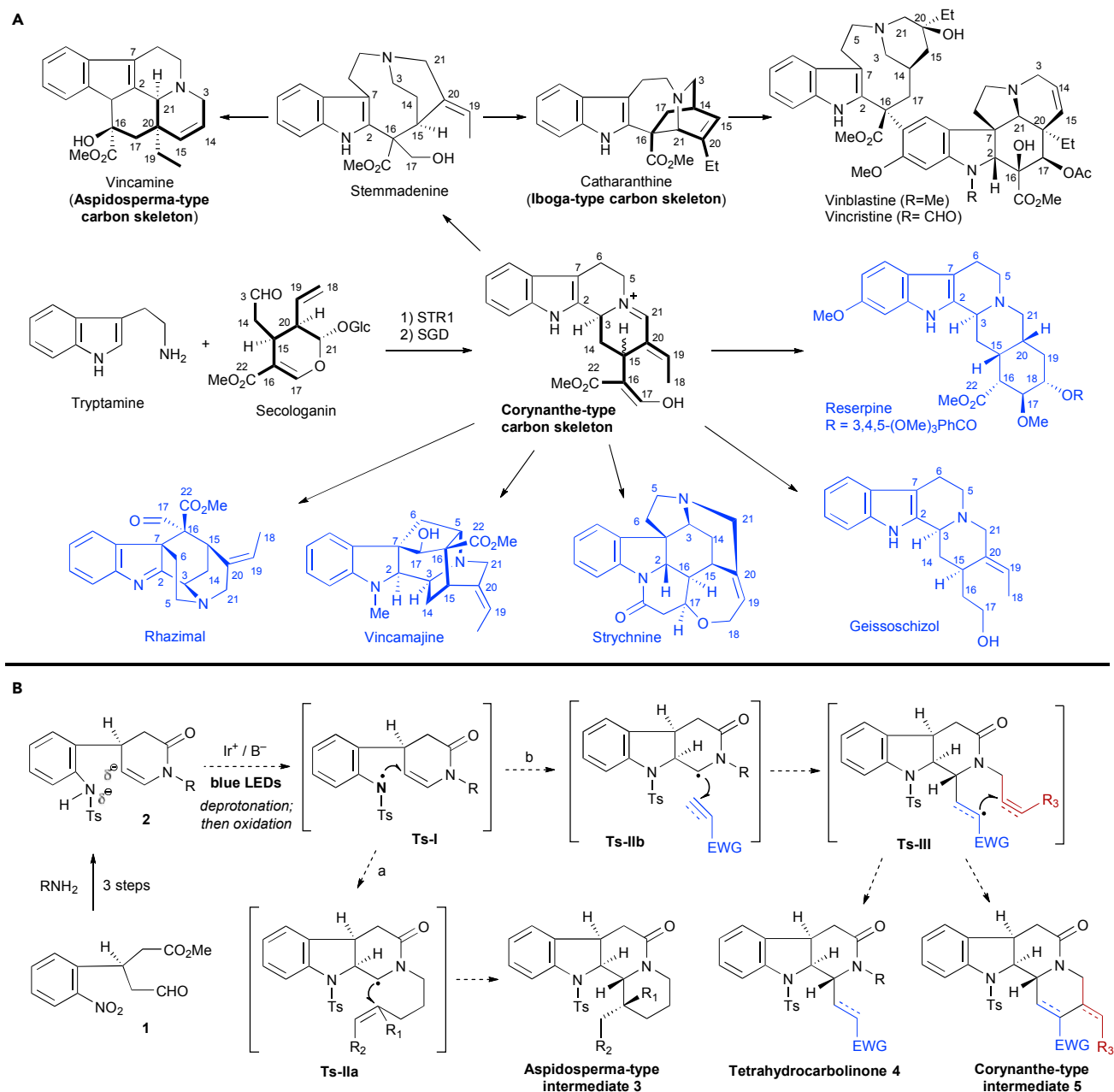
<sup>2</sup>School of Pharmaceutic Science, Chongqing University, Chongqing 401331, China

<sup>3</sup>These authors contributed equally

<sup>4</sup>Lead Contact

\*Correspondence: [yongqin@scu.edu.cn](mailto:yongqin@scu.edu.cn)

<http://dx.doi.org/10.1016/j.chempr.2017.04.007>

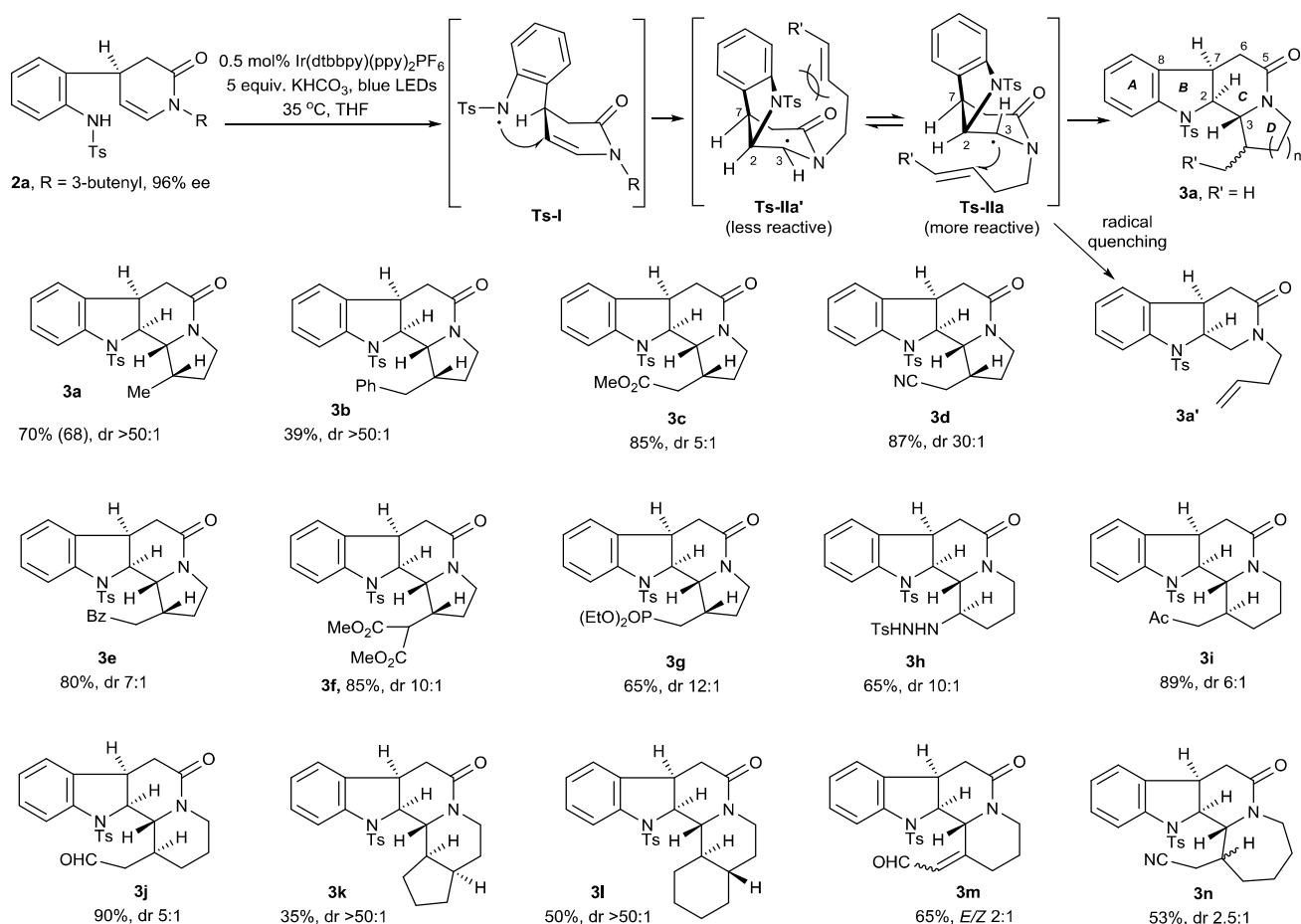


**Figure 1. Background and Synthetic Plan**

(A) Proposed biosynthetic pathway and structural categorization of monoterpene indole alkaloids.

(B) Envisioned photocatalytic radical cascade to generate aspidosperma-type intermediate 3 (path a), tetrahydrocarbolinone 4, and corynanthe-type intermediate 5 (path b) for the syntheses of monoterpene indole alkaloids. Abbreviations: D-A reaction, Diels-Alder reaction; STR1, strictosidine synthase; SG, strictosidine glucosidase.

indole-alkaloid synthesis in mind, we used tosyl-protecting aniline amide **2a** (Figures S8–S11) as a substrate for generating the nitrogen-centered radical via photocatalysis in order to test the designed two-step radical cascade (pathway a; Figure 1B). After extensive screening of photocatalysts, bases, solvents, and temperature, optimal conditions (0.5 mol % Ir(dtbbpy)(ppy)<sub>2</sub>PF<sub>6</sub>, 5 equiv KHCO<sub>3</sub>, degassed tetrahydrofuran [THF], 35°C, 5 W blue LEDs, Ar) were determined. Under these conditions, the radical cascade of **2a** proceeded smoothly to produce the desired **3a**



### Figure 2. Preparation of Aspidosperma-Type Derivatives 3

Optimal conditions: 0.5 mol % Ir(dtbbpy)(ppy)<sub>2</sub>PF<sub>6</sub>, 5 equiv KHCO<sub>3</sub>, degassed THF, 5 W blue LEDs, 35°C, Ar. The dr values were determined by LC-MS analysis. The relative carbon configurations at the C-ring and D-ring were determined by nuclear Overhauser effect experiments. **3a** and **3l**: the absolute configuration was determined by X-ray crystallography of the desotylated intermediates (see the [Supplemental Information](#)). **3a–3m**: the dr values or E/Z ratios were determined by LC-MS analysis. A dr > 50:1 indicated that other diastereoisomers were not detected in the LC-MS experiments. **3a**: the yield in parentheses was obtained with 50% aqueous THF as the solvent. **3n**: the dr value was determined by <sup>1</sup>H NMR analysis. Ir(dtbbpy)(ppy)<sub>2</sub>PF<sub>6</sub>, (4,4'-di-tert-butyl-2,2'-bipyridine)bis[(2-pyridinyl)phenyl]iridium(III) hexafluorophosphate. See also [Figures S8–S156](#).

([Figures S20–S22](#)) in 70% yield and >50:1 diastereomeric ratio (dr), along with a 2% yield of by-product **3a'** ([Figure 2](#); see also [Figures S23–S29](#)). Notably, the reaction for production of **3a** could be performed in aqueous THF without loss of yield and diastereoselectivity. The radical reaction did not take place under the same conditions when the Ts protecting group in **2a** was replaced with Me, CO<sub>2</sub>Me, Bz, and Boc (see the [Supplemental Experimental Procedures](#) and [Figures S12–S19](#)). Presumably, this could be due to their tendency for weaker deprotonation, which suppressed the initiation of a nitrogen-centered radical. In addition, a control experiment using a similar substrate without tosyl amide functionality was carried out under the same conditions; the starting material remained unchanged after 12 hr ([Scheme S1](#)), indicating that oxidation of the nitrogen anion to initiate a nitrogen-centered radical was crucial for the cascade reaction.

A variety of substrates (**2b–2n**; [Figures S30–S87](#)) with either an electron-rich double bond or an electron-deficient Michael acceptor linked to the enamine nitrogen were then used for the radical cascade. To our delight, all reactions afforded the

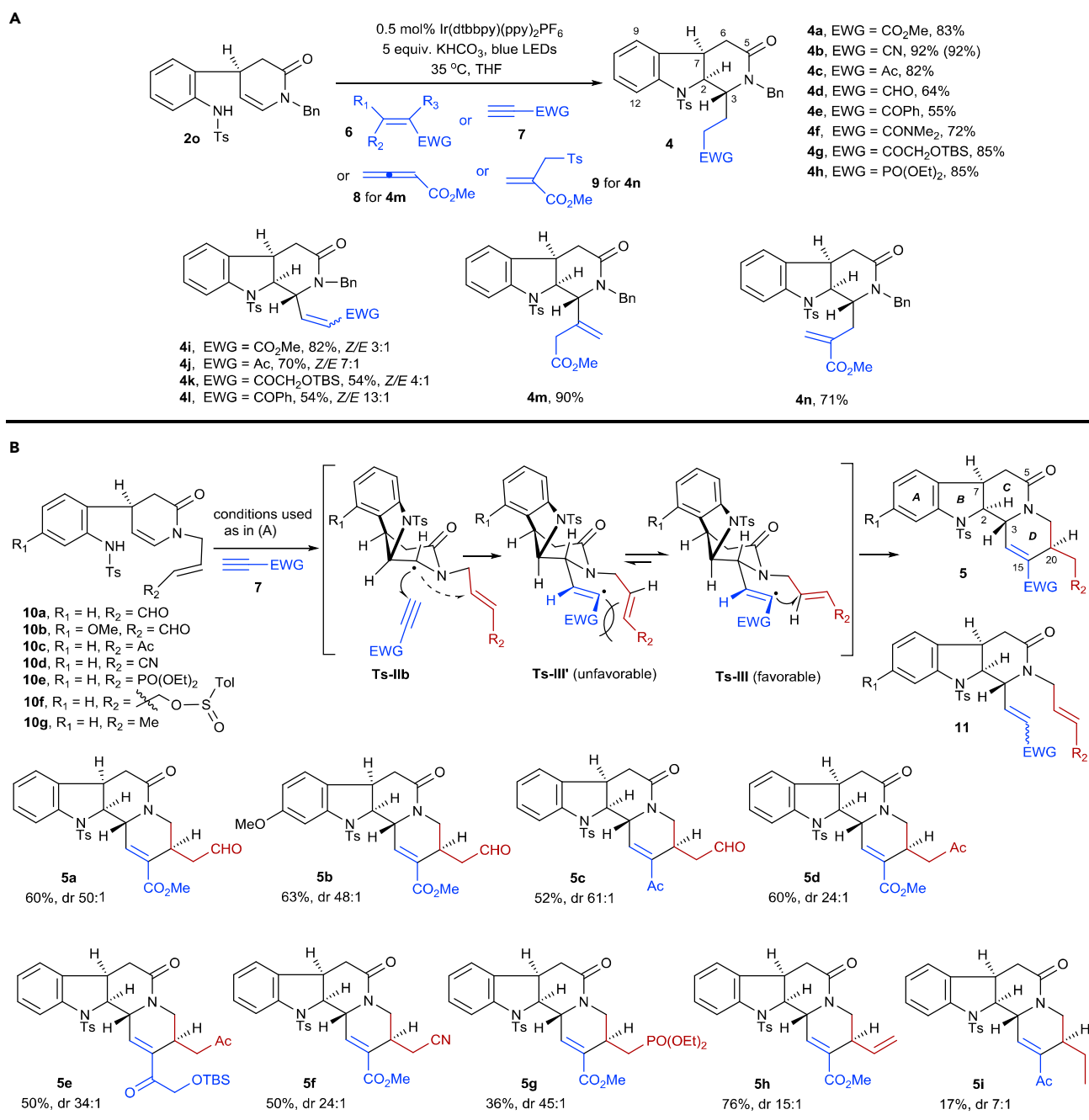
corresponding products **3b–3m** (Figures S90–S150) with a fused pyrrolidine or piperidine ring in moderate to high yields and high to excellent dr. An exceptionally low dr value (2.5:1) was observed in adduct **3n** (Figures S151 and S152), which has a more flexible azepane ring. This substrate-controlled cascade proceeded in a highly stereoselective manner to completely control the relative configurations of C2 and C3 as a *trans* relationship.

In view of the stereoselectivity for the radical cascade, the addition of the nitrogen-centered radical to the enamine double bond in the first step proceeded from the upper face (Ts-I; Figure 2) to give transition states Ts-IIa' and Ts-IIa, both possessing a *cis* relationship between H2 and H7. Ts-IIa could be more reactive than Ts-IIa', considering that twisting of the amide in Ts-IIa would dramatically increase the donating ability of the lone electron pair of the amide nitrogen,<sup>48</sup> thus rendering the radical much more nucleophilic. Furthermore, because the upper face of the piperidinone in Ts-IIa' should be blocked by the Ts-protected indoline group, addition of a radical to the double bond (triple bond for **3m**) from the upper face of the piperidinone was unfavorable because of steric repulsion. An equilibrium shift of Ts-IIa' to Ts-IIa resulted in a dominant intramolecular attack of the radical to the double bond (or triple bond) from the bottom face of the piperidinone ring, which gave adduct **3** with a *trans* relationship between H2 and H3. Direct quenching of the radical in Ts-IIa' or Ts-IIa before the addition to the double bond (or triple bond) provided the by-product **3a'**.

Having successfully achieved the two steps of the intra- and intramolecular radical cascade for generating aspidosperma-type derivatives **3**, we then chose **2o** (Figures S157–S160) with an inert *N*-benzyl (*N*-Bn) group as a substrate to explore the planned intra- and intermolecular radical cascade (Figure 3A). Under the same conditions as above, Michael acceptors **6–9** (1.1–4.0 equiv) were then used in the radical cascade to afford the corresponding tetrahydrocarbolinones **4a–4n** (Figures S161–S198) in moderate to high yields. Although the *E/Z* configuration at the side chain in **4i–4l** was not controllable, the newly generated stereocenters at C2 and C3 were formed exclusively in a *trans* configuration in **4a–4n**. Using Michael acceptors **8** and **9**, we were able to isolate **4m** and **4n** with a methylene group  $\alpha$  and  $\beta$  to C3, respectively. The reaction generating **4b** was also performed in aqueous THF without loss of yield and diastereoselectivity.

For the preparation of corynanthe-type derivatives **5**, we planned to use substrate **10** (Figures S199–S239) bearing a Michael acceptor or a double bond tethered to the piperidinone ring in an attempt to expand the radical chain reaction from the intermolecular radical addition (Ts-IIb) in the second step to the intramolecular radical addition (Ts-III) in the third step to give **5** (Figure 3B). In this case, the Ts-IIb conformer would be crucial for enabling intermolecular trapping by increasing the lifetime of the radical and disfavoring direct intramolecular 4-exo-trig cyclization with the double bond on the nitrogen side chain. According to this design, we then used alkynyl-type Michael acceptors **7a–7c** to perform the programmed radical cascade, which provided **5a–5h** (Figures S240–S278) in 36%–76% yields with excellent diastereoselectivities, as well as 7%–44% yields of by-product **11** in some cases (see the Supplemental Information). The minor diastereoisomers were the C20 epimers. The by-product **11** was produced by direct radical quenching of Ts-III' and Ts-III. With regard to the excellent stereocontrol for the D-ring formation, the transition-state Ts-III rather than Ts-III' might be responsible for generating the D ring with H20 located at the  $\alpha$  bond in adduct **5**. The strong steric repulsion between the electron-withdrawing group (EWG) and R<sub>2</sub> was thus avoided in Ts-III.

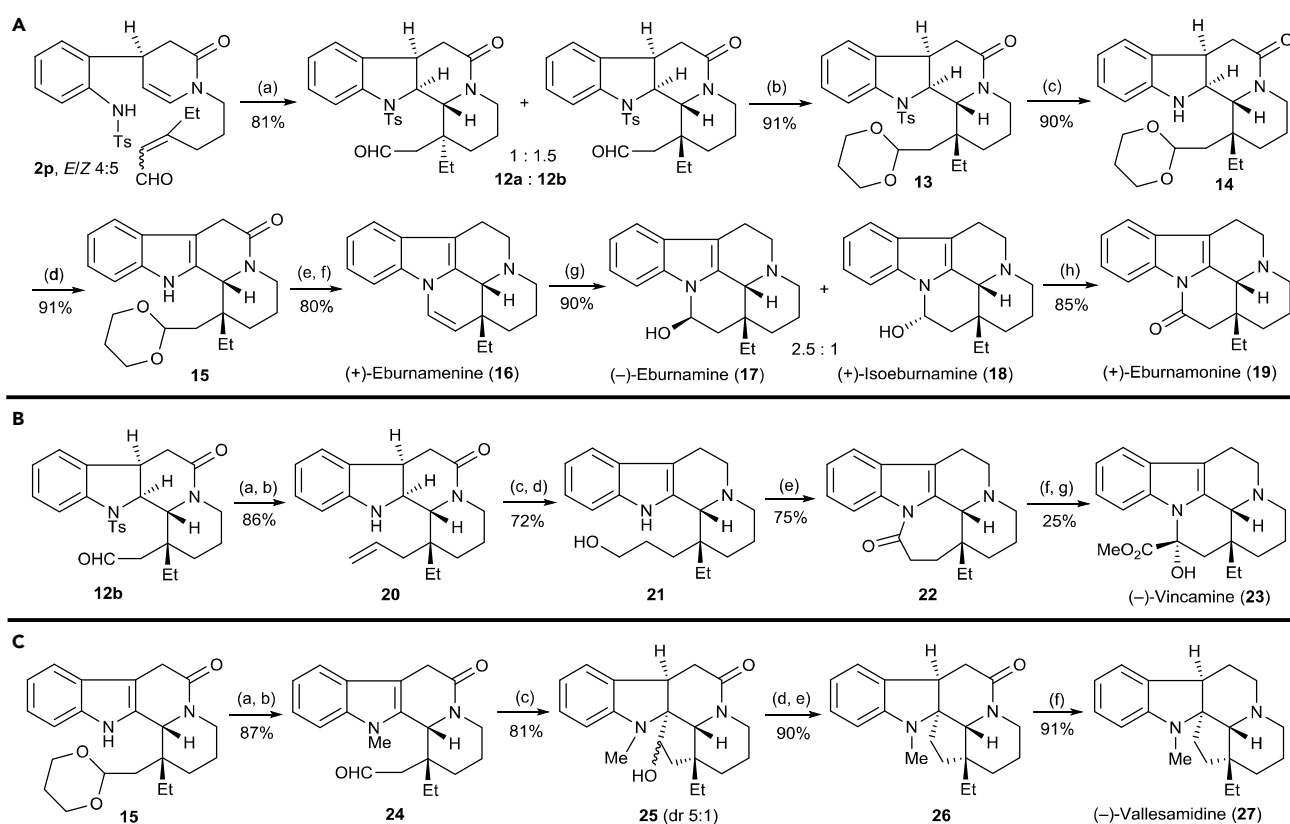




**Figure 3. Preparation of Tetrahydrocarbolinones 4 and Corynanthe-Type Derivatives 5**

(A) Optimal conditions: 0.5 mol % Ir(dtbbpy)(ppy)<sub>2</sub>PF<sub>6</sub>, 5 equiv KHCO<sub>3</sub>, degassed THF, 5 W blue LEDs, 35°C, Ar. For the syntheses of 4a–4h, 4m, and 4n, 1.1–2.5 equiv Michael acceptors 6, 8, and 9 were used. For the syntheses of 4i–4l, 4 equiv Michael acceptor 7 was used. 4b: the yield in parentheses was obtained with 50% aqueous THF as the solvent.

(B) 7: 2.5–5 equiv was used. 5a–5i: the dr values of 5 in (B) were determined by LC-MS analysis. The relative configurations of 5a, 5b, and 5d–5i were determined by comparison of their NMR spectra with that of 5c; the absolute configuration was confirmed by conversion of 5c to 28a and 29a (see Scheme 2 and the Supplemental Information for details). 5h: dioxane was used as the solvent. See also Figures S157–S283.



### Scheme 1. Total Syntheses of the Eburnamine-Vincamine Family Alkaloids

(A) Reagents and conditions: (a) 1 mol % Ir(dtbbpy) (ppy)<sub>2</sub>PF<sub>6</sub>, 5 equiv KHCO<sub>3</sub>, degassed acetonitrile, 30 W blue LEDs, 35°C, Ar; (b) *p*-TsOH, CH<sub>2</sub>Cl<sub>2</sub>, 1,3-propanediol, room temperature (RT); (c) sodium naphthalenide, THF, -78°C; (d) benzeneseleninic anhydride, THF, 40°C; (e) BH<sub>3</sub>·SMe<sub>2</sub>, THF, 0°C to RT; (f) trifluoroacetic acid (TFA), CH<sub>2</sub>Cl<sub>2</sub>, RT; (g) 0.5 M HCl (aq), RT; (h) pyridinium dichromate (PDC), CH<sub>2</sub>Cl<sub>2</sub>, RT.

(B) Reagents and conditions: (a) KO<sup>t</sup>Bu, THF, Ph<sub>3</sub>P<sup>+</sup>CH<sub>2</sub>Br<sup>-</sup>, 0°C to RT; (b) sodium naphthalenide, THF, -78°C; (c) benzeneseleninic anhydride, THF, 40°C; (d) BH<sub>3</sub>·SMe<sub>2</sub>, THF, 0°C to RT, then NaBO<sub>3</sub>; (e) tetrapropylammonium perruthenate, *N*-methyl morpholine-*N*-oxide, CH<sub>2</sub>Cl<sub>2</sub>, 4 Å molecular sieves, RT, then PDC, CH<sub>2</sub>Cl<sub>2</sub>, RT; (f) sodium bis(trimethylsilyl)amide (NaHMDS), <sup>t</sup>BuONO, PhMe, 50°C; (g) TsOH, paraformaldehyde, AcOH, 100°C; then KO<sup>t</sup>Bu, MeOH, RT.

(C) Reagents and conditions: (a) NaH, dimethylformamide, MeI, 0°C to RT; (b) 6 M HCl (aq)/THF (1:1 v/v), RT; (c) hexamethyl phosphoril triamide, Sml<sub>2</sub>, THF, reflux; (d) NaH, CS<sub>2</sub>, THF; then MeI, 0°C to RT; (e) azodiisobutyronitrile (AIBN), Bu<sub>3</sub>SnH, PhMe, 80°C; (f) 15 mol % tris(triphenylphosphine)rhodium(I) carbonyl hydride (Rh(H)(CO)(PPh<sub>3</sub>)<sub>3</sub>), PhSiH<sub>3</sub>, THF, RT. See also Figures S284–S345.

When the R<sub>2</sub> group was a methyl group, reaction of 10g with 7b (EWG = Ac) afforded 5i (Figures S279–S283) in a lower yield (17%) and a moderate dr value (7:1). The results were reasonable given that a simple double bond rather than a Michael acceptor in 10g was relatively inert toward the intramolecular attack of an olefin-type radical in the third step, and the steric repulsion between the methyl group and the acetyl group in Ts-III' was partially alleviated.

### Syntheses of the Eburnamine-Vincamine Family Alkaloids

Application of the established radical cascade to total syntheses of indole alkaloids was first demonstrated in the syntheses of eburnamine-vincamine family alkaloids. As shown in Scheme 1A, by conducting a two-step radical cascade of 2p (Figures S284–S297) on a 14 g scale, we were able to isolate two diastereomers, 12a and 12b (Figures S298–S303), in 81% combined yield and 1:1.5 ratio. After masking of the aldehyde in 12b as a dioxane, the tosyl (Ts)-protecting group in the resultant 13 was removed with sodium naphthalenide to afford amine 14 in excellent yield. Facile oxidation of the indoline moiety to indole (14 to 15), followed by amide

reduction and treatment with trifluoroacetic acid, gave (+)-eburnamenine (**16**; Figures S312 and S313) in 73% yield in three steps. Hydration of **16** with HCl/H<sub>2</sub>O resulted in (–)-eburnamine (**17**; Figures S314 and S315) and (+)-isoeburnamine (**18**; Figures S316 and S317). Further oxidation of the mixture of **17** and **18** led to the formation of the alkaloid (+)-eburnamonine (**19**; Figures S318–S321).<sup>49</sup>

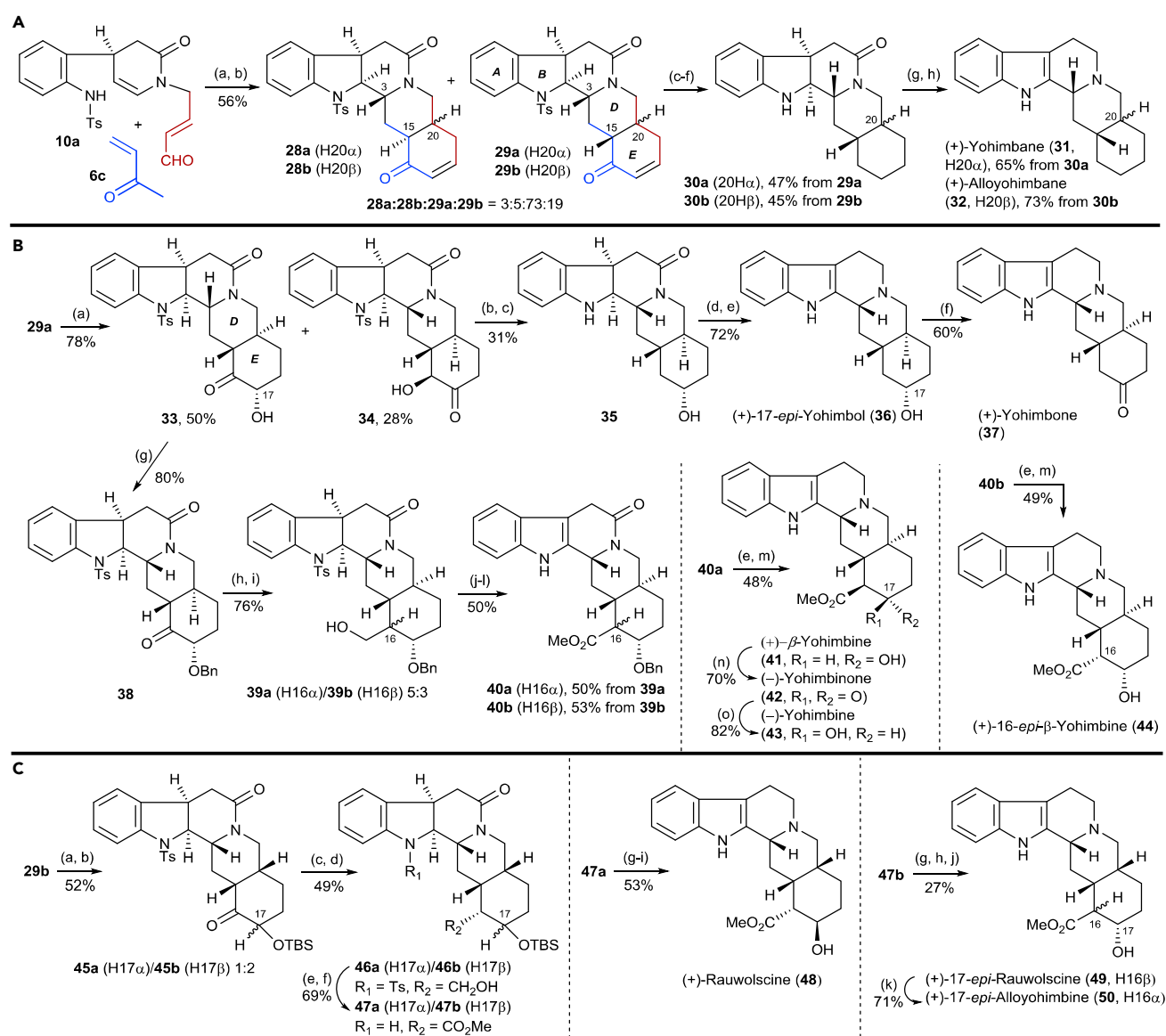
Intermediate **12b** was used for the synthesis of (–)-vincamine (**23**) in seven steps (Scheme 1B). Wittig methylenation of **12b** and removal of the Ts group afforded **20** in excellent yield. After oxidation of the indoline moiety, the double bond in **20** was then converted into a hydroxy group by hydroboration oxidation, which resulted in concomitant reduction of the amide to give alcohol **21**. Oxidation of the hydroxy group in **21** led to the formation of lactam **22**. Finally, **23** (Figures S332–S344) was synthesized from **22** according to a literature procedure.<sup>50</sup>

The synthesis of (–)-vallesamidine (**27**) was achieved with **15** as the starting material (Scheme 1C). After two steps of methylation and deprotection, aldehyde **24** was treated with SmI<sub>2</sub> to generate a ketyl radical, which was then added to the indole double bond to afford **25** as a pair of diastereomers. Removal of the hydroxy group in **25**, followed by reduction of the resulting **26** with rhodium(I) hydride,<sup>51</sup> provided **27** (Figures S342–S345) in excellent yield.

### Syntheses of the Yohimbine Family Alkaloids

In the analysis of the radical cascade in Figure 3B, we noticed that a yohimbine-type core could be easily constructed if methyl vinyl ketone (**6c**) was used as a Michael acceptor in place of the alkynyl-type counterpart (Scheme 2A). In this context, separable diastereoisomers **28a**, **28b**, **29a**, and **29b** (Figures S346–S355) were isolated in 56% combined yield and a 3:5:73:19 ratio if compounds **10a** and **6c** (1.2 equiv) were subjected to the radical cascade conditions on a 12 g scale, followed by treatment with *p*-TsOH in toluene. The absolute configurations of **28a**, **28b**, **29a**, and **29b** were determined by X-ray crystallography (see the Supplemental Information for details). Major isomers **29a** and **29b** were then used as starting materials for the syntheses of yohimbane (**31**) and alloyohimbane (**32**) via a six-step transformation. Specifically, four steps of individual hydrogenation, reduction, and the removal of hydroxy and Ts groups in **29a** and **29b** provided the corresponding amines **30a** and **30b**, respectively. Further indoline oxidation and amide reduction afforded **31** (Figures S376–S379) and **32** (Figures S380–S383), respectively.

For the syntheses of natural 17-*epi*-yohimbol (**36**), yohimbone (**37**), β-yohimbine (**41**), yohimbine (**43**), and the unnatural yohimbine (**42**) and 16-*epi*-β-yohimbine (**44**), intermediate **29a** with a *trans*-fused D/E ring system was used as the starting material (Scheme 2B). Mukaiyama hydration of enone **29a** led to the desired alcohol **33** as well as an unexpected by-product **34**.<sup>52</sup> It is clear that **34** was generated by enol rearrangement from the unstable 17-*epimer* of **33** under the chromatographic conditions, which were then used for the syntheses of **36** and **37**. Removal of the hydroxy group and the Ts group in **34** resulted in simultaneous stereoselective reduction of ketone to give **35** as a single diastereoisomer. The two subsequent steps of oxidation of the indoline moiety and reduction of the amide in **35** afforded **36** (Figures S394–S399). Further oxidation of **36** afforded **37** (Figures S400–S403) in 60% yield. However, after protection of the hydroxy group in **33**, Corey-Chaykovsky epoxidation of the resultant **38**, followed by opening of the epoxide ring,<sup>53</sup> generated two separable diastereoisomers, **39a** and **39b**. Compounds **39a** and **39b** were then individually converted to the corresponding esters **40a** and **40b** in approximately 50% yield. Further functional group transformation of **40a**, including reduction of the



### Scheme 2. Total Syntheses of the Yohimbane Family Alkaloids

(A) Reagents and conditions: (a) 0.5 mol % Ir(dtbbpy) (ppy)<sub>2</sub>PF<sub>6</sub>, 5 equiv KHCO<sub>3</sub>, THF, 30 W blue LEDs, 25°C; (b) *p*-TsOH, PhMe, 60°C; (c) Pd(OH)<sub>2</sub>, H<sub>2</sub>, EtOAc, RT; (d) NaBH<sub>4</sub>, MeOH, RT; (e) CS<sub>2</sub>, NaH, MeI, THF, 0°C; then AIBN, Bu<sub>3</sub>SnH, PhMe, 80°C; (f) Mg, MeOH, RT; (g) benzeneseleninic anhydride, THF, 40°C; (h) 15 mol % Rh(H)(CO)(PPh<sub>3</sub>)<sub>3</sub>, PhSiH<sub>3</sub>, THF, RT.

(B) Reagents and conditions: (a) tris(2,2,6,6-tetramethyl-3,5-heptanedionato)manganese(III) (Mn(dpm)<sub>3</sub>), PhSiH<sub>3</sub>, O<sub>2</sub>, <sup>i</sup>PrOH/CH<sub>2</sub>Cl<sub>2</sub> (1:4 v/v), RT; then silica gel; (b) 1,1'-thiocarbonyldiimidazole, 4-dimethylaminopyridine, 1,2-dichloroethane (DCE), RT; then AIBN, Bu<sub>3</sub>SnH, DCE, reflux; (c) Mg, MeOH, RT; (d) benzeneseleninic anhydride, THF, 40°C; (e) 15 mol % Rh(H)(CO)(PPh<sub>3</sub>)<sub>3</sub>, PhSiH<sub>3</sub>, THF, RT; (f) dicyclohexylcarbodiimide, Cl<sub>2</sub>CHCOOH, DMSO, 35°C; (g) BnBr, Ag<sub>2</sub>O, PhMe, 45°C; (h) Me<sub>3</sub>S<sup>+</sup>I<sup>-</sup>, KO<sup>t</sup>Bu, DMSO, RT; (i) Zn, Cp<sub>2</sub>TiCl<sub>2</sub>, 1,4-cyclohexadiene (1,4-CHD), THF, RT; (j) 2,2,6,6-tetramethyl-1-piperidyl-oxyl (TEMPO), PhI(OAc)<sub>2</sub>, MeCN/H<sub>2</sub>O (1:1 v/v); then NaClO<sub>2</sub>, NaH<sub>2</sub>PO<sub>4</sub>, 2-methyl-2-butene, <sup>t</sup>BuOH/H<sub>2</sub>O (1:1 v/v), RT; then trimethylsilyldiazomethane (TMSCHN<sub>2</sub>), PhMe/MeOH (5:1 v/v), RT; (k) Mg, MeOH, RT; (l) benzeneseleninic anhydride, THF, 45°C; (m) BBr<sub>3</sub>, CH<sub>2</sub>Cl<sub>2</sub>, -78°C; (n) Ac<sub>2</sub>O, DMSO, RT; (o) lithium triisobutylhydroborate, THF, -78°C, 43/41 6:1.

(C) Reagents and conditions: (a) Mn(dpm)<sub>3</sub>, PhSiH<sub>3</sub>, O<sub>2</sub>, <sup>i</sup>PrOH/CH<sub>2</sub>Cl<sub>2</sub> (1:4 v/v), RT; (b) *tert*-butyldimethylsilyl chloride, imidazole, CH<sub>2</sub>Cl<sub>2</sub>, RT; (c) Me<sub>3</sub>S<sup>+</sup>I<sup>-</sup>, <sup>n</sup>BuLi, THF, 0°C; (d) Zn, Cp<sub>2</sub>TiCl<sub>2</sub>, 1,4-CHD, THF, 50°C; (e) TEMPO, PhI(OAc)<sub>2</sub>, MeCN/H<sub>2</sub>O (1:1 v/v); then NaClO<sub>2</sub>, NaH<sub>2</sub>PO<sub>4</sub>, 2-methyl-2-butene, <sup>t</sup>BuOH/H<sub>2</sub>O (1:1 v/v), RT; then TMSCHN<sub>2</sub>, PhMe/MeOH (5:1 v/v), RT; (f) Mg, MeOH, RT; (g) benzeneseleninic anhydride, THF, 40°C; (h) 15 mol % Rh(H)(CO)(PPh<sub>3</sub>)<sub>3</sub>, PhSiH<sub>3</sub>, THF, RT; (i) 5 M HCl/THF (1:3 v/v), 30°C; (j) pyridine hydrofluoride, THF, 40°C; (k) 1 M MeONa in MeOH, 30°C. See also Figures S346–S467.

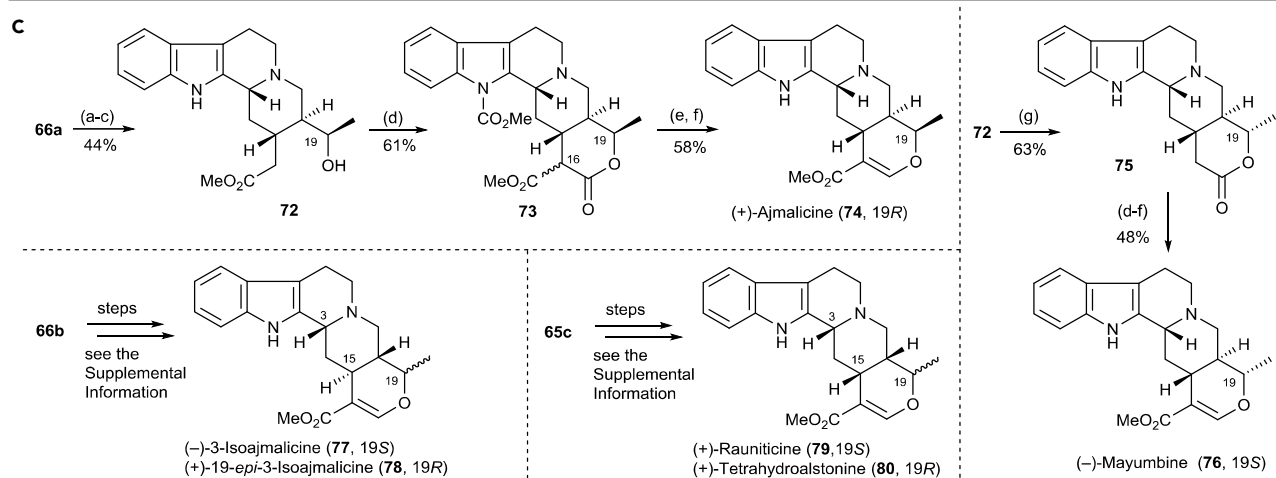
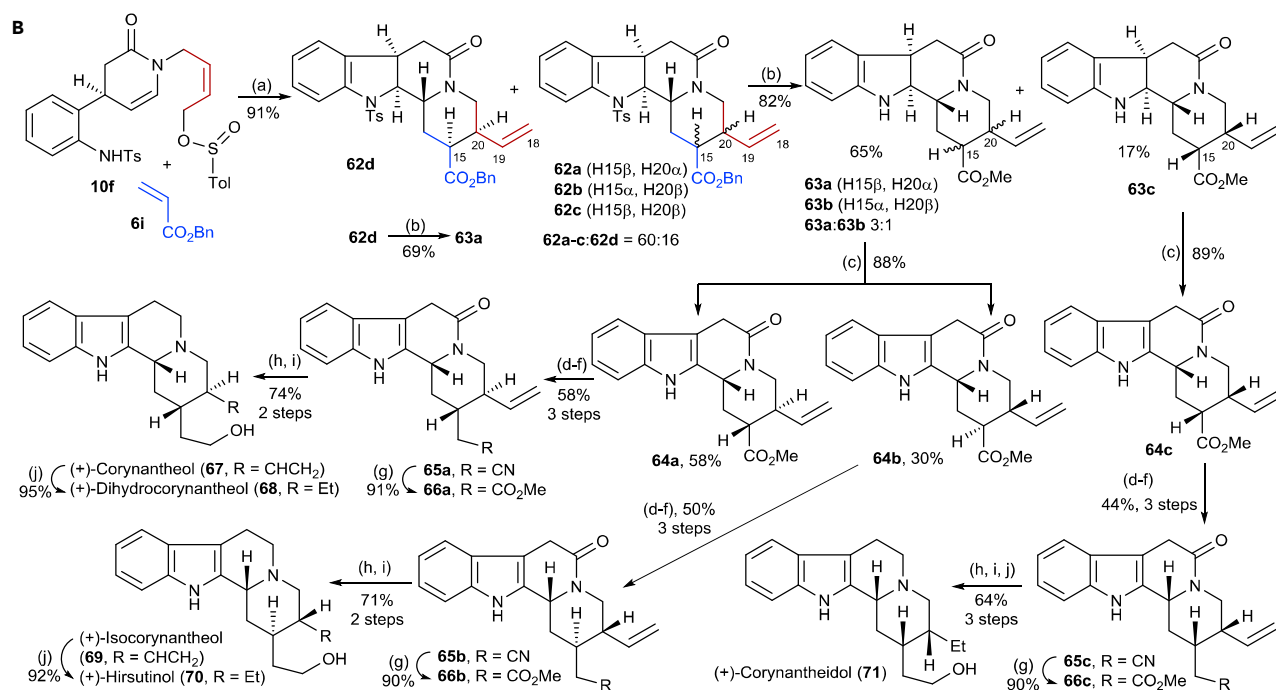
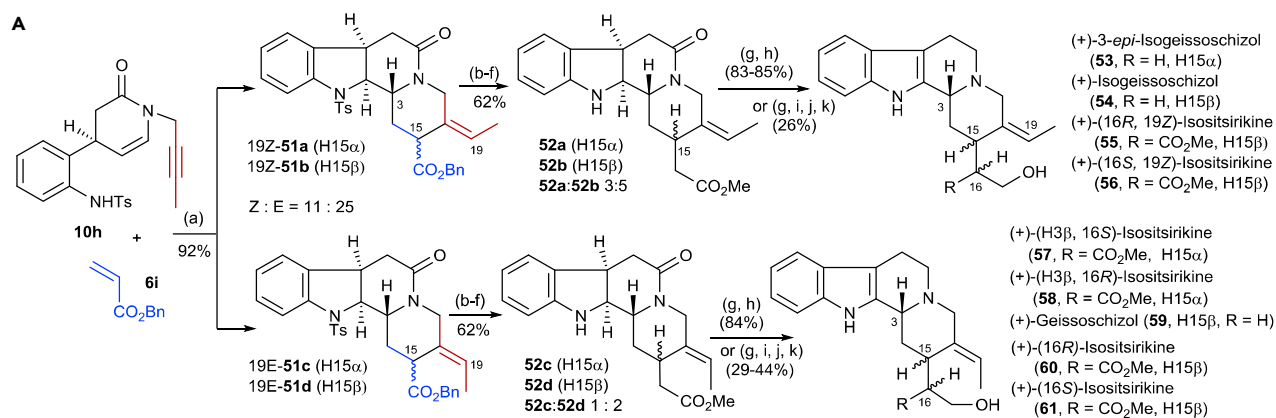
amide and O-debenzylation with  $\text{BBr}_3$ , afforded **41** (Figures S428–S431). Ultimately, a sequential oxidation-reduction of **41** via **42** (Figures S434 and S435) delivered (–)-yohimbine (**43**; Figures S436–S439).<sup>14,54</sup> Similarly, the diastereoisomer **44** (Figures S432 and S433) was synthesized from **40b** in 49% yield according to the same procedure as that applied for the synthesis of **41**.

Having developed a synthetic route to yohimbine (**43**) and related alkaloids from **29a**, we were able to synthesize natural rauwolscine (**48**), 17-*epi*-alloyohimbine (**50**), and the unnatural 17-*epi*-rauwolscine (**49**) from **29b**, which possessed a *cis*-fused D/E ring system (Scheme 2C). Unlike **29a**, Mukaiyama hydration of **29b** provided two inseparable diastereoisomers **45a** and **45b** in 52% yield and a 1:2 ratio after *tert*-butyldimethylsilyl (TBS) protection of the resultant hydroxy group. A mixture of **46a** and **46b** was obtained in 49% yield when Corey-Chaykovsky epoxidation, followed by opening of the epoxide ring, was performed. After oxidation of the hydroxy groups in **46a** and **46b** to esters, the Ts groups were removed to give two separable diastereoisomers, **47a** and **47b**, in 69% combined yield. Finally, three steps of indoline oxidation, amide reduction, and TBS deprotection from **47a** furnished rauwolscine (**48**; Figures S456–S459). In a similar procedure, **49** (Figures S464 and S465) was readily synthesized from **47b**, and **50** (Figures S466 and S467) was obtained by epimerization of **49** at C16.

### Syntheses of the Corynanthe and Heteroyohimbine Family Alkaloids

In addition to the divergent stereochemistry at C15 and C20, the distinction among the large members of the corynanthe family alkaloids is the geometric variation of the double bond at C19. Therefore, for syntheses of alkaloids in this family, we used **6i** (5 equiv) and **10h** (Figures S469–S472) with a 2-butynyl side chain to conduct a three-step radical cascade on a 20 g scale, which afforded two mixtures of the two diastereoisomers **51a–51b** and **51c–51d** in excellent combined yield (Scheme 3A; see also Figures S468 and S473–S480). The *E/Z* geometric isomers were completely separated at this stage. After homologation of the ester side chain at C15 and removal of the Ts group in **51** via a five-step transformation from individual mixtures of **51a–51d**, the four separable diastereoisomers **52a–52d** were obtained. Starting from each isomer, we were able to synthesize eight corynanthe family alkaloids, **54–61** (Figures S513–S520 and S527–S542), and unnatural 3-*epi*-isogeissoschizol (**53**; Figures S511 and S512) via two to four steps of functionality manipulations (see Supplemental Experimental Procedures).

For further syntheses of the corynanthe family alkaloids **67–71**, a strategy that introduces a C18–C19 terminal double bond at an early stage of synthesis was designed (Scheme 3B). This strategy also enabled the formation of a dihydropyran ring by converting the terminal alkene into a hydroxy group at C19, thus facilitating the syntheses of heteroyohimbine family alkaloids **74** and **76–80** with varied stereochemistry at C15, C19, and C20 (Scheme 3C).<sup>41</sup> To form a C18–C19 terminal double bond, we performed the radical cascade by using **6i** (5 equiv) and **10f** to provide a mixture of **62a–62c** (Figures S543 and S544) and a single diastereomer **62d** (Figures S545 and S546) in excellent yield. Removal of the Ts group in **62d** with Mg/MeOH readily effected epimerization at C15 to give **63a**. Coincidentally, there is no corynanthe family alkaloid that possesses the same stereochemistry at C3, C15, and C20 as that of **62d**. Treatment of the mixture of the three diastereoisomers **62a–62c** with Mg/MeOH afforded a mixture of two diastereoisomers **63a** and **63b** in 65% yield and a single diastereoisomer **63c** in 17% yield. After oxidation of the indoline moiety in **63a** and **63b**, diastereoisomers **64a** and **64b** were separated. Similarly, **64c** was obtained by oxidation of **63c**. After extension of the C15 ester chain by a



**Scheme 3. Total Syntheses of the Corynanthe and Heteroyohimbine Family Alkaloids**

(A) Reagents and conditions: (a) 1 mol % Ir(dtbbpy)(ppy)<sub>2</sub>PF<sub>6</sub>, 5 equiv KHCO<sub>3</sub>, THF, 30 W blue LEDs, 35°C, Ar; (b) LiBH<sub>4</sub>, THF, 0°C to RT; (c) methanesulfonyl chloride (MsCl), Et<sub>3</sub>N, CH<sub>2</sub>Cl<sub>2</sub>, RT; (d) trimethylsilyl cyanide (TMSCN), tetra-*n*-butylammonium fluoride (TBAF), THF, reflux; (e) HCl (g), MeOH, 0°C to RT; (f) Mg, MeOH, RT; (g) benzeneseleninic anhydride, THF, 40°C; (h) LiAlH<sub>4</sub>, PhMe, 0°C to RT; (i) 5 mol % Rh(H)(CO)(PPh<sub>3</sub>)<sub>3</sub>, PhSiH<sub>3</sub>, THF, RT; (j) lithium diisopropylamide, HCO<sub>2</sub>Me, THF, -78°C to RT; (k) AcOH, NaBH<sub>4</sub>, MeOH, 0°C.

(B) Reagents and conditions: (a) 0.5 mol % Ir(dtbbpy)(ppy)<sub>2</sub>PF<sub>6</sub>, 5 equiv KHCO<sub>3</sub>, acetonitrile, 15 W blue LEDs, Ar, 37°C; (b) Mg, MeOH, RT; (c) benzeneseleninic anhydride, THF, 40°C; (d) LiAlH<sub>4</sub>, THF, -30°C; (e) MsCl, Et<sub>3</sub>N, CH<sub>2</sub>Cl<sub>2</sub>, RT; (f) TMSCN, TBAF, THF, reflux; (g) HCl (g), MeOH, 0°C–60°C; (h) 7 mol % Rh(H)(CO)(PPh<sub>3</sub>)<sub>3</sub>, PhSiH<sub>3</sub>, THF, RT; (i) LiAlH<sub>4</sub>, THF, 0°C to RT; (j) H<sub>2</sub>, 10% PtO<sub>2</sub>, MeOH, RT.

(C) Reagents and conditions: (a) Pd(OAc)<sub>2</sub>, HClO<sub>4</sub>, 1,4-benzoquinone, MeCN/H<sub>2</sub>O (7:1 v/v), RT; (b) 7 mol % Rh(H)(CO)(PPh<sub>3</sub>)<sub>3</sub>, PhSiH<sub>3</sub>, THF, RT; (c) NaBH<sub>4</sub>, MeOH, -30°C; (d) NaHMDS or LiHMDS, NCCO<sub>2</sub>Me, THF, -78°C; (e) diisobutylaluminum hydride or NaBH<sub>4</sub>; (f) *p*-TsOH, CH<sub>2</sub>Cl<sub>2</sub>, reflux; then K<sub>2</sub>CO<sub>3</sub>, MeOH, RT; (g) Ph<sub>3</sub>P, diethyl azodicarboxylate, *p*-nitrobenzoic acid, THF, 0°C–30°C; then Cs<sub>2</sub>CO<sub>3</sub>, MeOH, RT. See also [Figures S468–S640](#).

four-step transformation (**64a** to **66a**), stepwise reduction of the amide and ester and then the double bond in **66a** generated **67** ([Figures S575 and S576](#)) and then **68** ([Figures S579–S582](#)), respectively. Similarly, **69–71** ([Figures S577, S578, and S583–S586](#)) were synthesized from **66b** and **66c** according to the above procedure for the syntheses of **67** and **68**, respectively.

For the syntheses of heteroyohimbine family alkaloids, **66a**, **66b**, and **65c** were used as starting materials ([Scheme 3C](#)). A three-step sequence of Wacker oxidation, amide reduction, and stereoselective ketone reduction was applied to **66a** to provide the single diastereoisomer **72** in 44% overall yield. Carbonylation of **72** resulted in the formation of the lactone ring and the introduction of two methoxycarbonyl groups in one pot to yield **73**. Further reduction and hydrolysis of **73** gave rise to ajmalicine (**74**; [Figures S601–S604](#)). Lactone **75** was obtained in 63% yield from **72** by Mitsunobu inversion of the C19 hydroxy group configuration, followed by hydrolysis. Mayumbine (**76**; [Figures S596–S598](#)) was prepared according to a procedure similar to that applied for the synthesis of ajmalicine (**74**). In addition, after similar functional-group manipulations, alkaloids **77–80**, possessing different stereochemistry at C15 and C19, were synthesized from **66b** and **65c**, respectively (see [Supplemental Experimental Procedures and Figures S605–S640](#)).

**Conclusion**

We have developed an innovative photocatalytic radical cascade that reverses the conventional reactivity between two electron-donating amine and enamine groups and allows highly efficient assembly of manifold core structures of indole alkaloids with divergent stereochemistry and functionalities from simple starting materials. The power of this radical cascade has been demonstrated by easy preparation of focused libraries of natural-product-like compounds with high to excellent diastereoselectivity. By using this radical cascade as a key reaction, we synthesized 33 indole alkaloids belonging to four families and four unnatural diastereoisomers in 6–14 steps, which are difficult to achieve by traditional methods. Promisingly, the radical cascade is green, water insensitive, and readily scalable ([Figure S641 and Table S1](#)). With the current success, we anticipate that generation of a nitrogen-centered radical from direct cleavage of an aniline N–H bond can be involved in many intermolecular reaction protocols. Expansion of such ideas would provide expedient access to more nitrogen-containing architectures, such as reserpine, strychnine, and vincamajine, which are of great value. Application of this method to the syntheses of other natural products and bioactive substances is in progress and will be reported in due course.

**EXPERIMENTAL PROCEDURES**

Full experimental procedures are provided in the [Supplemental Information](#).

## ACCESSION NUMBERS

The data for the X-ray crystallographic structures of detosylated derivatives of **3a** and **3l**, **28a**, **28b**, **29a**, and **29b** in this article have been deposited in the Cambridge Crystallographic Data Center under accession numbers CCDC: 1518109, 1520164, 1519507, 1519506, 1495501, and 1495500, respectively.

## SUPPLEMENTAL INFORMATION

Supplemental Information includes Supplemental Experimental Procedures, 641 figures, 1 table, 1 scheme, and 6 data files and can be found with this article online at <http://dx.doi.org/10.1016/j.chempr.2017.04.007>.

## AUTHOR CONTRIBUTIONS

Y.Q. conceived and directed all aspects of the research and wrote the manuscript with the assistance of X.-Y.L. The main experiments, which included methodology development and syntheses of natural products, were performed by X.W., D.X., W.Q., R.Z., X.Z., and Q.Z. W.L., X.D., and H.W. carried out the scale-up experiments of the radical cascade. S.W. and L.T. conducted the large-scale preparation of starting materials. D.Z., H.S., and all other authors analyzed the results and commented on the manuscript.

## ACKNOWLEDGMENTS

We thank the National Natural Science Foundation of China (21132006 and 21572140) and the National Science and Technology Major Projects for "Major New Drugs Innovation and Development" (2017ZX09101005 and 2017ZX09101003) for financial support. Daibing Luo is acknowledged for X-ray crystallographic analysis. We thank Litao Yuan for recording the high-resolution mass spectra. We would like to thank Prof. Weidong Li (Chongqing University) and Prof. Xiaoming Feng (Sichuan University) for helpful discussions.

Received: February 13, 2017

Revised: March 30, 2017

Accepted: April 19, 2017

Published: June 8, 2017

## REFERENCES AND NOTES

1. Newman, D.J., and Cragg, G.M. (2016). Natural products as sources of new drugs from 1981 to 2014. *J. Nat. Prod.* **79**, 629–661.
2. Nicolaou, K.C. (2016). Catalyst: synthetic organic chemistry as a force for good. *Chem* **1**, 331–334.
3. Seiple, I.B., Zhang, Z., Jakubec, P., Langlois-Mercier, A., Wright, P.M., Hog, D.T., Yabu, K., Allu, S.R., Fukuzaki, T., Carlsen, P.M., et al. (2016). A platform for the discovery of new macrolide antibiotics. *Nature* **533**, 338–345.
4. Creasey, W.A. (1983). The monoterpene indole alkaloids. In *Chemistry of Heterocyclic Compounds: Indoles*. E. Saxton, ed. (Wiley), pp. 783–829.
5. Dewick, P.M. (2009). *Medicinal Natural Products: A Biosynthetic Approach*, Third Edition (Wiley).
6. Neuss, N., and Neuss, M.N. (1990). Therapeutic use of bisindole alkaloids from *Catharanthus*. In *The Alkaloids: Chemistry and Pharmacology*. A. Brossi, ed. (Academic), pp. 229–240.
7. Mashour, N.H., Lin, G.I., and Frishman, W.H. (1998). Herbal medicine for the treatment of cardiovascular disease: clinical considerations. *Arch. Int. Med.* **158**, 2225–2234.
8. O'Connor, S.E., and Maresh, J.J. (2006). Chemistry and biology of monoterpene indole alkaloid biosynthesis. *Nat. Prod. Rep.* **23**, 532–547.
9. Woodward, R.B., Bader, F.E., Bickel, H., Frey, A.J., and Kierstead, R.W. (1956). The total synthesis of reserpine. *J. Am. Chem. Soc.* **78**, 2023–2025.
10. Woodward, R.B., Cava, M.P., Ollis, W.D., Hunger, A., Daeniker, H.U., and Schenker, K. (1954). The total synthesis of strychnine. *J. Am. Chem. Soc.* **76**, 4749–4751.
11. Adams, G.L., and Smith, A.B., III (2016). The chemistry of the akuammiline alkaloids. In *Alkaloids: Chemistry and Biology*, H.J. Knölker, ed. (Elsevier), pp. 171–257.
12. Smith, J.M., Moreno, J., Boal, B.W., and Garg, N.K. (2015). Cascade reactions: a driving force in akuammiline alkaloid total synthesis. *Angew. Chem. Int. Ed.* **54**, 400–412.
13. Mizoguchi, H., Oikawa, H., and Oguri, H. (2014). Biogenetically inspired synthesis and skeletal diversification of indole alkaloids. *Nat. Chem.* **6**, 57–64.
14. Lebold, T.P., Wood, J.L., Deitch, J., Lodewyk, M.W., Tantillo, D.J., and Sarpong, R. (2013). A divergent approach to the synthesis of the yohimbinoindole alkaloids venenatine and alstovenine. *Nat. Chem.* **5**, 126–131.
15. Lackner, G.L., Quasdorf, K.W., and Overman, L.E. (2013). Direct construction of quaternary carbons from tertiary alcohols via photoredox-catalyzed fragmentation of tert-alkyl



- N-phthalimidoyl oxalates. *J. Am. Chem. Soc.* **135**, 15342–15345.
16. Jamison, C.R., and Overman, L.E. (2016). Fragment coupling with tertiary radicals generated by visible-light photocatalysis. *Acc. Chem. Res.* **49**, 1578–1586.
17. Lo, J.C., Gui, J., Yabe, Y., Pan, C.-M., and Baran, P.S. (2014). Functionalized olefin cross-coupling to construct carbon–carbon bonds. *Nature* **516**, 343–348.
18. Yan, M., Lo, J.C., Edwards, J.T., and Baran, P.S. (2016). Radicals: reactive intermediates with translational potential. *J. Am. Chem. Soc.* **138**, 12692–12714.
19. Studer, A., and Curran, D.P. (2016). Catalysis of radical reaction: a radical chemistry perspective. *Angew. Chem. Int. Ed.* **55**, 58–102.
20. Jones, S.B., Simmons, B., Mastracchio, A., and MacMillan, D.W.C. (2011). Collective synthesis of natural products by means of organocascade catalysis. *Nature* **475**, 183–188.
21. Brill, Z.G., Grover, H.K., and Maimone, T.J. (2016). Enantioselective synthesis of anophiobolin sesterterpene via a programmed radical cascade. *Science* **352**, 1078–1082.
22. Asaba, T., Katoh, Y., Urabe, D., and Inoue, M. (2015). Total synthesis of crotophorbolone. *Angew. Chem. Int. Ed.* **54**, 14457–14461.
23. Nagatomo, M., Koshimizu, M., Masuda, K., Tabuchi, T., Urabe, D., and Inoue, M. (2014). Total synthesis of ryanodol. *J. Am. Chem. Soc.* **136**, 5916–5919.
24. Narayanam, J.M.R., and Stephenson, C.R.J. (2011). Visible light photoredox catalysis: applications in organic synthesis. *Chem. Soc. Rev.* **40**, 102–113.
25. Prier, C.K., Rankic, D.A., and MacMillan, D.W.C. (2013). Visible light photoredox catalysis with transition metal complexes: applications in organic synthesis. *Chem. Rev.* **113**, 5322–5363.
26. Nicewicz, D.A., and MacMillan, D.W.C. (2008). Merging photoredox catalysis with organocatalysis: the direct asymmetric alkylation of aldehydes. *Science* **322**, 77–80.
27. Johnson, C.P., Smith, R.T., Allmendinger, S., and MacMillan, D.W.C. (2016). Metallaphotoredox-catalysed  $sp^3$ – $sp^3$  cross-coupling of carboxylic acids with alkyl halides. *Nature* **536**, 322–325.
28. Ischay, M.A., Anzovino, M.E., Du, J., and Yoon, T.P. (2008). Efficient visible light photocatalysis of [2+2] enone cycloadditions. *J. Am. Chem. Soc.* **130**, 12886–12887.
29. Yoon, T.P., Ischay, M.A., and Du, J. (2010). Visible light photocatalysis as a greener approach to photochemical synthesis. *Nat. Chem.* **2**, 527–532.
30. Narayanam, J.M.R., Tucker, J.W., and Stephenson, C.R.J. (2009). Electron-transfer photoredox catalysis: development of a tin-free reductive dehalogenation reaction. *J. Am. Chem. Soc.* **131**, 8756–8757.
31. Dai, C., Narayanam, J.M.R., and Stephenson, C.R.J. (2011). Visible-light-mediated conversion of alcohols to halides. *Nat. Chem.* **3**, 140–145.
32. Weiss, M.E., and Carreira, E.M. (2011). Total synthesis of (+)-daphnadin E. *Angew. Chem. Int. Ed.* **50**, 11501–11505.
33. Furst, L., Narayanam, J.M.R., and Stephenson, C.R.J. (2011). Total synthesis of (+)-gliocladin C enabled by visible-light photoredox catalysis. *Angew. Chem. Int. Ed.* **50**, 9655–9659.
34. Schnermann, M.J., and Overman, L.E. (2012). A concise synthesis of (–)-aplyviolene facilitated by a strategic tertiary radical conjugate addition. *Angew. Chem. Int. Ed.* **51**, 9576–9580.
35. Sun, Y., Li, R., Zhang, W., and Li, A. (2013). Total synthesis of indotertine A and drimentines A, F, and G. *Angew. Chem. Int. Ed.* **52**, 9201–9204.
36. Takayama, H., and Sakai, S.I. (1998). Monoterpene indole alkaloid syntheses utilizing biomimetic reaction. In *The Alkaloids: Chemistry and Biology* G.A. Cordell, ed. (Academic), pp. 415–452.
37. Brandau, S., Landa, A., Franzén, J., Marigo, M., and Jørgensen, K.A. (2006). Organocatalytic conjugate addition of malonates to  $\alpha,\beta$ -unsaturated aldehydes: asymmetric formal synthesis of (–)-paroxetine, chiral lactams, and lactones. *Angew. Chem. Int. Ed.* **45**, 4305–4309.
38. Stöckigt, J., Antonchick, A.P., Wu, F., and Waldmann, H. (2011). The Pictet–Spengler reaction in natural and in organic chemistry. *Angew. Chem. Int. Ed.* **50**, 8538–8564.
39. Yu, J., Wang, T., Liu, X., Deschamps, J., Flippen-Anderson, J., Liao, X., and Cook, J.M. (2003). General approach for the synthesis of sarpagine indole alkaloids. Enantiospecific total synthesis of (+)-vellosimine, (+)-normacusine B, (–)-alkaloid Q3, (–)-panarine, (+)-N-methylvellosimine, and (+)-N-methyl-16-epipericyclivine. *J. Org. Chem.* **68**, 7565–7581.
40. Deiters, A., Chen, K., Eary, C.T., and Martin, S.F. (2003). Biomimetic entry to the sarpagan family of indole alkaloids: total synthesis of (+)-geissoschizine and (+)-N-methylvellosimine. *J. Am. Chem. Soc.* **125**, 4541–4550.
41. Stavrinides, A., Tatsis, E.C., Caputi, L., Foureau, E., Stevenson, C.E., Lawson, D.M., Courdavault, V., and O'Connor, S.E. (2016). Structural investigation of heteroyohimbine alkaloid synthesis reveals active site elements that control stereoselectivity. *Nat. Commun.* **7**, 12116.
42. Zard, S.Z. (2008). Recent progress in the generation and use of nitrogen-centered radicals. *Chem. Soc. Rev.* **37**, 1603–1618.
43. Stella, L. (2001). Nitrogen-centered radicals. In *Radicals in Organic Synthesis*, P. Renaud and M.P. Sibi, eds. (Wiley), pp. 407–426.
44. Choi, G.J., and Knowles, R.R. (2015). Catalytic alkene carboaminations enabled by oxidative proton coupled electron transfer. *J. Am. Chem. Soc.* **137**, 9226–9229.
45. Choi, G.J., Zhu, Q., Miller, D.C., Gu, C.J., and Knowles, R.R. (2016). Catalytic alkylation of remote C–H bonds enabled by proton couple electron transfer. *Nature* **539**, 268–271.
46. Chu, J.C.K., and Rovis, T. (2016). Amide-directed photoredox-catalysed C–C bond formation at unactivated  $sp^3$  C–H bonds. *Nature* **539**, 272–275.
47. Hu, X.-Q., Qi, X., Chen, J.-R., Zhao, Q.-Q., Wei, Q., Lan, Y., and Xiao, W.-J. (2016). Catalytic N-radical cascade reaction of hydrazones by oxidative deprotonation electron transfer and TEMPO mediation. *Nat. Commun.* **7**, 11188.
48. Vatsadze, S.Z., Loginova, Y.D., dos Passos Gomes, G., and Alabugin, I.V. (2017). Stereoelectronic chameleons: the donor–acceptor dichotomy of functional groups. *Chem. Eur. J.* **23**, 3225–3245.
49. Takano, S., Yonaga, M., Morimoto, M., and Ogasawara, K. (1985). Chiral synthesis of (+)-eburnamine, (–)-eburnarnenine, and (–)-eburnamonine. *J. Chem. Soc. Perkin Trans. 1*, 305–309.
50. Desmaële, D., Mekouar, K., and d'Angelo, J. (1997). Stereocontrolled elaboration of quaternary carbon centers through the asymmetric Michael-type alkylation of chiral imines/secondary enamines: enantioselective synthesis of (+)-vincamine. *J. Org. Chem.* **62**, 3890–3901.
51. Das, S., Li, Y., Bornschein, C., Pisiewicz, S., Kiersch, K., Michalik, D., Gallou, F., Junge, K., and Beller, M. (2015). Selective rhodium-catalyzed reduction of tertiary amides in amino acid esters and peptides. *Angew. Chem. Int. Ed.* **54**, 12389–12393.
52. Magnus, P., Payne, A.H., Waring, M.J., Scott, D.A., and Lynch, V. (2000). Conversion of  $\alpha,\beta$ -unsaturated ketones into  $\alpha$ -hydroxy ketones using an  $Mn^{III}$  catalyst, phenylsilane and dioxygen: acceleration of conjugate hydride reduction by dioxygen. *Tetrahedron Lett.* **41**, 9725–9730.
53. Barrero, A.F., Quilez del Moral, J.F., Sánchez, E.M., and Arteaga, J.F. (2006). Titanocene-mediated radical cyclization: an emergent method towards the synthesis of natural products. *Eur. J. Org. Chem.* **2006**, 1627–1641.
54. Abué, J., Ghosh, S., and Tanol, M. (1994). Symmetry-driven synthesis of indole alkaloids: asymmetric total syntheses of (+)-yohimbine, (–)-yohimbone, (–)-yohimbane, and (+)-alloyohimbane. *J. Am. Chem. Soc.* **116**, 9009–9018.

## Opinion

## Microalgal Cultivation in Treating Liquid Digestate from Biogas Systems

Ao Xia<sup>1,2</sup> and Jerry D. Murphy<sup>1,3,\*</sup>

**Biogas production via anaerobic digestion (AD) has rapidly developed in recent years. In addition to biogas, digestate is an important byproduct. Liquid digestate is the major fraction of digestate and may contain high levels of ammonia nitrogen. Traditional processing technologies (such as land application) require significant energy inputs and raise environmental risks (such as eutrophication). Alternatively, microalgae can efficiently remove the nutrients from digestate while producing high-value biomass that can be used for the production of biochemicals and biofuels. Both inorganic and organic carbon sources derived from biogas production can significantly improve microalgal production. Land requirement for microalgal cultivation is estimated as 3% of traditional direct land application of digestate.**

## Development of Biogas Industry

The global industry of **biogas** (see [Glossary](#)) has developed significantly in the past 10 years [1–3]. In Europe, Germany leads the biogas industry. A total of 10 020 biogas plants were in operation in 2014, generating over 144 PJ of energy; biogas produced 4.7% of electricity and 1% of heat demand in Germany [1]. In Asia, China is the largest biogas producer; in 2014, 41.5 million household digesters were in operation, annually generating 13.7 billion m<sup>3</sup> of biogas (293 PJ) [2]. The number of medium/large-scale biogas plants is also growing. In 2014, 99 957 biogas plants produced 2.1 billion m<sup>3</sup> of biogas (45 PJ) [2].

Currently, most biogas is used as a source for generation of heat and/or electricity. However, the use of upgraded biogas (biomethane after removal of CO<sub>2</sub> and impurities) as a transport fuel is growing. In Sweden, 54% of biogas was used as transport biofuel in 2013 [1]. Other countries, such as Switzerland, Germany, China, the USA, and France, are developing biogas-fuelled transport systems [4].

In addition to biogas, **digestate** is another important byproduct [5]. Digestate processing has become a major bottleneck in the development of a biogas industry [6]. Digestate may be separated into solid (10–20% by mass) and liquid (80–90% by mass) fractions by screw press or decanter centrifuge [6]. Solid digestate contains less water and is more stable; it can be easily transported and stored. Solid digestate can either be used as agricultural biofertiliser or be further converted to heat and/or value-added products (e.g., pyrochar, nanocellulose) via thermal processes [6,7]. By contrast, liquid digestate processing is more difficult. The simplest treatment method is to directly spread on local agricultural land; land application of liquid digestate, however, has some disadvantages. First, it leads to NH<sub>3</sub> volatilisation and nutrient loss, which may cause **eutrophication** of nearby water systems [8]. Second, it may cause chemical (e.g., heavy metals), biological (e.g., pathogens), or physical (e.g., plastics) contamination, which reduces the long-term crop productivity of soil [5,9]. Furthermore, the increasing

## Trends

Biogas production has developed rapidly in recent years. Digestate is an important byproduct of the biogas system. However, digestate processing has become a major bottleneck in the development of a biogas industry.

Biofuels and bioproducts from microalgae are promising for the future; nevertheless, the current microalgal cultivation cost is too high to allow commercial applications. Nutrient use may account for half of the cost in microalgal cultivation. The combining of on-site liquid digestate treatment and microalgal cultivation can significantly reduce the nutrient cost for cultivation.

Study of microalga-based digestate treatment has become a topic of much interest in the past few years. Microalgae can efficiently remove various nutrients from digestate, particularly nitrogen and phosphorus. However, there remain numerous challenges for such a process.

<sup>1</sup>MaREI Centre, Environmental Research Institute, University College Cork, Cork, Ireland

<sup>2</sup>Key Laboratory of Low-Grade Energy Utilization Technologies and Systems, Chongqing University, Chongqing 400044, China

<sup>3</sup>School of Engineering, University College Cork, Cork, Ireland

\*Correspondence: [jerry.murphy@ucc.ie](mailto:jerry.murphy@ucc.ie) (J.D. Murphy).

number and capacity of biogas plants may lead to an oversupply of digestate for local agricultural land; the value of liquid digestate after long-distance transport may become negative. Digestate is continuously produced. Land application is dependent on the crop growth stage, soil type, and time of year; it is not applied in winter months or in poor weather. Thus, digestate needs to be stored. The storage process can emit additional greenhouse gases (e.g., CH<sub>4</sub>, N<sub>2</sub>O) [7,9] as the digestion process rarely destroys all volatile solids. Other digestate treatment technologies, such as membrane separation and evaporation, can efficiently concentrate the nutrients; however, they require high energy input. For example, at an industrial scale, membrane separation consumes 16–25 kW<sub>e</sub>h (58–90 MJ) of electricity per m<sup>3</sup> treated digestate, while evaporation requires 300–350 kWh (1080–1260 MJ) of thermal energy per ton of water evaporated [6].

There are huge demands on agricultural land for application of digestate (in countries such as Germany) and in a number of countries (such as Ireland) authorisation for the application of digestate produced from the digestion of animal byproducts and wastes is very difficult to obtain. Solutions whereby digestate is not land applied are extremely beneficial to a biogas system. Aquatic **microalgae** may offer an alternative solution for digestate treatment [7,10]. The initial attempt to cultivate microalgae in digestate was conducted by Golueke and Oswald in the 1950s [11]. However, this process was not built upon until very recently. The primary driver for this work is the increasing demand for digestate processing from the biogas industry [1,6].

This opinion article aims to provide a perspective on microalgal cultivation for liquid digestate treatment. Recent trends of microalgae grown in digestate are reviewed. A quantitative model is proposed for a 2-MW<sub>e</sub> biogas plant to establish the savings in land area needed provided by a microalgal cultivation system as opposed to land application of digestate. The potential and the challenges associated with such a process are highlighted.

### Microalgae Grown in Liquid Digestate

Microalga-based biofuels and bioproducts are promising for the future; however, the current cultivation cost is too high to allow commercial applications [10,12,13]. Nutrient use (e.g., nitrogen, phosphorus) can account for half of the cost and energy input in cultivation [8,14]. The combining of on-site liquid digestate treatment and microalgal cultivation can significantly reduce the nutrient cost.

There are three main cultivation modes for microalgae: photoautotrophic, heterotrophic, and mixotrophic, as described in Box 1. For liquid digestate treatment, mixotrophic microalgae not only improve the biomass productivity and enhance nitrogen and phosphorus removal but also enable inorganic and organic carbon removal. Mixotrophic cultivation has higher biomass concentration and productivity and less photoinhibition/limitation than photoautotrophic cultivation [14–16]. Mixotrophic microalgae can achieve one to two magnitudes higher productivities than photoautotrophic cultures in outdoor photobioreactors [15].

Box 2 presents the effects of the main components of liquid digestate on microalgal growth. The composition of liquid digestate varies significantly and is mainly dependent on feedstock characteristics, the microbial community, AD process control (e.g., temperature, organic loading rate, trace element supply), and the configuration (e.g., batch or continuous, single stage or two stage).

### Trends in Microalgae Treating Liquid Digestate

Table 1 summarises recent studies of microalgal cultivation using liquid digestate. Most of the reported microalgae are naturally grown in either a freshwater environment (e.g., *Chlorella pyrenoidosa*, *Scenedesmus obliquus*) or a marine environment (e.g., *Nannochloropsis salina*) [17–19]. Alternatively, a mutant strain obtained by nuclear irradiation (e.g., *Chlorella* PY-ZU1)

### Glossary

**Anaerobic digestion (AD):** an anaerobic biological process comprising hydrolysis, acidogenesis, acetogenesis, and methanogenesis. AD degrades organic components such as animal manure, agricultural residues, energy crops, industrial wastes, and food wastes while producing biogas and digestate via a complex microorganism community. AD is efficient in organic component removal; however, it has minimal effect in removal of the inorganic component [14].

**Biogas:** a gas mixture mainly comprising CH<sub>4</sub> (ca. 60% by volume) and CO<sub>2</sub> (ca. 40% by volume). The gas usually contains trace amounts of water, H<sub>2</sub>S, NH<sub>3</sub>, N<sub>2</sub>, O<sub>2</sub>, CO, halogenated hydrocarbons, and siloxanes. Biogas has various applications, such as electricity, vehicle fuel, and heat.

**Biorefinery:** a sustainable process converting biomass to various products (such as chemicals, materials, and feeds) and energy (including electricity and/or heat and biofuels).

**Combined heat and power (CHP) generation:** simultaneous generation of electricity and heat via biogas combustion. Efficiencies of 35% and 50% respectively would be typical.

**Digestate:** a mixture of undigested substrates, microbial biomass, and metabolic products. Digestate contains high levels of nitrogen, phosphorus, and stabilised carbon [7].

**Eutrophication:** a phenomenon whereby an aquatic system is enriched with natural or artificial nutrients. This may cause explosive growth of algae and plants.

**Microalgae:** microscopic photosynthetic eukaryotic organisms (usually 1–10 μm in size) that live in freshwater and marine environments. They convert CO<sub>2</sub> and water to organic carbon components (e.g., glucose) and produce O<sub>2</sub> through photosynthesis. Cyanobacteria may also be referred to as microalgae, as they share many features [44,45,47].

**Two-stage fermentation:** separate hydrolytic and methanogenic reactors. The two reactors operate at the optimal pH for each stage (hydrolysis and methanation). In the first, hydrolytic reactor much of the organic component is hydrolysed and fermented to VFAs, while in the

### Box 1. Microalgal Cultivation Mode

Microalgae in general are photosynthetic microorganisms that use energy from light to extract electrons and protons from water and reduce CO<sub>2</sub> as organic compounds [14]. Nevertheless, many microalgal species use organic substrates under light or dark conditions (mixotrophic and heterotrophic growth) [12,16]. For instance, *Chlorella vulgaris*, *Arthrospira platensis*, and *Haematococcus pluvialis* can employ photoautotrophic, mixotrophic, and heterotrophic growth modes [16]. Table I presents a comparison of the three main cultivation modes.

Photoautotrophic cultivation has been widely reported for microalgal cultivation in both raceway ponds and photobioreactors [13,15]. Microalgae use light as an energy source and inorganic carbon as the carbon source (e.g., CO<sub>2</sub>, bicarbonate). Nevertheless, high microalgal biomass productivity and concentration are difficult to achieve due to the self-shading phenomenon caused by the accumulation of microalgal cells [15,24]. Furthermore, photoinhibition caused by high light intensity is a common problem in outdoor cultivation [12].

In heterotrophic cultivation, microalgae use organic compounds (e.g., sugars, VFAs) as energy and carbon sources. Drawbacks of light limitation and inhibition in photosynthesis are avoided; consequently, high biomass productivity and concentration can be achieved [15,16] with less land requirement. Heterotrophic cultivation may be considered a promising mode if a low-cost substrate can be sourced. However, the microalgal cultures are easily contaminated by other microorganisms. The maintenance of microalgal culture is a critical issue for heterotrophic cultivation that significantly increases the cultivation cost [15].

In mixotrophic cultivation, microalgae employ heterotrophy and photoautotrophy using both organic and inorganic carbon sources [15,16]. Organic carbon is assimilated via aerobic respiration and inorganic carbon is fixed via photosynthesis. Light is not a dominant limiting factor for mixotrophic microalgal growth as cultivation is not solely dependent on photosynthesis. The adverse effects of photoinhibition and limitation on microalgal growth can be reduced when the illumination is too high or too low. Combining photosynthesis and organic carbon compound utilisation, mixotrophic cultivation can improve growth rates, reduce cultivation duration, and enhance biomass productivity [14,15]. Furthermore, CO<sub>2</sub> released by aerobic respiration can be reused to enhance photosynthesis [16].

Table I. A Comparison of Photoautotrophic, Heterotrophic, and Mixotrophic Cultivation Modes for Microalgal Cultivation (Adapted from [15,16])

Parameter	Photoautotrophic	Heterotrophic	Mixotrophic
Reactor	Raceway pond and photobioreactor	Fermenter	Raceway pond and photobioreactor
Carbon source	Inorganic sources such as CO <sub>2</sub> and bicarbonate	Organic sources such as sugars and organic acids	Both organic and inorganic sources
Energy source	Light	Organic sources	Both light and organic sources
Biomass productivity	Low	High	High
Features	<ul style="list-style-type: none"> <li>• Energy-saving process</li> <li>• Capacity to produce light-induced high-value substances</li> </ul>	<ul style="list-style-type: none"> <li>• Independent of light</li> <li>• High growth rate and productivity</li> </ul>	<ul style="list-style-type: none"> <li>• Reduction of photo limitation and inhibition</li> <li>• High growth rate</li> <li>• Less biomass loss in absence of light</li> <li>• Cost reduction</li> </ul>

second, methanogenic reactor the organic effluents are further converted to CH<sub>4</sub> and CO<sub>2</sub>.

is used for liquid digestate treatment [10]. Liquid digestate is mainly derived from AD of agricultural wastes (e.g., livestock manure, slurry) and industrial wastes (e.g., vinasse) [10,18,20,21]. The biomass productivities and concentrations (dry weight) of microalgae cultivated in liquid digestate are in the ranges of 0.03–0.67 g/l/d and 0.4–4.8 g/l. These values are comparable with or slightly higher than those of photoautotrophic cultivation in synthetic medium [10,13]. However, the performance can be further improved by addressing the following inhibition and limitation factors.

### Turbidity and Ammonia Nitrogen Inhibition

The high turbidity of liquid digestate caused by suspended materials is a major issue, although microalgal cultivation can partly reduce the turbidity by removing the suspended materials [22]. As photosynthesis is dependent on the availability of photosynthetically active radiation (PAR)

### Box 2. Suitability of Liquid Digestate as Microalgal Cultivation Medium

Table I presents the main characteristics of liquid digestate derived from wet AD (total solids content in digester below 15%). Liquid digestate is usually slightly alkaline or neutral, with a pH value in the range 6.7–9.2. This is within the optimal range for freshwater microalgae (6–8) and alkaliphilic microalgae (8.5–10) [13,14,23,47].

Liquid digestate contains abundant nitrogen [total nitrogen (TN): 139–3456 mg/l] and phosphorus [total phosphorus (TP): 7–381 mg/l]. These are the primary nutrients required for microalgal growth.

Nitrogen is found in various biological substances (e.g., protein, nucleic acid, phospholipid) [19]. Ammonium is considered the preferred form of nitrogen for microalgal growth, as a redox reaction is not involved and less energy is required [34]. When ammonium is available, cyanobacteria do not use other nitrogen sources until ammonium is consumed [14]. In digestate, ammonia nitrogen, which is mainly in the form of ammonium nitrogen, is the major component of TN (65–98%); this enables fast growth of microalgae.

Phosphorus, preferably in the form of phosphate, is essential for microalgal growth and various cellular processes including energy transfer and synthesis of DNA and nucleic acids [23]. Phosphate is the dominant component of TP (82–90%) in digestate, which facilitates microalgal cultivation.

COD concentration in liquid digestate is in the range 210–6900 mg/l. COD includes VFAs such as acetate [10,17]. These organic carbon sources can enhance mixotrophic metabolism and boost the growth rate of microalgae [18]. Furthermore, the inorganic carbon sources (939–1353 mg/l), mainly in the form of bicarbonate, can play an important role in photosynthesis [25].

Other macronutrients (e.g., manganese, potassium, sulphur) and micronutrients (e.g., boron, cobalt, iron, molybdenum, nickel, zinc) exist in liquid digestate [10,14]. They are derived either from feedstock degradation or trace element supply in AD and are necessary for microalgal cultivation [10,13].

Table I. Characteristics of Liquid Digestate

Characteristic	Value Range	Refs
pH	6.7–9.2	[17–20,25,30,33,41,48–50]
COD, mg/l	210–6900	[17–20,24–26,30–33,41,49,51]
Total inorganic carbon (TIC) mg/l	939–1353	[20,48]
TN	139–3456	[8,10,17–20,22,25,31,33,36,41,48–52]
Percentage of ammonia nitrogen (TAN/TN)	65–98%	[8,10,17,18,22,25,33,48,49,52]
TP	7–381	[8,10,17–20,22,25,26,30,31,36,37,41,48–52]
Percentage of phosphate (PO <sub>4</sub> -P/TP)	82–90%	[17,18,49]
Aluminium (Al), mg/l	0.1–34	[18,52]
Boron (B), mg/l	0.9–4	[8,10,17,18,52]
Cadmium (Cd), mg/l	<1	[10,52]
Calcium (Ca), mg/l	65–1044	[8,10,17,18,24,52]
Chlorine (Cl), mg/l	160–438	[10,24]
Chromium (Cr), mg/l	<1.2	[52]
Cobalt (Co), mg/l	0.02–0.04	[17]
Copper (Cu), mg/l	0.09–21.4	[8,10,17,52]
Iron (Fe), mg/l	0.9–65	[8,10,17,18,52]
Lead (Pb), mg/l	0.03–2.8	[10,52]
Magnesium (Mg), mg/l	3–659	[8,10,17,18,24,52]
Manganese (Mn), mg/l	0.1–17	[8,10,17,18,52]
Molybdenum (Mo), mg/l	<1.8	[10,52]
Nickel (Ni), mg/l	<1.4	[52]
Potassium (K), mg/l	102–2707	[8,10,17,18,24,52]
Silicon (Si), mg/l	26–72	[52]
Sodium (Na), mg/l	126–709	[10,17,18,24,52]
Sulphur (S), mg/l	111–115	[52]
Zinc (Zn), mg/l	0.9–13	[10,18,52]

Table 1. Recent Trends and Performances of Microalgae Cultivated in Liquid Digestate

Inoculum	Digestate Origin	Digestate Pretreatment	Operation <sup>a</sup>	Biomass Productivity and Concentration <sup>b</sup>	Nutrient Removal Efficiency	Refs
<i>Chlorella pyrenoidosa</i>	Starch processing wastewater	<ul style="list-style-type: none"> <li>Filtration</li> <li>Sterilisation</li> <li>Mixed with alcohol wastewater</li> </ul>	Batch (9 d)	<ul style="list-style-type: none"> <li>0.58 g/l/d</li> <li>3.01 g/l</li> </ul>	<ul style="list-style-type: none"> <li>TN 91.6%</li> <li>TP 90.7%</li> <li>COD 75.8%</li> </ul>	[18]
<i>C. pyrenoidosa</i>	Starch processing wastewater	<ul style="list-style-type: none"> <li>Precipitation</li> <li>Filtration</li> </ul>	Outdoor batch (14 d) sparging with 5–9% CO <sub>2</sub>	<ul style="list-style-type: none"> <li>0.63 g/l/d</li> <li>2.05 g/l</li> </ul>	<ul style="list-style-type: none"> <li>TN 83.1%</li> <li>TP 97.0%</li> <li>COD 66.0%</li> </ul>	[17]
<i>Chlorella</i> PY-ZU1	Swine manure and sewage	<ul style="list-style-type: none"> <li>Centrifugation</li> <li>Autoclave</li> </ul>	Batch (13 d) sparging with 15% CO <sub>2</sub>	<ul style="list-style-type: none"> <li>0.601 g/l/d</li> <li>4.81 g/l</li> </ul>	<ul style="list-style-type: none"> <li>TAN 73%</li> <li>TP 95%</li> <li>COD 79%</li> </ul>	[10]
<i>Chlorella</i> sp.	Dairy manure	<ul style="list-style-type: none"> <li>Dilution</li> <li>Filtration</li> </ul>	Batch (21 d)	<ul style="list-style-type: none"> <li>1.71 g/l</li> </ul>	<ul style="list-style-type: none"> <li>TN 82.5%</li> <li>TAN 100%</li> <li>TP 74.5%</li> <li>COD 38.4%</li> </ul>	[22]
<i>Chlorella</i> sp.	NA	<ul style="list-style-type: none"> <li>Ultraviolet</li> <li>Filtration</li> </ul>	Batch (6 d) with biogas in headspace	<ul style="list-style-type: none"> <li>0.494 g/l</li> </ul>	<ul style="list-style-type: none"> <li>TN 73.1%</li> <li>TP 67.6%</li> <li>COD 78.9%</li> </ul>	[41]
<i>Chlorella</i> sp.	Wastewater sludge	<ul style="list-style-type: none"> <li>Mixed with wastewater treatment plant effluent</li> </ul>	Batch (until stationary phase)	<ul style="list-style-type: none"> <li>0.45 g/l/d</li> <li>2.11 g/l</li> </ul>	<ul style="list-style-type: none"> <li>TN 83.7%</li> <li>TP 94.2%</li> <li>COD 86.3%</li> </ul>	[26]
<i>Chlorella vulgaris</i>	Dairy manure	<ul style="list-style-type: none"> <li>Dilution</li> </ul>	Semicontinuous (30 d) with 2% CO <sub>2</sub>		<ul style="list-style-type: none"> <li>TN 93.6%</li> <li>TAN 100%</li> <li>TP 89.2%</li> <li>COD 55.4%</li> </ul>	[36]
<i>Chlorella minutissima</i> , <i>Chlorella sorokiniana</i> and <i>Scenedesmus bijuga</i>	Poultry litter	<ul style="list-style-type: none"> <li>Centrifugation</li> <li>Dilution</li> </ul>	Batch (12 d)	<ul style="list-style-type: none"> <li>0.076 g/l/d</li> <li>0.612 g/l</li> </ul>	<ul style="list-style-type: none"> <li>TN 60%</li> <li>TP 80%</li> </ul>	[52]
<i>C. vulgaris</i> , <i>Scenedesmus obliquus</i> , and <i>Neochloris oleoabundans</i>	Livestock waste	<ul style="list-style-type: none"> <li>Ultraviolet</li> <li>Filtration</li> </ul>	Batch (7 d) with biogas in headspace		<ul style="list-style-type: none"> <li>TN 76.0%</li> <li>TP 63.2%</li> <li>COD 63.1%</li> <li>CO<sub>2</sub> 62%</li> </ul>	[20]
<i>C. vulgaris</i> and nitrifying–denitrifying activated sludge	Vinasse	<ul style="list-style-type: none"> <li>Dilution</li> </ul>	Continuous (175 d) with synthetic biogas sparging	<ul style="list-style-type: none"> <li>11.8 g/m<sup>2</sup>/d</li> <li>0.6 g/l</li> </ul>	<ul style="list-style-type: none"> <li>TN 37%</li> <li>TP 71%</li> <li>COD 51%</li> <li>TOC 57%</li> <li>TIC 78%</li> <li>CO<sub>2</sub> 80%</li> </ul>	[21]
<i>C. vulgaris</i> , <i>N. oleoabundans</i> , and <i>S. obliquus</i>	Cattle slurry and raw cheese whey	<ul style="list-style-type: none"> <li>Dilution</li> </ul>	Batch (21 d) in CO <sub>2</sub> incubator	<ul style="list-style-type: none"> <li>0.26 g/l/d</li> </ul>	<ul style="list-style-type: none"> <li>TAN 99.9%</li> <li>PO<sub>4</sub>-P 97.3%</li> </ul>	[53]
<i>Chroococcus</i> sp.	<i>Chroococcus</i> sp.	<ul style="list-style-type: none"> <li>Dilution or mixed with wastewater or BG 11 medium</li> </ul>	Batch (12 d) with air sparging	<ul style="list-style-type: none"> <li>1.42 g/l</li> </ul>	<ul style="list-style-type: none"> <li>TAN 85.2%</li> <li>NO<sub>3</sub>-N 77.3%</li> <li>TP 89.3%</li> <li>COD 70%</li> </ul>	[30]
<i>Desmodesmus</i> sp.	Pig manure	<ul style="list-style-type: none"> <li>Filtration</li> <li>Dilution</li> </ul>	Batch (10 d)	<ul style="list-style-type: none"> <li>0.385 g/l</li> </ul>	<ul style="list-style-type: none"> <li>TN 75.6%</li> <li>TAN 92.7%</li> <li>PO<sub>4</sub>-P 100%</li> </ul>	[33]
			Fed-batch (40 d)	<ul style="list-style-type: none"> <li>1.039 g/l</li> </ul>	<ul style="list-style-type: none"> <li>TN 94.2%</li> <li>TAN 91.1%</li> <li>PO<sub>4</sub>-P 88.7%</li> </ul>	[33]

Table 1. (continued)

Inoculum	Digestate Origin	Digestate Pretreatment	Operation <sup>a</sup>	Biomass Productivity and Concentration <sup>b</sup>	Nutrient Removal Efficiency	Refs
<i>Desmodesmus</i> sp.	Pig manure	<ul style="list-style-type: none"> <li>Filtration</li> <li>Dilution</li> </ul>	Batch (14 d)	<ul style="list-style-type: none"> <li>0.029 g/l/d</li> <li>0.412 g/l</li> </ul>	<ul style="list-style-type: none"> <li>TN 100%</li> <li>TP 100%</li> </ul>	[49]
<i>Nannochloropsis salina</i>	Municipal wastewater	<ul style="list-style-type: none"> <li>Mixed with artificial seawater</li> </ul>	Batch (10 d) with air sparging	<ul style="list-style-type: none"> <li>0.092 g/l/d</li> <li>0.92 g/l</li> </ul>	<ul style="list-style-type: none"> <li>TN 100%</li> <li>TP 100%</li> </ul>	[31]
			Semicontinuous (18 d) with air sparging	<ul style="list-style-type: none"> <li>0.155 g/l/d</li> </ul>	<ul style="list-style-type: none"> <li>TN 89%</li> <li>TP 82.8%</li> </ul>	[31]
<i>N. salina</i> and <i>Synechocystis</i> sp.	Municipal wastewater	<ul style="list-style-type: none"> <li>Mixed with artificial seawater</li> </ul>	Batch (18 d) with air sparging	<ul style="list-style-type: none"> <li>0.151 g/l/d</li> </ul>	<ul style="list-style-type: none"> <li>TN 100%</li> <li>TP 100%</li> </ul>	[32]
			Semicontinuous (18 d) with air sparging	<ul style="list-style-type: none"> <li>0.212 g/l/d</li> </ul>	<ul style="list-style-type: none"> <li>TN 100%</li> <li>TP 100%</li> </ul>	[32]
<i>N. oleoabundans</i>	Dairy manure	<ul style="list-style-type: none"> <li>Dilution</li> </ul>	Batch (11 d) with 2–3% CO <sub>2</sub> sparging	<ul style="list-style-type: none"> <li>0.088 g/l/d</li> </ul>		[8]
<i>Scenedesmus accuminatus</i>	Livestock waste	<ul style="list-style-type: none"> <li>Filtration</li> <li>Autoclave</li> <li>Dilution</li> </ul>	Batch (5 d) with air sparging	<ul style="list-style-type: none"> <li>0.118 g/l/d</li> </ul>		[25]
			Semicontinuous (29 d) with air sparging	<ul style="list-style-type: none"> <li>0.214 g/l/d</li> </ul>	<ul style="list-style-type: none"> <li>TN 89%</li> </ul>	[25]
<i>Scenedesmus</i> sp.	Swine manure	<ul style="list-style-type: none"> <li>Autoclave</li> <li>Mixed with municipal wastewater</li> </ul>	Batch then continuous chemostats (45 d) with air sparging	<ul style="list-style-type: none"> <li>0.67 g/l/d</li> </ul>	<ul style="list-style-type: none"> <li>TAN &gt;95%</li> <li>PO<sub>4</sub>-P &gt;97%</li> </ul>	[29]
<i>S. obliquus</i>	Livestock waste	<ul style="list-style-type: none"> <li>Filtration</li> <li>Autoclave</li> <li>Dilution</li> </ul>	Batch (7 d) with biogas in headspace	<ul style="list-style-type: none"> <li>0.311 g/l/d</li> </ul>	<ul style="list-style-type: none"> <li>TN 74.6%</li> <li>TP 88.8%</li> <li>COD 75.3%</li> <li>CO<sub>2</sub> 73.8%</li> </ul>	[19]
Mixed microalgae dominated by <i>Scenedesmus</i> sp.	Wastewater	<ul style="list-style-type: none"> <li>Dilution</li> </ul>	Batch (7 d)	<ul style="list-style-type: none"> <li>2.6 g/l</li> </ul>		[24]
<i>Tetraselmis</i> sp.	<i>Tetraselmis</i> sp.	<ul style="list-style-type: none"> <li>Dilution</li> </ul>	Batch (10 d) with air sparging	<ul style="list-style-type: none"> <li>5 × 10<sup>8</sup> cells/l</li> </ul>		[37]

<sup>a</sup>Indoor experiment unless stated otherwise.

<sup>b</sup>Dry biomass weight unless stated otherwise.

(400–700 nm), high turbidity leads to low PAR, thereby reducing the growth of microalgae [7,22,23]. Various pretreatment methods, such as filtration [18], centrifugation [10], and precipitation [17], have been applied for removal of the solid particles from digestate to reduce the turbidity. Nevertheless, there is no quantitative study on the impact of digestate pretreatment methods on microalgal growth rates.

Inhibition from ammonia nitrogen is another critical issue. Although ammonium is a preferable form for microalgal utilisation, high total ammonia nitrogen (TAN) (both ammonium and free ammonia) levels may lead to inhibition. Inhibitory thresholds vary significantly and depend on the microalgal species and cultivation conditions. Levine *et al.* suggested that 50 mg/l of TAN is

the inhibitory threshold for *Neochloris oleoabundans* while 100 mg/l of TAN is toxic to microalgal cells [8]. By contrast, Uggetti *et al.* reported that 260 mg/l of TAN did not prevent the growth of a mixed microalgal culture dominated by *Scenedesmus* sp. [24]. Park *et al.* found that a TAN level of 100 mg/l did not suppress the cell growth of *Scenedesmus* sp. When TAN levels increased to 500 mg/l, the cell concentration was reduced by 30%, while the initial growth rate was not inhibited. Only 35% of the cell concentration was achieved at 1000 mg/l of TAN [25].

Free ammonia is mainly responsible for the TAN inhibition, as the microalgal cell membrane is highly permeability to free ammonia [26]. A 77% reduction in the growth rate of *Scenedesmus* sp. was found when the free ammonia nitrogen (FAN) level increased from 9 to 34 mg/l [24]. Photosynthesis rates of *S. obliquus* and *Dunaliella tertiolecta* can be reduced by 50% when the FAN level reached 17 mg/l [27]. The equilibrium between ammonia and ammonium is shown in Equation 1. The FAN concentration increases with increasing TAN, pH, and temperature (Equation 2) [28].



$$\text{FAN} = \frac{\text{TAN}}{1 + \frac{10^{-\text{pH}}}{10^{-\left(0.09018 + \frac{2729.92}{T(K)}\right)}}} \quad [2]$$

At room temperature (25 °C), FAN accounts for only 0.1% of TAN at pH 6; this significantly increases to 0.6%, 5%, and 36% at pH 7, 8, and 9, respectively. Therefore, pH control (e.g., by CO<sub>2</sub> sparging) is considered an important strategy for reduction of FAN inhibition [26].

TAN levels in liquid digestate are usually high (1000–3000 mg/l) and have the potential to inhibit microalgal growth. Most of the studies used dilution to reduce the inhibition effect caused by TAN, FAN, and turbidity (Table 1). However, microalgal biomass concentrations are reduced due to the dilution of the nutrient supply [24]. Furthermore, the dilution process consumes a large quantity of freshwater; this makes the overall process less attractive for industrial application. The use of wastewater [26,29,30] and seawater [31,32] as the dilution source is more sustainable. Alternatively, direct use of liquid digestate without dilution has recently been demonstrated in green microalgal cultivation [10,17,20]. Cheng *et al.* found *Chlorella* PY-ZU1 adapted to the liquid digestate from pig farms (initial TAN level: 1093 mg/l) with 15% CO<sub>2</sub> gas sparging under low pH conditions (6–6.5) [10]. In this case, FAN is at a low concentration (0.7–2.3 mg/l) and may not significantly inhibit microalgal growth. Most of the studies reported in Table 1 were conducted in batch culture systems; however, continuous flow cultures (e.g., fed batch, chemostat) are more advantageous in controlling nutrient levels because of their flexibility in nutrient supply. Consequently, the inhibition caused by excess TAN and turbidity can be reduced [23,29,33].

#### Phosphorus and Carbon Limitation

The optimal N/P mass ratio for microalgal growth is suggested to be around 7 [10,34]. In some cases, insufficient phosphorus supply can be a limited factor in liquid digestate applied to microalgal cultivation [6,10,20,26]. The growth rate of microalgae almost doubled through the addition of phosphate to liquid digestate [10]. Similarly, the C/N mass ratio of microalgae is in the range 4–8 [35], indicating that the carbon sources in digestate may be much lower than required. Both external inorganic sources (e.g., CO<sub>2</sub>, bicarbonate) and organic carbon sources [e.g., volatile fatty acids (VFAs), sugars] can be effectively supplied to boost microalgal growth and to improve nutrient removal [10,18,25,33,36].



### Bacterial Contamination

Bacteria present in liquid digestate may have either positive impacts (e.g., vitamin, ammonium, and CO<sub>2</sub> production, O<sub>2</sub> consumption) or negative impacts (e.g., competition for nutrients) on the microalgal cultivation [7,8,17,24,37]. Sterilisation process to maintain a monoculture of microalgae is not favourable for mass cultivation systems. The presence of bacteria is inevitable and should be accepted and controlled [27,37]. Moreover, other biological contamination sources, such as foreign algae, zooplankton, and viruses, may greatly inhibit the growth of the target microalgae [38]; the control strategies for biological contamination are important for future mass cultivation of microalgae.

Filtration (to remove large organisms) and chemical addition (to inhibit zooplankton) are effective approaches to control biological contamination during microalgal cultivation [38]. Nevertheless, the former method consumes energy whereas the later method may result in additional treatment processes for the cultivation effluent. Microalgal strain selection would be a more feasible approach; selection of a strain with resistance or non-susceptibility to biological contamination would be a key issue for mass cultivation [38,39]. Alternatively, control of environmental (e.g., light, temperature) and operational (e.g., hydraulic and biomass retention, nutrient supply, pH) parameters is a cost-effective strategy to reduce biological contamination in microalgal systems [40].

Currently, control of biological contamination in mass microalgal cultivation for liquid digestate treatment has not been achieved. It is necessary to develop our understanding of interactions between species to identify effective and economical methods to maintain microalgal dominance.

### Pollutant Removal

Nutrient removal efficiencies vary depending on the microalgal species, operational parameters, and the characteristics of the liquid digestate. Achieving 100% removal of nitrogen and phosphorus is possible under batch and semicontinuous operation [31–33]. However, not all removed nutrients are removed by microalgae. For instance, under alkaline conditions excess TAN removal can be caused by ammonia stripping, while phosphate removal can be caused by the formation of insoluble precipitates [17].

Approximately 50–90% of chemical oxygen demand (COD) can be removed by mixotrophic microalgae [10,17–21,26,30,36,41]. However, it is unlikely to achieve complete COD removal. This is because the remaining COD may comprise recalcitrant organic compounds that are hardly degradable by AD or through microalgal cultivation [17]. Alternatively, it may be attributed to the fact that organic compounds, which can be either naturally excreted via microalgal growth or suddenly released via cell lysis [42], have adverse effects on COD removal.

In addition to nutrient removal, microalgae are able to remove heavy metals [43]. Cheng *et al.* found that microalgae successfully reduced heavy metal levels (lead, arsenic, mercury, and cadmium) in liquid digestate, with removal efficiencies of 35–90%, while accumulating heavy metals in their biomass. However, the heavy metal levels of biomass were still below the maximum tolerable dietary levels for dairy cattle feed [10].

### Integration of Microalgal Cultivation with Biogas Industry

The produced microalgal biomass can be further integrated into a **biorefinery** approach to produce biochemicals, biofuels, animal and aquaculture feeds, and soil conditioners [10,12,22,44–46]. Box 3 presents a case study of the integration of liquid digestate treatment and microalgal cultivation. Biogas facilities not only provide abundant nitrogen and phosphorus sources in liquid digestate but also supply sufficient CO<sub>2</sub> as a carbon source for microalgal

### Box 3. Integration of Microalgal Digestate Treatment with Biogas Industry

The concept of microalgal cultivation coupled with biogas production is shown in Figure 1. Microalgae can simultaneously remove the nutrients in liquid digestate and fix CO<sub>2</sub> via biomass accumulation. Produced microalgal biomass can be further integrated into a biorefinery process to improve the economic feasibility and energy recovery. High-value compounds, such as astaxanthin, carotenoids, beta-carotene, and omega-3 fatty acids, can be extracted from microalgal biomass. The entire biomass or residual biomass after extraction can be used as animal feeds or soil conditioners or converted to biofuels such as biodiesel (via esterification), bioethanol (via fermentation), biogas (via AD), and electricity (via combustion) [10,12,22].

A 2-MW<sub>e</sub> agricultural biogas plant in Europe is modelled that annually consumes 46 000 t of biomass (fresh weight; e.g., maize silage, corn silage, grass silage, yard manure). Some water is added for dilution. Digestate production is 41 200 t of liquid and 10 400 t of solid digestate separated via a screw press unit [6,12]. Table I provides a case study of microalgal cultivation for liquid digestate treatment.

Allowing 90% conversion of nitrogen to biomass, 14.6 kg VS of microalgal biomass can be produced by treating 1 m<sup>3</sup> of liquid digestate. Carbon supply is far below the required level. Consequently, approximately 79% of the carbon should be supplied by an external carbon source such as CO<sub>2</sub>. Low-cost CO<sub>2</sub> is an important issue for large-scale microalgal cultivation [12]. However, the biogas facility can provide abundant CO<sub>2</sub>. Only 11% of the CO<sub>2</sub> in the biogas is required for microalgal cultivation. CO<sub>2</sub> can be derived from the biogas upgrading process (e.g., membrane separation) or from the exhaust of the **combined heat and power (CHP)** process. Allowing currently achievable microalgal productivity in outdoor raceway ponds during wastewater treatment (15 g VS/m<sup>2</sup>/d or 55 t VS/ha/a) [12], the land requirement for microalgal cultivation is estimated as 11 ha; this can be realised for a rural biogas plant. By contrast, the direct field application of liquid digestate would require 364 ha of land (based on the common maximum nutrient load of 170 kg N/ha/a) [9]. It should be noted that the real CO<sub>2</sub> demand may be significantly higher than the theoretical value, as CO<sub>2</sub>-to-cell transfer is limited in a raceway pond system [45].

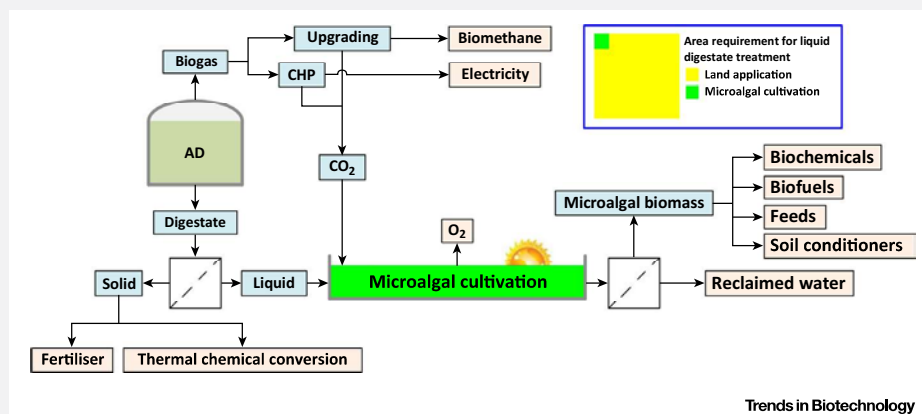


Figure 1. Microalgal Cultivation for Liquid Digestate Treatment.

Table I. Outdoor Microalgal Cultivation for Treatment of Liquid Digestate from 2-MW<sub>e</sub> Biogas Plant

Parameter	Result	Remarks and Refs
<i>Basic Elements of 2-MW<sub>e</sub> Agricultural Biogas Plant</i>		
Liquid digestate output	41 200 m <sup>3</sup> /a	Assuming the density of liquid equal to water [6]
Biogas output	10 160 000 m <sup>3</sup> /a	Data from [3]
CO <sub>2</sub> output	4 064 000 m <sup>3</sup> /a	40% CO <sub>2</sub> content in biogas [47]
<i>Microalgae Grown in Liquid Digestate</i>		
Microalgal biomass composition (mass percentage of VS)	C 52.4%; H 7.5%; O 29.7%; N 9.2%; P 1.3%	C <sub>106</sub> H <sub>181</sub> O <sub>45</sub> N <sub>16</sub> P [27]
Main nutrients in liquid digestate	TN 1500 mg/l; TP 210 mg/l; total carbon (TC) 2000 mg/l	Typical values in Box 2
Microalgal biomass production per m <sup>3</sup> liquid digestate treatment	14.6 kg VS/m <sup>3</sup>	90% of TN to biomass conversion

Table I. (continued)

Parameter	Result	Remarks and Refs
TC in microalgal biomass per m <sup>3</sup> liquid digestate treatment	7.7 kg/m <sup>3</sup>	
Carbon in microalgae sourced from liquid digestate	1.6 kg/m <sup>3</sup>	80% TC to biomass conversion
External carbon requirement	6.1 kg/m <sup>3</sup> equal to 22.2 kg CO <sub>2</sub> /m <sup>3</sup>	
Area productivity of microalgae	15 g VS/m <sup>2</sup> /d or 55 t VS/ha/a	In raceway pond [12]
Area capacity for liquid digestate treatment by microalgae	3742 m <sup>3</sup> /ha	Based on microalgal productivity and biomass yield from liquid digestate
External CO <sub>2</sub> fixation	83.2 t/ha	Based on area treatment capacity and external CO <sub>2</sub> requirement
<i>Microalgal Cultivation for Treating Liquid Digestate from 2-MW<sub>e</sub> Agricultural Biogas Plant</i>		
Area requirement	11 ha	
Annual external CO <sub>2</sub> requirement	917 t/a	
CO <sub>2</sub> fixed in biogas	11%	
Annual microalgal biomass output	603 t VS/a	
Annual microalgal energy equivalent	13 266 GJ/a	22 GJ/t VS of energy density

cultivation. One m<sup>3</sup> of liquid digestate can be used as the nutrient source to produce 14.6 kg volatile solids (VS) of microalgae while fixing 22.2 kg of CO<sub>2</sub> in biogas via microalgal photosynthesis. For a 2-MW<sub>e</sub> biogas plant, an area of 11 ha is expected for liquid digestate treatment, providing 603 t VS/a of microalgal biomass (13 266 GJ of energy equivalent or 316 t oil equivalent). This is equivalent to 6% of the energy in the biogas (ca. 210 TJ). The land requirement for microalgal cultivation is only approximately 3% of the direct land application (11 ha versus 364 ha). Furthermore, microalgae can be continuously cultivated around the year to treat digestate. Thus, the environmental risks associated with digestate storage and transport to field can be minimised.

### Concluding Remarks and Future Perspectives

Microalgae can efficiently extract the nutrients from biogas digestate while providing high-value biomass for biorefinery applications. Current developments of microalga-based digestate treatment are significant; however, there remain many challenges that need to be addressed (see Outstanding Questions). More research work should be devoted to the following areas.

- (i) An external carbon source can significantly boost microalgal growth in digestate. CO<sub>2</sub> derived from biogas is a desirable inorganic carbon source that can enhance the photosynthesis of microalgae. Alternatively, low-cost organic carbon sources have the potential to markedly increase microalgal productivity. **Two-stage fermentation** may be used to realise such a process. In the first stage, the hydrolytic reactor can produce an effluent rich in VFAs, part of which can be mixed with the liquid digestate obtained from the second, methanogenic reactor to improve mixotrophic microalgal growth.
- (ii) Most of the current studies are conducted under indoor batch conditions. For future application in the biogas industry, the stability and performance of long-term microalgal cultivation for digestate treatment needs to be evaluated under outdoor continuous operation, with particular focus on pollutant removal efficiencies, biomass productivity, and quality. The microalgal process is efficient in the removal of nitrogen and phosphorus from digestate; however, it may be less efficient for the removal of other pollutants such as COD and heavy metals. The reclaimed water quality should be carefully examined. Furthermore, the control strategies associated with biological contamination (e.g., bacteria, foreign microalgae) still need to be comprehensively investigated.

### Outstanding Questions

What is the most cost-effective strategy for the control of biological contamination (e.g., bacteria, foreign microalgae) during long-term outdoor microalgal cultivation for digestate treatment?

Can the quality of reclaimed water derived from microalga-based digestate treatment achieve discharge standards without additional post-treatment processes?

What is the most economical and sustainable microalgal processing pathway?

- (iii) Selection, breeding, and engineering of high-performance microalgae can efficiently enhance the digestate treatment process. System engineering is encouraged to enhance mass transfer from nutrients to cells and to improve the overall performance of microalgal cultivation.
- (iv) The extraction of high-value chemicals can improve the economic feasibility of microalgal cultivation; however, the global demands for such chemicals are relatively small. Production of microalgal biofuels and animal and aquaculture feeds are encouraged. Various microalgal harvesting and conversion processes require significantly different energy input and chemical usage; the pathway choice is very much dependent on the final use of the microalgal products. More detailed analyses of energy, greenhouse gas emission, and economic feasibility in microalgal cultivation, harvesting, and conversion based on digestate treatment should be conducted.

### Acknowledgments

This opinion article is based on work supported by Science Foundation Ireland (SFI) under grant nos 12/RC/2302 and 12/RC/2305s2. Researchers are employed by the SFI centre Marine Renewable Energy Ireland (MaREI). Industrial funding is provided by Gas Networks Ireland through The Green Gas Innovation Group and by ERVIA. The authors thank Dr David Wall and Mr Markus Voelklein for the helpful suggestions. A.X. acknowledges Chongqing University for start-up funds under the 'One Hundred Talents Program'.

### References

- IEA Bioenergy (2015) *Task 37 Country Reports Summary*. [www.iea-biogas.net/](http://www.iea-biogas.net/)
- Li, J. (2015) Biogas policy in China. In *3rd China International Bioenergy and Biomass Utilization Summit*, pp. 203–207 [www.bbs-summit.com/en](http://www.bbs-summit.com/en)
- Murphy, J. *et al.* (2011) Biogas from crop digestion. *IEA Bioenergy Task 37*, 1–23 [www.iea-biogas.net](http://www.iea-biogas.net)
- Borjesson, P. and Mattiasson, B. (2008) Biogas as a resource-efficient vehicle fuel. *Trends Biotechnol.* 26, 7–13
- Nkoa, R. (2014) Agricultural benefits and environmental risks of soil fertilization with anaerobic digestates: a review. *Agron. Sustain. Dev.* 34, 473–492
- Fuchs, W. and Drosig, B. (2013) Assessment of the state of the art of technologies for the processing of digestate residue from anaerobic digesters. *Water Sci. Technol.* 67, 1984–1993
- Monlau, F. *et al.* (2015) New opportunities for agricultural digestate valorization: current situation and perspectives. *Energy Environ. Sci.* 8, 2600–2621
- Levine, R.B. *et al.* (2011) *Neochloris oleoabundans* grown on anaerobically digested dairy manure for concomitant nutrient removal and biodiesel feedstock production. *Biomass Bioenerg.* 35, 40–49
- Lukehurst, C.T. *et al.* (2010) Utilisation of digestate from biogas plants as biofertiliser. *IEA Bioenergy Task 37*, 1–22 [www.iea-biogas.net](http://www.iea-biogas.net)
- Cheng, J. *et al.* (2015) Growth optimisation of microalga mutant at high CO<sub>2</sub> concentration to purify undiluted anaerobic digestion effluent of swine manure. *Bioresour. Technol.* 177, 240–246
- Golueke, C.G. and Oswald, W.J. (1959) Biological conversion of light energy to the chemical energy of methane. *Appl. Microbiol.* 7, 219–227
- Lundquist, T.J. *et al.* (2010) *A Realistic Technology and Engineering Assessment of Algae Biofuel Production*, Energy Biosciences Institute
- Zhu, L. (2015) Microalgal culture strategies for biofuel production: a review. *Biofuels Bioprod. Bioref.* 9, 801–814
- Markou, G. and Georgakakis, D. (2011) Cultivation of filamentous cyanobacteria (blue-green algae) in agro-industrial wastes and wastewaters: a review. *Appl. Energy* 88, 3389–3401
- Wang, J. *et al.* (2014) Mixotrophic cultivation of microalgae for biodiesel production: status and prospects. *Appl. Biochem. Biotechnol.* 172, 3307–3329
- Katarzyna, C. and Facundo-Joaquin, M.-R. (2004) Kinetic and stoichiometric relationships of the energy and carbon metabolism in the culture of microalgae. *Biotechnology* 3, 21–34
- Tan, X. *et al.* (2014) *Chlorella pyrenoidosa* cultivation using anaerobic digested starch processing wastewater in an airlift circulation photobioreactor. *Bioresour. Technol.* 170, 538–548
- Yang, L. *et al.* (2015) Nutrients removal and lipids production by *Chlorella pyrenoidosa* cultivation using anaerobic digested starch wastewater and alcohol wastewater. *Bioresour. Technol.* 181, 54–61
- Xu, J. *et al.* (2015) Nutrient removal and biogas upgrading by integrating freshwater algae cultivation with pigery anaerobic digestate liquid treatment. *Appl. Microbiol. Biotechnol.* 99, 6493–6501
- Zhao, Y. *et al.* (2015) Performance of three microalgal strains in biogas slurry purification and biogas upgrade in response to various mixed light-emitting diode light wavelengths. *Bioresour. Technol.* 187, 338–345
- Serejo, M.L. *et al.* (2015) Influence of biogas flow rate on biomass composition during the optimization of biogas upgrading in microalgal–bacterial processes. *Environ. Sci. Technol.* 49, 3228–3236
- Wang, L. *et al.* (2010) Anaerobic digested dairy manure as a nutrient supplement for cultivation of oil-rich green microalgae *Chlorella* sp. *Bioresour. Technol.* 101, 2623–2628
- Richmond, A. (2004) *Handbook of Microalgal Culture: Biotechnology and Applied Phycology*, Blackwell
- Uggetti, E. *et al.* (2014) Anaerobic digestate as substrate for microalgae culture: the role of ammonium concentration on the microalgae productivity. *Bioresour. Technol.* 152, 437–443
- Park, J. *et al.* (2010) Ammonia removal from anaerobic digestion effluent of livestock waste using green alga *Scenedesmus* sp. *Bioresour. Technol.* 101, 8649–8657
- Akerstrom, A.M. *et al.* (2014) Biomass production and nutrient removal by *Chlorella* sp as affected by sludge liquor concentration. *J. Environ. Manag.* 144, 118–124
- Peccia, J. *et al.* (2013) Nitrogen supply is an important driver of sustainable microalgae biofuel production. *Trends Biotechnol.* 31, 134–138
- Rajagopal, R. *et al.* (2013) A critical review on inhibition of anaerobic digestion process by excess ammonia. *Bioresour. Technol.* 143, 632–641
- Dickinson, K.E. *et al.* (2015) Simultaneous remediation of nutrients from liquid anaerobic digestate and municipal wastewater by the microalga *Scenedesmus* sp AMDD grown in continuous chemostats. *J. Appl. Microbiol.* 118, 75–83
- Prajapati, S.K. *et al.* (2014) Bioconversion of algae to methane and subsequent utilization of digestate for algae cultivation: a closed

- loop bioenergy generation process. *Bioresour. Technol.* 158, 174–180
31. Cai, T. *et al.* (2013) Cultivation of *Nannochloropsis sauna* using anaerobic digestion effluent as a nutrient source for biofuel production. *Appl. Energy* 108, 486–492
32. Cai, T. *et al.* (2013) Comparison of *Synechocystis* sp PCC6803 and *Nannochloropsis salina* for lipid production using artificial seawater and nutrients from anaerobic digestion effluent. *Bioresour. Technol.* 144, 255–260
33. Ji, F. *et al.* (2015) Fed-batch cultivation of *Desmodesmus* sp in anaerobic digestion wastewater for improved nutrient removal and biodiesel production. *Bioresour. Technol.* 184, 116–122
34. Cai, T. *et al.* (2013) Nutrient recovery from wastewater streams by microalgae: status and prospects. *Renew. Sust. Energy Rev.* 19, 360–369
35. Ward, A.J. *et al.* (2014) Anaerobic digestion of algae biomass: a review. *Algal Res.* 5, 204–214
36. Wang, L. *et al.* (2010) Semi-continuous cultivation of *Chlorella vulgaris* for treating undigested and digested dairy manures. *Appl. Biochem. Biotechnol.* 162, 2324–2332
37. Erkelens, M. *et al.* (2014) Microalgae digestate effluent as a growth medium for *Tetraselmis* sp in the production of biofuels. *Bioresour. Technol.* 167, 81–86
38. Wang, H. *et al.* (2013) The contamination and control of biological pollutants in mass cultivation of microalgae. *Bioresour. Technol.* 128, 745–750
39. Day, J.G. *et al.* (2012) Overcoming biological constraints to enable the exploitation of microalgae for biofuels. *Bioresour. Technol.* 109, 245–251
40. Park, J.B.K. *et al.* (2011) Wastewater treatment high rate algal ponds for biofuel production. *Bioresour. Technol.* 102, 35–42
41. Yan, C. and Zheng, Z. (2014) Performance of mixed LED light wavelengths on biogas upgrade and biogas fluid removal by microalga *Chlorella* sp. *Appl. Energy* 113, 1008–1014
42. Hadj-Romdhane, F. *et al.* (2013) The culture of *Chlorella vulgaris* in a recycled supernatant: effects on biomass production and medium quality. *Bioresour. Technol.* 132, 285–292
43. Alam, M.A. *et al.* (2015) Enhanced removal of  $Zn^{2+}$  or  $Cd^{2+}$  by the flocculating *Chlorella vulgaris* JSC-7. *J. Hazard. Mater.* 289, 38–45
44. Larkum, A.W.D. *et al.* (2012) Selection, breeding and engineering of microalgae for bioenergy and biofuel production. *Trends Biotechnol.* 30, 198–205
45. Christenson, L. and Sims, R. (2011) Production and harvesting of microalgae for wastewater treatment, biofuels, and bioproducts. *Biotechnol. Adv.* 29, 686–702
46. Passos, F. and Ferrer, I. (2015) Influence of hydrothermal pretreatment on microalgal biomass anaerobic digestion and bioenergy production. *Water Res.* 68, 364–373
47. Xia, A. *et al.* (2015) How do we optimize third-generation algal biofuels? *Biofuels Bioprod. Bioref.* 9, 358–367
48. Posadas, E. *et al.* (2014) Microalgae-based agro-industrial wastewater treatment: a preliminary screening of biodegradability. *J. Appl. Phycol.* 26, 2335–2345
49. Ji, F. *et al.* (2014) Biomass production and nutrients removal by a new microalgae strain *Desmodesmus* sp in anaerobic digestion wastewater. *Bioresour. Technol.* 161, 200–207
50. Kumar, M.S. *et al.* (2010) Influence of nutrient loads, feeding frequency and inoculum source on growth of *Chlorella vulgaris* in digested piggery effluent culture medium. *Bioresour. Technol.* 101, 6012–6018
51. Hollinshead, W.D. *et al.* (2014) Boosting D-lactate production in engineered cyanobacteria using sterilized anaerobic digestion effluents. *Bioresour. Technol.* 169, 462–467
52. Singh, M. *et al.* (2011) Microalgal system for treatment of effluent from poultry litter anaerobic digestion. *Bioresour. Technol.* 102, 10841–10848
53. Franchino, M. *et al.* (2013) Growth of three microalgae strains and nutrient removal from an agro-zootechnical digestate. *Chemosphere* 92, 738–744

ARTICLE

Received 23 Sep 2014 | Accepted 1 Dec 2014 | Published 14 Jan 2015

DOI: 10.1038/ncomms7013

OPEN

# A molecular nematic liquid crystalline material for high-performance organic photovoltaics

Kuan Sun<sup>1,2,3,\*</sup>, Zeyun Xiao<sup>1,\*</sup>, Shirong Lu<sup>1,\*</sup>, Wojciech Zajaczkowski<sup>4</sup>, Wojciech Pisula<sup>4</sup>, Eric Hanssen<sup>5</sup>, Jonathan M. White<sup>1</sup>, Rachel M. Williamson<sup>6</sup>, Jegadesan Subbiah<sup>1</sup>, Jianyong Ouyang<sup>2</sup>, Andrew B. Holmes<sup>1</sup>, Wallace W.H. Wong<sup>1</sup> & David J. Jones<sup>1</sup>

Solution-processed organic photovoltaic cells (OPVs) hold great promise to enable roll-to-roll printing of environmentally friendly, mechanically flexible and cost-effective photovoltaic devices. Nevertheless, many high-performing systems show best power conversion efficiencies (PCEs) with a thin active layer (thickness is  $\sim 100$  nm) that is difficult to translate to roll-to-roll processing with high reproducibility. Here we report a new molecular donor, benzodithiophene terthiophene rhodanine (BTR), which exhibits good processability, nematic liquid crystalline behaviour and excellent optoelectronic properties. A maximum PCE of 9.3% is achieved under AM 1.5G solar irradiation, with fill factor reaching 77%, rarely achieved in solution-processed OPVs. Particularly promising is the fact that BTR-based devices with active layer thicknesses up to 400 nm can still afford high fill factor of  $\sim 70\%$  and high PCE of  $\sim 8\%$ . Together, the results suggest, with better device architectures for longer device lifetime, BTR is an ideal candidate for mass production of OPVs.

<sup>1</sup>School of Chemistry, Bio21 Institute, The University of Melbourne, 30 Flemington Road, Parkville, Victoria 3010, Australia. <sup>2</sup>Department of Materials Science and Engineering, National University of Singapore, 7 Engineering Drive 1, Singapore 117574, Singapore. <sup>3</sup>Department of Renewable Energy, School of Power Engineering, Chongqing University, 174 Shazhengjie, Shapingba, Chongqing 400044, China. <sup>4</sup>Max Planck Institute for Polymer Research, Ackermannweg 10, 55128 Mainz, Germany. <sup>5</sup>Advanced Microscopy Facility, Bio21 Institute, The University of Melbourne, 30 Flemington Road, Parkville, Victoria 3010, Australia. <sup>6</sup>MX Beamlines, Australian Synchrotron, 800 Blackburn Road, Clayton, Victoria 3168, Australia. \* These authors contributed equally to this work. Correspondence and requests for materials should be addressed to J.O. (email: mseoj@nus.edu.sg) or to W.W.H.W. (email: wwwhong@unimelb.edu.au) or to D.J.J. (email: djones@unimelb.edu.au).

Despite recent developments in solid-state photovoltaic devices<sup>1–3</sup>, bulk-heterojunction (BHJ) organic photovoltaics (OPVs)<sup>4</sup> continue to be a promising low-cost renewable energy technology. The reasons for this outlook include the versatility of organic semiconducting materials and simple device architectures that can be constructed from a variety of printing techniques. The development of the BHJ OPVs has been rapid in recent years driven by a combination of organic material design, interface engineering and improvements in device geometry. The reported power conversion efficiency (PCE) of single-junction small-area devices is now routinely in the 6–8% range<sup>5–7</sup>.

Published reports of single-junction BHJ OPVs over 9% PCE are still rare. A handful of polymeric electron donor materials and only one molecular donor have been reported in devices that reached this benchmark<sup>8–13</sup>. Molecular OPVs are an attractive alternative to polymer-based OPVs. Higher material purity can be achieved with the well-defined discrete structure of molecules and this should ensure greater reproducibility in devices<sup>14–16</sup>. To achieve high photovoltaic conversion efficiency, the material should be capable of forming good films with high molecular order. This can be achieved by smart molecular design and control over crystallization processes. For molecular semiconductors, conjugated flat and rigid backbones are preferred for easy packing via  $\pi$ – $\pi$  interactions. Good solubility is conferred through employment of the appropriate number, type and length of side chains, without hindering the packing of the backbones. The desirable donor phase in BHJ OPVs needs well-ordered nanocrystals with sizes comparable to the exciton diffusion length for efficient charge generation. Strategies simultaneously to enhance molecular order and restrict crystal size have been reported, including thermal annealing, solvent additives, solid additives and solvent vapour annealing (SVA)<sup>7,17–22</sup>. Recent reports showed that the rapid SVA treatment was particularly useful in achieving high fill factor (FF) and PCE in molecular OPVs<sup>23,24</sup>. Solvent selection rules for SVA treatment were identified in our previous study<sup>23</sup>.

Despite the important progress achieved in small-area OPV devices fabricated in laboratories, the successful commercialization of OPV technology relies on the application of solution-processed roll-to-roll techniques for large-scale printing<sup>25</sup>. One of the challenges in printing OPV devices is in printing the optimal active layer thickness of 80–120 nm that many of the high-performing material systems require, while obtaining pinhole-free thin films reproducibly at high printing speed. This problem can be relieved by printing thick films with thickness over 200 nm<sup>26</sup>. Unfortunately, due to limited charge diffusion length, thick-film OPV devices often experience severe bimolecular recombination and space charge effect, leading to reduced FF and PCE<sup>27</sup>. So far only a few studies have achieved high photovoltaic performance on polymer-based OPVs, with active layers above 200 nm<sup>26,28–30</sup>. No report has been found for molecular OPVs.

In this work, a new molecular electron donor material, benzodithiophene terthiophene rhodanine (BTR), with a benzo[1,2-*b*:4,5-*b'*]dithiophene (BDT) core and rhodanine peripheral units was developed and used in OPV devices giving PCEs >9%. While its  $\pi$ -conjugated structure is analogous to a high-performance compound reported previously<sup>7,31</sup>, the strategic placement of the side chains provided BTR with strong intermolecular interactions, as evidenced by its liquid crystalline (LC) behaviour. Such interactions translated successfully into excellent hole transport properties; hole mobilities up to 0.1 and  $1.6 \times 10^{-3} \text{ cm}^2 \text{ V}^{-1} \text{ s}^{-1}$  were recorded by organic field-effect transistor (OFET) and space-charge-limited current (SCLC) methods, respectively. Thus, BTR-based OPVs with thick active layers (300–400 nm) could still afford PCEs of over 8%

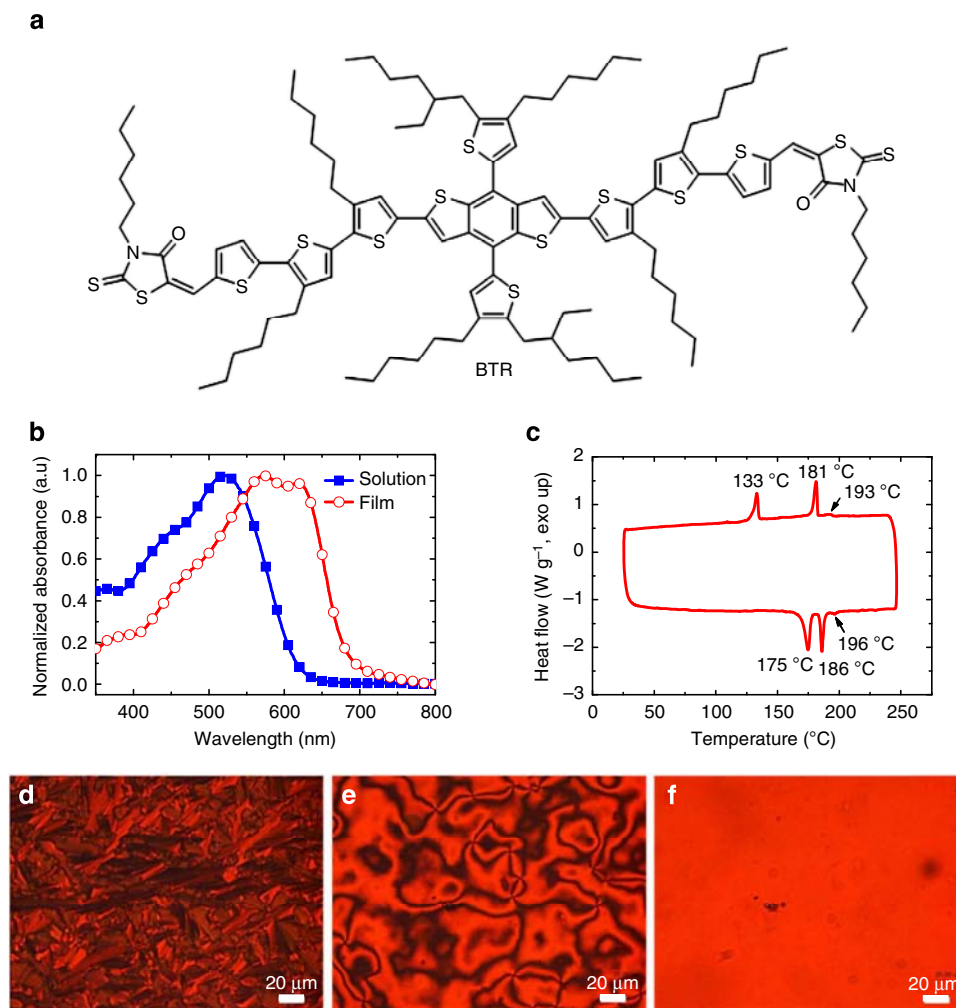
with high FF of  $\sim 70\%$ . Normal cell architecture employed in this study showed a moderate device lifetime. With better cell architectures or proper encapsulation for longer device lifetime, it is believed that BTR is a very attractive candidate for roll-to-roll printed OPV modules.

## Results

**Physical properties of BTR.** The BTR molecule was synthesized in two steps from known precursors in a good yield (Supplementary Fig. 1). The chemical structure of BTR is shown in Fig. 1a. The backbone consisting of the BDT unit, two terthiophenes and two rhodanine groups formed a coplanar structure. In comparison with analogous structures in the literature<sup>7,31</sup>, the side chains of BTR were shortened and positioned at the terthiophene building blocks in a regioregular manner to facilitate side-chain interdigitation<sup>32,33</sup>. In combination with the additional hexyl group on the thienyl-BDT unit, the side chains of BTR imparted LC behaviour (*vide infra*) that was not observed in previous reports.

BTR shows an excellent solubility of  $211 \text{ mg ml}^{-1}$  in chloroform, as derived from concentration and absorption data (Supplementary Fig. 2). BTR in solution displays an absorption maximum ( $\lambda_{\text{max}}$ ) at 523 nm, with an extinction coefficient ( $\epsilon$ ) of  $1.10 \times 10^5 \text{ M}^{-1} \text{ cm}^{-1}$  (Fig. 1b; Supplementary Table 1). The high  $\epsilon$  is attributed to the planarity of its backbone. The BTR solid film exhibits a red-shift of the  $\lambda_{\text{max}}$  to 572 nm relative to that in solution. Furthermore, an additional absorption peak at 620 nm appears in the absorption spectrum of a thin film. The red-shift and new absorption peak of the BTR film suggest the presence of strong intermolecular interaction and aggregation in the solid film. The absorption onset of the BTR film is at 681 nm, equivalent to an optical frontier orbital energy gap of 1.82 eV. Determined by cyclic voltammetry (CV) (Supplementary Fig. 3), the highest occupied molecular orbital (HOMO) and lowest unoccupied molecular orbital (LUMO) of BTR are  $-5.34$  and  $-3.52$  eV, respectively. The HOMO–LUMO gap of BTR is 1.82 eV, which is in good agreement with the optical energy gap. Because the open-circuit voltage ( $V_{\text{oc}}$ ) is largely determined by the HOMO–LUMO gap of the donor and acceptor, a deep-lying HOMO of BTR can potentially support a high  $V_{\text{oc}}$ . In combination with fullerene acceptor [6,6]-phenyl  $\text{C}_{71}$  butyric acid methyl ester ( $\text{PC}_{71}\text{BM}$ ), whose LUMO level is around  $-4.0$  eV, the LUMO energy offset of 0.48 eV between BTR and  $\text{PC}_{71}\text{BM}$  should provide enough driving force for exciton dissociation<sup>34</sup>.

The BTR molecule has good thermal stability with a decomposition temperature of 405 °C in nitrogen (5% weight loss in thermogravimetric analysis, Supplementary Fig. 4). BTR exhibits a sharp differential scanning calorimetry (DSC) peak at 175 °C (Fig. 1c), which is assigned to secondary crystalline phase transition by means of a structural analysis (*vide infra*). Furthermore, a melting temperature of 186 °C into a LC phase and a clearing temperature at 196 °C of small enthalpy into an isotropic melt were observed. Upon cooling, three exothermic peaks at 193, 181 and 133 °C were recorded. The first minor transition was attributed to the LC phase transition, while the two major ones were related to the crystallization process of the two crystalline phases. To observe directly the LC transition and precisely assign the phases, BTR powder was sandwiched in between two glass slides, heated and examined under a polarized optical microscope (POM). The BTR molecule was highly crystalline below a stage temperature of 185 °C (Fig. 1d). Between 185 and 195 °C, the crystalline solid was replaced by a liquid crystal nematic texture (Fig. 1e). The nematic phase suggests that BTR molecules have a rigid rod-like shape, which can maintain a long-range directional order with their long axes parallelly



**Figure 1 | BTR chemical structure and physical properties.** (a) Chemical structure of BTR. (b) Normalized UV-vis absorption spectra of BTR in chloroform ( $5 \text{ mg ml}^{-1}$ ) and in a spin-cast film. (c) DSC thermogram of BTR in nitrogen at a ramp rate of  $10 \text{ }^\circ\text{C min}^{-1}$ . The lower trace is from the heating cycle and upper trace from the cooling cycle. (d) BTR thin film sandwiched in between two glass slides observed under a polarized optical microscope (POM) at a stage temperature of  $185 \text{ }^\circ\text{C}$ . (e) The POM image of the same BTR thin film at the same settings when the stage temperature rises to  $195 \text{ }^\circ\text{C}$ . (f) The POM image taken at a stage temperature of  $197 \text{ }^\circ\text{C}$ .

aligned. They can thus have high crystallinity in solid state<sup>17,35–37</sup>. The liquid crystal transformed above  $196 \text{ }^\circ\text{C}$  into an isotropic melt, leaving no prominent feature under the POM (Fig. 1f). Thereby, the small transition enthalpy determined by DSC is in agreement with the low-ordered nematic phase. The nematic LC behaviour is an important feature of the BTR molecule, implying strong intermolecular interaction resulted from side-chain modifications, and potentially high charge carrier mobility due to three-dimensional (3D) charge transport<sup>38</sup>.

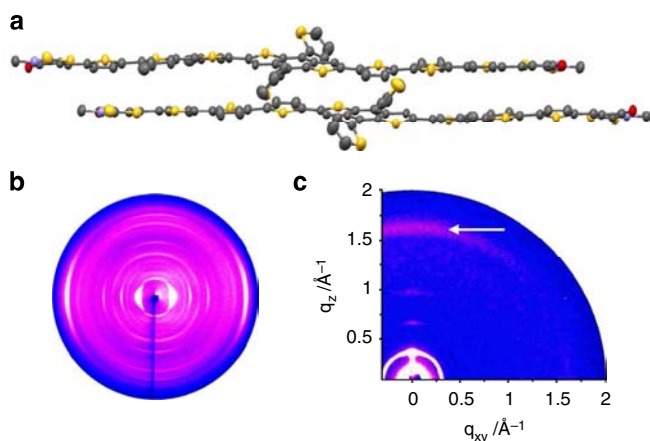
**Crystal packing of BTR molecules.** To obtain a better understanding of the packing of BTR molecules in the solid, X-ray quality single crystals of BTR were grown from a mixed solution of 2-propanol and dichloromethane by slow evaporation. The single crystal structure was solved using data from the MX2 beamline at the Australian Synchrotron<sup>39</sup> (Fig. 2a; Supplementary Figs 5–8). The X-ray crystal structure of the BTR molecule revealed a coplanar structure of the conjugated backbone, which should facilitate light absorption and also crystal stacking. The crystal packing is dominated by  $\pi$ -stacking between the individual BTR backbones that arrange themselves into  $\pi$ -stacked centrosymmetric dimers with an average inter-plane separation of ca  $3.60 \text{ \AA}$  (Fig. 2a). These individual dimers aggregate together

by  $\pi$ -stacking, with an average interplanar separation of  $3.62 \text{ \AA}$  (Supplementary Fig. 6). This type of packing is consistent with the bathochromic shifting of the absorption from solution to the solid film (*J*-aggregate).

The solid-state structure was also examined using two-dimensional wide-angle X-ray scattering (2D-WAXS) on neat BTR filaments. The samples were prepared by filament extrusion<sup>40</sup>, which imparted bulk orientation on the crystalline material. The 2D-WAXS pattern suggests a crystalline character of BTR in the low-temperature phase as evident by the high number of distinct reflections (Fig. 2b). The molecules are organized in a layered structure that is aligned in the direction of the fibre axis. An interlayer distance of  $18.3 \text{ \AA}$  is determined from reflections located in the equatorial small-angle range. On the same plane of the pattern, two  $\pi$ -stacking peaks appear that are related to distances of  $3.70$  and  $3.65 \text{ \AA}$  of stacked BTR dimers. These values are in the same range as found for the single crystal. Further meridional reflections are originated from intramolecular correlations along the extended conjugated BTR backbone. At  $179 \text{ }^\circ\text{C}$ , the sample maintains a crystalline phase, however, with a slightly smaller degree of order (Supplementary Fig. 9). The interlayer spacing remains identical at  $18.3 \text{ \AA}$ , while only one and a little larger stacking distance was observed at  $3.76 \text{ \AA}$ .



In a thin solid film, BTR organizes in two different molecular arrangements as indicated by the grazing incidence wide-angle X-ray scattering (GIWAXS) pattern in Fig. 2c. Reflections in the meridional plane (along  $q_{xy} = 0 \text{ \AA}^{-1}$ ) in the small- and middle-range scattering region are related to the formation of a layered structure with an interlayer distance of  $18.7 \text{ \AA}$ . In addition, 3rd-order reflections are visible typical for a long-range order, while their position on the meridional plane of the pattern is characteristic for an edge-on molecular organization. In this



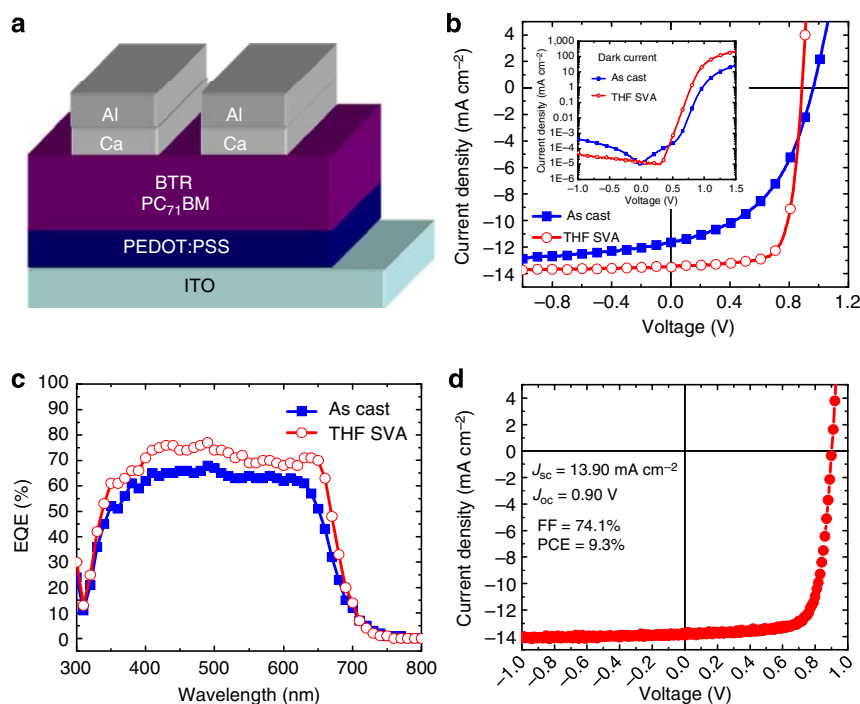
**Figure 2 | Crystal packing resolved by X-ray techniques.**

(a) Centrosymmetric  $\pi$ -stacked dimers of BTR molecules in its single crystal, the alkyl side chains have been omitted for clarity. (b) 2D-WAXS of BTR filament measured at  $30^\circ\text{C}$ . (c) GIWAXS of the as-cast BTR thin film on silicon wafer via spin coating ( $\pi$ -stacking reflection is indicated by an arrow).

arrangement, the backbone plane is aligned perpendicular to the surface. However, the corresponding equatorial  $\pi$ -stacking peak of the edge-on arranged molecules assembled in the layered structure is too weak to be detected. Instead, the  $\pi$ -stacking reflection related to a single distance of  $3.70 \text{ \AA}$  is located also on the meridional plane, which is typical for a face-on arrangement. These results imply two distinct surface organizations. In the first phase, the molecules are  $\pi$ -stacked and face-on arranged, but do not organize in a layered structure. In the second phase, the molecules are edge-on aligned with respect to the substrate, but are disordered within the layer organization. Because charge transport in organic semiconductors is mainly via hopping between adjacent molecules, the co-existence of edge-on and face-on orientations can potentially form a 3D network for hopping, thus beneficial to charge transport<sup>41</sup>.

**OFET mobility.** To study the charge carrier transport, OFETs using different procedures were built. For top-contact devices, BTR was spin-coated from a  $4.5\text{-mg ml}^{-1}$  toluene solution and subsequently annealed at  $179^\circ\text{C}$ . These transistors delivered hole mobilities up to  $0.01 \text{ cm}^2 \text{ V}^{-1} \text{ s}^{-1}$  (Supplementary Fig. 10). Bottom-contact OFET devices with the BTR molecules deposited by drop-casting gave mobility values as high as  $0.1 \text{ cm}^2 \text{ V}^{-1} \text{ s}^{-1}$  (Supplementary Fig. 11). It should be noted that the OFET devices were not intensively optimized. The primary purpose of the OFET experiments was to show the potential of the BTR material as a semiconductor.

**Photovoltaic performances.** The excellent solubility, strong intermolecular interaction, suitable absorption profile and energy levels, as well as encouraging semiconducting properties prompted us to explore the photovoltaic performance of the BTR



**Figure 3 | Device architecture and photovoltaic performances.** (a) Schematic diagram of a normal cell architecture used in this study. (b)  $J$ - $V$  characteristics of BTR:PC<sub>71</sub>BM BHJ solar cells with or without THF solvent vapour annealing tested in air under  $98 \text{ mW cm}^{-2}$  AM1.5G illumination. Inset: dark current plotted in a semi-log scale of the two solar cells. (c) EQE spectra of optimized BTR-based solar cells with or without THF SVA treatment. (d)  $J$ - $V$  curve of the most efficient BTR:PC<sub>71</sub>BM BHJ solar cell after 15 s of THF SVA measured by an independent research institute in nitrogen atmosphere under an illumination of  $100 \text{ mW cm}^{-2}$ .

molecule. The OPV cells adopted a simple normal architecture, with the BTR:PC<sub>71</sub>BM blend film sandwiched between a poly(3,4-ethylenedioxythiophene):poly(styrenesulfonate) (PEDOT:PSS)-coated indium tin oxide (ITO) transparent anode and a Ca/Al back cathode (Fig. 3a). We further treated the active layer with SVA, which has been shown to be effective in enhancing the performance of molecular OPVs<sup>22–24</sup>. The SVA treatment was carried out by exposing the as-cast active layer to solvent vapours. According to the solvent selection rules previously identified<sup>23</sup>, tetrahydrofuran (THF) was chosen for SVA owing to the moderate solubility of BTR in THF (89 mg ml<sup>-1</sup>).

The BTR-based OPVs with an optimal active layer thickness of 250 nm were encapsulated and tested in air. The current density (*J*)-voltage (*V*) curves of the best devices are shown in Fig. 3b, with the photovoltaic parameters summarized in Table 1. Without SVA treatment, the highest performance for the as-cast OPVs showed short-circuit current density (*J*<sub>sc</sub>) = 11.64 mA cm<sup>-2</sup>, *V*<sub>oc</sub> = 0.96 V, FF = 47% and PCE = 5.2%. SVA treatment significantly enhanced the photovoltaic performance. OPVs with 15 s of THF SVA exhibited *J*<sub>sc</sub> = 13.52 mA cm<sup>-2</sup>, *V*<sub>oc</sub> = 0.89 V, FF = 73% and PCE = 8.7%. Device assembly was reproducible with around 60 SVA-treated OPV devices having an average PCE of 8.3 ± 0.2%. Thermal annealing was found to diminish the device performance, due to the overgrowth of the phases (Supplementary Fig. 12).

The causes for the enhanced FF after SVA treatment were investigated by measuring dark currents (inset of Fig. 3b). Compared with an as-cast molecular OPV, the SVA-treated sample displayed notably higher current density under positive bias. In great contrast, the current density was one order of magnitude smaller in reverse bias. To further understand the SVA treatment effect, series resistance (*R*<sub>s</sub>) and shunt resistance (*R*<sub>sh</sub>) were extracted at 1.5 and 0 V of the dark curves (Table 1). Without SVA treatment, the OPV had a *R*<sub>s</sub> of 14.0 Ω cm<sup>2</sup> and a *R*<sub>sh</sub> of 5.5 MΩ cm<sup>2</sup>. SVA treatment led to a reduction of *R*<sub>s</sub> by six times and a slight increase of *R*<sub>sh</sub>. Together, the results suggest the SVA treatment can suppress leakage current and improve the diode behaviour.

The slight improvement in *J*<sub>sc</sub> after SVA treatment was monitored by external quantum efficiency (EQE) measurement (Fig. 3c). A high EQE of over 60% was measured in the visible region from 400 to 650 nm for the non-annealed OPV. The *J*<sub>sc</sub> calculated by integrating the product of photon flux and EQE at

each wavelength was 11.70 mA cm<sup>-2</sup>, which was in good agreement with the measured *J*<sub>sc</sub> (11.64 mA cm<sup>-2</sup>). The SVA treatment lifted the EQE in the entire absorption range. In particular, the EQE stayed above 70% between 400 and 650 nm, and a shoulder was found at 640 nm. As a result, the calculated *J*<sub>sc</sub> increased to 13.53 mA cm<sup>-2</sup>. The EQE result clearly indicates SVA treatment plays a positive role in charge generation, transport and/or collection.

Bearing in mind that OPVs with normal cell architecture are not stable in air, we fabricated a batch of 20 devices in Singapore and 8 devices in Australia and tested them under inert atmosphere using the facilities at Solar Energy Research Institute of Singapore and the Commonwealth Scientific and Industrial Research Organisation, respectively. The best BTR-based OPV fabricated in Singapore exhibited a record efficiency of 9.3%, with *J*<sub>sc</sub> = 13.90 mA cm<sup>-2</sup>, *V*<sub>oc</sub> = 0.90 V and FF = 74.1% (Fig. 3d; Table 1). The results were highly reproducible. The same PCE of 9.3% with a *J*<sub>sc</sub> of 13.40 mA cm<sup>-2</sup>, a *V*<sub>oc</sub> of 0.90 V and an extremely high FF of 77.0% was achieved in Australia (Table 1). This result demonstrates molecular OPVs can achieve comparable efficiencies attainable by polymer-based OPVs<sup>8–11</sup>. It is worth noting that the FF of 77.0% is among the highest FF value reported in the literature for solution-processed molecular OPVs<sup>12,42</sup>. The average photovoltaic parameters for the 28 devices were *J*<sub>sc</sub> = 13.49 ± 0.28 mA cm<sup>-2</sup>, *V*<sub>oc</sub> = 0.89 ± 0.01 V, FF = 74 ± 1% and PCE = 8.9 ± 0.2% (Table 1).

**OPVs of a thick active layer.** The high FF values suggest that the BTR-based OPVs can accommodate a greater range of active layer thicknesses. This is particularly important in roll-to-roll printing of very thin films, which are difficult to be precisely controlled, and pinholes are often found in thin-film devices. We were motivated to explore the thickness-dependent solar cell performance using the BTR molecule. Active layers with different thicknesses ranging from 80 to 400 nm were fabricated by tuning the solution concentrations and spin rates. Figure 4 and Supplementary Table 2 show that BTR-based OPVs maintain a nearly constant *V*<sub>oc</sub> between 0.87 and 0.90 V. The average *J*<sub>sc</sub> increases from ~10 to ~13 mA cm<sup>-2</sup> as the active layer thickness increases from 80 to 250 nm and then it saturates around 13 mA cm<sup>-2</sup> when the thickness further increases to 400 nm. Surprisingly, the FF values for BTR-based OPVs remain high and close to 70% even at

**Table 1 | Photovoltaic parameters of BTR:PC<sub>71</sub>BM BHJ solar cells fabricated and tested under different conditions**

<i>J</i> <sub>sc</sub> (mA cm <sup>-2</sup> )	<i>V</i> <sub>oc</sub> (V)	FF (%)	PCE (%)	<i>R</i> <sub>s</sub> <sup>*</sup> (Ω cm <sup>2</sup> )	<i>R</i> <sub>sh</sub> <sup>†</sup> (MΩ cm <sup>2</sup> )	μ <sub>h</sub> <sup>‡</sup> (cm <sup>2</sup> V <sup>-1</sup> s <sup>-1</sup> )	μ <sub>e</sub> <sup>‡</sup> (cm <sup>2</sup> V <sup>-1</sup> s <sup>-1</sup> )
<i>As-cast</i> <sup>§</sup>							
11.64 (11.20 ± 0.51)	0.96 (0.96 ± 0.01)	47 (42 ± 3)	5.2 (4.5 ± 0.4)	14.0 —	5.5 —	2.2 × 10 <sup>-4</sup>	3.5 × 10 <sup>-4</sup>
<i>THF SVA</i> <sup>§</sup>							
13.52 [12.16] (13.17 ± 0.43)	0.89 [0.90] (0.89 ± 0.01)	73 [76] (71 ± 2)	8.7 [8.3] (8.3 ± 0.2)	2.4 2.2 —	42 6.4 —	1.6 × 10 <sup>-3</sup>	9.6 × 10 <sup>-3</sup>
<i>THF SVA</i> <sup>  </sup>							
13.90 [13.40] (13.61 ± 0.16)	0.90 [0.90] (0.89 ± 0.01)	74 [77] (74 ± 1)	9.3 [9.3] (8.9 ± 0.2)	2.7 1.9 —	15 20 —		

FF, fill factor; PCE, power conversion efficiency; SCLC, space-charge-limited current; SVA, solvent vapour annealing; THF, tetrahydrofuran.

Data in brackets show the cell with the highest FF. Data in parentheses are average results out of 40 + encapsulated devices tested in air or 28 non-encapsulated devices tested in nitrogen.

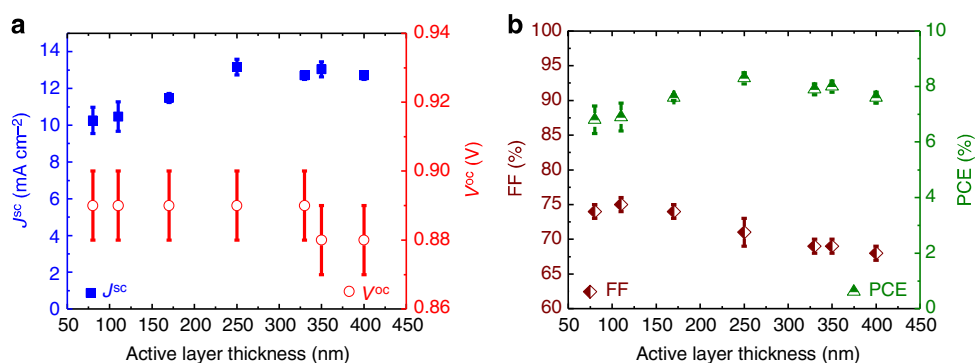
\*Series resistance of the device.

†Shunt resistance of the device.

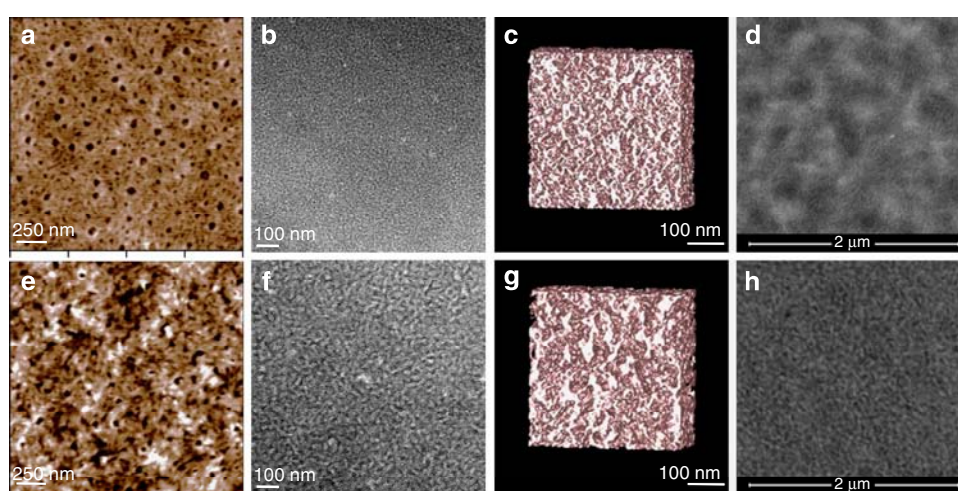
‡Charge mobility values obtained from SCLC experiments.

§Cells were tested in air with encapsulation, illumination intensity was 98 mW cm<sup>-2</sup>.

||Cells without encapsulation were tested in a glove box filled with dry nitrogen; illumination intensity was 100 mW cm<sup>-2</sup>.



**Figure 4 | Active layer thickness-dependent variation of photovoltaic performances.** (a) Plots of  $J_{sc}$  or  $V_{oc}$  vs active layer thickness ranging from 80 to 400 nm. (b) Plots of FF or PCE against active layer thickness. The results are an average value of >8 devices. The error bars represent the standard deviation from >8 devices.



**Figure 5 | Solvent vapor annealing induced morphological changes.** (a) AFM image shows the topography of an as-cast BTR:PC<sub>71</sub>BM (1:1 weight ratio) blend film. (b) TEM bright-field image of the as-cast film taken at a defocusing range of 3  $\mu$ m. (c) Computer model generated from the TEM tomogram of the as-cast film. (d) Low-energy HAADF STEM image of the as-cast film at focus using a beam energy of 15 keV. (e) AFM image of the BTR:PC<sub>71</sub>BM blend film after THF SVA for 15 s. (f) TEM bright-field image of the SVA-treated film at a defocusing range of 3  $\mu$ m. (g) Computer model of the THF SVA film. (h) HAADF STEM image of the blend film after SVA treatment.

thicknesses up to 400 nm. This is not commonly observed in thick-film OPVs, whether it is a molecular OPV or a polymer-based solar cell<sup>26–29,43</sup>. As a result, the overall PCEs formed a flat bell curve with a minimum average value of 6.8% and maximum average value of 8.3% at an active layer thickness of 250 nm. The large tolerance for the active layer thickness makes the BTR molecule a strong candidate for printed OPVs.

**Solvent vapour annealing.** To understand the effect of SVA treatment on the photovoltaic performance of BTR-based OPVs, we carried out studies on active layer morphology and the optoelectronic properties. The surface topography of the active layer was recorded by atomic force microscopy (AFM) operated in the tapping mode. Before the SVA treatment, Fig. 5a depicts a rather smooth surface, with root-mean-square roughness ( $R_{rms}$ ) of 0.61 nm. Fine crystal domains co-exist with random pinholes, which are believed to be related with the escaping of processing solvent. After a short THF SVA treatment of 15 s, the active layer exhibits a coarser surface (Fig. 5e). The  $R_{rms}$  value almost doubles to 1.04 nm. Transmission electron microscopy (TEM) is able to provide morphological information inside the active layer. The bright-field TEM images (Fig. 5b,f) suggest THF SVA treatment leads to larger and more well-defined domains. Because of the sharp contrast in the TEM images, we were able to obtain TEM tomograms

and computer models to view the morphological change in 3D (Fig. 5c,g; Supplementary Movies). Both the TEM tomograms and their computer models show that fine-sized domains in the as-cast active layer (Supplementary Movies 1 and 2) evolve into larger domains that are inter-connected to form networks throughout the entire active layer after THF SVA for 15 s (Supplementary Movies 3 and 4). Such networks resemble ‘3D charge highways’ that are beneficial to fast charge transport. The feature size on TEM images is verified by low-energy high-angle angular dark-field scanning TEM (HAADF STEM) images (Fig. 5d,h).

The SVA treatment can be monitored by colour change of the active layer. The inset of Supplementary Fig. 13 is a digital image of the active layer before and after the THF SVA treatment. The colour of the film changed from maroon to purple upon annealing by THF vapour. Such a colour change was reflected by the change in absorption profile (Supplementary Fig. 13). There was a slight red-shift of the absorption maximum from 555 to 565 nm. Besides, the shoulder at 620 nm became more prominent, suggesting good alignment of the rod-like molecules. The absorption enhancement at 620 nm directly translated to increased photocurrent, as suggested by the EQE plot (Fig. 3c).

GIWAXS measurements were performed to understand the organization of BTR in the active layer before and after SVA. In comparison with the BTR neat film, the edge-on layered

organization remains unchanged in the as-cast BTR:PC<sub>71</sub>BM blend film, while the  $\pi$ -stacking distance slightly increases to 3.80 Å and becomes randomly distributed towards the surface, as confirmed by the isotropic intensity of the corresponding peak (Supplementary Fig. 14a). The amorphous halo at  $q$ -range of ca.  $1.25 \text{ \AA}^{-1}$  is attributed to PC<sub>71</sub>BM domains. SVA improves the crystallinity and surface ordering of BTR. The interlayer distance is reduced to 17.75 Å, while the  $\pi$ -stacking distance decreases to 3.60 Å. The random orientation of  $\pi$ -stacking evolves into the co-existence of both edge-on and face-on arrangements after SVA, evidenced from the  $\pi$ -stacking reflections at ca.  $1.7 \text{ \AA}^{-1}$  in both  $q_{xy}$  and  $q_z$  directions (Supplementary Fig. 14b). Such a molecular arrangement is beneficial to 3D charge transport.

**SCLC mobilities.** The hole mobility was measured using the SCLC method with a cell architecture: ITO/PEDOT:PSS/BTR:PC<sub>71</sub>BM/Au. Without SVA treatment, the blend film exhibited a relatively high hole mobility of  $2.2 \times 10^{-4} \text{ cm}^2 \text{ V}^{-1} \text{ s}^{-1}$  (Supplementary Fig. 15; Table 1). The rigid and planar backbone facilitates easy stacking and strong intermolecular interaction due to side-chain modifications. The SVA treatment substantially enhanced the mobility by one order of magnitude to  $1.6 \times 10^{-3} \text{ cm}^2 \text{ V}^{-1} \text{ s}^{-1}$ , which is comparable to or greater than those reported for high-performing donor:acceptor blend systems<sup>7,31,41,44,45</sup>. The electron mobility derived from the SCLC method was also improved by one order of magnitude after SVA treatment (Supplementary Fig. 16; Table 1). Such an enhancement can be attributed to larger and more structured domains, as well as better molecular arrangement. The extremely high mobility would partially account for the high FF observed in BTR-based OPVs. However, we do not exclude other possible factors including vertical phase separation or removal of recombination centres and so on<sup>33</sup>.

**Solar cell stability.** For practical application, solar cell-stability experiments were carried out in both air and nitrogen environments. Due to the use of active metal-like calcium for the top electrode, the unencapsulated OPVs of the thick active layer (~400 nm) degraded to almost zero efficiency within three days of storage in air (Supplementary Fig. 17; Supplementary Table 3). However, a simple encapsulation with ultraviolet (UV)-curable epoxy and thin glass slides could greatly improve the device stability in air. The OPVs degraded three times slower than that without encapsulation (Supplementary Fig. 17; Supplementary Table 4). To minimize the degradation factor due to the oxidation of electrode and further explore the stability of the active layer, one BTR-based solar cell device was stored in a glove box filled with dry nitrogen and was monitored over a time span of 30 days. The cell retained 86% of initial PCE after 7 days, and it exhibited >50% of original PCE after 30 days of storage (Supplementary Fig. 18a,b; Supplementary Table 5). Further enhancement of device stability could be achieved by improved device architecture. Average of 10 OPV cells of thick active layer of 400 nm and an additional 30-nm-thick silver top electrode/protection layer with or without encapsulation retained 92 and 86% of initial average PCE after 30 days of storage in a glove box (Supplementary Fig. 18c; Supplementary Tables 6 and 7). We believe even better stability can be obtained if the cells were properly encapsulated or inverted cell architecture was employed.

## Discussion

In summary, we present a new molecular donor, BTR, which possesses a rigid and flat backbone and a large number of flexible side chains that could work synergistically to provide excellent processability, nematic liquid crystal behaviour and

optoelectronic properties. The neat BTR film exhibited hole mobilities up to  $0.1 \text{ cm}^2 \text{ V}^{-1} \text{ s}^{-1}$  in OFET devices. The solution-processed single-junction BHJ solar cells based on BTR and PC<sub>71</sub>BM demonstrated a reproducible record efficiency of 9.3%. The blend film also supported a high FF of 77% and a high SCLC hole mobility of  $1.6 \times 10^{-3} \text{ cm}^2 \text{ V}^{-1} \text{ s}^{-1}$  after SVA with THF. Thick-film molecular solar cells with an active layer thickness up to 400 nm were demonstrated, showing a low thickness dependence of photovoltaic performance. Together, the results suggest BTR is an ideal candidate for printed OPVs. Moreover, enhancing the intermolecular interaction through side-chain modification is a viable way further to enhance the efficiency of molecular solar cells in excess of 10%.

## Methods

**Materials.** Unless noted, all materials were reagent grade and used as received without further purification. Anhydrous solvents were prepared by drying HPLC-grade solvents using freshly activated molecular sieves.

**Synthesis of aldehyde compound 3.** Synthetic route could be found in Supplementary Fig. 1. Precursor 1 and 2 were prepared using literature methods<sup>46,47</sup>. In protection of N<sub>2</sub>, to a dry 250-ml flask were added compound 1 (1.07 g, 1.0 mmol), compound 2 (1.05 g, 2.0 mmol), Pd<sub>2</sub>(dba)<sub>3</sub> (46 mg, 0.04 mmol), P(*o*-tolyl)<sub>3</sub> (97 mg, 0.32 mmol) and 50 ml of toluene. The reaction mixture was refluxed at 125 °C for 12 h. The reaction mixture was filtered and the crude product was purified by silica gel column chromatography (petroleum spirit 40–60 °C: dichloromethane = 1:1.5, R<sub>f</sub> 0.5) to give the product as yellow solid (830 mg, 53%). mp 146–147 °C; infrared (IR) (neat)  $\nu$  2,955, 2,923, 2,855, 1,656, 1,432, 1,225, 1,058, 820, 786 and 663  $\text{cm}^{-1}$ ; <sup>1</sup>H NMR ( $\delta$ , CDCl<sub>3</sub>) 9.89 (s, 2H), 7.72 (d,  $J$  = 4.0 Hz, 2H), 7.68 (s, 2H), 7.23 (d,  $J$  = 4.0 Hz, 2H), 7.12 (s, 2H), 7.01 (s, 2H), 2.82 (m, 12H), 2.65 (m, 4H), 1.60–1.75 (m, 14H), 1.26–1.45 (m, 52H), 0.88 (m, 30H); <sup>13</sup>C NMR ( $\delta$ , CDCl<sub>3</sub>) 182.6, 146.1, 142.6, 142.2, 141.2, 139.6, 139.0, 138.6, 137.3, 137.2, 136.9, 136.0, 135.8, 134.8, 130.3, 129.8, 129.5, 129.1, 128.3, 125.9, 123.5, 119.5, 41.7, 32.7, 32.3, 31.8, 31.6, 30.8, 30.4, 30.2, 29.8, 29.6, 29.3, 29.2, 29.1, 28.9, 28.4, 26.0, 23.1, 22.7, 22.6, 14.2 and 13.1; mass spectrometry (MS) (matrix-assisted laser desorption/ionization (MALDI))  $m/z$  1,630 [M].

**Synthesis of BTR molecule.** To the solution of compound 3 (327 mg, 0.2 mmol) in dry chloroform (20 ml) was added rhodanine 4 (434 mg, 2.0 mmol) followed by one drop of 1,8-Diazabicyclo[5.4.0]undec-7-ene (DBU). The reaction mixture was then placed under continuous stirring at room temperature for 3 h. Reaction solvent was removed and the crude product was purified by silica gel column chromatography (petroleum spirit 40–60 °C: dichloromethane = 1:1, R<sub>f</sub> 0.8). The desired fractions were collected and the product was obtained as a purple solid (310 mg, 76%) after washing with acetone. mp 178–180 °C; IR (neat)  $\nu$  2,924, 2,855, 1,699, 1,575, 1,423, 1,327, 1,238, 1,180 and 820  $\text{cm}^{-1}$ ; <sup>1</sup>H NMR ( $\delta$ , CDCl<sub>3</sub>) 7.83 (s, 2H), 7.65 (s, 2H), 7.35 (d,  $J$  = 4.0 Hz, 2H), 7.23 (s, 2H), 7.20 (d,  $J$  = 4.0 Hz, 2H), 7.10 (s, 2H), 7.00 (s, 2H), 4.09 (t,  $J$  = 7.6 Hz, 4H), 2.81 (m, 12H), 2.78 (m, 4H), 1.60–1.75 (m, 18H), 1.26–1.45 (m, 64H), 0.88 (m, 36H); <sup>13</sup>C NMR ( $\delta$ , CDCl<sub>3</sub>) 192.2, 167.5, 144.3, 141.9, 141.0, 139.5, 139.0, 138.6, 137.3, 137.2, 137.1, 135.7, 135.6, 134.8, 134.6, 130.4, 129.8, 129.7, 129.0, 128.3, 126.5, 125.0, 123.5, 120.2, 119.5, 44.9, 41.7, 32.7, 32.4, 31.8, 31.7, 31.6, 31.3, 30.8, 30.4, 30.3, 29.8, 29.7, 29.3, 29.2, 29.1, 28.9, 28.4, 27.0, 26.4, 26.0, 23.1, 22.7, 22.6, 22.5, 14.2, 13.1; MS (MALDI)  $m/z$  2,028.7 [M]<sup>+</sup>. Elemental analyses calcd (%) for C<sub>114</sub>H<sub>152</sub>N<sub>2</sub>O<sub>2</sub>S<sub>14</sub> (BTR): C, 67.41; H, 7.54; N, 1.38; O, 1.58; S, 22.10; found: C, 67.64; H, 7.65; N, 1.24; O, 1.33; S, 21.87.

**Material characterizations.** IR spectra were obtained on a Perkin-Elmer Spectrum One Fourier transform infrared spectrometer and UV-visible spectra were recorded using a Cary 50 UV-visible spectrometer. Photoluminescence was measured with a Varian Cary Eclipse fluorimeter. Melting points were determined on a Büchi 510 melting point apparatus. <sup>1</sup>H NMR and <sup>13</sup>C NMR spectra were carried out on a 400-MHz spectrometer. All NMR data were referenced to the chloroform signal and peak multiplicity was reported as follows: s = singlet, d = doublet, t = triplet, q = quartet, p = pentet, dd = doublets of doublets, m = multiplet and br = broad. MALDI-time-of-flight MS was performed on a Bruker microflex instrument, using chloroform as solvent and dithranol as the assisted matrix. Elemental analyses were obtained commercially through Chemical & Analytical Services Pty Ltd. (Australia) an Exeter Analytical CE-440 elemental analyzer. Thermal gravimetric analysis experiments were carried out with a Mettler Toledo TGA/SDTA851e, and DSC experiments were performed on a Perkin-Elmer Sapphire DSC. CV experiments were performed at a sweep rate of 100 mV s<sup>-1</sup>. CVs were carried out in a three-electrode cell consisting of a glassy carbon working electrode, a platinum wire auxiliary electrode and a Ag/Ag<sup>+</sup> pseudo-reference electrode. The supporting electrolyte was 0.10 M tetrabutylammonium hexafluorophosphate (Bu<sub>4</sub>NPF<sub>6</sub>) in CH<sub>3</sub>CN. The solutions were deoxygenated by sparging with argon prior to each scan and blanketed with argon during the scans.

The glassy carbon working electrode was prepared by polishing with 5 mm alumina and washed and dried before the polymer was drop-casted on the electrode from chlorobenzene solution to form a film. Ferrocene/ferrocenium redox couple was used as the internal standard. The HOMO energy level was calculated from the onset of the oxidation potential of the polymer using the following:  $E_{\text{HOMO}} = -(4.8 + E_{\text{ox onset}}) \text{ eV}$ .

**Crystal structure determination.** Single-crystal data were collected on the MX2 beamline at The Australian Synchrotron at 100 K using a  $360^\circ$  rotation in steps of  $1^\circ$  with 1-s exposure time per step. The beamline was set to the Mo-K $\alpha$  edge (17.444 keV or 0.71073 Å). Crystal data for BTR: C112 H150 N2 O2 S14,  $M = 2,005.17$ ,  $T = 100.0(2) \text{ K}$ ,  $\lambda = 0.71073 \text{ Å}$ , Triclinic, space group  $P-1$ ,  $a = 314.257(3)$ ,  $b = 20.519(4)$ ,  $c = 21.795(4) \text{ Å}$ ,  $\alpha = 114.76(3)^\circ$ ,  $\beta = 98.08(3)^\circ$ ,  $\gamma = 02.00(3)^\circ$ ,  $V = 5,474(2) \text{ Å}^3$ ,  $Z = 2$ ,  $D_c = 1.217 \text{ Mg M}^{-3}$ ,  $\mu = 0.326 \text{ mm}^{-1}$ ,  $F(000) = 2,152$ , crystal size  $0.10 \times 0.05 \times 0.05 \text{ mm}$ .  $\theta_{\text{max}} = 27.47^\circ$ , 88,775 reflections measured, 22,889 independent reflections ( $R_{\text{int}} = 0.055$ ) the final  $R = 0.11$  ( $I > 2\sigma(I)$ , 14,445 data) and  $wR(F^2) = 0.3696$  (all data) GOOF = 1.371.

**Thin-film characterizations.** To study the liquid crystal property of BTR, we used a Nikon Eclipse LV100 POM equipped with Linkam LTS350 heating and cooling stage connected to a Linkam TMS 94 temperature programmer. GIWAXS samples were prepared by spin-coating chloroform solution of BTR onto PEDOT:PSS-coated silicon substrates. The measurements were performed by means of a solid anode X-ray tube (Siemens Kristalloflex X-ray source, copper anode X-ray tube operated at 35 kV and 40 mA), Osmic confocal MaxFlux optics, X-ray beam with pinhole collimation and a MAR345 image plate detector. The beam size was  $0.5 \times 0.5 \text{ mm}$  and samples were irradiated just below the critical angle for total reflection with respect to the incoming X-ray beam ( $\sim 0.18^\circ$ ). The scattering intensity was detected on a 2D image plate (MAR345) with a pixel size of  $100 \mu\text{m}$  ( $3,450 \times 3,450$  pixels). Data analysis was performed using the Datasqueeze 3.0.0 software. Atomic force microscopy images were acquired using an Asylum Research Cypher scanning probe microscope operated in tapping mode. Samples for electron microscopy were prepared by dissolving the PEDOT:PSS layer using water and transferring the floating active layer to TEM grids. TEM bright-field images were obtained by a FEI Tecnai TF30 TEM equipped with a beam-blank function. For TEM tomography, tilt series were acquired using the Xplore 3D software (FEI Company). Tomograms were recorded between  $-65$  and  $+65$  degrees at  $2^\circ$  intervals and aligned with IMOD. A 3D model rendering employed 3d mod software. Each model was generated from the aligned tomogram. The BTR donor phase was rendered in pink colour, while the PC<sub>71</sub>BM acceptor phase was represented by empty space in model movies. The scale bar was  $100 \text{ nm}$  in both the model movies and the tomogram movies. HAADF STEM was performed at a primary electron energy of 15 keV with a FEI Quanta 3D Microscope equipped with a HAADF STEM detector. To obtain hole and electron mobilities using SCLCs, hole-only devices (ITO/PEDOT:PSS/BTR:PC<sub>71</sub>BM/Au) and electron-only devices (ITO/Al/BTR:PC<sub>71</sub>BM/Al) were constructed. Their dark currents were recorded by a computer-programmed Keithley 2400 source meter and then fitted by the Mott-Gurney equation. Film thickness was determined by a Veeco Dektak 150+ Surface Profiler.

**Solvent vapour annealing.** SVA was conducted in a glove box filled with dried nitrogen. THF (1 ml) were injected into a 30-mm glass Petri dish. The Petri dish was closed for 1 min to let the vapour saturate the treatment chamber. Then as-cast films were attached on the backside of the Petri dish lid, which was quickly swapped with the lid covering the solvent-containing Petri dish. The film was about 1 cm above the solvent level during the SVA. After certain duration, the film was removed from the treatment chamber. The optimal duration in this study was 15 s.

**OFET fabrication and measurement.** OFETs were fabricated employing two types of device configurations: bottom-gate, bottom-contact and bottom-gate, top-contact on the 300-nm-thick silicon-dioxide dielectric covering the highly doped silicon that acted as the gate electrode. The source-drain channel length ( $L$ ) to channel width ( $W$ ) ratio was 1:70 for bottom-contact and 1:33 for top-contact configurations. The substrates were first cleaned by sonication in acetone and isopropanol for 20 min each, then dried under nitrogen flow and dipped into a freshly prepared piranha solution (7:3 v/v H<sub>2</sub>SO<sub>4</sub>/30% H<sub>2</sub>O<sub>2</sub>) at  $90^\circ \text{C}$  for 60 min. To remove residues of the piranha solution, substrates were rinsed with copious deionized water and dried under nitrogen flow. The BTR thin film was deposited via spin-coating (for top-contact OFETs) or drop-casting (bottom-contact OFETs) using  $4.5 \text{ mg ml}^{-1}$  toluene with subsequent annealing at  $60^\circ \text{C}$  for 60 min to remove residual solvent. In addition, the BTR films were measured after thermal annealing at 179 and  $190^\circ \text{C}$ . All the electrical measurements are performed in a glove box under nitrogen atmosphere by means of a Keithley 4200 SCS.

**Solar cell fabrication and characterization.** Patterned ITO glasses were washed sequentially by detergent, deionized water, acetone and 2-propanol in an ultrasonication bath and UV/ozone-treated. PEDOT:PSS (Clevios P VP Al 4083) was spin-coated at 6,000 r.p.m. and then baked at  $140^\circ \text{C}$  for 10 min in air. The

substrates were transferred to a glove box filled with dried nitrogen, where a chloroform solution of the donor-acceptor blend was spin coated at various spin rates on top of the substrate. The best PCE was achieved by spin coating 20 mg BTR and 20 mg PC<sub>71</sub>BM in 1 ml of chloroform at 1,000 r.p.m. The resulting film thickness was around 250 nm. Thicker or thinner films were produced by varying the solution concentration and spin rate from 1.6 to 2.0% and from 600 to 2,000 r.p.m., respectively. To obtain high photovoltaic performance, the films were solvent vapour annealed by THF. Then they were transferred to a thermal evaporator where 40 nm Ca and 100 nm aluminium were deposited through a shadow mask (active area was  $0.11 \text{ cm}^2$ ) at a base pressure of  $4 \times 10^{-7}$  mbar. The solar cells were encapsulated under nitrogen by UV-curable epoxy (Epotek OG112-6 by Epoxy Technology Inc.) and cover glass. They were tested in air with a computer-programmed Keithley 2400 source meter under a Newport Oriel class A solar simulator, which simulated the AM1.5 solar irradiance with energy density of  $98 \text{ mW cm}^{-2}$ . For accurate measurement and to avoid oxidation during testing, a batch of optimized solar cells were brought to a third-party research institute, Solar Energy Research Institute of Singapore, where the cells were tested under nitrogen and 1 SUN ( $100 \text{ mW cm}^{-2}$ ) condition provided by a 1 kW solar simulator (Sun 2000 Solar Simulator by ABET Technologies) that was calibrated by a silicon reference cell (Fraunhofer ISE) and a Schott visible-colour glass-filtered (KG5 colour filtered) Si diode (Hamamatsu S1133). OPVs made in Australia followed the same fabrication procedures, and were tested at Clayton Laboratories of Commonwealth Scientific and Industrial Research Organisation, where a 1-kW Oriel solar simulator with an AM 1.5G filter was used as the light source.

## References

- Burschka, J. *et al.* Sequential deposition as a route to high-performance perovskite-sensitized solar cells. *Nature* **499**, 316–319 (2013).
- Liu, M., Johnston, M. B. & Snaith, H. J. Efficient planar heterojunction perovskite solar cells by vapour deposition. *Nature* **501**, 395–398 (2013).
- Zhou, H. *et al.* Interface engineering of highly efficient perovskite solar cells. *Science* **345**, 542–546 (2014).
- Yu, G., Gao, J., Hummelen, J. C., Wudl, F. & Heeger, A. J. Polymer photovoltaic cells: enhanced efficiencies via a network of internal donor-acceptor heterojunctions. *Science* **270**, 1789–1791 (1995).
- Chen, H. Y. *et al.* Polymer solar cells with enhanced open-circuit voltage and efficiency. *Nat. Photon.* **3**, 649–653 (2009).
- Small, C. E. *et al.* High-efficiency inverted dithienogermole-thienopyrrolodione-based polymer solar cells. *Nat. Photon.* **6**, 115–120 (2012).
- Liu, Y. *et al.* Solution-processed small-molecule solar cells: breaking the 10% power conversion efficiency. *Sci. Rep.* **3**, 3356 (2013).
- He, Z. *et al.* Enhanced power-conversion efficiency in polymer solar cells using an inverted device structure. *Nat. Photon.* **6**, 591–595 (2012).
- Ye, L., Zhang, S., Zhao, W., Yao, H. & Hou, J. Highly efficient 2D-conjugated benzodithiophene-based photovoltaic polymer with linear alkythio side chain. *Chem. Mater.* **26**, 3603–3605 (2014).
- Liao, S.-H., Jhuo, H.-J., Cheng, Y.-S. & Chen, S.-A. Fullerene derivative-doped zinc oxide nanofilm as the cathode of inverted polymer solar cells with low-bandgap polymer (PTB7-Th) for high performance. *Adv. Mater.* **25**, 4766–4771 (2013).
- Guo, X. *et al.* Enhanced photovoltaic performance by modulating surface composition in bulk heterojunction polymer solar cells based on PBDTTT-C-T/PC<sub>71</sub>BM. *Adv. Mater.* **26**, 4043–4049 (2014).
- Gupta, V. *et al.* Barium: an efficient cathode layer for bulk-heterojunction solar cells. *Sci. Rep.* **3**, 1965 (2013).
- Li, C.-Z. *et al.* Suppressed charge recombination in inverted organic photovoltaics via enhanced charge extraction by using a conductive fullerene electron transport layer. *Adv. Mater.* **26**, 6262–6267 (2014).
- Walker, B., Kim, C. & Nguyen, T.-Q. Small molecule solution-processed bulk heterojunction solar cells. *Chem. Mater.* **23**, 470–482 (2010).
- Mishra, A. & Bäuerle, P. Small molecule organic semiconductors on the move: promises for future solar energy technology. *Angew. Chem. Int. Ed.* **51**, 2020–2067 (2012).
- Lin, Y., Li, Y. & Zhan, X. Small molecule semiconductors for high-efficiency organic photovoltaics. *Chem. Soc. Rev.* **41**, 4245–4272 (2012).
- Shin, W., Yasuda, T., Watanabe, G., Yang, Y. S. & Adachi, C. Self-organizing mesomorphic diketopyrrolopyrrole derivatives for efficient solution-processed organic solar cells. *Chem. Mater.* **25**, 2549–2556 (2013).
- Graham, K. R. *et al.* Improved performance of molecular bulk-heterojunction photovoltaic cells through predictable selection of solvent additives. *Adv. Funct. Mater.* **22**, 4801–4813 (2012).
- Wang, H. *et al.* The role of additive in diketopyrrolopyrrole-based small molecular bulk heterojunction solar cells. *Adv. Mater.* **25**, 6519–6525 (2013).
- Graham, K. R. *et al.* Tailor-made additives for morphology control in molecular bulk-heterojunction photovoltaics. *ACS Appl. Mater. Interfaces* **5**, 63–71 (2013).
- Zhou, J. *et al.* Small molecules based on benzo[1,2-b:4,5-b']dithiophene unit for high-performance solution-processed organic solar cells. *J. Am. Chem. Soc.* **134**, 16345–16351 (2012).

22. Wei, G., Wang, S., Sun, K., Thompson, M. E. & Forrest, S. R. Solvent-annealed crystalline squaraine: PC<sub>70</sub>BM (1:6) solar cells. *Adv. Energy Mater.* **1**, 184–187 (2011).
23. Sun, K. *et al.* The role of solvent vapor annealing in highly efficient air-processed small molecule solar cells. *J. Mater. Chem. A* **2**, 9048–9054 (2014).
24. Wessendorf, C. D. *et al.* Efficiency improvement of solution-processed dithienopyrrole-based A-D-A oligothiophene bulk-heterojunction solar cells by solvent vapor annealing. *Adv. Energy Mater.* **4**, 1400266 (2014).
25. Krebs, F. C. Fabrication and processing of polymer solar cells: a review of printing and coating techniques. *Sol. Energy Mater. Sol. Cells* **93**, 394–412 (2009).
26. Li, W. *et al.* Efficient small bandgap polymer solar cells with high fill factors for 300 nm thick films. *Adv. Mater.* **25**, 3182–3186 (2013).
27. Li, G., Shrotriya, V., Yao, Y. & Yang, Y. Investigation of annealing effects and film thickness dependence of polymer solar cells based on poly(3-hexylthiophene). *J. Appl. Phys.* **98**, 043704 (2005).
28. Murphy, L., Hong, W., Aziz, H. & Li, Y. Organic photovoltaics with thick active layers (~800 nm) using a high mobility polymer donor. *Sol. Energy Mater. Sol. Cells* **114**, 71–81 (2013).
29. Zeng, L., Tang, C. W. & Chen, S. H. Effects of active layer thickness and thermal annealing on polythiophene: fullerene bulk heterojunction photovoltaic devices. *Appl. Phys. Lett.* **97**, 053305 (2010).
30. Wang, N., Chen, Z., Wei, W. & Jiang, Z. Fluorinated benzothiadiazole-based conjugated polymers for high-performance polymer solar cells without any processing additives or post-treatments. *J. Am. Chem. Soc.* **135**, 17060–17068 (2013).
31. Zhou, J. *et al.* Solution-processed and high-performance organic solar cells using small molecules with a benzodithiophene unit. *J. Am. Chem. Soc.* **135**, 8484–8487 (2013).
32. Kline, R. J. *et al.* Critical role of side-chain attachment density on the order and device performance of polythiophenes. *Macromolecules* **40**, 7960–7965 (2007).
33. Kim, M. S., Kim, B. G. & Kim, J. Effective variables to control the fill factor of organic photovoltaic cells. *ACS Appl. Mater. Interfaces* **1**, 1264–1269 (2009).
34. Bredas, J. L., Norton, J. E., Cornil, J. & Coropceanu, V. Molecular understanding of organic solar cells: the challenges. *Acc. Chem. Res.* **42**, 1691–1699 (2009).
35. Schmidt-Mende, L. *et al.* Self-organized discotic liquid crystals for high-efficiency organic photovoltaics. *Science* **293**, 1119–1122 (2001).
36. Goel, M. & Jayakannan, M. Supramolecular liquid crystalline  $\pi$ -conjugates: the role of aromatic  $\pi$ -stacking and van der Waals forces on the molecular self-assembly of oligophenylenevinyls. *J. Phys. Chem. B* **114**, 12508–12519 (2010).
37. Kim, B.-G. *et al.* A molecular design principle of lyotropic liquid-crystalline conjugated polymers with directed alignment capability for plastic electronics. *Nat. Mater.* **12**, 659–664 (2013).
38. Hanna, J.-i., Ohno, A. & Iino, H. Charge carrier transport in liquid crystals. *Thin Solid Films* **554**, 58–63 (2014).
39. McPhillips, T. M. *et al.* Blu-Ice and the distributed control system: software for data acquisition and instrument control at macromolecular crystallography beamlines. *J. Synchrotron Radiat.* **9**, 401–406 (2002).
40. Guo, X., Puniredd, S. R., Baumgarten, M., Pisula, W. & Müllen, K. Benzotrithiophene-based donor-acceptor copolymers with distinct supramolecular organizations. *J. Am. Chem. Soc.* **134**, 8404–8407 (2012).
41. Guo, X. *et al.* Polymer solar cells with enhanced fill factors. *Nat. Photon.* **7**, 825–833 (2013).
42. Lin, Y. *et al.* Small-molecule solar cells with fill factors up to 0.75 via a layer-by-layer solution process. *Adv. Energy Mater.* **4**, 1300626 (2014).
43. Murphy, L., Hong, W., Aziz, H. & Li, Y. Influences of using a high mobility donor polymer on solar cell performance. *Org. Electron.* **14**, 3484–3492 (2013).
44. Liang, Y. *et al.* For the bright future: bulk heterojunction polymer solar cells with power conversion efficiency of 7.4%. *Adv. Mater.* **22**, E135–E138 (2010).
45. Kyaw, A. K. K. *et al.* Intensity dependence of current–voltage characteristics and recombination in high-efficiency solution-processed small-molecule solar cells. *ACS Nano* **7**, 4569–4577 (2013).
46. Qin, T. *et al.* Tailored donor–acceptor polymers with an A–D1–A–D2 structure: controlling intermolecular interactions to enable enhanced polymer photovoltaic devices. *J. Am. Chem. Soc.* **136**, 6049–6055 (2014).
47. Kumar, R. J., MacDonald, J. M., Singh, T. B., Waddington, L. J. & Holmes, A. B. Hierarchical self-assembly of semiconductor functionalized peptide  $\alpha$ -helices and optoelectronic properties. *J. Am. Chem. Soc.* **133**, 8564–8573 (2011).

## Acknowledgements

This research was supported by the Victorian Organic Solar Cell Consortium with funding from the Victorian Government (DSDBI) and the Australian Renewable Energy Agency (ARENA) through grants 2-A018, 1-GER001 and the ARENA funded Australian Centre for Advanced Photovoltaics. The research was also supported by the Ministry of Education, Singapore (R-284-000-113-112). W.W.H.W. is supported by an ARC Future Fellowship (FT130100500). We acknowledge the Monash Centre for Electron Microscopy (MCEM) at Monash University, the MX2 beamline at the Australian Synchrotron, CSIRO, Department of Materials Science & Engineering (DMSE) at National University of Singapore (NUS) and Solar Energy Research Institute of Singapore (SERIS) for sharing their facilities with us. We acknowledge Dr Doojin Vak at CSIRO, Dr Xi-Ya Fang at MCEM, Henche Kuan, Yeow Koon Liew, Drs Lei Chen and Pengcheng Li at DMSE NUS and Fang Jeng Lim at SERIS for experiment assistance and in-depth discussions.

## Author contributions

K.S. fabricated the solar cell device and characterized the film and device properties using POM, XRD, AFM, TEM, HAADF STEM and SCLC. Z.X. designed and performed materials synthesis and characterization including NMR, MS, CV and UV–vis absorption spectra for solution and thin film. S.L. scaled up the synthesis, grew single crystals and measured DSC, TGA, PL and solubility. W.Z. and W.P. fabricated OFET, measured and analysed OFET, 2D-XRD and GIWAXS data. E.H. constructed TEM tomograms and computer models. J.M.W. solved the crystal structure using XRD acquired by R.M.W. at Australian Synchrotron. J.S. reproduced the OPV results. K.S., Z.X. and S.L. prepared the manuscript. All authors discussed the results and commented on the manuscript. J.O., W.W.H.W., A.B.H. and D.J.J. supervised the project and revised the manuscript.

## Additional information

**Accession codes:** The crystallographic information file for BTR has been deposited with Cambridge Crystallographic Data Centre, and signed to CCDC code 1029304.

**Supplementary Information** accompanies this paper at <http://www.nature.com/naturecommunications>

**Competing financial interests:** The authors declare no competing financial interests.

**Reprints and permission** information is available online at <http://npg.nature.com/reprintsandpermissions/>

**How to cite this article:** Sun, K. *et al.* A molecular nematic liquid crystalline material for high-performance organic photovoltaics. *Nat. Commun.* **6**:6013 doi: 10.1038/ncomms7013 (2015).



This work is licensed under a Creative Commons Attribution 4.0 International License. The images or other third party material in this article are included in the article's Creative Commons license, unless indicated otherwise in the credit line; if the material is not included under the Creative Commons license, users will need to obtain permission from the license holder to reproduce the material. To view a copy of this license, visit <http://creativecommons.org/licenses/by/4.0/>

# Determination of the CYP1A-inducing potential of single substances, mixtures and extracts of samples in the micro-EROD assay with H4IIE cells

Andreas Schiwy<sup>1,7</sup>, Markus Brinkmann<sup>1,7</sup>, Ines Thiem<sup>2</sup>, Gabriele Guder<sup>2</sup>, Kerstin Winkens<sup>1</sup>, Kathrin Eichbaum<sup>1</sup>, Leonie Nüßer<sup>1</sup>, Beat Thalmann<sup>1</sup>, Sebastian Buchinger<sup>3</sup>, Georg Reifferscheid<sup>3</sup>, Thomas-Benjamin Seiler<sup>1</sup>, Brigitte Thoms<sup>2</sup> & Henner Hollert<sup>1,4–6</sup>

<sup>1</sup>Department of Ecosystem Analysis, Institute for Environmental Research, Aachen Biology and Biotechnology (ABBT), Rheinisch-Westfälische Technische Hochschule Aachen (RWTH) Aachen University, Aachen, Germany. <sup>2</sup>Food and Veterinary Institute Braunschweig/Hannover, Lower Saxony State Office for Consumer Protection and Food Safety (LAVES), Braunschweig, Germany. <sup>3</sup>Federal Institute of Hydrology (BFG), Department G3: Biochemistry, Ecotoxicology, Koblenz, Germany. <sup>4</sup>College of Resources and Environmental Science, Chongqing University, Chongqing, China. <sup>5</sup>College of Environmental Science and Engineering and State Key Laboratory of Pollution Control and Resource Reuse, Tongji University, Shanghai, China. <sup>6</sup>State Key Laboratory of Pollution Control and Resource Reuse, School of the Environment, Nanjing University, Nanjing, China. <sup>7</sup>These authors contributed equally to this work. Correspondence should be addressed to H.H. (Henner.Hollert@bio5.rwth-aachen.de).

Published online 8 October 2015; doi:10.1038/nprot.2015.108

**This protocol describes a quantitative and robust 96-well-plate-reader-based assay for the measurement of ethoxyresorufin-O-deethylase (EROD) activity using the rat hepatoma cell line H4IIE. The assay can be used to determine the cytochrome P450 subfamily 1A (CYP1A)-inducing potential of single substances, as well as of mixtures and extracts of samples. It is based on the aryl hydrocarbon receptor (AhR)-mediated induction of cytochrome P450 enzymes (subfamily 1A) in cells after exposure to dioxins and dioxin-like compounds. One enzymatic reaction catalyzed by CYP1A is the deethylation of the exogenous substrate 7-ethoxyresorufin to the fluorescent product resorufin, which is measured as EROD activity in the assay. The CYP1A-inducing potential of a sample can be reliably quantified by comparing the EROD activity with the concentration-response curve of the standard substance 2,3,7,8-tetrachlorodibenzo-*p*-dioxin, which can be detected at concentrations down to the picogram per liter range. A researcher familiar with the procedure can process up to 160 samples with four wells each within 3 d. The series described uses four plates with three concentrations per sample, which can be easily scaled to accommodate different sample sizes.**

## INTRODUCTION

Dioxins and dioxin-like chemicals (DLCs) are of high toxicological and environmental concern. They belong to the class of persistent organic pollutants that is characterized by low environmental degradation rates through physical, chemical or biological processes<sup>1</sup>. Consequently, their environmental half-lives are rather high, ranging from months to over several years and decades, meaning that they tend to accumulate in soils and sediments<sup>2,3</sup>. It is because of their high lipophilicity and their low rate of biotransformation that dioxins and DLCs are highly bioaccumulative. This leads to increased levels in wildlife, animal feed, meat, and dairy products<sup>4–6</sup>. The resulting elevated risk of human exposure through contaminated food is particularly alarming in light of the variety of acute and chronic toxic effects that dioxins and DLCs are known to provoke. These toxic effects include neurotoxicity, immunotoxicity and hepatotoxicity, reproductive toxicity, and ultimately even certain types of cancer<sup>7–12</sup>. Activation of the nuclear AhR and subsequent induction of CYP1A-dependent monooxygenases is a well-studied effect of dioxins and DLCs<sup>13</sup>.

Polychlorinated dibenzo-*p*-dioxins and dibenzofurans (often summarized as 'dioxins') are mostly produced unintentionally as by-products of chemical reactions involving chlorine, and during industrial or domestic combustion processes<sup>14</sup>. Polychlorinated biphenyls (PCBs) had been extensively used in technical applications, such as transformer oil or cutting liquids, because of their favorable physical and chemical properties—i.e., their chemical inertness and high thermal conductivity. Therefore, dioxin-like

PBCs (dl-PCBs) are probably the most prevalent class of DLCs in the environment. As their environmental and toxicological impacts became apparent, production of PCBs was globally restricted and finally banned<sup>15</sup>. Although emissions substantially decreased, dioxins and DLCs are still re-distributed in the environment by processes that are still poorly understood. This became evident during the Belgian dioxin and PCB crisis in 1999 (ref. 16) and the extensive contamination of eggs and different types of meat in Germany in 2011 (ref. 17) because of contaminated animal feed. In 2012 and 2013, the European Rapid Alert System for Food and Feed (RASFF) reported a total number of 29 dioxin limit exceedances in feed samples<sup>18,19</sup>. As a consequence, national and multinational regulations were implemented or revised to reduce the risk for consumer health. The European Commission proposed a two-step approach for reducing the amount of dioxins, furans and PCBs in food and feed<sup>20–26</sup>.

Instrumental chemical analysis of dioxins and DLCs, which is typically performed using high-resolution gas chromatography with high-resolution mass spectrometry (HRGC/HRMS), is costly and requires highly specialized personnel. This clearly limits the number of samples that can be investigated and the applicability for developing countries<sup>25,27,28</sup>. It became quickly evident that more rapid and economic methods are needed to efficiently protect consumer safety and to uncover the toxicological burden present in the environment.

A powerful and promising solution to the problem is the use of cell-based *in vitro* bioassays for prescreening of a large number

of samples<sup>29–32</sup>. This type of analytical tool does not allow for exact quantification of single compounds, but it greatly facilitates the assessment of a sample's overall CYP1A-inducing potential<sup>33</sup>. Several methods applying different, untransfected or genetically engineered cell lines exist for this purpose, all of which use the activation of AhR by agonists that are present in a given sample<sup>34</sup>. Differences in affinity exist between different Ah receptors, with the rodent AhR showing a greater affinity to 2,3,7,8-tetrachlorodibenzo-*p*-dioxin (TCDD) than the human receptor<sup>35</sup>. Although this is an advantage in terms of sensitivity of the assay, it does not allow for straightforward extrapolations to effects on human health<sup>35,36</sup>. Among the most frequently used assays is the commercial DR CALUX assay. It is based on H4IIE cells that have been stably transfected and thus genetically modified with a luciferase-reporter gene that is expressed upon receptor binding<sup>37</sup>.

### Development of the protocol

Here we describe a protocol for the EROD assay using the untransfected rat hepatoma cell line H4IIE, which is approximately ten times more sensitive to TCDD than human cell lines<sup>35,38</sup>. Our protocol is based on the original method of Schwirzer *et al.*<sup>39</sup>, as modified and applied by Thiem *et al.*<sup>40–42</sup> for routine dioxin screening, which is based on the pioneering work of Donato *et al.*<sup>43,44</sup>, Safe<sup>45</sup> and Tillitt *et al.*<sup>46</sup>. It is regularly applied at the Institute for Environmental Research, RWTH Aachen University, Aachen, Germany and at the Food and Veterinary Institute Braunschweig/Hannover, Lower Saxony State Office for Consumer Protection and Food Safety (LAVES), Germany. The method is based on the endogenous AhR-mediated induction of CYP1A in particular, which is triggered by dioxins and DLCs. The induced CYP1A-dependent monooxygenases catalyze the deethylation of the exogenous substrate 7-ethoxyresorufin (ETX) to the fluorescent product resorufin. It can be easily quantified fluorometrically in a 96-well-plate reader. The CYP1A-inducing potential of a given sample can be reliably quantified when comparing the activity induced by the sample with the concentration-response curve of a well-characterized standard substance—e.g. TCDD, benzo[*a*]pyrene or  $\beta$ -naphthoflavone.

It has been shown that the EROD assay is compliant with the regulations of the European Commission for dioxin screening of food and feed<sup>26,40</sup>. These include various criteria for dioxin screening,

e.g., false-compliance rate with respect to the maximum levels lower than 5%, repeatability (relative standard deviation ( $RSD_r$ )) of <20% and within-laboratory reproducibility ( $RSD_R$ ) of <25% referring to the matrix validation. Other criteria are more bioassay-specific—e.g., that the relative standard deviations of technical triplicates should not exceed 15%.

### Comparison with other methods, applications and potential limitations

Recently, our group published a literature review on the analytical performance of different cell-based bioassays for assessing the CYP1A-inducing potential of chemicals, mixtures and extracts of environmental samples<sup>34</sup>. Although the commercially available DR CALUX achieved the lowest limits of detection, the micro-EROD bioassay described here showed the highest sensitivity to TCDD; i.e., the lowest effective concentrations of all compared assays. An advantage in comparison with the reporter gene assays is that it uses untransfected H4IIE cells, which are often referred to as 'wild type' (Fig. 1a). Therefore, it can be carried out in laboratories without containment level for genetically modified cells. Furthermore, the cell line is readily available via the American Type Culture Collection (ATCC). In addition, the assay procedure has been economically optimized, as expensive substrates, e.g., for the determination of luciferase activity, or the addition of co-substrates such as NADPH are not required.

The assay can be applied to various sample types, including single substances, mixtures and extracts of environmental samples, food and feed. It had been used to assess soils, sediments, exhaust from domestic and industrial combustion processes, fish, eggs, meat and dairy products, plant materials, and sewage sludge (Table 1). It is important to note that different matrices require different extraction and cleanup procedures to prepare samples for the bioassay. Expert knowledge is necessary, as some matrix components can drastically influence the results of the bioassay. In particular, the removal of fat from biological samples is required. Depending on the analytical aim, readily degradable inducers can be extracted.

For the analysis of stable inducers such as dioxins, the oxidation of these degradable inducers is recommended. Such compounds

**Figure 1** | Summary of the micro-EROD bioassay with H4IIE cells. (a) Confluent H4IIE rat hepatoma cells in culture. Scale bar, 50  $\mu$ m. (b) Flowchart of the micro-EROD bioassay. The corresponding steps are described in detail in the PROCEDURE section of the protocol. Optional steps or steps that are only necessary for certain sample matrices are indicated by a dashed outline, and they are not detailed in this protocol. (c) Exemplary result for the solvent control (SC), the TCDD standard and the polychlorinated dibenzo-*p*-dioxins and dibenzofuran fraction of a sediment extract from the Elbe River (Zollelbe, Magdeburg, Germany) after treatment with sulfuric acid, as well as multilayer and carbon/Celite fractionation.

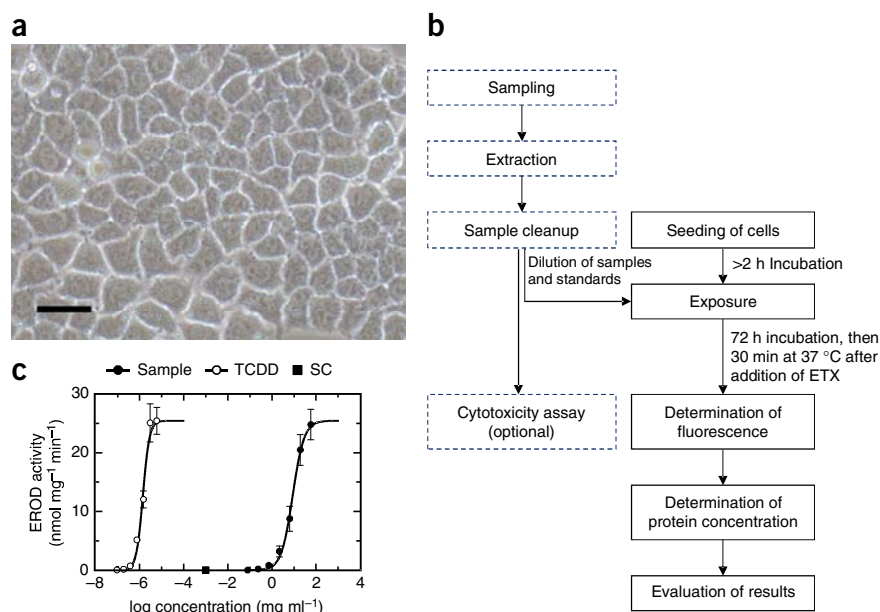




TABLE 1 | Examples of typical applications for the micro-EROD assay.

Sample matrix	Example references
Single substances and technical mixtures	Hanberg <i>et al.</i> <sup>56</sup> , Peters <i>et al.</i> <sup>57</sup> , Sanderson <i>et al.</i> <sup>47</sup> and Schmitz <i>et al.</i> <sup>58</sup>
Soils and sediment	Behnisch <i>et al.</i> <sup>59</sup> , Gale <i>et al.</i> <sup>60</sup> , Li <i>et al.</i> <sup>61</sup> and Schwirzer <i>et al.</i> <sup>39</sup>
Sewage sludge	Schwirzer <i>et al.</i> <sup>39</sup>
Plant materials	Li <i>et al.</i> <sup>61</sup>
Fish	Hanberg <i>et al.</i> <sup>56</sup> , Hewitt <i>et al.</i> <sup>62</sup> and Jiang <i>et al.</i> <sup>63</sup>
Feed	Behnisch <i>et al.</i> <sup>59</sup> and Summer <i>et al.</i> <sup>64</sup>
Meat and dairy products	Thiem <i>et al.</i> <sup>40</sup> and Valdovinoso <i>et al.</i> <sup>65</sup>
Fly ash, industrial and domestic emissions	Behnisch <i>et al.</i> <sup>59</sup> , Li <i>et al.</i> <sup>61</sup> , Schramm <i>et al.</i> <sup>66</sup> and Schwirzer <i>et al.</i> <sup>39</sup>
Transformer PCB-oil	Behnisch <i>et al.</i> <sup>59</sup>

might be transformed by xenobiotic metabolizing enzymes during the assay within 24–48 h. Depending on their receptor affinity, they can markedly alter the assay result. The exposure time of 72 h reduces the results to the contribution of the most stable inducers, such as dioxins and dl-PCBs. A number of suitable cleanup procedures can be found in the literature, e.g., in Schwirzer *et al.*<sup>39</sup>.

#### Experimental design

**Overview.** A flowchart of the assay procedure is shown in **Figure 1b**. After seeding the cells and incubating for 2–16 h, samples and standards are added directly to the wells. After an incubation period of 68–72 h, the exposure medium is removed and a solution of the substrate ETX is added. During the subsequent incubation step (30 min, 37 °C), ETX is converted by EROD to the fluorescent product resorufin. To avoid reductive degradation of resorufin, the reductase inhibitor dicoumarol is added to the incubation mixture. After incubation, methanol is added to terminate the reaction, and the amount of resorufin

in each well is determined by means of fluorescence spectroscopy. Thereafter, the corresponding protein concentration is measured. It can be used as a validity criterion in comparison with wells containing solvent and negative controls (≥80%), to exclude any cytotoxicity or contaminations, as well as erroneous handling. Furthermore, it can be used to calculate the specific EROD activity relative to the protein content of the wells. A concentration-response curve can be plotted for the standard and sample, from which biological TCDD equivalents (BEQs) can be calculated (**Fig. 1c**).

**Controls.** The micro-EROD bioassay has been optimized with special emphasis on high sample throughput and economic considerations. The assay is performed in a 96-well format with H4IIE cells (**Fig. 1a**), and it mostly requires basic cell culture. To meet the requirement for improved sample throughput, only the most necessary standards and controls are included—i.e., TCDD and protein standards, as well as a negative control

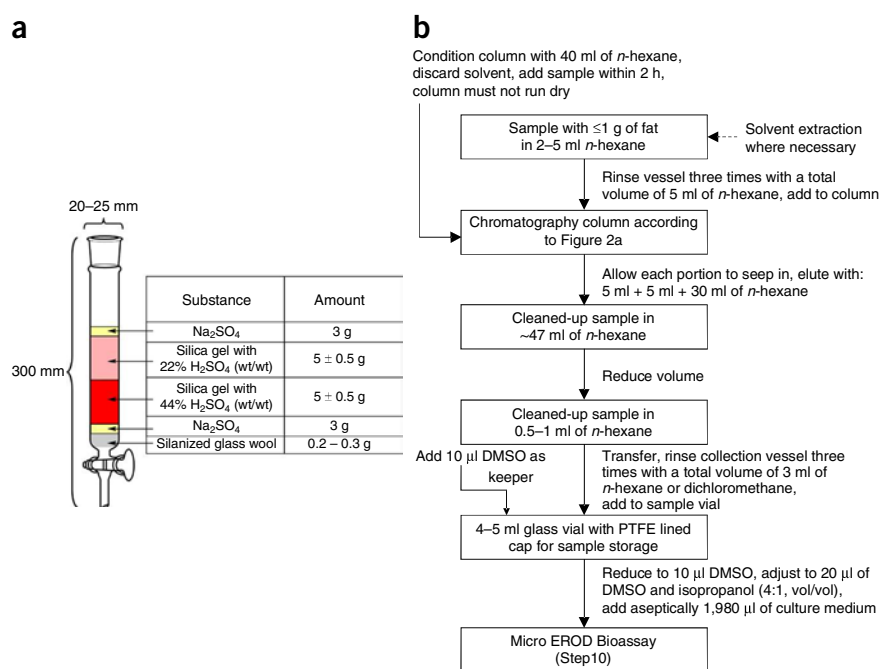
### Box 1 | Exemplary acidic silica column cleanup procedure

The protocol required for extraction and a subsequent cleanup before processing a sample in the micro-EROD bioassay highly depends on the matrix of the sample and the compounds of interest (see Gizzi *et al.*<sup>49</sup> and Thiem *et al.*<sup>40</sup>). **Figure 2** presents a cleanup procedure for samples with a maximum of 1 g of fat content. This cleanup is optimized for samples with low cytotoxicity and comparably low content of CYP1A inducers. For matrices anticipated to exhibit higher cytotoxicity or content of inducers, a modification of this procedure is necessary—e.g., the amounts of column components (sulfuric silica gel, solvent, column dimensions) can be scaled and the final volume of DMSO can be increased. Alternatively, other extraction and cleanup methods such as pressurized solvent extraction with in-cell cleanup might be more suitable.

In summary, the procedure is designed to remove components that interfere with the bioassay and to concentrate the persistent inducers. A sulfuric acid treatment is used to remove fat and readily degradable inducers such as PAHs. The sequence of two separate sulfuric acid silica gel layers with different acid concentrations helps reduce the formation of an impermeable layer within the column. The volatile solvent *n*-hexane is used to elute the CYP1A inducers. *N*-hexane or dichloromethane can be used to transfer the extract to a sample vial. DMSO is applied as a nonvolatile keeper and as the final solvent for the bioassay. For reliable results, all components of the cleanup process have to be evaluated in the micro-EROD bioassay to exclude any induction originating in the process itself. For each batch of solvents, chemicals or chromatography materials, a control needs to be implemented. Furthermore, a procedure blank and preferably a recovery control should be included. In addition, all chemicals have to be of high purity, and all materials in contact with the sample must be specially prepared and cleaned.



**Figure 2** | Cleanup procedure for the removal of up to 1 g of fat content and unstable CYP1A inducers before analysis in the micro-EROD bioassay. **(a)** Dimensions and composition of the chromatography column. **(b)** Workflow of steps necessary for the cleanup procedure.



consisting of the same lot and solvent concentration as the TCDD standard. Solvent controls from the sample cleanup should be included where required. Unlike with many other EROD assays, the protocol does not include a resorfin standard curve, as it is not necessary for comparative analysis of samples and standards<sup>47,48</sup>. Furthermore, no sample transfer to a second plate is necessary, as described in previous methods<sup>39</sup>.

**Sample preparation.** Depending on the nature of the tested samples, different sample preparation steps will be necessary. Single substances need to be dissolved in appropriate solvents—e.g., a mixture of DMSO and isopropanol (4:1, vol/vol). Always choose the same solvent for standards and samples. Keep the final solvent concentration constant for all wells. The compatibility and a suitable concentration range of any unknown solvent needs to be verified beforehand in the assay. We have had a good experience with a mixture of DMSO and isopropanol (4:1, vol/vol). For environmental, food and feed samples, adequate extraction and cleanup techniques, e.g., pressurized liquid extraction, liquid–liquid extraction, multilayer column chromatography, treatment with sulfuric acid, gel permeation chromatography, or HPLC fractionation need to be applied. These procedures should be evaluated with appropriate recovery controls. If different lots of solvent are used for the sample cleanup than for standards, a solvent control for the sample should be included. An example cleanup scheme

for the preparation of food and feed samples with a maximum of 1 g of fat content—according to Gizzi *et al.*<sup>49</sup> and Thiem *et al.*<sup>40</sup>—is provided in **Box 1** and **Figure 2**.

**Data evaluation.** The current data evaluation strategy described in the PROCEDURE (Steps 33–38) has been optimized to use the H4IIE micro-EROD assay for food or feed samples—i.e., to conform to the needs of maximum sample throughput and thus a low number of tested concentrations. Please be aware that different sample matrices and management criteria will require other data evaluation strategies, e.g., for mass-balance analyses of sediments. Good starting points can be found in the reviews of Safe *et al.*<sup>50</sup>, Whyte *et al.*<sup>48</sup>, Thiem and Boehmler<sup>42</sup> and Eichbaum *et al.*<sup>34</sup>, as well as in the general considerations by Villeneuve *et al.*<sup>51</sup> and Hädrich *et al.*<sup>52</sup>.

## MATERIALS

### REAGENTS

- H4IIE rat hepatoma cell line (ATCC, cat. no. CRL 1548)
  - ▲ **CRITICAL** The cell passage number has to be recorded, and the cell quality should be regularly verified microscopically. Contamination with mycoplasma must be excluded, and the cultures should be screened regularly.
- 2,3,7,8-Tetrachlorodibenzo-*p*-dioxin (TCDD) standard stock solutions, 50 μg ml<sup>-1</sup> (CIL, cat. no. ED-901-B). Alternatively, working solutions in the appropriate range can be obtained directly from the manufacturer after consultation. **CAUTION** TCDD is a known human carcinogen and a developmental toxicant in animals. It should be handled with care. As for any other chemicals used in this protocol, appropriate institutional and governmental safety guidelines need to be followed. Please refer to the respective MSDSs.
- Bicinchoninic acid (BCA) assay kit for protein determination (Sigma-Aldrich, cat. no. BCA1)
- Dicoumarol (Sigma-Aldrich, cat. no. M1390)
- Tris (Sigma-Aldrich, cat. no. 252859)
- Sodium hydroxide (NaOH; Sigma-Aldrich, cat. no. 38210)
- DMEM cell culture medium, low glucose, without glutamine, without phenol red (Life Technologies, cat. no. 11054-020)
- FBS (BioWest, cat. no. S1810-500)

- L-Glutamine 200 mM, sterile, suitable for cell culture (Life Technologies, cat. no. 25030-081), or GlutaMAX solution, 200 mM, sterile, suitable for cell culture (Life Technologies, cat. no. 35050-061)
- HEPES buffer, 1 M, sterile, suitable for cell culture (Sigma-Aldrich, cat. no. H0887)
- DMSO, cell culture tested, >97.5% (Sigma-Aldrich, cat. no. D2650)
- Methanol, laboratory reagent (Sigma-Aldrich, cat. no. 179957)
- Isopropanol, reagent grade (Sigma-Aldrich, cat. no. 190764)
- 7-Ethoxyresorufin (ETX; Sigma-Aldrich, cat. no. E3763)
- Dulbecco's PBS (DPBS) solution, with calcium, magnesium, without phenol red (Life Technologies, cat. no. 14040-091)
- 10× trypsin-EDTA solution (0.5% (wt/vol) trypsin; 0.2% (wt/vol) EDTA; BIOCHROM, cat. no. L2153)
- Sterile water suitable for cell culture (Life Technologies, cat. no. A1287301)

### EQUIPMENT

#### Apparatus

- CO<sub>2</sub> incubator for tissue culture (37 °C, 5–7% (vol/vol) CO<sub>2</sub>, >95% relative humidity)
- Microplate spectrofluorometer and spectrophotometer
- Liquid handling and aspiration apparatus with appropriate accessories
- Inverted phase-contrast microscope for inspection of cells

## PROTOCOL

- Sterile workbench suitable for cell culture
- Pipette, 10  $\mu$ l
- Refrigerator (2–8 °C)
- Freezer ( $\leq$ –18 °C)
- Ultrasonic bath for volumes of at least 50 ml (~35 kHz)
- Electronic multichannel pipette, 20–300  $\mu$ l
- Electronic multichannel pipette, 50–1,200  $\mu$ l
- Electronic pipetting aid (pipettor)
- Shaker suitable for multiwell plates
- Water bath, 30–37 °C
- Hemocytometer (Neubauer) or automated cell counter

### General equipment and consumables

- Disposable laboratory gloves (nitrile or latex)
- Standard tissue and cell culture flasks (TPP, cat. no. 90026 or 90076)
- Sterile 96-well tissue culture plates (Sarstedt, cat. no. 83.1835.300)
- Pipette tips: 2–20  $\mu$ l, 10–300  $\mu$ l and 50–1,200  $\mu$ l, sterile or autoclaved
- Sterile serological pipettes: 1, 5, 10 and 25 ml
- Sterile reaction tubes, 2 ml (VWR, cat. no. 2112165)
- Sterile reagent reservoirs minimum 50 ml, suitable for 12-channel pipettes (VWR, cat. no. 612-6572)
- Paper towels and 70% (vol/vol) ethanol
- Glass vials with polytetrafluoroethylene (PTFE)-lined caps (volume of 4–5 ml)

### REAGENT SETUP

**Complemented DMEM cell culture medium (culture medium)** Complement 500 ml of DMEM without phenol red with 50 ml of FBS and 9.9 ml of 200 mM L-glutamine or 200 mM GlutaMAX solution and 12.5 ml of 1 M HEPES buffer under aseptic conditions. Culture medium should be stored refrigerated at 2–8 °C for no longer than 4 weeks. In addition, the number of warming and cooling cycles should not exceed 12, and a sterility control should be conducted weekly. To avoid partial medium component degradation, each warming period should not exceed 30 min.

**TCDD standard working stock solutions (30–1,200 pg ml<sup>-1</sup>; optional)** An example preparation is shown in **Table 2**. Depending on the test setup, other solvents or mixtures with different concentrations may be chosen. Pre-dilute the original TCDD solution (50  $\mu$ g ml<sup>-1</sup>) with DMSO to a concentration of 3,000 pg ml<sup>-1</sup> in a 1-ml volume. This parent solution is stable at 2–8 °C for the storage life of DMSO (2 years). We recommend using a mixture of DMSO and isopropanol (4:1, vol/vol) as a solvent. Prepare the stock solution by adding 250  $\mu$ l of isopropanol to 1 ml of the parent solution, which results in a TCDD stock concentration of 2,400 pg ml<sup>-1</sup>. This stock solution can be stored at 2–8 °C for 12 months. Prepare the different concentrations of TCDD working stock solutions according to **Table 2** by diluting the stock

solution with the solvent mixture (DMSO and isopropanol; 4:1, vol/vol). Only experienced staff should conduct this procedure, and all work should be done under a laboratory hood. Take sufficient precautionary measures. Store the solution at 2–8 °C in glass vials with polytetrafluoroethylene (PTFE)-lined caps for up to 12 months. To reduce concentration artifacts due to evaporation, dilute the parent or original solution with volatile solvents in volumes smaller than the annual consumption. Choose a storage vessel with minimal volume.

**Solvent mixture (DMSO and isopropanol; 4:1, vol/vol)** Prepare a mixture of DMSO and isopropanol (4:1, vol/vol). As an example, mix 400  $\mu$ l of DMSO with 100  $\mu$ l of isopropanol. This solvent mixture can be stored at 2–8 °C for the storage life of DMSO. Use the same lot as that used for the preparation of TCDD standards.

**ETX stock solution (800  $\mu$ M)** Dissolve 5 mg of ETX in 25.5 ml of methanol. Close it quickly to prevent evaporation of the solvent. Store ETX stock solutions in glass vials with PTFE lids at 2–8 °C and protected from direct light for up to 36 months. Contamination of the ETX stock solution or a spontaneous conversion to resorufin should be regularly excluded by means of fluorescence spectroscopy<sup>53</sup>.

**Dicoumarol stock solution (1 mM)** Dissolve 16.5 mg of dicoumarol in 50  $\mu$ l of 0.1 M NaOH solution and add 48 ml of 50 mM Tris. Dissolution can be accelerated by ultrasonication. Do not exceed temperatures of 40 °C for the solution. Store aliquots of 2–5 ml at  $\leq$ –18 °C for a maximum time of 12 months. Thaw each aliquot no more than three times.

**ETX working solution (8  $\mu$ M ETX and 10  $\mu$ M dicoumarol in DPBS, with calcium and magnesium)** For each 96-well plate, 9.6 ml of ETX working solution is required. For a typical set of four plates with sufficient reserve volume, combine the following volumes freshly each day and use the solution within 2 h of preparation: 410  $\mu$ l of dicoumarol stock solution (1 mM), 410  $\mu$ l of ETX stock solution (800  $\mu$ M) and 40.18 ml of DPBS. Use an ultrasonic bath to dissolve any particles under dimmed light for ~15 min. Verify before proceeding whether the particles remain visible. If necessary, prolong ultrasonication. Keep the solution at room temperature (20–26 °C) protected from direct light. The excess volume will be needed for the protein standard.

**BCA working solution** Prepare fresh BCA working solution according to the manufacturer's protocol and use it within 12 h.

**Protein standard (BSA) diluted in ETX working solution** Store the BSA stock standard supplied within the BCA kit according to the manufacturer's specifications. More-concentrated protein solutions can be diluted to 1 mg ml<sup>-1</sup> with sterile water and stored at 2–8 °C for up to 3 months. Freezing is not recommended.

**TABLE 2** | Sequence of the preparation and storage of the TCDD standard solution.

Name of solution	Concentration	Storage
Original ↓	50 $\mu$ g ml <sup>-1</sup> TCDD in DMSO	As recommended by the manufacturer
Parent ↓	3,000 pg ml <sup>-1</sup> TCDD in DMSO	Up to the storage life of DMSO at 2–8 °C
Stock ↓	2,400 pg ml <sup>-1</sup> TCDD in DMSO and isopropanol (4:1, vol/vol)	12 months at 2–8 °C
	No.                      1                      2                      3                      4                      5                      6                      7	
Working stock <sup>a</sup> ↓ (pg ml <sup>-1</sup> )	In D/I                      1,200                      800                      400                      240                      120                      60                      30	12 months at 2–8 °C
Ready to use <sup>b</sup> (pg ml <sup>-1</sup> )	In culture medium                      1.200                      0.800                      0.400                      0.240                      0.120                      0.060                      0.030	Maximum of 15 min in reaction tubes
Per well <sup>c</sup> (picograms per well)	In culture medium                      0.600                      0.400                      0.200                      0.120                      0.060                      0.030                      0.015                      —	

See Reagent Setup.

<sup>a</sup>Annual preparation of working stock solution in DMSO and isopropanol (4:1, vol/vol). <sup>b</sup>10  $\mu$ l of each working stock solution in 990  $\mu$ l of culture medium. <sup>c</sup>Addition of 50  $\mu$ l of each ready-to-use standard to wells containing 50  $\mu$ l of culture medium and cells, resulting in a final solvent concentration of 0.5% DMSO and isopropanol (D/I; 4:1, vol/vol).

**TABLE 3** | Dilution of the BSA standard in ETX working solution.

Protein standard	Well	Concentration per well ( $\mu\text{g well}^{-1}$ ) <sup>a</sup>	Stock concentration ( $\mu\text{g ml}^{-1}$ ) <sup>b</sup>
1	A1	50.00	500.00
2	B1	25.00	250.00
3	C1	12.50	125.00
4	D1	6.25	62.50
5	E1	3.13	31.25
6	F1	1.56	15.63
7	G1	0.78	7.81
8	H1	0	ETX working solution

See Reagent Setup.

<sup>a</sup>This concentration per well results from the addition of 100  $\mu\text{l}$  of the corresponding BSA standard concentration to each well. <sup>b</sup>This is the concentration that needs to be prepared as a serial dilution in ETX working solution.

Prepare the BSA standard dilutions according to **Table 3** freshly each day. Use excess volume of ETX working solution from Step 18 of the same day.

**▲ CRITICAL** The BSA protein standard supplied with the BCA kit contains a preservative. It can interfere with protein determination methods other than the BCA method.

**Trypsin/EDTA working solution (0.05% trypsin, 0.02% EDTA)** Dilute the stock solution 1:10 (vol/vol) with sterile water. After opening, Trypsin/EDTA solutions should be stored frozen in sterile 10-ml aliquots at  $-20\text{ }^{\circ}\text{C}$  for no longer than the manufacturer's expiration date. Thawed, ready-to-use solutions should be stored at  $2\text{--}8\text{ }^{\circ}\text{C}$  for no longer than 2 weeks.

**Dilution medium (culture medium with solvent mixture)** Add 1% (vol/vol) of the solvent mixture to the culture medium freshly each day, e.g., for four plates (16 samples with three concentrations). Add 100  $\mu\text{l}$  of the solvent mixture to 9.9 ml of culture medium to obtain the dilution medium.

**▲ CRITICAL** DMSO tends to sink to the bottom owing to its higher density. Shake the vials before processing the responding solution. Do not prepare larger volumes for storage.

**EQUIPMENT SETUP**

**Equipment preparation** Prepare the cell culture bench and clean it thoroughly with 70% (vol/vol) ethanol. All materials should be cleaned with 70% ethanol and, where possible, they should be sterilized or autoclaved to reduce the risk of contamination. Temper cell culture medium and trypsin/EDTA solution to  $30\text{--}37\text{ }^{\circ}\text{C}$ . Adjust the electronic pipette for the various liquid handling steps such as pipetting, dispensing and mixing. The use of electronic pipettes reduces the handling time and results in an improved accuracy.

**PROCEDURE**

**Sample preparation ● TIMING 1–3 d**

1| Prepare single substance or biological (e.g., environmental, food, or feed) samples for analysis. The preparation procedure will depend on the sample of interest. Refer to the Experimental design section in the INTRODUCTION for more information.

**▲ CRITICAL STEP** Fat or other matrix compounds might have a negative effect on the performance of the bioassay, and they need to be removed using appropriate protocols (see Experimental design and **Box 1**).

**Cytotoxicity evaluation ● TIMING 3 d**

2| (Optional) Depending on the test design and the cytotoxicity of the chosen matrix, samples may be evaluated before conducting the micro-EROD bioassay to exclude potential masking of the dioxin-like effects of interest. If required, follow the recommended procedure as previously described by Repetto *et al.*<sup>54</sup>.

**▲ CRITICAL STEP** Cytotoxicity of a sample can alter the results of the micro-EROD bioassay. It causes a reduced response and leads to potentially false-negative results. The maximum concentration applied in the micro-EROD bioassay should not cause any cytotoxicity. Alternatively, assess the cytotoxicity of a given sample in Step 33 and exclude it from further calculations if necessary.

**Seeding of cells into tissue culture plates ● TIMING 1 h–1 h 30 min**

3| Verify the quality of the cells with an inverted phase-contrast microscope. Exclude contaminated samples before proceeding with the assay. The cell monolayer should reach a desired confluence of 60–90%. Select appropriate flasks with cells and transfer them into the laminar flow cabinet.

**▲ CRITICAL STEP** All of the steps for the first day (Steps 3–9) must be performed under aseptic conditions in a laminar flow cabinet. Flasks exceeding 90% confluence are not recommended for the bioassay, as they are expected to show a lower metabolic rate.

4| Aspirate the medium of a cell culture flask preferably with a liquid handling apparatus and add 1 ml of the trypsin/EDTA working solution. Gently agitate the solution over the monolayer of cells and carefully remove it.

5| Add another 1 ml of trypsin/EDTA working solution, and then incubate the cell culture flask at  $33\text{--}37\text{ }^{\circ}\text{C}$  for 4–8 min.

6| Tap the flask to detach the cells and add 5 ml of culture medium. Mechanically dissociate the cell layer into a suspension of single cells by gently aspirating and expelling the cells into the flask with a serological pipette. Repeat this step 5–10 times until all macroscopically visible clusters of cells have dissociated.

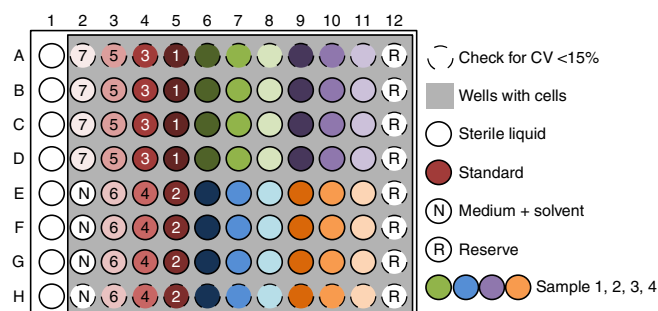
**▲ CRITICAL STEP** Proceed quickly to the next step in order to avoid recurring adhesion of the cells to the flask.

**? TROUBLESHOOTING**



## PROTOCOL

**Figure 3** | Layout for the exposure of H4IIE cells in 96-well tissue culture plates. In the current example, seven concentrations (S1–S7) for the standard and a negative control (N) containing the solvent of the standard are presented. In addition, four different samples can be tested in three different dilutions (indicated by the color gradient) with  $n = 4$  technical replicates. The wells labeled with 'R' can be additionally used—e.g., for additional solvent controls. Outer wells on the plate should be used with caution, as an edge effect can occur (check for CV <15%). The wells in column 1 are filled with a sterile liquid. Subsequently, in Step 27, the protein standard (Table 3) is located in these wells. All wells highlighted in gray contain cells. Depending on the study design, schemes with less samples and more tested concentrations could be applied.



7| Determine the cell density within the suspension using a hemocytometer or an automated cell counter. During manual counting, the viability of the cells can be verified using trypan blue staining. The cell viability should be >95%.

8| Dilute the cell suspension to 200,000 cells per ml with culture medium in a sterile reagent reservoir. Immediately dispense 50  $\mu$ l of the cell suspension into wells A2–H12 (Fig. 3). The resulting cell density is 10,000 cells per well. Each plate requires ~5 ml of the cell suspension.

▲ **CRITICAL STEP** Thoroughly mix the cell suspension in the reagent reservoir before adding it into the tissue culture plates to ensure an even distribution of the cells throughout all wells. Repeat mixing periodically, at least between every two plates, and dispense quickly using an electronic multichannel pipette.

### ? TROUBLESHOOTING

9| After addition of the cells, gently tilt the well plates to ensure an even distribution of cells within the wells. Cover the plates with a lid, label the plates and transfer them into an incubator (33–37 °C, 5–7% CO<sub>2</sub>, 95% humidity). During this incubation step, the cells are supposed to attach to the bottom of the tissue culture plates and grow a monolayer.

▲ **CRITICAL STEP** Do not agitate the plates in a circular manner, as this will result in a central cell cluster.

### ? TROUBLESHOOTING

■ **PAUSE POINT** Samples and standards should be added not earlier than after 2 h, and at the latest after 16 h.

### Preparation of samples and standards ● TIMING 1 h 40 min

10| Prepare the dilutions of samples and standards freshly before exposure of the cells in the solvent of choice. This procedure describes the use of a mixture of DMSO and isopropanol (4:1, vol/vol) as a solvent for all samples and controls. The dilution scheme for the samples must be individually developed according to the study design. Here we present an example for three sample concentrations: a sample stock and two further dilutions.

First, prepare 2 ml of a sample stock solution in sterile conditions by adjusting the sample or sample extract (Box 1) to 20  $\mu$ l with a 4:1 DMSO and isopropanol volumetric ratio. Next, without touching the cap of the vials, add 1,980  $\mu$ l of culture medium to the sample and agitate it for at least 10 min on a shaker at 300–600 r.p.m.

Next, fill two reaction tubes per sample with 250  $\mu$ l of dilution medium containing 1% solvent mixture (Reagent Setup). These tubes will be used for a subsequent serial dilution of the samples (Step 12) and they can be prepared up to 4 h in advance. Close all tubes until use.

▲ **CRITICAL STEP** 15–30 min of contact between the dioxins and the plastic tubes causes a substantial reduction in the cell response. When applying this protocol, the contact time is shorter than 2 min per concentration.

11| For each standard concentration (S1–S7) and the negative control, dispense 990  $\mu$ l of culture medium into eight reaction tubes. Stock solutions will be added just before pipetting onto the plate. This volume is sufficient for four tissue culture plates and can be prepared up to 4 h in advance.

▲ **CRITICAL STEP** The volume of standard and negative control dilution depends on the number of samples investigated. For each plate, 200  $\mu$ l is needed. To reduce pipetting errors, a minimum of 990  $\mu$ l of culture medium for 1 ml of final solution should be dispensed. Hence, the maximum dilution is 100-fold. When different lots of solvents for standards and samples are used, include an additional solvent control for the samples.

### Dosing of cells with the samples ● TIMING 1 h

12| Perform sample dilutions using tubes prepared in Step 10. Dilute 250  $\mu$ l of the sample stock in one of the reaction tubes containing 250  $\mu$ l of dilution medium to create dilution 1. Then, take 250  $\mu$ l of dilution 1 and add it to the second tube to create dilution 2.

Dispense a volume of 50  $\mu$ l of sample stock, dilution 1 and dilution 2 to four wells each. For an exemplary plate layout, see Figure 3. Add the sample stock and the two dilutions to the cells before proceeding with the next sample or the standards. Standards should subsequently be added to all plates at once (Step 13). Do not exceed the time span of 1 h

between the first sample and the last standard. If this cannot be guaranteed, e.g., because of a high sample number, subdivide the sample set and prepare separate standards for each subset.

**▲ CRITICAL STEP** We recommend using an electronic multichannel pipette for this step. The dilution and dispensing process per concentration can be combined and furthermore be performed for two samples in parallel for quick succession.

**▲ CRITICAL STEP** As 50 µl of the cell suspension is already inside the wells, all sample concentrations are diluted during this step. Calculate the concentrations accordingly (Step 10). For the chosen example, the resulting final solvent concentration is 0.5% within all wells.

**? TROUBLESHOOTING**

### Dosing of cells with TCDD standard and negative control ● TIMING 15 min

**13|** Add 10 µl of the corresponding standard working stock solutions and negative control to the reaction tubes with 990 µl of culture medium (Step 11). Mix the resulting standard dilution immediately. Dispense 50 µl into the four corresponding wells per concentration of all previously prepared plates (Step 9), as indicated in **Figure 3**.

**▲ CRITICAL STEP** Prepare a maximum of four reaction tubes with standard dilution at once, as TCDD shows a strong sorption to plastics. Handle the standards quickly to reduce the contact time in the tubes to <2 min. As 50 µl of the cell suspension is already inside the well, standards are diluted during this step. For the chosen example, the resulting final solvent concentration is 0.5% within all wells.

**? TROUBLESHOOTING**

**14|** To avoid extensive evaporation, fill all wells without sample or controls with 100 µl of culture medium or excess solvent control.

**15|** Verify that the addition of all components was successful. Each well should now contain 100 µl of liquid.

**▲ CRITICAL STEP** If drops of liquids are not mixed and adhere to the wells, carefully tip the plates to ensure successful addition of all components.

**? TROUBLESHOOTING**

**16|** Cover the plates with lids, and label and record the exact time. Transfer the plates into the incubator for 68–72 h.

**! CAUTION** Collect all remaining standard solutions and discard them properly as toxic waste. Handle them with care and adhere to all governmental and institutional safety regulations.

**? TROUBLESHOOTING**

**■ PAUSE POINT** Depending on the test design, the plates can be incubated for different periods. In the protocol, we chose 68–72 h in order to measure stable inducers of the AhR. Shorter periods give different results, as unstable compounds may be still measurable. When using sample extract procedure blanks (i.e., extraction process controls) and samples, they usually showed higher EROD activity after 24 or 48 h of incubation.

### Preparation for EROD activity measurement ● TIMING 1 h

**17|** Cool methanol, pipette tips and a reagent reservoir at 2–8 °C. The following parts of the protocol do not require sterile conditions.

**18|** Prepare the ETX working solution freshly before use (Reagent Setup).

**▲ CRITICAL STEP** All steps involving handling the ETX working solution (Steps 18–25) should be conducted under dimmed light conditions. The required time can be reduced when performing the visual plate examination (Step 19) and the ultrasonication of the ETX working solution (Step 18) in parallel.

**19|** After 68–72 h, verify proper cell growth and sterility for each plate and at least one well per sample with an inverted phase-contrast microscope. Record any problems.

**20|** Carefully aspirate the medium from each well of all plates, including the wells that were filled with liquid only. Do no damage the cell layer.

**! CAUTION** Collect all of the aspirated media and discard them properly as toxic waste. Handle them with care and adhere to all governmental and institutional safety regulations.

**▲ CRITICAL STEP** Accidental aspiration or damage of cells will result in reduced EROD activity and protein concentration, thus leading to false assay results. Uneven distribution of medium leftovers results in higher coefficients of variation (CVs). Tilt the plate to 40–70° and aspirate the liquid out of the corner to achieve best results. Use an aspiration rake for quick parallel handling of several rows.

**? TROUBLESHOOTING**

## PROTOCOL

21| Dispense 100  $\mu\text{l}$  of room-temperature ETX working solution to each well containing cells (sparse column A1–H1). Cover the plates with lids and transfer them into an incubator at 33–37  $^{\circ}\text{C}$  for 30 min.

▲ **CRITICAL STEP** Exact incubation timing for each plate is vital for an accurate result. Use a timer and work at a constant speed.  
? **TROUBLESHOOTING**

### Addition of methanol ● **TIMING 10 min**

22| Remove the tempered methanol, pipette tips and reagent reservoir (Step 17) from the refrigerator. Add methanol into the reservoir and aspirate with the multichannel pipette. Aspirate and dispense the complete volume a few times and verify that the methanol does not leak or drip from the tips. To stop the reaction, quickly add 75  $\mu\text{l}$  of methanol to all wells of the incubated plates, including column A1–H1, and then cover the plate with a lid.

▲ **CRITICAL STEP** Keep the concentration gradient in mind and avoid cross-contamination. For the example layout (**Fig. 3**), dispensing from row D to row A and from row E to row H is recommended. Change the tips after the first half of the plate or rinse them with methanol, discarding one full aspiration of methanol into a second reservoir.

? **TROUBLESHOOTING**

23| Transfer the plates to a shaker and shake them for at least 2 min at 300 r.p.m. in darkness—e.g., by covering the plate shaker with a box.

■ **PAUSE POINT** Plates can be covered with polyolefin film for storage. The film allows the transmission of fluorescence and is almost impermeable to methanol. The loss of fluorescence intensity when measuring through the film is ~15%. At ambient temperature, the results are stable for at least 3 d (ref. 37). Cooling can result in condensed water inside the wells and thus increase the CV. Adjust amplification in the plate reader, if applicable.

### Determination of resorufin using fluorescence spectroscopy ● **TIMING 30 min**

24| Prepare the fluorescence spectrometer for the measurement. The following settings should be applied: excitation wavelength, 544–572 nm; emission wavelength, 584–590 nm; 10 flashes; position delay, 0.2 s.

▲ **CRITICAL STEP** The excitation and emission wavelengths might require adjustments for the particular fluorometer used. Resorufin has an excitation maximum at 572 nm and an emission maximum at 584 nm. 7-Ethoxyresorufin has an excitation maximum at 494 nm and an emission maximum at 576 nm (ref. 53). Adjust the settings to achieve the highest ratio between the values of the negative control and the highest TCDD standard induction. Especially for devices with variable amplification (also referred to as gain, zoom and so on) and a dynamic range, further adjustment shall be conducted. The outer well with the highest TCDD standard shall be adjusted to 75–90% of the working range of the device. Excessive amplification will result in an overflow of the photomultiplier, and the data for this measurement point will be lost. If applicable, the measurement setting 'optimal gain' can be used to determine the best parameters. Verify the setting before a measurement.

25| Measure the fluorescence units (FU) in each well of all plates with the corresponding settings.

▲ **CRITICAL STEP** Until this step, all plates and solutions should have been handled under dimmed light conditions.

### Measurement of protein amount ● **TIMING 1 h–1 h 40 min**

26| Prepare the BCA working solution freshly before use according to Reagent Setup. Freshly prepare dilutions of protein standard (BSA, see Reagent Setup) to obtain the concentrations given in **Table 3**. There should be sufficient ETX working solution left from Step 18 from the same day for use.

27| Add 100  $\mu\text{l}$  of each concentration of the protein standard to the corresponding wells without cells (column A1–H1; **Fig. 3**).

28| Add 100  $\mu\text{l}$  of the BCA working solution to all wells of the plate. Now all wells contain a volume of 275  $\mu\text{l}$ .

▲ **CRITICAL STEP** Take care that the reagent reservoir is clean and does not contain any proteins or tissue fibers. Do not cross-contaminate the wells containing cells with the protein standard. Rinse the tips with BCA working solution between the samples and the protein standard.

? **TROUBLESHOOTING**

29| Cover the plates with lids. Incubate the plates at room temperature for 45–90 min. Keep temperatures below 40  $^{\circ}\text{C}$  and work in well-ventilated areas or under a laboratory hood.

! **CAUTION** Methanol is a flammable and toxic liquid; avoid overheating and inhalation. Do not use an incubator for this step.

? **TROUBLESHOOTING**

■ **PAUSE POINT** Incubation at room temperature takes 45–90 min. Covering the plates with the lid is sufficient. After incubation, firmly seal the plates, e.g., with polyolefin film, after which they can be stored at 2–8  $^{\circ}\text{C}$  overnight. Before measurement, allow the plates to reach room temperature. Be aware of condensed water inside the wells.

**30** | Measure the absorbance units (AU) in each well at the wavelength of 550–570 nm by means of a microplate spectrophotometer. **▲ CRITICAL STEP** The absorption wavelength might require adjustments for the particular microplate spectrophotometer used. The measured BCA/copper complex of the BCA protein assay has an absorption maximum at 562 nm (ref. 55). The ratio between the absorbance of protein negative control and that of wells with cells should be at least 2. The ratio between the protein negative control and the highest value of the protein standard should be ~3. If these ratios are not met, a prolonged incubation is recommended. Evaporation can be minimized by sealing the plates.

**31** | Store all measurements in a proper file format for subsequent data analysis.

**32** | Properly discard the solutions as toxic waste according to governmental and institutional safety regulations, as the BCA working solution contains copper, and discard the plates.

**■ PAUSE POINT** Evaluation of the previously documented results can be performed at any time after the measurement.

**Data evaluation ● TIMING 15 min**

**33** | Calculate the protein content in each well by interpolation from the BSA standard curve using linear regression. To verify the quality of the curve, slope, position of the single values along the curve and the coefficient of determination ( $R^2$ ) have to be evaluated. The  $R^2$  value should be above 0.975. The protein content in each well containing sample should be at least 80% of the mean value from wells containing standards and negative controls (row 2–5).

**▲ CRITICAL STEP** If the protein content of a single well is suspicious, it can be assumed to be a bacterial contamination or a handling artifact. The value should be removed from analysis. Increasing protein content with higher dilution can be observed with toxic sample compounds.

**34** | Evaluate the fluorescence values of the four technical replicates of each concentration of standards and samples if the CV is below 15%. If needed, one of the four values can be excluded, which typically affects the outer wells (evaporation and growth differences). If the CV of the remaining three wells still exceeds 15%, that concentration must be disregarded from further calculation.

**▲ CRITICAL STEP** Calculate the data using FU or specific EROD activity (Step 35) depending on the chosen evaluation strategy. The following steps describe the latter.

**35** | For all individual wells, calculate the specific EROD activity ( $\text{FU min}^{-1} \text{mg protein}^{-1}$ ) according to equation 1, where FU is the fluorescence intensity,  $t$  is the time of incubation (that is, 30 min) and  $C_{\text{protein}}$  is the protein content within the well (Step 33).

$$\text{EROD} = \frac{\text{FU}}{t \cdot C_{\text{protein}}} \quad (1)$$

**36** | Plot the TCDD standard curve using four-parameter logistic regression (Hill function) of the data points using equation 2, where top is the  $y$ -value of the upper asymptote, bottom is the  $y$ -value of the lower asymptote, the half-maximal effective concentration ( $\text{EC}_{50}$ ) is the point of inflection and slope is the slope factor, which corresponds to the steepness of the curve at  $\text{EC}_{50}$ . The  $x$  axis corresponds to the concentration (pg per well), and the  $y$  axis corresponds to the specific EROD activity (Step 35). If the curve is plotted with logarithmic  $x$  axis, it will result in a sigmoidal shape. For a good representation of the curve, the value of at least one of the two highest standard concentrations has to be higher than  $\text{EC}_{80}$ .

$$y = \frac{\text{bottom} - \text{top}}{1 + \left(\frac{x}{\text{EC}_{50}}\right)^{\text{slope}}} + \text{top} \quad (2)$$

**37** | Subtract the average specific EROD activity of the negative control from the activities of the standards. The bottom value is then equal to zero. Fit curves by means of least squares fit between expected and measured values of the standard concentrations. For a better fit of the curve especially at lower concentrations, perform weighting of the values through variances. Calculate the weighted sum of squared residuals (WSSR) according to Hädrich *et al.*<sup>52</sup> using equation 3, where  $y_i$  is the measured value,  $\hat{y}$  is the corrected value,  $i = 1$  to  $N$  the different concentrations of the standard and  $w_i$  is the weighting factor that equals the inverse of the variance of  $y_i$ .

$$\text{WSSR} = \sum_{i=1}^N w_i (y_i - \hat{y}_i)^2 \quad (3)$$

**▲ CRITICAL STEP** When you are using different lots of solvents for standards and samples, include an additional solvent control for the samples and correct data accordingly.



## PROTOCOL

**38** | Subtract the average specific EROD activity of the corresponding solvent control from the activities of the samples (Step 35). Use the resulting values to interpolate the corresponding TCDD concentration from the standard curve. Express the results as picograms of BEQ per well and then back-calculate to the corresponding concentration within the original sample.

### ? TROUBLESHOOTING

Troubleshooting advice can be found in **Table 4**.

**TABLE 4** | Troubleshooting table.

Step	Problem	Possible reason	Solution
6, 8, 9	Unevenly distributed fluorescence and/or unevenly distributed protein content CV within one concentration >15%	Cell aggregates	Use more force to dissociate the cell layer and separate cells, ensuring that cell survival remains over 95%  Microscopically verify separation into single cells
		Unevenly distributed cells because of Pipetting error, sedimentation of cells, or central cell cluster	The pipette might need maintenance. Frequently agitate the suspension and dispense it in fewer steps. Do not agitate the plate circularly
12, 13, 15	Variation of fluorescence between samples of the same concentration	Time spent pipetting samples is too long	Time needed for the addition of samples should be minimized to less than 12 min per plate; keep the contact time of sample and standard solution in the reaction vessel below 2 min
	Fluorescence between samples of the same concentration is uneven, although measured protein content is comparable	Uneven distribution of samples or standards during pipetting	The pipette might need maintenance; use an optical pattern to keep track of the dosed wells
	Values are erroneously distributed	Plate layout is not followed properly	If possible, allocate the samples to the correct sample, and repeat the bioassay
16, 21, 22, 29	Activity in the outer wells is higher than that in the inner wells	Evaporation of media	Ventilation is too high, relative humidity is too low; cover the plates
20	Unevenly distributed fluorescence; Unevenly distributed protein content CV within one concentration >15%	Residual liquids within wells; dilution effects	Visually inspect whether the residues are present; if applicable, aspirate the medium from the corresponding wells individually
		Damage of the cell layer	Microscopically evaluate whether damage occurred; if applicable, aspirate more gently
21	Fluorescence is systematically lower or higher in one row per plate	Displacement of an additional volume before first full dispensing volume	If applicable, expel positive displacement before dispensing
22	Nonhomogeneous fluorescence and absorption values show a corresponding gradient	Temperature gradient between methanol, pipette and tips with uneven methanol distribution	Rinse the tips with cool methanol directly before dispensing at least twice to cool down air inside the pipette. Ensure that no dripping occurs and that full volumes are dispensed. Then proceed quickly
28	Protein concentration is systematically higher or lower in one row per plate	Displacement of an additional volume before first full dispensing volume	Expel the residual substrate solution before dispensing
	Unevenly distributed protein values	BCA solution is cloudy or impure	Mix properly and avoid dust from paper towels. Use room-temperature solution
	Protein concentration decreases with column number 2>3>4...	Carryover of protein standard	Row 1 should receive the BCA solution last; rinse the tips with BCA working solution

● **TIMING**

**Days 1–3**

Step 1, sample preparation

Allow 3 days for complete chromatography column preparation, sample cleanup and cleaning. The column chromatography with subsequent volume reduction and solvent transfer can be performed within 8 h. Pure chemicals can be dissolved in a solvent of choice within a few minutes.

**Days 4–6**

Step 2, cytotoxicity evaluation (optional)

The recommended protocol by Repetto *et al.*<sup>54</sup> requires 3 d to obtain results. The total handling time for this protocol is 4 h 15 min.

**Day 7**

Steps 3–9, seeding of cells into tissue culture plates: 1 h–1 h 30 min

Steps 10 and 11, preparation of samples and standards: 1 h 40 min

Step 12, dosing of cells with the samples: 1 h

Steps 13–16, dosing of cells with TCDD standard and solvent control: 15 min

**Day 9**

Steps 17–21, preparation for EROD activity measurement: 1 h

Steps 22 and 23, addition of methanol: 10 min

Steps 24–25, determination of resorufin using fluorescence spectroscopy: 30 min

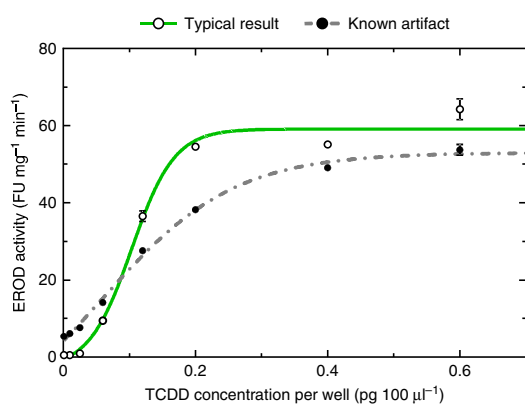
Steps 26–32, measurement of protein amount: 1 h–1 h 40 min

Steps 33–38, Data evaluation: 15 min

**ANTICIPATED RESULTS**

TCDD standard curves show a characteristic shape, and their parameters have been proven to be useful as quality criteria (Fig. 4 and Table 5). If applicable, the requirements of the European Commission should be considered as well<sup>25,26</sup>. The example TCDD concentrations, shown in Table 2, result in S-shaped concentration-response curves with lower and upper asymptotes. For a well-defined upper asymptote, the EC<sub>80</sub> must be reached by at least one of the two highest standard concentrations. During a pre-round robin test, curves without upper asymptotes occurred, which led to erroneous sample results (Fig. 5, 0.5% DMSO+I, artifact). A change in the lot of cells resulted in a regular shape. Higher background fluorescence resulting in decreasing slopes and FU ratios, respectively, can be observed in aged or stressed cells. Possible stressors are cryopreservation, infection with mycoplasma and excessive solvent concentrations or confluence before seeding. Other reasons for similar results are suboptimal measurement conditions (e.g., filter settings), degraded or contaminated ETX stock solution, and incubation with ETX below 30 °C (Step 21). Changes in EC<sub>50</sub> can be signs of alterations in the TCDD standard stock solutions.

Within one test, solvent composition and concentrations should be equal in all wells. Differences can result in variable substance uptake into the cells. Thus, misinterpretation of sample results could be possible (Fig. 5). For several substances, other curve shapes compared with TCDD are known<sup>33,41</sup>. Very high amounts of AhR active



**Figure 4** | Specific EROD activity for TCDD with typical curve shape and parameters. The typical result plot represents a curve of TCDD (EC<sub>50</sub> = 0.11 pg TCDD per well, slope = 3.11, FU ratio = 118). The plot for known artifact represents a curve from a mycoplasma-infected cell line (EC<sub>50</sub> = 0.15 pg TCDD per well, slope = 1.72, FU ratio = 11). Error bars represent the s.d. of *n* = 4 replicates.

**TABLE 5** | Typical curve parameters and quality criteria for TCDD after incubation for 68–72 h in the Micro-EROD bioassay.

Criterion	Acceptable performance	Comments
FU ratio (FU <sub>max</sub> to FU <sub>N</sub> ) <sup>a,b</sup>	>15	Good cell lines show values of 60–120
EC <sub>50</sub> in pg BEQ per well	0.12 ± 0.06	Observed for FU and specific EROD activity, respectively
Slope	3.00 ± 1.00	
Ratio of EC <sub>50</sub> (TCDD) to EC <sub>50</sub> (PCB-126)	0.08 ± 0.03	
CV of triplicates	<15%	In an experienced laboratory, ~5% is typical

<sup>a</sup>FU<sub>max</sub> = Highest measured fluorescence for a standard concentration, alternatively the upper asymptote of the curve. <sup>b</sup>FU<sub>N</sub> = Fluorescence for the negative control.

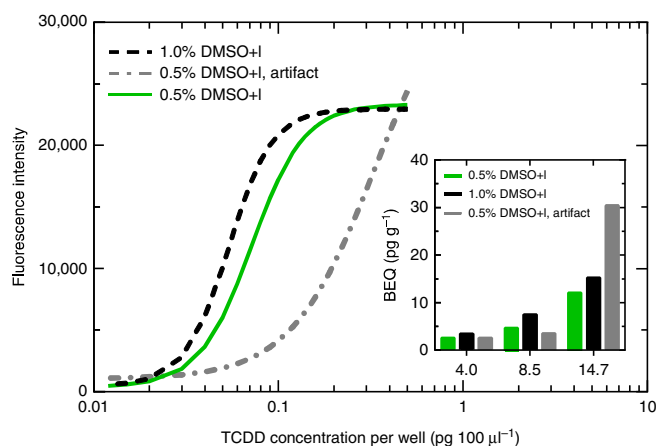


## PROTOCOL

**Figure 5** | Example result from a pre-round robin test. Fluorescence intensity for TCDD using a final solvent concentration of 0.5 and 1%, respectively. Sample results are from fish oil after cleanup with sulfuric acid. The artifact represents an incomplete standard curve (missing upper asymptote). This resulted in an overestimation of the sample's potency for the highest contamination level but in an underestimation of the medium contamination level. DMSO+I, DMSO and isopropanol, 4:1, vol/vol. Error bars represent s.d. of  $n = 4$  replicates.

compounds may lead to cytotoxicity, competing receptor activity or other artifacts. Higher dilution of samples may prove necessary.

When choosing standard substance concentrations, the following criteria should be considered: a minimum of seven concentrations should be included. Two of these concentrations should define the asymptotes of the curves with values of  $<EC_{20}$  and  $>EC_{80}$ , respectively. One of these concentrations should represent the  $EC_{50}$ . At least one concentration should be between  $EC_{20}$  and  $EC_{50}$ . A negative control representing the solvent of the same lot and concentration as for the standard dilution should be included.



For a curve calculation via four-parameter fit, at least six valid concentrations are needed. Make sure that the former quality control parameters presented in **Table 5** are valid. Always check data from newly prepared standards with a verified working stock. The relative difference between identical concentrations should be  $<15\%$ .

**ACKNOWLEDGMENTS** This protocol was applied within the §64-LFGB working group 'Wirkungsbezogene Analytik' (effect directed analysis) for a pre-round robin test. The authors acknowledge the federal office of Consumer Protection and Food Safety (BVL) for their support in this project. The protocol was used and further adopted in context of the project 'DioRAMA—Assessment of the dioxin-like activity in sediments and fish for sediment evaluation' that received funds from the German Federal Ministry of Transport and Digital Infrastructure. The authors acknowledge the German National Academic Foundation ('Studienstiftung des deutschen Volkes') for a personal scholarship granted to M.B. H.H. was supported by the Chinese 111 Program (College of Environmental Science and Engineering and Key Laboratory of Yangze Water environment, Ministry of Education, Tongji University).

**AUTHOR CONTRIBUTIONS** All authors contributed extensively to the work presented in this paper, read and edited it, and gave their final approval for publication. A.S. and M.B. have contributed equally to the work and share first authorship. A.S. has adopted the protocol from an initial version of I.T., G.G. and B.T., and established it together with K.W., L.N. and K.E. in our laboratory. M.B. and A.S. wrote the manuscript and compiled the protocol. T.-B.S. B.T., S.B., G.R. and H.H. gave technical support and conceptual advice.

**COMPETING FINANCIAL INTERESTS** The authors declare no competing financial interests.

Reprints and permissions information is available online at <http://www.nature.com/reprints/index.html>.

1. Sinkkonen, S. & Paasivirta, J. Degradation half-life times of PCDDs, PCDFs and PCBs for environmental fate modeling. *Chemosphere* **40**, 943–949 (2000).
2. Weber, R. *et al.* Dioxin- and POP-contaminated sites—contemporary and future relevance and challenges. *Environ. Sci. Pollut. Res. Int.* **15**, 363–393 (2008).
3. Brack, W. Effect-directed analysis: a promising tool for the identification of organic toxicants in complex mixtures? *Anal. Bioanal. Chem.* **377**, 397–407 (2003).
4. Theelen, R.M.C., Liem, A.K.D., Slob, W. & Van Wijnen, J.H. Intake of 2,3,7,8-chlorine-substituted dioxins, furans, and planar PCBs from food in the Netherlands: Median and distribution. *Chemosphere* **27**, 1625–1635 (1993).
5. Spagnoli, J.J. & Skinner, L.C. PCBs in fish from selected waters of New York State. *Pestic. Monit. J.* **11**, 69–87 (1977).
6. La Rocca, C. & Mantovani, A. From environment to food: the case of PCB. *Ann. Ist. Super. Sanità* **42**, 410–416 (2006).
7. Denison, M.S. & Heath-Pagliuso, S. The Ah receptor: a regulator of the biochemical and toxicological actions of structurally diverse chemicals. *Bull. Environ. Contam. Toxicol.* **61**, 557–568 (1998).
8. Denison, M.S. & Nagy, S.R. Activation of the aryl hydrocarbon receptor by structurally diverse exogenous and endogenous chemicals. *Annu. Rev. Pharmacol. Toxicol.* **43**, 309–334 (2003).
9. Brouwer, A. *et al.* Functional aspects of developmental toxicity of polyhalogenated aromatic hydrocarbons in experimental animals and human infants. *Eur. J. Pharmacol.* **293**, 1–40 (1995).
10. Van den Berg, M. *et al.* Toxic equivalency factors (TEFs) for PCBs, PCDDs, PCDFs for humans and wildlife. *Environ. Health Perspect.* **106**, 775–792 (1998).
11. Poland, A. & Knutson, J.C. 2,3,7,8-tetrachlorodibenzo-*p*-dioxin and related halogenated aromatic hydrocarbons: examination of the mechanism of toxicity. *Annu. Rev. Pharmacol. Toxicol.* **22**, 517–554 (1982).
12. Giesy, J.P., Ludwig, J.P. & Tillitt, D.E. Deformities in birds of the Great Lakes region. Assigning causality. *Environ. Sci. Technol.* **28**, 128A–135A (1994).
13. Dencker, L. The role of receptors in 2,3,7,8-tetrachlorodibenzo-*p*-dioxin (TCDD) toxicity. *Arch. Toxicol. Suppl.* **8**, 43–60 (1985).
14. Huang, H. & Buekens, A. On the mechanisms of dioxin formation in combustion processes. *Chemosphere* **31**, 4099–4117 (1995).
15. Lallas, P.L. The Stockholm Convention on persistent organic pollutants. *Am. J. Int. Law* 692–708 (2001).
16. Covaci, A. *et al.* The Belgian PCB/dioxin crisis—8 years later: an overview. *Environ. Toxicol. Pharmacol.* **25**, 164–170 (2008).
17. Abraham, K. *et al.* Review: incidents regarding dioxin in feedstuff in Germany 2011—a consumer health risk? *Arch. Lebensmittelhyg.* **62**, 108–115 (2011).
18. European Commission. *The Rapid Alert System for Food and Feed 2013: Annual Report*. Report No. 978-92-79-38196-6, (OP, 2014).
19. European Commission. *The Rapid Alert System for Food and Feed 2012: Annual Report*. Report No. 978-92-79-28611-7, (OP, 2013).
20. European Commission. Communication of 16 April 2002 from the Commission to the Council, the European parliament, the Economic and Social Committee and the Committee of the regions: Towards a thematic strategy for soil protection. *Official Journal of the European Union, L series (OJ L)* **179** (2002).
21. European Commission. Commission Regulation (EC) No. 1881/2006 of 19 December 2006 setting maximum levels for certain contaminants in foodstuffs. *OJ L* **364** (2006).
22. European Commission. Commission Recommendation (EC) No. 711/2013 of 3 December 2013 on the reduction of the presence of dioxins, furans and PCBs in feed and food. *OJ L* **323** (2013).

23. European Commission. Commission Recommendation (EC) No. 663/2014 of 11 September 2014 amending the Annex to Recommendation 2013/711/EU on the reduction of the presence of dioxins, furans and PCBs in feed and food. *OJ L* **272** (2014).
24. European Commission. Commission Regulation (EC) No. 277/2012 of 28 March 2012 amending Annexes I and II to Directive 2002/32/EC of the European Parliament and of the Council as regards maximum levels and action thresholds for dioxins and polychlorinated biphenyls. *OJ L* **91** (2012).
25. European Commission. Commission Regulation (EC) No. 589/2014 of 2 June 2014 laying down methods of sampling and analysis for the control of levels of dioxins, dioxin-like PCBs and non-dioxin-like PCBs in certain foodstuffs and repealing Regulation (EU) No. 252/2012. *OJ L* **164** (2014).
26. European Commission. Commission Regulation (EC) No 278/2012 of 28 March 2012 amending Regulation (EC) No. 152/2009 as regards the determination of the levels of dioxins and polychlorinated biphenyls. *OJ L* **91** (2012).
27. Jordaan, I. *et al.* The Contribution of dioxin-like compounds from platinum mining and processing samples. *Miner. Eng.* **20**, 191–193 (2007).
28. Nieuwoudt, C. *et al.* A pilot-study of dioxin-like compounds in soil and sediment from residential and industrial areas in central South Africa. *Chemosphere* **76**, 744–783 (2008).
29. Wölz, J. *et al.* Changes in toxicity and Ah receptor agonist activity of suspended particulate matter during flood events at the rivers Neckar and Rhine—a mass balance approach using *in vitro* methods and chemical analysis. *Environ. Sci. Pollut. Res.* **15**, 536–553 (2008).
30. Keiter, S. *et al.* Activities and identification of aryl hydrocarbon receptor agonists in sediments from the Danube river. *Anal. Bioanal. Chem.* **390**, 2009–2019 (2008).
31. Olsman, H. *et al.* Relative differences in aryl hydrocarbon receptor-mediated response for 18 polybrominated and mixed halogenated dibenzo-*p*-dioxins and -furans in cell lines from four different species. *Environ. Toxicol. Chem.* **26**, 2448–2454 (2007).
32. Wernersson, A.-S. *et al.* The European technical report on aquatic effect-based monitoring tools under the water framework directive. *Env. Sci. Eur.* **27**, 7 (2015).
33. Behnisch, P.A., Hosoe, K. & Sakai, S.-i. Combinatorial bio/chemical analysis of dioxin and dioxin-like compounds in waste recycling, feed/food, humans/wildlife and the environment. *Environ. Int.* **27**, 495–519 (2001).
34. Eichbaum, K. *et al.* *In vitro* bioassays for detecting dioxin-like activity—application potentials and limits of detection, a review. *Sci. Total Environ.* **487**, 37–48 (2014).
35. Van den Berg, M. *et al.* The 2005 World Health Organization reevaluation of human and mammalian toxic equivalency factors for dioxins and dioxin-like compounds. *Toxicol. Sci.* **93**, 223–241 (2006).
36. Novotna, A., Pavek, P. & Dvorak, Z. Novel stably transfected gene reporter human hepatoma cell line for assessment of aryl hydrocarbon receptor transcriptional activity: construction and characterization. *Environ. Sci. Technol.* **45**, 10133–10139 (2011).
37. Murk, A.J. *et al.* Chemical-activated Luciferase Gene Expression (CALUX): a novel *in vitro* bioassay for Ah receptor active compounds in sediments and pore water. *Fundam. Appl. Toxicol.* **33**, 149–160 (1996).
38. Pitot, H.C., Peraino, C., Morse, P.A. Jr. & Potter, V.R. Hepatomas in tissue culture compared with adapting liver *in vivo*. *J. Natl. Cancer Inst. Monogr.* **13**, 229–245 (1964).
39. Schwirzer, S.M. *et al.* Establishment of a simple cleanup procedure and bioassay for determining 2,3,7,8-tetrachlorodibenzo-*p*-dioxin toxicity equivalents of environmental samples. *Ecotoxicol. Environ. Saf.* **41**, 77–82 (1998).
40. Thiem, I., Boehmler, G. & Thoms, B. Modification of the micro EROD-bioassay and validation for routine analysis demonstrated for beef and milk. *Organohalogen Compd.* **76**, 161–164 (2014).
41. Thiem, I. & Boehmler, G. Step-by-step analysis of recovery rates of dioxin-like compounds in beef using the micro-EROD-bioassay. *Organohalogen Compd.* **73**, 2128–2131 (2011).
42. Thiem, I. & Boehmler, G. Model for interpretation of coupled data from biotests based on the dioxin-like response of Ah-receptors. *Organohalogen Compd.* **73**, 2124–2127 (2011).
43. Donato, M.T., Castell, J.V. & Gómez-Lechón, M.J. A rapid and sensitive method for measuring monoxygenase activities in hepatocytes cultured in 96-well plates. *J. Tissue Cult. Methods* **14**, 153–157 (1992).
44. Donato, M.T., Gomez-Lechon, M.J. & Castell, J.V. A microassay for measuring cytochrome P450IA1 and P450IIB1 activities in intact human and rat hepatocytes cultured on 96-well plates. *Anal. Biochem.* **213**, 29–33 (1993).
45. Safe, S. Development of bioassays and approaches for the risk assessment of 2,3,7,8-tetrachlorodibenzo-*p*-dioxin and related compounds. *Environ. Health Perspect.* **101** (suppl. 3): 317–325 (1993).
46. Tillitt, D.E., Giesy, J.P. & Ankley, G.T. Characterization of the H4IIE rat hepatoma cell bioassay as a tool for assessing toxic potency of planar halogenated hydrocarbons in environmental samples. *Environ. Sci. Technol.* **25**, 87–92 (1991).
47. Sanderson, J.T. *et al.* Comparison of Ah receptor-mediated luciferase and ethoxyresorufin-*O*-deethylase induction in H4IIE cells: Implications for their use as bioanalytical tools for the detection of polyhalogenated aromatic hydrocarbons. *Toxicol. Appl. Pharmacol.* **137**, 316–325 (1996).
48. Whyte, J., Schmitt, C. & Tillitt, D. The H4IIE cell bioassay as an indicator of dioxin-like chemicals in wildlife and the environment. *Crit. Rev. Toxicol.* **34**, 1–83 (2004).
49. Gizzi, G., Hoogenboom, L.A.P., Von Holst, C., Rose, M. & Ankam, E. Determination of dioxins (PCDDs/PCDFs) and PCBs in food and feed using the DR CALUX (R) bioassay: results of an international validation study. *Food Addit. Contam.* **22**, 472–481 (2005).
50. Safe, S., Rodriguez, L. & Goldstein, L. Toxic equivalency factor approach for risk assessment of combustion by-products. *Toxicol. Environ. Chem.* **49**, 181–191 (1995).
51. Villeneuve, D.L., Blankenship, A.L. & Giesy, J.P. Derivation and application of relative potency estimates based on *in vitro* bioassay results. *Environ. Toxicol. Chem.* **19**, 2835–2843 (2000).
52. Hädrich, J. *et al.* Considerations on the working range in bioassays dose-response curves: curve fit and assay background response. *Organohalogen Compd.* **74**, 177–181 (2012).
53. Radenac, G., Coteur, G., Danis, B., Dubois, P. & Warnau, M. Measurement of EROD activity: caution on spectral properties of standards used. *Mar. Biotechnol.* **6**, 307–311 (2004).
54. Repetto, G., del Peso, A. & Zurita, J.L. Neutral red uptake assay for the estimation of cell viability/cytotoxicity. *Nat. Protoc.* **3**, 1125–1131 (2008).
55. Smith, P.K. *et al.* Measurement of protein using bicinchoninic acid. *Anal. Biochem.* **150**, 76–85 (1985).
56. Hanberg, A., Stahlberg, M., Georgellis, A., de Wit, C. & Ahlberg, U.G. Swedish dioxin survey: evaluation of the H-4-IIE bioassay for screening environmental samples for dioxin-like enzyme induction. *Pharmacol. Toxicol.* **69**, 442–449 (1991).
57. Peters, A. *et al.* Effects of polybrominated diphenyl ethers on basal and TCDD-induced ethoxyresorufin activity and cytochrome P450-1A1 expression in MCF-7, HepG2, and H4IIE cells. *Toxicol. Sci.* **82**, 488–496 (2004).
58. Schmitz, H.-J. *et al.* CYP1A1-inducing potency in H4IIE cells and chemical composition of technical mixtures of polychlorinated biphenyls. *Environ. Toxicol. Pharmacol.* **1**, 73–79 (1996).
59. Behnisch, P.A., Hosoe, K., Brouwer, A. & Sakai, S.-i. Screening of dioxin-like toxicity equivalents for various matrices with wildtype and recombinant rat hepatoma H4IIE cells. *Toxicol. Sci.* **69**, 125–130 (2002).
60. Gale, R.W., Long, E.R., Schwartz, T.R. & Tillitt, D.E. Evaluation of planar halogenated and polycyclic aromatic hydrocarbons in estuarine sediments using ethoxyresorufin-*O*-deethylase Induction of H4IIE cells. *Environ. Toxicol. Chem.* **19**, 1348–1359 (2000).
61. Li, W., Wu, W.Z., Barbara, R.B., Schramm, K.W. & Ketrup, A. A new enzyme immunoassay for PCDD/F TEQ screening in environmental samples: comparison to micro-EROD assay and to chemical analysis. *Chemosphere* **38**, 3313–3318 (1999).
62. Hewitt, L.M. *et al.* Characteristics of ligands for the Ah receptor and sex steroid receptors in hepatic tissues of fish exposed to bleached kraft mill effluent. *Environ. Sci. Technol.* **34**, 4327–4334 (2000).
63. Jiang, Q.T. *et al.* Human health risk assessment of organochlorines associated with fish consumption in a coastal city in China. *Environ. Pollut.* **136**, 155–165 (2005).
64. Summer, C.L., Bursian, S.J. & Kubiak, T.J. Effects induced by feeding organochlorine contaminated carp from Saginaw Bay, Lake Huron to laying White Leghorn hens. I Effects on health of adult hens egg production and fertility. *J. Toxicol. Environ. Health* **49**, 389–408 (1996).
65. Valdovinoso, C., Sotomayora, P., Stecha, R., Schoffera, J. & Bustos-López, C. Application of the EROD-H4IIE bioassay for the determination of dioxins in pork in comparison to high resolution gas chromatography coupled to high resolution mass spectrometry. *Arch. Med. Vet.* **45**, 173–181 (2013).
66. Schramm, K.W., Klimm, C., Hofmaier, A. & Ketrup, A. Comparison of dioxin-like-response *in vitro* and chemical analysis of emissions and materials. *Chemosphere* **42**, 551–557 (2001).

ARTICLE

Received 8 Sep 2013 | Accepted 22 Jan 2014 | Published 13 Feb 2014

DOI: 10.1038/ncomms4297

OPEN

# Twinning-like lattice reorientation without a crystallographic twinning plane

Bo-Yu Liu<sup>1</sup>, Jian Wang<sup>2</sup>, Bin Li<sup>3</sup>, Lu Lu<sup>4</sup>, Xi-Yan Zhang<sup>5</sup>, Zhi-Wei Shan<sup>1</sup>, Ju Li<sup>1,6</sup>, Chun-Lin Jia<sup>4</sup>, Jun Sun<sup>1</sup> & Evan Ma<sup>1,7</sup>

Twinning on the  $\{10\bar{1}2\}$  plane is a common mode of plastic deformation for hexagonal-close-packed metals. Here we report, by monitoring the deformation of submicron-sized single-crystal magnesium compressed normal to its prismatic plane with transmission electron microscopy, the reorientation of the parent lattice to a 'twin' lattice, producing an orientational relationship akin to that of the conventional  $\{10\bar{1}2\}$  twinning, but without a crystallographic mirror plane, and giving plastic strain that is not simple shear. Aberration-corrected transmission electron microscopy observations reveal that the boundary between the parent lattice and the 'twin' lattice is composed predominantly of semicoherent basal/prismatic interfaces instead of the  $\{10\bar{1}2\}$  twinning plane. The migration of this boundary is dominated by the movement of these interfaces undergoing basal/prismatic transformation via local rearrangements of atoms. This newly discovered deformation mode by boundary motion mimics conventional deformation twinning but is distinct from the latter and, as such, broadens the known mechanisms of plasticity.

<sup>1</sup>Center for Advancing Materials Performance from the Nanoscale (CAMP-Nano) and Hysitron Applied Research Center in China (HARCC), State Key Laboratory for Mechanical Behavior of Materials, Xi'an Jiaotong University, Xi'an 710049, China. <sup>2</sup>MST-8, Los Alamos National Laboratory, Los Alamos, New Mexico 87545, USA. <sup>3</sup>Center for Advanced Vehicular Systems, Mississippi State University, Starkville, Mississippi 39762, USA. <sup>4</sup>International Center of Dielectric Research, Xi'an Jiaotong University, Xi'an 710049, China. <sup>5</sup>School of Materials Science and Engineering, Chongqing University, Chongqing 400044, China. <sup>6</sup>Department of Nuclear Science and Engineering and Department of Materials Science and Engineering, Massachusetts Institute of Technology, Cambridge, Massachusetts 02139, USA. <sup>7</sup>Department of Materials Science and Engineering, Johns Hopkins University, Baltimore, Maryland 21218, USA. Correspondence and requests for materials should be addressed to Z.-W.S. (email: zwshan@mail.xjtu.edu.cn).

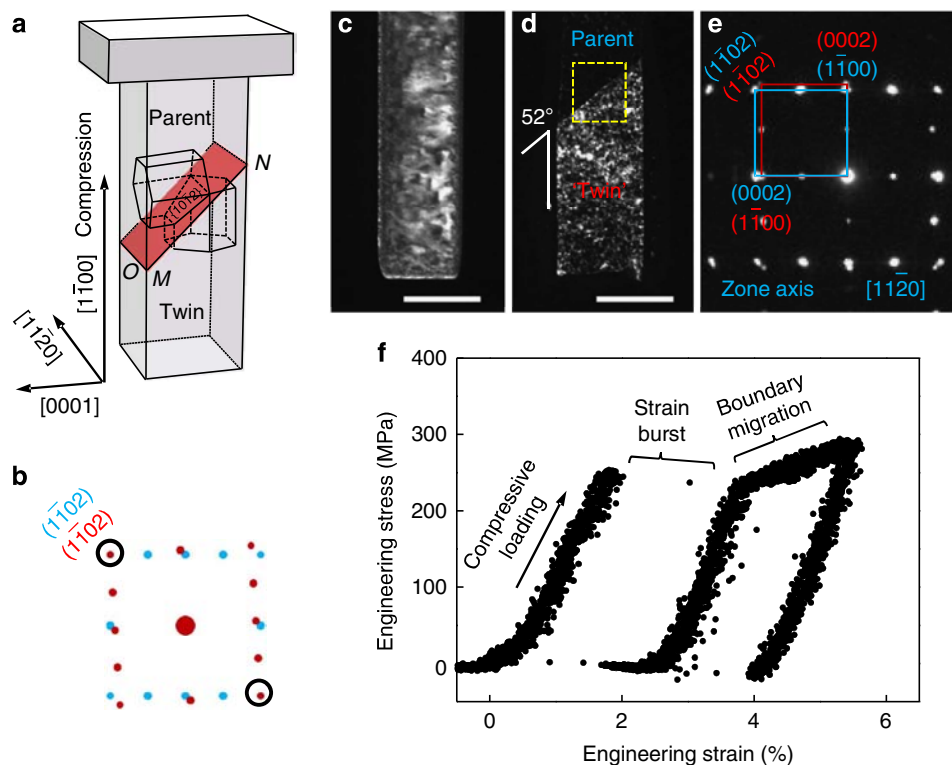
Deformation twinning (DT) is a major mode of plastic deformation for metals with the hexagonal-close-packed (HCP) structure<sup>1–6</sup>, owing to their very limited number of slip systems available for dislocation glide. However, twinning mechanisms for such HCP metals are much less understood when compared with face-centred-cubic metals, for which twin boundary (TB) migration is well established to be accomplished via the glide of Shockley partial dislocations on the twinning plane<sup>1,5,7</sup>. For the  $\{10\bar{1}2\}$  DT that is prevalent in almost all HCP metals, both mobile disconnections<sup>8–15</sup> acting as twinning dislocations and atomic shuffling<sup>16–21</sup> have been argued to be the dominating and rate-limiting element. These debates suggest that there is a pressing need to better understand the details of the deformation dynamics in HCP-structured metals experimentally.

In this work, we choose to study submicron-sized single-crystal pure magnesium. On one hand, submicron-sized samples are sufficiently thin to be electron transparent, which allows us to monitor and record the nucleation and propagation of DT at high spatial resolution. On the other hand, submicron-sized crystals may be much stronger than their bulk counterparts, according to the well-established tenet of ‘smaller is stronger’. Consequently, our study may reveal unusual deformation mechanisms under high-stress conditions, which may also exist in bulk magnesium due to local stress concentrators such as grain boundary or precipitates. The samples were fabricated using focused ion beam (FIB) micromachining and then tested inside a transmission electron microscopy (TEM) employing the Hysitron PI95 Picoindenter<sup>22</sup>, which enables one-to-one correspondence between the external applied stress/strain and the microstructure evolution of the deforming material. The sample/loading orientation is shown schematically in Fig. 1a. When viewed along the  $[1\bar{1}20]$  direction, the angle between the trace of

the  $(1\bar{1}02)$  plane and the loading axis is  $43.1^\circ$ . The  $\{10\bar{1}2\}$  DT is expected to be activated in this configuration when the specimen is compressed.

## Results

**‘Deformation twinning’.** For the testing condition in Fig. 1a,  $\{10\bar{1}2\}$  ‘deformation twinning’ appeared to be all that had happened, at the first glance. One typical example is shown in Fig. 1c–f. The initial dimensions of this sample are  $400 \times 500 \times 1,600 \text{ nm}^3$  (Fig. 1c). During compression, a strain burst ( $\sim 2\%$ ) set in at  $\sim 250 \text{ MPa}$  (Fig. 1f), which is much higher than the yield strength of bulk single-crystal magnesium with same orientation. At the same time, a twin-like feature formed. The fast release of the accumulated elastic energy made it difficult to differentiate the ‘twin’ nucleation and the following quick growth process. However, the measured strain generated by the ‘twinned’ volume during the strain burst agrees well with that predicted by theoretical calculations. As the test was controlled under a fixed displacement rate, the flat punch probe detached from the sample at the moment of the burst, which in turn slowed down and stopped the ‘twin’ growth temporally. Correspondingly, an apparently straight boundary running across the gauge part of the sample can be seen clearly. After the flat punch probe caught up with the sample to continue the compression, this boundary migrated continuously until the end of the programmed total displacement (Supplementary Movie 1). The trace of the boundary looks quite smooth and straight (Fig. 1d) at this magnification, as expected for the TB of the  $\{10\bar{1}2\}$  DT. The DT is supposed to generate a plastic strain of  $\sim 6\%$ ; here the strain burst and the following boundary migration swept about 60% of the sample in its length direction (Fig. 1d), such that



**Figure 1 | *In situ* compression test on a submicron-sized single-crystal Mg pillar.** (a) Schematic illustration of the crystal, compression-loaded in  $[1\bar{1}00]$  orientation. The  $\{10\bar{1}2\}$  plane is highlighted in red. (b) SADP for ideal  $\{10\bar{1}2\}$  twins. (c,d) Dark-field TEM images showing the pillar before and after loading, respectively. Scale bars, 400 nm. (e) SADP taken from the framed area, demonstrating that  $\{10\bar{1}2\}$  diffraction spots are separated instead of overlapping with each other. The zone axis is  $[1\bar{1}20]$  for parent lattice. (f) The corresponding stress-strain curve.

the plastic strain generated should be ~3.6%, as found in the experiment data in Fig. 1f.

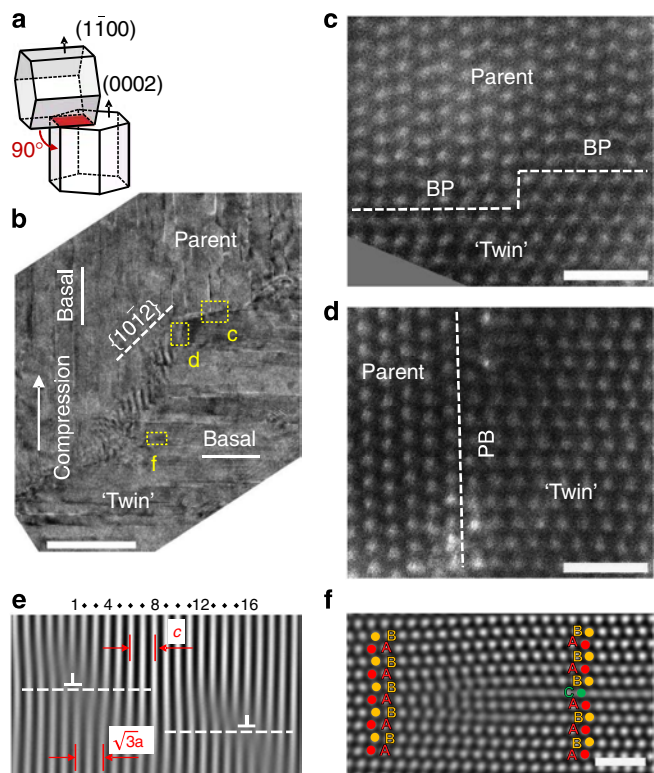
However, a close examination revealed that several features are inconsistent with {10 $\bar{1}2$ } deformation twinning. First, the inclination angle (52°) of the boundary shows a pronounced deviation from that expected from the {10 $\bar{1}2$ } plane, by as much as 9°. Second, for {10 $\bar{1}2$ } DT, the {10 $\bar{1}2$ } diffraction spots should overlap in the corresponding selected area diffraction pattern (SADP), as shown in Fig. 1b. However, the SADP acquired across the boundary shows that the {10 $\bar{1}2$ } diffraction spots are actually separated (Fig. 1e), and the angle between the basal planes of the parent and the deformed regions is close to 90° rather than the 86.3° expected for {10 $\bar{1}2$ } DT. It thus appears that while we seem to have activated {10 $\bar{1}2$ } DT, the reoriented lattice in the deformed region does not hold a rigorously crystallographic (rational) orientational relationship with the parent lattice as expected for {10 $\bar{1}2$ } twinning.

**Basal/prismatic interfaces.** Figure 2a schematically illustrates the actual orientational relationship as indicated by the SADP in Fig. 1e. To characterize the atomic structure of the boundary (marked by red colour), the sample shown in Fig. 1d was further thinned and examined inside a spherical aberration-corrected TEM. The high-resolution TEM observations reveal that the straight boundary in Fig. 1d in fact has a rugged structure

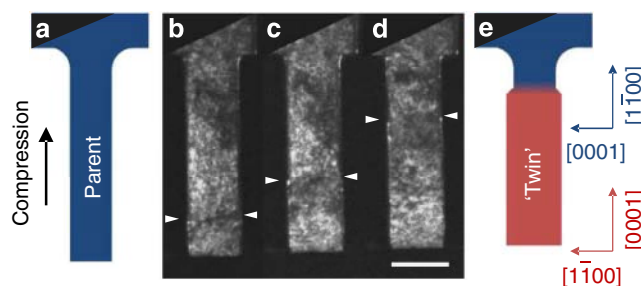
(Fig. 2b) throughout the entire boundary. The Moiré fringes observed at the boundary areas are a result of the overlap between two crystals, the parent and the ‘twin’ regions. On the atomic level, the ‘twin’/parent boundary actually consists of two types of interfaces: basal/prismatic interface (Fig. 2c) and prismatic/basal interface (Fig. 2d). The existence of such interfaces was predicted recently by computer simulations<sup>23,24</sup>. These two types of interfaces, perpendicular to each other, constitute a stepped boundary between the deformed and undeformed regions. In other words, while {10 $\bar{1}2$ } TBs are present in some local regions, along the boundary the {10 $\bar{1}2$ } segments are few and far between. Zooming in down to the atomic level, the majority of the boundary is instead composed of (pairs of) basal/prismatic and prismatic/basal interfaces. This is also true for samples deformed in tensile tests (loaded along the [0001] direction), see Supplementary Fig. 1. There is no rational crystallographic orientational mirror symmetry established across these basal/prismatic interfaces. The boundary is therefore not a TB *per se*, and the 90° twin-like orientation relationship described in the preceding paragraph is established via reorientation actions at the basal/prismatic interfaces rather than on a crystallographic, invariant twinning plane. However, considering that the atomistically wavy boundary appears ‘straight’ at low magnifications (Fig. 1) and the orientation relationship between the parent and ‘twin’ regions is close to that in {10 $\bar{1}2$ } DT, we refer the two regions in all the figures of this paper as the parent lattice and the ‘twin’ lattice, respectively.

The basal/prismatic and prismatic/basal interfaces are semi-coherent because of the lattice mismatch, as confirmed by the existence of misfit dislocations at the interfaces: the dislocation separation spacing is counted to be 15 lattice fringes (Fig. 2e). In many regions, the basal plane of the parent lattice is not exactly parallel to the prismatic plane of the ‘twin’ lattice: this is a result of local strains near the boundary or other defects (see Supplementary Note 1 and Supplementary Table 1). Basal stacking faults were observed on both sides of the boundary, but the density is much lower in the parent region than that in the ‘twinned’ region. Figure 2f shows a high-resolution image of one of such stacking faults.

**‘Twin’ propagation.** We found that the lattice reorientation is reversible when the loading direction was switched from tensile to compression. Most surprisingly, we found that the ‘twin’ boundary can propagate without an obvious twinning shear, as shown in Fig. 3. This sample was initially in dog-bone shape and was deformed under uniaxial tension along the [0001] direction. This led to the parent-to-‘twin’ conversion, much like the case of



**Figure 2 | Atomic structure of the deformation boundary.** (a) Schematic showing the orientation relationship between the ‘twin’ and its parent lattice. (b) High-resolution TEM image showing the rugged boundary (see atomic resolution images in c and d), with stacking faults on both sides of the boundary. Scale bar, 50 nm. (c,d) Scanning TEM images of typical basal/prismatic interface and prismatic/basal interface, respectively. (e) One-dimensional lattice fringe image obtained by a fast Fourier transform filtering process showing two misfit dislocations at the basal/prismatic interface. (f) A noise-filtered image of a stacking fault in the deformed volume. Scale bars, 1 nm (c,d,f). The e-beam direction is [11 $\bar{2}0$ ].



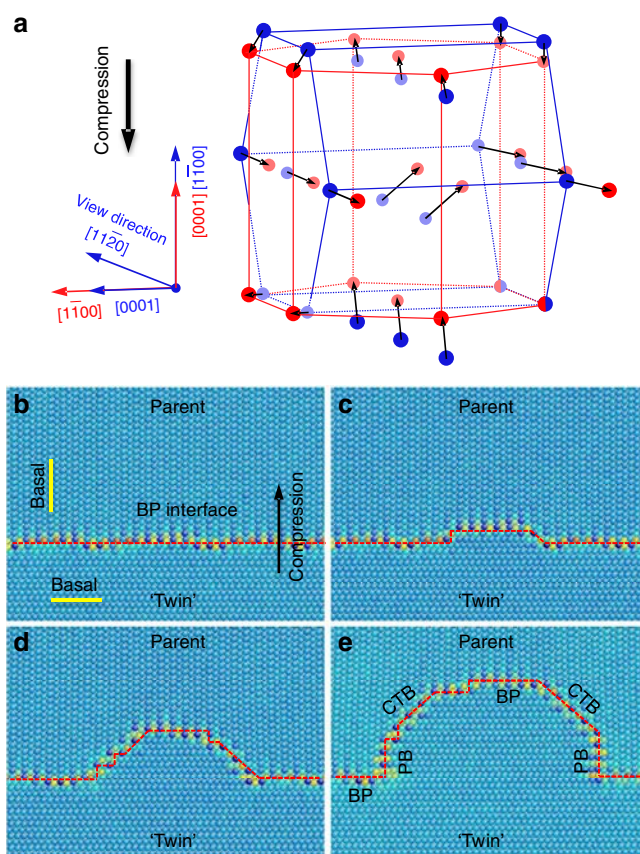
**Figure 3 | Basal/prismatic interfaces mediated boundary migration.** Panels a and e Schematically showing the sample condition before and after the compression test, respectively. Panels b–d are snapshots extracted from the recorded movie showing the boundary (marked by a pair of white arrows) movement with time. Note that the sample swells towards both sides and shrink in the loading direction. Scale bar, 400 nm.

compression in the direction perpendicular to [0001] (the scenario described in Fig. 1). We then took the ‘twinned’ sample out of the TEM and made it into a pillar with FIB by chopping off the T-shaped free end (Fig. 3a). The pillar was then subjected to programmed compressive loading (Fig. 3b), now along the direction perpendicular to the (newly formed) prismatic plane. The orientation is now the same as that in Fig. 1 and the only difference is that the sample has already gone through the basal/prismatic transformation once to reach this orientation. The ensuing deformation is therefore a reverse transformation, or ‘de-twinning’, process (see diffraction patterns in Supplementary Fig. 2). As expected, following the nucleation of ‘de-twinning’ at the free end, the deformation boundary propagated gradually towards the root part of the pillar along with compression deformation, with the moving boundary nearly perpendicular to the loading axis. Most interestingly, the ‘de-twinned’ part (Fig. 3e) uniformly swelled towards both sides of the pillar, rather than sheared in a specific direction, during the entire deformation process (Supplementary Movie 2). The observation in Fig. 3 and Supplementary Movie 2 demonstrates that the propagation of the boundary is not coupled to simple shear, but rather, tetragonal compression. This is in sharp contrast with any DT mechanism where the lattice reorientation is carried predominantly by twin shear.

**Twinning-like lattice reorientation.** To recap, the interesting finding from our experiments is that in many regions a transformation process can take over to directly convert basal plane to prismatic plane, and *vice versa*. Although the chain of transformation events at numerous basal/prismatic and prismatic/basal interfaces achieves a crystal reorientation that appears not far off from the  $\{10\bar{1}2\}$  DT, a close look probing the boundary reveals that this net result is accomplished through a distinctly different mechanism. While DT requires a single, crystallographic mirror plane (the invariant plane), the new deformation mode relies on coordinated motion of basal/prismatic interface couples, without establishing crystallographic mirror orientational relationship right across the interfaces. The combination of a large number of basal/prismatic interfaces intermixed with prismatic/basal interfaces, with varying segment lengths, can lead to different inclination angles when viewed from a distance, including those (such as  $52^\circ$ ) that deviate considerably from what is known for the  $\{10\bar{1}2\}$  DT.

## Discussion

Our newly discovered deformation mode mimics conventional DT but is distinct in two important aspects. A textbook definition of DT is that it achieves simple shear of a crystal, while possessing a crystallographic invariant plane or twinning plane. Our deformation mode can achieve tetragonal compression (Supplementary Movie 2) instead of simple shear, and it does not possess a crystallographic characteristic plane seen at the larger-length scale. In term of the atomistic mechanism for lattice reorientation, neither the well-known pole mechanism<sup>1,3</sup> nor the disconnection mechanism<sup>8–15</sup> for DT can explain the nucleation, propagation and structure of the deformation boundary observed in this work. While further studies are clearly needed, in the following we discuss the mechanism in a qualitative manner. Two HCP frames are schematically shown in Fig. 4a, with one HCP embryo parasitizing inside another. The red and blue symbols outline the ‘twin’ and its parent lattice, respectively. The two structures are rotated  $90^\circ$  relative to one another. When a sufficiently high compressive stress is applied normal to the prismatic plane, the blue HCP can transform to the red one. The arrows indicate the possible route for the required atomic



**Figure 4 | Atomic view of the basal/prismatic transformation.** (a) The parent HCP frame (blue) and ‘twin’ HCP frame (red) as well as their possible transformation route via shuffling atomic rearrangements. The right-bottom atoms (half blue and half red) were chosen to be the reference point. (b–e) MD simulations showing the migration of basal/prismatic (BP) and prismatic/basal (PB) interfaces under compressive loading. The coherent TB (CTB) is present despite of the  $90^\circ$  (rather than  $86^\circ$ ) lattice orientational relationship, because there are coexisting dislocations at the boundary. See Supplementary Information for simulation details.

rearrangements. The prismatic planes in the parent body transform into the basal planes of the new lattice, creating the basal/prismatic interface with misfit dislocations. Such a mechanism and the migration of the basal/prismatic interfaces can in fact be visualized in molecular dynamics (MD) simulations (Fig. 4b–e). When a 1.5-GPa compressive stress is applied perpendicular to a basal/prismatic interface, we observe a disconnection with a height of two atomic layers (Fig. 4c) moving upwards with the step of  $2n$  atomic layers (where  $n$  is an integer). Concurrent with this DT, the nearby basal/prismatic interface also migrates, with accompanying formation of prismatic/basal interface, which is what is observed in our experimental samples.

The next question to address is why the basal/prismatic transformation mode becomes prevalent in our submicron samples. We note that, as expected from the well-established tenet of ‘smaller is stronger’, the stress required for activating twinning dislocations on  $\{10\bar{1}2\}$  planes will increase with decreasing sample size<sup>25</sup>. The availability of disconnections assisting DT is limited in small-volume samples. Since our crystal is compressed perpendicular to its prismatic plane, the high normal stress facilitates the short-range rearrangement of atoms to form a new basal plane. This may render basal/prismatic



conversion kinetically more favourable than the motion of the coherent  $\{10\bar{1}2\}$  interface, although the latter has a lower interfacial energy ( $125 \text{ mJ m}^{-2}$ ) relative to the basal/prismatic interface ( $170 \text{ mJ m}^{-2}$ ). As such, the basal/prismatic conversion at numerous basal/prismatic interfaces assists and accommodates the DT to produce plastic strain. Our submicron-sized sample provides a high free-surface-to-volume ratio, possibly making it easier to accommodate the strains associated with the lattice reorientation and the misfit dislocations generated at the basal/prismatic interface. However, it is noteworthy that the basal/prismatic interfaces were also observed in a bulk magnesium alloy deformed under high strain rates (see Supplementary Discussion and Supplementary Fig. 3). This suggests that the basal/prismatic conversion mode may be activated under many high-stress conditions and thus be of general importance in HCP metals.

The newly revealed transformations at the basal/prismatic interfaces may also have implications for alloy design. For example, basal/prismatic interfaces may have different propensity for trapping solute atoms<sup>26</sup> when compared with coherent twin boundaries. The propagation of basal/prismatic interface may be less sensitive to precipitates that are traditionally important for age hardening<sup>27</sup>.

Before closing, we point out several open questions for future exploration. First, Yu *et al.*<sup>28</sup> carried out similar tests on single-crystal magnesium in a similar size range, but they observed populous  $\{10\bar{1}2\}$  coherent twin boundaries. Further experiments are necessary to clarify whether the difference is related to compositional difference. Second, copious stacking faults parallel to the basal planes have been observed on both sides of the boundary (in the deformed and undeformed regions). It remains to be seen whether these stacking faults can improve strain hardening<sup>29</sup>, thereby improving the ductility of magnesium alloys. Finally, the transformation at the moving basal/prismatic interfaces can be regarded as a special case of stress-driven grain boundary migration<sup>30–32</sup> but disagreeing with the conventional theory of shear-coupled grain boundary motion. Our new mechanism at the sweeping boundary (Supplementary Movie 2) produces a sizable plastic strain of tetragonal compression character instead of simple shear.

## Methods

**TEM and *in situ* mechanical testing.** The submicron-sized samples were fabricated via FIB micromachining. *In situ* mechanical test was conducted using a Hysitron PicoIndenter (PI95) inside a JEOL 2100FEG TEM (200 keV). More than 30 tests were conducted successfully on 27 samples (for more details see Supplementary Table 2 and Supplementary Note 2). The strain rate was of the order of  $10^{-3} \text{ s}^{-1}$ . To investigate the atomic structure of the boundaries, the deformed sample was further thinned by using M1040 Nano Mill (Fischione Inc). The atomic resolution TEM images were acquired using an ARM200F spherical aberration-corrected TEM, under scanning TEM (200 keV) imaging mode.

**Measures taken to minimize the potential artefacts.** We have designed our experiments carefully to minimize the effects from the following factors: sample taper, stress concentrations, misalignment and FIB effects. In the following, we will detail the measures we have adopted. (1) Taper: to minimize the taper, we used FIB to fabricate the pillar with square cross-section and carefully adjusted the cutting angles in the final steps. As shown in Supplementary Fig. 4, the taper angle for as-fabricated samples is quite small. (2) Stress concentration: stress concentration did exist at the contact interface between the probe and pillar, which was evidenced by the fact that the apparent nucleation stress observed in pillar samples is much lower than that in ‘dog-bone’ samples (Supplementary Fig. 5). This is conceivable because it will be very difficult to make the free-end surface of the tested sample exactly parallel to probe surface. Comparably speaking, the ‘dog-bone’ shape samples do not have such drawbacks. Therefore, we employed both pillar and ‘dog-bone’ samples to confirm that our findings are the intrinsic properties of the tested material instead of artefacts resulted from the stress concentration. The fact that boundary migration stresses in both ‘dog-bone’ samples and pillars are on the same level suggests that stress concentration resulted from the contact interface has much less effect on boundary migration. (3) Misalignment: all our *in situ* tests have been designed carefully under the guidance of electron beam. Therefore, misalignment is unlikely to play a significant role. (4) The following measures were

adopted to minimize the effect from FIB. First, we fabricated the sample via glancing cutting on the lateral surface. Second, a low-energy (5 keV) ion beam was used to clean the sample surface and minimize the damage layer thickness. TEM observation confirmed that the FIB influenced layer was usually less than a few nanometres. As our samples have dimensions of about 400 nm, the effects from FIB should be insignificant.

**MD simulation.** Atomistic simulations were performed for Mg with empirical interatomic potentials<sup>33</sup>. A bicrystal model is constructed with periodic boundary conditions in all three dimensions. Two identical semicoherent basal/prismatic interfaces are created in the  $x$ - $z$  plane. The equilibrium, relaxed model has the dimensions of 49.8 nm in the  $x$  direction, 15.98 nm in the  $z$  direction and 15 nm for each crystal in the  $y$  direction. Owing to the mismatch of lattices in the  $x$  direction  $2(\sqrt{3}-\kappa)/(\sqrt{3}+\kappa)$  ( $\kappa$  is the  $c/a$  ratio), the semicoherent basal/prismatic contain an array of misfit dislocations, which can be described as  $\langle 0001 \rangle \{ \bar{1}100 \}$  with respect to the prismatic plane or  $\langle \bar{1}100 \rangle \{ 0001 \}$  with respect to the basal plane. The average spacing is 8.3 nm, suggesting that the misfit dislocation would not be present in short basal/prismatic interfaces. We performed MD at a temperature of 10 K under a compressive stress perpendicular to the basal/prismatic interface plane. During compression, the nucleation and motion of interface disconnections commence at a compressive stress of 1.5 GPa. The analysis of the relative displacements in Fig. 4b–d confirms that interface disconnections are  $2n$ -layer thick and no shear deformation is associated with the motion of interface disconnections.

## References

- Christian, J. W. & Mahajan, S. Deformation twinning. *Prog. Mater. Sci.* **39**, 1–157 (1995).
- Cahn, R. W. Twinned crystals. *Adv. Phys.* **3**, 363–445 (1954).
- Bilby, B. A. & Crocker, A. G. Theory of the crystallography of deformation twinning. *Proc. R. Soc. Lond. A* **288**, 240–255 (1965).
- Weertman, J. & Weertman, J. R. *Elementary Dislocation Theory* (Macmillan, 1964).
- Zhu, Y. T., Liao, X. Z. & Wu, X. L. Deformation twinning in nanocrystalline materials. *Prog. Mater. Sci.* **57**, 1–62 (2012).
- Yoo, M. H. Slip, twinning, and fracture in hexagonal close-packed metals. *Metall. Trans. A* **12**, 409–418 (1981).
- Mahajan, S. & Chin, G. Y. Formation of deformation twins in fcc crystals. *Acta Metall.* **21**, 1353–1363 (1973).
- Serra, A. & Bacon, D. J. Computer-simulation of twin boundaries in the hcp metals. *Philos. Mag. A* **54**, 793–804 (1986).
- Serra, A. & Bacon, D. J. Computer-simulation of twinning dislocation in magnesium using a many-body potential. *Philos. Mag. A* **63**, 1001–1012 (1991).
- Serra, A. & Bacon, D. J. A new model for  $\{10\bar{1}\text{over-bar}2\}$  twin growth in hcp metals. *Philos. Mag. A* **73**, 333–343 (1996).
- Serra, A., Bacon, D. J. & Pond, R. C. The crystallography and core structure of twinning dislocations in hcp metals. *Acta Metall.* **36**, 3183–3203 (1988).
- Serra, A., Bacon, D. J. & Pond, R. C. Dislocations in interfaces in the hcp metals - I. Defects formed by absorption of crystal dislocations. *Acta Mater.* **47**, 1425–1439 (1999).
- Serra, A., Pond, R. C. & Bacon, D. J. Computer-simulation of the structure and mobility of twinning dislocations in hcp metals. *Acta Metall. Mater.* **39**, 1469–1480 (1991).
- Wang, J., Hirth, J. P. & Tome, C. N.  $\{10\bar{1}\text{over-bar}2\}$  Twinning nucleation mechanisms in hexagonal-close-packed crystals. *Acta Mater.* **57**, 5521–5530 (2009).
- Wang, J. *et al.* Nucleation of a  $\{10\bar{1}\text{over-bar}2\}$  twin in hexagonal close-packed crystals. *Scr. Mater.* **61**, 903–906 (2009).
- Wang, J., Yadav, S. K., Hirth, J. P., Tomé, C. N. & Beyerlein, I. J. Pure-shuffle nucleation of deformation twins in hexagonal-close-packed metals. *Mater. Res. Lett.* **1**, 126–132 (2013).
- Li, B. & Ma, E. Atomic shuffling dominated mechanism for deformation twinning in magnesium. *Phys. Rev. Lett.* **103**, 035503 (2009).
- Li, B. & Ma, E. Reply to comment on ‘Atomic shuffling dominated mechanism for deformation twinning in magnesium’. *Phys. Rev. Lett.* **104**, 029604 (2010).
- Serra, A., Bacon, D. J. & Pond, R. C. Comment on ‘Atomic shuffling dominated mechanism for deformation twinning in magnesium’. *Phys. Rev. Lett.* **104**, 029603 (2010).
- Zhang, X. Y. *et al.* Twin boundaries showing very large deviations from the twinning plane. *Scr. Mater.* **67**, 862–865 (2012).
- Li, B. & Zhang, X. Y. Global strain generated by shuffling-dominated twinning. *Scr. Mater.* **71**, 45–48 (2014).
- Shan, Z. W. *In situ* TEM investigation of the mechanical behavior of micronanoscaled metal pillars. *JOM* **64**, 1229–1234 (2012).
- Wang, J., Liu, L., Tomé, C. N., Mao, S. X. & Gong, S. K. Twinning and detwinning via glide and climb of twinning dislocations along serrated coherent twin boundaries in hexagonal-close-packed metals. *Mater. Res. Lett.* **1**, 81–88 (2013).

24. Xu, B., Capolungo, L. & Rodney, D. On the importance of prismatic/basal interfaces in the growth of (1012) twins in hexagonal close packed crystals. *Scr. Mater.* **68**, 901–904 (2013).
25. Yu, Q. *et al.* Strong crystal size effect on deformation twinning. *Nature* **463**, 335–338 (2010).
26. Nie, J. F., Zhu, Y. M., Liu, J. Z. & Fang, X. Y. Periodic segregation of solute atoms in fully coherent twin boundaries. *Science* **340**, 957–960 (2013).
27. Stanford, N. & Barnett, M. R. Effect of particles on the formation of deformation twins in a magnesium-based alloy. *Mater. Sci. Eng. A* **516**, 226–234 (2009).
28. Yu, Q. *et al.* The nanostructured origin of deformation twinning. *Nano Lett.* **12**, 887–892 (2012).
29. Jian, W. W. *et al.* Ultrastrong mg alloy via nano-spaced stacking faults. *Mater. Res. Lett.* **1**, 61–66 (2013).
30. Cahn, J. W., Mishin, Y. & Suzuki, A. Coupling grain boundary motion to shear deformation. *Acta Mater.* **54**, 4953–4975 (2006).
31. Rupert, T. J., Gianola, D. S., Gan, Y. & Hemker, K. J. Experimental observations of stress-driven grain boundary migration. *Science* **326**, 1686–1690 (2009).
32. Zhang, Y., Sharon, J. A., Hu, G. L., Ramesh, K. T. & Hemker, K. J. Stress-driven grain growth in ultrafine grained Mg thin film. *Scr. Mater.* **68**, 424–427 (2013).
33. Liu, X. Y., Adams, J. B., Ercolessi, F. & Moriarty, J. A. EAM potential for magnesium from quantum mechanical forces. *Modelling Simul. Mater. Sci. Eng.* **4**, 293–303 (1996).

### Acknowledgements

This work was supported by Grants from NSFC (50925104, 11132006, 51231005 and 51321003) and 973 Program of China (2010CB631003). We also appreciate the support from the 111 Project of China (B06025). J.W. was supported by Office of Basic Energy Sciences, Project FWP 06SCPE401, under US DOE Contract number W-7405-ENG-36.

B.L. gratefully acknowledges the support from Center for Advanced Vehicular Systems, Mississippi State University. J.L. acknowledges the support by NSF DMR-1240933 and DMR-1120901. E.M. acknowledges an adjunct professorship at XJTU. X.Y.Z. thanks the support from NSFC under Grant numbers 50890170, 51071183 and 51271208. We thank J.C. Wan, C.S. Ma and G. Yang for assistance in TEM experiments.

### Author contributions

Z.-W.S., J.S. and E.M. designed and supervised the project. B.-Y.L. carried out the *in situ* experiments. L.L. performed spherical aberration-corrected (S) TEM experiments under the supervision of C.-L.J.; J.W. conducted the MD simulations in consultation with B.L.; X.-Y.Z. supervised the sample selection and carried out the *ex situ* experiments on bulk samples. B.-Y.L., J.W., J.L., Z.-W.S. and E.M. wrote the paper. All authors contributed to discussion of the results.

### Additional information

**Supplementary Information** accompanies this paper at <http://www.nature.com/naturecommunications>

**Competing financial interests:** The authors declare no competing financial interests.

**Reprints and permission** information is available online at <http://npg.nature.com/reprintsandpermissions/>

**How to cite this article:** Liu, B.-Y. *et al.* Twinning-like lattice reorientation without a crystallographic twinning plane. *Nat. Commun.* 5:3297 doi: 10.1038/ncomms4297 (2014).



This work is licensed under a Creative Commons Attribution-NonCommercial-NoDerivs 3.0 Unported License. To view a copy of this license, visit <http://creativecommons.org/licenses/by-nc-nd/3.0/>

# Chalcogenide glass-on-graphene photonics

Hongtao Lin<sup>1\*</sup>, Yi Song<sup>2</sup>, Yizhong Huang<sup>1,3</sup>, Derek Kita<sup>1</sup>, Skylar Deckoff-Jones<sup>1</sup>, Kaiqi Wang<sup>1</sup>, Lan Li<sup>1</sup>, Junying Li<sup>1,4</sup>, Hanyu Zheng<sup>1</sup>, Zhengqian Luo<sup>1,3</sup>, Haozhe Wang<sup>2</sup>, Spencer Novak<sup>5</sup>, Anupama Yadav<sup>5</sup>, Chung-Che Huang<sup>6</sup>, Ren-Jye Shiue<sup>2</sup>, Dirk Englund<sup>2</sup>, Tian Gu<sup>1</sup>, Daniel Hewak<sup>6</sup>, Kathleen Richardson<sup>5</sup>, Jing Kong<sup>2</sup> and Juejun Hu<sup>1\*</sup>

**Two-dimensional (2D) materials are of tremendous interest to integrated photonics, given their singular optical characteristics spanning light emission, modulation, saturable absorption and nonlinear optics. To harness their optical properties, these atomically thin materials are usually attached onto prefabricated devices via a transfer process. Here, we present a new route for 2D material integration with planar photonics. Central to this approach is the use of chalcogenide glass, a multifunctional material that can be directly deposited and patterned on a wide variety of 2D materials and can simultaneously function as the light-guiding medium, a gate dielectric and a passivation layer for 2D materials. Besides achieving improved fabrication yield and throughput compared with the traditional transfer process, our technique also enables unconventional multilayer device geometries optimally designed for enhancing light-matter interactions in the 2D layers. Capitalizing on this facile integration method, we demonstrate a series of high-performance glass-on-graphene devices including ultra-broadband on-chip polarizers, energy-efficient thermo-optic switches, as well as graphene-based mid-infrared waveguide-integrated photodetectors and modulators.**

The isolation of single-layer graphene in 2004 triggered intensive investigations into two-dimensional (2D) crystals consisting of one or a few monolayers of atoms. With their remarkable optical properties, these materials have garnered enormous interest for their photonic applications as light emitters<sup>1</sup>, modulators<sup>2,3</sup>, photodetectors<sup>4,5</sup>, saturable absorbers<sup>6</sup> and plasmonic sensors<sup>7</sup>. On-chip integration of 2D materials with photonic devices generally relies on layer transfer, where exfoliated or delaminated 2D membranes are attached onto prefabricated devices<sup>8</sup>. Despite its widespread implementation, the transfer approach has its limitations. When transferring these atomically thin crystals onto a substrate with uneven topology, the 2D materials tend to rupture at the pattern step edges. To circumvent such damage, an additional planarization step is often mandated prior to 2D material transfer, which complicates the process<sup>9–12</sup>. Furthermore, the transferred 2D layer resides on top of the prepatterned devices and only interacts with the optical mode through the relatively weak evanescent waves.

To resolve these issues, an alternative 2D material integration route entails growing an optically thick (comparable to optical wavelength in the medium) film directly on 2D materials and lithographically patterning it into functional photonic devices. Besides improved processing yield and throughput compared to the traditional transfer process, this ‘monolithic’ approach also offers several critical advantages: it enables accurate alignment of photonic components with 2D material structures (for example, in-plane heterojunctions) with lithographic precision, which is difficult to attain using transfer, it allows flexible placement of 2D material layers inside a photonic structure to maximally enhance light-matter interactions and last but not least, it heralds a truly monolithic, wafer-scale integration process with 2D material systems where

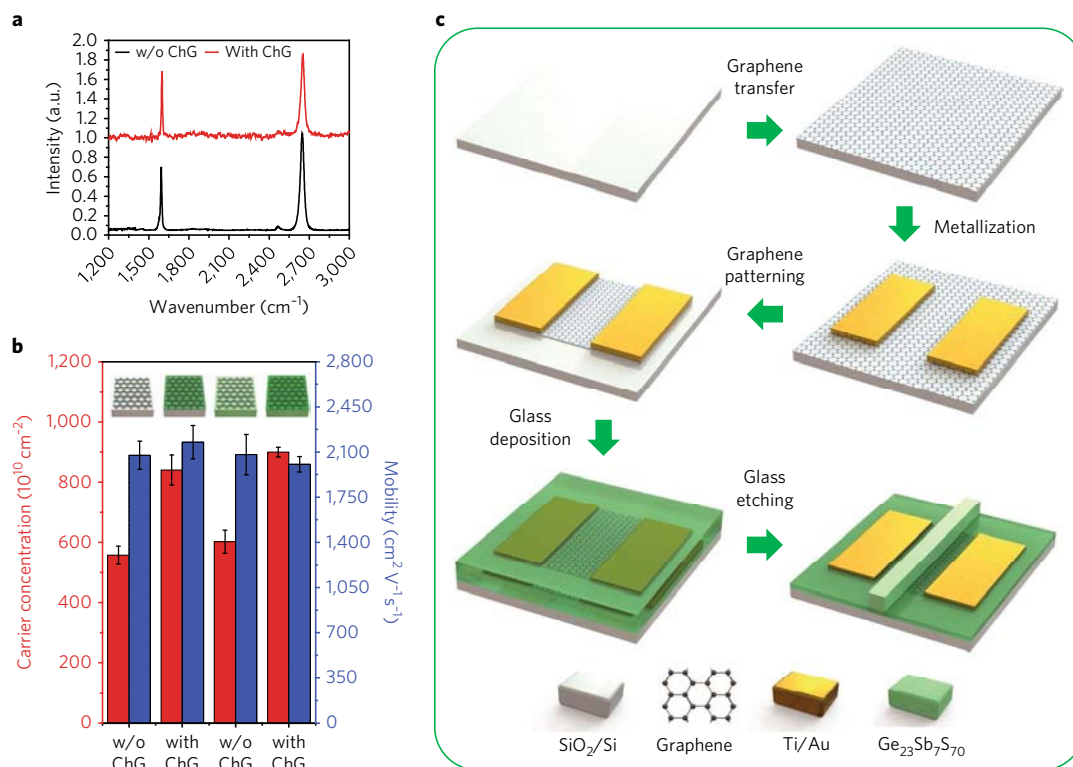
catalyst-free, large-area continuous growth on semiconductor or dielectric substrates has been realized (for example, graphene on SiC<sup>13</sup>, MoS<sub>2</sub> and MoTe<sub>2</sub> on SiO<sub>2</sub>/Si<sup>14,15</sup>).

Growth of optically thick dielectric films on 2D materials is not a trivial task, however. Integration on graphene, the archetypal 2D material, epitomizes the challenge. Graphene has a chemically inert surface that makes nucleation and growth of a uniform dielectric film on its surface difficult<sup>16</sup>. Surface modification using ozone<sup>17</sup>, NO<sub>2</sub><sup>18</sup>, or perylene tetracarboxylic acid<sup>19</sup> catalyses nucleation, albeit at the expense of carrier mobility in graphene. Electron-beam evaporation can form continuous dielectric films (for example, SiO<sub>2</sub> and TiO<sub>2</sub>) without surface functionalization, although the harsh deposition environment tends to severely degrade graphene quality (Supplementary Section I). Atomic layer deposition (ALD) has been widely adopted for gate dielectric deposition on graphene<sup>20</sup>; however, growing an optically thick layer using ALD is impractical. Alternatively, plasma-enhanced chemical vapour deposition (PECVD) has been attempted for silicon nitride coating on graphene, although the process requires low-density, low-power plasma with a reduced deposition rate to mitigate plasma damage to the graphene surface<sup>21</sup>. Recently, a simple spin-coating process was devised for direct polymer waveguide modulator fabrication on graphene<sup>22</sup>. Nevertheless, the large modal area in low-index-contrast polymer waveguides limits the resulting device footprint and performance. For other 2D materials, especially less stable ones such as black phosphorous<sup>23</sup>, protection of the material’s structural integrity from high temperatures, plasma and reactive chemicals imposes additional constraints on the integration process.

Here, we present a generic route for photonic integration of 2D materials using chalcogenide glass (ChG) as the backbone

<sup>1</sup>Department of Materials Science & Engineering, Massachusetts Institute of Technology, Cambridge 02139 MA, USA. <sup>2</sup>Department of Electrical Engineering & Computer Science, Massachusetts Institute of Technology, Cambridge 02139 MA, USA. <sup>3</sup>Department of Electronic Engineering, Xiamen University, Xiamen 361005, China. <sup>4</sup>Key Laboratory of Optoelectronic Technology & System, Education Ministry of China, Chongqing University, Chongqing 400044, China. <sup>5</sup>The College of Optics & Photonics, University of Central Florida, Orlando 32816 FL, USA. <sup>6</sup>Optoelectronics Research Centre, University of Southampton, Southampton SO17 1TW, UK. Hongtao Lin, Yi Song, Yizhong Huang, and Derek Kita contributed equally to this work.

\*e-mail: [hometown@mit.edu](mailto:hometown@mit.edu); [hujuejun@mit.edu](mailto:hujuejun@mit.edu)



**Fig. 1 | Chalcogenide glass–graphene integration.** **a**, Raman spectra of as-transferred monolayer CVD graphene (black) and graphene covered with a  $\text{Ge}_{23}\text{Sb}_7\text{S}_{70}$  glass layer (red). Background Raman signal from the  $\text{Ge}_{23}\text{Sb}_7\text{S}_{70}$  glass film has been subtracted. **b**, Hall carrier concentration and mobility measured in graphene (results averaged over five samples of each type). From left to right: Graphene transferred onto an oxidized silicon wafer; graphene transferred onto an oxidized silicon wafer and then covered with a  $\text{Ge}_{23}\text{Sb}_7\text{S}_{70}$  glass film; graphene transferred onto a  $\text{Ge}_{23}\text{Sb}_7\text{S}_{70}$  glass film; graphene sandwiched between two  $\text{Ge}_{23}\text{Sb}_7\text{S}_{70}$  glass layers. **c**, Schematic fabrication process flow to integrate chalcogenide glass photonic devices with graphene.

optical material. Chalcogenide glasses, namely the amorphous compounds containing S, Se and/or Te, are emerging photonic materials known for their broadband transparency, high and continuously tunable refractive indices ( $n \approx 2\text{--}3.5$ ) and large Kerr non-linearity<sup>24, 25</sup>. In addition to their exceptional optical properties, ChGs are also uniquely poised for 2D material integration. These glasses can be deposited at high rates exceeding  $100 \text{ nm min}^{-1}$  via simple single-source thermal evaporation with the substrate held near room temperature<sup>26</sup>. Combined with their amorphous nature and good van der Waals adhesion to different substrates without surface modification, the extremely low thermal budget allows epitaxy-free ChG coating with minimal thermal and structural damage to the substrate. Here we show that ChGs can be deposited on a wide variety of 2D materials without disrupting their structure and optoelectronic properties. Figure 1a displays the Raman spectra of monolayer graphene synthesized using CVD before and after coating with a 450-nm-thick thermally evaporated  $\text{Ge}_{23}\text{Sb}_7\text{S}_{70}$  ChG film. No defect-related peaks (D, D' or D+G) were observed after ChG deposition, indicating that the low-temperature glass deposition does not introduce structural defects into graphene<sup>27</sup>. We further confirm that other 2D materials ( $\text{MoS}_2$ , black phosphorus, InSe and hexagonal BN) similarly remain intact after ChG deposition (Supplementary Section II). Such integration compatibility facilitates the fabrication of unconventional multilayer structures incorporating 2D materials to optimally engineer their interactions with the optical mode. As an example, we exploit the giant optical anisotropy of graphene and modal symmetry in graphene-sandwiched waveguides to demonstrate an ultra-broadband polarizer and a thermo-optic switch with energy efficiency an order of magnitude higher compared to previous reports.

In addition to being an optical guiding medium, the insulating  $\text{Ge}_{23}\text{Sb}_7\text{S}_{70}$  glass can function as a gate dielectric and as an effective passivation barrier to prevent 2D materials from degradation inflicted by ambient air, moisture or corrosive chemicals (Supplementary Section III). Figure 1b evaluates the impact of  $\text{Ge}_{23}\text{Sb}_7\text{S}_{70}$  glass deposition on transport properties of monolayer CVD graphene transferred onto an oxidized silicon wafer or a  $\text{Ge}_{23}\text{Sb}_7\text{S}_{70}$  film on silicon. Notably, despite the increased p-doping (which normally reduces mobility), carrier mobility in graphene remains unchanged after ChG encapsulation, in contrast to most other deposited dielectrics, which tend to degrade carrier mobility due to surface damage during deposition and hence increased defect density<sup>28</sup>. In this Article we harness this feature to demonstrate the first mid-infrared graphene waveguide modulator, where the multifunctional ChG material serves simultaneously as the waveguide and as a gate dielectric to electrostatically modulate the Fermi level in graphene.

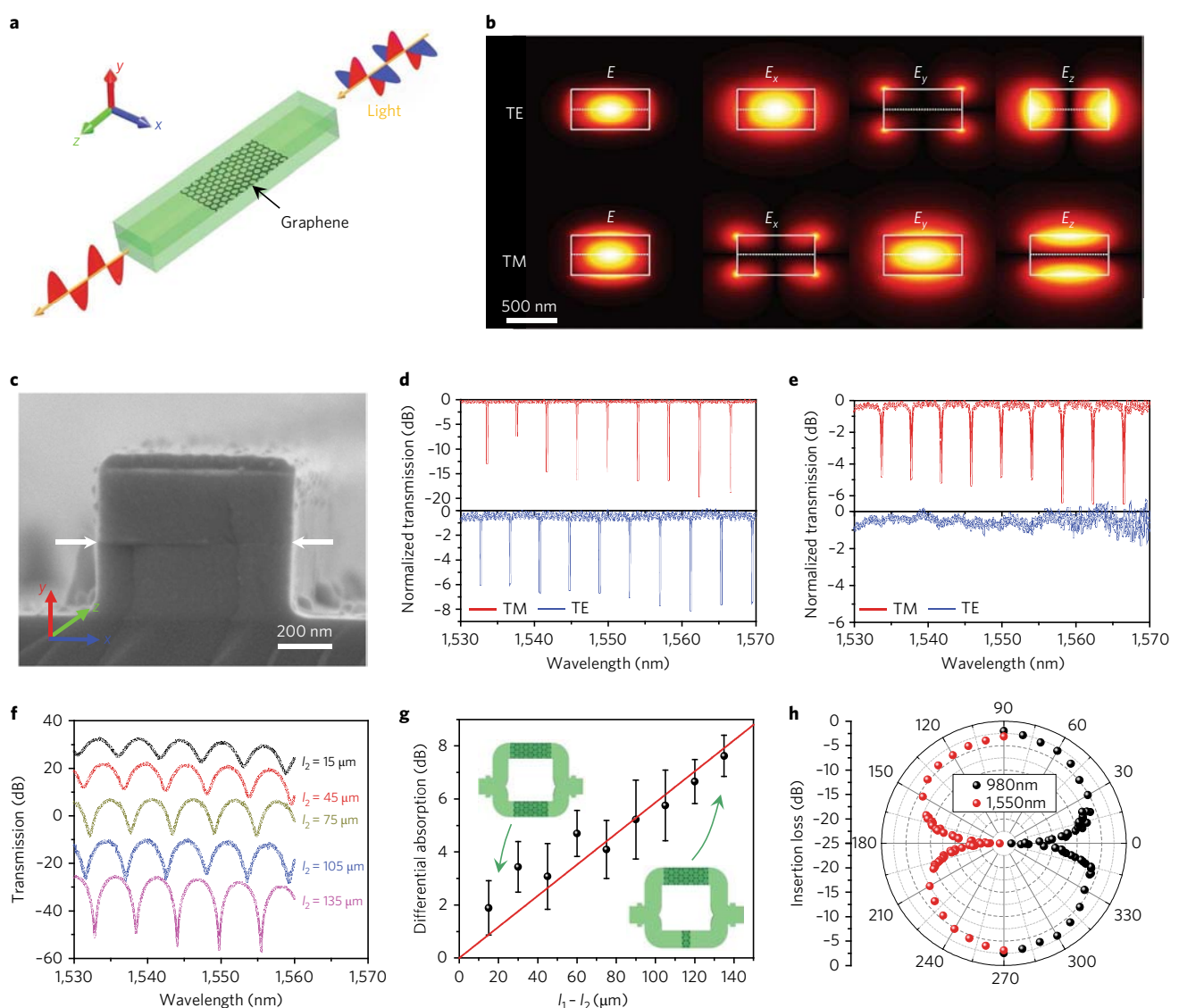
## Results

Figure 1c illustrates the baseline fabrication protocols for the ChG-on-graphene photonic devices. Details of the fabrication process are provided in the Methods. The following sections present four classes of novel devices leveraging the new integration strategy to reap unique performance benefits. We note that although the devices described herein were fabricated using the specific combination of thermally evaporated  $\text{Ge}_{23}\text{Sb}_7\text{S}_{70}$  glass and graphene, we have validated the integration process based on other 2D materials and ChG compositions formed using alternative methods including solution processing and nanoimprint<sup>29</sup> (Supplementary Section IV). The ChG/2D material integration process is therefore generic and can be adapted to meet diverse device design and application needs.

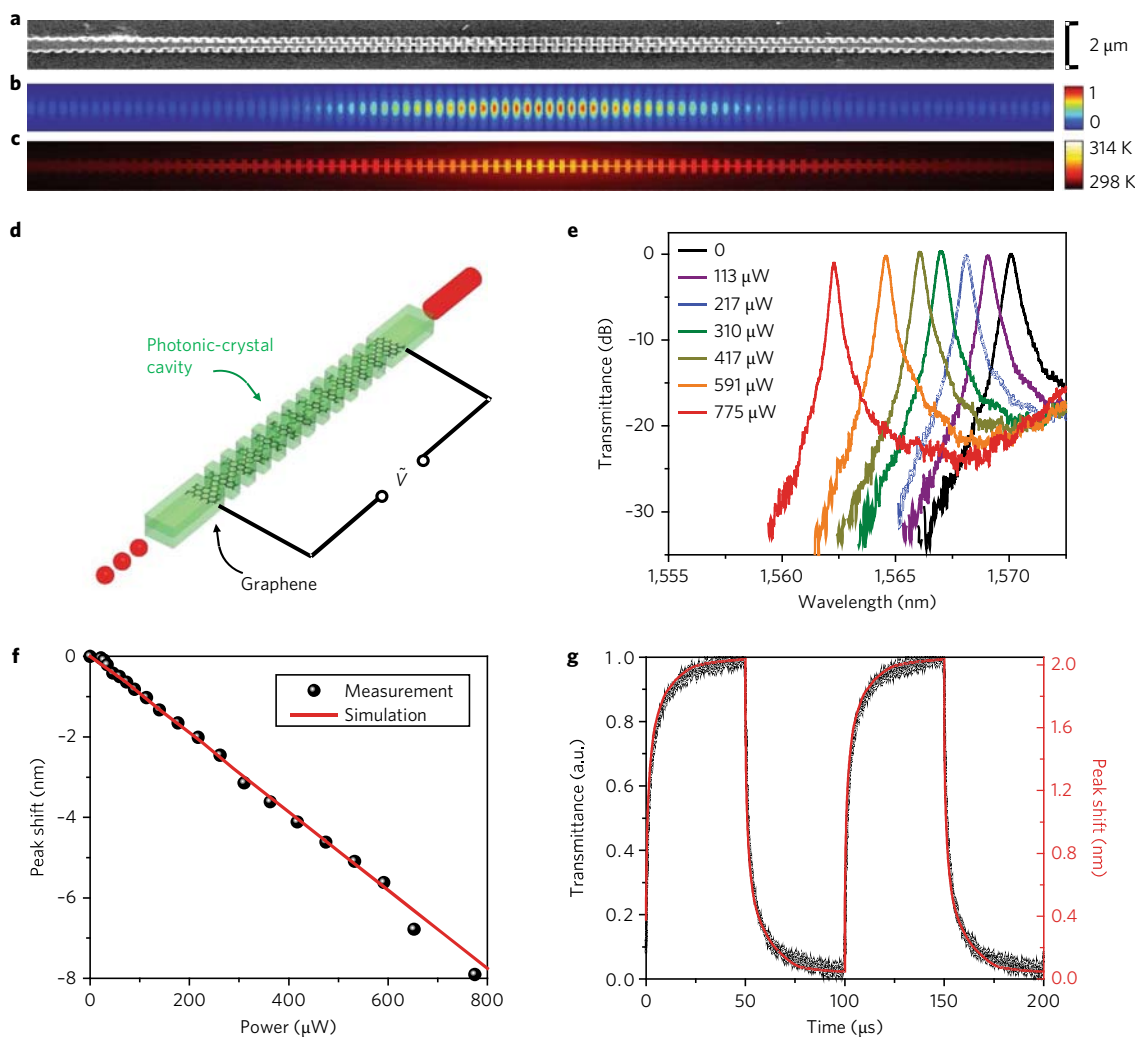
**Ultra-broadband on-chip waveguide polarizer.** Unlike traditional graphene-integrated devices where the transferred graphene layer is located outside the waveguide core, here we introduce a new multi-layer waveguide platform comprising a graphene monolayer situated at the centre of a symmetrically cladded strip waveguide (Fig. 2a). Figure 2c shows a scanning electron microscopy (SEM) image of a fabricated waveguide where a graphene film is sandwiched between two  $\text{Ge}_{23}\text{Sb}_7\text{S}_{70}$  layers of equal thickness. The waveguide behaves as a polarizer as a result of the large optical anisotropy of graphene and the polarization-dependent symmetric properties of waveguide modes. To illustrate its working principle, Fig. 2b depicts the electric field components of the fundamental TM (transverse magnetic) and TE (transverse electric) modes supported in the waveguide at a wavelength of 1,550 nm. For TM polarization, its in-plane electric field components ( $E_x$  and  $E_z$ ) are antisymmetric with respect to the centre plane and thus vanish at the graphene layer. Because

graphene acts as an optically absorbing metal in-plane and as a lossless dielectric along the out-of-plane direction<sup>30</sup>, the waveguide becomes transparent to the TM mode. In contrast, both in-plane electric-field components of the TE mode reach their maxima at the waveguide centre, leading to strong optical attenuation. Using experimental Fermi-level data from Hall measurements, we modelled the propagation losses for the TM and TE modes as  $0\text{--}1.5\text{ dB cm}^{-1}$  and  $575 \pm 1.5\text{ dB cm}^{-1}$ , respectively, at a wavelength of 1,550 nm, where the error bars (Fig. 2g) take into account glass thickness deviations based on realistic fabrication tolerances (Supplementary Section V).

To precisely quantify the large polarization-dependent losses in the waveguide, we employed two device structures: ring resonators to characterize the low-loss TM mode and unbalanced Mach-Zehnder interferometers (MZI) to gauge the much higher TE-mode loss. Protocols of loss extraction are summarized in



**Fig. 2 | Broadband graphene-sandwiched waveguide polarizer.** **a**, Schematic diagram showing the graphene-sandwiched waveguide polarizer. **b**, Simulated modal intensity and electric-field component profiles for fundamental TE and TM modes in the graphene-sandwiched waveguide. **c**, SEM image of the fabricated polarizer cross-section: white arrows mark graphene location. **d, e**, Optical transmittance through microring resonators without graphene (**d**) and with embedded graphene (**e**). **f**, Transmittance spectra of unbalanced MZIs with graphene strips of different lengths ( $l_1$  and  $l_2$ ) embedded in their arms. Here  $l_1 = 150\ \mu\text{m}$  and  $l_2$  varies from 15  $\mu\text{m}$  to 135  $\mu\text{m}$ . **g**, Differential absorption induced by graphene. Error bars correspond to standard deviations of measurements performed on 10 devices at each  $l_1 - l_2$  value. **h**, Polar diagram showing the polarizer performance at 980 nm and 1,550 nm wavelengths. The polar angle represents the angle between the input polarization plane and the substrate.



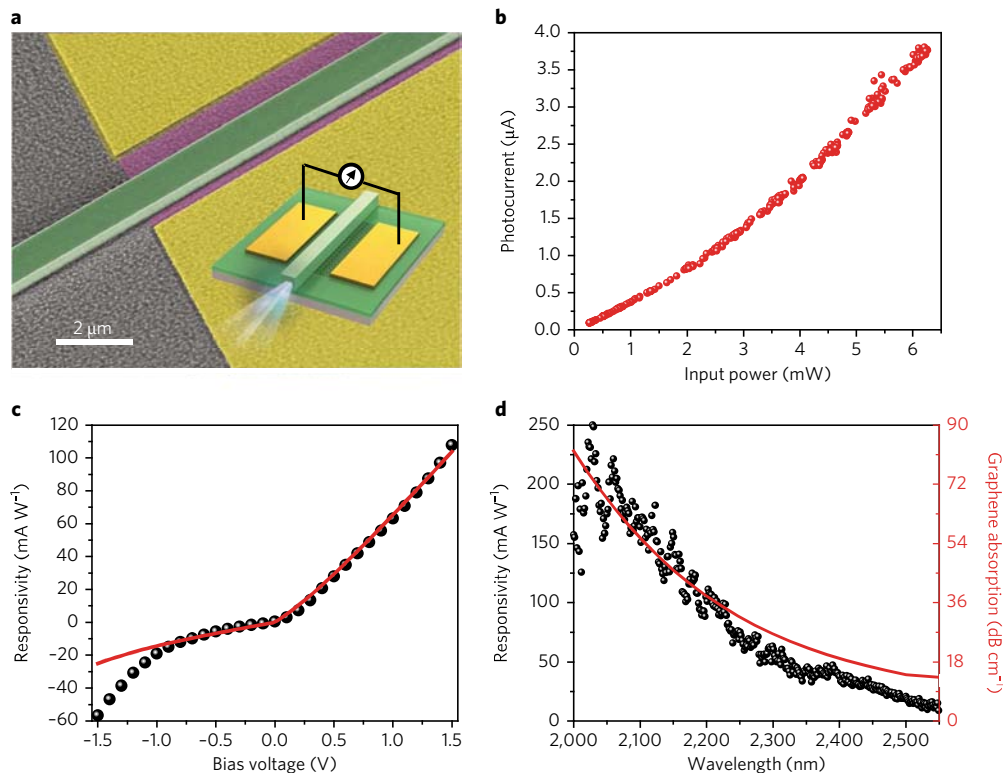
**Fig. 3 | Graphene-sandwiched photonic-crystal thermo-optic switch.** **a**, Top-view SEM micrograph of the photonic-crystal thermo-optic switch. **b**, Simulated optical mode profile in the photonic crystal cavity. **c**, Temperature distribution in the device when electric current is flowing through the embedded graphene heater. **d**, Schematic illustration of the thermo-optic switch structure, which consists of a graphene layer embedded in the centre of a photonic-crystal nanobeam cavity. **e**, Optical transmission spectra of the switch at varying input power levels into the graphene heater. **f**, Thermo-optic resonant wavelength shift: the solid line represents finite element method simulation results, whereas the dots are experimental data. **g**, Time-domain response of the switch to a square-wave driving current at 10 kHz.

Supplementary Section VI. Figure 2d,e plots examples of transmission spectra of ring resonators without and with the embedded graphene layer. Although TM-mode resonances are clearly visible for both types of device, the TE-mode resonances disappear in the graphene-sandwiched waveguide, signalling significant TE polarization-selective absorption by graphene. Using the classical coupled-wave transfer matrix formalism, we calculated the excess TM-mode loss induced by graphene to be  $20 \text{ dB cm}^{-1}$  at  $1,550 \text{ nm}$ , which we attribute to unevenness of graphene caused by polymer residues from the transfer process (Supplementary Section V). The TE-mode loss was assessed based on the unbalanced MZI transmission spectra in Fig. 2f, where the extinction ratio (ER) of the transmittance undulation correlates with the differential optical attenuation induced by graphene embedded in the MZI arms. Figure 2g plots the calculated differential TE-mode absorption by graphene as a function of embedded graphene length difference in the two arms, from which we infer a TE-mode loss of  $590 \text{ dB cm}^{-1}$  near  $1,550 \text{ nm}$ , which agrees well with our theoretical predictions. The results correspond to  $23 \text{ dB ER}$  and  $0.8 \text{ dB insertion loss}$  in a  $400\text{-}\mu\text{m}$ -long polarizer device operating at  $1,550 \text{ nm}$  wavelength

and a large figure of merit (FOM, defined as the ratio of ER to insertion loss) of 29.

Importantly, because the polarizer design operates on material anisotropy and modal symmetry, both of which are wavelength-independent, the device is broadband in nature. To demonstrate broadband operation of the polarizer, a  $400\text{-}\mu\text{m}$ -long polarizer device was characterized at  $980 \text{ nm}$  and  $1,550 \text{ nm}$  wavelengths and the results are summarized in the polar diagram in Fig. 2h. The measurement procedures are elaborated in Supplementary Section VII. Consistent with the experimental results, our theoretical model confirms that the same device can operate over a broad spectral range from  $940 \text{ nm}$  to  $1,600 \text{ nm}$  with a polarization extinction ratio exceeding  $20 \text{ dB}$ , which represents the largest operation bandwidth for on-chip waveguide polarizers (Supplementary Section VII).

**Energy-efficient photonic-crystal thermo-optic switch.** The TM-transparent sandwich waveguide provides an example where graphene is embedded inside a waveguide without incurring excess optical loss. This counterintuitive observation opens up the application of graphene as a broadband transparent heater to realize a



**Fig. 4 | Waveguide-integrated graphene mid-infrared photodetector.** **a**, SEM tilted-view micrograph of the mid-infrared waveguide-integrated detector. Inset: Schematic diagram of the device. **b**, Zero-bias photocurrent recorded as a function of input optical power from the waveguide at 2,185 nm wavelength. **c**, Responsivity of the detector device to 2,185 nm waveguide input. **d**, Mid-infrared broadband spectral dependences of the detector's responsivity (at 1.5 V bias) and calculated optical absorption in the graphene layer.

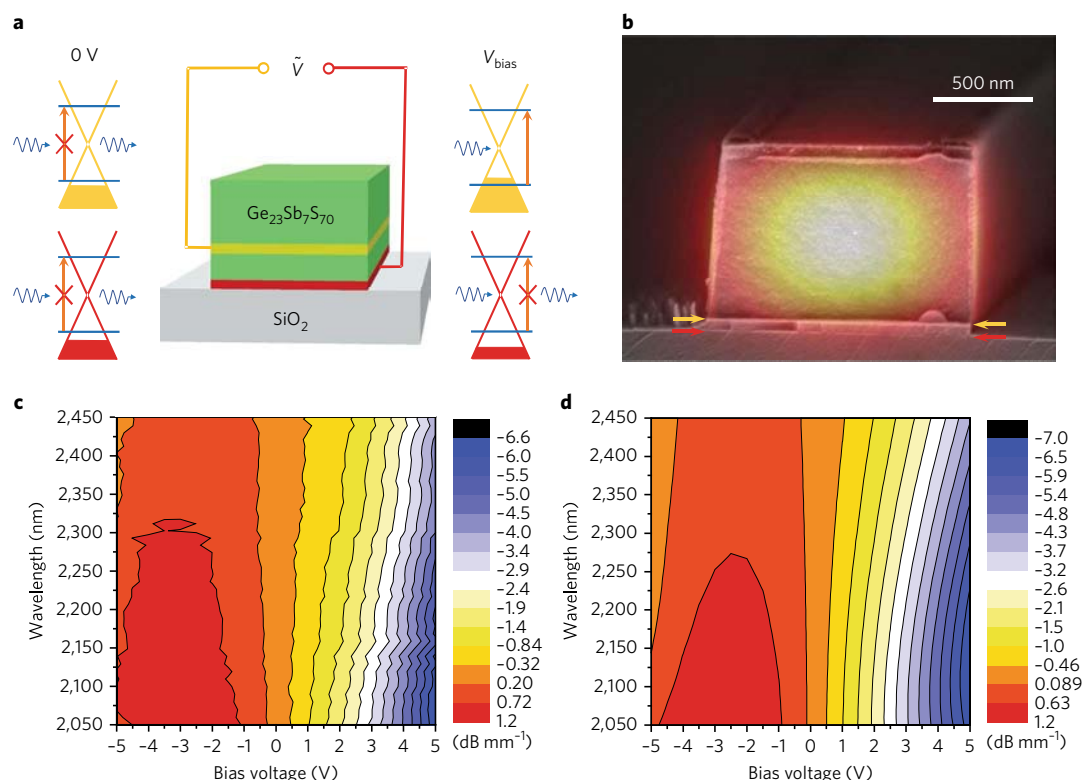
thermo-optic switch with unprecedented energy efficiency. Unlike metal heaters, which have to be placed several micrometres away from the waveguide to suppress parasitic absorption, the waveguide-integrated graphene heater offers superior energy efficiency because of the much smaller thermal mass and large spatial overlap of the optical mode with the heating zone.

Figure 3d schematically illustrates the device structure consisting of a waveguide-coupled photonic-crystal nanobeam cavity formed through depth modulation of side Bragg gratings<sup>31</sup>. A graphene monolayer is embedded in the centre of the nanobeam cavity waveguide and connected to a pair of electrodes as described in Supplementary Section VIII. Figure 3a shows a top-view SEM micrograph of the graphene-embedded nanobeam, which supports a single resonant mode near 1,570 nm (Fig. 3b). When a bias voltage is applied across the electrodes, the graphene and the cavity are resistively heated, leading to a thermo-optic spectral drift of the cavity resonance. Figure 3c depicts the simulated temperature profile as a result of resistive heating in graphene. Because the graphene conductor is placed directly inside the waveguide core, this unique geometry leads to strong thermal confinement and large spatial overlap between the heating zone and the cavity mode, both of which contribute to improved energy efficiency. Figure 3e presents the transmission spectra of the cavity showing progressive resonance detuning with increasing input power. As is shown in Fig. 3f, the measured resonance shift agrees well with our finite element modelling (Supplementary Section IX). The slope of the curve indicates a record energy efficiency of  $10 \text{ nm mW}^{-1}$ , which represents almost an order of magnitude improvement compared to the best values previously reported in on-chip thermo-optic switches and tuning devices<sup>32</sup>.

To elucidate the device physics underlying the exceptional energy efficiency, we analysed the switch's performance character-

istics using a lumped element model (Supplementary Section X). A FOM for thermo-optic switches, defined as the inverse of the product of rise time and power consumption, is often cited when drawing comparison between different technologies<sup>33</sup>. With a low switching energy of 0.11 mW and a 10–90% rise time of 14  $\mu\text{s}$  (Fig. 3g), our device features a FOM of  $0.65 \text{ mW}^{-1} \mu\text{s}^{-1}$ , which is among the highest values reported in an on-chip thermo-optic switch (Supplementary Section XI).

**Mid-infrared waveguide-integrated photodetector.** Our integration scheme equally applies to optoelectronic devices where graphene becomes the active medium. The broadband infrared transparency of ChGs makes them particularly appealing for integration with graphene, whose zero-gap nature potentially enables broadband optical detection. Our approach simplifies the graphene detector and waveguide integration process through direct deposition and patterning of ChG waveguides and metal contacts on monolayer CVD graphene (Fig. 4a, inset). The device was characterized by launching mid-infrared TE-polarized light into the waveguide and Fig. 4b depicts the detector's photoresponse at zero bias. Three possible mechanisms contribute to photoresponse in graphene: photothermoelectric, photovoltaic (PV) and bolometric effects. To elucidate the origin of the photoresponse, we attempted to fit the data with models for these three response mechanisms (Supplementary Section XIII). The best fit was obtained for the PV mechanism (Fig. 4c). In this fit, the hot carrier relaxation time was taken as a free fit parameter, producing  $\tau = 2.3 \text{ ps}$ , in good agreement with directly measured values<sup>34,35</sup>. The increasing responsivity with bias voltage is due to improved carrier collection. The asymmetric shape of the curve is attributed to the off-centred waveguide configuration, as shown in Fig. 4a. The discrepancy of the PV effect for bias  $< -1 \text{ V}$  could be attributed to the difference in



**Fig. 5 | Mid-infrared waveguide modulator.** **a**, Centre: Schematic diagram of the mid-infrared waveguide modulator, where the top and bottom graphene layers are labelled with yellow and red colours, respectively. Left and right: Band profiles of the two graphene layers. Brown arrows represent energy of incident photons. **b**, Overlay of simulated TE optical mode profile in the modulator waveguide and an SEM cross-sectional image of the device. Arrows point to the locations of the two graphene layers. **c,d**, Measured (**c**) and simulated (**d**) colour contour maps showing wavelength- and bias-dependent modulation depth of the device in  $\text{dB mm}^{-1}$  (relative to its transmittance at zero bias).

electron and hole mobility<sup>36</sup>, which requires further investigation. The device exhibits a broadband photoresponse over the entire scanning range of our tunable laser (2.0–2.55  $\mu\text{m}$ ) with a peak responsivity of  $250 \text{ mA W}^{-1}$  at a wavelength of 2.03  $\mu\text{m}$  (Fig. 4d). The responsivity figure is on par with, or in some cases superior to, state-of-the-art waveguide-integrated graphene detectors operating in the mid-infrared<sup>37</sup> and near-infrared<sup>9, 11, 38, 39</sup>. Hall measurements indicate that the Fermi level of graphene used in the device is located at 0.34 eV below the Dirac point owing to substrate doping<sup>40</sup>. Consequently, the reduced responsivity observed at longer wavelengths manifests the onset of Pauli blocking and decreased optical absorption in the p-type graphene. We modelled the wavelength-dependent absorption in graphene, and the predicted wavelength scaling of graphene absorption is plotted in Fig. 4d. The agreement between the calculated graphene absorption spectrum and the measured responsivity trend validates the hypothesis.

As well as simplifying the integration of graphene detectors with waveguides on silicon, the use of ChGs further opens up photonic integration on unconventional plastic substrates to enable mechanically flexible photonic systems. Leveraging our previously developed flexible substrate integration protocols<sup>41, 42</sup>, we have demonstrated a waveguide-integrated graphene detector on flexible polymer membranes. Detailed fabrication and characterization outcomes are presented in Supplementary Section XIV.

**Broadband mid-infrared waveguide modulator.** As previously discussed, the  $\text{Ge}_{23}\text{Sb}_7\text{S}_{70}$  glass can function not only as the waveguiding medium, but also as a gate dielectric to control the Fermi level inside graphene. As its Fermi level changes across a threshold value corresponding to half the photon energy, optical absorption

of graphene is drastically modified due to Pauli blocking, an effect that has been harnessed to realize near-infrared waveguide modulators<sup>3, 43–46</sup> and electro-optic manipulation of free-space mid-infrared light<sup>47–49</sup>. Here, we utilize the versatile ChG material to demonstrate the first graphene-based waveguide modulator operating in the mid-infrared. Figure 5a illustrates the device layout and Fig. 5b shows an overlay of the TE modal profile at 2  $\mu\text{m}$  wavelength and an SEM cross-sectional micrograph of the waveguide. The device working principle is similar to that of double-layer graphene modulators developed by Liu and co-authors<sup>50</sup>. In our case, the active region is formed by two graphene sheets separated by a  $\text{Ge}_{23}\text{Sb}_7\text{S}_{70}$  glass gate dielectric of 50 nm in thickness. When a gate bias is applied, charges of opposite signs are electrostatically deposited in the two graphene layers, resulting in shifts of their Fermi levels towards opposite directions. Optical transmission in the waveguide (also made of  $\text{Ge}_{23}\text{Sb}_7\text{S}_{70}$  glass) is consequently modulated via Pauli blocking. Using this mechanism, we demonstrate broadband optical modulation for the TE mode across the 2.05–2.45  $\mu\text{m}$  band with modulation depth up to  $8 \text{ dB mm}^{-1}$ , as shown in Fig. 5c. A thorough theoretical analysis taking into consideration the starting Fermi levels in the two graphene layers as well as Fermi–Dirac carrier distribution is presented in Supplementary Section XV. The theoretically predicted waveguide transmittance as a function of gate bias (Fig. 5d) agrees well with experimental measurements. The current device geometry and our characterization set-up are not optimized for high-speed tests and limit the modulation time constant to 7  $\mu\text{s}$ , being mainly restricted by the large electrical probe capacitance and series resistance. Our calculations show that with improved device design and measurement schemes the attainable modulation bandwidth can be enhanced by five orders of magnitude to



warrant gighertz operation using the same device architecture (Supplementary Section XVI).

## Conclusion

In summary, we have established a new paradigm for integrating 2D materials with planar photonic circuits. Unlike traditional methods that rely on post-fabrication transfer, our approach capitalizes on low-temperature ChG deposition to process devices directly on 2D materials without disrupting their extraordinary optoelectronic properties. In addition to streamlining the 2D material integration process, our approach envisages novel multilayer structures with unprecedented control of light–matter interactions in the 2D layers. As an example, we implemented a graphene-sandwiched waveguide architecture to experimentally achieve ultra-broadband on-chip polarization isolation and thermo-optic switching with record energy efficiency. We further leverage the zero-gap nature of graphene to realize ChG waveguide-integrated broadband mid-infrared detectors and modulators, the latter of which also makes use of the multifunctional ChG as the gate dielectric for electrostatic tuning of the Fermi level in graphene. We foresee that the versatile glass-on-2D-material platform will significantly expedite and expand integration of 2D materials to enable new photonic functionalities.

## Methods

Methods, including statements of data availability and any associated accession codes and references, are available at <https://doi.org/10.1038/s41566-017-0033-z>.

Received: 4 March 2017; Accepted: 27 September 2017;  
Published online: 30 October 2017

## References

- Withers, F. et al. Light-emitting diodes by band-structure engineering in van der Waals heterostructures. *Nat. Mater.* **14**, 301–306 (2015).
- Sun, Z., Martinez, A. & Wang, F. Optical modulators with 2D layered materials. *Nat. Photon.* **10**, 227–238 (2016).
- Liu, M. et al. A graphene-based broadband optical modulator. *Nature* **474**, 64–67 (2011).
- Xia, F., Mueller, T., Lin, Y.-m., Valdes-Garcia, A. & Avouris, P. Ultrafast graphene photodetector. *Nat. Nanotech.* **4**, 839–843 (2009).
- Youngblood, N., Chen, C., Koester, S. J. & Li, M. Waveguide-integrated black phosphorus photodetector with high responsivity and low dark current. *Nat. Photon.* **9**, 247–252 (2015).
- Bao, Q. et al. Atomic-layer graphene as a saturable absorber for ultrafast pulsed lasers. *Adv. Funct. Mater.* **19**, 3077–3083 (2009).
- Grigorenko, A., Polini, M. & Novoselov, K. Graphene plasmonics. *Nat. Photon.* **6**, 749–758 (2012).
- Bonaccorso, F., Sun, Z., Hasan, T. & Ferrari, A. Graphene photonics and optoelectronics. *Nat. Photon.* **4**, 611–622 (2010).
- Gan, X. et al. Chip-integrated ultrafast graphene photodetector with high responsivity. *Nat. Photon.* **7**, 883–887 (2013).
- Li, H., Anugrah, Y., Koester, S. J. & Li, M. Optical absorption in graphene integrated on silicon waveguides. *Appl. Phys. Lett.* **101**, 111110 (2012).
- Schall, D. et al. 50 GBit/s photodetectors based on wafer-scale graphene for integrated silicon photonic communication systems. *ACS Photon.* **1**, 781–784 (2014).
- Hu, Y. et al. Broadband 10 Gb/s operation of graphene electro-absorption modulator on silicon. *Laser Photon. Rev.* **10**, 307–316 (2016).
- Nyakiti, L. et al. Enabling graphene-based technologies: toward wafer-scale production of epitaxial graphene. *MRS Bull.* **37**, 1149–1157 (2012).
- Huang, C.-C. et al. Scalable high-mobility MoS<sub>2</sub> thin films fabricated by an atmospheric pressure chemical vapor deposition process at ambient temperature. *Nanoscale* **6**, 12792–12797 (2014).
- Zhou, L. et al. Large-area synthesis of high-quality uniform few-layer MoTe<sub>2</sub>. *J. Am. Chem. Soc.* **137**, 11892–11895 (2015).
- Colombo, L., Wallace, R. M. & Ruoff, R. S. Graphene growth and device integration. *Proc. IEEE* **101**, 1536–1556 (2013).
- Lee, B. et al. Characteristics of high-*k* Al<sub>2</sub>O<sub>3</sub> dielectric using ozone-based atomic layer deposition for dual-gated graphene devices. *Appl. Phys. Lett.* **97**, 043107 (2010).
- Williams, J., DiCarlo, L. & Marcus, C. Quantum Hall effect in a gate-controlled pn junction of graphene. *Science* **317**, 638–641 (2007).
- Wang, X., Tabakman, S. M. & Dai, H. Atomic layer deposition of metal oxides on pristine and functionalized graphene. *J. Am. Chem. Soc.* **130**, 8152–8153 (2008).
- Zheng, L. et al. Improvement of Al<sub>2</sub>O<sub>3</sub> films on graphene grown by atomic layer deposition with pre-H<sub>2</sub>O treatment. *ACS Appl. Mater. Inter.* **6**, 7014–7019 (2014).
- Zhu, W., Neumayer, D., Perebeinos, V. & Avouris, P. Silicon nitride gate dielectrics and band gap engineering in graphene layers. *Nano Lett.* **10**, 3572–3576 (2010).
- Kleinert, M. et al. Graphene-based electro-absorption modulator integrated in a passive polymer waveguide platform. *Opt. Mater. Express* **6**, 1800–1807 (2016).
- Ling, X., Wang, H., Huang, S., Xia, F. & Dresselhaus, M. S. The renaissance of black phosphorus. *Proc. Natl Acad. Sci. USA* **112**, 4523–4530 (2015).
- Eggleton, B. J., Luther-Davies, B. & Richardson, K. Chalcogenide photonics. *Nat. Photon.* **5**, 141–148 (2011).
- Taeed, V. G. et al. Ultrafast all-optical chalcogenide glass photonic circuits. *Opt. Express* **15**, 9205–9221 (2007).
- Hu, J. et al. Fabrication and testing of planar chalcogenide waveguide integrated microfluidic sensor. *Opt. Express* **15**, 2307–2314 (2007).
- Childres, I., Jauregui, L. A., Park, W., Cao, H. & Chen, Y. P. in *New Developments in Photon and Materials Research* (ed. Jang, J. I.) Ch. 19 (Nova Science, New York, 2013).
- Yang, M., Feng, Y. & Wang, S. in *Graphene Science Handbook: Electrical and Optical Properties* (ed. Aliofkhaezai, M. et al.) 15–24 (CRC Press, Boca Raton, 2016).
- Zou, Y. et al. Solution processing and resist-free nanoimprint fabrication of thin film chalcogenide glass devices: inorganic–organic hybrid photonic integration. *Adv. Opt. Mater.* **2**, 759–764 (2014).
- Kwon, M.-S. Discussion of the epsilon-near-zero effect of graphene in a horizontal slot waveguide. *IEEE Photon. J.* **6**, 6100309 (2014).
- Quan, Q., Deotare, P. B. & Loncar, M. Photonic crystal nanobeam cavity strongly coupled to the feeding waveguide. *Appl. Phys. Lett.* **96**, 203102 (2010).
- Yu, L., Yin, Y., Shi, Y., Dai, D. & He, S. Thermally tunable silicon photonic microdisk resonator with transparent graphene nanoheaters. *Optica* **3**, 159–166 (2016).
- Watts, M. R. et al. Adiabatic thermo-optic Mach–Zehnder switch. *Opt. Lett.* **38**, 733–735 (2013).
- Urich, A., Unterrainer, K. & Mueller, T. Intrinsic response time of graphene photodetectors. *Nano Lett.* **11**, 2804–2808 (2011).
- Graham, M. W., Shi, S. F., Ralph, D. C., Park, J. & McEuen, P. L. Photocurrent measurements of supercollision cooling in graphene. *Nat. Phys.* **9**, 103–108 (2013).
- Chen, J. H. et al. Charged-impurity scattering in graphene. *Nat. Phys.* **4**, 377–381 (2008).
- Wang, X., Cheng, Z., Xu, K., Tsang, H. K. & Xu, J.-B. High-responsivity graphene/silicon-heterostructure waveguide photodetectors. *Nat. Photon.* **7**, 888–891 (2013).
- Shiue, R.-J. et al. High-responsivity graphene–boron nitride photodetector and autocorrelator in a silicon photonic integrated circuit. *Nano Lett.* **15**, 7288–7293 (2015).
- Wang, J. et al. High-responsivity graphene-on-silicon slot waveguide photodetectors. *Nanoscale* **8**, 13206–13211 (2016).
- Goniszewski, S. et al. Correlation of p-doping in CVD graphene with substrate surface charges. *Sci. Rep.* **6**, 22858 (2016).
- Li, L. et al. Integrated flexible chalcogenide glass photonic devices. *Nat. Photon.* **8**, 643–649 (2014).
- Zou, Y. et al. High-performance, high-index-contrast chalcogenide glass photonics on silicon and unconventional non-planar substrates. *Adv. Opt. Mater.* **2**, 478–486 (2014).
- Mohsin, M. et al. Graphene based low insertion loss electro-absorption modulator on SOI waveguide. *Opt. Express* **22**, 15292–15297 (2014).
- Ye, C., Khan, S., Li, Z. R., Simsek, E. & Sorger, V. J.  $\lambda$ -size ITO and graphene-based electro-optic modulators on SOI. *IEEE J. Sel. Top. Quant.* **20**, 40–49 (2014).
- Phare, C. T., Lee, Y.-H. D., Cardenas, J. & Lipson, M. Graphene electro-optic modulator with 30 GHz bandwidth. *Nat. Photon.* **9**, 511–514 (2015).
- Dalir, H., Xia, Y., Wang, Y. & Zhang, X. Athermal broadband graphene optical modulator with 35 GHz speed. *ACS Photon.* **3**, 1564–1568 (2016).
- Yao, Y. et al. Electrically tunable metasurface perfect absorbers for ultrathin mid-infrared optical modulators. *Nano Lett.* **14**, 6526–6532 (2014).
- Emani, N. K. et al. Electrical modulation of Fano resonance in plasmonic nanostructures using graphene. *Nano Lett.* **14**, 78–82 (2013).
- Gao, W. et al. Excitation and active control of propagating surface plasmon polaritons in graphene. *Nano Lett.* **13**, 3698–3702 (2013).
- Liu, M., Yin, X. & Zhang, X. Double-layer graphene optical modulator. *Nano Lett.* **12**, 1482–1485 (2012).

## Acknowledgements

The authors thank L.C. Kimerling and A. Agarwal for providing access to device measurement facilities, Q. Du, P.-c. Shen, W.S. Leong, J. Michon and Y. Zou for assistance with device processing and characterization and M. Mondol for technical support with electron-beam lithography. Funding support is provided by the National Science Foundation under award nos. 1453218, 1506605 and 1509197. This material is based upon work supported by the National Science Foundation Graduate Research Fellowship under grant no. 1122374. R.-J.S. and D.E. gratefully acknowledge funding support by the the Center for Excitronics, an Energy Frontier Research Center funded by the US Department of Energy, Office of Science, Office of Basic Energy Sciences under award no. DE-SC0001088. C.-C.H. and D.H. were funded in part through the Future Photonics Manufacturing Hub (EPSRC EP/N00762X/1). The authors also acknowledge fabrication facility support by the MIT Microsystems Technology Laboratories and the Harvard University Center for Nanoscale Systems, the latter of which is supported by the National Science Foundation under award no. 0335765.

## Author contributions

H.L. conceived the device designs and carried out device fabrication and testing. Y.S. prepared and characterized the 2D materials. Y.H. characterized the polarizer and thermo-optic switch devices. D.K. constructed the mid-infrared testing system and measured the

detector and modulator devices. S.D.-J. prepared the black phosphorus and InSe samples and performed Raman and passivation tests. K.W. performed numerical modelling of the thermo-optic switch. J.L. and H.Z. deposited the ChG films. S.D.-J., L.L. and Z.L. contributed to device characterization. S.N. and A.Y. synthesized the ChG materials. H.W. and C.-C.H. assisted with 2D material preparation. R.-J.S. assisted in detector design and performed detector device modelling. J.H., T.G., J.K., K.R., D.E. and D.H. supervised and coordinated the research. All authors contributed to technical discussions and writing the paper.

## Competing interests

The authors declare no competing financial interests.

## Additional information

**Supplementary information** is available for this paper at <https://doi.org/10.1038/s41566-017-0033-z>

**Reprints and permissions information** is available at [www.nature.com/reprints](http://www.nature.com/reprints).

**Correspondence and requests for materials** should be addressed to H.L. or J.H.

**Publisher's note:** Springer Nature remains neutral with regard to jurisdictional claims in published maps and institutional affiliations.

## Methods

**Device fabrication.** Device fabrication was performed at the MIT Microsystems Technology Laboratories and the Harvard Center for Nanoscale Systems. For the mid-infrared detector and modulator, the starting substrate was a silicon wafer coated with 3  $\mu\text{m}$  thermal oxide (Silicon Quest International), whereas for the polarizer and the thermo-optic switch an additional  $\text{Ge}_{23}\text{Sb}_7\text{S}_{70}$  layer was deposited onto the wafer before graphene transfer. Monolayer graphene grown using CVD on Cu foils was then transferred onto the substrate following the standard poly(methyl-methacrylate) (PMMA)-based wet transfer process<sup>51</sup>. In all cases, the substrate has a planar surface finish, ensuring a high transfer yield. The graphene layer was subsequently patterned using electron-beam lithography on an Elionix ELS-F125 electron-beam lithography system followed by oxygen plasma etching. Ti/Au (10/50 nm) contact metals were electron-beam evaporated and patterned using PMMA as the liftoff resist. A  $\text{Ge}_{23}\text{Sb}_7\text{S}_{70}$  glass film was then deposited via thermal evaporation using a custom-designed system (PVD Products)<sup>26,52</sup>. Small flakes of  $\text{Ge}_{23}\text{Sb}_7\text{S}_{70}$  crushed from bulk glass rods prepared using the standard melt quenching technique were used as the evaporation source material<sup>53</sup>. The deposition rate was monitored in real time using a quartz crystal microbalance and was stabilized at 20  $\text{\AA s}^{-1}$ . The substrate was not actively cooled although the substrate temperature was maintained below 40  $^{\circ}\text{C}$  throughout the deposition as measured by a thermocouple. The  $\text{Ge}_{23}\text{Sb}_7\text{S}_{70}$  devices were defined using fluorine-based plasma etching (detailed etching protocols are discussed elsewhere<sup>24</sup>). If needed, the graphene transfer and glass deposition process can be repeated multiple times to create complex multilayer geometries.

**Device characterization.** The on-chip polarizers were tested using a fibre end-fire coupling scheme and the characterization set-up and protocols are described in detail in Supplementary Section VI. The thermo-optic switch devices were measured on a home-built grating coupling system used in conjunction with an

external cavity tunable laser (Luna Technologies) with a built-in optical vector analyser. Laser light was coupled into and out of the devices using single-fibre probes. The d.c. electrical power was supplied and monitored by a Keithley 2401 Source Measure Unit (SMU). For the dynamic test, the a.c. electrical power was provided by a Keysight 33521A function generator while the optical output was recorded on an oscilloscope. The mid-infrared detector and modulator devices were interrogated using a tunable  $\text{Cr}^{2+}:\text{ZnS}/\text{Se}$  mid-infrared laser covering wavelengths of 2.0–2.55  $\mu\text{m}$  (IPG Photonics). The mid-infrared laser waveguide coupling and real-time wavelength monitoring system is similar to that described in an earlier publication<sup>55</sup> and is illustrated in Supplementary Section XVII.

**Data availability.** The data that support the plots within this paper and other findings of this study are available from the corresponding authors on reasonable request.

## References

- Hong, J. Y. et al. A rational strategy for graphene transfer on substrates with rough features. *Adv. Mater.* **28**, 2382–2392 (2016).
- Musgraves, J. et al. Comparison of the optical, thermal and structural properties of Ge–Sb–S thin films deposited using thermal evaporation and pulsed laser deposition techniques. *Acta Materialia* **59**, 5032–5039 (2011).
- Petit, L. et al. Compositional dependence of the nonlinear refractive index of new germanium-based chalcogenide glasses. *J. Solid State Chem.* **182**, 2756–2761 (2009).
- Du, Q. et al. Low-loss photonic device in Ge–Sb–S chalcogenide glass. *Opt. Lett.* **41**, 3090–3093 (2016).
- Han, Z. et al. On-chip chalcogenide glass waveguide-integrated mid-infrared PbTe detectors. *Appl. Phys. Lett.* **109**, 071111 (2016).





重慶大學

近十年《Cell》《Nature》《Science》及子刊  
论文汇编

2018年



科学技术发展研究院

地址：重庆市沙坪坝区沙正街174号

电话：023-65102303

邮编：400044

前沿交叉学科研究院

地址：重庆市沙坪坝区沙正街174号

电话：023-65103065

邮编：400044